Journal of Oncology

Pharmacological Targeting DNA Repair and Replication, PARP Inhibitors and Beyond

Lead Guest Editor: Guo Chen
Guest Editors: Fu Wang and Xue Gao

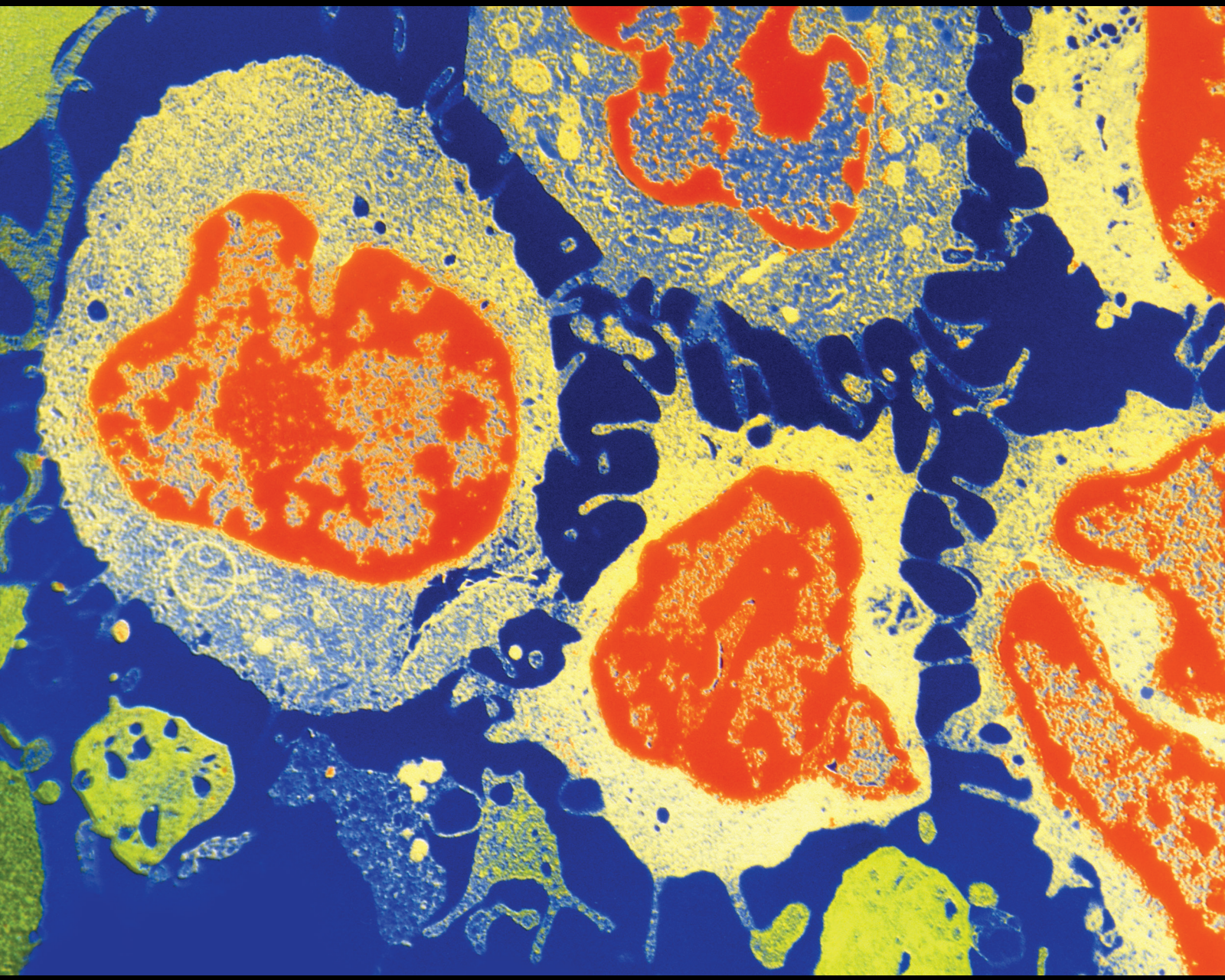

Pharmacological Targeting DNA Repair and Replication, PARP Inhibitors and Beyond

Journal of Oncology

Pharmacological Targeting DNA Repair and Replication, PARP Inhibitors and Beyond

Lead Guest Editor: Guo Chen
Guest Editors: Fu Wang and Xue Gao

Contents

Contents

Contents

Hindawi
Journal of Oncology
Volume 2022, Article ID 8890434, 8 pages
https://doi.org/10.1155/2022/8890434

Research Article

Bone Mesenchymal Stem Cell-Derived Exosome-Enclosed miR-181a Induces $CD4^+CD25^+FOXP3^+$ Regulatory T Cells via SIRT1/Acetylation-Mediated FOXP3 Stabilization

Renyong Wang,[1] **Ruixue Li**,[1] **Tiehan Li**,[1] **Lei Zhu**,[1] **Zongze Qi**,[2] **Xiaokui Yang**,[1] **Huan Wang**,[1] **Baoquan Cao**,[1] **and Hong Zhu**[1]

[1]*First Department of Hepatobiliary and Pancreatic Surgery, The Second Affiliated Hospital of Kunming Medical University, Kunming, China*
[2]*Department of General Surgery, The First People's Hospital of Xundian Hui and Yi Autonomous County, Kunming, China*

Correspondence should be addressed to Hong Zhu; zhhong519@163.com

Received 11 January 2022; Revised 22 March 2022; Accepted 24 March 2022; Published 26 May 2022

Academic Editor: Fu Wang

Bone marrow mesenchymal stem cells (BMSCs) have been identified as a potential therapeutic approach to immune-related diseases. Here, we show that BMSC-derived exosomes promote FOXP3 expression and induce the conversion of $CD4^+$ T cells into $CD4^+CD25^+FOXP3^+$ Treg cells, which is significant for immunosuppressive activity. We found that miR-181a-5p is upregulated in BMSC-derived exosomes and can be transferred to $CD4^+$ T cells. In $CD4^+$ cells, miR-181a directly targets SIRT1 and suppresses its expression. Moreover, downregulated SIRT1 enhances FOXP3 via protein acetylation. In conclusion, our data demonstrated that BMSC-derived exosomal miR-181a is critical in the maintenance of immune tolerance. Furthermore, our results reveal that BMSC-derived exosomal miR-181a induces the production of $CD4^+CD25^+FOXP3^+$ Treg cells via SIRT1/acetylation/FOXP3.

1. Introduction

Pancreas transplantation is widely used for treating diabetes mellitus [1, 2]. However, recurrent autoimmunity and conventional allograft rejection are significant obstacles to pancreas transplantation [1, 2]. Learned tolerance is a hallmark of the immune system, and the induction of immune tolerance is considered a promising way to improve the success of pancreas transplantation [3, 4].

MSCs are multipotent stromal cells that play a significant role in the immune response via immune suppression [5]. Zhang et al. showed the role of MSC-mediated immunosuppression in immune thrombocytopenia [6]. Mounayar et al. suggested that PI3kα and STAT1 modulate immunosuppressive activity by MSCs [7]. Exosomes are a type of membrane microvesicles approximately 40–150 nm in diameter [8] that are involved in Treg cell development [8, 9] and can mediate cellular communication by carrying miRNAs to neighboring cells [10]. Research suggests that stem cell-derived exosomes could be a new strategy for the treatment of neurodegenerative diseases [11]. In addition, accumulating evidence indicates that MSC-derived exosomal miRNAs are critical for immunosuppression regulation. Du et al. showed that MSC-derived cells promote immunosuppression of regulatory T cells in asthma [12]. Shahir et al. indicated that MSC-derived exosomes could induce mouse tolerogenic dendritic cells [13]. Moreover, MSC-derived exosomal miRNAs function in immunosuppression [14]. MSC-derived exosomes can transfer microRNAs (miRNAs) to receptors, subsequently affecting immune homeostasis [15–17].

Moreover, previous studies found that MSCs seem to play a significant role in inducing FOXP3-expressing Treg cells [18, 19]. Forkhead box protein 3 (FOXP3)-expressing $CD4^+CD25^+$ Treg cells are critical for immune tolerance maintenance, for example, Nemo-like kinase-enhanced

FOXP3 participates in Treg cell-mediated immune tolerance [20]. FOXP3$^+$ Treg cells promote transplantation tolerance via neuropilin-1 [21]. POH1 contributes to immune tolerance by maintaining FOXP3$^+$ Treg cells [22]. Increasing evidence suggests that the maintenance of FOXP3 expression is critical for Treg cell development and function. Jang et al. indicated that Hhex suppresses Treg cells by inhibiting FOXP3 [23]. Chen demonstrated that dysregulation of FOXP3 by hypermethylation impairs the function of Treg cells [24]. FOXP3 also plays a central role in immune tolerance; thus, stabilization of FOXP3 expression may provide an acceptable way to maintain immune tolerance and improve the success of pancreas transplantation [25]. Researchers have demonstrated that FOXP3 expression and activity could be controlled by posttranslational modifications. Moreover, posttranslational modifications of FOXP3 contribute to Treg cell function [26]. Kagoya et al. indicated that arginine methylation of FOXP3 plays a crucial role in the suppressive activity of Treg cells [27]. Lin et al. suggested that kaempferol promotes the suppressive function of Treg cells by inhibiting PIMI-mediated FOXP3 phosphorylation [28]. In addition, the deacetylation of FOXP3 by sirtuin 1 (SIRT1) also functions in Treg cell regulation [29–31]. It was reported that acetylation of FOXP3 modulates the suppressive function of CD4$^+$CD25$^+$ FOXP3$^+$ Treg cells [29, 30]. Zhang et al. showed that miR-23a-3p-mediated FOXP3 acetylation could induce Treg function [32]. In abdominal aortic aneurysm (AAA), SIRT1-regulated acetylation of FOXP3 modulates Treg function [30]. Forkhead box protein 3 (FOXP3)-expressing CD4$^+$CD25$^+$ Treg cells play an essential role in immune tolerance maintenance [33]. Sustained FOXP3 expression is the most specific marker for characterizing CD4$^+$CD25$^+$FOXP3$^+$ Treg cells [23, 34]. Therefore, the regulation of FOXP3 may provide a potential method for immunosuppression. Epigenetic regulation, such as acetylation and methylation, of FOXP3 has been well studied [35].

In this study, we uncovered the underlying mechanism by which BMSC-derived exosomal miR-181a induces CD4$^+$CD25$^+$FOXP3$^+$ Treg cells via SIRT1/acetylation/FOXP3, providing a potential way to improve the success of pancreas transplantation.

2. Materials and Methods

2.1. Cell Culture. BMSCs were purchased from Cyagen Biosciences (MUBMX-01001). Then, the cells were cultured in Mouse Mesenchymal Stem Cell Growth Medium (MUCMX-90011, Cyagen Biosciences) and cultured at 37°C and 5% CO_2. CD34 and CD44 surface markers were used for BMSC analysis.

2.2. BMSC-Exosome Isolation and Identification. When the density of BMSCs reached approximately 80%, the culture medium was discarded, and serum-free medium for BMSCs was added. After culturing for 24 h, the supernatant was aspirated into a 50 ml centrifuge tube and subjected to gradient centrifugation (300 g, 10 min; 2000 g, 10 min; 10000 g, 30 min) at 4°C. The supernatant was transferred to an exosome extraction ultracentrifuge tube and subjected to centrifugation (100000 g, 70 min). The supernatant was discarded, and the sediment was washed with PBS and subjected to centrifugation (100000 g, 70 min). The exosomes were resuspended in 150 μl PBS and identified with transmission electron microscopy as described previously [36].

2.3. CD4$^+$ T Cell Isolation and Purification. CD4$^+$ T cells from the spleen were isolated using magnetic activated cell sorting (MACS). Briefly, a spleen cell suspension was obtained by grinding the tissue. After lysis, the cells were resuspended in PBE buffer. Anti-CD4 magnetic beads (Miltenyi) were used to isolate CD4$^+$ T cells following the manufacturer's protocol.

2.4. Flow Cytometry. Flow cytometry analysis was performed to determine the percentage of Treg cells in CD4$^+$ T cells. Treg cells were measured by flow cytometry with FOXP3$^+$ as the marker. Briefly, the cells were first stained with anti-CD4-FITC (ab218745, Abcam), anti-CD25-PE (ab210334, Abcam), and anti-FOXP3-APC (ab200568, Abcam) antibodies. Fluorescence signals were measured by a FACS Fortessa system (BD).

2.5. Cell Transfection. Cells were transfected with miR-181a inhibitor (5′-ACUCACCGACAGCGUUGAAUGUU-3′) and miR-181a NC (5′-CAGUACUUUUGUGUAGUACAA-3′) using Lipofectamine 2000 reagent (Invitrogen) according to the manufacturer's instructions.

2.6. Reverse Transcription-Quantitative (RT-q) PCR Analysis. RT-qPCR was used to examine the expression of miR-181a. Total RNA was isolated using TRIzol reagent (R0016, Beyotime), and 1 μg RNA was used as a template for cDNA synthesis using SuperScript III RT (18080093, Invitrogen). The primers used in this study were as follows: miR-181a-5p forward primer: 5′-CGGCAACATTCAACGCTGT-3′ and reverse primer: 5′-GTGCAGGGTCCGAGGTATTC-3′; U6 forward primer: 5′-CTTCGGCAGCACATATAC-3′ and reverse primer: 5′-GAACGCTTCACGAATTTGC-3′. RT-qPCR was performed at 95°C for 3 min, 95°C for 5 s, 56°C for 10 s, 75°C for 25 s (39 cycles), 65°C for 5 s, and 95°C for 50 s.

2.7. Western Blotting. Total proteins were extracted by RIPA lysis buffer (Beyotime, P0013B), and the concentration of the proteins was measured by a BCA kit (Beyotime, P0012). Equal amounts of protein lysates were loaded on a sodium dodecyl sulfonate-polyacrylamide gel (SDS–PAGE) and transferred to a polyvinylidene fluoride membrane. The membrane was blocked with 5% nonfat milk and incubated with antibodies at 4°C overnight. The primary antibodies used were as follows: anti-CD81 (1 : 1000, Cell Signaling Technology, 56039), anti-CD63 (1 : 1000, Abcam, ab68418), anti-CD9 (1 : 1000, Abcam, ab223052), anti-SIRT1 (1 : 1000,

Abcam, ab263965), and anti-FOXP3 (1 : 2000, Abcam, ab10901). GAPDH was used as a loading control. Then, a horseradish peroxidase (HRP)-labeled secondary antibody was used to detect the specific protein bands.

2.8. Immunoprecipitation. The acetylation of FOXP3 was detected using an IP kit (Absin, abs955-50 tests) according to the manufacturer's instructions. Briefly, the collected cells were washed with PBS and lysed with IP lysis buffer on ice for 5 min. Cells were scraped from the plate and transferred to a microcentrifuge tube. After ultrasonic disruption 3 times, the cells were subjected to centrifugation (14,000 g, 10 min) at 4°C, and the supernatant (cell lysate) was transferred to a new tube. Cell lysates (200–1000 μg total protein) were mixed with anti-FOXP3 antibody. After overnight incubation at 4°C, the protein A/G plus agarose was added to the sample and incubated on a rotator at 4°C for 2 hours. The mixture was centrifuged at 12,000 g for 1 minute to retain the precipitate, and it was washed with wash buffer. The acetylation of FOXP3 was determined by Western blotting with antiacetylated-lysine antibody (Cell Signaling Technology, 9941) and anti-FOXP3 antibody (Abcam, ab10901).

2.9. Luciferase Reporter Assay. The wild (WT) or mutant (MUT) type of the 3′-UTR of SIRT1 was inserted into the pGL3 promoter vector (Promega, E1761). SIRT1 WT or SIRT1 MUT and miR-181a control or miR-181a mimic were transfected into HEK-293T cells (Procell, CL-0005). The luciferase activities were measured by the Dual-Luciferase Reporter Assay System.

2.10. Statistical Analysis. All of the data are presented as the mean ± SD as indicated for at least three independent experiments and were tested with Student's *t*-test for between-group differences. $P < 0.05$ was considered statistically significant.

3. Results

3.1. Characterization of BMSCs and BMSC-Derived Exosomes. We first identified BMSCs by detecting the CD34 and CD44 surface markers of the cells (Figure 1(a)). Exosomes derived from MSCs were identified with transmission electron microscopy (Figure 1(b)). Western blotting results indicated that the exosome markers CD9, CD63, and CD81 in the exosomes were significantly higher than those in the BMSC lysate (Figure 1(c)).

3.2. miR-181a Is Highly Expressed in BMSC-Derived Exosomes. To determine the expression of miR-181a in the BMSC-derived exosomes, we first performed RT-qPCR to detect miR-181a expression in the BMSC-derived exosomes and BMSC lysates. As shown in Figure 2(a), the expression of miR-181a was upregulated in the BMSC-derived exosomes. In addition, after coculturing with the BMSC-derived exosomes, miR-181a expression was increased in the $CD4^+$ cells (Figure 2(b)).

3.3. BMSC-Derived Exosome miR-181a Treatment Triggers the Conversion of Effector T Cells into FOXP3$^+$ Expressing Tregs. We next determined the role of MSC-derived exosome miR-181a (BMSC-exo-miR-181a) in the stimulation of $CD4^+CD25^+FOXP3^+$ Treg cells. $CD4^+$ cells were treated with BMSC-exo-miR-181a, and the frequency of $CD4^+CD25^+FOXP3^+$ Treg cells was analyzed by flow cytometry. As shown in Figure 3(a), the frequency of $CD4^+CD25^+FOXP3^+$ Treg cells in the BMSC-exo-miR-181a treated group was higher than that in the BMSC lysate treated group.

We next knocked down miR-181a by miR-181a inhibitor transfection into BMSCs and isolated exosomes from the knockdown BMSCs. The expression of miR-181a in exosomes derived from miR-181a inhibitor-transfected BMSCs was measured (Figure 3(b)). After inhibition of miR-181a, the exosomes no longer increased the frequency of $CD4^+CD25^+FOXP3^+$ Treg cells (Figure 3(c)). These results revealed the function of BMSC-exo-miR-181a in maintaining $CD4^+CD25^+FOXP3^+$ Treg cells.

3.4. BMSC-Derived Exosomal miR-181a Regulates FOXP3 via SIRT1-Mediated Acetylation. miRNAs were previously reported to modulate target genes by binding to their 3′UTRs. Based on bioinformatics analysis, miR-181a could directly target a deacetylase, SIRT1 (Figure 4(a)). According to the dual-luciferase reporter assay, there was a relationship between miR-181a and SIRT1 (Figure 4(b)). After BMSC-exo-miR-181a treatment, the expression of SIRT1 in $CD4^+$ cells decreased (Figure 4(c)). Inhibition of miR-181a rescued SIRT1 expression (Figure 4(d)).

Accumulating evidence has demonstrated that SIRT1 modulates FOXP3 expression via protein deacetylation. Here, we detected FOXP3 and acetylation levels in $CD4^+$ cells treated with BMSC-exo-miR-181a. BMSC-exo-miR-181a promoted FOXP3 and acetylation (Figures 4(c) and 4(e)). The suppression of miR-181a decreased FOXP3 and acetylation levels (Figures 4(d) and 4(f)).

4. Discussion

Here, we demonstrate the effect of exosomes derived from bone marrow mesenchymal stem cells (BMSCs) on immunosuppressive regulation. Our results indicate that BMSC-derived exosomes can induce the transformation of $CD4^+$ T cells into $CD4^+CD25^+FOXP3^+$ Treg cells. $CD4^+CD25^+FOXP3^+$Treg cells play a key role in the aggressiveness of diseases and cancers by regulating the immune response. In recent years, with advances in research, the regulatory mechanism of $CD4^+CD25^+Foxp3^+$Treg cells in the process of controlling autoimmunity and maintaining immune tolerance has been gradually understood [37, 38].

In our study, it was demonstrated that miR-181A was highly expressed in BMSC-derived exosomes, and miR-181A, miR-181b, miR-181c, and miR-181D jointly formed

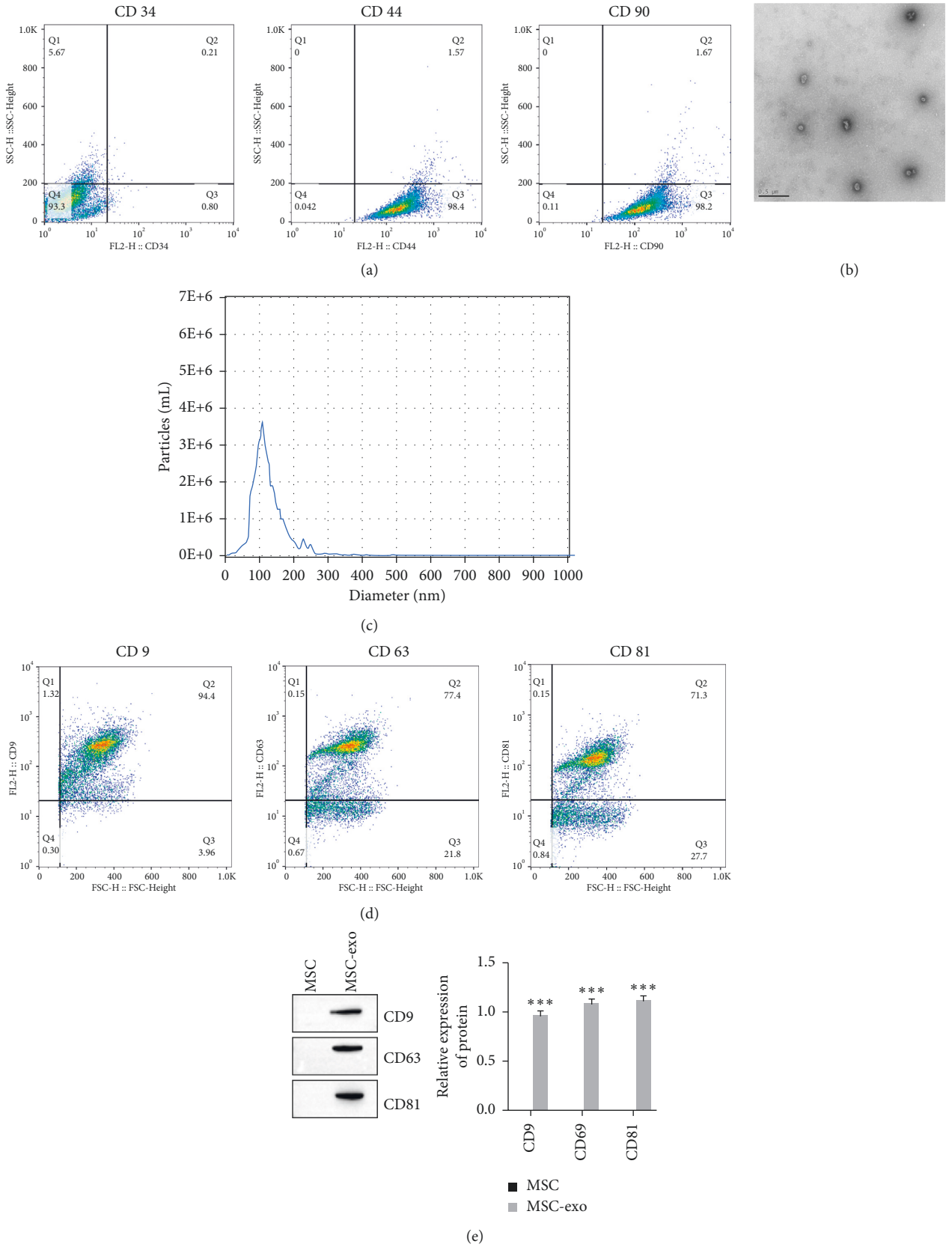

Figure 1: Characterization of BMSC and BMSC-derived exosomes. (a) CD34, CD44, and CD90 surface markers of the cells measured by flow cytometry. (b) Exosomes isolated from BMSCs detected by transmission electron microscopy. (c) Exosome diameter measured by dynamic light scattering (DLS). (d) Expression of exosome markers detected by flow cytometry. (e) Expression of exosome markers detected by Western blot.

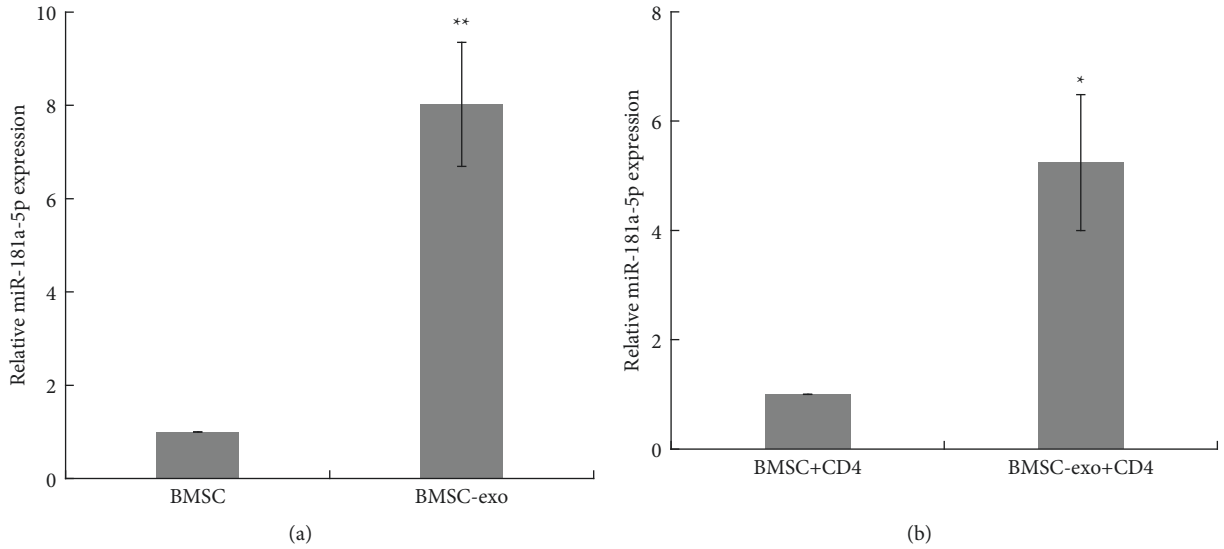

Figure 2: miR-181a is highly expressed in BMSC-derived exosomes. (a) Expression of miR-181a in BMSC-derived exosomes measured by RT-qPCR assay. $^{**}P < 0.01$. (b) Expression of miR-181a in $CD4^+$ T cells treated with BMSC-derived exosomes measured by RT-qPCR assay. $^{*}P < 0.05$. Data are the mean ± SD ($n = 3$ biological replicates).

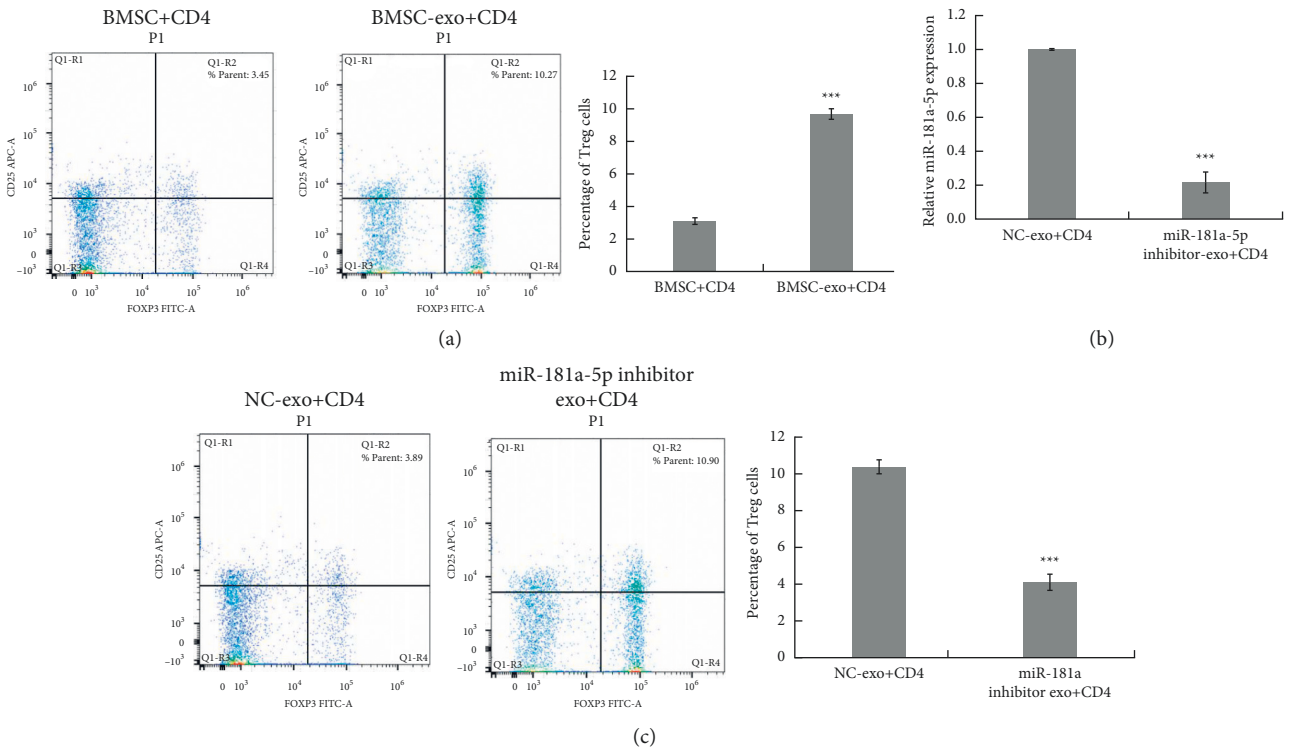

Figure 3: BMSC-derived exosome miR-181a treatment triggers the conversion of effector T cells into $FOXP3^+$-expressing Tregs. (a) The frequency of $CD4^+CD25^+FOXP3^+$ Treg cells in $CD4^+$ T cells cocultured with BMSC-derived exosomes analyzed by flow cytometry. $^{***}P < 0.001$. (b) miR-181a expression in $CD4^+$ T cells treated with NC or miR-181a inhibitor-transfected BMSC-derived exosomes measured by RT-qPCR assay. $^{***}P < 0.001$. (c) The frequency of $CD4^+CD25^+FOXP3^+$ Treg cells in $CD4^+$ T cells treated with NC or miR-181a inhibitor-transfected BMSC-derived exosomes analyzed by flow cytometry. $^{***}P < 0.001$. Data are the mean ± SD ($n = 3$ biological replicates).

the miR-181 family, which is one of the most abundant miRNAs in lymphatic tissues [39]. mir-181a plays an important role in B cell development in bone marrow [40, 41] and immune function [42]. We found that miR-181A can be internalized by $CD4^+$ cells and that miR-181A in $CD4^+$ cells directly target SIRT1. SIRT1 is a protein deacetylase that

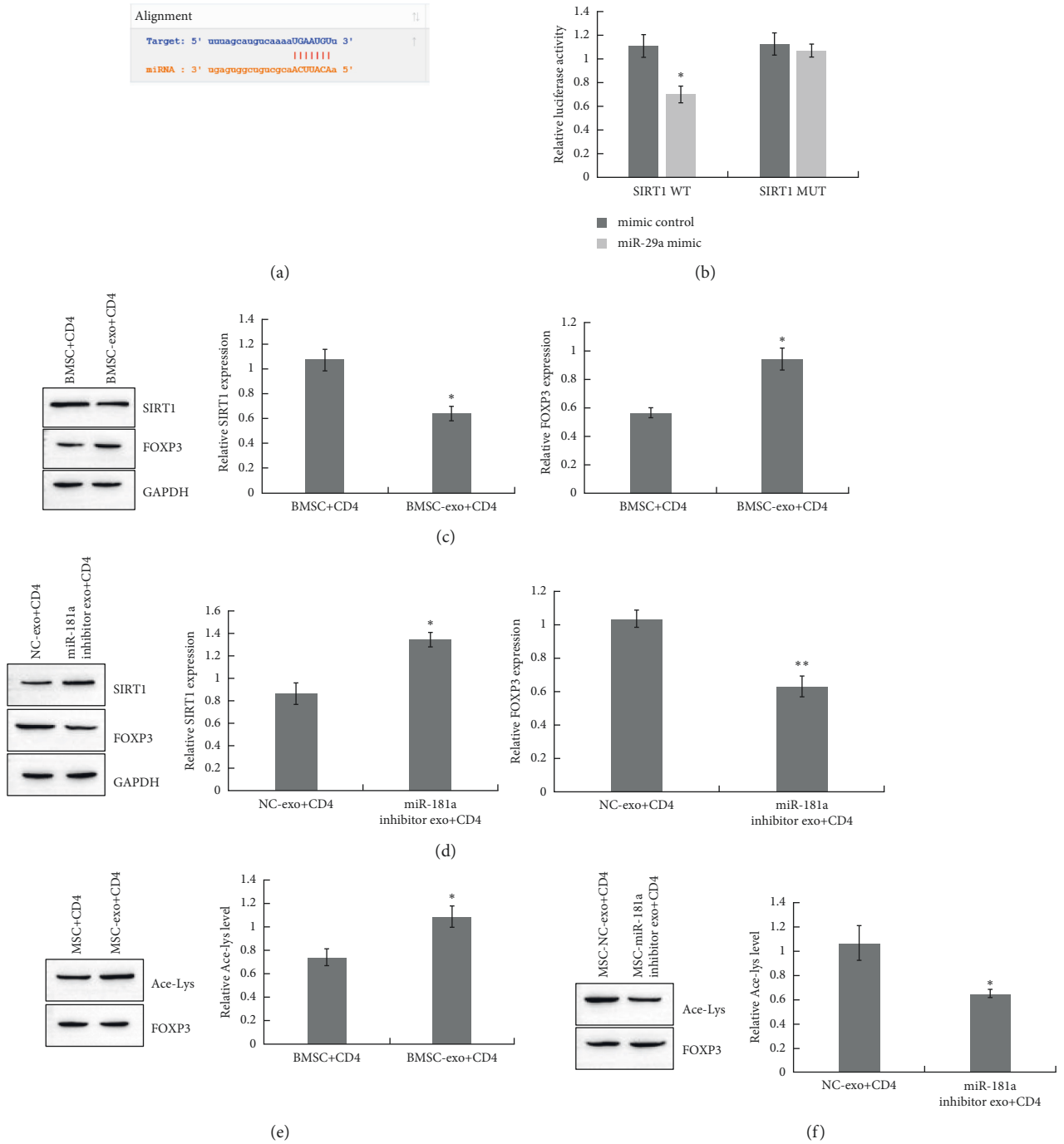

Figure 4: BMSC-derived exosomal miR-181a regulates FOXP3 via SIRT1-mediated acetylation. (a) The binding site of miR-181a and SIRT1 predicted by StarBase. (b) The interaction of SIRT1 and miR-181a determined by a dual-luciferase reporter assay. $^*P < 0.05$. (c) Expression of SIRT1 and FOXP3 in $CD4^+$ T cells treated with BMSC-derived exosomes detected by Western blot. $^*P < 0.05$. (d) Expression of SIRT1 and FOXP3 in $CD4^+$ T cells transfected with NC or miR-181a inhibitor BMSC-derived exosomes detected by Western blot. $^*P < 0.05$. (e) FOXP3 acetylation in $CD4^+$ T cells treated with BMSC-derived exosomes detected by immunoprecipitation. $^*P < 0.05$. (f) FOXP3 acetylation in $CD4^+$ T cells with $CD4^+$ T cells transfected with NC or miR-181a inhibitor and BMSC-derived exosomes detected by immunoprecipitation. $^*P < 0.05$. Data are the mean ± SD ($n = 3$ biological replicates).

regulates protein expression through deacetylation. miRNA and host cell protein expression are important regulatory mechanisms. Studies have shown that HCV impairs the T cell response through miR-181a-mediated DUSP6 expression [43]. miR-181A not only regulates T cell response-related proteins but also balances immune-mediated virus clearance with inflammatory damage and enhances immune tolerance [44]. This study demonstrated that miR-181A has a targeted relationship with SIRT1, a deacetylase that regulates protein expression. In future

studies, the proteins related to miR-181A that have roles in the process of immune tolerance can be further studied, and the related mechanisms can be explored. Our results suggest that the suppression of SIRT1 enhances FOXP3 activity by increasing acetylation levels. In addition, our results suggest that BMSC-derived exosomes trigger $CD4^+CD25^+FOXP3^+$Treg cells through mir-181A/SIRT1-mediated FOXP3 acetylation.

Collectively, our data show that exosomes from bone marrow mesenchymal stem cells (BMSCs) induce the transformation of $CD4^+$ T cells into $CD4^+CD25^+FOXP3^+$ Treg cells. miR-181a is preferentially expressed in exosomes derived from bone marrow mesenchymal stem cells and can be transferred to $CD4^+$ T cells. miR-181a directly targets SIRT1 in $CD4^+$ T cells and reduces SIRT1 expression. Inhibition of SIRT1 enhances FOXP3 expression by promoting acetylation of FOXP3. We found that bmSC-derived exosomes carrying miR-181A induced the production of $CD4^+CD25^+FOXP3^+$ Treg cells by regulating FOXP3 expression. In addition, we revealed the mechanism by which exosomal miR-181A enhances FOXP3 expression through sirT1-catalyzed acetylation. A limitation of this study is that we did not verify this mechanism in vivo.

Data Availability

The data used to support the findings of this study are included within the article.

Conflicts of Interest

The authors declare that they have no conflicts of interest.

Authors' Contributions

Renyong Wang and Ruixue Li contributed equally to the present work.

Acknowledgments

This work was supported by the National Natural Science Foundation of China (81460132) and Yunnan Packnrovincial Department of Science, Technology-Kunming Medical University Applied Basic Research Joint Special Fund Project (2018FE001 (-224)), and Yunnan Clinical Medical Center for Hepatobiliary-pancreatic Diseases.

References

[1] D. S. Tai, J. Hong, R. W. Busuttil, and G. S. Lipshutz, "Low rates of short- and long-term graft loss after kidney-pancreas transplant from a single center," *JAMA Surgery*, vol. 148, no. 4, pp. 368–373, 2013.

[2] J. L. Larsen, "Pancreas transplantation: indications and consequences," *Endocrine Reviews*, vol. 25, no. 6, pp. 919–946, 2004.

[3] Z. J. Jiang, Q. H. Shen, H. Y. Chen, Z. Yang, M. Q. Shuai, and S. Zheng, "Galectin-1 Restores Immune Tolerance to Liver Transplantation through Activation of Hepatic Stellate Cells," *Cellular Physiology and Biochemistry*, vol. 48, no. 3, pp. 863–879, 2018.

[4] H. Huang, Y. Lu, T. Zhou, G. Gu, and Q. Xia, "Innate immune cells in immune tolerance after liver transplantation," *Frontiers in Immunology*, vol. 9, p. 2401, 2018.

[5] L. Chow, V. Johnson, J. Coy, D. Regan, and S. Dow, "Mechanisms of immune suppression utilized by canine adipose and bone marrow-derived mesenchymal stem cells," *Stem Cells and Development*, vol. 26, no. 5, pp. 374–389, 2017.

[6] J. M. Zhang, F. Feng, Q. Wang et al., "Platelet-derived Growth factor-BB protects mesenchymal stem cells (MSCs) derived from immune thrombocytopenia patients against Apoptosis and Senescence and maintains MSC-mediated immunosuppression," *Stem Cells Translational Medicine*, vol. 5, no. 12, pp. 1631–1643, 2016.

[7] M. Mounayar, E. Kefaloyianni, B. Smith et al., "PI3kα and STAT1 interplay regulates human mesenchymal stem cell immune polarization," *Stem Cells (Dayton, Ohio)*, vol. 33, no. 6, pp. 1892–1901, 2015.

[8] Q. Zhang, L. Fu, Y. Liang et al., "Exosomes originating from MSCs stimulated with TGF-β and IFN-γ promote Treg differentiation," *Journal of Cellular Physiology*, vol. 233, no. 9, pp. 6832–6840, 2018.

[9] B. Zhang, R. W. Y. Yeo, R. C. Lai, E. W. K. Sim, K. C. Chin, and S. K. Lim, "Mesenchymal stromal cell exosome-enhanced regulatory T-cell production through an antigen-presenting cell-mediated pathway," *Cytotherapy*, vol. 20, no. 5, pp. 687–696, 2018.

[10] J. H. Lee, J. A. Kim, S. Jeong, and W. J. Rhee, "Simultaneous and multiplexed detection of exosome microRNAs using molecular beacons," *Biosensors and Bioelectronics*, vol. 86, pp. 202–210, 2016.

[11] N. Fayazi, M. Sheykhhasan, S. Soleimani Asl, and R. Najafi, "Stem cell-derived exosomes: a new strategy of neurodegenerative disease treatment," *Molecular Neurobiology*, vol. 58, 2021.

[12] Y. M. Du, Y. Zhuansun, R. Chen, L. Lin, Y. Lin, and J. Li, "Mesenchymal stem cell exosomes promote immunosuppression of regulatory T cells in asthma," *Experimental Cell Research*, vol. 363, no. 1, pp. 114–120, 2018.

[13] M. Shahir, S. Mahmoud Hashemi, A. Asadirad et al., "Effect of mesenchymal stem cell-derived exosomes on the induction of mouse tolerogenic dendritic cells," *Journal of Cellular Physiology*, vol. 235, no. 10, pp. 7043–7055, 2020.

[14] C. Harrell, N. Jovicic, V. Djonov, N. Arsenijevic, and V. Volarevic, "Mesenchymal stem cell-derived exosomes and other extracellular vesicles as new remedies in the therapy of inflammatory diseases," *Cells*, vol. 8, 2019.

[15] M. Reis, E. Mavin, L. Nicholson, K. Green, A. M. Dickinson, and Xn Wang, "Mesenchymal stromal cell-derived extracellular vesicles attenuate dendritic cell Maturation and function," *Frontiers in Immunology*, vol. 9, p. 2538, 2018.

[16] L. Kilpinen, A. Parmar, D. Greco et al., "Expansion induced microRNA changes in bone marrow mesenchymal stromal cells reveals interplay between immune regulation and cell cycle," *Aging (Albany NY)*, vol. 8, no. 11, pp. 2799–2813, 2016.

[17] Z. Bolandi, N. Mokhberian, M. Eftekhary et al., "Adipose derived mesenchymal stem cell exosomes loaded with miR-10a promote the differentiation of Th17 and Treg from naive $CD4^+$ T cell," *Life Sciences*, vol. 259, Article ID 118218, 2020.

[18] Z. X. Wang, C. Q. Wang, X. Y. Li et al., "Mesenchymal stem cells alleviate atherosclerosis by elevating number and function of $CD4^+CD25^+FOXP3^+$ regulatory T-cells and inhibiting macrophage foam cell formation," *Molecular and Cellular Biochemistry*, vol. 400, pp. 163–172, 2015.

[19] D. Darlan, D. Munir, A. Putra, and N. K. Jusuf, "MSCs-released TGFβ1 generate CD4CD25Foxp3 in T-reg cells of human SLE PBMC," *Journal of the Formosan Medical Association = Taiwan yi zhi*, vol. 120, 2020.

[20] V. Fleskens, C. M. Minutti, X. Wu et al., "Nemo-like kinase drives Foxp3 stability and is critical for maintenance of immune tolerance by regulatory T cells," *Cell Reports*, vol. 26, no. 13, pp. 3600–3612.e6, 2019.

[21] M. Campos-Mora, P. Contreras-Kallens, F. Galvez-Jiron et al., "$CD4^+Foxp3^+$T regulatory cells promote transplantation Tolerance by modulating effector $CD4^+$ T Cells in a neuropilin-1-dependent manner," *Frontiers in Immunology*, vol. 10, p. 882, 2019.

[22] Y. Liu, L. Zhang, B. Wang et al., "Requirement for POH1 in differentiation and maintenance of regulatory T cells," *Cell Death and Differentiation*, vol. 26, no. 4, pp. 751–762, 2019.

[23] S. W. Jang, S. S. Hwang, H. S. Kim et al., "Homeobox protein Hhex negatively regulates Treg cells by inhibiting Foxp3 expression and function," *Proceedings of the National Academy of Sciences of the United States of America*, vol. 116, no. 51, pp. 25790–25799, 2019.

[24] J. Chen, C. Zhan, L. Zhang et al., "The hypermethylation of Foxp3 promoter impairs the function of Treg cells in EAP," *Inflammation*, vol. 42, no. 5, pp. 1705–1718, 2019.

[25] L. Lu, J. Barbi, and F. Pan, "The regulation of immune tolerance by FOXP3," *Nature Reviews Immunology*, vol. 17, no. 11, pp. 703–717, 2017.

[26] G. Deng, X. Song, S. Fujimoto, C. A. Piccirillo, Y. Nagai, and M. I. Greene, "Foxp3 post-translational Modifications and Treg suppressive activity," *Frontiers in Immunology*, vol. 10, p. 2486, 2019.

[27] Y. Kagoya, H. Saijo, Y. Matsunaga et al., "Arginine methylation of FOXP3 is crucial for the suppressive function of regulatory T cells," *Journal of Autoimmunity*, vol. 97, pp. 10–21, 2019.

[28] F. Lin, X. Luo, A. Tsun, Z. Li, D. Li, and B. Li, "Kaempferol enhances the suppressive function of Treg cells by inhibiting FOXP3 phosphorylation," *International Immunopharmacology*, vol. 28, no. 2, pp. 859–865, 2015.

[29] X. Yang, Y. Lun, H. Jiang et al., "SIRT1-Regulated abnormal Acetylation of FOXP3 induces regulatory T-cell function Defect in hashimoto's thyroiditis," *Thyroid*, vol. 28, no. 2, pp. 246–256, 2018.

[30] H. Jiang, S. Xin, Y. Yan, Y. Lun, X. Yang, and J. Zhang, "Abnormal acetylation of FOXP3 regulated by SIRT-1 induces Treg functional deficiency in patients with abdominal aortic aneurysms," *Atherosclerosis*, vol. 271, pp. 182–192, 2018.

[31] S. Chadha, L. Wang, W. W. Hancock, and U. H. Beier, "Sirtuin-1 in immunotherapy: a Janus-headed target," *Journal of Leukocyte Biology*, vol. 106, no. 2, pp. 337–343, 2019.

[32] D. Zhang, X. Qiu, J. Li, S. Zheng, L. Li, and H. Zhao, "MiR-23a-3p-regulated abnormal acetylation of FOXP3 induces regulatory T cell function defect in Graves' disease," *Biological Chemistry*, vol. 400, no. 5, pp. 639–650, 2019.

[33] S. Tsuda, A. Nakashima, T. Shima, and S. Saito, "New paradigm in the role of regulatory T cells during pregnancy," *Frontiers in Immunology*, vol. 10, p. 573, 2019.

[34] P. Zafari, K. Yari, S. Mostafaei et al., "Analysis of Helios gene expression and Foxp3 TSDR methylation in the newly diagnosed Rheumatoid Arthritis patients," *Immunological Investigations*, vol. 47, no. 6, pp. 632–642, 2018.

[35] A. Colamatteo, F. Carbone, S. Bruzzaniti et al., "Molecular mechanisms controlling Foxp3 expression in health and autoimmunity: from epigenetic to post-translational regulation," *Frontiers in Immunology*, vol. 10, p. 3136, 2020.

[36] C. Théry, S. Amigorena, G. Raposo, and A. Clayton, "Isolation and characterization of exosomes from cell culture supernatants and biological fluids," *Current Protocols in Cell Biology*, 2006.

[37] M. Buggert, S. Nguyen, L. M. McLane et al., "Limited immune surveillance in lymphoid tissue by cytolytic CD4+ T cells during health and HIV disease," *PLoS Pathogens*, vol. 14, no. 4, Article ID e1006973, 2018.

[38] S. Ranasinghe, M. Flanders, S. Cutler et al., "HIV-specific CD4 T cell responses to different viral proteins have discordant associations with viral load and clinical outcome," *Journal of Virology*, vol. 86, no. 1, pp. 277–283, 2012.

[39] C. Kim, Z. Ye, C. M. Weyand, and J. J. Goronzy, "miR-181a-regulated pathways in T-cell differentiation and aging," *Immunity & Ageing*, vol. 18, no. 1, p. 28, 2021.

[40] C. Z. Chen, L. Li, H. F. Lodish, and D. P. Bartel, "MicroRNAs modulate hematopoietic lineage differentiation," *Science*, vol. 303, no. 5654, pp. 83–86, 2004.

[41] R. Fragoso, T. Mao, S. Wang et al., "Modulating the strength and threshold of NOTCH oncogenic signals by mir-181a-1/b-1," *PLoS Genetics*, vol. 8, no. 8, Article ID e1002855, 2012.

[42] C. X. Lim, B. Lee, O. Geiger et al., "miR-181a modulation of ERK-MAPK signaling sustains DC-SIGN expression and limits activation of monocyte-derived dendritic cells," *Cell Reports*, vol. 30, no. 11, pp. 3793–3805, 2020.

[43] G. Y. Li, Y. Zhou, R. S. Ying et al., "Hepatitis C virus-induced reduction in miR-181a impairs $CD4^+$T-cell responses through overexpression of DUSP6," *Hepatology*, vol. 61, no. 4, pp. 1163–1173, 2015.

[44] G. Li, M. Yu, W. W. Lee et al., "Decline in miR-181a expression with age impairs T cell receptor sensitivity by increasing DUSP6 activity," *Nature Medicine*, vol. 18, no. 10, pp. 1518–1524, 2012.

Hindawi
Journal of Oncology
Volume 2022, Article ID 2956888, 13 pages
https://doi.org/10.1155/2022/2956888

Research Article

Hax-1 Regulates Radiation-Induced Mitochondrial-Dependent Apoptosis of Uveal Melanoma Cells through PI3K/AKT/eNOS Pathway

Sha Wang,[1,2] **Jia Tan**,[1,2] **Lu Chen**,[1,2] **and Jinwei Wang**[1,2]

[1]*Eye Center of Xiangya Hospital, Central South University, 87 Xiangya Road, Changsha, China 410008*
[2]*Hunan Key Laboratory of Ophthalmology, 87 Xiangya Road, Changsha, China 410008*

Correspondence should be addressed to Jia Tan; tanjia1009@126.com

Received 28 December 2021; Revised 21 March 2022; Accepted 30 March 2022; Published 13 May 2022

Academic Editor: Fu Wang

Uveal melanoma is an aggressive skin cancer that remains insurmountable and is accompanied by inferior prognostic results. The proliferative and survival mechanisms of uveal melanoma cells need to be further investigated to improve the treatment of uveal melanoma. According to reports, HAX-1 is an antiapoptotic protein vital for multiple malignancies. Nevertheless, the role and causal link of HAX-1 in uveal melanoma are still elusive. The survival diversity of uveal melanoma sufferers with diverse haX-1 expressing levels was studied by TCGA database. Patients in the $risk_{high}$ group exhibited greater levels of HAX-1 in contrast to the $risk_{low}$ group, and individuals with higher HAX-1 levels displayed inferior survival times. The outcomes of CCK-8 and clonogenesis revealed that the proliferative rate of haX-1 knockout cells was slower. The result of scratch experiment shows that the ability of scratch recovery after HAX-1 is reduced. Transwell migration and tumor cell pelletization experiments showed that siHAX-1 significantly reduced cell migration and tumor cell pelletization. After haX-1 was knocked out, the loss of MMP was decreased, the transfer of CyT C was elevated, and the protein expression of Bax, Caspase 3, and Bcl2 was elevated, suggesting that mitochondria-induced apoptosis was increased. Sihax-1 treatment remarkably decreased the phosphonation of phosphatidylinositol 3-kinase (PI3K)/AKT/mammalian target of rapamycin (mTOR)/endothelial NO synthase (eNOS) in mum-2B and C918. Pretreatment with LY294002 significantly restored iHAX-1-induced decline in PI3K/AKT/mTOR/eNOS phosphorylation. Therefore, our results suggest that haX-1 induces radiation-dependent apoptosis of UM cells via the PI3K/AKT/eNOS signal path.

1. Introduction

UM is one of the most seen primary intraocular malignancies in adults. It is mainly derived from uveal melanocytes and has the features of high proliferation activity and easy metastases [1, 2]. The prevalence of melanoma rises incessantly in many nations and has become one of the major causes of tumor-associated incidence and death across the globe [3]. Due to the special structure of the eye, the initial tumor symptoms are not obvious, and the patient's attention is not paid attention to. This has caused many patients with liver or systemic metastases at the time of diagnosis, which often leads to higher mortality [4, 5]. The treatment methods of UM mainly include eyeball enucleation, local tumor resection, local radiotherapy (external scleral application radiotherapy, stereo radiotherapy, and proton beam therapy), and laser photocoagulation therapy (transpupillary thermotherapy and photodynamic therapy) [6, 7]. At present, extrascleral application radiotherapy is a more effective method for the treatment of UM, which can not only increase the effective transmission speed of radiation but also reduce the damage of radiation to normal tissues [8, 9]. As current treatment methods still face challenges in improving patients' clinical survival and visual function,

studying the molecular mechanism of UM is imperative for early diagnosis and ameliorating the long-term prognosis of patients.

Apoptosis is one of the methods of programmed cell death (CD), and it is vital for the elimination of impaired cells [10]. Apoptotic events have evident morphology and biochemistry variations and are pivotal for the growth and developmental process of organs and tissues, immunity, metabolism, and the elimination of abnormal cells [11]. Caspase is a protease that promotes cell apoptosis and plays a central role in the network of cellular apoptotic mechanisms [12]. Researches have shown that Caspases can induce cell apoptosis in three main ways: (1) death receptor pathway (exogenous) apoptosis, (2) mitochondrial pathway (endogenous pathway), and (3) internal apoptosis of the plasma reticulum stress pathway [13, 14].

The key effects of mitochondria on apoptotic events have been broadly revealed [15]. In the process of apoptotic events, the permeability of the mitochondrial membrane increases, releasing soluble mitochondrial membrane interstitial proteins and further destroying the cell structure. Among these lethal proteins, some (Cyt c, Smac/DIABLO, Omi/HtrA2, etc.) can activate caspases, while others (endo G, AIF, Omi/HtrA2, etc.) act in a non-caspase-dependent manner. The releasing of those proteins is the result of the destruction of the completeness of the mitochondria OM via permeabilisation [16, 17]. The kinetic events in mitochondria eventually decide the onset of apoptotic events, highlighting the tight association between mitochondria function disorder and CD. In addition, Bcl-2 family protein is also vital for the occurrence of apoptotic events. Bcl-2 family members modulate the mitochondria apoptosis signal path via regulating the permeation of the mitochondrial OM. Upon apoptosis stimulation, Bax/Bak translocates to the mitochondrial membrane, promotes the releasing of Cyt c from the inner mitochondrial membrane space into the cytoplasm, and induces the occurrence of cell apoptosis [18]. HS-1 related protein-1 (HAX) -1) is a +35 kDa protein, found everywhere in mitochondria [19]. On the foundation of its low sequencing homology with Nip3 and structure similarity with Bcl-2 family protein, as a mitochondrial antiapoptotic protein, HAX-1 is considered to participate in apoptotic events or programmed CD regulation, and its abnormal expression is related to many serious diseases, including neurodevelopmental delay, cancer, and cardiovascular disease [20, 21]. A report pointed out that HAX-1 can regulate the cell death process in myocardial ischemia-reperfusion injury through ERS and mitochondrial stability [22]. Recently, a research showed that the decomposition of HAX-1 induced CD in mankind B-cell lymphomas, confirming the critical effects of HAX-1 on regulating cellular survival [23]. Another study pointed out that the abnormal expression of HAX-1 protein is vital for suppressing the apoptosis of glioblastoma cells [24]. Yan et al. revealed that HAX-1 can suppress the apoptotic events of prostate oncocytes via the inactivation of yellow membrane-9 [25]. According to Oncomine, the tumor microarray database, the expression of HAX-1 is high in many diseases like lung carcinoma, lymphoma, melanoma, and myeloma [26]. However, the molecular mechanism of HAX-1's effect on uveal melanoma has not been studied.

Here, our team was the first to reveal that HAX-1 knockout affects the viability, migration, and tumor cell spheroidizing ability of UM cells. The effects of HAX-1 on mitochondrial-dependent induction of uveal melanoma cell apoptosis are caused by activating the PI3K/AKT/eNOS signal path and favorable modulation of Bax, caspase 3, and Bcl2.

In this research, the TCGA database was employed to study the survival differences of patients with uveal melanoma with diverse expression levels of HAX-1. Our team found that the expression of HAX-1 in the $risk_{high}$ group was greater in contrast to the $risk_{low}$ group, and the survival duration of patients with higher HAX-1 levels was inferior. In addition, we also discovered that HAX-1 participates in the modulation of uveal melanoma cellular viability, metastasis, and tumor ring formation via modulating PI3K/AKT/eNOS and triggers UM cell apoptosis via mitochondria dependence. For that reason, the present research primarily discusses the expressing features of HAX-1 in uveal melanoma and the causal link affecting cell apoptosis.

2. Methods

2.1. Data Collection. Download RNA-seq data of uveal melanoma patients from TCGA database and relevant clinical data of patients. The extracted clinical data included overall survival time (OS.time), age, sex, and IDH gene mutation status. Data from 88 patients with uveal melanoma were extracted by matching the samples with RNA-SEQ data, CNV data, and relevant clinic information for analysis.

2.2. Differential Analysis of the Expression Profile of UM Patients with Different HAX-1 Expression. For 88 UM expression spectrum data in TCGA, HAX1_H:40 and HAX1_L:40 were used as grouping basis. DESeq2 package was used for difference analysis and screen $P < 0.05$ and absolute value $\text{Log2}(\text{fold change}) > 1$ as the significant gene for difference. Finally, the difference genes were shown by volcano map. Differentially expressed genes in heat map were stratified and clustered. The correlation between HAX1 gene expressing and OS rate was analyzed by univariable Cox based on the clinical information data of UM in TCGA database.

2.3. Differential Gene GO Analysis and KEGG Pathway Analysis. TCGA expression profile chip was corrected, edgeR of R language was used for differential gene analysis, and pheatmap package was used to draw differential gene volcano map and cluster analysis heatmap. The screening conditions were $\text{logFC} \geq 1$ or ≤ -1, and $P < 0.05$ had significance on statistics. DAVID online program and clusterProfiler package were employed to study the differentially expressed EC genes. Finally, Gene Ontology (GO) analysis with $\text{FDR} < 0.05$ was selected as the result of enrichment function, and the GGploT2 package of R language was used for mapping. KEGG pathway analysis is functionally

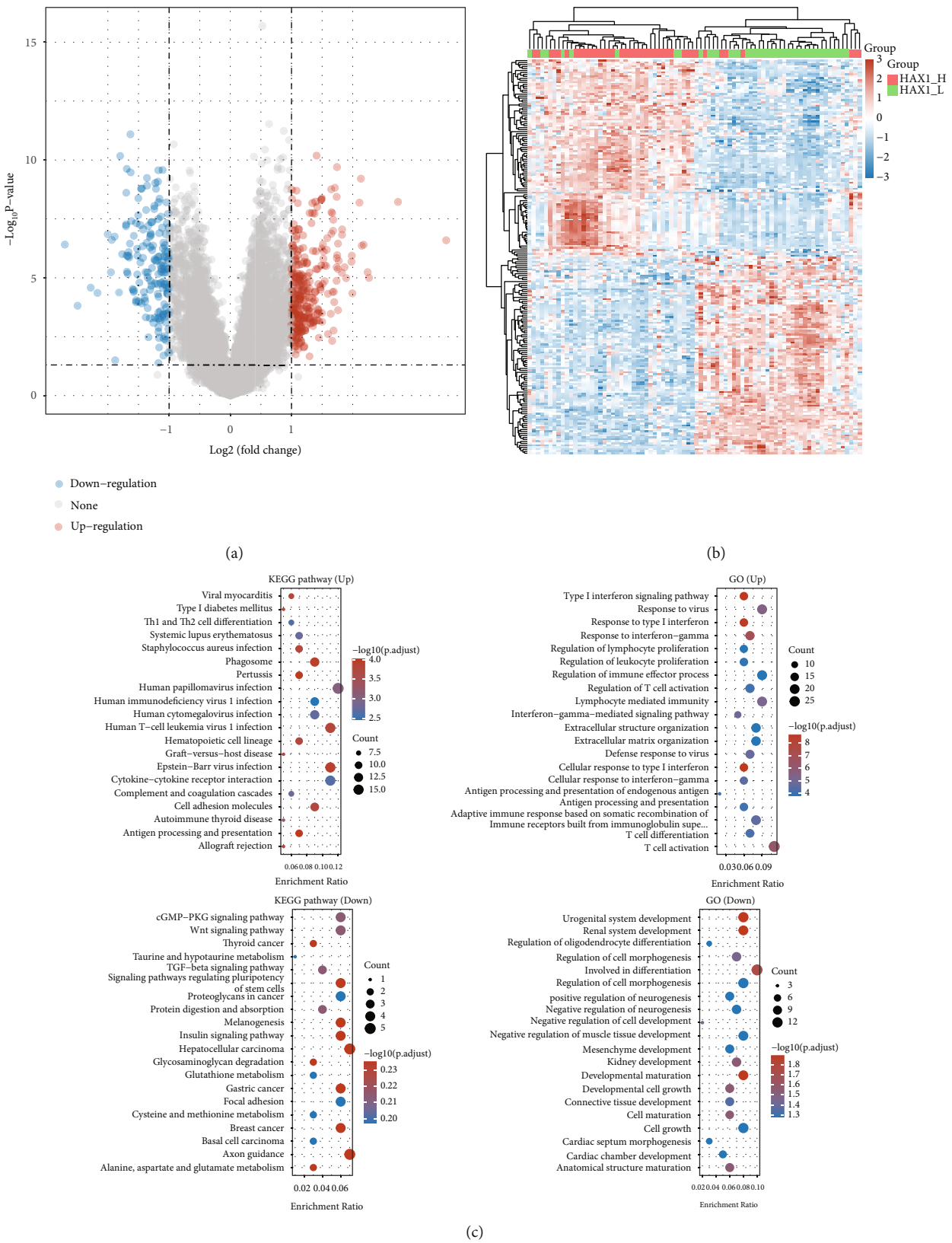

Figure 1: Difference analyses of HAX-1 overexpression and normal expression in patients with uveal melanoma. (a) TCGA volcano map of differentially expressed genes in patients with uveal melanoma in different survival periods. (b) Layer clustering thermograph of differential genes. (c) Enrichment analysis of the upregulated and downregulated genes GO and KEGG in the survival group of patients with uveal melanoma in TCGA.

classified and enriched by a hypergeometric distribution. The dataset was analyzed by KEGG pathway via the "Limma" R package for differential analysis.

2.4. Subsistence Analysis. The Kaplan-Meier survival curve was drawn, and logrank rank-sum test was employed to evaluate the overall survival of patients in the $risk_{high}$ group and $risk_{low}$ group. ROC curves were employed to evaluate the prediction power of the prognostic risk model at 1, 3, and 5 years of survival, and heat maps of the $risk_{high}$ group and $risk_{low}$ group were drawn. The univariable and multivariable Cox regressive analyses were employed to evaluate the correlation of clinical variables and risk scores with patient prognoses. The pictures were drawn using R software and SPSS 22.0 (IBM, Armonk, NY, USA).

2.5. MUM-2B and C918 Cells and their Cultivation. UM lineage cells Mum-2B and C918 were bought from SICB, CAS. The uveal melanoma lineage cells mum-2B and C918 were cultivated in DMEM intermediary with 10% serum, and 1% PNC/Streptomycin double antibody solution was added into the medium. The cell incubator temperature was set at 37°C and CO_2 content was 5%. The fresh medium was replaced every 2 days. When the medium was replaced, the cell surface was washed with PBS solution to remove some metabolic substances secreted by cells. When the cells adhered to the wall and grew to 80%~90%, 0.25% trypsin was added for digestion and passage of cells. Stable and well-growing third-generation melanoma cells were collected for subsequent experimental operations.

2.6. Synthesis of HAX-1 siRNA. According to the design principle of siRNA sequence and according to the sequence of HAX-1 gene (no. NM006118) in GenBank database, the 540-640 nucleotide of CDS sequence was selected as siRNA sequence, and this sequence was compared with the homology of other genes and EST sequences in NCBI database, which confirmed that there was no homology with other genes and EST sequences. The following two haX-1 siRNA target sequences with BglII and HindIII sticky ends were designed and synthesized:

5,—CATCCCCAACCAGAGAGGACAATGATCTTTC AAGAGAAGATCATTGTCCTCTCTGGTTTTTTTA—37

5,—AGCTTAAAAAAACCAGAGAGGACAATGATCT TCTCTTGAAAGATCATTGTCCTCTCTGGTTGGG—37

2.7. Cell Proliferation Detected by CCK8 Method. The cells from each group were digested by trypsin to prepare cell suspension and inoculated on 96-well dishes with inoculation density of 5 × 103/well. The cells were continued to be cultured at 37°C, and 100 μL CCK 8 liquor was supplemented into all wells at 0 h, 24 h, 48 h, and 72 h, separately, and cultivated under 37°C for 30 min under dark conditions. The OD result of all wells at 450 nm was measured on a multifunctional micro plate analyzer, and the cellular activity (%) − (experiment group optical density/control group optical density) × 100% was calculated. Three multiple holes were set at each time point in every group, and the assay was performed in triplicate.

2.8. Clone Formation Experiment. Mum-2b and C918 cells were seeded to 6-well dishes with about 500 cells in each well and grouped according to Method 1.3. After 7 days of culture, the supernatant was discarded, 4% paraformaldehyde was subjected to fixation for 20 min, and 0.1% gentian violet was dyed for 15 min. After washing and drying, the number of clones formed was observed under a microscope, and the clone forming rate was computed. Cell clone forming rate (%) = overall cell clones/seeded cells × 100%.

2.9. Scratch Healing Test. Mum-2b and C918 cells were seeded into 6-well dishes, and 1 × 106 cells were inoculated in every well and cultured to 90%-100% fusion degree. The bottom of 6-well plates was gently scratched with 200 μL spear head, a vertical line and a horizontal line were drawn, and the cells were cleaned with PBS for two times. The 6-well plate was observed under an inverted microscopic device. Images were captured near the junction of vertical and horizontal lines and taken again at the same position 24 hours later. Use ImageJ software to measure the scratch width, mobility/% = (0 h scratch width − 24 h scratch width)/ 0 h scratch width × 100%. Each dosing group was set with 3 multiple wells, and the assay was independently performed in triplicate.

2.10. Transwell Assay Detected by Cell Migration. Matrigel matrix adhesive was diluted 9 : 1 in precooled culture medium, and 40 μL Matrigel diluent was added to each well in the upper chamber of Transwell chamber and cultivated under RT for 5 h. Mum-2b and C918 cells of logarithmic growth uveal melanoma cells were precooled and washed with PBS, subjected to digestion by 0.25% trypsin, and then added with culture medium without fetal bovine serum to prepare single cell suspension (5 × 104 cells/mL). 200 μL single cell suspension was supplemented to each well of the upper chamber. 600 μL culture intermediary with 10% FBS was supplemented into each well in the lower chamber, cultivated for 24 h under 37°C within an incubating device at 5% carbon dioxide, cleaned in PBS, subjected to fixation in PFA for 10 min, dyed in 0.1% gentian violet for 10 min, and wiped with cotton swabs for nonmigrated cells. The number of transplanted cells was observed under microscope.

2.11. Flow Cytometry Apoptosis Detection. The cells were inoculated on 6-well dishes and apoptotic events were identified via flow cell technique using Annexin V-FITC/PI dyeing (Nanjing KGI Biotechnology Development Co., Ltd.). Flow cytometry apoptosis detection is as follows: 24 h posterior to transfection, the cells were digested by trypsin and harvested and then suspended and washed with 100 μL 1×Binding Buffer (Shanghai Biyantian Biotechnology Co., Ltd.) for each tube. Annexin V-APC 5 μL reagent was added and incubated for 15 min. Apoptotic events were identified via flow cell technique at 4°C.

2.12. Western Blot Detection. The cells were harvested 3648 h posterior to transfection and subjected to centrifugation at 600 r/min for 3 rains, and the supernate was removed. The cells were cleaned with 5 mL ice precooled PBS for 2 times

Table 1: Top 20 upregulated genes and top 20 downregulated genes.

Upregulated genes				Downregulated genes			
Gene name	LogFC	*P* value	Adjusted *P* value	Gene name	LogFC	*P* value	Adjust *P* value
HTR2B	3.53	2.55E-07	1.66E-05	SYNPR	-2.70	3.89E-07	2.24E-05
CHAC1	2.74	6.01E-09	1.28E-06	SPP1	-2.50	1.53E-04	1.73E-03
SLC38A5	2.27	1.00E-05	2.22E-04	MSC	-2.28	2.63E-05	4.51E-04
VGF	2.24	5.76E-06	1.47E-04	GSTA3	-2.17	4.39E-05	6.61E-04
TRPV2	2.18	3.95E-07	2.27E-05	PDE3A	-2.00	1.40E-07	1.07E-05
ECM1	2.15	4.35E-07	2.38E-05	HPGD	-1.95	5.84E-06	1.49E-04
AHNAK2	2.13	6.21E-10	3.72E-07	ENPP2	-1.94	2.46E-07	1.61E-05
ISM1	2.11	6.47E-09	1.29E-06	IL12RB2	-1.89	1.79E-07	1.26E-05
IFI27	1.99	4.56E-05	6.83E-04	BEX1	-1.82	4.21E-05	6.39E-04
COL9A3	1.99	1.15E-06	4.79E-05	ROPN1B	-1.80	6.76E-11	1.16E-07
VTN	1.98	2.08E-06	7.09E-05	BCHE	-1.77	9.90E-07	4.25E-05
MYEOV	1.89	1.03E-05	2.27E-04	GPR27	-1.70	6.57E-08	6.48E-06
PSMB9	1.87	3.56E-06	1.04E-04	LNP1	-1.70	5.37E-08	5.63E-06
WARS1	1.83	8.82E-08	7.75E-06	MTUS1	-1.70	2.45E-09	7.87E-07
GRID1	1.83	1.50E-07	1.12E-05	RNF43	-1.69	2.37E-10	1.99E-07
TNFRSF19	1.82	6.11E-06	1.53E-04	CLEC11A	-1.69	5.45E-06	1.42E-04
RARRES2	1.77	1.89E-06	6.60E-05	LIMS2	-1.68	1.19E-06	4.86E-05
PLN	1.76	2.37E-04	2.42E-03	MLIP	-1.67	6.84E-06	1.66E-04
FERMT3	1.76	3.55E-07	2.09E-05	COL11A1	-1.66	1.18E-06	4.86E-05
LAG3	1.76	4.26E-06	1.18E-04	KCNK2	-1.66	8.05E-07	3.65E-05

to collect cell precipitates. 200 μL single detergent lysis solution containing protease inhibitor was supplemented into a 60 mm diameter cultivation plate, followed by an ice bath of about 18 rains and centrifugation of 13000 r/min for 10 rains. The supernate was taken, and the total protein was quantitatively determined and moved onto PVDF film by SDS-PAGE. The cells were sealed with 5% skim milk powder, sealed with primary antibody (1 : 1000, Protein Tech Group, USA) under 4°C nightlong, and cleaned three times in TBST, 300 s each. The second antisubstance (1 : 500, Protein Tech Group, USA) was incubated under RT for 60 min and afterwards cleaned three times in TBST, and ECL chemiluminescence was performed. FluorChemFC2 imager from CELLBIOSCIENCES was used for luminescence development.

2.13. Statistical Analysis. Using R (V3.6.1) and SPSS 20.00, the univariable Cox regressive analyses were completed on the expressing level of HAX-1 and overall survival in UM clinical case data. Statistical tests were conducted by bilateral tests. $P < 0.05$ had significance on statistics.

3. Results

3.1. Differential Analysis of the Expression Profile of HAX-1 Overexpression and Normal Expression in Uveal Melanoma. Raw counts and corresponding clinical information of RNA sequence (level 3) from 80 UVM tumors were acquired from TCGA dataset. Using the high and low expression of HAX1 as grouping basis (HAX1_H:40 and HAX1_L:40), Limma software of R program was employed to explore the differentially expressed mRNA. According to the screening criteria modified $P < 0.05$ and absolute value Log2(fold change) > 1. A total of 407 mRNA genes were screened, including 252 upregulated genes and 155 downregulated genes (Figure 1(a)), and top 20 upregulated genes and top 20 downregulated genes are shown in Table 1. Figure 1(b) thermograph shows layer clustering of expressing levels of DEGs. To identify the potential capabilities of underlying targets, the data was studied through feature enrichment. GO is a extensively utilized method to annotate functional genes, particularly MF, BP, and CC. KEGG enrichment analysis is useful for analyzing gene function and related high-level genomic function data. To further reveal the carcinogenic effects of targeted genes, the clusterProfiler package in R was employed to study the GO function of underlying mRNAS and realize the KEGG pathway enrichment. Cytokine enriching assay revealed that the upregulated genes were mainly distributed in viral arditis, type 1 diabetes mellitus, Th1 and Th2 cellular differentiation, systemic lupus erythematosus, SA infection, phagosome, pertussis, human papillomavirus infection, HIV-1 infection, and HCMV infection. KEGG pathway analyses revealed that downregulated genes were mainly distributed in Wnt signal path, thyroid cancer, TGF-beta, signal path, signal paths modulating pluripotency of stem cells, proteoglycans in carcinoma, etc. GO term enrichment outcomes revealed that the upregulated genes were primarily distributed in type I interferon signaling pathway, reaction to viruses, reaction to type I IFN, reaction to IFN-γ, modulation of lymphocyte proliferation, and other pathways. GO term enrichment showed developmental maturation, developmental cell growth,

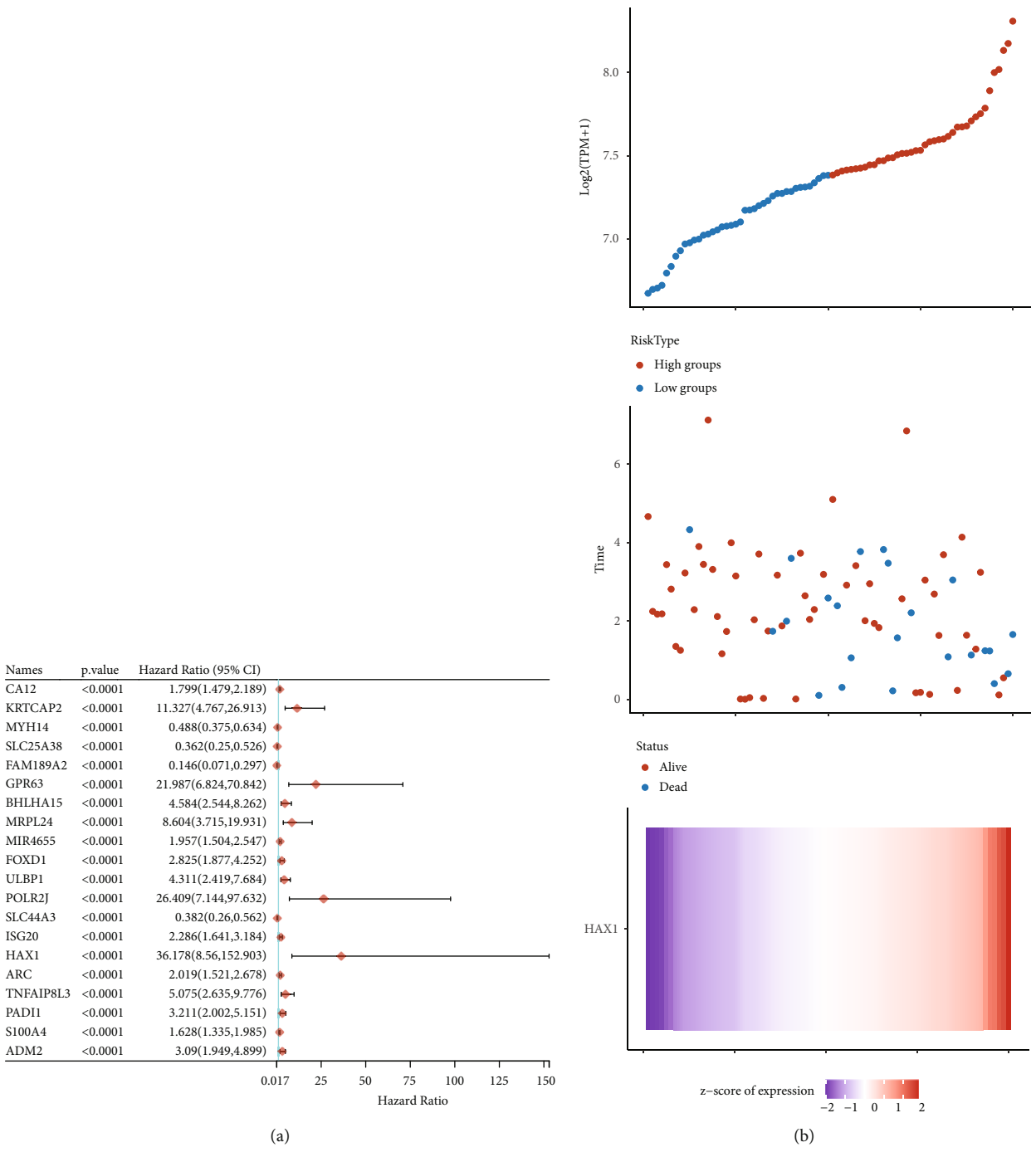

Figure 2: Cox analysis of correlation between haX-1 expressing and OS. (a) Forest map of 20 differentially expressed genes related to OS in whole-gene Cox regressive analysis. (b) Risk factor association diagram of differential expression gene prognostic model. Above: $risk_{high}$ (red) and $risk_{low}$ (blue) in a prognostic model. Risk score distribution of uveal melanoma patients. Middle image: scatter plot shows the survival of patients with GBM in the model. Red dots are patients who died and blue dots are patients who survived. Figure below: a calorimetric map of the genetic expression of haX-1 in the model.

connective tissue development, cell maturation, cell growth, cardiac septum morphogenesis, cardiac chamber development, and packet structure Hood isotherm pathway (Figure 1(c)).

3.2. Cox Analysis of the Correlation between HAX-1 Expression and Overall Survival. To further study the effect of HAX-1 on the prognosis of uveal melanoma, the DEGs were obtained, univariate Cox regression analysis was performed, and forest maps were drawn. As shown in Figure 2(a), the Cox risk regression analysis identified 20 optimal differentially expressed genes. As you can see from the risk factor association graph, there were significantly more deaths and fewer survivors in the $risk_{high}$ group. In

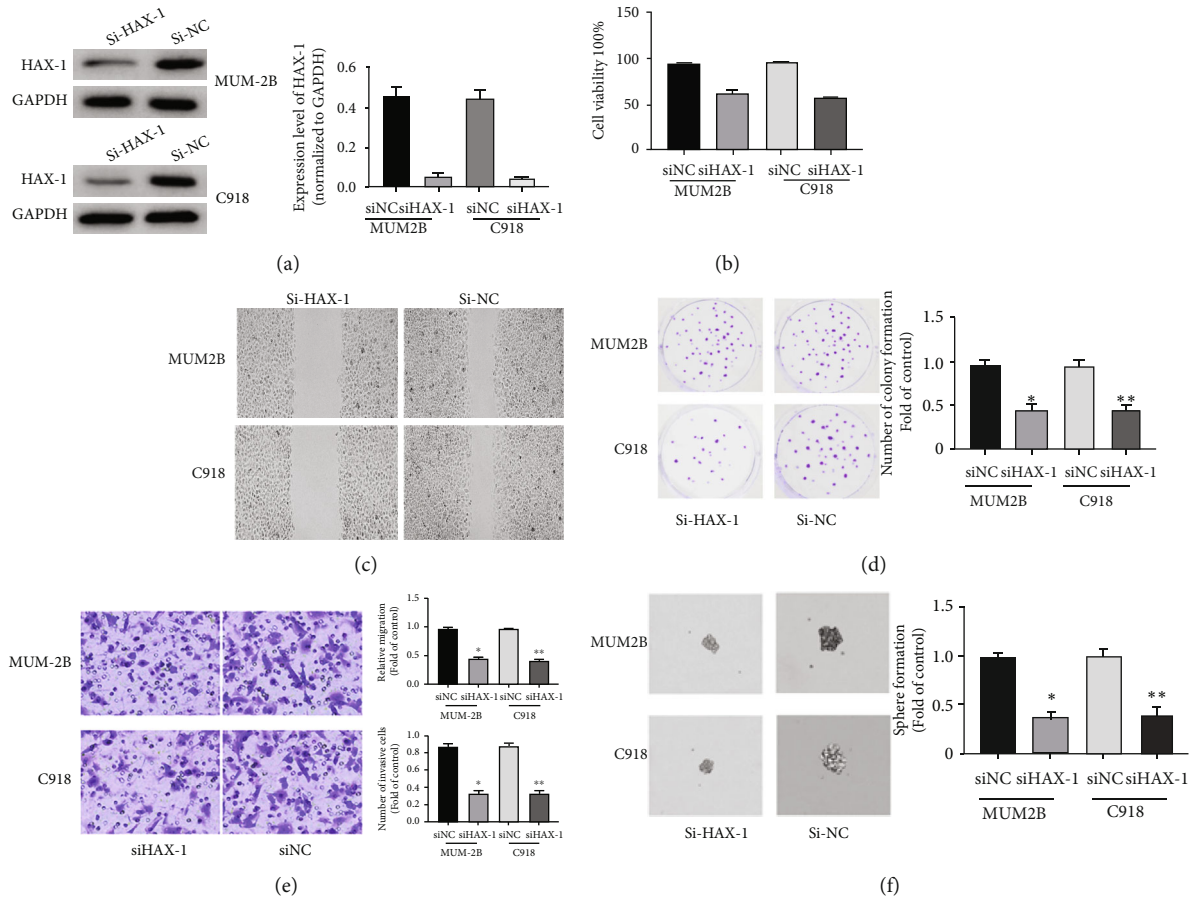

Figure 3: HAX-1 knockout affects the viability and migration of UM cells and the ability of tumor cells to form balls. (a) WB assay of HAX-1 protein expressing levels in uveal melanoma lineage cells MUM-2B and C91. (b) CCK-8 method was employed to identify the proliferative effect of transfected siHAX-1 and si control on MUM-2B and C91 cells. siHAX-1 vs. control group, $^{*}P < 0.05$ and $^{**}P < 0.01$. (c) Scratch test to assess the effect of HAX-1 on the migration of MUM-2B and C91 cells. (d) The clone formation experiment detects the effect of HAX-1 on the proliferative ability of MUM-2B and C91 cells. siHAX-1 vs. the controls, $^{*}P < 0.05$ and $^{**}P < 0.01$. (e) Migration test (using Matrigel Transwell chambers) is used to study cell migration. siHAX-1 vs. the controls, $^{*}P < 0.05$ and $^{**}P < 0.01$. (f) Tumor sphere formation ability experiment to assess the roles of HAX-1 in the tumor sphere formation capability of MUM-2B and C91 cells.

addition, the expressing level of haX-1 was greater in the risk$_{high}$ group in contrast to the risk$_{low}$ group (Figure 2(b)). K-M survival analyses were used to evaluate the OS of sufferers in diverse groups. The OS of sufferers in the risk$_{low}$ group (blue) was remarkably higher in contrast to the risk$_{high}$ group (red) ($P < 0.05$) and the difference was statistically significant (Figure 2(c)). On the foundation of the prognosis gene model, the overall survival rate of 1, 3, and 5 years in the future was predicted by ROC curve. The results showed that the constructed model exhibited satisfactory prediction capability (Figure 2(d)).

3.3. HAX-1 Knockout Affects UM Cell Viability, Migration, and Oncocyte Spheroidizing Ability. To better explore the roles of HAX-1 in UM cells, our team used chemically synthesized siRNA to knock down haX-1 expression in mum-2B and C918 cells. At 48 h after transfection, WB was employed to evaluate the efficiency of siRNA knockout. The outcomes showed that HAX-1 siRNA effectively reduced the protein expressing level of HAX-1 in mum-2B and C918 cells (Figure 3(a)). By CCK-8 detection, we found that cell proliferation rates of Mum-2B and C918 cells subjected to siRNA treatment were remarkably lower in contrast to those subjected to siRNA treatment (Figure 3(b)). In scratch experiments, siHAX-1's ability to recover scratch was remarkably improved in mum-2B and C918 cells compared with siRNA control cells (Figure 3(c)). Results of clone forming assays revealed that siHAX-1 remarkably reduced the quantity of colony formation in soft AGAR (Figure 3 (d)). In Transwell migration experiment, siHAX-1 significantly reduced cell migration in mum-2B and C918 cells in contrast to siRNA control cells (Figure 3(e)). In addition, haX-1 knockout significantly reduced the pellet-forming ability of UM cells in contrast to the controls (Figure 3(f)). Those results reveal that HAX-1 knockout affects UM cellular activity, metastasis, and oncocyte pelletogenesis.

3.4. HAX-1 Induces Apoptosis in the Mitochondrial-Dependent Pathway. We next examined whether HAX-1 triggered apoptosis in uveal melanoma cells. In apoptotic events identified via flow cell technique, siHAX-1 triggered

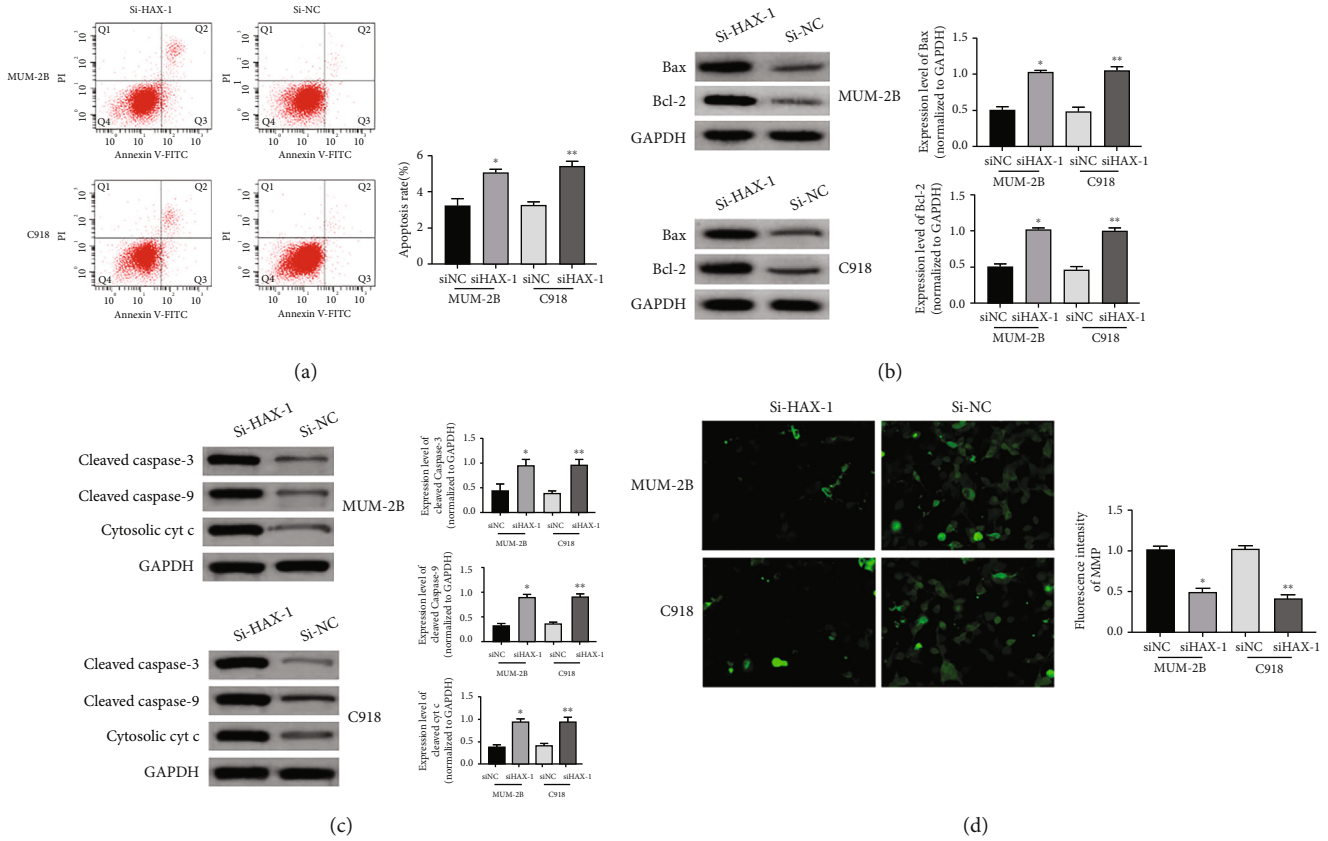

Figure 4: HAX-1 induces apoptosis in the mitochondrial-dependent pathway. (a) Flow cytometry to detect flow cytometry cycle distribution. (b) WB assay to identify Bax and Bcl-2 protein expressing levels in UM lineage cells MUM-2B and C91. (c) Western blot analysis to detect the expression levels of caspase-3/9 and cytosolic Cyt c protein in the uveal melanoma cell lines MUM-2B and C91. (d) Immunofluorescence detection of MMP expressing in UM lineage cells MUM-2B and C91.

programmed cell death in mum-2B and C918 cells in contrast to siRNA control cells (Figure 4(a)). In addition, siHAX-1 increased protein expressing levels of Bax mum-2B and C918 cells (Figure 4(b)). Stimulation of caspase-9, reduction of MMP, and transfer of Cyt c from the mitochondrion to cytosol can verify the occurrence of mitochondrial apoptosis. For that reason, to better verify the effects of mitochondria on haX-1-triggered apoptotic events, we examined variations in protein expressing levels of caspase-3/9 and cytochrome C levels. The outcomes revealed that siHAX-1 elevated the expression of Caspase-3/9 and Cytosol cyt C in mum-2B and C918 cells in contrast to the controls (Figure 4(c)). Moreover, siHAX-1 remarkably decreased MMP in mitochondrial pathways in mum-2B and C918 cells compared to the controls (Figure 4(d)). Those results reveal that HAX-1 triggers programmed cell death in uveal melanoma cells in a mitochondrion-reliant signal path.

3.5. HAX-1 Induces UM Cell Apoptosis through AKT/eNOS Signal Path. To investigate the causal link involved in the apoptosis-inducing role of HAX-1, WB was employed to identify the expression and phosphonation of PI3K/AKT/mTOR/eNOS. Treatment with SihaX-1 remarkably decreased the phosphonation of PI3K/AKT/mTOR/eNOS in mum-2B and C918 (Figure 5(a)). Pretreatment with 740-YP significantly restored the decrease in PI3K and AKT phosphorylation induced by SihaX-1 (Figure 5(b)). These data suggest that the apoptosis-inducing effect of SiHAX-1 in mum-2B and C918 cells might be under the mediation of the PI3K/AKT/mTOR/eNOS signal path.

3.6. HAX-1 Regulates UM Cell Viability, Migration, Oncocyte Spheroidization Ability, and Mitochondrial-Dependent Apoptosis by Regulating the AKT/eNOS Signal Path. It is known to all that the AKT/eNOS signal path is pivotal for the genesis and development of tumors. It is vital for cellular proliferation, differentiation, and cell viability modulation [27]. The gain or loss of function caused by abnormal expression of related genes and molecules in this pathway can lead to abnormal proliferation, apoptosis, and invasion of tumor cells [28]. Tumor progression is related to aberrant genetic stimulation in those signal paths as well, which might induce elevated cellular growth and survival [29]. Next, we examined whether haX-1 affects uveal melanoma cells through the AKT/eNOS pathway. 48 h after transfection, Western blot results showed that the decrease in PI3K and AKT phosphonation caused by HAX-1 knockdown was significantly restored by LY294002 in mum-2B and C918 cells (Figures 5(a) and 5(b)). By CCK-8 assay, we found that LY294002 preconditioning restored the decrease in mum-2B and C918 cellular proliferative rates caused by siHAX-1 treatment (Figure 6(a)). In the scratch experiment,

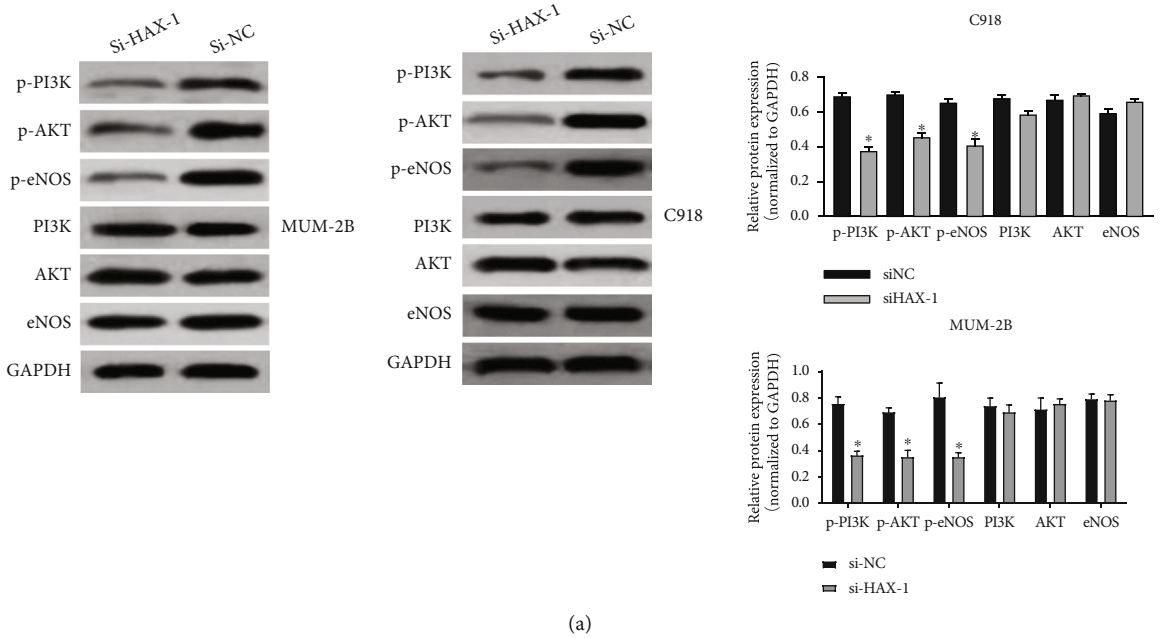

(a)

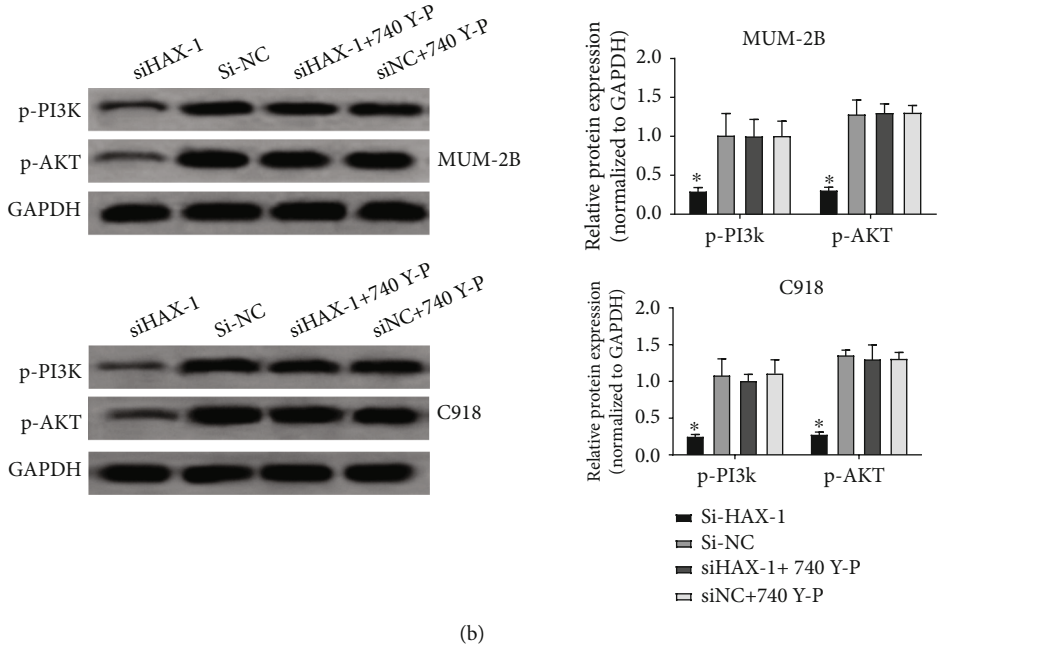

(b)

Figure 5: HAX-1 induces uveal melanoma programmed cell death via the AKT/eNOS signal path. (a) WB assay to identify the effect of HAX-1 on PI3K/AKT/mTOR/eNOS pathway. (b) WB assay to assess the roles of siHAX-1+740 Y-P in the expressing levels of phosphorylated PI3K and AKT proteins.

LY294002 pretreatment restored the reduced scratch recovery ability of SIHAX-1 in mum-2B and C918 cells (Figure 6(b)). The results of clone formation experiments showed that LY294002 pretreatment restored the reduction in the number of colonies formed in soft AGAR caused by SiHAX-1 (Figure 6(c)). In Transwell migration experiment, pretreatment with LY294002 restored the decrease in cell migration induced by SIHAX-1 in mum-2B and C918 cells (Figure 6(d)). These results suggest that haX-1 knockout reduced uveal melanoma cell viability and migration ability reversed by LY294002. In addition, LY294002 also reversed the tumor-forming ability of uveal melanoma cells reduced by HAX-1 knockdown (Figure 6(e)), as well as the apoptosis of uveal melanoma cells induced by HAX-1 in the mitochondria-dependent pathway (Figure 6(f)). Those results reveal that haX-1 affects UM cell viability, the ability of migrating tumor cells to form pellets, and mitochondria-dependent apoptosis via the AKT/eNOS pathway.

4. Discussion

Uveal melanoma (UM) is a commonly seen malignancy in the eye. Its incidence is second only to retinoblastoma. It has a high degree of malignancy, proliferation, and

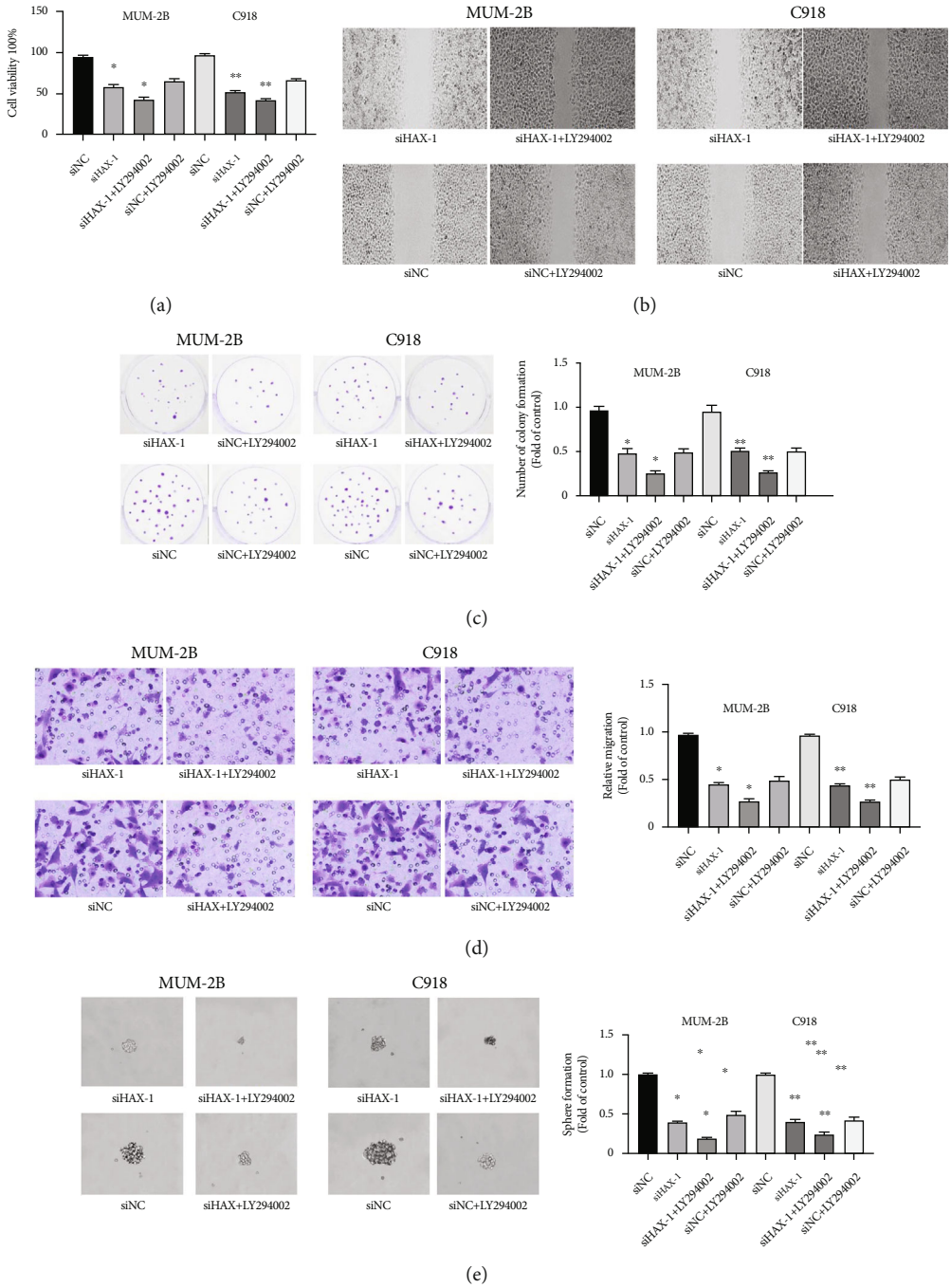

Figure 6: Continued.

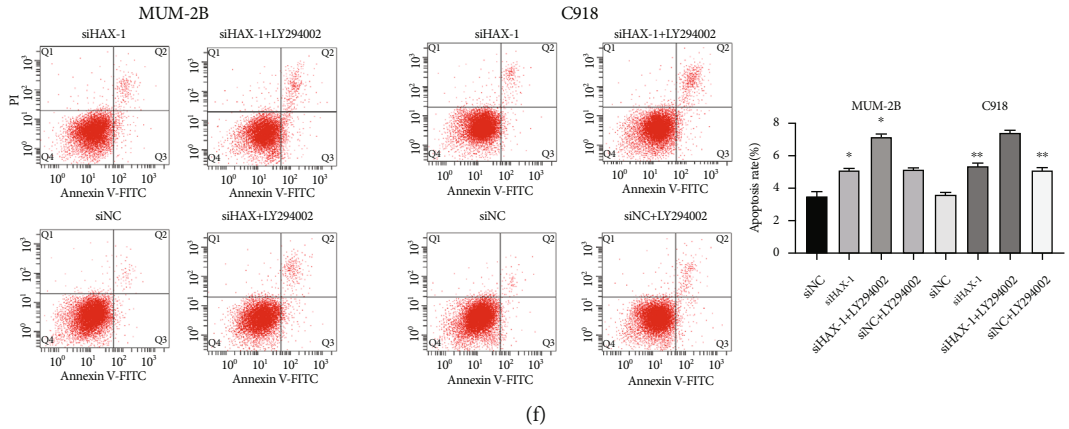

(f)

Figure 6: HAX-1 regulates uveal melanoma cell viability, migration, tumor cell spheroidization ability, and mitochondrial-dependent apoptosis by regulating the AKT/eNOS pathway. (a) CCK-8 method was employed to identify the proliferative effect of MUM-2B and C91 cells in siHAX-1+ LY294002 and siNC+LY294002 groups. siHAX-1 vs. the controls, $^{*}P < 0.05$ and $^{**}P < 0.01$; siHAX-1+LY294002 vs. siNC+LY294002, $^{*}P < 0.05$ and $^{**}P < 0.01$. (b) Scratch test to evaluate the effect of HAX-1+LY294002 on the migration of MUM-2B and C91 cells. (c) The clone formation experiment detects the effect of siHAX-1+LY294002 on the proliferation of MUM-2B and C91 cells. siHAX-1 vs. the controls, $^{*}P < 0.05$ and $^{**}P < 0.01$; siHAX-1+LY294002 vs. siNC+LY294002, $^{*}P < 0.05$ and $^{**}P < 0.01$. (d) Migration test (using Matrigel Transwell chambers) is used to study cell migration. siHAX-1 vs. control group, $^{*}P < 0.05$ and $^{**}P < 0.01$; siHAX-1+LY294002 vs. siNC+LY294002, $^{*}P < 0.05$ and $^{**}P < 0.01$. (e) Tumor spherule forming ability experiment to assess the role of siHAX-1+LY294002 in the tumor spherule forming capability of MUM-2B and C91 cells. siHAX-1 vs. the controls, $^{*}P < 0.05$ and $^{**}P < 0.01$; siHAX-1+LY294002 vs. siNC+LY294002, $^{*}P < 0.05$ and $^{**}P < 0.01$. (f) Flow cytometry experiment to assess the roles of siHAX-1 +LY294002 in the apoptotic capability of MUM-2B and C91 cells. siHAX-1 vs. the controls, $^{*}P < 0.05$ and $^{**}P < 0.01$; siHAX-1 +LY294002 vs. siNC+LY294002, $^{*}P < 0.05$ and $^{**}P < 0.01$.

invasiveness and can metastasize at an early stage [30]. Some studies have pointed out that metastasis, especially the distant metastasis that breaks through the orbit, is an important cause of death [31]. Surgery is still one of the most effective treatments for the disease, but the 5-year survival rate of sufferers remains not optimistic. However, more than 50% of surgical patients have blood metastases, most of which involve the liver, and eventually cause liver failure and death. Surgical resection did not significantly improve the patient's quality of life and did not achieve the effect of radical treatment of the tumor [32, 33]. Therefore, further research of the molecular causal link of the occurrence and metastasis of UM and the search for tumor molecular markers and new therapeutic targets have important significance and clinical application value.

Apoptosis, that is, programmed CD, can happen through the external pathway of the cell death receptor mediator or the internal pathway of the mitochondrial mediator. Many stimuli induce programmed cell death, such as ROS, RNS, hormones, cell-cell interactions, growing factor extraction, antigens, and chemotherapy [34, 35]. The development of cancer is related to decreased apoptosis and cancer cell proliferation [36]. For that reason, apoptotic induction is considered a valid way of tumor treatment. Herein, our team discovered that HAX-1 triggers programmed cell death in a mitochondrial-reliant signal path. In addition, our team also explored the signaling pathways that might exert impacts on the apoptotic events of uveal melanoma cells triggered by HAX-1. As far as we know, the present research is the first to link HAX-1 to uveal melanoma cell lines and shows that HAX-1 mediated mitochondrion-dependent apoptosis is through the AKT/eNOS pathway.

As an antiapoptotic protein, HAX-1 is crucial for cellular protection via suppressing the stimulation of mitochondria and endoplasm reticulum stress-associated apoptosis signal paths [19]. More and more researches have revealed that the expression of HAX-1 is high in a variety of malignancies, affecting tumor cell proliferation, migration, and apoptosis [37]. Deng et al. discovered that the expression of HAX-1 is high in glioma samples and lineage cells and is related to the clinicopathology features and prognoses of glioma; moreover, it promotes the proliferation of glioblastoma cells and inhibits tumor cell apoptosis. [24] Studies have also found that HAX-1 promotes the proliferative, migratory, invasive abilities, and epithelial interstitial transform of liver carcinoma cells. Another research revealed that HAX-1 suppresses the programmed cell death of prostate carcinoma cells via inhibiting the activation of caspase-9 [38]. Nevertheless, the roles and molecular causal link of HAX-l in the occurrence and progression of UM are still unclear. This study was the first to discover that HAX-1 promotes radiation-induced mitochondrion-reliant programmed cell death of UM cells via the AKT/eNOS signal path, inhibits cell proliferation, and has potential clinical application value.

In this study, the TCGA database first analyzed survival differences in patients with uveal melanoma with diverse haX-1 expressing levels. The results showed that the gene expression level of haX-1 was greater in the $risk_{high}$ group in contrast to the $risk_{low}$ group, and sufferers with higher HAX-1 levels displayed an inferior survival time. For that reason, HAX-1 was chosen as an investigation target. There

is increasing proofs that the overexpression of HAX-1 occurs in a variety of malignancies, especially affecting proliferation and invasion. We were interested in the roles and causal link of HAX-1 in uveal melanoma, so we used chemically synthesized siRNA to knock out HAX-1 expression in mum-2B and C918 cells. To evaluate the siRNA knockout efficiency, WB was employed to evaluate the siRNA knockout efficiency. We found that HAX-1 siRNA effectively reduced protein expression of HAX-1 in mum-2B and C918 cells. By CCK-8 analysis, our team discovered that cellular proliferative rates of Mum-2B and C918 cells subjected to siRNA treatment were remarkably lower in contrast to those subjected to siRNA treatment. Those outcomes suggest that HAX-1 can facilitate the development of cancer via regulating uveal melanoma cell proliferation. Consistent with this concept, we further found that haX-1 knockdown inhibited cell proliferation in mum-2B and C918 cells. Transwell migration analysis showed that siHAX-1 significantly reduced the cell migration ability in mum-2B and C918 cells in contrast to siRNA control cells. In addition, haX-1 knockout significantly reduced the pellet-forming ability of uveal melanoma cells compared to the control group.

Internal apoptosis induced by mitochondria triggered by death receptors is represented by activation of caspase-9 [39]. In this study, Sihax-1 mediated the activation of Caspase-3/9 and Cytosolic cyt C, and sihax-1 significantly inhibited MMP in the mitochondrial pathway. In addition, Bcl-2 and Bax are tightly associated with programmed cell death as well. Bcl-2 primarily acts as a global mitochondria membrane protein and produces heterosomes with Bax to avoid mitochondria variations during programmed cell death. The outcomes herein revealed that siHAX-1 remarkably decreased the increased expression of Bcl-2 and Bax in mum-2B and C918 cells. Those outcomes suggest that HAX-1 induces uveal melanoma cell apoptosis mainly through mitochondrial dependence.

Finally, this research demonstrates for the first time that HAX-1 triggers uveal melanoma cell apoptosis via mitochondria dependence via the stimulation of PI3K/AKT/eNOS signal path and favorable modulation of Bax, Caspase 3, and Bcl2. The results of this study suggest that haX-1 activates uveal melanoma cells through PI3K/AKT/eNOS by mediating mitochondrial dependent apoptotic pathways that trigger apoptosis, including loss of MMP, transfer of CyT C, and favorable modulation of Bax, Caspase 3, and Bcl2 as key events associated with apoptosis. Those discoveries reveal that PI3K/AKT/eNOS/mitochondrial signal path plays a pivotal role in haX-1 induction of uveal melanoma cell apoptosis.

Abbreviations

HAX-1: Hematopoietic matrix-1-related protein X-1
UM: Uveal melanoma
BP: Biological pathways
OS: Overall survival
GO: Gene Ontology
KEGG: Kyoto Encyclopedia of Genes and Genomes
ROC: Receiver operating characteristic
PBS: Phosphate buffer solution
IFN: Interferon
MF: Molecular functions
CC: Cellular components
RNS: Reactive nitrogen species
OM: Outer membrane
CD: Cell death
SICB: Shanghai Institute of Cell Biology
PNC: Penicillin
RT: Room temperature
PFA: Paraformaldehyde
WB: Western blot
DEGs: Differentially expressed genes
K-M: Kaplan-Meier
Cyt c: Cytochrome c
CAS: Chinese Academy of Sciences
SA: Staphylococcus aureus
HCMV: Human cytomegalovirus
FBS: Fetal bovine serum.

Data Availability

The data used to support the findings of this study are available from the corresponding author by request.

Conflicts of Interest

The authors declare that they have no competing interest.

References

[1] A. D. Singh, E. C. Zabor, and T. Radivoyevitch, "Estimating cured fractions of uveal melanoma," *JAMA Ophthalmology*, vol. 139, no. 2, pp. 174–181, 2021.

[2] A. D. Singh, C. L. Shields, and J. A. Shields, "Prognostic factors in uveal melanoma," *Melanoma Research*, vol. 132, no. 5, pp. 806-807, 2001.

[3] E. A. Seftor, P. S. Meltzer, D. A. Kirschmann et al., "Molecular determinants of human uveal melanoma invasion and metastasis," *Clinical & Experimental Metastasis*, vol. 19, no. 3, pp. 233–246, 2002.

[4] J. J. Augsburger, Z. Corrêa, and A. H. Shaikh, "Effectiveness of treatments for metastatic uveal melanoma," *American Journal of Ophthalmology*, vol. 148, no. 1, pp. 119–127, 2009.

[5] M. G. Field and J. W. Harbour, "Recent developments in prognostic and predictive testing in uveal melanoma," *Current Opinion in Ophthalmology*, vol. 25, no. 3, pp. 234–239, 2014.

[6] B. Tarlan and H. Kıratlı, "Uveal Melanoma: current trends in diagnosis and management," *Turkish Journal of Ophthalmology*, vol. 46, no. 3, pp. 123–137, 2016.

[7] J. Wu, M. X. Lei, X. Y. Xie et al., "Rosiglitazone inhibits high glucose-induced apoptosis in human umbilical vein endothelial cells through the PI3K/Akt/eNOS pathway," *Canadian Journal of Physiology & Pharmacology*, vol. 87, no. 7, pp. 549–555, 2009.

[8] C. Nalley, "Uveal melanoma: current treatments & new approaches on the horizon," *Oncology Times*, vol. 43, no. 5, pp. 6-7, 2021.

[9] J. Karlsson, L. M. Nilsson, S. Mitra et al., "Molecular profiling of driver events in metastatic uveal melanoma," *Nature Communications*, vol. 11, no. 1, 2020.

[10] C. Brenner and G. Kroemer, "Apoptosis. Mitochondria–the death signal integrators," *Science (New York, N.Y.)*, vol. 289, no. 5482, pp. 1150-1151, 2019.

[11] I. E. Gerard and H. V. Karen, "Proliferation, cell cycle and apoptosis in cancer," *Nature*, vol. 411, no. 6835, pp. 342–348, 2001.

[12] T. J. Fan, L. H. Han, R. S. Cong, and J. Liang, "Caspase family proteases and apoptosis," *Acta Biochimica et Biophysica Sinica*, vol. 37, no. 11, pp. 719–727, 2005.

[13] R. M. Friedlander, "Apoptosis and caspases in neurodegenerative diseases," *New England Journal of Medicine*, vol. 348, no. 14, pp. 1365–1375, 2003.

[14] C. Huang, H. F. Lu, Y. H. Chen, J. C. Chen, W. H. Chou, and H. C. Huang, "Curcumin, demethoxycurcumin, and bisdemethoxycurcumin induced caspase-dependent and –independent apoptosis via Smad or Akt signaling pathways in HOS cells," *BMC Complementary Medicine and Therapies*, vol. 20, no. 1, p. 68, 2020.

[15] E. Jacotot, A. Deniaud, A. Borgne-Sanchez et al., "Therapeutic peptides: targeting the mitochondrion to modulate apoptosis," *Biochimica et Biophysica Acta*, vol. 1757, no. 9-10, pp. 1312–1323, 2006.

[16] N. Zamzami and G. Kroemer, "The mitochondrion in apoptosis: how Pandora's box opens," *Nature Reviews Molecular Cell Biology*, vol. 2, no. 1, pp. 67–71, 2001.

[17] P. Caroppi, F. Sinibaldi, L. Fiorucci, and R. Santucci, "Apoptosis and human diseases: mitochondrion damage and lethal role of released cytochrome c as proapoptotic protein," *Current Medicinal Chemistry*, vol. 16, no. 31, pp. 4058–4065, 2009.

[18] C. Hetz, P. A. Vitte, A. Bombrun et al., "Bax channel inhibitors prevent mitochondrion-mediated apoptosis and protect neurons in a model of global brain ischemia," *Journal of Biological Chemistry*, vol. 280, no. 52, pp. 42960–42970, 2005.

[19] L. Cilenti, M. M. Soundarapandian, G. A. Kyriazis et al., "Regulation of HAX-1 anti-apoptotic protein by Omi/HtrA2 protease during cell death," *Journal of Biological Chemistry*, vol. 279, no. 48, pp. 50295–50301, 2004.

[20] B. Fadeel and E. Grzybowska, "HAX-1: a multifunctional protein with emerging roles in human disease," *BBA - General Subjects*, vol. 1790, no. 10, pp. 1139–1148, 2009.

[21] V. Yedavalli, H. M. Shih, Y. P. Chiang et al., "Human immunodeficiency virus type 1 Vpr interacts with antiapoptotic mitochondrial protein HAX-1," *Journal of Virology*, vol. 79, no. 21, pp. 13735–13746, 2005.

[22] P. A. Bidwell, K. Haghighi, and E. G. Kranias, "The antiapoptotic protein HAX-1 mediates half of phospholamban's inhibitory activity on calcium cycling and contractility in the heart," *The Journal of Biological Chemistry*, vol. 293, no. 1, pp. 359–367, 2018.

[23] U. Baumann, V. Fernández-Sáiz, M. Rudelius et al., "Disruption of the PRKCD-FBXO25-HAX-1 axis attenuates the apoptotic response and drives lymphomagenesis," *Nature Medicine*, vol. 20, no. 12, pp. 1401–1409, 2014.

[24] X. Deng et al., "HAX-1 protects glioblastoma cells from apoptosis through the Akt1 pathway," *Frontiers in Cellular Neuroscience*, vol. 11, p. 420-, 2017.

[25] X. Deng, L. Song, W. Zhao, Y. Wei, and X. B. Guo, "HAX-1 inhibits apoptosis in prostate cancer through the suppression of caspase-9 activation," *Oncology Reports*, vol. 34, no. 5, pp. 2776–2781, 2015.

[26] X. Li, J. Jiang, R. Yang et al., "Expression of HAX-1 in colorectal cancer and its role in cancer cell growth," *Molecular Medicine Reports*, vol. 12, no. 3, pp. 4071–4078, 2015.

[27] C. Y. Huang, U. Batzorig, W. L. Cheng et al., "Glucose-regulated protein 94 mediates cancer progression via AKT and eNOS in hepatocellular carcinoma," *Tumor Biology*, 2016.

[28] H. Zhou, X. Liu, L. Liu et al., "Oxidative stress and apoptosis of human brain microvascular endothelial cells induced by free fatty acids," *Journal of International Medical Research*, vol. 37, no. 6, pp. 1897–1903, 2009.

[29] C. Liang, Y. Ren, H. Tan et al., "Rosiglitazone via upregulation of Akt/eNOS pathways attenuates dysfunction of endothelial progenitor cells, induced by advanced glycation end products," *British Journal of Pharmacology*, vol. 158, no. 8, pp. 1865–1873, 2009.

[30] R. D. Carvajal, J. A. Sosman, J. F. Quevedo et al., "Effect of selumetinib vs chemotherapy on progression-free survival in uveal melanoma: a randomized clinical trial," *Jama the Journal of the American Medical Association*, vol. 311, no. 23, pp. 2397–2405, 2014.

[31] N. Singh, L. Bergman, S. Seregard, and A. D. Singh, "Uveal melanoma: epidemiologic aspects," in *Clinical Ophthalmic Oncology*, pp. 75–87, Springer, Berlin Heidelberg, 2014.

[32] M. Maio, R. Danielli, V. Chiarion-Sileni et al., "Efficacy and safety of ipilimumab in patients with pre-treated, uveal melanoma," *Annals of Oncology Official Journal of the European Society for Medical Oncology*, vol. 24, no. 11, pp. 2911–2915, 2013.

[33] B. Damato, C. Duke, S. E. Coupland et al., "Cytogenetics of uveal melanoma," *Ophthalmology*, vol. 114, no. 10, pp. 1925–1931.e1, 2007.

[34] S. Desagher and J. C. Martinou, "Mitochondria as the central control point of apoptosis," *Trends in Cell Biology*, vol. 10, no. 9, pp. 369–377, 2000.

[35] Y. A. Chelyshev, G. V. Cherepnev, and K. I. Saitkulov, "Apoptosis in the nervous system," *Russian Journal of Developmental Biology*, vol. 32, no. 2, pp. 92–102, 2001.

[36] S. W. Lowe and A. W. Lin, "Apoptosis in cancer," *Carcinogenesis*, vol. 21, no. 3, pp. 485–495, 2000.

[37] X. J. Wei, S. Y. Li, B. Yu, G. Chen, J. F. Du, and H. Y. Cai, "Expression of HAX-1 in human colorectal cancer and its clinical significance," *Tumor Biology*, vol. 35, no. 2, pp. 1411–1415, 2014.

[38] Y. Wang, X. Huo, Z. Cao et al., "HAX-1 is overexpressed in hepatocellular carcinoma and promotes cell proliferation," *International Journal of Clinical and Experimental Pathology*, vol. 8, no. 7, pp. 8099–8106, 2015.

[39] J. Dörrie, H. Gerauer, Y. Wachter, and S. J. Zunino, "Resveratrol induces extensive apoptosis by depolarizing mitochondrial membranes and activating caspase-9 in acute lymphoblastic leukemia cells," *Cancer Research*, vol. 61, no. 12, pp. 4731–4739, 2001.

Hindawi
Journal of Oncology
Volume 2022, Article ID 7981711, 14 pages
https://doi.org/10.1155/2022/7981711

Research Article

PITPNA-AS1/miR-98-5p to Mediate the Cisplatin Resistance of Gastric Cancer

Zhongling Ma,[1] **Gang Liu**,[2] **Suhong Hao**,[2] **Tianfu Zhao**,[2] **Wei Chang**,[2] **Jiansheng Wang**,[3] **Hong Ren**,[3] **and Xinhan Zhao**[1]

[1]*Department of Oncology, The First Affiliated Hospital of Xi'an Jiaotong University, 277 West Yanta Road, Xi'an, 710061 Shaanxi Province, China*
[2]*Department of Oncology, Xi'an Chang'an District Hospital, No. 120 Wenyuan Middle Road, Chang'an District, Xi'an, 710100 Shaanxi Province, China*
[3]*Department of Surgical Thoracic, The First Affiliated Hospital of Xi'an Jiaotong University, 277 West Yanta Road, Xi'an, 710061 Shaanxi Province, China*

Correspondence should be addressed to Hong Ren; renhong@xjtu.edu.cn and Xinhan Zhao; zhaoxinhan@mail.xjtu.edu.cn

Received 7 January 2022; Revised 7 March 2022; Accepted 23 March 2022; Published 7 May 2022

Academic Editor: Guo Chen

Gastric cancer (GC) is the most deadly gastrointestinal malignancy with high incidence and mortality. Although, molecular mechanisms which drive gastric cancer progression are extensively investigated, the roles of long noncoding RNA (lncRNA) in gastric cancer growth and drug sensitivity remain unclear. Platinum is a mainstay to treat gastric cancer, and platinum resistance always leads to the local recurrence of gastric cancer. Therefore, it is important to identify biomarkers or therapeutic targets to sensitize gastric cancer to platinum. In this study, we employ noncoding RNA sequencing and found that lncRNA PITPNA-AS1 is overexpressed in gastric cancer tissues and associated with poor survival of gastric cancer patients. Kockdown of PITPNA-AS1 in gastric cancer cells significantly inhibited cell growth and triggered apoptotic cell death in gastric cancer cells. Also, cisplatin treatment could decrease PITPNA-AS1 levels in gastric cancer cells through inhibiting H3K27ac. Besides, PITPNA-AS1 is elevated in cisplatin-resistant gastric cancer cells and tissues, PITPNA-AS1 knockdown could sensitize gastric cancer cells to cisplatin treatment. Furthermore, we identified that PITPNA-AS1 directly interacts and inhibits miR-98-5p. Therefore, PITPNA-AS1 could be served as a potential biomarkers and curative therapeutic targets for gastric cancer progression.

1. Introduction

Gastric cancer (GC) is the fourth most commonly diagnosed cancer and the second most common cancer-related mortality globally, with approximately 738,000 people died of GC each year worldwide [1, 2]. Despite the remarkable progressive improvement in surgical and medical techniques, prognosis of patients with GC remains relatively poor, mainly due to its high recurrence and metastasis incidence [3]. Neoadjuvant chemotherapy improves overall survival of GC patients in comparison to traditional chemotherapy or surgery alone. 5-Fluorouracil combined with cisplatin has been convincingly proved survival benefits for HER-2-positive patients [4–6]. As the main chemotherapy treatment for postoperative GC patients, the efficacy of platinum has been largely limited due to the chemo-resistance [7]. Laboratory studies illustrated that resistance to platinum is almost multifactorial, which includes impaired cellular uptake of platinum drug [8], reinforced endocellular detoxification by glutathione and metallothionein systems [9], enhanced DNA repair capacity, enhanced tolerance to DNA damage [10], and rising restore of DNA damage [8, 11].

Long noncoding RNAs (LncRNAs) are a class of noncoding RNAs longer than 200 nt without protein coding potential. Several lncRNAs were confirmed as biotargets for modulating cisplatin resistance in cancer through the cell cycle, apoptosis, and Wnt pathways [12], which acts as a competing endogenous RNA or directly binding to mRNAs

or proteins and regulating their expression and functions [13]. LncRNA PITPNA antisense RNA 1 (PITPNA-AS1) is located in chromosome 17p13.3, with the function of regulating cell growth and motility of hepatocellular carcinoma via miR-876-5p/WNT5A pathway, which was affirmed by rescue and in vivo experiments [14]. Furthermore, PITPNA-AS1 was found to be involved in promoting EMT process to promote proliferation and metastasis of non-small-cell lung cancer. Based on the fact that EMT is an important mechanism for regulating platinum resistance, we hypothesized that PITPNA-AS1 took part in mediating platinum resistance as well.

MiRNAs are another type of noncoding RNAs with 19-24 nt in length, which could posttranscriptionally repress gene expression via binding to the 3′-untranslated region (3′-UTR) of mRNA [15]. Wei et al. summarized expression levels and potential targets of 53 microRNAs (miRNAs) which participated in platinum resistance of gastric cancer [16]. It has been reported that several oncogenic miRNAs can promote platinum resistance of gastric cancer, such as miR-20a [17] and miR-106a [18], while tumor suppressive miRNAs can reverse platinum resistance, such as miR-508p [19] and miR-129-5p [20]. As a valid tumor suppressor, microRNA-98-5p (miR-98-5p), which is one member of let-7 family, is usually downregulated in various cancers, such as nasopharyngeal carcinoma [21] and endometrial cancer [22]. But increased expression of miR-98-5p has been observed in primary breast cancer swatches [23]. Perhaps miR-98 has completely opposite obligation in different types of cancers. A series of assays have elucidated that MiR-98-5p was expressed significantly lower in pancreatic ductal adenocarcinoma tissues compared with normal tissue and its expression was highly associated with tumor size, TNM stage, lymph node metastasis, and survival. And it could negatively regulate MAP4K4 and inhibit MAPK/ERK signaling [24]. Until now, few studies implemented the function of miR-98-5p in GC.

Although recent advanced studies identify molecular elements of GC, the precise mechanisms of tumourigenesis remain largely unknown [25]. Therefore, the clarification of new pathogenesis is vital for practical targeted treatment for GC; many studies verified that lncRNA and miRNA played vital functions in the development and therapeutic resistance of cancers and their aberrant expression emerged as important hallmarks of multiple cancers [26–28]. However, few studies reported the molecular mechanisms of PITPNA-AS1 and miR-98-5p in GC, especially when it comes to their relationship with platinum resistance. Thus, we investigate the role of PITPNA-AS1 and miR-98-5p in GC and their connection with platinum resistance.

2. Results

2.1. RNA Sequencing for lncRNA and MicroRNA in 3 Gastric Cancer Patients. To identify the differentiated expression noncoding RNA (ncRNA) in cisplatin sensitive and cisplatin resistant gastric cancer tissues, we have performed ncRNA sequencing including lncRNA and microRNA using gastric cancer tissue (cisplatin sensitive vs. resistant). The top 20 upregulated lncRNAs and microRNAs including PITPNA-AS1 are shown in Figure 1. Elevated expression of PITPNA-AS1 was previously detected in gastric cancers; our ncRNA sequencing further showed that PITPNA-AS1 was downregulated in cisplatin resistant gastric cancer. To identify the downstream effector of PITPNA-AS1, we used DIANA on-line software, which is a website-based tool to prediction miRNA-lncRNA interactions, and found that miR-98-5p might be the target of PITPNA-AS1.

2.2. PITPNA-AS1 Expression Was Correlated with Local Recurrence in Gastric Cancer Patients. To further confirm the PITPNA-AS1 expression in gastric cancer tissues compared with their matched normal tissue, we have measured PITPNA-AS1 expression in 153 gastric cancer tissues compared with para-cancer tissues and found that PITPNA-AS1 was significantly increased cancer tissues; meanwhile, the level of its putative target miR-98-5p significantly downregulated in cancer tissues (Figures 2(a) and 2(b)). In addition, the patients' survival analysis showed that the high expression of PITPNA-AS1 was associated with poor survival (Figure 2(c)). On the contrary, the high level of miR-98-5p was associated with better overall survival (Figure 2(d)). Besides, the expression of PITPNA-AS1 was negatively correlated with miR-98-5p expression in gastric cancer tissues (Figure 2(e)). Furthermore, significant higher level of PITPNA-AS1 has been detected in local recurrent gastric cancer patients compared with non-recurrent cancer tissues, while miR-98-5p was downregulated in local recurrent gastric cancer tissues (Figures 2(f) and 2(g)).

2.3. PITPNA-AS1/miR-98-5p Regulated Cell Proliferation and Inhibits Apoptosis in Gastric Cancer Cell Lines. Next, we measured the PITPNA-AS1 levels in gastric cancer cells, and found that PITPNA-AS1 was overexpressed in human gastric cancer cell lines including MKN45 and AGS, but not in in normal gastric mucosal cell line GES-1 (Figure 3 (a) and Sup Figure 1). Meanwhile the expression of miR-98-5p was lower in MKN45 and AGS than that in GSE-1 cell line (Figure 3(b)). To investigate the biological roles of PITPNA-AS1 in gastric cancer, knocked down the expression of PITPNA-AS1 in MKN45 and AGS cells (Sup Figures 2a and 2b), and found that silence of PITPNA-AS1 significantly inhibited cancer cell proliferation (Figures 3(c) and 3(d)). Also, PITPNA-AS1 knockdown caused apoptotic cell death in MKN45 and AGS cells, as evidenced by significant increased caspase 3/7 activity. In contrast with PITPNA-AS1, ectopic expression of miR-98-5p (Sup Figures 2c and 2d) could significantly decreased cell proliferation rate and enhanced cell apoptosis rate (Figures 3(g)–3(j)).

2.4. PITPNA-AS1 Negatively Regulated the Expression of miR-98-5p. To validate whether miR-98-5p could be the target of PITPNA-AS1, we examined the miR-98-5p expression after PITPNA-AS1 knockdown and found that silence of PITPNA-AS1 significantly increased the level of miR-98-5p (Figures 4(a) and 4(b)). Then, we performed dual luciferase

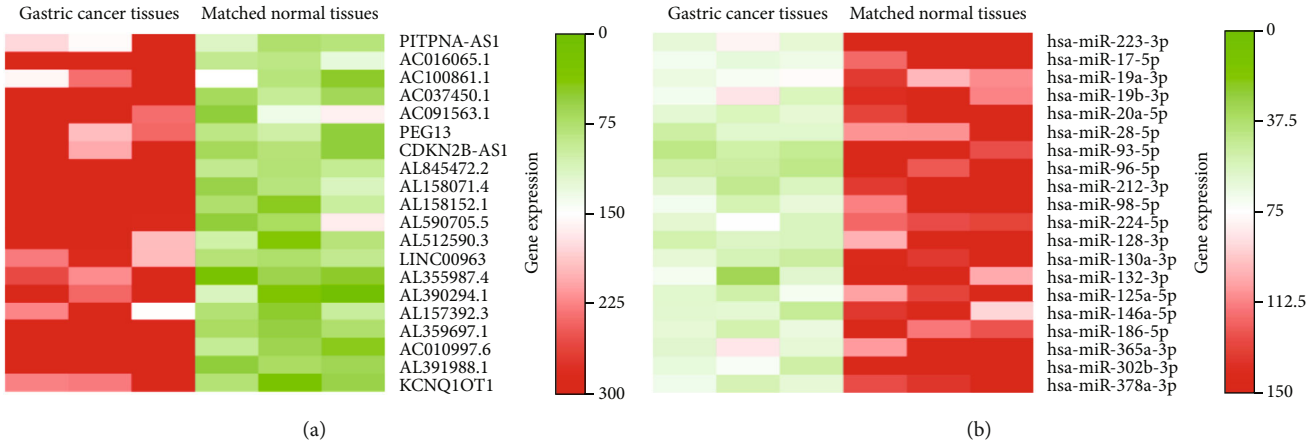

Figure 1: RNA sequencing for lncRNA and microRNA in 3 gastric cancer patients. (a) Heatmap based on the lncRNA NGS between gastric cancer and matched normal tissues to show the top 20 differentially expressed genes. (b) Heatmap based on the microRNA NGS between gastric cancer and matched normal tissues to show the top 20 differentially expressed microRNAs in gastric cancer.

reporter gene assay and found that PITPNA-AS1 was associated with miR-98-5p in cell (Figures 4(c) and 4(d)). We further performed *in vitro* RNA pulldown assay and found that PITPNA-AS1 directly interacted with miR-98-5p (Figures 4(e) and 4(f)).

2.5. PITPNA-AS1 Expression Can Be Suppressed by Cisplatin in Gastric Cancer Cell Lines. PITPNA-AS1 was decreased in the cisplatin-resistant gastric cancer tissues; we then examined whether cisplatin treatment whether could affect PITPNA-AS1 expression. As shown in Figure 5(a), the half maximal inhibitory concentration (IC50) of CDDP in MKN45 is 0.52μg/mL and the IC50 in AGS is 0.59 μg/mL (Figure 5(b)). We used CDDP (0.52 μg/mL) to treat MKN45 and CDDP (0.59 μg/mL) to treat AGS cells for 24 hours and found that PITPNA-AS1 expression can be significantly suppressed after cisplatin treatment (Figures 5(c) and 5(d)).

In the meantime, we also detected that CDDP treatment could significantly increase expression of miR-98-5p in MKN45 (0.52 μg/mL) and in AGS cells (0.59 μg/mL) (Figures 5(e) and 5(f)). To study the mechanism which leads to PITPNA-AS1 downregulation during cisplatin treatment, we examined H3K27ac levels after cisplatin treatment, since H3K27ac is a well-established marker for active enhancers and promoters. As shown in Figure 5(g), we found that H3K27ac expression was significantly suppressed in MKN45 and AGS cells when treated with CDDP.

2.6. PITPNA-AS1/miR-98-5p Regulated by H3K27ac Influenced the Effect of Platinum. We have generated cisplatin-resistant MKN45 cells (MKN45-CDDPR), the IC50 of which is 2.60 μg/mL, which MKN45 parental cell has a IC50 of 0.59μg/mL (Figure 6(a)). Then, we checked PITPNA-AS1 expression in MKN45 parental and cisplatin resistant cells, and we found that PITPNA-AS1 was overexpressed in MKN45-CDDPR compared with parental cells (Figure 6(b)); meanwhile, we also detected that miR-98-5p was downregulated in cisplatin-resistant cells (Figure 6(c)).

Furthermore, we also found that H3K27ac was upregulated in MKN45-CDDPR cells (Figure 6(d)), which could be significantly suppressed by cisplatin treatment (Figure 6(e)). Furthermore, Chip assay showed that H3K27ac enriched more in the promotor region of PITPNA-AS1 in MKN45-CDDPR cells than in parental cells (Figures 6(f) and 6(g)). By treating with C646, the expression of PITPNA-AS1 in MKN45-CDDPR could be significantly suppressed (Figure 6(h)). Then, we transfected PITPNA-AS1-WT plasmids and found that PITPNA-AS1 knock down could suppress IC50 of MKN45-CDDPR, which could be reversed by miR-98-5p knock down (Figure 6(i)).

3. Discussion

Collectively, in this study, we discovered the role of PITPNA-AS1 and miR-98-5p in gastric cancer through gain and loss-of-function assays and analyzed the mechanism by which PITPNA-AS1 regulates apoptosis and drug resistance through the miR-98-5p targeting axis.

Gastric cancer is one of the leading public health problems worldwide because of its high incidence, morbidity, and mortality rate [29]. Currently, lacking of screening methods and early symptom, patients are most often diagnosed at advanced stages, with metastatic at distant sites and somber prognosis (median overall survival is 10-12 months) [30, 31]. For locally advanced disease, adjuvant or neoadjuvant therapy which recognized as the optimal therapeutic option is usually introduced with surgery owing to its curability [30]. Fluoropyrimidine plus oxaliplatin doublet is considered as the preferred first-line regimen due to its comparable survival benefits and lower toxicity [32]. Overcoming resistance is still a challenge in GC chemotherapy.

LncRNAs are associated with the tumor recurrence and poor prognosis, and abnormal expression has been observed in various tumors [33]. Mounting evidence elucidated that lncRNAs could act as oncogenes or tumor suppressors by modulating the gene expression or function in tumorigenesis [34], which possibly induce significant influence on the

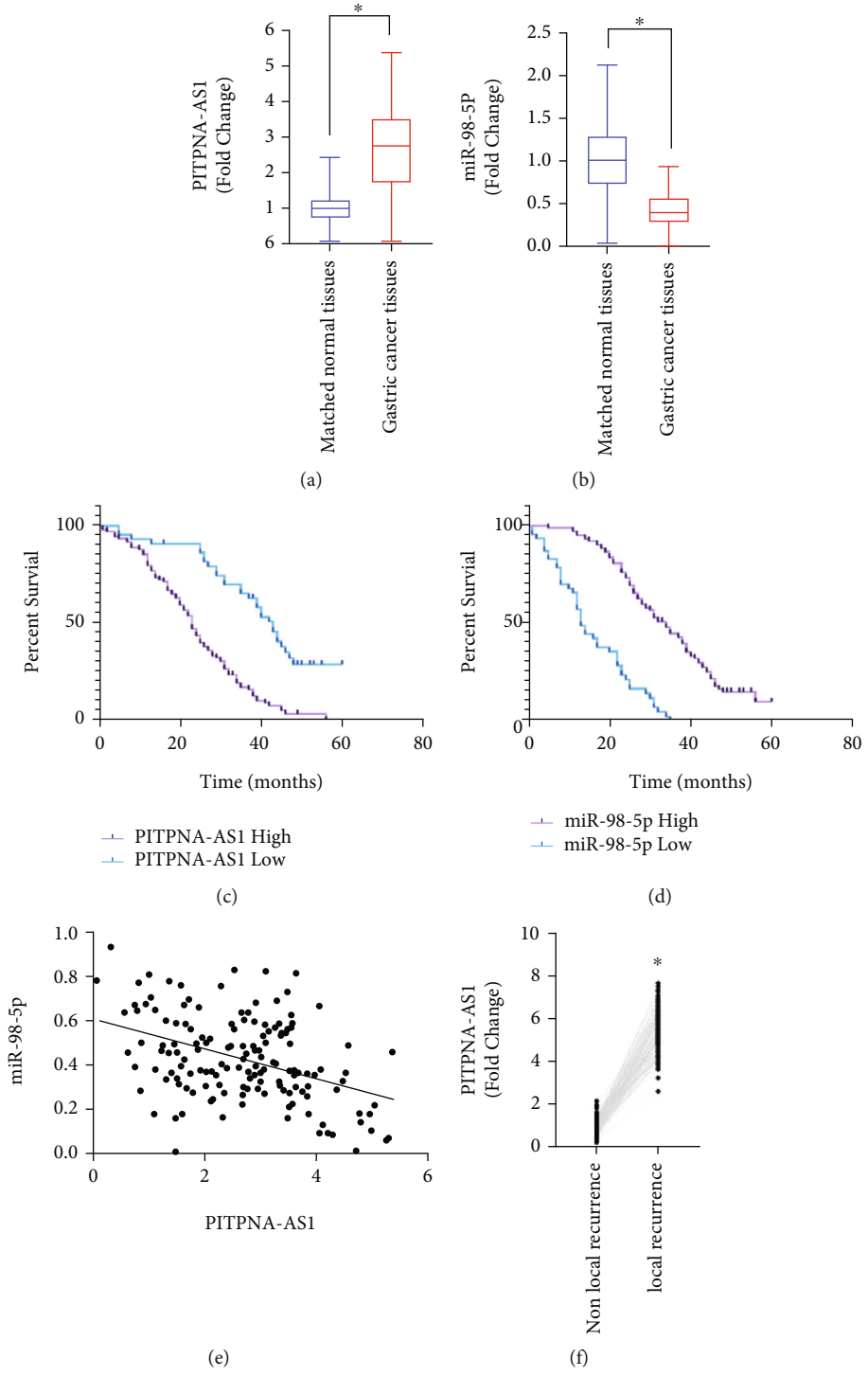

Figure 2: Continued.

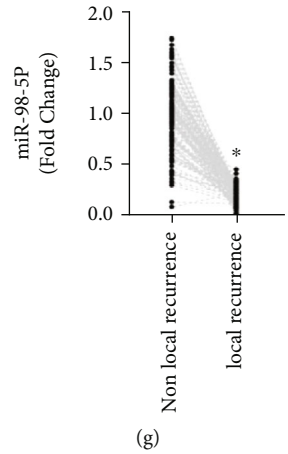

Figure 2: PITPNA-AS1 expression was correlated with local recurrence in gastric cancer patients. (a) PITPNA-AS1 expression was measured using qRT-PCR method in gastric cancer tissues compared with matched normal tissues. (b) miR-98-5p expression was measured using qRT-PCR method in gastric cancer tissues compared with matched normal tissues. (c) Survival analysis shown as KM-plot for PITPNA-AS1 high-expression group and low-expression group in gastric cancer patients. (d) Survival analysis shown as KM-plot for miR-98-5p high-expression group and low-expression group in gastric cancer patients. (e) The correlation of PITPNA-AS1 and miR-98-5p based on qRT-PCR method in gastric cancer patients. (f) PITPNA-AS1 expression was measured by qRT-PCR in gastric cancer patients stratified by local recurrence and nonlocal recurrence. (g) miR-98-5p expression was measured by qRT-PCR in gastric cancer patients stratified by local recurrence and nonlocal recurrence.

alterations of cell proliferation, metastasis, autophagy, and apoptosis [35, 36]. Our study indicated that lncRNA PITPNA-AS1 was highly expressed in gastric cancer patients and was associated with poor prognosis. Alteration of gene expression is correlated with the cancer specific survival of patients. PITPNA-AS1 was overexpressed in MKN45 cell line while knocking down PITPNA-AS1 resulted in inhibiting cell proliferation rate and increasing apoptosis rate. We first time inspected the role of PITPNA-AS1 in GC, which founding the basis for further exploration.

Next, we investigated the potential mechanism underlying PITPNA-AS1. Biased on current study, mechanism assays unveiled that PITPNA-AS1 targeted miR-98-5p. Dual-luciferase reporter gene assay, RNA pull-down assay, and RIP consequence provided powerful evidence that PITPNA-AS1 could interact with miR-98-5p. Moreover, knocking down of PITPNA-AS1 resulted in decreased expression of miR-98-5p, which confirmed this discovery again. The antitumor function of miR-98-5p has been documented yet. For instances, Fu et al. recognized miR-98-5p underexpression as biomarkers for predicting poor prognosis in pancreatic ductal adenocarcinoma (PDAC) patients because miR-98-5p inhibits proliferation and metastasis via targeting MAP4K4 [24]. Acting as a tumor suppressor, miR-98 could decelerate cancer aggressiveness by inhibiting TWIST expression in non-small-cell lung cancers [37]. In hepatocellular carcinoma (HCC), miR-98-5p could restrain cell proliferation and induce cell apoptosis via inhibition of its target gene IGF2BP1 [38]. As for colon cancer, miR-98 plays the role of tumor suppressor gene and inhibits Warburg effect by targeting HK2 (HK2 involves in miR-98-mediated suppression of glucose uptake, lactate production, and cell proliferation, whose expression was negatively correlated with miR-98) in colon cancer cells, which provided promising therapeutic candidate for clinical treatments [39].

In our study, miR-98-5p was shown to be downregulated in GC. Overexpression of miR-98-5p led to decreased cell proliferation rate and ascended apoptosis rate. Moreover, inhibition of miR-98-5p partially reversed the inhibitory effects of PITPNA-AS1 on GC cell proliferation and apoptosis. Thus, we draw the conclusion that PITPNA-AS1 exerts its tumor-promotion effect in GC via negatively modulating the expression of miR-98-5p. Laboratory findings were consistent with literature reports. Guo et al. revealed that lncRNA PITPNA-AS facilitates the cervical cancer progression on the proliferation, cell cycle, and apoptosis by targeting the miR-876-5p/c-MET axis [40].

It is well-established that aberrant lncRNA expression is strongly implicated in drug resistance in some cancers [41, 42]. Our experiments uncovered that cisplatin (CDDP) and lobaplatin (LBP) could suppress PITPNA-AS1 expression and induce expression of miR-98-5p in GC cell lines. Besides, PITPNA-AS1 was overexpressed in MKN45-CDDPR and MKN45-LBPR, which could confer GC cell resistance to platinum drugs, compared with their parental cells. However, miR-98-5p has the opposite effects. Furthermore, PITPNA-AS1-WT could reverse the inhibitory effect of platinum. These data demonstrated that PITPNA-AS1/miR-98-5p had a major role in regulating platinum-resistant in GC cells. Consistent with aforementioned findings, Wang's studies have identified that elevated expression of miR-98-5p is associated with resistance to cisplatin treatment through directly targeting Dicer1 and poor clinical outcomes in epithelial ovarian cancer patients [43]. Guo's studies have illustrated that cancer-associated fibroblast-derived exosomal who carrying overexpressed miR-98-5p promoted cisplatin resistance in ovarian cancer by

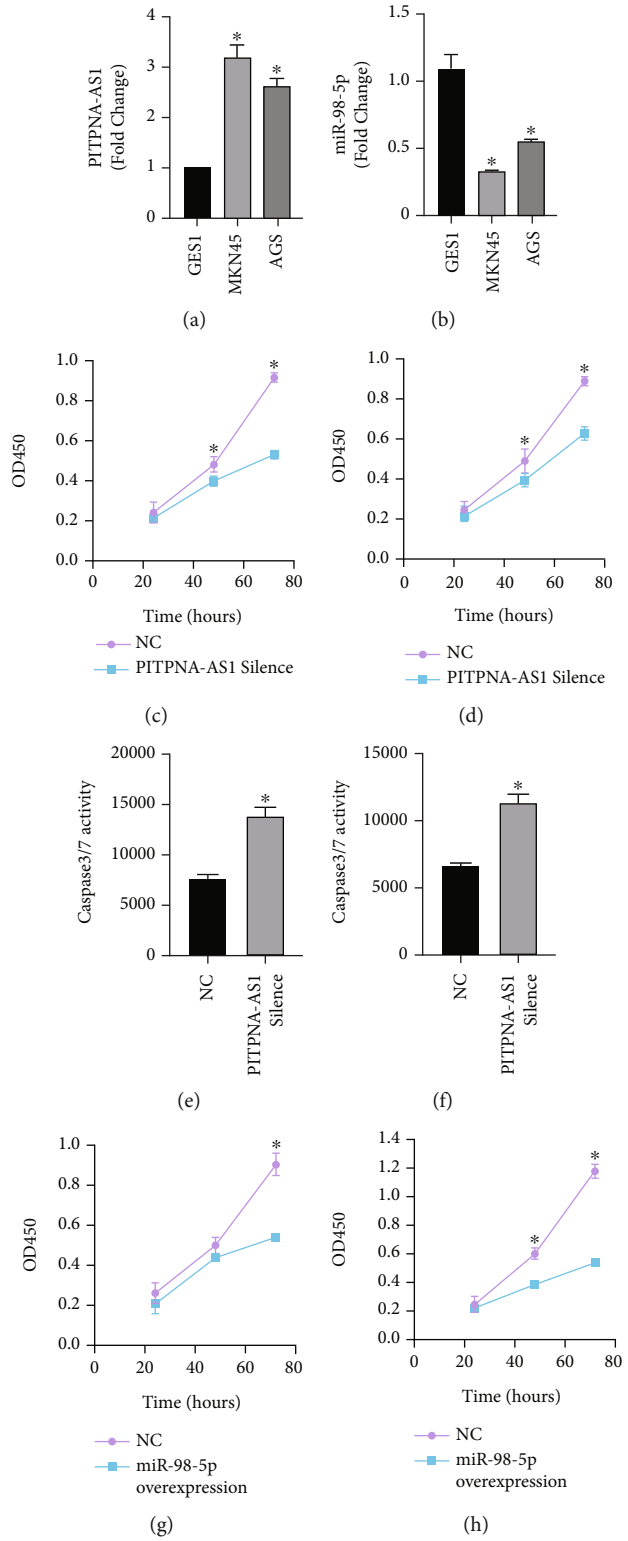

Figure 3: Continued.

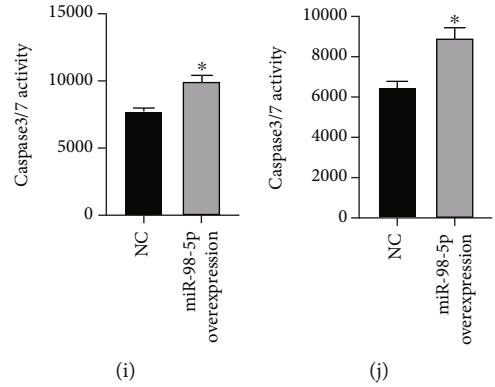

Figure 3: PITPNA-AS1/miR-98-5p regulated cell proliferation and inhibits apoptosis in gastric cancer cell lines. (a) PITPNA-AS1 expression was measured by qRT-PCR in gastric cancer cells, MKN45 and AGS compared with normal gastric cell GES1. (b) miR-98-5p expression was measured by qRT-PCR in gastric cancer cells, MKN45 and AGS compared with normal gastric cell GES1. (c) Cell viability was measured by CCK-8 assay for PITPNA-AS1 silence AGS cells and negative control plasmids transduced AGS cells. (d) Cell viability was measured by CCK-8 assay for PITPNA-AS1 silence MKN45 cells and negative control plasmids transduced MKN45 cells. (e) Apoptosis was measured by caspase 3/7 activity kit for PITPNA-AS1 silence AGS cells and negative control plasmids transduced AGS cells. (f) Apoptosis was measured by caspase 3/7 activity kit for PITPNA-AS1 silence MKN45 cell line and negative control plasmids transduced MKN45 cells. (g) Cell viability was measured by CCK-8 assay for miR-98-5p overexpression AGS cells and negative control plasmids transduced AGS cells. (h) Cell viability was measured by CCK-8 assay for miR-98-5p overexpression MKN45 cells and negative control plasmids transduced MKN45 cells. (i) Apoptosis was measured by caspase 3/7 activity kit for miR-98-5p overexpression AGS cells and negative control plasmids transduced AGS cells. (j) Apoptosis was measured by caspase 3/7 activity kit for miR-98-5p overexpression MKN45 cells and negative control plasmids transduced MKN45 cells.

downregulating CDKN1A [44]. An existing study has revealed that miR-129 could enhance chemosensitivity to cisplatin by suppressing P-gp protein in GC cells [45].

Conjointly, these results suggest that miR-98-5p could be served as a novel prognostic factors and critical therapeutic target in GC by enhancing chemo-sensitivity for platinum treatment against GC. However, downstream signal molecule and other biological processes are required further investigation.

4. Materials and Methods

4.1. Gastric Cancer Patients. The GC tissues and local recurrence GC tissues, as well as the corresponding para-cancer tissues, were collected from the patients who were diagnosed as GC by surgical resection at the First Affiliated Hospital of Xi'an Jiao Tong University. All patients were treated with 800 mg/m^2 fluorouracil (civ 24 h, d1~5) and 80 mg/m^2 cisplatin (ivgtt, d1) for 2 cycles before surgery and 2-4 cycles after surgery. Routine blood test and chest and abdominal CT were performed every 2 months during the follow-up. Local recurrence was determined based on the CT results. All of the samples were pathologically diagnosed and stored in liquid nitrogen. All of the patients had signed a written informed consent. The present study gained approval from the Ethics Committee of The First Affiliated Hospital of Xi'an Jiao tong University. And all experiments were conducted in accordance with relevant guidelines and regulations, which is consistent with the Declaration of Helsinki regulations.

4.2. Cell Culture. The human GC cell lines MKN45 and AGS were purchased from Shanghai Gaining Biological Technology Co., Ltd. (Shanghai, China), and the human gastric epithelial cell line GES-1 was obtained from American Type Culture Collection (Virginia, USA). All the cells were cultured in DMEM medium (HyClone, USA) containing 10% fetal bovine serum (Gibco, USA) and 1% penicillin-streptomycin (HyClone, USA) in a 37°C and 5% CO2 incubator. The GC cells were then treated with continuous low-dose of cisplatin in a stepwise manner to developed cisplatin resistant GC (MKN45-CDDPR) cells.

4.3. Cell Transfection. The PITPNA-AS1 knockdown and miR-98-5p overexpression plasmids were purchased from GeneChem (Shanghai, China). The above plasmids were delivered into MKN45 and AGS cell lines by using the Lipofectamine 3000 (Invitrogen, Carlsbad, CA, USA) reagent according to the manufacturer's instruction.

4.4. RNA Sequencing. The RNA sequencing process was guided and supported by GeneChem (Shanghai, China). In brief, total RNA was extracted from 3 GC patients' tissues and corresponding normal tissues by using TRIzol (Invitrogen, Carlsbad, CA). And the RNA purification was performed by using the RNA Clean XP Kit (Beckman Coulter, Kraemer Boulevard Brea, CA) and the RNase-Free DNase Set (QIAGEN, GmbH, Germany). Finally, the Illumina HiSeq 2000/2500 (Illumina Inc., San Diego, CA) was used for RNA sequencing.

4.5. qRT-PCR. Total RNA was extracted from GC tissues and cell lines by using Trizol reagent (Invitrogen, Carlsbad, CA, USA). The cDNA was generated by using the first-strand cDNA synthesis kit (Tiangen Biotech, Beijing, China). The expression levels of PITPNA-AS1 was tested by conducting

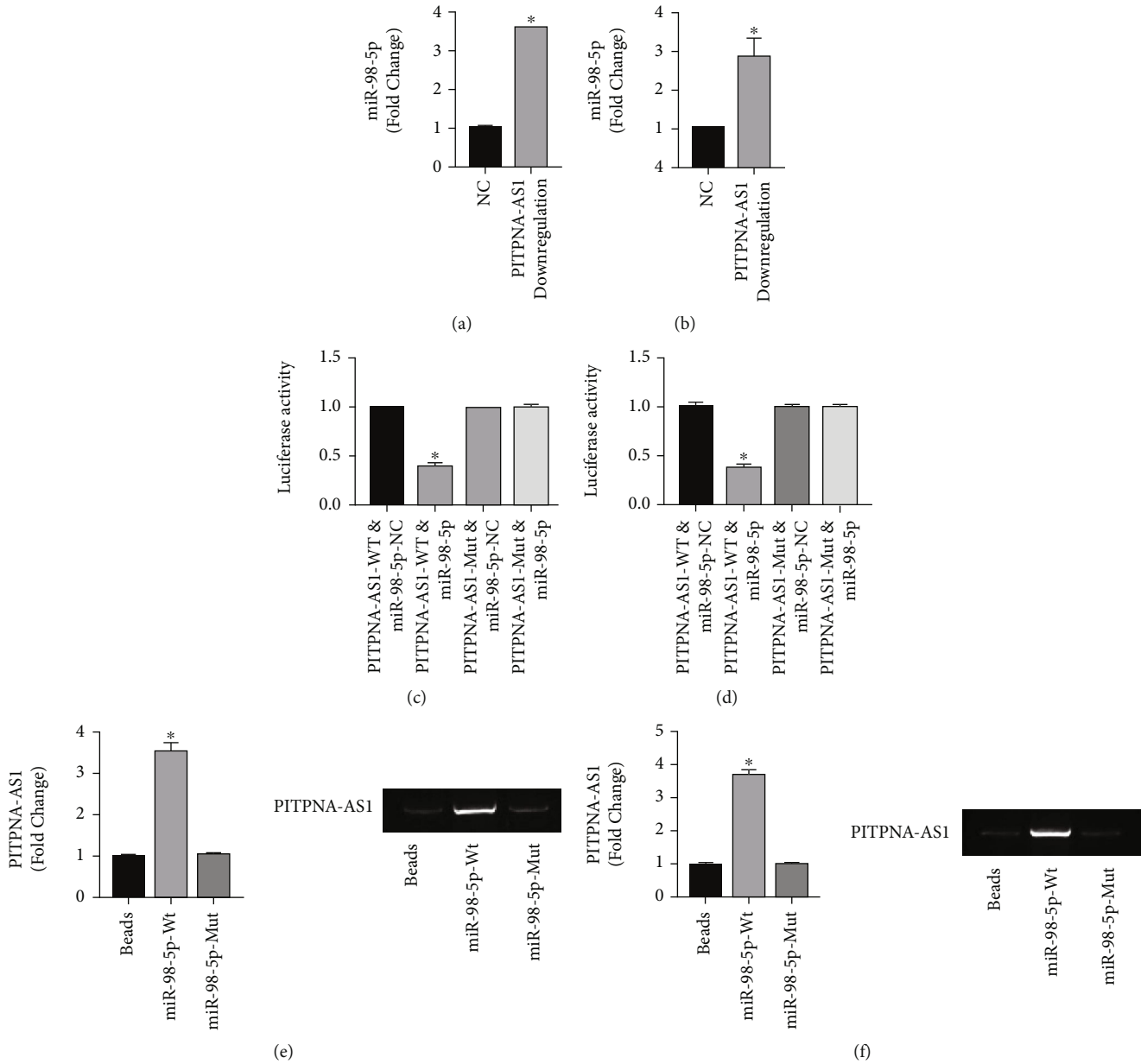

Figure 4: PITPNA-AS1 negatively regulated the expression of miR-98-5p. (a) miR-98-5p expression was measured by qRT-PCR in PITPNA-AS1 silence AGS cells. (b) miR-98-5p expression was measured by qRT-PCR in PITPNA-AS1 silence MKN45 cells. (c) Dual-luciferase reporter gene assay was used to investigate the interaction between miR-98-5p and PITPNA-AS1 in AGS cell line. (d) Dual-luciferase reporter gene assay was used to investigate the interaction between miR-98-5p and PITPNA-AS1 in MKN45 cell line. (e) RNA pull down assay following qRT-PCR and PCR agarose gel electrophoresis was used to investigate the interaction between miR-98-5p and PITPNA-AS1 in AGS cell line. (f) RNA pull down following qRT-PCR and PCR agarose gel electrophoresis was used to investigate the interaction between miR-98-5p and PITPNA-AS1 in MKN45 cell line.

qRT-PCR using SYBR® Premix Dimer Eraser kit (Takara Shiga, Japan). And β-actin was used as the inner reference. The miScript microRNA RT PCR kit (Qiagen, Toronto, ON, Canada) was used for cDNA synthesis and qRT-PCR process for miR-98-5p expression. U6 was used as the internal reference. ABI 7500 Real-Time PCR system (Applied Biosystems, Carlsbad, CA, USA) was conducted to perform the qRT-PCR process. The expression level was calculated by $2 - \Delta\Delta$Ct method.

4.6. Western Blot. The total proteins were extracted from GC cells by using RIPA lysis buffer (Sigma-Aldrich, Darmstadt, Germany) and were quantified by BCA Protein Assay Kit (Beyotime, Shanghai, China). Then, proteins were diverted onto PVDF membranes (Millipore, USA) after separated by SDS-PAGE. The transferred PVDF membranes were blocked by using 5% skim milk and then were incubated overnight at 4°C with primary antibodies, which is including H3K27ac (1 : 1000, CST, Shanghai,

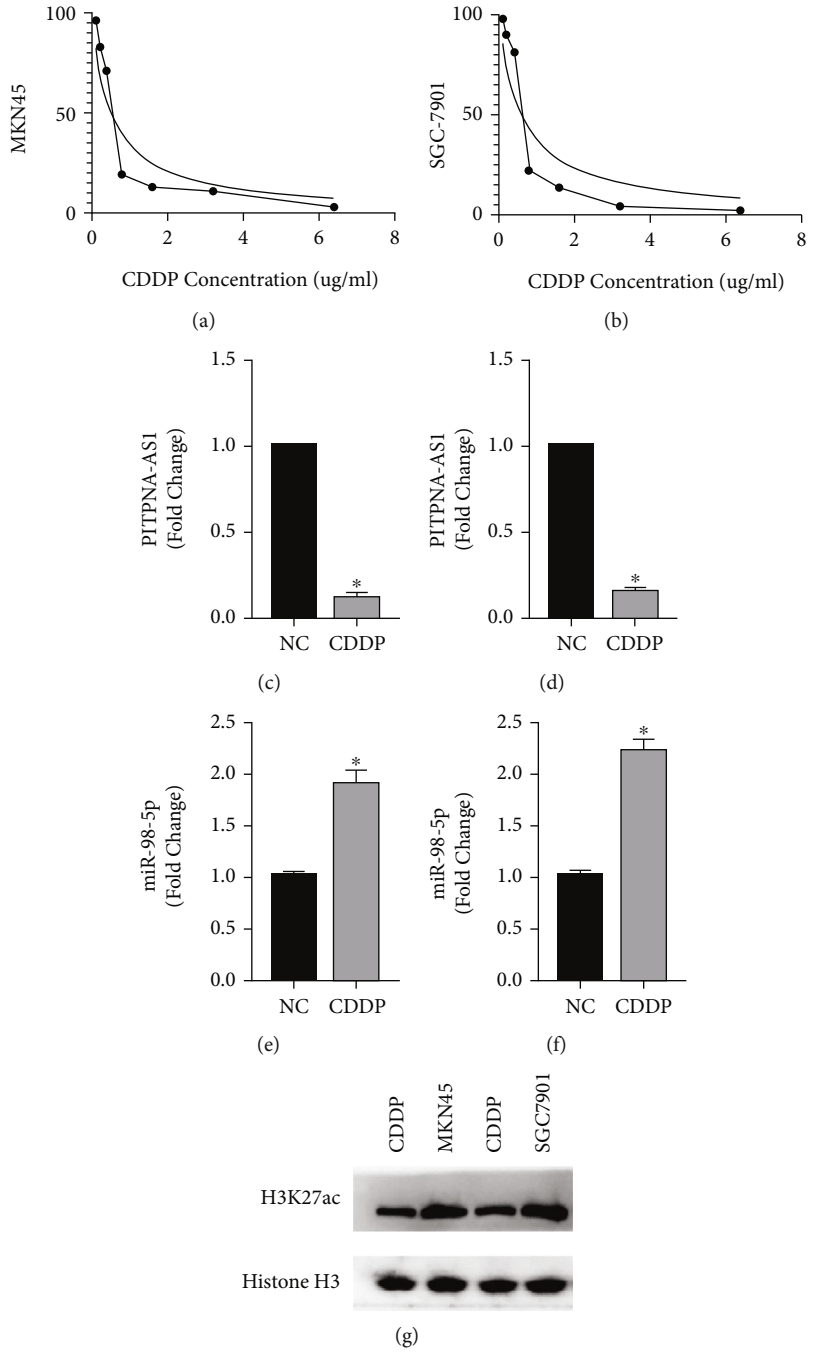

Figure 5: PITPNA-AS1 expression can be suppressed by cisplatin in gastric cancer cell lines. (a) IC50 of AGS to CDDP was detected by CCK-8 assay. (b) IC50 of MKN45 to CDDP was detected by CCK-8 assay. (c) CDDP suppressed PITPNA-AS1 expression, which was measured by qRT-PCR, in AGS cell line. (d) CDDP, which was measured by qRT-PCR, suppressed PITPNA-AS1 expression in MKN45 cell line. (e) CDDP induced miR-98-5p expression, which was measured by qRT-PCR, in AGS cell line. (f) CDDP induced miR-98-5p expression, which was measured by qRT-PCR, in MKN45 cell line. (g) CDDP suppressed H3K27ac expression, which was measured by Western blot, in MKN45 and AGS cell lines.

China) and Histone H3 (1 : 2000, CST, Shanghai, China). Subsequently, the membranes were incubated with the secondary antibody (1 : 10000, Beyotime, Shanghai, China). Then, the enhanced chemiluminescence (ECL, Beyotime, Shanghai, China) was used to quantify the protein expression levels.

4.7. Cell Proliferation. In order to evaluate the proliferation and cisplatin resistance of GC cells, the cell counting kit-8 (CCK-8) kit (AbMole, USA) was used according to the manufacturer's protocol. Briefly, GC cells were seeded in 96-well plates with a density of 5×10^3 cells per well, then 10 μL of CCK-8 reaction solution was supplemented into each well

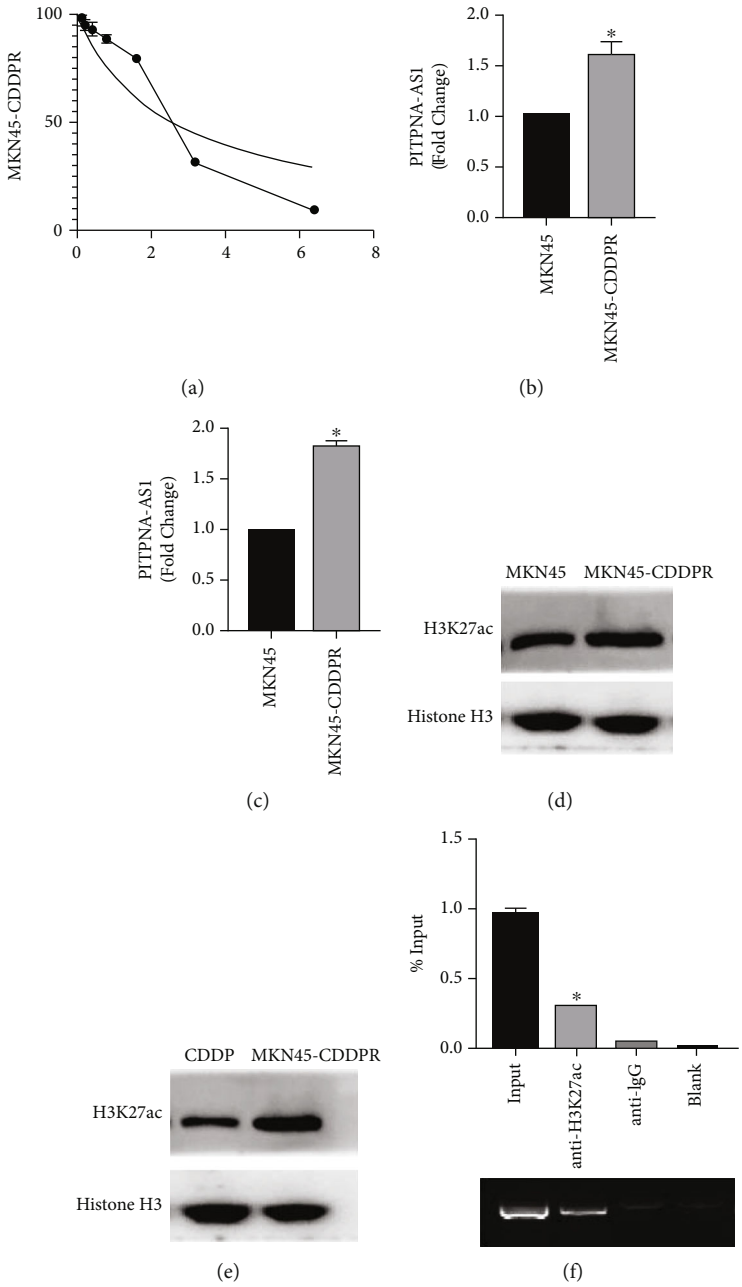

Figure 6: Continued.

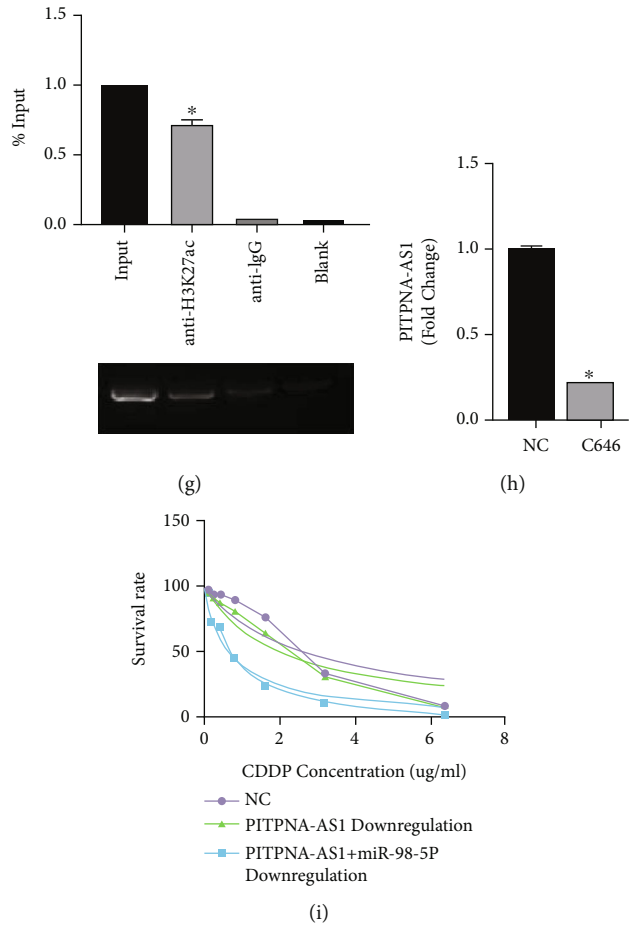

Figure 6: PITPNA-AS1/miR-98-5p regulated by H3K27ac influenced the effect of platinum. (a) IC50 of MKN45-CDDPR to CDDP was detected by CCK-8 assay. (b) PITPNA-AS1 expression, which was measured by qRT-PCR, in MKN45-CDDPR cell line was detected by CCK-8 assay. (c) miR-98-5p expression, which was measured by qRT-PCR, in MKN45-CDDPR cell line. (d) H3K27ac expression, which was measured by Western blot, in MKN45-CDDPR cell line. (e) CDDP suppressed the H3K27ac expression, which was measured by Western blot, in MKN45-CDDPR cell line. (f) RIP assay was performed to show that H3K27ac enriched in the promotor region of PITPNA-AS1 in parental cells. (g) RIP assay was performed to show that H3K27ac enriched more in the promotor region of PITPNA-AS1 in MKN45-CDDPR cell line. (h) C646 suppressed the PITPNA-AS1 expression, which was measured by qRT-PCR. (i) CCK-8 assay showed that PITPNA-AS1 knock down suppressed IC50 of MKN45-CDDPR, which be reversed by miR-98-5p knock down.

every 24 h followed by incubation for 2 h. Then, the optical density (OD) values of GC cells at 450 nm were detected to assess cell proliferation of GC.

4.8. Cell Apoptosis Assay. The Caspase 3/7 Activity Apoptosis Assay Kit (Invitrogen) was used to detect the apoptosis rate of GC cells. According to the manufacturer's instruction, GC cells were plated into the 96-well plate overnight at 20000 cells per well. Then, 50 μL of caspase 3/7 substrate (component A) was added into 10 mL of assay buffer (component B) to make caspase 3/7 assay loading solution. GC cells were incubated in a 37°C, 5% CO2, incubator for 6 h after treated with camptothecin to induce apoptosis. Then, GC cells were added with 100 μL/well of caspase 3/7 assay loading solution, followed by supplemented with the assay loading solution at room temperature under dark conditions for 1 h of incubation. Finally, GC cells were centrifuged at 800 rpm for 2 min, then the fluorescence intensity at Ex/Em = 490/525 nm was monitored to evaluate cell apoptosis rate.

4.9. Dual-Luciferase Reporter Gene Assay. The plasmids of PITPNA-AS1 wild-type (PITPNA-AS1-WT) and PITPNA-AS1 mutant type (PITPNA-AS1-Mut) were cotransfected with the miR-98-5p-NC mimic into GC cells by using Lipofectamine 2000 (Invitrogen, USA). And then the miR-98-5p-WT and miR-98-5p-Mut vectors were transfected into GC cells as well. Then, dual-luciferase reporter system (Promega, Madison, WI, USA) was conducted to estimate the luciferase activities based on the manufacturer's instruction.

4.10. RNA Pull-Down Assay. Biotin-labeled miR-98-5p-WT and miR-98-5p-Mut were synthesized by GeneCreate (Wuhan, China) and were transfected into GC cells which were incubated with lysis buffer (Ambion, Austin, Texas, USA). Then, the GC cell lysates were incubated with the

streptavidin Dynabeads (Invitgen, USA) precoated with RNase-free bovine serum albumin (BSA) and yeast tRNA (Sigma-Aldrich, USA) overnight at 4°C. After washed with washing buffer, the bound RNA was purified by using Trizol. Finally, the enrichment of PITPNA-AS1 was identified and estimated by performing qRT-PCR.

4.11. Statistics. The SPSS 18.0 software and the GraphPad Prism 8.2 software were used to analyze and visualize the data involved in this study. The Limma package were used for RNA sequencing analysis. A paired Student's t-test was used to evaluate the statistical differences between two groups. And one-way ANOVA was applied for multiple-group comparison. The Kaplan-Meier survival analysis was used to estimate the prognosis of GC patients. Each assay was independently repeated at least three times, and all the statistical results presented in this work were expressed as mean ± standard deviation (SD). A p value of <0.05 was indicative of statistically significant difference.

Data Availability

Data would be made available on request by sending e-mail to the corresponding author.

Conflicts of Interest

The authors declare that they have no competing interests.

Authors' Contributions

Zhongling Ma designed and performed the experiments in this study and completed the writing of the manuscript. XinhanZhao and Hong Ren supervised the progression of the study. Gang Liu completed the statistical analyses of the data and contributed to the manuscript editing. Xiaojuan Zhao plotted the statistic graphs. Suhong Hao helped to edit the manuscript. All authors gave final approval of the version to be published, and agreed to be accountable for all aspects of the work.

Acknowledgments

We thanked for the contribution of Dr. Wang's team to this article. A preprint has previously been published [10.21203/rs.3.rs-156344/v1] [46]. This study was financially supported by the Innovation Capability Supporting Plan of Shaanxi Province (2020TD-045).

Supplementary Materials

Sup1 Figure 1: FISH assay was used to show that PITPNA-AS1 mainly resided in the plasma of MKN45 and AGS. Sup Figure 2: (A) qRT-PCR was used to detect the expression of PITPNA-AS1 in PITPNA-AS1 silence AGS cells to show the knocking down efficiency. (B) qRT-PCR was used to detect the expression of PITPNA-AS1 in PITPNA-AS1 silence MKN45 cells to show the knocking down efficiency. (C) qRT-PCR was used to detect the expression of miR-98-5p in miR-98-5p overexpression AGS cells to show the overexpression efficiency. (D) qRT-PCR was used to detect the expression of miR-98-5p in miR-98-5p overexpression MKN45 cells to show the overexpression efficiency. *(Supplementary Materials)*

References

[1] A. Jemal, M. M. Center, C. DeSantis, and E. M. Ward, "Global patterns of cancer incidence and mortality rates and trends," *Cancer Epidemiology, Biomarkers & Prevention*, vol. 19, no. 8, pp. 1893–1907, 2010.

[2] J. Ferlay, H. R. Shin, F. Bray, D. Forman, C. Mathers, and D. M. Parkin, "Estimates of worldwide burden of cancer in 2008: GLOBOCAN 2008," *International Journal of Cancer*, vol. 127, no. 12, pp. 2893–2917, 2010.

[3] A. E. Dassen, J. L. Dikken, C. J. H. van de Velde, M. W. J. M. Wouters, K. Bosscha, and V. E. P. P. Lemmens, "Changes in treatment patterns and their influence on long-term survival in patients with stages I–III gastric cancer in The Netherlands," *International Journal of Cancer*, vol. 133, no. 8, pp. 1859–1866, 2013.

[4] A. D. Wagner, N. L. X. Syn, M. Moehler et al., "Chemotherapy for advanced gastric cancer," *Cochrane Database of Systematic Reviews*, vol. 8, p. CD004064, 2017.

[5] L. Jiang, K. H. Yang, Q. L. Guan, Y. Chen, P. Zhao, and J. H. Tian, "Survival benefit of neoadjuvant chemotherapy for resectable cancer of the gastric and gastroesophageal junction a meta-analysis," *Journal of Clinical Gastroenterology*, vol. 49, no. 5, pp. 387–394, 2015.

[6] GASTRIC, "Benefit of adjuvant chemotherapy for resectable gastric cancer," *Journal of the American Medical Association*, vol. 303, no. 17, pp. 1729–1737, 2010.

[7] J. Pan, Z. Xiang, Q. Dai, Z. Wang, B. Liu, and C. Li, "Prediction of platinum-resistance patients of gastric cancer using bioinformatics," *Journal of Cellular Biochemistry*, vol. 120, no. 8, pp. 13478–13486, 2019.

[8] D. P. Gately and S. B. Howell, "Cellular accumulation of the anticancer agent cisplatin: a review," *British Journal of Cancer*, vol. 67, no. 6, pp. 1171–1176, 1993.

[9] "Positive correlation between cellular glutathione and acquired cisplatin resistance in human ovarian cancer cells," *Cell Biology and Toxicology*, vol. 11, no. 5, pp. 273–281, 1995.

[10] S. W. Johnson, R. P. Perez, A. K. Godwin et al., "Role of platinum-DNA adduct formation and removal in cisplatin resistance in human ovarian cancer cell lines," *Biochemical Pharmacology*, vol. 47, no. 4, pp. 689–697, 1994.

[11] H. Masuda, R. F. Ozols, G. M. Lai, A. Fojo, M. Rothenberg, and T. C. Hamilton, "Increased DNA repair as a mechanism of acquired resistance to cis-diamminedichloroplatinum (II) in human ovarian cancer cell lines," *Cancer Research*, vol. 48, no. 20, pp. 5713–5716, 1988.

[12] N. Abu, K. W. Hon, S. Jeyaraman, and R. Jamal, "Long non-coding RNAs as biotargets in cisplatin-based drug resistance," *Future Oncology*, vol. 14, no. 29, pp. 3085–3095, 2018.

[13] L. Yuan, Z. Y. Xu, S. M. Ruan, S. Mo, J. J. Qin, and X. D. Cheng, "Long non-coding RNAs towards precision medicine in gastric cancer: early diagnosis, treatment, and drug resistance," *Molecular Cancer*, vol. 19, no. 1, p. 96, 2020.

[14] J. Sun, Y. Zhang, B. Li et al., "PITPNA-AS1 abrogates the inhibition of miR-876-5p on WNT5A to facilitate hepatocellular

carcinoma progression," *Cell Death & Disease*, vol. 10, no. 11, p. 844, 2019.

[15] G. C. Shukla, J. Singh, and S. Barik, "MicroRNAs: processing, maturation, target recognition and regulatory functions," *Molecular and Cellular Pharmacology*, vol. 3, no. 3, pp. 83–92, 2011.

[16] L. Wei, J. Sun, N. Zhang et al., "Noncoding RNAs in gastric cancer: implications for drug resistance," *Molecular Cancer*, vol. 19, no. 1, pp. 62–79, 2020.

[17] X. Li, Z. Zhang, M. Yu et al., "Involvement of miR-20a in promoting gastric cancer progression by targeting early growth response 2 (EGR2)," *International Journal of Molecular Sciences*, vol. 14, no. 8, pp. 16226–16239, 2013.

[18] Y. Fang, H. Shen, H. Li et al., "miR-106a confers cisplatin resistance by regulating PTEN/Akt pathway in gastric cancer cells," *Acta Biochim Biophys Sin (Shanghai)*, vol. 45, no. 11, pp. 963–972, 2013.

[19] Y. Shang, Z. Zhang, Z. Liu et al., "miR-508-5p regulates multidrug resistance of gastric cancer by targeting ABCB1 and ZNRD1," *Oncogene*, vol. 33, no. 25, pp. 3267–3276, 2014.

[20] Q. Wu, Z. Yang, L. Xia et al., "Methylation of miR-129-5p CpG island modulates multi-drug resistance in gastric cancer by targeting ABC transporters," *Oncotarget*, vol. 5, no. 22, pp. 11552–11563, 2014.

[21] N. M. Alajez, W. Shi, A. B. Y. Hui et al., "Enhancer of Zeste homolog 2 (EZH2) is overexpressed in recurrent nasopharyngeal carcinoma and is regulated by miR-26a, miR-101, and miR-98," *Cell Death & Disease*, vol. 1, no. 10, p. e85, 2010.

[22] H. Panda, T. D. Chuang, X. Luo, and N. Chegini, "Endometrial miR-181a and miR-98 expression is altered during transition from normal into cancerous state and target PGR, PGRMC1, CYP19A1, DDX3X, and TIMP3," *The Journal of Clinical Endocrinology and Metabolism*, vol. 97, no. 7, pp. E1316–E1326, 2012.

[23] L. X. Yan, X. F. Huang, Q. Shao et al., "MicroRNA miR-21 overexpression in human breast cancer is associated with advanced clinical stage, lymph node metastasis and patient poor prognosis," *Ribonucleic Acid*, vol. 14, no. 11, pp. 2348–2360, 2008.

[24] Y. Fu, X. Liu, Q. Chen et al., "Downregulated miR-98-5p promotes PDAC proliferation and metastasis by reversely regulating MAP4K4," *Journal of Experimental & Clinical Cancer Research*, vol. 37, no. 1, p. 130, 2018.

[25] N. Nagarajan, D. Bertrand, A. M. Hillmer et al., "Whole-genome reconstruction and mutational signatures in gastric cancer," *Genome Biology*, vol. 13, pp. 1–10, 2012.

[26] X. Jiao, X. Qian, L. Wu et al., "microRNA: the impact on cancer stemness and therapeutic resistance," *Cell*, vol. 9, no. 1, 2019.

[27] X. D. Xiong, X. Ren, M. Y. Cai, J. W. Yang, X. Liu, and J. M. Yang, "Long non-coding RNAs: an emerging powerhouse in the battle between life and death of tumor cells," *Drug Resistance Updates*, vol. 26, pp. 28–42, 2016.

[28] A. G. Ewan, J. B. Carolyn, and L. L. Wan, "The functional role of long non-coding RNA in human carcinomas," *Molecular Cancer*, vol. 10, no. 1, p. 38, 2011.

[29] S. Nagini, "Carcinoma of the stomach: a review of epidemiology, pathogenesis, molecular genetics and chemoprevention," *World Journal of Gastrointestinal Oncology*, vol. 4, no. 7, pp. 156–169, 2012.

[30] E. Van Cutsem, X. Sagaert, B. Topal, K. Haustermans, and H. Prenen, "Gastric cancer," *The Lancet*, vol. 388, no. 10060, pp. 2654–2664, 2016.

[31] A. Digklia and A. D. Wagner, "Advanced gastric cancer: current treatment landscape and future perspectives," *World Journal of Gastroenterology*, vol. 22, no. 8, pp. 2403–2414, 2016.

[32] J. Cheng, M. Cai, X. Shuai, J. Gao, G. Wang, and K. Tao, "First-line systemic therapy for advanced gastric cancer: a systematic review and network meta-analysis," *Therapeutic Advances in Medical Oncology*, vol. 11, p. 1758835919877726, 2019.

[33] J. Li, W. Wang, P. Xia et al., "Identification of a five-lncRNA signature for predicting the risk of tumor recurrence in patients with breast cancer," *International Journal of Cancer*, vol. 143, no. 9, pp. 2150–2160, 2018.

[34] Y. Yu, L. Li, Z. Zheng, S. Chen, E. Chen, and Y. Hu, "Long noncoding RNA linc00261 suppresses gastric cancer progression via promoting slug degradation," *Journal of Cellular and Molecular Medicine*, vol. 21, no. 5, pp. 955–967, 2017.

[35] Y.-L. Xiu, K. X. Sun, X. Chen et al., "Upregulation of the lncRNA Meg3 induces autophagy to inhibit tumorigenesis and progression of epithelial ovarian carcinoma by regulating activity of ATG3," *Oncotarget*, vol. 8, no. 19, pp. 31714–31725, 2017.

[36] J. Li, D. S. Zhai, Q. Huang, H. L. Chen, Z. Zhang, and Q. F. Tan, "LncRNA DCST1-AS1 accelerates the proliferation, metastasis and autophagy of hepatocellular carcinoma cell by AKT/mTOR signaling pathways," *European Review for Medical and Pharmacological Sciences*, vol. 23, no. 14, pp. 6091–6104, 2019.

[37] H. Zhou, Z. Huang, X. Chen, and S. Chen, "miR-98 inhibits expression of TWIST to prevent progression of non-small cell lung cancers," *Biomedicine & Pharmacotherapy*, vol. 89, pp. 1453–1461, 2017.

[38] T. Jiang, M. Li, Q. Li et al., "MicroRNA-98-5p inhibits cell proliferation and induces cell apoptosis in hepatocellular carcinoma via targeting IGF2BP1," *Oncology Research*, vol. 25, no. 7, pp. 1117–1127, 2017.

[39] W. Zhu, Y. Huang, Q. Pan, P. Xiang, N. Xie, and H. Yu, "MicroRNA-98 suppress Warburg effect by targeting HK2 in colon cancer cells," *Digestive Diseases and Sciences*, vol. 62, no. 3, pp. 660–668, 2017.

[40] Q. Guo, L. Li, Q. Bo, L. Chen, L. Sun, and H. Shi, "Long noncoding RNA PITPNA-AS1 promotes cervical cancer progression through regulating the cell cycle and apoptosis by targeting the miR-876-5p/c-MET axis," *Biomedicine & Pharmacotherapy*, vol. 128, p. 110072, 2020.

[41] Z. Chen, T. Pan, D. Jiang et al., "The lncRNA-GAS5/miR-221-3p/DKK2 axis modulates ABCB1-mediated adriamycin resistance of breast cancer via the Wnt/β-catenin signaling pathway," *Molecular Therapy-Nucleic Acids*, vol. 19, pp. 1434–1448, 2020.

[42] D. Fu, C. Lu, X. Qu et al., "LncRNA TTN-AS1 regulates osteosarcoma cell apoptosis and drug resistance via the miR-134-5p/MBTD1 axis," *Aging (Albany NY)*, vol. 11, no. 19, pp. 8374–8385, 2019.

[43] Y. Wang, W. Bao, Y. Liu et al., "miR-98-5p contributes to cisplatin resistance in epithelial ovarian cancer by suppressing miR-152 biogenesis via targeting Dicer1," *Cell Death & Disease*, vol. 9, no. 5, p. 447, 2018.

[44] H. Guo, C. Ha, H. Dong, Z. Yang, Y. Ma, and Y. Ding, "Cancer-associated fibroblast-derived exosomal microRNA-98-5p

promotes cisplatin resistance in ovarian cancer by targeting CDKN1A," *Cancer Cell International*, vol. 19, no. 1, p. 347, 2019.

[45] C. Lu, Z. Shan, C. Li, and L. Yang, "MiR-129 regulates cisplatin-resistance in human gastric cancer cells by targeting P-gp," *Biomedicine & Pharmacotherapy*, vol. 86, pp. 450–456, 2017.

[46] Y. Liu, X. Zhao, Y. Chen, G. Guo, J. Wang, and S. He, "PITPNA-AS1 activated by H3K27ac sponged miR-98-5p to regulate cisplatin resistance in gastric cancer," *Research Square*, 2021.

Hindawi
Journal of Oncology
Volume 2022, Article ID 8777697, 17 pages
https://doi.org/10.1155/2022/8777697

Research Article

The tRNA-Derived Fragment tRF-24-V29K9UV3IU Functions as a miRNA-like RNA to Prevent Gastric Cancer Progression by Inhibiting GPR78 Expression

Hui Wang,[1,2] **Weikang Huang**,[2] **Xirui Fan**,[2] **Xiaoxue He**,[2] **Sijin Chen**,[2] **Su Yu**,[2] **and Yan Zhang**[1]

[1]*Department of Gastroenterology, West China Hospital, Sichuan University, Chengdu, China*
[2]*Department of Gastroenterology, The Affiliated YanAn Hospital of Kunming Medical University, Kunming, China*

Correspondence should be addressed to Yan Zhang; hxzyan@163.com

Received 22 January 2022; Accepted 10 March 2022; Published 29 April 2022

Academic Editor: Fu Wang

Emerging studies have proved that tRNA-derived fragments (tRFs) play vital roles in tumor metastasis; however, the function of tRFs in gastric cancer (GC) remains largely unclear. We investigated the role of tRF-24-V29K9UV3IU in growth and metastasis of GC using a xenograft mouse model. Differential gene expression downstream of tRF-24-V29K9UV3IU was identified by transcriptome sequencing, and interaction was then verified by a dual luciferase reporter and RNA immunoprecipitation. MKN-45 cells were also used to explore the biological functions of tRF-24-V29K9UV3IU *in vitro*. Here, knockdown of tRF-24-V29K9UV3IU promoted tumor growth and metastasis of GC *in vivo*. The expression of tRF-24-V29K9UV3IU and E-cadherin (epithelial cell marker) was down-regulated in tumors of mice following tRF-24-V29K9UV3IU knockdown, whereas the mesenchymal cell markers N-cadherin and vimentin displayed an opposite trend. Transcriptome sequencing identified 87 differentially expressed genes (DEGs) down-regulated in the tRF-24-V29K9UV3IU-overexpressed groups compared with the control group. Among them, G-protein–coupled receptor 78 (GPR78), the most significantly down-regulated DEG, was also predicted to be a target of tRF-24-V29K9UV3IU. Moreover, tRF-24-V29K9UV3IU could function as a miRNA-like fragment and bind to AGO2 and directly silence GPR78 expression by complementing with the 3′-untranslated region of the GPR78 mRNA. Functionally, overexpression of tRF-24-V29K9UV3IU significantly suppressed proliferation, migration, and invasion and promoted apoptosis of MKN-45 cells, whereas GPR78 attenuated these effects. Therefore, our data suggest that tRF-24-V29K9UV3IU functions as a miRNA-like fragment to suppress GPR78 expression and thus inhibit GC progression. These observations suggest that the tRF-24-V29K9UV3IU/GPR78 axis serves as a potential therapeutic target in GC.

1. Introduction

Gastric cancer (GC) ranks second in morbidity and mortality of various cancers in China, only after lung cancer [1]. Most GC patients already demonstrate advanced disease and metastasis at the time of diagnosis; these patients cannot be cured by simple radical surgical resection, which is accompanied by an extremely high recurrence rate [2]. Epidemiological studies have shown that GC is most prevalent in patients aged >55 years [3]. As the aging population of China grows proportionally larger, the social burden caused by GC will also rise; however, clinical treatment of these patients is hampered by the lack of a clear understanding of the molecular mechanisms underlying GC development [4]. Therefore, revealing the molecular mechanisms underlying invasion and metastasis in GC and finding non-invasive, simple, and feasible new biomarkers to prevent and control this malignant disease are of great importance.

tRNA-derived fragments (tRFs) are short non-coding RNAs derived from tRNA, approximately 16–40 nucleotides in length [5], which originate from mitochondrial or nuclear tRNAs [6]. Currently, tRFs are known to be involved in various physiological and pathological processes, such as infectious diseases and tumor formation, and in

neurodegenerative diseases [7]. Schimmel reported that the events of tRF production responded to many stresses such as hyperosmotic stress, pro-oncogenic transcription under hypoxia, and regulation of hematopoiesis [8]. The regulatory role of tRFs on tumor progression has been extensively studied. tiRNA-Gly, a kind of 5′-tRNA halve, promotes migration and proliferation of papillary thyroid cancer cell through binding to RBM17 and inducing alternative splicing [9]. The tRF Lys-CTT-010 promoted malignant progression of triple-negative breast cancer through glucose metabolism regulation [10]. tRF-Leu-CAG promotes the proliferation and cell cycle progression of non-small-cell lung cancer cells [11]. These studies suggested that abnormally expressed tRFs are associated with changes in tumor biological function, and it is expected that tRFs can serve as tumor diagnostic or prognostic markers or even tumor therapeutic targets. However, there are few studies on the role of tRFs in GC, and the mechanism by which tRFs regulate biological functions in GC remains unclear.

In our previous study, using small RNA sequencing, we identified that tRF-24-V29K9UV3IU was prominently down-regulated in GC tissues relative to adjacent tissues [12]; the available genomes is *Homo sapiens* (hg19/GRCh37). Moreover, pathway analysis showed that the target genes of tRF-24-V29K9UV3IU were involved in biological processes related to cancer occurrence and metastasis, such as cell adhesion and connection, cell migration, and the cAMP signaling, Wnt signaling, MAPK signaling, and cancer signaling pathways. Therefore, we attempted to further explore the function and regulatory mechanisms of tRF-24-V29K9UV3IU on the invasion and metastasis of GC cells *in vivo* and *in vitro* using a xenograft tumor mouse model and transcriptome sequencing.

2. Materials and Methods

2.1. Sample Collection of GC Patients. Ethics approval of this study was received from the Ethics Committee of Kunming Medical University. A total of 19 tumor tissues and 19 normal tissues were collected from a GC patient who underwent surgical resection. All patients in this study read and signed the informed consent. Preoperatively, the GC patient showed no pathological changes in other organs, and did not receive chemoradiotherapy and immunotherapy. The tissue was instantaneously frozen in liquid nitrogen after isolation until the experiment.

2.2. Cell Culture and Transfection. The human gastric cancer cell line MKN-45 and 293T/17 cells were purchased from Procell. GC cells were cultured in RPMI 1640 medium (Corning, USA), contained with 10% fetal bovine serum (FBS) and 1% penicillin/streptomycin (PS), in an incubator at 37°C containing 5% CO_2. For gain-of-function, experiments, we designed a tRF-24-V29K9UV3IU sequence with a 5′ phosphate group (5′-P-UAGGAUGGGGUGUGAU AGGUGGCA-3′), and tRF-24-V29K9UV3IU mimics and control sequences were transfected into MKN-45 cells using Lipofectamine 2000 following the manufacturer's protocol. All sequences are shown in Supplemental Table 1.

2.3. Construction of a Stable Lentiviral Cell Line. The lentivirus-mediated tRF-24-V29K9UV3IU knockdown (LV-tRF-24-inhibitor sponge) vector and a negative control (NC) vector were purchased from Genepharma (China). The catalogue number of vector was C09004. In belief, the LV3(H1/GFP&Puro)-tRF-24-inhibitor sponge vector was constructed to express RNA sequences containing three mature tRF-24 binding sites, and the mature tRF-24 was bound by adsorption, thus exerting the inhibition effect of tRF-24. Virus packaging was performed using 293T tool cells, when cells reached 80–90% fusion, shuttle plasmid (LV3-tRF-24-inhibitor sponge) and packaging plasmid (pGag/Pol, pRev, pVSV-G) were added, and 300 μL RNAi-mate was also added. The virus was collected after 72 h of culture. Then, when the confluence of MKN-45 cells reached 50%–70%, 50–200 μL virus solution was added to each well and mixed. To find the optimal concentration of puromycin for selection, MKN-45 cells were treated with 0, 3, 6, 9, 12, and 15 μg/mL puromycin (Selleck, China) for 1–4 days. To obtain stable transfections, MKN-45 cells with lentiviral infection of NC or LV-tRF-24-inhibitor sponge were cultured at optimal puromycin concentration for 14 days. The surviving cells were collected for subsequent experiments.

2.4. Xenografts in Mice. To establish the xenograft mouse model, 40 male BALB/c nude mice (5-week-old) were distributed at random into two groups (20 rats per group): a LV-tRF-24-inhibitor group and an NC group. For *in vivo* tumor growth assays ($n = 5$) [13], approximately 5×10^6 MKN-45 cells were subcutaneously injected into the axilla of the BALB/c nude mice. Tumor volume (mm^3) was calculated every 3 days with a caliper and calculated as (length × width^2)/2. All mice were euthanized after 21 days using CO_2 inhalation followed by decapitation. The collected tumor tissue was used for qRT-PCR and hematoxylin and eosin (H&E) staining. For *in vivo* tumor metastasis assays ($n = 5$) [14], approximately 2×10^6 MKN-45 cells were injected into the tail veins of BALB/c nude mice. After 50 days, lung tissues from all BALB/c nude mice were subjected to H&E staining. All experiments in mice were approved by the Ethics Committee of Kunming Medical University.

2.5. H&E Staining. Tumor tissues ($n = 3$) and lung tissues ($n = 5$) from each group of mice were harvested for H&E staining to detect the tumorigenicity of tRF-24-V29K9UV3IU. Tumor and lung tissues were fixed in 10% formalin and paraffin embedded, then routine cut into 5 μm sections, and mounted on slides. Following staining with H&E staining, tissues were imaged under a light microscope (Olympus, Japan).

2.6. qRT-PCR Analysis. TRIzol Reagent (Invitrogen, USA) was used to extract total RNA from tumor and adjacent peritumoral tissues of mice and then quality of RNA was assessed by NanoDrop 2000 (Thermo Scientific, USA). For tRF-24-V29K9UV3IU detection, to distinguish precursors from mature tRF, we used a two-end adaptor method for qRT-PCR. An adaptor was ligated at the 3′-ends of RNAs followed by hybridized with 3′ primers and ligated a 5′

adaptor. Finally, the product was amplified to create a cDNA using the Thermo Scientific revertaid first strand cDNA synthesis kit (Thermo Scientific, USA). For mRNA detection, conventional cDNA synthesis and PCR amplification were used. The specific PCR primers were designed and utilized to measure specific tRF and mRNAs by qRT-PCR using ABsolute Blue SYBR Green Master Mix (Thermo Scientific, USA) on the QuantStudio 6 Flex Real-Time PCR System (Thermo Fisher Scientific, Inc.) according to the product instructions. All primers used in this study were custom synthesized by Shanghai Sangon Biotech and are shown in Supplemental Table 1. The relative gene expression was normalized to *GAPDH* and determined by the $2^{-\Delta\Delta Cq}$ method [15].

2.7. Western Blotting. The method for western blotting was adapted from previously described [16]. Total protein was isolated from the tumors using RIPA lysis buffer and quantified using the BCA Protein Assay Kit (Thermo Scientific, USA). Next, equal amounts of protein were subjected to 10% SDS-PAGE, after that the proteins were transferred onto PVDF membranes. The PVDF membranes were blocked for nonspecific binding with 5% nonfat milk and incubated with primary antibodies: vimentin (1 : 1000, Abcam, ab8978), anti-Snail (1 : 1000, CST, 3879), and GAPDH (1 : 1000, Proteint, 60004-1-Lg), at 4°C overnight. Then, membranes were incubated with goat anti-mouse IgG H&L (HRP-conjugated secondary antibodies) (1: 10000, Abcam, ab205719) at room temperature for 1 h. In the end, the gels were photographed performed on the Bio-Rad ChemiDoc XRS system.

2.8. Transcriptome Sequencing and Bioinformatics Analysis. GC cells were harvested for transcriptome sequencing in triplicates after transfection with tRF-24-V29K9UV3IU mimics or NC. Total RNA was isolated using the TRIzol Reagent and qualified using the NanoDrop 2000 (Thermo Scientific, USA). Next, RNA was reversed transcribed and amplified into a cDNA library using the RNA Seq Library Preparation Kit for Transcriptome Discovery (Questgenomics, Nanjing, China), and RNA sequencing was performed on an Illumina HiSeq 2500 platform. The fragments per kilobase per million were used to normalize the expression of sequences, and the normalized expression was used to identify differentially expressed genes (DEGs) using the DEGSeq algorithm. The DEGs parameter was set to the absolute value of $\log_2$ (fold change, FC) was greater than 1 and P was less than 0.05. DEGs were used for GO classification and KEGG analysis.

2.9. Network Construction. To illustrate the regulatory network of tRF-24-V29K9UV3IU on the basis of target gene and KEGG analysis, we selected 8 DEGs and related pathways to perform the network. The network was centered on tRF-24-V29K9UV3IU, with target gene-mediated pathways, and it was imaged using the Cytoscape version 3.6.1.

2.10. Dual Luciferase Activity Assay. G-protein–coupled receptor 78 (GPR78) containing the wild-type (WT) or mutant (MUT) putative binding sites of tRF-24-V29K9UV3IU was synthesized by GenePharma (Shanghai, China) and cloned into psiCHECK-2 vectors (Promega, USA). Next, psiCHECK-2-GPR78-WT and psiCHECK-2-GPR78-MUT reporters were co-transfected into 293T/17 cells (CL-0469, Procell, China) with tRF-24-V29K9UV3IU mimics or controls (NC) using Lipofectamine 2000. After 48 h of transfection, luciferase activity was measured utilizing the Dual-Luciferase Reporter Assay System (Promega, USA). All sequences are shown in Supplemental Table 1.

2.11. Argonaute 2 (AGO2) and RNA Immunoprecipitation (RIP). The RNA immunoprecipitation (RIP) assay was conducted by the Magna RIP™ RNA-Binding Protein Immunoprecipitation Kit (Cat. 17-701, Millipore, USA) according to the manufacturer's instructions. Shortly, cells were lysed in RIP lysis buffer (Magna RIP Kit, Millipore, MA, USA) and incubated with anti-pan-AGO antibodies (MABE56; Millipore), control IgG antibodies. Then, the RNA and proteins in the immunoprecipitates were harvested in the TRIzol Reagent or lysis buffer, respectively, for subsequent analysis.

2.12. CCK8 Assay. The proliferation ability of GC cells was assessed by CCK8 assays. Shortly, about 1×10^4 cells were seeded into 96-well plates. Each group contained six replicate wells. Then, 10 μL of CCK-8 (Beyotime Biotechnology) assay solution was mixed to each well and another cultured for 1 h. Finally, OD values at 450 nm were obtained using a microplate reader.

2.13. Transwell Migration and Invasion Assays. The Transwell system was used to assess the migration and invasion of GC cells. Transwell chambers (Corning, NY, USA) were covered with a layer of matrigel mix for invasion assays and not coated for migration assays. GC cells were seeded into the upper chamber and normal culture medium filled the bottom chamber. After incubating for 24 h, the upper chamber was removed, fixed, and stained with crystal violet (Beyotime Biotechnology). Cells were visualized and counted in five randomly selected fields under a microscope (×100).

2.14. Flow Cytometry Analysis. Cell apoptosis was accessed by flow cytometry; for this purpose, theharvested cell was gently washed by PBS and centrifuged with high-speed to remove the supernatant. Next, a cell suspension with a density approximately of $2–5 \times 10^5$ cells/mL was precipitated using 195 μL Binding Buffer and mixed with 5 μL Annexin V-FITC solution (C1062, Beyotime, China) following incubated for 15 min at 25°C in the dark. Subsequently, cell mixture underwent centrifugation and re-suspension and washed by Binding Buffer. Finally, cells were incubated with 10 μL propidium iodide. The stained cells were analyzed by FACSVerse™ (BD Biosciences, USA), and apoptosis data was processed using the Flowjo V10 software (Tree Star, San Francisco, CA, USA).

2.15. Statistical Analysis. Statistical analysis of all data was processed using SPSS 16.0 and significant differences between two groups were assessed by t test, one-way ANOVA followed by Tukey's test used for four groups. For all data, a P value less than 0.05 was deemed statistically significant. Data are presented as means ± SD.

3. Results

3.1. Knockdown of tRF-24-V29K9UV3IU Facilitates the Growth and Metastasis of Xenograft Tumors In Vivo. The tRF-24-V29K9UV3IU was identified by small RNA sequencing in our previous study [12]. As shown in Figure 1(a), tRF-24-V29K9UV3IU (Sequence: TAGGAT GGGGTGTGATAGGTGGCA) was a 5′-tRF type cleaved from tRNA-Gln-TTG, which was predicted by MINTbase v2.0 (a database for the interactive exploration of mitochondrial and nuclear tRFs, https://cm.jefferson.edu/). We also predicted the secondary structure of tRNA-Gln who produced tRF-24-V29K9UV3IU on the RNAstructure database (http://rna.urmc.rochester.edu/RNAstructureWeb/ Servers/ Predict1/Predict1.html); it was exhibited a typically cloverleaf structure (Figure 1(b)). The Cancer Genome Atlas (TCGA) data showed that tRF-24-V29K9UV3IU was expressed in multiple tumor samples, and compared with non-TCGA, tRF-24-V29K9UV3IU was low expressed in most tumor tissues, including colon adenocarcinoma (COAD), esophageal carcinoma (ESCA), and stomach adenocarcinoma (STAD) (Figure 1(c)). In short, tRF-24-V29K9UV3IU is a novel small molecule that may be involved in GC progression.

Next, to verify the function of tRF-24-V29K9UV3IU, lentiviral vectors were used to interfere with the expression of it. After 14 days of puromycin selection, we obtained an MKN-45 cell line with stable lentivirus-mediated knockdown of tRF-24-V29K9UV3IU, and the interference efficacy is shown in Figure 2(a). To observe the potential biological effects of tRF-24-V29K9UV3IU in GC tumor cells, MKN-45 cells stably transfected with LV-tRF-24-V29K9UV3IU-inhibitor sponge or NC vectors were injected subcutaneously into BALB/c nude mice (Figures 2(b) and 2(c)). Compared with the NC vector, knockdown of tRF-24-V29K9UV3IU significantly increased tumor growth, as determined by tumor weights and tumor volumes (Figures 2(d) and 2(e)). The tumor burden of mice gradually increased with time, but the volume of tumors in the LV-tRF-24-V29K9UV3IU-inhibitor group was always significantly bigger than in the NC group (Figure 2(d)). tRF-24-V29K9UV3IU knockdown-promoted tumor growth was confirmed by H&E staining (Figure 2(f)). We also detected the expression of tRF-24-V29K9UV3IU in tumor tissues; as expected, the larger the tumor volume, the lower the expression of tRF-24-V29K9UV3IU in the tumor (Figure 2(g)). Moreover, in the BALB/c nude mice, tail vein injection of MKN-45 cells stably transfecting LV-tRF-24-V29K9UV3IU-inhibitor sponge resulted in higher number of lung metastatic nodules than the injection of NC vector, as shown by H&E staining (Figure 2(h)). To further confirm the promotion of tumor metastasis after knocking down tRF-24-V29K9UV3IU, qRT-PCR and western blotting were performed for measuring the expression of epithelial–mesenchymal transition markers in tumor tissues. E-cadherin expression was decreased and the expression of N-cadherin and vimentin was up-regulated at the mRNA level, whereas Snail and vimentin was also up-regulated at the protein level, supporting that the knockdown of tRF-24-V29K9UV3IU promoted the epithelial–mesenchymal transition of tumor cells (Figures 2(i)–2(k)). These results suggested that tRF-24-V29K9UV3IU has a tumor suppressor role in tumorigenesis and aggressiveness.

3.2. Gene Expression Profile Alterations Triggered by tRF-24-V29K9UV3IU. To take an overview of molecular alteration of tRF-24-V29K9UV3IU effect on GC cells, we first analyzed the gene expression profile overexpression of tRF-24-V29K9UV3IU by transfection with RNA mimics. Compared with the NC group, tRF-24-V29K9UV3IU was significantly overexpressed (Figure 3(a)). The overall gene expression profile alterations triggered by tRF-24-V29K9UV3IU is shown in Supplemental Table 2. Moreover, a total of 159 DEGs were identified, including 72 up-regulated and 87 down-regulated genes in the tRF-24-V29K9UV3IU-overexpressing MKN-45 cells relative to NC MKN-45 cells (Figure 3(b)). A heat map indicated significant dysregulation of mRNAs in the tRF-24-V29K9UV3IU-overexpressing MKN-45 cells compared with NC MKN-45 cells (Figure 3(c)). Therefore, we obtained the expression profile of GC cells after overexpression of tRF-24-V29K9UV3IU.

3.3. Functional and Pathway Analysis. To further investigate the potential molecules that respond to tRF-24-V29K9UV3IU overexpression, all DEGs were annotated in the GO and KEGG databases. Functional GO analysis showed that these DEGs were mainly enriched in the negative regulation of monocyte chemotaxis, negative regulation of the inflammatory response, and positive regulation of NF-kappaB import into the nucleus (Figure 4(a)). KEGG analysis revealed that these DEGs were mainly involved in pathways associated with cancer and metastasis, such as microRNAs in cancer, thyroid cancer, and cell adhesion molecule pathways (Figure 4(b)). Therefore, we speculated that the tRF-24-V29K9UV3IU might regulate the GC progress by the above DEG-mediated pathways.

3.4. tRF-24-V29K9UV3IU Inhibits GPR78 Expression by Directly Binding to Its 3′-Untranslated Region (3′-UTR). Considering that tRF-24-V29K9UV3IU is down-regulated in tumor tissues, we focused on the DEGs predicted to be targets of tRF-24-V29K9UV3IU via overlap in the Miranda and RNAhybrid databases. There were a total of 8 DEGs that met these conditions and attracted our focus (Figure 5(a)). We constructed a network diagram to visualize the predicted regulatory network for tRF-24-V29K9UV3IU. The GPR78, ventricular zone expressed pH domain-containing 1 (VEPH1), and oxidized low-density lipoprotein (lectin-like) receptor 1 (OLR1), elastin (ELN), and selectin L (SELL) were down-regulation (green) in tRF-24-V29K9UV3IU-overexpressing MKN-45 cells compared with NC MKN-45 cells, whereas the three remaining predicted target genes were up-regulated (red) (Figure 5(b)). To verify whether the expression of these genes was suppressed in GC cells after tRF-24-V29K9UV3IU overexpression according to our transcriptome data, we selected three genes with the highest abundance for qRT-PCR validation (GPR78, VEPH1, and

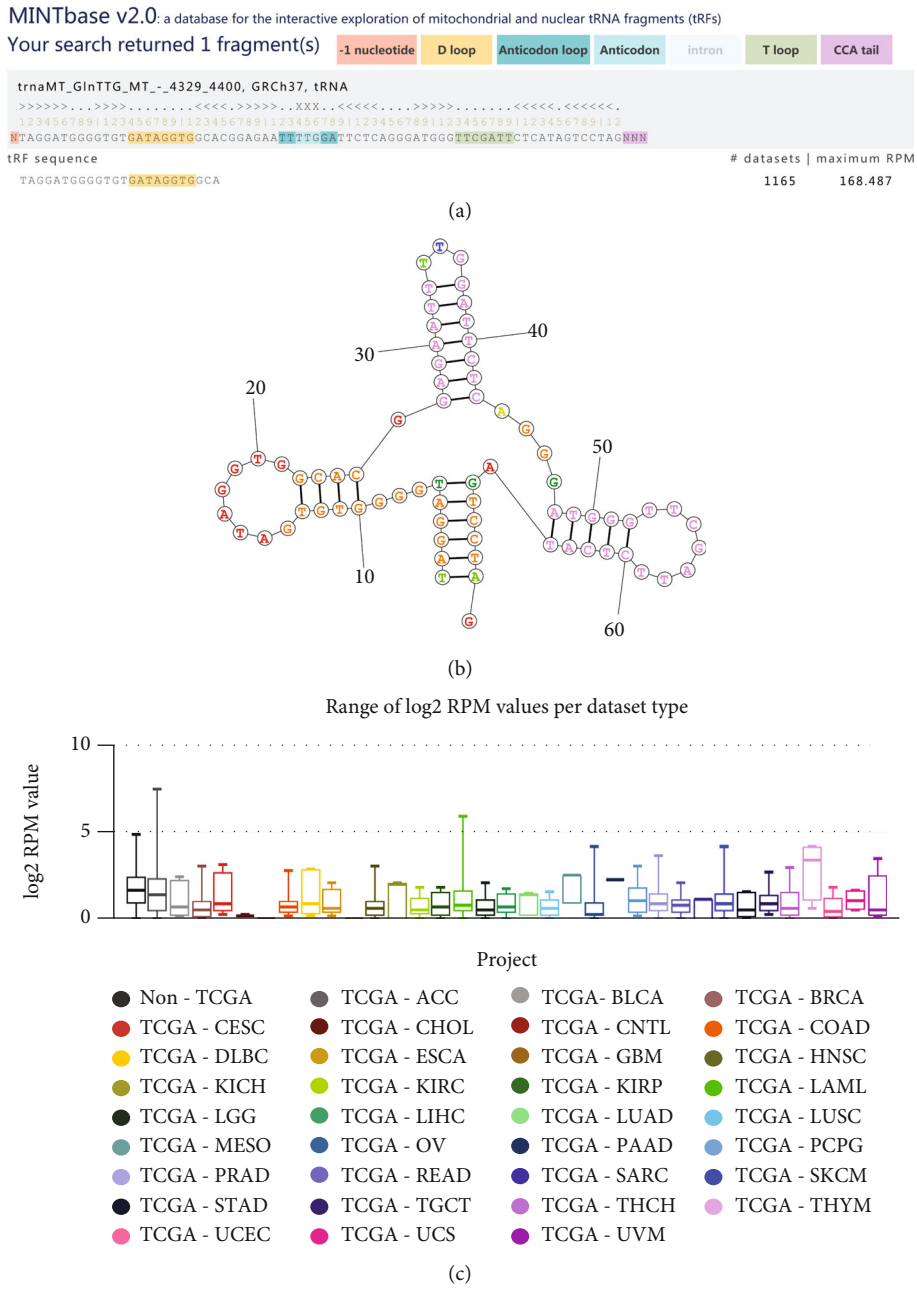

Figure 1: The information of tRF-24-V29K9UV3IU. (a) The sequence information of tRF-24-V29K9UV3IU, which was a 5′-tRF type cleaved from tRNA-Gln-TTG, in MINTbase v2.0. (b) Secondary structure of total tRNA-Gly. (c) The expression of tRF-24-V29K9UV3IU in different tumors predicted by TCGA.

OLR1). Results showed that only down-regulation of GPR78 was confirmed in tRF-24-V29K9UV3IU-overexpressing MKN-45 cells compared with NC MKN-45 cells by qRT-PCR, while the expressions of VEPH1 and OLR1 were inconsistent with the RNA sequencing data (Figures 5(c)–5(e)). Therefore, GPR78 expression was selected as a downstream marker of tRF-24-V29K9UV3IU for subsequent experiments.

Next, we explored the interaction between tRF-24-V29K9UV3IU and GPR78. The full-length and mutant sequence of the 3′-UTR of wild-type GPR78 (GPR78-WT) and mutant GPR78 (GPR78-MUT) containing the predicted tRF-24-V29K9UV3IU binding sites was cloned into psiCHECK-2 vectors (Figure 5(f)). A luciferase reporter assay indicated that only the GPR78-WT plasmids significantly decreased luciferase activity in tRF-24-V29K9UV3IU mimics group, whereas there was no difference in the GPR78 mutants (Figure 5(g)). These results indicated that there might be a direct interaction between tRF-24-V29K9UV3IU and GPR78 at the 3′-UTR. Increasing articles have demonstrated that tRFs can bind to the Argonaute (AGO) complex and exert functions similar to

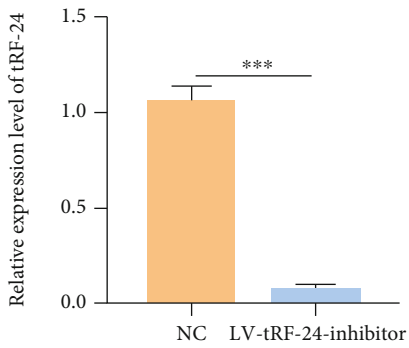

(a)

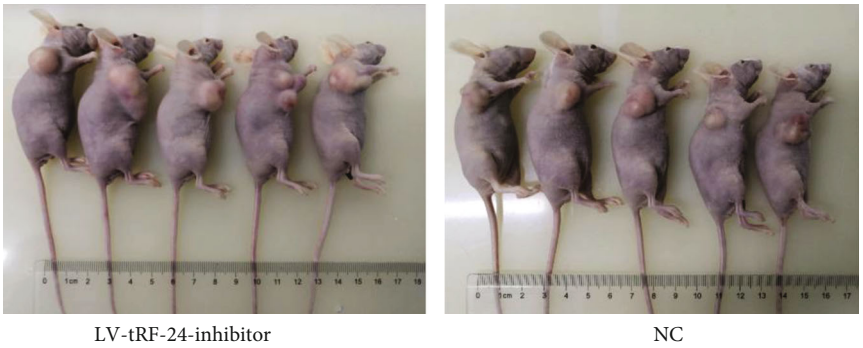

(b)

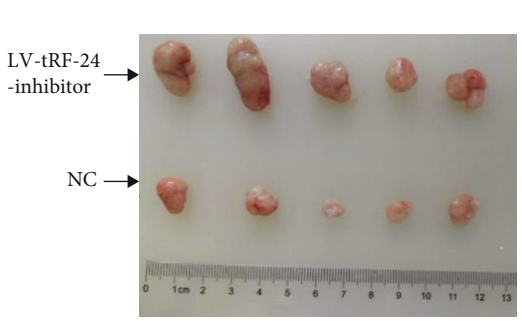

(c)

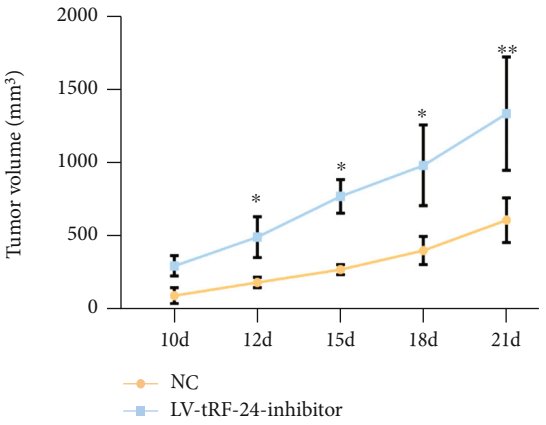

(d)

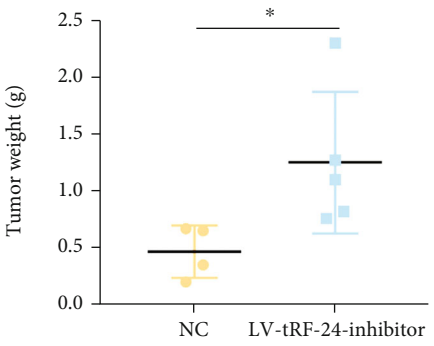

(e)

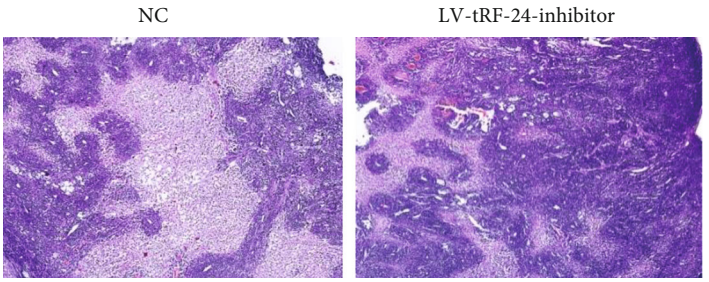

(f)

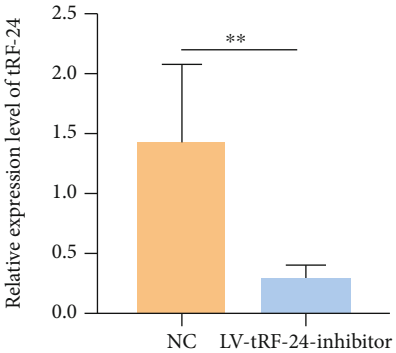

(g)

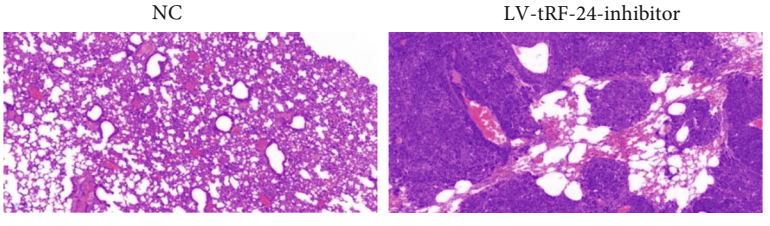

(h)

Figure 2: Continued.

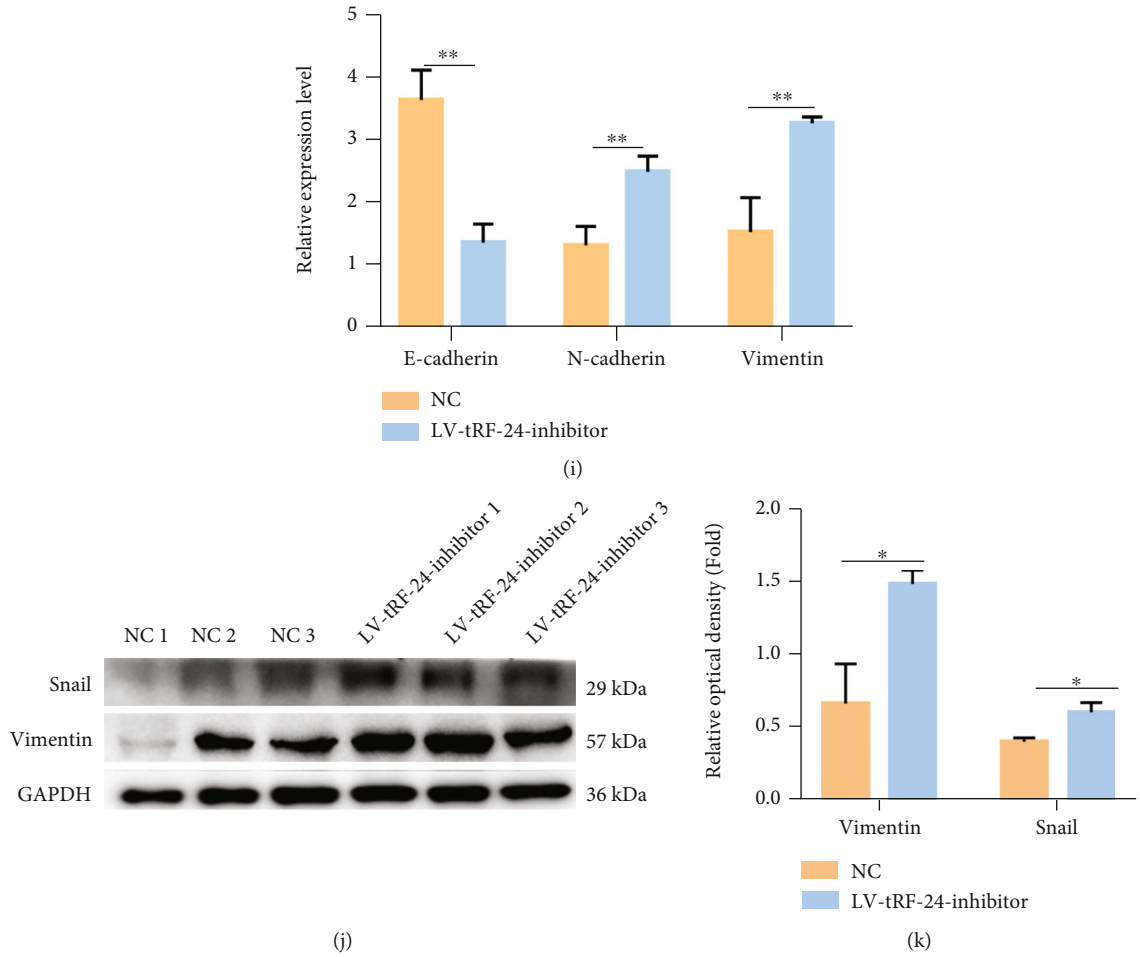

Figure 2: Knockdown of tRF-24-V29K9UV3IU facilitates growth and metastasis of xenograft tumors *in vivo*. (a) The efficacy of lentivirus interfering with tRF-24-V29K9UV3IU expression detected by qRT-PCR ($n = 3$). (b) Representative images of subcutaneous tumor formation in mice after LV-tRF-24-V29K9UV3IU-inhibitor-expressing or NC MKN-45 cell inoculation ($n = 5$). (c) Representative images of subcutaneous tumor tissues in mice ($n = 5$). The tumor (d) volume and (e) weight statistics after LV-tRF-24-V29K9UV3IU-inhibitor-expressing or NC MKN-45 cell inoculation ($n = 5$). (f) Representative images for H&E staining in tumors ($n = 3$). Magnification 20x. These results implicated that knockdown of tRF-24-V29K9UV3IU facilitates growth of GC. (g) The expression of tRF-24-V29K9UV3IU in tumor tissues after LV-tRF-24-V29K9UV3IU-inhibitor or NC MKN-45 cell inoculation ($n = 3$). (h) Representative images of H&E staining in lung tissue following LV-tRF-24-V29K9UV3IU-inhibitor-expressing MKN-45 cell injection ($n = 5$). Magnification 20x. (i) mRNA expression of E-cadherin, N-cadherin, and vimentin in tumor tissues after LV-tRF-24-V29K9UV3IU-inhibitor-expressing or NC MKN-45 cell inoculation, detected by qRT-PCR ($n = 3$). ((j) and (k)) Protein expression of vimentin and Snail in tumor tissues after LV-tRF-24-V29K9UV3IU-inhibitor-expressing or NC MKN-45 cell inoculation, detected by western blotting ($n = 3$). These results implicated that knockdown of tRF-24-V29K9UV3IU facilitates lung metastasis of GC. *t* test, $*P < 0.05$, $**P < 0.01$, $***P < 0.001$.

miRNAs by complementarily binding to the 3′-UTRs of mRNAs [17, 18]. Therefore, we performed an AGO2-RIP assay in MKN-45 cells to pull down RNA transcripts bound to AGO2. We found that tRF-24-V29K9UV3IU was significantly enriched by AGO2-pulldown compared with the input control, implying molecular interaction between AGO2 and tRF-24-V29K9UV3IU (Figure 5(h)). In the previous study, we examined the expression of tRF-24-V29K9UV3IU in tumor tissues and normal tissues [12]. To interrogate whether the expression of GPR78 and tRF-24-V29K9UV3IU is correlated in tumor tissues, we examined GPR78 expression in 19 paired tumor tissues and normal tissues, followed by Pearson's analysis. The results showed that the expression of GPR78 in tumor tissues was strongly higher than that in normal tissues (Figure 5(i)), and GPR78 expression was significantly negatively correlated with tRF-24-V29K9UV3IU ($P < 0.001$) (Figure 5(j)). Cumulatively, tRF-24-V29K9UV3IU down-regulates GPR78 expression by binding to AGO2 and complementing with the 3′-UTR of GPR78.

3.5. tRF-24-V29K9UV3IU Inhibits the Biological Function of GC Cells by Regulating GPR78. To explore whether tRF-24-V29K9UV3IU exerts biological effects in GC cells via regulation of GPR78 expression, we conducted a series of

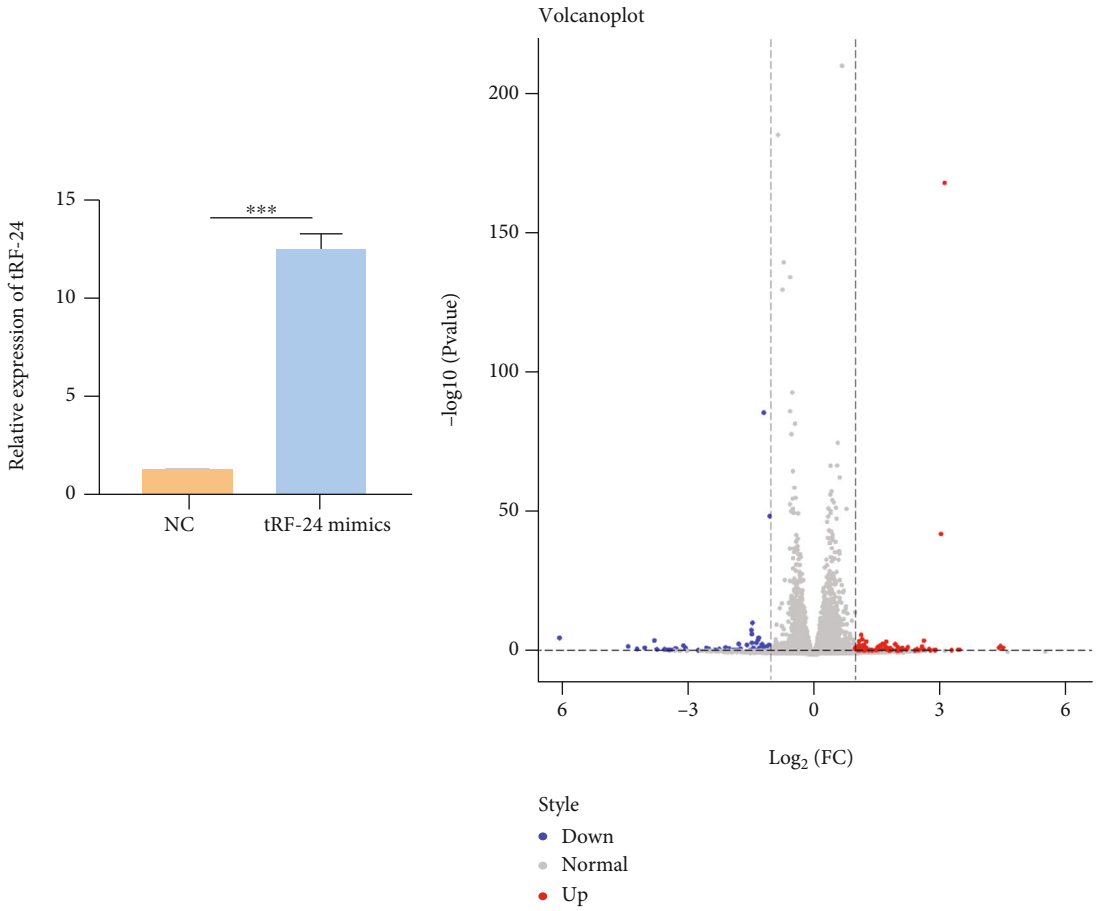

(a) (b)

Figure 3: Continued.

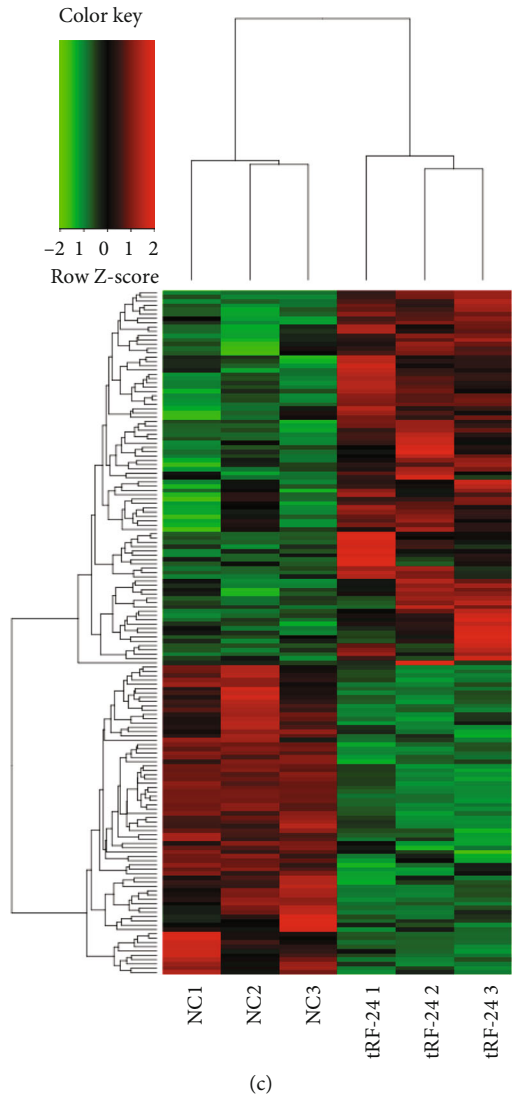

Figure 3: Gene expression profile after overexpression of tRF-24-V29K9UV3IU. (a) The efficacy of tRF-24-V29K9UV3IU overexpression by qRT-PCR. (b) Volcano plot of DEGs in MKN-45 cells after overexpression of tRF-24-V29K9UV3IU compared with the NC group. Red means up-regulated DEGs, and blue means down-regulated DEGs. (c) Heat map showing the DEGs in MKN-45 cells after the overexpression of tRF-24-V29K9UV3IU compared with the NC group. Red means up-regulated DEGs, and green means down-regulated DEGs. "tRF-24" indicates cells overexpressing tRF-24-V29K9UV3IU. $n = 3$, t test, $*** P < 0.001$.

rescue experiments. Flow cytometry results showed that the overexpression of tRF-24-V29K9UV3IU prominently increased apoptosis in MKN-45 cells; conversely, GPR78 overexpression significantly reduced the apoptosis of MKN-45 cells (Figures 6(a) and 6(b)). In addition, the cotransfection of tRF-24-V29K9UV3IU mimics and oe-GPR78 partially eliminated the effect on MKN-45 cells (Figures 6(a) and 6(b)). Similarly, growth curves suggested that overexpression of tRF-24-V29K9UV3IU prominently decreased the proliferative ability of MKN-45 cells, and GPR78 overexpression had the opposite effect, whereas the cotransfection of tRF-24-V29K9UV3IU mimics and oe-GPR78 counteracted each other (Figure 6(c)). Transwell assays implicated that the migratory and invasive capabilities of MKN-45 cells were significantly inhibited by tRF-24-V29K9UV3IU mimics but significantly enhanced by the overexpression of GPR78 (Figures 6(d) and 6(e)). Simultaneous action of tRF-24-V29K9UV3IU mimics and oe-GPR78 could partially dilute the effect (Figures 6(d) and 6(e)). Therefore, these results supported that tRF-24-V29K9UV3IU altered the biological functions of GC cells by down-regulating GPR78 expression.

4. Discussion

Accumulation studies prove that non-coding RNAs are widely involved in the occurrence and development of tumors [19]. Importantly, tRFs are expected to be an important target in cancer treatment owing to their role in tumor progression [20]. In this study, we provided evidences that the low expression of tRF-24-V29K9UV3IU in GC *in vivo* was related to the promotion of growth and

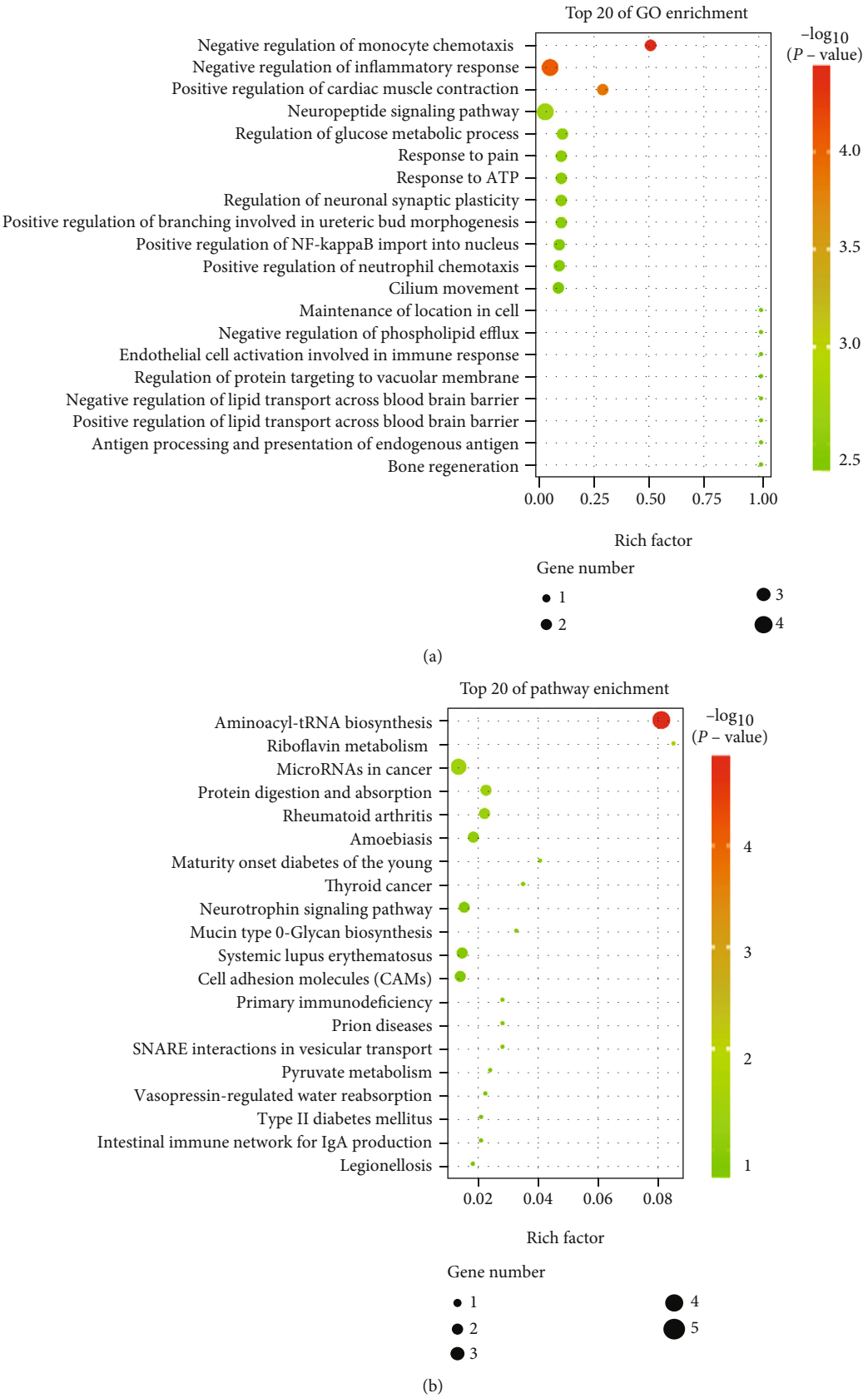

Figure 4: Functional analysis of DEGs. (a) Top 20 GO terms and (b) top 20 KEGG pathways identified among enriched DEGs. Circle size indicates the number of DEGs enriched, and red color indicates significant enrichment.

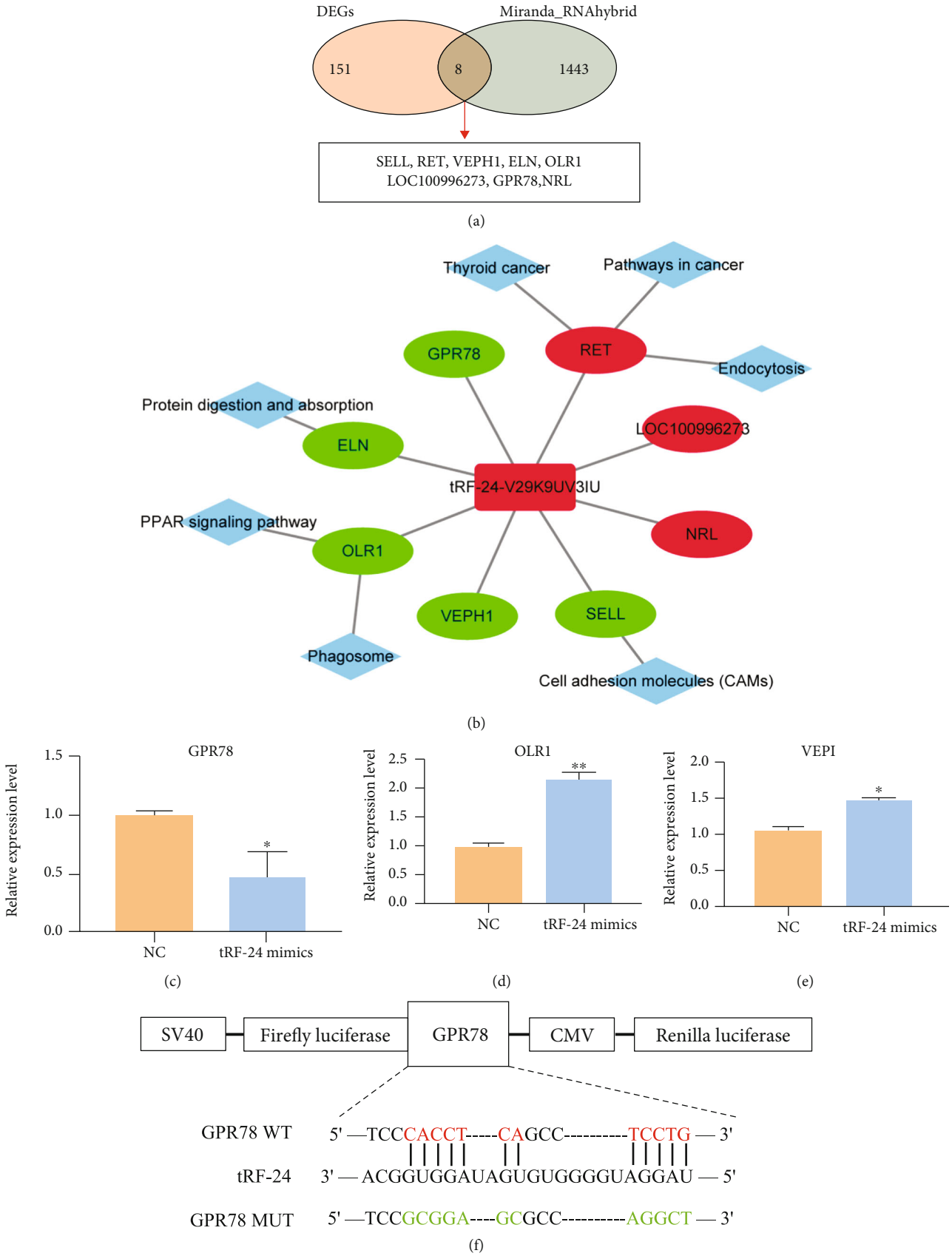

Figure 5: Continued.

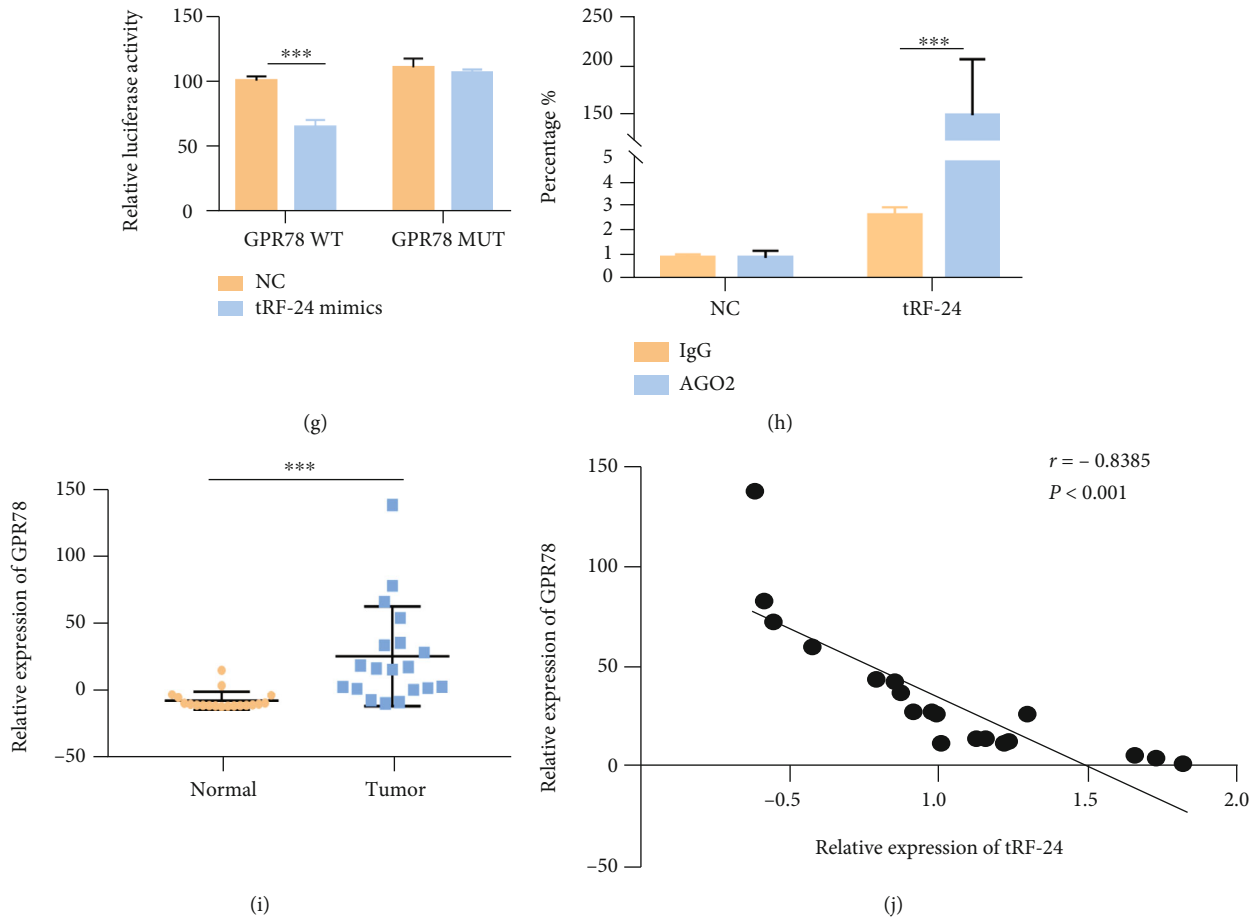

Figure 5: tRF-24-V29K9UV3IU inhibits GPR78 expression by binding its 3′-UTR in GC cells. (a) Eight DEGs predicted to possibly bind tRF-24-V29K9UV3IU through overlap of DEGs and the Miranda and RNAhybrid database. (b) The regulatory network of tRF-24-V29K9UV3IU. The rounded rectangle represents tRF-24-V29K9UV3IU, the ellipse represents mRNA, the diamond represents a pathway, and the red/green color indicates upregulation and down-regulation, respectively. ((c)–(e)) Expression of *GPR78*, *OLR1*, and *VEPH1* as verified by qRT-PCR. (f) Putative binding site of tRF-24-V29K9UV3IU on GPR78. (g) The luciferase activity of GPR78 in MKN-45 cells after cotransfection with tRF-24-V29K9UV3IU mimics or NC. (h) An AGO2-RIP assay was conducted to confirm that tRF-24-V29K9UV3IU associates with AGO2. (i) Expression of *GPR78* in 19 pairs tumor and normal tissues detected by qRT-PCR. Expression of *GPR78* was up-regulated in tumor compared to normal tissues. (j) The expression of *GPR78* and tRF-24-V29K9UV3IU was negatively correlated, which was analyzed by Pearson's correlation in tumors. The above experiments were repeated three times. *t* test, $*P < 0.05$, $**P < 0.01$, $*** P < 0.001$.

metastasis of tumor cells. In addition, we found that tRF-24-V29K9UV3IU directly inhibited GPR78 expression to suppress the proliferation, invasion, and metastasis and promote apoptosis of GC cells.

Increasing studies have showed that tRFs serve a pivotal role in the development of tumors. For instance, tRFs (e.g., derived from the nuclear $tRNA^{Gly}$ and $tRNA^{Leu}$, the mitochondrial $tRNA^{Val}$ and $tRNA^{Pro}$) and isoforms of miRNAs (isomiRs) contributed to the race disparities in triplen-negative breast cancer [21]. Londin et al. reported the abundance profiles and biases in lengths of tRFs associated with metastatase and patient survival in uveal melanoma [22]. A novel mitochondrial tRF of i-tRF-Phe is a molecular prognostic biomarker in chronic lymphocytic leukemia [23]. The tRF-24-V29K9UV3IU is a mitochondrial 5′-tRF discovered in our previous work [12], and here, we demonstrate that it plays a negative regulatory role in GC. Also, we found that tRF-24-V29K9UV3IU is not only expressed in GC, but also lowly expressed in TCGA STAD and other TCGA COAD cancers. These results encourage us to believe that tRF-24-V29K9UV3IU plays a key role in the progression of GC and induces us to further explore its mechanism of function.

Accumulating evidence has demonstrated that tRFs have a functional mechanism similar to that of miRNAs. For example, tRNA-derived fragments of CU1276 can interact with AGO1-4 proteins, functioning just as miRNAs to modulate the proliferation and DNA damage response in B cell lymphoma [17]. Green et al. found that tRF-3003a was enriched in the AGO2/RNA-induced silencing complex, and the inhibitory effects of tRF-3003a on JAK3 were abolished by AGO2 knockdown [24]. $5'\text{-tRF}^{His\text{-}GTG}$ has also been identified as a miRNA-like small non-coding RNA whose function relied on AGO2 [25]. Thus, perhaps as

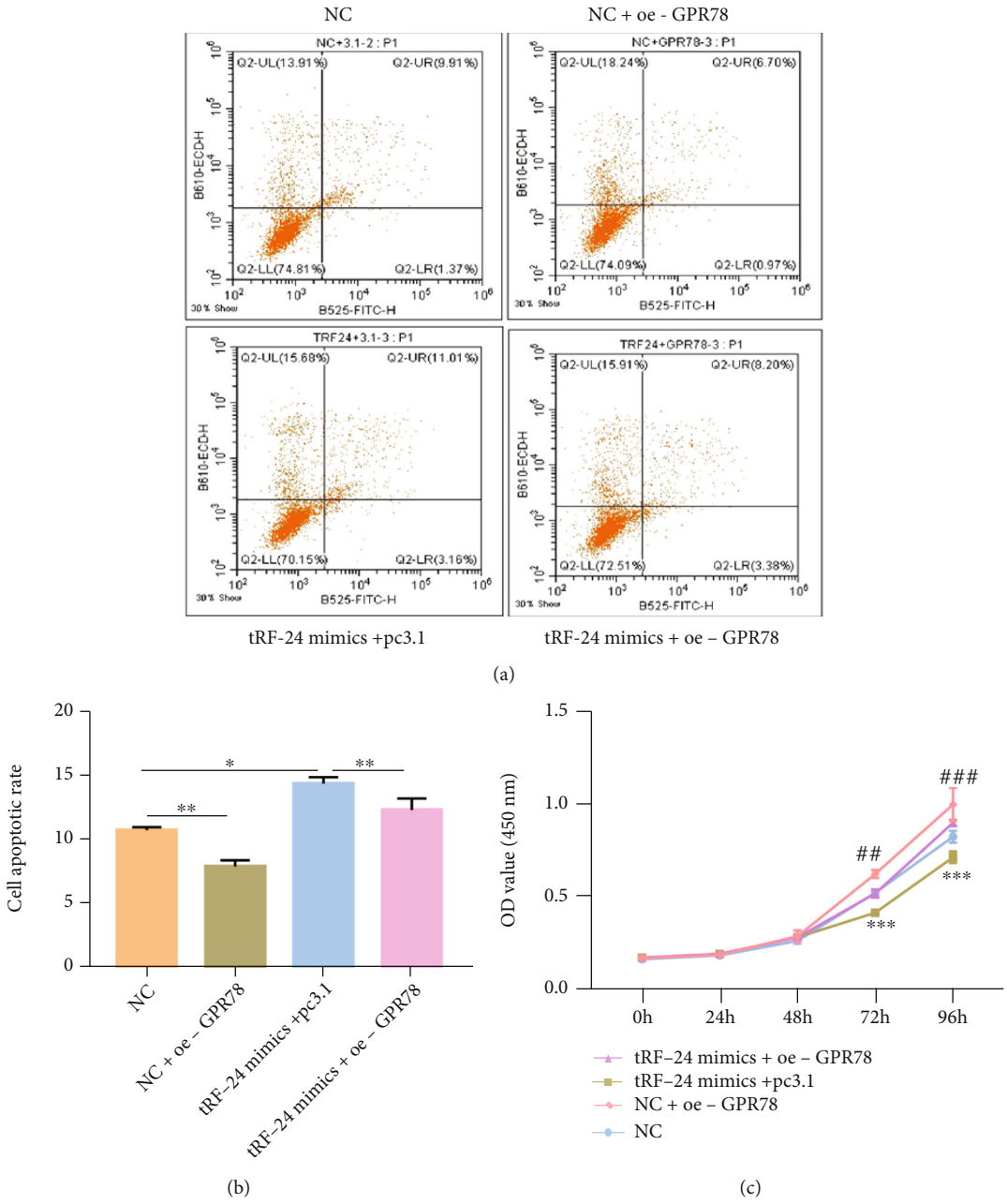

Figure 6: Continued.

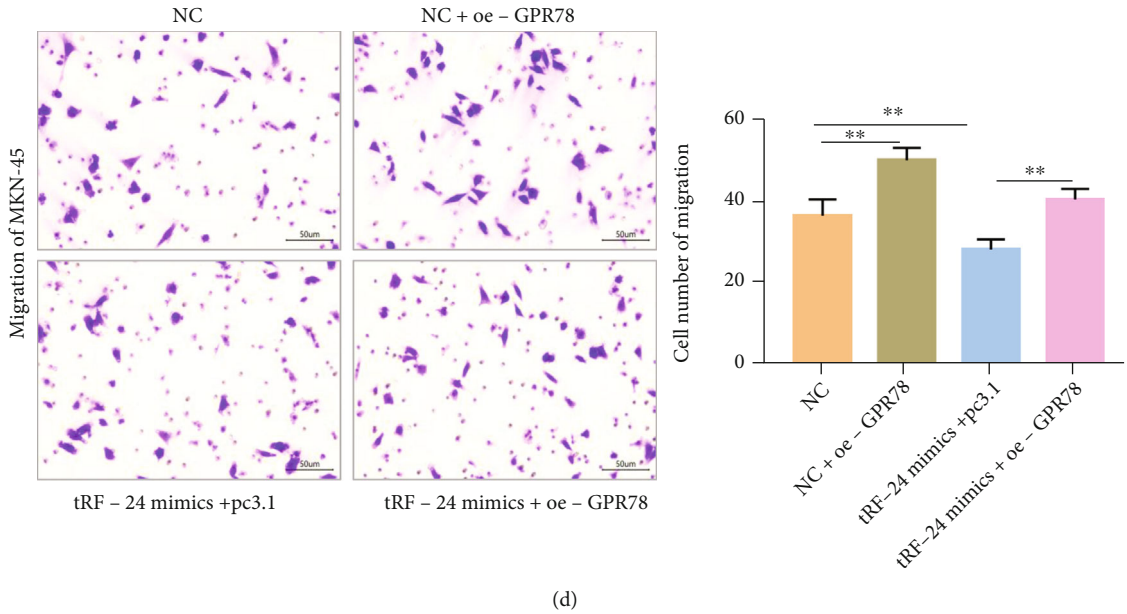

(d)

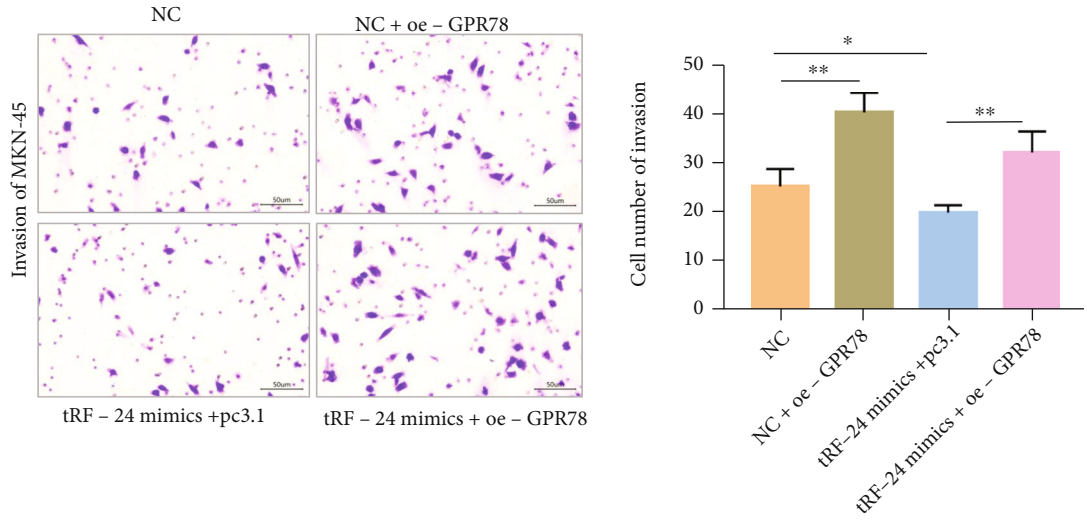

(e)

Figure 6: tRF-24-V29K9UV3IU inhibits the biological functions of GC cells by regulating GPR78 expression. (a) Representative images and (b) statistical results of flow cytometry analysis utilized to determine the number of apoptotic cells in four groups. (c) Cell proliferation assays of MKN-45 cells overexpressing tRF-24-V29K9UV3IU. (d) Transwell assays were used to detect the effect of overexpression of tRF-24-V29K9UV3IU on MKN-45 cell migration (d) and invasion (e). These results showed that overexpression of tRF-24-V29K9UV3IU promoted apoptosis, suppressed proliferation, migration, and invasion, while overexpression of BBB was opposite, and overexpression of GPR78 weakened the function of tRF-24-V29K9UV3IU. The above experiments were repeated three times. One-way ANOVA followed by Tukey's test, $*P < 0.05$, $**P < 0.01$.

reviewed by Venkates et al., tRFs usually masqueraded as miRNA [26]. We hypothesize that tRF-24-V29K9UV3IU also acts in this manner. Because the function of miRNAs depends on the AGO2 protein, we explored the relationship between tRF-24-V29K9UV3IU and AGO2, and AGO2–RIP revealed that the tRF-24-V29K9UV3IU was significantly enriched by AGO2 antibody rather than IgG. Therefore, tRF-24-V29K9UV3IU might bind to AGO2 and function as a miRNA-like RNA to regulate target gene activity and thus inhibit the progression of GC.

In addition, our results of transcriptome sequencing and luciferase assay show that GPR78 is physically bound and transcriptionally regulated by tRF-24-V29K9UV3IU. GPR78 belongs to the G-protein–coupled receptor superfamily, which is composed of approximately 800 different members, functioning as central nodes of many different signaling pathways participated in various aspects of human physiology [27]. The function of members of the GPR Class A orphan subfamily in regulating tumor progression has been widely reported. For instance, GPR48/LGR4 overexpression promoted thyroid tumor growth, lymph node metastasis, and recurrence *in vivo* and proliferation and migration of thyroid cancer cells *in vitro* [28]. The CXCL17-CXCR8 (GPR35) signaling axis promotes

the proliferation and migration of breast cancer cells *in vitro* and *in vivo* [29]. Therefore, it is reasonable to speculate that GPR78 is involved in the regulation of tumor progression, and this has been partially confirmed. GRP78 promotes malignant phenotype of hepatocellular carcinoma by activating the Wnt/HOXB9 signaling pathway and chaperoning LRP6 [30]. GPR78 activates the Gαq-Rho GTPase pathway to promote lung cancer cell migration and metastasis [31]. In this study, GPR78 was shown to significantly block the inhibition of proliferation, migration, and invasion of GC cells caused by the overexpression of tRF-24-V29K9UV3IU, suggesting that GPR78 promotes GC progression, but its activity is regulated by tRF-24-V29K9UV3IU. These results were consistent with those of the abovementioned studies. Therefore, we speculate that the inhibition effect of tRF-24-V29K9UV3IU on GC is achieved by physically regulating GPR78 expression.

Moreover, it is worth noting that in our previous studies, We found that tRF-24-V29K9UV3IU inhibited the biological function of GC cells [12], which was consistent with the results of this study. Also, using target and function prediction found that tRF target genes were major enriched in focal adhesion, stem cell differentiation regulation, cancer proteoglycan synthesis, Wnt, MAPK, and calcium signaling pathways. However, in this study, the pathway of KEGG enrichment was microRNAs in cancer, thyroid cancer, and cell adhesion molecule (CAM) pathways. The reason for this discrepancy may be related to the experimental design. In the previous study , the KEGG analysis was based on target gene prediction and enrichment of miRNA-like mechanism for all DEtRFs between tumor and adjacent tissues, whereas this study was performed enrichment for DEGs after tRF-24-V29K9UV3IU knockdown, these DEGs included those regulated by tRF-24-V29K9UV3IU through other mechanisms than miRNA-like. In summary, the analyzed tRF and the based regulatory mechanisms are different, so the enriched pathways will be different.

Interestingly, according to the results of MINTbase v2.0, tRF-24-V29K9UV3IU may be originated from mitochondrial tRNAs. Telonis et al. first reported the existence of multiple sequences in human mitochondrial tRNAs that are highly similar to human nuclear chromosomes, and called it mitochondrial tRNA-lookalikes [6, 32]. The plenty of mitochondrial tRNA-lookalikes, repetitive representation of tRNA templates in the nuclear genome, make it challenging to definitively determine the source of tRFs. Only a few specific and sensitive methods like MINTbase v2.0 can distinguish between mitochondrial tRFs and nuclear tRFs [33]. Thus, we tentatively believe that tRF-24-V29K9UV3IU originates from mitochondria. To date, a few studies have described the presence of mitochondrial tRFs and provided clue for their mitochondrial origin and function [34, 35]. Meseguer proposed two models of mitochondrial tRF biogenesis: 1) one of mitochondrial tRF translocated out of the mitochondria into cytoplasm where Dicer prepared them and then incorporated with AGO2 to regulate the expression of nuclear-encoded genes; 2) mitochondrial tRF processed by Dicer and loaded in AGO2 was occurred in the mitochondria, and then control the expression of mitochondrial DNA-encoded genes [36]. In our study, tRF-24-V29K9UV3IU incorporated with AGO2 and function as a miRNA-like RNA to regulate GPR78. Therefore, we speculate that the working mechanism of tRF-24-V29K9UV3IU is more plausible with the first model.

5. Conclusion

In summary, tRF-24-V29K9UV3IU inhibits growth and metastasis of GC *in vivo*. Moreover, tRF-24-V29K9UV3IU exerts a miRNA-like function and down-regulates GPR78, thereby inhibiting the proliferation, invasion, and migration as well as promoting apoptosis of GC cells *in vitro*. This study identifies novel targets and diagnostic biomarkers to develop molecular therapies for treatment of GC.

Data Availability

The datasets used and/or analyzed in this study are available from the corresponding author upon reasonable request.

Ethical Approval

All experimental procedures and animal care performed were approved according to the relevant guidelines and regulations of the ethics committee of Kunming Medical University.

Conflicts of Interest

The authors declare that there are no conflicts of interest.

Authors' Contributions

All authors made substantial contributions to the conception and design, acquisition of data, or analysis and interpretation of data; took part in drafting the article or revising it critically for important intellectual content; agreed on the journal to which the article will be submitted; gave final approval of the version to be published; and agreed to be accountable for all aspects of the work.

Acknowledgments

This work was supported by the National Natural Science Foundation of China (81860424).

Supplementary Materials

Supplementary 1. Supplemental Table 1. Primers information used in this study.

Supplementary 2. Supplemental Table 2. Clean data quality control and statistics.

References

[1] W. Chen, R. Zheng, P. D. Baade et al., "Cancer statistics in China, 2015," *CA: a Cancer Journal for Clinicians*, vol. 66, no. 2, pp. 115–132, 2016.

[2] V. Catalano, R. Labianca, G. D. Beretta, G. Gatta, F. de Braud, and E. Van Cutsem, "Gastric cancer," *Critical Reviews in Oncology/Hematology*, vol. 71, no. 2, pp. 127–164, 2009.

[3] Y. Mizota and S. Yamamoto, "How long should we continue gastric cancer screening? From an epidemiological point of view," *Gastric Cancer*, vol. 22, no. 3, pp. 456–462, 2019.

[4] T. Abrams, L. M. Hess, Y. E. Zhu, W. Schelman, A. M. Liepa, and C. Fuchs, "Predictors of heterogeneity in the first-line treatment of patients with advanced/metastatic gastric cancer in the U.S," *Gastric Cancer*, vol. 21, no. 5, pp. 738–744, 2018.

[5] R. Magee and I. Rigoutsos, "On the expanding roles of tRNA fragments in modulating cell behavior," *Nucleic Acids Research*, vol. 48, no. 17, pp. 9433–9448, 2020.

[6] A. Telonis, P. Loher, Y. Kirino, and I. Rigoutsos, "Nuclear and mitochondrial tRNA-lookalikes in the human genome," *Frontiers in Genetics*, vol. 5, p. 344, 2014.

[7] K. K. Pandey, D. Madhry, Y. S. Ravi Kumar et al., "Regulatory roles of tRNA-derived RNA fragments in human pathophysiology," *Mol Ther Nucleic Acids*, vol. 26, pp. 161–173, 2021.

[8] P. Schimmel, "The emerging complexity of the tRNA world: mammalian tRNAs beyond protein synthesis," *Nature Reviews Molecular Cell Biology*, vol. 19, no. 1, pp. 45–58, 2018.

[9] L. Han, H. Lai, Y. Yang et al., "A 5'-tRNA halve, tiRNA-Gly promotes cell proliferation and migration via binding to RBM17 and inducing alternative splicing in papillary thyroid cancer," *Journal of experimental & clinical cancer research: CR*, vol. 40, no. 1, p. 222, 2021.

[10] P. Zhu, J. Lu, X. Zhi et al., "tRNA-derived fragment tRFLys-CTT-010 promotes triple-negative breast cancer progression by regulating glucose metabolism via G6PC," *Carcinogenesis*, vol. 42, no. 9, pp. 1196–1207, 2021.

[11] Y. Shao, Q. Sun, X. Liu, P. Wang, R. Wu, and Z. Ma, "tRF-Leu-CAG promotes cell proliferation and cell cycle in non-small cell lung cancer," *Chemical Biology & Drug Design*, vol. 90, no. 5, pp. 730–738, 2017.

[12] X. Dong, X. Fan, X. He et al., "Comprehensively identifying the key tRNA-derived fragments and investigating their function in gastric cancer processes," *Oncotargets and Therapy*, vol. 13, pp. 10931–10943, 2020.

[13] M. Yu, L. Ren, F. Liang et al., "Effect of epiberberine from _Coptis chinensis_ Franch on inhibition of tumor growth in MKN-45 xenograft mice," *Phytomedicine*, vol. 76, p. 153216, 2020.

[14] F. Kong, T. Sun, X. Kong, D. Xie, Z. Li, and K. Xie, "Krüppel-like factor 4 suppresses serine/threonine kinase 33 activation and metastasis of gastric cancer through reversing epithelial-mesenchymal transition," *Clinical Cancer Research*, vol. 24, no. 10, pp. 2440–2451, 2018.

[15] K. J. Livak and T. D. Schmittgen, "Analysis of relative gene expression data using real-time quantitative PCR and the $2^{-\Delta\Delta\ -C-}{}_{T}$ method," *Methods*, vol. 25, no. 4, pp. 402–408, 2001.

[16] H. J. Kim, Y. Joe, S. K. Kim et al., "Carbon monoxide protects against hepatic steatosis in mice by inducing sestrin-2 _via_ the PERK-eIF2 α-ATF4 pathway," *Free Radical Biology & Medicine*, vol. 110, pp. 81–91, 2017.

[17] R. L. Maute, C. Schneider, P. Sumazin et al., "tRNA-derived microRNA modulates proliferation and the DNA damage response and is down-regulated in B cell lymphoma," *Proceedings of the National Academy of Sciences of the United States of America*, vol. 110, no. 4, pp. 1404–1409, 2013.

[18] L. Tong, W. Zhang, B. Qu et al., "The tRNA-derived fragment-3017A promotes metastasis by inhibiting NELL2 in human gastric cancer," *Frontiers in Oncology*, vol. 10, p. 570916, 2020.

[19] V. Boivin, L. Faucher-Giguere, M. Scott, and S. Abou-Elela, "The cellular landscape of mid-size noncoding RNA," *Wiley Interdiscip Rev RNA*, vol. 10, no. 4, article e1530, 2019.

[20] Y. Hu, A. Cai, J. Xu et al., "An emerging role of the 5′ termini of mature tRNAs in human diseases: Current situation and prospects," *Biochim Biophys Acta Mol Basis Dis*, vol. 1868, no. 2, p. 166314, 2022.

[21] A. Telonis and I. Rigoutsos, "Race disparities in the contribution of miRNA isoforms and tRNA-derived fragments to triple-negative breast cancer," *Cancer Research*, vol. 78, no. 5, pp. 1140–1154, 2018.

[22] E. Londin, R. Magee, C. Shields, S. Lally, T. Sato, and I. Rigoutsos, "IsomiRs and tRNA-derived fragments are associated with metastasis and patient survival in uveal melanoma," *Pigment Cell & Melanoma Research*, vol. 33, no. 1, pp. 52–62, 2020.

[23] P. Karousi, P. Adamopoulos, S. Papageorgiou, V. Pappa, A. Scorilas, and C. Kontos, "A novel, mitochondrial, internal tRNA-derived RNA fragment possesses clinical utility as a molecular prognostic biomarker in chronic lymphocytic leukemia," *Clinical Biochemistry*, vol. 85, pp. 20–26, 2020.

[24] J. A. Green, M. Y. Ansari, H. C. Ball, and T. M. Haqqi, "tRNA-derived fragments (tRFs) regulate post-transcriptional gene expression via AGO-dependent mechanism in IL-1β stimulated chondrocytes," *Osteoarthritis and Cartilage*, vol. 28, no. 8, pp. 1102–1110, 2020.

[25] Y. Li, X. Wu, H. Gao et al., "Abstract LB-247: 5′-tRFHis-GTG, a novel tRNA-derived novel mi RNA-like small non-coding RNA, aberrantly expressed in metastatic renal cell carcinoma by promoting tumor cell proliferation, migration and invasion," *Cancer Research*, vol. 73, pp. LB-247–LB-247, 2013.

[26] T. Venkatesh, P. S. Suresh, and R. Tsutsumi, "tRFs: miRNAs in disguise," *Gene*, vol. 579, no. 2, pp. 133–138, 2016.

[27] A. S. Hauser, M. M. Attwood, M. Rask-Andersen, H. B. Schioth, and D. E. Gloriam, "Trends in GPCR drug discovery: new agents, targets and indications," *Nature Reviews. Drug Discovery*, vol. 16, no. 12, pp. 829–842, 2017.

[28] Y. E. Kang, J. M. Kim, K. S. Kim et al., "Upregulation of RSPO2-GPR48/LGR4 signaling in papillary thyroid carcinoma contributes to tumor progression," *Oncotarget*, vol. 8, no. 70, pp. 114980–114994, 2017.

[29] Y. J. Guo, Y. J. Zhou, X. L. Yang, Z. M. Shao, and Z. L. Ou, "The role and clinical significance of the CXCL17-CXCR8 (GPR35) axis in breast cancer," *Biochemical and Biophysical Research Communications*, vol. 493, no. 3, pp. 1159–1167, 2017.

[30] H. Xiong, H. Xiao, C. Luo et al., "GRP78 activates the Wnt/HOXB9 pathway to promote invasion and metastasis of hepatocellular carcinoma by chaperoning LRP6," *Experimental Cell Research*, vol. 383, no. 1, p. 111493, 2019.

[31] D. D. Dong, H. Zhou, and G. Li, "GPR78 promotes lung cancer cell migration and metastasis by activation of Gαq-Rho GTPase pathway," *BMB Reports*, vol. 49, no. 11, pp. 623–628, 2016.

[32] A. Telonis, Y. Kirino, and I. Rigoutsos, "Mitochondrial tRNA-lookalikes in nuclear chromosomes: could they be functional?," *RNA Biology*, vol. 12, no. 4, pp. 375–380, 2015.

[33] V. Pliatsika, P. Loher, R. Magee et al., "MINTbase v2.0: a comprehensive database for tRNA-derived fragments that includes nuclear and mitochondrial fragments from all The Cancer Genome Atlas projects," *Nucleic Acids Research*, vol. 46, no. D1, pp. D152–D159, 2018.

[34] R. Magee, E. Londin, and I. Rigoutsos, "TRNA-derived fragments as sex-dependent circulating candidate biomarkers for Parkinson's disease," *Parkinsonism & Related Disorders*, vol. 65, pp. 203–209, 2019.

[35] S. Meseguer, C. Navarro-González, J. Panadero et al., "The MELAS mutation m.3243A>G alters the expression of mitochondrial tRNA fragments," *Biochimica et biophysica acta Molecular cell research*, vol. 1866, no. 9, pp. 1433–1449, 2019.

[36] S. Meseguer, "MicroRNAs and tRNA-derived small fragments: key messengers in nuclear-mitochondrial communication," *Frontiers in Molecular Biosciences*, vol. 8, pp. 643575–643575, 2021.

Hindawi
Journal of Oncology
Volume 2022, Article ID 3447185, 11 pages
https://doi.org/10.1155/2022/3447185

Research Article

Blocking TGF-β Expression Attenuates Tumor Growth in Lung Cancers, Potentially Mediated by Skewing Development of Neutrophils

Yifei Fang,[1] **Xiyao Li**,[2] **Yuxuan Jiang**,[3] **and Zhihan Ge**[4]

[1]*Faculty of Art and Science, University of Toronto (St. George Campus), Toronto, Ontario, Canada M5S 1A1*
[2]*Nanjing University, Nanjing, Jiangsu 210033, China*
[3]*Qingdao Academy, Qingdao, Shandong 266114, China*
[4]*College of Life Science and Technology, Changchun University of Science and Technology, Changchun, Jilin 130013, China*

Correspondence should be addressed to Yifei Fang; evelyn.fang@mail.utoronto.ca

Received 4 January 2022; Accepted 2 March 2022; Published 21 April 2022

Academic Editor: Fu Wang

In the tumor microenvironment (TME), cells secrete a cytokine known as transforming growth factor-β (TGF-β), which polarizes tumor-associated neutrophils (TANs) towards a protumor phenotype. In this work, C57BL/6 mice with *TGF-β1* gene knocked out selectively in myofibroblasts receive orthotopic implantation of Lewis lung carcinoma (LLC). Then, TANs' differentiation and tumor growth are studied both *in vivo* and *in vitro*, to examine the potential effects of TGF-β levels in TME on neutrophil polarization and cancer progression. Possible results are anticipated and discussed from various aspects. Though tumor suppression via inhibition of TGF-β signaling has been widely studied in this field, this study is the first to present a detailed experimental design for evaluating the potential antitumor effects of blocking TGF-β expression. This work provides a creative approach for cancer treatment targeting specific cytokines, and the experimental design presented here may apply to future research on other cytokines, promoting the development of novel cancer-treating strategies.

1. Introduction

1.1. NSCLC: Lethal Diseases That Lack Effective Diagnosis and Treatment Strategies. Nonsmall cell lung cancer (NSCLC) is a potentially lethal disease, whose incidence is rising rapidly worldwide, especially in the past 50 years. In 2020, there were about 19.3 million new cancer cases and 10.0 million deaths worldwide, with lung cancer accounting for 11.4% of new cases and 18% of deaths, making it the leading cause of cancer death [1]. Apart from the high incidence, the severity of NSCLC may be attributed to the difficulty in its diagnosis. The asymptomatic early stages of NSCLC cause the tumors in almost two-thirds of patients to develop into the advanced stages even before diagnosis.

To attenuate tumor growth, patients with NSCLC are usually treated surgically and postoperative chemotherapy and/or radiotherapy. However, patients with advanced lung cancer are not eligible for surgery, while conventional chemotherapy and radiotherapy do not increase patients' survival rate effectively and have severe adverse effects. To improve NSCLC patients' survival and quality of life, new strategies for NSCLC treatment are in urgent need.

It is worth noticing that NSCLC tumor cells produce multiple inflammatory cytokines, which recruit inflammatory cells such as neutrophils to the tumor microenvironment (TME) and activate them to promote cancer progression [2]. The recruited immune cells and the cytokines that activate them may be potential targets for cancer treatment. This study will be focusing on the tumor-associated neutrophils (TANs) and the transforming growth factor-β (TGF-β), a cytokine that is believed to influence the phenotypes of TANs. By exploring the effect of blocking the

production of TGF-β on neutrophils differentiation and, therefore, cancer progression, this study hereby proposes a novel hypothetical treatment approach.

1.2. Vital Roles of Neutrophils in the Tumor Microenvironment. Neutrophils play a key role in the immune system and polarize into different phenotypes in response to environmental signals [3]. They facilitate adaptive immunity by contributing to B lymphocyte maturation via effector molecules and cytokines including BAFF and APRIL [4]. In addition, neutrophils mediate innate immune destruction of invading microorganisms through phagocytosis, releasing lyase, and producing reactive oxygen-species (ROS) [4]. They also release the neutrophils extracellular traps (NETs) that disarm pathogens. These extracellular fibrillary networks mainly consist of DNA and antimicrobial proteins, which kill microbes extracellularly and prevent further spread of pathogens [5].

Neutrophils play dual roles in the development of tumors, depending on their phenotypes and effector molecules produced [6]. To distinguish subsets of TANs, neutrophils with antitumor activities are known as N1 and the protumorigenic neutrophils are known as N2 [6]. N1 and N2 have different influences on TME, both directly and indirectly through the recruitment and activation of other cells. N1 neutrophils are capable of killing cancer cells by releasing of reactive oxygen species and reactive nitrogen species, as well as activating cytotoxic T cells and recruiting proinflammatory macrophages [7]. In contrast, N2 neutrophils promote tumor growth by inhibiting natural killer cell function and releasing matrix metalloproteinase 9 (MMP9), which stimulates angiogenesis and dissemination of cancer cells [7]. N2 neutrophils also recruit anti-inflammatory macrophages and regulatory T cells, which further facilitate cancer progression.

The role of TANs in NSCLC has not been extensively studied. However, during the treatment of patients with NSCLC, the neutrophil to lymphocyte ratio (NLR) is a commonly used prognostic marker of immunotherapy [8]. This suggests that neutrophils may have important effects on the progression of NSCLC and can be a potential target for NSCLC treatment.

1.3. TGF-β: Functions and Origins. The phenotypic switch in TANs is thought to be regulated by TGF-β, which is the most well-studied cytokine in the TGF-β superfamily. As a multifunctional cytokine, TGF-β has a great influence on the inflammatory response, bone remodeling, and cell differentiation. More importantly, it has been shown that TGF-β contributes to the growth of tumor cells, which makes it a potentially suitable target for cancer treatment. One of the major ways by which TGF-β stimulates tumor growth is that it induces N2 polarization of TANs, which inhibits the antitumor function of T cell and NK cells [9]. It has been demonstrated that blocking TGF-β activity inhibits the progression of the colorectal cancer (CRC) via the polarization of TANs towards N1 [10]. However, the antitumor effect of inhibiting TGF-β has not yet been tested in NSCLC.

In TME, tumors can promote TGF-β production through different pathways. For instance, TC-1 and B16-OVA tumor cells can secrete TGF-β in order to suppress the immunological function of plasmacytoid dendritic cells (pDC) [11]. Tumor cells can stimulate platelets to release large amounts of TGF-β to assist metastasis [12], and osteoclasts during tumor bone metastasis produce a large amount of TGF-β [13]. Thus, identifying and blocking the source of the TGF-β surge in TME would be a viable cancer treatment option. Hence, the authors hypothesize that blocking the expression of TGF-β *in vivo* will attenuate tumor growth in NSCLC, potentially mediated by skewing development of TANs' subpopulations.

Several research papers that have led to the novel immunotherapeutic approach to treat NSCLC are described in the following section. The chosen papers have provided evidence for the significance of the antitumor neutrophils subpopulation in resistance against selected cancers, as well as the vital roles of TGF-β in the polarization of neutrophils towards protumor phenotypes. The papers have also demonstrated that inhibiting TGF-β activities leads to tumor suppression, which has provided the foundation for the hypothetic treatment for NSCLC by blocking the expression of TGF-β.

2. Approach

2.1. Summary of Primary Research

2.1.1. Function of Neutrophils in Tumor Microenvironment. In [7], neutrophils are a key player in the tumor microenvironment and are considered to be associated with cancer progression. By performing both bulk and single-cell RNA sequencing (scRNA-seq) assays on gene knockout mice, the researchers demonstrated that neutrophils are required for the activation of an interferon-gamma-dependent pathway of immune resistance, mediated by the polarization of a subset of $CD4^{-}CD8^{-}$ unconventional $\alpha\beta$ T cells (UTC$\alpha\beta$). In selected human tumors, the researchers found that neutrophil infiltration was associated with a type 1 immune response and better clinical outcome. To conclude, these experiments showed the importance of neutrophils in resistance against murine sarcomas and selected human tumors.

2.1.2. Anti-TGF-β Inhibits Cancer Progression via the Polarization of TANs to an anti-Tumor Phenotype. The [10] investigated the role of anti-TGF-β on the polarization of TANs towards a tumor-suppressive phenotype. Firstly, the researchers found that patients with colorectal cancer (CRC) showed higher TANs' infiltration and increased levels of TGF-β compared to the control. To further evaluate the roles of TANs and TGF-β in TME, SW480 cells established from a primary adenocarcinoma of the colon were cultured *in vitro* with primed neutrophils, which can be considered as TANs. Anti-TGF-β was added to block TGF-β in order to polarize TANs. The addition of anti-TGF-β not only suppressed the tumor migration by decreasing the metastasis chemoattractant produced by TANs but also promoted the apoptosis of cancer cells by increasing the cytotoxicity of TANs. This altered phenotype of TANs was potentially due to increased GM-CSF and INF-γ expression, which are

cytokines that regulate the polarization of TANs. Further immunoblotting showed that the tumor-suppressive effect was mediated by the inhibition of PI3K/AKT signaling pathways in TANs and TGF-β/Smad signaling pathways in the tumor cells. Lastly, to explore the tumor-suppressive effect of anti-TGF-β *in vivo*, mice models were treated with anti-TGF-β. The tumors in the treated mice were significantly smaller and showed reverse tumorigenesis. To conclude, this study provided evidence that inhibiting TGF-β by anti-TGF-β could attenuate cancer progression via the polarization of TANs towards an antitumor phenotype, providing novel ways to cancer treatment.

2.1.3. Integrin Subunit α_V Expressed by Tumor Cells Activates TGF-β. The [19] study showed that cancer cells express an integrin subunit known as α_V, which activates TGF-β in the tumor microenvironment (TME). When first secreted, TGF-β is bound to latency associated protein and has no effector functions. The activation of TGF-β reshapes TME by polarizing the neutrophils towards a protumor phenotype, helping the tumor cells to evade the attack of the immune systems. Additionally, the inhibition of TGF-β maturation via α_V knockout promotes the differentiation of activated cytotoxic T cells to granzyme B-producing CD103+CD69+ resident memory T cells, which induce apoptosis in tumor cells. To conclude, this study demonstrated how the tumor cells evade the immune responses via TGF-β activation, suggesting that TGF-β may be a good target for cancer treatment.

2.1.4. Finding and Inhibiting the Origin of TGF-β in TME. In [13], the authors revealed the role of TGF-β in the differences in the effectiveness of immune checkpoint therapy (ICT) in subcutaneous and skeletal castration-resistant prostate cancer (CRPC) models. They discovered that Th17 cells without antitumor function replace antitumor Th1 cells in the presence of abnormally high levels of TGF-β, which is closely related to Th17 differentiation. Next, they hypothesized the TGF-β surge results from the overabundance of osteoclastic cells in bone metastases. To further support the hypothesis, the writers blockaded the osteoclast differentiation and activated factor NF-κB, significantly suppressing the osteoclasts in the femur. Consequently, TGF-β levels were significantly reduced while no significant changes in other cytokine levels were observed. Thus, they identified the main source of TGF-β overabundance in bone metastases as the osteoclast cells. Lastly, the authors found that the survival rate of bone metastatic CPRC mice was significantly enhanced after anti-TGF-β injection, and increased levels of CD8+ Tc, a marker for ICT, were detected, confirming that blocking TGF-β can be an effective way to strengthen the effect of ICT. Considering TGF-β is a vital protumor cytokine, the ideas provided in this paper for discovering and inhibiting the origin of TGF-β in the tumor microenvironment may have great potential in the treatment of other tumors.

The studies discussed above have demonstrated the importance of TGF-β in the polarization of TANs towards tumor-suppressive phenotypes, which have been identified as a key player in the immunity against cancers. The activity of TGF-β may also be inhibited to suppress tumor by skewing the development of TANs subsets. Combining these findings, the authors of this work hypothesize that inhibiting the expression of TGF-β *in vivo* assists in NSCLC treatment, potentially via the polarization of TANs' subpopulations. The general approach and detailed experiment designs are discussed in the next section.

2.2. Method and Materials

2.2.1. General Approach. A series of experiments will be performed on four groups of C57BL/6 mice. The treatment group is mice with the *TGF-β1* gene knocked out specifically in myofibroblasts, showing low production of TGF-β in TME. One control group is wild type, healthy mice with normal level of TGF-β in TME. The second control group represents mice with TGF-β overexpression and consists of wild type mice with frequent injections of purified TGF-β to keep the level of TGF-β in TME high. The last group is comprised of mice treated with 1D11, which is the monoclonal antibody specific to TGF-β. The blockade of TGF-β has been shown to polarize TANs towards N1 and induce antitumor response [10]; thus, this group of mice is set up to examine the effectiveness of *TGF-β1* gene knockout therapy compared to the known antitumor effect of direct TGF-β inhibition.

The level of TGF-β in TME will be measured, and their N1 and N2 will be quantified to show how TGF-β level affects TANs' differentiation. The progression of cancer in each group will be examined by studying tumor phenotypes and marker expression. In addition, four media will be prepared, each of which will contain Lewis lung carcinoma cells, primed neutrophils, and myofibroblasts obtained directly from a specific group of mice model. The media allow the experiments to be repeated *in vitro*, so that it can be more confidently concluded that the findings of this work solely result from the change in TGF-β level in TME.

2.2.2. Mice Model and Animal Care. Pathogen-free C57BL/6 mice with mixed genders at 6 weeks old will be used in this study. All mice will have free access to a standard laboratory diet and water *ad libitum*. The mice will be kept under controlled temperature and a 12 h light and dark cycle. The experimental procedures will be performed based on institutional animal care guidelines.

2.2.3. Tumor Cell Line. Lewis lung carcinoma (LLC) cell line originated from mouse lung will be used in this study. LLC cells will be maintained as monolayer cultures in Dulbecco's Modified Eagle Medium (DMEM) with 10% fetal bovine serum (FBS) and penicillin/streptomycin and kept within 5% CO_2 chamber and under 37 degrees Celsius.

2.2.4. Orthotopic Intrapulmonary Implantation of LLC. C57BL/6 mice will be anesthetized with ether before surgery. A limited skin incision to the left chest with a length of approximately 5 mm will be made to each mouse, and 3×10^4 LLC cells will be suspended in PBS buffer and orthotopically injected into the lung parenchyma. After injection, the

skin incision will be closed by a surgical skin clip. Throughout the implantation procedure, the vital signs of mice including respiration rate and heart rate will be monitored. The transplanted tumors are allowed to develop for two weeks before the mice are sacrificed by euthanasia.

2.2.5. Tissue Specific Knock-out Mice via Cre-loxP System. C57BL/6 mice that are homozygous for a *TGF-β1* gene flanked by *loxP* sites will mate with C57BL/6 mice that are hemizygous for myofibroblast-specific *cre* transgene and homozygous for *TGF-β1* genes that are not floxed. The cross will generate mice that are heterozygous for the floxed allele and hemizygous for the *cre* transgene. The F1 generation will then mate with the homozygous floxed mice. One fourth of the offspring will be homozygous for the floxed allele and hemizygous for the *cre* transgene, and they will be the *TGF-β1* knock-out mice used in further experiments. The *cre* transgenic mice without any *loxP*-flanked alleles will have normal TGF-β expression and will be one of the control groups. If the *Cre-loxP* system fails, then CRISPR-Cas9 will be used as an alternative gene editing tool.

2.2.6. Tissue-Specific Gene Knockout via CRISPR-Cas9. Single guide RNA (sgRNA) will be designed via GenScript, whose algorithm is developed and validated by Feng Zhang lab, Broad Institute of Harvard and MIT. A px330 plasmid coding Cas9, sgRNA, and a myofibroblast-specific promoter will be introduced to fertilized, one-celled oocytes of C57BL/6 mice. The oocytes will then be transferred to pseudopregnant females. In this way, C57BL/6 mice with *TGF-β1* gene specifically knocked out in myofibroblasts will be generated via a Nonhomologous End Joining (NHEJ) approach.

2.2.7. Direct Inhibition of TGF-β via Monoclonal Antibody 1D11. TGF-β antibody 1D11 (R&D Systems, Inc., MN, USA) is a highly potent TGF-β inhibitor that simultaneously inhibits TGF-β1, TGF-β2, and TGF-β3, with the most significant inhibitory effect on TGF-β1 signaling [14]. One of the four groups of mice will be treated with 1D11 three times per week, i.p, 5 mg/Kg to inhibit TGF-β signaling *in vivo*. To inhibit TGF-β signaling in the TME *in vitro*, one of the four media will be prepared by coculturing LLC cells, primed neutrophils, and myofibroblasts from wild-type mice in the presence of 1D11.

2.2.8. LLC Conditioned Medium. LLC cells will be plated under the conditions described in the "*Tumor cell line*" section. When the cells are 50% confluent, the medium will be replaced by DMEM with 1% FBS. After 48 hours, the conditioned medium will be collected and used for neutrophils priming.

2.2.9. Purification of Neutrophils. Around 10 mL of blood will be obtained from healthy, wild-type C57BL/6 mice and anticoagulated with heparin. The neutrophils will be isolated by density centrifugation, and their viability will be checked via trypan blue exclusion. The purity of neutrophils may be checked by Wright staining of cytocentrifuge slides.

2.2.10. Neutrophil Priming. Before being cocultured with LLC cells in the presence or absence of 1D11, the purified neutrophils need to be primed by culturing in the conditioned medium of LLC cells for 6 hours. The primed neutrophils will adjust to the tumor microenvironment and may be considered as TANs in subsequent *in vitro* assays.

2.2.11. Enzyme-Linked Immunosorbent Assay (ELISA). This assay employs a quantitative sandwich enzyme immunoassay technique, using AssayMax Mouse TGF-β1 ELISA (Enzyme-Linked Immunosorbent Assay) kit to detect TGF-β1 in the supernatants of cell lysate and the plasma. TGF-β1 molecules in the standard solutions and the samples will be fixed to the plate by the immobilized antibody. Then, they will be bound by biotinylated polyclonal antibodies specific to mouse TGF-β1, which can be recognized by a streptavidin-peroxidase conjugate. All the unbound substances are then washed away, and a peroxidase enzyme substrate is added for the color to develop. The color development will be stopped and the absorbance at a certain wavelength will be measured. Concentrations of TGF-β1 will be calculated by comparing the absorbance with a standard curve generated by ELISA assays on TGF-β1 in standards.

2.2.12. Measurement of Tumor Size and Weight. After the mice are sacrificed, the tumors will be removed by surgery. The weight of the tumors will then be measured, along with the length (longest dimension) and width (shortest dimension) of the tumors. The size of the tumor can then be calculated by the formula $V = 1/2\,(L \times W)^2$ [15].

2.2.13. Electrochemiluminescence Immunoassay (ECLI). Tumor markers are molecules present in or produced by malignant cells or tumor-associated cells, and their upregulation often correlates with tumor growth. In this study, CEA, CA125, NSE, and cyfra21-1 are selected as the tumor markers for NSCLC, because increases in their serum concentrations are often detected in NSCLC patients. Prior to ECLI, blood will be collected from all groups of mice and centrifuged to obtain the serum. The level of the tumor markers in the serum will be quantified, by measuring their chemical electroluminescence. Elecsys1010 and kits provided by Roche in Germany will be used in the ECLI assay.

2.2.14. Immunohistochemical Analysis. DAB staining will be performed on paraffin sections of lung tissues according to the instructions of DAB staining kit (Abcam). Antibodies specific to CD31 (Thermo Fisher) will be used in this study.

2.2.15. Fluorescence-Activated Cell Sorting (FACS). FACS will be performed on the cells in TME to quantify N1 and N2 neutrophils, which allows the researchers to study the effect of blocking TGF-β expression on TANs' polarization. The cells in TME will be harvested and washed to prepare a single cell suspension in ice cold FACS Buffer (PBS, 0.5-1% BSA or 5-10% FBS, 0.1% NaN_3 sodium azide). To identify the TANs in the suspension, antibodies specific to LyG6 (Proteintech) will be added, which is expressed extensively on neutrophils [16]. To further distinguish N1 from N2 neutrophils, the cells will be labelled with antibodies specific to

CD206 (Abcam), which is expressed on the surface of N2 but not N1. The two types of antibodies have unique fluorescent tags attached to them, so the labelled cells will emit light with different wavelengths when analyzed with a flow cytometer, allowing the identification of the distinct cell types.

3. Anticipated Results

3.1. TGF-β Expression in TME. To study the efficiency of manipulating the expression of TGF-β in TME by specifically knocking out *TGF-β1* gene in mice myofibroblasts, the serum TGF- β1 level in mice will be quantified via ELISA. Additionally, the TGF-β1 level in the media containing purified LLC cells, TANs, and myofibroblasts will also be measured via ELISA. Since the level of TGF-β is not directly influenced in mice treated with 1D11 or in the medium prepared in the presence of 1D11, ELISA is not performed for these two groups of samples. The two possible results for the rest of the samples are shown in Figure 1 below.

3.2. Change in Tumor Growth in Response to TGF-β Level in TME. All mice will be sacrificed 2 weeks after orthotopic transplantation of NSCLC cells, and the size and weight of the NSCLC tumor will be measured. The four possible outcomes are shown in Figure 2.

3.3. Immunohistochemical Analysis. The lung tissues of mice will be sliced and stained with H and E and immunohistochemistry. It is expected that more blurred tumor margins and more microvascular infiltration around the tumor tissue are observed in mice with injections of additional TGF-β. In *TGF-β1* gene knockout mice and 1D11-treated mice, clearer tumor tissue margins, less microvascular infiltration, and fewer necrotic areas within the tumor sections are expected.

3.4. Detection of Tumor Markers. The level of tumor markers CEA, CyFRA21-1, NSE, and CA125 in mice serum is measured to further study the progression of NSCLC under different TGF-β levels [17]. The two possible results are shown in Figure 3.

3.5. The Relative Abundance of N1 and N2 TANs in TME. To study the effect of inhibiting TGF-β production in myofibroblasts on the differentiation of TANs, FACS would be performed on the cells in TME to quantify N1 and N2 subpopulations. The anticipated results are shown in Figure 4.

4. Discussion

4.1. TGF-β Expression in the Tumor Microenvironment (TME). The expected results are shown in Figure 1(a), where the level of TGF-β decreases in TME with *TGF-β1* knocked out myofibroblasts. This confirms that the tissue-specific gene knockout is successful, and myofibroblasts are a major source of TGF-β. In Figure 1(b), however, similar TGF-β levels are observed in the wild type and the *TGF-β1* knockout models, indicating that the gene knockout is not effective. Before any further assay, the tissue-specific gene knockout needs to be redone via CRISPR-Cas9. Alternatively, the ineffective knockout may be because myofibroblasts are not a significant source of TGF-β in TME. Therefore, in future experiments, *TGF-β1* may be knocked out in a different cell type or more than one cell type. Additionally, if the injection of purified TGF-β only leads to significantly higher TGF-β level *in vitro* but not *in vivo*, it is highly likely due to the catabolism of TGF-β *in vivo*, which may be compromised by more frequent injections of TGF-β.

4.2. Tumor Size and Weight. In Figure 2(a), no significant difference in the growth rate of tumors can be observed in four groups of models. In this case, TGF-β has little effect on tumor growth and the hypothesis is refuted. In Figure 2 (b), *TGF-β1* knockout mice develop larger tumors than wild-type mice, while 1D11 treatment suppresses tumor growth. The reason behind the different outcomes between the two inhibition mechanisms may be that 1D11 only inhibits TGF-β in TME, while *TGF-β1* knockout blocks TGF-β expression in all myofibroblast cells throughout the body. Since TGF-β1 is a multifunctional cytokine widely present in the body, the knockout of *TGF-β1* may have an overall immune-suppressive effect, hence facilitating the development of cancer. Figure 2(c) shows no significant difference in tumor growth rate between the *TGF-β1* knockout group and the wild-type mice, while mice with injections of TGF-β develop larger tumors. It is likely that the gene knockout in myofibroblasts does not effectively reduce the TGF-β level in TME. As previously discussed, the tissue-specific gene knockout method needs to be revised. Lastly, in Figure 2(d), compared to the wild-type mice, tumor growth in the *TGF-β1* knockout mice is attenuated and the mice with higher levels of TGF-β develop larger tumors. Thus, reducing the expression of TGF-β shows antitumor effects and the hypothesis is supported. The difference in the limitation of tumor growth between the *TGF-β1* knockout treatment and the 1D11 treatment also reflects the effectiveness of tumor suppression by blocking TGF-β production. However, the measurements of tumor size and weight only examine the growth of primary NSCLC tumors, while providing no information regarding tumor metastasis. Thus, follow-up experiments are required to study the effect of TGF-β level on tumor metastasis.

4.3. Immunohistochemical Analysis. More irregular tumor tissue boundaries and increased microvascular infiltration typically represent a more malignant tumor. Thus, if clearer tumor tissue margins and less microvascular infiltration are observed in the *TGF-β1* knockout mice compared to the wild type mice, then inhibition of TGF-β expression is shown to attenuate tumor growth, supporting the hypothesis. If the morphology of the tumors shows no appreciable differences among the mice models, the hypothesis might be refuted. However, the qualitative nature of tumor morphology makes the analysis inevitably subjective. Hence, the results need to be analyzed with quantitative data from other experiments in order to draw a more reliable conclusion.

4.4. The Level of Tumor Markers. Tumor markers such as CEA, CyFRA21-1, NSE and CA125 are commonly used in

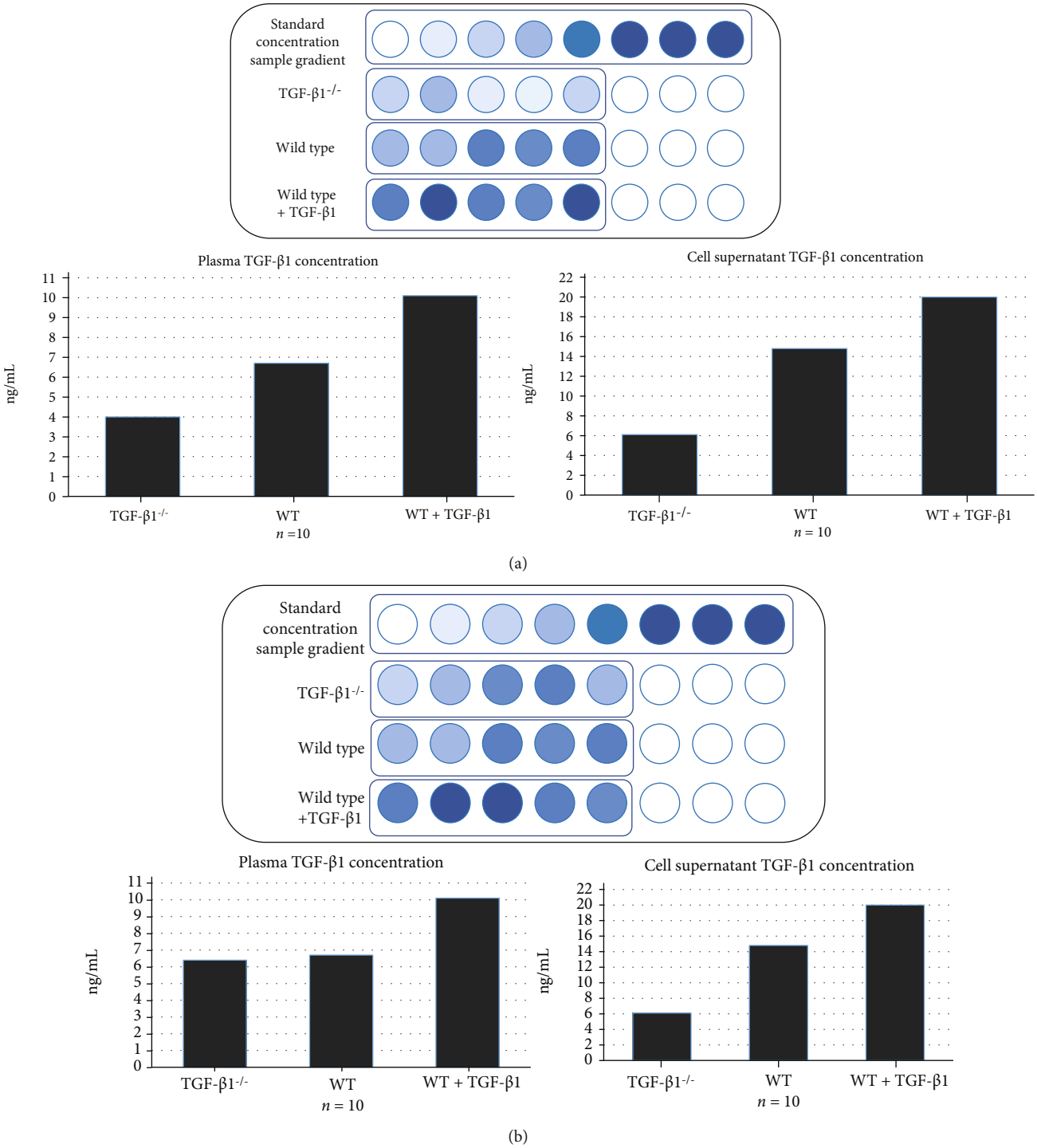

Figure 1: Predicted plasma TGF-β1 concentration and TGF-β1 concentration *in vitro* (a) Blood TGF-β1 concentration in TGF-β1 knockout mice is reduced compared with wild-type mice. In addition, the TGF-β1 concentration of mice with injection of purified TGF-β1 is significantly higher than that of wild-type mice. (b) Compared with the wild-type mice, there is no significant decrease in blood TGF-β1 concentration in the *TGF-β1* knockout group, indicating that the gene knockout model is not successful.

cancer diagnosis. Their abnormal upregulation often precedes clinical symptoms and other detection signals [18], so their concentrations may be measured to study the tumor growth. In Figure 3(a), the levels of most tumor markers decrease in mice with lower TGF-β expression, indicating that blocking the production of TGF-β in TME inhibits tumor growth, supporting the hypothesis. The effectiveness of *TGF-β1*-knockout therapy may be inferred by comparing the level of tumor markers in knockout mice and mice treated with 1D11, which has been shown to limit tumor growth via TGF-β inhibition [10]. In Figure 3(b), the levels of most tumor markers

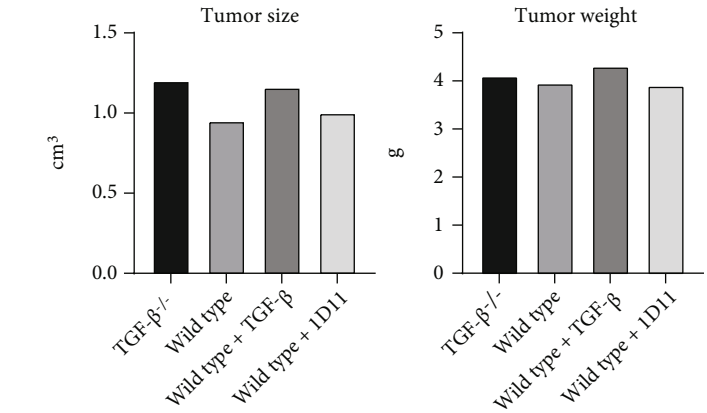

(a)

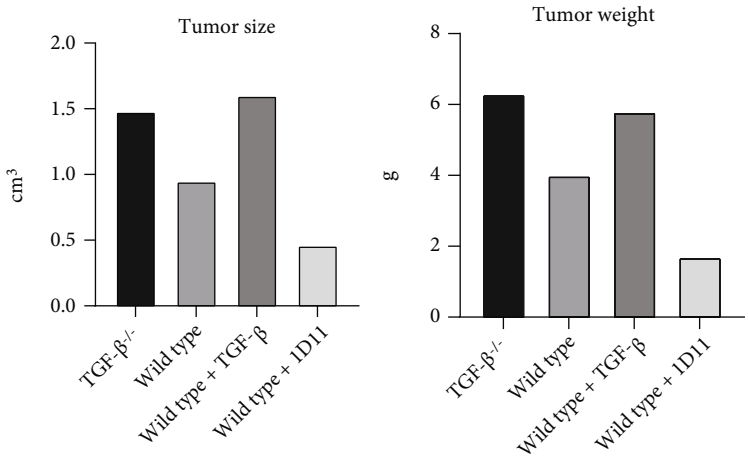

(b)

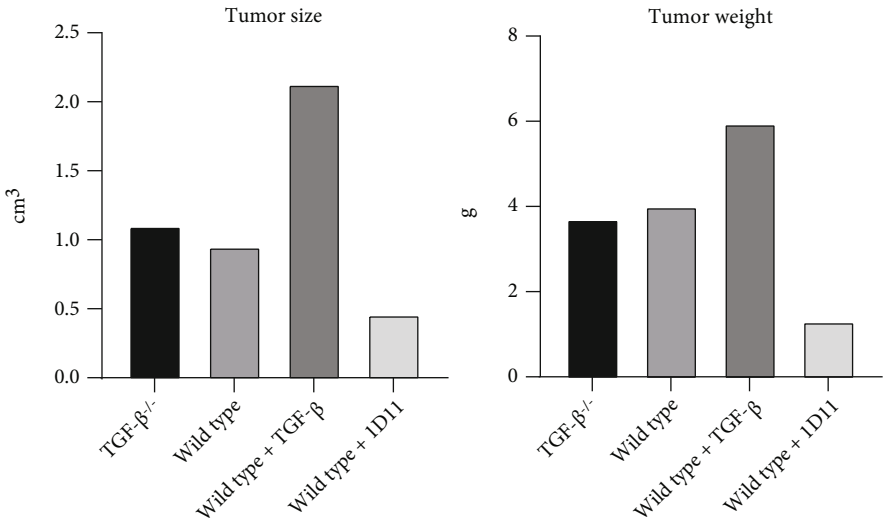

(c)

Figure 2: Continued.

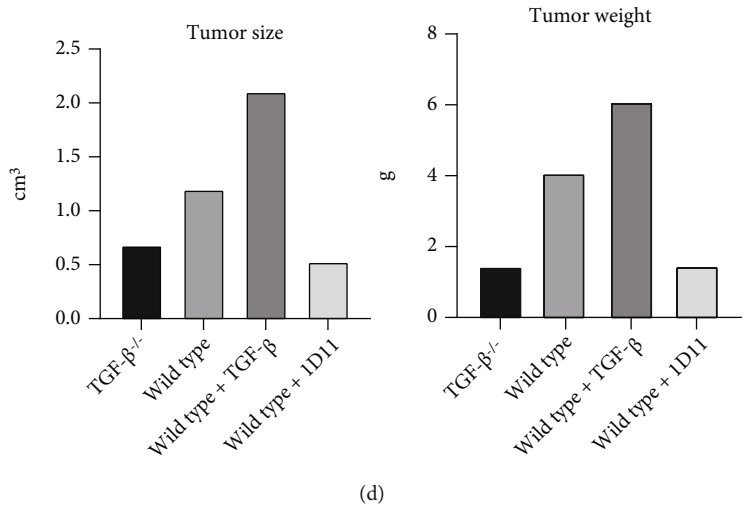

(d)

Figure 2: Predicted tumor size and weight (a) There is no significant difference in tumor growth among all mice. (b) *TGF-β1* gene knockout mice and mice injected with additional TGF-β develop larger and more severe tumors than wild-type mice, while the injection of 1D11 leads to reduced tumor growth. (c) There is no significant difference in tumor growth rate between the *TGF-β1* knockout group and the wild-type mice, while the tumors in mice injected with additional TGF-β are larger and heavier. The tumors in mice treated with 1D11 have reduced size and weight compared to those in wild-type mice. (d) In comparison to wild-type mice, the tumors in the gene knockout mice and 1D11-treated mice are smaller, while the tumors in mice treated with additional TGF-β develop more rapidly.

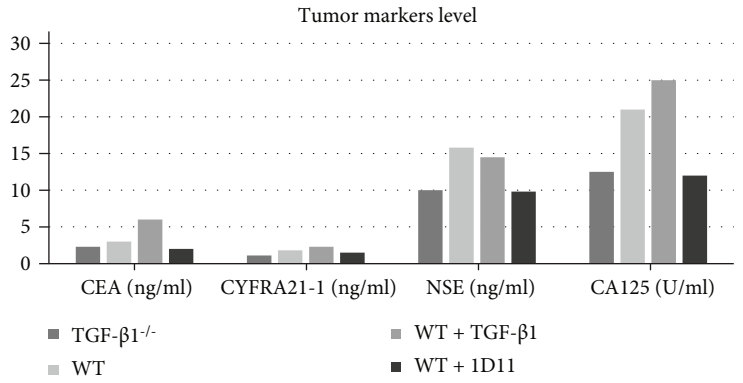

(a)

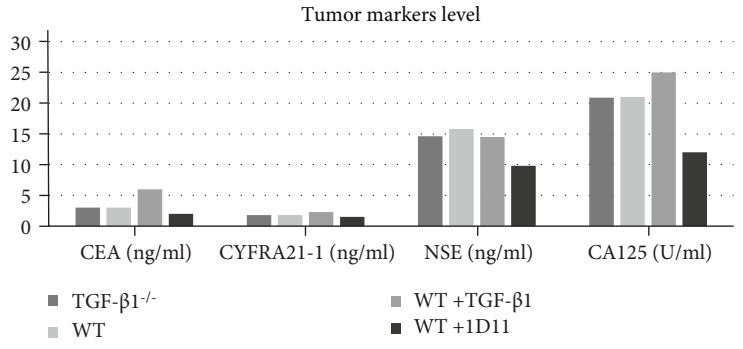

(b)

Figure 3: Predicted level of tumor markers in serum (a) Compared with wild-type mice, the concentrations of various tumor markers in both *TGF-β1* gene knockout mice and 1D11-treated mice decrease, while the concentrations of most tumor markers in the additional TGF-β1 injection group significantly increase. (b) Although additional TGF-β1 injections results in higher levels of most cancer markers, the gene knockout does not reduce the concentrations of tumor markers, suggesting that *TGF-β1* knockout therapy is ineffective.

are higher in mice with TGF-β overexpression, demonstrating the protumor effects of TGF-β. However, the gene knockout does not reduce the expression of tumor markers, suggesting that *TGF-β1* knockout in myofibroblasts is not effective and CRISPR-Cas9 should be used as an alternative gene editing tool.

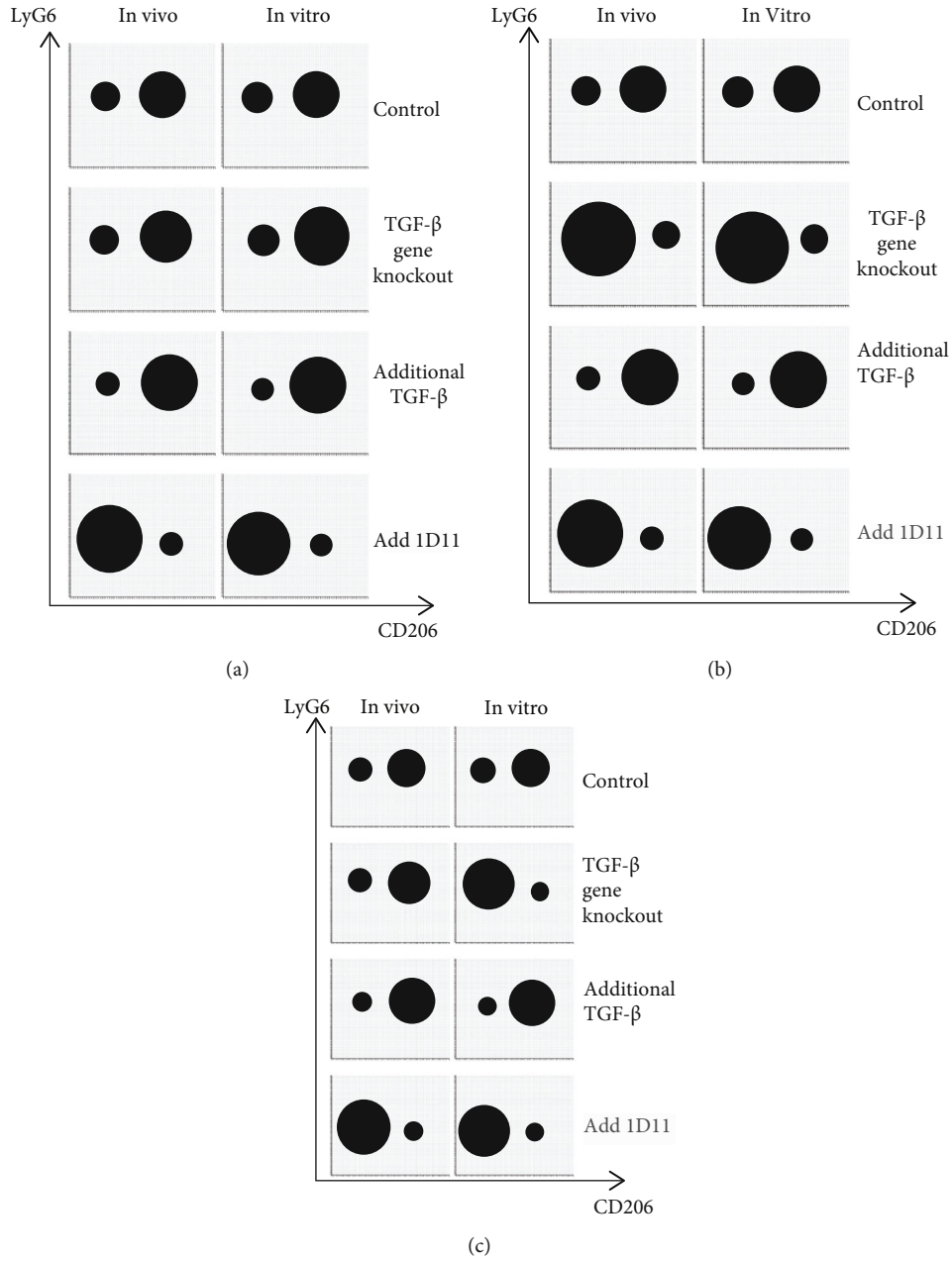

Figure 4: Predicted abundance of N1 TANs and N2 TANs quantified by flow cytometry. In each diagram, one solid black circle represents one population of cells, and the area of the circle correlates with the number of cells in that population. (a) Compared with the control group, the abundance of N1 (Ly6G+/CD206-) and N2 (Ly6G+/CD206+) cells in TME after gene knockout of TGF-β producing gene in myofibroblasts might not change significantly, and N2 (Ly6G+/CD206+) subgroup might be still more than the N1 (Ly6G+/CD206-) subgroup. After the addition of additional TGF based on the control group, the number of N2 (Ly6G+/CD206+) subgroup cells might further increase, and the number of N1 (Ly6G+/CD206-) subgroup cells might further decrease. The addition of 1D11 leads to increased N1 and decreased N2 population. (b) Compared with the control group, the number of N1 (Ly6G+/CD206-) subgroup significantly increases, and N2 (Ly6G+/CD206+) subgroup significantly decreases after the knockout of TGF-β producing gene in myofibroblasts. After the addition of additional TGF-β based on the control group, the number of N2 (Ly6G+/CD206+) subgroup cells might further increase, and the number of N1 (Ly6G+/CD206-) subgroup cells might further decrease. The addition of 1D11 results in expanded N1 and reduced N2. (c) There can be little difference between *in vivo* and *in vitro* controls. *In vivo*, compared with the control group, gene knockout of TGF-β producing gene in myofibroblasts might not affect the differentiation of N1 (Ly6G+/CD206-) and N2 (Ly6G +/CD206+). However, *in vitro*, gene knockout of TGF-β producing gene in myofibroblasts might result in a significant increase in the N1 (Ly6G+/CD206-) population and a significant decrease in the N2 (Ly6G+/CD206+) population. After the addition of additional TGF-β based on the control group, the number of N2 (Ly6G+/CD206+) subgroup cells might further increase, and the number of N1 (Ly6G+/CD206-) subgroup cells might decrease further. The addition of 1D11 promotes N1 and suppresses N2 differentiation.

4.5. The Relative Quantity of N1 and N2 TANs in TME. In Figure 4(a), the differentiation of TANs into N1 and N2 both *in vivo* and *in vitro* is not significantly affected by the *TGF-β1* gene knockout of myofibroblasts, indicating that myofibroblasts may not be an important source of TGF-β. In future experiments, the *TGF-β1* gene may be knocked out in other types of cells to significantly reduce the amount of TGF-β in TME. If the decrease in TGF-β level still has no appreciable influence on neutrophils polarization, the hypothesis may be refuted. In Figure 4(b), both *in vivo* and *in vitro*, the tumor microenvironment (TME) with *TGF-β1* knocked out myofibroblasts contains increased amount of N1 and reduced amount of N2, compared to the control group. In TME with overexpression of TGF-β, however, the number of N1 decreases while the number of N2 increases. The results show a positive correlation between the TGF-β level and the polarization of TANs towards N2, which promotes tumor growth. Therefore, blocking the expression of TGF-β in TME shifts the differentiation of TANs towards an antitumor phenotype, supporting the hypothesis. As shown in Figure 4(c), the differentiation of TANs *in vivo* is not significantly affected by *TGF-β1* knockout, but more N1 and fewer N2 are observed in the *in vitro* media with *TGF-β1* knocked out myofibroblasts. The skewed differentiation observed *in vitro* indicates that myofibroblast is indeed a major source of TGF-β and that inhibiting TGF-β expression in TME polarizes TANs towards N1. However, there are more than one type of cells producing TGF-β *in vivo,* so the reduced production of TGF-β due to *TGF-β1* knocked out myofibroblasts may be compromised by other cells, leading to TANs' differentiation similar to the wild type models. In future experiments, *TGF-β1* may be knocked out in more TGF-β producing cell types. Under all three circumstances, the inhibition of TGF-β signaling via 1D11 is predicted to shift the differentiation of TANs towards antitumor (N1) phenotype, according to the results of Qin et al. [10].

4.6. Limitations. In this study, the production of TGF-β is selectively blocked in mice myofibroblasts, but not other tissues. The choice of myofibroblasts is based on the fact that myofibroblasts are one of the most abundant TGF-β-producing cells present in the NSCLC TME. Nonetheless, other cells like thrombocytes and tumor cells are also major contributors of TGF-β expression in TME. Hence, future experiments may be performed with selective *TGF-β1* knockout in a different type of cells or multiple types of cells. Another limitation is that the progression of cancer is only monitored via the growth of primary tumor, while the metastasis of NSCLC is not examined. Besides, the mechanism by which TGF-β contributes to the polarization of TANs is still a mystery. More in-depth research is in need to characterize the signaling pathway of TAN differentiation.

5. Conclusion

Tumor-associated neutrophils (TANs) significantly influence the progression of nonsmall cell lung cancer (NSCLC), and their effector functions are affected by a cytokine known as transforming growth factor-β (TGF-β), which polarizes the TANs towards a protumor phenotype. Thus, blocking the production of TGF-β may attenuate tumor growth through the polarization of TANs towards a tumor-suppressive phenotype. In this study, the C57BL/6 mice are divided into four groups, one with the *TGF-β1* gene knocked out in myofibroblasts, one with frequent injections of purified TGF-β, one containing wild type, healthy mice with normal expression of TGF-β, the other containing wild type mice treated with anti-TGF-β (1D11). After orthotopic intrapulmonary implantation of Lewis lung carcinoma (LLC), the mice's N1 and N2 in TME are quantified by flow cytometry to investigate to what extent TGF-β level influences TANs' differentiation. The morphology of the tumors and the level of tumor markers in serum are also examined to study the tumor growth under different TGF-β levels. The experiments are then repeated *in vitro* on media containing LLC cells, TANs, and myofibroblasts obtained from the mice model. Possible results are anticipated and discussed from various aspects. To conclude, this study provides experimental designs for studying the potential antitumor effects of blocking TGF-β production. Since most current studies in this field focus on the therapeutic potential of directly inhibiting TGF-β signaling, rather than blocking the production of TGF-β in TME, this study fills the knowledge gap and presents a creative direction for cancer therapy targeting specific cytokines. Combining with other cancer treatments, the tissue-specific blockade of TGF-β production may lead to promising outcomes and may have clinical applications. Furthermore, the experimental design presented in this study may apply to other cytokines, facilitating the development of novel cancer therapies.

Data Availability

The data used to support the findings of this study are included within the article.

Conflicts of Interest

The authors declare that they have no competing interest.

Authors' Contributions

Yifei Fang, Xiyao Li, Yuxuan Jiang, and Zhihan Ge contributed equally to this work.

References

[1] H. Sung, J. Ferlay, R. L. Siegel et al., "Global cancer statistics 2020: GLOBOCAN estimates of incidence and mortality worldwide for 36 cancers in 185 countries," *CA: a Cancer Journal for Clinicians*, vol. 71, no. 3, pp. 209–249, 2021.

[2] M. R. Galdiero, E. Bonavita, I. Barajon, C. Garlanda, A. Mantovani, and S. Jaillon, "Tumor associated macrophages and neutrophils in cancer," *Immunobiology*, vol. 218, no. 11, pp. 1402–1410, 2013.

[3] A. Mantovani, M. A. Cassatella, C. Costantini, and S. Jaillon, "Neutrophils in the activation and regulation of innate and adaptive immunity," *Nature Reviews Immunology*, vol. 11, no. 8, pp. 519–531, 2011.

[4] C. Nathan, "Neutrophils and immunity: challenges and opportunities," *Nature Reviews Immunology*, vol. 6, no. 3, pp. 173–182, 2006.

[5] V. Brinkmann, U. Reichard, C. Goosmann et al., "Neutrophil extracellular traps kill bacteria," *Science*, vol. 303, no. 5663, pp. 1532–1535, 2004.

[6] X. Wang, L. Qiu, Z. Li, X. Y. Wang, and H. Yi, "Understanding the multifaceted role of neutrophils in cancer and autoimmune diseases," *Frontiers in Immunology*, vol. 9, p. 2456, 2018.

[7] A. Ponzetta, R. Carriero, S. Carnevale et al., "Neutrophils Driving Unconventional T cells mediate resistance against murine sarcomas and selected human tumors," *Cell*, vol. 178, no. 2, pp. 346–360.e24, 2019.

[8] S. Diem, S. Schmid, M. Krapf et al., "Neutrophil-to-lymphocyte ratio (NLR) and platelet-to-lymphocyte ratio (PLR) as prognostic markers in patients with non-small cell lung cancer (NSCLC) treated with nivolumab," *Lung Cancer*, vol. 111, pp. 176–181, 2017.

[9] R. Derynck, S. J. Turley, and R. J. Akhurst, "TGFβ biology in cancer progression and immunotherapy," *Nature Reviews. Clinical Oncology*, vol. 18, no. 1, pp. 9–34, 2021.

[10] F. Qin, X. Liu, J. Chen et al., "Anti-TGF-β attenuates tumor growth via polarization of tumor associated neutrophils towards an anti-tumor phenotype in colorectal cancer," *Journal of Cancer*, vol. 11, no. 9, pp. 2580–2592, 2020.

[11] M. Terra, M. Oberkampf, C. Fayolle et al., "Tumor-derived TGFβ alters the ability of plasmacytoid dendritic cells to respond to innate immune signaling," *Cancer Research*, vol. 78, no. 11, pp. 3014–3026, 2018.

[12] M. Labelle, S. Begum, and R. O. Hynes, "Direct signaling between platelets and cancer cells induces an epithelial-mesenchymal-like transition and promotes metastasis," *Cancer Cell*, vol. 20, no. 5, pp. 576–590, 2011.

[13] S. Jiao, S. K. Subudhi, A. Aparicio et al., "Differences in tumor microenvironment dictate T helper lineage polarization and response to immune checkpoint therapy," *Cell*, vol. 179, no. 5, pp. 1177–1190.e13, 2019.

[14] X. Liang, H. W. Schnaper, T. Matsusaka, I. Pastan, S. Ledbetter, and T. Hayashida, "Anti-TGF-β Antibody, 1D11, Ameliorates glomerular fibrosis in mouse models after the onset of proteinuria," *PLoS One*, vol. 11, no. 5, article e0155534, 2016.

[15] L. Zhang, N. Yang, J. R. Garcia et al., "Generation of a syngeneic mouse model to study the effects of vascular endothelial growth factor in ovarian carcinoma," *The American Journal of Pathology*, vol. 161, no. 6, pp. 2295–2309, 2002.

[16] J. M. Daley, A. A. Thomay, M. D. Connolly, J. S. Reichner, and J. E. Albina, "Use of Ly6G-specific monoclonal antibody to deplete neutrophils in mice," *Journal of Leukocyte Biology*, vol. 83, no. 1, pp. 64–70, 2008, Epub 2007 Sep 20.

[17] M. A. Giese, L. E. Hind, and A. Huttenlocher, "Neutrophil plasticity in the tumor microenvironment," *Blood*, vol. 133, no. 20, pp. 2159–2167, 2019.

[18] J. Yang, A. Tang, J. Ma, X. Sun, and L. Ming, "The reference intervals for CA125, CA15-3, CA19-9, CA72-4, AFP, CEA, NSE and CYFRA21-1," *Scandinavian Journal of Clinical and Laboratory Investigation*, vol. 79, no. 1-2, pp. 71–74, 2019.

[19] I. Malenica, J. Adam, S. Corgnac et al., "Integrin-αV-mediated activation of TGF-β regulates anti-tumour CD8 T cell immunity and response to PD-1 blockade," *Nat Commun*, vol. 12, no. 1, p. 5209, 2021.

Hindawi
Journal of Oncology
Volume 2022, Article ID 6586354, 13 pages
https://doi.org/10.1155/2022/6586354

Research Article

Construction of a miRNA Signature Using Support Vector Machine to Identify Microsatellite Instability Status and Prognosis in Gastric Cancer

Ya-nan Wang,[1] Ya-ning Wei,[2] Xiang-yu Fan,[1] Fang Xu,[1] Zheng-yang Dong,[3] Shu-jie Cheng,[4] and Jin-ku Zhang[5]

[1]*Department of Pathology, Affiliated Hospital of Hebei University, Baoding, China*
[2]*Department of Oncology, Affiliated Hospital of Hebei University, Baoding, China*
[3]*Department of Pathology, The Fourth Hospital of Hebei Medical University, Shijiazhuang, China*
[4]*Department of Surgery, Affiliated Hospital of Hebei University, Baoding, China*
[5]*Department of Pathology, No.1 Central Hospital of Baoding, Baoding, China*

Correspondence should be addressed to Shu-jie Cheng; csj326647@sina.com and Jin-ku Zhang; jinkuzhang@stu.ncwu.edu.cn

Received 9 January 2022; Revised 5 March 2022; Accepted 9 March 2022; Published 15 April 2022

Academic Editor: Fu Wang

Background. The specific role and prognostic value of DNA repair and replication-associated miRNAs in gastric cancer (GC) have not been clearly elucidated. Therefore, comprehensive analysis of miRNAs in GC is crucial for proposing therapeutic strategies and survival prediction. *Methods*. Firstly, clinical information and transcriptome data of TCGA-GC were downloaded from the database. In the entire cohort, we performed differential analysis in all miRNAs and support vector machine (SVM) was used to eliminate redundant miRNAs. Subsequently, we combined survival data and cox regression analysis to construct a miRNA signature in the training cohort. In addition, we used PCA, Kaplan-Meier, and ROC analysis to explore the prognosis value of risk score in the training and testing cohort. It is worth noting that multiple algorithms were used to evaluate difference of immune microenvironment (TME), microsatellite instability (MSI), tumor mutational burden (TMB), and immunotherapy in different risk groups. Finally, we investigated the potential mechanism about miRNA signature. *Results*. We constructed miRNA signature based on the following 4 miRNAs: hsa-miR-139-5p, hsa-miR-139-3p, hsa-miR-146b-5p, and hsa-miR-181a-3p. Univariate and multivariate Cox regression analyses suggested that risk score is a risk factor and an independent prognostic factor in GC patients. The AUC value of ROC analysis showed a robust prediction accuracy in each cohort. Moreover, significant differences in immune functions, immune cell content, immune checkpoint, MSI status, and TMB score were excavated in different groups distinguished by risk score. Finally, based on the above four miRNA target genes, we revealed that the signature was enriched in DNA repair and replication. *Conclusion*. We have developed a robust risk-formula based on 4 miRNAs that provides accurate risk stratification and prognostic prediction for GC patients. In addition, different risk subgroups may potentially guide the choice of targeted therapy.

1. Introduction

Gastric cancer (GC) is one of the most common causes of death across the world [1]. Its overall 5-year survival rate is less than 20%, and although considerable progress has been made in the treatment of GC, only slight improvements have been seen in the past 20 years [2]. Microsatellite instability (MSI) increases the rate of replication mistakes and hypermutation state, increasing the risk of oncogene or tumor suppressor gene alterations. Importantly, MSI status in patients with GC has been proved to be useful for treatment outcome prediction [3]. However, research combining several miRNAs to predict MSI status and prognosis is relatively uncommon.

Meanwhile, miRNAs are endogenous noncoding RNAs ranging in length from 17 to 25 nucleotides that influence

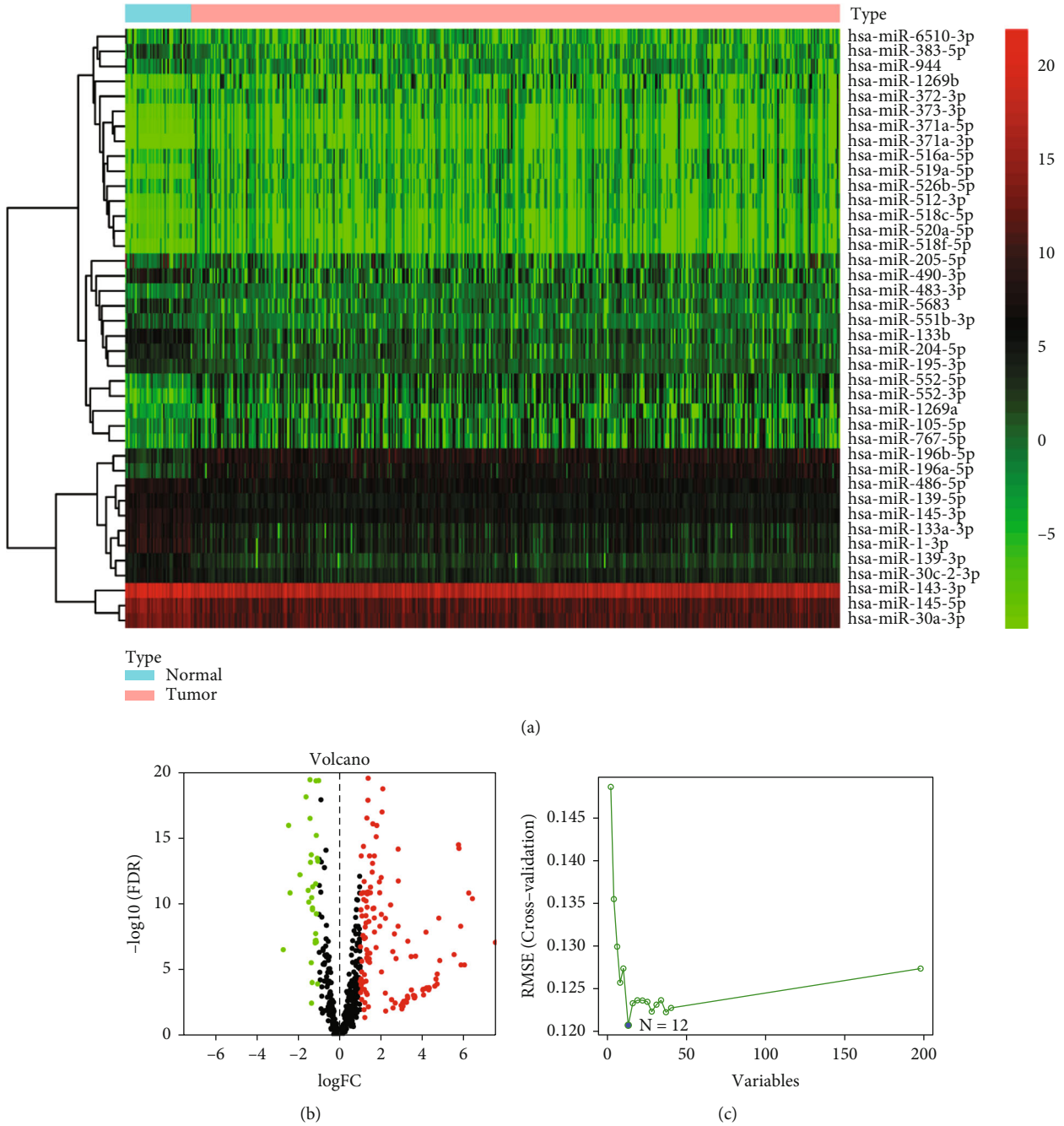

Figure 1: Screening of miRNAs: (a) the heat map of different expression miRNAs (DEmiRNAs); (b) volcano plot of DEmiRNAs; (c) the results of SVM.

gene expression posttranscriptionally [4]. Increasing data indicates that miRNA expression is varied in GC and is linked with survival prognosis [5]. Numerous research published in the last few years have identified miRNAs as possible diagnostic or prognostic indications for GC; however, the findings have been conflicting, although recent studies suggest that miRNAs play a complex role in tumorigenesis, drug resistance, and cancer therapy. Studies of miRNAs in GC still require more evidence at this time, as most studies have only looked at a small number of miRNAs in cell lines. In addition, support vector machine (SVM) is a robust machine learning method and is widely used in classification [6].

Although there are a large number of studies based on Cox and LASSO regression analysis to identify risk signatures, there are fewer studies on signature in GC patients with the SVM method. In order to obtain robust and stable results, we used SVM and Cox regression analysis to construct a miRNA signature. In conclusion, the construction of a novel miRNA signature is critical for the prognosis prediction of GC patients with the goal of exploring potential

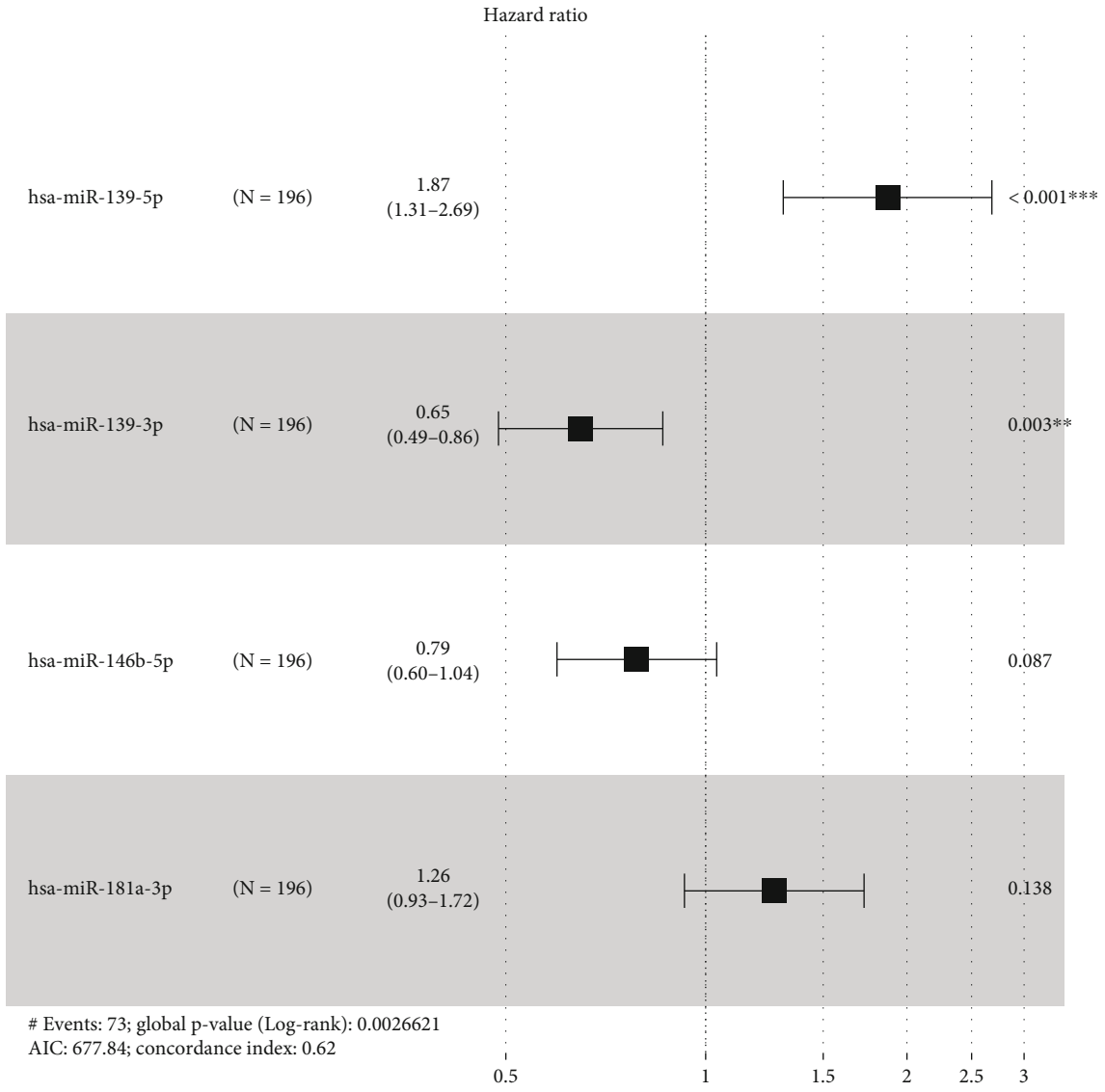

(a)

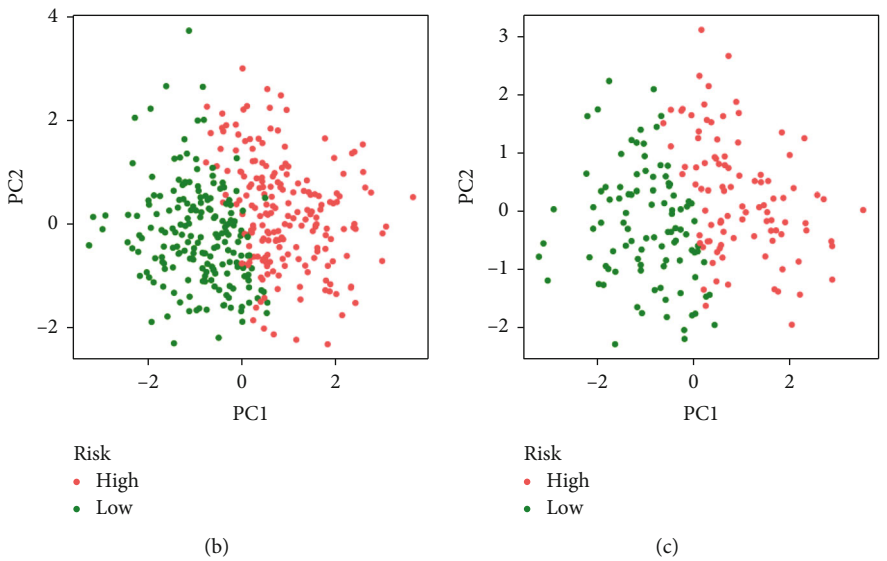

(b) (c)

Figure 2: Continued.

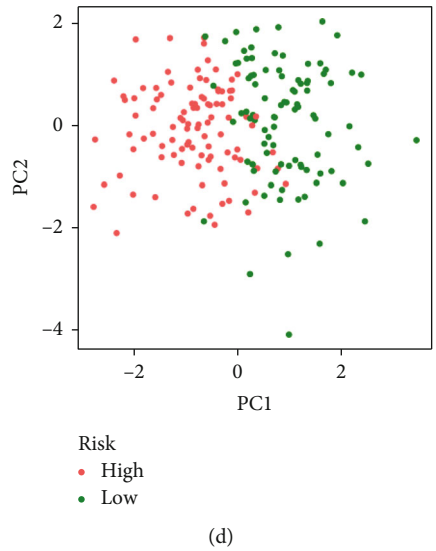

(d)

Figure 2: Construction of risk model. (a) A forest plot for results of multivariate Cox regression. PCA analysis of the entire cohort (b), training cohort (c), and testing cohort (d).

effects of miRNAs on immunotherapy, TME, biological processes, and MSI status.

2. Materials and Methods

2.1. Datasets. The Cancer Genome Atlas (TCGA) database was searched for transcriptome data and included 45 normal samples and 389 GC samples. The UCSC Xena Browser contains clinical data on TCGA-GC. Their survival information, clinicopathology, and genetics were retrieved and analyzed further. TCGA-GC cohort was randomly divided into 1 : 1 and represented as training set and testing set. The RNA-seq transcriptome data in CPM format and corresponding clinical data of GC patients were extracted from the database, and only genes with CPM greater than 1 were considered.

2.2. Calculation of Risk Score. Clinical data from GC cases in TCGA cohort were used to screen prognostic miRNAs linked with OS using univariate Cox regression analysis, and support vector machine (SVM) was used to eliminate redundant miRNAs. We selected miRNAs with p value less than 0.05 to undertake multivariate Cox regression analysis. The expression levels of the miRNAs and coefficients were then used to construct risk signature. The following formula was used to calculate the risk score for each patient:

$$\sum_{i=1}^{n} \mathrm{Coef}_i * \mathrm{miRNA}_i. \quad (1)$$

We calculated the median score in TCGA-GC cohort to divide patients into two groups and identify the most significant differences in prognosis between the risk subgroups. To analyze the prediction performance of prognostic features on overall survival, Kaplan-Meier survival curves and ROC curves were used.

2.3. Biological Function Analysis. Differential expression analysis (mRNAs and miRNAs) was performed using the limma package. TargetScan, miRTarBase, and miRDB tools were used to screen out target mRNAs. We overlapped target mRNAs and differential expression mRNAs. Finally, the above genes were analyzed for gene enrichment.

2.4. Comprehensive Analysis. We used ssGSEA, XCELL, TIMER, QUANTISEQ, MCPCOUNT, EPIC, CIBERSORT, CIBERSORT-ABS, ESTIMETA, and TIDE algorithms for estimating the abundance of immune cells, immune-related pathway, immunotherapeutic response, and microsatellite instability (MSI) status. p values and Pearson correlation coefficients were obtained based on the study. Immune checkpoint-related gene and human leukocyte antigen (HLA) gene expression levels may be linked to immune checkpoint inhibitor therapy response. We explored the difference in gene expression levels between the two groups.

3. Results

3.1. Calculation of Risk Score in GC Patients. Using 45 normal samples as a control, we revealed that 138 were upregulated miRNAs and 60 were downregulated miRNAs. The volcano plot and heat map showed the 198 miRNA expression landscape (Figures 1(a) and 1(b)). In addition, SVM was used to screen robust 18 miRNAs in the above miRNAs (Figure 1(c)). Subsequently, multivariate Cox regression analysis was applied to 18 miRNA expression data in the training cohort for avoiding overfitting (Figure 2(a)). In detail, the risk score was determined according to the coefficients of each miRNA in the result of multivariate Cox regression analysis, and the formula is as follows: risk score = hsa − miR − 139 − 5p expression × 0.6271 + hsa − miR − 139 − 3p expression × −0.4345 + hsa − miR − 146b − 5 p expression × −0.2398 + hsa − miR − 181a − 3p expression × 0.2347. According to the above formula, the risk score of each patient in TCGA-GC cohort was calculated.

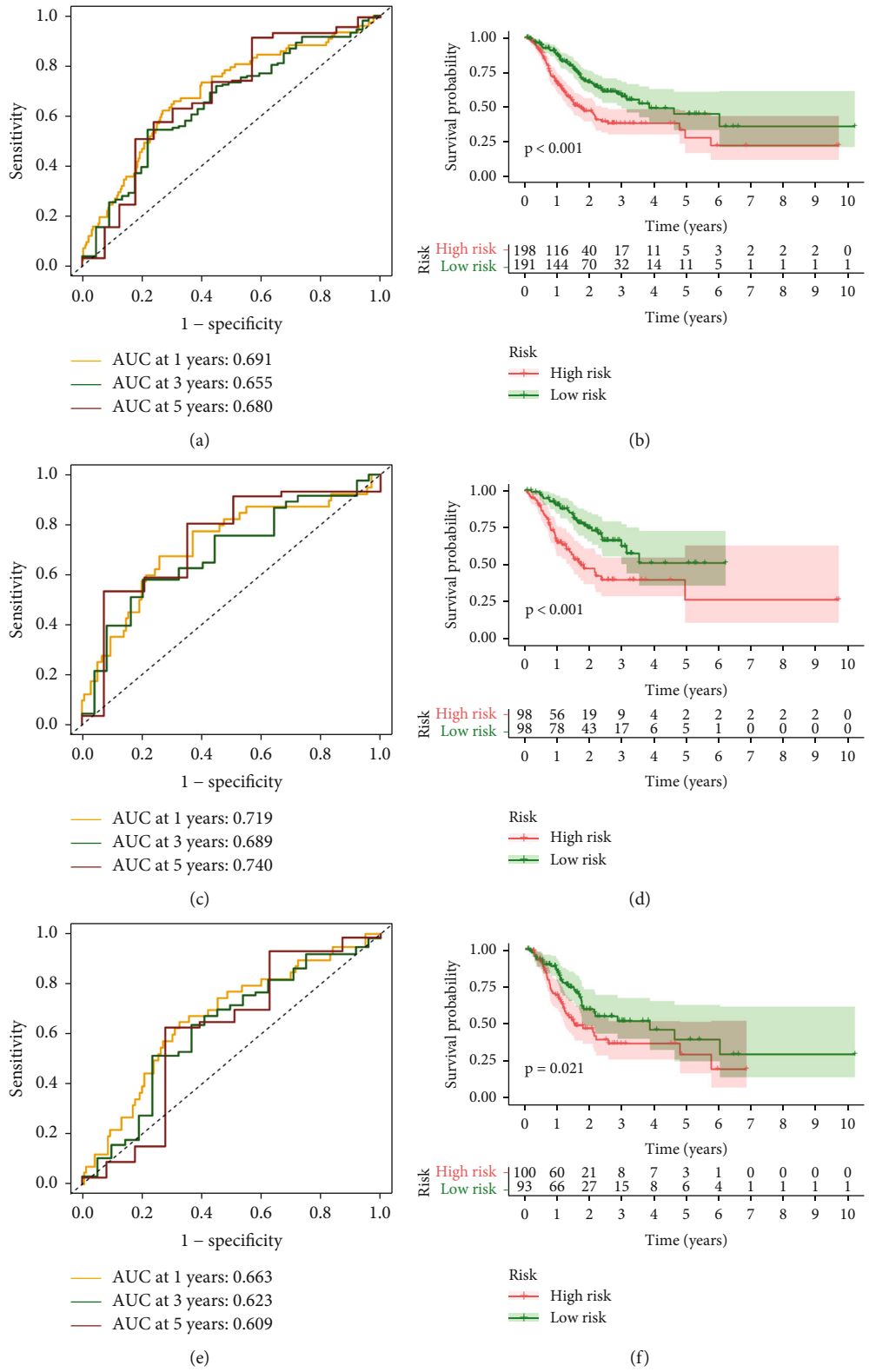

Figure 3: Prognostic value of risk score. ROC analysis of the entire cohort (a), training cohort (c), and testing cohort (e). Kaplan-Meier survival analysis of the entire cohort (b), training cohort (d), and testing cohort (f).

Subsequently, based on the median of risk score in the training cohort, we divided patients into two risk subgroups. PCA analysis showed that all samples from the different risks could be well distinguished in the entire cohort (Figure 2(b)), training cohort (Figure 2(c)), and testing cohort (Figure 2(d)).

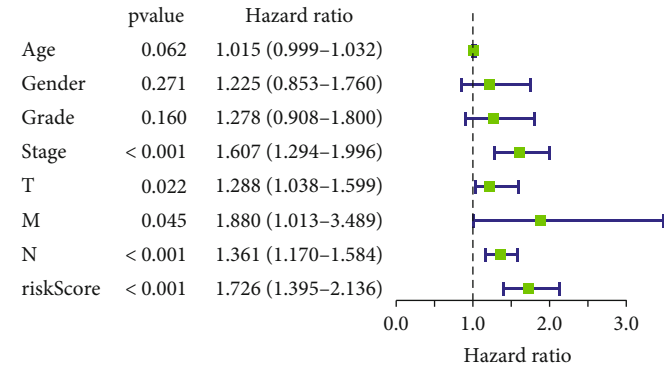

(a)

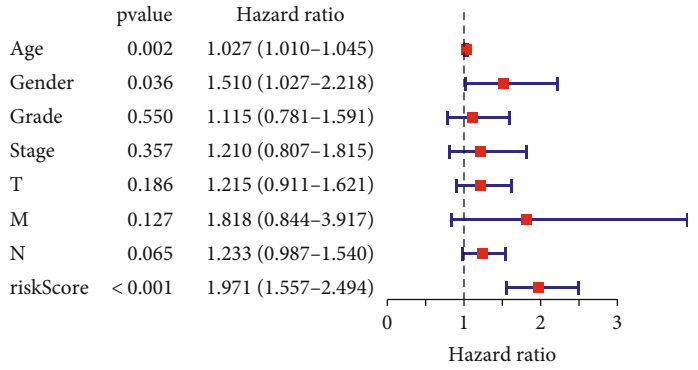

(b)

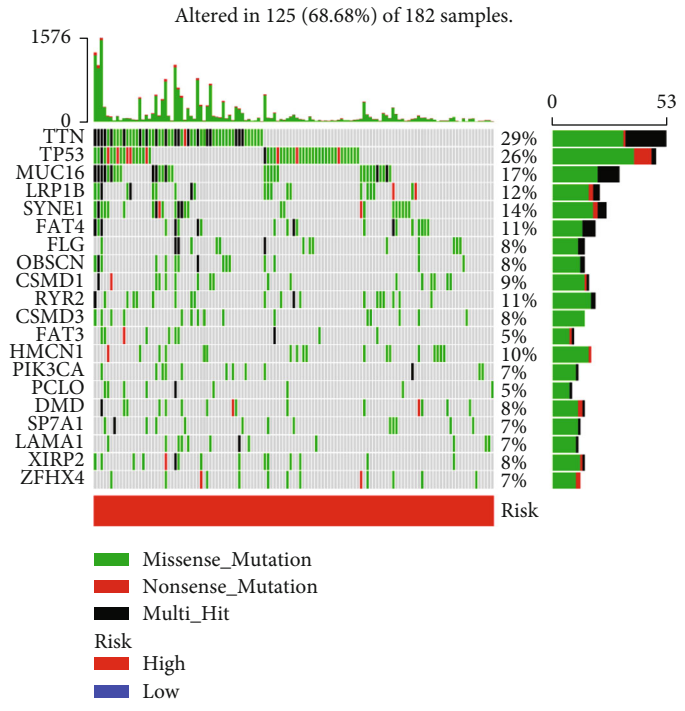

(c)

Figure 4: Continued.

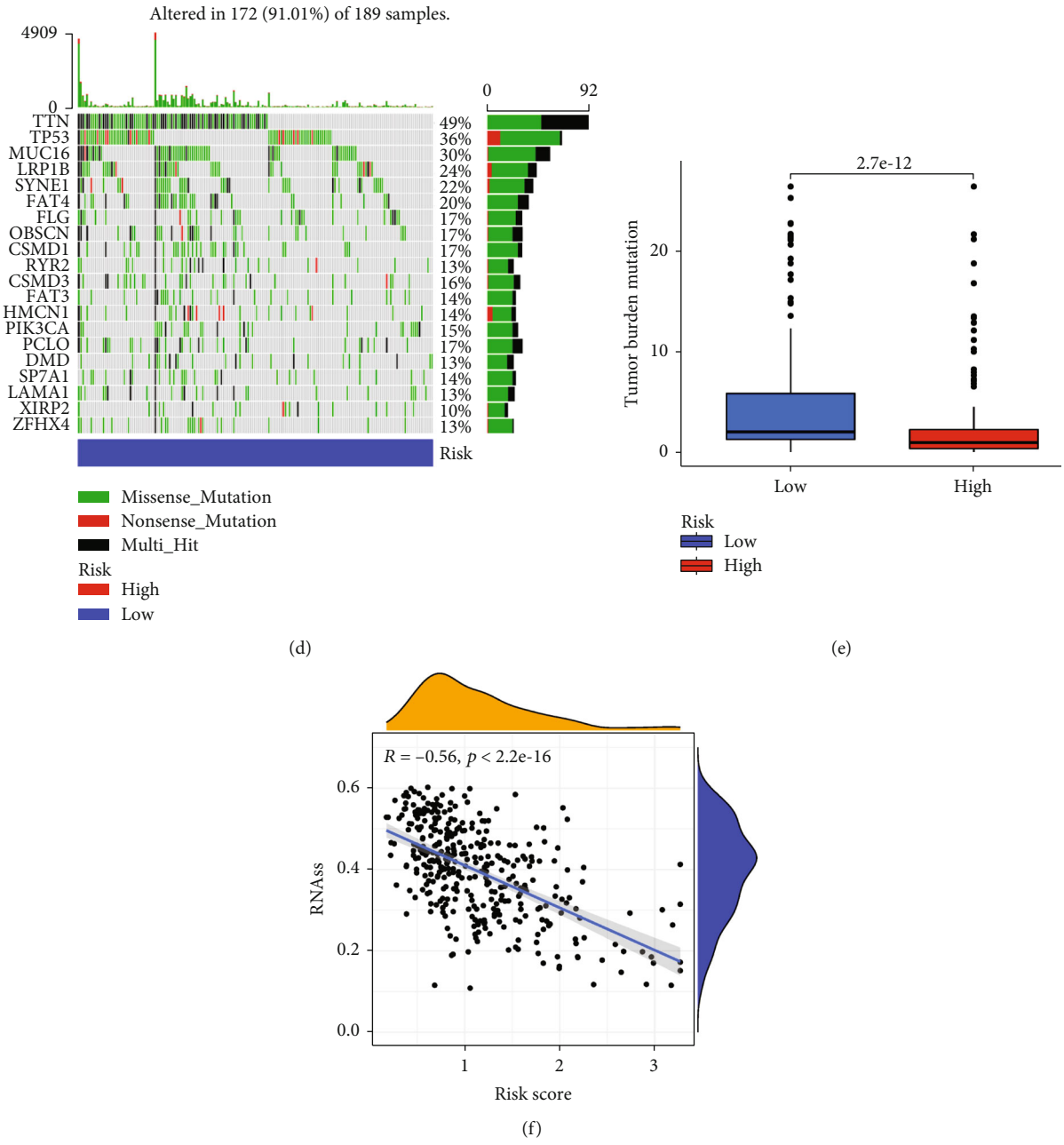

Figure 4: Somatic mutation analysis: (a) forest plot of univariate Cox regression analysis; (b) forest plot of multivariate Cox regression analysis; (c) somatic mutation analysis in the high-risk group; (d) somatic mutation analysis in the low-risk group; (e) analysis of differences in TMB in different risk groups; (f) correlation analysis between RNAs and risk score.

3.2. Exploring Prognostic Value of Risk Score. To better evaluate the prognostic value of risk score, we performed ROC analysis, and the AUC value showed a robust prediction accuracy (AUC > 0.7) in each cohort, as shown in Figures 3(a), 3(c), and 3(e). Meanwhile, the Kaplan-Meier analysis and log-rank test were used to estimate the predictive ability of the model for the clinical outcomes of GC patients ($p < 0.05$). The results showed that the OS of patients with low risk was better than those of high-risk patients in the entire cohort (Figure 3(b)), training cohort (Figure 3(d)), and testing cohort (Figure 3(f)). To determine whether risk score is an independent prognostic factor in GC patients, we included risk score and other clinical parameters in Cox regression analyses. Excitingly, univariate and multivariate Cox regression analyses suggested that risk score is a risk factor (Figure 4(a)) and an independent prognostic factor (Figure 4(b)). Specifically, in univariate and multivariate regression, HR value of risk score is 1.726 and 1.971, respectively ($p < 0.001$).

3.3. Somatic Mutation and Cell Stemness Analysis. We further analyzed the relationship between risk score and somatic mutation. The waterfall plot showed that patients in the low-risk group exhibited a wider range of mutations

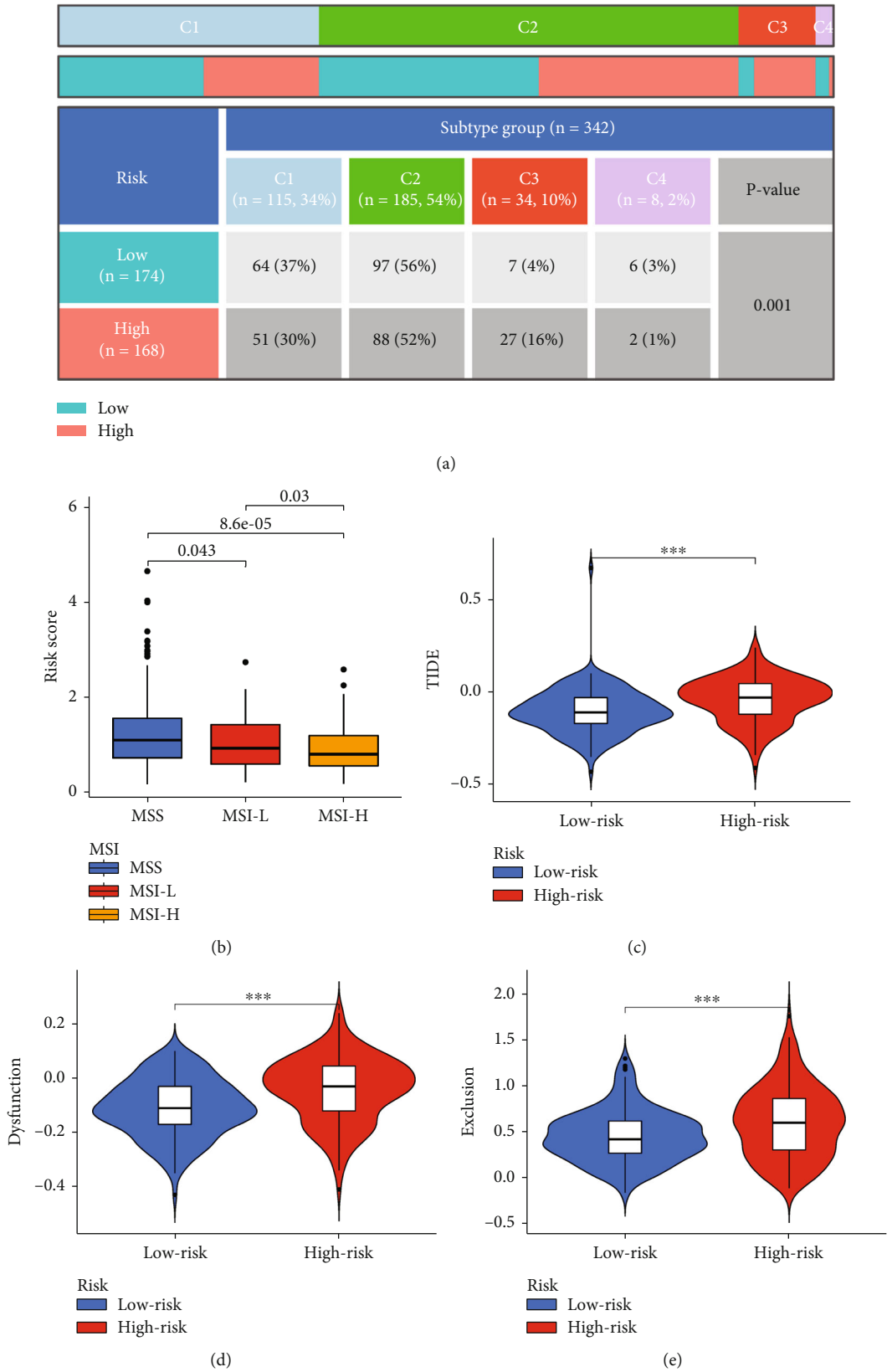

Figure 5: MSI status and immune subtype analysis: (a) distribution of immune subtypes and risk subgroups; (b) analysis of differences in TMB in different risk groups; (c) analysis of differences in MSI status, TIDE, dysfunction, and exclusion in different risk groups.

Figure 6: Difference analysis of immune cells and risk subgroups.

(Figures 4(a) and 4(b)). However, in different risk groups, TTN, TP53, MUC16, and LRP1B were the major mutation genes. In addition, the boxplot showed that low-risk patients have a higher TMB score (Figure 4(c)). Considering the effect of cell stemness on prognosis, we also analyzed cell stemness of patients with risk score and found that they were negatively related (Figure 4(d)).

3.4. Comprehensive Evaluation of Immune Function by Multiple Algorithms. We performed ANOVA for different risk patients and immune subtypes, and the differences were statistically significant (Figure 5(a)). We also analyzed microsatellite instability (MSI) of patients with different risks and found that the MSI-H grouping has a lower risk score (Figure 5(b)). The above results provide another potential explanation for the poor prognosis of patients with high risk score. Based on tumor pretreatment expression profiles, this TIDE module can estimate multiple published transcriptomic biomarkers to predict patient response [7]. In our risk subgroups, the high-risk group had higher TIDE score (Figure 5(c)), dysfunction score (Figure 5(d)), and exclusion score (Figure 5(e)) than the low-risk group. Moreover, XCELL, TIMER, QUANTISEQ, MCPCOUNT, EPIC, CIBERSORT, and, CIBERSORTABS algorithms were used to evaluate the content and correlation of immune infiltrating cells in different risk groups. In the person correlation analysis, we found that most of the immune cells calculated by 6 algorithms were negatively correlated with the risk score. In the difference analysis, B cell and T cell showed significant differences in most algorithm results, as shown in Figure 6. Subsequently, we explored the tumor microenvironment using the ESTIMATE algorithm, and we found that the high-risk group had higher estimate score, immune score, and stromal score compared with the low-risk group (Figure 7(a)). The ssGSEA algorithm also suggested that there are also significant differences in immune function between the different risk groups, including APC costimulation, CCR, MHC class I, parainflammation, and IFN response (Figure 7(b)). We selected 46 immune checkpoints commonly used in treatment, and the results showed that 24 immune checkpoints were significantly different between patients in the high- and low- risk groups (Figure 7(c)). Interestingly, immunofunctional analysis confirmed significant differences in HLA-related genes between the low-risk and high-risk groups in TCGA and GEO cohorts, as shown in Figure 7(d).

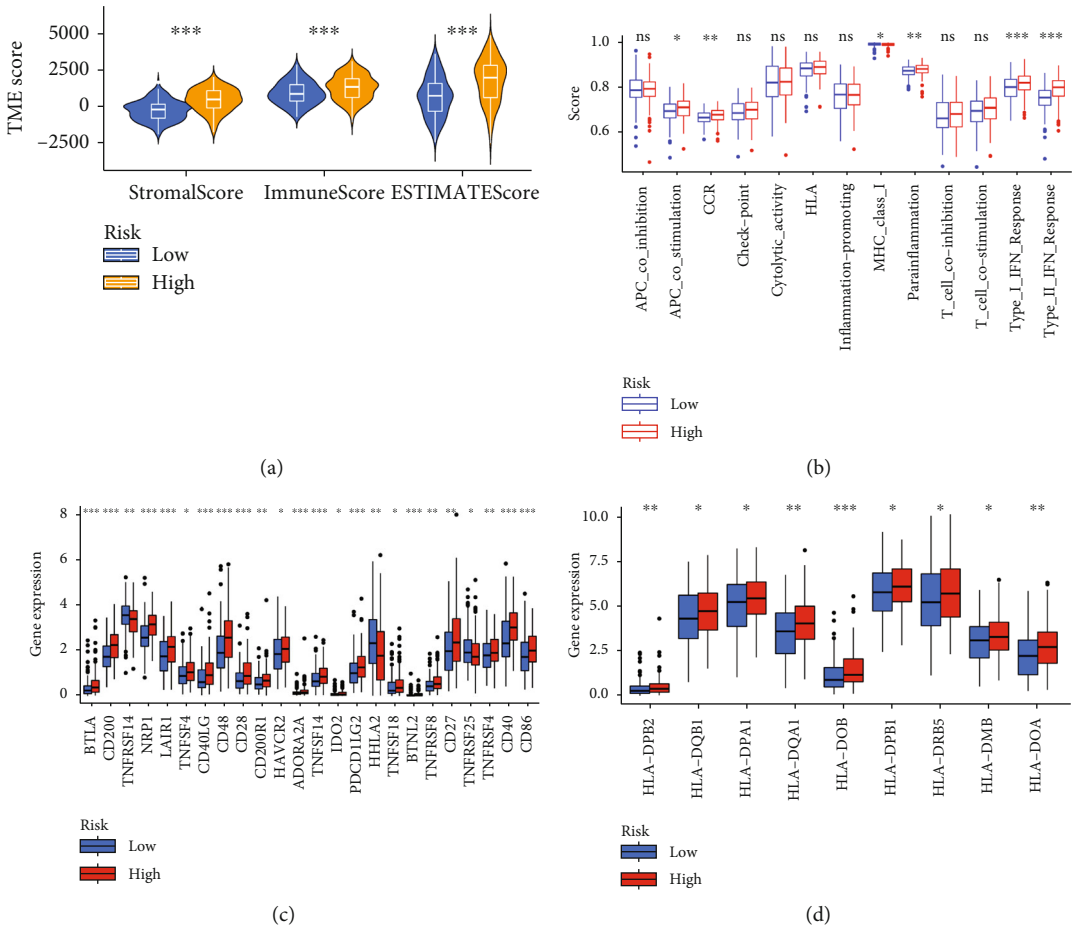

Figure 7: Immune function and immune checkpoint analysis in risk subgroups: (a) estimate analysis in different risk subgroups; (b) differential analysis of immune function; (c) differential expression analysis of immune checkpoint-related genes; (d) differential expression analysis of HLA-related genes.

3.5. miRNAs Participating in Signature May Be Revolved in DNA Repair and Replication. TargetScan, miRTarBase, and miRDB tools were used to screen out target mRNAs in 4 miRNAs participating in signature. Subsequently, we overlapped target mRNAs and differential expression mRNAs. Finally, a potential functional regulation network is constructed (Figure 8(a)). To better understand the underlying molecular mechanisms and functions of the above mRNAs, interestingly, in KEGG analysis, we found that the above mRNAs were associated with DNA repair, DNA replication, and homologous recombination (Figure 8(b)).

4. Discussion

Gastric cancer (GC) is widely regarded as one of the most common malignant tumors of the digestive system, with high morbidity and mortality, and has attracted more and more attention. A series of discoveries of miRNAs have made significant progress in the field of cancer, especially in immune [8]. In recent years, a number of critical discoveries have highlighted the growing interest in understanding the mechanisms of miRNAs. And with the development of artificial intelligence, more new tools have been applied in the life sciences [9, 10]. However, the specific role and prognostic value of miRNAs in GC have not been clearly elucidated. In this study, using SVM-Cox model, we were able to construct a risk score formula based on 4 miRNAs. The training and testing cohorts were used to validate the performance of the risk score that was made. We also used the KEGG enrichment analyses to investigate the function of these miRNAs. XCELL, TIMER, QUANTISEQ, MCPCOUNT, EPIC, CIBERSORT, and, CIBERSORTABS algorithms were used to evaluate the content and correlation of immune infiltrating cells in different risk groups. The findings of the study imply that risk score has a significant impact on survival risk in GC patients and could be used as biomarkers for therapeutic targets.

The four miRNAs involved in the modeling have been studied in gastric cancer. For example, SNHG3 functions in an oncogenic manner to drive GC proliferation, migration, and invasion by regulating the miR-139-5p/MYB axis [11]. In addition, circ-PTPDC1 promotes the proliferation, migration, and invasion of GC cell lines via sponging miR-139-3p by regulating ELK1 [12]. In the current study, quantitative analyses revealed that the high-risk group had a higher percentage of immune-related cells and functions. Previous research has demonstrated that ferroptosis can emit damage-associated molecular or lipid mediators that

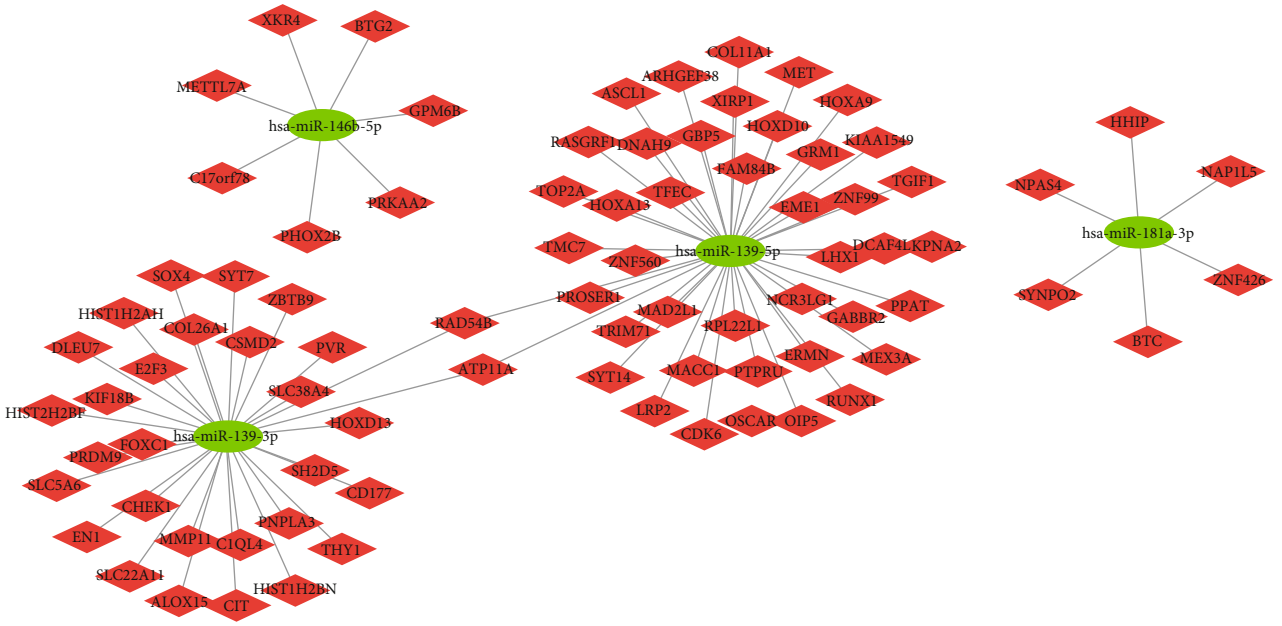

(a)

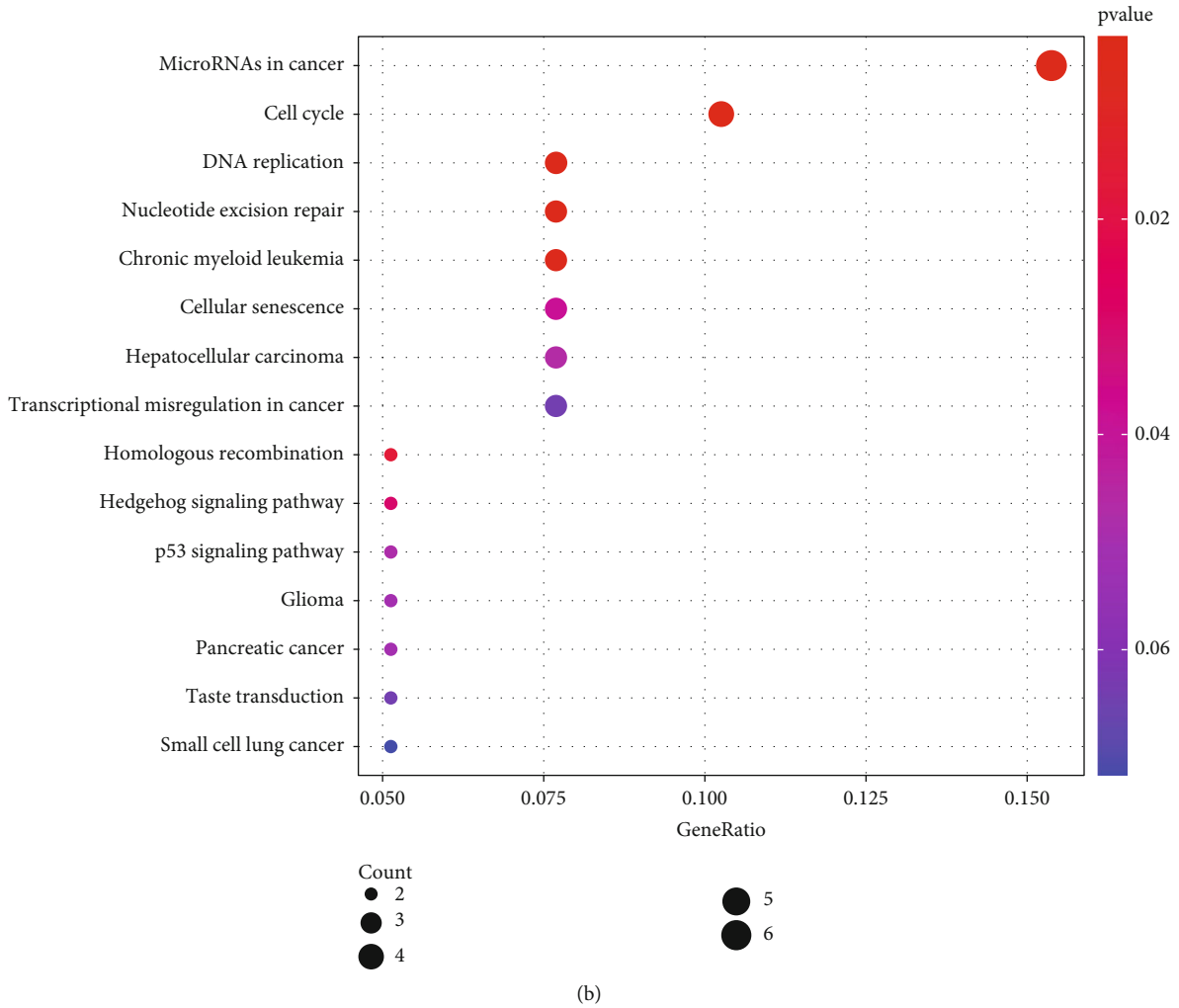

(b)

Figure 8: miRNA-mRNA network: (a) miRNA-mRNA network; (b) a bubble plot for the results of KEGG analysis.

attract antigen-presenting cells, triggering a cascade of innate and adaptive immune responses [13]. Consistent with previous studies, our study also shows that cells and functions associated with the antigen presentation process are significantly activated in the low-risk group, particularly in T cells and B cells [14]. It is also noteworthy that both T cells and B cells have a significant effect on the effect of antitumor activity of OSCC. Furthermore, ferroptosis combined with immune checkpoint inhibitors (ICIs) synergistically enhance antitumor activity, even in ICI-resistant types [12]. We identified several immune checkpoints that may guide our future targeted therapy options in OSCC patients, such as CD27, CD276, CD40, CD44, LAG3, LIGIT, TMIGD2, and TNFSF15. We found that many types of immune cells are different in different risk groups. In the current study, $CD8^+$ T lymphocytes have also been demonstrated to cause lipid peroxidation in cancer cells and make cells more susceptible to ferrogenesis by releasing IFN [15]. As a result, we believe that further research into the involvement of these immune cells in ferroptosis and immune evasion is required in the future. Finally, based on the findings of this study, we can speculate that the poorer prognosis in the high-risk group may be due to dysregulation of antitumour immune function, which raises a more in-depth question: whether the development of GC can be caused by miRNA imbalance affecting antitumour immune function.

In conclusion, this study utilized comprehensive bioinformatics to analyze and establish 4-miRNA risk score formula, including hsa-miR-139-5p, hsa-miR-139-3p, hsa-miR-146b-5p, and hsa-miR-181a-3p, ultimately to identify potential biomarkers for predicting GC progression. And further analysis and study finally revealed the functions and mechanisms of these miRNAs. Due to the small sample size of the control group used for miRNA analysis in this study, only limited data can be presented in the paper. In summary, our data need to be further investigated and validated in a larger patient population and explored in future research together.

Data Availability

Data is available at TCGA database (https://portal.gdc.cancer.gov/).

Disclosure

The authors are accountable for all aspects of the work in ensuring that questions related to the accuracy or integrity of any part of the work are appropriately investigated and resolved.

Conflicts of Interest

The authors declare that they have no conflicts of interest.

Authors' Contributions

Y.W. conceived and designed the study. X.F. was responsible for materials. F.X. drafted the article. Z.D., S.C., and J.Z. revised the article critically. All authors had the final approval of the submitted versions. Ya-nan Wang and Ya-ning Wei contributed equally to this work.

Acknowledgments

This study was funded by the Department of Science and Technology of Hebei Province (grant number 162777241).

References

[1] Global Burden of Disease Cancer Collaboration, "The global burden of cancer 2013," *JAMA Oncology*, vol. 1, no. 4, pp. 505–527, 2015.

[2] N. Coburn, R. Cosby, L. Klein et al., "Staging and surgical approaches in gastric cancer: a systematic review," *Cancer Treatment Reviews*, vol. 63, pp. 104–115, 2018.

[3] F. Pietrantonio, R. Miceli, A. Raimondi et al., "Individual patient data meta-analysis of the value of microsatellite instability as a biomarker in gastric cancer," *Journal of Clinical Oncology*, vol. 37, no. 35, pp. 3392–3400, 2019.

[4] C. Wang, X. Leng, Y. Zhang et al., "Transcriptome-wide analysis of dynamic variations in regulation modes of grapevine microRNAs on their target genes during grapevine development," *Plant Molecular Biology*, vol. 84, no. 3, pp. 269–285, 2014.

[5] Z. Yan, Y. Xiong, W. Xu et al., "Identification of recurrence-related genes by integrating microRNA and gene expression profiling of gastric cancer," *International Journal of Oncology*, vol. 41, no. 6, pp. 2166–2174, 2012.

[6] Z. Sun, J. Yang, X. Li, and J. Zhang, "DPWSS: differentially private working set selection for training support vector machines," *PeerJ Computer Science*, vol. 7, article e799, 2021.

[7] J. Fu, K. Li, W. Zhang et al., "Large-scale public data reuse to model immunotherapy response and resistance," *Genome Medicine*, vol. 12, no. 1, p. 21, 2020.

[8] S. Nagata and M. Tanaka, "Programmed cell death and the immune system," *Nature Reviews. Immunology*, vol. 17, no. 5, pp. 333–340, 2017.

[9] H. Huang, N. Wu, Y. Liang, X. Peng, and S. Jun, "SLNL: a novel method for gene selection and phenotype classification," *International Journal of Intelligent Systems*, 2022.

[10] H. H. Huang, X. D. Peng, and Y. Liang, "SPLSN: an efficient tool for survival analysis and biomarker selection," *International Journal of Intelligent Systems*, vol. 36, no. 10, pp. 5845–5865, 2021.

[11] Y. Xie, L. Rong, M. He et al., "LncRNA SNHG3 promotes gastric cancer cell proliferation and metastasis by regulating the miR-139-5p/MYB axis," *Aging (Albany NY)*, vol. 13, no. 23, pp. 25138–25152, 2021.

[12] Z. Li, Y. Cheng, K. Fu et al., "Circ-PTPDC1 promotes the progression of gastric cancer through sponging Mir-139-3p by regulating ELK1 and functions as a prognostic biomarker," *International Journal of Biological Sciences*, vol. 17, no. 15, pp. 4285–4304, 2021.

[13] J. P. Friedmann Angeli, D. V. Krysko, and M. Conrad, "Ferroptosis at the crossroads of cancer-acquired drug resistance and immune evasion," *Nature Reviews. Cancer*, vol. 19, no. 7, pp. 405–414, 2019.

[14] R. Tang, J. Xu, B. Zhang et al., "Ferroptosis, necroptosis, and pyroptosis in anticancer immunity," *Journal of Hematology & Oncology*, vol. 13, no. 1, p. 110, 2020.

[15] W. Wang, M. Green, J. E. Choi et al., "$CD8^+$ T cells regulate tumour ferroptosis during cancer immunotherapy," *Nature*, vol. 569, no. 7755, pp. 270–274, 2019.

Hindawi
Journal of Oncology
Volume 2022, Article ID 3794021, 17 pages
https://doi.org/10.1155/2022/3794021

Research Article

Screening and Validation of Significant Genes with Poor Prognosis in Pathologic Stage-I Lung Adenocarcinoma

Yujie Deng,[1,2,3] Xiaohui Chen,[4,5] Chuanzhong Huang,[6] Jun Song,[1,2] Sisi Feng,[1,2] Xuzheng Chen,[1,2] and Ruixiang Zhou[1,2]

[1]*School of Basic Medical Sciences, Fujian Medical University, Fuzhou 350108, Fujian, China*
[2]*Key Laboratory of Gastrointestinal Cancer, Ministry of Education, Fujian Medical University, Fuzhou 350108, Fujian, China*
[3]*Molecular Oncology Research Institute, The First Affiliated Hospital of Fujian Medical University, Fuzhou 350005, Fujian, China*
[4]*Department of Thoracic Surgery, Fujian Medical University Cancer Hospital, Fujian Cancer Hospital, Fuzhou, Fujian Province 350014, China*
[5]*College of Clinical Medicine for Oncology, Fujian Medical University, Fuzhou, China*
[6]*Laboratory of Immuno-Oncology, Fujian Medical University Cancer Hospital, Fujian Cancer Hospital, Fuzhou, Fujian 350014, China*

Correspondence should be addressed to Ruixiang Zhou; rxzhou@fjmu.edu.cn

Yujie Deng and Xiaohui Chen contributed equally to this work.

Received 19 November 2021; Accepted 5 February 2022; Published 11 April 2022

Academic Editor: Fu Wang

Background. Although more pathologic stage-I lung adenocarcinoma (LUAD) was diagnosed recently, some relapsed or distantly metastasized shortly after radical resection. The study aimed to identify biomarkers predicting prognosis in the pathologic stage-I LUAD and improve the understanding of the mechanisms involved in tumorigenesis. *Methods*. We obtained the expression profiling data for non-small cell lung cancer (NSCLC) patients from the NCBI-GEO database. Differentially expressed genes (DEGs) between early-stage NSCLC and normal lung tissue were determined. After function enrichment analyses on DEGs, the protein-protein interaction (PPI) network was built and analyzed with the Search Tool for the Retrieval of Interacting Genes (STRING) and Cytoscape. Overall survival (OS) and mRNA levels of genes were performed with Kaplan–Meier analysis and Gene Expression Profiling Interactive Analysis (GEPIA). qPCR and western blot analysis of hub genes in stage-I LUAD patients validated the significant genes with poor prognosis. *Results*. A total of 172 DEGs were identified, which were mainly enriched in terms related to management of extracellular matrix (ECM), receptor signaling pathway, cell adhesion, activity of endopeptidase, and receptor. The PPI network identified 11 upregulated hub genes that were significantly associated with OS in NSCLC and highly expressed in NSCLC tissues compared with normal tissues by GEPIA. Elevated expression of ANLN, EXO1, KIAA0101, RRM2, TOP2A, and UBE2T were identified as potential risk factors in pathologic stage-I LUAD. Except for ANLN and KIAA0101, the hub genes mRNA levels were higher in tumors compared with adjacent non-cancerous samples in the qPCR analysis. The hub genes protein levels were also overexpressed in tumors. In vitro experiments showed that knockdown of UBE2T in LUAD cell lines could inhibit cell proliferation and cycle progression. *Conclusions*. The DEGs can probably be used as potential predictors for stage-I LUAD worse prognosis and UBE2T may be a potential tumor promoter and target for treatment.

1. Introduction

Lung cancer is still the leading cause of cancer incidence and mortality both in China and worldwide [1, 2]. Although the 5-year survival rate of stage-I non-small cell lung cancer (NSCLC) is between 70% and 92%, there is still much progress such as screening, early detection, and genome analyses that have been made for lung cancer [3, 4], and they shed light on the possibility of developing more reliable prognostic biomarkers and sensitive predisposing genes in the carcinogenesis of lung cancer, better understanding the underlying mechanism and improving the treatment effect.

Although more and more pathologic stage-I non-small cell lung cancer (NSCLC) patients had been diagnosed and cured, some of them still suffered from early relapse and distant metastasis after surgery. Thus, the discrimination of specific biomarkers to predict the clinical outcome of early-stage NSCLC patients is indispensably necessary. Many researchers had worked out a variety of schemes in the prediction of resectable lung cancer patients [5, 6], while few focused on the outcome foretelling especially in pathologic stage-I patients. The use of gene chips can quickly detect differentially expressed genes (DEGs) within cancerous and normal tissues, identifying novel genetic predictors of lung cancer, facilitating improvements to early detection, and elucidating the mechanisms influencing carcinogenesis [7].

Ubiquitin-conjugating enzyme E2T (UBE2T) is a member of the E2 family in the ubiquitin-proteasome pathway that is located on chromosome 1q32.1. As one of the post-translational modifications, the ubiquitin-proteasome system regulates protein ubiquitination and stability and is recognized as a key regulator of cell proliferation, invasion, and differentiation [8]. UBE2T plays an important role in the Fanconi anemia pathway [9] by ubiquitinating FANCD2 and inducing the DNA damage response (DDR). Overexpression of UBE2T has been detected in different tumor types. UBE2T promotes tumor progression by downregulation of BRCA1 in breast cancer [10] and p53 ubiquitination in hepatocellular carcinoma cells [11]. However, the role of UBE2T in early-stage LUAD remains unclear. In vitro, we found that UBE2T promoted the proliferation of LUAD cells, which verified its functions.

2. Materials and Methods

2.1. Patients and Tissue Samples. The study was approved by the Ethics Committee of Clinical Research of Fujian Cancer Hospital. LUAD and paired non-cancerous tissues were obtained from seven patients diagnosed with stage-I lung adenocarcinoma who underwent surgical resection at Fujian Cancer Hospital between March 2014 and December 2014. All the patients were pathologically confirmed. None of the patients had received prior radiotherapy or chemotherapy. Fresh frozen samples were stored at −80°C.

2.2. Microarray Data Acquisition and DEGs Data Processing. Gene expression profile of GSE18842, GSE31210, and GSE33532 NSCLC and normal lung tissues were obtained from NCBI-GEO. All these microarray data were derived from GPL570 platforms ((HG-U133_Plus_2) Affymetrix Human Genome U133 Plus 2.0 Array). GSE18842 included 46 tumors and 45 controls; GSE31210 included 226 lung adenocarcinomas and 20 normal lung tissues; and GSE33532 had 80 tumors and 20 matched normal lung tissues. DEGs were identified via GEO2R online tools. The DEGs between NSCLC and normal lung tissue were selected by the criteria of $|\log FC| > 2$ as well as an adjusted P value <0.05. The raw data in TXT format were analyzed in Venn software online (http://bioinformatics.psb.ugent.be/webtools/Venn/) to evaluate the commonly DEGs within these 3 data sets. The DEGs with $\log FC > 0$ was taken as upregulated genes and $\log FC < 0$ as downregulated genes.

2.3. Gene Oncology and PPI Network Analysis. Gene ontology analysis (GO) is used to define genes and their RNA or protein products to identify unique biological properties. The Database for Annotation, Visualization, and Integrated Discovery (David) was utilized to determine these DEGs enrichment, including molecular function (MF), cellular component (CC), biological process (BP), and Kyoto Encyclopedia of Gene and Genome (KEGG) pathways ($P < 0.05$). Protein-protein interaction (PPI) was constructed via STRING (https://www.string-db.org/). The STRING database was used to determine the potential correlation between these DEGs. Then Cytoscape (version 3.7.1) was applied to visualize the PPI network. Modules of the PPI network was validated by the MCODE app in Cytoscape (degree cutoff = 2, node score cutoff = 0.2, k-core = 2, and max. depth = 100).

2.4. RNA Expression of Core Genes and Survival Analysis. Gene Expression Profiling Interactive Analysis (GEPIA) website was applied to analyze the DEGs mRNA expression between NSCLC and normal tissues ($P < 0.05$). Kaplan–Meier plotter (http://kmplot.com/analysis/index.php?p=service&cancer=lung) was used to determine the effect of genes on survival based on GEO (Affymetrix microarrays only). Survival within groups was compared by log-rank estimates ($P < 0.05$).

2.5. ROC Curve, Forest Plot, and Volcano Plot. The receiver operating characteristic curve (ROC) analysis was applied to evaluate the specificity and sensitivity of the core genes. The pROC R packages were installed, and the area under the curve (AUC) and P value were calculated (TCGA). Forest plot R packages were installed and the forest plot of subgroup analysis related to the stage of the candidate genes was drawn. The ggplot2 R packages were installed to draw the volcano plot labeled with hub genes.

2.6. Human Protein Atlas. The Human Protein Atlas (https://www.proteinatlas.org/) is an online website that includes pathology atlas of nearly 20 types of malignant tumors. In our study, immunohistochemical data of ANLN, TOP2A, and RRM2 were used to compare the expression in normal and lung adenocarcinoma tissues. The intensity of antibody staining indicated the protein expression of hub genes.

2.7. Real-Time Quantitative Reverse Transcription Polymerase Chain Reaction and Western Blot Analysis. Total RNA of fresh frozen tissues and cells were isolated using TRIzol reagent (Invitrogen) and was transferred to cDNA using Evo M-MLV RT Kit with gDNA Clean for qPCR (Accurate biology, AG). The SYBR® Green Premix Pro Taq HS qPCR Kit (Accurate biology, AG) and ROX Reference Dye (4 μM)

(Accurate biology, AG) were used to perform PCR amplification on Agilent Mx3000p real-time PCR system. The primers were synthesized by Sunya Biotechnology Co. Ltd. (Fuzhou, China); GAPDH was used as the internal control. Each measurement was performed in triplicate. The expression levels of hub gene mRNAs were evaluated using a relative quantification approach ($2^{-\Delta\Delta Ct}$ method) against GAPDH levels. Many more details of primer sequences for qRT-PCR were in a supplementary appendix online (Supplementary Table S2).

The cell lines were collected and lysed on ice with radioimmunoprecipitation assay (RIPA) buffer containing 0.1 mg/ml PMSF (Sangon Biotech, Shanghai) and cocktail (MCE). The fresh frozen tissues from seven patients paired with lung adenocarcinoma (T) and adjacent non-cancerous control tissues (N) were minced into small pieces before being lysed. The protein lysates were obtained from the supernatant through centrifugation at 12,000 g for 20 min at 4°C. The total amount of protein for each sample was 25 μg, run on 8%–12% gradient SDS-polyacrylamide gels, and then transferred onto a PVDF membrane (Immobilon-P^{SQ}, Millipore, Merck, USA). The membranes were probed with primary antibodies at 4°C overnight after blocking with 0.5% BSA blocking buffer for 1 h at room temperature. The membranes were then incubated with the appropriate secondary antibodies at room temperature for 1 hour and finally were detected by using an ECL blotting analysis system (ImageQuant LAS 4000 mini, GE, USA). The details of antibodies information can be found in Supplementary Table S3).

2.8. In Vitro Experiment

2.8.1. Cell Culture and siRNA Transfection. The A549 and H1299 LUAD cell lines obtained from Laboratory of Radiation Oncology and Radiobiology, Fujian Medical University Cancer Hospital, were cultured in RPMI-1640 (cytiva) containing 10% fetal bovine serum (Biological Industries) with 100 units/mL penicillin and 100 μg/mL streptomycin (Gibco) in a humidified 5% CO_2 incubator at 37°C. Three small interfering RNAs (si-UBE2T) against UBE2T (si-UBE2T-homo-192, 5′-CUCCUCAG AUCCGAUUUCUTT-3′; si-UBE2T-homo-374, 5′-GCUGACAUAUCCUCAGAA UTT-3′; and si-UBE2T-homo-97, 5′-CCUGCGAGCUCAAAUAUUATT-3′) and negative control siRNAs (si-NC, 5′-UUCUCCGAACGUGUCACGUTT), which were obtained from GenePharma (Shanghai, China), were transfected into cell lines using siRNA-mate transfection reagent (GenePharma, Shanghai, China) according to the manufacturer's instructions.

2.8.2. Cell Proliferation Assays. Cell proliferation was assessed by Cell Counting Kit-8 (CCK-8) and colony-forming assays. A total of 5×10^3 transfected cells in 100 μL medium per well were added to a 96-well plate for 4, 8, 24, 48, and 72 hours. At the indicated times, 10 μL (at a concentration of 10%) CCK-8 solution (Vazyme, Nanjing, China) was added to each well and incubated for 1 hour at room temperature. The absorbance was assessed at a 450 nm wavelength under a plate reader (BioTek ELx800). For the Colony-forming assays, transfected A549 and H1299 cell lines were seeded (1×10^3 cells/well) into six-well plates with 2 mL complete medium and divided into an si-NC and si-UBE2T groups. The colonies were fixed with 4% methanol (Solarbio) after 7–10 days of culture and then stained with 0.1% crystal violet solution (Biosharp, China). After 15 min, the cells were washed gently with PBS 3 times and then air-dried. Finally, the colony-forming units (consisting of ≥50 cells) were observed under an inverted microscope (ZEISS Primo Vert) and counted using ImageJ software. All experiments were performed in triplicate.

2.8.3. Flow Cytometry. LUAD cells were added into 6-well plates at a density of 1.3×10^5 cells per well for transfection after 24 hours incubation. Transfected cells were digested by 0.25% trypsin-EDTA (Gibco), collected into a centrifuge tube, and then fixed in 70% precooled ethanol overnight at −20°C. The cells were washed twice with PBS. After recollection by centrifugation at 1,500 rpm for 5 min, the cells were stained by 500 μL PI/RNase staining buffer (BD, USA). Culturing for 15 min at 37°C in dark, the cells were analyzed by LSRFortessaX-20 (BD Biosciences). All experiments were performed in triplicate.

2.9. Statistical Analysis. SPSS 18.0, GraphPad Prism 8.0, R software (version 4.0.2), and ModFit LT were used to conduct the analysis and generate graphs. The in vitro experiments were repeated in triplicate, and all data from the experiments were expressed as mean ± SE. *T*-test was used to evaluate the statistical significance of differences between experimental groups. A paired-samples *t*-test was used to assess the difference in hub genes expression between LUAD and non-cancerous tissues. $^*P < 0.05$ was considered statistically significant.

3. Results

3.1. Identification of DEGs in NSCLCs. In total, 352 NSCLC and 85 normal lung tissues were included. A total of 1,044, 626, and 818 DEGs were extracted from GSE18842, GSE31210, and GSE33532 by GEO2R online tool, respectively (Table S1 and Table 1). A total of DEGs including 49 upregulated genes (logFC > 0) and 123 downregulated genes (logFC < 0) were determined through Venn diagram software (Figures 1(a)–1(b) and 2(b)).

3.2. DEGs Gene Ontology Analysis in NSCLCs. All 172 DEGs analyzed by David online tools and GO analysis indicated roles in biological process (BP), cell component (CC), and molecular function (MF). For BP, upregulated DEGs were enriched in the regulation of collagen catabolic process, extracellular matrix disassembly, proteolysis, collagen fibril organization, sensory perception of sound, and inner ear morphogenesis, and downregulated DEGs were mainly enriched in angiogenesis, vasculogenesis, cell surface. For

Table 1: Patients' demographic characteristics of three GEO data sets.

GEO accession	GSE18842	GSE31210	GSE33532
No. of patients			
Normal	45	20	20
Tumor	46	226	80
Mean age (years)	NR	59	64
Gender			
Male	NR	105	64
Female		121	16
Histology			
LUAD	14	226	40
LUSC	32	0	16
Others	0	0	24
pTNM stage			
I	38	168	56
II	4	58	24
III-IV	4	0	0
Smoking history			
Yes	NR	122	NR
No		104	
Driven gene status			
EGFR mutation	NR	127	NR
KRAS mutation		20	
EML4-ALK fusion		11	
Triple negative		68	

CC, proteinaceous ECM, collagen trimer, extracellular region, and space were the main function that the upregulated DEGs were enriched in. As indicated in Table 2, downregulated DEGs consisted mainly of integral component of plasma membrane, membrane raft, and integral component of membrane. And molecular function of the DEGs majorly lay in metalloendopeptidase activity, endopeptidase activity, serine-type endopeptidase activity, and receptor activity.

3.3. PPI Network and Modular Analysis. All 172 DEGs were imported into the network that screened a total of 119 nodes and 283 edges, including 39 upregulated and 80 downregulated genes (Figure 1(c)). Fifty-three out of 172 DEGs were not in the DEGs PPI network. Then Cytoscape MCODE analysis demonstrated 11 core nodes among the 119, which were all upregulated genes (Figure 1(d)).

3.4. Analysis of Core Genes by GEPIA and the Kaplan–Meier Plotter. The expression level of the 11 core genes among cancerous as well as normal lung tissues was assessed via GEPIA, showing that in comparison to normal lung tissue, ANLN, CCNA2, CDCA7, DEPDC1, DLGAP5, EXO1, HMMR, KIAA0101, RRM2, TOP2A, and UBE2T were indeed highly expressed in both adenocarcinoma and squamous cell cancerous tissue (Figures 3(a)–3(k)). Kaplan–Meier plotter was used to identify the prognostic values of these 11 core genes, demonstrating all 11 genes were significantly correlated with worse prognosis and shorter OS (Table 3) in NSCLC patients. These 11 genes were then individually studied the different roles that would play in the different histology of NSCLC, finding that none of them demonstrated a significant effect on OS in lung squamous cell carcinoma (LUSC; Table 3), while the other 9 genes, including ANLN, CCNA2, DEPDC1, DLGAP5, EXO1, KIAA0101, RRM2, TOP2A, and UBE2T, demonstrated potential in the prediction of survival based on the expression level in LUAD (Figures 3(l)–3(t)) rather than CDCA7 and HMMR (Table 3).

Further analysis was then managed to uncover the prognostic effect of these genes on different pathologic stages of lung adenocarcinoma patients. Interestingly, the results of forest plot showed that genes such as ANLN (HR = 1.67; 95% CI: 1.1–2.53; $P = 0.0143$), EXO1 (HR = 2.68; 95% CI: 1.76–4.07; $P < 0.0001$), KIAA0101 (HR = 2.41; 95% CI: 1.59–3.64; $P < 0.0001$), RRM2 (HR = 1.63; 95% CI: 1.09–2.42; $P = 0.0151$), TOP2A (HR = 1.88; 95% CI: 1.25–2.32; $P = 0.002$), and UBE2T (HR = 3.48; 95% CI: 2.16–5.61; $P < 0.0001$) demonstrated significantly prognostic effect in early disease, especially in pathologic stage-I lung adenocarcinoma patients. The risk ratio (HR) for UBE2T is the most obvious. In addition, KIAA0101 also exhibited potential in the prediction of OS in stage-II LUAD patients (HR = 2.04; 95% CI: 1.25–3.33; $P = 0.0037$). CCNA2, DEPDC1, and DLGAP5 demonstrated no difference in different pathologic stage patients (Figure 2(a)). The distributions of six hub genes have been labeled in volcano plot (Figure 2(b)).

3.5. ROC Curves of the Candidate Genes. According to ROC curve analysis, in the pathologic stage-I LUAD, the AUCs of ANLN, EXO1, KIAA0101, RRM2, TOP2A, and UBE2T were 0.976 (95% CI: 0.960–0.988), 0.979 (95% CI: 0.964–0.991), 0.968 (95% CI: 0.949–0.984), 0.960 (95% CI: 0.938–0.978), 0.986 (95% CI: 0.974–0.995), and 0.990 (95% CI: 0.981–0.997), respectively (Figure 2(c); $P < 0.001$).

3.6. The 6 Hub Genes Were up-Regulated in Stage-I LUAD Compared with Normal Lung Tissues. To further determine the clinical significance of the six hub genes, we investigated the expression of UBE2T, ANLN, TOP2A, RRM2, KIAA0101, and EXO1 in seven randomly selected pairs of stage-I LUAD and adjacent non-cancerous tissues. The seven patients' characteristics were listed in Table 4. qRT-PCR analysis showed that mRNA expression of UBE2T ($P = 0.046$), TOP2A ($P = 0.047$), RRM2 ($P = 0.007$), and EXO1 ($P = 0.032$) were significantly higher in the LUAD tissues than in the adjacent non-cancerous tissues (Figure 4(a)). We tried to explore the protein expression of hub genes using Human Protein Atlas (HPA) after studying the mRNA expression. Immunohistochemistry assays from HPA showed that TOP2A and RRM2 protein was not expressed in normal lung tissues. TOP2A staining was high or medium in most LUAD tissues compared to low. However, RRM2 was not detected in eight LUAD tissues. There were also some IHC data of ANLN showing high and medium staining in cancer samples, although mRNA expression levels were not significantly different between

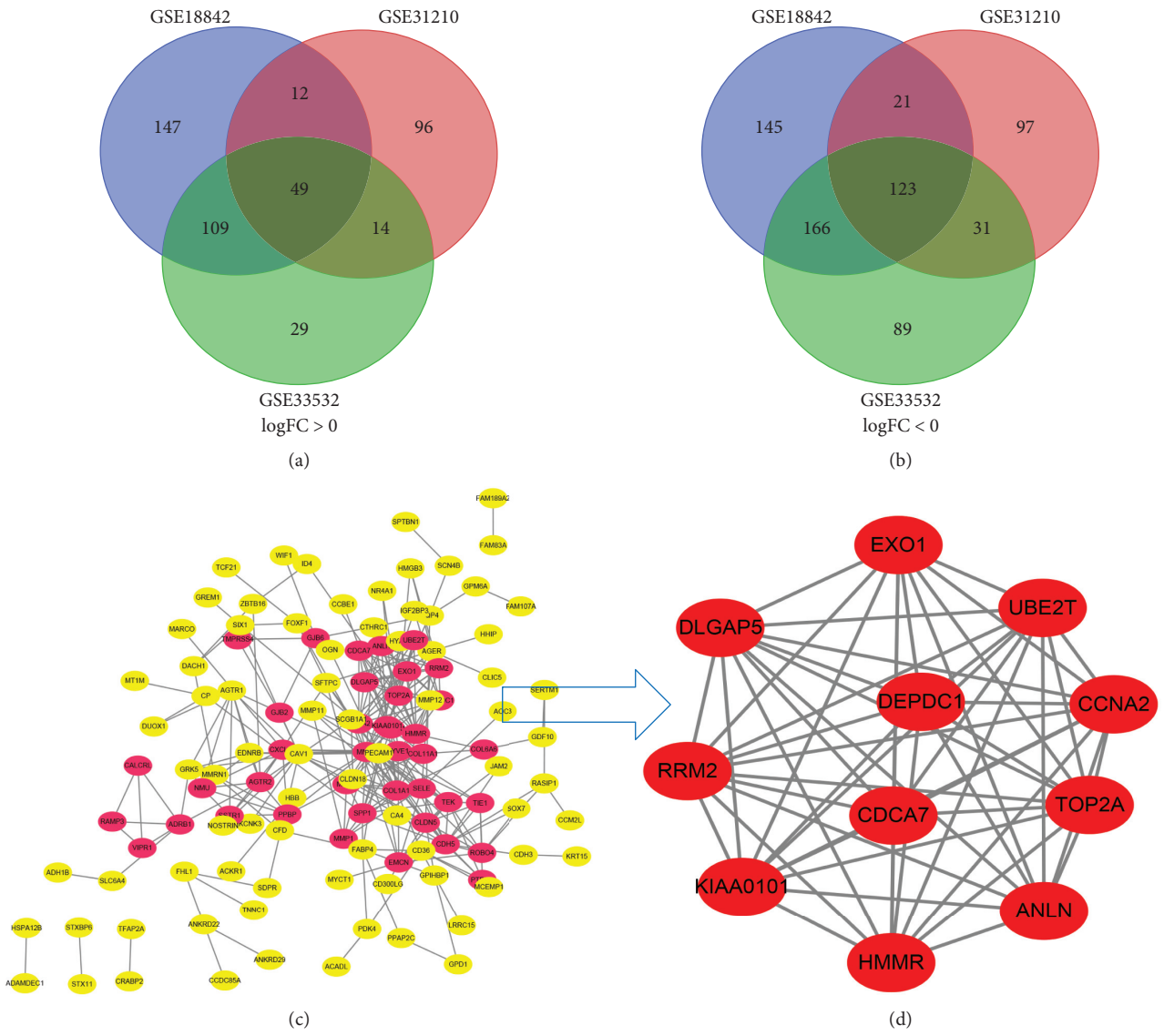

Figure 1: A total of 172 DEGs in the data sets (GSE18842/GSE31210/GSE33532) via the Venn diagrams website and PPI network constructed by STRING online platform and Cytoscape software. (a and b) 49 and 123 DEGs were upregulated (logFC > 0) and downregulated (logFC < 0) in the three data sets, respectively. (c) A total of 119 DEGs in the PPI network complex. Nodes: proteins; edges: interaction of proteins; red nodes were upregulated DEGs; and and yellow ones were downregulated DEGs. (d) Module analysis via Cytoscape software (degree cutoff = 2, node score cutoff = 0.2, k-core = 2, and max. depth = 100).

cancerous and non-cancerous samples in our seven patients (Figure 4(b)). Finally, we investigated the protein expression of UBE2T, ANLN, TOP2A, RRM2, KIAA0101 (PAF15), and EXO1 in the seven pairs of tissues. The results from western blot analysis also indicated that these six hub genes were overexpressed in tumor samples (Figure 4(c)). These results indicated that hub genes are overexpressed in stage-I LUAD and might promote tumor genesis.

3.7. Validation of UBE2T in Vitro That Promoted LUAD Cell Proliferation. Interestingly, the hazard ratio (HR) of UBE2T was the most obvious. And both mRNA and protein levels showed differences between LUAD and adjacent non-cancerous tissues.

To explore the biological function of UBE2T in LUAD progression, A549 and H1299 cells with transient UBE2T knockdown were established. We transfected LUAD cells with three independent small interfering RNAs (siRNAs) and a negative control vector (si-NC group; Table 5). Transfection efficiency was verified in UBE2T knockdown cells using real-time quantitative PCR and western blot (Figures 5(a) and 5(b)). Compared with the si-NC group, the mRNA expression level of UBE2T in A549 cells was markedly reduced by the transfection of the si-UBE2T vectors (Figure 5(a)). UBE2T protein expression was effectively downregulated in si-UBE2T-192 transfected A549 cell line than that of si-UBE2T-374 and si-UBE2T-97 (Figure 5(b)). The same results were observed in H1299 cell lines (Figures 5(a) and 5(b)). So we chose si-UBE2T-192 for further experiments in vitro.

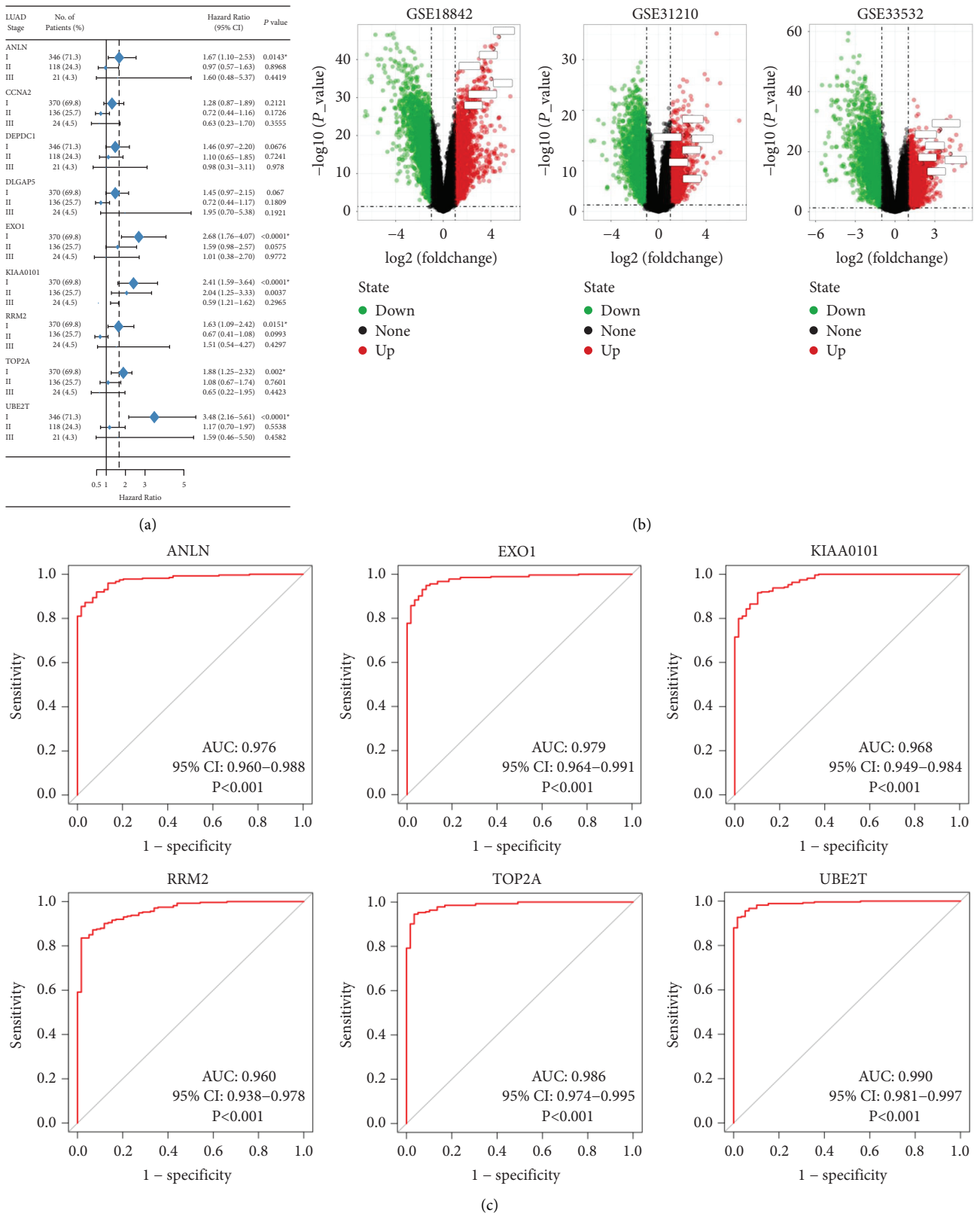

Figure 2: The OS for stage-I–III LUAD of nine candidate genes and ROC analysis: (a) six genes had a significantly worse survival in stage-I lung adenocarcinoma, while three had no significant ($^*P < 0.05$); (b) the distribution of all DEGs and six genes in volcano plots including GSE18842, GSE31210, and GSE33532; and (c) the ROC curves of six genes in pathologic stage-I LUAD. ROC: receiver operating characteristic and AUC: area under the curve.

Table 2: Gene ontology analysis of DEGs in NSCLC.

Expression	Category	Term	Count	*P*-value	FDR
Upregulated	GOTERM_BP_DIRECT	GO:0030574~collagen catabolic process	8	$4.6E-10$	$6.5E-7$
	GOTERM_BP_DIRECT	GO:0022617~extracellular matrix disassembly	6	$2.2\ E-6$	0.003069
	GOTERM_BP_DIRECT	GO:0007605~sensory perception of sound	6	$3.4E-5$	0.047394
	GOTERM_BP_DIRECT	GO:0030199~collagen fibril organization	4	$1.7E-4$	0.244070
	GOTERM_BP_DIRECT	GO:0006508~proteolysis	7	0.002578	3.540562
	GOTERM_BP_DIRECT	GO:0042472~inner ear morphogenesis	3	0.009302	12.233335
	GOTERM_CC_DIRECT	GO:0005578~proteinaceous extracellular matrix	8	$5.2E-06$	0.005507
	GOTERM_CC_DIRECT	GO:0005581~collagen trimer	5	$9.2E-05$	0.096644
	GOTERM_CC_DIRECT	GO:0005576~extracellular region	13	$6.1E-04$	0.638880
	GOTERM_CC_DIRECT	GO:0005615~extracellular space	9	0.020704	19.761271
	GOTERM_MF_DIRECT	GO:0004222~metalloendopeptidase activity	6	$1.08E-05$	0.012389
	GOTERM_MF_DIRECT	GO:0004175~endopeptidase activity	4	$3.7E-04$	0.425928
	GOTERM_MF_DIRECT	GO:0004252~serine-type endopeptidase activity	6	$5.1E-04$	0.578533
	GOTERM_MF_DIRECT	GO:0003682~chromatin binding	6	0.003359	3.771756
Downregulated	GOTERM_BP_DIRECT	GO:0001525~angiogenesis	11	$7.1E-07$	0.001095
	GOTERM_BP_DIRECT	GO:0001570~vasculogenesis	5	$3.2E-04$	0.492091
	GOTERM_BP_DIRECT	GO:0007166~cell surface receptor signaling pathway	8	0.001115	1.718397
	GOTERM_BP_DIRECT	GO:0007155~cell adhesion	10	0.001443	2.218739
	GOTERM_BP_DIRECT	GO:0031623~receptor internalization	4	0.002008	3.075026
	GOTERM_BP_DIRECT	GO:0002576~platelet degranulation	5	0.003101	4.711874
	GOTERM_CC_DIRECT	GO:0005887~integral component of plasma membrane	24	$7.3E-06$	0.008643
	GOTERM_CC_DIRECT	GO:0045121~membrane raft	8	$2.3E-04$	0.267090
	GOTERM_CC_DIRECT	GO:0016021~integral component of membrane	49	$2.5E-04$	0.292185
	GOTERM_CC_DIRECT	GO:0005886~plasma membrane	41	$4.8E-04$	0.562068
	GOTERM_CC_DIRECT	GO:0009897~external side of plasma membrane	7	0.001690	1.978880
	GOTERM_CC_DIRECT	GO:0016324~apical plasma membrane	8	0.001739	2.035373
	GOTERM_MF_DIRECT	GO:0004872~receptor activity	6	0.007296	9.063121
	GOTERM_MF_DIRECT	GO:0008201~heparin binding	5	0.012256	14.785944
	GOTERM_MF_DIRECT	GO:0044325~ion channel binding	4	0.025214	28.204372

The results from the Cell Counting Kit-8 (CCK-8) assays revealed that UBE2T knockdown (si-UBE2T-192) significantly reduced the LUAD cell lines' proliferative ability (Figure 5(c)). Similarly, the colony-forming assays suggested that UBE2T knockdown inhibited A549 cell line clonogenic ability. We also detected the tendency of decreased number of colonies after being transfected with si-UBE2T-192 in an H1299 cell line, although there was no statistically significant difference (Figure 5(d)). In addition, we analyzed cell cycle distribution using flow cytometry and showed that decreased UBE2T inhibited cell cycle progression with the accumulation of LUAD cell lines in G1-phase and reduction in S-phase (Figure 5(e)). These results demonstrated that as one of the 6 hub genes, UBE2T depletion did inhibit the proliferation of LUAD cells in vitro, and it might be a potential biomarker for early-stage LUAD diagnosis and prognosis.

4. Discussion

With the development of lung cancer screening and low-dose CT (LDCT) scan technology, many pathologic stage-I non-small cell lung cancer (NSCLC) patients have been diagnosed and cured. However, some still suffered from early relapse and distant metastasis after surgery, and few researchers focused on the outcome foretelling especially in pathologic stage-I LUAD patients. Therefore, there is a substantial need for novel therapeutic targets. In this study, bioinformatics analysis was performed to identify the candidate core genes correlated with early-stage LUAD.

We analyzed RNA sequencing data from the three profile data sets of early-stage NSCLC from the GEO data sets (GSE18842, GSE31210, and GSE33532) via GEO2R and Venn software, discriminated 172 DEGs including 49 upregulated and 123 downregulated genes compared to normal lung tissue. The 172 DEGs were detected by GO terms analyses. The BP of upregulated DEGs was particularly enriched in the management of extracellular matrix (ECM) that facilitated tumor metastasis, and that of downregulated DEGs was mainly enriched in cell surface receptor signaling pathway, cell adhesion, and receptor internalization, which might in part accelerate cellular detachment and eventually promote distant metastasis. The CCs of upregulated DEGs were also enriched in proteinaceous ECM, extracellular region, and space. For MF, DEGs were significantly focused on the activity of endopeptidase and receptor. The GO terms analysis revealed that the DEGs were obviously associated with ECM-related functions. A previous study showed that the extracellular matrix has crucial roles in lung cancer metastasis [12, 13]. Next, the DEGs PPI network of 119 nodes and 283 edges was built, and eventually, 11 out of 39 upregulated genes were screened. Further validation of these genes via GEPIA analysis indicated that all 11 genes exhibited higher expression levels in both histologies (LUAD

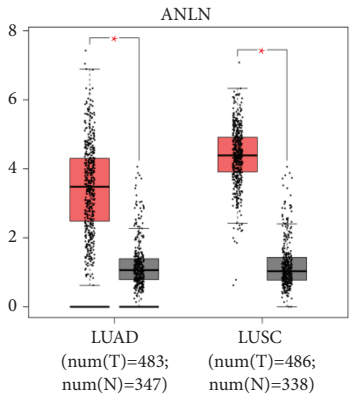

(a)

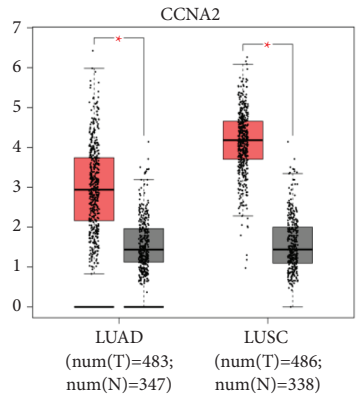

(b)

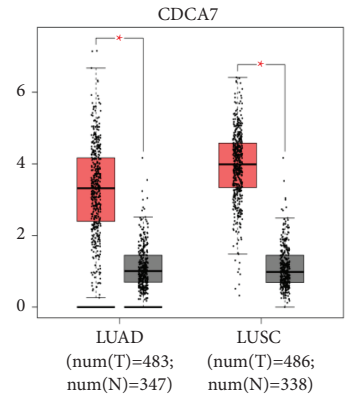

(c)

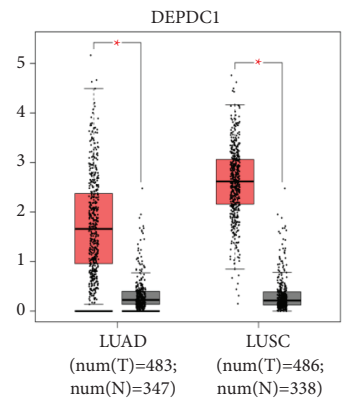

(d)

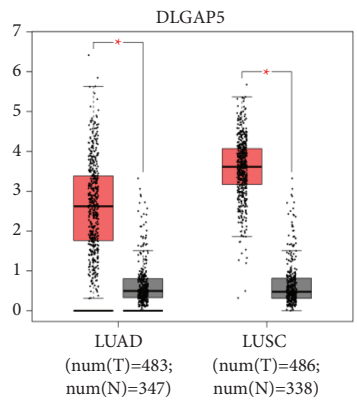

(e)

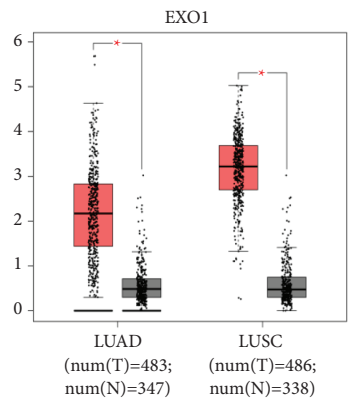

(f)

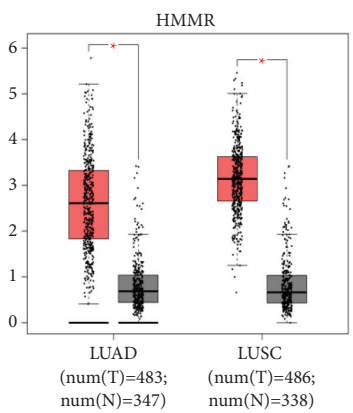

(g)

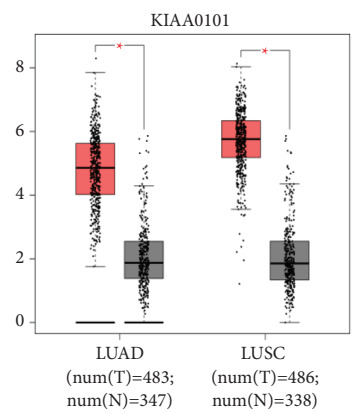

(h)

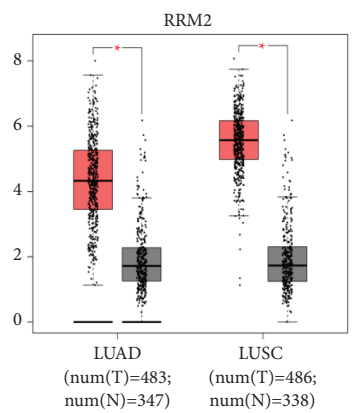

(i)

Figure 3: Continued.

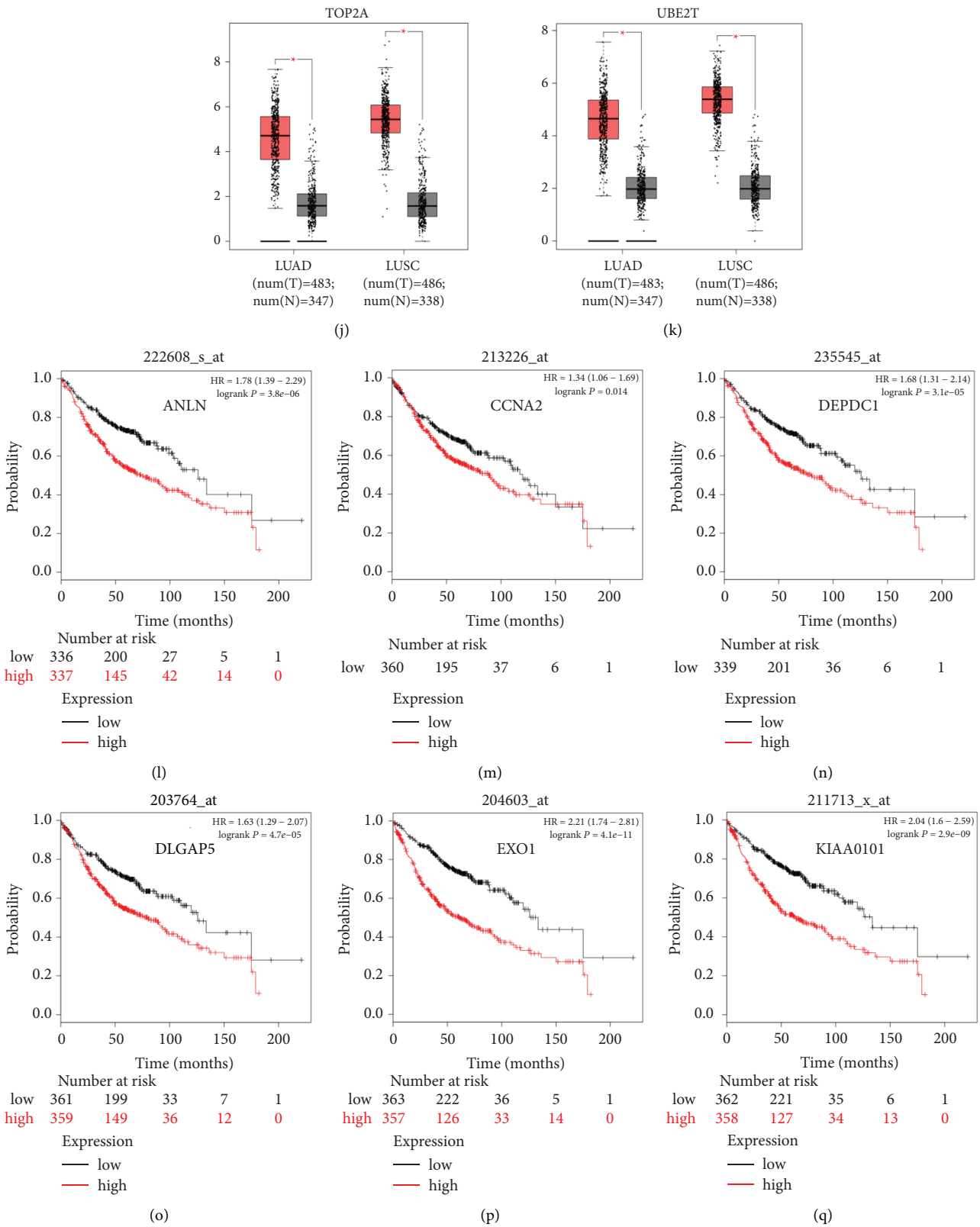

Figure 3: Continued.

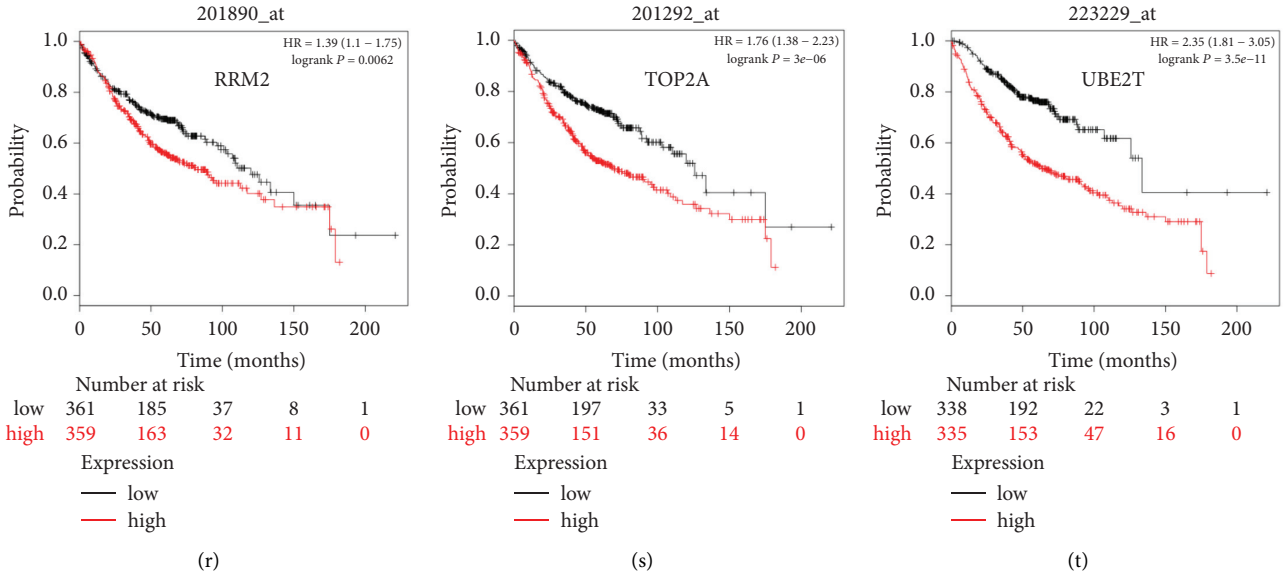

Figure 3: The expression of the 11 hub genes analyzed by the GEPIA website and the prognosis identified by Kaplan–Meier plotter online tools. (a–k) All the 11 genes demonstrated enhanced expression in both LUAD and LUSC compared to the normal specimen (*$P < 0.05$). Red and grey color stood for tumor and normal lung tissue, respectively. (l–t) Nine of 11 genes had a significantly worse survival ($P < 0.05$) in LUAD.

Table 3: The expression and prognosis of 11 core genes.

Category	Genes
Highly expressed genes in NSCLCs compared to normal tissues ($P < 0.05$)	ANLN CCNA2 CDCA7 DEPDC1 DLGAP5 EXO1 HMMR KIAA0101 RRM2 TOP2A UBE2T
Genes with significantly worse OS in NSCLC ($P < 0.05$)	ANLN CCNA2 CDCA7 DEPDC1 DLGAP5 EXO1 HMMR KIAA0101 RRM2 TOP2A UBE2T
Genes without significantly worse OS in LUSC ($P < 0.05$)	ANLN CCNA2 CDCA7 DEPDC1 DLGAP5 EXO1 HMMR KIAA0101 RRM2 TOP2A UBE2T
Genes with significantly worse OS in LUAD ($P < 0.05$)	ANLN CCNA2 DEPDC1 DLGAP5 EXO1 KIAA0101 RRM2 TOP2A UBE2T

OS, overall survival; LUSC, lung squamous cell carcinoma; and LUAD, lung adenocarcinoma.

and LUSC) of NSCLC in comparison to normal lung tissue. We then evaluated their prognostic effect on NSCLC patients via Kaplan–Meier plotter analysis and found them having a significantly worse survival. Interestingly, final analyses showed that none of the 11 genes had any significance on the outcome of patients with LUSC histology (all $P > 0.05$), while 6 of the 11 genes (ANLN, EXO1, KIAA0101, RRM2, TOP2A, and UBE2T) demonstrated statistical significance on worse prognosis in patients with pathologic stage-I LUAD histology (all $P < 0.05$). Chen et al. [14] also verified that UBE2T and KIAA0101 were highly expressed in early-stage lung adenocarcinoma through bioinformatic analysis and experiments in vitro. Moreover, to explore the predictive ability of the six hub genes, the ROC curves were performed. Notably, all six genes enabled a relatively high capacity for discrimination stage-I LUAD patients, with better clinical accuracy and higher diagnostic value.

Much effort has been tried to discriminate different genetic subgroups of surgically resected pathologic stage-I NSCLCs that would probably relapse and metastasize, including gene panel biomarkers [3, 15] and tumor genotyping [16, 17]. In the present study, we demonstrated that enhanced expression of either ANLN, EXO1, KIAA0101, RRM2, TOP2A, or UBE2T genes in pathologic stage-I LUAD patients was a risk factor of inferior outcome and shorter OS, although this finding might need further validation in larger sample size or in real-world studies.

ANLN overexpression correlated with worse outcomes in a wide spectrum of malignancies including lung [18–21], breast [22], and gastric cancer [23]. ANLN expression [18] was essential for the growth of lung cancer cell lines, as well as the maintenance of cellular motility and cytokinesis. Interestingly, the endogenous ANLN could be detected in various patterns of localization, either in nuclei and/or cytoplasm, and NSCLC patients with nuclear localization of ANLN had a significantly worse outcome compared to the cytoplasmic pattern. Intracellular ANLN level was found to change dynamically during mitosis, increase at a transition period from G1 to S phase, peak at S phase, and decrease in G2/M phase. The reduction of ANLN induced apoptosis and thus inhibited tumor proliferation in pancreatic cancer [24]. ANLN downregulation inhibited cell migration and

Table 4: The seven patients' characteristics of the fresh frozen samples.

# No.	Age (y. o.)	Sex	Smoking history/ brinkman index	Location	Surgery	TNM	Histology/predominant growth patterns	TTF-1	Bronchial involvement/ lymphovascular invasion	Relapse	Status
No. 1	52	F	No	LLL	VATS radical resection	T2aN0M0, IB	Ade/acinar + micropapillary	(+)	No	No	Alive
No. 2	58	M	Yes/400	LUL	Left pneumonectomy	T1aN0M0, IA1	Ade/acinar	(+)	No	No	Alive
No. 3	59	F	No	LLL	VATS radical resection	T1cN0M0, IA3	Ade/acinar	NA	No	No	Alive
No. 4	48	F	No	RUL	VATS radical resection	T2aN0M0, IB	Ade/acinar + papillary	(+)	No	Yes (bone/ liver/brain)	Dead
No. 5	48	M	Yes/300	LLL	VATS radical resection	T1cN0M0, IA3	Ade/ acinar + micropapillary + solid	(+)	No	No	Alive
No. 6	61	M	Yes/200	LLL	VATS exploration plus radical resection	T1bN0M0, IA2	Ade/acinar + solid	(+)	No	Yes (local)	Alive
No. 7	64	F	No	RUL	VATS radical resection	T2aN0M0, IB	Ade/acinar	NA	No	No	Alive

y. o., years old; F, female; M, male; LLL, left lower lobe; LUL, left upper lobe; RUL, right upper lobe; VATS, video-assisted thoracoscopic surgery; TTF-1, positive thyroid transcription factor-1; and NA, no application.

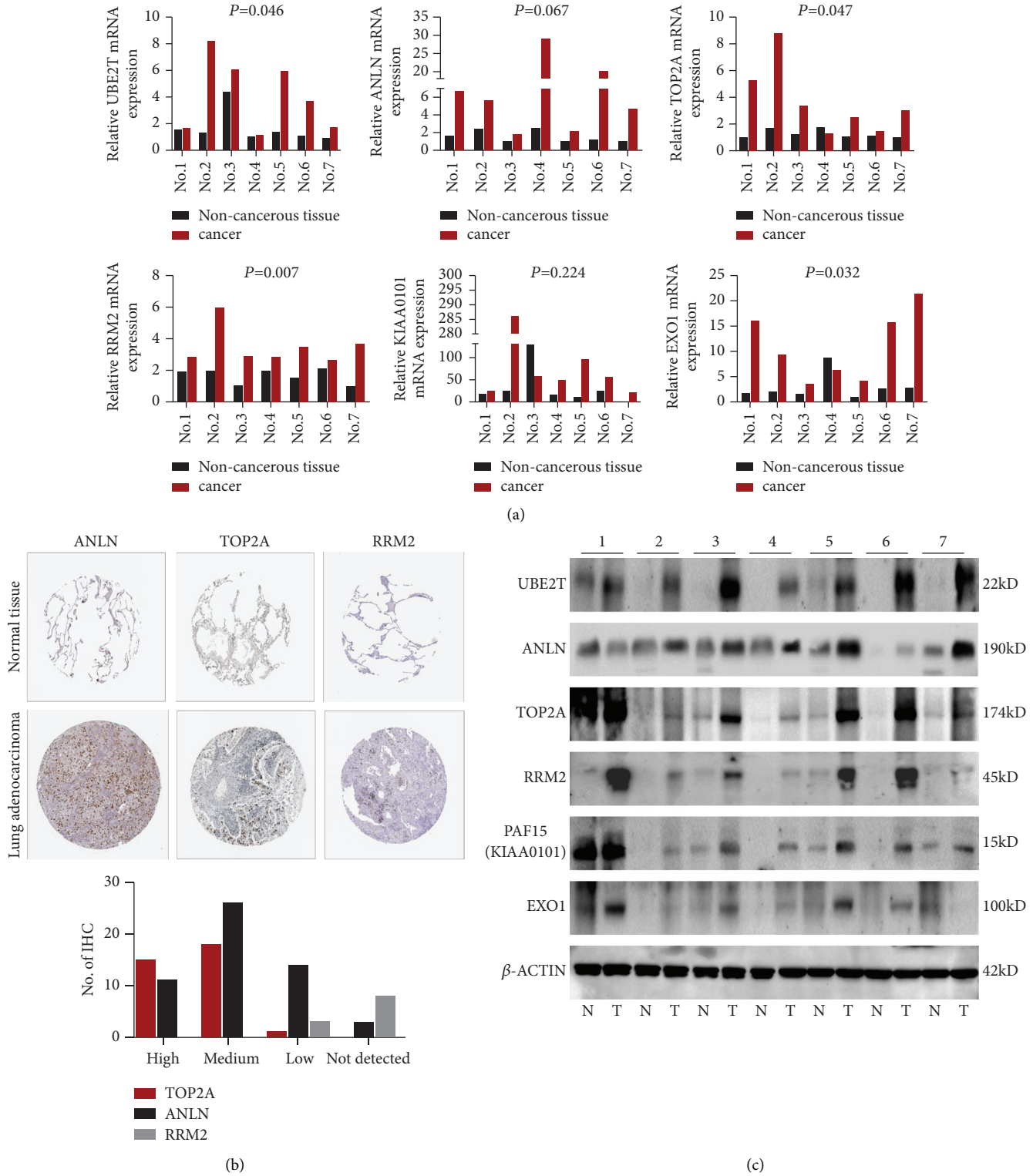

Figure 4: The expression of six genes in stage-I LUAD: (a) the mRNA level expressions of six genes were analyzed in lung adenocarcinoma and adjacent non-cancerous control samples from seven patients, using qRT-PCR ($^*P < 0.05$); (b) immunohistochemical analysis of ANLN, TOP2A, and RRM2 in normal and lung adenocarcinoma tissues from the Human Protein Atlas (HPA); and (c) western blot of six markers protein level expression in stage-I lung adenocarcinoma (T) and adjacent non-cancerous control samples (*N*) from seven patients. *β*-ACTIN was used as an internal control.

Table 5: Sequence of si-UBE2T and si-negative control group.

Category	Forward primer (5′------3′)	Reverse primer (5′------3′)
si-UBE2T-192	CUCCUCAGAUCCGAUUUCUTT	AGAAAUCGGAUCUGAGGAGTT
si-UBE2T-374	GCUGACAUAUCCUCAGAAUTT	AUUCUGAGGAUAUGUCAGCTT
si-UBE2T-97	CCUGCGAGCUCAAAUAUUATT	UAAUAUUUGAGCUCGCAGGTT
si-NC	UUCUCCGAACGUGUCACGUTT	ACGUGACACGUUCGGAGAATT

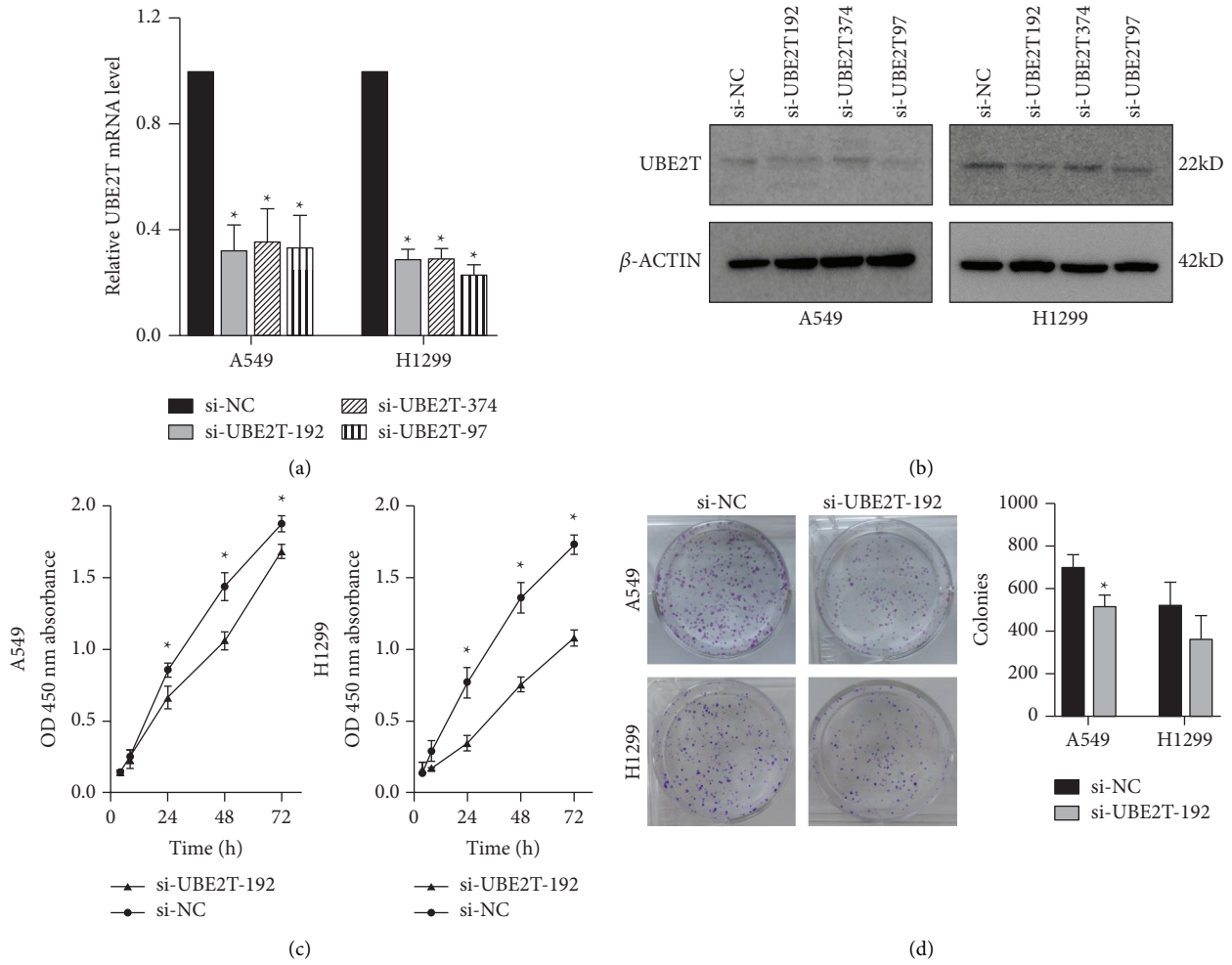

Figure 5: Continued.

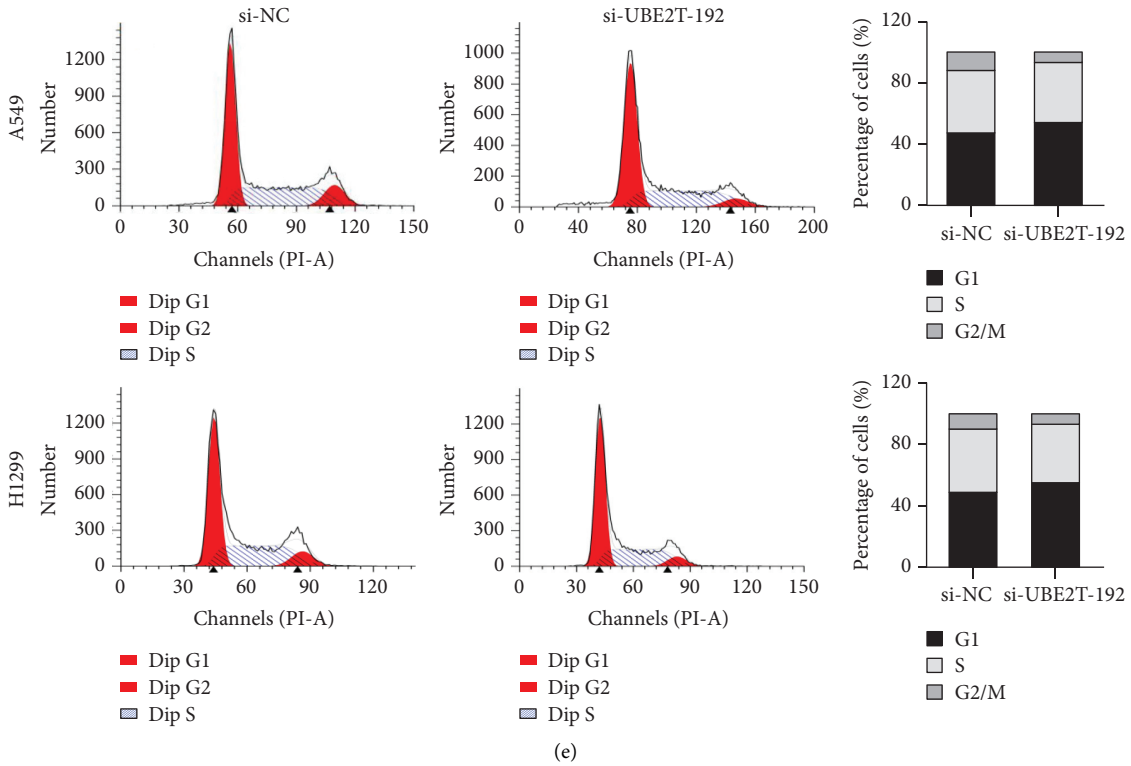

Figure 5: UBE2T promotes the malignant biological behaviour of LUAD cells: (a and b) the relative mRNA and protein expression in A549 and H1299 cell lines after being transfected with small interfering RNAs (siRNAs) against UBE2T, by qRT-PCR (* $P < 0.05$); (c) CCK-8 assay showed the inhibition of proliferation ability of LUAD cells with transient UBE2T knockdown (* $P < 0.05$); (d) clone formation assay showed the inhibition of proliferation ability of LUAD cells with transient UBE2T knockdown (* $P < 0.05$); and (e) flow cytometry showed G0/G1 arrested in LUAD cells with transient UBE2T knockdown. si-UBE2T group: A549 and H1299 cell lines transfected with si-UBE2T vector and si-NC group: LUAD cells transfected with control vector.

invasion in breast cancer, which was considered a biomarker for global genomic instability and to play a vital role in replicative immortality of tumor cells. Based on its adverse prognostic effect onstage-I LUAD patients, we speculated that ANLN over-expression might probably be an early event in the carcinogenesis of NSCLC.

Exonuclease 1 (EXO1) gene locates at 1q42–43 and encodes an 846 amino acid protein [25]. Owing to its role in DNA repair, maintenance of chromatin stability, and modulation of DNA recombination, the relationship between polymorphisms of EXO1 and the risk of cancer had been well studied, with at least nine genetic variants identified [26–29]. However, its expressions in carcinogenesis and prognosis in cancer entities were limited. Several studies indicated EXO1 was remarkably overexpressed and correlated with unfavorable patient prognosis in the colorectum, liver, pancreas, prostate, and so on [30–33]. However, the expression and prognostic value of EXO1 in NSCLC especially early-stage LUAD remains undefined, although some reported several EXO1 SNPs were correlated with worse prognosis in patients with NSCLC [27]. Here, we defined enhanced EXO1 expression as a risk factor in pathologic stage-I LUAD patients.

High expression of KIAA0101 (proliferating cell nuclear antigen (PCNA) associated factor 15 (PAF15)), containing a PCNA-binding motif and playing a key role in DNA repair, cellular apoptosis, and cell cycle, had been observed in a variety of human tumors including lung cancer [34–37]. High KIAA0101 level was significantly associated with shorter survival in NSCLC patients, especially in LUAD [34], which was consistent with our findings that KIAA0101 was bioinformatically identified as a negative prognostic factor in patients with pTNM stage-I (HR: 2.41; 95% CI: 1.59–3.64; $P < 0.0001$) and stage-II (HR: 2.04; 95% CI: 1.25–3.33; $P = 0.0037$). As a potential cell proliferation-related factor, KIAA0101 might probably become a treatment target either in human nasopharyngeal carcinoma [38] or in lung cancer patients with poor response to immune checkpoint inhibitors (ICIs) [35]. Further validation of this finding in real-world prospective studies would be necessary for our future studies.

Ribonucleotide reductase M2 subunit (RRM2), a small subunit of the ribonucleotide reductase complex that acts as an oncogenic role under pathological conditions, and its overexpression was found in various cancers including NSCLCs [39, 40]. Tabbal et al. [41] revealed that RRM2 overexpression was associated with poor prognosis and inhibition of RRM2 blocked cell proliferation, induced apoptosis, and inhibited cell migration. Recent studies also rendered RRM2 as a target in anti-cancer drug designation for treatment with anti-RRM2 drugs could reduce ribonucleotide reductase activity and consequently decreased the synthesis of dNTPs with concomitant inhibition of DNA

replication, arrest of cells at S-phase, DNA damage, and finally apoptosis [42].

Topoisomerase-II alpha (TOP2A) is an essential nuclear enzyme regulating the topological state of DNA during transcription and is involved in the processes of chromosome condensation and chromatid separation [43]. As a marker of proliferation and chemotherapy resistance, a higher TOP2A level was indicative of poor prognosis in many human cancers and also the target for some most widely used anti-cancer drugs [44, 45]. A recent study [46] found that resistance of esophageal cancer cells to paclitaxel can be reduced by the knockdown of the long non-coding RNA DDX11-AS1 through TAF1/TOP2A inhibition. Wang et al. [47] revealed that TOP2A had prognostic significance in early-stage lung cancer patients, and its expression correlated with the levels of immune cell infiltration, especially dendritic cells.

UBE2T (ubiquitin-conjugating enzyme, E2T), a typical ubiquitin-conjugating enzyme, connects with a particular E3 ubiquitin ligase to degrade related substrates [48]. In normal lung tissue, basal cells of pseudostratified ciliated columnar epithelium with high self-renewal and differentiation ability showed positive UBE2T immunohistochemistry staining, suggesting that UBE2T was closely related to cell proliferation [49]. UBE2T not only involved in DNA repair [50] but also regulated the protease in the glucose metabolism of tumor tissue, leading to its ubiquitination and degradation, ultimately promoting the tumor by glucose metabolism [51, 52]. UBE2T knockdown inhibited NSCLC proliferation and invasion by suppressing the Wnt/b-catenin signaling pathway [53]. Tu et al. [20] found that high UBE2T and ANLN expression correlated with worse outcomes in NSCLCs, regardless of their histology. Neither their histologic features nor combined diseases had been clarified, which was quite different from the results of our study.

We verified both the mRNA and protein expression levels of the six hub genes in stage-I LUAD. It was determined that EXO1, RRM2, TOP2A, and UBE2T expression was significantly upregulated in stage-I LUAD patients. Although there was no significant difference in the mRNA expression of ANLN and KIAA0101 between tumor and normal lung tissues, the tendency of increased relative mRNA expression could be detected, which also were probably ascribed to much few of the matching specimens. Interestingly, the hazard ratio (HR) of UBE2T was the most obvious. To further support the results of our bioinformatics analyses, we carried out UBE2T-related in vitro experiments. The proliferative ability and cell cycle progression of LUAD cell lines were inhibited after the knockdown of the UBE2T in A549 and H1299 cell lines. These results indicated the hub genes might be potential biomarkers for early-stage LUAD diagnosis and prognosis and played a vital role in stage-I LUAD. UBE2T overexpression might also promote cancer development. Nevertheless, more stage-I tumor samples would be needed to verify the expression of the hub genes. We also planned to verify the gene function in vitro and in vivo in our further study, and the underlying molecular mechanisms of the hub genes in the development and progression of early-stage LUAD remain to be further explored.

5. Conclusion

Our bioinformatic analyses identified six DEGs (ANLN, EXO1, KIAA0101, RRM2, TOP2A, and UBE2T) that could probably be used as potential biomarkers in the prediction of worse clinical outcomes in surgically resected stage-I LUADs and could facilitate the selection of some defined patients with a higher risk of postoperative relapse or distant metastasis. We also concluded that UBE2T enhanced LUAD cells' proliferative ability and cell cycle progression. The finding claims further validation with a larger sample size and underlying molecular mechanisms of the hub genes in the development and progression of early-stage LUAD.

Abbreviations

LUAD: Lung adenocarcinoma
DEGs: Differentially expressed genes
STRING: Search tool for the retrieval of interacting genes
PPI: Protein-protein interaction
GEPIA: Gene expression profiling interactive analysis
ROC: Receiver operating characteristic curve.

Data Availability

The data sets generated and/or analyzed during the current study are available in the Gene Expression Omnibus: GEO accession viewer (nih.gov); STRING: functional protein association networks (string-db.org); Gene Expression Profiling Interactive Analysis: GEPIA (cancer-pku.cn); Kaplan–Meier plotter (Lung; kmplot.com); and The Human Protein Atlas. All data can be obtained from the first author or corresponding author.

Disclosure

The abstract was accepted to be presented at the ELCC Annual Meeting 2020 in Geneva.

Conflicts of Interest

The authors declare that there are no conflicts of interest regarding the publication of this article.

Authors' Contributions

Y Deng, X Chen, and R Zhou conceptualized and designed the study; J Song and R Zhou provided the administrative support; C Huang, S Feng, and X Chen provided the study materials or patients; Y Deng and X Chen contributed to collection and assembly of data; Y Deng and X Chen contributed to data analysis and interpretation; All authors contributed to writing the manuscript and approved the final version of the manuscript. Y Deng and X Chen contributed equally.

Acknowledgments

This study was supported by Fujian Provincial Health Technology Project (Grant nos. 2018-2-20 to Y Deng and

2019-ZQN-13 to X Chen). The authors thank Professor Xiandong Lin, Laboratory of Radiation Oncology and Radiobiology, Fujian Medical University Cancer Hospital, Mingfang Zhang, the School of Basic Medical Sciences, Fujian Medical University, for kindly providing LUAD cells A549 and H1299.

Supplementary Materials

Supplementary Table 1: A total of 172 differentially expressed genes (DEGs) were detected from the three data sets, including 49 upregulated and 123 downregulated genes in NSCLC tissues compared to normal tissues. Supplementary Table 2: Sequence of primers for quantitative reverse transcription-polymerase chain reaction. Supplementary Table 3: Antibodies for western blot analysis. (*Supplementary Materials*)

References

[1] W. Chen, C. Xia, R. Zheng et al., "Disparities by province, age, and sex in site-specific cancer burden attributable to 23 potentially modifiable risk factors in China: a comparative risk assessment," *Lancet Global Health*, vol. 7, no. 2, pp. e257–e269, 2019.

[2] R. L. Siegel, K. D. Miller, H. E. Fuchs, and A. Jemal, "Cancer statistics, 2021," *CA: A Cancer Journal for Clinicians*, vol. 71, no. 1, pp. 7–33, 2021.

[3] S. Ren, S. Zhang, T. Jiang et al., "Early detection of lung cancer by using an autoantibody panel in Chinese population," *OncoImmunology*, vol. 7, no. 2, Article ID e1384108, 2018.

[4] P. Goldstraw, K. Chansky, J. Crowley et al., "The IASLC lung cancer staging Project: proposals for revision of the TNM stage groupings in the forthcoming (eighth) edition of the TNM classification for lung cancer," *Journal of Thoracic Oncology: Official Publication of the International Association for the Study of Lung Cancer*, vol. 11, no. 1, pp. 39–51, 2016.

[5] H. Y. Wu, Y. Y. Pan, A. T. Kopylov et al., "Assessment of serological early biomarker candidates for lung adenocarcinoma by using multiple reaction monitoring-mass spectrometry," *Proteomics-Clinical Applications*, vol. 14, no. 4, Article ID e1900095, 2020.

[6] X. Zhang, Y. He, K. Jia et al., "Does selected immunological panel possess the value of predicting the prognosis of early-stage resectable non-small cell lung cancer?" *Translational Lung Cancer Research*, vol. 8, no. 5, pp. 559–574, 2019.

[7] C. M. O'Keefe, D. Giammanco, S. Li, T. R. Pisanic, and T.-H. J. Wang, "Multilayer microfluidic array for highly efficient sample loading and digital melt analysis of DNA methylation," *Lab on a Chip*, vol. 19, no. 3, pp. 444–451, 2019.

[8] L. N. Micel, J. J. Tentler, P. G. Smith, and G. S. Eckhardt, "Role of ubiquitin ligases and the proteasome in oncogenesis: novel targets for anticancer therapies," *Journal of Clinical Oncology*, vol. 31, no. 9, pp. 1231–1238, 2013.

[9] Y. J. Machida, Y. Machida, Y. Chen et al., "UBE2T is the E2 in the Fanconi anemia pathway and undergoes negative autoregulation," *Molecular Cell*, vol. 23, no. 4, pp. 589–596, 2006.

[10] T. Ueki, J.-H. Park, T. Nishidate et al., "Ubiquitination and downregulation of BRCA1 by ubiquitin-conjugating enzyme E2T overexpression in human breast cancer cells," *Cancer Research*, vol. 69, no. 22, pp. 8752–8760, 2009.

[11] L.-p. Liu, M. Yang, Q.-z. Peng et al., "UBE2T promotes hepatocellular carcinoma cell growth via ubiquitination of p53," *Biochemical and Biophysical Research Communications*, vol. 493, no. 1, pp. 20–27, 2017.

[12] A. L. Parker and T. R. Cox, "The role of the ECM in lung cancer dormancy and outgrowth," *Frontiers in Oncology*, vol. 10, Article ID 1766, 2020.

[13] D. M. Gilkes, G. L. Semenza, and D. Wirtz, "Hypoxia and the extracellular matrix: drivers of tumour metastasis," *Nature Reviews Cancer*, vol. 14, no. 6, pp. 430–439, 2014.

[14] Y. Chen, L. Jin, Z. Jiang, S. Liu, and W. Feng, "Identifying and validating potential biomarkers of early stage lung adenocarcinoma diagnosis and prognosis," *Frontiers in Oncology*, vol. 11, Article ID 644426, 2021.

[15] X.-C. Zhang, J. Wang, G.-G. Shao et al., "Comprehensive genomic and immunological characterization of Chinese non-small cell lung cancer patients," *Nature Communications*, vol. 10, no. 1, p. 1772, 2019.

[16] R. W. Jansen, P. van Amstel, R. M. Martens et al., "Non-invasive tumor genotyping using radiogenomic biomarkers, a systematic review and oncology-wide pathway analysis," *Oncotarget*, vol. 9, no. 28, pp. 20134–20155, 2018.

[17] X. Zhuang, C. Zhao, J. Li et al., "Clinical features and therapeutic options in non-small cell lung cancer patients with concomitant mutations of EGFR , ALK , ROS1 , KRAS or BRAF," *Cancer Medicine*, vol. 8, no. 6, pp. 2858–2866, 2019.

[18] C. Suzuki, Y. Daigo, N. Ishikawa et al., "ANLN plays a critical role in human lung carcinogenesis through the activation of RHOA and by involvement in the phosphoinositide 3-kinase/AKT pathway," *Cancer Research*, vol. 65, no. 24, pp. 11314–11325, 2005.

[19] M. Skrzypski, E. Jassem, M. Taron et al., "Three-gene expression signature predicts survival in early-stage squamous cell carcinoma of the lung," *Clinical Cancer Research*, vol. 14, no. 15, pp. 4794–4799, 2008.

[20] H. Tu, M. Wu, W. Huang, and L. Wang, "Screening of potential biomarkers and their predictive value in early stage non-small cell lung cancer: a bioinformatics analysis," *Translational Lung Cancer Research*, vol. 8, no. 6, pp. 797–807, 2019.

[21] C. Wang, J. Qiu, S. Chen et al., "Prognostic model and nomogram construction based on autophagy signatures in lower grade glioma," *Journal of Cellular Physiology*, vol. 236, no. 1, pp. 235–248, 2021.

[22] A. M. Sadi, D. Y. Wang, B. J. Youngson et al., "Clinical relevance of DNA microarray analyses using archival formalin-fixed paraffin-embedded breast cancer specimens," *BMC Cancer*, vol. 11, pp. 1–13, 2011.

[23] N. S. Pandi, M. Manimuthu, P. Harunipriya, M. Murugesan, G. V. Asha, and S. Rajendran, "In silico analysis of expression pattern of a Wnt/β-catenin responsive gene ANLN in gastric cancer," *Gene*, vol. 545, no. 1, pp. 23–29, 2014.

[24] N. M. Tuan and C. H. Lee, "Role of anillin in tumour: from a prognostic biomarker to a novel target," *Cancers*, vol. 12, no. 6, 2020.

[25] A. Morgan and R. D. Burgoyne, "Exol and Exo2 proteins stimulate calcium-dependent exocytosis in permeabilized adrenal chromaff in cells," *Nature*, vol. 355, no. 6363, pp. 833–836, 1992.

[26] W. Eid, D. Hess, C. König, C. Gentili, and S. Ferrari, "The human Exonuclease-1 interactome and phosphorylation sites," *Biochemical and Biophysical Research Communications*, vol. 514, no. 3, pp. 567–573, 2019.

[27] S. Zienolddiny, D. Campa, H. Lind et al., "Polymorphisms of DNA repair genes and risk of non-small cell lung cancer," *Carcinogenesis*, vol. 27, no. 3, pp. 560–567, 2006.

[28] G. Jin, H. Wang, Z. Hu et al., "Potentially functional polymorphisms of EXO1 and risk of lung cancer in a Chinese population: a case-control analysis," *Lung Cancer*, vol. 60, no. 3, pp. 340–346, 2008.

[29] N. Y. Hsu, H. C. Wang, C. H. Wang et al., "Lung cancer susceptibility and genetic polymorphisms of Exo1 gene in Taiwan," *Anticancer Research*, vol. 29, no. 2, pp. 725–730, 2009.

[30] G. L. De' Angelis, L. Bottarelli, C. Azzoni et al., "Microsatellite instability in colorectal cancer," *Acta BioMedica*, vol. 89, no. 9-S, pp. 97–101, 2018.

[31] Y. Dai, Z. Tang, Z. Yang et al., "EXO1 overexpression is associated with poor prognosis of hepatocellular carcinoma patients," *Cell Cycle (Georgetown, Tex.)*, vol. 17, no. 19-20, pp. 2386–2397, 2018.

[32] S. Alimirzaie, A. Mohamadkhani, S. Masoudi et al., "Mutations in known and novel cancer susceptibility genes in young patients with pancreatic cancer," *Archives of Iranian Medicine*, vol. 21, no. 6, pp. 228–233, 2018.

[33] F. Luo, Y. Z. Wang, D. Lin, J. Li, and K. Yang, "Exonuclease 1 expression is associated with clinical progression, metastasis, and survival prognosis of prostate cancer," *Journal of Cellular Biochemistry*, vol. 120, 2019.

[34] T. Kato, Y. Daigo, M. Aragaki, K. Ishikawa, M. Sato, and M. Kaji, "Overexpression of KIAA0101 predicts poor prognosis in primary lung cancer patients," *Lung Cancer*, vol. 75, no. 1, pp. 110–118, 2012.

[35] S. Pabla, J. M. Conroy, M. K. Nesline et al., "Proliferative potential and resistance to immune checkpoint blockade in lung cancer patients," *Journal for ImmunoTherapy of Cancer*, vol. 7, no. 1, p. 27, 2019.

[36] Y. Cheng, K. Li, D. Diao et al., "Expression of KIAA0101 protein is associated with poor survival of esophageal cancer patients and resistance to cisplatin treatment in vitro," *Laboratory Investigation*, vol. 93, no. 12, pp. 1276–1287, 2013.

[37] M. J. Emanuele, A. Ciccia, A. E. H. Elia, and S. J. Elledge, "Proliferating cell nuclear antigen (PCNA)-associated KIAA0101/PAF15 protein is a cell cycle-regulated anaphase-promoting complex/cyclosome substrate," *Proceedings of the National Academy of Sciences*, vol. 108, no. 24, pp. 9845–9850, 2011.

[38] H. Zhao, M. Chen, J. Wang, G. Cao, W. Chen, and J. Xu, "PCNA-associated factor KIAA0101 transcriptionally induced by ELK1 controls cell proliferation and apoptosis in nasopharyngeal carcinoma: an integrated bioinformatics and experimental study," *Aging (Albany NY)*, vol. 12, no. 7, pp. 5992–6017, 2020.

[39] S. Fan, J. Tang, N. Li et al., "Integrative analysis with expanded DNA methylation data reveals common key regulators and pathways in cancers," *Npj Genomic Medicine*, vol. 4, no. 1, p. 2, 2019.

[40] W. X. Chen, L. G. Yang, L. Y. Xu et al., "Bioinformatics analysis revealing prognostic significance of RRM2 gene in breast cancer," *Bioscience Reports*, vol. 39, no. 4, 2019.

[41] H. Tabbal, A. Septier, M. Mathieu et al., "EZH2 cooperates with E2F1 to stimulate expression of genes involved in adrenocortical carcinoma aggressiveness," *British Journal of Cancer*, vol. 121, no. 5, pp. 384–394, 2019.

[42] C.-W. Chen, Y. Li, S. Hu et al., "DHS (trans–4,4'-dihydroxystilbene) suppresses DNA replication and tumor growth by inhibiting RRM2 (ribonucleotide reductase regulatory subunit M2)," *Oncogene*, vol. 38, no. 13, pp. 2364–2379, 2019.

[43] A. A. Riccio, M. J. Schellenberg, and R. S. Williams, "Molecular mechanisms of topoisomerase 2 DNA-protein crosslink resolution," *Cellular and Molecular Life Sciences*, vol. 77, no. 1, pp. 81–91, 2020.

[44] A. Grenda, J. Błach, M. Szczyrek et al., "Promoter polymorphisms of TOP2A and ERCC1 genes as predictive factors for chemotherapy in non-small cell lung cancer patients," *Cancer Medicine*, vol. 9, no. 2, pp. 605–614, 2020.

[45] Z. Gatalica, S. Vranic, B. Krušlin et al., "Comparison of the biomarkers for targeted therapies in primary extra-mammary and mammary Paget's disease," *Cancer Medicine*, vol. 9, no. 4, pp. 1441–1450, 2020.

[46] S. Zhang, H. Jiang, Z. Xu et al., "The resistance of esophageal cancer cells to paclitaxel can be reduced by the knockdown of long noncoding RNA DDX11-AS1 through TAF1/TOP2A inhibition," *American journal of cancer research*, vol. 9, no. 10, pp. 2233–2248, 2019.

[47] K. Wang, R. Chen, Z. Feng et al., "Identification of differentially expressed genes in non-small cell lung cancer," *Aging (Albany NY)*, vol. 11, no. 23, pp. 11170–11185, 2019.

[48] M. J. Cornwell, G. J. Thomson, J. Coates et al., "Small-molecule inhibition of ube2t/FANCL-mediated ubiquitylation in the Fanconi anemia pathway," *ACS Chemical Biology*, vol. 14, no. 10, pp. 2148–2154, 2019.

[49] J. Hao, A. Xu, X. Xie et al., "Elevated expression of UBE2T in lung cancer tumors and cell lines," *Tumor Biology*, vol. 29, no. 3, pp. 195–203, 2008.

[50] A. Alpi, F. Langevin, G. Mosedale, Y. J. Machida, A. Dutta, and K. J. Patel, "UBE2T, the Fanconi anemia core complex, and FANCD2 are recruited independently to chromatin: a basis for the regulation of FANCD2 monoubiquitination," *Molecular and Cellular Biology*, vol. 27, no. 24, pp. 8421–8430, 2007.

[51] M. Shen, S. Schmitt, D. Buac, and Q. P. Dou, "Targeting the ubiquitin-proteasome system for cancer therapy," *Expert Opinion on Therapeutic Targets*, vol. 17, no. 9, pp. 1091–1108, 2013.

[52] L. Barbin, F. Eisele, O. Santt, and D. H. Wolf, "The Cdc48-Ufd1-Npl4 complex is central in ubiquitin-proteasome triggered catabolite degradation of fructose-1,6-bisphosphatase," *Biochemical and Biophysical Research Communications*, vol. 394, no. 2, pp. 335–341, 2010.

[53] J. Liu and X. Liu, "UBE2T silencing inhibited non-small cell lung cancer cell proliferation and invasion by suppressing the wnt/beta-catenin signaling pathway," *International Journal of Clinical and Experimental Pathology*, vol. 10, no. 9, pp. 9482–9488, 2017.

Hindawi
Journal of Oncology
Volume 2022, Article ID 2750193, 15 pages
https://doi.org/10.1155/2022/2750193

Research Article

Digital Image Analysis-Based Evaluation of Claudin-1 and Claudin-7 Delocalization in Cutaneous Squamous Cell Carcinoma and in Its Precancerous State

Lina Xu, Yunlei Pan, Shunli Tang, Juan Bai, Yinhua Wu, Jianjun Qiao, and Hong Fang

Department of Dermatology, The First Affiliated Hospital, College of Medicine, Zhejiang University, Hangzhou 310003, China

Correspondence should be addressed to Jianjun Qiao; qiaojianjun@zju.edu.cn and Hong Fang; fanghongzy@zju.edu.cn

Received 14 December 2021; Revised 7 March 2022; Accepted 11 March 2022; Published 6 April 2022

Academic Editor: Fu Wang

Accumulating evidence has revealed that delocalization of the transmembrane proteins, Claudin-1 and Claudin-7, to the cytoplasm and/or nucleus occurs in various tumors. However, their subcellular distribution in terms of the membrane, cytoplasm, and nucleus and relationship with signaling pathways have not been elucidated during carcinogenesis. We first determined the expression of these proteins in the membrane, cytoplasm, and nucleus using ImageJ software and automatically collected the immunohistochemical quantification of dysplasia (actinic keratosis (AK)), carcinoma in situ (CIS; Bowen's disease (BD)), and invasive cutaneous squamous cell carcinoma (SCC) for digital image analysis (DIA). The activity of p-ERK, p-AKT, and p-mTOR and their correlation with subcellular Claudin-1 and Claudin-7 were also performed. Finally, we validated Claudin-1 and Claudin-7 delocalization at the cytoplasm and nucleus in cultured human normal keratinocytes and cutaneous SCC cells. Claudin-1 and Claudin-7 were delocalized as revealed by membranous, cytoplasmic, and nuclear staining in sun-exposed skin, AK, BD, and SCC. In BD, both membranous and cytoplasmic Claudin-1 (nuclear Claudin-1 decrease but no significant difference) were higher than AK, while Claudin-7 almost had the opposite situation. In SCC, cytoplasmic and nuclear Claudin-1 (membranous Claudin-1 no significant difference) was lower than in AK and sun-exposed skin, while Claudin-7 had higher membranous and cytoplasmic but lower nuclear expression. Moreover, p-AKT and p-mTOR (but not p-ERK) were downregulated in the SCC. Subcellular Claudin-1 and Claudin-7 were not only correlated with each other, but also correlated with p-ERK in BD and p-AKT and p-mTOR in SCC. Together, these results imply the delocalization of Claudin-1 and Claudin-7 and their correlation with MAPK/ERK and PI3K-AKT-mTOR signaling pathways in tumorigenesis and infiltration in cutaneous SCC.

1. Introduction

The incidence of cutaneous squamous cell carcinoma (SCC) is on the rise, making it the second-most-common keratinocyte-derived carcinoma [1]. Its classic multistep carcinogenesis involves several events, ranging from cumulative sun exposure to precursor actinic keratosis (AK), carcinoma in situ (CIS; Bowen's disease (BD)), and invasive cutaneous SCC. There are at least two pathways involved in cutaneous SCC: phosphatidylinositol 3-kinase- (PI3K-) AKT-mammalian target of rapamycin (mTOR) pathway and the mitogen-activated protein kinases/extracellular signal-regulated kinase (MAPK/ERK) pathway. Overactivation of PI3K-AKT-mTOR is observed in cutaneous SCC and its inhibition suppresses the growth of human cutaneous SCC, both *in vitro* and *in vivo* [2–5]. The level of phosphorylated-ERK1/2 (p-Erk1/2) is correlated with the size of cutaneous SCC, but not with its metastasis [3]. However, the dynamic activities of these pathways in tumorigenesis and infiltration of cutaneous SCC are not well understood and, therefore, need to be clarified.

Claudins contain 27 transmembrane-protein-family members which play important roles in tight junction (TJ)

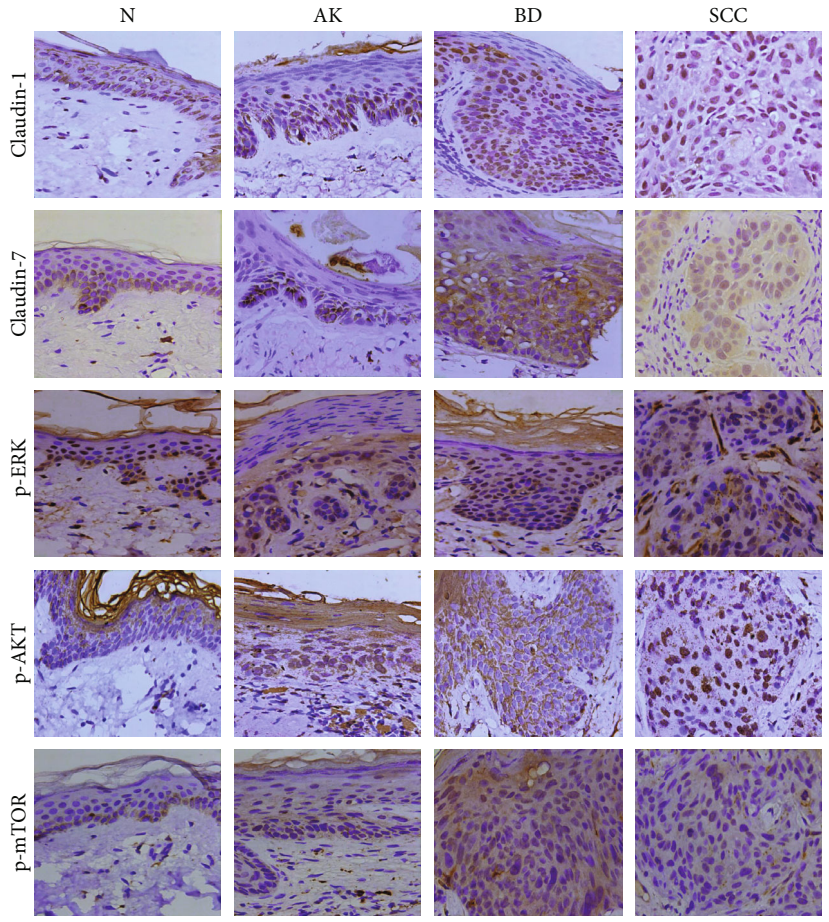

(a)

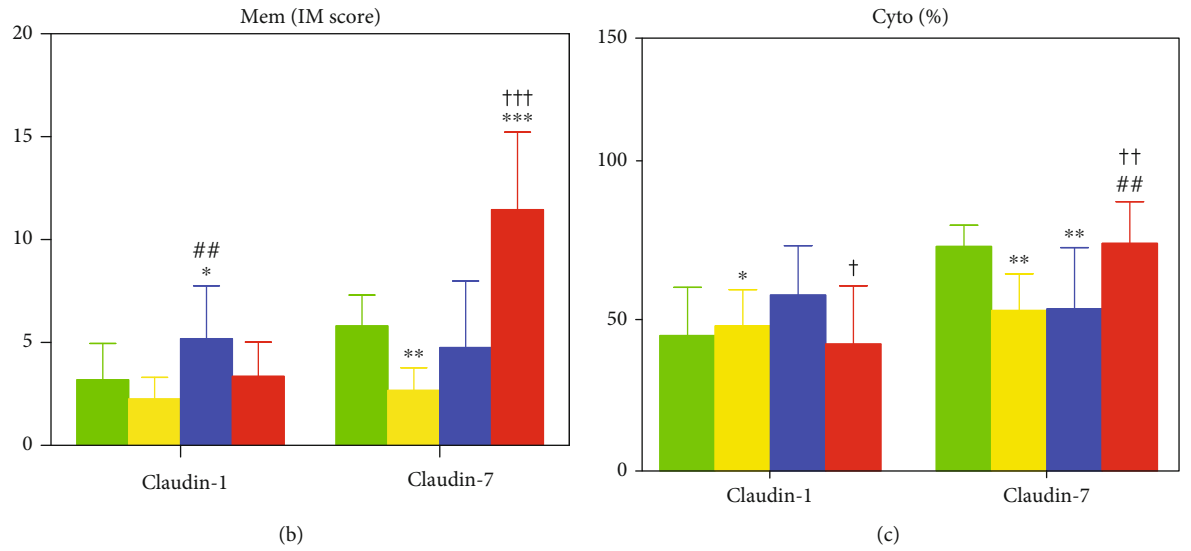

(b)

(c)

Figure 1: Continued.

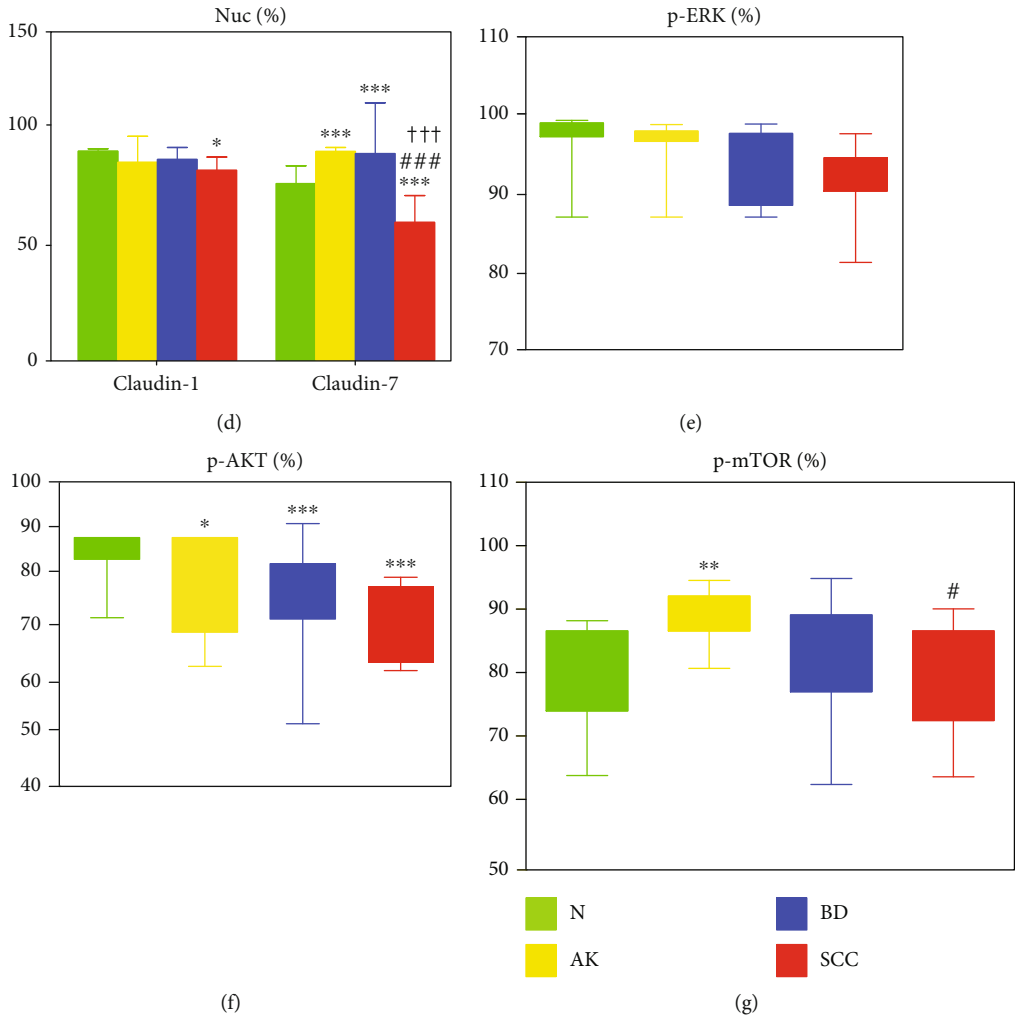

FIGURE 1: Immunohistochemical analysis. (a) Subcellular localization of Claudin-1 and Claudin-7 and p-ERK, p-AKT, and p-mTOR expression in sun-exposed skin, precancerous actinic keratosis (AK), in situ Bowen's disease (BD), and invasive cutaneous squamous cell carcinoma (SCC) (×400). Quantitative analysis of Claudin-1 and Claudin-7 immunostaining for (b) membrane (Mem, IM scores), (c) cytoplasm (Cyto, %), and (d) nucleus (Nuc, %) localization reflected by positive percentages in sun-exposed skin (green), AK (yellow), BD (blue), and SCC (red). A comparison of positive percentages of (e) p-ERK, (f) p-AKT, and (g) p-mTOR. Relative to sun-exposed skin: $^{*}P < 0.05$; $^{**}P < 0.01$; $^{***}P < 0.001$. Relative to AK tissue: $^{\#}P < 0.05$; $^{\#\#}P < 0.01$; $^{\#\#\#}P < 0.001$. Relative to BD tissue: $^{\dagger}P < 0.05$; $^{\dagger\dagger}P < 0.01$; $^{\dagger\dagger\dagger}P < 0.001$.

formation and regulate paracellular permeability, as well as cell polarity in epithelial and endothelial cells. The TJ integrity is often decreased in cancerous cells due to dysregulation of tight junction proteins (TJPs), such as up- or downregulation or delocalization of Claudins. Claudin-1 expression in the membrane, cytoplasm, and nucleus is altered in human malignancies including colon cancer [6], nasopharynx carcinoma [7], thyroid carcinoma [8], breast cancer [9], and melanoma [10, 11]. Moreover, subcellular Claudin-1 correlates with aggressive tumor behaviors such as enhanced cell migration, invasion, and proliferation, as well as decreased apoptosis [7, 8]. Claudin alterations have also been reported in cutaneous SCC and its precancerous lesions [12, 13], whereby a faint or strong cytoplasmic, rather than primary membranous, localization of Claudin-1 was found to be parallel with the cutaneous SCC carcinogenesis process. Additionally, Claudin-1 expression was found to be heterogeneous between keratinized and unkeratinized cutaneous SCC [14]. However, digital image analysis of membranous/cytoplasmic/nuclear Claudin-1 and Claudin-7 in multisteps of carcinogenesis in cutaneous SCC has not been performed. In this study, two auto-scored plugins of ImageJ software, ImmunoMembrane plugin exclusive for membrane proteins [15] and IHC profiler plugin for cytoplasmic/nuclear molecules [16], were developed for a series of cutaneous SCC, BD, AK, and sun-exposed skin to avoid subjective visual and qualitative estimation.

Claudin-1 and Claudin-7 delocalization was determined using membranous, cytoplasmic, and nuclear staining of sun-exposed normal skin, AK, BD, and SCC. Both membranous and delocalized cytoplasmic Claudin-1 was increased in BD, compared with AK, but delocalized nuclear Claudin-1 was decreased in SCC. Similarly, both membranous and cytoplasmic Claudin-7 staining was found to be

Table 1: Staining expression value of tight junction proteins and signaling pathway proteins.

Specimens	Claudin-1 Mean ± SEM	*n*	Claudin-7 Mean ± SEM	*n*	p-ERK Mean ± SEM	*n*	p-AKT Mean ± SEM	*n*	p-mTOR Mean ± SEM	*n*
NS										
Mem										
IM scores	3.19 ± 1.77		5.81 ± 1.49		—		—		—	
Cyto										
HP (%)	2.13 ± 2.69		1.63 ± 1.81		16.78 ± 8.33		4.35 ± 0.79		1.54 ± 1.49	
P (%)	11.78 ± 8.10		12.86 ± 6.15		43.50 ± 10.44		26.83 ± 0.31		13.98 ± 7.36	
LP (%)	30.07 ± 7.35		58.30 ± 3.69		37.71 ± 15.87		37.02 ± 1.56		48.81 ± 7.17	
Neg (%)	56.03 ± 15.64	14	27.36 ± 7.01	7	2.00 ± 2.43	14	31.80 ± 0.99	4	35.67 ± 13.29	11
Nuc										
HP (%)	24.99 ± 9.75		18.22 ± 7.39		44.28 ± 9.25		20.73 ± 9.52		21.47 ± 5.31	
P (%)	54.18 ± 5.31		30.91 ± 4.96		43.36 ± 4.70		36.31 ± 3.36		35.02 ± 5.00	
LP (%)	19.20 ± 7.56		33.95 ± 3.87		10.85 ± 4.61		31.17 ± 5.52		33.79 ± 4.00	
Neg (%)	1.63 ± 1.06		16.91 ± 8.44		1.50 ± 0.74		11.79 ± 6.72		9.72 ± 3.82	
AK										
Mem										
IM scores	2.25 ± 1.05		2.67 ± 1.12		—		—		—	
Cyto										
HP (%)	1.83 ± 1.81		0.75 ± 1.00		25.20 ± 15.00		2.53 ± 2.61		7.24 ± 6.42	
P (%)	12.13 ± 7.84		9.64 ± 6.02		49.75 ± 7.72		14.06 ± 4.35		34.85 ± 11.21	
LP (%)	33.11 ± 3.90		41.53 ± 6.96		23.32 ± 10.20		30.15 ± 4.35		44.88 ± 10.80	
Neg (%)	52.93 ± 11.71	9	47.97 ± 11.97	10	1.72 ± 1.09	10	53.26 ± 13.21	7	13.03 ± 7.49	10
Nuc										
HP (%)	31.14 ± 13.10		42.70 ± 10.52		47.20 ± 6.25		38.56 ± 5.45		37.72 ± 10.42	
P (%)	39.28 ± 12.1		41.68 ± 3.80		33.62 ± 4.65		37.67 ± 4.79		31.31 ± 4.05	
LP (%)	22.77 ± 12.35		13.82 ± 7.89		16.54 ± 4.23		20.86 ± 3.74		22.62 ± 5.49	
Neg (%)	6.83 ± 12.2		1.79 ± 1.85		3.66 ± 1.72		3.97 ± 2.68		8.35 ± 5.68	
BD										
Mem										
IM scores	5.19 ± 2.57		4.75 ± 3.23		—		—		—	
Cyto										
HP (%)	5.79 ± 8.40		0.97 ± 1.13		17.83 ± 11.54		3.03 ± 2.52		3.09 ± 4.06	
P (%)	19.16 ± 10.35		9.83 ± 8.52		41.46 ± 8.50		19.73 ± 12.91		25.60 ± 12.36	
LP (%)	32.16 ± 4.20		41.79 ± 14.18		36.30 ± 14.32		30.97 ± 9.17		51.33 ± 6.88	
Neg (%)	42.83 ± 15.93	14	47.54 ± 19.35	14	4.42 ± 3.01	13	46.27 ± 21.93	15	19.98 ± 13.97	14
Nuc										
HP (%)	25.37 ± 11.70		31.07 ± 11.63		38.77 ± 18.44		26.33 ± 7.72		24.72 ± 10.85	
P (%)	42.98 ± 7.11		47.35 ± 11.99		34.23 ± 7.67		42.83 ± 4.47		30.60 ± 3.56	
LP (%)	26.15 ± 11.01		18.83 ± 8.00		21.41 ± 12.67		25.75 ± 7.27		30.52 ± 6.15	
Neg (%)	5.53 ± 5.63		2.46 ± 1.68		5.60 ± 5.61		5.09 ± 3.73		14.05 ± 7.17	
SCC										
Mem										
IM scores	3.36 ± 1.67		11.46 ± 3.77		—		—		—	
Cyto		11		8		10		11		9
HP (%)	1.92 ± 2.22		1.34 ± 2.06		7.28 ± 4.68		3.90 ± 3.67		2.62 ± 2.80	

Table 1: Continued.

Specimens	Claudin-1	*n*	Claudin-7	*n*	p-ERK	*n*	p-AKT	*n*	p-mTOR	*n*
	Mean ± SEM		Mean ± SEM		Mean ± SEM		Mean ± SEM		Mean ± SEM	
P (%)	11.51 ± 8.91		16.01 ± 14.35		34.25 ± 12.91		14.94 ± 6.84		27.12 ± 11.11	
LP (%)	33.11 ± 3.90		56.48 ± 4.89		49.56 ± 8.95		29.41 ± 5.33		52.87 ± 5.58	
Neg (%)	58.83 ± 18.82		26.23 ± 13.54		8.90 ± 9.60		51.75 ± 12.73		17.39 ± 8.95	
Nuc										
HP (%)	17.69 ± 8.64		11.31 ± 12.40		24.10 ± 8.20		22.65 ± 6.97		16.69 ± 12.22	
P (%)	36.58 ± 10.1		20.54 ± 5.57		40.03 ± 6.26		42.96 ± 7.17		24.47 ± 7.22	
LP (%)	35.14 ± 9.36		33.05 ± 6.39		29.47 ± 8.26		29.79 ± 8.62		35.00 ± 6.19	
Neg (%)	10.3 ± 6.26		35.10 ± 12.59		6.39 ± 3.08		4.59 ± 2.41		23.84 ± 13.10	

NS: sun-exposed skin; AK: actinic keratosis; BD: Bowen's disease; SCC: squamous cell carcinoma; Mem: membrane; Cyto: cytoplasm; Nuc: nucleus; HP: high positive; P: positive; LP: low positive; Neg: negative.

elevated in SCC when compared to AK and BD, while its delocalized nucleus staining was reduced. Furthermore, the relationships between Claudin-1 and Claudin-7 subcellular localization and their correlation with p-ERK, p-AKT, and p-mTOR were examined to analyze their alterations in sun-exposed skin, AK, BD, and SCC.

2. Materials and Methods

2.1. Skin Samples. Sun-exposed skin (apparently normal skin, abbreviated as N) samples were obtained from patients with head-face orthopedics. According to the diagnosis by two pathologists, all AK, BD, and SCC tissue sections obtained from the head and face regions were selected and fixed with paraffin. In addition, SCC samples were obtained from skins without metastasis. There were no age and gender differences among the patients. Skin samples were obtained with the patient's written informed consent after pathological diagnosis.

2.2. Immunohistochemistry (IHC). All 4 μm thick sections were first deparaffinized and rehydrated, followed by antigen retrieval by heating in a microwave oven for 30 min. The specimens were then treated with 3% H_2O_2 for 10 min to block endogenous peroxidase activity. All slides were incubated with primary antibodies for 1 h at room temperature and then with secondary antibody (DAKO) for 30 min at room temperature to detect the antibody-antigen complex. Subsequently, the samples were stained with a chromogenic substrate, 3,3′-diaminobenzidine tetrahydrochloride (DAB substrate chromogen, DAKO), for different durations according to our preliminary tests. The primary antibodies used were the following: Anti-Claudin1 (1 : 200; ab15098, Abcam, UK), Anti-Claudin7 (1 : 500; ab27487, Abcam), Anti-p-ERK (1 : 400; 4376S, Cell Signaling Technology, USA), Anti-p-Akt (1 : 250; 66444-1-Ig, Proteintech, USA), and Anti-p-mTOR (1 : 100; 2976S, Cell Signaling Technology).

2.3. Image Acquisition. Images were captured in triplicate at ×40 magnification using a light microscope (Leica™ DM2500) with CCD (Leica DFC320) by manual exposure and white balance with identical parameters for each marker. Identical contrast and brightness conditions were applied for each antibody. All the images were saved in the TIFF format.

2.4. ImageJ Analysis. The ImmunoMembrane plugin running in ImageJ was used to establish membrane-binding proteins. Firstly, regions of interest (ROI) for each slide were visually demarcated by two pathologists. Secondly, digital image analysis (DIA) was automatically performed by defined custom cutoff values using the ImmunoMembrane (IM) score (0-20 points), depending on the membrane staining intensity and completeness, finally the *M* score for each case.

At the same time, the DIA of the cytoplasmic and nuclear expression was automatically scored using the IHC profiler plugin running in ImageJ. The ROIs were selected before the staining intensity was automatically assigned into a four-tier system (high positive, positive, low positive, and negative) for each image, all of which were in percentage form. All data was presented as the average of the triplicates for each case.

2.5. Cell Culture. Human cutaneous squamous carcinoma A431 cell line and human immortalized HaCaT keratinocytes (Institute of Biochemistry and Cell Biology, Shanghai, China) were cultured in Dulbecco's modified Eagle's medium (DMEM), supplemented with both 10% heat-inactivated Fetal Bovine Serum (FBS, Invitrogen) and 1% antibiotic-antimycotic (Invitrogen) at 37°C and 5% CO_2 in a 95% humidified incubator.

2.6. Protein Extraction and Western Blot (WB) Analysis. Nuclear and cytoplasmic proteins were isolated by Nuclear and Cytoplasmic Protein Extraction Kit (Beyotime, Haimen, China) following the manufacturer's protocols. After quantification determined by the Enhanced BCA Protein Assay Kit (Beyotime, Haimen, China), the protein samples were separated by sodium dodecyl sulphate-polyacrylamide gel electrophoresis (SDS-PAGE). Upper stacking gels (5%, 90 V) and lower separating gels (12%, 120 V) were orderly run containing 30 μg samples, which were later transferred to

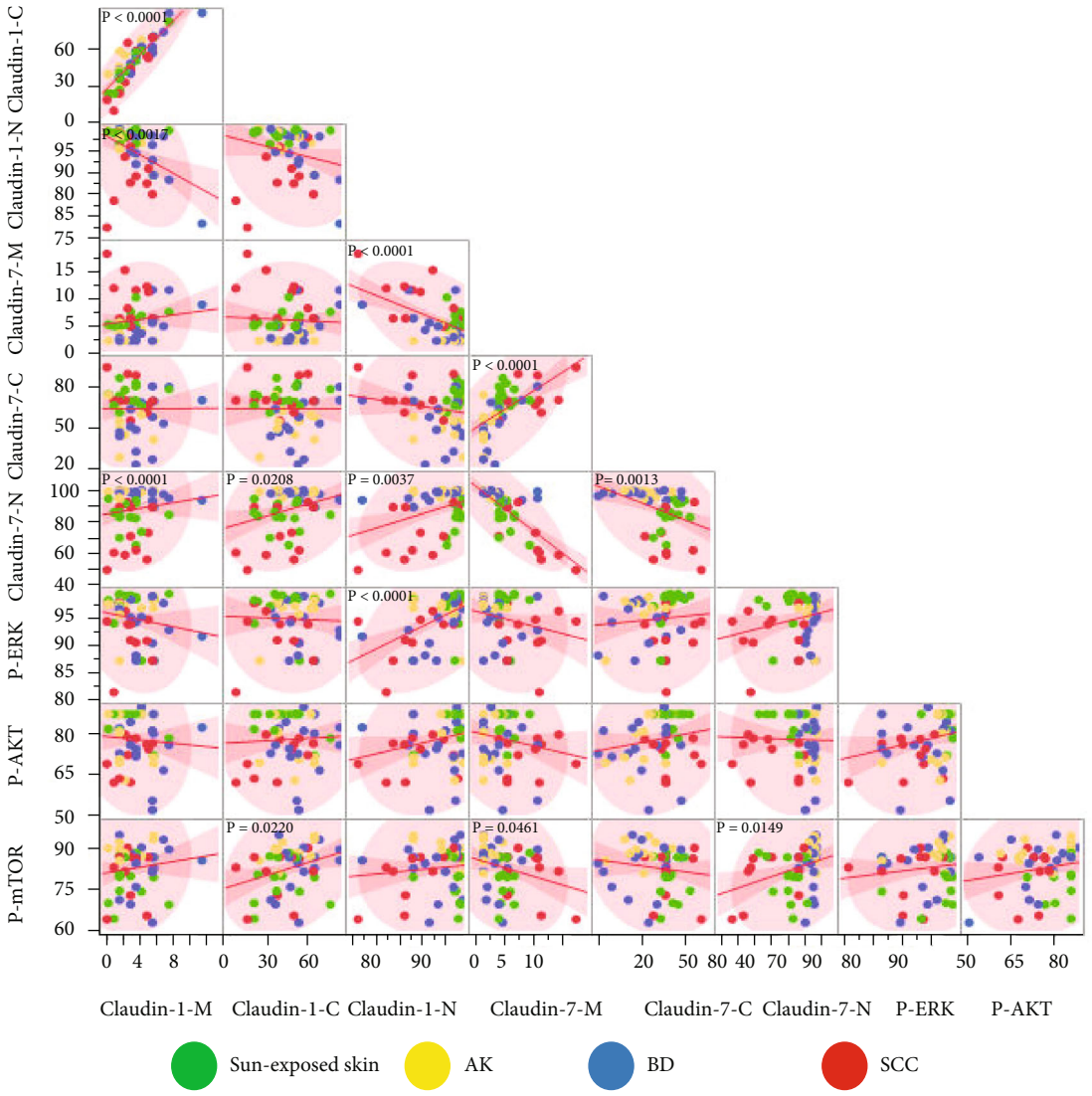

(a)

Figure 2: Continued.

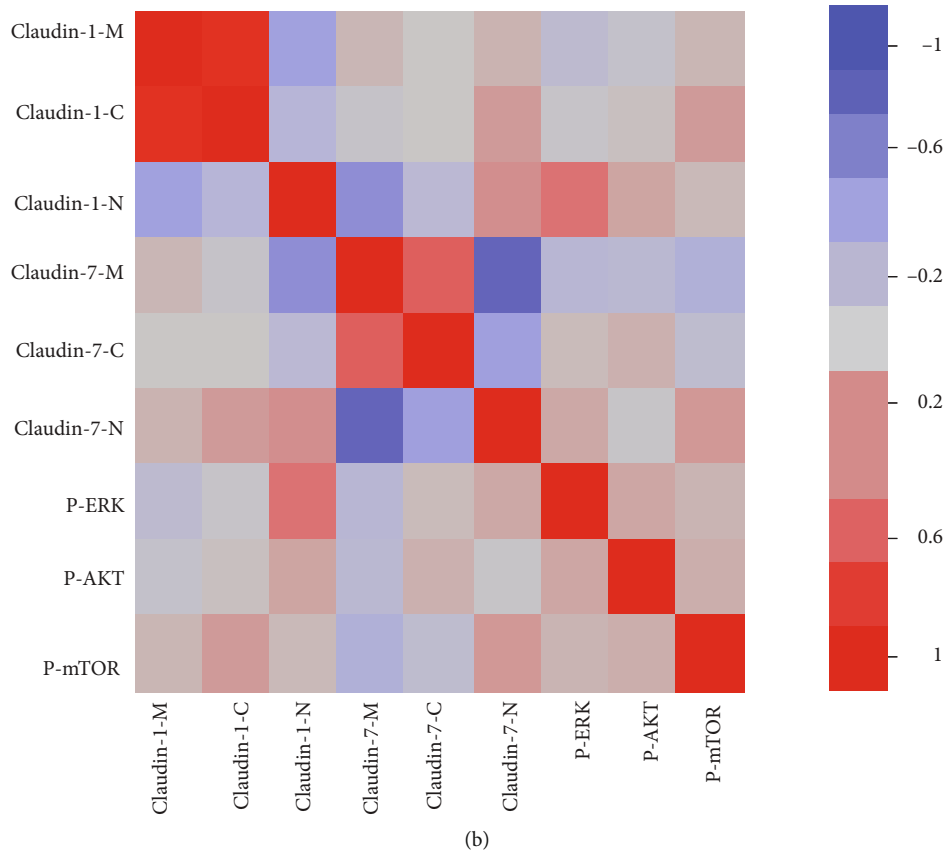

Figure 2: Data correlation analysis. (a) Scatterplot matrix indicating correlations within the entire data set (all four groups: sun-exposed skin, AK, BD, and SCC). Pairwise correlation analyses include the tight junction protein (TJPs) characteristics of membrane (Claudin-1-M, Claudin-7-M), cytoplasm (Claudin-1-C, Claudin-7-C), and nucleus (Claudin-1-N, Claudin-7-N) and signaling pathway proteins (p-ERK, p-AKT, and p-mTOR). Data about different groups is represented by different colors (sun-exposed skin, green; AK, yellow; BD, blue; SCC, red). The red line represents the pairwise linear regression slope, while the pink shaded clouds represent the 95% bivariate normal density ellipse. (b) Heatmap representation for the data set.

polyvinylidene fluoride (PVDF) microfiltration membrane by Trans-Blot® Turbo™ Transfer System (BIO-RAD, Hercules, CA, USA) under 200 mA at 1 min/kDa. After TBST containing 5% skimmed milk sealing nonspecific sites for 1 h at room temperature, the PVDF membrane was incubated overnight at 4°C with corresponding antibodies against Claudin-1, Claudin-7, and Histone (15 kDa, AF1684, Beyotime) and enhanced by chemiluminescence (ECL) substrate (BIO-RAD, Hercules, CA, USA) and then quantified by the ChemiDoc™ Touch Imaging System (BIO-RAD, Hercules, CA, USA).

2.7. Statistical Analyses. Results are presented as mean ± SEM. Statistical significance was calculated using the paired *t*-test. Multivariate analysis was performed by two-way ANOVA using GraphPad Prism 5 (GraphPad Software, La Jolla, CA, USA). Scatterplot matrices and heatmaps are displayed by pairwise Pearson correlation coefficients using JMP statistical software release 10.0 (JMP, a trademark of SAS Institute).

3. Results

3.1. Claudin-1 and Claudin-7 Displayed Altered Membrane Expression and Delocalized Subcellular Location in SCC. We first detected the expression of Claudin-1 and Claudin-7 in each tissue using IHC (Figure 1(a)) and subsequently analyzed their staining expression values by ImageJ (Table 1). Membranous Claudin-1 was upregulated in BD, relative to N and AK. Similarly, membranous Claudin-7 was significantly increased in SCC compared to BD, AK, and N (Figure 1(b)). The cytoplasmic Claudin-1 was increased in BD and N, but decreased in SCC compared to BD. Cytoplasmic Claudin-7 was obviously downregulated in AK and BD compared to N, but elevated in SCC compared to AK and BD (Figure 1(c)). Nuclear Claudin-1 was downregulated in SCC, while nuclear Claudin-7 was reduced in AK, BD, and SCC (Figure 1(d)).

3.2. p-AKT and p-mTOR (but Not p-ERK) Participate in Tumorigenesis and Infiltration in Cutaneous SCC. Intracellular staining revealed that the activation level of p-AKT was

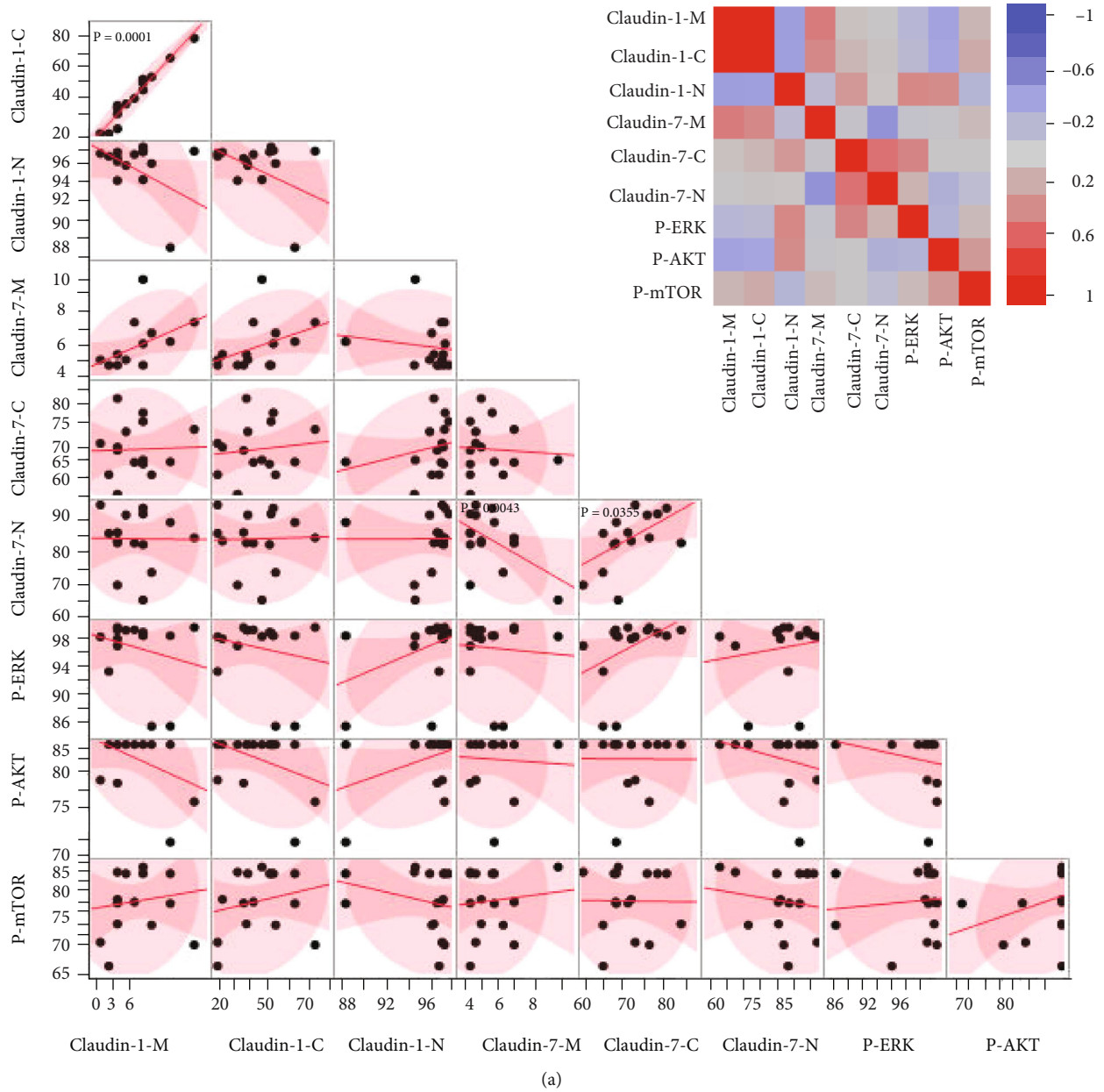

(a)

Figure 3: Continued.

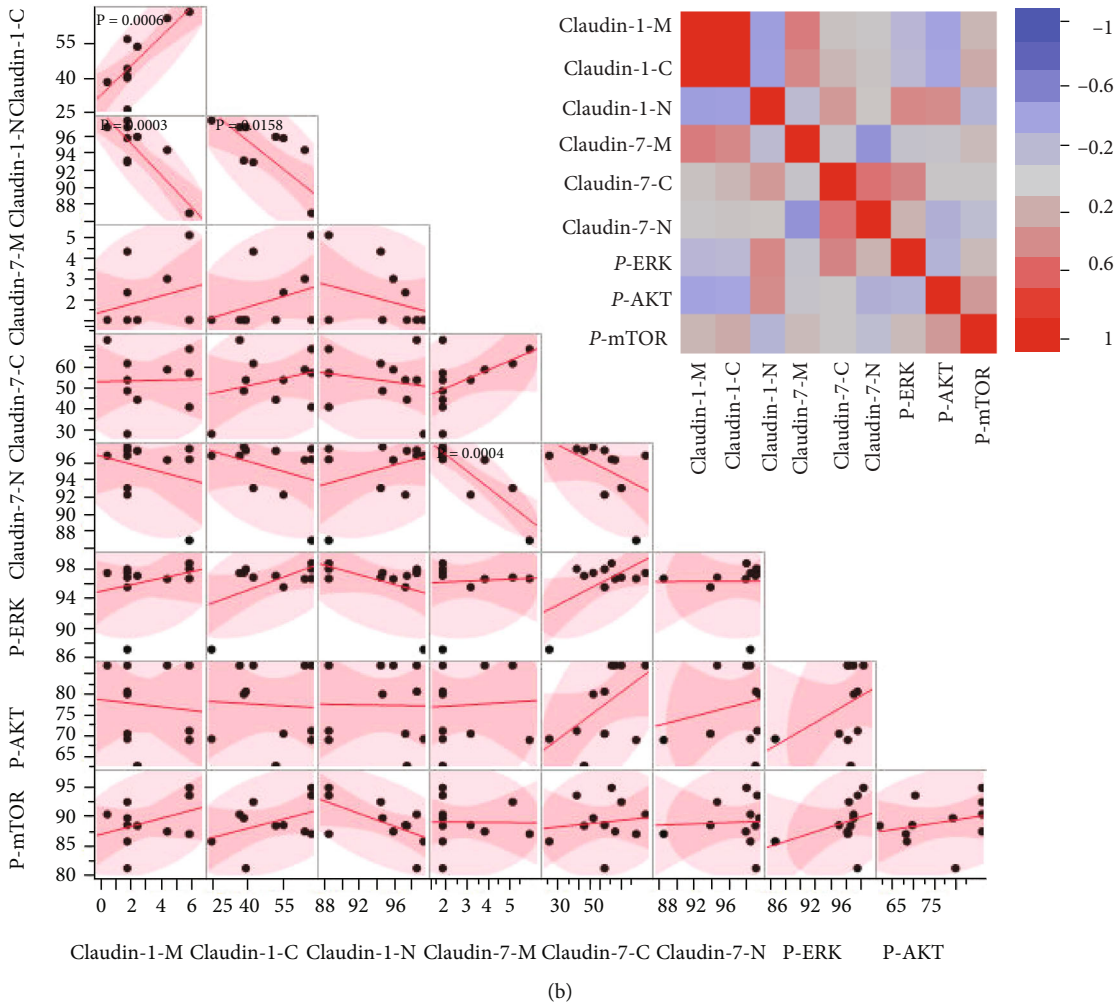

(b)

Figure 3: Continued.

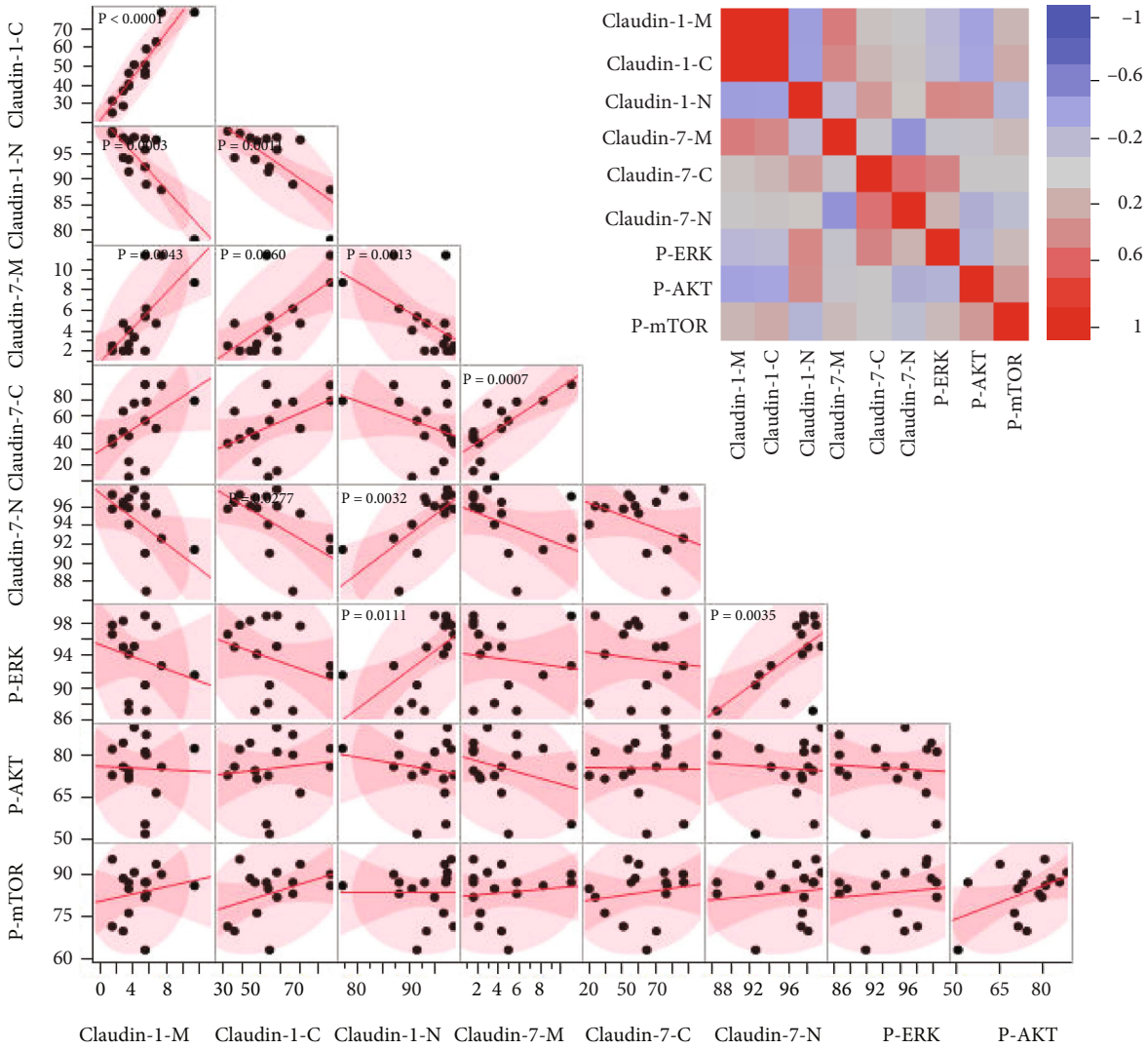

(c)

Figure 3: Continued.

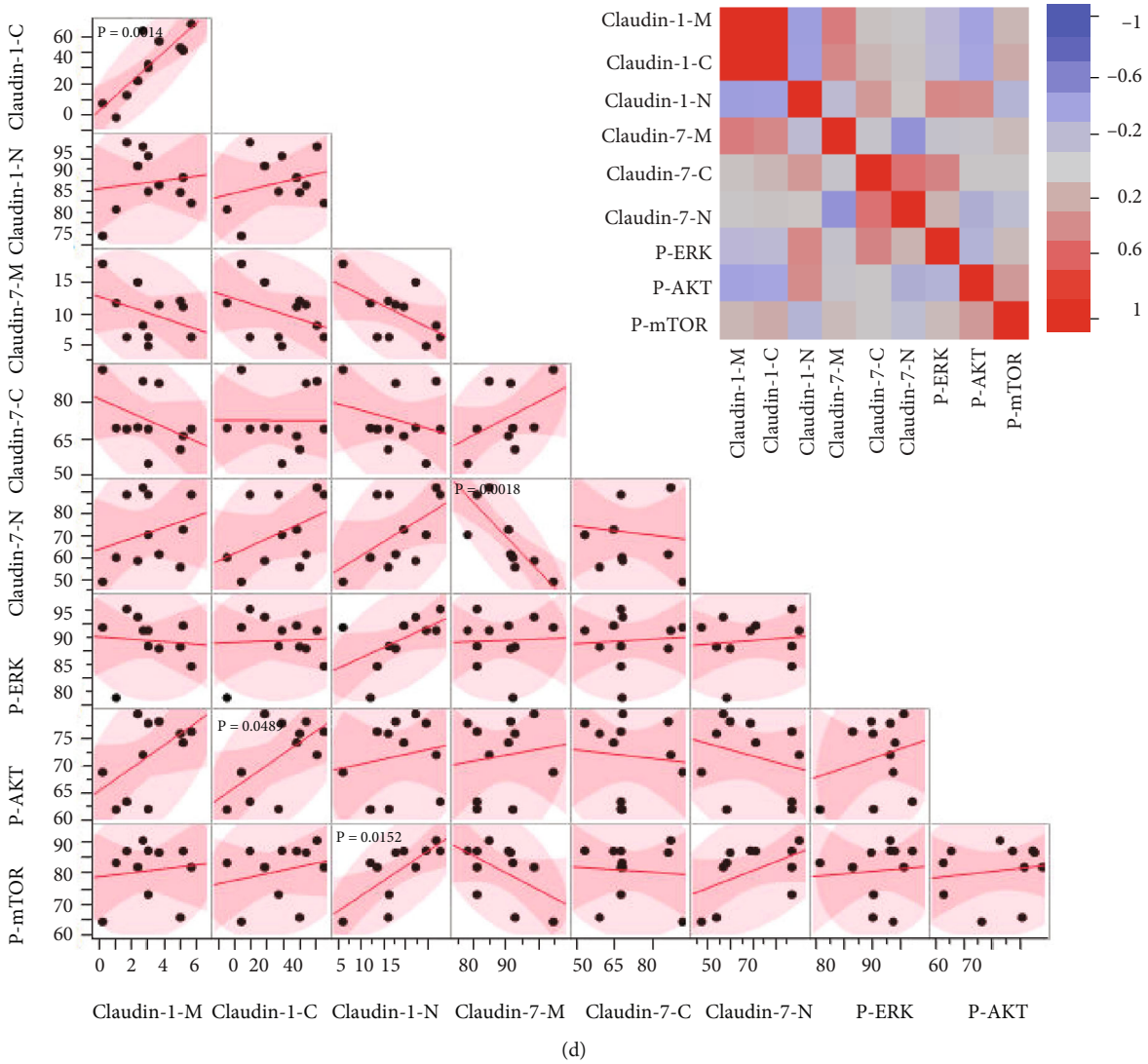

(d)

Figure 3: Data correlation analysis for different groups. The same correlation analysis as in Figure 2 for (a) sun-exposed skin, (b) AK, (c) BD, and (d) SCC.

reduced (Figure 1(f)). p-mTOR increased in AK but decreased in SCC (Figure 1(g)) while the level of activated p-ERK was not altered (Figure 1(e)). Collectively, these findings suggest that the p-AKT and p-mTOR signaling pathways closely are associated with tumorigenesis and infiltration of cutaneous SCC.

3.3. Correlations among Subcellular Claudin-1 and Claudin-7 and p-ERK, p-AKT, and p-mTOR in Different Stages of Cutaneous SCC. Pairwise correlation analyses for TJPs (localization of membrane, M; cytoplasm, C; nucleus, N), p-ERK, p-AKT, and p-mTOR in all samples are shown in Figures 2 and 3. The data (Figures 2(a) and 2(b)) showed a moderate positive correlation between Claudin-1-N and p-ERK. p-mTOR exhibited a weak positive correlation with Claudin-1-C and Claudin-7-N, but a weak negative correlation with Claudin-7-M. Claudin-1-M had a strong positive correlation with Claudin-1-C, but a moderate negative correlation with Claudin-1-N, and a weak correlation with Claudin-1-C and Claudin-1-N. Although Claudin-7-M showed a moderate positive correlation with Claudin-7-C, it was not correlated with Claudin-7-N, and there was a weak negative correlation between Claudin-7-C and Claudin-7-N. Claudin-7-N exhibited a moderate negative correlation with Claudin-1-M, but a weaker positive correlation with Claudin-1-C and Claudin-1-N. Additionally, a moderate negative correlation was found between Claudin-7-M and Claudin-1-N.

For sun-exposed skin, a strong positive correlation was observed between Claudin-1-M and Claudin-1-C. Moreover, Claudin-7-N was positively correlated with Claudin-7-M, but negatively correlated with Claudin-7-C. There was no correlation between subcellular TJPs and p-ERK, p-AKT, or p-mTOR in sun-exposed skin (Figure 3(a)). For AK skin, there was a significant negative correlation between Claudin-1-M or Claudin-1-C and Claudin-1-N, while a strong positive correlation was found between Claudin-1-M and Claudin-1-C. Similarly, Claudin-7-N was negatively

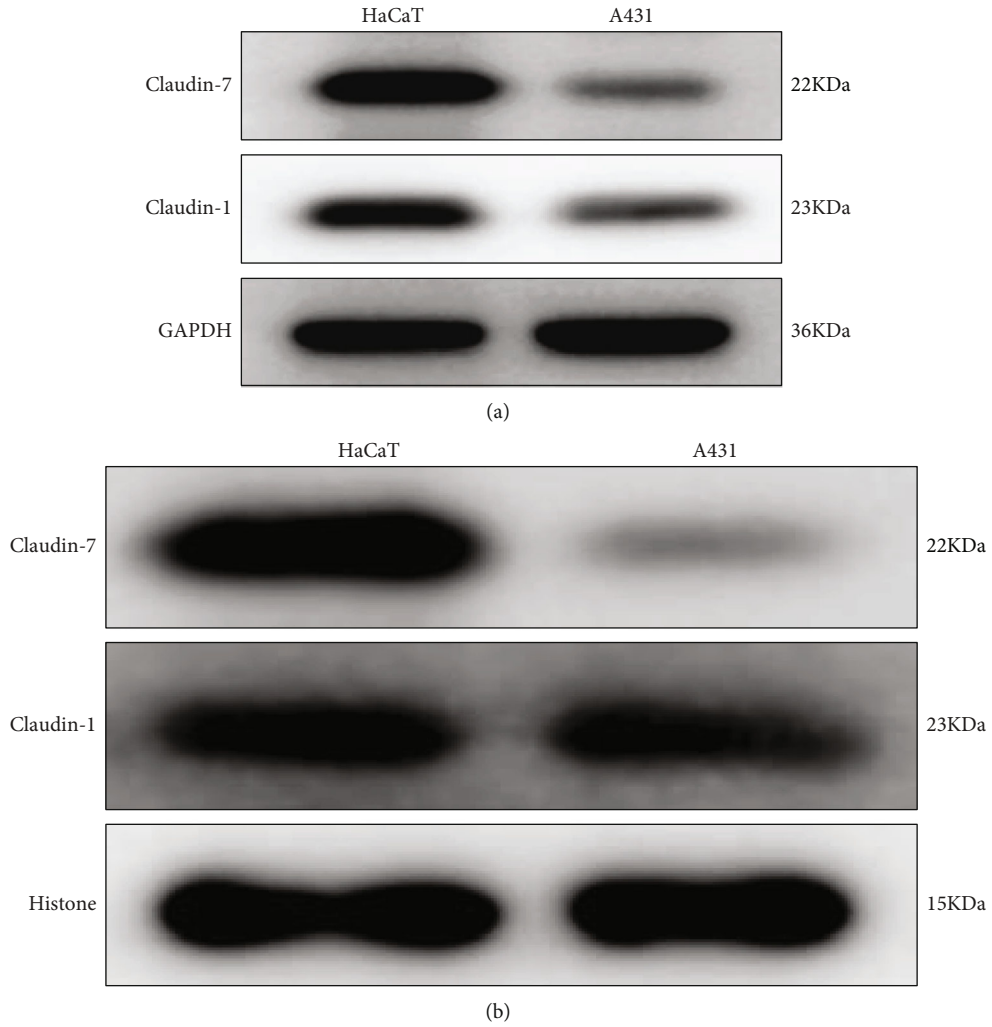

Figure 4: Delocalization of Claudin-1 and Claudin-7 in HaCaT and A431 cells as demonstrated by western blotting. (a) Expression of Claudin-1 and Claudin-7 in the cytoplasm in HaCaT and A431 cells. (b) Expression of Claudin-1 and Claudin-7 in the nucleus in HaCaT and A431 cells.

correlated with Claudin-1-M. Like in sun-exposed skin, there was no correlation between subcellular TJPs and p-ERK or p-AKT and p-mTOR in the AK group (Figure 3(b)). In the BD group, Claudin-1-C was strongly positively correlated with Claudin-1-M, while Claudin-1-N was negatively correlated with Claudin-1-M and Claudin-1-C, but positively correlated with Claudin-7-N. Meanwhile, Claudin-7-M was positively correlated with Claudin-1-M, Claudin-1-C, and Claudin-7-C, but negatively correlated with Claudin-1-N. Claudin-1-N exhibited a moderate positive correlation with Claudin-7-N. Surprisingly, there were obvious positive correlations among p-ERK, Claudin-1-N, and Claudin-7-N (Figure 3(c)). In SCC samples, there was a strong positive correlation between Claudin-1-C and Claudin-1-M and a strong negative correlation between Claudin-7-N and Claudin-7-M. Significant positive correlations were also found between p-AKT and Claudin-1-C and p-mTOR and Claudin-1-N (Figure 3(d)).

3.4. Delocalization of Claudin-1 and Claudin-7 in HaCaT and A431 Cell Lines. To further confirm the observation of Claudin-1 and Claudin-7 delocalization in cutaneous SCC and its precancerous lesions, we successively extracted cytoplasmic and nuclear proteins from both HaCaT and A431 cells by western blot analysis. As shown in Figure 4, both Claudin-1 and Claudin-7 were delocalized to the cytoplasm and nucleus of the two types of cells. Inconsistent with markedly reduced Claudin-1 and Claudin-7 delocalization to the cytoplasm (Figure 4(a)), nuclear Claudin-1 was examined with slight reduction but no significant alternation in A431 cells compared with HaCaT cells (Figure 4(b)). However, Claudin-7 remained dramatically nuclear delocalization in A431 cells relative to HaCaT cells (Figure 4(b)). Collectively, the overall reduced Claudin-1 and Claudin-7 delocalization to the cytoplasm and nucleus in A431 cells might indicate their roles in tumorigenesis.

4. Discussion

In this study, we determined the subcellular distribution of TJPs in stepwise skin malignancies, such as epithelial dysplasia (AK), CIS (BD), and cutaneous SCC, along with their

associated signaling pathway proteins, followed by support of normal HaCaT keratinocytes and cutaneous SCC A431 cells experiment *in vitro*. We found that they participated in tumorigenesis and infiltration of cutaneous SCC.

TJPs were aberrantly expressed in the subcellular skin regions with malignant lesions. Although Claudin-1 and Claudin-7 were found to have intact membranous expression in sun-exposed skin, slight cytoplasmic and strong positive nuclear immunostaining was observed. In both BD and SCC, nuclear Claudin-1 and Claudin7 were significantly low. Although they displayed no or impaired membrane-integrity, their membranous and cytoplasmic immunoexpression remained high. These findings are in contrast to those obtained from three previous reports on Claudin-1 in cutaneous SCC. Heterogeneously expressed Claudin-1 after keratinization was reported in one study [14], while another reported overexpressed Claudin-1 with focal loss of staining in poorly differentiated areas [12], but a third study showed diminished membranous Claudin-1 in AK compared to normal skin and exclusive cytoplasmic Claudin-1 expression in cutaneous SCC [13]. Several factors relating to technology, experimental settings, and patient group selection in this study might have contributed to these discrepant findings. One drawback of this study is the lack of clinical data on cutaneous SCC and precancerous cases. On the other hand, overexpressed, but actually destructive TJPs might lack membrane integrity accompanied by reduced nuclear Claudin-1 and Claudin-7 translocation in cutaneous SCC processes.

The reason for the translocation of Claudin-1 and Claudin-7 from the membrane to the cytoplasm or nucleus is not clearly known in sun-exposed skin, AK, BD, and SCC. A similar result was obtained in melanocytic lesions; Claudin-1 exhibited reduced nuclear localization but high expression in the cytoplasm in both subcutaneous and visceral metastases. However, there was no nuclear localization in lymph node metastases, indicating its metastatic potential [10]. Overexpression of Claudin-1 directly contributed to melanoma cell invasion, while Claudin-1 knockdown inhibited invasion, which further supports the findings in this study [10]. In addition, subcellular localization of Claudin-1 was reported to be deactivated by protein kinase A (PKA), but not protein kinase C (PKC), resulting in Claudin-1 nuclear sequestration, from the nucleus to the cytoplasm, although both PKA and PKC phosphorylation resulted in Claudin-1 cytoplasmic distribution [11]. Surprisingly, despite the existence of rich phosphorylated PKA, reduced nuclear Claudin-1 was inexplicable, and therefore, we hypothesize that a designated Claudin-1 threshold is required before exclusion from the nucleus [11]. Consequently, PKC-rich metastatic melanoma cells possess high nuclear Claudin-1, and PKA phosphorylation leads to the translocation of nuclear Claudin-1 to the cytoplasm [11]. Based on the above studies on melanoma, it can be concluded that delocalization of Claudin-1 and Claudin-7 is linked to carcinogenesis, invasiveness, and metastasis. Therefore, it remains to be determined whether the subcellular localization of Claudin-1 and Claudin-7 contributes to cutaneous SCC.

Contrary to these results, several studies have reported that Claudin-1 translocated from the membrane to the cytoplasm and nucleus, which was also associated with carcinogenesis, invasiveness, metastasis, and apoptosis. Claudin-1 was found to be expressed in the membrane and cytoplasm in normal thyroid tissue, although it was found to be slightly expressed in the nucleus in follicular adenoma and primary follicular thyroid carcinoma. Additionally, it was not expressed in the membrane but was highly expressed in the nucleus in metastatic follicular thyroid carcinoma [8]. Transiently transfected nuclear Claudin-1 augmented migration and invasion, and suppression of Claudin-1 by siRNA inhibited migration and invasion [8]. Claudin-1-transduced MDA-MB 361 breast tumor cell spheroids induced significant apoptosis [9]. Cytoplasmic and nuclear Claudin-1 delocalization was associated with decreased apoptosis in nasopharyngeal carcinoma cell lines [7]. Unlike the subjects selected in this study including hyperplasia, dysplasia, in situ, and invasive carcinoma, most above-mentioned findings were limited to the carcinoma group versus normal group and only presented decreased or increased cytoplasm or nuclear expression and location in the simple background of it. Since carcinogenesis is a multistep, multistage, and multifactor process, it should be analyzed in detail throughout all carcinogenic stages, rather than in isolated cancers or noncancer contexts. Consequently, the higher membranous and cytoplasmic Claudin-1 and Claudin-7 expression in SCC might mean classical membranous structure loss, dysfunctions, and even further tumorigenesis. However, reduced nuclear delocalization would indicate its propensity for carcinogenesis, invasiveness, metastasis, and apoptosis in cutaneous SCC by automatic quantification which was already applied in oral precancerous tissues and oral squamous cell carcinoma [17].

The mechanism behind subcellular localization and alternation of TJPs in cancers remains to be explored. Here, we propose the following hypotheses. Firstly, considerable attention should be given to the nutrient supply hypothesis, in which tumor cells adopt uncontrolled and unlimited access to nutrients due to increased paracellular permeability caused by TJP deficiency [18, 19]. Claudin-1-transduced 3D in breast tumor spheroid culture displayed plasma membrane homing and reduced paracellular flux, which further supports this hypothesis [9]. Interestingly, this study presents a paradoxical situation, where membranous Claudin-1 in BD and Claudin-7 in SCC were highly scored, compared to the classical membrane location, which further indicates that dysregulation of TJ dynamics is linked to carcinogenesis. Additionally, Claudin-1 is a cancer invasion/metastasis suppressor, prognostic predictor, and a potential drug [20]. Accordingly, it was speculated that Claudin-1-transduced cutaneous SCC, although its precancerous cell might show similar membrane homing, paracellular flux inhibition, and increased apoptotic capacity, implying that it could be a therapeutic strategy.

Correlations among subcellular Claudin-1, Claudin-7, p-ERK, p-AKT, and p-mTOR were analyzed at different stages of cutaneous SCC. Subcellular distribution of Claudin-1 and Claudin-7 was correlated with the progress of cutaneous

SCC, possibly indicating that altered membrane expression contributes to their mislocalization and potential Claudin-Claudin interaction. These possibilities need to be explored further [21, 22]. Additionally, it was observed that p-ERK correlated with Claudin-1-N and Claudin-7-N in BD, which might explain why p-ERK participates in Claudin-1 and Claudin-7 nuclear delocalization as well as in carcinogenesis. Moreover, p-AKT was positively correlated with Claudin-1-C, while p-mTOR was correlated with Claudin-1-N in cutaneous SCC, which points to their role in carcinogenesis.

5. Conclusion

In conclusion, the results presented here indicate that the subcellular localization of Claudin-1 and Claudin-7 and the correlations between them, and with PI-3K/AKT and MEK/ERK signaling pathways, play roles in cutaneous SCC tumorigenesis. The mechanism behind the TJPs delocalization and its associated signaling pathways in cutaneous SCC tumorigenesis, infiltration, and metastases requires further research.

Data Availability

The data used to support the findings of this study are included within the article. Further inquiries can be directed to the corresponding author.

Conflicts of Interest

The authors declare no conflict of interest.

Acknowledgments

This study was supported by the National Natural Science Foundation of China (No. 81972931).

References

[1] K. A. Burton, K. A. Ashack, and A. Khachemoune, "Cutaneous squamous cell carcinoma: a review of high-risk and metastatic disease," *American Journal of Clinical Dermatology*, vol. 17, no. 5, pp. 491–508, 2016.

[2] C. Hafner, M. Landthaler, and T. Vogt, "Activation of the PI3K/AKT signalling pathway in non-melanoma skin cancer is not mediated by oncogenic PIK3CA and AKT1 hotspot mutations," *Experimental Dermatology*, vol. 19, no. 8, pp. e222–e227, 2010.

[3] L. Rittié, S. Kansra, S. W. Stoll et al., "Differential ErbB1 signaling in squamous cell versus basal cell carcinoma of the skin," *The American Journal of Pathology*, vol. 170, no. 6, pp. 2089–2099, 2007.

[4] N. Lin, Y. Moroi, H. Uchi et al., "Significance of the expression of phosphorylated-STAT3, -Akt, and -ERK1/2 in several tumors of the epidermis," *Journal of Dermatological Science*, vol. 48, no. 1, pp. 71–73, 2007.

[5] Y. Zou, M. Ge, and X. Wang, "Targeting PI3K-AKT-mTOR by LY3023414 inhibits human skin squamous cell carcinoma cell growth _in vitro_ and _in vivo_," *Biochemical and Biophysical Research Communications*, vol. 490, no. 2, pp. 385–392, 2017.

[6] P. Dhawan, A. B. Singh, N. G. Deane et al., "Claudin-1 regulates cellular transformation and metastatic behavior in colon cancer," *The Journal of Clinical Investigation*, vol. 115, no. 7, pp. 1765–1776, 2005.

[7] J. W. Lee, W. T. Hsiao, H. Y. Chen et al., "Upregulated claudin-1 expression confers resistance to cell death of nasopharyngeal carcinoma cells," *International Journal of Cancer*, vol. 126, no. 6, pp. 1353–1366, 2010.

[8] D. Zwanziger, J. Badziong, S. Ting et al., "The impact of CLAUDIN-1 on follicular thyroid carcinoma aggressiveness," *Endocrine-Related Cancer*, vol. 22, no. 5, pp. 819–830, 2015.

[9] T. Hoevel, R. Macek, K. Swisshelm, and M. Kubbies, "Reexpression of the TJ protein CLDN1 induces apoptosis in breast tumor spheroids," *International Journal of Cancer*, vol. 108, no. 3, pp. 374–383, 2004.

[10] P. D. Leotlela, M. S. Wade, P. H. Duray et al., "Claudin-1 overexpression in melanoma is regulated by PKC and contributes to melanoma cell motility," *Oncogene*, vol. 26, no. 26, pp. 3846–3856, 2007.

[11] A. D. French, J. L. Fiori, T. C. Camilli et al., "PKC and PKA phosphorylation affect the subcellular localization of claudin-1 in melanoma cells," *International Journal of Medical Sciences*, vol. 6, no. 2, pp. 93–101, 2009.

[12] A. Ouban, H. Hamdan, A. Hakam, and A. A. Ahmed, "Claudin-1 expression in squamous cell carcinomas of different organs: comparative study of cancerous tissues and normal controls," *International Journal of Surgical Pathology*, vol. 20, no. 2, pp. 132–138, 2012.

[13] H. R. Hintsala, M. Siponen, K. M. Haapasaari, P. Karihtala, and Y. Soini, "Claudins 1, 2, 3, 4, 5 and 7 in solar keratosis and squamocellular carcinoma of the skin," *International Journal of Clinical and Experimental Pathology*, vol. 6, no. 12, pp. 2855–2863, 2013.

[14] K. Morita, S. Tsukita, and Y. Miyachi, "Tight junction-associated proteins (occludin, ZO-1, claudin-1, claudin-4) in squamous cell carcinoma and Bowen's disease," *The British Journal of Dermatology*, vol. 151, no. 2, pp. 328–334, 2004.

[15] H. O. Helin, V. J. Tuominen, O. Ylinen, H. J. Helin, and J. Isola, "Free digital image analysis software helps to resolve equivocal scores in HER2 immunohistochemistry," *Virchows Archiv*, vol. 468, no. 2, pp. 191–198, 2016.

[16] F. Varghese, A. B. Bukhari, R. Malhotra, and A. De, "IHC Profiler: an open source plugin for the quantitative evaluation and automated scoring of immunohistochemistry images of human tissue samples," *PLoS One*, vol. 9, no. 5, article e96801, 2014.

[17] D. R. Mane, A. D. Kale, and C. Belaldavar, "Validation of immunoexpression of tenascin-C in oral precancerous and cancerous tissues using ImageJ analysis with novel immunohistochemistry profiler plugin: an immunohistochemical quantitative analysis," *J Oral Maxillofac Pathol*, vol. 21, no. 2, pp. 211–217, 2017.

[18] J. M. Mullin, "Potential interplay between luminal growth factors and increased tight junction permeability in epithelial carcinogenesis," *The Journal of Experimental Zoology*, vol. 279, no. 5, pp. 484–489, 1997.

[19] J. M. Mullin, K. V. Laughlin, N. Ginanni, C. W. Marano, H. M. Clarke, and A. Peralta Soler, "Increased tight junction permeability can result from protein kinase C activation/translocation and act as a tumor promotional event in epithelial cancers," *Annals of the New York Academy of Sciences*, vol. 915, no. 1, pp. 231–236, 2000.

[20] Y. C. Chao, S. H. Pan, S. C. Yang et al., "Claudin-1 is a metastasis suppressor and correlates with clinical outcome in lung adenocarcinoma," *American Journal of Respiratory and Critical Care Medicine*, vol. 179, no. 2, pp. 123–133, 2009.

[21] J. Piorntek, L. Winkler, H. Wolburg et al., "Formation of tight junction: determinants of homophilic interaction between classic claudins," *The FASEB Journal*, vol. 22, no. 1, pp. 146–158, 2008.

[22] T. Inai, "The coculture method to examine interactions between claudin isoforms in tight junction-free HEK293 cells and tight junction-bearing MDCK II cells," *Methods in Molecular Biology*, vol. 762, pp. 101–114, 2011.

Hindawi
Journal of Oncology
Volume 2022, Article ID 2800488, 12 pages
https://doi.org/10.1155/2022/2800488

Research Article

The PARP1 Inhibitor Niraparib Represses DNA Damage Repair and Synergizes with Temozolomide for Antimyeloma Effects

Hong-Yuan Shen,[1] **Hai-Long Tang**,[1] **Yan-Hua Zheng**,[1] **Juan Feng**,[1] **Bao-Xia Dong**,[1] **and Xie-Qun Chen**[1,2,3]

[1]*Department of Hematology, Xijing Hospital, Air Force Medical University, Xi'an, 710032 Shaanxi, China*
[2]*Institute of Hematology, Northwest University, Xi'an, 710069 Shaanxi, China*
[3]*Department of Hematology, Affiliated Hospital, Northwest University, Xi'an, 710082 Shaanxi, China*

Correspondence should be addressed to Bao-Xia Dong; freshupdbx@hotmail.com and Xie-Qun Chen; xiequnchen@fmmu.edu.cn

Received 17 January 2022; Revised 15 February 2022; Accepted 9 March 2022; Published 5 April 2022

Academic Editor: Guo Chen

Purpose. Poly(ADP-ribose) polymerase 1 (PARP1) is necessary for single-strand break (SSB) repair by sensing DNA breaks and facilitating DNA repair through poly ADP-ribosylation of several DNA-binding and repair proteins. Inhibition of PARP1 results in collapsed DNA replication fork and double-strand breaks (DSBs). Accumulation of DSBs goes beyond the capacity of DNA repair response, ultimately resulting in cell death. This work is aimed at assessing the synergistic effects of the DNA-damaging agent temozolomide (TMZ) and the PARP inhibitor niraparib (Nira) in human multiple myeloma (MM) cells. *Materials and Methods*. MM RPMI8226 and NCI-H929 cells were administered TMZ and/or Nira for 48 hours. CCK-8 was utilized for cell viability assessment. Cell proliferation and apoptosis were detected flow-cytometrically. Immunofluorescence was performed for detecting γH2A.X expression. Soft-agar colony formation assay was applied to evaluate the antiproliferative effect. The amounts of related proteins were obtained by immunoblot. The combination index was calculated with the CompuSyn software. A human plasmacytoma xenograft model was established to assess the anti-MM effects *in vivo*. The anti-MM activities of TMZ and/or Nira were evaluated by H&E staining, IHC, and the TUNEL assay. *Results*. The results demonstrated that cotreatment with TMZ and Nira promoted DNA damage, cell cycle arrest, and apoptotic death in cultured cells but also reduced MM xenograft growth in nude mice, yielding highly synergistic effects. Immunoblot revealed that TMZ and Nira cotreatment markedly increased the expression of p-ATM, p-CHK2, RAD51, and γH2A.X, indicating the suppression of DNA damage response (DDR) and elevated DSB accumulation. *Conclusion*. Inhibition of PARP1 sensitizes genotoxic agents and represents an important therapeutic approach for MM. These findings provide preliminary evidence for combining PARP1 inhibitors with TMZ for MM treatment.

1. Introduction

Multiple myeloma (MM) represents a hematologic cancer caused by clonal plasma cell growth in the bone marrow [1]. Combination of proteasome inhibitor and immunomodulatory drug and myeloablative high-dose treatment plus autologous stem cell transplantation (ASCT) is efficient therapeutic approach for MM [2, 3]. However, almost all MM patients eventually develop refractory disease and relapse. To date, MM remains an incurable disease, and new treatment approaches are urgently required for improving patient outcome. MM features common chromosomal instability and deranged DNA repair [4, 5]. Cells can initiate multiple DNA repair mechanisms to cope with genotoxic stress such as nucleobase adduct removal and single- (SSB) and/or double-strand DNA break (DSB) repair. Suppressing DNA repair is considered a reasonable sensitization strategy to improve genotoxic therapy [6].

PARP1 represents an important component of the base excision repair (BER) of SSBs [6]. PARP1 suppression promotes SSB accumulation and PARP1-DNA interactions. Insufficient SSB repair results in DSBs during DNA

replication, and PARP1 trapping inhibits replication fork generation [7]. Inhibition of PARP1 alters DNA repair, indicating PARP1 suppressors could enhance the cytotoxicity of drugs. Mounting evidence suggests PARP1 suppressors enhance the antitumor properties of alkylating agents such as cisplatin, oxaliplatin, cyclophosphamide, and temozolomide [8–10]. Temozolomide (TMZ) is an alkylating product employed in glioma and leukemia treatment. TMZ damages the DNA via methyl adduct addition to N^7 guanine (70% of all adducts), N^3 adenine (9%), and O^6 guanine (5%) [11]. TMZ causes SSBs, cell cycle arrest, and apoptotic death [12]. However, the doses applied for TMZ monotherapy are usually high enough to cause intolerable toxicity to normal cells. Thus, a combination strategy based on synergistic effects may be a better approach to counter tumor progression and reduce toxicity, ultimately improving disease prognosis. PARP inhibitors have been examined in multiple tumors, e.g., small-cell lung cancer, non-small-cell lung cancer, lymphoma, pancreatic cancer, ovarian cancer, breast cancer, prostate cancer, and Ewing's sarcoma, and improve TMZ's anticancer activities *in vitro* and in xenograft models [13–16]. However, in the field of MM therapy, combination of TMZ and PARP inhibitors has not been previously reported.

Here, TMZ and the PARP inhibitor niraparib were examined for synergism. We hypothesized that TMZ could cause SSBs in MM cells, resulting in SSB buildup and DNA replication fork collapse as well as the generation of lethal DSBs in combination with PARP1 inhibitors. The results provide evidence PARP inhibition has little effects when used as a single agent on MM cells but could remarkably enhance TMZ cytotoxicity both in cultured cells and in mice.

2. Materials and Methods

2.1. Cell Lines. Human MM RPMI8226 and NCI-H929 cells, provided by the American Type Culture Collection (ATCC), underwent culture in RPMI 1640 (Gibco) containing 10% fetal bovine serum (FBS; Sigma) and 1% penicillin/streptomycin (Hyclone) at 37°C in a humid atmosphere with 5% CO_2.

2.2. Drugs and Chemicals. TMZ (MedChemExpress), Nira (MK4827; MedChemExpress), and niraparib hydrochloride (MK4827 hydrochloride; MedChemExpress) were maintained dissolved in dimethyl sulfoxide (DMSO). DMSO level was always below 5% in all treatments. Antibodies against-gamma H2A.X (phospho S139) (γH2A.X) (ab81299), ATM (ab32420), ATM (phospho S1981, ab81292), RAD51 (ab133534), cyclin D1 (ab134175), CHK2 (ab109413), CHK2 (phospho T68, ab32148), and GAPDH (ab128915) were obtained from Abcam; antibodies targeting cleaved caspase-3 (9664S) and anti-rabbit HRP secondary antibodies (7074) were provided by Cell Signaling Technology.

2.3. Cell Viability Assay. A total of 2×10^4 indicated MM cells underwent seeding into a 96-well plate and culture for 4 h, followed by the administration of different doses of TMZ and/or Nira for 48 h. After drug exposure for a specific time, cell viability was examined with Cell Counting Kit-8 (CCK8, China). After exposure for 48 h with the drugs, adding 20 μL of CCK-8 solution to each well, the absorbance at 450 nm with a microplate reader was recorded after incubation for 2 h. CCK-8 kit uses a water-soluble tetrazolium salt to quantify the number of live cells by producing an orange formazan dye. The amount of formazan produced is directly proportional to the number of living cells.

2.4. Cell Apoptosis Analysis. RPMI8226 and NCI-H929 underwent seeding in a 6-well plate at 2.0×10^5/well. Cells were treated for 48 h with DMSO, 30 μM TMZ (RPMI8226), 20 μM TMZ (NCI-H929), and 3 μM Nira, respectively, for both cell lines, or combined 3 μM Nira and 30 μM (RPMI8226) or 20 μM (NCI-H929) TMZ for 48 h. The Annexin V/propidium iodide (PI) detection kit (BD Pharmingen™) was utilized for apoptosis quantitation. In brief, after treatment with specific drugs for 48 h, the cells underwent incubation, shielded from light at ambient, with Annexin V/FITC and PI for 15 min. Analysis was performed flow-cytometrically with an Epics flow cytometer. After treatment for 48 h with the drugs, adding 5 μL Annexin V and 15 μL PI for each sample, and incubation in the dark for 15 min, apoptosis analysis was performed by flow cytometer. Cells that were Annexin V/FITC positive (with translocation of membrane phospholipid phosphatidylserine (ps) from the inner to the outer leaflet of the plasma membrane) and PI negative (with intact cellular membrane excluding PI) were regarded as early apoptotic cells, whereas positivity for both Annexin V/FITC and PI was considered as late apoptotic or necrotic cells.

2.5. EdU Assay. An EdU Staining Proliferation Kit (iFluor 647) (Abcam, ab222421) was utilized in these assays. After drug treatment, the culture medium was supplemented with 20 μM EdU staining solution and incubated for 2 h at 37°C. This was followed by 4% formalin fixation. An Epics flow cytometer was utilized for analysis. After exposure for 48 h with the drugs, cells were incubated with 20 μM EdU (Abcam, ab222421) for 2 h, followed by fixation, permeabilization, and EdU staining according to the manufacturer's instructions; the EdU-positive cells were determined using flow cytometer.

2.6. Soft-Agar Clonogenic Assay. Actively growing cells underwent counting and resuspension in 0.3% agar in RPMI 1640 (maintained liquid at 41°C) containing 10% FCS and specific drugs. This was followed by plating on 0.5% agar in a 24-well plate (1×10^4/well) and incubation under standard conditions for 14–21 days. Colonies in each well underwent 0.5% crystal violet staining. Colony counting was performed under an inverted microscope (Leica, Germany).

2.7. Immunofluorescence. RPMI8226 and NCI-H929 cells were incubated with specific drugs at 37°C for 48 h in four groups (DMSO, TMZ, Nira, and TMZ plus Nira). After treatment, cells were harvested, washed, and dropped on adhesive slides. This was followed by fixation with 4% formalin for 15 min and permeabilization and blocking using PBS with 0.4% Triton X-100 and 2% BSA in PBS,

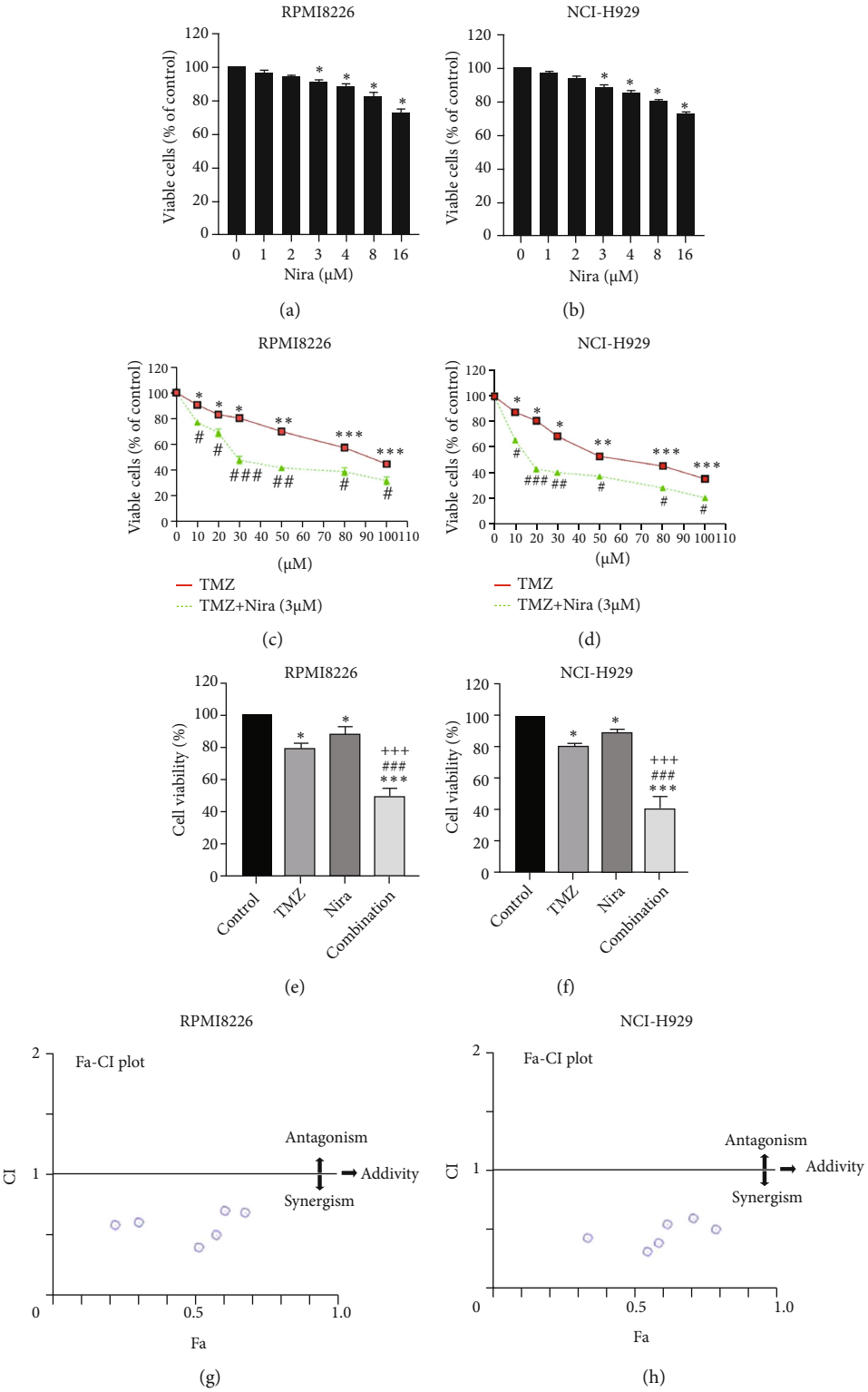

Figure 1: Nira induces synergistic cytotoxicity with TMZ in MM cell lines. (a) RPMI8226 and (b) NCI-H929 cells were exposed to increased Nira amounts for 48 h, before CCK-8 assay analysis of cell viability. (c) D MM cells were incubated for 48 h with increasing doses of TMZ and Nira (3 μM), either alone or in combination, followed by the CCK-8 assay. (e, f) MM cells were administered TMZ and/or Nira for 48 h (RPMI8226 cells, 30 μM and 3 μM, respectively, and NCI-H929 cells, 20 μM and 3 μM, respectively), followed by the CCK-8 assay. (g, h) Fa–CI plots according to the Chou–Talalay equation, generated by CompuSyn v1.0. Round symbol indicates CI (combination index) for a given Fa (fraction affected) at each dose. $^{*}P < 0.05$, $^{**}P < 0.01$, and $^{***}P < 0.001$ versus control group; $^{\#}P < 0.05$, $^{\#\#}P < 0.01$, and $^{\#\#\#}P < 0.001$ versus TMZ group; $^{+++}P < 0.001$ versus Nira group. TMZ: temozolomide; Nira: niraparib.

Table 1: Combination index data for TMZ and Nira in RPMI8226 cells.

Dose TMZ (μM)	Dose Nira (μM)	Combination effect*	CI value
10	3	0.23	0.56554
20	3	0.31	0.58787
30	3	0.52	0.38529
50	3	0.58	0.49207
80	3	0.61	0.6861
100	3	0.68	0.67125

Notes: Combination index (CI) values for TMZ and Nira were based on the Chou–Talalay's method at 48 h. CI < 1, CI = 1, and CI > 1 reflect synergistic, additive, and antagonistic effects, respectively. Independent experiments were performed thrice. *Mean value of three replicates. In each condition, standard deviation is less than 10%. Abbreviations: TMZ: temozolomide; Nira: niraparib.

Table 2: Combination index data for TMZ and Nira in NCI-H929 cells.

Dose TMZ (μM)	Dose Nira (μM)	Combination effect*	CI value
10	3	0.34	0.42312
20	3	0.55	0.3069
30	3	0.59	0.37772
50	3	0.62	0.54191
80	3	0.71	0.58941
100	3	0.79	0.49808

Notes: Combination index (CI) values for TMZ and Nira were based on the Chou–Talalay's method at 48 h. CI < 1, CI = 1, and CI > 1 reflect synergistic, additive, and antagonistic effects, respectively. Independent experiments were performed thrice. *Mean value of three replicates. In each condition, standard deviation is less than 10%. Abbreviations: TMZ: temozolomide; Nira: niraparib.

respectively. Next, successive incubations with rabbit monoclonal anti-γH2A.X antibodies (Abcam, 1 : 200) and Cy3-linked goat anti-rabbit secondary antibodies were followed by DAPI counterstaining. Cells with >10 nuclear foci were assessed for percentage, among at least 100 cells counted in total.

2.8. Immunoblot. After treatment, the RIPA buffer containing protease inhibitors (Thermo Fisher) was utilized for cell lysis. A BCA assay kit (Beyotime) was used for protein quantitation. Proteins underwent separation by 10-12% SDS-PAGE and electrotransfer onto PVDF (polyvinylidene difluoride) membranes (Millipore), which were blocked with 5% skimmed milk in 1× TBST. This was followed by successive incubations with primary and HRP-linked secondary antibodies (CST). SuperSignal reagent (Millipore) was used for visualizing immunoreactive bands.

2.9. In Vivo Xenograft Mouse Model. All procedures were carried out following the Guide for the Care and Use of Laboratory Animals by the US National Institutes of Health. The study had approval from the Animal Ethics Committee of Xijing Hospital, Air Force Military Medical University. Briefly, 4–6-week-old female BALB/c nude mice (16–20 g, Charles River Laboratories) underwent subcutaneous inoculation of 1.0×10^7 RPMI8226 cells in 150 μl 50% Matrigel (Corning) in serum-free RPMI 1640. About 7-10 days post-cell injection, with tumors measuring about 100 mm^3, the animals were randomly assigned to 4 groups (each $N = 5$): control group (saline containing 50% PEG300, intraperitoneally (i.p.) administered 5 days/week), TMZ (30 mg/kg injected i.p. 5 days/week), Nira hydrochloride (20 mg/kg administered i.p. 5 days/week), and the TMZ and Nira combination group. A Vernier caliper was utilized to measure the tumors' long- (a) and short- (b) axis diameters for 21 days at 3-day interval. Tumor volume was derived as $V = 0.5a \times b^2$. The mouse weight was also recorded by an electronic balance. At study end, euthanasia was carried out with humane methods. The xenografts were histologically analyzed.

2.10. Immunohistochemical Staining and TUNEL Assay. Tumor xenograft tissue samples underwent fixation with formalin, paraffin embedding, and sectioning at 5 μm. The sections underwent deparaffinization and rehydration with graded alcohol dilutions for immunohistochemistry. After sequential incubation with primary (overnight at 4°C) and secondary (37°C for 30 min) antibodies, the specimens underwent treatment with streptavidin-HRP. The DAB kit was utilized for visualization. Anti-Ki67 (Abcam, 1 : 200), anti-cleaved caspase-3 (1 : 200, CST), anti-RAD51 (Abcam, 1 : 200), and anti-γH2A.X (Abcam, 1 : 200) primary antibodies were utilized. For histological analysis, specimens were examined after hematoxylin and eosin (H&E) staining to identify morphological changes. Tissue specimens were examined using a light microscope (Zeiss, Germany). Furthermore, detection of in situ apoptosis was carried out by TUNEL assay with the In Situ Cell Death Detection Kit, POD (Roche, USA) as directed by the manufacturer.

2.11. Drug Synergy and Combination Index. The CompuSyn software was utilized for combination index assessment [17], with CI < 1, CI = 1, and CI > 1 indicating synergistic, additive, and antagonistic effects, respectively.

2.12. Statistical Analysis. Data analysis utilized GraphPad Prism v8.0 (San Diego, CA). One-way analysis of variance was performed with Statistical Package for Social Sciences (SPSS) v22.0. All assays were performed thrice, and data are mean ± standard deviation (SD).

3. Results

3.1. Nira Enhances the Toxicity of TMZ in MM Cell Lines. For treatment of ovarian cancer, the recommended dose of niraparib is 300 mg per day for 21 days every 28-day cycle, with plasma C max approximating 2 μM following the initial treatment and rising to 3.5~4.2 μM at day 21 [18]. We first tested whether the PARP inhibitor Nira monotherapy could elicit direct cytotoxicity on MM cells *in vitro*. At physiological concentrations (≤3.5 μM), Nira caused no significant cytotoxicity in RPMI8226 and NCI-H929 cells, as depicted in Figures 1(a) and 1(b). Next, the effects of fixed low-dose

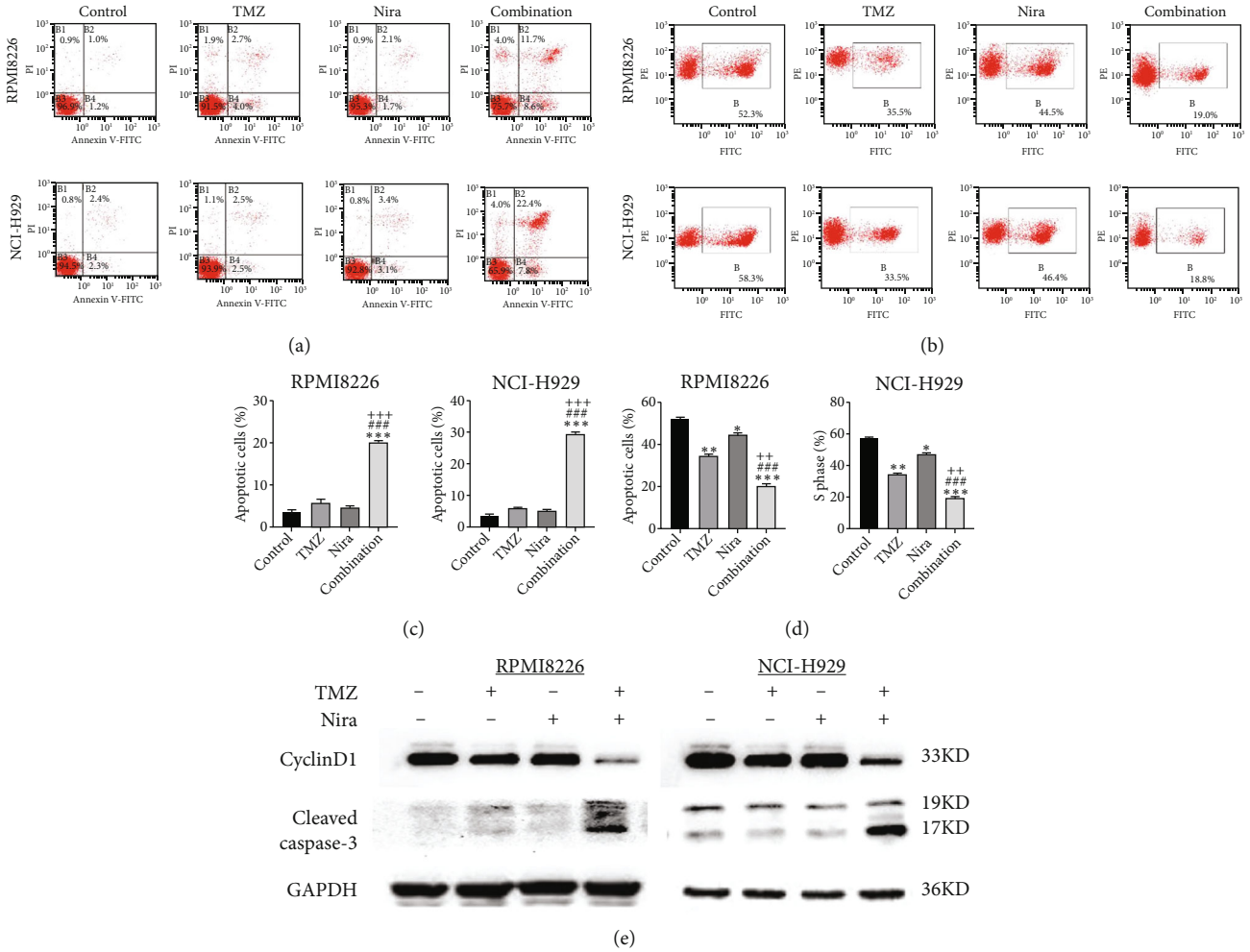

Figure 2: Effects of TMZ and/or Nira on proliferation and apoptotic death in MM cells. (a) RPMI8226 and NCI-H929 cells were administered TMZ and/or Nira for 48 h, and apoptosis was examined flow-cytometrically after Annexin V–FITC/PI staining. (b) RPMI8226 and NCI-H929 cells were administered TMZ and/or Nira for 48 h, and S-phase cells were detected flow-cytometrically by the EdU assay. (c, d) Quantification of apoptotic and S-phase cells shown in (a). (e) Cell cycle-related and apoptosis-associated proteins in RPMI8226 and NCI-H929 cells were quantitated by immunoblot. $^{*}P < 0.05$, $^{**}P < 0.01$, and $^{***}P < 0.001$ versus control group; $^{\#\#}P < 0.01$ and $^{\#\#\#}P < 0.001$ versus TMZ group; $^{++}P < 0.01$ and $^{+++}P < 0.001$ versus Nira group. TMZ: temozolomide; Nira, niraparib.

concentrations of Nira combined with TMZ on the viability of MM cells were examined with CCK-8. Upon 48 h of incubation, TMZ monotherapy markedly suppressed viability in MM cells in comparison with control cells, concentration-dependently (Figures 1(c) and 1(d)). We used the physiological concentration of Nira at 3 μM for subsequent experiments. When cells were cotreated with a fixed dose of Nira and different doses of TMZ, as depicted in Figures 1(c) and 1(d), the IC_{50} of TMZ in RPMI8226 cells was significantly reduced from 85 μM to 30 μM; the IC_{50} of TMZ in NCI-H929 cells declined from 65 μM to 20 μM. Combination of Nira and TMZ showed very good therapeutic potential for MM cell lines (Figures 1(e) and 1(f)). The CompuSyn software was used to generate CI and Fa-CI plots for varying concentrations of TMZ with fixed dose of Nira to determine the synergistic effects. Figures 1(g) and 1(h) and Tables 1 and 2 indicated synergistic effects for all the doses tested. Combination of TMZ at 30 μM (RPMI8226 cells) and 20 μM (NCI-H929 cells) with 3 μM Nira showed the strongest synergistic effects. These doses were selected for the next experiments to test whether this combination was optimal.

3.2. Effects of TMZ and/or Nira on Apoptosis. In order to assess whether administration of TMZ and/or Nira for 48 h affects apoptosis in MM cells, Annexin V/PI staining of RPMI8226 and NCI-H929 cells was carried out. As presented in Figures 2(a) and 2(c), single-agent TMZ or Nira did not induce significant apoptosis. However, combined treatment with TMZ and Nira induced more apoptosis (25% apoptosis) ($P < 0.01$). We also evaluated the effects of TMZ and/or Nira on apoptosis-associated protein levels in MM cells by immunoblot. Cleaved caspase-3 protein amounts in the combination group were markedly higher compared with controls and TMZ and Nira monotherapies (Figure 2(e)).

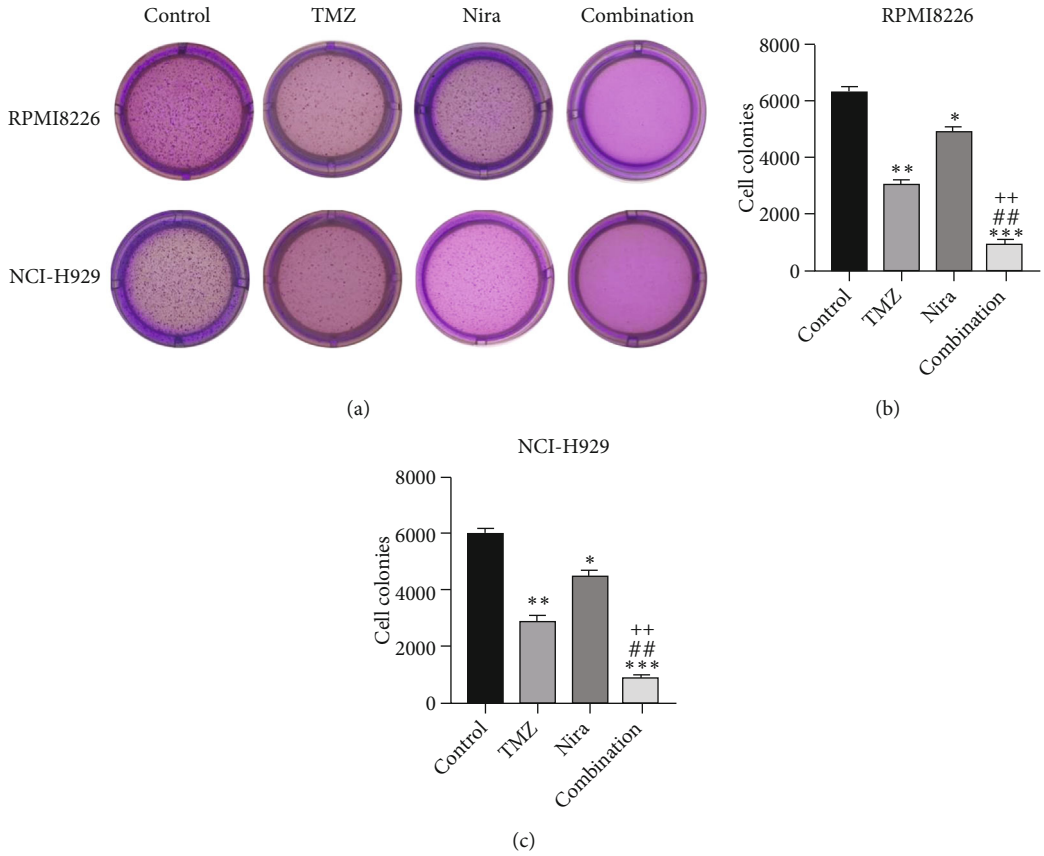

Figure 3: Effects of TMZ and/or Nira on colony formation in MM cells. (a) RPMI8226 and NCI-H929 cells were administered TMZ and/or Nira for 14-21 days, and colony formation ability was determined by soft-agar clonogenic assay. (b, c) Quantification of colonies shown in (a). $^{*}P < 0.05$, $^{**}P < 0.01$, and $^{***}P < 0.001$ versus control group; $^{\#\#}P < 0.01$ versus TMZ group; $^{++}P < 0.01$ versus Nira group. TMZ: temozolomide; Nira: niraparib.

3.3. Effects of TMZ and/or Nira on Cell Proliferation. To further examine the above synergistic effects of TMZ and Nira in the present study, this optimal drug combination was assessed for its effects on the S-phase distribution of MM cells treated with TMZ and/or Nira, for 48 h flow-cytometrically. Figures 2(b) and 2(d) show TMZ reduced the proportion of cells in the S-phase at 48 h. Cotreatment with TMZ and Nira significantly enhanced this effect compared with TMZ alone. Furthermore, we performed soft-agar colony formation assay to assess the antiproliferative effect of Nira-TMZ. As depicted in Figures 3(a)–3(c), the amounts of colonies following Nira-TMZ treatment were starkly diminished in comparison with the TMZ monotherapy, Nira monotherapy, and untreated control groups of MM cells. These data suggested that combination of TMZ and Nira markedly inhibited cell proliferation, with potent synergistic cytotoxicity in MM cells. Accordingly, immunoblot showed that the cell cycle-associated protein cyclin D1 was significantly decreased in the combination group compared with the Nira or TMZ alone group (Figure 2(e)).

3.4. Combination of Nira and TMZ Induces γH2A.X Foci Formation and Blunts DNA Damage Repair in MM Cell Lines. We used immunofluorescence to detect whether histone H2A.X phosphorylation (γH2A.X) forms nuclear foci after exposure to TMZ and/or Nira treatment for 48 h. The number of γH2A.X foci is considered to be tightly associated with the amounts of cellular DSBs. The majority cells in the control group had no γH2A.X foci in the nuclei, while TMZ or Nira alone treatment caused sparse γH2A.X foci in MM cells. The proportion of γH2A.X-positive cells and the number of γH2A.X foci per nucleus were overtly increased after Nira plus TMZ treatment ($P < 0.05$) (Figures 4(a)–4(c)), suggesting that the combination induced significant DNA damage. This revealed that the PARP inhibitor Nira hindered DNA damage response (DDR) aroused by TMZ cytotoxicity.

3.5. Effects of Nira and/or TMZ on DDR Signaling in MM Cells. In order to elucidate the mechanism responsible for the synergistic effects of Nira and TMZ, the protein levels of DDR signaling effectors were examined. Cotreatment with TMZ plus Nira led to significantly increased p-ATM, p-CHK2, RAD51, and γH2A.X compared with monotherapy (Figure 5), indicating that TMZ-Nira combination therapy could function via the DNA damage response. These proteins are core members of the DDR when DNA confronts genotoxic challenges such as genotoxic chemotherapy.

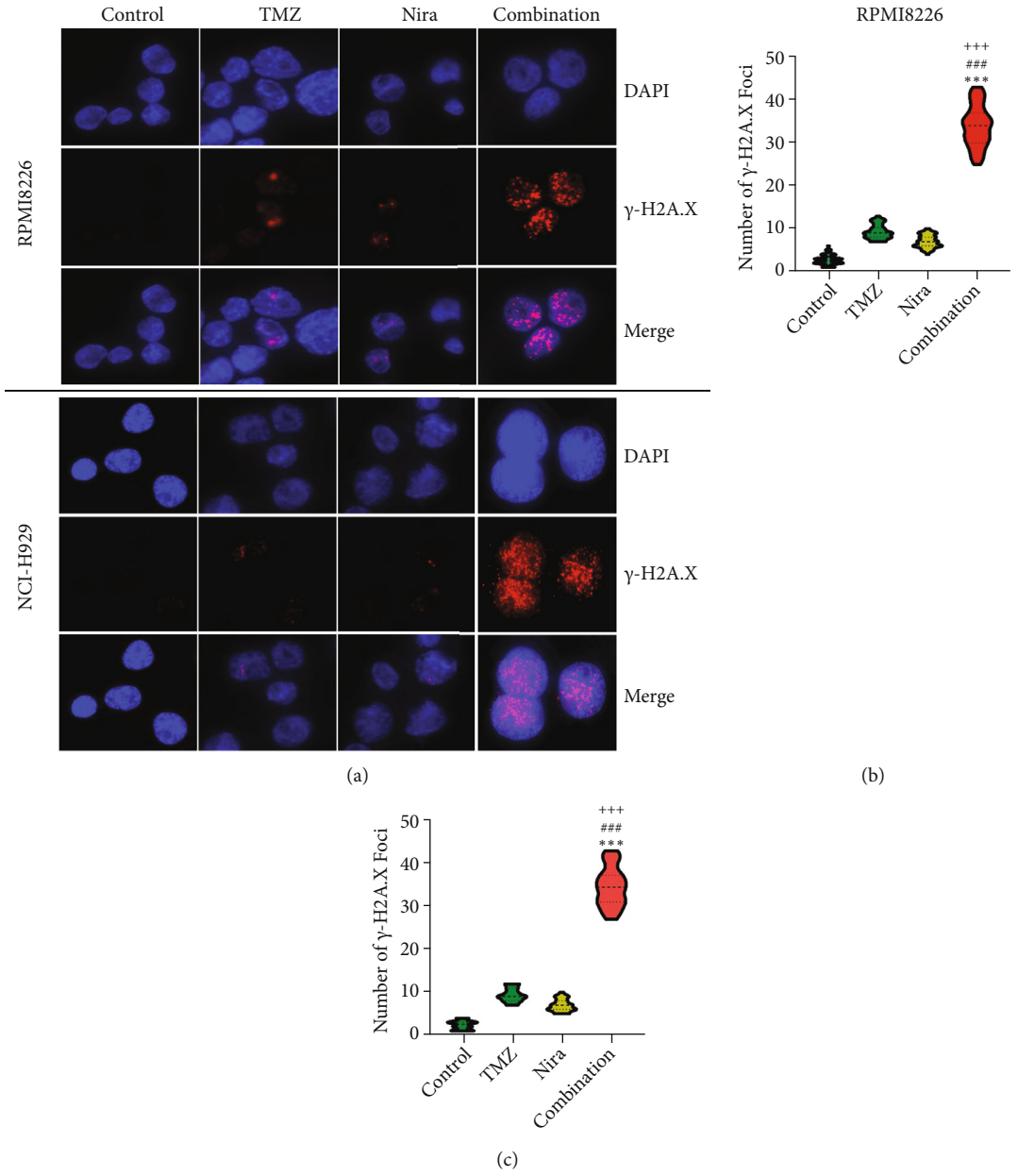

Figure 4: TMZ and/or Nira induce γH2A.X foci formation and block DNA damage repair in MM cell lines. (a) Immunofluorescent staining showing high amounts of γH2A.X foci in MM cells administered the TMZ/Nira combination regimen (TMZ at 30 μM and 20 μM for RPMI8226 and NCI-H929 cells, respectively, and Nira at 3 μM) for 48 h. (b, c) Quantitation of (a). $^{***}P < 0.001$ versus control group; $^{###}P < 0.001$ versus TMZ group; $^{+++}P < 0.001$ versus Nira group. TMZ: temozolomide; Nira: niraparib.

Mounting evidence suggests the BER pathway efficiently removes DNA nucleobase adducts and prevents DNA damage and cell death associated with DNA alkylating agents, including TMZ, cyclophosphamide, and carmustine [19]. Here, the PARP1 inhibitor Nira hampered the recruitment of some core DNA repair proteins of the PARP/BER pathway. Pharmacologically, the PARP1 inhibitor Nira hampered the recruitment of some core DNA repair proteins of the PARP/BER pathway, blocked SSB repair to some extent, and caused SSB accumulation [20, 21]. And thus, unrepaired SSBs were converted into lethal DSBs causing cell death and proliferation arrest in MM cells, which could explain the synergistic effects of TMZ and Nira.

3.6. In Vivo Effects of Nira and/or TMZ in an RPMI8226 Xenograft Model. The effects of daily TMZ (35 mg/kg) and/or Nira (20 mg/kg), administered i.p. 5 days per week, on RPMI8226 cell growth were examined in a human plasmacytoma xenograft model via subcutaneous injection. TMZ plus Nira regimen resulted in significantly reduced tumor volume and weight over time, compared with the vehicle and single-agent treatment groups (Figures 6(a)–6(c)). During the three weeks of treatment, the combination regimen showed no significant weight loss, and the animals showed good general health and activity, with no signs of discomfort, which showed a good tolerability for the Nira and TMZ combination.

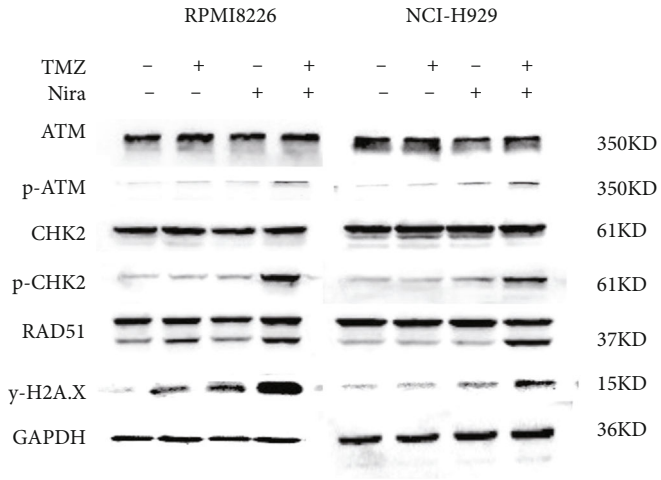

Figure 5: Effects of Nira and/or TMZ on DDR signaling in MM cells. RPMI8226 and NCI-H929 cells were administered TMZ and/or Nira for 48 h at various amounts, and immunoblot was carried out for quantitating proteins. GAPDH was utilized for normalization. TMZ: temozolomide; Nira: niraparib.

At the end of drug administration, euthanasia was performed, and tumors were extracted and analyzed by immunohistochemistry (IHC) for Ki67 and cleaved caspase-3, which are proliferative and apoptotic biomarkers in tumors. The tumors were also examined by TUNEL assay to assess in situ apoptosis to further confirm the above findings. Apoptotic (TUNEL- and cleaved caspase-3-positive) cells in the combination group were extensively increased as well as the morphologic features of apoptosis (Figures 6(d) and 6(e)). On the contrary, proliferative (Ki67-positive) cells were overtly decreased (Figure 6(e)), in accordance with the previously observed proliferation arrest. Moreover, we demonstrated that γH2A.X and RAD51 expression levels were starkly higher in the combination treatment group (Figure 6(e)), which suggested that the combination regimen enhanced DNA damage and blocked DNA repair. Jointly, these *in vivo* findings about tumor proliferation corroborated those obtained in cultured cells, further verifying our hypothesis that TMZ-Nira cotreatment produces excellent synergistic effects.

4. Discussion

MM comprises ~10% of all hematologic cancer cases. MM cases show good response to alkylating agents initially, but the quasi-totality of patients relapse eventually, including those who achieved complete remission (CR) [22]. In addition, many patients develop refractory disease because of multidrug resistance (MDR). Recently, although novel therapeutic approaches (newer proteasome inhibitors, IMiDs, CD38 monoclonal antibody, CAR-T therapy, and autologous stem cell transplantation (ASCT)) have extended survival, many patients still inevitably relapse and die of comorbidities [23]. Many patients are ineligible for auto-ASCT due to advanced age at diagnosis. It is imperative to identify more effective therapeutic options to improve curative effects in elderly and advanced-stage patients [24]. Genotoxic agent-based chemotherapeutic regimens are important in MM treatment. MDR represents the major obstacle hindering prognosis improvement in MM cases. Many factors contribute to MRD such as elevated drug efflux, altered drug resistance-related genes, increased DNA damage repair, and reduced apoptosis [25, 26]. Previous reports have suggested that PARP1 inhibitors synergize with several conventionally applied chemotherapeutics such as TMZ. As shown above, in combination with the PARP1 inhibitor Nira, the IC_{50} of TMZ was reduced significantly. An early event following DNA DSBs is the generation of phosphorylated histone H2AX (γH2A.X), which is considered the gold standard for DSB detection [27]. Therefore, γH2A.X amounts reflect DNA damage resulting from chemotherapeutic agents in cancer cells, representing an index of cell sensitivity to chemotherapy [28]. As shown above, after exposure to combination treatment, upregulation of γH2A.X indicated increased DSBs and enhanced drug sensitivity. RAD51 represents the most important protein that promotes strand pairing and exchange between homologous DNAs during homologous recombination repair (HRR) [29]. In this study, immunoblot and IHC analysis demonstrated elevated expression of RAD51 in the combination group, suggesting severe and lethal DNA DSB accumulation. Tumor cell sensitivity to chemotherapeutics promoting DNA damage is function of the balance between DNA damage and repair. Consequently, targeting key factors in DNA repair response that protect cells from death represent a promising approach for enhancing the curative effect of routine cytotoxic molecules.

PARP1 mainly contributes to SSB repair, particularly via the BER pathway. A PARP1 inhibitor was first successfully used as monotherapy based on the concept of "synthetic lethal therapy" for the treatment of cancers exhibiting intrinsic DNA repair anomalies. BRCA1/2-mutated cancers with abnormal DNA homogenous repair are vulnerable to further DNA repair pathway suppression [30, 31]. The PARP1/BER pathway is critical in clearing chemotherapy-induced DNA adducts, which prevents cell cycle arrest and death. When

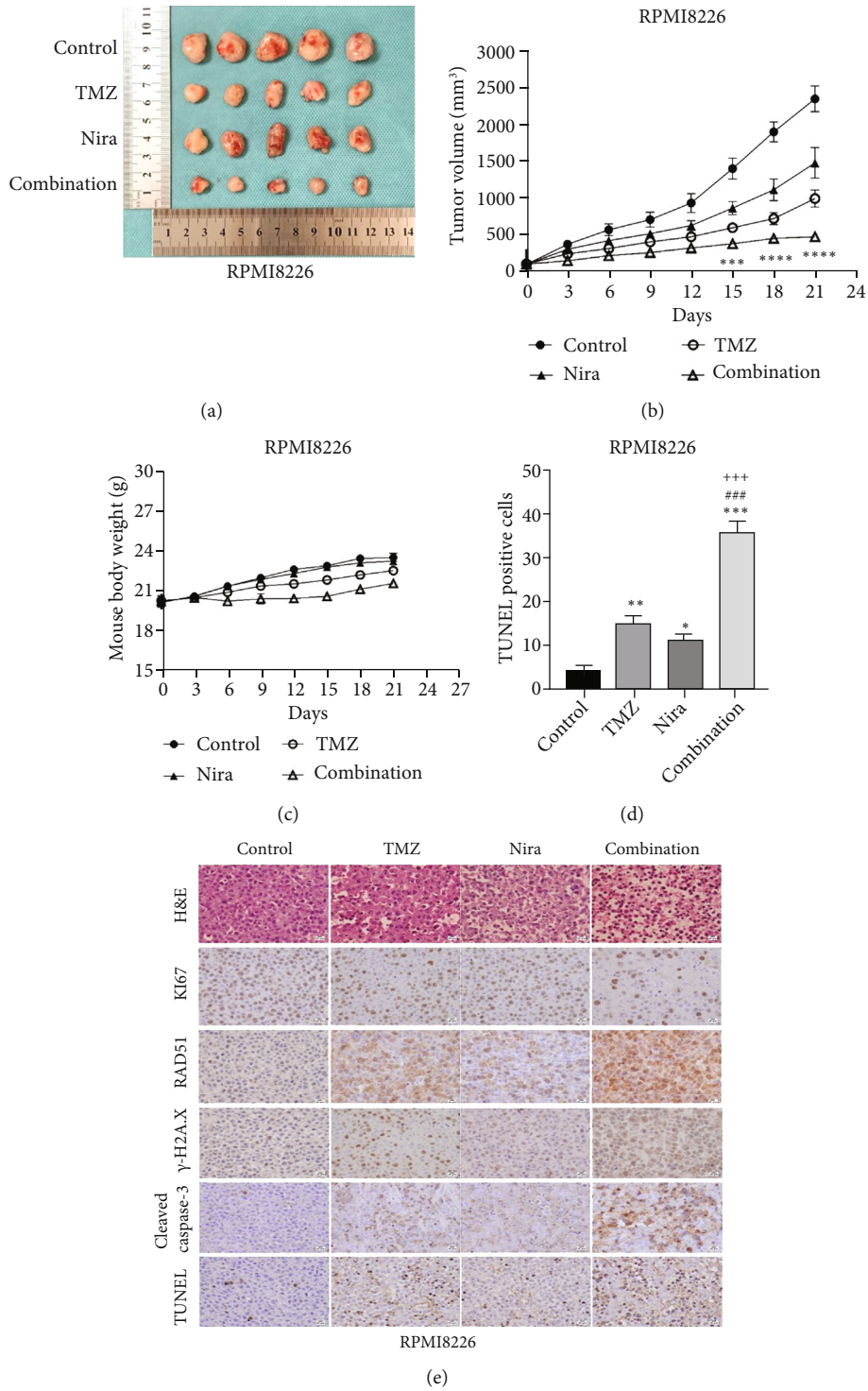

Figure 6: The TMZ/Nira regimen suppresses plasmacytoma xenograft *in vivo*. (a) Human MM cell-derived xenograft model was built using RPMI8226 cells to confirm the synergistic effects of TMZ and Nira. The animals had decreased tumor volumes upon administration of the TMZ-Nira combination compared with the TMZ and Nira monotherapy and control groups. (b, c) Tumor size and weight measurements revealed decreased plasmacytoma xenograft growth after TMZ/Nira cotreatment. (d) The percentages of TUNEL-positive cells were obtained by ImageJ. (e) Apoptotic and proliferating cells in tumor specimens, respectively, were detected by the TUNEL assay, H&E staining, and immunochemistry. The expression levels of γH2A.X, RAD51, Ki67, and cleaved caspase-3 were determined by immunohistochemistry. Reduced expression of Ki67 and elevated expression of γH2A.X, RAD51, and cleaved caspase-3 were found in the TMZ plus Nira group. Mean ± SD ($n = 5$ per group). Significant differences were indicated as follows: $^{*}P < 0.05$, $^{**}P < 0.01$, $^{***}P < 0.001$, and $^{****}P < 0.0001$ versus control group; $^{\#\#\#}P < 0.001$ versus TMZ group; $^{+++}P < 0.001$ versus Nira group. Scale bar, 20 μm. Original magnification, ×400. TMZ: temozolomide; Nira: niraparib.

DNA damage occurs, DNA lesions are recognized by DNA glycosylase that performs hydrolysis of the altered base to produce an apurinic-apyrimidinic (AP) base. This AP base undergoes removal by AP endonuclease for generating a DNA nick, which interacts with PARP1, resulting in DNA polymerase h (Pol h) and DNA ligase complex recruitment for repairing the DNA [32–34]. Temozolomide introduces DNA damage through DNA alkylation or methylation. Under normal conditions, temozolomide promotes methyl adduct formation in DNA at guanine's N7, guanine's O6, and adenine's N3. Since methylpurines (N7-MeG and N3-MeA) undergo repair quickly via BER, cytotoxicity mostly results from methylation at guanine's O6. PARP suppressors affect PARP1 and PARP2, blunt BER, and sensitize malignant cells to temozolomide [35, 36], constituting potential combinatory agents for use with temozolomide in cancer.

This study explored the mechanism by which temozolomide cytotoxicity was potentiated by the PARP suppressor Nira. As demonstrated above, Nira monotherapy yielded about 10% of cell viability inhibition (IC_{10}) at the clinical dose. In this study, temozolomide's effect was starkly enhanced by Nira. Indeed, we showed that in MM cells, 48 h of exposure to Nira plus TMZ achieved TMZ potentiation to a large extent. We hypothesized that temozolomide-dependent nucleotide methylation was not effectively repaired with BER blocking by Nira. The produced SSBs were subsequently converted into DSBs, causing MM cell apoptosis and proliferation arrest. Indeed, the amounts of DSBs, reflected by γH2A.X expression, were markedly elevated after combined administration of temozolomide and Nira. The elevated amounts of DSBs are correlated with enhanced cytotoxicity under these conditions. Bryant and Helleday suggested PARP suppression alters endogenous SSB repair, resulting in collapsed DNA replication forks [37]. This study provides some evidence that DSBs are important in temozolomide-dependent cytotoxicity in MM cells. Meanwhile, γH2A.X level was confirmed in the current work as a useful index for assessing the impact of PARP suppression on DNA repair.

PARP suppressors as chemosensitizing agents are scarcely applied in the clinical setting, probably because of the complexities of combination therapies, e.g., identifying the optimal dose [10]. Cotreatment with PARP1 inhibitors and conventional chemotherapeutics was shown to highly enhance the efficacy of chemotherapy that exerts cancer suppressive effects at reduced doses [38].

The combination regimen not only inhibited cancer cell proliferation and induced apoptosis but also reduced human plasmacytoma xenograft growth in mice. Histologic analysis confirmed that suppression of proliferative markers, appearance of severer DNA damage and breaks, and enhanced cell apoptosis corroborated xenograft growth suppression.

A limitation of this study is that the dosing and scheduling of TMZ (30 mg/kg, i.p. ×5, three cycles) used in this animal model were different from the regimen employed in clinical practice. Although the animals in this research did not show signs of discomfort and significant weight loss in the monotherapy and combination groups, the cooperative mechanism of genotoxic agents and PARP1 inhibitors remains to be further elucidated.

5. Conclusion

This study confirmed that Nira remarkably enhanced temozolomide's anticancer effects both in cultured cells and in mice. The above preclinical findings provide a sound rationale for the use of Nira for chemosensitization of MM cases to temozolomide in clinic. This research also provides a novel treatment strategy for MM, particularly in patients who have exhausted other treatment modalities. Nira has excellent pharmacokinetic features in many species and could cross the blood-brain barrier [8], making it particularly suitable for combined use with temozolomide for treating intracranial tumors in clinical practice.

Data Availability

All data throughout the manuscript were generated by our experiments on cells and mice. And data can be obtained by communicating with corresponding author or three co-first authors.

Ethical Approval

All procedures were carried out following the Guide for the Care and Use of Laboratory Animals by the US National Institutes of Health. The study had approval from the Animal Ethics Committee of Xijing Hospital, Air Force Medical University.

Conflicts of Interest

The authors report no conflicts of interest in this work.

Authors' Contributions

Hong-Yuan Shen, Hai-Long Tang, and Yan-Hua Zheng contributed equally to this article as co-first authors.

Acknowledgments

The present study was funded by the National Natural Science Foundation of China (No. 81870103) granted to Professor Baoxia Dong.

References

[1] C. Röllig, S. Knop, and M. Bornhäuser, "Multiple myeloma," *Lancet*, vol. 385, no. 9983, pp. 2197–2208, 2015.

[2] S. K. Kumar, V. Rajkumar, R. A. Kyle et al., "Multiple myeloma," *Nature Reviews. Disease Primers*, vol. 3, article 17046, 2017.

[3] S. K. Kumar, F. K. Buadi, and S. V. Rajkumar, "Pros and cons of frontline autologous transplant in multiple myeloma: the debate over timing," *Blood*, vol. 133, no. 7, pp. 652–659, 2019.

[4] M. A. Shammas, R. J. Shmookler Reis, H. Koley, R. B. Batchu, C. Li, and N. C. Munshi, "Dysfunctional homologous

recombination mediates genomic instability and progression in myeloma," *Blood*, vol. 113, no. 10, pp. 2290–2297, 2009.

[5] M. R. Velangi, E. C. Matheson, G. J. Morgan et al., "DNA mismatch repair pathway defects in the pathogenesis and evolution of myeloma," *Carcinogenesis*, vol. 25, no. 10, pp. 1795–1803, 2004.

[6] G. E. Ronson, A. L. Piberger, M. R. Higgs et al., "PARP1 and PARP2 stabilise replication forks at base excision repair intermediates through Fbh1-dependent Rad51 regulation," *Nature Communications*, vol. 9, no. 1, p. 746, 2018.

[7] H. Farmer, N. McCabe, C. J. Lord et al., "Targeting the DNA repair defect in BRCA mutant cells as a therapeutic strategy," *Nature*, vol. 434, no. 7035, pp. 917–921, 2005.

[8] C. K. Donawho, Y. Luo, Y. Luo et al., "ABT-888, an orally active poly(ADP-ribose) polymerase inhibitor that potentiates DNA-damaging agents in preclinical tumor models," *Clinical Cancer Research*, vol. 13, no. 9, pp. 2728–2737, 2007.

[9] H. Cheng, Z. Zhang, A. Borczuk et al., "PARP inhibition selectively increases sensitivity to cisplatin in ERCC1-low non-small cell lung cancer cells," *Carcinogenesis*, vol. 34, no. 4, pp. 739–749, 2013.

[10] Y. Lu, Y. Liu, Y. Pang, K. Pacak, and C. Yang, "Double-barreled gun: combination of PARP inhibitor with conventional chemotherapy," *Pharmacology & Therapeutics*, vol. 188, pp. 168–175, 2018.

[11] R. N. Trivedi, K. H. Almeida, J. L. Fornsaglio, S. Schamus, and R. W. Sobol, "The role of base excision repair in the sensitivity and resistance to temozolomide-mediated cell death," *Cancer Research*, vol. 65, no. 14, pp. 6394–6400, 2005.

[12] X. Cao, Y. Lu, Y. Liu et al., "Combination of PARP inhibitor and temozolomide to suppress chordoma progression," *Journal of Molecular Medicine (Berlin, Germany)*, vol. 97, no. 8, pp. 1183–1193, 2019.

[13] B. H. Lok, E. E. Gardner, V. E. Schneeberger et al., "PARP inhibitor activity correlates with SLFN11 expression and demonstrates synergy with temozolomide in small cell lung cancer," *Clinical Cancer Research*, vol. 23, no. 2, pp. 523–535, 2017.

[14] L. Tentori, C. Leonetti, M. Scarsella et al., "Combined treatment with temozolomide and poly(ADP-ribose) polymerase inhibitor enhances survival of mice bearing hematologic malignancy at the central nervous system site," *Blood*, vol. 99, no. 6, pp. 2241–2244, 2002.

[15] J. P. Palma, Y. C. Wang, L. E. Rodriguez et al., "ABT-888 confers broad in vivo activity in combination with temozolomide in diverse tumors," *Clinical Cancer Research*, vol. 15, no. 23, pp. 7277–7290, 2009.

[16] S. J. Gill, J. Travers, I. Pshenichnaya et al., "Combinations of PARP inhibitors with temozolomide drive PARP1 trapping and apoptosis in Ewing's sarcoma," *PLoS One*, vol. 10, no. 10, article e0140988, 2015.

[17] T. C. Chou, "Drug combination studies and their synergy quantification using the Chou-Talalay method," *Cancer Research*, vol. 70, no. 2, pp. 440–446, 2010.

[18] L. Booth, J. L. Roberts, R. Rais, A. Poklepovic, and P. Dent, "Valproate augments niraparib killing of tumor cells," *Cancer Biology & Therapy*, vol. 19, no. 9, pp. 797–808, 2018.

[19] N. Kondo, A. Takahashi, K. Ono, and T. Ohnishi, "DNA damage induced by alkylating agents and repair pathways," *Journal of Nucleic Acids*, vol. 2010, Article ID 543531, 7 pages, 2010.

[20] R. Krishnakumar and W. L. Kraus, "The PARP side of the nucleus: molecular actions, physiological outcomes, and clinical targets," *Molecular Cell*, vol. 39, no. 1, pp. 8–24, 2010.

[21] D. Slade, "PARP and PARG inhibitors in cancer treatment," *Genes & Development*, vol. 34, no. 5-6, pp. 360–394, 2020.

[22] N. van de Donk, C. Pawlyn, and K. L. Yong, "Multiple myeloma," *Lancet*, vol. 397, no. 10272, pp. 410–427, 2021.

[23] C. S. Chim, S. K. Kumar, R. Z. Orlowski et al., "Management of relapsed and refractory multiple myeloma: novel agents, antibodies, immunotherapies and beyond," *Leukemia*, vol. 32, no. 2, pp. 252–262, 2018.

[24] C. L. Zuch de Zafra, F. Fajardo, W. Zhong et al., "Targeting multiple myeloma with AMG 424, a novel anti-CD38/CD3 bispecific T-cell-recruiting antibody optimized for cytotoxicity and cytokine release," *Clinical Cancer Research*, vol. 25, no. 13, pp. 3921–3933, 2019.

[25] B. S. Vinod, T. T. Maliekal, and R. J. Anto, "Phytochemicals as chemosensitizers: from molecular mechanism to clinical significance," *Antioxidants & Redox Signaling*, vol. 18, no. 11, pp. 1307–1348, 2013.

[26] M. T. Tomicic and B. Kaina, "Topoisomerase degradation, DSB repair, p53 and IAPs in cancer cell resistance to camptothecin-like topoisomerase I inhibitors," *Biochimica et Biophysica Acta*, vol. 1835, no. 1, pp. 11–27, 2013.

[27] N. J. Curtin, L. Z. Wang, A. Yiakouvaki et al., "Novel poly(-ADP-ribose) polymerase-1 inhibitor, AG14361, restores sensitivity to temozolomide in mismatch repair-deficient cells," *Clinical Cancer Research*, vol. 10, no. 3, pp. 881–889, 2004.

[28] B. Kopp, L. Khoury, and M. Audebert, "Validation of the γH2AX biomarker for genotoxicity assessment: a review," *Archives of Toxicology*, vol. 93, no. 8, pp. 2103–2114, 2019.

[29] E. Laurini, D. Marson, A. Fermeglia, S. Aulic, M. Fermeglia, and S. Pricl, "Role of Rad51 and DNA repair in cancer: a molecular perspective," *Pharmacology & Therapeutics*, vol. 208, article 107492, 2020.

[30] M. W. Audeh, J. Carmichael, R. T. Penson et al., "Oral poly(ADP-ribose) polymerase inhibitor olaparib in patients with BRCA1 or BRCA2 mutations and recurrent ovarian cancer: a proof-of-concept trial," *Lancet*, vol. 376, no. 9737, pp. 245–251, 2010.

[31] K. A. Gelmon, M. Tischkowitz, H. Mackay et al., "Olaparib in patients with recurrent high-grade serous or poorly differentiated ovarian carcinoma or triple-negative breast cancer: a phase 2, multicentre, open-label, non-randomised study," *The Lancet Oncology*, vol. 12, no. 9, pp. 852–861, 2011.

[32] V. Schreiber, J. C. Amé, P. Dollé et al., "Poly(ADP-ribose) polymerase-2 (PARP-2) is required for efficient base excision DNA repair in association with PARP-1 and XRCC1," *The Journal of Biological Chemistry*, vol. 277, no. 25, pp. 23028–23036, 2002.

[33] G. L. Dianov, K. M. Sleeth, I. I. Dianova, and S. L. Allinson, "Repair of abasic sites in DNA," *Mutation Research*, vol. 531, no. 1-2, pp. 157–163, 2003.

[34] M. Masson, C. Niedergang, V. Schreiber, S. Muller, J. Menissier-de Murcia, and G. de Murcia, "XRCC1 is specifically associated with poly(ADP-ribose) polymerase and negatively regulates its activity following DNA damage," *Molecular and Cellular Biology*, vol. 18, no. 6, pp. 3563–3571, 1998.

[35] O. Erice, M. P. Smith, R. White et al., "MGMT expression predicts PARP-mediated resistance to temozolomide," *Molecular Cancer Therapeutics*, vol. 14, no. 5, pp. 1236–1246, 2015.

[36] C. L. Cheng, S. P. Johnson, S. T. Keir et al., "Poly(ADP-ribose) polymerase-1 inhibition reverses temozolomide resistance in a DNA mismatch repair-deficient malignant glioma xenograft," *Molecular Cancer Therapeutics*, vol. 4, no. 9, pp. 1364–1368, 2005.

[37] H. E. Bryant and T. Helleday, "Inhibition of poly (ADP-ribose) polymerase activates ATM which is required for subsequent homologous recombination repair," *Nucleic Acids Research*, vol. 34, no. 6, pp. 1685–1691, 2006.

Hindawi
Journal of Oncology
Volume 2022, Article ID 7521934, 13 pages
https://doi.org/10.1155/2022/7521934

Research Article

DNA Repair Protein HELQ and XAB2 as Chemoresponse and Prognosis Biomarkers in Ascites Tumor Cells of High-Grade Serous Ovarian Cancer

Fang Zhu[1,2] **Siyu Yang**[1,2] **Ming Lei**[1,2] **Qiongqiong He**[3,4] **Lisha Wu**[2,5] **and Yu Zhang**[1,2,6]

[1]*Department of Gynecology, Xiangya Hospital, Central South University, Changsha, Hunan, China*
[2]*Gynecological Oncology Research and Engineering Center of Hunan Province, Changsha, Hunan, China*
[3]*Department of Pathology, Xiangya Hospital, Central South University, Changsha, Hunan, China*
[4]*Department of Pathology, School of Basic Medicine, Central South University, Changsha, Hunan, China*
[5]*Institute of Medical Science, Xiangya Hospital, Central South University, Changsha, Hunan, China*
[6]*National Clinical Research Center for Geriatric Disorders, Xiangya Hospital, Central South University, Changsha, Hunan, China*

Correspondence should be addressed to Lisha Wu; lishawu@csu.edu.cn and Yu Zhang; xyzhangyu@csu.edu.cn

Received 26 December 2021; Accepted 10 March 2022; Published 29 March 2022

Academic Editor: Guo Chen

Nucleotide excision repair (NER) is an important mediator for responsiveness of platinum-based chemotherapy. Our study is aimed at investigating the NER-related genes expression in ascites tumor cells and its application in the prediction of chemoresponse in high-grade serous ovarian cancer (HGSC) patients. The relationship between 16 NER-related genes and the prognosis of ovarian cancer was analyzed in the TCGA database. NER-related genes including HELQ and XAB2 expressions were determined via immunocytochemistry in ascites cell samples from 92 ovarian cancer patients prior to primary cytoreduction surgery. Kaplan-Meier analysis and Cox model were used to investigate the association between NER-related gene expression and prognosis/chemotherapeutic response. Predicting models were constructed using a training cohort of 60 patients and validated in a validation cohort of 32 patients. We found that high expression of HELQ and XAB2 in the training cohort was associated with poor prognosis (for HELQ, $P = 0.001$, HR = 2.83, 95% CI: 1.46-5.49; for XAB2, $P = 0.008$, HR = 2.38, 95% CI: 1.23-4.63) and platinum resistance (for HELQ, $P < 0.001$; for XAB2, $P = 0.006$). In the validation cohort, the combination of HELQ and XAB2 (AUC = 0.863) showed the highest AUC. The expression levels of HELQ (RR 5.7, 95% CI 1.7-19.2) and XAB2 (RR 3.2, 95% CI 0.9-10.8) in ascites tumor cells were positively correlated to the risk of platinum resistance. In summary, we revealed that the expression levels of HELQ and XAB2 are candidate predictors for primary chemotherapy responsiveness and prognosis in HGSC. Ascites cytology is applicable as a promising method for chemosensitivity prediction in HGSC.

1. Introduction

Epithelial ovarian cancer (EOC) is the second most lethal gynecologic cancer worldwide [1], with a 5-year survival of 46%. Primary cytoreductive surgery followed by platinum-based chemotherapy has been the standard treatment of EOC over the past decades [2, 3]. However, chemoresistance is common in the later course of EOC. Unresponsiveness to chemotherapy is associated with poorer prognosis in EOC patients [4, 5]. Currently, the widely used predictor of the response to platinum-based chemotherapy in ovarian cancer has been the platinum-free interval (PFI). However, PFI is not a valid predictor. The PFI is a retrospective evaluation and may be influenced by the frequency and types of

investigations a patient receives during follow-up. For platinum-resistant patients, they cannot benefit from treatment and have to endure the side effects of chemotherapy drugs. Therefore, the prediction of chemosensitiveness before primary treatment in EOC is a major clinical issue.

Platinum-based chemotherapy, such as carboplatin or cisplatin, causes DNA damage by intercalating DNA through interstrand cross-links (ICLs) between purine bases, resulting in DNA double-strand breaks (DSBs) [6, 7]. In response to genotoxic stress, cells activate the checkpoints to prevent further progression through the cell cycle and initiate DNA repair [8], whereas in cancer cells, inappropriate or aberrant activation of the DNA damage response network is associated with resistance to platinum [9, 10]. Previous studies have shown that NER was an important mediator for responsiveness of platinum-based chemotherapy. NER and high activity of NER was correlated with platinum resistance in EOC [11, 12]. Therefore, the identification of the key elements in NER pathways could provide biomarkers for early detection of platinum chemoresistance.

It is acknowledged that advanced stage EOC is prone to metastasize to the entire abdominal cavity via peritoneal dissemination and large amount of ascites generally ensues. Ascites cytology is a promising alternative to primary tumor tissue sampling, especially for the elderly or patients with poor general condition, in whom invasive procedures may be postponed due to comorbidities [13]. Zivadinovic et al. have observed good concordance between ascites cytology and primary tumor tissue sampling. The sensitivity of cytology was 98.92%, and the specificity was 93.6% [14]. It has been reported that the introduction of immunohistochemistry (IHC) staining of cell blocks obtained from ascitic fluid further improved that accuracy of diagnosis [15].

In this study, we first analyzed the correlation between NER-related genes and the prognosis of ovarian cancer cases from the TCGA database and found that the high-expression levels of Helicase POLQ-like (HELQ), Xeroderma pigmentosum group A-binding protein2 (XAB2), and replication protein A2 (RPA2) were associated with the poor prognosis of ovarian cancer. Then, we further evaluated the role of HELQ and XAB2 in ascites cell samples as a predictive biomarker. The predictive performance of ascites cytology was compared with paired primary tumor tissues.

2. Materials and Methods

2.1. Bioinformatics Analysis of TCGA Dataset. The normalized mRNA high-throughput sequencing data and clinical information of tubo-ovarian high-grade serous carcinoma were downloaded from The Cancer Genome Atlas (TCGA, https://portal.gdc.cancer.gov) via open access in December 2018. Sixteen NER-related genes (HELQ, ERCC1, ERCC3, ERCC4, ERCC5, ERCC6, ERCC8, DDB2, RAD23A, RAD23B, RPA1, RPA2, RPA3, XAB2, XPA, and XPC) were included in the study [16]. Patients who have not undergone platinum-based chemotherapy or incomplete follow-up information were excluded. The rest of 339 patients were divided into high and low according to the mRNA expression of each gene. The receiver operating characteristic (ROC) curve was employed to determine the optimal cut-off point for expression level. And the value at maximum Youden's index (sensitivity+specificity-1) was selected as the cut-off value [17, 18]. Survival analysis of overall survival (OS) and progression-free survival (PFS) was performed.

2.2. Study Cohorts and Clinical Information Collection. All eligible patients of the study were from the Xiangya Hospital of Central South University, China, between January 2014 to September 2019 and were treated in strict accordance with the version 1 2021 NCCN guidelines [19]. Eligible patients had to meet the following criteria: (1) The diagnosis of ovarian adenocarcinoma was reached by morphology and IHC of the ascites and tissue samples. The protocol for IHC staining was described in the study by Uehara et al. IHC stains that showed PAX8 (+), WT1 (+), CA125 (+), CK7 (+), CDX-2 (-), CK20 (-), and CEA (-) were recognized as ovarian origin [20], (2) treated by surgical debulking and histologically confirmed as high-grade serous ovarian cancer (HGSC), and (3) underwent at least three cycles of platinum-based chemotherapy after surgery. Patients who met the following criteria were excluded: (1) accompanied with other systemic malignancies; (2) received radiotherapy, chemotherapy, and biological therapy before cytological evaluation or debulking; (3) treated with platinum drugs other than cisplatin or carboplatin; (4) with incomplete clinical information; (5) loss of follow-up; and (6) lack of available biopsy specimens. A total of 92 patients were included in the study, including 60 in the training cohort and 32 in the validation cohort. Detailed description of the process of participants through the research was shown in Figure S1. The following clinical parameters were retrieved from medical records: age, pretreatment level of CA-125, volume of ascites, residual lesion, the International Federation of Gynecology and Obstetrics (FIGO) stage, chemotherapy regimen, OS, and PFS. Patient follow-up was terminated on November 1st, 2020. Patients were deemed as platinum resistant if they had disease progression during primary chemotherapy or disease recurrence within 6 months after completion of primary chemotherapy, while those without disease progression after 6 months from the end of primary chemotherapy were deemed as platinum sensitive. Surveillance was implemented upon completion of the initial treatment with 3-4 m interval during the first 2 years, 4-6 m interval from year 2 to year 3, 6 m internal from years 3-5, and annual visits after 5 years. These visits included symptom management, examination including a pelvic examination, chest/abdominal/pelvic CT and CA-125 or other tumor markers measurements. Subsequent imaging workup was indicated for patients with elevated CA-125, including ultrasound, CT, MRI, or PET-CT. If the lesion is found, it will indicate the recurrence or progression. PFI > 6 months predicts favorable response to retreatment; <6-month PFI is defined as platinum resistant [16, 21]. The study was approved by the Ethics Committee Xiangya Hospital of Central South University (No. 2017068222).

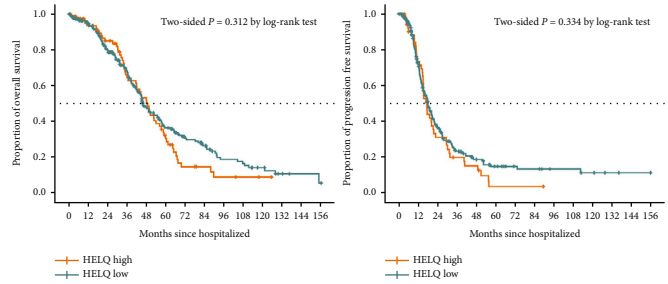

(a)

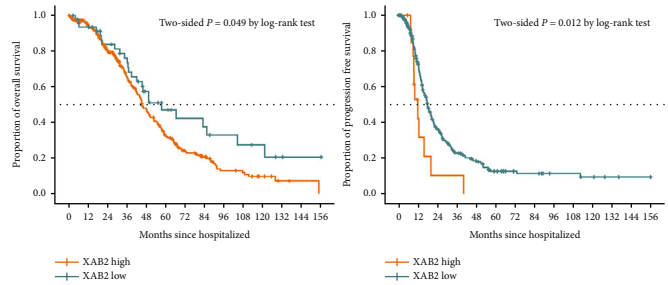

(b)

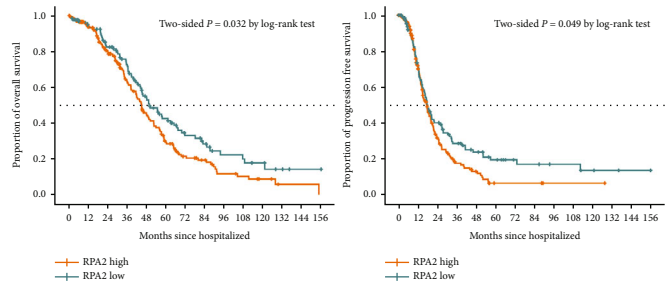

(c)

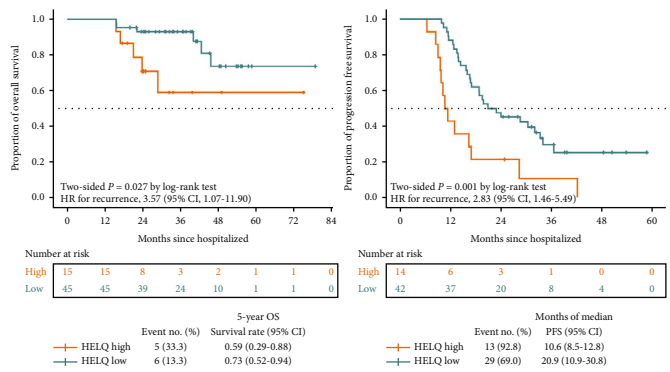

(d)

Figure 1: Continued.

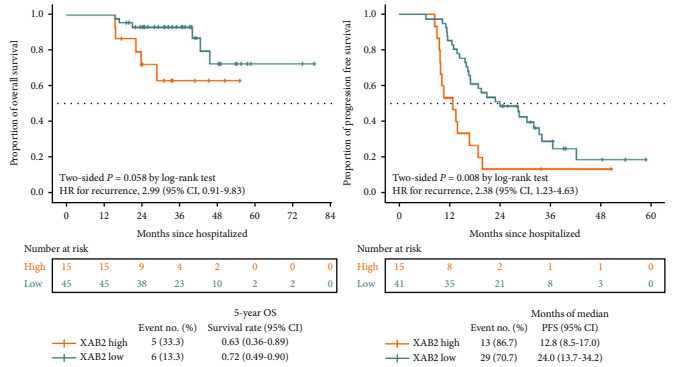

(e)

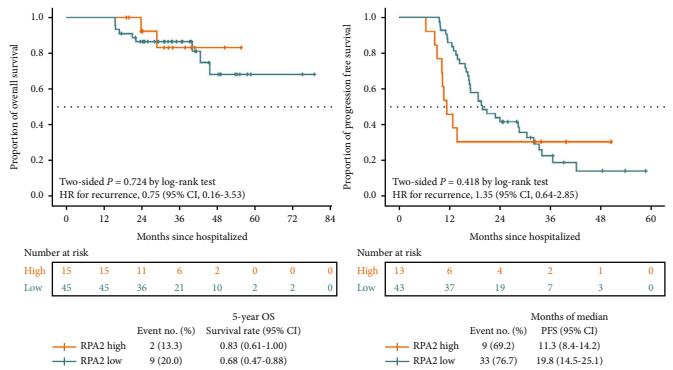

(f)

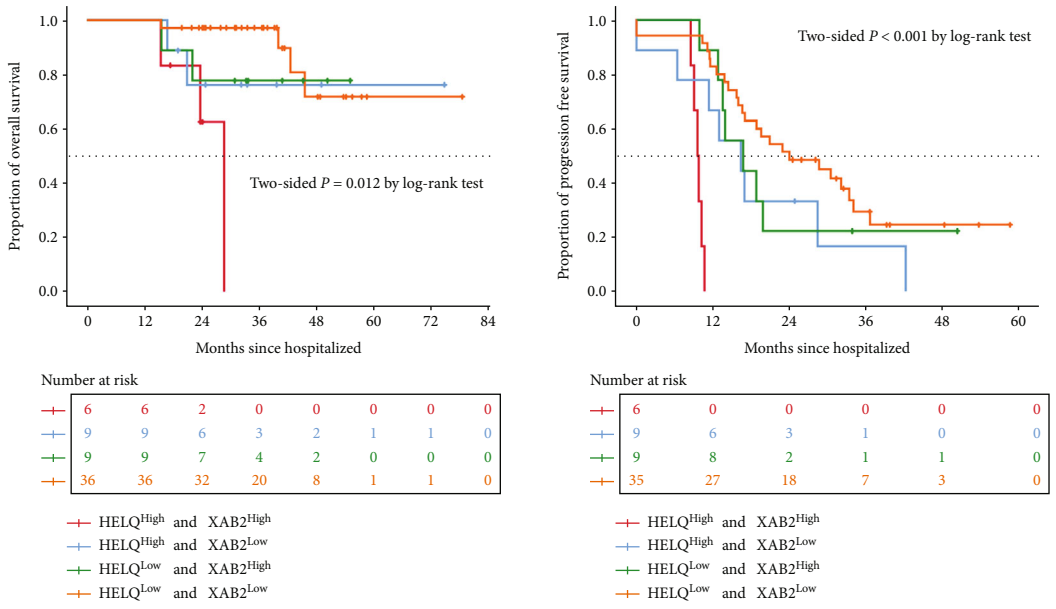

(g)

Figure 1: HELQ and XAB2 were associated with poor survival in patients with ovarian cancer. (a–c) Kaplan-Meier curves of OS and PFS according to the expressions of HELQ, XAB2, and RPA2 in TCGA tuboovarian high-grade serous carcinoma. (d–f) Kaplan-Meier survival curves for OS and PFS of patients with HGSC from the study cohort according to expressions of HELQ, XAB2, and RPA2 in ascites tumor cells. (g) Kaplan-Meier survival curves for OS and PFS of patients with HGSC from the study cohort according to HELQ-XAB2 stratification in ascites tumor cells. HELQ: helicase, POLQ like; RPA2: replication protein A2; XAB2: XPA binding protein 2; TCGA: The Cancer Genome Atlas; OS: overall survival; PFS: progression-free survival; HGSC: high-grade serous ovarian cancer.

Table 1: Clinicopathologic characteristics of 60 HGSC patients in Xiangya hospital.

Clinicopathologic parameters	Frequency (%)	Expression level in ascites tumor cells					
		HELQ			XAB2		
		High	Low	*P*	High	Low	*P*
Age (year)				0.153			>0.99
≤60	48 (80)	10	38		12	36	
>60	12 (20)	5	7		3	9	
FIGO stage				—			—
I-II	3 (5)	0	3		0	3	
III-IV	57 (95)	15	42		15	42	
Residual disease				0.637			0.428
R0	14 (23)	2	12		2	12	
R1	29 (48)	8	21		7	22	
>R1	17 (28)	5	12		6	11	
Ascitic fluid (ml)				0.313			0.313
≤500	15 (25)	2	13		2	13	
>500	45 (75)	13	32		13	32	
Chemotherapy response				<0.001			0.006
Sensitive	48 (80)	6	42		8	40	
Resistant	12 (20)	9	3		7	5	

P value was calculated by chi-square test. HGSC: high-grade serous ovarian cancer; FIGO: International Federation of Gynecology and Obstetrics. Statistically significant ($P < 0.05$).

2.3. Ascites Cell Samples, Paired with Primary Tumor Tissues, Immunohistochemistry. To clarify the relationship between the expression levels of HELQ and XAB2 in ascites tumor cells and clinical characteristics in HGSC patients, ascites samples were obtained for immunocytochemistry staining. In newly diagnosed ovarian cancer patients, ascites was collected during peritoneal puncture before initial cytoreductive surgery. Firstly, all samples of ascites were submitted for routine cytologic examination. Approximately 20 to 50 ml ascites was spun down at 600 g for 5 minutes. After discarding the upper layer, the samples were fixed in 10% formalin overnight, embedded in paraffin and finally stained with hematoxylin-eosin (HE) or immunocytochemistry. All paired tumor tissue specimens were collected via surgical resection and paraffin-embedded for immunocytochemistry analysis in the Pathology Department of Xiangya Hospital. Paraffin-embedded ascitic fluid cells and tissue blocks were sliced into sections with a thickness of 2.5 μm. Sections were dewaxed by turpentine, hydrated by gradient alcohol, and heated by microwave in citric acid buffer (pH = 6.0) at 100°C for 30 min to antigen retrieval. After natural cooling at room temperature, we used 3% hydrogen peroxide solution to block endogenous peroxidase and 5% bovine serum albumin to reduce nonspecific binding. After being washed once or twice in PBS, the sections were incubated with a HELQ antibody (Abclonal, A12661, 1 : 300) and a XAB2 antibody (Abcam, ab228006, 1 : 400) at 4°C overnight. The following day, the sections were washed twice in PBS and kept at room temperature for 1 h of secondary antibody incubation. The immunohistochemical reaction was observed with 3,3,0-diaminobenzidine (DAB), and hematoxylin was used for nuclear staining of all the tissue sections. Stained slides were scanned into digital images by the automatic scanning system. Five fields with highest positive expression were selected for each slice by 200x and 400x magnification and then analyzed by Vectra 2 system. All assessments were blinded with respect to clinical patient data.

2.4. Statistical Analysis. Kaplan-Meier analyses and log-rank test were used to analyze the OS and PFS of patients. Univariate analyses with enter method were performed by Cox regression survival analyses. The correlation between gene expression and clinicopathological features was estimated by the chi-square test, Fisher's exact test (for categorical variables), and binary logistic regression (for numerical variables). ROC curve analysis was used to assess the accuracy of the predicted probabilities. A *P* value of < 0.05 was considered statistically significant. All statistical analyses were performed with IBM-Microsoft SPSS version 22.0, GraphPad Prism 8.0, and R version 4.1.0.

3. Results

3.1. HELQ and XAB2 Were Associated with Poorer Prognosis of EOC Patients. We analyze the survival of 16 NER-related gene expressions in EOC patients from the TCGA database. The results showed that high expression levels of XAB2 (for OS, $P = 0.049$; for PFS, $P = 0.012$, Figure 1(b)) and RPA2 (for OS, $P = 0.032$; for PFS, $P = 0.049$, Figure 1(c)) were associated with poorer prognosis. According to our previous study demonstrating HELQ as a novel indicator of platinum-based chemoresistance for EOC [22], we included HELQ in this study, even though it was not statistically significant in this

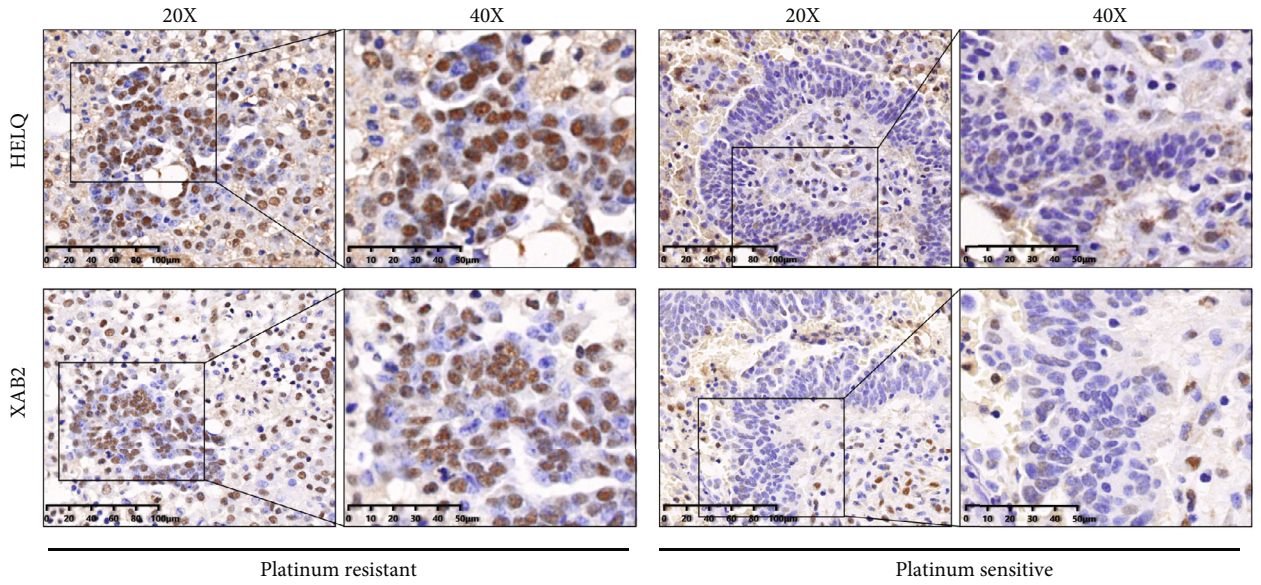

(a)

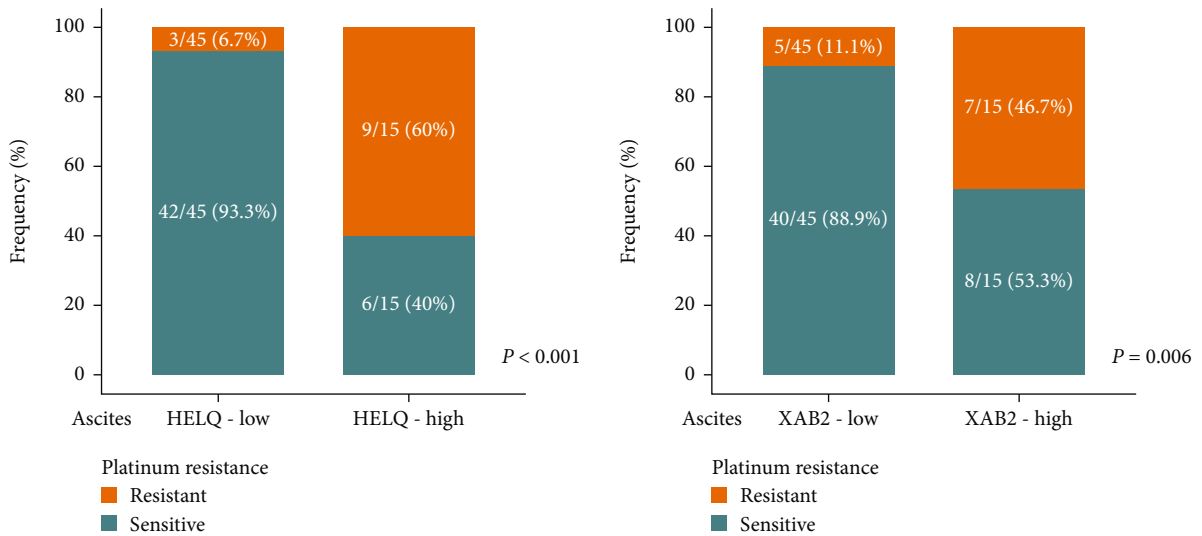

(b)

Figure 2: Continued.

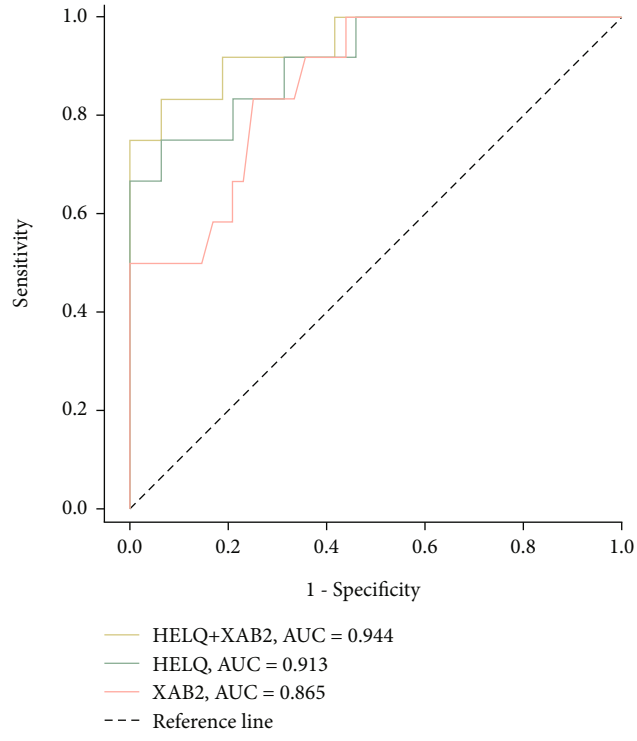

(c)

Figure 2: HELQ and XAB2 expressions in ascites tumor cells associated with platinum-resistant phenotype. (a) Representative immunohistochemistry images of HELQ and XAB2 in patients with platinum-resistant and platinum-sensitive phenotypes. (b) Frequency of platinum-resistant patients from the study cohort was compared according to HELQ and XAB2 expressions. (c) Receiver operator characteristic curves with AUC according to relative expressions of HELQ and XAB2 in ascites tumor cells of patients with HGSC. AUC: area under the curve.

Table 2: Diagnostic performances of HELQ and XAB2 expression levels in ovarian cancer with platinum resistance.

Triage	Diagnostic accuracy (95% CI)			
	Sensitivity	Specificity	PPV	NPV
High expression of HELQ	75% (43-93)	87.5% (74-95)	60% (33-83)	93.3% (81-98)
High expression of XAB2	58.3% (29-84)	83.3% (69-92)	46.7% (22-73)	88.9% (75-96)
High expression of both HELQ and XAB2	50% (22-78)	100% (91-100)	100% (52-100)	88.9% (77-95)

PPV: positive predictive value; NPV: negative predictive value.

analysis (for OS, $P = 0.312$; for PFS, $P = 0.334$, Figure 1(a)). Details of 16 genes involved in the NER pathway are shown in Table S1. In the training cohort of 60 patients, better survival was strongly associated with low expression of HELQ (Figure 1(d)) and XAB2(Figure 1(e)) in ascites tumor cells. Given that RPA2 expression in ascites tumor cells (5-year survival rate, 0.83 vs 0.68, $P = 0.724$; median PFS, 11.3 months vs. 19.8 months, $P = 0.418$) was weakly correlated with poor prognosis of HGSC patients in training cohort (Figure 1(f)), it was not included in subsequent analyses.

Next, we stratified samples into 4 groups based on the combination of the HELQ and XAB2 expressions in ascites tumor cells: a high-expression HELQ/high-expression XAB2 group, a high-expression HELQ/low-expression XAB2 group, a low-expression HELQ/high-expression XAB2 group, and a low-expression HELQ/low-expression XAB2 group. We subsequently performed a survival analysis. Comparisons were made between the 4 groups. The median PFS was 22.6, 16.8, 16.6, and 15.0 months, respectively ($P < 0.001$), and the median OS was 55.1, 49.5, 38.6, and 38.6 months ($P = 0.012$), respectively (Figure 1(g)).

3.2. High Expression of HELQ and XAB2 in Ascites Tumor Cells Were Correlated with Platinum Resistance in HGSC Patients. The characteristics of the 60 HGSC patients were summarized in Table 1. Subsequent analyses of HELQ and XAB2 expressions in ascites tumor cells and clinical data showed statistically significant increased distribution of platinum resistance in patients with high-expression of HELQ ($P < 0.001$) and XAB2 ($P = 0.006$). Other clinical features

Table 3: Clinicopathologic characteristics of 32 HGSC patients in validation cohort.

Clinicopathologic parameters	Frequency (%)	Expression level in ascites tumor cells					
		HELQ			XAB2		
		High	Low	*P*	High	Low	*P*
Age (year)				0.590			0.590
≤60	25 (78)	4	21		4	21	
>60	7 (22)	2	5		2	5	
FIGO stage				1.00			1.00
I-II	1 (4)	0	1		0	1	
III-IV	31 (97)	6	25		6	25	
Residual disease*				0.049			0.040
R0	13 (41)	0	13		0	13	
R1	12 (38)	4	8		4	8	
>R1	6 (19)	1	5		2	4	
Ascitic fluid (ml)				0.361			0.059
≤500	13 (41)	1	12		0	13	
>500	19 (59)	5	14		6	13	
Chemotherapy response				0.012			0.101
Sensitive	25 (78)	2	23		3	22	
Resistant	7 (22)	4	3		3	4	

*With one patient whose residual disease was unavailable. HGSC: high-grade serous ovarian cancer; FIGO: International Federation of Gynecology and Obstetrics.

such as age, stage, and residual disease did not harbor any significant distribution variation.

To confirm the correlation between HELQ and XAB2 expressions and platinum-based chemotherapy response in HGSC, we noticed that high expression of HELQ and XAB2 in ascites tumor cells were strongly correlated with platinum resistance (Figure 2(a)). In addition, we compared the frequency of platinum-resistant phenotype in cases with high or low expression level of HELQ and XAB2. We observed platinum resistance enrichment in the high expression of HELQ (9/15 vs. 3/45, $P < 0.001$) and XAB2 (7/15 vs. 5/45, $P = 0.006$) (Figure 2(b)), suggesting that HELQ and XAB2 expressions in ascites tumor cells could be predictors of platinum resistance in HGSC.

Then, we investigated the relative expression of HELQ and XAB2 in ascites tumor cells utilizing ROC curves, to evaluate the performance of HELQ and XAB2 as predictors. ROC curves for HELQ alone, XAB2 alone, and combination of HELQ and XAB2 demonstrated the highest area under the curve (AUC) for the combination of HELQ and XAB2 (AUC = 0.944), followed by HELQ alone (AUC = 0.913) and lastly by XAB2 alone (AUC = 0.865) (Figure 2(c)).

Table 2 showed the diagnostic performance of HELQ and XAB2 expression levels in ovarian cancer with platinum resistance in study cohort. Positive predictive values (PPV) for high expression of HELQ and XAB2 individually in platinum resistance were 60% and 46.7%, respectively. PPV for platinum resistance improved (100%) when using dual markers.

3.3. Expression of HELQ and XAB2 in Ascites Tumor Cells Was Positively Correlated with Chemoresistance in HGSC Patients in Validation Cohort. The clinicopathologic characteristics of 32 HGSC in the validation cohort were summarized in Table 3. A higher frequency of platinum resistance in patients with high expression of HELQ (4/6 vs 3/26, $P = 0.012$) was observed in validation cohort. However, the platinum resistance enrichment in the high expression of XAB2 was insignificant (3/6 vs. 4/26, $P = 0.101$) (Figure 3(a)). Consistent with the study cohort, ROC curves showed the highest AUC for the combination of HELQ and XAB2 (AUC = 0.863), followed by HELQ alone (AUC = 0.843) and lastly by XAB2 alone (AUC = 0.720) (Figure 3(b)). We observed a 5.7 times higher risk of developing platinum resistance in cases with high expression of HELQ in ascites tumor cells (relative risk (RR) 5.7, 95% CI 1.7-19.2). The platinum resistance risk was also higher in cases with high expression of XAB2 (RR 3.2, 95% CI 0.9-10.8) and with coexpression of HELQ and XAB2 (RR 5.2, 95% CI 1.8-15.2) (Figure 3(c)).

To validate the reliability of HELQ and XAB2 results in ascites tumor cells, we also determined the expression of HELQ and XAB2 in paired primary tumor tissues (Figure 4(a)). Consistent with ascites samples, a trend toward platinum resistance enrichment was observed in cases with high expression of HELQ and XAB2 in paired tumor tissues (Figures 4(b) and 4(c)), which supported HELQ and XAB2 as predictors of platinum resistance.

4. Discussion

Platinum-based chemotherapy has drastically improved the prognosis of EOC patients. Unfortunately, resistance to platinum drugs frequently occurs and limits the efficacy of chemotherapy. However, the absence of an effective

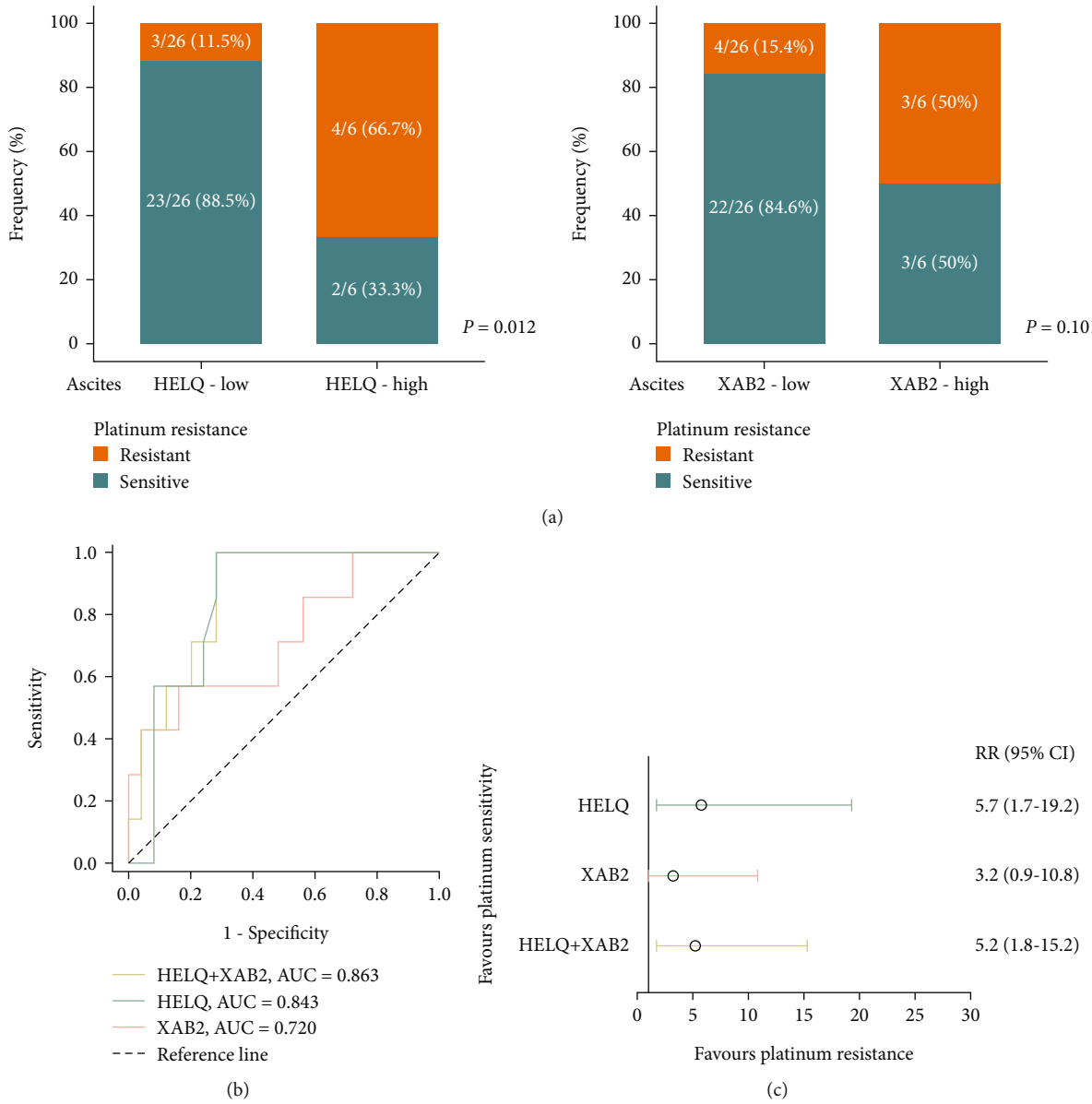

Figure 3: Expressions of HELQ and XAB2 in ascites tumor cells were positively correlated with chemoresistance of HGSC patients in validation cohort. (a) Frequency of platinum-resistant patients from the validation cohort was compared according to HELQ and XAB2 expressions. (b) Receiver operator characteristic curves with AUC according to relative expressions of HELQ and XAB2 in ascites tumor cells of patients with HGSC. (c) Forest plot for relative risk of the high expressions of HELQ and XAB2 in ascites tumor cells. RR: relative risk.

predictor of chemoresistance prior to systemic therapy initiation has resulted in patients receiving unindividualized chemotherapy regimen regardless [23, 24]. DNA damage repair (DDR) plays a critical role in the occurrence and development of numerous cancers [25–28]. Abnormal activation of DNA damage repair, such as the NER pathway, has been confirmed to be associated with the prognosis and platinum resistance in ovarian cancer [22, 29]. Previous study had confirmed that the high expression of HELQ in EOC tissues was associated with poor prognosis and platinum resistance [30].

70% of ovarian cancer is diagnosed at advanced stages, accompanied by extensive pelvic-abdominal metastasis and large amounts of ascites [31, 32]. Systemic therapy is indicated for these patients, and it is of great importance to obtain an accurate pathological diagnosis prior to the initiation of treatment. Ascites cytology, as a less invasive and more accessible alternative to primary tumor tissue biopsy, also provides prediction of chemoresistance. Therefore, the number of studies concerning ascites in ovarian cancer has been increasing. Goto et al. suggested that p16INK4a expression in ascites cells was a candidate marker in predicting primary response to chemotherapy and prognosis [4]. However, concerns have been raised about the application of ascites cytology in ovarian cancer regarding its reliability [33]. Previously, ascites cytology has been investigated as

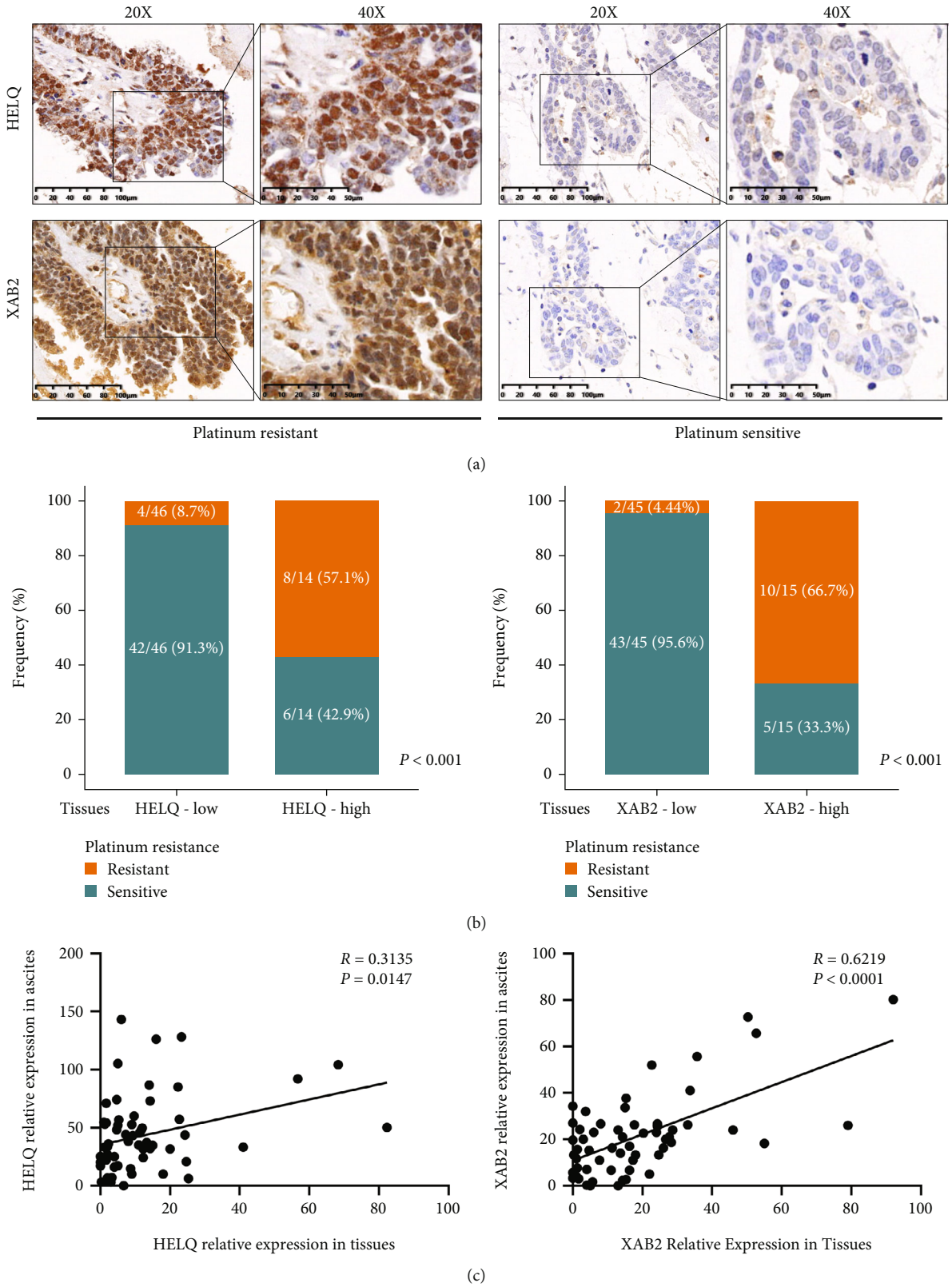

Figure 4: HELQ and XAB2 expressions in tumor tissues were correlated with that in ascites tumor cells. (a) Representative immunohistochemistry images of HELQ and XAB2 in tumor tissues of HGSC patients with platinum-resistant and platinum-sensitive phenotypes. (b) Frequency of platinum-resistant patients from the study cohort was compared according to HELQ and XAB2 expressions in tumor tissues. (c). Expressions of HELQ and XAB2 in ascites tumor cells were used to analyze the correlation with that in matched tumor tissues.

part of the diagnostic module for ovarian cancer and its efficacy has been proved [34, 35]. Additionally, ascites cytology has demonstrated noninferiority to primary tumor tissue sampling and blood samples in the determination of the patient's BRCA status [36, 37]. Our current finding showed that HELQ and XAB2 expressions in the ascites tumor cells correlated with HGSC patient's response to platinum-based chemotherapy and clinical outcomes indicate the potentiality of HELQ and XAB2 as independent biomarkers to predict HGSC patients' response to platinum drugs. More importantly, we observed good accordance of HELQ and XAB2 expressions between ascites tumor cells and paired tumor tissues tumor tissues in our study. Hence, the assessment of HELQ and XAB2 expression levels in ascites tumor cells may help clinicians to design individualized treatment strategies for HGSC patients.

Our study has confirmed that ovarian cancer patients with the high expression of HELQ or XAB2 had decreased PFS and OS, respectively. HELQ, an ATP-dependent $3'$-$5'$ DNA helicase, plays a pivotal role in DNA processing, including homologous recombination (HR) repair [30], by regulating related proteins in the NER pathway which, in turn, contributes to cellular response to cisplatin and patients' response to platinum-based chemotherapy [20]. In this study, the high expression of HELQ and XAB2 in ascites tumor cells may lead to an increase of the ability of DNA damage repair, such as the HR or NER pathway, and a decrease in apoptosis, which led to tumor cell tolerance to platinum drugs. As a member of the NER pathway, XAB2 protein participates in many biological processes such as transcription-couple DNA repair, ATRA-induced cellular differentiation, splicing, mRNA export, and transcription [38, 39]. Recent studies indicated that XAB2 also participated in the end step of HR [40]. However, the mechanism of HELQ and XAB2 leading to platinum resistance in ovarian cancer needs further exploration.

This study was limited by a relatively small number of cases and possible selection bias. Further analysis by a large prospective study is needed to confirm our findings. However, the results of our study suggested the assessment of HELQ and XAB2 expression levels in cytology of ascites could be a less invasive and convenient predictive method in HGSC especially in consideration of chemotherapy.

5. Conclusion

In summary, our findings demonstrated that immunocytochemistry for HELQ and XAB2 expressions in ascites tumor cells are applicable in prediction of the primary response to chemotherapy and prognosis. We recommend a large multicenter prospective study to confirm the clinical significance of HELQ and XAB2 in ascites tumor cells in HGSC be performed.

Data Availability

Publicly available datasets were analyzed in this study (https://portal.gdc.cancer.gov).

Conflicts of Interest

No potential conflicts of interest were disclosed.

Authors' Contributions

Fang Zhu contributed to the conceptualization, methodology, validation, investigation, and writing—original draft. Siyu Yang contributed to the conceptualization, software acquisition, formal analysis, and writing—original draft. Ming Lei contributed to the writing—reviewing and editing. Qiongqiong He contributed to the acquisition of resources and validation. Li-Sha Wu contributed to the conceptualization and writing—reviewing and editing. Yu Zhang contributed to the conceptualization, resources, supervision, and project administration. All authors read and approved the final manuscript.

Acknowledgments

The authors are grateful to the contributors of data to the public TCGA database. And this study was supported by the National Science and Nature Foundation (No. 82073323), Clinical Research Foundation of Xiangya Hospital (No. 2020LNJJ11), Natural Science Foundation of Hunan Province (No. 2021JJ31106) and Fundamental Research Funds for the Central Universities of Central South University (No. 2019zzts341).

Supplementary Materials

Figure S1. the flow diagram of high-grade serous ovarian cancer patients. Table S1: correlation between NER gene expression and survival in 339 ovarian cancer patients from TCGA. *(Supplementary Materials)*

References

[1] H. Sung, J. Ferlay, R. L. Siegel et al., "Global cancer statistics 2020: GLOBOCAN estimates of incidence and mortality worldwide for 36 cancers in 185 countries," *CA: a Cancer Journal for Clinicians*, vol. 71, no. 3, pp. 209–249, 2021.

[2] M. Markman, "Optimizing primary chemotherapy in ovarian cancer," *Hematology/Oncology Clinics of North America*, vol. 17, no. 4, pp. 957–968, 2003.

[3] M. A. Lisio, L. Fu, A. Goyeneche, Z. H. Gao, and C. Telleria, "High-grade serous ovarian cancer: basic sciences, clinical and therapeutic standpoints," *International Journal of Molecular Sciences*, vol. 20, no. 4, p. 952, 2019.

[4] T. Goto, M. Takano, J. Hirata et al., "p16INK4a expression in cytology of ascites and response to chemotherapy in advanced ovarian cancer," *International Journal of Cancer*, vol. 125, no. 2, pp. 339–344, 2009.

[5] D. A. Dungl, E. N. Maginn, and E. A. Stronach, "Preventing damage limitation: targeting DNA-PKcs and DNA double-strand break repair pathways for ovarian cancer therapy," *Frontiers in Oncology*, vol. 5, p. 240, 2015.

[6] W. R. Wiedemeyer, J. A. Beach, and B. Y. Karlan, "Reversing platinum resistance in high-grade serous ovarian carcinoma: targeting BRCA and the homologous recombination system," *Frontiers in Oncology*, vol. 4, p. 34, 2014.

[7] M. Shih Ie and R. J. Kurman, "Ovarian tumorigenesis: a proposed model based on morphological and molecular genetic analysis," *The American Journal of Pathology*, vol. 164, no. 5, pp. 1511–1518, 2004.

[8] S. P. Jackson and J. Bartek, "The DNA-damage response in human biology and disease," *Nature*, vol. 461, no. 7267, pp. 1071–1078, 2009.

[9] M. Goldstein and M. B. Kastan, "The DNA damage response: implications for tumor responses to radiation and chemotherapy," *Annual Review of Medicine*, vol. 66, no. 1, pp. 129–143, 2015.

[10] E. C. Friedberg, "How nucleotide excision repair protects against cancer," *Nature Reviews. Cancer*, vol. 1, no. 1, pp. 22–33, 2001.

[11] K. V. Ferry, T. C. Hamilton, and S. W. Johnson, "Increased nucleotide excision repair in cisplatin-resistant ovarian cancer cells: role of ERCC1-XPF," *Biochemical Pharmacology*, vol. 60, no. 9, pp. 1305–1313, 2000.

[12] R. Agarwal and S. B. Kaye, "Ovarian cancer: strategies for overcoming resistance to chemotherapy," *Nature Reviews. Cancer*, vol. 3, no. 7, pp. 502–516, 2003.

[13] D. Grisaru, N. Michaan, L. Gortzak-Uzan, and I. Laskov, "The accuracy of ascites cytology in diagnosis of advanced ovarian cancer in postmenopausal women prior to neoadjuvant chemotherapy; methodological issues - answer," *Menopause*, vol. 27, no. 8, pp. 964-965, 2020.

[14] R. Zivadinovic, A. Petric, D. Krtinic, and J. Stevanovic Milosevic, "Ascites in ovarian carcinoma - reliability and limitations of cytological analysis," *The West Indian Medical Journal*, vol. 64, no. 3, pp. 236–240, 2015.

[15] J. L. Dennis, T. R. Hvidsten, E. C. Wit et al., "Markers of adenocarcinoma characteristic of the site of origin: development of a diagnostic algorithm," *Clinical Cancer Research*, vol. 11, no. 10, pp. 3766–3772, 2005.

[16] A. Basu and S. Krishnamurthy, "Cellular responses to cisplatin-induced DNA damage," *Journal of Nucleic Acids*, vol. 2010, 16 pages, 2010.

[17] M. Okour, P. A. Jacobson, A. Israni, and R. C. Brundage, "Comparative evaluation of median versus Youden index dichotomization methods: exposure-response analysis of mycophenolic acid and acyl-glucuronide metabolite," *European Journal of Drug Metabolism and Pharmacokinetics*, vol. 44, no. 5, pp. 629–638, 2019.

[18] E. Cholongitas, I. Goulis, M. Ioannidou, S. Soulaidopoulos, P. Chalevas, and E. Akriviadis, "Urine albumin-to-creatinine ratio is associated with the severity of liver disease, renal function and survival in patients with decompensated cirrhosis," *Hepatology International*, vol. 11, no. 3, pp. 306–314, 2017.

[19] K. A. Deborah, D. A. Ronald, and N. B. Jamie, *The NCCN Ovarian Cancer/Fallopian Tube Cancer/Primary Peritoneal Cancer clinical practice guidelines in oncology (Version 1.2021)[EB/OL]*, NCCN, Fort Washington, 2021.

[20] T. Uehara, H. Yoshida, M. Fukuhara et al., "Efficacy of ascitic fluid cell block for diagnosing primary ovarian, peritoneal, and tubal cancer in patients with peritoneal carcinomatosis with ascites," *Gynecologic Oncology*, vol. 157, no. 2, pp. 398–404, 2020.

[21] S. L. Cooke and J. D. Brenton, "Evolution of platinum resistance in high-grade serous ovarian cancer," *The Lancet Oncology*, vol. 12, no. 12, pp. 1169–1174, 2011.

[22] J. Long, J. Y. Zhu, Y. B. Liu et al., "Helicase POLQ-like (HELQ) as a novel indicator of platinum-based chemoresistance for epithelial ovarian cancer," *Gynecologic Oncology*, vol. 149, no. 2, pp. 341–349, 2018.

[23] R. Cornelison, D. C. Llaneza, and C. N. Landen, "Emerging therapeutics to overcome chemoresistance in epithelial ovarian cancer: a mini-review," *International Journal of Molecular Sciences*, vol. 18, no. 10, p. 2171, 2017.

[24] J. F. Goodwin, M. J. Schiewer, J. L. Dean et al., "A hormone-DNA repair circuit governs the response to genotoxic insult," *Cancer Discovery*, vol. 3, no. 11, pp. 1254–1271, 2013.

[25] M. Majidinia and B. Yousefi, "DNA repair and damage pathways in breast cancer development and therapy," *DNA Repair (Amst)*, vol. 54, pp. 22–29, 2017.

[26] J. Mateo, G. Boysen, C. E. Barbieri et al., "DNA repair in prostate cancer: biology and clinical implications," *European Urology*, vol. 71, no. 3, pp. 417–425, 2017.

[27] J. S. Saldivar, X. Wu, M. Follen, and D. Gershenson, "Nucleotide excision repair pathway review I: implications in ovarian cancer and platinum sensitivity," *Gynecologic Oncology*, vol. 107, no. 1, pp. S56–S71, 2007.

[28] J. Kang, A. D. D'Andrea, and D. Kozono, "A DNA repair pathway-focused score for prediction of outcomes in ovarian cancer treated with platinum-based chemotherapy," *Journal of the National Cancer Institute*, vol. 104, no. 9, pp. 670–681, 2012.

[29] X. Han, L. Zhao, and X. Li, "HELQ in cancer and reproduction," *Neoplasma*, vol. 63, no. 6, pp. 825–835, 2016.

[30] C. A. Adelman, R. L. Lolo, N. J. Birkbak et al., "HELQ promotes RAD51 paralogue-dependent repair to avert germ cell loss and tumorigenesis," *Nature*, vol. 502, no. 7471, pp. 381–384, 2013.

[31] J. A. Doherty, L. C. Peres, C. Wang, G. P. Way, C. S. Greene, and J. M. Schildkraut, "Challenges and opportunities in studying the epidemiology of ovarian cancer subtypes," *Current Epidemiology Reports*, vol. 4, no. 3, pp. 211–220, 2017.

[32] S. Lheureux, C. Gourley, I. Vergote, and A. M. Oza, "Epithelial ovarian cancer," *Lancet*, vol. 393, no. 10177, pp. 1240–1253, 2019.

[33] P. E. Schwartz and W. Zheng, "Neoadjuvant chemotherapy for advanced ovarian cancer: the role of cytology in pretreatment diagnosis," *Gynecologic Oncology*, vol. 90, no. 3, pp. 644–650, 2003.

[34] Y. Wang, Y. Wang, J. Li et al., "PAX8: a sensitive and specific marker to identify cancer cells of ovarian origin for patients prior to neoadjuvant chemotherapy," *Journal of Hematology & Oncology*, vol. 6, no. 1, p. 60, 2013.

[35] S. Baransi, N. Michaan, L. Gortzak-Uzan et al., "The accuracy of ascites cytology in diagnosis of advanced ovarian cancer in postmenopausal women prior to neoadjuvant chemotherapy," *Menopause*, vol. 27, no. 7, pp. 771–775, 2020.

[36] A. Gornjec, S. Novakovic, V. Stegel et al., "Cytology material is equivalent to tumor tissue in determining mutations of BRCA 1/2 genes in patients with tubo-ovarian high grade serous carcinoma," *BMC Cancer*, vol. 19, no. 1, p. 296, 2019.

[37] C. Fumagalli, A. Rappa, C. Casadio et al., "Next-generation sequencing-based BRCA testing on cytological specimens from ovarian cancer ascites reveals high concordance with tumour tissue analysis," *Journal of Clinical Pathology*, vol. 73, no. 3, pp. 168–171, 2020.

[38] I. Kuraoka, S. Ito, T. Wada et al., "Isolation of XAB2 complex Involved in pre-mRNA splicing, transcription, and transcription-coupled repair," *The Journal of Biological Chemistry*, vol. 283, no. 2, pp. 940–950, 2008.

[39] K. Ohnuma-Ishikawa, T. Morio, T. Yamada et al., "Knockdown of XAB2 enhances all-trans retinoic acid-induced cellular differentiation in all-trans retinoic acid-sensitive and -resistant cancer cells," *Cancer Research*, vol. 67, no. 3, pp. 1019–1029, 2007.

[40] D. O. Onyango, S. M. Howard, K. Neherin, D. A. Yanez, and J. M. Stark, "Tetratricopeptide repeat factor XAB2 mediates the end resection step of homologous recombination," *Nucleic Acids Research*, vol. 44, no. 12, pp. 5702–5716, 2016.

Hindawi
Journal of Oncology
Volume 2022, Article ID 1087399, 21 pages
https://doi.org/10.1155/2022/1087399

Research Article

Analysis of the Heterogeneity of the Tumor Microenvironment and the Prognosis and Immunotherapy Response of Different Immune Subtypes in Hepatocellular Carcinoma

Jian Hu,[1] **Feifei Mao**,[2] **Lifang Li**,[3] **Xiaoqian Wang**,[1] **Depei Cai**,[4] **Longmei He**,[5] **Qian Wu**,[1] **Cong Wang**,[1] **Ning Zhang**,[1] **Yanfen Ma**,[1] **Xia Wu**,[6] **Kai Qu**,[7] **and Xiaoqin Wang**[1]

[1]*Department of Clinical Laboratory, The First Affiliated Hospital of Xi'an Jiaotong University, Xi'an, 710061 Shaanxi Province, China*
[2]*Tongji University Cancer Center, Shanghai Tenth People's Hospital, School of Medicine, Tongji University, Shanghai 200072, China*
[3]*Emergency Department, The First Affiliated Hospital of Xi'an Jiaotong University, Xi'an, 710061 Shaanxi Province, China*
[4]*Department of Clinical Laboratory, Xi'an Aerospace General Hospital, Xi'an, 710061 Shaanxi Province, China*
[5]*Department of Clinical Laboratory, Shaanxi Provincial Hospital of Chinese Medicine, Xi'an, 710082 Shaanxi Province, China*
[6]*Department of Clinical Laboratory, Xi'an Chest Hospital, Xi'an, 710061 Shaanxi Province, China*
[7]*Department of Hepatobiliary Surgery, The First Affiliated Hospital of Xi'an Jiaotong University, Xi'an, 710061 Shaanxi Province, China*

Correspondence should be addressed to Xiaoqian Wang; wangxiaoqian9510@163.com and Kai Qu; joanne8601@163.com

Received 21 January 2022; Accepted 4 March 2022; Published 29 March 2022

Academic Editor: Guo Chen

Purpose. The current clinical classification of hepatocellular carcinoma (HCC) cannot well predict the patient's possible response to the treatment plan, nor can it predict the patient's prognosis. We use the gene expression patterns of patients with hepatocellular carcinoma to reveal the heterogeneity of hepatocellular carcinoma and analyze the differences in prognosis and immunotherapy response of different immune subtypes. *Methods*. Firstly, using the hepatocellular carcinoma expression profile data of TCGA, combined with the single sample gene set enrichment analysis (ssGSEA) algorithm, the immune enrichment of the patient's tumor microenvironment was analyzed. Subsequently, the spectral clustering algorithm was used to extract different classifications, and the cohort of hepatocellular carcinoma was divided into 3 subtypes, and the correlation between immune subtypes and clinical characteristics and survival prognosis was established. The patient's risk index is obtained through the prognostic prediction model, suggesting the correlation between the risk index and various types of immune cells. *Results*. We can divide the liver cancer cohort into three subtypes: stromal cell activated immune-enriched type (A-IS), general immune-enriched type (N-IS), and non-immune-enriched type (non-IS). The 3-year survival rate of TCGA's A-IS is higher than that of N-IS and non-IS, and the three components are significantly different ($p = 0.017$). The 3-year survival rates of ICGC's A-IS and N-IS groups were higher than those of the non-IS group. The analysis of the correlation between the risk index and immune cells showed that the patient's disease risk was significantly positively correlated with cancer-associated fibroblast (CAF) stimulated cell, activated stroma cell, and anti-PD-1 resistant cell. *Conclusion*. The tumor gene expression characteristics of patients with hepatocellular carcinoma can be used as a basis for clinical patient classification. Different immune subtypes are closely related to survival prognosis. Different immune cell states of patients may lead to different disease risk levels. All these provide important references for the clinical identification and prognosis prediction of hepatocellular carcinoma.

1. Introduction

Liver cancer is still a global health challenge, which is expected to have more than 1 million cases by 2025. Hepatocellular carcinoma (HCC) is the most common form of liver cancer, accounting for 90% of cases [1, 2]. Its main risk factors include hepatitis B virus (HBV) and hepatitis C virus (HCV) infections [3–6], and metabolic syndrome and alcohol intake are becoming more common risk factors [7, 8].

The classification of HCC is based on the Barcelona-Clinical-Liver Cancer (BCLC) classification [2, 9, 10]. The system defines five subcategories of HCC and provides specific treatment recommendations for each category, including surgical resection, liver transplantation, radiofrequency ablation, chemoembolization, and multikinase inhibitor sorafenib [2]. However, the high recurrence rate of resectable liver cancer leads to a poor prognosis [11]. Recurrence seriously affects the long-term survival of HCC patients [12]. Due to the emergence of primary and secondary drug resistance, sorafenib only works in some patients with HCC, and its therapeutic effect is limited. Primary drug resistance is mainly due to genetic heterogeneity [13]. To make matters worse, almost all patients will develop secondary resistance to sorafenib within 6 months, and the recurrence rate of patients has not been significantly reduced [14]. At present, it is generally believed that the high heterogeneity of HCC, including genetic heterogeneity and immune heterogeneity, is the main reason for treatment failure [15, 16]. Among them, immune heterogeneity is one of the main reasons why current therapies are ineffective against most types of cancer, including HCC. Therefore, a comprehensive and accurate understanding of the heterogeneity of the tumor immune microenvironment of HCC is essential to improve the efficiency of personalized treatment of HCC.

In recent years, analysis and research based on HCC high-throughput data expression profile have been devoted to unraveling the molecular characteristics of HCC heterogeneity [17–20]. Although researchers have stratified clinical samples based on molecular markers, they have not yet fully clarified the correlation between the new subtypes and clinic pathological characteristics. Recently, researchers have divided HCC patients into three subgroups from the perspective of metabolism, namely, metabolic subgroup (S-Mb), microenvironment disorder subgroup (S-Me), and proliferation subgroup. Among them, the S-Me subtype enriched in proteins involved in immunity and inflammation and has a worse prognosis than S-Mb [21].

We evaluated the expression profile characteristics, immune enrichment characteristics, matrix enrichment characteristics, prognostic value, and other information of the HCC cohort, aiming to characterize the molecular characteristics of HCC by developing immune and matrix-related gene expression profiles. Comprehensive analysis was performed using the metadata set of 371 HCC human samples from The Cancer Genome Atlas (TCGA), and GSE144269 ($n = 70$), GSE14520_cohort1 ($n = 22$), GSE14520_cohort2 ($n = 225$), GSE25097_GPL10687 ($n = 268$), GSE36376_GPL10558 ($n = 240$), and ICGC_LIRI_JP ($n = 232$) data sets are used to verify the enrichment of immune-related molecules.

All samples are associated with clinical information, and the correlation between patient subtype and survival rate is verified in the ICGC data set. Three subtypes of HCC have been preliminarily identified: stromal cell-activated immune-enriched type (A-IS), general immune-enriched type (N-IS), and non-immune-enriched type (non-IS). Then, we analyzed the metadata set of immune activity characteristics, clinical characteristics, and prognostic value. Subclass A-IS shows active stromal enrichment, high immunological activity, and good prognosis. The subtype N-IS exhibits normal stromal activity, average middle immune activity, and normal survival. The subtype non-IS shows low matrix enrichment, low immune-related enrichment, and poor prognosis. In this study, a new classification of HCC was established based on the gene expression profile of immunity and matrix, thereby further revealing the diversity of human HCC.

2. Results

2.1. Classification of Gene Expression Patterns in Patients Presenting with Hepatocellular Carcinoma. We applied the spectral clustering algorithm to extract expression patterns from liver cancer samples in TCGA cohort, based on the expression profile data of TCGA (Figure 1(a)). At the same time, we used t-Distributed Stochastic Neighbor Embedding (tSNE) to show the subgroups among samples (Figure 1(b)). Based on the above classification, we further analyzed the immune enrichment situation of the tumor microenvironment of each subgroup through the single sample gene set enrichment analysis (ssGSEA) algorithm. The immune-related gene set comes from the following references (Table 1).

The analysis results showed that there was a subtype with immune-related genetic enrichment (IS) in the cohort, and the rest were non-IS types, that is, types with less immune infiltration (Figure 1(c)). We found that patients with immune-enriched subtypes were significantly enriched in the characteristics of identifying immune cells or immune responses ($p < 0.05$). In addition, even in the presence of massive immune cells, stromal cells play an essential role in tumor immune escape. Therefore, we further dissected the enrichment of stromal cells in the gene expression profile of immune enrichment subtypes. Likewise, we found that there are features of activated stromal response in the cohort by ssGSEA (Figure 1(c)). Overall, we divided hepatocellular carcinoma cohort into three subtypes: A-IS, N-IS, and non-IS.

2.2. Validation of Immune Subtype Classification of Cohort Patients. As shown below, the three subtypes have the following immune differences (Figure 2(a)). Compared with non-IS and N-IS (Figure 2(a), blue box), A-IS subtypes showed significant enrichment in identifying immune cells or immune response characteristics (all $p < 0.01$) including B cells, immune enrichment score, macrophages, mast cells, and Th1 cells. We further compared the differentially

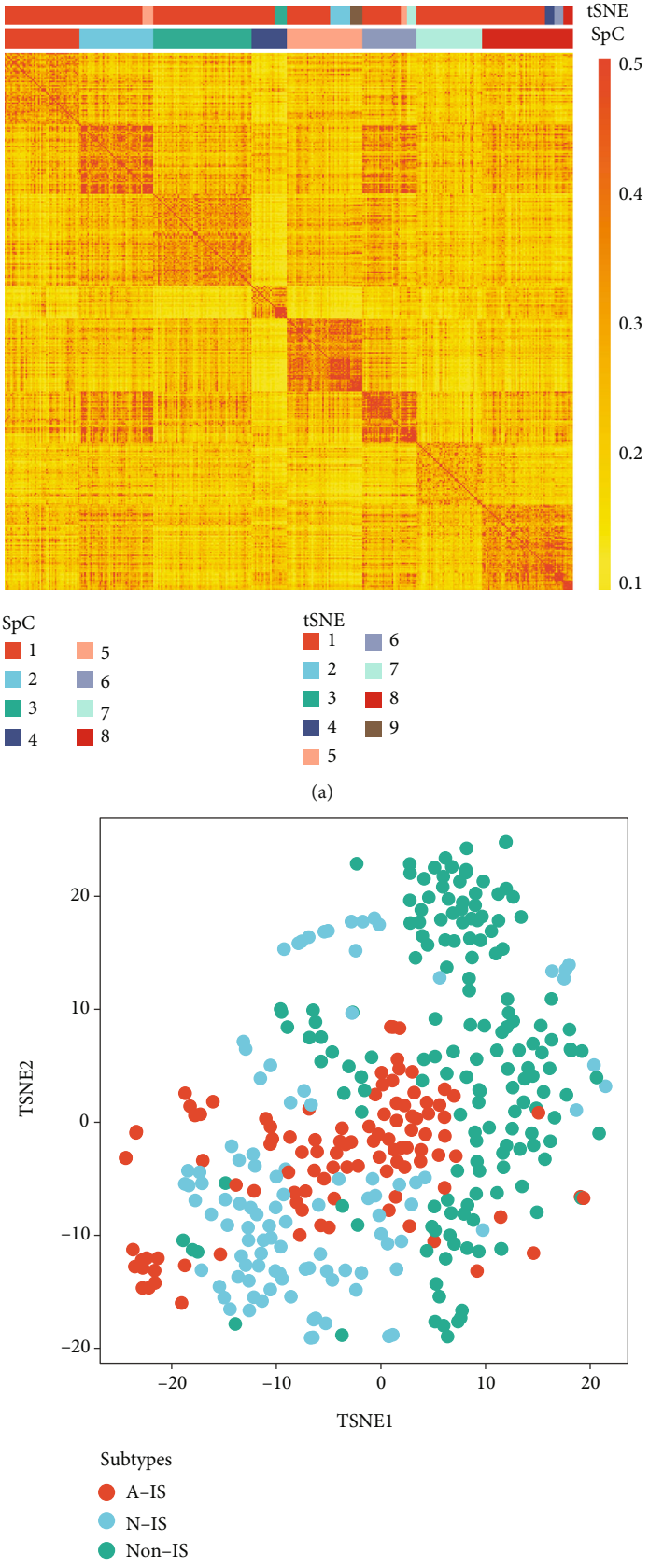

Figure 1: Continued.

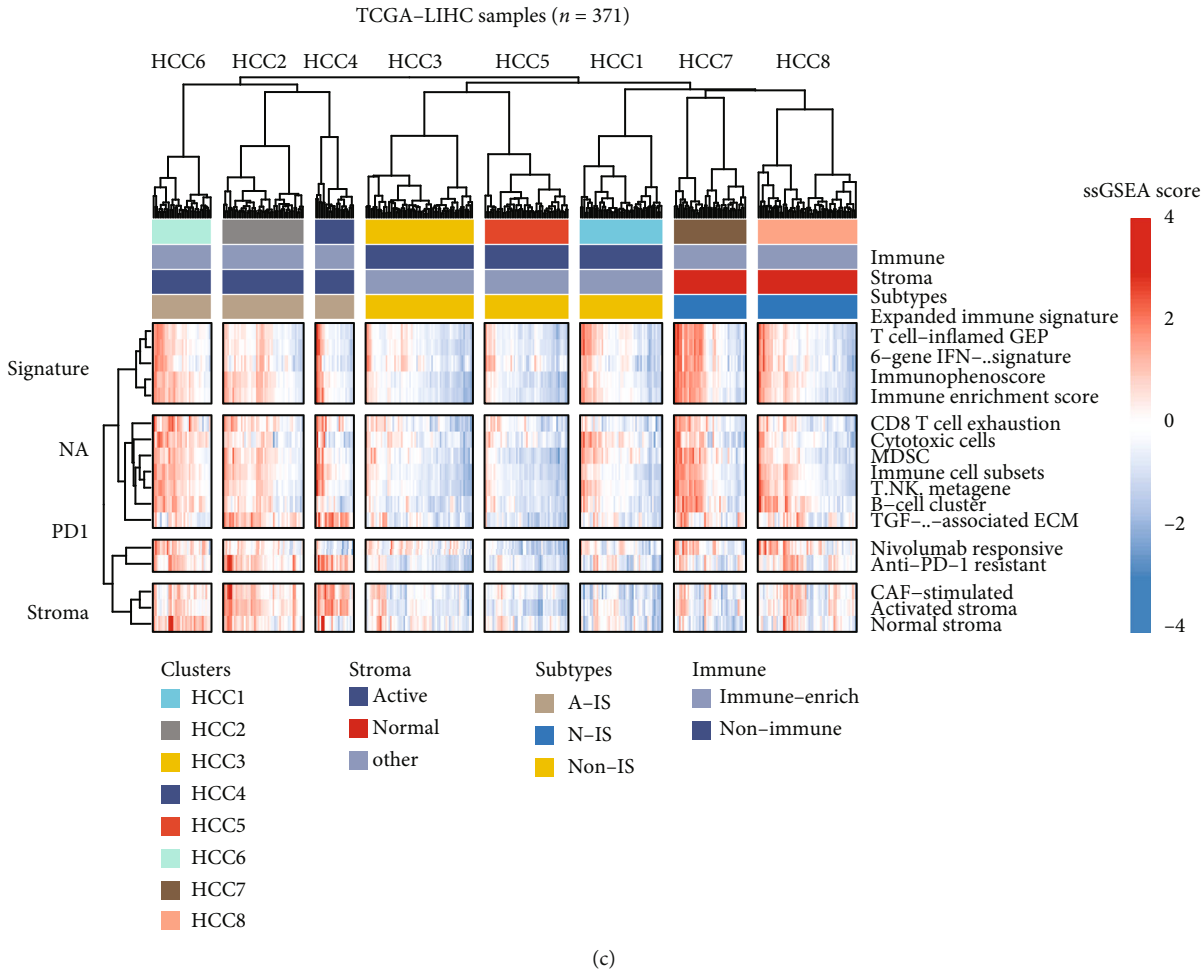

(c)

Figure 1: Classification of gene expression patterns in patients presenting with hepatocellular carcinoma. (a) Classification of gene expression patterns of hepatocellular carcinoma patients. The spectral clustering algorithm is used to extract expression patterns from hepatocellular carcinoma samples in TCGA cohort. According to different expression patterns, patients can be divided into 8 subgroups including HCC1, HCC2, HCC3, HCC4, HCC5, HCC6, HCC7, and HCC8. SpC stands for spectral clustering. (b) The plot shows the tSNE clustering of different subsets, and the distribution of each subtype is relatively concentrated. (c) The ssGSEA algorithm reveals the immune enrichment of the tumor microenvironment of each subtype, and divides all patients into three subgroups based on immunity and stromal-related features. The latest taxa included stromal cell-activated immune-enriched subtype (A-IS), normal immune-enriched subtype (N-IS) and non-immune-enriched subtype (non-IS).

expressed genes of IS (including A-IS and N-IS) and non-IS subtypes, mainly using the limma algorithm and $p < 0.05$ as the criterion for significant differences (Table S1). At the same time, the genes with significant differences between A-IS and N-IS subtypes were compared (Table S2). We found that representative genes with significant differences are closely related to immune recognition and immune response. In order to verify the accuracy and consistency of the analysis method, we use the same strategy to verify it in other independent data. Our verification strategy is to select the top 50 genes that are differentially upregulated to construct a gene set and use the ssGSEA algorithm to predict the enrichment of other data. In addition, we selected cells with significant differences in immunological activity for verification. The analysis results were shown below including the GSE144269 data set (Figure 2(b), $n = 70$), the GSE14520_cohort1_test data set (Figure 2(c), $n = 22$), the GSE14520_cohort2_train samples (Figure 2(d), $n = 225$), the GSE25097_GPL10687 samples (Figure 2(e), $n = 268$), GSE36376_GPL10558 (Figure 2(f), $n = 240$) data set, and ICGC_LIRI_JP samples (Figure 2(g), $n = 232$). In the Mongolian hepatocellular carcinoma (HCC) patient cohort, we found that compared with the HCC1 patient population, immune and stromal enrichment was common in the HCC2 patient population (Figure 2(b)). Each subject in the HCC2 panel has hepatitis virus HDV and HBV infection [22]. Studies have shown that HDV RNA pattern recognition can activate immunity [23], and it has also been reported that L-HDAg, consisting of 214 amino acids, can directly induce IFN signaling [24]. Moreover, HBV-HDV coinfection shows a strong immune response [23]. xCell-aDC, B cells, immune enrichment score, myeloid-derived suppressor cells (MDSC), activated stroma, and other immune- and stromal-related features represented in

Table 1: Immune-related signatures and references.

Signature name	Reference
Immune enrichment score	Yoshihara et al. Nat Commun. 2013 [37]
6-gene IFN-γ signature	Chow et al. J Clin Oncol. 2016 (suppl) [56]
Activated stroma	Moffitt et al. Nat Genet. 2015 [43]
Immune cell subsets	Cancer Genome Atlas Network. Cell. 2015 [57]
T cells	Bindea et al. Immunity. 2013 [58]
CD8 T cells	Bindea et al. Immunity. 2013 [58]
T. NK. metagene	Alistar et al. Genome Med. 2014 [59]
B-cell cluster	Iglesia et al. Clin Cancer Res. 2014 [60]
Macrophages	Bindea et al. Immunity. 2013 [58]
Cytotoxic cells	Bindea et al. Immunity. 2013 [58]
Immunophenoscore	Charoentong et al. Cell Rep. 2017 [61]
T cell-inflamed GEP	Cristescu et al. Science. 2018 [36]
Expanded immune signature	Ayers et al. J Clin Invest. 2017 [62]
TGF-β-associated ECM	Chakravarthy et al. Nat Commun. 2018 [35]
MDSC	Yaddanapudi et al. Cancer Immunol Res. 2016 [63]
CAF	Calon et al. Cancer Cell. 2012 [64]
TAM M2/M1	Beyer et al. PLoS One. 2012 [65]
CD8 T cell exhaustion	Giordano et al. EMBO J. 2015 [66]
T cell exhaustion early/late stage	Philip et al. Nature 2017 [67]
Nivolumab responsive	Riaz et al. Cell. 2017 [68]

most of HCC2 in GSE14520_cohort1 (Figure 2(c)). Similarly, certain subgroups of GSE14520_cohort2, mainly including HCC1 (pink box) and HCC3 (blue box), arose the enrichment of immune and stromal signatures (Figure 2(d)). HCC3, HCC5, HCC6 and HCC7 in the GSE25097_GPL10687 cohort showed biomarker enrichment on the immune and stoma response (Figure 2 (e)). Certain subgroups in the ICGC_LIRI_JP cohort, mainly including HCC6, HCC4, and HCC7, have enrichment of immune and stromal features (Figure 2(f)). However, in the GSE36376_GPL10558 (Figure 2(e)) cohort, multiple subtypes have patients with both immune- and matrix-related enrichment and nonenriched. It suggests that the existing HCC classification method cannot cover all patients. Our research strategy might provide more references for the clinical classification of HCC patients.

2.3. Differences in Immune Subtypes Are Related to Clinical Features and Survival Prognosis. We have preliminarily determined that different patient subsets have differences in immune- and matrix-related signatures. So, whether or what clinical information might be associated with immune alterations? Firstly, we collected and sorted out the clinical information of all patients within three immune subtypes (Table 2). The statistical results showed that clinical indicators such as age_at_initial_pathologic_diagnosis, neoplasm_histologic_grade, and vascular_tumor_cell_type in different subgroups are strikingly different among three subpopulations ($p < 0.01$). The value of albumin_result_upper_limit of the A-IS subgroup is significantly larger than that of the N-IS and non-IS subgroups, since the age at initial pathologic diagnosis has differential survival advantages in fibrolamellar hepatocellular carcinoma (FLHCC) and hepatocellular carcinoma (HCC) [25]. And, the albumin/globulin ratio can provide guidance for the postoperative prognosis and survival prediction of HCC patients [26]. Therefore, prognostic inquiry among all subtypes matters hugely. Fortunately, we found that the three-year survival of A-IS was higher than that of N-IS and non-IS, and there is significance of intergroup variations (p value < 0.05) in TCGA cohort (Figure 3(a)). Nevertheless, the five-year survival of A-IS was not improving in the same cohort (Figure 3(b)). Similarly, the three-year (Figure 3(c)) and ten-year (Figure 3(d)) survival of patients in the ICGC cohort was compared in detail, which exhibited similar trends; that is, A-IS and N-IS have higher survival than non-IS.

2.4. Prognostic Prediction Model Based on Signatures of Tumor Microenvironment. In order to clarify the molecular markers related to the prognosis of HCC patients, we screened the characteristic genes of immune subtypes, combined with the random forest algorithm to construct a predictive model. We took TCGA data as the training set and filter to the following signatures. At the same time, the risk coefficient (β value) of Cox multiple regression is introduced to predict the risk coefficient of each patient. We calculated the risk score (risk score) of each patient based on the expression of the 96-gene panel and the multiple Cox regression coefficient (Table 3). These 96 genes were enriched in the calcium signaling pathway and neuroactive ligand-receptor interaction pathway, which have been known to be involved in the HCC. The risk index is used to analyze

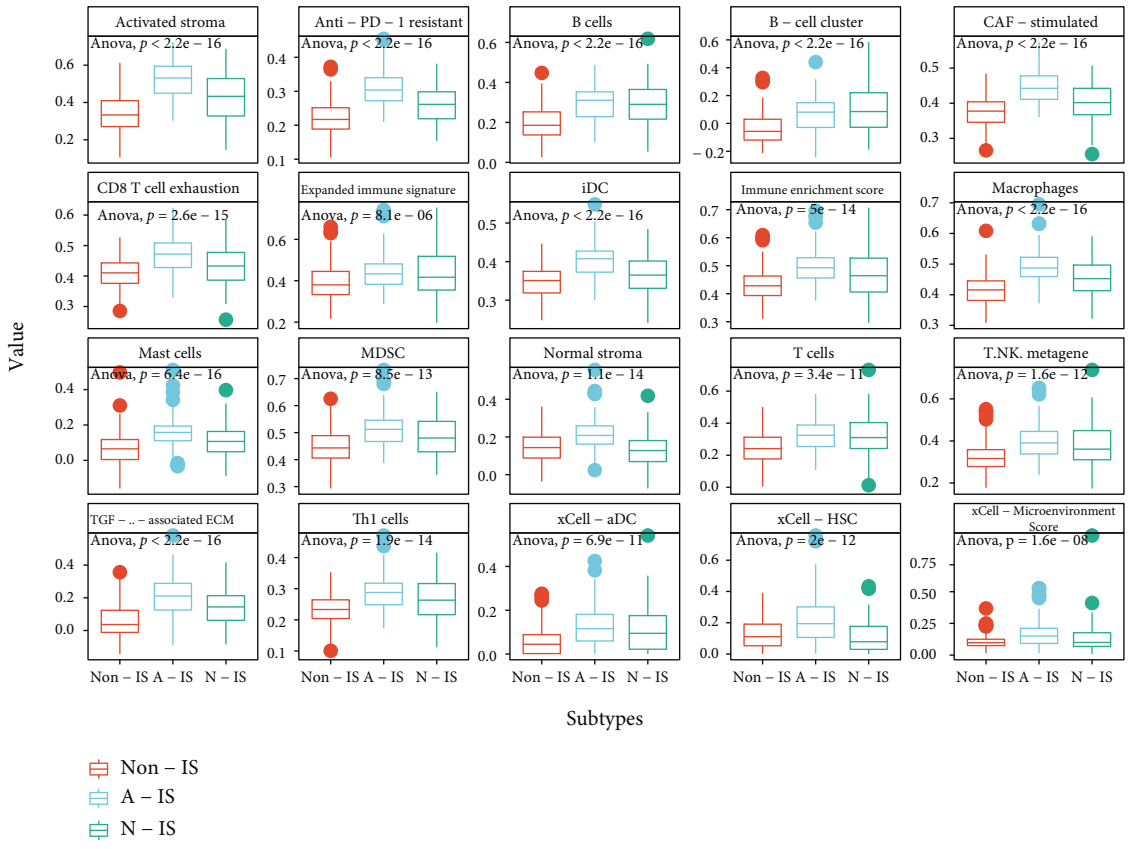

(a)

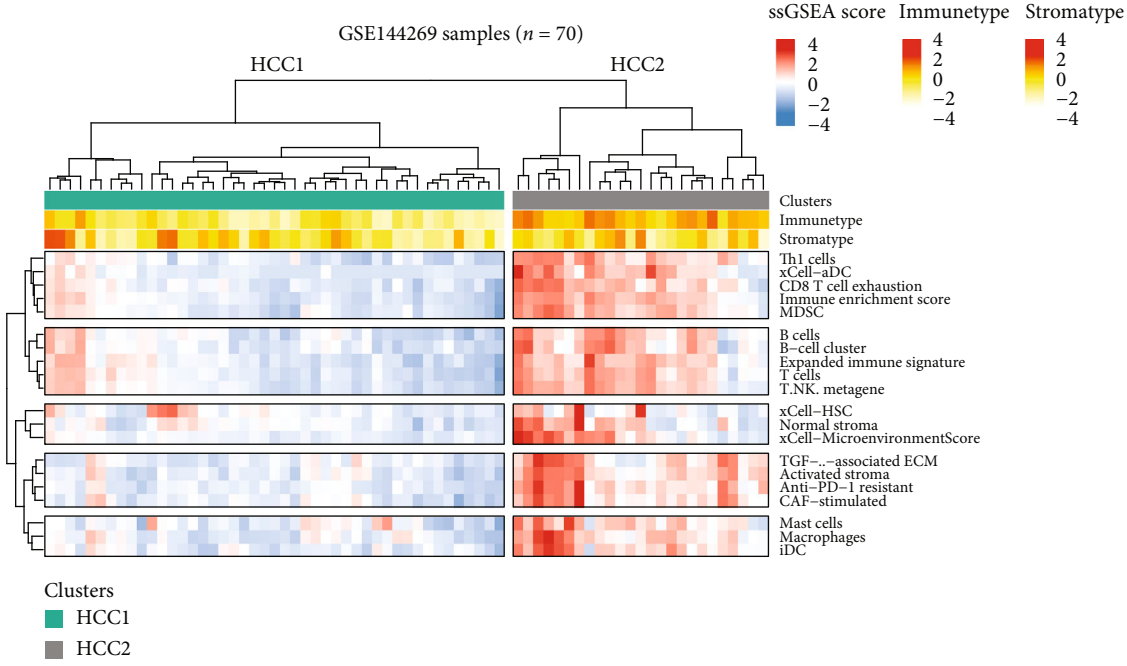

(b)

Figure 2: Continued.

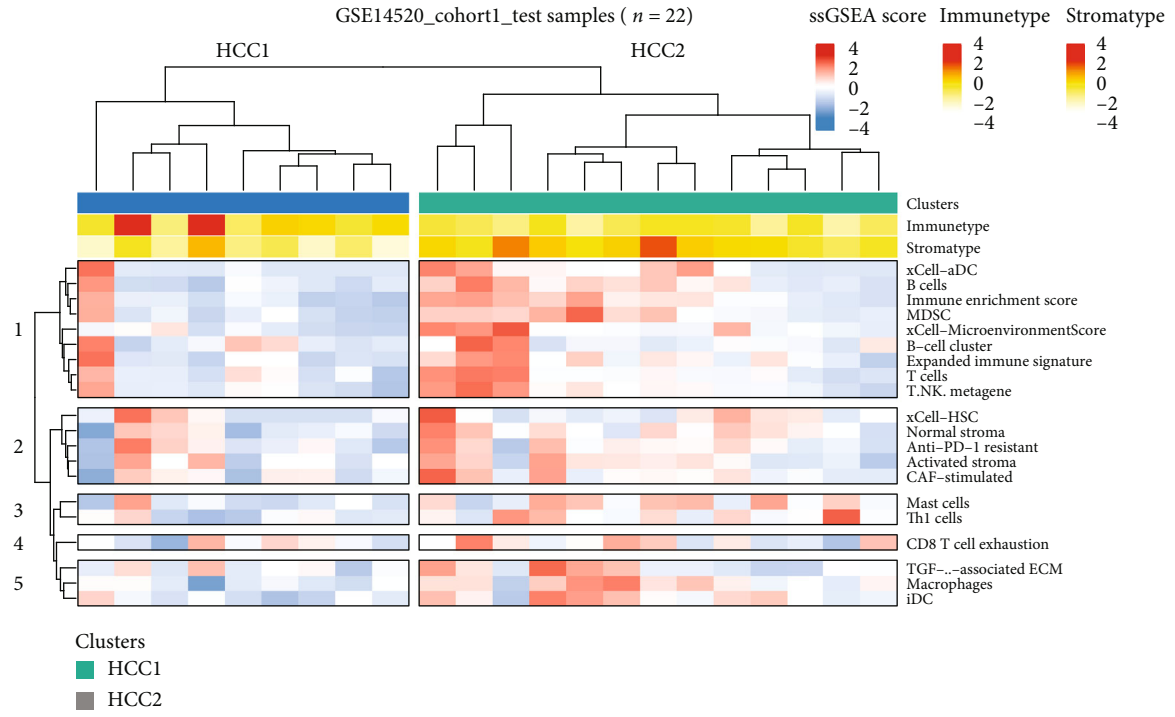

(c)

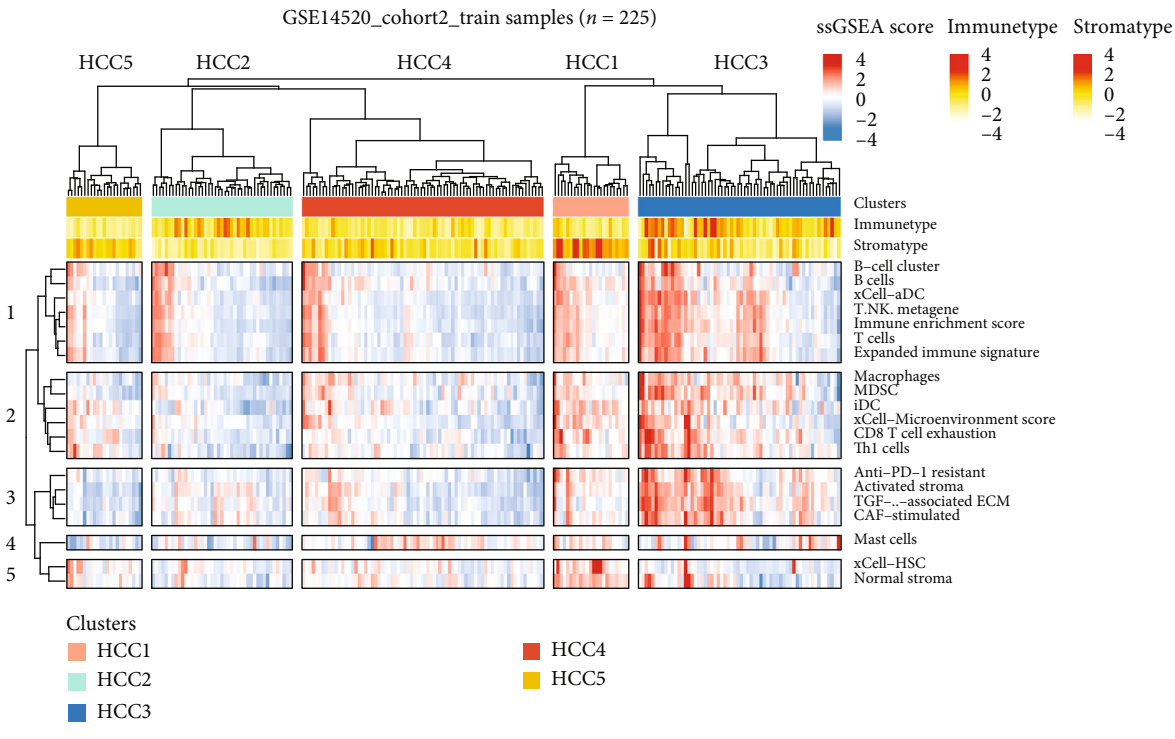

(d)

Figure 2: Continued.

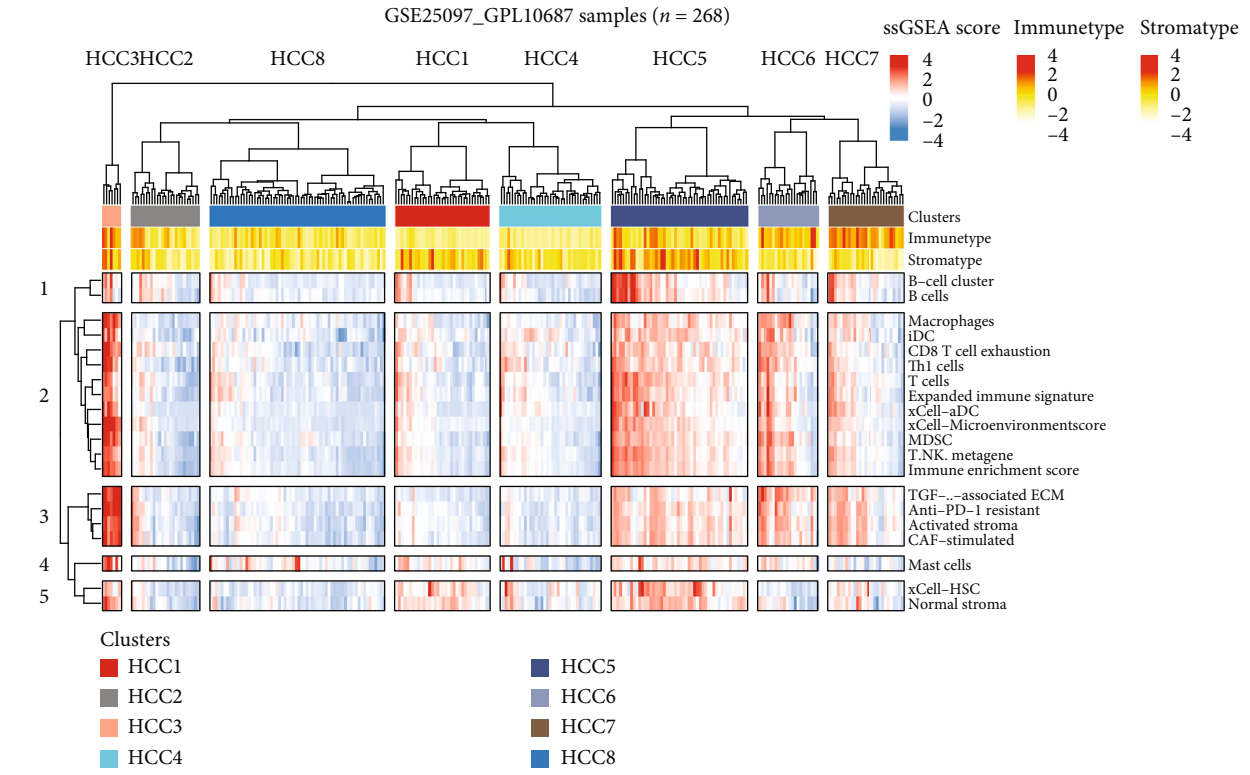

(e)

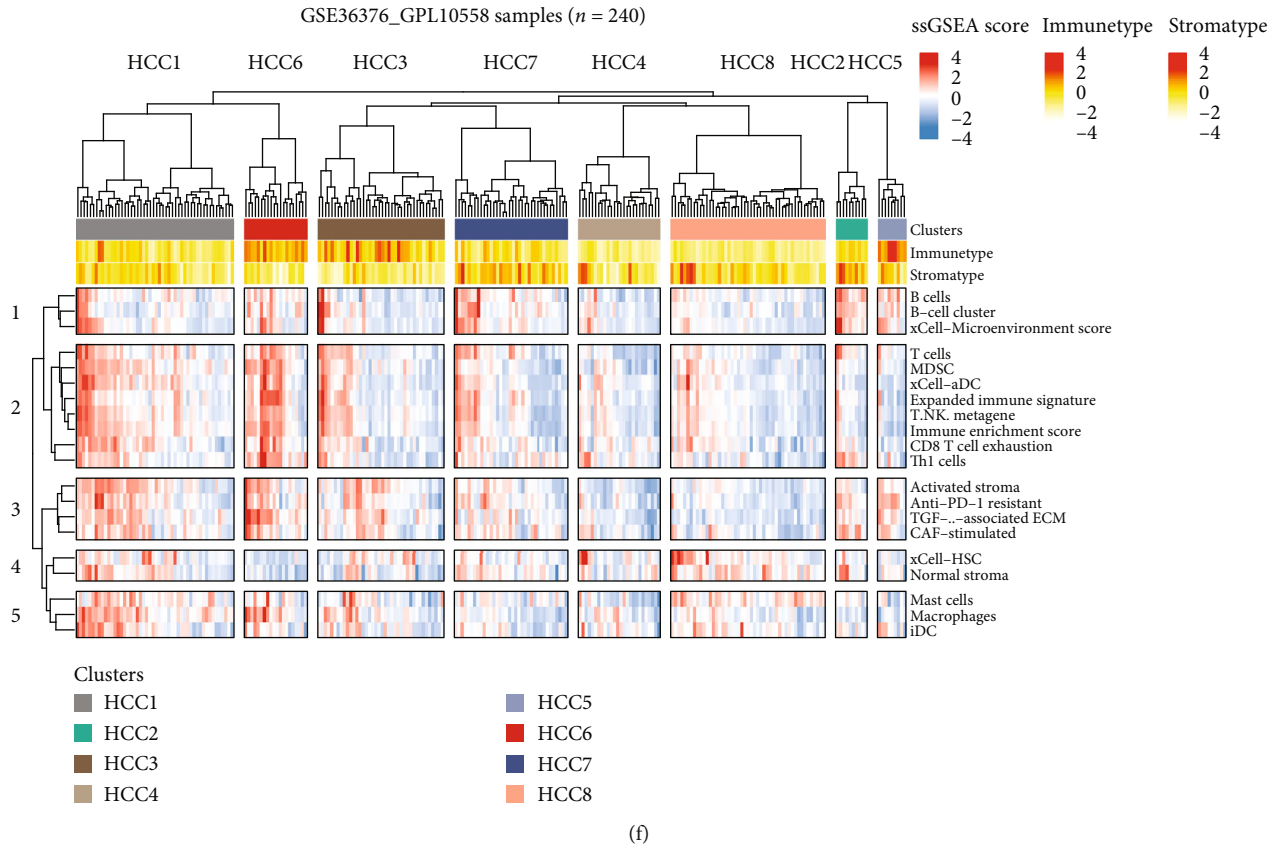

(f)

Figure 2: Continued.

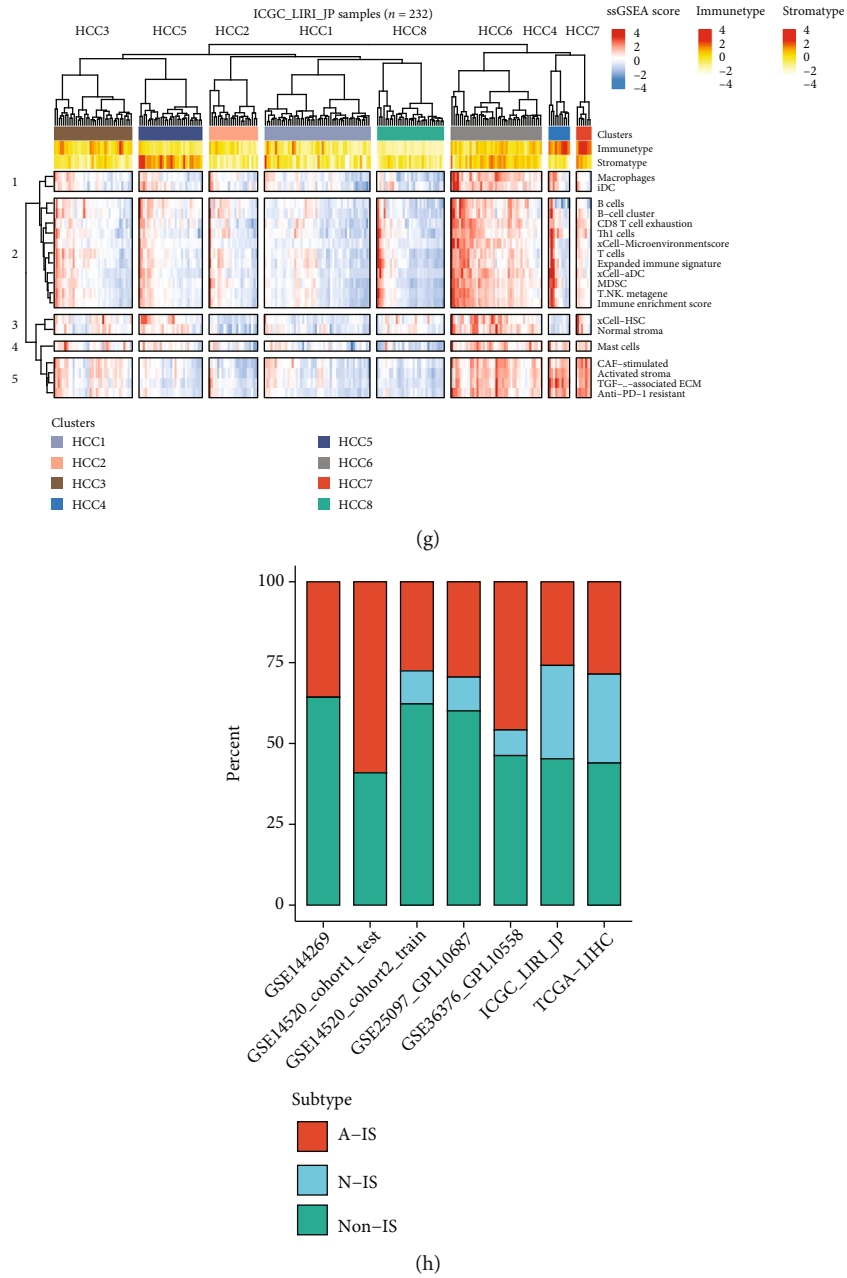

Figure 2: Validation of immune subtype classification of cohort patients. (a) Comparison of the striking differences in the immune microenvironment of the three subtypes. The red box represents non-immune-enriched subtype (non-IS), the blue box represents stromal cell-activated immune-enriched subtype (A-IS), and the green box represents normal immune-enriched subtype (N-IS). Anti-PD-1 resistant, B cell, immune enrichment score, macrophages, and other immune characteristics were significantly different among three subgroups (ANOVA test, $p < 0.01$). (b) The ssGSEA algorithm was performed on the GSE144269 data set ($n = 70$). Th1 cells, CD8 T cell exhaustion, MDSC, expanded immune signature, and other immune signatures were enriched in HCC2 subtypes instead of HCC1. (c) The ssGSEA algorithm was performed on the GSE14520 (cohort1_test) data set ($n = 22$). Compared with HCC1, majority of HCC2 subjects showed an enrichment of immune and stromal-related features. It specifically included B cells, immune enrichment score, MDSC, macrophages, and other signatures. (d) Molecular marker enrichment of patients in the GSE14520 (cohort2_train) data set ($n = 225$). Among existing clusters, HCC3 subclass showed strong immunity and stroma enrichment, followed by HCC1. (e) Enrichment of immune and stromal marker in subjects from the GSE25097_GPL10687 data set ($n = 268$). Among existing clusters, HCC3 subclass showed strong immunity and stroma enrichment, followed by HCC5 and HCC6. (f) Enrichment of immune and stromal marker in subjects from the GSE25097_GPL10558 data set ($n = 240$). Among existing clusters, HCC1 and HCC6 subclass showed moderate immunity and stroma enrichment. (g) Enrichment of immune and stromal marker in subjects from the ICGC_LIRI_JP data set ($n = 232$). Among existing clusters, HCC6 subclass showed strong immunity and stroma enrichment, followed by HCC4 and HCC7. (h) A stack barplot for percentage of patients in non-IS, A-IS, and N-IS subtypes among the data sets.

Table 2: Clinical index of three subtypes.

		Stroma				
	Level	A-IS	N-IS	Non-IS	*p*	Test
n		16	16	38		
Adjacent_hepatic_tissue_inflammation_extent_type (%)		2 (12.5)	6 (37.5)	7 (18.4)	5.60*E*-01	Fisher_exact
	Mild	7 (43.8)	4 (25.0)	12 (31.6)		
	None	7 (43.8)	6 (37.5)	16 (42.1)		
	Severe	0 (0.0)	0 (0.0)	3 (7.9)		
Age_at_initial_pathologic_diagnosis (median [IQR])		61.50 [57.75, 67.25]	64.00 [56.00, 69.50]	64.50 [56.25, 72.00]	8.47*E*-01	Nonnorm
Albumin_result_lower_limit (median [IQR])		3.50 [3.48, 3.50]	3.50 [3.38, 3.50]	3.50 [3.50, 3.50]	3.74*E*-01	Nonnorm
Albumin_result_specified_value (median [IQR])		4.05 [3.77, 4.53]	4.00 [3.58, 4.32]	4.05 [3.50, 4.50]	7.34*E*-01	Nonnorm
Albumin_result_upper_limit (median [IQR])		5.00 [4.95, 5.00]	5.00 [5.00, 5.00]	5.00 [5.00, 5.00]	3.69*E*-01	Nonnorm
Bilirubin_lower_limit (median [IQR])		0.10 [0.10, 0.20]	0.20 [0.10, 0.20]	0.10 [0.10, 0.20]	2.08*E*-01	Nonnorm
Bilirubin_upper_limit (median [IQR])		0.70 [0.67, 0.93]	0.65 [0.38, 1.00]	0.60 [0.50, 0.90]	3.07*E*-01	Nonnorm
Cancer_first_degree_relative (median [IQR])		1.00 [1.00, 1.00]	1.00 [1.00, 2.00]	1.00 [1.00, 2.00]	2.34*E*-01	Nonnorm
Child_Pugh_classification_grade (%)		2 (12.5)	5 (31.2)	5 (13.2)	2.35*E*-01	Fisher_exact
	A	12 (75.0)	8 (50.0)	29 (76.3)		
	B	1 (6.2)	3 (18.8)	4 (10.5)		
	C	1 (6.2)	0 (0.0)	0 (0.0)		
Creatinine_lower_level (median [IQR])		0.60 [0.50, 0.80]	0.70 [0.60, 0.80]	0.70 [0.60, 0.80]	3.51*E*-01	Nonnorm
Creatinine_upper_limit (median [IQR])		1.30 [1.20, 1.40]	1.40 [1.20, 1.50]	1.25 [1.10, 1.40]	2.32*E*-01	Nonnorm
Creatinine_value_in_mg_dl (median [IQR])		0.80 [0.70, 1.00]	0.90 [0.75, 1.00]	0.95 [0.80, 1.10]	2.71*E*-01	Nonnorm
Inter_norm_ratio_lower_limit (median [IQR])		4.60 [0.88, 8.40]	8.30 [0.97, 8.33]	8.30 [0.90, 8.40]	8.18*E*-01	Nonnorm
Neoplasm_histologic_grade (%)	G1	3 (18.8)	0 (0.0)	7 (18.4)	4.14*E*-02	Fisher_exact
	G2	10 (62.5)	9 (56.2)	26 (68.4)		
	G3	2 (12.5)	7 (43.8)	3 (7.9)		
	G4	1 (6.2)	0 (0.0)	2 (5.3)		
Pathologic_M (%)	M0	7 (43.8)	10 (62.5)	29 (76.3)	7.96*E*-02	Fisher_exact
	M1	0 (0.0)	0 (0.0)	1 (2.6)		
	MX	9 (56.2)	6 (37.5)	8 (21.1)		
Pathologic_N (%)	N0	8 (50.0)	10 (62.5)	27 (71.1)	2.48*E*-01	Fisher_exact
	N1	0 (0.0)	1 (6.2)	0 (0.0)		
	NX	8 (50.0)	5 (31.2)	11 (28.9)		
Person_neoplasm_cancer_status (%)		6 (37.5)	6 (37.5)	11 (28.9)	8.52*E*-01	
	TUMOR FREE	5 (31.2)	5 (31.2)	17 (44.7)		
	WITH TUMOR	5 (31.2)	5 (31.2)	10 (26.3)		

Table 2: Continued.

		Stroma				
Platelet_result_count (median [IQR])		196.00 [174.75, 232.00]	232.50 [206.25, 308.50]	206.50 [164.75, 263.25]	2.38*E*-01	Nonnorm
Prothrombin_time_result_value (median [IQR])		5.15 [1.10, 9.88]	9.40 [1.15, 10.33]	8.85 [1.02, 10.97]	8.37*E*-01	Nonnorm
Relative_family_cancer_history (%)	NO	3 (18.8)	2 (12.5)	2 (5.3)	3.28*E*-01	Fisher_exact
	YES	13 (81.2)	14 (87.5)	36 (94.7)		
Vascular_tumor_cell_type (%)		1 (6.2)	4 (25.0)	2 (5.3)	1.42*E*-02	Fisher_exact
	Macro	2 (12.5)	3 (18.8)	1 (2.6)		
	Micro	0 (0.0)	2 (12.5)	9 (23.7)		
	None	13 (81.2)	7 (43.8)	26 (68.4)		
Weight (median [IQR])		86.00 [69.00, 102.00]	72.00 [63.50, 82.50]	70.00 [61.00, 92.50]	2.09*E*-01	Nonnorm
Gender.demographic (%)	Female	3 (18.8)	11 (68.8)	15 (39.5)	1.57*E*-02	Fisher_exact
	Male	13 (81.2)	5 (31.2)	23 (60.5)		
Race.demographic (%)	Asian	2 (12.5)	1 (6.2)	10 (26.3)	3.11*E*-01	Fisher_exact
	Black or African American	0 (0.0)	2 (12.5)	2 (5.3)		
	Not reported	1 (6.2)	0 (0.0)	3 (7.9)		
	White	13 (81.2)	13 (81.2)	23 (60.5)		
Vital_status.demographic (%)	Alive	11 (68.8)	7 (43.8)	23 (60.5)	3.34*E*-01	
	Dead	5 (31.2)	9 (56.2)	15 (39.5)		
BMI.exposures (median [IQR])		29.20 [25.64, 31.92]	27.49 [24.29, 32.87]	23.74 [21.03, 30.07]	1.63*E*-01	Nonnorm

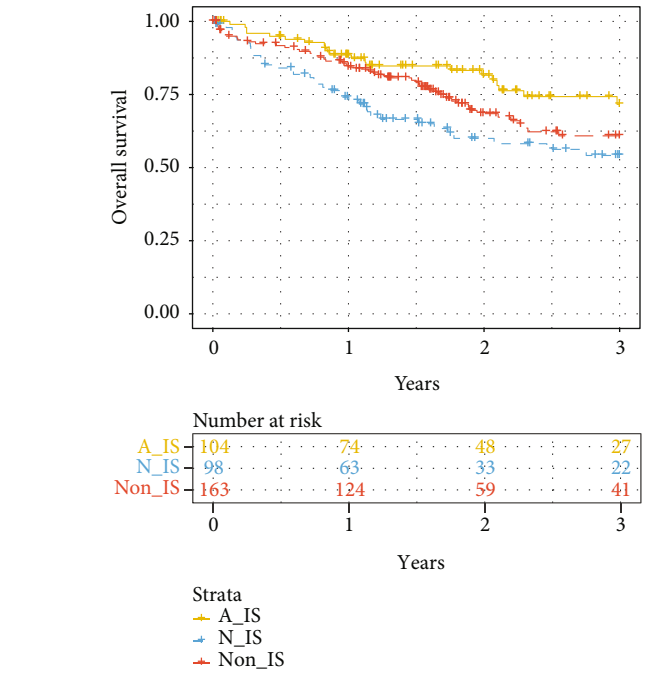

(a)

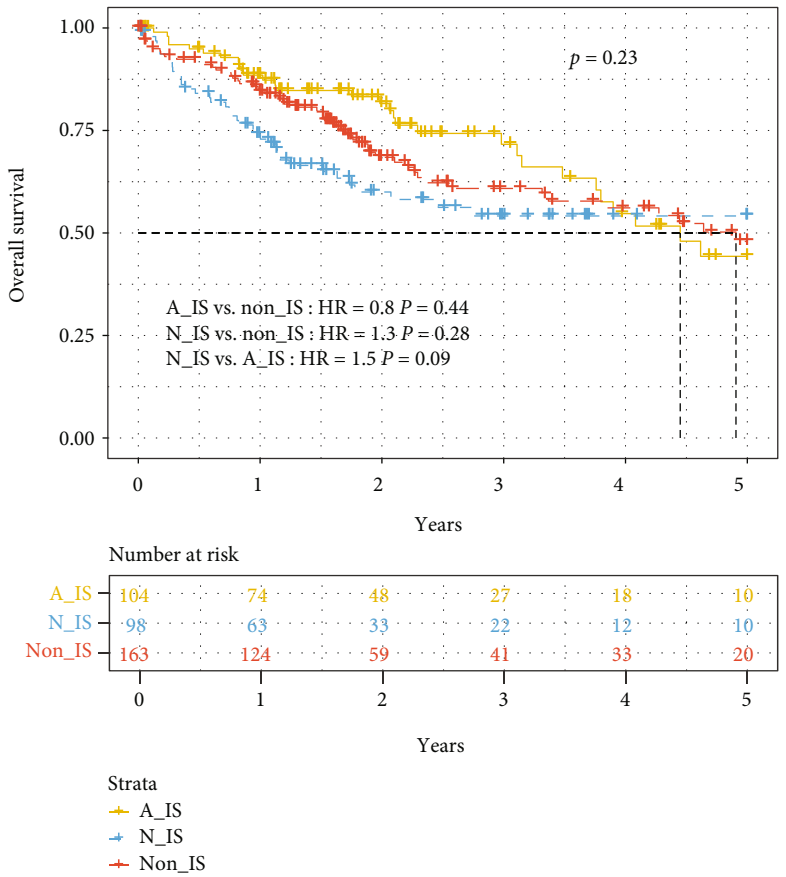

(b)

Figure 3: Continued.

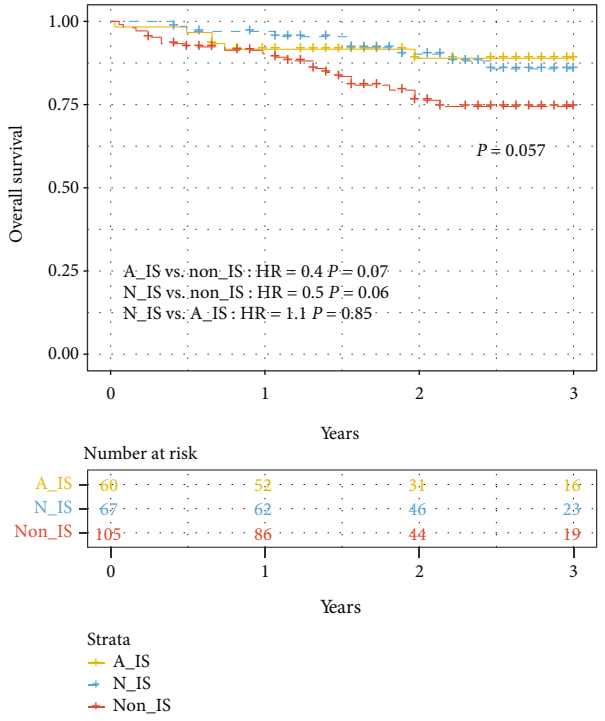

(c)

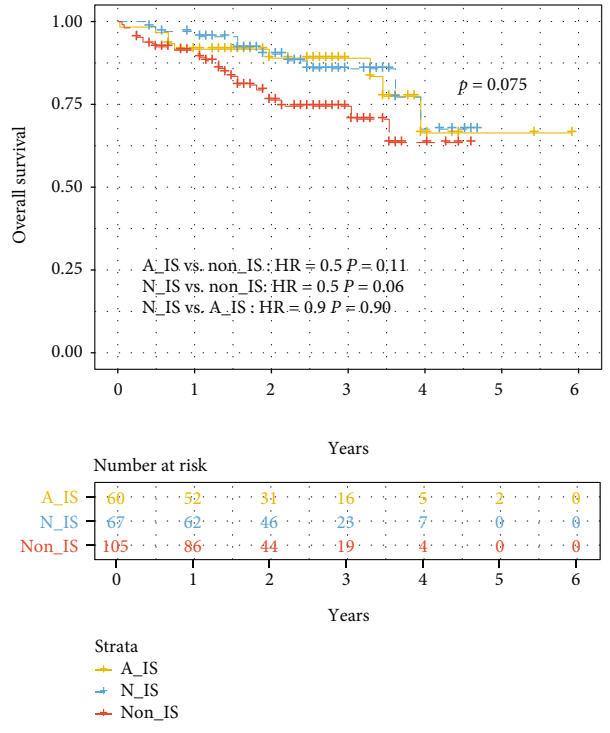

(d)

Figure 3: Differences in immune subtypes are related to clinical features and survival prognosis. (a) Comparison of 3-year survival among subgroups in TCGA cohort. The survival of patients was significantly different ($p = 0.017$) among the three types, and the survival of the A-IS subgroup (yellow line) was higher than that of N-IS (blue line) and non-IS (red line). (b) Comparison of 5-year survival rate of TCGA cohort. The analysis results showed that there was no significant difference among subtypes ($p = 0.23$). (c) Comparison of 3-year survival rate of the ICGC cohort. The survival was different among subgroups, and the survival of the A-IS subgroup (yellow line) was slightly higher than that of N-IS (blue line) and much higher than that of non-IS (red line). (d) Comparison of 6-year survival rates of ICGC patients. Compared with N-IS and non-IS subtypes (5 years), the overall survival of A-IS (6 years) is longer.

Table 3: Genes in the signature of survival prediction model.

Features	Multi_beta	Multi_HR	Multi_95%_CI_for_HR	Multi_*p*.value
ACRV1	0.284056	1.32851	0.974712-1.81072	0.0722009
AXDND1	0.666513	1.94743	1.493-2.54019	8.83*E*-07
B3GALT2	-1.88552	0.15175	0.0940178-0.244934	1.17*E*-14
ATP6V0D2	-0.266228	0.766265	0.628065-0.934874	0.00869992
ACPT	-0.532479	0.587148	0.465202-0.74106	7.36*E*-06
BRDT	0.890815	2.43711	1.7581-3.37837	8.98*E*-08
C10orf90	-0.321027	0.725404	0.590832-0.890626	0.00216696
BCO2	-0.606966	0.545002	0.369291-0.804318	0.00223885
ADAM32	0.740927	2.09788	1.61513-2.72492	2.81*E*-08
APOC4	-0.44861	0.638515	0.492737-0.827422	0.000692331
BSND	0.177579	1.19432	0.979831-1.45577	0.0787091
C12orf56	0.651933	1.91925	1.47251-2.50152	1.42*E*-06
C3orf36	-0.51696	0.596331	0.471639-0.753988	1.57*E*-05
CCNJL	0.807457	2.2422	1.47032-3.41929	0.000176535
DRD1	-0.731418	0.481226	0.373178-0.620558	1.72*E*-08
BAI2	1.06687	2.90626	1.99042-4.24349	3.31*E*-08
ERMN	-1.53079	0.216365	0.146571-0.319394	1.32*E*-14
ADAM12	3.4097	30.2563	12.0407-76.0287	4.08*E*-13
ADRA1A	-0.520536	0.594202	0.462577-0.763281	4.62*E*-05
GPR17	0.60065	1.8233	1.45229-2.2891	2.29*E*-07
HOXD10	0.174129	1.19021	0.989576-1.43152	0.0644995
C6orf223	-0.451106	0.636924	0.515442-0.787036	2.94*E*-05
SPAG6	-0.237856	0.788316	0.663102-0.937174	0.0070345
ACADL	-1.0514	0.349449	0.253158-0.482365	1.63*E*-10
CACNA1G	-0.410589	0.663259	0.532399-0.826285	0.000250567
CCDC36	0.37175	1.45027	1.14484-1.83719	0.00206295
CLEC2L	0.659235	1.93331	1.54772-2.41497	6.31*E*-09
CRISPLD1	-1.56237	0.209639	0.139785-0.314403	4.17*E*-14
FAM163B	0.347517	1.41555	1.09563-1.82888	0.00784528
HAVCR1	-0.281462	0.754679	0.62655-0.909011	0.0030281
MAMDC2	-1.1539	0.315405	0.204155-0.487279	2.00*E*-07
SFTPD	0.383284	1.46709	1.16916-1.84095	0.000934926
TKTL1	0.302278	1.35294	1.11067-1.64806	0.0026775
PPP2R2C	-0.546543	0.578948	0.46423-0.722013	1.23*E*-06
RTL1	0.444023	1.55897	1.22861-1.97815	0.000257703
TMC2	0.228553	1.25678	1.00585-1.57031	0.0442939
CYP19A1	0.410575	1.50768	1.23172-1.84548	6.88*E*-05
EPO	0.440563	1.55358	1.24005-1.94638	0.000127753
NKPD1	-0.297478	0.742689	0.575869-0.957833	0.0219126
SLC4A10	0.390634	1.47792	1.1312-1.9309	0.00418663
C15orf43	0.345474	1.41266	1.13902-1.75205	0.00166174
CLDN18	-0.545319	0.579657	0.462226-0.726921	2.34*E*-06
DPYSL4	1.17553	3.23985	2.29182-4.58003	2.82*E*-11
GNG4	0.383981	1.46812	1.16163-1.85547	0.0013088
GPM6A	0.777221	2.17542	1.57699-3.00094	2.19*E*-06
GPR18	-0.660017	0.516843	0.358506-0.74511	0.000405541
MYOCD	-0.409451	0.664015	0.474862-0.928514	0.0166865
NAV2.AS4	0.368257	1.44521	1.16618-1.791	0.000766567

Table 3: Continued.

Features	Multi_beta	Multi_HR	Multi_95%_CI_for_HR	Multi_*p*.value
PGA5	0.648481	1.91263	1.4807-2.47057	6.85*E*-07
SLC35F3	0.229401	1.25785	1.07694-1.46914	0.00378439
SOX8	-0.482409	0.617294	0.443993-0.858238	0.00411509
CD79A	-2.0343	0.130772	0.073325-0.233227	5.52*E*-12
HOXC6	0.250183	1.28426	1.07384-1.53591	0.0061387
MAGEA10	-0.87019	0.418872	0.317794-0.552099	6.58*E*-10
NKAIN1	-0.316253	0.728875	0.602838-0.881263	0.00109518
NKX3.2	0.497165	1.64405	1.28246-2.1076	8.74*E*-05
POU3F2	-0.604137	0.546546	0.428564-0.697007	1.12*E*-06
PSAPL1	-0.189652	0.827247	0.692495-0.988221	0.0365659
RCOR2	-0.505268	0.603344	0.455672-0.798872	0.000418987
TRAT1	1.94154	6.96945	3.92159-12.3861	3.65*E*-11
UBASH3A	-2.19459	0.111404	0.0547494-0.226683	1.41*E*-09
CDH10	0.579573	1.78528	1.39972-2.27703	3.03*E*-06
CHRND	0.165047	1.17945	1.00318-1.38669	0.0456736
CLEC17A	-0.482991	0.616935	0.468195-0.812928	0.000600521
COL25A1	-0.198214	0.820195	0.673116-0.99941	0.0493201
COLEC10	0.563006	1.75594	1.27602-2.41638	0.000547644
CRHBP	1.5943	4.92489	2.96712-8.17444	6.97*E*-10
DHH	0.719224	2.05284	1.44977-2.90677	5.06*E*-05
FAM129C	0.676126	1.96625	1.41399-2.7342	5.84*E*-05
FAM72D	0.509919	1.66516	1.16518-2.37967	0.00512327
GABRQ	0.287478	1.33306	0.99848-1.77976	0.0512178
GPR182	-0.322767	0.724142	0.533903-0.982168	0.0379242
HOXD3	0.755311	2.12827	1.62083-2.79459	5.48*E*-08
IGJ	0.333382	1.39568	0.896479-2.17286	0.139915
MAGEA6	-0.372357	0.689108	0.565764-0.839343	0.000215221
MS4A1	0.565355	1.76007	1.26789-2.44331	0.00072941
OGN	-0.228948	0.79537	0.647752-0.976629	0.0288351
OR13A1	0.299903	1.34973	1.10913-1.64252	0.00275417
SAA2	1.17003	3.22208	2.18463-4.75219	3.60*E*-09
VCX3A	0.585063	1.7951	1.36651-2.35812	2.63*E*-05
DLX2	-0.2672	0.76552	0.621962-0.942213	0.0116782
GFRA3	-0.263969	0.767997	0.644168-0.91563	0.00325573
KIF5A	0.319303	1.37617	1.09699-1.7264	0.00577724
MEP1A	0.354055	1.42483	1.18877-1.70777	0.000127605
PAGE2	-0.463863	0.62885	0.504242-0.78425	3.84*E*-05
PANX3	0.720169	2.05478	1.47722-2.85816	1.89*E*-05
PIP5K1B	-1.29461	0.274003	0.190459-0.394195	3.03*E*-12
PNCK	-0.505915	0.602954	0.485959-0.748116	4.29*E*-06
PRICKLE1	2.16419	8.70756	4.44639-17.0524	2.77*E*-10
RGS6	-0.611302	0.542644	0.41516-0.709275	7.67*E*-06
RSPO3	-0.412661	0.661887	0.493666-0.88743	0.00581211
SLC22A8	-0.259751	0.771243	0.6545-0.908811	0.00192368
SLC30A8	-0.295976	0.743806	0.565241-0.978781	0.0345933
TCF24	-0.526444	0.590702	0.448147-0.778603	0.000187066
TDRD5	0.277834	1.32027	1.11272-1.56653	0.00145269
XCR1	0.29765	1.34669	1.01721-1.78289	0.0376024

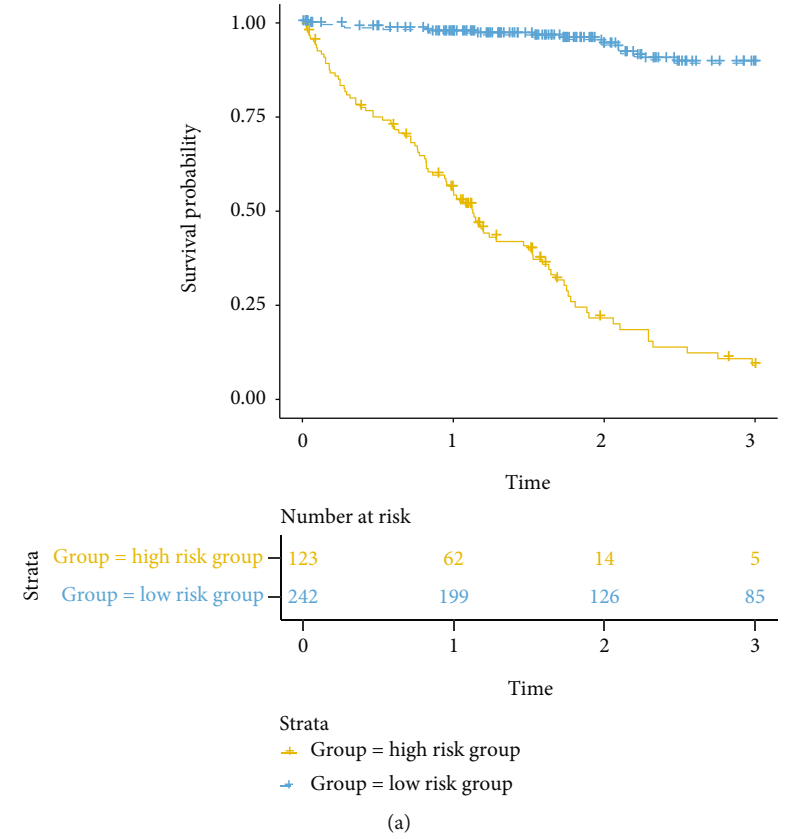

(a)

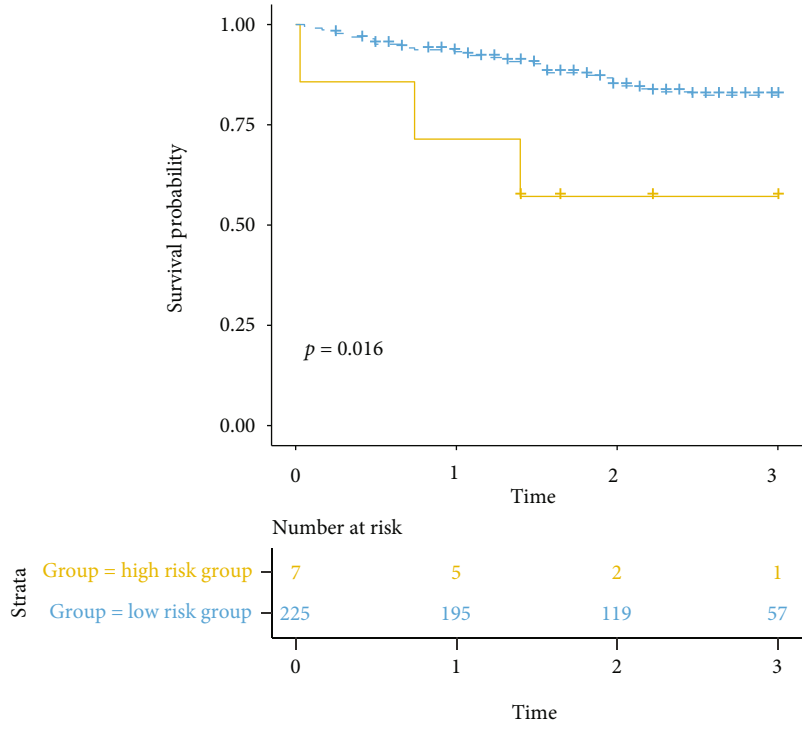

(b)

Figure 4: Continued.

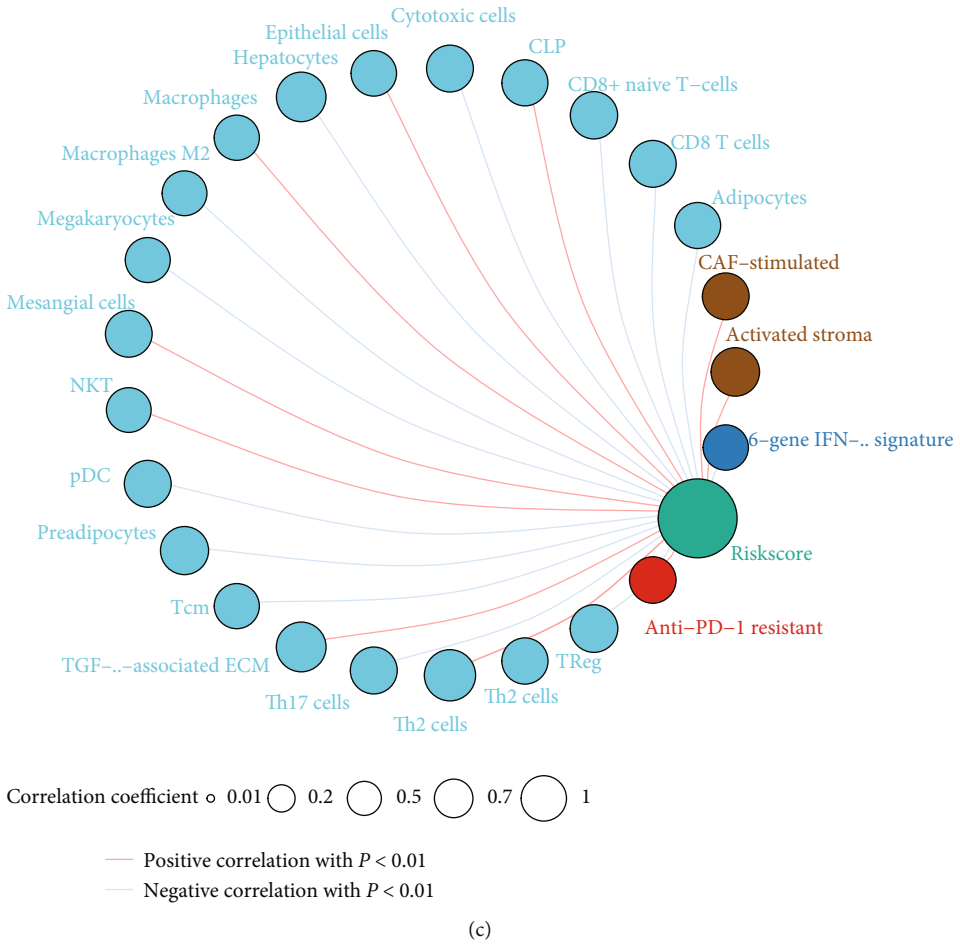

(c)

Figure 4: Prognostic prediction model based on signatures of tumor microenvironment. (a) Kaplan-Meier survival curve of the high- and low-risk groups in TCGA training set. The horizontal axis represents time (unit: year); the vertical axis represents survival probability. The low-risk group (blue line) presented a high three-year survival probability (35.12%); however, the high-risk group (yellow) presented a low three-year survival rate (4.07%). (b) Kaplan-Meier survival curve of the high- and low-risk groups in the ICGC testing set. The low-risk group (blue line) presented a high three-year survival probability (25.33%); however, the high-risk group (yellow) presented a low three-year survival rate (14.29%). (c). Immune cells associated with the risk index of TCGA patients. The red line indicates a positive correlation between the risk index and immune cells, and the gray line indicates a negative correlation between the risk index and immune cells. The size of the circle indicates different correlation coefficients, and the larger the area of the circle, the larger the correlation coefficient.

its relationship with patient survival and to draw the K-M survival curve (Figure 4(a)). Similarly, we use the patient's risk index to verify in the test set of the ICGC database (Figure 4(b)).

Based on the patient's immune subtypes and differences in survival, we want to know which immune cells are related to the patient's disease risk. Therefore, by establishing the correlation between the patient's risk index and immune cells in TCGA cohort, and taking $p < 0.05$ as the significant correlation, the immune cells related to the patient's disease risk were screened out (Figure 4(c)).

3. Discussion

The HCC ecosystem, which is mainly composed of tumor cells and immune cells, is complex and dynamic. Due to drug resistance or immune escape, the heterogeneity at all levels from single cells to lesions reduces the therapeutic effect [27]. In the past decade, many efforts have been made to use multiregional and high-throughput analysis to study intratumoral heterogeneity [28–30]. Most studies focus on the genetic changes of HCC cells; this study is an attempt to use computational biology to study the immune-related heterogeneity of HCC at the genomic level. In this study, we tried to construct its correlation with survival prognosis based on the patient's immunotype and the differential genes screened. Our findings confirm that the prognostic survival of A-IS is significantly higher than that of N-IS. These findings are consistent with existing studies, namely, other microenvironmental factors (for example, angiogenesis and extracellular matrix contribute more immune heterogeneity) [27]. Therefore, intervention in the immune status of the HCC microenvironment may be a suitable strategy, because such treatments may affect all lesions of the individual and

may also be applicable for a group of patients. More importantly, many new tools for immunotherapy have been developed and improved. In addition, through comprehensive analysis, we have observed that some immune cells are significantly related to patient classification and disease risk, providing a comprehensive new understanding of immunophenotyping and risk prediction, and proposed possible targets for intervention in HCC.

Enhancing host immunity may be beneficial to the cure of cancer. Researchers found infiltrating T cells in HCC and discovered the enrichment of Treg cells and the depletion of CD8+ T cells [31]. Studies have confirmed the enrichment of immunosuppressive cells in patients with HCC [32, 33]. Researchers revealed significant differences between immune cells infiltrating HCC [34]. The similarity of the immune microenvironment of some HCC patients not only facilitates classification but also facilitates the implementation of personalized treatment. In this case, according to our new classification scheme, HCC patients can be divided into three subtypes. More importantly, we use an independent cohort of HCC patients to confirm the classification results. Although there is significant heterogeneity in the immune status among patients, the three subtypes of HCC are clearly identified, indicating that this classification method can be applied to the HCC patient population. Patients with N-IS subtype generally had normal lymphocyte infiltration, but some patients have abundant expression of immune-related genes. The upregulation of features included expanded immune signature [35], T cell-inflamed gene expression profile (GEP) [36], and immune enrichment score [37]. T cell inflammation gene expression profile (GEP) contains genes related to antigen presentation, chemokine expression, cytotoxic activity, and adaptive immune resistance [35]. They can divide cancer into different subgroups and correspond to corresponding biological patterns. Capturing immune-related feature sets can provide accurate reference for reasonable construction and evaluation of treatment plans [36]. Non-IS is like a "cold" tumor, with almost no enrichment of immune- and matrix-related molecules. For such patients, combination therapy is more effective [38–40]. Enhanced T cell trafficking or suppression of inhibitory MDSC may increase the response of these HCC patients to immune checkpoint inhibitors [41, 42].

The three HCC subtypes we identified represent the clinical situation of human patients. A-IS subtype patients have relatively strong immune enrichment of stromal cell activation, although in pancreatic ductal adenocarcinoma, compared with patients with normal stromal subtype (N-IS), patients with activated stromal subtype samples (A-IS) have a worse survival [43]. But in HCC patients, the situation is different; that is, the 3-year survival performance of patients with an activated stroma subtype is better than that of patients with a normal stroma subtype (Figure 3(a)). However, the 5-year survival of different patient subgroups did not differ significantly (Figure 3(b)).

The current WHO classification of HCC highlights subtypes with stromal characteristics [44] which include lymphocyte-rich HCC. It is featured by lymphocyte infiltration into tumor and related to a better prognosis notably [45]. Studies have shown that different tumor subtypes have different types of immune microenvironments [46, 47] usually related to intratumoral heterogeneity [48]. The composition of the tumor immune microenvironment has been analyzed by methods such as gene expression analysis, single-cell RNA sequencing, and flow cytometry analysis [16, 31, 48–50]. In liver cancer, studies have shown that the number of immune cell infiltration, especially cytotoxic T cells [51–53], and the molecular classification of the immune microenvironment have clinicopathological significance [16, 48, 54]. In our study, the stroma activation of immune activity can indeed divide HCC patients into three subgroups (Figure 1(c)), and it is significantly associated with individuals' survival (Figure 3(a)).

4. Methods

4.1. Project and Sample. Data sets of 371 liver hepatocellular carcinoma donors were downloaded from TCGA database with detailed clinical information (https://xenabrowser.net/datapages/?dataset=TCGA-LIHC). The independent data sets used for verification come from the GSE144269 data set ($n = 70$) (https://www.ncbi.nlm.nih.gov/geo/query/acc.cgi?acc=GSE144269), the GSE14520_cohort1_test data set ($n = 22$), the GSE14520_cohort2_train samples ($n = 225$) (https://www.ncbi.nlm.nih.gov/geo/query/acc.cgi?acc=GSE14520), the GSE25097_GPL10687 samples ($n = 268$) (https://www.ncbi.nlm.nih.gov/geo/query/acc.cgi?acc=GSE25097), the GSE36376_GPL10558 ($n = 240$) (https://www.ncbi.nlm.nih.gov/geo/query/acc.cgi?acc=GSE36376) data set, and ICGC_LIRI_JP samples ($n = 232$) (https://dcc.icgc.org/projects/LIRI-JP).

4.2. Bioinformatics Analysis

(1) ssGSEA algorithm: use the R package "GSVA (version 1.30.0)," and use ssGSEA to explore the HCC expression profile data of TCGA-LIHC cohort, and analyze the immune enrichment of each patient's tumor microenvironment. According to the immune enrichment status and stroma status of HCC samples, they are divided into A-IS, N-IS, and non-IS subtypes. According to the ssGSEA score obtained by each sample, the spectral clustering algorithm is used to extract different classifications. In addition, the R package "limma (version 3.41.18)" was used to analyze immunoenriched and non-immune-enriched patients, as well as the significantly different genes of stromal cell enrichment and nonmatrix enrichment, and $p < 0.05$ was taken as the significant difference

(2) The unsupervised clustering of the data set was performed mainly based on tSNE which is embedded in t-distributed random neighborhoods [55]. In this study, we use tSNE to show the different subgroups of TCGA-LIHC cohort

(3) We performed Kaplan-Meier survival analysis on the samples and plotted survival curves. Survival analysis divided the samples into high-index groups and low-

index groups based on the median. Data visualization is mainly done in the R environment (version 4.1.0). Kaplan-Meier survival analysis relies on the use of the "survival (version 3.1-8)" package. The ROC curve is drawn based on the "survivalROC (version 1.0.3)" package

(4) Prognosis prediction model establishment process: (a) use the training set to perform unit Cox regression on each gene to initially screen disease-related genes; (b) after obtaining all Cox significant genes in all units, perform 1000X LASSO regression to calculate the frequency of each gene and rank it; (c) according to the sorting result of the previous step, build the gene set incrementally. Use each gene set to perform multiple Cox regression to get the contribution of each gene; (d) obtain the optimal gene set according to the gene contribution degree, and perform multiple Cox regression analysis on these genes. Finally, we determined the regression coefficient of each gene; (e) calculate the death risk score of each patient through regression coefficients; (f) the death risk score model is tested in the training set (comparing the predicted situation with the actual situation); (g) the same model is tested in the independent testing set at the beginning (comparison of the predicted situation with the actual situation)

(5) Construct the optimal multivariate Cox model based on the LASSO algorithm. This analysis uses the LASSO algorithm for gene screening: in the field of statistics and machine learning, LASSO algorithm (least absolute shrinkage and selection operator, also translated as minimum absolute shrinkage and selection operator, LASSO algorithm) is a regression analysis method that simultaneously performs feature selection and regularization (mathematics). It is aimed at enhancing the predictive accuracy and interpretability of statistical models. LASSO adopts the linear regression method of L1-regularization, so that the weight of some learned features is 0, so as to achieve the purpose of sparseness, selection of variables, and construction of the best model. The characteristic of LASSO regression is to perform variable selection and regularization while fitting a generalized linear model. Therefore, regardless of whether the target dependent variable (dependent/response variable) is continuous, binary, or discrete, it can be modeled by LASSO regression and then predicted

(6) We use the random forest algorithm to select the best gene model based on the Cox multiple regression model and finally draw the unit Cox regression model forest diagram based on the gene panel as follows: we calculate the risk score (risk score) of each patient based on the expression of the gene panel and the multiple regression coefficient. The formula is as follows:

$$\text{Risk score} = \sum_{i=1}^{n} \beta_i * x_i. \quad (1)$$

where x_i represents the expression level of each gene in the panel and β_i is the multivariate Cox regression beta value (multi_beta) corresponding to each gene

Data Availability

The data used to support the findings of this study are included within the article.

Conflicts of Interest

The authors declare that they have no competing interest.

Authors' Contributions

Jian Hu, Feifei Mao, Lifang Li, and Xiaoqian Wang contributed equally to this work.

Acknowledgments

This work was financially supported by National Natural Science Foundation of China (82002480), Youth project of Natural Science Basic Research Program of Shaanxi Province (GR2022JQ-866), and Key Research and Development program of Shaanxi Province (2022SF-243).

Supplementary Materials

Supplementary 1. Table S1: significantly differently expressed genes between immune and nonimmune subtypes.

Supplementary 2. Table S2: significantly differently expressed genes between stroma and nonstroma subtypes.

References

[1] A. Forner, M. Reig, and J. Bruix, "Hepatocellular carcinoma," *Lancet*, vol. 391, no. 10127, pp. 1301–1314, 2018.

[2] European Association for the Study of the Liver and European Organisation for Research and Treatment of Cancer, "EASL-EORTC clinical practice guidelines: management of hepatocellular carcinoma," *Journal of Hepatology*, vol. 56, no. 4, pp. 908–943, 2012.

[3] J. M. K. Llovet, R. Kate, A. Villanueva et al., "Hepatocellular carcinoma," *Nature Reviews Disease Primers*, vol. 7, no. 1, p. 6, 2021.

[4] H. Wang, P. Men, Y. Xiao et al., "Hepatitis B infection in the general population of China: a systematic review and meta-analysis," *BMC Infectious Diseases*, vol. 19, no. 1, p. 811, 2019.

[5] K. Mohd Hanafiah, J. Groeger, A. D. Flaxman, and S. T. Wiersma, "Global epidemiology of hepatitis C virus infection: new estimates of age-specific antibody to HCV seroprevalence," *Hepatology*, vol. 57, no. 4, pp. 1333–1342, 2013.

[6] R. E. Omer, A. Kuijsten, A. M. Y. Kadaru et al., "Population-attributable risk of dietary aflatoxins and hepatitis B virus infection with respect to hepatocellular carcinoma," *Nutrition and Cancer*, vol. 48, no. 1, pp. 15–21, 2004.

[7] D. A. Wheeler, L. R. Roberts, and Cancer Genome Atlas Research Network, "Comprehensive and Integrative Genomic Characterization of Hepatocellular Carcinoma," *Cell*, vol. 169, no. 7, pp. 1327–1341.e23, 2017.

[8] J. D. Yang and L. R. Roberts, "Hepatocellular carcinoma: a global view," *Nature Reviews Gastroenterology & Hepatology*, vol. 7, no. 8, pp. 448–458, 2010.

[9] J. Bruix and M. Sherman, "Management of hepatocellular carcinoma: an update," *Hepatology*, vol. 53, no. 3, pp. 1020–1022, 2011.

[10] A. Forner, J. M. Llovet, and J. Bruix, "Hepatocellular carcinoma," *Lancet*, vol. 379, no. 9822, pp. 1245–1255, 2012.

[11] P. T. Kim, J. H. Jang, E. G. Atenafu et al., "Outcomes after hepatic resection and subsequent multimodal treatment of recurrence for multifocal hepatocellular carcinoma," *British Journal of Surgery*, vol. 100, no. 11, pp. 1516–1522, 2013.

[12] J. Bruix, M. Reig, and M. Sherman, "Evidence-based diagnosis, staging, and treatment of patients with hepatocellular carcinoma," *Gastroenterology*, vol. 150, no. 4, pp. 835–853, 2016.

[13] L. Niu, L. Liu, S. Yang, J. Ren, P. B. S. Lai, and G. G. Chen, "New insights into sorafenib resistance in hepatocellular carcinoma: Responsible mechanisms and promising strategies," *Biochimica et Biophysica Acta (BBA) - Reviews on Cancer*, vol. 1868, no. 2, pp. 564–570, 2017.

[14] J. Bruix, T. Takayama, V. Mazzaferro et al., "Adjuvant sorafenib for hepatocellular carcinoma after resection or ablation (STORM): a phase 3, randomised, double-blind, placebo-controlled trial," *The Lancet Oncology*, vol. 16, no. 13, pp. 1344–1354, 2015.

[15] R. K. Kelley, "Adjuvant sorafenib for liver cancer: wrong stage, wrong dose," *The Lancet Oncology*, vol. 16, no. 13, pp. 1279–1281, 2015.

[16] D. Sia, Y. Jiao, I. Martinez-Quetglas et al., "Identification of an Immune-specific Class of Hepatocellular Carcinoma, Based on Molecular Features," *Gastroenterology*, vol. 153, no. 3, pp. 812–826, 2017.

[17] S. Boyault, D. S. Rickman, A. de Reyniès et al., "Transcriptome classification of HCC is related to gene alterations and to new therapeutic targets," *Hepatology*, vol. 45, no. 1, pp. 42–52, 2007.

[18] Y. Hoshida, S. M. B. Nijman, M. Kobayashi et al., "Integrative transcriptome analysis reveals common molecular subclasses of human hepatocellular carcinoma," *Cancer Research*, vol. 69, no. 18, pp. 7385–7392, 2009.

[19] J. S. Lee, I. S. Chu, J. Heo et al., "Classification and prediction of survival in hepatocellular carcinoma by gene expression profiling," *Hepatology*, vol. 40, no. 3, pp. 667–676, 2004.

[20] Y. Hou, H. Guo, C. Cao et al., "Single-cell triple omics sequencing reveals genetic, epigenetic, and transcriptomic heterogeneity in hepatocellular carcinomas," *Cell Research*, vol. 26, no. 3, pp. 304–319, 2016.

[21] Q. Gao, H. Zhu, L. Dong et al., "Integrated Proteogenomic characterization of HBV-related hepatocellular carcinoma," *Cell*, vol. 179, no. 2, pp. 561–577.e22, 2019.

[22] J. Candia, E. Bayarsaikhan, M. Tandon et al., "The genomic landscape of Mongolian hepatocellular carcinoma," *Nature Communications*, vol. 11, no. 1, p. 4383, 2020.

[23] S. Jung, S. M. Altstetter, and U. Protzer, "Innate immune recognition and modulation in hepatitis D virus infection," *World Journal of Gastroenterology*, vol. 26, no. 21, pp. 2781–2791, 2020.

[24] V. Williams, S. Brichler, N. Radjef et al., "Hepatitis delta virus proteins repress hepatitis B virus enhancers and activate the alpha/beta interferon-inducible MxA gene," *Journal of General Virology*, vol. 90, no. 11, pp. 2759–2767, 2009.

[25] V. A. Chaudhari, K. Khobragade, M. Bhandare, and S. V. Shrikhande, "Management of fibrolamellar hepatocellular carcinoma," *Chinese Clinical Oncology*, vol. 7, no. 5, p. 51, 2018.

[26] X. J. Qian, Q. Xu, M. J. Yao et al., "Prognostic significance of albumin/globulin ratio on postoperative survival of patients with hepatocellular carcinoma," *Zhonghua Gan Zang Bing Za Zhi*, vol. 26, no. 9, pp. 670–675, 2018.

[27] J. Liu, H. Dang, and X. W. Wang, "The significance of intertumor and intratumor heterogeneity in liver cancer," *Experimental & Molecular Medicine*, vol. 50, no. 1, article ???, 2018.

[28] M. Duan, J. Hao, S. Cui et al., "Diverse modes of clonal evolution in HBV-related hepatocellular carcinoma revealed by single-cell genome sequencing," *Cell Research*, vol. 28, no. 3, pp. 359–373, 2018.

[29] A. Huang, X. Zhao, X. R. Yang et al., "Circumventing intratumoral heterogeneity to identify potential therapeutic targets in hepatocellular carcinoma," *Journal of Hepatology*, vol. 67, no. 2, pp. 293–301, 2017.

[30] S. Ling, Z. Hu, Z. Yang et al., "Extremely high genetic diversity in a single tumor points to prevalence of non-Darwinian cell evolution," *Proceedings of the National Academy of Sciences*, vol. 112, no. 47, pp. E6496–E6505, 2015.

[31] C. Zheng, L. Zheng, J. K. Yoo et al., "Landscape of infiltrating T cells in liver cancer revealed by single-cell sequencing," *Cell*, vol. 169, no. 7, pp. 1342–1356.e16, 2017.

[32] C. J. Lim, Y. H. Lee, L. Pan et al., "Multidimensional analyses reveal distinct immune microenvironment in hepatitis B virus-related hepatocellular carcinoma," *Gut*, vol. 68, no. 5, pp. 916–927, 2019.

[33] V. Chew, L. Lai, L. Pan et al., "Delineation of an immunosuppressive gradient in hepatocellular carcinoma using high-dimensional proteomic and transcriptomic analyses," *Proceedings of the National Academy of Sciences*, vol. 114, no. 29, pp. E5900–E5909, 2017.

[34] Q. Zhang, Y. Lou, J. Yang et al., "Integrated multiomic analysis reveals comprehensive tumour heterogeneity and novel immunophenotypic classification in hepatocellular carcinomas," *Gut*, vol. 68, no. 11, pp. 2019–2031, 2019.

[35] M. Ayers, J. Lunceford, M. Nebozhyn et al., "IFN-γ-related mRNA profile predicts clinical response to PD-1 blockade," *Journal of Clinical Investigation*, vol. 127, no. 8, pp. 2930–2940, 2017.

[36] R. A.-O. Cristescu, R. Mogg, M. Ayers et al., "Pan-tumor genomic biomarkers for PD-1 checkpoint blockade-based immunotherapy," *Science*, vol. 362, no. 6411, article eaar3593, 2018.

[37] K. Yoshihara, M. Shahmoradgoli, E. Martínez et al., "Inferring tumour purity and stromal and immune cell admixture from expression data," *Nature Communications*, vol. 4, no. 1, p. 2612, 2013.

[38] A. A.-O. Samson, K. J. Scott, D. Taggart et al., "Intravenous delivery of oncolytic reovirus to brain tumor patients immunologically primes for subsequent checkpoint blockade," *Science Translational Medicine*, vol. 10, no. 422, article eaam7577, 2018.

[39] M. A.-O. Bourgeois-Daigneault, D. G. Roy, A. S. Aitken et al., "Neoadjuvant oncolytic virotherapy before surgery sensitizes

triple-negative breast cancer to immune checkpoint therapy," *Science Translational Medicine*, vol. 10, no. 422, article eaao1641, 2018.

[40] A. Ribas, R. Dummer, I. Puzanov et al., "Oncolytic virotherapy promotes intratumoral T cell infiltration and improves Anti-PD-1 immunotherapy," *Cell*, vol. 174, no. 4, pp. 1031-1032, 2018.

[41] E. A.-O. Allen, A. Jabouille, L. B. Rivera et al., "Combined anti-angiogenic and anti-PD-L1 therapy stimulates tumor immunity through HEV formation," *Science Translational Medicine*, vol. 9, no. 385, article eaak9679, 2017.

[42] C. Wu, H. Ning, M. Liu et al., "Spleen mediates a distinct hematopoietic progenitor response supporting tumor-promoting myelopoiesis," *Journal of Clinical Investigation*, vol. 128, no. 8, pp. 3425–3438, 2018.

[43] R. A. Moffitt, R. Marayati, E. L. Flate et al., "Virtual microdissection identifies distinct tumor- and stroma-specific subtypes of pancreatic ductal adenocarcinoma," *Nature Genetics*, vol. 47, no. 10, pp. 1168–1178, 2015.

[44] WHO Classification of Tumours, *Digestive Systen Tumours*, International Agency for Research on Cancer, 5th ed edition, 2019.

[45] A. W. Chan, J. H. M. Tong, Y. Pan et al., "Lymphoepithelioma-like hepatocellular carcinoma," *American Journal of Surgical Pathology*, vol. 39, no. 3, pp. 304–312, 2015.

[46] J. Calderaro, M. Ziol, V. Paradis, and J. Zucman-Rossi, "Molecular and histological correlations in liver cancer," *Journal of Hepatology*, vol. 71, no. 3, pp. 616–630, 2019.

[47] J. Calderaro, G. Couchy, S. Imbeaud et al., "Histological subtypes of hepatocellular carcinoma are related to gene mutations and molecular tumour classification," *Journal of Hepatology*, vol. 67, no. 4, pp. 727–738, 2017.

[48] Y. Kurebayashi, H. Ojima, H. Tsujikawa et al., "Landscape of immune microenvironment in hepatocellular carcinoma and its additional impact on histological and molecular classification," *Hepatology*, vol. 68, no. 3, pp. 1025–1041, 2018.

[49] M. Garnelo, A. Tan, Z. Her et al., "Interaction between tumour-infiltrating B cells and T cells controls the progression of hepatocellular carcinoma," *Gut*, vol. 66, no. 2, pp. 342–351, 2017.

[50] Q. Gao, S. J. Qiu, J. Fan et al., "Intratumoral balance of regulatory and cytotoxic T cells is associated with prognosis of hepatocellular carcinoma after Resection," *Journal of Clinical Oncology*, vol. 25, no. 18, pp. 2586–2593, 2007.

[51] M. E. Hoekstra, L. Bornes, F. E. Dijkgraaf et al., "Long-distance modulation of bystander tumor cells by $CD8^+$ T-cell-secreted IFN-γ," *Nature Cancer*, vol. 1, no. 3, pp. 291–301, 2020.

[52] D. H. Raulet and N. Guerra, "Oncogenic stress sensed by the immune system: role of natural killer cell receptors," *Nature Reviews Immunology*, vol. 9, no. 8, pp. 568–580, 2009.

[53] B. A.-O. Silva-Santos, S. A.-O. Mensurado, and S. A.-O. Coffelt, "$\gamma\delta$ T cells: pleiotropic immune effectors with therapeutic potential in cancer," *Nature Reviews Cancer*, vol. 19, no. 7, pp. 392–404, 2019.

[54] S. Job, D. Rapoud, A. Dos Santos et al., "Identification of four immune subtypes characterized by distinct composition and functions of tumor microenvironment in intrahepatic cholangiocarcinoma," *Hepatology*, vol. 72, no. 3, pp. 965–981, 2020.

[55] L. Van der Maaten and G. Hinton, "Visualizing data using t-SNE," *Journal of Machine Learning Research*, vol. 1, pp. 1–48, 2008.

[56] L. Q. M. Chow, R. Haddad, S. Gupta et al., "Antitumor activity of pembrolizumab in biomarker-unselected Patients With recurrent and/or metastatic head and neck squamous cell carcinoma: results from the phase Ib KEYNOTE-012 expansion Cohort," *Journal of Clinical Oncology*, vol. 34, no. 32, pp. 3838–3845, 2016.

[57] A. Abeshouse, J. Ahn, R. Akbani et al., "The Molecular Taxonomy of Primary Prostate Cancer," *Cell*, vol. 163, no. 4, pp. 1011–1025, 2015.

[58] G. Bindea, B. Mlecnik, M. Tosolini et al., "Spatiotemporal dynamics of intratumoral immune cells reveal the immune landscape in human cancer," *Immunity*, vol. 39, no. 4, pp. 782–795, 2013.

[59] A. Alistar, J. W. Chou, S. Nagalla, M. A. Black, R. D'Agostino, and L. D. Miller, "Dual roles for immune metagenes in breast cancer prognosis and therapy prediction," *Genome Medicine*, vol. 6, no. 10, p. 80, 2014.

[60] M. D. Iglesia, B. G. Vincent, J. S. Parker et al., "Prognostic B-cell signatures using mRNA-seq in patients with subtype-specific breast and ovarian cancer," *Clinical Cancer Research*, vol. 20, no. 14, pp. 3818–3829, 2014.

[61] P. Charoentong, F. Finotello, M. Angelova et al., "Pan-cancer immunogenomic analyses reveal genotype-immunophenotype relationships and predictors of response to checkpoint blockade," *Cell Reports*, vol. 18, no. 1, pp. 248–262, 2017.

[62] M. Ayers, J. Lunceford, M. Nebozhyn et al., "IFN-γ–related mRNA profile predicts clinical response to PD-1 blockade," *The Journal of Clinical Investigation*, vol. 127, no. 8, pp. 2930–2940, 2017.

[63] K. Yaddanapudi, B. E. Rendon, G. Lamont et al., "MIF Is Necessary for Late-Stage Melanoma Patient MDSC Immune Suppression and Differentiation," *Cancer Immunology Research*, vol. 4, no. 2, pp. 101–112, 2016.

[64] A. Calon, E. Espinet, S. Palomo-Ponce et al., "Dependency of Colorectal Cancer on a TGF-β-Driven Program in Stromal Cells for Metastasis Initiation," *Cancer Cell*, vol. 22, no. 5, pp. 571–584, 2012.

[65] M. Beyer, M. R. Mallmann, J. Xue et al., "High-resolution transcriptome of human macrophages," *PLoS One*, vol. 7, no. 9, article e45466, 2012.

[66] M. Giordano, C. Henin, J. Maurizio et al., "Molecular profiling of CD8 T cells in autochthonous melanoma identifies Maf as driver of exhaustion," *The EMBO Journal*, vol. 34, no. 15, pp. 2042–2058, 2015.

[67] M. Philip, L. Fairchild, L. Sun et al., "Chromatin states define tumour-specific T cell dysfunction and reprogramming," *Nature*, vol. 545, no. 7655, pp. 452–456, 2017.

[68] N. Riaz, J. J. Havel, V. Makarov et al., "Tumor and microenvironment evolution during immunotherapy with nivolumab," *Cell*, vol. 171, no. 4, pp. 934–949.e16, 2017.

Hindawi
Journal of Oncology
Volume 2022, Article ID 4221756, 17 pages
https://doi.org/10.1155/2022/4221756

Research Article

A Risk-Scoring Model Based on Evaluation of Ferroptosis-Related Genes in Osteosarcoma

Mingyang Jiang,[1] **Zifan Wang**,[2] **Xiaoyu He**,[3] **Yang Hu**,[1] **Mingjing Xie**,[1] **Yiji Jike**,[1] **Zhandong Bo**,[1] **and Wentao Qin**[1]

[1]*Department of Bone and Joint Surgery, First Affiliated Hospital of Guangxi Medical University, Nanning 530021, China*
[2]*Department of Burn Plastic and Wound Repair, The Affiliated Hospital of Youjiang Medical University for Nationalities, Baise 533000, China*
[3]*Department of Thoracic Surgery, The Shenzhen Bao'an District Songgang People's Hospital, Shenzhen, China*

Correspondence should be addressed to Wentao Qin; qwt1713974028@163.com

Mingyang Jiang, Zifan Wang, and Xiaoyu He contributed equally to this work.

Received 21 January 2022; Revised 2 March 2022; Accepted 3 March 2022; Published 28 March 2022

Academic Editor: Fu Wang

Background. Osteosarcoma (OS) is a bone malignancy frequently seen in pediatrics and has high mortality and incidence. Ferroptosis is an important cell death process in regulating the apoptosis and invasion of tumor cells, so constructing the risk-scoring model based on OS ferroptosis-related genes (FRGs) will benefit the evaluation of both treatment and prognosis. *Methods*. The OS dataset was screened from the Therapeutically Applicable Research to Generate Effective Treatments (TARGET) database, and OS-related FRGs were found through the Ferroptosis Database (FerrDb) using a multivariate Cox regression model, followed by the generation of the risk scores and a risk-scoring prediction model. Further systematical exploration for immune cell infiltration and assessing the prediction of response to targeted drugs was conducted. *Results*. Based on OS-related FRGs, a risk-scoring model of FRGs in OS was constructed. The six FRGs played a role in the carbon metabolism, glutathione metabolism, and pentose phosphate pathways. Results from targeted drug sensitivity analyses were concordant to pathway analyses. The response to targeted drugs statistically differed between the two groups with different risks, and the high-risk group presented a high sensitivity to targeted drugs. *Conclusions*. We identified a 6-ferroptosis-gene-based prognostic signature in OS and created and verified a risk-scoring model to predict the prognosis of OS at 1, 3, and 5 years for OS patients independently.

1. Introduction

Osteosarcoma (OS) is one of the malignancies frequently seen in pediatrics with high disability rates and mortality [1]. The 5-year survival rate of OS patients is improved to 50–60% with developed understanding of cancer pathogenesis and the updating of diagnostic methods [2]. The understanding of tumor biology has advanced considerably over the past decades [3]. As one of the vital cell death processes participating in the pathophysiology of cells, ferroptosis is involved in regulating apoptosis, invasion, and metastasis of tumor cells [4]. As a new programmed cell death, ferroptosis is iron-dependent and in contrast to apoptosis, cell necrosis, and autophagy. The primary mechanism is that unsaturated fatty acids from the cell membrane are catalyzed in the presence of divalent iron or ester oxygenase, which activates lipid peroxidation and induces cell death.

With the exploration of ferroptosis, plenty of evidence may hold out molecularly targeted therapies for OS patients. A previous study indicated that the mitogenic actions on osteoblasts were related to stimulation of G6PD activity [5]. Marinkovic et al. demonstrated that the correlation of p63 with G6PD and PGD predicts a poor prognosis using bioinformatics [6]. The other four FRGs were not subject

to OS-related evidence, but they also played essential roles in other tumor pathways. For example, ACSF2 could be one of the FRGs to predict breast cancer [7]. Similarly, FADS2 was proved as a predicting FRG of bladder cancer.

As yet, the traditional approaches based on histopathologic diagnosis and tumor staging system for prognostic prediction of OS patients are not sufficient for precisely evaluating the outcomes [8]. It forces the development of robust and accurate prognostic biomarkers to assist clinicians to optimize therapy strategies. Hence, establishing an effective risk-scoring model based on FRGs in OS could assist in evaluating therapy and prognosis.

There are many online databases now, but there are few samples in the data set about OS. As a database for pediatric tumors, the TARGET database utilizes an integrative genomic approach to determine the molecular alterations during the onset and development of pediatric tumors and is aimed at using data to help guide the development of more effective and less toxic therapies [9]. And through data analysis, it generates useful drug targets and prognostic markers for researchers to develop new and more effective treatment options [10].

In this study, an OS dataset from TARGET was downloaded for the prediction of the OS occurrence based on ferroptosis. FRGs were screened and normalized. Then, a risk-scoring prediction model was constructed through the multiple COX regression model [11], and the Kyoto Encyclopedia of Genes and Genomes (KEGG) and gene ontology (GO) database were utilized to determine related biological process enrichment signaling pathways of FRGs.

Table 1: Clinicopathological characteristics of OS patients from TARGET database.

Characteristics		Patients ($N = 85$)	
		No.	%
Sex	Female	37	43.53
	Male	47	55.29
	Unknown	1	1.18
Age	≤14 (median)	44	51.76
	>14 (median)	40	47.06
	Unknown	1	1.18
Race	Race	51	60.00
	Asian	6	7.06
	Black or African American	7	8.24
	Unknown	21	24.71
Disease at diagnosis	Metastatic disease	21	24.71
	Nonmetastatic disease	63	74.12
	Unknown	1	1.18
Primary tumor site	Arm/hand	6	7.06
	Leg/foot	76	89.41
	Pelvis	2	2.35
	Unknown	1	1.18
Vital status	Dead	27	31.76
	Alive	58	68.24

2. Methods

2.1. Data Preparation. The gene set information including 85 samples (TARGET-OS) was contained as a training set derived from the TARGET database [11]. The patient information consisted of survival time and status, sex, age, disease at diagnosis, primary tumor site, specific tumor region, and eventual surgery (Table 1). The Ferroptosis Database (FerrDb) was utilized for the ferroptosis information collection of FRG selection [12].

2.2. Model Establishment. To establish our model, we combined univariate Cox-LASSO–multivariate Cox regression with the clinical factors and finally constructed the risk-scoring model using the selected FRGs. Univariate and multivariate Cox regression analyses were performed using R's "survival" package, and $P < 0.01$ was used as the filtering condition of univariate Cox [13]. To prevent large variance, we performed LASSO regression analysis using R's "GLMNET" package and determined K value by minimum lambda [11]. The gene at the minimum of the Akaike information criterion (AIC) was calculated and used as the variable to be included in the model, and each patient's gene expression level was used to evaluate the risk score, with the algorithm according to the previous studies [14, 15]. The median risk score of each patient is considered the reference standard for classifying the high and low groups, followed by the analysis of the survival of the two groups and drawing the survival curves using the Kaplan-Meier method (K-M method) [16]. In virtue of the critical parameters and model scores and in combination with various clinical factors, we drew a clinically relevant nomogram to predict the 1-, 3-, and 5-year survival, and the scales on nomograms represented the numerical ranges of each variable [17].

2.3. Model Validation. We used the package of "Survival ROC" to draw receiver operating characteristic curves (ROC) and "RMS" for the calibration to evaluate the accuracy of the predicted survival rates and ROC curves for the validation of each grouping variable [18].

2.4. GO and KEGG Analysis. We investigated the cellular components (CC), BP, and molecular function (MF) in the FRGs from the GO database. Furthermore, screened FRGs were analyzed for the functional pathway analysis of KEGG and for the functional enrichment analysis using R software and ClusterProfiler package [19]. We then used the "corrplot" package to analyze the relationships between FRGs by Pearson's correlation coefficient.

2.5. Gene Set Enrichment Analysis (GSEA). GSEA is implemented to enrich gene sets and determine the distribution differences between whole gene sets and phenotypes, thereby achieving enrichment. The grouping file of the FRG expression differences and the downloaded expression matrix file of OS common transcription group were input into GSEA4.0.3 software [20]. The data sets used

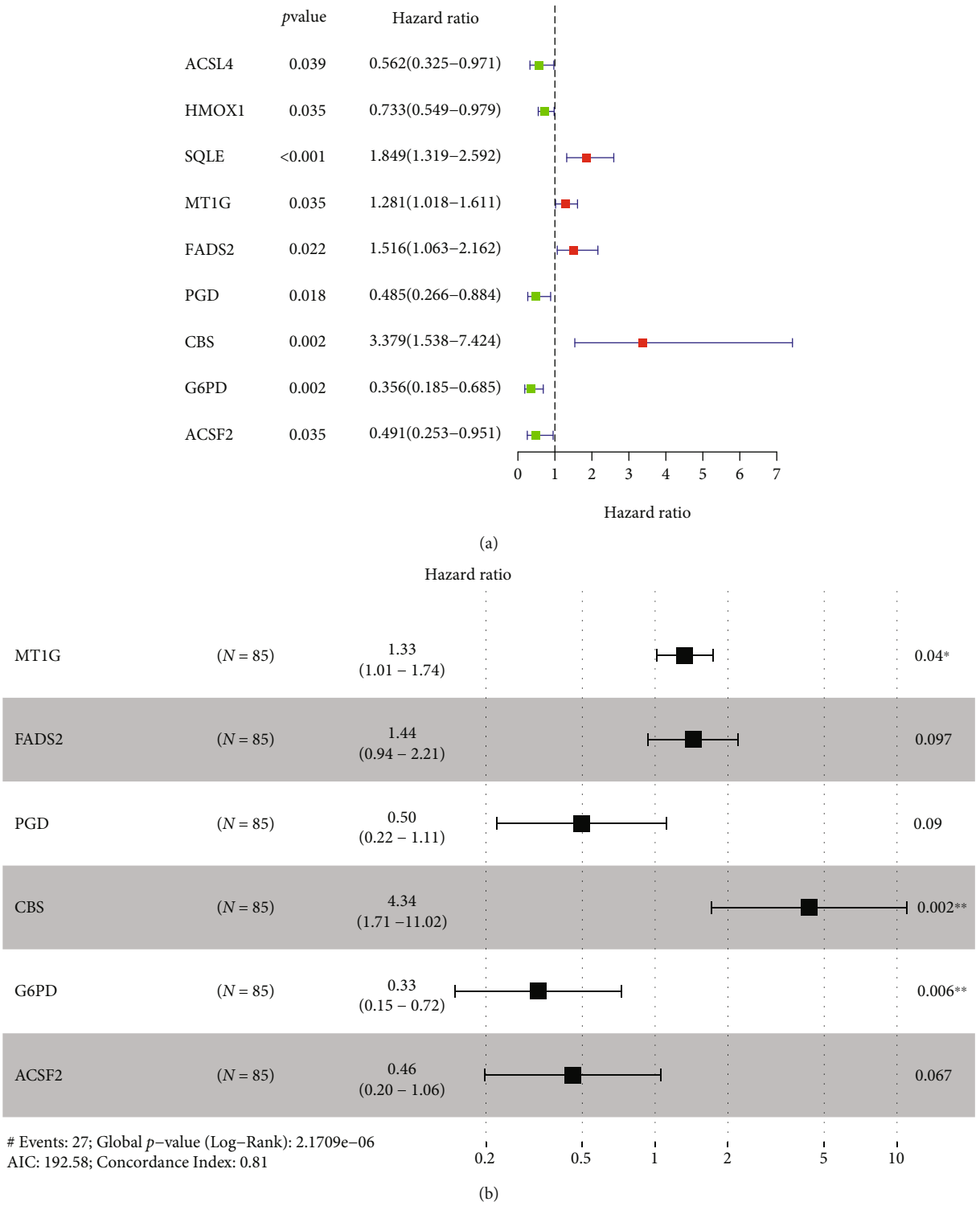

Figure 1: Development of prognostic ferroptosis-associated gene signature. (a) Forrest plot of univariate Cox regression. (b) Forrest plot of multivariate Cox regression.

for enrichment were C2 and C5 molecular sets from the Molecular Characteristic Database (MSigDB), and the output results were adjusted to 100 sheets [21]. Finally, the enrichment gene sets were screened according to Normalized Enrichment Score (NES) > 1, False-Discovery Rate (FDR) < 0.25, and $P < 0.05$.

2.6. Immune Cell Infiltration. The visualization was conducted for proportions of immune cell signatures in the training set. The cell infiltration level and the stromal content for OS samples were collected through the single-sample GSEA (ssGSEA) algorithm, and consensus clustering through the "ConsensuClusterPlus" package.

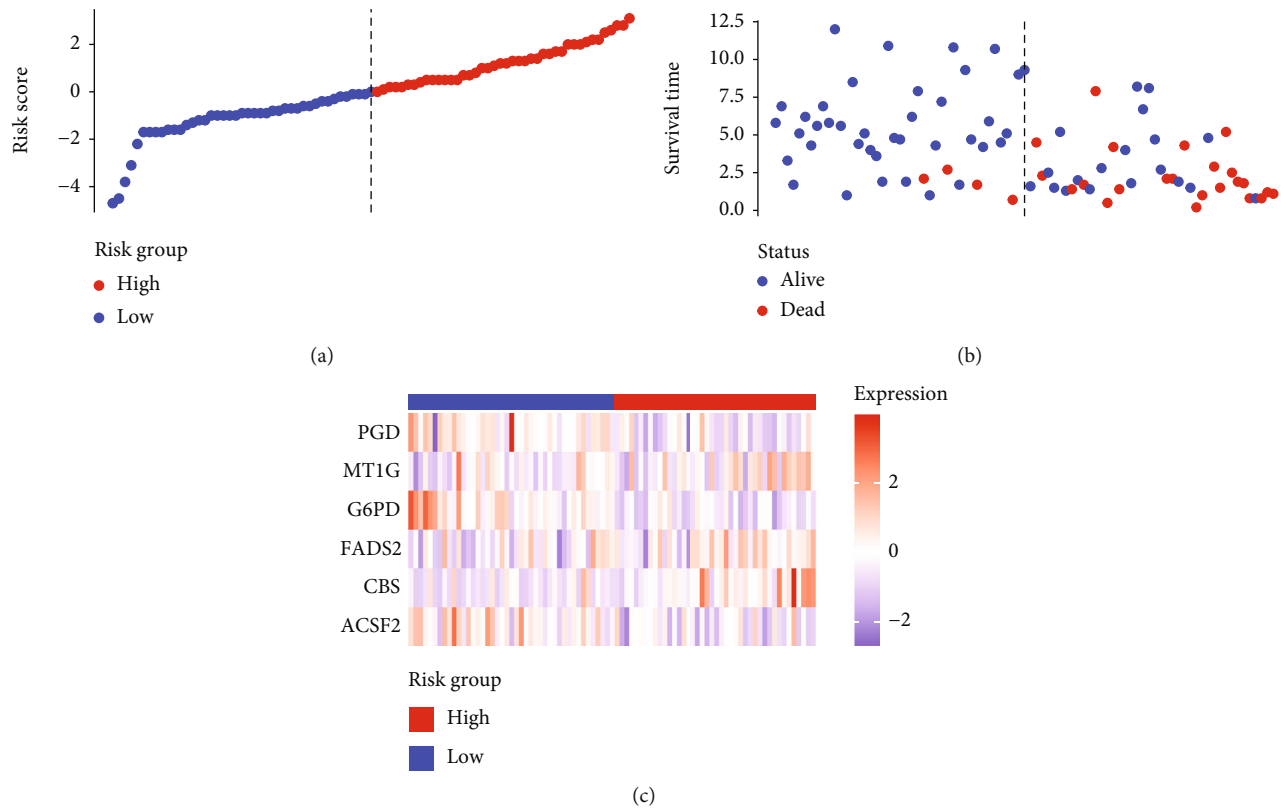

Figure 2: Establishment and validation of prognostic ferroptosis-associated gene signature. (a) Risk score plot, (b) survival status scatter plot, and (c) heatmap for the levels of *ACSF2*, *CBS*, *FADS2*, *G6PD*, *MT1G*, and *PGD*.

2.7. Prediction of Response to Targeted Therapy. Half-maximal inhibitory concentrations (IC_{50}) of targeted therapeutic drugs were plotted using R's "ggplot2" and "pRRophetic" packages. Box plots represented the connection of the IC_{50}s to two risk groups.

3. Results

3.1. Collation of FRGs. Combining gene expression information of 85 OS patients obtained from TARGET and 61 FRGs on FerrDb, the OS-related FRGs as well as the expression information and clinical information were found. Nine survival-related FRGs were obtained as shown in Figure 1(a). We then used multivariate Cox regression and LASSO method to generate a categorizer to forecast OS according to the expression of FRGs. Finally, a combination of six genes (*ACSF2*, *CBS*, *FADS2*, *G6PD*, *MT1G*, and *PGD*) remained as predictors in the model (Figure 1(b)).

3.2. Data Preprocessing and Risk-Scoring Model Establishment. Based on the median risk score in the training set, the patients were separated into two risk groups: the low and the high. Survival analysis between groups showed that the risk score negatively correlated to the prognosis in the OS patients (Figures 2(a) and 2(b)). A heatmap was drawn to display the six genes level from their signatures (Figure 2(c)), showing lower expression of *PGD*, *G6PD*, and *ACSF2* of the high-risk group, together with higher levels of *MT1G*, *FADS2*, and *CBS*. The survival rates and gene expression levels of each hub FRG are shown in Figures 3 and 4.

3.3. Nomogram Development and Verification. As shown in Figure 5, an OS risk estimation nomogram was formed combining the risk score and five independently related risk factors, including sex, age, disease at diagnosis, definitive surgery, and risk score. K-M curves indicated that over time, the survival rate of the low-risk group was higher than that of the high-risk group (Figure 6(a)). The prediction accuracy was evaluated in *C*-index (0.822) and calibration curve (Figures 6(b) and 6(c)).

3.4. KEGG and GO Analysis. The KEGG signaling pathway and GO functional process analysis were carried out specifying the biology pathways and processes associated with the six FRGs. The results indicated that these FRGs were functional in ferroptosis-related processes such as carbon metabolism, glutathione metabolism, and pentose phosphate pathway (Figure 7).

3.5. GSEA. The stratification was conducted in OS patients depending on the median risk scores. The results disclosed the enrichment of six FRGs in the provenzani metastasis, peroxisomal protein import, neutrophil degranulation, amino acids regulating mTORC1, peroxisome, T cell receptor signaling pathway, regulation of calcium-mediated

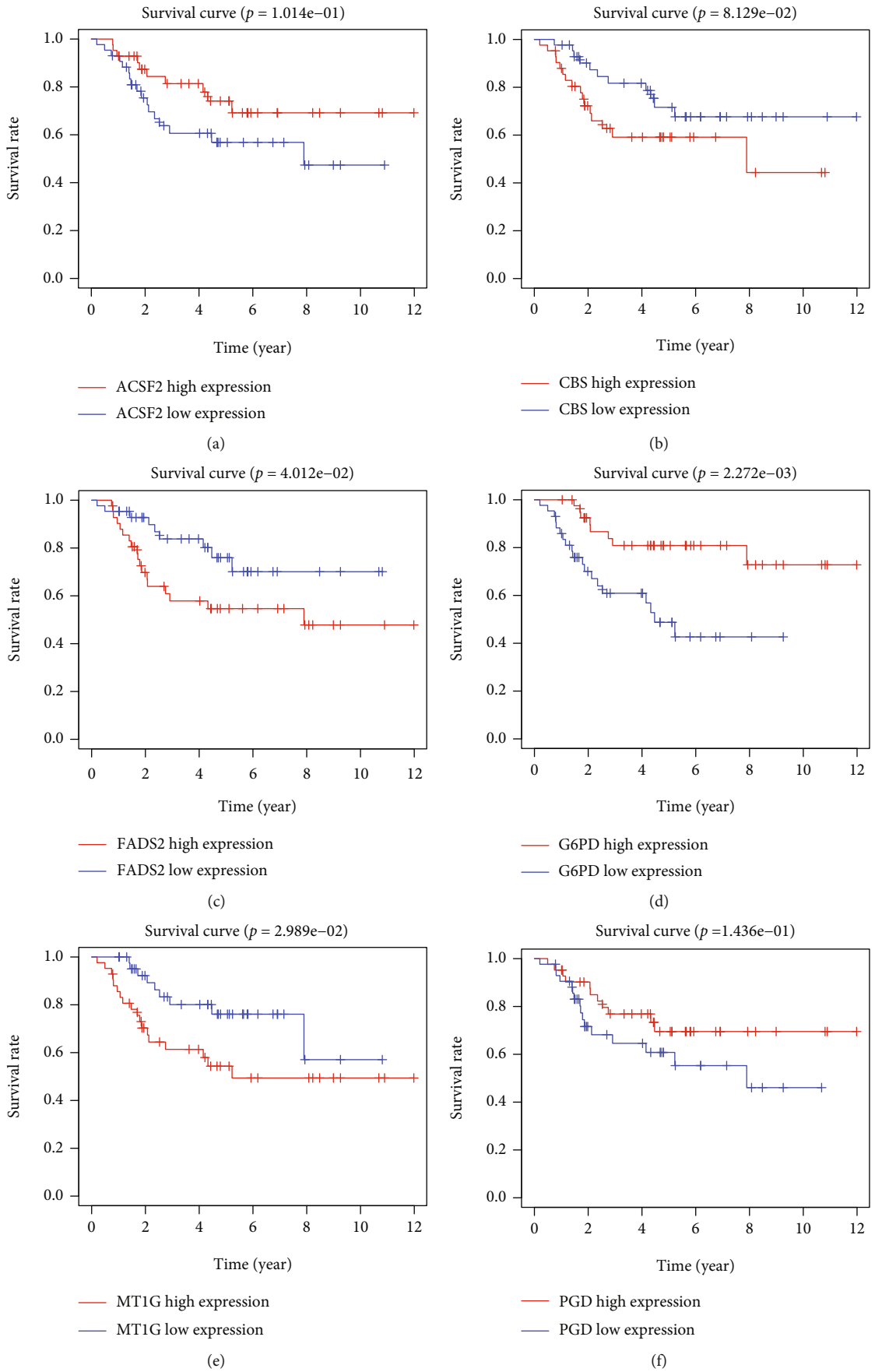

Figure 3: Survival rates of *ACSF2*, *CBS*, *FADS2*, *G6PD*, *MT1G*, and *PGD*.

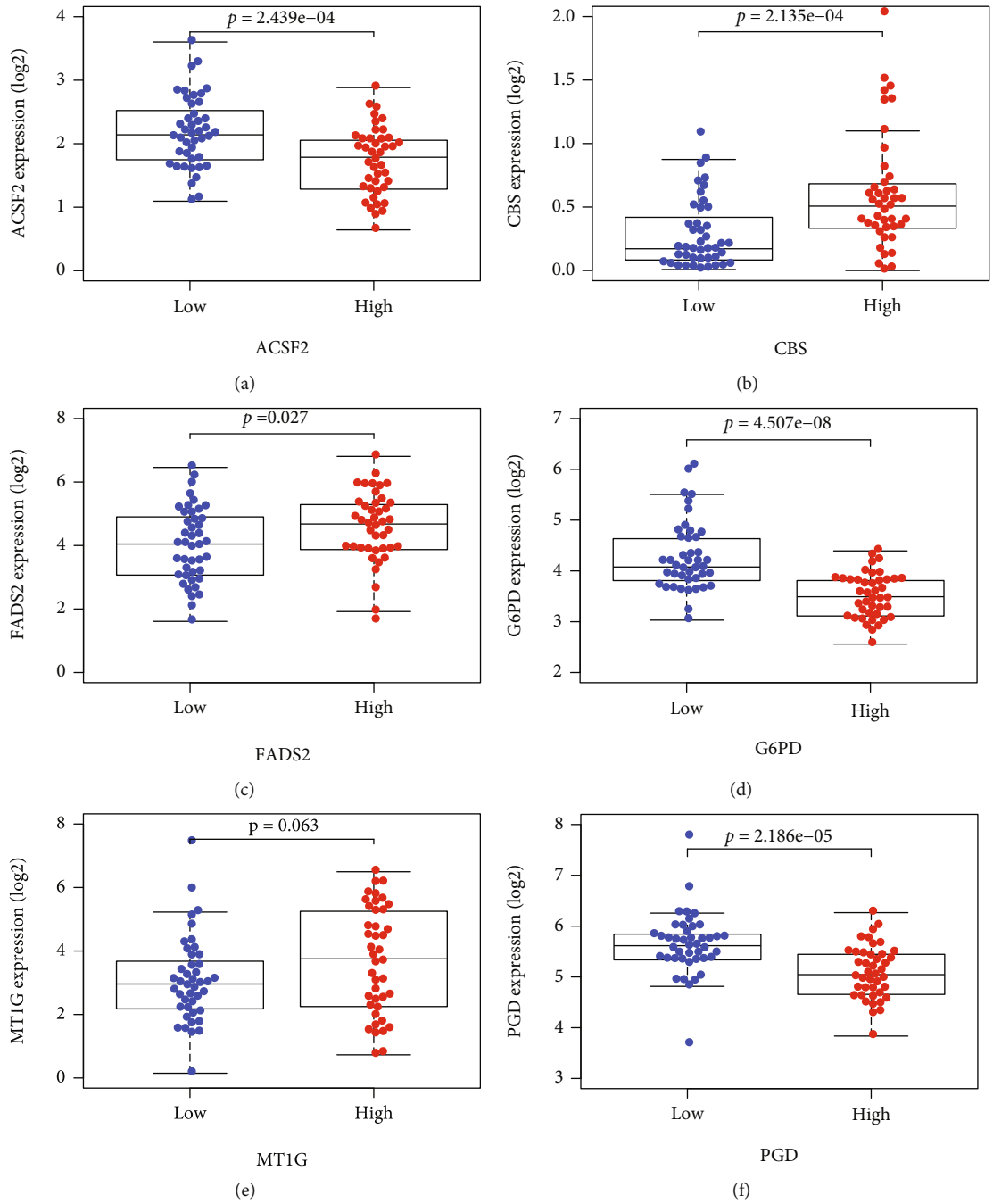

Figure 4: Expressions of *ACSF2*, *CBS*, *FADS2*, *G6PD*, *MT1G*, and *PGD*.

signaling, positive regulation of protein targeting to the mitochondrion, and B cell activation involved in immune response (Figure 8).

3.6. Immune Infiltrating. Except for activated dendritic cells (aDCs) and immature dendritic cells (iDCs), the numbers of other immune cells and immune functions of the low-risk group were significantly eminent compared to that of the high-risk group (Figures 9(a)–9(c)).

3.7. Response to Targeted Therapy. Based on the predicted IC_{50}s, the response to various targeted drugs differed significantly between the two groups with different risks. IC_{50}s were lower in the high-risk group, indicating a higher sensitivity to targeted drugs (Figure 10).

4. Discussion

OS is the most common malignant tumor originated from mesenchymal tissue, which is prone to teenagers, recurrence, and lung metastasis with a poor prognosis. The main treatment of osteosarcoma is extensive or radical amputation, combined with chemotherapy. However, the multidrug resistance of osteosarcoma restricts its chemotherapy effect

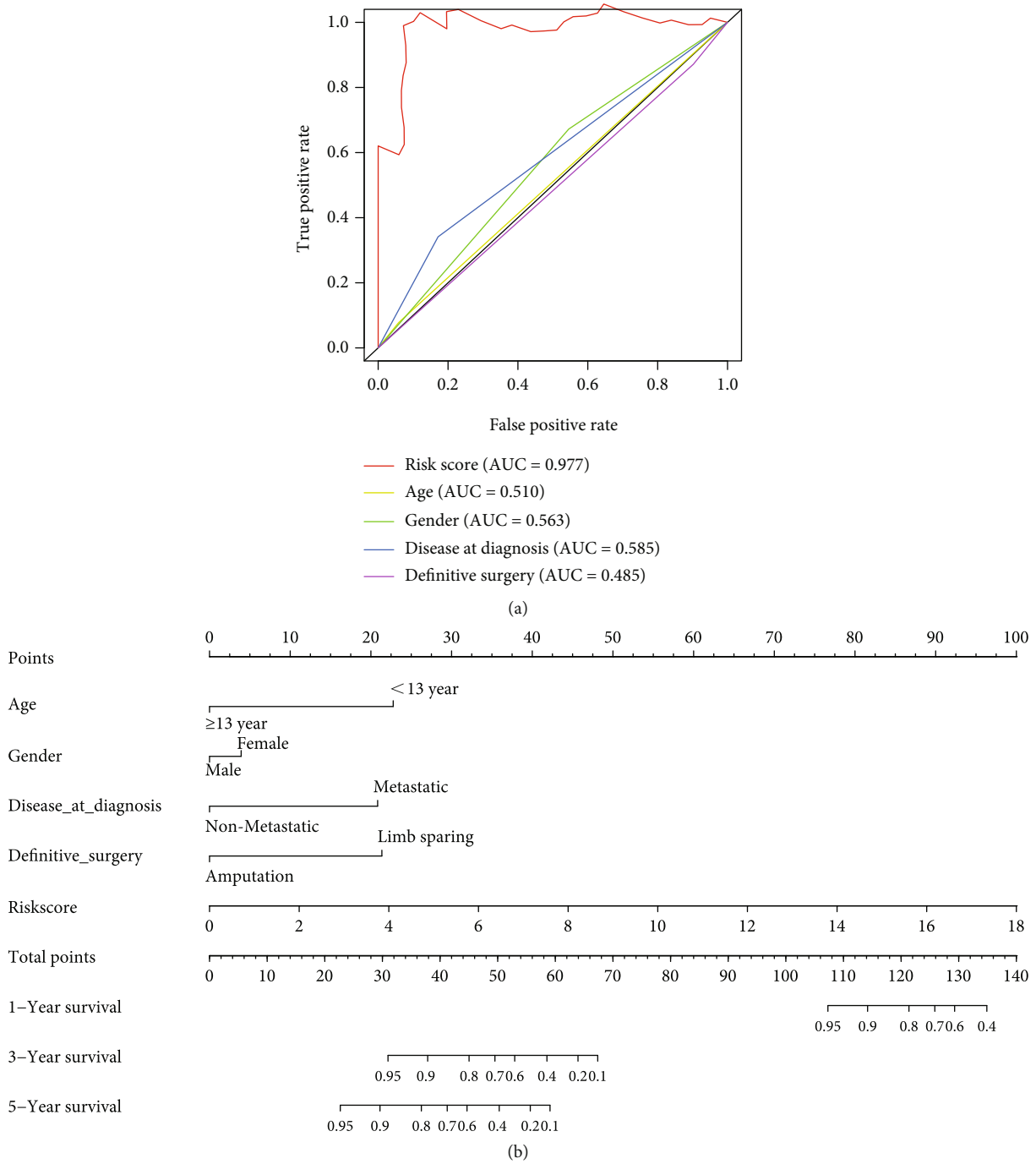

Figure 5: Construction of a predictive nomogram. (a) Independent related risk factors (sex, age, disease at diagnosis, definitive surgery, and risk score) were selected in the nomogram. (b) Nomogram for predicting 1-, 3-, and 5-year survival.

and long-term prognosis. Therefore, it is necessary to find new treatment methods.

Our research sifted six FRGs relating to OS that were possibly targeted for novel molecular therapy. The results from the risk prediction model in accordance with these six key FRGs showed noticeably separated survival curves between the two risk groups. In the time-dependent model, the risk score and death number have been elevated remarkably over time, suggesting the critical importance of these six FRGs on the prognosis prediction of OS. The key FRGs were good predictors of prognosis for OS patients, as shown by the ROC prediction results of 1-, 3-, and 5-year survival rates. Similarly, the six FRGs have shown promising outcomes in terms of clinical characterization studies.

According to the enrichment analyses results, OS's ferroptosis is closely related to carbon metabolism, glutathione metabolism, and the pentose phosphate pathway. Metabolic adaptation of cancer occurs as efficient cellular energy and biomass production alterations are indispensable for cancer onset and progression [22]. The catabolic and anabolic

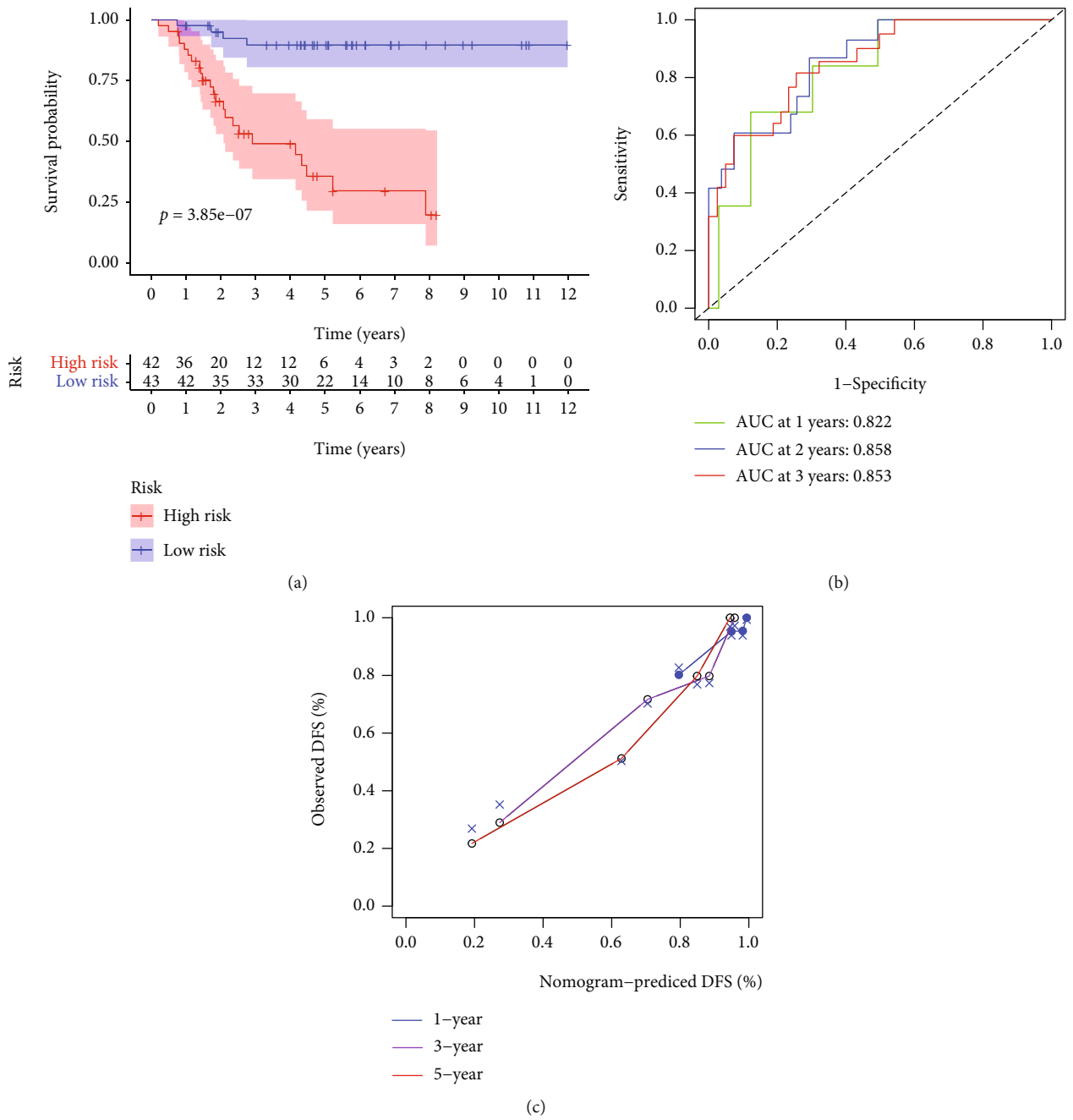

Figure 6: Validation of a predictive nomogram. (a) Kaplan-Meier curve comparing the survival rates, (b) ROC curve, and (c) calibration curve to judge the accuracy of the nomogram.

procedures in cancer metabolism can easily adjust to the elevated energy, and biological mass demands resulting from rapidly proliferating tumors. Malignant and metastatic cells of OS have elevated energy metabolism in comparison with the benign cells [23]. Among these metabolic pathways, the cysteine synthesis glutathione (GSH) pathway plays a leading role in the initiation of ferroptosis (Erastin induction pathway). Erastin is one of the small molecules found in chemical screening that can induce iron death in carcinogenic Ras mutant cell lines [24, 25]. In the process of iron death induced by Erastin, glutamate cysteine transporter, also known as X-C system, is the most important target of Erastin molecule. Cystine (the main form of intracellular cysteine) is mainly transferred into cells through glutamate cysteine transporter in the ratio of 1 : 1. Then, GSH and glutathione peroxidase 4 (GPX4) are synthesized in cells. GSH is mainly used as a cofactor in the process of protecting cells from oxidative damage, and GPX4 catalyzes the reduction of lipid peroxide to alcohols [26]. Therefore, targeting to cancer metabolism is ongoing to develop new therapies for cancer.

The risk-scoring model revealed the positive correction of risk scores with the sensitivity to targeted drugs. Prior investigations documented the effect of these drugs on cancer cytology. For example, axitinib is a potent and selective

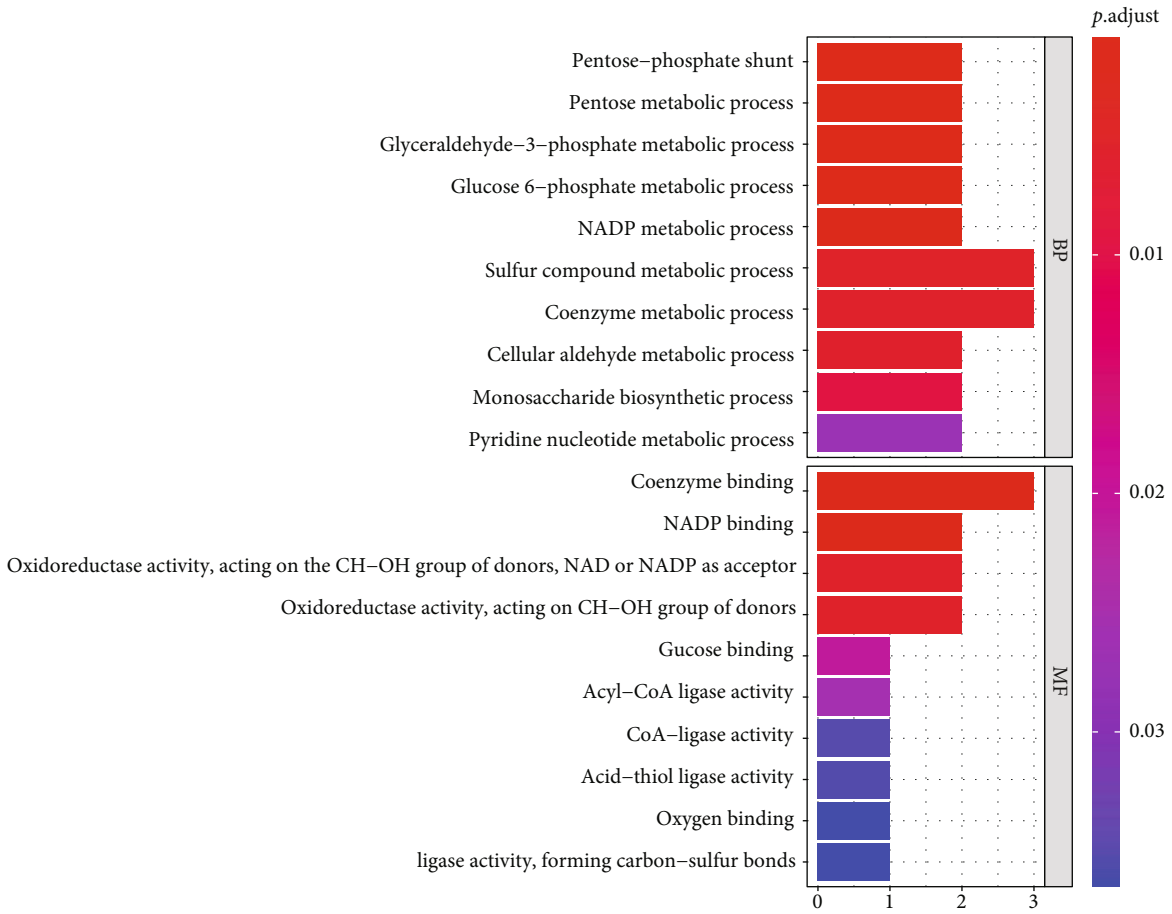

(a)

Figure 7: Continued.

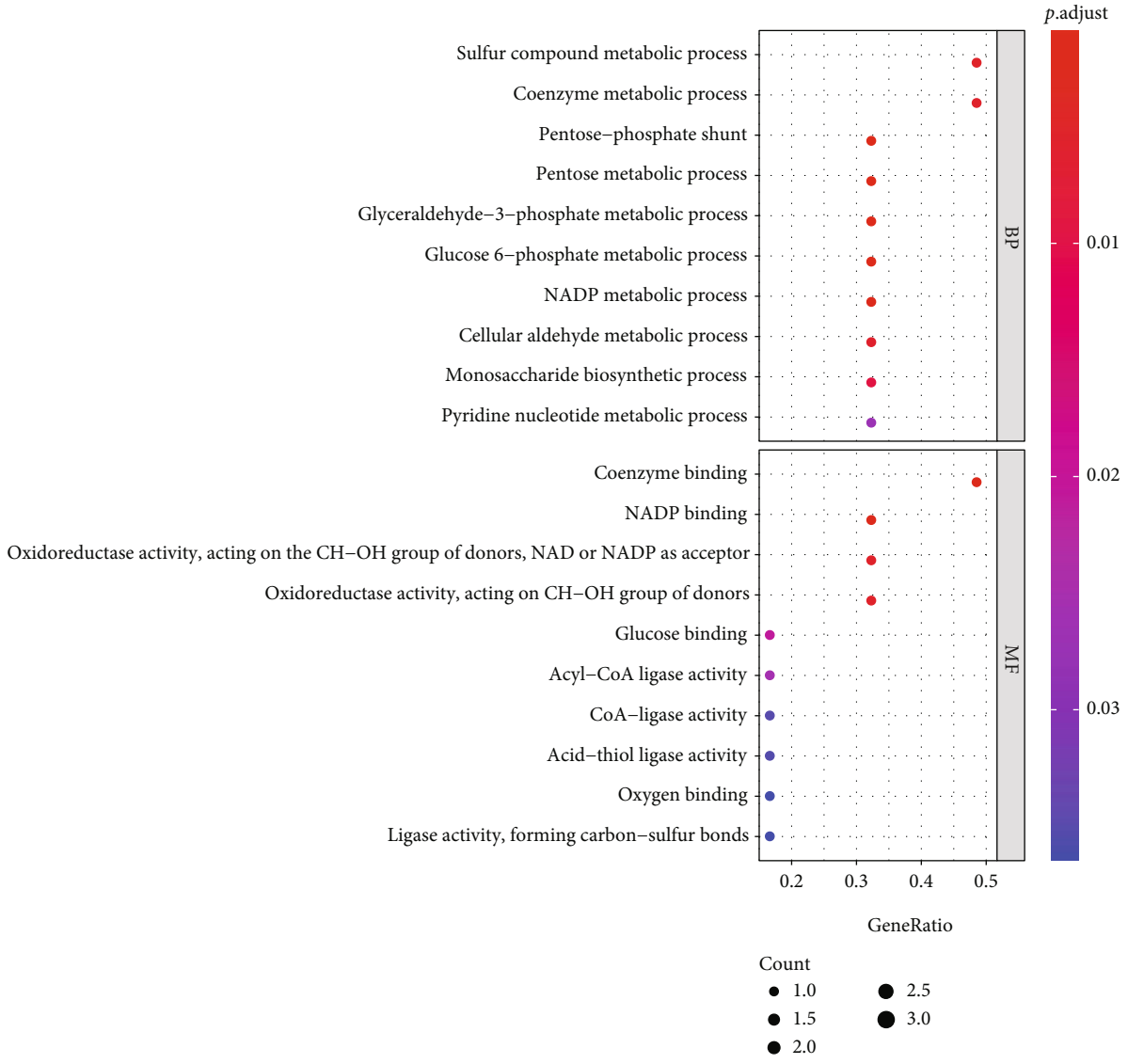

(b)

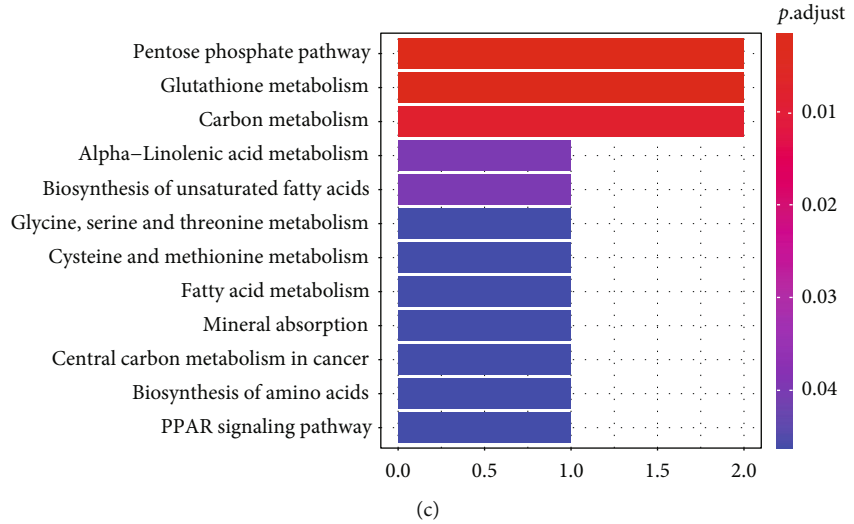

(c)

Figure 7: Continued.

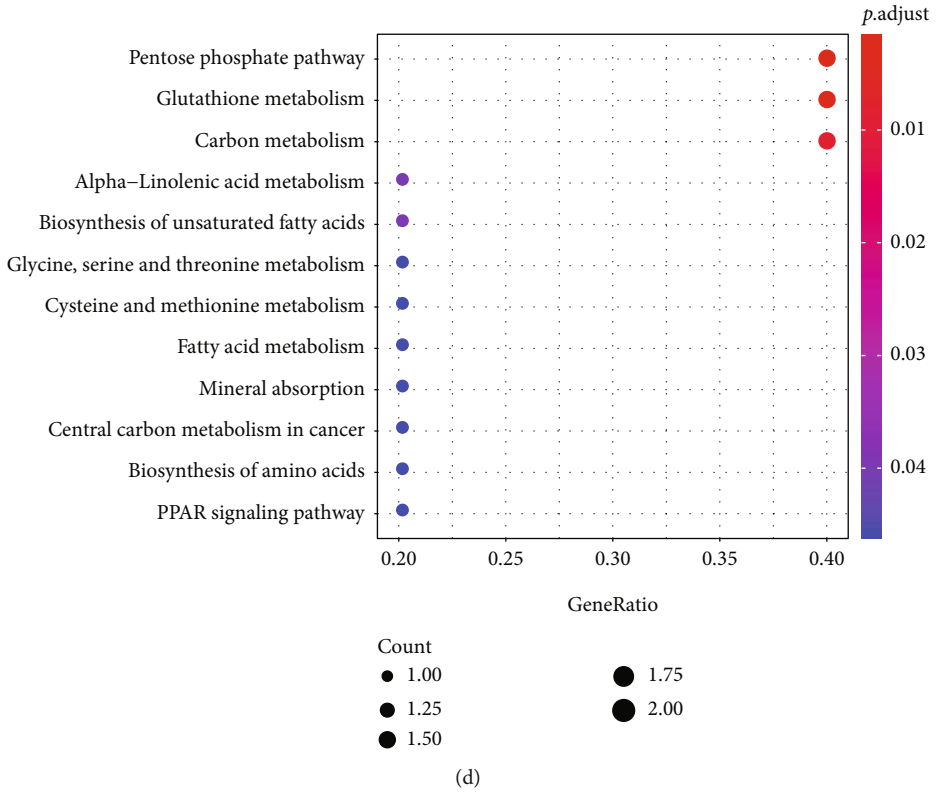

Figure 7: Significantly enriched GO annotations and KEGG pathways. (a) Bar plot and (b) bubble plot of gene ontology (GO) enrichment pathway. (c) Bar plot and (d) bubble plot of KEGG enrichment pathway.

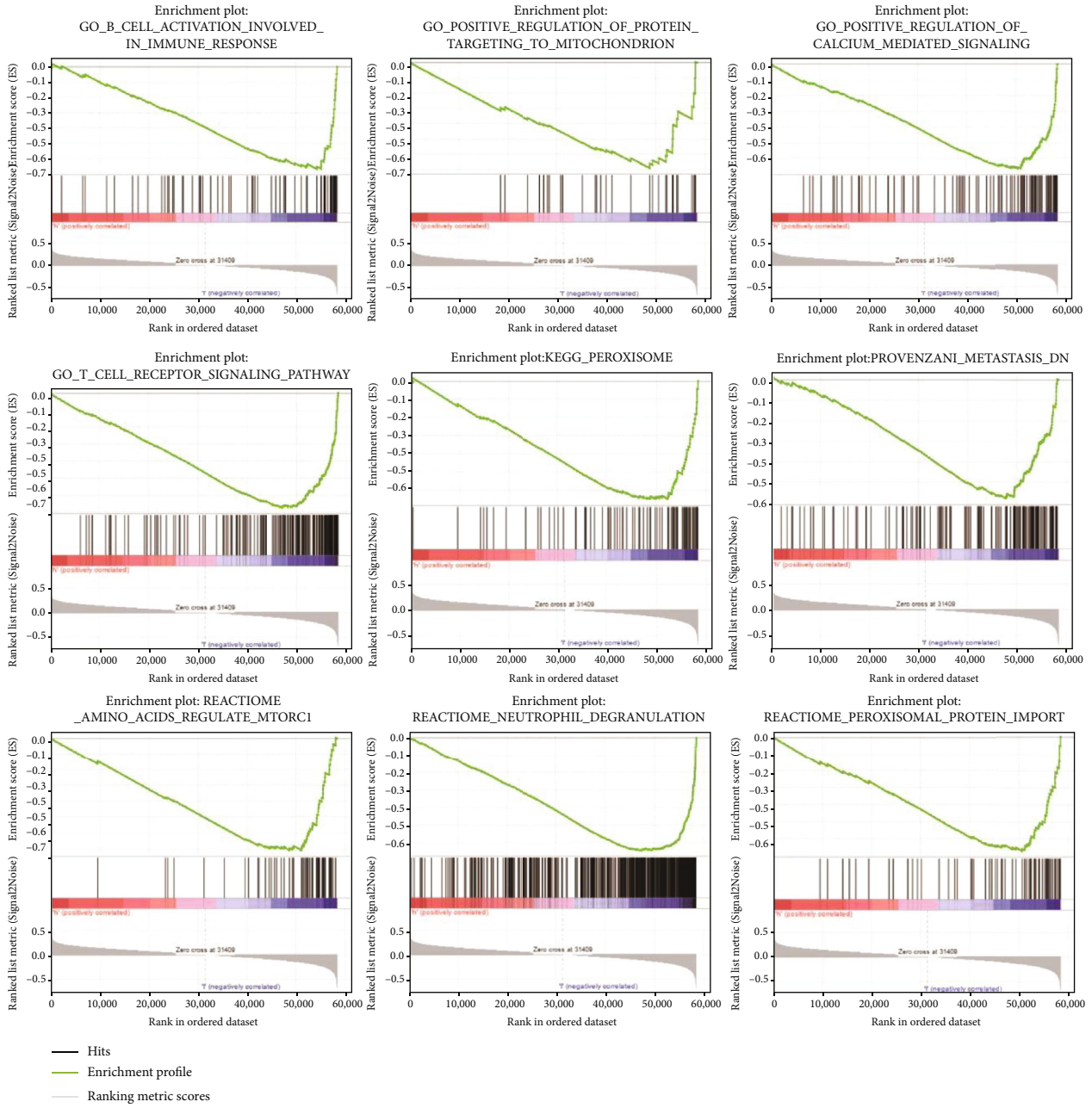

Figure 8: Gene set enrichment analysis results for *ACSF2*, *CBS*, *FADS2*, *G6PD*, *MT1G*, and *PGD*.

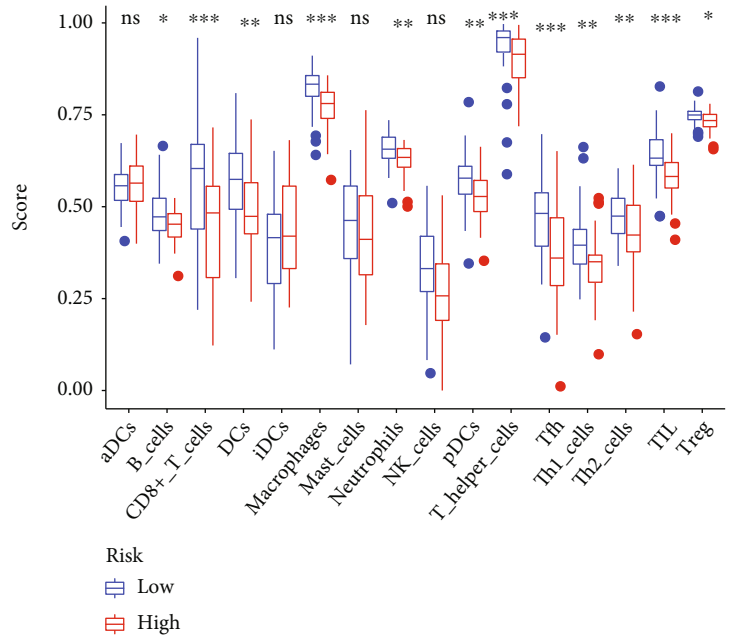

(a)

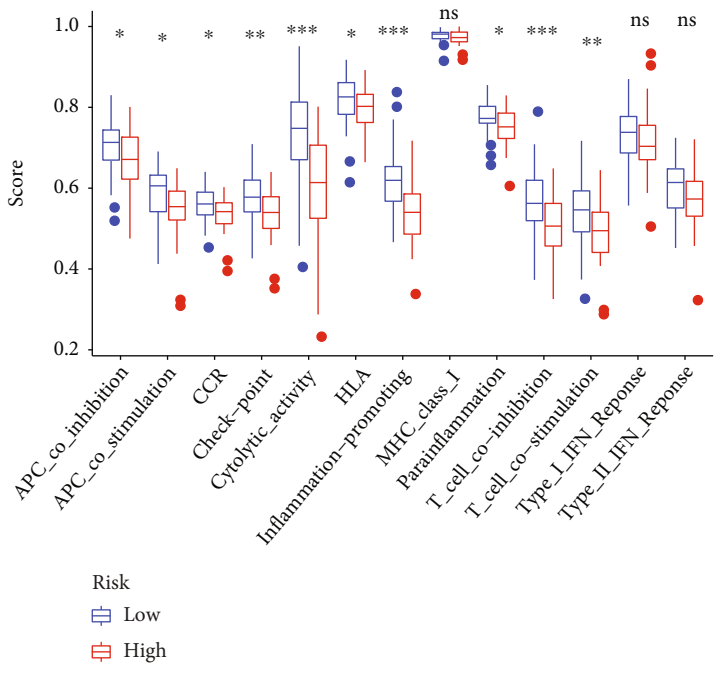

(b)

Figure 9: Continued.

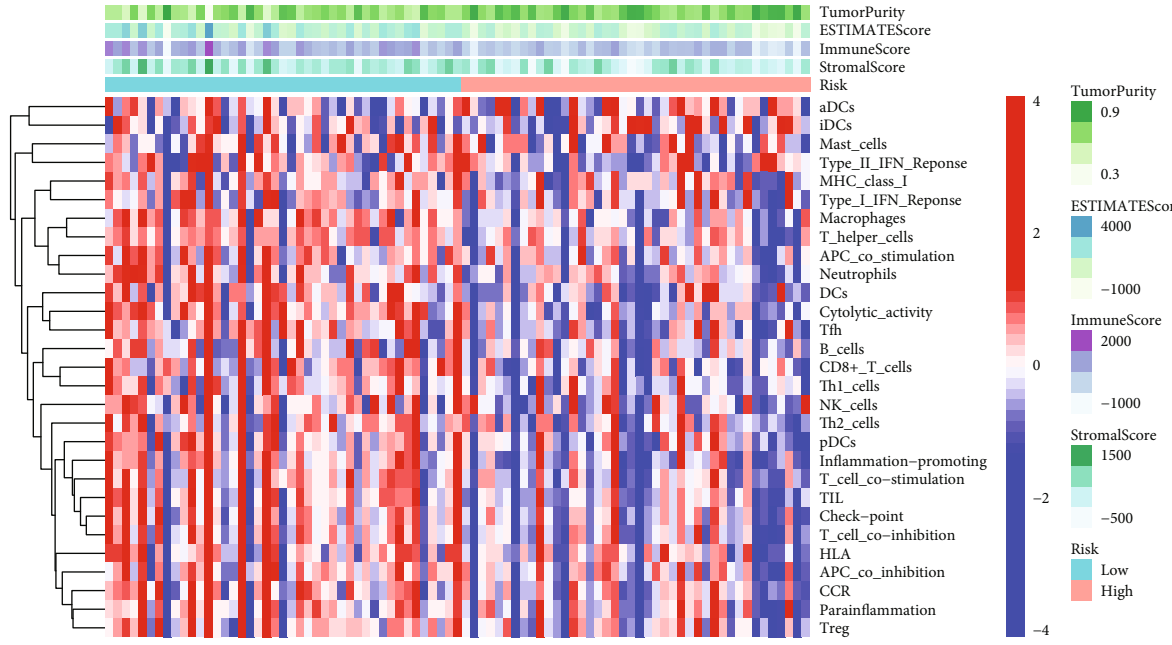

(c)

Figure 9: Tumor immune cell infiltration. (a) The 16 levels of immune cell infiltration. (b) The immune function. (c) Heatmap showing the infiltration level of immune signatures in different groups.

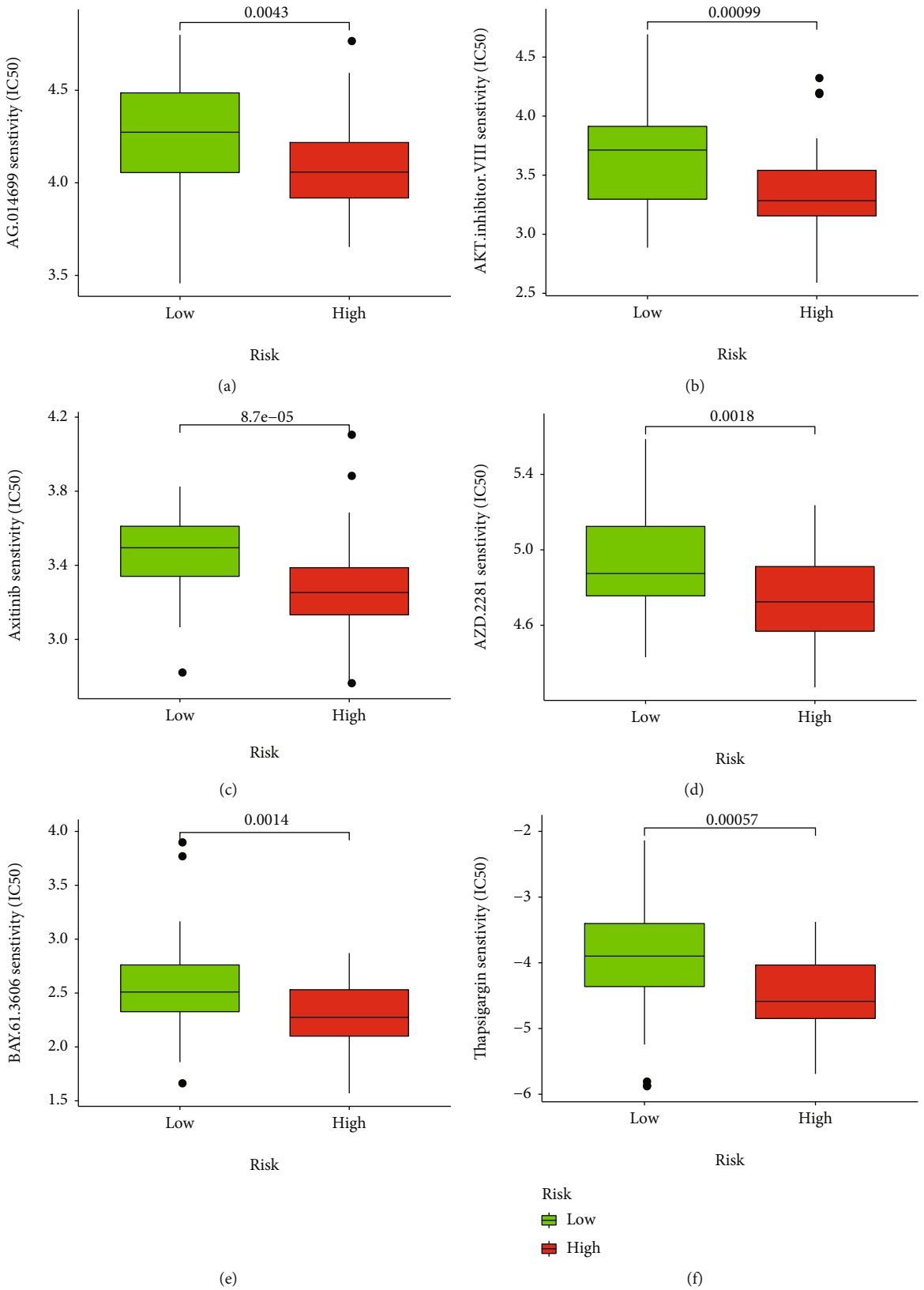

Figure 10: Prediction of response to targeted drugs. (a) AG.014699. (b) AKT.inhibitor.VIII. (c) Axitinib. (d) AZD.2281. (e) BAY.61.3606. (f) Thapsigargin.

inhibitor of VEGFR-1–3. In transfected or endogenous RTK-expressing cells, axitinib potently blocked growth factor-stimulated phosphorylation of VEGFR-2 and VEGFR-3, thereby effectively inhibiting tumor growth, angiogenesis, and distant metastasis [27, 28]. Fritsche-Guenther et al. proved that AKT2 is a critical signal molecule in the insulin signaling pathway, which needs to induce glucose transport [29]. In our study, the group with high risk presented high sensitivity to AKT inhibitor VIII. Therefore, inhibiting AKT to interfere with glucose metabolism and then controlling the occurrence or development of ferroptosis can be considered the future research direction.

It has been reported that ferroptosis can improve the antitumor effect of immunotherapy by activating CD8+ T cells, but whether FRG affects the occurrence and development of OS by regulating the immune state of the tumor microenvironment is still unclear [30]. In the process of establishing and verifying the risk-scoring model, we found that OS patients with different FRG expression matrixes showed different immune states, and patients with more active immune states had better prognosis. The tumor-associated immune response vitally partakes in tumor cell infiltration, whereas ferroptosis critically regulates the tumor-related immune responses [31]. The immune cell infiltration analysis in this study indicated that the immune functions and the numbers of immune cells, except for aDCs and iDCs, are noticeably higher in the low-risk group, indicating the ferroptosis-related, antitumor immune response processes that reduce the risk of death in low-risk patients.

Some limitations exist in this study. For example, the sample size is comparatively insufficient, which needs future study to include more samples to evaluate the model performance further and elucidate the latent mechanism.

5. Conclusions

To sum up, a prognostic signature of OS based upon six FRGs was determined, and a risk-scoring model based on six OS-related FRGs was established. This risk-scoring model shows commendable performance to independently evaluate the prognosis of OS at 1, 3, and 5 years, which will provide the potential guidance of OS targeted therapy.

Data Availability

The data used to support the findings of this study are included within the article.

Ethical Approval

This study was approved by Guangxi Medical University First Affiliated Hospital Ethical Review Committee [approval No.: 2021 (KY-E-125)].

Conflicts of Interest

All authors have no conflicts of interest to declare and have completed the ICMJE uniform disclosure form (available at https://doi.org/xxxx).

Authors' Contributions

Mingyang Jiang, Zifan Wang, and Xiaoyu He contributed equally to this work and are co-first authors. The authors are responsible for all aspects of the work in ensuring that issues related to the accuracy or integrity of any part of the work are appropriately investigated and resolved.

Acknowledgments

This work was supported by the Guangxi Natural Science Foundation (2017JJA10088). The authors thank the First Affiliated Hospital of Guangxi Medical University for the assistance offered with data collection.

References

[1] B. Pingping, Z. Yuhong, L. Weiqi et al., "Incidence and mortality of sarcomas in shanghai, China, during 2002-2014," *Frontiers in Oncology*, vol. 9, p. 662, 2019.

[2] L. C. Sayles, M. R. Breese, A. L. Koehne et al., "Genome-informed targeted therapy for osteosarcoma," *Cancer Discovery*, vol. 9, no. 1, pp. 46–63, 2019.

[3] C. Farquharson, J. Milne, and N. Loveridge, "Mitogenic action of insulin-like growth factor-i on human osteosarcoma mg-63 cells and rat osteoblasts maintained in situ: the role of glucose-6-phosphate dehydrogenase," *Bone and Mineral*, vol. 22, no. 2, pp. 105–115, 1993.

[4] A. D'Alessandro, I. Amelio, C. R. Berkers et al., "Metabolic effect of TAp63α: enhanced glycolysis and pentose phosphate pathway, resulting in increased antioxidant defense," *Oncotarget*, vol. 5, no. 17, pp. 7722–7733, 2014.

[5] D. Wang, G. Wei, J. Ma et al., "Identification of the prognostic value of ferroptosis-related gene signature in breast cancer patients," *BMC Cancer*, vol. 21, no. 1, p. 645, 2021.

[6] M. Marinkovic, M. Sprung, M. Buljubasic, and I. Novak, "Autophagy modulation in cancer: current knowledge on action and therapy," *Oxidative Medicine and Cellular Longevity*, vol. 2018, Article ID 8023821, 18 pages, 2018.

[7] B. Jin, D. Jin, Z. Zhuo, B. Zhang, and K. Chen, "Mir-1224-5p activates autophagy, cell invasion and inhibits epithelial-to-mesenchymal transition in osteosarcoma cells by directly targeting plk 1 through pi3k/akt/mtor signaling pathway," *Oncotargets and Therapy*, vol. Volume 13, pp. 11807–11818, 2020.

[8] J. Levy, C. G. Towers, and A. Thorburn, "Targeting autophagy in cancer," *Nature Reviews Cancer*, vol. 17, no. 9, pp. 528–542, 2017.

[9] L. Fan, J. Ru, T. Liu, and C. Ma, "Identification of a novel prognostic gene signature from the immune cell infiltration landscape of osteosarcoma," *Frontiers in Cell and Development Biology*, vol. 9, article 718624, 2021.

[10] R. Nagarajan, B. J. Weigel, R. C. Thompson, and J. P. Perentesis, "Osteosarcoma in the first decade of life," *Medical and Pediatric Oncology*, vol. 41, no. 5, pp. 480–483, 2003.

[11] S. Dong, H. Huo, Y. Mao, X. Li, and L. Dong, "A risk score model for the prediction of osteosarcoma metastasis," *FEBS Open Bio*, vol. 9, no. 3, pp. 519–526, 2019.

[12] K. Homma, K. Suzuki, and H. Sugawara, "The autophagy database: an all-inclusive information resource on autophagy that provides nourishment for research," *Nucleic Acids Research*, vol. 39, no. Database, pp. D986–D990, 2011.

[13] J. Li, Y. Li, X. Wu, and Y. Li, "Identification and validation of potential long non-coding RNA biomarkers in predicting survival of patients with head and neck squamous cell carcinoma," *Oncology Letters*, vol. 17, no. 6, pp. 5642–5652, 2019.

[14] D. J. Birnbaum, P. Finetti, A. Lopresti et al., "A 25-gene classifier predicts overall survival in resectable pancreatic cancer," *BMC Medicine*, vol. 15, no. 1, p. 170, 2017.

[15] Y. Mao, Z. Fu, Y. Zhang et al., "A six-microRNA risk score model predicts prognosis in esophageal squamous cell carcinoma," *Journal of Cellular Physiology*, vol. 234, no. 5, pp. 6810–6819, 2019.

[16] B. Han, H. Zhang, Y. Zhu et al., "Subtype-specific risk models for accurately predicting the prognosis of breast cancer using differentially expressed autophagy-related genes," *Aging (Albany NY)*, vol. 12, no. 13, pp. 13318–13337, 2020.

[17] S. Liao, J. He, C. Liu et al., "Construction of autophagy prognostic signature and analysis of prospective molecular mechanisms in skin cutaneous melanoma patients," *Medicine (Baltimore)*, vol. 100, no. 22, article e26219, 2021.

[18] Y. Jiao, Z. Fu, Y. Li, L. Meng, and Y. Liu, "High EIF2B5 mRNA expression and its prognostic significance in liver cancer: a study based on the TCGA and GEO database," *Cancer Management and Research*, vol. Volume 10, pp. 6003–6014, 2018.

[19] R. S. Zhou, E. X. Zhang, Q. F. Sun et al., "Integrated analysis of lncRNA-miRNA-mRNA ceRNA network in squamous cell carcinoma of tongue," *BMC Cancer*, vol. 19, no. 1, p. 779, 2019.

[20] A. Subramanian, P. Tamayo, V. K. Mootha et al., "Gene set enrichment analysis: a knowledge-based approach for interpreting genome-wide expression profiles," *Proceedings of the National Academy of Sciences of the United States of America*, vol. 102, no. 43, pp. 15545–15550, 2005.

[21] A. Liberzon, C. Birger, H. Thorvaldsdottir, M. Ghandi, J. P. Mesirov, and P. Tamayo, "The molecular signatures database hallmark gene set collection," *Cell Systems*, vol. 1, no. 6, pp. 417–425, 2015.

[22] D. Hanahan and R. A. Weinberg, "Hallmarks of cancer: the next generation," *Cell*, vol. 144, no. 5, pp. 646–674, 2011.

[23] R. Fritsche-Guenther, Y. Gloaguen, M. Kirchner, P. Mertins, P. U. Tunn, and J. A. Kirwan, "Progression-dependent altered metabolism in osteosarcoma resulting in different nutrient source dependencies," *Cancers*, vol. 12, no. 6, 2020.

[24] H. Yu, P. Guo, X. Xie, Y. Wang, and G. Chen, "Ferroptosis, a new form of cell death, and its relationships with tumourous diseases," *Journal of Cellular and Molecular Medicine*, vol. 21, no. 4, pp. 648–657, 2017.

[25] Y. Zhao, Y. Li, R. Zhang, F. Wang, T. Wang, and Y. Jiao, " The role of erastin in ferroptosis and its prospects in cancer therapy ," *Oncotargets and Therapy*, vol. Volume 13, pp. 5429–5441, 2020.

[26] T. Lei, H. Qian, P. Lei, and Y. Hu, "Ferroptosis-related gene signature associates with immunity and predicts prognosis accurately in patients with osteosarcoma," *Cancer Science*, vol. 112, no. 11, pp. 4785–4798, 2021.

[27] D. D. Hu-Lowe, H. Y. Zou, M. L. Grazzini et al., "Nonclinical antiangiogenesis and antitumor activities of axitinib (ag-013736), an oral, potent, and selective inhibitor of vascular endothelial growth factor receptor tyrosine kinases 1, 2, 3," *Clinical Cancer Research*, vol. 14, no. 22, pp. 7272–7283, 2008.

[28] B. M. Fenton and S. F. Paoni, "The addition of ag-013736 to fractionated radiation improves tumor response without functionally normalizing the tumor vasculature," *Cancer Research*, vol. 67, no. 20, pp. 9921–9928, 2007.

[29] C. W. Lindsley, Z. Zhao, W. H. Leister et al., "Allosteric akt (pkb) inhibitors: discovery and Sar of isozyme selective inhibitors," *Bioorganic & Medicinal Chemistry Letters*, vol. 15, no. 3, pp. 761–764, 2005.

[30] W. Wang, M. Green, J. E. Choi et al., "$CD8^+$ T cells regulate tumour ferroptosis during cancer immunotherapy," *Nature*, vol. 569, no. 7755, pp. 270–274, 2019.

[31] C. Marar, B. Starich, and D. Wirtz, "Extracellular vesicles in immunomodulation and tumor progression," *Nature Immunology*, vol. 22, no. 5, pp. 560–570, 2021.

Hindawi
Journal of Oncology
Volume 2022, Article ID 9465124, 11 pages
https://doi.org/10.1155/2022/9465124

Research Article

Study on Mechanism of Yiqi Yangyin Jiedu Recipe Inhibiting Triple Negative Breast Cancer Growth: A Network Pharmacology and *In Vitro* Verification

Xin Sun,[1,2,3] **Panling Xu**,[3] **Fengli Zhang**,[3] **Ting Sun**,[3] **Haili Jiang**,[3] **Mei Zhang**,[3] **and Ping Li**[1,2,3]

[1]*Anhui Provincial Hospital, Cheeloo College of Medicine, Shandong University, Jinan, Shandong 250012, China*
[2]*Anhui Provincial Hospital, Hefei, Anhui 230032, China*
[3]*Department of Chinese Integrative Medicine Oncology, The First Affiliated Hospital of Anhui Medical University, Hefei, Anhui 230022, China*

Correspondence should be addressed to Ping Li; 1964liping@sina.com

Received 21 January 2022; Revised 6 March 2022; Accepted 9 March 2022; Published 27 March 2022

Academic Editor: Fu Wang

Background. The present study explores the potential mechanism of Yiqi yangyin jiedu Recipe (YQYYJDR) on triple negative breast cancer via adopting network pharmacology and experimental validation. *Materials and Methods*. The potential active compounds and target genes of YQYYJDR were screened out from TCMSP database with OB ≥ 30% and DL index ≥ 0.18. The potential pathways and function enrichment were identified from Metascape website. MDA-MB-231 and MDA-MB-468 cells were tested for cell viability, invasion, and apoptosis by *in vitro* and *in vivo* experiments. *Results*. A total of 153 bioactive compounds and 281 target genes of YQYYJDR were retrieved from TCMSP database. The top 5 enrichment pathways of YQYYJDR target genes include pathways in cancer, AGE-RAGE signaling pathway in diabetic complications, proteoglycans in cancer, IL-17 signaling pathway, and platinum drug resistance. 65 target genes were included in the pathway of cancer. Biological function enrichment analysis of 65 genes showed YQYYJDR inhibited tumor growth mainly through apoptotic pathway. *In vitro* experiments showed that YQYYJDR could inhibit the proliferation and invasion of MDA-MB-231 and MDA-MB-468 cells, arrest cells in S stage, and induce cell apoptosis. YQYYJDR upregulated BAX, caspase3, and cleaved caspase3 expression and downregulated BCL2 expression. *In vivo* experiments showed that YQYYJDR could inhibit tumor growth. *Conclusions*. In this study, network pharmacology and experiment were used to explore the mechanism of YQYYJDR on triple negative breast cancer. *In vitro* and *in vivo* experiments showed that YQYYJDR could inhibit the growth of triple negative breast cancer and induce cell apoptosis. Apoptosis pathway plays a significant role in the treatment of triple negative breast cancer.

1. Introduction

Triple negative breast cancer (TNBC) is an aggressive cancer with poor prognosis, which accounts for less than 30% in breast cancer [1]. It is characterized by negative expression of estrogen receptor (ER), progesterone receptor (PR), and human epidermal growth factor receptor 2 (HER-2) [2]. The recurrence and disease metastasis rates in TNBC are high, and the median survival for patients with advanced disease is about 18 months [3], which emphasizes the importance of developing more effective therapies for patients. The current treatments on TNBC include chemotherapy, targeted therapy, and immunotherapy. However, these treatments do not work well, and patients' quality of life is impaired [4]. Therefore, it is very important to find an alternative treatment for TNBC.

Yiqi yangyin jiedu Recipe (YQYYJDR) is a representative prescription for the treatment on breast cancer. YQYYJDR is composed of Angelica Sinensis, Astragalus Membranaceus, Radix Pseudostellariae, Prepared Radix Rehmanniae, Fructus

Amomi, Radix Scrophulariae, Semen Coicis, Fructus Lycii, Rhizoma Atractylodis, Radix Isatidis, Lonicera Japonica, Chrysanthemum, Fructus Forsythiae, Glossy Privet Fruit, Subprostrate Sophora, and Chinese Yam. Researches had proved that YQYYJDR can improve the clinical effect of breast cancer treatment [5]. However, the efficacy and mechanism of YQYYJDR against TNBC still need to be elucidated.

Network pharmacology is an emerging subject for explaining the mechanism of drug acting on disease [6]. The "drug-target-gene" model provides new perspective and methods to explore the potential targets in compound preparations, and furthermore, network pharmacology provides a more efficient platform to reveal the interactions and internal relationships between drugs and diseases [7]. In recent years, network pharmacology has been widely employed in compound preparation mechanism exploration [8, 9]. However, the reports on pharmacology network analysis of YQYYJDR has not been seen yet.

In this study, the active chemical compounds and target genes of YQYYJDR were searched using network pharmacology methods. And the drug-gene-disease network and function pathways were analyzed. *In vitro* and *in vivo* experiments were used to validate the antitumor effect and potential targets of YQYYJDR treating on TNBC.

2. Material and Methods

2.1. YQYYJDR-Related Compounds and Potential Targets. Active compounds and potential targets of YQYYJDR were searched in Traditional Chinese Medicine Database and Analysis Platform (TCMSP, https://tcmsp-e.com/), with the oral bioavailability $(\mathrm{OB}) \geq 30\%$ and drug – likeness $(\mathrm{DL}) \geq 0.18$. OB represents the percentage of drugs that reach the systemic circulation at the same oral dose; DL is used to assess the degree to which a desired compound is "drug-like," which helps to optimize drug pharmacokinetics and drug properties such as solubility and chemical stability [10]. Compounds that meet the above criteria will be considered as bioactive compounds. Then, the potential targets screened from TCMSP were imported into UniProt (http://www.uniprot.org/) to search their information, including gene name, functions, and gene ID [11].

2.2. Construction of YQYYJDR Network. The screened active compounds and potential targets were introduced into Cytoscape 3.7.2 (http://www.cytoscape.org/) to draw the activity "herb-compounds-targets" network [12]. The nodes in this network represent the active ingredients and targets of YQYYJDR; the interactions and internal relationships between the active compounds and the targets were encoded by edges.

2.3. Potential Pathways of YQYYJDR. The targets of YQYYJDR were inputted into Metascape website (https://metascape.org/) for analyzing Kyoto Encyclopedia of Genes and Genomes (KEGG) pathway and Gene Ontology Consortium (GO) Biological Processes. KEGG and GO analyses were enriched with p value < 0.01. Metascape is a comprehensive annotated and analytical resource for experimental biologists [13].

2.4. Preparation of YQYYJDR Aqueous Extract. YQYYJDR consisted of 20 g Angelica Sinensis, 30 g Astragalus Membranaceus, 15 g Radix Pseudostellariae, 18 g Prepared Radix Rehmanniae, 6 g Fructus Amomi, 15 g Radix Scrophulariae, 30 g Semen Coicis, 15 g Fructus Lycii, 15 g Rhizoma Atractylodis, 12 g Radix Isatidis, 20 g Lonicera Japonica, 20 g Chrysanthemum, 15 g Fructus Forsythiae, 15 g Glossy Privet Fruit, 15 g Subprostrate Sophora, and 15 g Chinese Yam. All crude herbs were provided by the Department of Pharmacy, The First Affiliated Hospital of Anhui Medical University. 1000 mL water was prepared to boil all above mixed herbs for 2 h, and the herbal extract of YQYYJDR was got. The obtained herbal extract was centrifuged for 30 min at 10000 rpm, then extracted twice, mixed with supernatants, and evaporated to dryness. The herbal powder was redissolved in water at a concentration of 40 mg/mL and then filtered with a 0.22 μm pore-size filter. Finally, the Chinese herb liquors were stored at -20°C for further use.

2.5. Cell Culture. The human breast cancer cell lines MDA-MB-231 and MDA-MB-468 were purchased from American Type Culture Collection (ATCC, USA). MDA-MB-231 and MDA-MB-468 cells were maintained in Leibovitz's L-15 medium (Gibco, Massachusetts, USA), which supplemented with 10% fetal bovine serum (FBS, Gibco, Massachusetts, USA), 100 U/mL penicillin, and 100 mg/mL streptomycin (Gibco, Massachusetts, USA). All cells were incubated at 37°C in a humidified incubator with 5% CO2. The morphology of the cell lines was regularly assessed.

2.6. Cell Viability Assay. MTT assay was used to detect the cytotoxicity of YQYYJDR on TNBC cell lines. In brief, 100 μL cell suspension (1×10^5 cells/mL) was seeded into 96-well plates; after incubation overnight, several concentrations of YQYYJDR were added into each well followed by a 48 h incubation. 10 μL 3-(4,5-dimethyl-2-thiazolyl)-2,5-diphenyl-2-H-tetrazolium bromide (MTT, 5 mg/mL; Sigma, USA) in phosphate-buffered saline (PBS, Gibco, USA) was added and incubated at 37°C for 4 h to produce formazan. 100 μL DMSO (Sigma, USA) was added, and the absorbance of the microplate reader was measured at 490 nm (SpectraMax ABS plus, Molecular Devices, USA).

2.7. Cell Cycle Analysis. A cell cycle and apoptosis analysis kit was used to test for cell cycle arrest. 5×10^5 cells were inoculated in each well of 6-well plates. After the cells were incubated overnight, they were treated with increasing doses of YQYYJDR for 48 hours. The cells were digested with trypsin to obtain the cell deposits, which were then fixed with precooled 70% ethanol; the cells were stained with propidium iodide solution and then detected by flow cytometry.

2.8. Apoptosis Assay. An Annexin V-FITC Apoptosis Detection Kit (Beyotime, Shanghai, China) was used to analyze cell apoptosis level. In brief, MDA-MB-231 and MDA-MB-468 cells (5×10^5 cells/mL) were seeded in 6-well plates, then

preincubated for 24 h. Different doses of YQYYJDR were added in 6-well plates and then incubated at 37°C for 48 h. Annexin V-FITC and propidium iodide staining solution were added to incubate for 20 minutes. Then, the cell apoptosis level was evaluated using a flow cytometer (CytoFLEXS, Beckman COULTER, USA).

2.9. Transwell Analysis. Cell invasion efficiency was verified by transwell assay. In brief, 200 μL Matrigel matrix was added into each well of a 24-well plate, 2×10^5 cells were cultured DMEM without FBS for 8 h, then inoculated in each well of a 24-well plate, and DMEM with 20% FBS were added into the bottom. After incubation for 24 hours, cells in upper chamber were fixed with 4% paraformaldehyde stained and stained with crystal violet staining solution after wiping the matrix. An optical microscope was used to observe.

2.10. RT-PCR. Total RNA from TNBC cells was extracted by using TRIzol reagent (Invitrogen, USA). Then, cDNA were obtained using TaKaRa PrimeScript RT reagent Kit. ABI 7900HT Real-Time PCR system (Applied Biosystems, USA) was used to amplify cDNA for comparing gene expression between different experimental groups. All reactions were run in triplicate. The sequences of the primers for genes are shown in Table 1.

2.11. Western Blotting. In order to verify the related pathways of drug action on cells, the cell protein samples were extracted by RIPA lysis buffer. The protein concentration of each protein sample was tested by BCA protein assay kit. SDS-PAGE protein loading buffer was added to protein samples for protein denaturation. After electrophoresis, transfer, and blocking, primary antibody was used to incubating with 0.22 μm PVDF membrane for 1 hour, followed by secondary antibody incubation and detection. The primary antibody in this study was shown below: α-Tubulin Rabbit Polyclonal Antibody (AF0001, Beyotime, China), Anti-BAX rabbit polyclonal antibody (D220073, BBI, China), Anti-BCL2 rabbit polyclonal antibody (D160117, BBI, China), and Anti-CASP3 rabbit polyclonal antibody (D320074, BBI, China).

2.12. In Vivo Experiment. Twelve BALB/c nude mice were obtained from GemPharmatech Co., Ltd. These mice were kept in the Laboratory Animal Center, Anhui Medical University. After one week of adaptive feeding, 1×10^7 MDA-MB-231 cells were injected under the skin of the right armpit of the mice. 7 days after injection, these mice were randomly divided into 3 groups with 6 mice in each group. One group was intragastric with 0.2 mL normal saline, and the other two groups were intragastric with 20 mg/kg and 40 mg/kg YQYYJDR once a day. 7 days after subcutaneous tumor injection, tumor length and diameter, as well as body weight of mice, were recorded every 3 days. After 21 days drug intervention, pentobarbital sodium was used at 250 mg/kg for mice anesthesia; subcutaneous tumors were broken off. The tumors were fixed in 4% paraformaldehyde for further detection.

2.13. Hematoxylin-Eosin Staining and Immunohistochemistry. Tumors fixed with 4% paraformaldehyde were embedded in paraffin, then sliced into 4 μm slices. Hematoxylin and Eosin Staining Kit was used to stain slices for 10 minutes, and then, a light microscope was used for analysis. As for immunohistochemistry, paraffin sections were dewaxed and sealed with goat serum; primary antibodies and second antibodies were incubated with paraffin sections. Tissue is then visualized under a light microscope (200x, Leica, Wetzlar, Germany).

2.14. Statistical Analysis. Statistical analysis was performed with the GraphPad Prism 9 software. All data were obtained from three independent experiments; data were analyzed by using Student's t-test and described as the mean ± SD. P values between groups were less than 0.05, indicating statistically significant differences.

3. Results

3.1. Identification of Bioactive Compounds and Targets in YQYYJDR. With the OB threshold ≥ 30% and DL index ≥ 0.18, a total of 153 bioactive compounds were retrieved from YQYYJDR, 2 of which belong to Angelica Sinensis, 18 of which belong to Astragalus Membranaceus, 6 to Radix Pseudostellariae, 2 to Prepared Radix Rehmanniae, 9 to Fructus Amomi, 5 to Radix Scrophulariae, 6 to Semen Coicis, 36 to Fructus Lycii, 4 to Rhizoma Atractylodis, 35 to Radix Isatidis, 17 to Lonicera Japonica, 18 to Chrysanthemum, 19 to Fructus Forsythiae, 9 to Glossy Privet Fruit, 13 to Subprostrate Sophora, 12 to Chinese Yam. 281 targets were predicted out of the 153 bioactive compounds. A "herb-compounds-targets" network was constructed (Figure 1). The network consists of 450 nodes (153 bioactive compounds and 281 targets). It is worth noting that this network includes some compounds with multiple targets, particularly the compounds quercetin (MOL000098), kaempferol (MOL000422), beta-sitosterol (MOL000358), wogonin (MOL000173), and 7-O-methylisomucronulatol (MOL000378) with degree ≥ 45.

3.2. Potential Pathways of YQYYJDR. KEGG pathway enrichment analysis was performed in Metascape website. In total, forty pathways were observed to be significantly associated with the gene input group ($P < 0.001$); the top 20 pathways are shown in Figure 2(a). The main pathways included pathways in cancer, AGE-RAGE signaling pathway in diabetic complications, proteoglycans in cancer, IL-17 signaling pathway, and platinum drug resistance. 65 target genes were included in the pathway of cancer. Biological function enrichment analysis of 65 genes showed YQYYJDR inhibited tumor growth mainly through the apoptotic pathway, shown as Figure 2(b).

3.3. Apoptosis Network of YQYYJDR. A total of 30 apoptosis genes in YQYYJDR were obtained. The apoptosis genes/compounds/YQYYJDR network was drawn by Cytoscape 3.7.2, as shown in Figure 3. It can be seen that the main compounds of YQYYJDR are quercetin (MOL000098), beta-sitosterol (MOL000358), luteolin (MOL000006), kaempferol (MOL000422), and acacetin (MOL001689).

Table 1: The sequences of the primers for genes.

Gene	Forward	Reverse
AKT1	TGACCATGAACGAGTTTGAGTA	GAGGATCTTCATGGCGTAGTAG
AR	CTACATCAAGGAACTCGATCGT	CATGTGTGACTTGATTAGCAGG
BAD	ATGTTCCAGATCCCAGAGTTTG	ATGATGGCTGCTGCTGGTT
BAX	CGAACTGGACAGTAACATGGAG	CAGTTTGCTGGCAAAGTAGAAA
BCL2	GACTTCGCCGAGATGTCCAG	GAACTCAAAGAAGGCCACAATC
BCL2L1	GCATATCAGAGCTTTGAACAGG	GAAGGAGAAAAAGGCCACAATG
CASP3	CCAAAGATCATACATGGAAGCG	CTGAATGTTTCCCTGAGGTTTG
CASP8	CAAACTTCACAGCATTAGGGAC	ATGTTACTGTGGTCCATGAGTT
CASP9	GGAACTCTTCTGCTGCCACTTCTG	GCCCAGGTCTCCAACACAAACAG
CDKN1A	GATGGAACTTCGACTTTGTCAC	GTCCACATGGTCTTCCTCTG
CTNNB1	TGGATTGATTCGAAATCTTGCC	GAACAAGCAACTGAACTAGTCG
E2F1	ATAGTGTCACCACCACCATCAT	GAAAGGCTGATGAACTCCTCAG
E2F2	GAAAGGTCTTGCTGCCCACACTC	GTGATACTGCTGCTGCTGGTCTG
FASLG	CACAGCATCATCTTTGGAGAAG	GTACAGCCCAGTTTCATTGATC
GSK3B	AGGAGAACCCAATGTTTCGTAT	ATCCCCTGGAAATATTGGTTGT
HIF1A	AGTAATGGGATGGCTGGGTCAAATG	GTGCTGGAGAGGATGTGGAGAAAC
JUN	CAAACCTCAGCAACTTCAACC	CTGGGACTCCATGTCGATG
MAPK8	ACACCACAGAAATCCCTAGAAG	CACAGCATCTGATAGAGAAGGT
MDM2	CTTCTAGGAGATTTGTTTGGCG	ATGTACCTGAGTCCGATGATTC
MMP9	CAGTACCGAGAGAAAGCCTATT	CAGGATGTCATAGGTCACGTAG
NKX3-1	GGAAGTTCAGCCATCAGAAGTA	TCGCTTAGTCTTATAGCGTCTG
PPARD	GATCCACGACATCGAGACATT	CGCCATACTTGAGAAGGGTAA
PRKCA	GGTGAAGGACCACAAATTCATC	CACCCGGACAAGAAAAAGTAAC
PTEN	GACCAGAGACAAAAAGGGAGTA	ACAAACTGAGGATTGCAAGTTC
PTGS2	TGTCAAAACCGAGGTGTATGTA	AACGTTCCAAAATCCCTTGAAG
RAF1	TAAGACAAGCAACACTATCCGT	CAGTATTCCAATCTAAGCGTGC
TGFB1	CTGTACATTGACTTCCGCAAG	TGTCCAGGCTCCAAATGTAG
TP53	TTCCTGAAAACAACGTTCTGTC	AACCATTGTTCAATATCGTCCG
RELA	GCAGAGAAGTGGAGTGTCAGGTAAC	GCAGTGTGGGTCAGTGTGTCTAAC
RB1	ATACACGCACAGATACGCTCCTTTC	GGTTAGTGACGCCAGTGACTTCAG
GAPDH	GGAGTGAGTGGAAGACAGAATGGAAG	CCTACAGCAGAGAAGCAGACAGTTATG

3.4. YQYYJDR Suppressed Cell Growth and Induced Cell Apoptosis In Vitro. To verify the efficacy of YQYYJDR on TNBC cancer cells, the cell viability assay of MDA-MB-231 and MDA-MB-468 cells was performed. YQYYJDR showed a dose-dependent effect on the viability of cancer cells in increasing concentrations (0-40 mg/mL) at 48 h. The IC_{50} value at 48 h was 6.095 mg/mL for MDA-MB-231 cells and 7.877 mg/mL for MDA-MB-468 cells, as shown in Figure 4 (a). Based on the observed IC_{50} values, YQYYJDR was used at concentrations of 0, 2.5, and 5 mg/mL in subsequent analysis. FITC/PE staining was used to evaluate cell apoptosis in cancer cells treated with YQYYJDR. YQYYJDR could induce cancer cell apoptosis, as shown in Figure 4(b). YQYYJDR arrested MDA-MB-231 and MDA-MB-468 cells in the S phase and inhibited cell invasion, as shown in Figures 4(c) and 4(d).

3.5. Apoptotic Mechanism Plays a Significant Role in the Inhibition of YQYYJDR on TNBC. These apoptotic genes were validated by RT-PCR *in vitro*, as shown in Figure 5; the mRNA expressions of CASP8, BAX, CDKN1A, PTEN, BAD, CASP3, MAPK8, GSK3B, and NKX3-1 were upregulated in cancer cells, and the mRNA expressions of AR, FASLG, HIF1A, MMP9, PPARD, RELA, BCL2L1, TGFB1, PTGS2, RAF1, RB1, CASP9, AKT1, PRKCA, BCL2, CTNNB1, E2F1, E2F2, JUN, MDM2, and TP53 were downregulated in cancer cells after the treatment with YQYYJDR. The results showed that YQYYJDR could induce cell apoptosis. Apoptosis-related proteins, such as BAX, BCL2, caspase3, and cleaved caspase3, were validated by western blotting *in vitro*; the results showed that YQYYJDR upregulated BAX, caspase3, and cleaved caspase3 expression and downregulated BCL2 expression, as shown in Figure 6.

3.6. YQYYJDR Inhibited TNBC Tumor Growth In Vivo. MDA-MB-231 mouse xenograft tumors were used to evaluate the tumor suppressive effect of YQYYJDR. The result showed that YQYYJDR at 40 mg/kg inhibited tumor growth

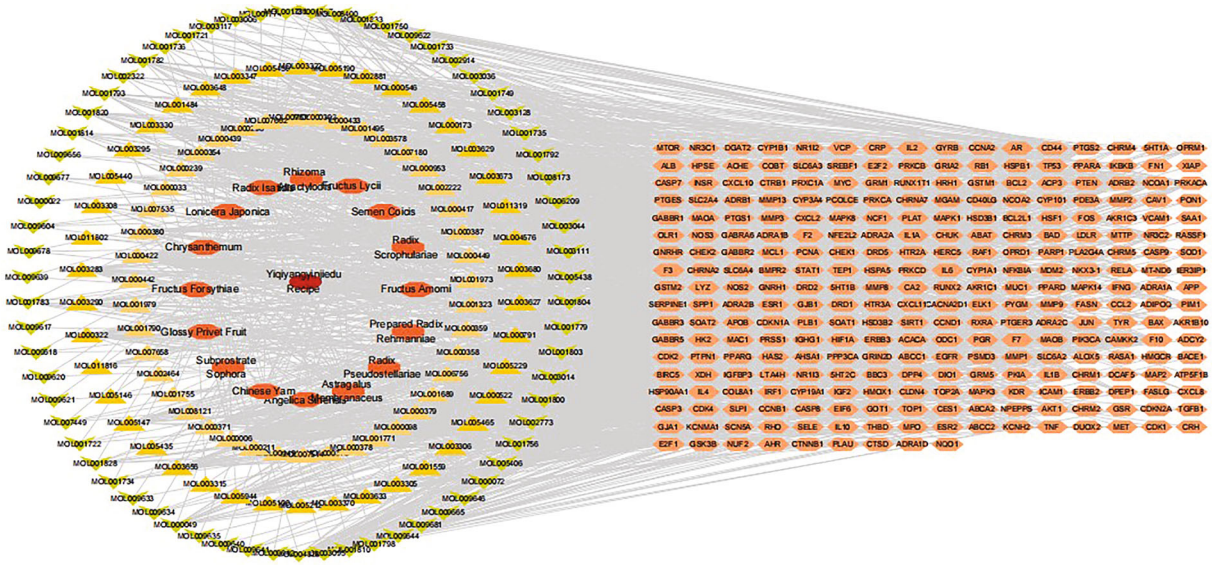

Figure 1: The "herb-compounds-targets" network diagram of YQYYJDR.

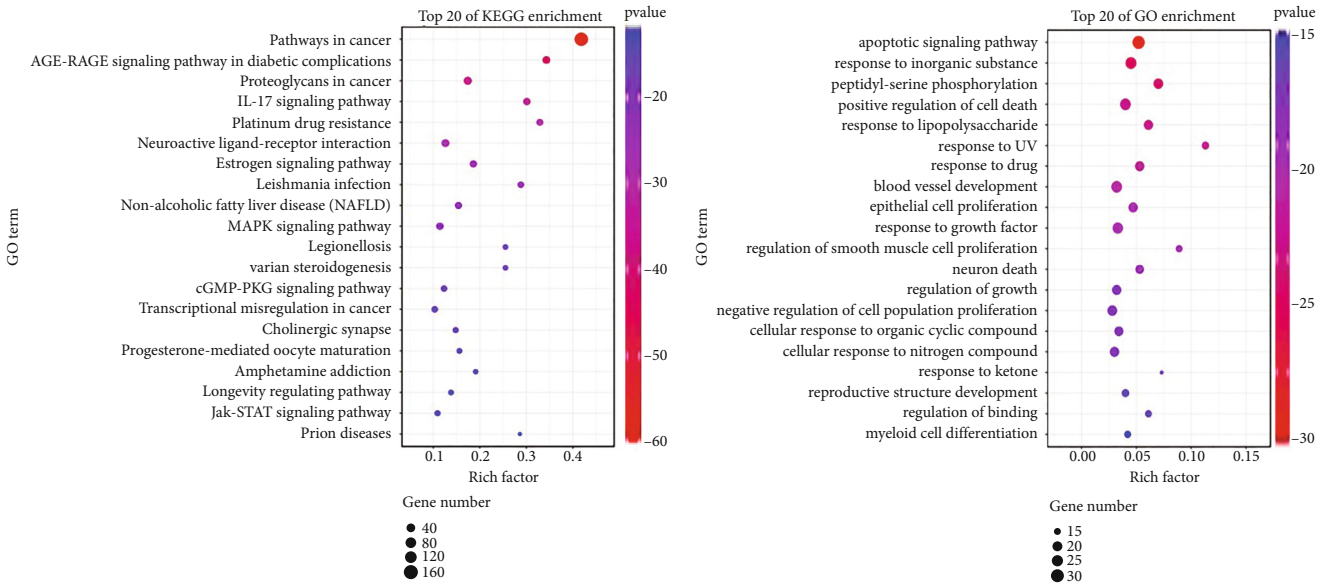

Figure 2: The KEGG pathway and GO Biological Processes of YQYYJDR.

significantly with 53% inhibition rate ($P < 0.01$). And YQYYJDR had no toxic effect on the body weight of the mice. HE and immunohistochemistry results showed that YQYYJDR inhibited the expression of Ki-67 protein in tumors, as shown in Figure 7.

4. Discussion

YQYYJDR has been used in clinic for breast cancer treatment [5]. Its main compounds include quercetin, kaempferol, beta-sitosterol, wogonin, and 7-O-methylisomucronulatol. Quercetin and wogonin have been reported to suppress cell proliferation and metastasis and induce cell apoptosis in TNBC cancer cells [14–17]. Kaempferol can suppress proliferation and induce apoptosis and autophagy in human lung cancer cells [18]. beta-Sitosterol could induce G1 arrest and cause depolarization of mitochondrial membrane potential and sensitize cells to TRAIL-induced apoptosis in breast carcinoma MDA-MB-231 cells [19, 20]. However, the mechanism of YQYYJDR on TNBC has not been reported. A variety of compounds in YQYYJDR have anticancer effect, which suggests that the compound preparation of various herbs will receive certain attention in the future research.

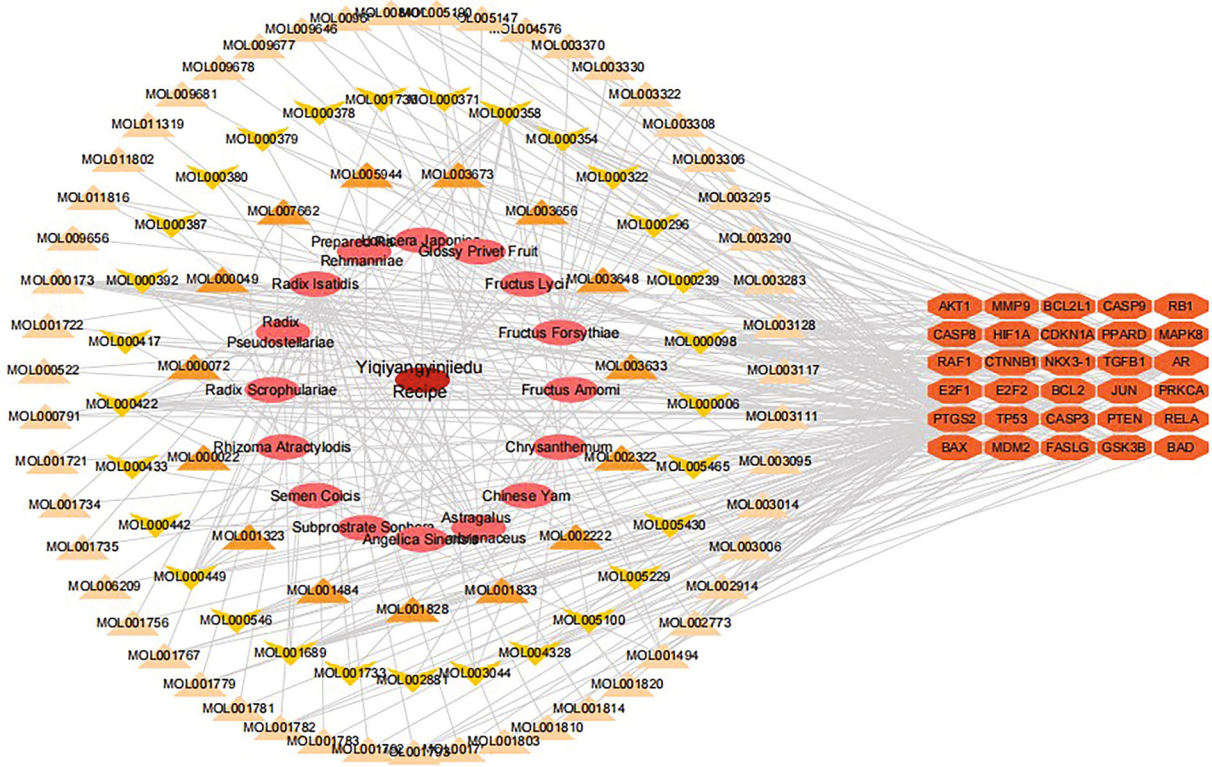

Figure 3: The apoptosis genes/compounds/YQYYJDR network.

The active compounds and target genes of traditional herbs have been widely explored by using network pharmacology methods, and it provides a new thought in the research of traditional medicine [21]. However, some new problems are also emerging, such as mixed research, decentralized and irregular data, and lack of scientific validation [22]. Recently, the Network Pharmacology Evaluation Method Guidance has been issued to solve these new problems [22]. In this study, the data of traditional herbs were extracted from TCMSP database, and the KEGG pathways were found out in Metascape database and proofed by experiments, thus exploring the mechanism of YQYYJDR on TNBC. As the information of compound targets in TCMSP database is collected from existing research data, some medicinal materials with little research may not be comprehensive in the database, which leads to certain selection bias in the prediction of compound preparation targets. However, this problem will be improved with the perfection of database information.

The network pharmacology results of YQYYJDR show that apoptotic mechanism may play a significant role in the inhibitory effects of YQYYJDR on TNBC. Main compounds that exert apoptosis-inducing functions include quercetin, beta-sitosterol, luteolin, kaempferol, and acacetin. The *in vitro* experiment showed that YQYYJDR could inhibit MDA-MB-231 and MDA-MB-468 cell proliferation and invasion, induce cells apoptosis, arrest cells in S stage, and regulate mRNA expression. The upregulation RNAs include CASP8, BAX, CDKN1A, PTEN, BAD, CASP3, MAPK8, GSK3B, and NKX3-1, and the mRNA expressions of AR, FASLG, HIF1A, MMP9, PPARD, RELA, BCL2L1, TGFB1, PTGS2, RAF1, RB1, CASP9, AKT1, PRKCA, BCL2, CTNNB1, E2F1, E2F2, JUN, MDM2, and TP53 were downregulated. The result of western blotting showed that YQYYJDR can induce cell apoptosis by regulating the expression of BAX, BCL2, and caspase3. Combined with above results, YQYYJDR induced apoptosis of triple negative breast cancer cells by regulating apoptosis-related proteins, thus playing a role in inhibiting tumor growth.

Key compounds that regulate apoptosis in YQYYJDR include quercetin, beta-sitosterol, and luteolin. Quercetin had been reported to potentiate the antimetastatic effect of 5-fluorouracil and docetaxel on the MDA-MB-231 cell line through induction of apoptosis and modulation of PI3K/AKT, MAPK/ERK, and JAK/STAT3 signaling pathways [23, 24]. Additionally, quercetin increased abundance of the proapoptotic protein Bax and decreased the levels of antiapoptotic protein Bcl-2 [25]. There are few such studies about the mechanism beta-sitosterol on MDA-MB-231; only few articles had shown that it induces cell apoptosis [20, 26]. Luteolin could enhance paclitaxel-induced apoptosis in human breast cancer MDA-MB-231 cells by blocking STAT3 [27]. Most of the existing studies focus on the mechanism of TCM monomers enhancing the efficacy of chemotherapy for breast cancer, partly because of the poor tumor suppressive effect of TCM monomers in mice, and on the other hand, TCM monomers are in the early stage of basic research and cannot be applied in clinical practice. As compound preparations of these monomers, YQYYJDR has been widely used in clinical practice, so their clinical significance

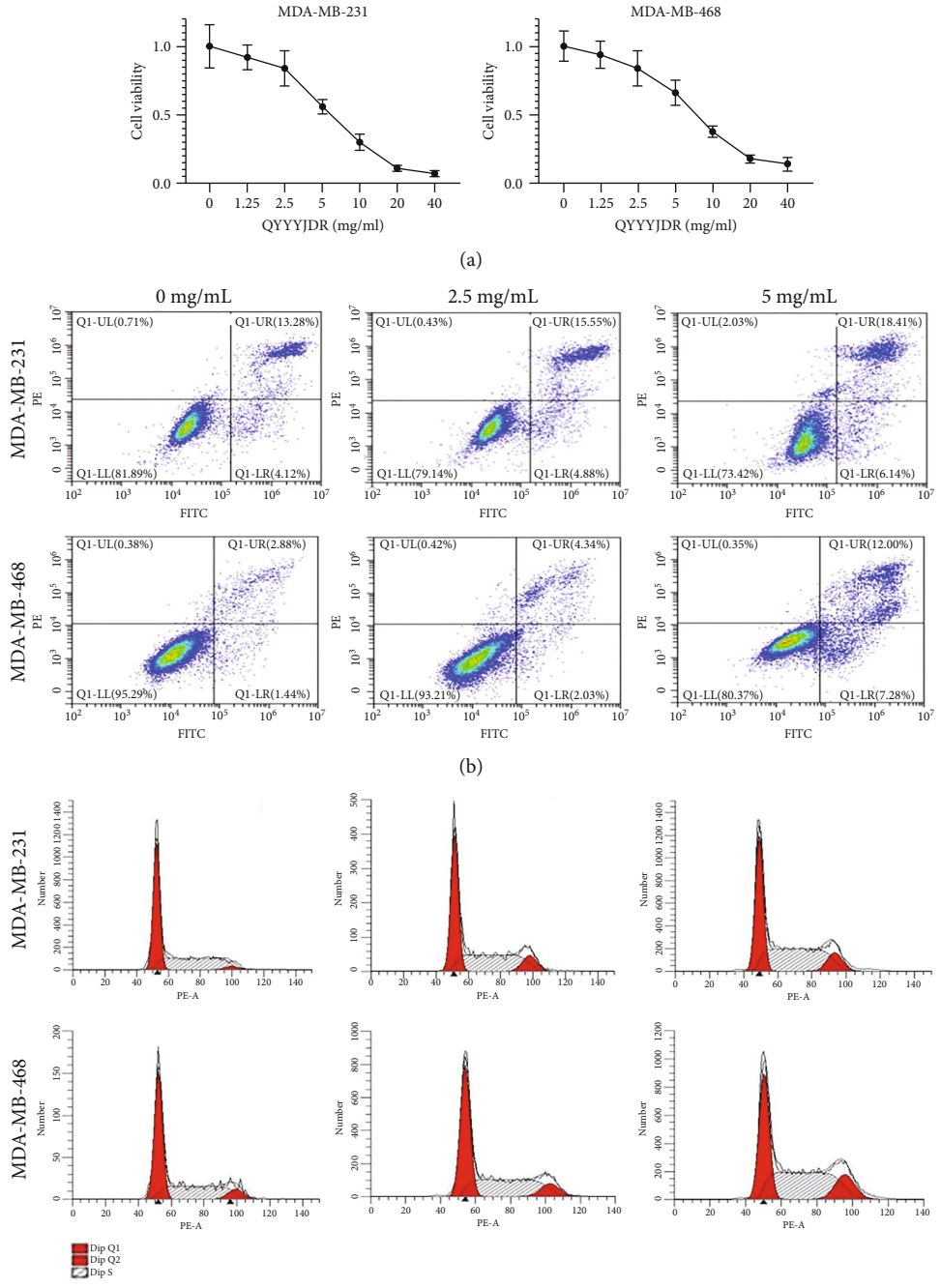

Figure 4: Continued.

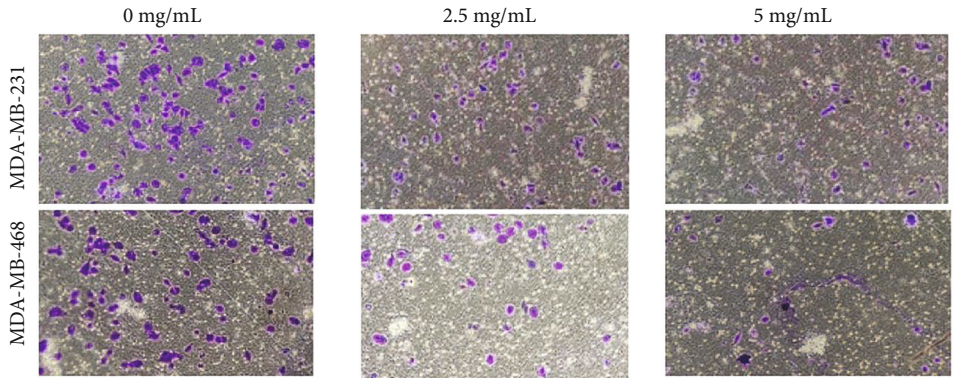

(d)

Figure 4: YQYYJDR suppressed in *vitro* triple negative breast cancer cell growth. (a) YQYYJDR showed a dose-dependent effect on the viability of breast cancer cells. (b) YQYYJDR induced MDA-MB-231 and MDA-MB-468 cell apoptosis. (c) YQYYJDR blocked MDA-MB-231 and MDA-MB-468 cells in the S phase. (d) YQYYJDR inhibited MDA-MB-231 and MDA-MB-468 cell invasion.

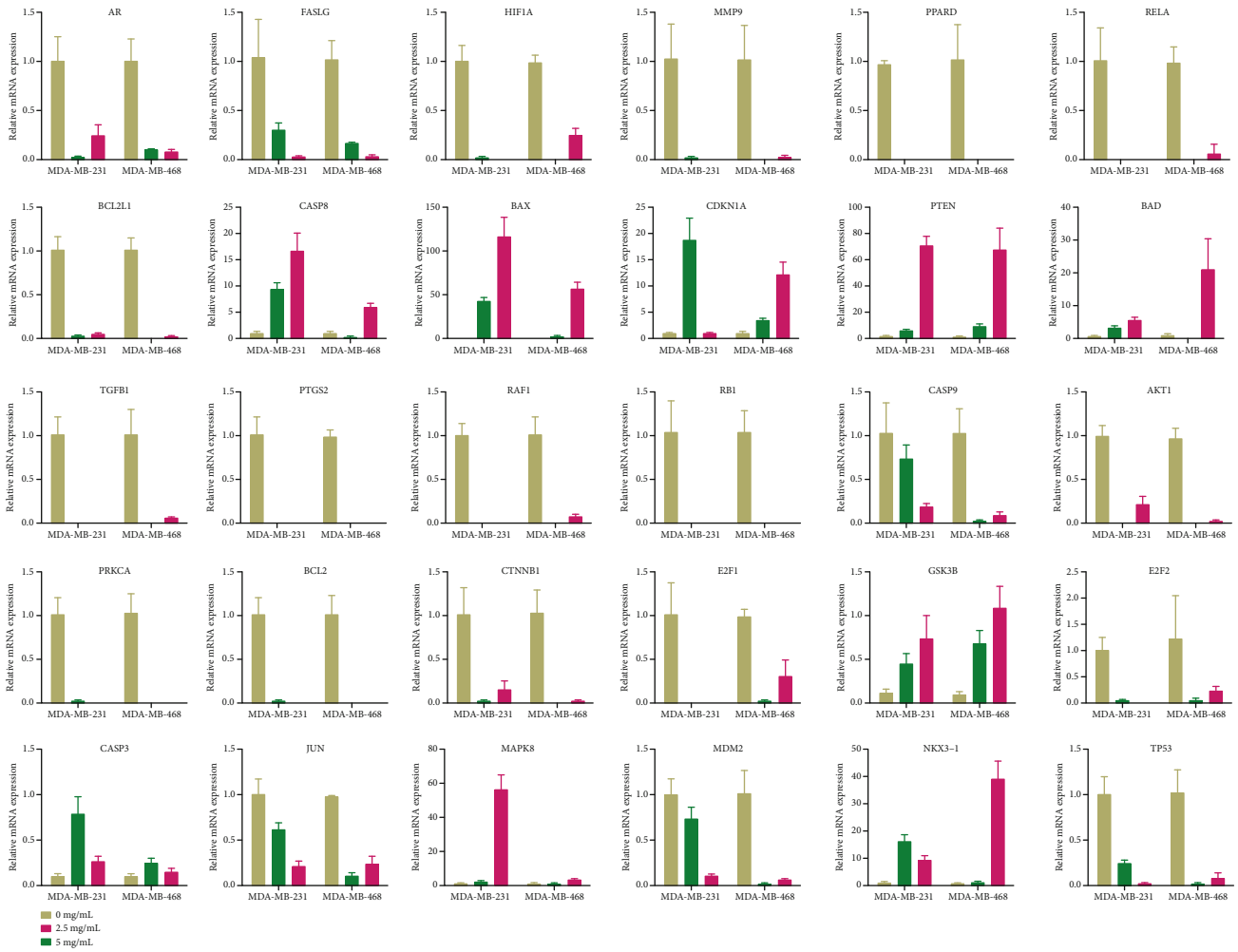

Figure 5: The mRNA expression of apoptosis-related genes after the treatment of YQYYJDR. The mRNA expressions of CASP8, BAX, CDKN1A, PTEN, BAD, CASP3, MAPK8, GSK3B, and NKX3-1 were upregulated in cancer cells, and the mRNA expressions of AR, FASLG, HIF1A, MMP9, PPARD, RELA, BCL2L1, TGFB1, PTGS2, RAF1, RB1, CASP9, AKT1, PRKCA, BCL2, CTNNB1, E2F1, E2F2, JUN, MDM2, and TP53 were downregulated in cancer cells after the treatment with YQYYJDR.

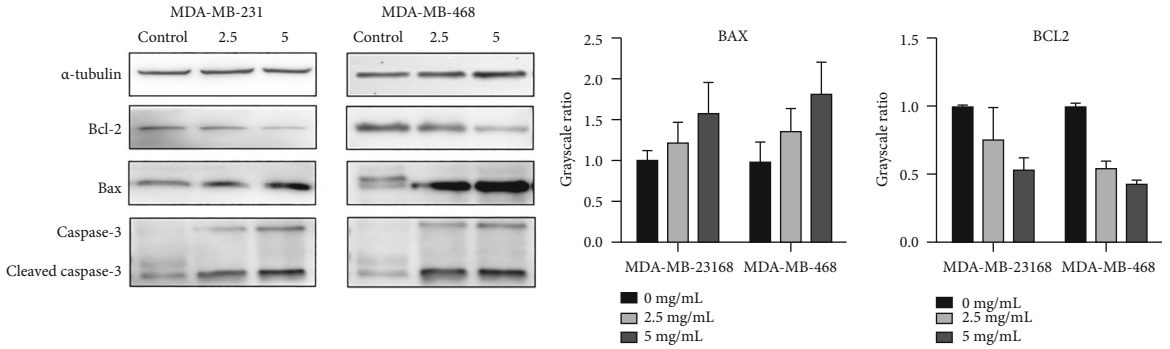

Figure 6: Protein expression in MDA-MB-231 and MDA-MB-468 cells after YQYYJDR intervention. YQYYJDR upregulated BAX, caspase3, and cleaved caspase3 and downregulated BCL2 expression.

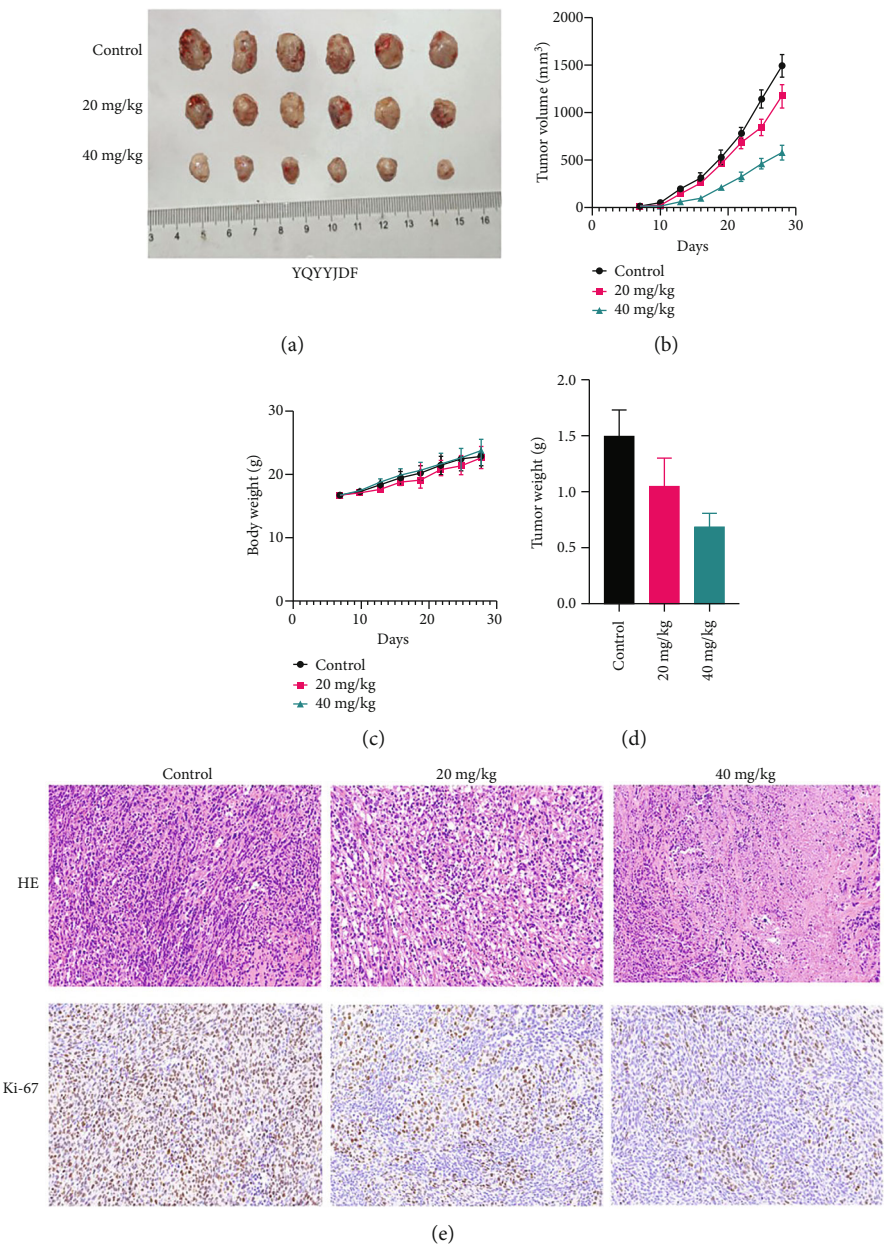

Figure 7: YQYYJDR inhibited tumor growth in mice. (a, b, d) YQYYJDR inhibited MDA-MB-231 mouse xenograft tumor growth. (c) YQYYJDR had no effect on mouse weight. (e) YQYYJDR inhibited Ki-67 expression in tumor tissues.

is greater than that of traditional Chinese medicine monomers. Combined with the *in vivo* results in our study, we believe that the compound preparation has better tumor inhibition effect.

There are several limitations to this study. First, molecular docking between drugs and target proteins was not used to predict possible drug targets in this study; second, the target proteins of apoptosis were not knocked out or overexpression to determine whether apoptotic targets are the main targets of drug action; third, animal experiments were used in this study to verify the efficacy of YQYYJDR; however, the mechanism of action *in vivo* remains unclear; fourth, the HPLC result and pharmacokinetics of compound preparations have not been studied *in vivo*. Therefore, it is necessary to further explore the effect of YQYYJDR on TNBC and clarify its mechanism.

5. Conclusions

In this study, network pharmacology techniques and experimental methods were used to explore the mechanism on triple negative breast cancer with YQYYJDR. *In vitro* and *in vivo* experiments showed that YQYYJDR could inhibit the growth of triple negative breast cancer and induce cell apoptosis. Apoptosis pathway plays a significant role in the treatment of triple negative breast cancer.

Data Availability

The data used to support the findings of this study are included within the article.

Ethical Approval

The study was conducted in accordance with the Declaration of Helsinki (as revised in 2013). The authors are accountable for all aspects of the work in ensuring that questions related to the accuracy or integrity of any part of the work are appropriately investigated and resolved.

Conflicts of Interest

The authors have no conflicts of interest to declare.

Acknowledgments

This study was supported by the Anhui Provincial Key Research and Development Plan (202104a07020021).

References

[1] D. D. Singh and D. K. Yadav, "TNBC: potential targeting of multiple receptors for a therapeutic breakthrough, nanomedicine, and immunotherapy," *Biomedicines*, vol. 9, no. 8, p. 876, 2021.

[2] M. Nedeljković and A. Damjanović, "Mechanisms of chemotherapy resistance in triple-negative breast cancer-how we can rise to the challenge," *Cells-Basel*, vol. 8, no. 9, p. 957, 2019.

[3] E. Vagia, D. Mahalingam, and M. Cristofanilli, "The landscape of targeted therapies in TNBC," *Cancers*, vol. 12, no. 4, p. 916, 2020.

[4] J. Jhan and E. R. Andrechek, "Triple-negative breast cancer and the potential for targeted therapy," *Pharmacogenomics*, vol. 18, no. 17, pp. 1595–1609, 2017.

[5] C. Nie, *Clinical Observation on Efficacy of Estrogen Receptoer Positive Breast Cancer Treated by Yi Qi Yang Ying Jie du Fang Combined with Tamoxifen*, Nanjing University of Chinese Medicine, 2018.

[6] T. T. Luo, Y. Lu, S. K. Yan, X. Xiao, X. L. Rong, and J. Guo, "Network pharmacology in research of Chinese medicine formula: methodology, application and prospective," *Chinese Journal of Integrative Medicine*, vol. 26, no. 1, pp. 72–80, 2020.

[7] B. Boezio, K. Audouze, P. Ducrot, and O. Taboureau, "Network-based approaches in pharmacology," *Inform*, vol. 36, no. 10, p. 10, 2017.

[8] X. Wang, Z. Y. Wang, J. H. Zheng, and L. I. Shao, "TCM network pharmacology: A new trend towards combining computational, experimental and clinical approaches," *Chin J Nat Med*, vol. 19, no. 1, pp. 1–11, 2021.

[9] S. He, T. Wang, C. Shi, Z. Wang, and X. Fu, "Network pharmacology-based approach to understand the effect and mechanism of Danshen against anemia," *Journal of Ethnopharmacology*, vol. 282, article 114615, 2022.

[10] J. Ru, P. Li, J. Wang et al., "TCMSP: a database of systems pharmacology for drug discovery from herbal medicines," *Journal of Cheminformatics*, vol. 6, no. 1, p. 13, 2014.

[11] The UniProt Consortium, "UniProt: The universal protein knowledgebase in 2021," *Nucleic Acids Research*, vol. 49, no. D1, pp. D480–D489, 2021.

[12] P. Shannon, A. Markiel, O. Ozier et al., "Cytoscape: a software environment for integrated models of biomolecular interaction networks," *Genome Research*, vol. 13, no. 11, pp. 2498–2504, 2003.

[13] Y. Zhou, B. Zhou, L. Pache et al., "Metascape provides a biologist-oriented resource for the analysis of systems-level datasets," *Nature Communications*, vol. 10, no. 1, p. 1523, 2019.

[14] L. Schroder, P. Marahrens, J. G. Koch et al., "Effects of green tea, matcha tea and their components epigallocatechin gallate and quercetin on MCF-7 and MDA-MB-231 breast carcinoma cells," *Oncology Reports*, vol. 41, no. 1, pp. 387–396, 2019.

[15] A. Kabala-Dzik, A. Rzepecka-Stojko, R. Kubina et al., "Flavonoids, bioactive components of propolis, exhibit cytotoxic activity and induce cell cycle arrest and apoptosis in human breast cancer cells MDA-MB-231 and MCF-7- a comparative study," *Cellular and Molecular Biology (Noisy-le-Grand, France)*, vol. 64, no. 8, pp. 1–10, 2018.

[16] A. A. Abd El-Hafeez, H. O. Khalifa, E. A. M. Mahdy et al., "Anticancer effect of nor-wogonin (5, 7, 8-trihydroxyflavone) on human triple-negative breast cancer cells via downregulation of TAK1, NF-κB, and STAT3," *Pharmacological Reports: PR*, vol. 71, no. 2, pp. 289–298, 2019.

[17] J. Go, J. Wei, J. Park, K. Ahn, and J. Kim, "Wogonin suppresses the LPS-enhanced invasiveness of MDA-MB-231 breast cancer cells by inhibiting the 5-LO/BLT2 cascade," *International Journal of Molecular Medicine*, vol. 42, no. 4, pp. 1899–1908, 2018.

[18] L. Zhu and L. Xue, "Kaempferol suppresses proliferation and induces cell cycle arrest, apoptosis, and DNA damage in breast

cancer cells," *Oncology Research*, vol. 27, no. 6, pp. 629–634, 2019.

[19] C. Park, D. O. Moon, C. H. Ryu et al., "β-Sitosterol sensitizes MDA-MB-231 cells to TRAIL-induced apoptosis," *Acta Pharmacologica Sinica*, vol. 29, no. 3, pp. 341–348, 2008.

[20] S. S Vundru, R. K. Kale, and R. P. Singh, "beta-Sitosterol induces G1 arrest and causes depolarization of mitochondrial membrane potential in breast carcinoma MDA-MB-231 cells," *BMC Complement Altern Med*, vol. 13, p. 280, 2013.

[21] C. Nogales, Z. M. Mamdouh, M. List, C. Kiel, A. I. Casas, and H. Schmidt, "Network pharmacology: curing causal mechanisms instead of treating symptoms," *Trends in Pharmacological Sciences*, vol. 43, no. 2, pp. 136–150, 2022.

[22] Z. Y. Wang, X. Wang, D. Y. Zhang, Y. J. Hu, and S. Li, "Traditional Chinese medicine network pharmacology: development in new era under guidance of network pharmacology evaluation method guidance," *Zhongguo Zhong Yao Za Zhi*, vol. 47, no. 1, pp. 7–17, 2022.

[23] M. Roshanazadeh, R. H. Babaahmadi, and M. Rashidi, "Quercetin synergistically potentiates the anti-metastatic effect of 5-fluorouracil on the MDA-MB-231 breast cancer cell line," *Iranian Journal of Basic Medical Sciences*, vol. 24, no. 7, pp. 928–934, 2021.

[24] A. Safi, E. Heidarian, and R. Ahmadi, "Quercetin synergistically enhances the anticancer efficacy of docetaxel through induction of apoptosis and modulation of PI3K/AKT, MAPK/ERK, and JAK/STAT3 signaling pathways in MDA-MB-231 breast cancer cell line," *International Journal of Molecular and Cellular Medicine*, vol. 10, no. 1, pp. 11–22, 2021.

[25] S. Y. Chien, Y. C. Wu, J. G. Chung et al., "Quercetin-induced apoptosis acts through mitochondrial- and caspase-3-dependent pathways in human breast cancer MDA-MB-231 cells," *Human & Experimental Toxicology*, vol. 28, no. 8, pp. 493–503, 2009.

[26] A. B. Awad, A. C. Downie, and C. S. Fink, "Inhibition of growth and stimulation of apoptosis by beta-sitosterol treatment of MDA-MB-231 human breast cancer cells in culture," *International Journal of Molecular Medicine*, vol. 5, no. 5, pp. 541–545, 2000.

[27] J. Lee, S. H. Park, J. Lee et al., "Differential effects of luteolin and its glycosides on invasion and apoptosis in MDA-MB-231 triple-negative breast cancer cells," *EXCLI Journal*, vol. 18, pp. 750–763, 2019.

Hindawi
Journal of Oncology
Volume 2022, Article ID 9175402, 22 pages
https://doi.org/10.1155/2022/9175402

Research Article

A Pan-Cancer Analysis on the Systematic Correlation of MutS Homolog 2 (MSH2) to a Malignant Tumor

Hai Yao,[1] Zhidong Cao,[1] Haochuan Yong,[1] Xiaoxing Zhang,[1] Xin Zhang,[1] Wei Li,[2] Shenshen Zhi,[2] and Wenyan Wu[2]

[1]*Department of Orthopaedic Surgery, Chongqing Emergency Medical Center, Chongqing University Center Hospital, School of Medicine, Chongqing University, Chongqing 400014, China*
[2]*Department of Clinical Laboratory, Chongqing Emergency Medical Center, Chongqing University Center Hospital, School of Medicine, Chongqing University, Chongqing 400014, China*

Correspondence should be addressed to Wenyan Wu; wuwenyan009@163.com

Received 18 January 2022; Revised 2 March 2022; Accepted 4 March 2022; Published 24 March 2022

Academic Editor: Fu Wang

MutS homolog 2 (MSH2) is a crucial participant in human DNA repair, and lots of the studies functionally associated with it were begun with hereditary nonpolyposis colorectal cancer (HNPCC). MSH2 has also been reported to take part in the progresses of various tumors' formation. With the help of GTEx, CCLE, and TCGA pan-cancer databases, the analysis of MSH2 gene distribution in both tumor tissues and normal control tissues was carried out. Kaplan-Meyer survival plots and COX regression analysis were conducted for the assessment into the MSH2's impact on tumor patients' clinical prognosis. In an investigation to the association of MSH2 expression with immune infiltration level of various tumors and a similar study on tumor immune neoantigens, microsatellite instability was subsequently taken. It was found that high expression of MSH2 is prevalent in most cancers. MSH2's efficacy on clinical prognosis as well as immune infiltration in tumor patients revealed a fact that expression of MSH2 in prostate adenocarcinoma (PRAD), brain lower-grade glioma (LGG), breast-invasive carcinoma (BRCA), and head and neck squamous cell carcinoma (HNSC) posed a significant correlation with the immune cell infiltration level of patients. Likewise as above, MSH2's expression comes in a similar trend with tumor immune neoantigens and microsatellite instability. MSH2's expression in the majority of tumors is a direct factor to the activation of tumor-associated pathways as well as immune-associated pathways. MSH2's early screening or even therapeutic target role for sarcoma (SARC) diagnosis is contributing to the efficiency of early screening and overall survival in SARC patients.

1. Introduction

Protein MutS homolog 2 (MSH2, ENSG00000095002) is a component of DNA damage repair by guiding the generation of critical relevant protein. This protein helps repair errors arising when DNA is replicated for cell division proteins (the MSH2 protein binds to one of the MSH6 or MSH3 (each produced by a different gene)) to form a dimer of the two-protein complex [1], which recognizes the error-occurring sites on DNA that begets in the course of DNA replication. The MLH1-PMS2 dimer is formed with another set of proteins, which subsequently combine with the MSH2 dimer to initiate the process of error repair by removing mismatched DNAs and replicating a new fragment [2, 3]. DNA damage is an inducement of cancer genesis; hence, the defection of DNA repair genes is primarily responsible for many cancers' initiation and development [4, 5]. Methylation in a promoter might contribute to a decline in DNA repair via the 4 pathways where MSH2 is involved: the repair to DNA loss of match, transcription-coupled repair, homologous recombination, and the repair to base excision [6–8]. This reduction in repair capacity might bring forth accumulation of DNA damage and lead to carcinogenesis [9]. It was reported in hereditary nonpolyposis colorectal cancer (HNPCC) that 40% of the genetic variants are the disease-associated ones of MSH2 and they are the primary

inducements of HNPCC development [10]. A study on the MSH2 in non-small-cell lung cancer (NSCLC) suggested that although the gene was not mutated, 29% of NSCLC cases were found with decline in epigenetic expression of MSH2 [11].

Likewise in the case of no MSH2 mutation found, MSH2 promoter methylation was found in 43% patients and 86% relapsed patients [12, 13]. Our study is the first attempt to conduct a pan-cancer analysis on MSH2 by using databases of The Cancer Genome Atlas (TCGA), Genotype-Tissue Expression (GTEx), Cancer Cell Line Encyclopedia (CCLE), and others integratedly with relevant factors including gene expression, survival status, genetic alterations, immune infiltration, and associated cellular pathways, and we eventually elucidated MSH2's role in the pathogenesis or the prognosis of cancers. We found that MSH2 expression was positively correlated with the survival prognosis, the immune infiltration, and the tumor load of various tumors, whose correlation with sarcoma (SARC) is more significant.

In the present study, MSH2 expression levels in SARC were significantly associated with genetic differences, tumor immune cell infiltration, and so on, and are likely to be used as target genes for early screening or even therapeutic targets in SARC, which can help improve more than the efficiency of early screening but also the overall survival of SARC patients.

2. Materials and Methods

2.1. Acquisition of Transcriptional Information. Our analysis to the gene expression patterns in 31 tissues was accomplished with the Genotype-Tissue Expression (GTEx) dataset (https://http://commonfund.nih.gov/GTEx/). Then, the subsequent analysis went along with the information from the CCLE (Cancer Cell Line Encyclopedia) database (https://portals.broadhttp://institute.org/ccle/), which was downloaded for each tumor cell line. The gene expression patterns in 21 tissues were subjected to the analysis according to tissue origin. Then, mRNA information was downloaded from the database of TCGA (https://www.cancer.gov/about-nci/organization/ccg/research/structural-genomics/tcga), which was for an analysis to 31 tumor samples.

The Kruskal-Wallis test was implemented through the R language version 3.6.3 (R Foundation for Statistical Computing, Austria) (https://www.r-project.org/) to determine the expression differences amid organs.

2.2. Differential Gene Expression Analysis. We downloaded the datasets of TCGA pan-cancer and GTEx from the UCSC Xena database (https://xena.ucsc.edu/) to figure out the differences in MSH2 expression patterns within our tumor samples and their control normal tissues. First of all, distinction of MSH2 expression patterns within tumor tissues and their control normal tissues in 20 tumor samples was obtained from TCGA database. Given the tiny amount of normal tissue samples in TCGA, we only make an integration of the information about the normal tissues separately from the GTEx database and TCGA tumor tissues, so that our analysis to the gene expression differences in 27 tumors could be performed. Distinction with a threshold of $P < 0.05$ was calculated in R language.

2.3. Survival Analysis at the Pan-Cancer Level. To figure out the association amid MSH2 expression patterns and the prognosis of 33 tumors in TCGA cohort, taking into account the possible presence of nontumor mortality factors during follow-up, we performed univariate COX regression analysis by using a threshold of COX ($P < 0.05$) for overall survival (OS), disease-free survival (DFS), disease-specific survival (DSS), disease-free interval (DFI), and progression-free interval (PFI). Summary forest plotting was performed using the R language forest plot package [14]. The tumors with a significant correlation in the regression analysis were selected, and our subjects were divided into two groups of high and low expression on the basis of the median of MSH2 expressions. Our Kaplan-Meier survival analysis was conducted with our R language packages of survival version 3.2.3 and survminer version 0.4.8. A log-rank test with a threshold of $P < 0.05$ was used to calculate the significance of the differences in survival rates.

2.4. Relationship between MSH2 Expression Levels and Immunity. Detectable level of tumor-infiltrating lymphocytes (TILs) in tumorous microenvironment suggests an improvement in prognosis and an efficient treatment outcome to different types of cancer [15]. We conducted an investigation to the correlation within MSH2 expression and the level of immune infiltration in different types of tumors. And our exploration on the MSH2's relationship with the immune infiltration level within all the association amid MSH2 expression and tumor-infiltrating lymphocytes in TCGA tumors (B cells, CD4+ T cells, CD8+ T cells, macrophages, neutrophils, and dendritic cells) was carried out by using the Immune-Gene module at the TIMER2 (tumor immune estimation resource, version 2, http://timer.cistrome.org/) online. According to the relevant literature, we chose different study methods for different TILs to improve the accuracy. We used the EPIC method to calculate the relative proportions of B cells, CD4+ T cells, and macrophages of multiple tumors and the QUANTISEQ method to calculate the relative proportions of CD8+ T cells in multiple tumors. After that, we calculated the relative proportions of neutrophils and dendritic cells with the MCPCOUNTER method [16]. When our association analysis came with the QMCPCOUNTER method, we used the function of Purity Adjustment, which means the usage of the partial Spearman's correlation. When it came to the EPIC and QUANTISEQ methods, we affirmed that the parameters of tumor purity and immune infiltration would be negatively correlated; hence, the adjustment to purity became unnecessary [17]. Immune cell infiltration level was estimated with the ESTIMATE method in R language, which comprised the immune microenvironment score as well as the stromal score of 33 tumorous cell samples from TCGA cohort [18]. We determined the association within MSH2 and the immune cell scores above with the Spearman correlation method.

2.5. Relationship between MSH2 and Neoantigen, TMB, and MSI. Point mutations, deletion mutations, gene fusions, and so on are the primary reasons of genetic mutations in tumor cells, and most of the mutated genes encode the nascent antigen named neoantigen. New abnormal proteins differ from the ones produced by normal cells. These proteins are enzymatically cleaved to form peptide fragments that are delivered to T cells, which facilitate T cells to be mature activated T cells which could specifically recognize tumor neoantigens and have themselves proliferate [19].

We hence had an estimation to the neoantigen amount in each tumor sample and conducted an analysis on the MSH2 expressions with immune neoantigens in a way of using the Spearman correlation method gene marker correlation [20]. Tumor mutational burden is a parameter usually presented as the somatic mutation amount (nonsynonymous mutations) begetting in an average of 1 Mb bases within the coding region (episomal region) in tumor genomes, which is even straightly shown as the total number of nonsynonymous mutations, as well as the types of mutations which mainly include single-nucleotide variants (SNV) and the insertions/deletions of small fragments' various forms of mutations. Here, we made a calculation separately to the tumor mutational burden (TMB) of each tumor sample and an analysis on the association amid MSH2 expression and TMB with correlation coefficient of Spearman's rank.

Microsatellite instability (MSI) is a term to describe any change in microsatellite length resulting from the insertion or the deletion of repeat units in the particular microsatellite of tumors versus normal tissue. Furthermore, emergence of a new microsatellite allele could be deemed as a genetic phenomenon [21]. We made use of the R data package "PreMSIm" for the prediction on MSI from the gene expression profiles of 33 cancers and commenced an analysis to the relationship within gene expression and MSI by the way of using the Spearman rank correlation coefficient [22].

2.6. Mutation Patterns of the MSH2 Gene in TCGA Tumor Samples. Our mutation data were downloaded from TCGA database for 33 malignant tumors, and the changes of the MSH2 gene in these tumors were analyzed. We used the R data package "maftools" to visualize the tumors with the most MSH2 mutations [23].

2.7. Gene Enrichment Analysis of Pan-Cancer Patients in TCGA. We first used the STRING website (https://string-db.org/) to query the name "MSH2" using a single protein and "organism" selected from "Homo sapiens." We then set the following main parameters: minimum required interaction score "low confidence (0.150)," meaning of network edges "confidence," max number of interactors to show "no more than 50 interactors" in the 1st shell, and active interaction sources "experiments." Finally, the available MSH2-binding proteins for the experimental assays were obtained.

We used the "Similar Gene Detection" model of Gene Expression Profiling Interactive Analysis 2 (GEPIA2, http://gepia2.cancer-pku.cn/#index) to obtain the top 100 MSH2-related target genes based on data from all TCGA tumors and associated normal tissues. We also performed the Pearson correlation analysis of MSH2 by "correlation analysis" mode of GEPIA2, and the scatter plots were obtained using log2 TPM, P value, and the correlation coefficient (P value). Value and the correlation coefficient (R) have been represented in the graph. In addition, we used the "Gene_Corr" model of TIMER2 to obtain heat map data for the selected genes, including partial correlation (cor) and purity-adjusted Spearman's rank correlation test (s rank correlation test).

We combined the two sets of data from the relevant target genes and the binding protein genes for Kyoto Encyclopedia of Genes and Genomes (KEGG) pathway analysis. Briefly, we selected identifier ("OFFICIAL_GENE_ SYMBOL") and species ("Homo sapiens") in the DAVID (Database for Annotation, Visualization, and Integrated Discovery) website to obtain functional annotation chart data. The final visualization of the enrichment pathways was obtained through the Sangerbox website (http://sangerbox.com), where we also performed GO (Gene Ontology) enrichment analysis, biological process (BP), cellular component (CC), and molecular function (MF) data visualized as centplots, and two-tailed $P < 0.05$ was considered statistically significant.

3. Results

3.1. Gene Expression Analysis Data. We analyzed the differences in gene expression between cancer and paracancer in individual tumor samples obtained from TCGA database, as shown in Figure 1(c). In bladder urothelial carcinoma (BLCA), BRCA, cholangiocarcinoma (CHOL), colon adenocarcinoma (COAD), esophageal carcinoma (ESCA), HNSC, kidney chromophobe (KICH), liver hepatocellular carcinoma (LIHC), lung adenocarcinoma (LUAD), lung squamous cell carcinoma (LUSC), rectum adenocarcinoma (READ), stomach adenocarcinoma (STAD), uterine corpus endometrial carcinoma (UCEC) (P value <0.001), LGG, and thyroid carcinoma (THCA) (P value <0.05), the tumors in TCGA cohort did not show MSH2 expression levels lower than those of the relevant control normal tissues.

After using normal tissues from the GTEx dataset as controls, we further evaluated the differences of MSH2 expression in adrenocortical carcinoma (ACC), cervical squamous cell carcinoma and endocervical adenocarcinoma (CESC), acute myeloid leukemia (LAML), ovarian serous cystadenocarcinoma (OV), testicular germ cell tumors (TGCT), and uterine carcinosarcoma (UCS). As shown in Figure 1(d), the MSH2 expression levels in ACC, CESC, OV, TGCT, and UCS (P value <0.001) were higher than those in the relevant control normal group tissues.

In addition, the Kruskal-Wallis test showed significant differences in MSH2 expression levels among organs (Figures 1(a) and 1(b)), while MSH2 expression levels were significantly higher in bone marrow tissues with a value of $\log2\,(\mathrm{TPM} + 1) > 6$.

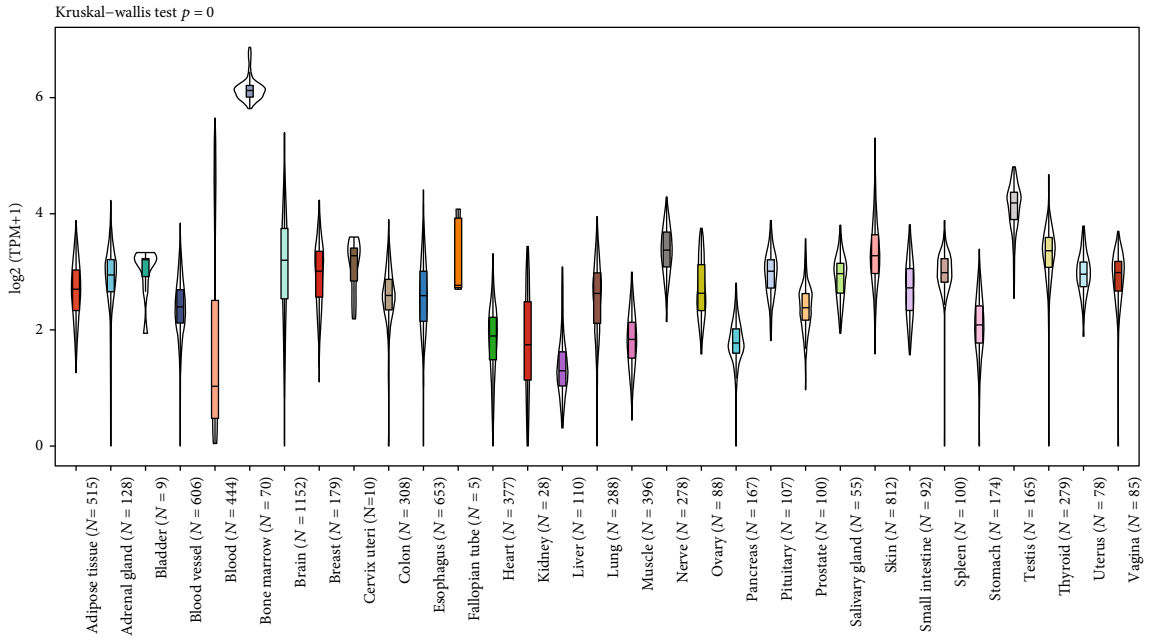

(a)

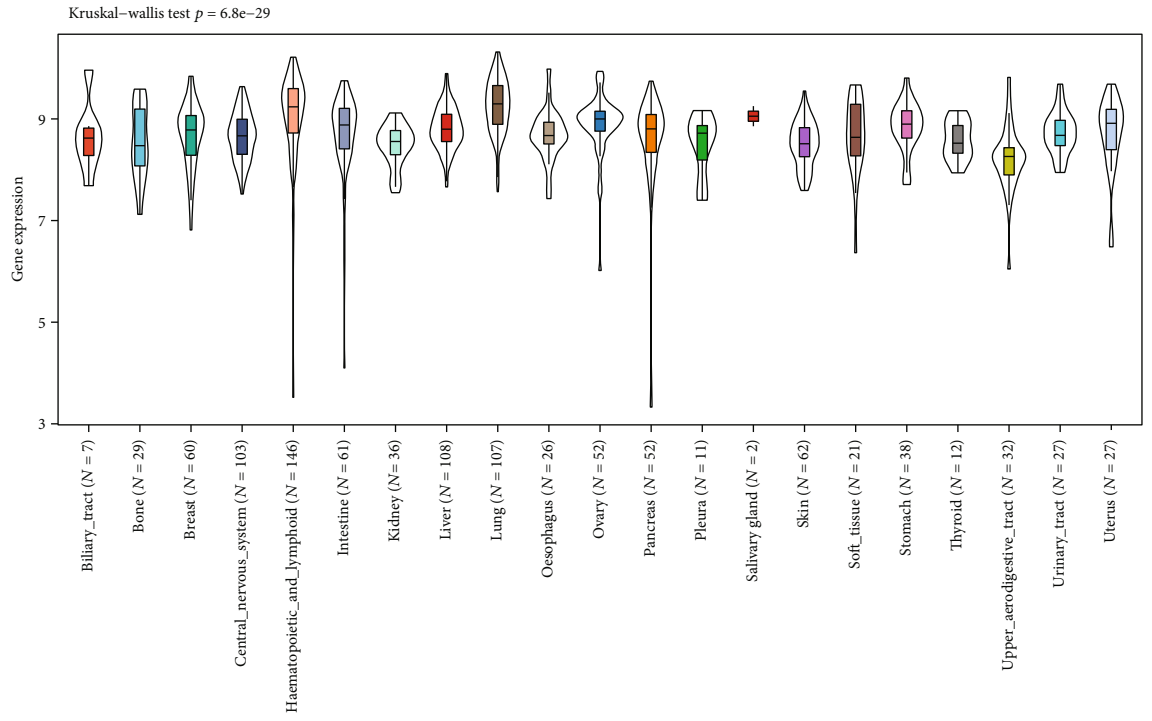

(b)

Figure 1: Continued.

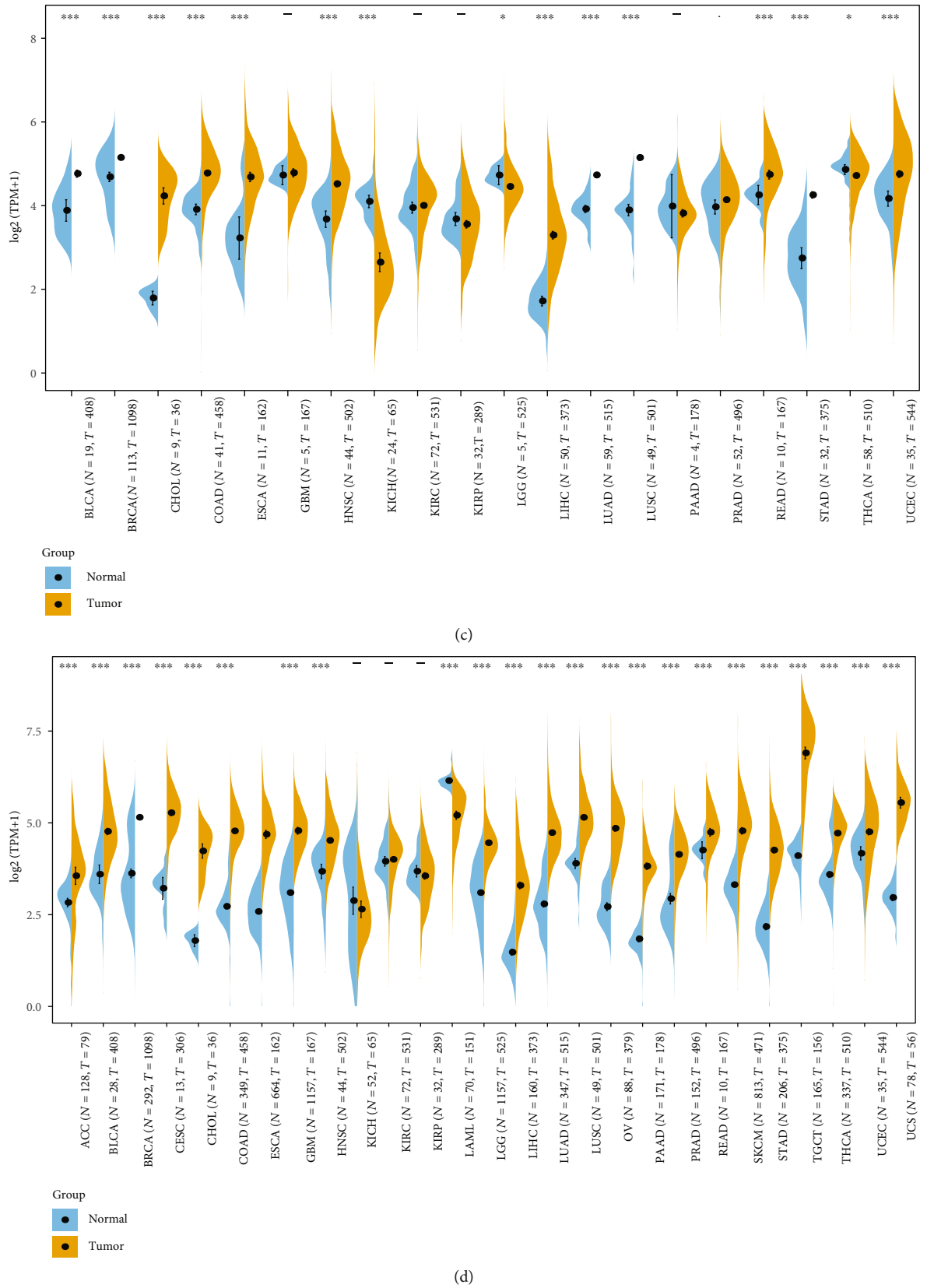

Figure 1: MSH2 expression level in 31 normal tissues across (a) the GTEx dataset and (b) the CCLE database. We downloaded the information of the distinction samples from (c) TCGA database and (d) GTEx datasets on individual gene expression between cancer and paracancer.

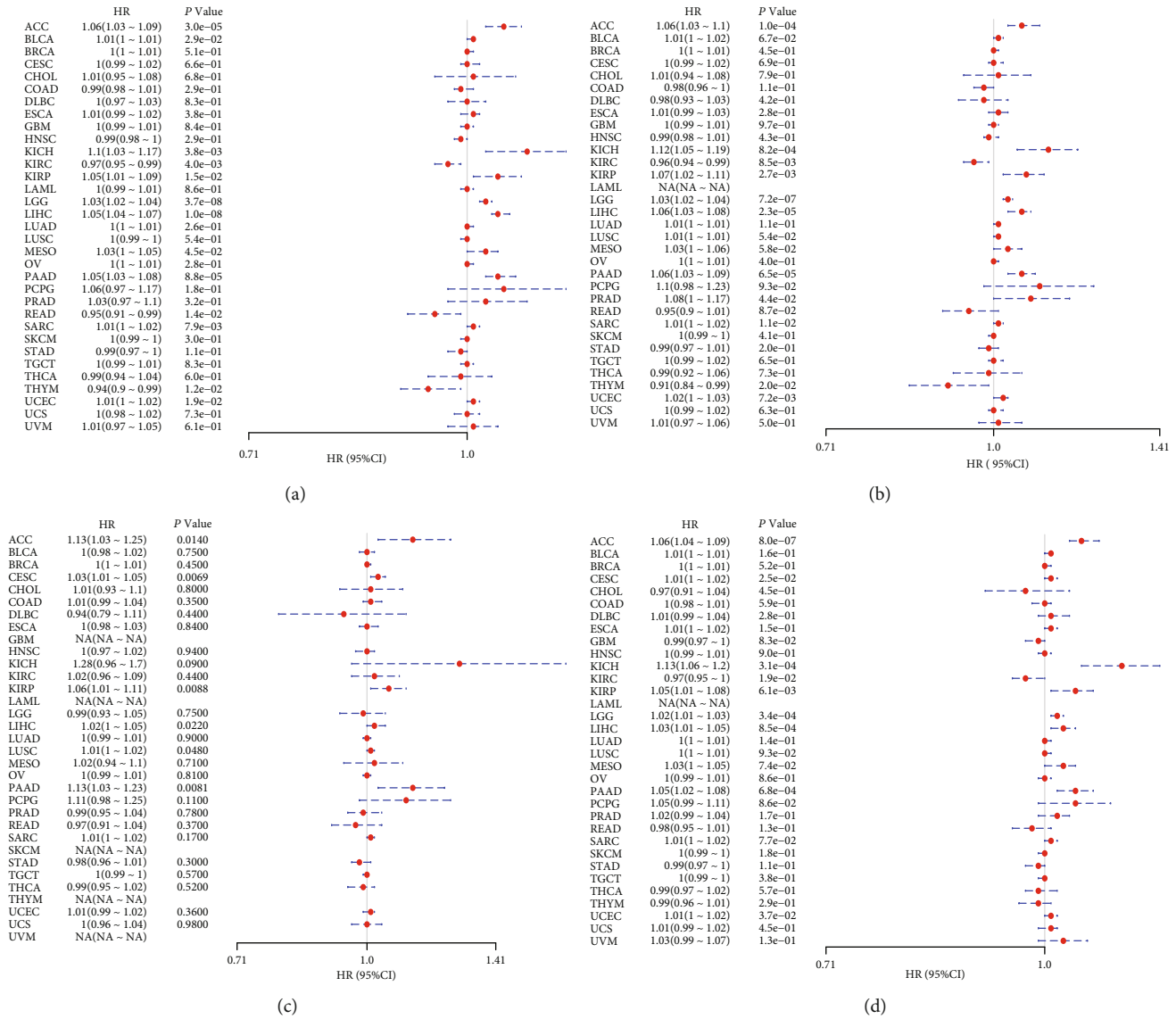

FIGURE 2: The relationship between expression and OS (a), DSS (b), DFI (c), and PFI (d) in 33 tumors of TCGA. Outcomes of univariate COX regression analysis were shown through the forest plot.

3.2. Survival Analysis Data. We investigated the relationship between MSH2 expression levels and survival prognosis in patients with different tumors. We first analyzed the relationship between expression and prognostic OS in 33 tumors of TCGA using gene expression profile data and univariate survival analysis. The forest plots in 33 tumors are shown in Figure 2(a), and among the significant tumors, ACC, BLCA, KICH, kidney renal clear cell carcinoma (KIRC), kidney renal papillary cell carcinoma (KIRP), LGG, LIHC, mesothelioma (MESO), pancreatic adenocarcinoma (PAAD), READ, SARC, thymoma (THYM), and UCEC are selected as prognostic KM curves. We divided cancer cases into high- and low-expression groups according to the median expression level of MSH2 and mainly applied the databases of TCGA and GEO to investigate the relationship between MSH2 expression and prognosis of patients with different tumors. According to Figure 3(a) high expression of MSH2 was associated with poorer prognosis in ACC, BLCA, KICH, KIRP, LGG, LIHC, MESO, PAAD, SARC, and UCEC, while low expression of MSH2 was associated with poorer prognosis in KIRC, READ, and THYM.

Also, considering the possibility of non-tumor-related deaths during follow-up, we analyzed the relationship between gene expression and DSS in 33 tumors of TCGA cohort (Figure 2(b)); among the significant tumors, ACC, KICH, KIRC, KIRP, LGG, LIHC, PAAD, PRAD, SARC, THYM, and UCEC are selected as prognostic KM curves. Cancer cases were divided into high- and low-expression groups according to the median expression level of MSH2 for prognostic KM curves. As shown in Figure 3(b) MSH2 was expressed in ACC, KICH, KIRP, LGG, LIHC, PAAD, PRAD, SARC, and UCEC in which high expression levels were significantly associated with their poorer DSS, while in KIRC and THYM, low MSH2 expression levels were associated with poorer DSS.

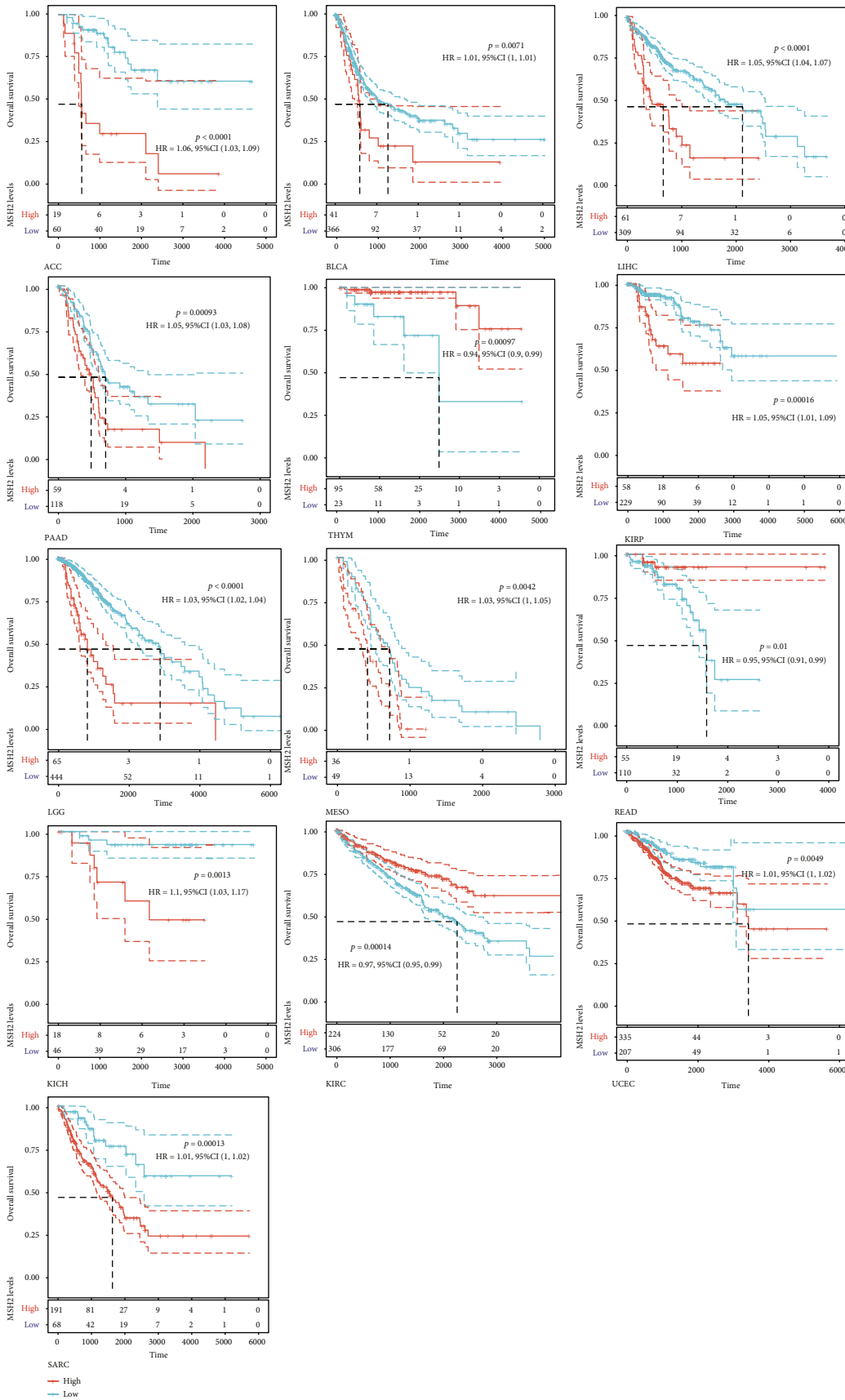

(a)

Figure 3: Continued.

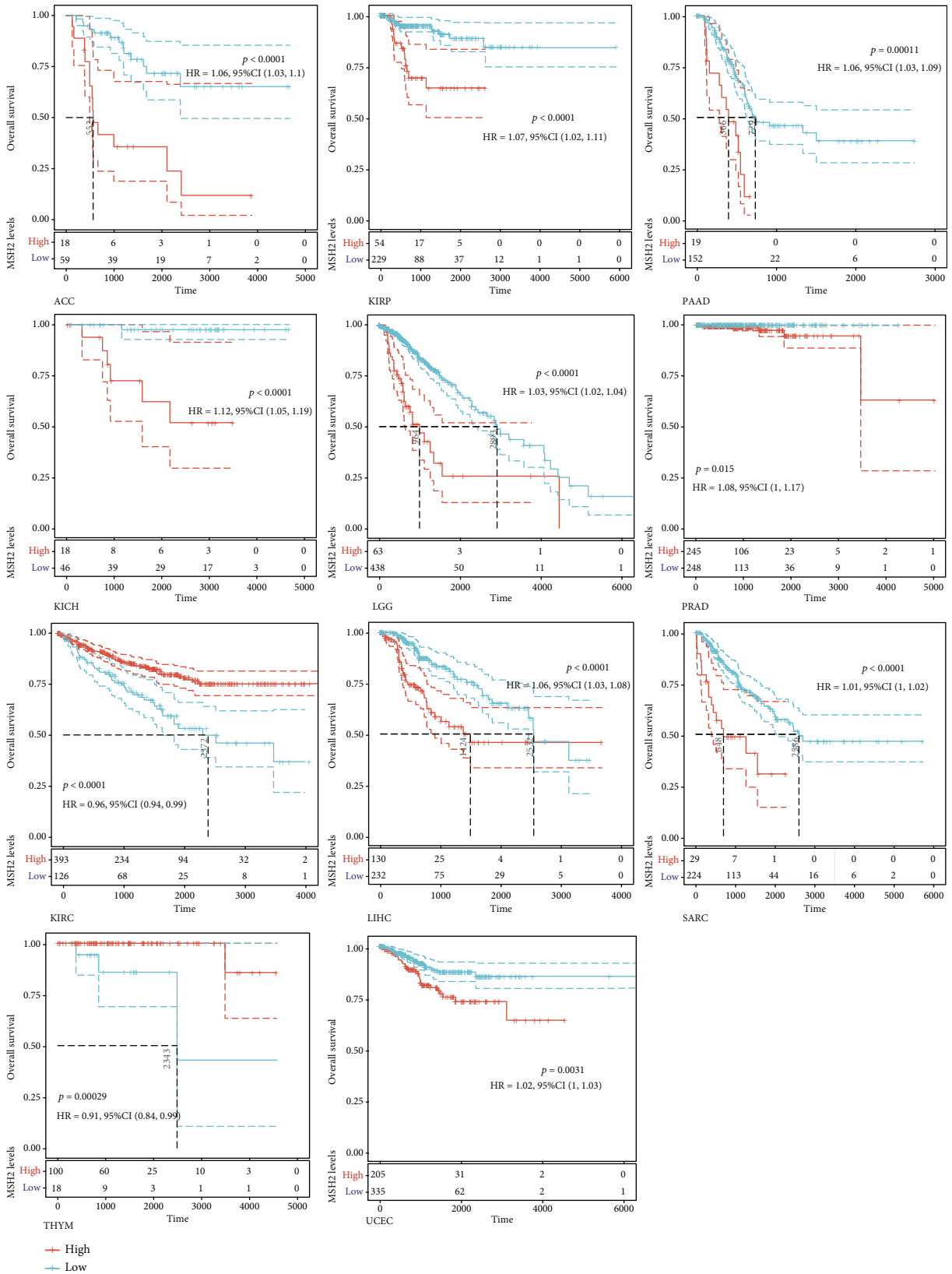

(b)

Figure 3: Continued.

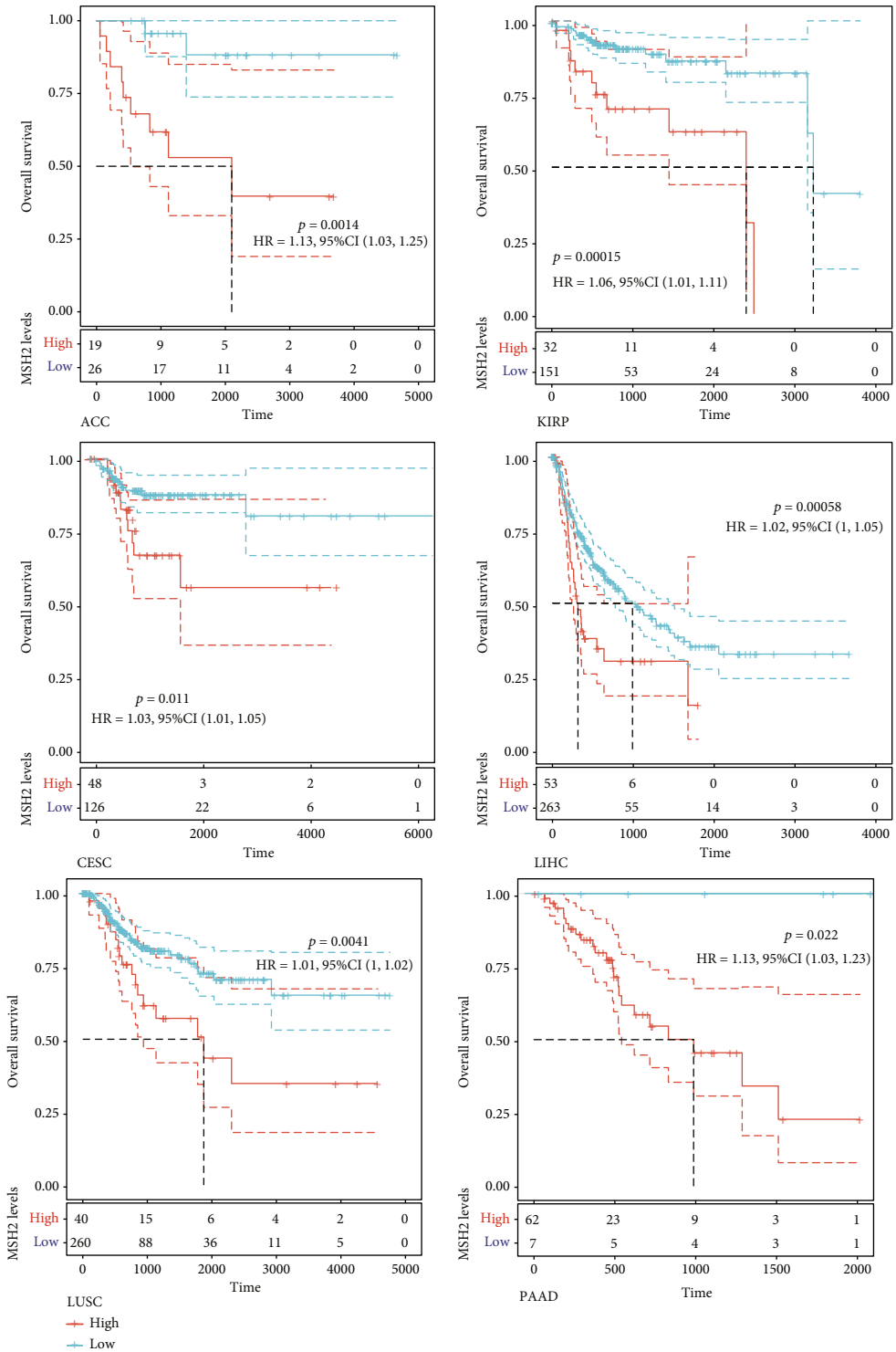

(c)

Figure 3: Continued.

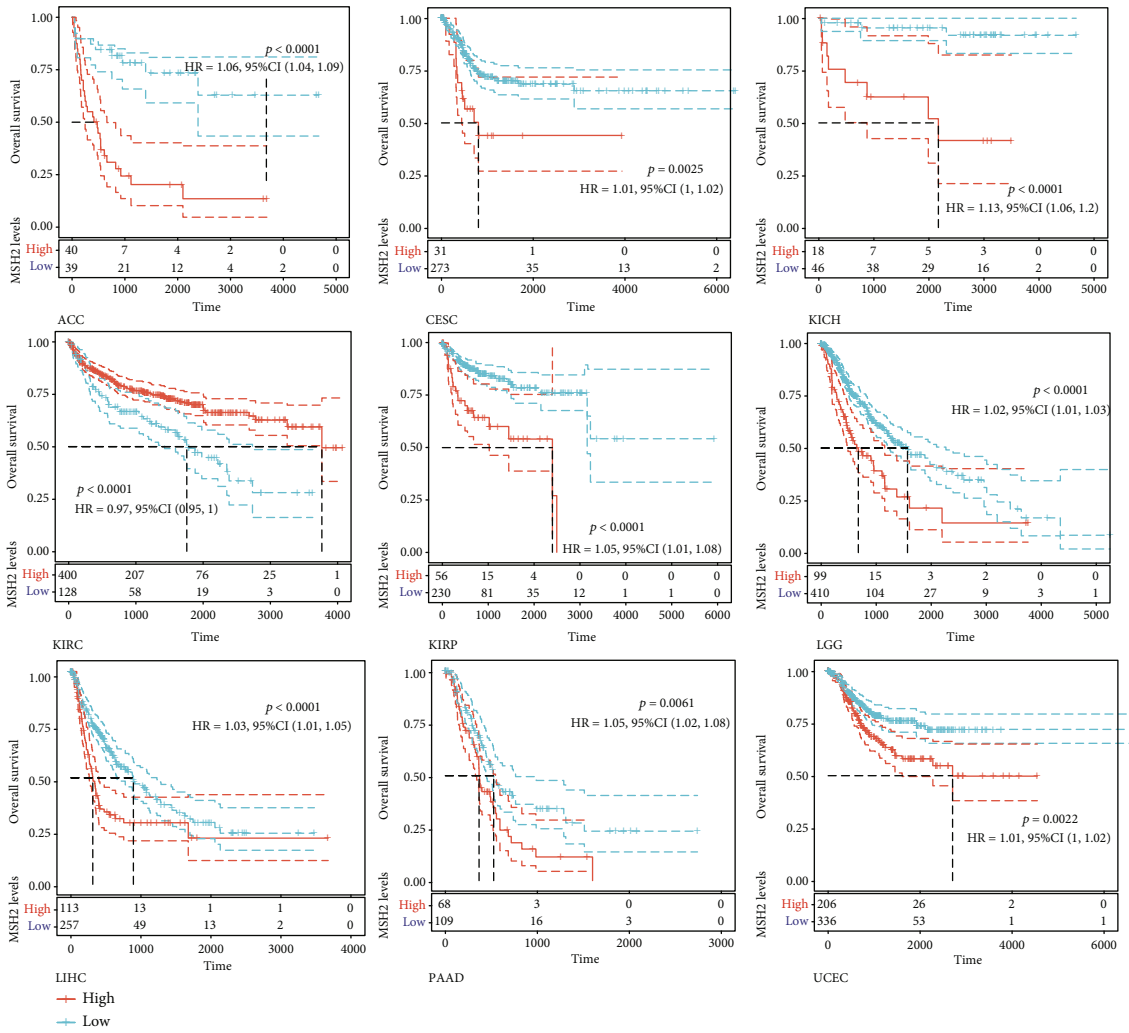

(d)

Figure 3: A log-rank test was conducted for the determination on the significance of the overall survival differences (a), DSS differences (b), DFI differences (c), and PFI distinctions (d) with a threshold of $P < 0.05$, whose results were presented by the way of Kaplan-Meier survival curves versus the patients' survival rates of low and high MSH2 expression in tumors.

We further analyzed the relationship between gene expression and DFI (Figure 2(c)) and PFI (Figure 2(d)) in the 33 tumors of TCGA cohort. Significant tumors (ACC, CESC, KIRP, LIHC, LUSC, PAAD and ACC, CESC, KICH, KIRC, KIRP, LGG, LIHC, PAAD, and UCEC) were selected in DFI and PFI survival analysis, and cancer cases were divided into high- and low-expression groups according to MSH2 expression levels for prognostic KM curves. As shown in Figure 3(c), in the DFI survival analysis, high expression of MSH2 was all associated with poorer prognosis in ACC, CESC, KIRP, LIHC, LUSC, and PAAD. As shown in Figure 4 (d), in the PFI survival analysis, high expression of MSH2 was associated with poorer prognosis in ACC, CESC, KICH, KIRP, LGG, LIHC, PAAD, and UCEC. And low expression of MSH2 was associated with a worse prognosis for KIRC patients.

3.3. Relationship between Gene Expression and Immunity in Individual Tumors. Tumor-infiltrating lymphocytes are independent predictors of anterior lymph node status and survival in cancer [24]. We investigated whether this gene expression correlated with the level of immune infiltration in different types of cancers.

The results showed that MSH2 expression levels were significantly correlated with the level of B cell infiltration in 18 cancers, CD4+ T cell infiltration in 23 cancers, CD8+ T cells in 10 cancers, macrophages in 12 cancers, neutrophils in 26 cancers, and dendritic cells in 12 cancers. The three most significantly correlated tumors in each immune cell were selected. B cell infiltration levels were significantly correlated with MSH2 expression levels in LGG, KIRP, and PRAD. CD4+ T cell infiltration level was significantly correlated with MSH2 expression levels in THCA, HNSC, and KIRC. CD8+ T cell infiltration level was significantly correlated with MSH2 expression levels in THYM, LIHC, and SARC. Macrophage infiltration levels were significantly correlated with MSH2 expression levels in LIHC, glioblastoma multiforme (GBM), and SARC. Neutrophil infiltration levels

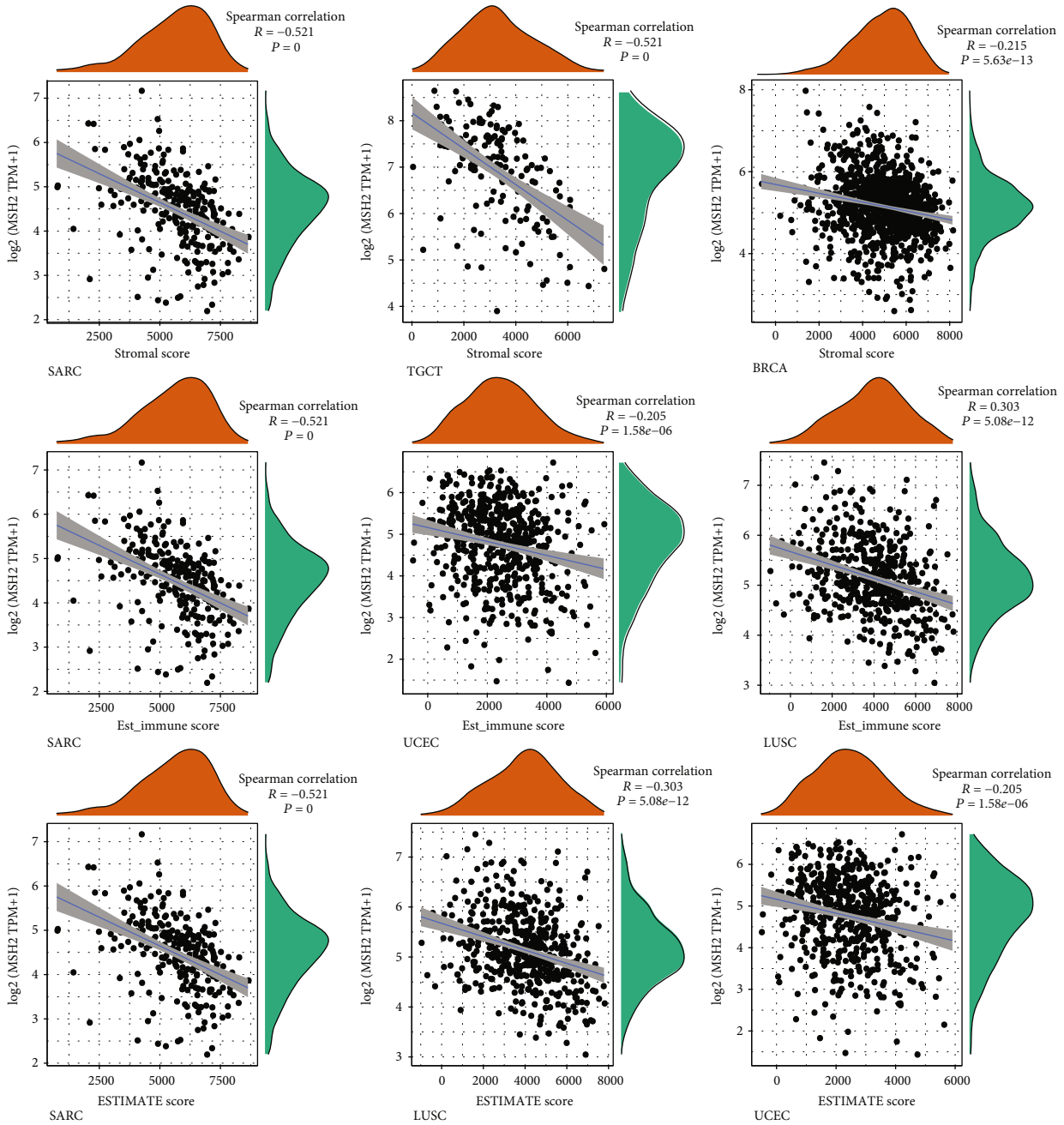

Figure 4: Correlation of MSH2 expression with the stromal score, immune score, and ESTIMATE score in SARC, LUSC, UCEC, TGCT, and BRCA.

were significantly correlated with MSH2 expression levels in THYM, KIRC, and PRAD. Dendritic cell infiltration levels were significantly correlated with MSH2 expression levels in BRCA, HNSC, and LIHC.

An increasing number of reports suggest that the tumor immune microenvironment has an important role in tumor development [25]. We observed the relationship between gene expression and the immune score, stromal score, and ESTIMATE score in 33 tumors and selected the three tumors with the most significant relationship among each score as shown in Figure 4. The results showed that the expression levels of MSH2 in SARC, TGCT, and BRCA were significantly and negatively correlated with the stromal score. The MSH2 gene expression levels in SARC, UCEC, and LUSC were significantly and positively correlated with the immune score. In SARC, LUSC, and UCEC, MSH2 gene expression levels were significantly and positively correlated with the ESTIMATE score.

Under normal conditions, immune cells can recognize and remove tumor cells from the tumor microenvironment [26]. Tumor immunotherapy approaches control and eliminate immune cells by restarting and maintaining the tumor immune cycle as a means to repair the normal antitumor immune response in the body. Immune checkpoint genes

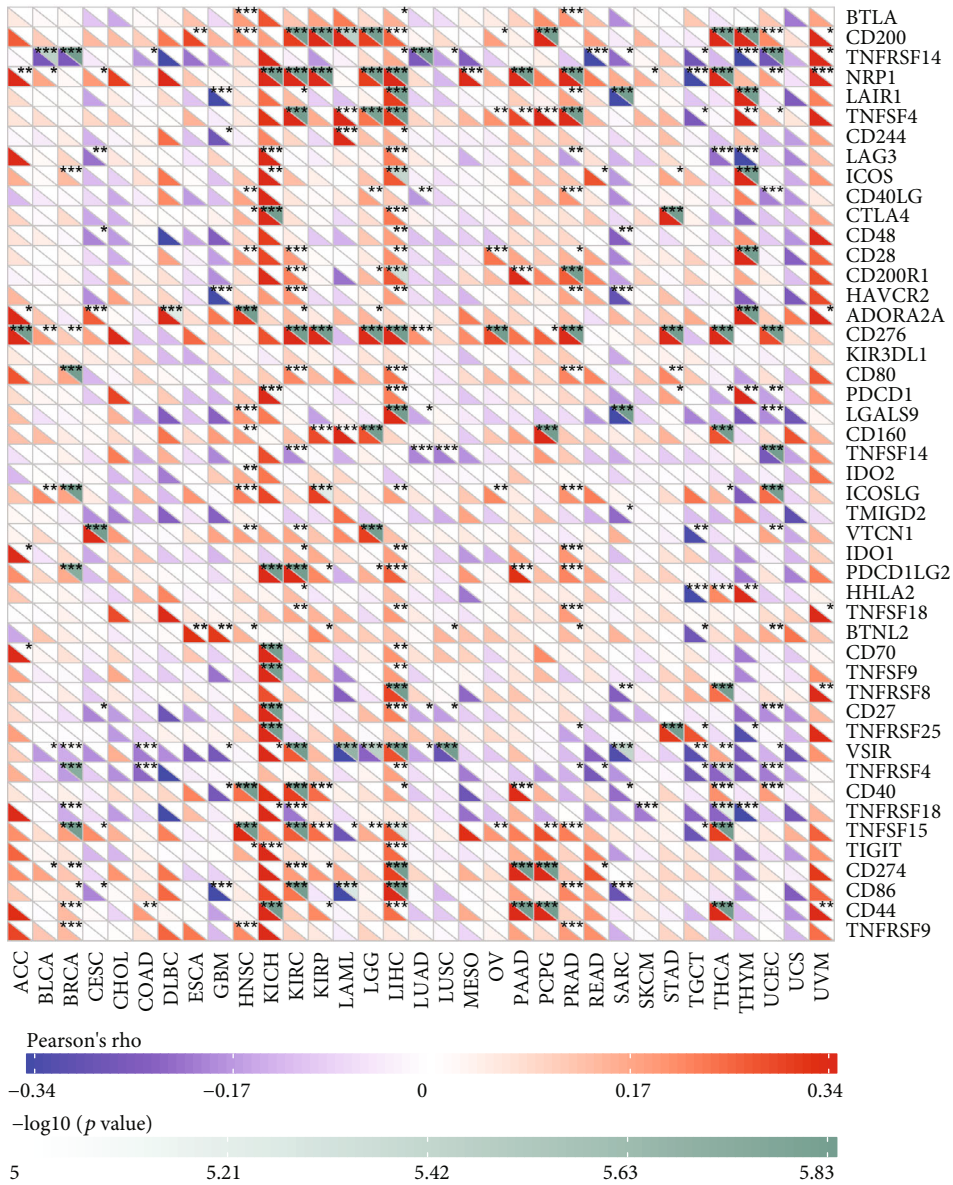

Figure 5: MSH2's relationship with immune checkpoint gene expression was presented in a way of a heat map. The horizontal coordinates indicate the 33 selected tumors, and the vertical coordinates indicate the relevant immune checkpoints, where $*$ indicates correlation ($P < 0.05$), $**$ indicates high correlation ($P < 0.01$), and $***$ indicates significant correlation ($P < 0.001$).

include monoclonal antibody-based immune checkpoint inhibitors, therapeutic antibodies, cancer vaccines, cell therapy, and small-molecule inhibitors [27]. As shown in Figure 5, the horizontal coordinates indicate the 33 selected tumors and the vertical coordinates indicate the relevant immune checkpoints. We found that the expression of MSH2 was positively correlated with the expression levels of immune checkpoint genes in KICH, KIRC, and LICH, while the expression of MSH2 was negatively correlated with the expression levels of immune checkpoint genes in SARC.

3.4. Relationship between Gene Expression and Immune Neoantigens, TMB, and Microsatellite Instability. The immune activity of tumor neoantigens and neoantigen vaccines can be designed and synthesized according to the mutation of tumor cells and immunized to patients to achieve therapeutic effects [28]. Here, we counted the number of neoantigens in each tumor sample separately to analyze the relationship between MSH2 expression and the number of antigens. As shown in Figure 6, the expression levels of MSH2 in LUAD, LUSC, BRCA, STAD, THCA, BLCA, PRAD, and LGG were found positively correlated with the number of immune neoantigens.

TMB is used to reflect the number of mutations contained in tumor cells and is a quantifiable biomarker. Here, we counted TMB for each tumor sample separately using Spearman's rank correlation coefficient and analyzed the relationship between gene expression and TMB as shown in Figure 7(a). MSH2 gene expression level results such as

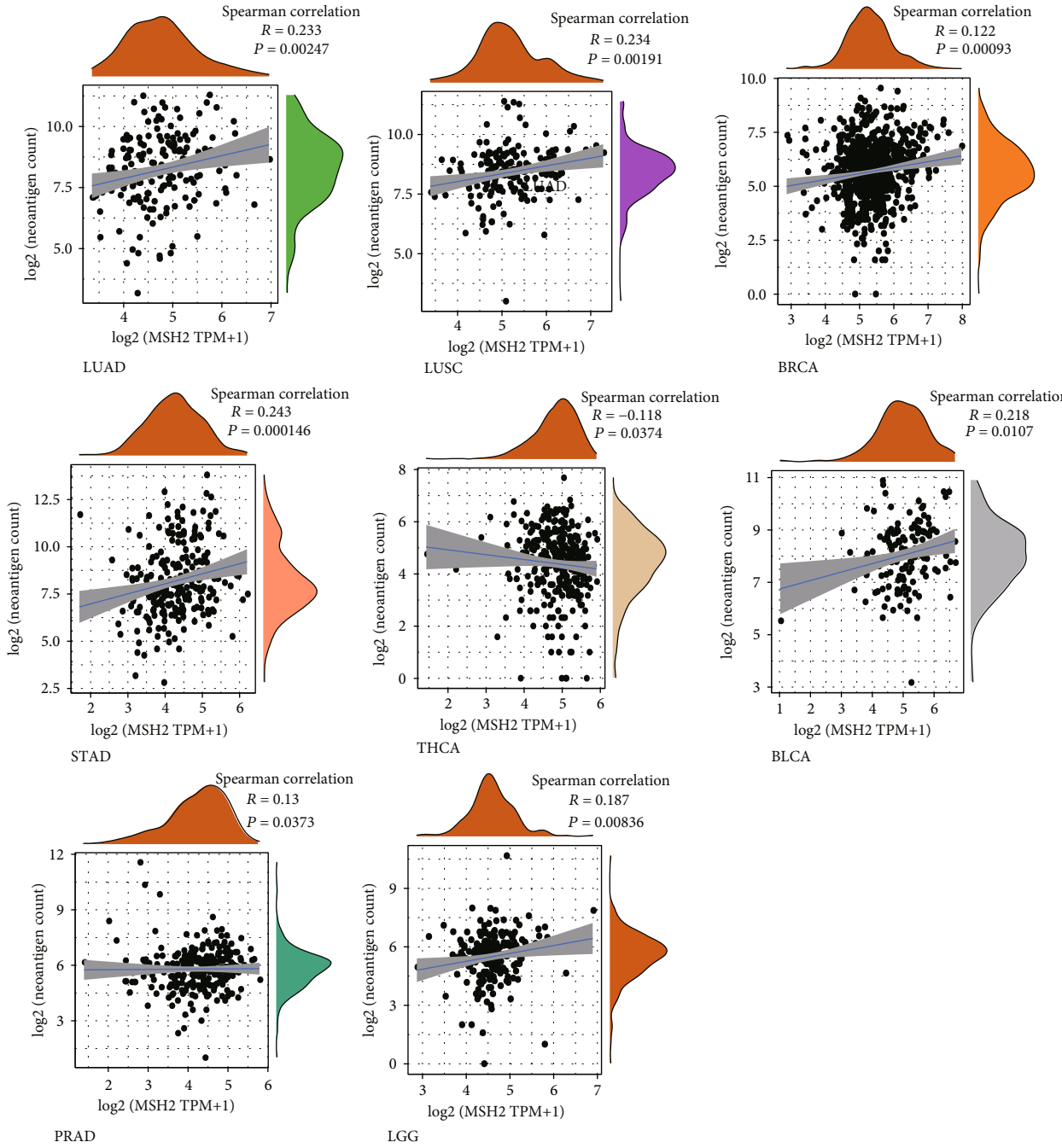

Figure 6: MSH2's correlation with neoantigens. Expression of MSH2 was positively correlated with the immune neoantigens' amount in LUAD, LUSC, BRCA, STAD, THCA, BLCA, PRAD, and LGG.

BLCA, BRCA, LAML, LGG, LUAD, LUSC, PRAD, skin cutaneous melanoma (SKCM), and STAD were significantly and positively correlated with TMB, while ESCA, KIRC, KIRP, THCA, and THYM showed a negative correlation between MSH2 gene expression levels and TMB.

We analyzed the correlation between gene expression and MSI using the Spearman rank correlation coefficient as shown in Figure 7(b). The results were as follows: MSH2 gene expression levels in KIRC, LUSC, STAD, and UCEC were positively correlated with MSI, while lymphoid neoplasm diffuse large B cell lymphoma (DLBC), PRAD, and THCA showed a negative correlation between MSH2 gene expression levels and MSI.

3.5. Mutation Patterns of Genes in Individual Tumor Samples. We obtained mutation data from TCGA database for 33 tumors and analyzed the mutations of MSH2 in these tumors. As shown in Figure 8, MSH2 was observed to mutate in BLCA, BRCA, COAD, GBM, LUAD, OV, PRAD, SKCM, STAD, and UCEC. The top three tumors with the highest MSH2 mutation rate were UCEC (rate = 7.36%), COAD (rate = 4.51%), and BRCA (rate = 2.43%).

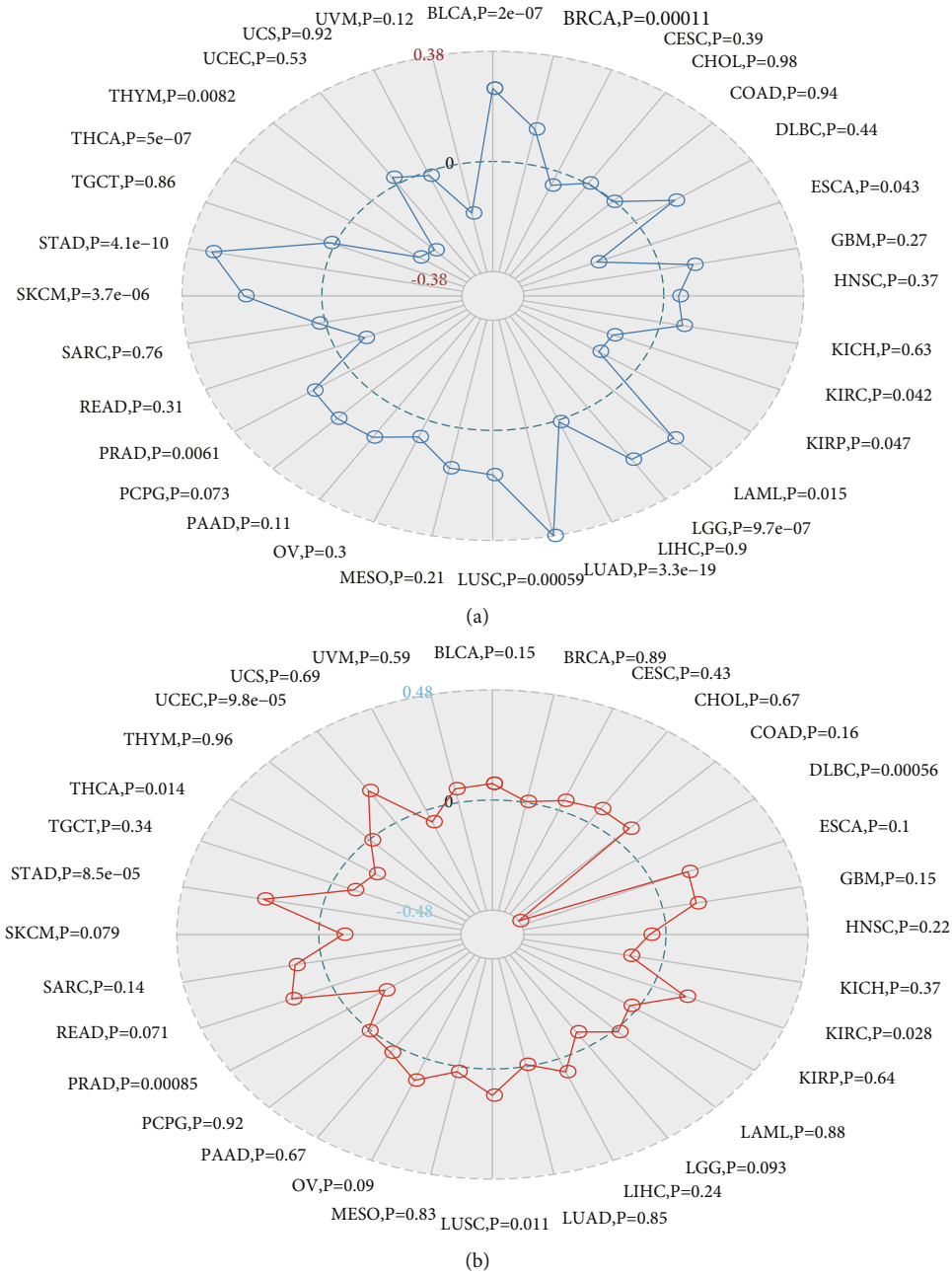

Figure 7: MSH2's correlation separately with TMB (a) and microsatellite instability (b).

3.6. Enrichment Analysis of MSH2-Related Partners. To further understand the molecular mechanisms of MSH2 in tumorigenesis, we screened for MSH2-binding proteins and MSH2 expression-related genes for a series of enrichment analyses. Based on the STRING website, we obtained a total of 50 MSH2-binding proteins supported by experimental evidence. The network diagram of the interactions of these proteins is shown in Figure 9(a). Using the GEPI A2 website, we combined the expression data of all tumor and normal tissues in TCGA to obtain the top 100 genes associated with MSH2 expression. As shown in Figure 9(b), MSH2 expression levels were positively correlated with MSH6, WDHD1, CDC25A, ERCC6L, and RCC2 (all $P < 0.001$). The corresponding heat map data also showed a positive correlation between MSH2 and the above five genes in most cancer types (Figure 9(d)). The intersection of the above two datasets showed three common genes, MSH6, FANCD2, and EXO1 (Figure 9(c)).

We combined these two datasets to perform KEGG and GO enrichment analysis, as shown in Figure 10, where the KEGG data suggest that the "cell cycle" may be involved in the influence of MSH2 on tumor pathogenesis, and the GO enrichment analysis data further suggest that the molecular mechanisms of these genes are mostly related to DNA metabolic pathways or chromosomal cell biology, such as "regulation of DNA metabolic process" and "DNA replication."

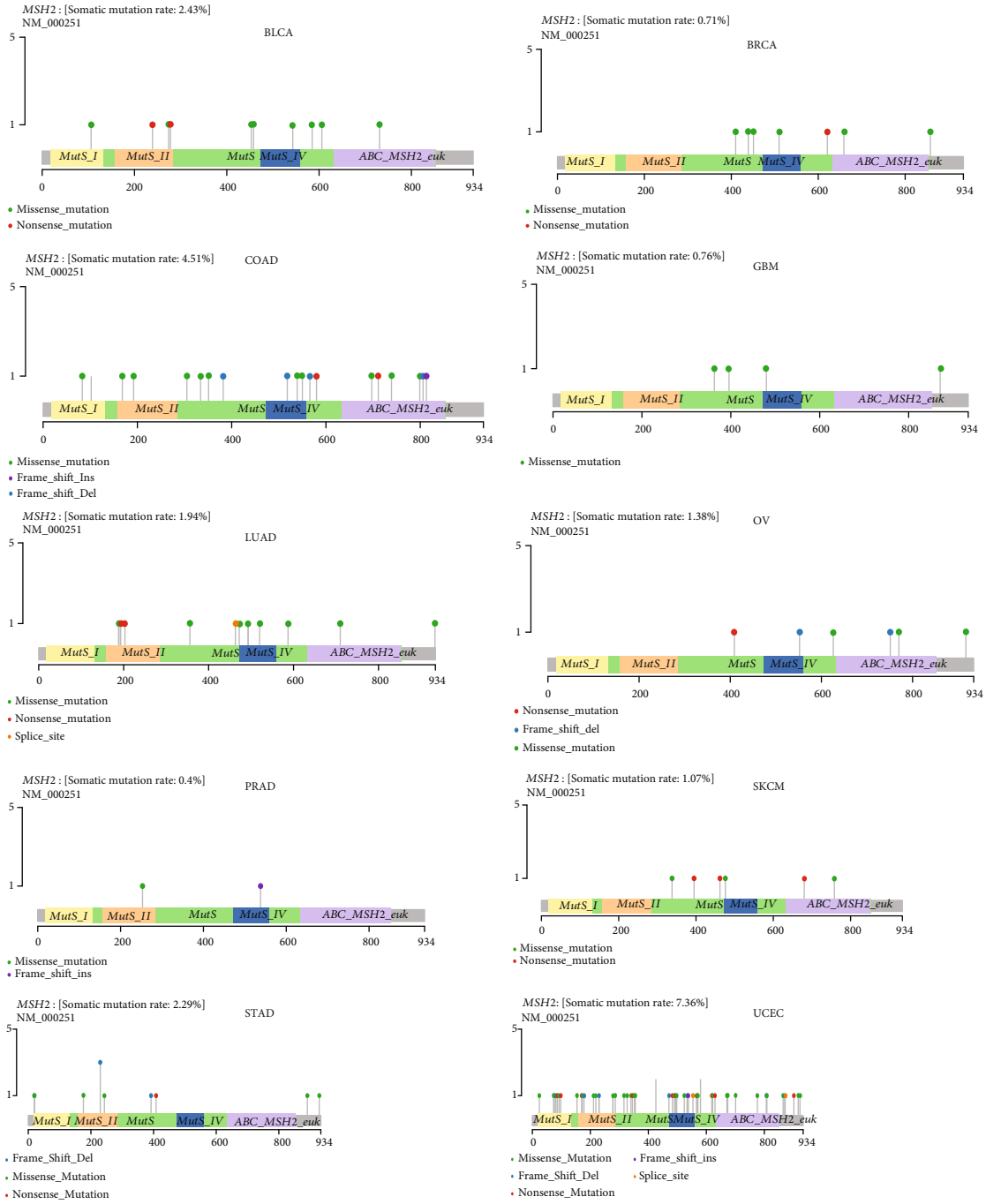

Figure 8: MSH2 gene mutation patterns in several tumors.

4. Discussion and Conclusions

China is the country with the most population worldwide; with the rising amount of its aging population, the burden of cancer in China comes to be severe [29]. Meanwhile, since the novel coronavirus pandemic in 2019, studies have shown that cancer patients in a state of systemic immunosuppression are considered highly vulnerable to the COVID-19 epidemic [30, 31].

We made a comprehensive examination on the MSH2 gene with a total of 33 different tumors in TCGA cohort based on data from TCGA, CCLE, UCSC Xena, and GTEx databases, as well as gene expression, gene variants, methylation, immune infiltration, and enrichment analysis [32]. Then, it turned out that expression of MSH2 was significantly related to prognosis and immunity in several different tumors. Therefore, we could assume that MSH2 might be a screening indicator and a possible factor for multiple tumors in the future.

We observed differences in MSH2 expression within cancers and its control normal tissues. Moreover, MSH2 was significantly more highly expressed in sarcoma,

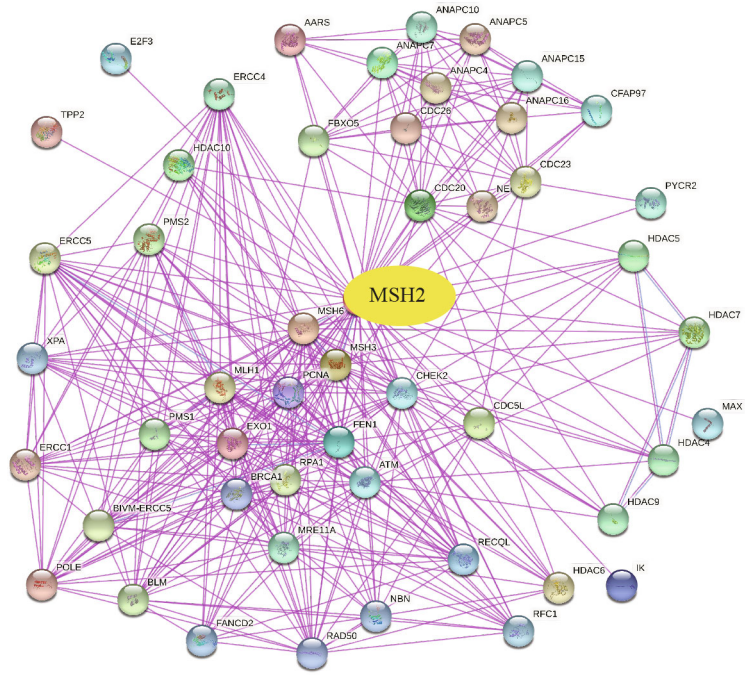

(a)

Figure 9: Continued.

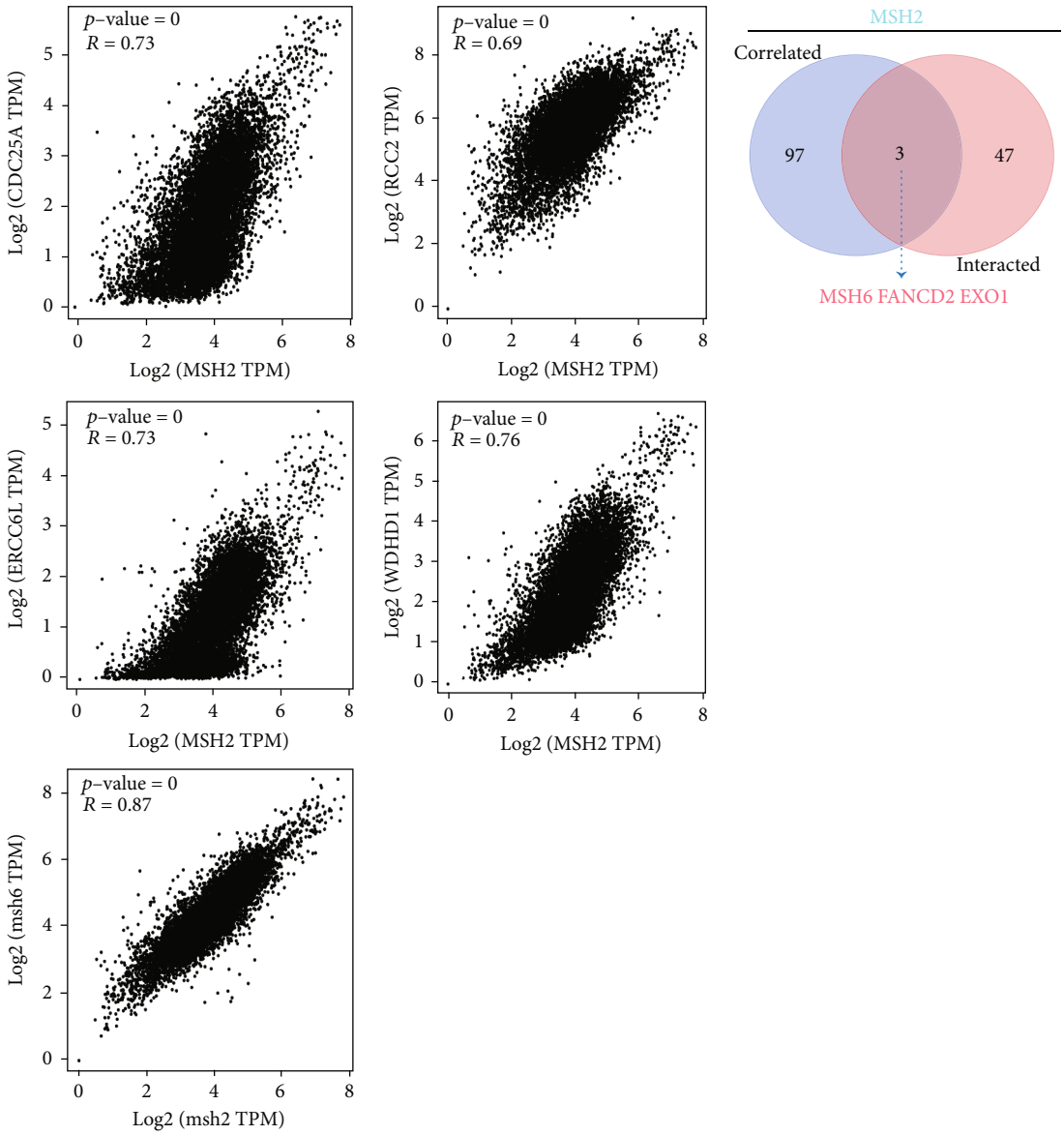

Figure 9: Continued.

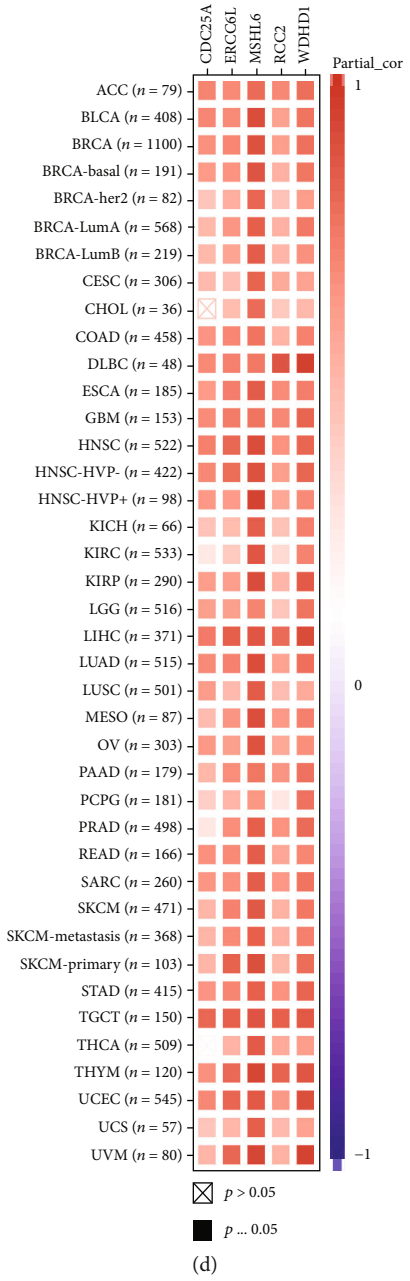

Figure 9: Enrichment analysis of MSH2-binding proteins and MSH2 expression-related genes. (a) We obtained the result of the experimentally available determination to the MSH2-binding proteins with the STRING tool. (b) We obtain 100 of the genes with the closest association with MSH2 expression. MSH2 expression levels were most positively correlated with MSH6, WDHD1, CDC25A, ERCC6L, and RCC2. (c) The intersection of the above two datasets showed three common genes, MSH6, FANCD2, and EXO1. (d) Information of the corresponding heat map also presented us a positive relationship amid MSH2 and the five genes above in most cancer types.

hepatocellular carcinoma, lung cancer, bile duct cancer, prostate cancer, gastric cancer, thyroid cancer, and common genital tumors versus normal tissues, with MSH2 expression being significantly higher in bone marrow tissues. The deletion of MSH2 protein was associated with the inactivation of MSH2, high mutation, and high tumor-infiltrating lymphocyte density in high-grade primary tumors [33]. Because MSH2 protein directs the production of proteins that modulates DNA repair, the MSH2 gene was also considered an oncogene in past studies [34], which is consistent with our analysis that high MSH2 expression was associated with OS in ACC, BLCA, and KICH patients. KIRP, LGG, LIHC, MESO, PAAD, SARC, and UCEC were associated with poorer prognosis in OS, and only KIRC and READ were associated with better prognosis in our analysis. Based on previous clinical studies, MSH2 plays different roles in different cancers, and high MSH2 expression in early-stage lung cancer is significantly associated with poorer prognosis

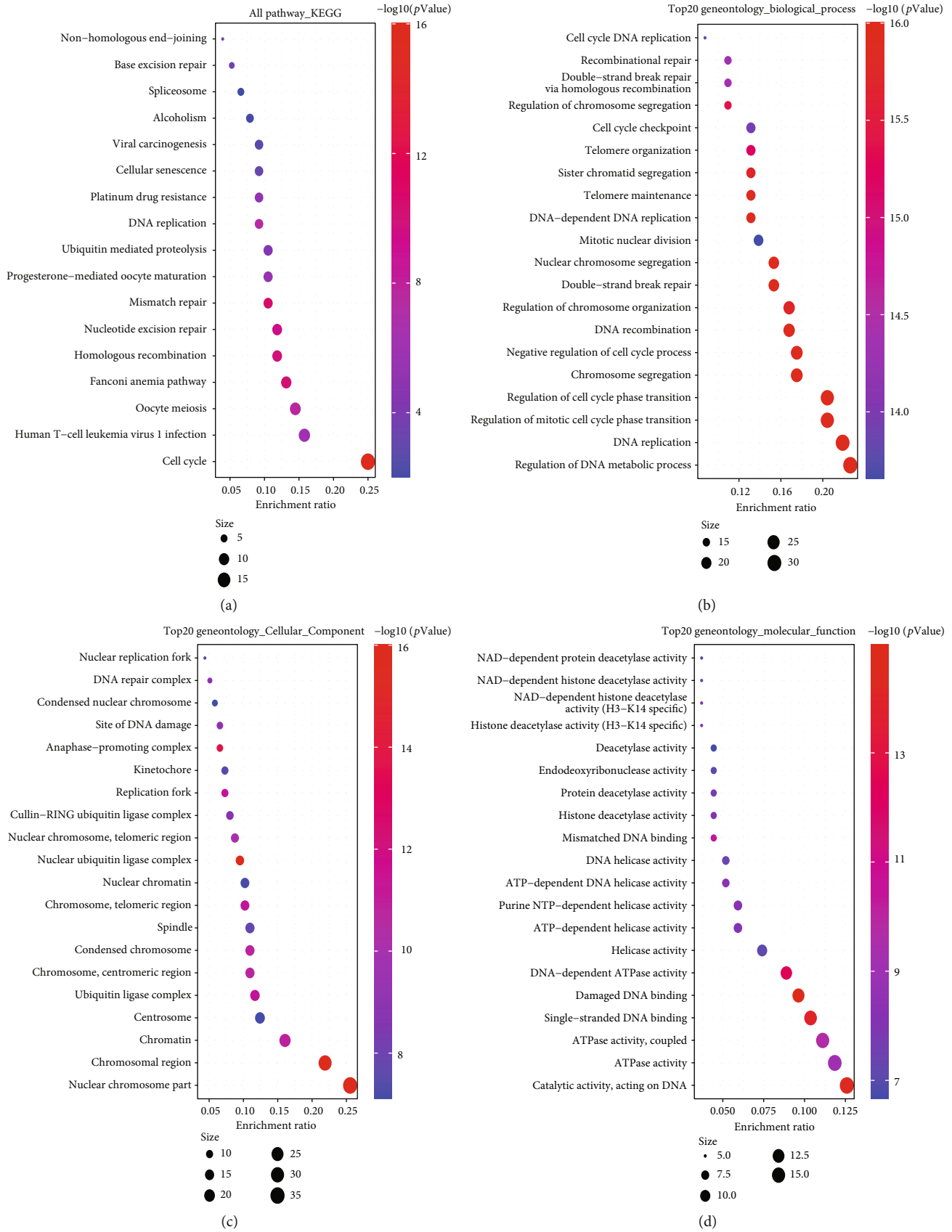

Figure 10: KEGG pathway GO enrichment analysis was performed on the basis of MSH2-binding and interacted genes. (a) KEGG pathway analysis. (b) Biological process, (c) cellular component, and (d) molecular function information of GO analysis was presented as a bubble plot.

[35], and high expression of MSH2 in NSCLC could be used as a prognostic indicator for prolonged survival [36]. This may be because the action of MSH2 protein depends on the regulation of tumor microenvironment; for example, both class IIb HDACsh and MSH2 may influence tumor pathogenesis through the cell cycle, and the deacetylation of MSH2 by HDAC10 may lead to DNA mismatch repair activity [37].

Our analysis to MSH2 expressions and immunity showed that the MSH2 expression in SARC showed a negative correlation with B cells, CD4+ T cells, CD8+ T cells, macrophages, neutrophils, and dendritic cells; it was also alike in the immune score, stromal score, and ESTIMATE score of ESTIMATE analysis. Progress of tumor development is complex, where the interplays within the cancer cells, microenvironment, and immune system hold impacts on tumorigenesis and progression [38]. Immune cells, by eliminating pathogens, have an important secondary role in maintaining tissue integrity and normal function in different states of homeostasis, infection, and noninfectious disturbances of the body and have an impact on the clinical outcome of tumors [39]. In addition, it has been shown that high or moderate immune scores in SARC can lead to better DFS or OS. Therefore, fortified MSH2 expression associated with worse prognosis in SARC patients may be related to the fact that MSH2 expression suppresses the infiltration of immune cells in the tumor microenvironment and decreases immune scores. Besides that, the MSH2 expressions in SARC presented a significantly negative correlation with most immune check genes, especially LGALS9 and VSIR. Immune checkpoints are various immunosuppressive pathways that hold the balance of self-tolerance, regulating the duration as well as the magnitude of immune responses in the physical state [40]. Immune checkpoint blockade can reduce immune escape of tumor cells and limit tumor growth.

It was reported that the abnormal expression of MSH2 in osteosarcoma cells has been proven a possible sign of drug resistance to chemotherapeutic drugs [41], and case reports have revealed the relationship between MSH2 variants and the development of osteosarcoma, and the accumulation of genetic damage due to MSH2 variants may contribute to the development of osteosarcoma [42]. In a related study on osteosarcoma tissue microarray, local expressions of MSH6 and MSH2/6 were significantly related to shorter survival time, especially in chemotherapy-naive patients and patients with metastatic tumors [43], which is consistent with our findings. However, the study is limited in public databases, and further investigation in MSH2 expression affecting the diagnosis and prognosis of different cancer types is needed. In particular, a potential role of MSH2 indicates the SARC and contributes to the immunotherapy of SARC. This inspirits the future research on verification of the specific role of MSH2 expression on sarcoma and exploring the mechanism of it. In conclusion, the present study firstly conducted the pan-cancer analysis on MSH2 in gene expression, survival status, genetic alterations, immune infiltration, and associated cellular pathways. The study revealed that MSH2 may be an ideal prognostic indicator for SARC as well as a therapeutic target for immunotherapy in the clinical setting to improve patient prognosis and increase survival rates.

Data Availability

All data generated or analyzed during this study are included in this published article.

Additional Points

Highlights. (1)The expression of MSH2 is found high in sarcoma and low in normal tissues. (2) High MSH2 in tumors accounts for unfavorable OS in SARC patients. (3) MSH2 may be used as a prognostic indicator for SARC or a therapeutic target for immunotherapy.

Conflicts of Interest

The authors declare that they have no competing interests.

Authors' Contributions

All authors conceptualized and designed the study. Hai Yao, Zhidong Cao, and Haochuan Yong were responsible for the administrative support. Hai Yao was responsible for the provision of study materials. Xiaoxing Zhang, Xin Zhang, Wei Li, Shenshen Zhi, and Wenyan Wu were responsible for the collection and assembly of data. Hai Yao, Shenshen Zhi, Wenyan Wu, and S Pan were responsible for the data analysis and interpretation. All authors wrote the manuscript. All authors gave the final approval of the manuscript.

Acknowledgments

This work was supported by the Scientific and Health Joint Medical Research Program of Chongqing (No. 2021MSXM238) and Senior Medical Talents Program of Chongqing for Young and Middle-aged (Young and Middle-aged Senior Medical Talents Studio of Chongqing) (No. 2015HBRC014).

References

[1] N. de Wind, M. Dekker, N. Claij et al., "HNPCC-like cancer predisposition in mice through simultaneous loss of Msh3 and Msh6 mismatch-repair protein functions," *Nature Genetics*, vol. 23, pp. 359–362, 1999.

[2] J. M. Carethers, "High predictability for identifying lynch syndrome via microsatellite instability testing or immunohistochemistry in all lynch-associated tumor types," *Translational Cancer Research*, vol. 8, Suppl 6, pp. S559–s563, 2019.

[3] T. J. Kinsella, E. Gurkan-Cavusoglu, W. Du, and K. A. Loparo, "Integration of principles of systems biology and radiation biology: toward development of in silico models to optimize IUdR-mediated radiosensitization of DNA mismatch repair deficient damage tolerant human cancers," *Frontiers in Oncology*, vol. 1, p. 20, 2011.

[4] F. Dietlein and H. C. Reinhardt, "Molecular pathways: exploiting tumor-specific molecular defects in DNA repair pathways for precision cancer therapy," *Clinical cancer research : an*

official journal of the American Association for Cancer Research, vol. 20, no. 23, pp. 5882–5887, 2014.

[5] M. Kastan, "DNA damage responses: mechanisms and roles in human Disease," *Molecular Cancer Research : MCR*, vol. 6, no. 4, pp. 517–524, 2008.

[6] B. Elliott and M. Jasin, "Repair of double-strand breaks by homologous recombination in mismatch repair-defective mammalian cells," *Molecular and Cellular Biology*, vol. 21, no. 8, pp. 2671–2682, 2001.

[7] J. F. Villemure, C. Abaji, I. Cousineau, and A. Belmaaza, "MSH2-deficient human cells exhibit a defect in the accurate termination of homology-directed repair of DNA double-strand breaks," *Cancer Research*, vol. 63, no. 12, pp. 3334–3339, 2003.

[8] I. Mellon, D. K. Rajpal, M. Koi, C. R. Boland, and G. N. Champe, "Transcription-coupled repair deficiency and mutations in human mismatch repair genes," *Science*, vol. 272, no. 5261, pp. 557–560, 1996.

[9] P. Pitsikas, D. Lee, and A. J. Rainbow, "Reduced host cell reactivation of oxidative DNA damage in human cells deficient in the mismatch repair gene hMSH2," *Mutagenesis*, vol. 22, no. 3, pp. 235–243, 2007.

[10] R. Janavicius and P. Elsakov, "Novel germline MSH2 mutation in lynch syndrome patient surviving multiple cancers," *Hereditary Cancer in Clinical Practice*, vol. 10, no. 1, p. 1, 2012.

[11] Y. C. Wang, Y. P. Lu, R. C. Tseng et al., "Inactivation of hMLH1 and hMSH2 by promoter methylation in primary non-small cell lung tumors and matched sputum samples," *The Journal of Clinical Investigation*, vol. 111, no. 6, pp. 887–895, 2003.

[12] C. X. Wang, X. Wang, H. B. Liu, and Z. H. Zhou, "Aberrant DNA methylation and epigenetic inactivation of hMSH2 decrease overall survival of acute lymphoblastic leukemia patients via modulating cell cycle and apoptosis," *Asian Pacific Journal of Cancer Prevention : APJCP*, vol. 15, no. 1, pp. 355–362, 2014.

[13] B. Diouf, Q. Cheng, N. F. Krynetskaia et al., "Somatic deletions of genes regulating MSH2 protein stability cause DNA mismatch repair deficiency and drug resistance in human leukemia cells," *Nature Medicine*, vol. 17, no. 10, pp. 1298–1303, 2011.

[14] C. J. Ryan, M. R. Smith, J. S. de Bono et al., "Abiraterone in metastatic prostate cancer without previous chemotherapy," *The New England Journal of Medicine*, vol. 368, no. 2, pp. 138–148, 2013.

[15] E. J. de Ruiter, M. L. Ooft, L. A. Devriese, and S. M. Willems, "The prognostic role of tumor infiltrating T-lymphocytes in squamous cell carcinoma of the head and neck: a systematic review and meta-analysis," *Oncoimmunology*, vol. 6, no. 11, article e1356148, 2017.

[16] G. Sturm, F. Finotello, F. Petitprez et al., "Comprehensive evaluation of transcriptome-based cell-type quantification methods for immuno-oncology," *Bioinformatics Oxford, England*, vol. 35, no. 14, pp. i436–i445, 2019.

[17] T. Li, J. Fu, Z. Zeng et al., "TIMER2.0 for analysis of tumor-infiltrating immune cells," *Nucleic Acids Research*, vol. 48, no. W1, pp. W509–w514, 2020.

[18] K. Yoshihara, M. Shahmoradgoli, E. Martínez et al., "Inferring tumour purity and stromal and immune cell admixture from expression data," *Nature Communications*, vol. 4, no. 1, p. 2612, 2013.

[19] R. M. Srivastava, T. A. Purohit, and T. A. Chan, "Diverse neoantigens and the development of cancer therapies," *Seminars in Radiation Oncology*, vol. 30, no. 2, pp. 113–128, 2020.

[20] S. Boegel, J. C. Castle, J. Kodysh, T. O'Donnell, and A. Rubinsteyn, "Bioinformatic methods for cancer neoantigen prediction," *Progress in Molecular Biology and Translational Science*, vol. 164, pp. 25–60, 2019.

[21] R. Bonneville, M. A. Krook, E. A. Kautto et al., "Landscape of microsatellite instability across 39 cancer types," *JCO Precision Oncology*, vol. 2017, no. 1, pp. 1–15, 2017.

[22] L. Li, Q. Feng, and X. Wang, "PreMSIm: an R package for predicting microsatellite instability from the expression profiling of a gene panel in cancer," *Computational and Structural Biotechnology Journal*, vol. 18, pp. 668–675, 2020.

[23] L. Yin, L. Xiao, Y. Gao et al., "Comparative bioinformatical analysis of pancreatic head cancer and pancreatic body/tail cancer," *Medical Oncology*, vol. 37, no. 46, 2020.

[24] M. Yusuf, J. Gaskins, S. Mandish et al., "Tumor infiltrating lymphocyte grade in Merkel cell carcinoma: relationships with clinical factors and independent prognostic value," *Acta oncologica Stockholm, Sweden*, vol. 59, no. 12, pp. 1409–1415, 2020.

[25] D. Dai, L. Liu, H. Huang et al., "Nomograms to predict the density of tumor-infiltrating lymphocytes in patients with high-grade serous ovarian cancer," *Frontiers in Oncology*, vol. 11, article 590414, 2021.

[26] F. Massari, M. Santoni, C. Ciccarese, and D. Santini, "The immunocheckpoints in modern oncology: the next 15 years," *Expert Opinion on Biological Therapy*, vol. 15, no. 7, pp. 917–921, 2015.

[27] L. Danilova, W. J. Ho, Q. Zhu et al., "Programmed cell death ligand-1 (PD-L1) and CD8 expression profiling identify an immunologic subtype of pancreatic ductal adenocarcinomas with favorable survival," *Cancer Immunology Research*, vol. 7, no. 6, pp. 886–895, 2019.

[28] L. Li, S. P. Goedegebuure, and W. E. Gillanders, "Preclinical and clinical development of neoantigen vaccines," *Annals of Oncology*, vol. 28, suppl_12, pp. xii11–xii17, 2017.

[29] D. Sun, H. Li, M. Cao et al., "Cancer burden in China: trends, risk factors and prevention," *Cancer Biology & Medicine*, vol. 17, no. 4, pp. 879–895, 2020.

[30] S. Yang, Y. Zhang, J. Cai, and Z. Wang, "Clinical characteristics of COVID-19 after gynecologic oncology surgery in three women: a retrospective review of medical records," *The Oncologist*, vol. 25, no. 6, pp. e982–e985, 2020.

[31] J. Song, J. Han, F. Liu et al., "Systematic analysis of coronavirus disease 2019 (COVID-19) receptor ACE2 in malignant tumors: pan-cancer analysis," *Frontiers in Molecular Biosciences*, vol. 7, article 569414, 2020.

[32] Y. Yi, Q. Zhang, Y. Shen et al., "System analysis of adaptor-related protein complex 1 subunit mu 2 (AP1M2) on malignant tumors: a pan-cancer analysis," *Journal of Oncology*, vol. 2022, Article ID 7945077, 17 pages, 2022.

[33] L. B. Guedes, E. S. Antonarakis, M. T. Schweizer et al., "MSH2 loss in primary prostate cancer," *Clinical Cancer Research*, vol. 23, no. 22, pp. 6863–6874, 2017.

[34] M. Fang, M. L. Pak, L. Chamberlain, W. Xing, H. Yu, and M. R. Green, "The CREB coactivator CRTC2 is a lymphoma tumor suppressor that preserves genome integrity through transcription of DNA mismatch repair genes," *Cell Reports*, vol. 11, no. 9, pp. 1350–1357, 2015.

[35] G. Levallet, F. Dubois, P. Fouret et al., "MSH2/BRCA1 expression as a DNA-repair signature predicting survival in early-stage lung cancer patients from the IFCT-0002 phase 3 trial," *Oncotarget*, vol. 8, no. 3, pp. 4313–4329, 2017.

[36] M. Bonomi, S. Pilotto, M. Milella et al., "Adjuvant chemotherapy for resected non-small-cell lung cancer: future perspectives for clinical research," *Journal of Experimental & Clinical Cancer Research : Cr*, vol. 30, no. 1, p. 115, 2011.

[37] Y. Li and E. Seto, "HDACs and HDAC inhibitors in cancer development and therapy," *Cold Spring Harbor Perspectives in Medicine*, vol. 6, no. 10, 2016.

[38] D. S. Chen and I. Mellman, "Elements of cancer immunity and the cancer-immune set point," *Nature*, vol. 541, no. 7637, pp. 321–330, 2017.

[39] S. Sui, X. An, C. Xu et al., "An immune cell infiltration-based immune score model predicts prognosis and chemotherapy effects in breast cancer," *Theranostics*, vol. 10, no. 26, pp. 11938–11949, 2020.

[40] D. M. Pardoll, "The blockade of immune checkpoints in cancer immunotherapy," *Nature Reviews. Cancer*, vol. 12, no. 4, pp. 252–264, 2012.

[41] H. Fujii, K. Honoki, T. Tsujiuchi, A. Kido, K. Yoshitani, and Y. Takakura, "Sphere-forming stem-like cell populations with drug resistance in human sarcoma cell lines," *International Journal of Oncology*, vol. 34, no. 5, pp. 1381–1386, 2009.

[42] H. Ahmed, A. Salama, S. E. Salem, and A. A. Bahnassy, "A case of synchronous double primary breast carcinoma and osteosarcoma: mismatch repair genes mutations as a possible cause for multiple early onset malignant tumors," *The American Journal of Case Reports*, vol. 13, pp. 218–223, 2012.

[43] T. Jentzsch, B. Robl, M. Husmann, B. Bode-Lesniewska, and B. Fuchs, "Expression of MSH2 and MSH6 on a tissue microarray in patients with osteosarcoma," *Anticancer Research*, vol. 34, no. 12, pp. 6961–6972, 2014.

Hindawi
Journal of Oncology
Volume 2022, Article ID 8736575, 14 pages
https://doi.org/10.1155/2022/8736575

Research Article

Identify a DNA Damage Repair Gene Signature for Predicting Prognosis and Immunotherapy Response in Cervical Squamous Cell Carcinoma

Hong Zhou,[1] **Limei Wu**,[2] **Lijun Yu**,[3] **Yabing Yang**,[4] **Lili Kong**,[3] **Shuo Liu**,[3] **Wenhui Chen**,[2] **and Ruiman Li**[1]

[1]*Department of Obstetrics and Gynecology, The First Affiliated Hospital of Jinan University, Guangzhou 510632, China*
[2]*Department of Oncology, The First Affiliated Hospital of Jinan University, Guangzhou 510632, China*
[3]*Department of Gynecology, Beijing Rehabilitation Hospital Capital Medical University, Beijing, China*
[4]*Department of General Surgery, The First Affiliated Hospital of Jinan University, Guangzhou 510632, China*

Correspondence should be addressed to Wenhui Chen; wenhuichen221@126.com and Ruiman Li; hqyyck@126.com

Received 10 January 2022; Revised 21 February 2022; Accepted 28 February 2022; Published 23 March 2022

Academic Editor: Fu Wang

The DNA damage repair (DDR) genes are increasingly gaining attention as potential therapeutic targets in cancers. In this study, we identified the DDR genes associated with the tumor mutation burden (TMB) and prognosis of cervical squamous cell carcinoma (CESC) based on The Cancer Genome Atlas (TCGA) database. Through LASSO Cox regression, the prognostic signature involving five DDR genes (ACTR2, TEX12, UBE2V1, HSF1, and FBXO6) was established, and the risk score was identified as an independent risk factor for CESC. The nomogram consisting of the five genes accurately predicted the overall survival (OS) and the immunotherapeutic response of CESC patients. Finally, the loss of the copies of the transcription factor (TF) SP140 in CESC patients may decrease the expression of FBXO6, improve DNA repair function, and reduce the diversity of neoantigens, thereby lowering the response to immunotherapies. Therefore, the DDR gene signature is a novel prognostic model and a biomarker for immunotherapies in CESC patients.

1. Background

With 530,000 newly diagnosed cases each year, cervical squamous cell carcinoma (CESC) is the fourth most common cancer worldwide and the third most common cancer in women [1, 2]. Almost all CESC cases are the result of human papillomavirus (HPV) infection [3]. While cervical screening and antiHPV vaccination are effective preventive measures, CESC remains the leading cause of cancer-related mortality with approximately 270,000 deaths per year [2, 4]. Currently, the primary treatment for CESC patients consists of radiation and/or cisplatin-containing chemotherapy in addition to surgical resection. Unfortunately, the majority of the patients are at an advanced stage that limits therapeutic success when diagnosed. Both local and distant recurrence is common, which highlights the need for improved therapeutic options [5, 6]. The clinical trials of therapeutic HPV vaccines, adoptive T cell therapy, and immune checkpoint inhibitors have shown promising response rates [7–10]. It is nevertheless crucial to identify more effective prognostic biomarkers for CESC and modify the current treatment strategies.

The DNA damage repair (DDR) response maintains genome stability and protects cells against endogenous and exogenous DNA damage [11]. Variations in the DDR genes in tumor cells are frequently associated with high somatic mutation load, which in turn triggers the production of tumor-specific neoantigens [12–15]. Consistently, as reported in a recent study, the DDR gene signature of glioma cells was predictive of patient prognosis and intratumoral immune cell infiltration [16]. Furthermore, the Arg399Gln polymorphism of the X-ray repair cross-complementing group 1 (XRCC1) gene is associated with the prognosis of nonsmall cell lung cancer (NSCLC) patients receiving platinum therapy, and the patients with the Gln/Gln genotype

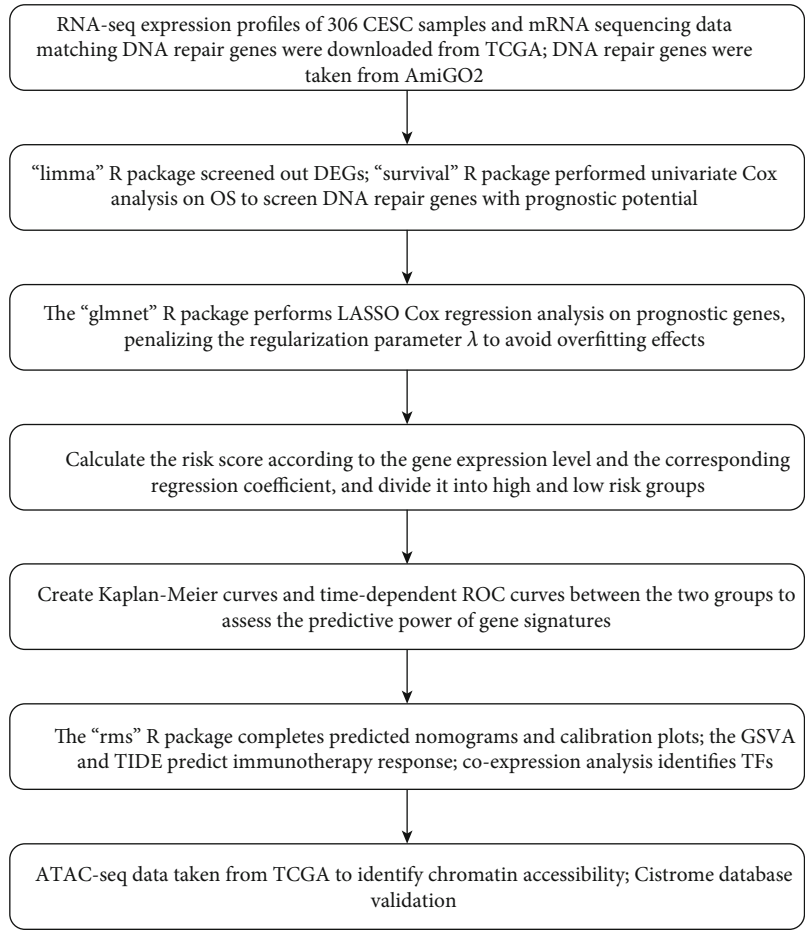

Figure 1: The flow chart of the analysis process. CESC: cervical squamous cell carcinoma; TCGA: The Cancer Genome Atlas; DEGs: differentially expressed genes; OS: overall survival; GSVA: Gene Set Variation Analysis; TIDE: tumor immune dysfunction and exclusion; TFs: transcription factors.

have a survival benefit [17]. Another study reported a correlation between polymorphisms of DDR genes and the response metastatic urothelial cancer patients to PD-1/PD-L1 blockers [18]. Thus, DNA repair defects are potentially novel biomarkers of immune checkpoint blockade response [12]. Mutations in the DNA polymerase required during DNA repair can also improve the overall survival rate of patients by increasing mutations in DDR genes [19]. In addition, mutations in DDR genes are closely related to the resistance of tumors to radiotherapy and chemotherapy [20, 21]. Few studies have reported the clinical significance of DDR genes in CESC, and so far, only XRCC4 has been associated with the progression of cervical cancer [22]. These studies indicate that DDR genes are emerging biomarkers of the clinical prognosis and immunotherapeutic response of various cancers. Furthermore, most DDR genes are regulated by upstream transcription factors (TFs), such as p53, BRCA1, AP-1, and NF-κB [23], which offers new insights into the mechanisms underlying their role in cancer prognosis.

The aim of this study was to identify novel DDR biomarkers for the prognosis and immunotherapeutic response of CESC. To this end, we screened for the differentially expressed DDR genes in CESC from TCGA (The Cancer Genome Atlas) and analyzed their relationship with the immune microenvironment in CESC. A five-DDR gene signature was identified that can predict CESC prognosis and immunotherapeutic response with high sensitivity.

2. Materials and Methods

2.1. Data Collection. RNA-seq data as well as clinical information (age, days to death, vital status, clinical stage, mutations, copy number variations, etc.) of 306 CESC samples were obtained from TCGA database (https://portal.gdc.cancer). Besides, samples with incomplete clinical information were excluded. DDR gene data was downloaded from AmiGO2. (http://amigo.geneontology.org/).

2.2. Identification of Differentially Expressed Genes. The RNA-seq data of DDR genes were processed using the "limma" package. For high-tumor mutation burden (TMB) and low-TMB samples, the differentially expressed genes (DEGs) were screened between them. Univariate Cox regression of the overall survival (OS) was performed using the

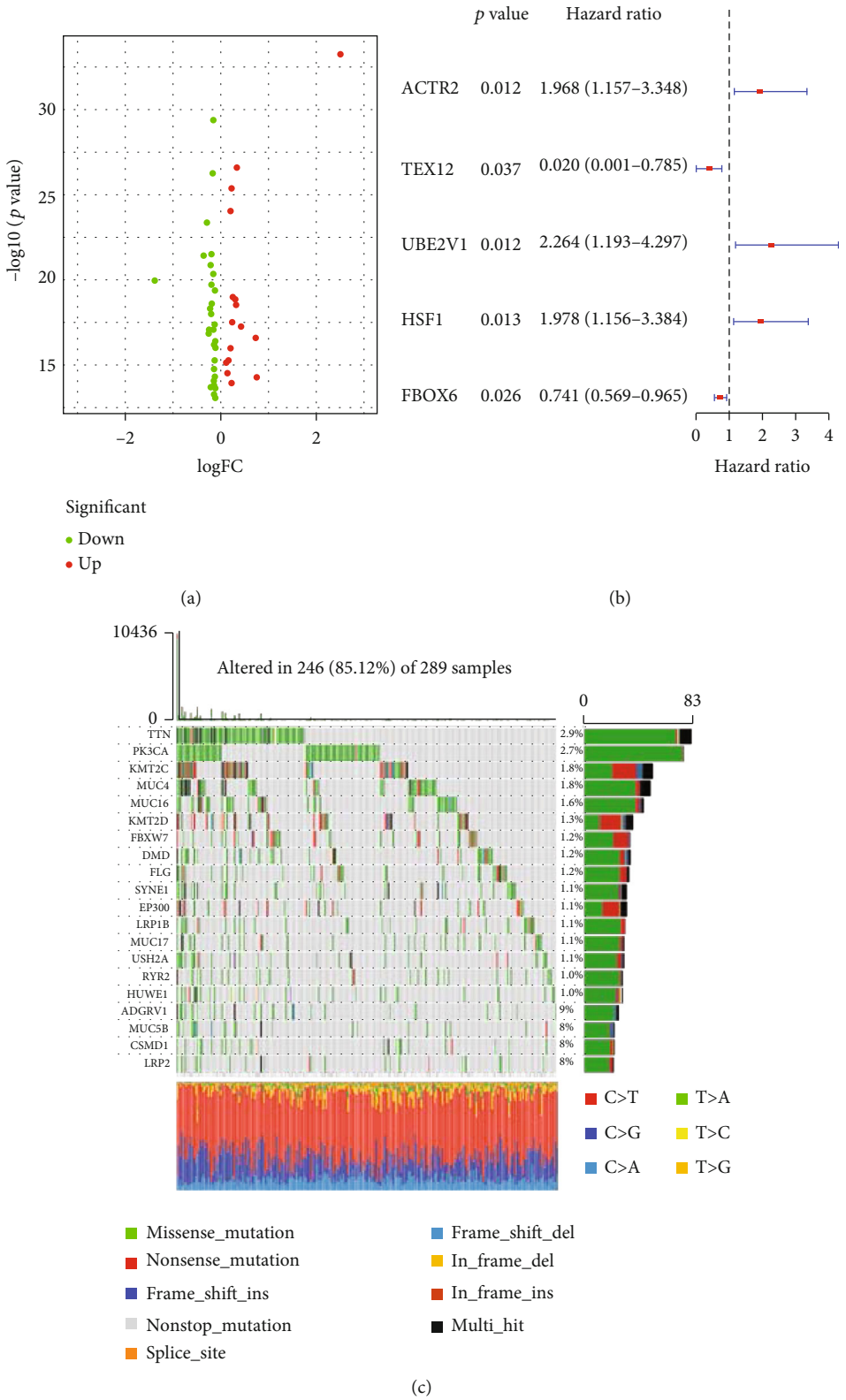

Figure 2: Continued.

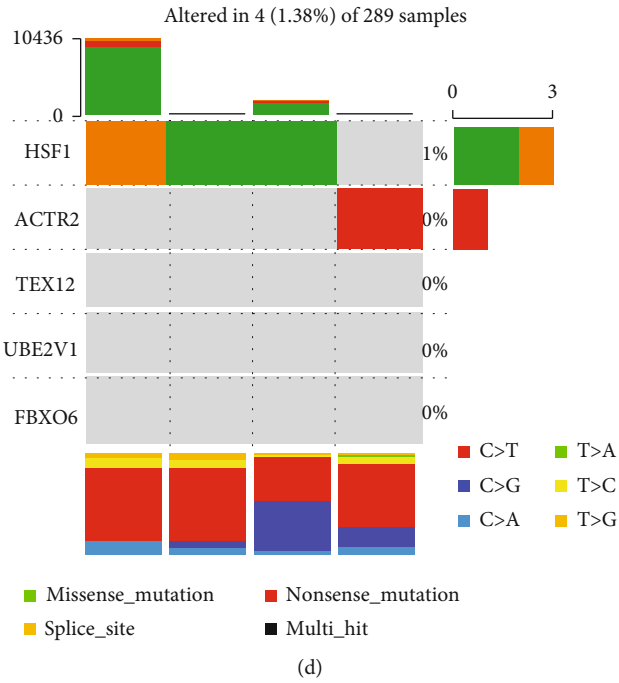

(d)

Figure 2: Identification of prognostic genes related to DNA damage repair: (a) Differentially expressed genes in the high and low TMB groups; (b) univariate Cox regression analysis to determine potential prognostic genes; (c) the incidence of major somatic mutations in CESC; (d) the mutation frequency of 5 DNA damage repair genes.

"survival" R package to identify DDR genes with prognostic relevance.

2.3. Identification of Prognostic Genes as well as Establishment of Prognostic Model. Analysis of the prognostic genes was performed by LASSO Cox regression based on the "glmnet" R package. To avoid overfitting, ten-fold cross-validation was adopted to determine the penalized regularization parameter λ in the model. For each patient, the risk score was calculated as following: risk score = SUM (expression level of each gene × corresponding coefficient). Based on the median of the risk score, CESC patients were then categorized into the low-/high-risk groups. The Kaplan-Meier curves of both groups were plotted using the "survminer" R package. The "survivalROC" R package was used to plot the time-dependent ROC curve in order to evaluate the predictive power of the gene signature. The independent prognostic predictors of OS were determined by Cox regression using TCGA data. The nomograms and corresponding calibration plots were constructed based on the independent predictors with the "rms" R package, and the predictive power of the nomogram was determined by ROC curve analysis.

2.4. Predictors of Immunotherapeutic Response. Single-sample gene set enrichment analysis (ssGSEA) was carried out on thirteen immune-related pathways. Meanwhile, the infiltration of sixteen immune cell types was evaluated using the "gsva" R package. The response of the CESC patients to ICB was predicted on the basis of pretreatment genomics using the tumor immune dysfunction and exclusion (TIDE) program (http://tide.dfci.harvard.edu/).

2.5. Identification of the Upstream TFs. TFs coexpressed with the key genes significantly were identified if their correlation coefficients >0.50.

2.6. Validation of the Regulatory Mechanism of TFs. For CESC samples, their ATAC-seq data was retrieved from TCGA, and the accessibility of the chromatin located at these biomarker genes were determined. The binding of the TFs to the putative targets was validated by the Cistrome database (http://cistrome.org/db/#/).

2.7. Statistical Analysis. Statistical analysis was carried out using R software 4.0.3. For the gene expression levels, Student t-test (2-sided) was used to compare the difference of CESC and adjacent nontumor tissues. Besides, Kaplan-Meier method was adopted to evaluate the OS, and log-rank test was used for the comparison between groups. The ssGSEA scores of immune pathways or cells were compared using Mann–Whitney U test. $p < 0.05$ indicated statistical significance.

3. Results

3.1. Identification of Prognostic DDR Genes in CESC. The procedure of bioinformatics analysis is summarized in Figure 1. To identify the prognostic DDR genes, CESC patients were divided into the high and low TMB groups according to the median TMB, and the differentially expressed DDR genes were screened (Figure 2(a)). Univariate Cox regression analysis revealed ACTR2, TEX12, UBE2V1, HSF1, and FBXO6 as the potential prognostic DDR genes (Figure 2(b)). We summarized the incidence of

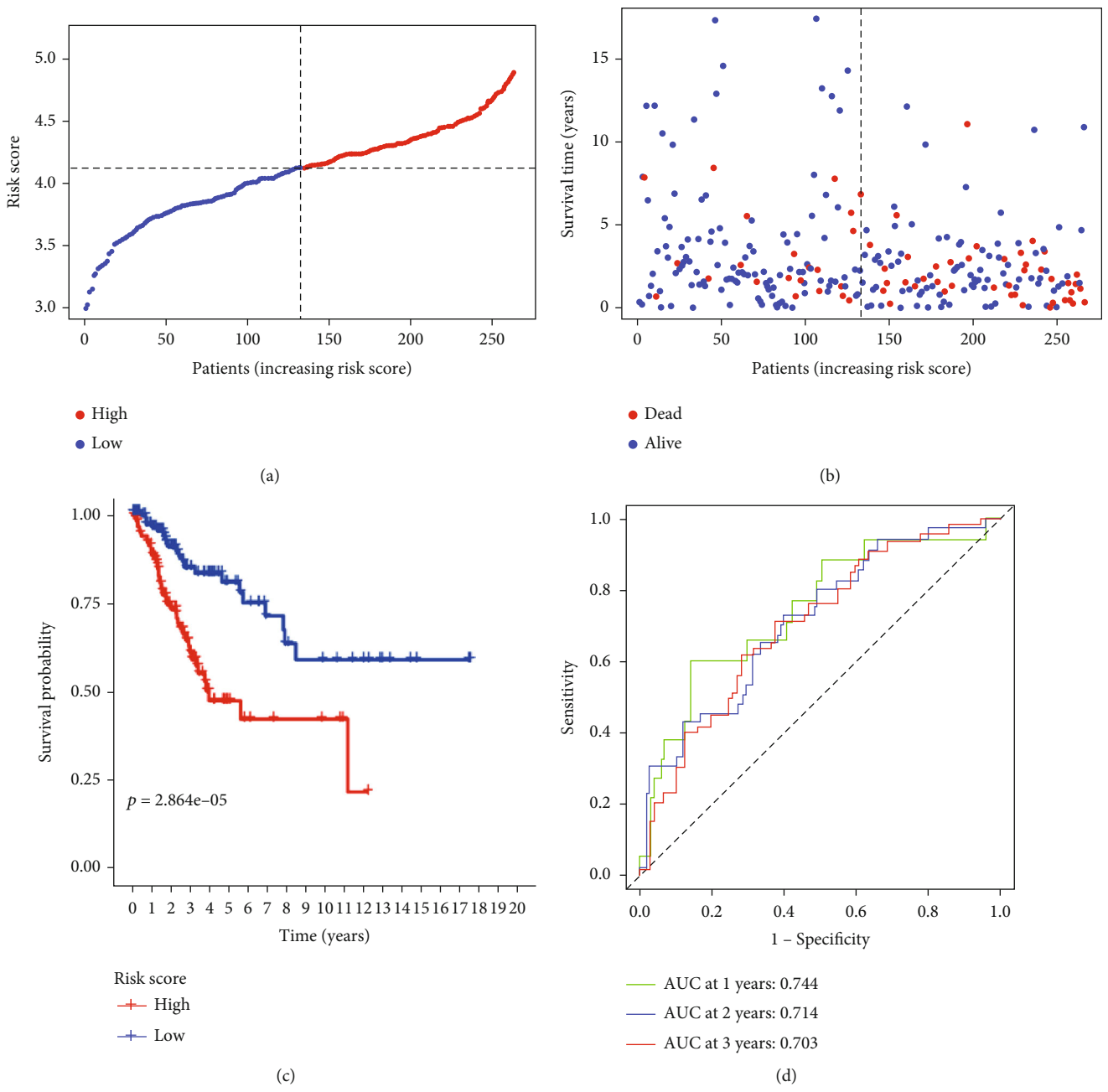

Figure 3: Prognostic analysis of the 5-gene marker in TCGA cohort: (a) risk score of samples from TCGA cohort; (b) the overall survival in TCGA cohort; (c) Kaplan-Meier curves showing the overall survival of the high-/low-risk groups in TCGA cohort; (d) the area under receiver operating characteristic curve showing the prognostic performance of the risk score.

main somatic mutations in CESC (Figure 2(c)) and detected low somatic mutation frequency in the above genes (Figure 2(d)).

3.2. Correlation with Prognosis of CESC Patients. The prognostic model consisting of ACTR2, TEX12, UBE2V1, HSF1, and FBXO6 was established based on LASSO Cox regression. The total risk score of these five genes was calculated as $(0.418 \times \text{expression of ACTR2}) + (-1.995 \times \text{expression of TEX12}) + (0.147 \times \text{expression of UBE2V1}) + (0.543 \times \text{expression of HSF1}) + (-0.217 \times \text{expression of FBXO6})$. Considering the median of the risk score as the cutoff, the samples were categorized into low-/high-risk groups (Figure 3(a)). Compared to the low-risk group, the mortality rate of patients was higher in the high-risk group with statistical significance (Figure 3(b)). Consistently, compared to the high-risk patients, Kaplan-Meier analysis discovered a better OS in low-risk group (Figure 3(c), $p < 0.05$). The areas under the receiver operating characteristic curve (*AUROCs*) for 1-, 2- and 3-year OS were 0.744, 0.714 and 0.703, respectively (Figure 3(d)).

3.3. Construction and Verification of DDR-Related Prognostic Model in CESC. For the risk score of DDR gene, univariate

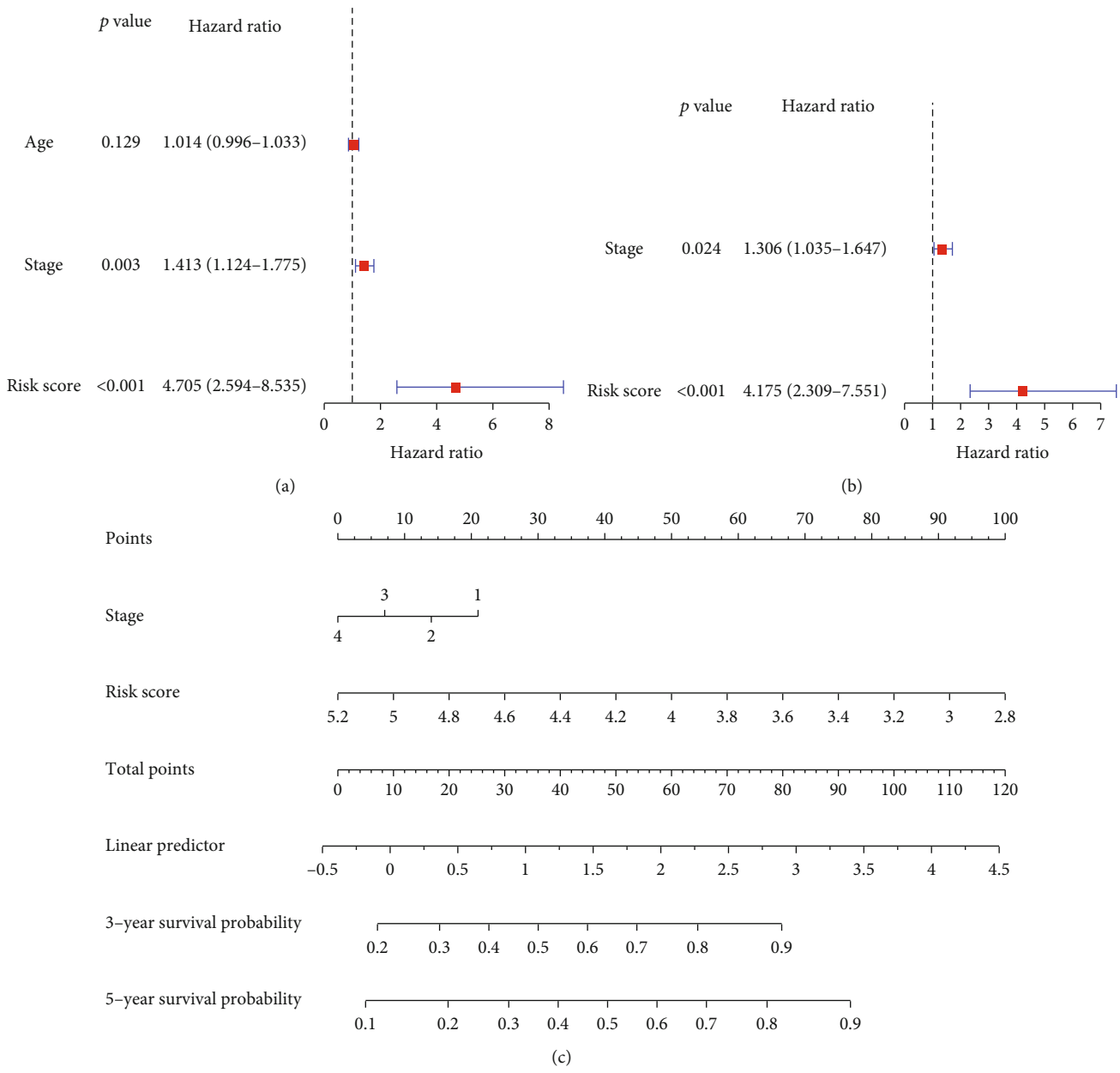

Figure 4: Continued.

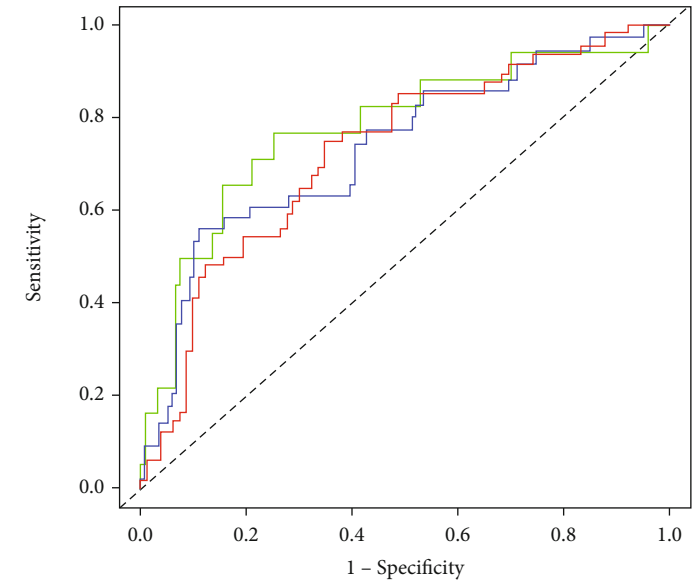

(d)

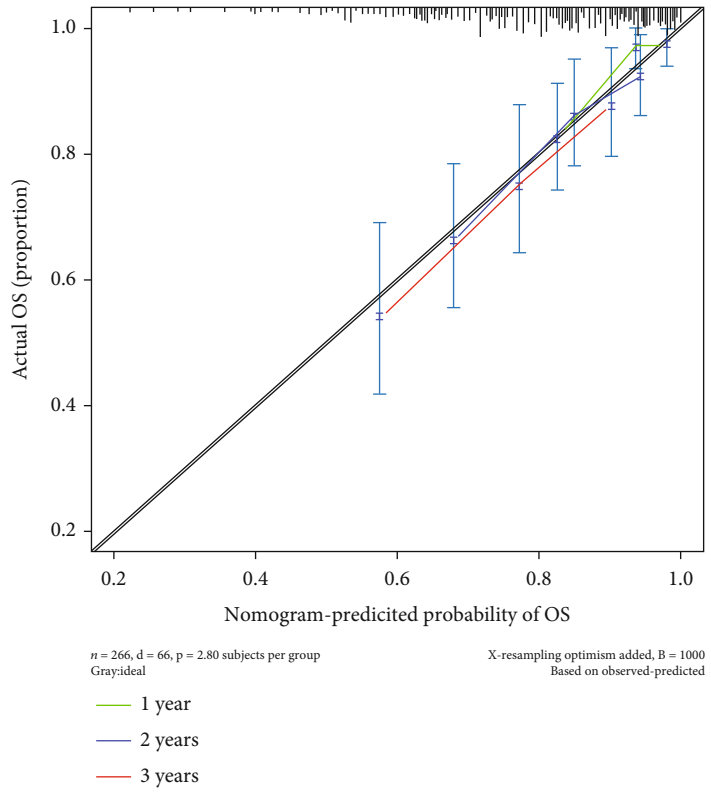

(e)

Figure 4: Construction and verification of the prognostic model: (a) the results of the univariate Cox regression analysis for the overall survival in TCGA cohort; (b) the results of multivariate Cox regression analysis; (c) nomogram construction; (d) verification of area under receiver operating characteristic curve.

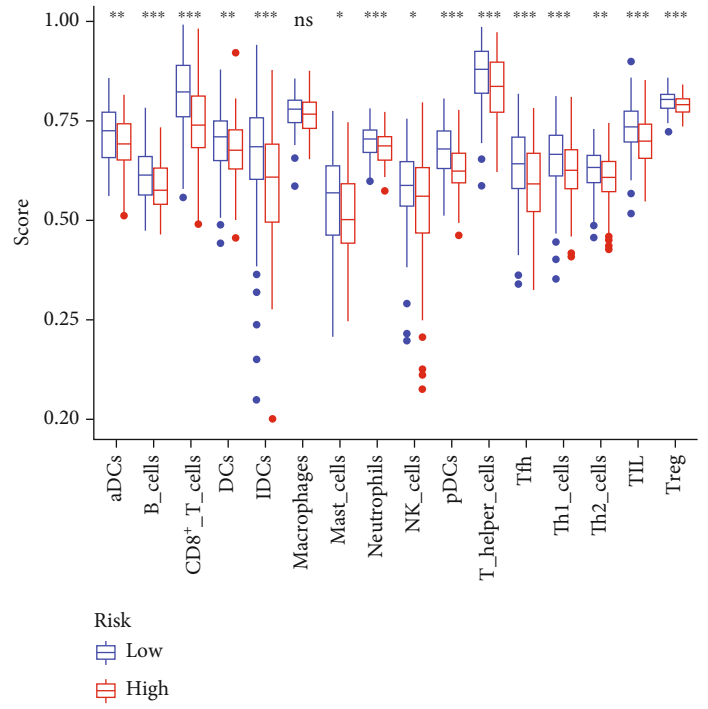

(a)

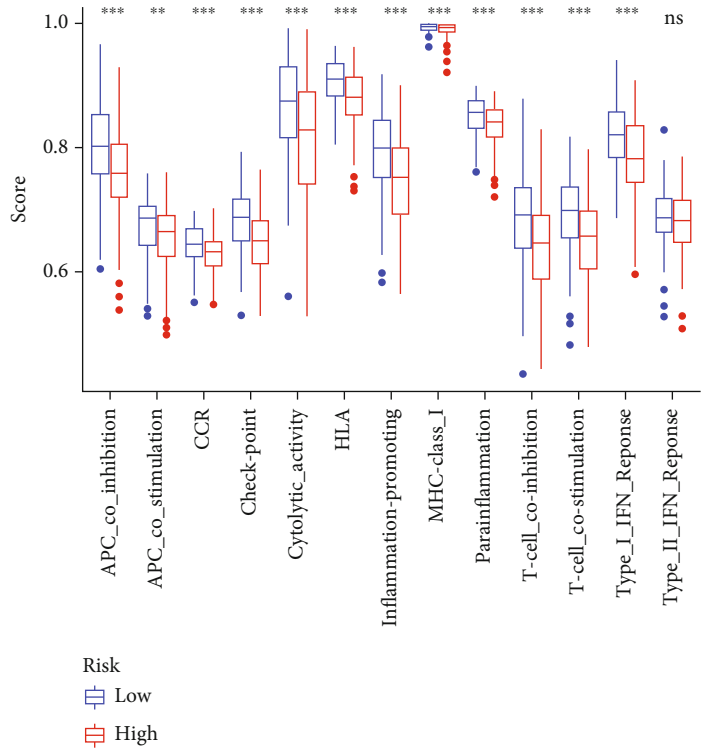

(b)

Figure 5: Continued.

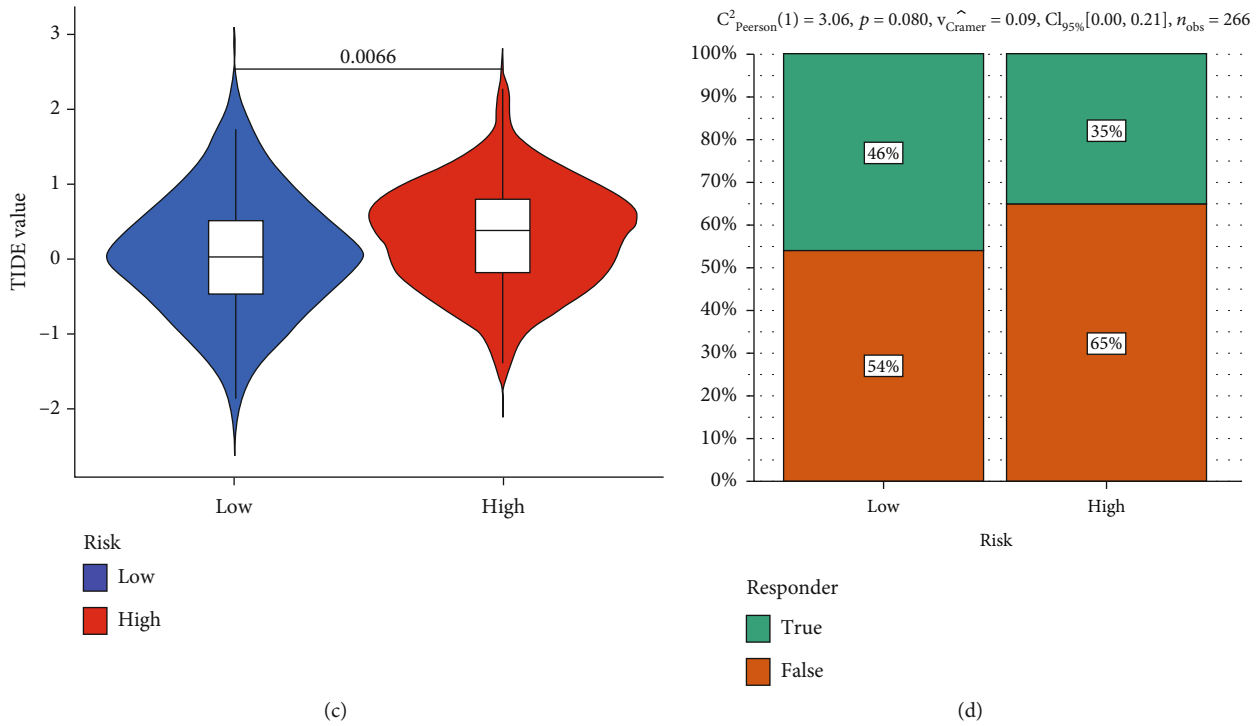

Figure 5: Comparison of ssGSEA scores between low-/high-risk groups in the TCGA cohort: (a) scores for the infiltration of sixteen immune cells; (b) scores for the functional activity of thirteen immune-related pathways; (c) immunotherapy response predicted by TIDE; (d) immunotherapy response rate.

analysis was used to assess the prognostic value in different subgroups of CESC patients. The risk score and tumor stage were significantly associated with the survival rate of CESC patients, and the risk score had a greater impact. However, no significant difference was observed in the survival rates of patients in terms of age (Figure 4(a)). Multivariate analysis further revealed tumor stage as well as risk score to be prognostic factors for CESC in TCGA cohort (Figure 4(b)). A nomogram consisting of the risk scores and tumor stages was then constructed to put the risk score into clinical prediction (Figure 4(c)). We found that the nomogram could predict the 3- and 5-year OS of cervical cancer patients, and the risk score was the main influencing factor. AUCs were 0.775, 0,734, and 0.726 for 1-, 2-, and 3-year OS, respectively (Figure 4(d)). The prognostic nomogram also showed good predictive ability and clinical value in terms of calibration and decision curve analysis (DCA) (Figure 4(e)). Taken together, the risk score consisting of DDR genes can effectively predict the survival outcomes of CESC patients.

3.4. Association between Risk Score and Immunotherapeutic Response of CESC Patients. To determine the correlation between risk score and immunotherapeutic response, we quantified the different immune cell subpopulations and activity of immune-related pathways using ssGSEA. Next, the distribution of immune cells and activity score of immune-related pathways between the high-risk group and the low-risk group is used as reliable evidence to assess the infiltration of immune cells. Compared to the low-risk group, the infiltration of 15 immune cell types was lower in the high-risk group with statistical significance, whereas macrophage infiltration showed no difference (Figure 5(a)). Furthermore, all but the type II IFN response immune pathways scored significantly higher in the low-risk group (Figure 5(b)). TIDE results further showed that CESC patients with lower risk score had less immune deficiency (Figure 5(c)) and were able to mount a more potent immune response (Figure 5(d)). In other words, compared to the high-risk patients, those with low-risk scores of DDR gene responded better to immunotherapies. Therefore, the risk score of DDR gene is a reliable biomarker for predicting the immunotherapeutic response in CESC.

3.5. FBXO6 Is Downregulated in CESC due to Loss of SP140. Thirty-five upstream TFs significantly associated with the DDR genes were identified by coexpression analysis, of which SP140 showed maximum copy number loss in CESC (Figure 6(a)). There was clear correlation between the expression levels of SP140 and FBXO6 ($R = 0.523$, $p < 0.001$) (Figure 6(b)). To further explore the underlying mechanisms, we used the ATAC-seq data of SP140 and FBXO6 in CESC samples from TGCA and verified their binding in the Cistrome database. As shown in Figure 6(c), there are multiple open chromatin regions in the promoter of FBXO6, indicating that it is transcriptionally regulated in CESC. We also detected multiple binding peaks corresponding to SP140 in the FBXO6 sequence according to

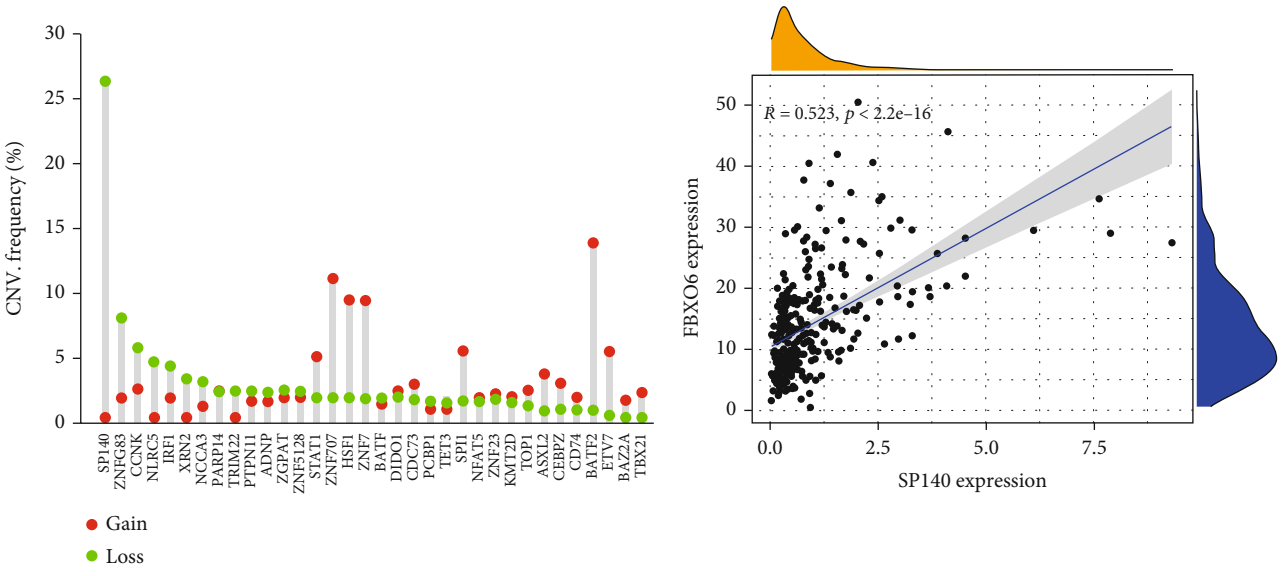

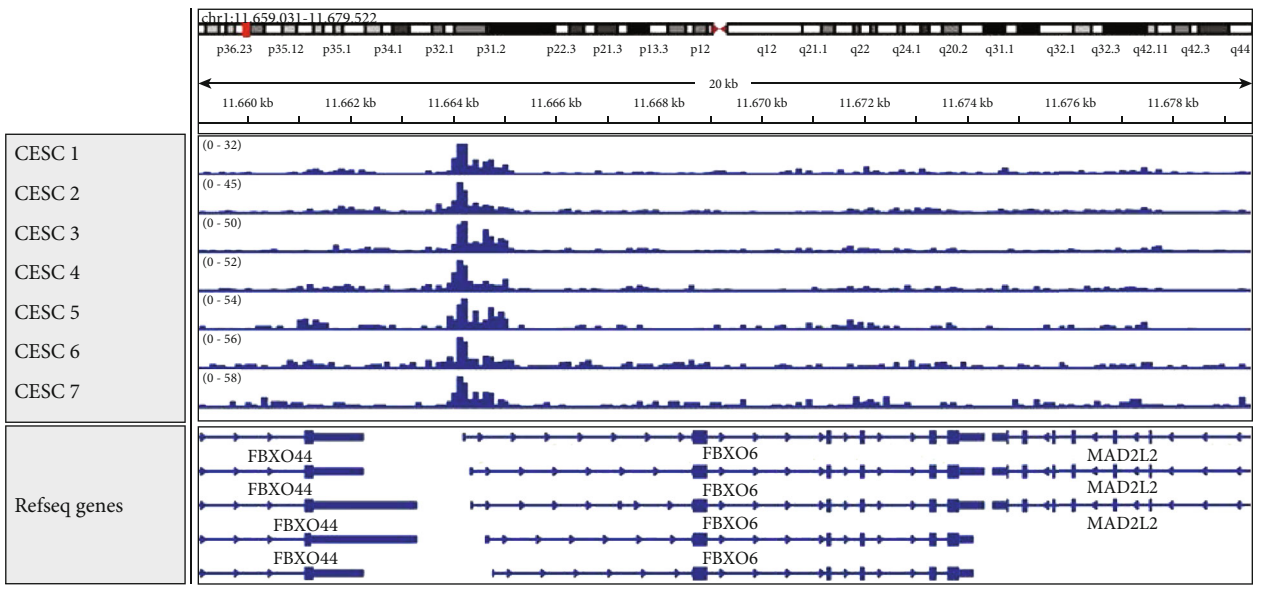

Figure 6: Continued.

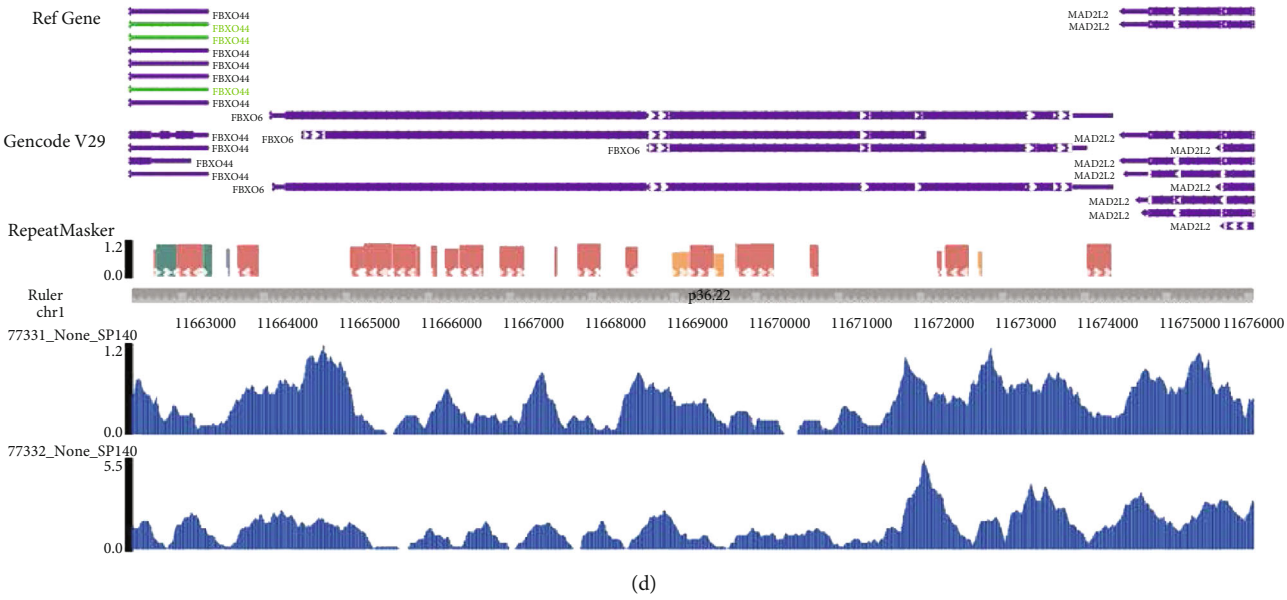

(d)

Figure 6: FBXO6 is positively regulated by SP140: (a) volcano map of TFs significantly related to DDR gene, CNV (gene copy number) of SP140 was the least; (b) SP140 is coexpressed with FBXO6; (c) multiple open chromatin regions in the FBXO6 promoter; (d) multiple peaks binding to SP140 in the FBXO6 sequence.

the chip sequence data of SP140 in the Cistrome database (Figure 6(d)). Therefore, the loss of copy number of SP140 in CESC may be a critical factor for FBXO6 downregulation.

4. Discussion

DNA carries genetic information which is necessary to synthesize RNA and proteins. Hence, to maintain the structural and functional integrity of DNA is critical for the normal development of all organisms. DNA damage due to endogenous events (oxidative damage, replication fork collapse, or errors that occur naturally during DNA replication or immune cell maturation) or by exogenous factors (ultraviolet rays, ionizing radiation, or chemical reagents) can result in mutations, eventually leading to malignant transformation [24–27]. In order to maintain the integrity of the cellular genome, a series of DNA damage responses, such as repair mechanisms, have evolved that can eliminate or adapt to damage [28].

DDR pathways were consisted of direct repair (DR), base excision repair (BER), nucleotide excision repair (NER), double-strand break repair (DSBR), and interstrand cross-link repair (ICLR) [28] and are regulated by specific genes and their upstream TFs [23]. More than one DDR pathway is often inactivated during cancer initiation and progression, and mutations among DDR genes have been linked to the chemoresistance of tumor cells as well [29, 30]. Thus, DDR genes are prognostically relevant and can be used to predict treatment response along with the overall prognosis of cancer patients. Based on above, we established a prognostic model for CESC involving five DDR genes, which accurately predicted the survival, immune infiltration, and the efficacy of immunotherapy in CESC patients. Thus, this novel prognostic signature can be used to select suitable patients for immunotherapy.

Referring to the expression levels of the five DDR genes, CESC patients are divided into low-/high-risk groups, and the former exhibited worse prognosis in terms of the OS rates. The TNM staging and risk scores of the low-/high-risk groups were significantly different, whereas age did not have a significant impact on the prognosis. Furthermore, the risk score was identified as an independent prognostic factor. The nomogram indicated high predictive power of the risk score for 3- and 5-year OS, whereas ROC analysis showed that 1-, 2-, and 3-year OS could be predicted by the risk score. The accuracy of this prognostic model was also validated by the decision curve analysis (DCA). Thus, the DDR gene-based risk score can precisely forecast the survival outcome of CESC patients and, at the same time, provide more therapeutic options.

Interestingly, for the low-/high-risk groups, the infiltration of 15 immune cell types differed significantly, whereas the infiltration of macrophages was similar. The low-risk group showed greater immune cell infiltration, especially that of T-helper cells, Treg cells, and CD8+ T cells. Furthermore, 13 immune-related pathways scored higher in the low-risk group, while type II IFN response showed no significant difference between groups. In addition, the association between the risk score of CESC and immunotherapeutic response was evaluated by TIDE program and revealed 46% and 35% positive responders in the low-risk and high-risk groups, respectively, which further underscores the role of DDR genes in determining the response of CESC patients to immunotherapy.

The checkpoint kinase CHK1 (CHEK1) recognizes DNA damage, delays the cell cycle, and initiates DNA repair [31]. FBXO6 can specifically recognize activated CHEK1 and

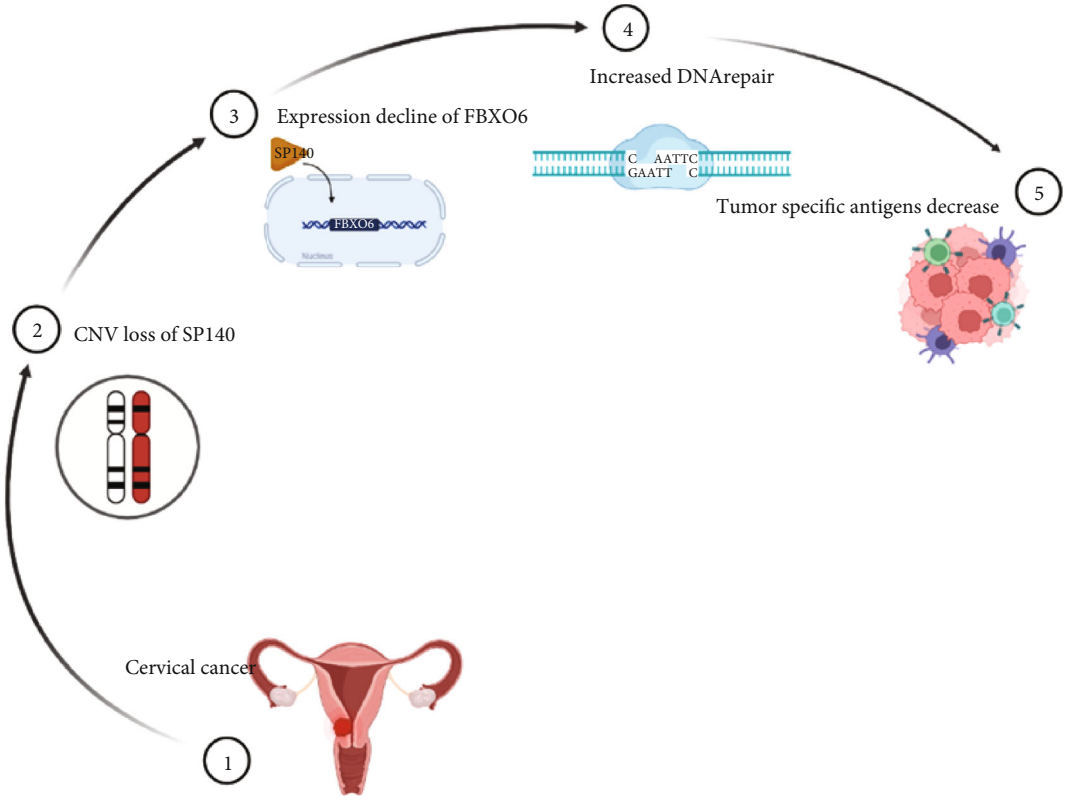

Figure 7: Schematic representation of the mechanism of FBXO6 and SP140 in CESC.

promote its ubiquitin-dependent degradation [32], thereby inhibiting DNA repair and function and eventually leading to increased neoantigen diversity and sensitivity to immunotherapy. Studies show that FBXO6 expression is related to the OS of NSCLC patients, and *in vitro* experiments have shown that FBXO6 inhibits cell proliferation, promotes apoptosis, and sensitizes the cells to cisplatin [33]. Furthermore, FBXO6 also inhibits the antiviral response by interfering with the production of IFN-I [34]. Ji et al. reported that the high expression levels of FBXO6 in tissues were correlated with poor survival of patients with advanced ovarian cancer. FBXO6 directly interacts with the tumor suppressor gene RNASET2 to target it for ubiquitin-dependent degradation, thus functioning as an oncogene in ovarian cancer [35]. Wang et al. found that FBXO6 is one of the coexpressed genes on CD8+ T cells and promotes infiltration of the cells into urothelial carcinoma tumors, which affects the clinical phenotype and the immune microenvironment [36].

TFs are the main regulators of gene expression in eukaryotic cells [37]. SP140 belongs to the speck protein (SP) family of TFs that are also known as human chromatin "readers." A chromatin reader is the core interpreter of the epigenome that promotes cell-specific transcription and is a therapeutic target for cancer and inflammation [38, 39]. SP140 is involved in various immune-related diseases such as Crohn's disease, chronic lymphocytic leukemia, and multiple sclerosis [40–42] and has recently been identified as the main regulator of the immune response in ovarian cancer [43]. We detected a significant decrease in the copy number of SP140 in CESC patients, which correlated with the downregulation of its downstream target FBX06.

Our study is the first to show that SP140-FBXO6 is related to the prognosis as well as immune microenvironment of CESC. Loss of SP140 in CESC cells downregulated the DNA repair gene FBXO6, which resulted an increased DNA repair and decreased generation of tumor-specific antigens (Figure 7). Thus, DDR genes are promising biomarkers of prognosis and immunotherapeutic response of CESC. Further studies are necessary to elucidate mechanism of SP140/FBXO6 in cervical cancer. In addition, it will be challenging to combine the DDR gene status with other known biomarkers for clinical applications.

5. Conclusion

We identified five DDR genes that are related to the OS of CESC patients, and the gene signature can predict prognosis and the response to immunotherapy. Nevertheless, the markers will have to be verified by functional analyses and clinical tests, and further research on the molecular mechanism of these genes is urgently needed.

Data Availability

The datasets generated during and/or analyzed during the current study are available from the corresponding author on reasonable request.

Conflicts of Interest

The authors declare no conflicts of interest in this work.

Authors' Contributions

Hong Zhou, Limei Wu, and Lijun Yu contributed equally to this work. Hong Zhou and Limei Wu performed the study and wrote the paper; Lijun Yu and Yabing Yang performed the data processing and statistics; Lili Kong and Shuo Liu worked on collecting data; Wenhui Chen and Ruiman Li designed the study and revised the paper.

Acknowledgments

This work was supported by a grant from the National Key Research and Development Program of China (Grant No. 2019YFC0121904) and Pilot Specialist Construction Project-Obstetrics and Gynecology (Grant No. 711008) of the First Affiliated Hospital of Jinan University.

References

[1] F. Bray, ,J. Ferlay, I. Soerjomataram, R. L. Siegel, L. A. Torre, and A. Jemal, "Global cancer statistics 2018: GLOBOCAN estimates of incidence and mortality worldwide for 36 cancers in 185 countries," *CA: A Cancer Journal for Clinicians*, vol. 68, no. 6, pp. 394–424, 2018.

[2] W. J. Small, ,M. A. Bacon, A. Bajaj et al., "Cervical cancer: a global health crisis," *Cancer*, vol. 123, no. 13, pp. 2404–2412, 2017.

[3] M. L. Gillison, A. K. Chaturvedi, and D. R. Lowy, "HPV prophylactic vaccines and the potential prevention of noncervical cancers in both men and women," *Cancer*, vol. 113, no. S10, pp. 3036–3046, 2008.

[4] E. J. Crosbie, M. H. Einstein, S. Franceschi, and H. C. Kitchener, "Human papillomavirus and cervical cancer," *The Lancet*, vol. 382, no. 9895, pp. 889–899, 2013.

[5] S. Gupta, ,A. Maheshwari, P. Parab et al., "Neoadjuvant chemotherapy followed by radical surgery versus concomitant chemotherapy and radiotherapy in patients with stage IB2, IIA, or IIB squamous cervical cancer: a randomized controlled trial," *Journal of Clinical Oncology*, vol. 36, no. 16, pp. 1548–1555, 2018.

[6] P. T. Ramirez, ,M. Frumovitz, R. Pareja et al., "Minimally invasive versus abdominal radical hysterectomy for cervical cancer," *The New England Journal of Medicine*, vol. 379, no. 20, pp. 1895–1904, 2018.

[7] J. Paavonen, ,P. Naud, J. Salmerón et al., "Efficacy of human papillomavirus (HPV)-16/18 AS04-adjuvanted vaccine against cervical infection and precancer caused by oncogenic HPV types (PATRICIA): final analysis of a double-blind, randomised study in young women," *The Lancet*, vol. 374, no. 9686, pp. 301–314, 2009.

[8] S. Stevanovic, L. M. Draper, M. M. Langhan et al., "Complete regression of metastatic cervical cancer after treatment with human papillomavirus-targeted tumor-infiltrating T cells," *Journal of Clinical Oncology*, vol. 33, no. 14, pp. 1543–1550, 2015.

[9] J.-S. Frenel, C. le Tourneau, B. O'Neil et al., "Safety and efficacy of pembrolizumab in advanced, programmed death ligand 1-positive cervical cancer results from the phase Ib KEYNOTE-028 trial," *Journal of Clinical Oncology*, vol. 35, no. 36, pp. 4035–4041, 2017.

[10] H. C. Chung, W. Ros, J. P. Delord et al., "Efficacy and safety of pembrolizumab in previously treated advanced cervical cancer: results from the phase II KEYNOTE-158 study," *Journal of Clinical Oncology*, vol. 37, no. 17, pp. 1470–1478, 2019.

[11] X. Li and W. D. Heyer, "Homologous recombination in DNA repair and DNA damage tolerance," *Cell Research*, vol. 18, no. 1, pp. 99–113, 2008.

[12] K. W. Mouw, M. S. Goldberg, P. A. Konstantinopoulos, and A. D. D'Andrea, "DNA damage and repair biomarkers of immunotherapy response," *Cancer Discovery*, vol. 7, no. 7, pp. 675–693, 2017.

[13] K. C. Strickland, B. E. Howitt, S. A. Shukla et al., "Association and prognostic significance of BRCA1/2-mutation status with neoantigen load, number of tumor-infiltrating lymphocytes and expression of PD-1/PD-L1 in high grade serous ovarian cancer," *Oncotarget*, vol. 7, no. 12, pp. 13587–13598, 2016.

[14] N. A. Rizvi, M. D. Hellmann, A. Snyder et al., "Cancer immunology. Mutational landscape determines sensitivity to PD-1 blockade in non-small cell lung cancer," *Science*, vol. 348, no. 6230, pp. 124–128, 2015.

[15] Y. K. Chae, A. A. Davis, K. Raparia et al., "Association of tumor mutational burden with DNA repair mutations and response to anti–PD-1/PD-L1 therapy in non–small-cell lung cancer," *Clinical Lung Cancer*, vol. 20, pp. 86–96, 2019.

[16] G. Wang, H. Zhou, L. Tian et al., "A prognostic DNA damage repair genes signature and its impact on immune cell infiltration in glioma," *Frontiers in Oncology*, vol. 11, article 682932, 2021.

[17] D. F. Giachino, P. Ghio, S. Regazzoni et al., "Prospective assessment of XPD Lys751Gln and XRCC1 Arg399Gln single nucleotide polymorphisms in lung cancer," *Clinical Cancer Research*, vol. 13, no. 10, pp. 2876–2881, 2007.

[18] M. Y. Teo, K. Seier, I. Ostrovnaya et al., "Alterations in DNA damage response and repair genes as potential marker of clinical benefit from PD-1/PD-L1 blockade in advanced urothelial cancers," *Journal of Clinical Oncology*, vol. 36, pp. 1685–1694, 2018.

[19] J. Ying, L. Yang, J. C. Yin et al., "Additive effects of variants of unknown significance in replication repair-associated DNA polymerase genes on mutational burden and prognosis across diverse cancers," *Journal for Immunotherapy of Cancer*, vol. 9, no. 9, article e002336, 2021.

[20] T. Kojima, M. A. Shah, K. Muro et al., "Randomized phase III KEYNOTE-181 study of pembrolizumab versus chemotherapy in advanced esophageal cancer," *Journal of Clinical Oncology*, vol. 38, no. 35, pp. 4138–4148, 2020.

[21] K. M. Turner, Y. Sun, P. Ji et al., "Genomically amplified Akt3 activates DNA repair pathway and promotes glioma progression," *Proceedings of the National Academy of Sciences of the United States of America*, vol. 112, no. 11, pp. 3421–3426, 2015.

[22] M. K. Gupta, A. S. Kushwah, R. Singh, and M. Banerjee, "Genotypic analysis of XRCC4 and susceptibility to cervical cancer," *British Journal of Biomedical Science*, vol. 77, no. 1, pp. 7–12, 2020.

[23] M. Christmann and B. Kaina, "Transcriptional regulation of human DNA repair genes following genotoxic stress: trigger mechanisms, inducible responses and genotoxic adaptation," *Nucleic Acids Research*, vol. 41, no. 18, pp. 8403–8420, 2013.

[24] J. Cadet and J. R. Wagner, "DNA base damage by reactive oxygen species, oxidizing agents, and UV radiation," *Cold Spring Harbor Perspectives in Biology*, vol. 5, no. 2, 2013.

[25] A. Maya-Mendoza, P. Moudry, J. M. Merchut-Maya, M. H. Lee, R. Strauss, and J. Bartek, "High speed of fork progression induces DNA replication stress and genomic instability," *Nature*, vol. 559, no. 7713, pp. 279–284, 2018.

[26] W. L. Santivasi and F. Xia, "Ionizing radiation-induced DNA damage, response, and repair," *Antioxidants & Redox Signaling*, vol. 21, no. 2, pp. 251–259, 2014.

[27] M. C. Poirier, "Chemical-induced DNA damage and human cancer risk," *Nature Reviews. Cancer*, vol. 4, no. 8, pp. 630–637, 2004.

[28] A. Sancar, L. A. Lindsey-Boltz, K. Unsal-Kacmaz, and S. Linn, "Molecular mechanisms of mammalian DNA repair and the DNA damage checkpoints," *Annual Review of Biochemistry*, vol. 73, no. 1, pp. 39–85, 2004.

[29] C. R. R. Rocha, M. M. Silva, A. Quinet, J. B. Cabral-Neto, and C. F. M. Menck, "DNA repair pathways and cisplatin resistance: an intimate relationship," *Clinics (São Paulo, Brazil)*, vol. 73, Supplement 1, p. e478s, 2018.

[30] G. Damia and M. Broggini, "Platinum resistance in ovarian cancer: role of DNA repair," *Cancers (Basel)*, vol. 11, no. 1, p. 119, 2019.

[31] J. Smith, L. M. Tho, N. Xu, and D. A. Gillespie, "The ATM-Chk2 and ATR-Chk1 pathways in DNA damage signaling and cancer," *Advances in Cancer Research*, vol. 108, pp. 73–112, 2010.

[32] Y. Tu, H. Liu, X. Zhu et al., "Ataxin-3 promotes genome integrity by stabilizing Chk1," *Nucleic Acids Research*, vol. 45, no. 8, pp. 4532–4549, 2017.

[33] L. Cai, J. Li, J. Zhao et al., "Fbxo6 confers drug-sensitization to cisplatin via inhibiting the activation of Chk1 in non-small cell lung cancer," *FEBS Letters*, vol. 593, no. 14, pp. 1827–1836, 2019.

[34] X. Du, F. Meng, D. Peng et al., "Noncanonical role of FBXO6 in regulating antiviral immunity," *The Journal of Immunology*, vol. 203, pp. 1012–1020, 2019.

[35] M. Ji, Z. Zhao, Y. Li et al., "FBXO6-mediated RNASET2 ubiquitination and degradation governs the development of ovarian cancer," *Cell Death & Disease*, vol. 12, no. 4, p. 317, 2021.

[36] Y. Wang, K. Yan, J. Lin et al., "CD8+ T cell co-expressed genes correlate with clinical phenotype and microenvironments of urothelial cancer," *Frontiers in Oncology*, vol. 10, article 553399, 2020.

[37] J. M. Vaquerizas, S. K. Kummerfeld, S. A. Teichmann, and N. M. Luscombe, "A census of human transcription factors: function, expression and evolution," *Nature Reviews. Genetics*, vol. 10, no. 4, pp. 252–263, 2009.

[38] S. Mehta and K. L. Jeffrey, "Beyond receptors and signaling: epigenetic factors in the regulation of innate immunity," *Immunology and Cell Biology*, vol. 93, no. 3, pp. 233–244, 2015.

[39] I. Fraschilla and K. L. Jeffrey, "The speckled protein (SP) family: immunity's chromatin readers," *Trends in Immunology*, vol. 41, no. 7, pp. 572–585, 2020.

[40] A. Franke, D. P. B. McGovern, J. C. Barrett et al., "Genome-wide meta-analysis increases to 71 the number of confirmed Crohn's disease susceptibility loci," *Nature Genetics*, vol. 42, no. 12, pp. 1118–1125, 2010.

[41] F. C. Sille, R. Thomas, M. T. Smith, L. Conde, and C. F. Skibola, "Post-GWAS functional characterization of susceptibility variants for chronic lymphocytic leukemia," *PLoS One*, vol. 7, no. 1, article e29632, 2012.

[42] International Multiple Sclerosis Genetics Consortium (IMSGC) 1, A. H. Beecham, N. A. Patsopoulos et al., "Analysis of immune-related loci identifies 48 new susceptibility variants for multiple sclerosis," *Nature Genetics*, vol. 45, pp. 1353–1360, 2013.

[43] S. Zhang, Y. Jing, M. Zhang et al., "Stroma-associated master regulators of molecular subtypes predict patient prognosis in ovarian cancer," *Scientific Reports*, vol. 5, no. 1, article 16066e, 2015.

Hindawi
Journal of Oncology
Volume 2022, Article ID 6358707, 14 pages
https://doi.org/10.1155/2022/6358707

Research Article

Survival Analysis and a Novel Nomogram Model for Progression-Free Survival in Patients with Prostate Cancer

Yuefu Han,[1,2,3] Xingqiao Wen,[1,4] Dong Chen,[3] Xiaojuan Li,[5] Qu Leng,[2] Yuehui Wen,[6] Jun Li,[2] and Weian Zhu[4]

[1]*Department of Urology, Shenzhen Hospital, The Third College of Clinical Medicine, Southern Medical University, Shenzhen, 518100 Guangdong, China*
[2]*Department of Urology, Zhujiang Hospital, Southern Medical University, Guangzhou, 510282 Guangdong, China*
[3]*Department of Urology, Yuebei People's Hospital Affiliated to Medical College of Shantou University, Shaoguan, 512026 Guangdong, China*
[4]*Department of Urology, Third Hospital of Sun Yat-sen University, Guangzhou, 510630 Guangdong, China*
[5]*Department of Health Care, Shenzhen Hospital, The Third College of Clinical Medicine, Southern Medical University, Shenzhen, 518100 Guangdong, China*
[6]*Department of Urology, Nanfang Hospital, Southern Medical University, Guangzhou, 510515 Guangdong, China*

Correspondence should be addressed to Xingqiao Wen; wenxq@mail.sysu.edu.cn

Received 13 January 2022; Revised 18 February 2022; Accepted 22 February 2022; Published 22 March 2022

Academic Editor: Fu Wang

Background. This study sought to perform a survival analysis and construct a prognostic nomogram model based on the Gleason grade, total prostate-specific antigen (tPSA), alkaline phosphate (ALP), and TNM stage in patients with prostate cancer (PCa). *Methods*. The progression-free survival (PFS) of 255 PCa patients was analyzed in this study. The prognostic value of tPSA and ALP was evaluated using the Kaplan-Meier survival curves and Cox regression analysis, and a nomogram model based on the Gleason grade, tPSA, ALP, and TNM stage was further established for PFS prediction in PCa patients. *Results*. PCa patients with different Gleason grades, tPSA and ALP levels, and TNM stages presented distinct PFS. The Gleason grade, tPSA, ALP, and TNM stage were four independent prognostic indicators. The C-index of the established nomogram was 0.705 for PFS in the test cohort and 0.687 for the validation cohort, and the calibration curves indicated a good consistency between predicted and actual PFS in PCa patients. *Conclusion*. The data of this study demonstrated that the Gleason grade, tPSA, ALP, and TNM stage of PCa patients are independently correlated with PFS, and a nomogram model based on these indicators may be valuable for the PFS prediction in PCa patient.

1. Introduction

Prostate cancer (PCa) is one of the most common malignant tumors in male. The incidence of PCa has gradually increased in recent years, which seriously threatens male health [1]. Since the lack of obvious clinical symptoms, most of PCa patients are diagnosed with advanced tumor stage, leading to the significant increase in PCa mortality rate [2, 3]. Despite the progresses in tumor therapeutic approaches, the clinical outcomes and survival prognosis of PCa remain unfavorable [4]. Therefore, it is important to early identify patients with high risk of disease progression or death, which may assist the clinical treatment and intervention in patients with PCa [5].

Prostate-specific antigen (PSA) and serum alkaline phosphate (ALP) have been identified as two critical molecular biomarkers for the occurrence and development of PCa [6, 7]. Blood PSA with a concentration of >4.0 ng/mL is an indicator for PCa screening, which has been widely used for PCa clinical diagnosis [8]. Serum ALP can be used to predict bone diseases and serves as an indicator for bone metastasis in human malignancies [9]. There are about more than 85% PCa-related deaths resulted from bone metastasis, implying the potential relationship between ALP and PCa prognosis

Table 1: Comparison of baseline characteristics of PCa patients between test set and validation set.

Features	Test set ($n = 196$)	Validation set ($n = 59$)	χ^2	P value
Age, n (%)			3.098	0.212
≤60 years	19 (9.7)	10 (16.9)		
60-70 years	50 (25.5)	17 (28.8)		
>70 years	127 (64.8)	32 (54.2)		
History of diabetes			0.624	0.430
Yes	20 (10.2)	4 (6.8)		
No	176 (89.8)	55 (93.2)		
History of hypertension			0.034	0.854
Yes	41 (20.9)	13 (22.0)		
No	155 (79.1)	46 (78.0)		
Bone metastasis			2.682	0.101
Yes	146 (74.5)	50 (84.7)		
No	50 (25.5)	9 (15.3)		
Indwelling catheter			0.002	0.968
Yes	47 (24.0)	14 (23.7)		
No	149 (76.0)	45 (76.3)		
Urinary tract infection			1.094	0.295
Yes	23 (11.7)	10 (16.9)		
No	173 (88.3)	49 (83.1)		
Gleason grade			7.130	0.129
1	3 (1.5)	0 (0.0)		
2	22 (11.2)	4 (6.8)		
3	37 (18.9)	6 (10.2)		
4	75 (38.3)	22 (37.5)		
5	59 (30.1)	27 (45.8)		
TNM stage			5.477	0.140
I	4 (2.0)	0 (0.0)		
II	25 (12.8)	3 (5.1)		
III	11 (5.6)	4 (6.8)		
VI	156 (79.6)	52 (88.1)		
Soloway grade			4.660	0.198
0	47 (24.0)	8 (13.6)		
I	29 (14.8)	7 (11.9)		
II	25 (12.8)	12 (20.3)		
III	95 (48.5)	32 (54.2)		
tPSA (ng/mL)			8.897	0.064
≤10	15 (7.7)	0 (0.0)		
10.1-20	10 (5.1)	5 (8.5)		
20.1-50	30 (15.3)	8 (13.6)		
50.1-100	32 (16.3)	5 (8.5)		
>100	109 (55.6)	41 (69.5)		
ALP (U/L)			7.149	0.067
≤67.0	46 (23.5)	19 (32.2)		
67.1-83.0	55 (28.1)	7 (11.9)		
83.1-135.0	46 (23.5)	18 (30.5)		
>135.0	49 (25.0)	15 (25.4)		

tPSA: total prostate-specific antigen; ALP: alkaline phosphate.

[10]. However, there is no uniform conclusion on the role of total PSA (tPSA) and ALP in the prediction of PCa prognosis.

Nomogram is an important statistical model to predict cancer prognosis, which can easily and accurately calculate survival probability by adding multiple variables that closely associated with disease prognosis [11]. This study analyzed the relationship between clinicopathological characteristics and clinical outcomes in PCa patients and provided evidence for tPSA, ALP, Gleason grade, and TNM stage as independent indicators for PFS of PCa. A nomogram model based on tPSA, ALP, Gleason grade, and TNM stage was constructed, and their predictive value for PFS (progression-free survival) was assessed and verified in PCa patients. The established nomogram may help to predict PCa progression more intuitively and accurately and provides a basis for the optimal clinical treatment decisions.

2. Material and Methods

2.1. Patients and Sample Collection. The data analyzed in this study were collected from 255 PCa patients, who underwent therapy in the Third Hospital of Sun Yat-sen University (Guangzhou, China) and Yuebei People's Hospital (Shaoguan, China) from January 2012 to December 2018. The regular follow-up was conducted to obtain their prognosis status. Following are the inclusion and exclusion criteria for patient recruitment:

The inclusion criteria were as follows: (1) tumor tissues were histopathologically diagnosed with PCa; (2) patients had biochemical recurrence or progressed to castration-resistant PCa after ADT therapy; (3) patients were followed up regularly.

The exclusion criteria were as follows: patients suffered from other tumors, prostatitis, hepatobiliary diseases, or other conditions that might affect the detection results of tPSA and ALP.

The included PCa patients were randomly divided into test cohort ($n = 196$) and validation cohort ($n = 59$) with a ratio of 3 : 1. Table 1 summarizes the demographic and clinicopathological characteristics of the patients, including age, history of diabetes and hypertension, bone metastasis, indwelling catheter condition, urinary tract infection, Gleason grade, TNM stage, Soloway grade, and levels of tPSA and ALP at initial diagnosis. The Gleason grades of the patients were determined with the Gleason grading system of the International Society for Urological Pathology (ISUP), the TNM stage was confirmed according to American Joint Committee on Cancer TNM 6th edition (2002), and the criteria by Soloway grade were used for different bone metastasis number. The electrochemiluminescence

Table 2: Univariate and multivariate Cox regression analysis results.

Characteristics	Univariate analysis		Multivariate analysis	
	HR (95% CI)	*P*	HR (95% CI)	*P*
Gleason grade				
1	Reference		Reference	
2	0.686 (0.475, 0.990)	0.044	0.706 (0.480, 1.040)	0.078
3	0.503 (0.321, 0.790)	0.003	0.527 (0.334, 0.832)	0.006
4	0.354 (0.204, 0.612)	<0.001	0.557 (0.308, 1.009)	0.054
5	0.418 (0.130, 1.350)	0.145	0.314 (0.089, 1.112)	0.073
tPSA (ng/mL)				
≤10	Reference		Reference	
10.1-20	1.866 (0.768, 4.532)	0.168	1.842 (0.687, 4.935)	0.225
20.1-50	2.031 (0.983, 4.199)	0.056	1.835 (0.828, 4.065)	0.135
50.1-100	3.608 (1.746, 7.456)	0.001	2.516 (1.103, 5.738)	0.028
>100	3.854 (1.992, 7.457)	<0.001	2.322 (1.076, 5.008)	0.032
ALP (U/L)				
≤67.0	Reference		Reference	
67.1-83.0	1.348 (0.876, 2.076)	0.175	1.234 (0.795, 1.913)	0.349
83.1-135.0	1.943 (1.246, 3.031)	0.003	1.831 (1.148, 2.920)	0.011
>135.0	2.235 (1.437, 3.476)	<0.001	1.600 (1.006, 2.544)	0.047
TNM stage				
I	Reference		Reference	
II	0.239 (0.084, 0.679)	0.007	0.593 (0.296, 1.187)	0.140
III	0.342 (0.205, 0.572)	<0.001	0.483 (0.270, 0.864)	0.014
VI	0.530 (0.271, 1.038)	0.064	0.592 (0.171, 2.045)	0.407
Bone metastasis				
Yes	Reference		—	—
No	0.447 (0.308, 0.648)	<0.001	—	—
Soloway grade				
0	Reference		—	—
I	1.357 (0.792, 2.325)	0.266	—	—
II	1.868 (1.087, 3.210)	0.024	—	—
III	3.144 (2.097, 4.712)	<0.001	—	—
Age (years)				
≤60	Reference		—	—
60-70	0.966 (0.557, 1.674)	0.901	—	—
>70	1.030 (0.622, 1.703)	0.909	—	—
History of diabetes				
Yes	Reference		—	—
No	0.795 (0.474, 1.333)	0.384	—	—
History of hypertension				
Yes	Reference		—	—
No	0.827 (0.571, 1.198)	0.316	—	—
Indwelling catheter				
Yes	Reference		—	—
No	1.413 (0.973, 2.050)	0.069	—	—
Urinary tract infection				
Yes	Reference		—	—
No	1.399 (0.820, 2.188)	0.244	—	—

tPSA: total prostate-specific antigen; ALP: alkaline phosphate.

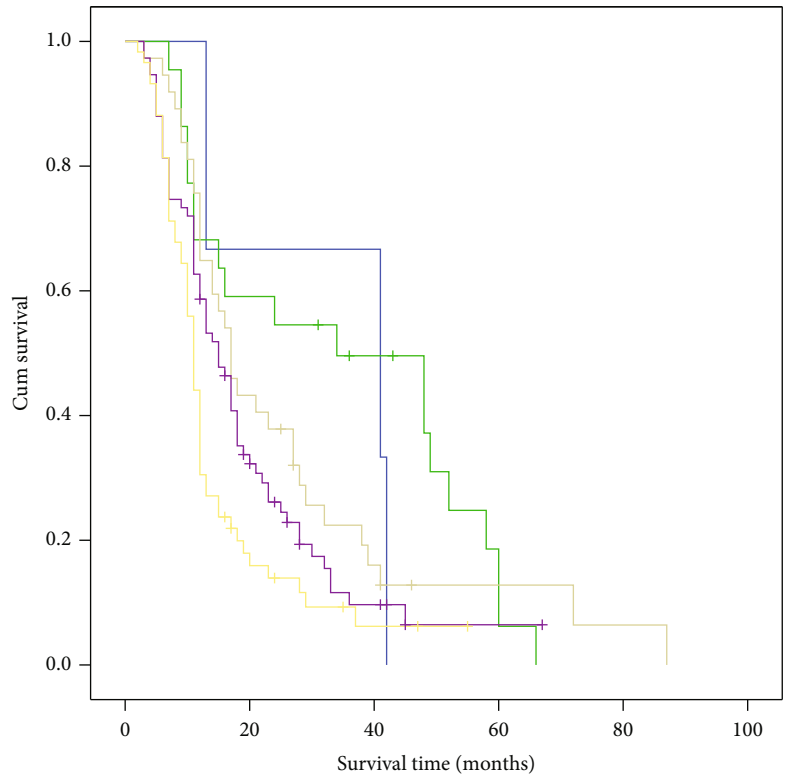

(a)

Figure 1: Continued.

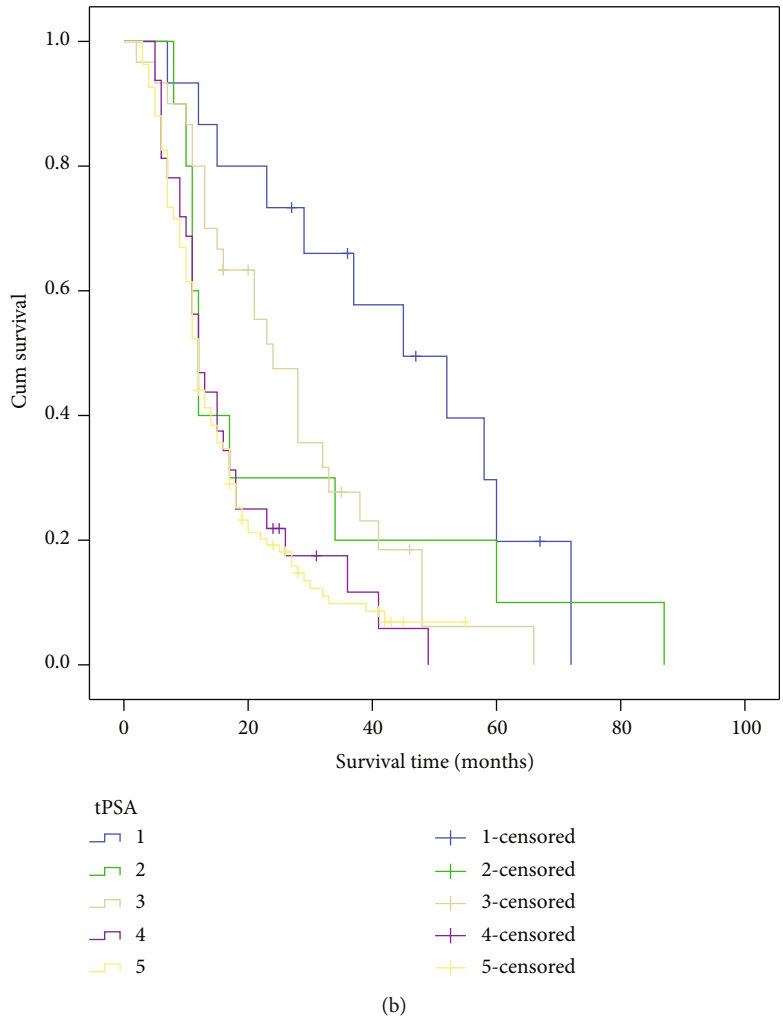

(b)

Figure 1: Continued.

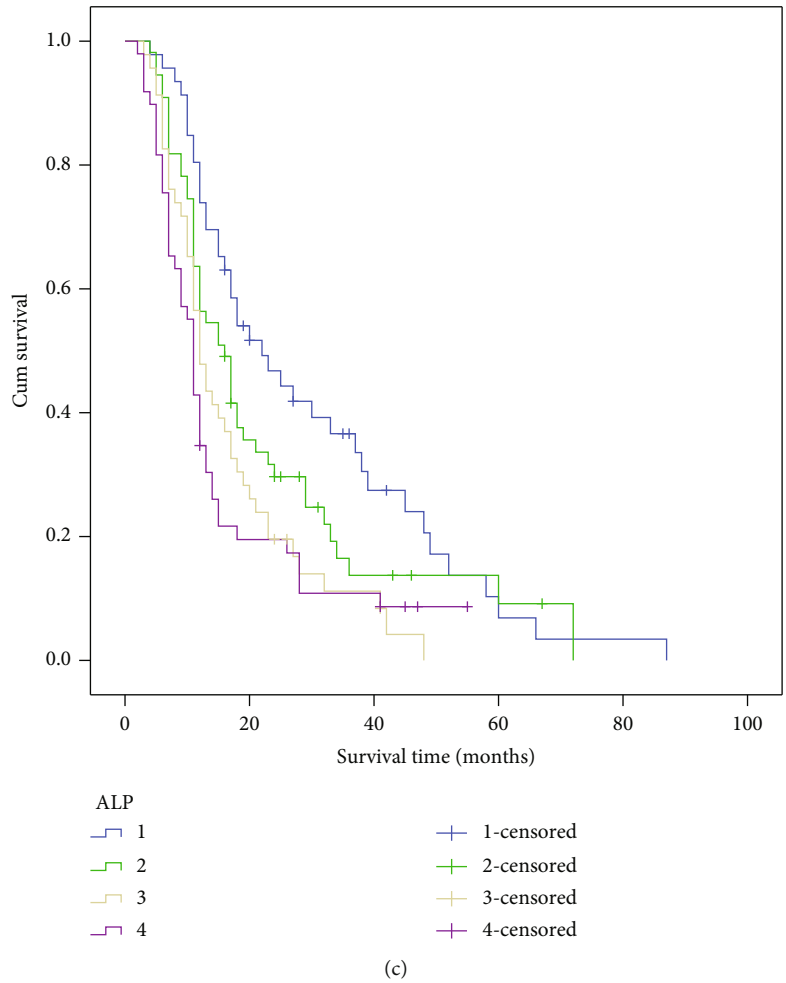

(c)

Figure 1: Continued.

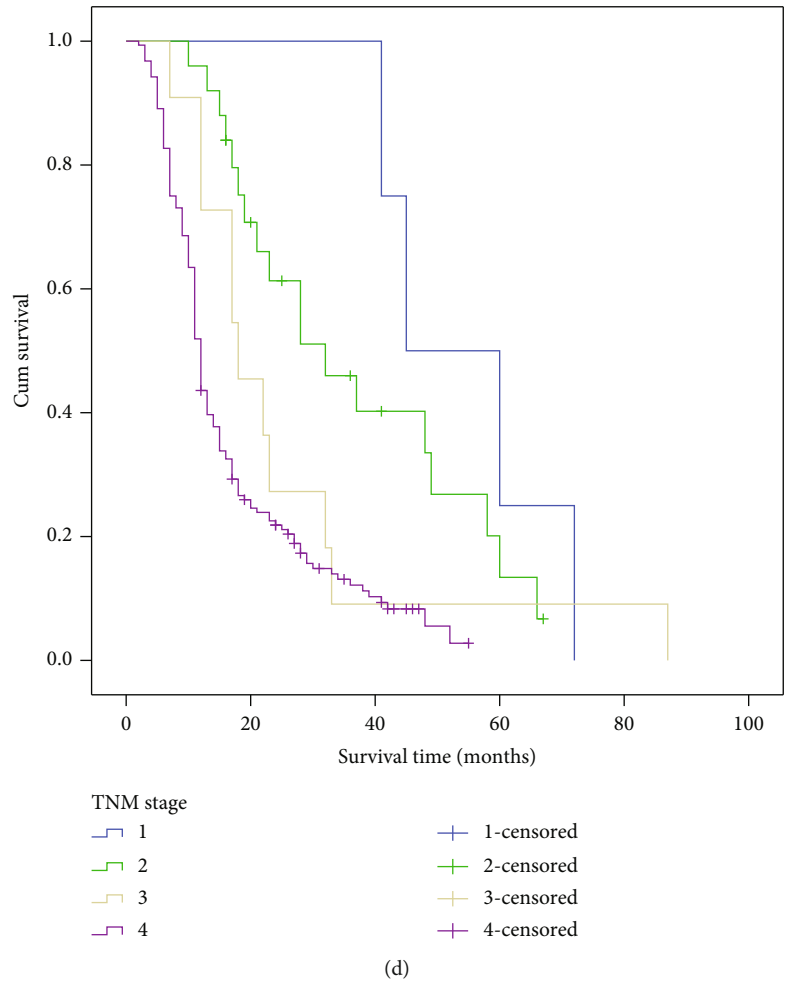

Figure 1: Kaplan-Meier curves for the PFS in patients with different Gleason grade, tPSA, ALP, and TNM stage. (a) Kaplan-Meier curves based on Gleason scores. (b) Kaplan-Meier curves based on tPSA levels. (c) Kaplan-Meier curves based on ALP concentration. (d) Kaplan-Meier curves based on TNM stages. $^*P < 0.05$.

immunoassay by Roche cobas e8000 was used for the detection of tPSA, and the colorimetry by Roche cobas c702 methods was applied for the analysis of ALP. The protocols of this study were approved by the Ethics Committee of our organization, and a signed informed consent was provided by each participant.

2.2. Statistical Analysis. To facilitate the data analysis, tPSA levels were organized into 5 groups based on ≤10, 10.1-20, 20.1-50, 50.1-100, and >100 ng/mL, and ALP was divided into 4 groups by the quartile ranges (≤25%, 25.1-50%, 50.1-75%, and >75%). All the data were expressed as frequency (percentage) and analyzed using SPSS 19.0 software (IBM, Armonk, New York). The R 3.6.1. Kaplan-Meier method was used to compare the differences of PFS between groups. The univariate and multivariate Cox regression analysis was conducted to examine the effect of tPSA, ALP, and other risk factors on PFS in PCa patients. A nomogram model for predicting 1-3-year PFS of PCa patients was conducted based on the independent prognostic indicators. Harrell's concordance index (C-index) was calculated to verify the discrimination of the model. The consistency of the nomogram model using calibration curves was predicted by the internal and external validation. The results were considered statistically significant when the two-sided P value was less than 0.05.

3. Results

3.1. Clinicopathological Characteristic Comparison between Test and Validation PCa Cohorts. The 255 PCa patients included 196 cases in test cohort and 59 cases in validation cohort. The demographic and clinical features of the patients were recorded and compared. The results summarized in Table 1 showed that there were no statistically significant differences between the two groups in age, diabetes history, hypertension history, bone metastasis, indwelling catheter condition, urinary tract infection, Gleason grade, TNM stage, Soloway grade, and levels of tPSA and ALP (all $P > 0.05$).

Table 3: Comparison of median PFS in patients with different Gleason grade, tPSA, ALP, and TNM stage.

Grouping	Median (95% CI) (months)	χ^2	P value
Gleason grade		19.654	0.001
1	41.0 (0.0, 85.8)		
2	34.0 (3.2, 64.8)		
3	17.0 (13.4, 20.6)		
4	15.0 (11.8, 18.2)		
5	11.0 (9.9, 12.1)		
tPSA (ng/mL)		25.082	<0.001
≤10	45.0 (22.7, 67.3)		
10.1-20	12.0 (10.5, 13.5)		
20.1-50	24.0 (17.4, 30.6)		
50.1-100	12.0 (9.2, 14.8)		
>100	12.0 (10.9, 13.1)		
ALP (U/L)		16.938	0.001
≤67.0	22.0 (13.8, 30.2)		
67.1-83.0	16.0 (11.5, 20.5)		
83.1-135.0	12.0 (9.8, 14.2)		
>135.0	11.0 (9.9, 12.1)		
TNM grade		26.078	<0.001
I	45.0 (26.4, 63.6)		
II	32.0 (17.9, 46.1)		
III	18.0 (9.9, 26.1)		
VI	12.0 (11.2, 17.8)		

tPSA: total prostate-specific antigen; ALP: alkaline phosphate.

3.2. Factors Associated with the PFS of PCa Patients. All of the clinicopathological parameters, including tPSA and ALP, were included in a Cox regression analysis to screen the factors that might be associated with the PFS of PCa patients. With the univariate analysis, the Gleason grade, tPSA, ALP, TNM stage, bone metastasis, and Soloway grade performed correlation with PFS (all $P < 0.05$, Table 2). The subsequent multivariate analysis that includes all the significant factors obtained from univariate analysis demonstrated that the Gleason grade, tPSA, ALP, and TNM stage were independently associated with the PFS of PCa patients (all $P < 0.05$). Meanwhile, the values of P could represent the significance of the index. Specifically, the smaller value of P , the higher significance is.

3.3. PFS in PCa Patients with Different Gleason Grades, tPSA, ALP, and TNM Stages. Given the independent association of the Gleason grade, tPSA, ALP, and TNM stage with PFS in PCa patients, the PFS in patients grouped based on these indicators was compared using Kaplan-Meier method. The Kaplan-Meier survival curves is shown in Figure 1, which indicated that PCa patients with high Gleason grade, high levels of tPSA or ALP, or advanced TNM stage had a poor PFS compared with those patients with low Gleason grade, tPSA, ALP, or early TNM stage ($P < 0.05$). In addition, the median PFS data in different groups was assessed, and the results listed in Table 3 revealed that the Gleason classification, TNM stage, and serum ALP are inversely proportional to the survival time of progression-free survival in patients with PCa. As the classification is higher, the median progression-free survival period is shorter. However, with the increase of tPSA value, the median progression-free survival of patients showed a fluctuating trend, which may be due to the influence of external factors on tPSA value.

3.4. Establishment of a Prognostic Nomogram Model for PFS in PCa Patients. A nomogram model was constructed using the Gleason grade, tPSA, ALP, and TNM stage, which were identified as independent prognostic factors of PFS after the multivariate Cox regression analysis (Figure 2). The results showed that TNM stage contributed most to PFS, followed by the Gleason grade, tPSA, and ALP. The likelihood of survival of PCa patients could be calculated by adding the scores of each variable, and the total score range was 0-30. The 1-year PFS of PCa patients accounted 0.9-0.2 when the total score was 6 to 29, and the 2-year and 3-year PFS could also be predicted by the constructed nomogram. Table 4 lists the risk scores of the subgroups of each independent variable included in the nomogram model. The 1-3-year PFS could be predicted easily by summing up the scores of the Gleason grade, tPSA, ALP, and TNM stage for each PCa patients.

3.5. Nomogram Validation. In order to further formalize the validity of the nomogram, this study used data from the test set for internal verification. The results showed that C-index (95% CI) was 0.705 (0.699, 0.711), suggesting a good discrimination. The consistency test results shown in Figure 3 indicated that the predicted 1-3-year PFS was in excellent agreement with the actual PFS in the PCa patients from test set. Moreover, the C-index obtained by external validation in patients from validation test was 0.687 (95% CI of 0.664, 0.710), indicating that the discrimination was within limits of acceptability. The calibration curves shown in Figure 4 revealed that the predicted 1-3-year PFS in validation cohort was slightly lower than that in the test cohort but still presents a considerable agreement with the actual observation.

4. Discussion

PCa remains the most frequent malignant tumor occurred in males. This study analyzed the relationship between clinicopathological characteristics and PFS in PCa patients, aiming to screen the variables that independently associated with PFS. The Gleason grade, tPSA, ALP, and TNM stage were demonstrated to be four independent prognostic indicators for PFS prediction in PCa patients. Furthermore, a prognostic nomogram was constructed based on the identified variables, which could assist the prediction of 1-3-year PFS and showed good discrimination in the validation from both internal and external levels. In addition, the calibration curves revealed that the nomogram model could predict 1-3-year PFS accurately.

PSA is widely used for clinical screening of prostate diseases, which greatly improves the early diagnosis of PCa [12,

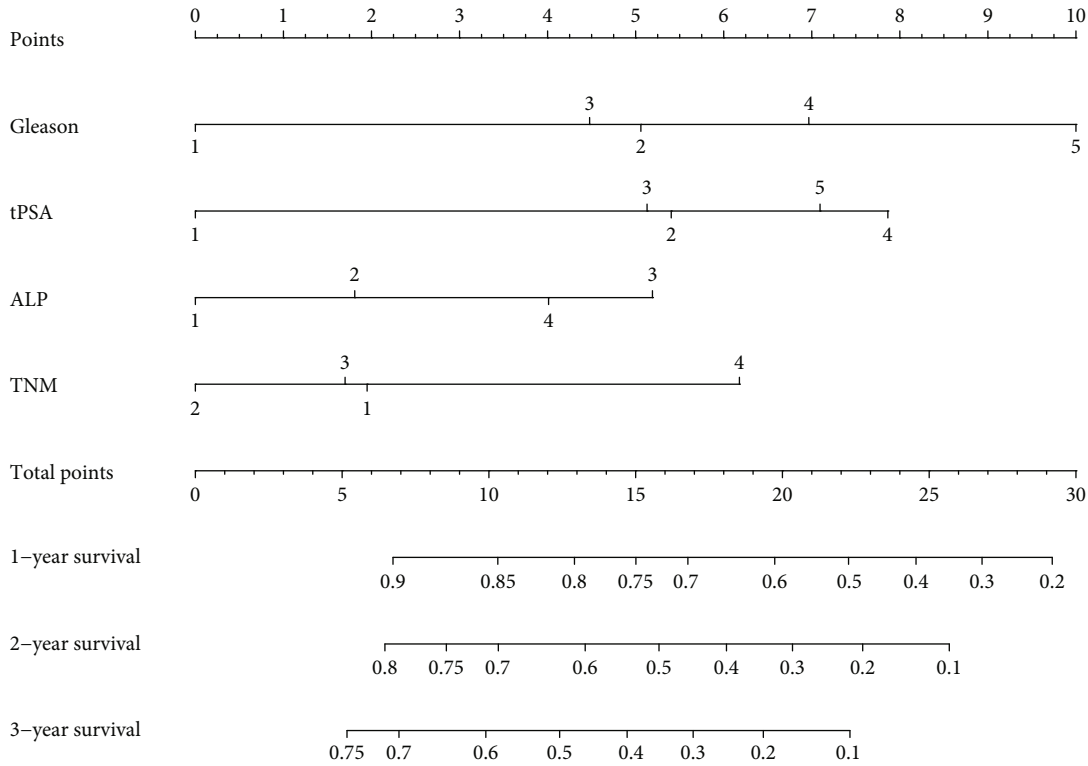

Figure 2: Nomogram based on the Gleason grade, tPSA, ALP, and TNM stage for predicting 1-3-year PFS in PCa patients.

Table 4: Scores of factors involved in the prediction nomogram model.

Gleason grade	Score	tPSA (ng/mL)	Score	ALP (U/L)	Score	TNM grade	Score
5	10	≤10	0	≤67.0	0	VI	6
4	7	10.1-20	5	67.1-83.0	2	III	2
3	4	20.1-50	5	83.1-135.0	5	II	0
2	5	50.1-100	8	>135.0	4	I	2
1	0	>100	7				

tPSA: total prostate-specific antigen; ALP: alkaline phosphate.

13]. During the development of prostate diseases, PSA levels are significantly elevated and associated with the disease progression [14]. Likewise, this study also observed that the PCa patients with high PSA levels had a poor PFS compared with those low PSA cases. Patients with PSA levels of 4-10 ng/mL are considered with benign prostate hyperplasia, and those with ≥10 ng/mL of PSA are considered with high risk of PCa. However, some PCa cases also show PSA levels of less than 10 ng/mL, leading to the application limitation of PSA [15]. Among the PCa patients included in this study, there were 15 cases with tPSA ≤10 ng/mL, accounting 5.9% of all the 255 PCa patients. Previous evidence and the survival analysis results of this study demonstrated the correlation of elevated PSA with the reduced survival in patients with PCa [16]. Nevertheless, PSA as a detection index for PCa lacks of accuracy, owing that PSA is a detection index for prostate rather than PCa [17]. It is considered that prostate infection, inflammation, or benign prostatic hyperplasia can also lead to the fluctuations of PSA levels [18]. In this study, the median PFS results in patients with different levels of PSA supported this view. Therefore, as an important indicator for PCa diagnosis and prognosis, the clinical use of PSA urgently needs to be improved.

ALP is important to indicate osteoblastic activity, which can be detected from the liver, kidney, intestinal mucosa, and bone tissues [19]. It is determined to be a predictive biomarker for tumor metastasis, especially for the metastasis to the bone [20]. There are approximately 85% PCa-related deaths caused by bone metastasis, implying the poor prognosis of PCa cases with positive bone metastasis [21]. In PCa patients, the serum upregulation of ALP has been documented to possess high predictive value for the occurrence of bone metastasis [22]. Thus, as the close relationship with bone metastasis, high levels of ALP generally predict a poor

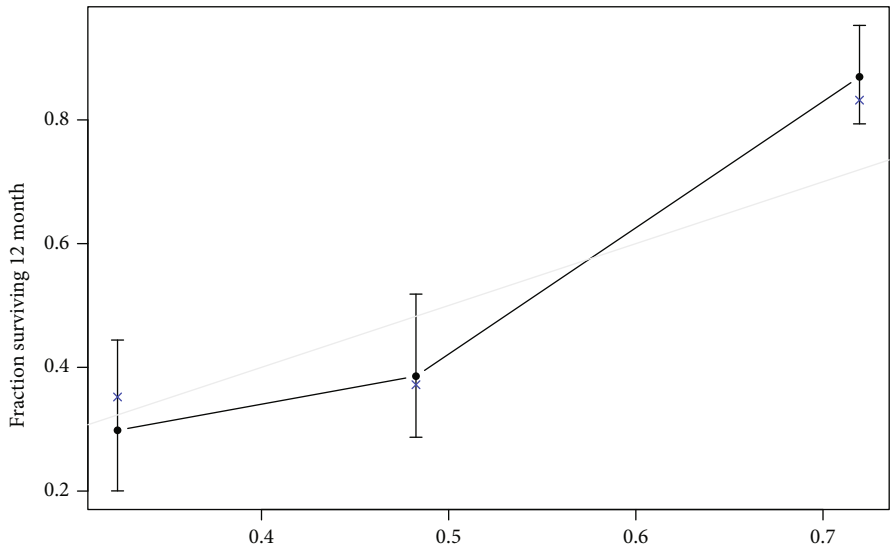

(a)

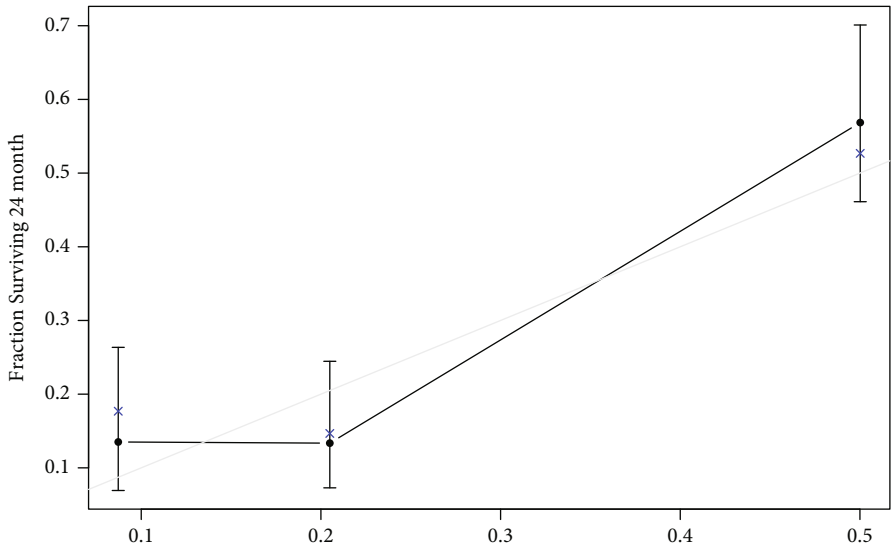

(b)

Figure 3: Continued.

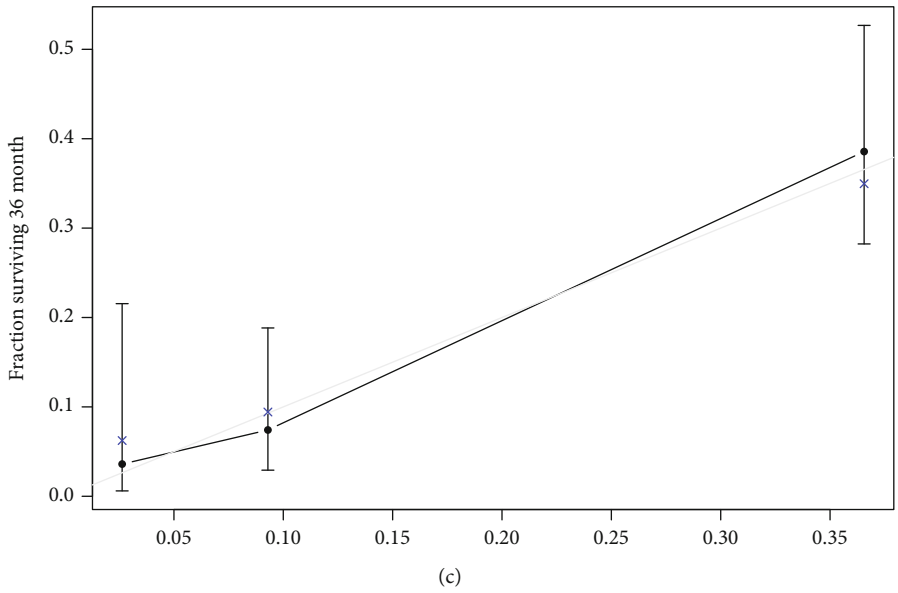

Figure 3: Internal calibration curves of the nomogram for predicting 1-3-year PFS in PCa patients. (a) Internal calibration curves for 1-year PFS. (b) Internal calibration curves for 2-year PFS. (c) Internal calibration curves for 3-year PFS.

prognosis in PCa patients. In this study, ALP levels were found to be independently associated with the PFS of PCa patients, and the median PFS was reduced as the ALP concentration increases. However, a study by Wei et al. reported that ALP only increased significantly after extensive bone metastasis with limited sensitivity, and its clinical use for prognosis prediction should be performed by the combination with other parameters [7].

Currently, the Gleason grade and TNM stage are two critical references for prognosis prediction in PCa patients [23]. This study also demonstrated the independent association of the Gleason grade and TNM stage with the PFS of PCa. There are five grades (grades 1-5) in the Gleason grading system and four stages (stages I, II, III, and IV) in the TNM staging system. However, the clinical decision for PCa management based only on the Gleason grade or TNM stage maybe ambiguous and has to be confirmed by some clinical experiences. Thus, the more intuitively and accurately prognosis predictive methods are urgently needed. Nomogram as a statistical model has been applied in the prognosis prediction in various human malignancies [24, 25]. It can accurately calculate the survival for each patient by summing up multiple variables that are related with prognosis. In PCa, Brockman et al. have established a nomogram predicting model for the mortality in PCa patients with biochemical recurrence after radical prostatectomy [26]. Hou et al. have developed a prognostic nomogram to predict bone metastasis in PCa patients according to the date from SEER database [27]. The nomograms efficiently assist the clinicians to predict the clinical outcomes of patients by assessing their individualized parameters.

Considering the pivotal role of PSA and ALP in PCa development, the two indicators were included in the survival analysis, and the Gleason grade, tPSA, ALP, and TNM stage were confirmed as four important prognostic indicators by multivariate analysis. Subsequently, a nomogram model was constructed based on the four selected variables. According to the scores in the nomogram, it is easy to predict the 1-3-year PFS of PCa patients by calculating the scores of the Gleason grade, tPSA, ALP, and TNM stage. In addition, by evaluating the survival data in the test and validation sets, we confirmed the discrimination and the predictive accuracy of the nomogram model. To our knowledge, this is the first time to develop a prognosis predictive nomogram considering PSA and ALP levels in PCa patients. The prediction of PFS may be more easy and accurate with the help of this predictive nomogram model. However, several limitations are included in this study. First, the sample size is small, which may limit the identification of significant prognostic indicators. Second, some critical clinical features are missing in this study, such as smoking history, alcohol abuse, and therapy. Thus, further investigations are necessary with a larger cohort and more complete clinicopathological data. Additionally, it is necessary to establish a regression equation, which could summarize the specific role of each factor in the prediction of PFS, which should attract special attention in the future studies.

The Gleason grade, tPSA, ALP, and TNM stage are four independent prognostic factors for the PFS of PCa patients, which are used to construct a predictive nomogram model. The established nomogram can accurately predict the 1-3-year PFS of PCa with a good discrimination. In clinical practice, the nomogram model may predict individualized survival risk and guild adjuvant therapy decisions for PCa patients.

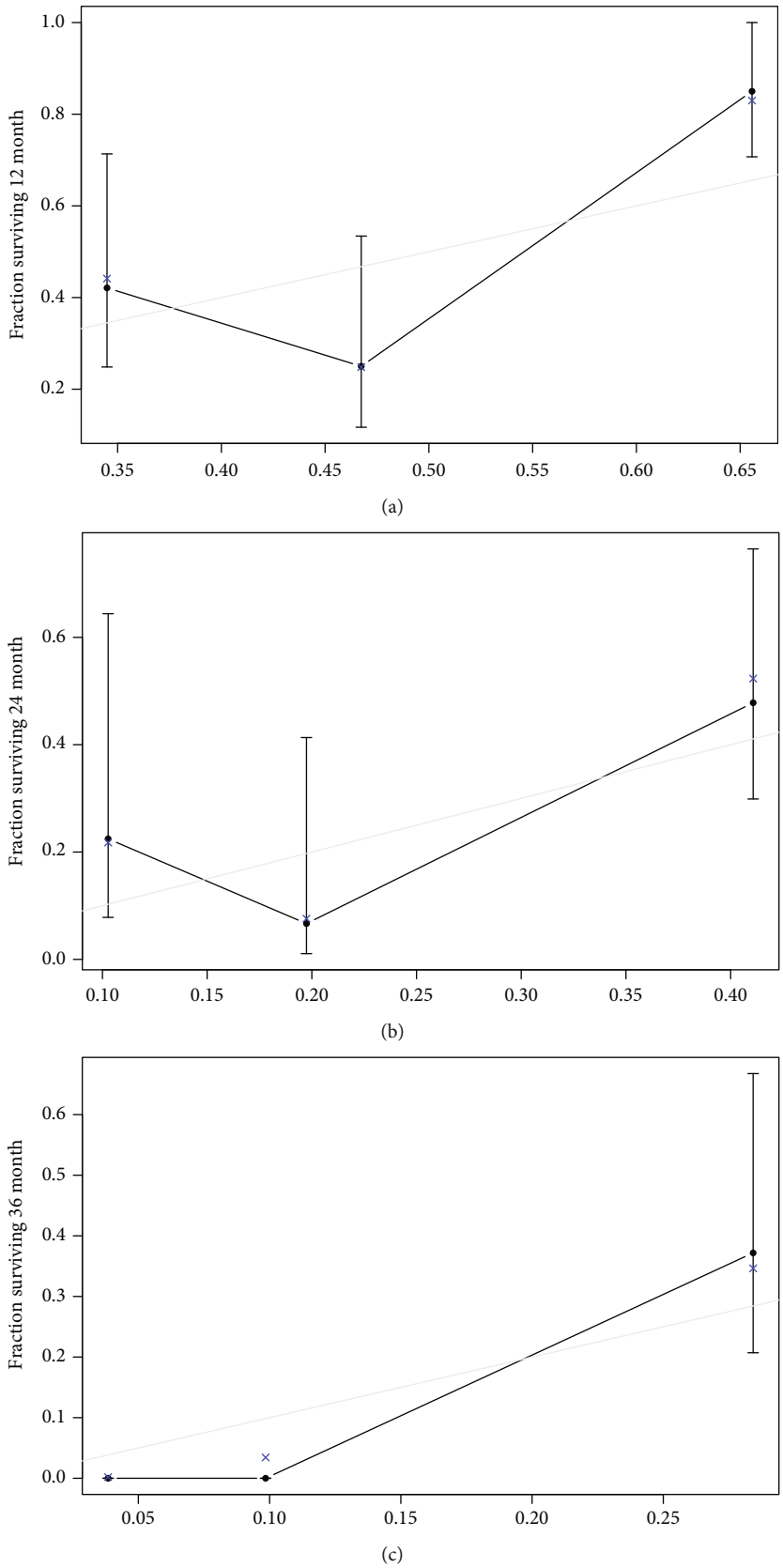

Figure 4: External calibration curves of the nomogram for predicting 1-3-year PFS in PCa patients. (a) External calibration curves for 1-year PFS. (b) External calibration curves for 2-year PFS. (c) External calibration curves for 3-year PFS.

Data Availability

Data are available on request from the authors.

Ethical Approval

This study was approved by the Ethics Committee of the Third Hospital of Sun Yat-sen University ([2020]02-105) and the Yuebei People Hospital Affiliated to Medical College of Shantou University (KY-2020-015).

Consent

The need for informed consent was waived due to the retrospective nature of the study.

Conflicts of Interest

The authors declare that they have no conflict of interests.

Authors' Contributions

XW conceived and designed the research, obtained funding, and revised the manuscript for important intellectual content; DC and XL were responsible for the acquisition of data; QL and YW analyzed and interpreted the data; JL and WZ were responsible for the statistical analysis; YH drafted the manuscript. All authors read and approved the final manuscript.

Acknowledgments

This study was supported by grants from the Natural Science Foundation of China (81874095 and 82072820) and the Guangdong Basic and Applied Basic Research Project Major Program of China (2019B1515120007).

References

[1] T. Guo, X. X. Wang, H. Fu, Y. C. Tang, B. Q. Meng, and C. H. Chen, "Early diagnostic role of PSA combined miR-155 detection in prostate cancer," *European Review for Medical and Pharmacological Sciences*, vol. 22, no. 6, pp. 1615–1621, 2018.

[2] Y. Hashimoto, M. Shiina, P. Dasgupta et al., "Upregulation of miR-130b contributes to risk of poor prognosis and racial disparity in African-American prostate cancer," *Cancer Prevention Research (Philadelphia, Pa.)*, vol. 12, no. 9, pp. 585–598, 2019.

[3] C. Ritch and M. Cookson, "Recent trends in the management of advanced prostate cancer," *F1000Research*, vol. 7, 2018.

[4] S. Y. Ku, M. E. Gleave, and H. Beltran, "Towards precision oncology in advanced prostate cancer," *Nature Reviews. Urology*, vol. 16, no. 11, pp. 645–654, 2019.

[5] T. Grozescu and F. Popa, "Prostate cancer between prognosis and adequate/proper therapy," *Journal of Medicine and Life*, vol. 10, no. 1, pp. 5–12, 2017.

[6] A. Castello, H. A. Macapinlac, E. Lopci, and E. B. Santos, "Prostate-specific antigen flare induced by 223RaCl2 in patients with metastatic castration-resistant prostate cancer," *European Journal of Nuclear Medicine and Molecular Imaging*, vol. 45, no. 13, pp. 2256–2263, 2018.

[7] R. J. Wei, T. Y. Li, X. C. Yang, N. Jia, X. L. Yang, and H. B. Song, "Serum levels of PSA, ALP, ICTP, and BSP in prostate cancer patients and the significance of ROC curve in the diagnosis of prostate cancer bone metastases," *Genetics and Molecular Research*, vol. 15, no. 2, 2016.

[8] E. Mulhem, N. Fulbright, and N. Duncan, "Prostate cancer screening," *American Family Physician*, vol. 92, no. 8, pp. 683–688, 2015.

[9] B. K. Sarvari, D. Sankara Mahadev, S. Rupa, and S. A. Mastan, "Detection of bone metastases in breast cancer (BC) patients by serum tartrate-resistant acid phosphatase 5b (TRACP 5b), a bone resorption marker and serum alkaline phosphatase (ALP), a bone formation marker, in lieu of whole body skeletal scintigraphy with technetium99m MDP," *Indian Journal of Clinical Biochemistry*, vol. 30, no. 1, pp. 66–71, 2015.

[10] S. C. Lin, L. Y. Yu-Lee, and S. H. Lin, "Osteoblastic factors in prostate cancer bone metastasis," *Current Osteoporosis Reports*, vol. 16, no. 6, pp. 642–647, 2018.

[11] M. Truong, B. Wang, J. B. Gordetsky et al., "Multi-institutional nomogram predicting benign prostate pathology on magnetic resonance/ultrasound fusion biopsy in men with a prior negative 12-core systematic biopsy," *Cancer*, vol. 124, no. 2, pp. 278–285, 2018.

[12] R. Kirby, "The role of PSA in detection and management of prostate cancer," *Practitioner*, vol. 260, no. 17-21, p. 13, 2016.

[13] C. Pezaro, H. H. Woo, and I. D. Davis, "Prostate cancer: measuring PSA," *Internal Medicine Journal*, vol. 44, no. 5, pp. 433–440, 2014.

[14] M. J. Barry and L. H. Simmons, "Prevention of prostate cancer morbidity and mortality: primary prevention and early detection," *The Medical Clinics of North America*, vol. 101, no. 4, pp. 787–806, 2017.

[15] S. Saini, "PSA and beyond: alternative prostate cancer biomarkers," *Cellular Oncology (Dordrecht)*, vol. 39, no. 2, pp. 97–106, 2016.

[16] C. Franzese, L. Di Brina, G. D'Agostino et al., "Predictive factors for survival outcomes of oligometastatic prostate cancer patients treated with metastases-directed therapy: a recursive partitioning-based analysis," *Journal of Cancer Research and Clinical Oncology*, vol. 145, no. 10, pp. 2469–2479, 2019.

[17] Z. Zhou, Y. Xu, Q. Li et al., "Prognostic significance of a novel indicator (PSA_{postd3}/PSA_{pre}) for PSA recurrence in patients after radical prostatectomy," *Cancer Management and Research*, vol. 11, pp. 5777–5783, 2019.

[18] T. Nordstrom, O. Akre, M. Aly, H. Gronberg, and M. Eklund, "Prostate-specific antigen (PSA) density in the diagnostic algorithm of prostate cancer," *Prostate Cancer and Prostatic Diseases*, vol. 21, no. 1, pp. 57–63, 2018.

[19] X. Wang, Y. Zhang, J. Choukroun, S. Ghanaati, and R. J. Miron, "Effects of an injectable platelet-rich fibrin on osteoblast behavior and bone tissue formation in comparison to platelet-rich plasma," *Platelets*, vol. 29, no. 1, pp. 48–55, 2018.

[20] S. Chen, L. Wang, K. Qian et al., "Establishing a prediction model for prostate cancer bone metastasis," *International Journal of Biological Sciences*, vol. 15, no. 1, pp. 208–220, 2019.

[21] R. B. Berish, A. N. Ali, P. G. Telmer, J. A. Ronald, and H. S. Leong, "Translational models of prostate cancer bone metastasis," *Nature Reviews. Urology*, vol. 15, no. 7, pp. 403–421, 2018.

[22] D. Li, H. Lv, X. Hao, B. Hu, and Y. Song, "Prognostic value of serum alkaline phosphatase in the survival of prostate cancer:

evidence from a meta-analysis," *Cancer Management and Research*, vol. 10, pp. 3125–3139, 2018.

[23] M. K. Buyyounouski, P. L. Choyke, J. K. McKenney et al., "Prostate cancer - major changes in the American Joint Committee on Cancer eighth edition cancer staging manual," *CA: a Cancer Journal for Clinicians*, vol. 67, no. 3, pp. 245–253, 2017.

[24] M. Roberto, A. Botticelli, L. Strigari et al., "Prognosis of elderly gastric cancer patients after surgery: a nomogram to predict survival," *Medical Oncology*, vol. 35, no. 7, p. 111, 2018.

[25] Y. Xiong, W. You, M. Hou, L. Peng, H. Zhou, and Z. Fu, "Nomogram integrating genomics with clinicopathologic features improves prognosis prediction for colorectal cancer," *Molecular Cancer Research*, vol. 16, no. 9, pp. 1373–1384, 2018.

[26] J. A. Brockman, S. Alanee, A. J. Vickers et al., "Nomogram predicting prostate cancer-specific mortality for men with biochemical recurrence after radical prostatectomy," *European Urology*, vol. 67, no. 6, pp. 1160–1167, 2015.

[27] G. Hou, Y. Zheng, D. Wei et al., "Development and validation of a SEER-based prognostic nomogram for patients with bone metastatic prostate cancer," *Medicine (Baltimore)*, vol. 98, no. 39, article e17197, 2019.

Hindawi
Journal of Oncology
Volume 2022, Article ID 4586729, 9 pages
https://doi.org/10.1155/2022/4586729

Research Article

Pretreatment Low Serum Sodium as a Prognostic Factor for Patients with Esophageal Cancer Treated with Radiotherapy or Chemoradiotherapy

Jianchao Lu, Yi Wang, Mei Lan, Jiahua Lv, Tao Li, Lei Wu, Qifeng Wang, and Jinyi Lang

Department of Radiation Oncology, Sichuan Cancer Hospital and Institution, Sichuan Cancer Center, School of Medicine, University of Electronic Science and Technology of China, Radiation Oncology Key Laboratory of Sichuan Province, Chengdu, China

Correspondence should be addressed to Lei Wu; wuleidoctor@163.com and Qifeng Wang; littlecancer@163.com

Received 21 January 2022; Accepted 3 March 2022; Published 21 March 2022

Academic Editor: Fu Wang

Low serum sodium levels have been associated with poor prognoses for several cancers. However, the prognostic value of low serum sodium levels in esophageal carcinoma (EC) has not been well elucidated. We examined the prognostic value of low baseline serum sodium levels before radiotherapy or chemoradiotherapy for EC patients. A retrospective analysis of data from EC patients who received radiotherapy or chemoradiotherapy at a single cancer center was performed. Patients were divided into low serum sodium level (≤140.0 mmol/L) or high serum sodium level (>140.0 mmol/L) groups according to the median pretreatment serum sodium level. The Kaplan–Meier model and Cox proportional hazards model were used for survival analyses. The 5-year progression-free survival (PFS) and overall survival (OS) rates in the whole group were 16.9% and 21.8%, respectively. The PFS and OS rates of patients in the low serum sodium levels group were significantly lower than those in the high serum sodium levels group ($p < 0.001$). A similar association between PFS/OS and sodium levels was observed in the treatment subgroups. The univariate analysis showed that low serum sodium levels, Karnofsky performance status (KPS), clinical N stage, tumor site, clinical stage, and treatment mode were the influencing factors of OS. Multivariate analyses indicated that low baseline serum sodium levels were an independent prognostic marker of poor PFS (HR, 1.744; 95% CI, 1.248-2.437; $p = 0.001$) and OS (hazard ratio (HR), 2.125; 95% confidence interval (CI), 1.555-2.904; $p < 0.001$). Pretreatment levels of low serum sodium could be a new and helpful serum biomarker of the prognosis of EC patients receiving radiotherapy or chemoradiotherapy.

1. Introduction

Esophageal carcinoma (EC) is a common malignancy, ranking seventh in terms of prevalence and sixth in terms of mortality worldwide. It is well established that the incidence of EC and the mortality of EC patients vary among geographic areas in China, with some areas reporting an incidence rate up to 116.87 per 100,000 and a mortality rate of 95.76 per 100,000 [1]. The 5-year overall survival (OS) rate ranges from 15% to 25% worldwide [2]. Squamous cell carcinoma is the main pathological type and is one of the most prevalent and lethal types, with a mortality rate of almost 90% in China [2]. Although there have been significant developments in the pathology of EC and comprehensive treatments are available, patient outcomes need to be improved. Little attention has been focused on biomarkers that can predict the prognosis. Therefore, it is necessary to explore biomarkers as new prognostic indicators that could potentially guide clinical practice.

Hyponatremia is a common serum disorder of electrolytes that frequently occurs in patients with solid tumors [3–5]. Numerous studies have revealed that hyponatremia is related to poor prognoses for several solid tumors, including tumors of the bladder, lung, breast, liver, colon,

Table 1: Patient and tumor characteristics in relation to serum sodium levels.

Characteristic	Total N (%)	Sodium levels (mmol/L) Low serum sodium group N (%)	High serum sodium group N (%)	p value
N	256	133 (52.0)	123 (48.0)	
Age (years)		64.38 ± 10.61	64.47 ± 10.25	0.942*
Sex				0.127
Male	196 (76.6)	107 (80.5)	89 (72.4)	
Female	60 (23.4)	26 (19.5)	34 (27.6)	
KPS				0.184†
70	25 (9.8)	14 (10.5)	11 (8.9)	
80	134 (52.3)	74 (55.6)	60 (48.8)	
90	97 (37.9)	45 (33.8)	52 (42.3)	
Tumor sites				0.302†
Cervical	24 (9.4)	8 (6.0)	16 (13.0)	
Upper	76 (29.7)	42 (31.6)	34 (27.6)	
Middle	112 (43.8)	58 (43.6)	54 (43.9)	
Lower	44 (17.2)	25 (18.8)	19 (15.4)	
Histopathology				0.480‡
Squamous	255 (99.6)	133 (100)	122 (99.2)	
Nonsquamous	1 (0.4)	0 (0)	1 (0.8)	
T stage				0.123†
T2	30 (11.7)	18 (13.5)	12 (9.8)	
T3	138 (53.9)	75 (56.4)	63 (51.2)	
T4a	36 (14.1)	16 (12.0)	20 (16.3)	
T4b	52 (20.3)	24 (18.0)	28 (22.8)	
Clinical N stage				0.514†
N0	16 (6.3)	8 (6.0)	8 (6.4)	
N1	120 (46.9)	62 (46.6)	58 (47.2)	
N2	107 (41.8)	52 (39.1)	55 (44.7)	
N3	13 (5.1)	11 (8.3)	2 (1.6)	
M stage				0.624
M0	207 (80.9)	106 (79.7)	101 (82.1)	
M1	49 (19.1)	27 (20.3)	22 (17.9)	
Clinical stage				0.713†
IIB	9 (3.5)	3 (2.3)	6 (4.9)	
IIIA	15 (5.9)	7 (5.3)	8 (6.5)	
IIIB	127 (49.6)	69 (51.9)	58 (47.2)	
IVA	59 (23.0)	29 (22.8)	30 (24.4)	
IVB	46 (18.0)	25 (18.8)	21 (17.1)	
Treatment types				0.106
Radiotherapy	92 (35.9)	54 (40.6)	38 (30.9)	
Chemoradiation	164 (64.1)	79 (59.4)	85 (69.1)	

Abbreviation: KPS: Karnofsky performance status. *t-test. †Mann–Whitney test; ‡Fisher's exact test. Other p values were tested by Pearson's chi-square (χ^2) test. Serum sodium levels: low sodium: ≤140.0 mmol/L; high sodium: >140.0 mmol/L.

and rectum, as well as head and neck [3, 6–9]. Serum sodium is widely recognized as a time-saving, economical, repeatable, and routine prognostic biomarker that can predict patient prognosis. Previous studies have shown that hyponatremia is an adverse event that emerges in 16% to 59% of EC patients who undergo chemotherapy or chemoradiotherapy [10–12].

To our knowledge, few studies have investigated the relationship between baseline serum sodium levels and survival of EC patients. The incidence and prognostic value of serum

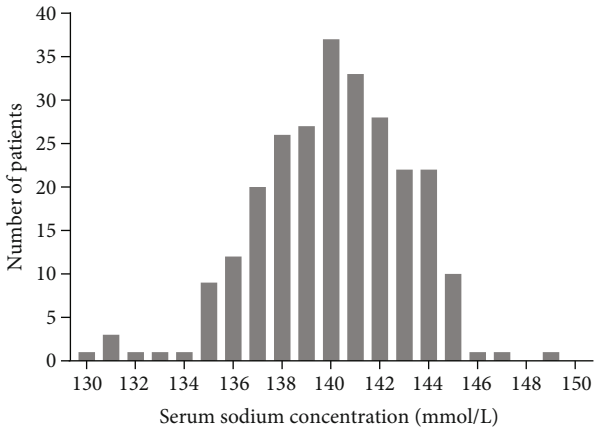

Figure 1: Graph showing distribution of serum sodium concentration in 256 patients.

sodium levels before any treatment for EC patients have been underestimated. Therefore, we retrospectively reviewed 271 EC patients to address this issue. Pretreatment serum sodium concentrations were assessed in association with OS and progression-free survival (PFS). Additionally, the association of pretreatment serum sodium levels with OS and PFS after different types of procedures was analyzed.

2. Materials and Methods

Our study received approval from the Ethics Committee of Sichuan Cancer Hospital, and informed consent was exempted by the ethics committee. Patients with biopsy-proven EC who had undergone radical radiotherapy or chemoradiotherapy were enrolled at the Sichuan Cancer Hospital between March 2006 and October 2016.

The inclusion criteria were as follows: Karnofsky score ≥ 70 points, pathologically confirmed EC, underwent radical radiotherapy or chemoradiotherapy, no history of malignant disease, and underwent a routine blood test and biochemical examination within 1 week before any treatment. In contrast, the exclusion criteria were as follows: severe medical disorders, underwent treatment at other institutions, had not received radiation doses of above 50.4 Gy, and insufficient information or incomplete laboratory or clinicopathological parameters.

Radical radiotherapy was administered for more than five weeks with a cumulative dose of 50.4 to 60.0 Gy. Some of these patients underwent radiation therapy concomitant with platinum-based chemotherapy. The patients were stratified by treatment modalities and divided into low and high serum sodium groups according to the median value.

2.1. Data Collection and Definition. The pretreatment serum sodium concentration was acquired from venous blood within one week before radiotherapy or chemoradiotherapy and was conventionally available from the hospital's laboratory at Sichuan Cancer Hospital. The baseline serum sodium concentration was recorded as the median value. A low serum sodium level was defined as ≤140.0 mmol/L, and a high serum sodium level was defined as >140 mmol/L. Clinical factors and demographic data were retrospectively collected manually from the medical records. Clinicopathological data included the date of diagnosis, age, sex, Karnofsky score, tumor histology, tumor site, staging, serum sodium level, and follow-up information. All patients were pathologically confirmed to have EC. The pathological stage was reassessed based on the TNM classification system, as defined by the American Joint Committee on Cancer (8th edition). All cases were examined and followed up at least every three months during the first two years, every six months for the following one to three years, and every 12 months after five years. The information collected during the follow-up period included the results of physical examinations, endoscopic examinations, imaging, and laboratory tests. Prognostic information included PFS and OS. PFS and OS were defined as the length of time between the initiation of treatment and the date of either death or disease progression and the length of time between the initiation of treatment and the date of all-cause death, respectively.

2.2. Statistical Analysis. Sample characteristics were compiled using descriptive statistics. Pearson's chi-square (χ^2) test and Student's t-test (the Mann–Whitney U test was performed if the data were not normally distributed) were used to assess the relationship between the patient's tumor characteristics and serum sodium levels. The Kaplan–Meier model and Cox proportional hazards model were used for survival analyses. Univariate and multivariable Cox proportional hazards models were employed to assess factors associated with esophageal cancer prognosis. After assessing the p value (p) from the univariate model, variables with $p < 0.1$ were introduced into multivariable Cox proportional hazards models. Statistical analyses were conducted using SPSS software version 24.0 (SPSS Inc., Chicago, IL, USA).

3. Results

3.1. Patient Characteristics. In total, 271 patients of biopsy-proven EC stage I-IVB were enrolled at Sichuan Cancer Hospital from March 1, 2006, to October 31, 2016. However, fifteen patients with the following criteria were excluded from the analysis: recurrent EC that had been previously treated ($n = 4$); patients with metastases to distant organs ($n = 5$); patients who stopped any of the treatments ($n = 1$); noncompletion of the treatment ($n = 2$); and incomplete available information, such as follow-up data and clinicopathological or laboratory parameters ($n = 3$). Therefore, only 256 patients were eligible for further analysis, including 92 patients who underwent radiotherapy alone and 164 patients who underwent chemoradiotherapy (Table 1). The average age of all patients was 64 years (range, 35-92 years). There were 196 men and 60 women with a Karnofsky score ≥ 70 points. According to the reference range of serum sodium levels (135-145 mmol/L), the rate of hypernatremia (>145 mmol/L) and the rate of hyponatremia (<135 mmol/L) for the enrolled patients were 1.6% and 6.3%, respectively.

The last follow-up was completed in February 2018, and the median follow-up time was 35 months (range, 12.4-81.2 months). The median baseline serum sodium level was

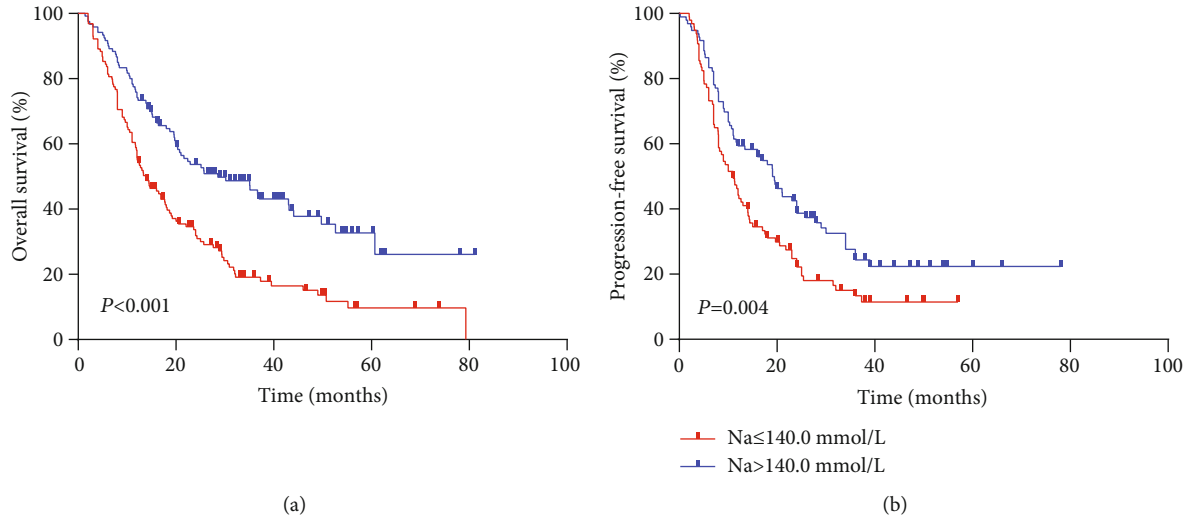

Figure 2: (a) Kaplan–Meier survival curves of the serum sodium concentration at the median cutoff value (140.0 mmol/L) are shown ($p < 0.001$). (b) Kaplan–Meier survival curves of the serum sodium concentration at the median cutoff value (140.0 mmol/L) are shown ($p = 0.004$).

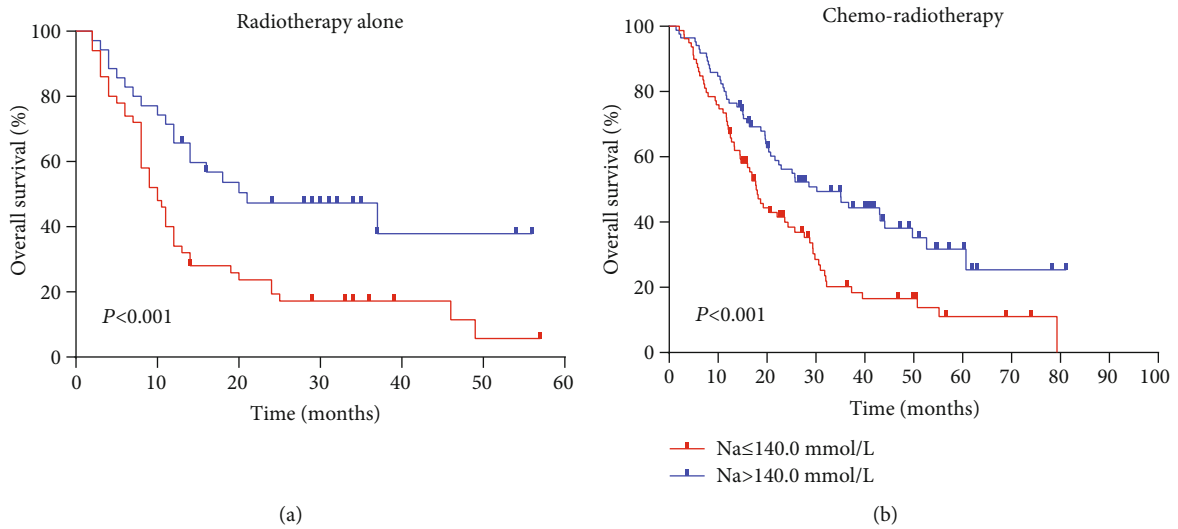

Figure 3: (a) Kaplan–Meier survival curves for OS according to the serum sodium concentration in the radiotherapy alone subgroup. (b) Kaplan–Meier survival curves for OS according to the serum sodium concentration in the chemoradiotherapy subgroup.

140.0 mmol/L (range, 130.0-149.0 mmol/L) (Figure 1). Of the 256 patients, 123 fell into the high serum sodium group and 133 fell into the low serum sodium group. Of all the patients, 76.6% were male, 47.3% were older than 65 years, and 9.4% had a Karnofsky performance score of 70 points. In addition, 99.6% of the patients had squamous cell carcinoma, and 43.8% of tumors were localized in the middle of the esophagus. None of the clinicopathological characteristics (age, sex, Karnofsky score, tumor site, histopathology, T and clinical N stage TNM classification, and type of treatment regimen) was statistically associated with serum sodium concentrations assessed before treatment (Table 1).

3.2. Survival Outcomes. The median PFS and OS for all evaluable patients were 12.6 months and 16.9 months, respectively. The overall 5-year PFS and OS rates were 16.9% and 21.8%, respectively. Analysis results indicated that outcomes in the high serum sodium group were better than those in the low serum sodium group (Figures 2(a) and 2(b)) (OS $p < 0.001$, PFS $p = 0.004$). The 5-year PFS rates were 22.4% and 11.5%, and the 5-year OS rates were 32.7% and 11.7% in the high and low serum sodium groups, respectively.

Next, we performed a subgroup analysis according to treatment modes. An analysis of OS with radiotherapy alone

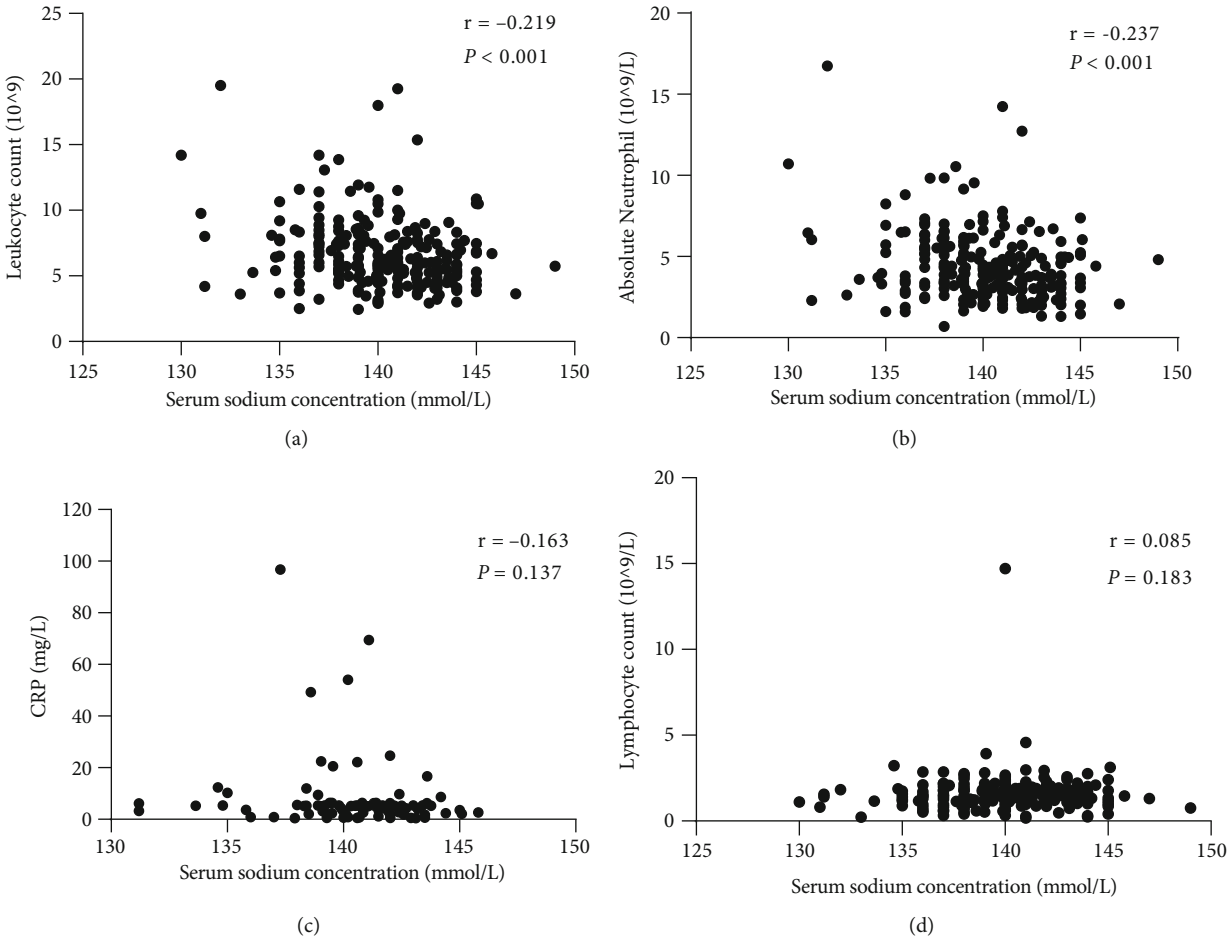

Figure 4: The association of serum sodium concentration with blood indicators. (a) Scatterplot for relationship between sodium and leukocyte count. (b) Scatterplot for relationship between sodium and neutrophil. (c) Scatterplot for relationship between sodium and CRP. (d) Scatterplot for relationship between sodium and lymphocyte.

and chemoradiotherapy (Figures 3(a) and 3(b)) showed that the high serum sodium group also had improved outcomes compared to the low serum sodium group (both $p < 0.001$).

3.3. Association of Serum Sodium Concentration with Inflammatory Response. Furthermore, we observed a significant negative correlation between low pretreatment concentration of serum sodium and neutrophil and leukocyte levels (Figures 4(a) and 4(b)).

The relationships among clinicopathological factors and serum sodium concentration are shown in Table 2. These data clearly show that the neutrophil count was negatively associated with the baseline serum sodium level ($p < 0.001$), and a significant negative correlation was observed between the serum sodium level and the neutrophil-to-lymphocyte ratio (NLR) ($p < 0.001$). The trend of the negative association between C-reactive protein (CRP) levels and serum sodium concentrations was not statistically significant ($p = 0.137$) (Figure 4(c)). In addition, there was no correlation between serum sodium levels and lymphocyte counts ($p = 0.183$) (Figure 4(d)). Alternatively, there was no association between the neutrophil count and CRP level ($p = 0.325$).

Table 2: Spearman's correlation analysis of interrelationships among hematological indicators.

Hematological Indices		r_s	p value
Serum sodium	Leukocyte	-0.219	<0.001
	Neutrophil	-0.237	<0.001
	CRP	-0.163	0.137
	Lymphocyte	0.085	0.183
	NLR	-0.247	<0.001
Leukocyte	Neutrophil	0.910	<0.001
	CRP	0.186	0.088
	Lymphocyte	0.363	<0.001
	NLR	0.381	<0.001
Neutrophil	CRP	0.108	0.325
	Lymphocyte	0.088	0.167
	NLR	0.634	<0.001
CRP	Lymphocyte	0.068	0.533
	NLR	0.029	0.792

Abbreviation: NLR, neutrophil-to-lymphocyte ratio; CRP, C-reactive protein. r_s: Spearman's correlation coefficient.

Table 3: Cox regression analysis of clinical characteristics of overall survival of EC patients who underwent radiotherapy alone or chemoradiotherapy.

	Univariate			Multivariate		
	HR	p value	95% CI	HR	p value	95% CI
KPS	2.207	<0.001***	1.408-3.462	2.974	<0.001***	1.862-4.751
70						
80-90						
Tumor sites						
Cervical	1 (reference)					
Upper	1.753	0.096	0.906-3.393			
Middle	1.979	0.034*	1.052-3.723			
Lower	2.611	0.005	1.331-5.119			
Clinical N stage						
N0	1 (reference)			1 (reference)		
N1	1.964	0.112	0.855-4.512	3.617	0.003**	1.529-8.558
N2-3	2.690	0.019*	1.175-6.158	5.205	<0.001***	2.175-12.455
Clinical stage	1.371	0.038*	1.017-1.848	1.473	0.017*	1.070-2.026
II-III						
IV						
Treatment models	0.665	0.011*	0.487-0.910	0.475	<0.001***	0.340-0.663
Radiotherapy						
Chemoradiotherapy						
Serum sodium	1.966	<0.001***	1.448-2.669	2.125	<0.001***	1.555-2.904
>140 mmol/L						
≤140 mmol/L						

Abbreviation: EC: esophageal carcinoma; HR: hazard ratio; CI: confidence interval; KPS: Karnofsky performance status. *$p < 0.05$. **$p < 0.01$. ***$p < 0.001$.

3.4. Univariate and Multivariate Analyses. The univariate analysis showed that low serum sodium levels (≤140.0 mmol/L), Karnofsky performance status (KPS), clinical N stage, tumor site, clinical stage, and treatment mode were the influencing factors of OS ($p < 0.05$) (Table 3). Similarly, the prognostic factors that significantly and independently affected PFS were the clinical stage of the carcinoma ($p = 0.002$), Karnofsky performance score ($p = 0.022$), and serum sodium level ($p = 0.005$) (Table 4).

In the multivariate Cox proportional hazards regression models, the serum sodium levels ($p < 0.001$), Karnofsky score ($p < 0.001$), treatment type ($p < 0.001$), clinical stage ($p = 0.017$), and clinical N stage ($p < 0.001$) were identified as significant and independent unfavorable outcome prognostic factors (Table 3).

According to the results of stratified and multivariate Cox proportional hazards model analysis for PFS and OS, the low serum sodium group's PFS ($p = 0.001$; HR [95% CI], 1.744 [1.248-2.437]) and OS ($p < 0.001$; HR [95% CI], 2.125 [1.555-2.904]) hazards ratios were higher than those of the high serum sodium group. In other words, patients with baseline serum sodium concentrations ≤ 140.0 mmol/L had a lower survival rate than those with serum sodium levels > 140.0 mmol/L (Figures 2(a) and 2(b), Tables 3 and 4). This suggests that a low baseline serum sodium level is an independent and significant prognostic factor for poor survival.

4. Discussion

In the present study, we assessed the prognostic value of baseline factors and pretreatment serum sodium levels by performing a retrospective analysis of 256 EC patients. The incidences of hypernatremia and hyponatremia (routinely classified in the laboratory) for untreated patients were 1.6% and 6.25%, respectively. This observation is in accordance with the previously reported incidence of hyponatremia (range, 4–47%) [5, 13].

We confirmed that EC patients with baseline serum sodium levels ≤ 140.0 mmol/L had significantly shorter survival than those with high serum sodium levels ($p < 0.001$). Similar results were obtained by performing a subset analysis of the different treatment groups ($p < 0.001$ for both comparisons). In addition, Cox proportional hazards model analysis showed that the risk of mortality in the low serum sodium level group was 2.15 times that of the high serum sodium level group, and the risk of disease progression was 1.744 times.

Our study demonstrated that the decrease in serum sodium concentrations before initial treatment was inversely associated with the outcomes of EC patients. A previous study indicated that the reduction in serum sodium levels (per 3 mmol/L decrease) was significantly related to a 19% increased risk of death [9]. However, the mechanisms

Table 4: Cox regression analysis of clinical characteristics of progression-free survival of EC patients who underwent radiotherapy alone or chemoradiotherapy.

	Univariate			Multivariate		
	HR	p value	95% CI	HR	p value	95% CI
KPS	1.785	0.022*	1.088-2.928	1.707	0.035*	1.040-2.802
70						
80-90						
Tumor sites						
Cervical	1 (reference)					
Upper	1.444	0.225	0.798-2.615			
Middle	1.618	0.097	0.916-2.857			
Lower	2.11	0.018*	1.136-3.922			
Clinical N stage						
N0	1 (reference)					
N1	1.623	0.298	0.652-4.038			
N2-3	2.113	0.105	0.855-5.220			
Clinical stage	1.689	0.002**	1.220-2.338	1.846	<0.001***	1.325-2.573
II-III						
IV						
Treatment models	0.892	0.617	0.571-1.395			
Radiotherapy						
Chemoradiotherapy						
Serum sodium	1.594	0.005**	1.149-2.213	1.744	0.001**	1.248-2.437
>140 mmol/L						
≤140 mmol/L						

Abbreviation: EC: esophageal carcinoma; HR: hazard ratio; CI: confidence interval; KPS: Karnofsky performance status. *$p < 0.05$. **$p < 0.01$. ***$p < 0.001$.

underlying the development of low serum sodium levels remain unclear, particularly for EC patients. Recently, an increasing number of biological markers have been identified that may have an essential role in cancer patients with serum sodium level abnormalities. Poor appetite, weight loss, and cachexia are commonly found in malignant diseases and particularly in EC patients who may develop malnutrition. Decreased oral intake, in particular, leads to decreased serum sodium levels.

Moreover, high tumor burden, gastrointestinal fluid loss, and renal fluid loss may disturb the serum sodium balance, which induces vomiting and diarrhea, resulting in hypovolemic hyponatremia [14]. Abnormal secretion of antidiuretic hormone in tumor patients may increase the reabsorption of water from the distal renal tubule and decrease plasma osmolality [15, 16]. A systemic inflammatory response is likely an additional factor that alters the serum sodium levels. Furthermore, a vicious cycle of the exacerbation of the production of inappropriate antidiuretic hormones might exist between inflammatory states and serum sodium levels [17].

We evaluated the association between low serum sodium levels and inflammation. Concomitantly, we found that the pretreatment serum sodium concentration was inversely associated with CRP, leukocyte count, neutrophil count, and NLR; however, it was positively associated with lymphocyte count in EC patients. Notably, no statistical differences were observed in the association between pretreatment serum sodium and CRP levels or lymphocyte counts. Similary, no significant correlation was found between the neutrophil count and CRP levels. This may be attributed to variations in detection levels over time and incomplete CRP data. A previous study consistently showed that white blood cell count was the risk factor in EC patients [11]. It has also been reported that CRP, IL-6, IL-1β, and neutrophil counts are associated with hyponatremia. Furthermore, this observation has been reported for nonmalignant diseases [18]. Secretion of antidiuretic hormones from neurons is promoted by the proinflammatory cytokines IL-6 and IL-1β in the internal milieu [19, 20], and the inflammatory response is further promoted through inflammasome activation in macrophages, which might be induced by cell swelling-stimulated osmolality [21]. Increasing evidence has suggested that ion channels and pumps not only have a major role in maintaining intracellular and extracellular pH and regulating membrane potential stability but also have critical roles in the regulation of cell migration [22]. These findings also suggest that decreased serum sodium levels could be a prognostic marker, although the underlying molecular mechanism remains unclear.

In the present study, the 5-year OS for patients treated with radiotherapy was 17.5%, which was lower than the 5-year OS of 34% reported by Lin et al. [23]. This could be partially due to the fact that 36.2% of the patients recruited

for their study had stage I or II tumors, whereas only 3.5% of the patients in our study had stage I or II. In the present review, the 5-year OS rate for chemotherapy and radiotherapy (23.6%) was significantly higher than that for radiotherapy alone (17.5%) ($p = 0.01$), which is similar to other findings [24, 25] and in accordance with the Radiation Therapy Oncology Group 8501 data [26]. At 5 years of follow-up, the OS for combined modality therapy was 26% compared with 0% after radiation therapy. Based on previous clinical data, chemoradiation is a standard strategy for EC patients.

The prognostic value of the tumor site in EC patients has been previously reported. We found that cervical EC had a better prognosis than carcinoma at other sites. However, further multifactor analysis did not show statistical significance. This may have been caused by confounding factors that could have influenced our results, such as patient selection.

It is commonly recognized that the N stage has emerged as a prognostic marker of outcomes of EC patients. Concomitantly, performance status has been determined to be a predictor of outcomes. Previous studies revealed that better performance status is associated with better tolerance of chemoradiation in EC patients [27]. Our study found that patients with a Karnofsky performance status of 70 had a worse prognosis than those with a Karnofsky performance status of 80 to 90 ($p < 0.001$).

To the best of our knowledge, this study is the first to demonstrate the predictive and prognostic values of baseline serum sodium concentrations of EC patients treated with radiotherapy alone or chemoradiotherapy. Moreover, serum sodium is regularly, quickly, and economically obtained during routine blood tests. Nevertheless, the causal associations among low serum sodium levels, ion channels and pumps, and inflammation for EC patients remain unclear and require further study.

Our study had several limitations. First, it was a retrospective, single-center analysis that spanned almost 10 years. Additionally, the sample size was relatively small. Finally, kinematic data of serum sodium were not collected.

5. Conclusions

We confirmed that low pretreatment serum sodium levels are associated with poorer OS and PFS for patients treated with radiotherapy alone or chemoradiotherapy. Serum sodium concentrations have the potential to be a significant prognostic factor of EC patients. However, a prospective large-scale study of EC patients is needed to fully understand the prognostic role of low serum sodium levels.

Data Availability

Data used and analyzed during the current study will be available from the corresponding authors upon reasonable request.

Acknowledgments

We owe thanks to all participating patients and their family members. We also thank Editage (http://www.editage.cn) for English language editing. This work was supported by grants from the Sichuan Science and Technology Department Key Research and Development Project Fund (2019YFS0378) and new service model of tumor radiotherapy based on "Internet+": the systemic development and application research of "Precision cloud radiotherapy" (project number: 2017YFC0113100).

Disclosure

The funding sources played no role in the study's design, data analysis, or decision to publish the findings.

Conflicts of Interest

The authors declare that there is no conflict of interest regarding the publication of this paper.

References

[1] F. Bray, J. Ferlay, I. Soerjomataram, R. L. Siegel, L. A. Torre, and A. Jemal, "Global cancer statistics 2018: GLOBOCAN estimates of incidence and mortality worldwide for 36 cancers in 185 countries," *CA: a Cancer Journal for Clinicians*, vol. 68, no. 6, pp. 394–424, 2018.

[2] A. Pennathur, M. K. Gibson, B. A. Jobe, and J. D. Luketich, "Oesophageal carcinoma," *Lancet*, vol. 381, no. 9864, pp. 400–412, 2013.

[3] J. J. Castillo, I. G. Glezerman, S. H. Boklage et al., "The occurrence of hyponatremia and its importance as a prognostic factor in a cross-section of cancer patients," *BMC Cancer*, vol. 16, no. 1, p. 564, 2016.

[4] J. B. Sorensen, M. K. Andersen, and H. H. Hansen, "Syndrome of inappropriate secretion of antidiuretic hormone (SIADH) in malignant disease," *Journal of Internal Medicine*, vol. 238, no. 2, pp. 97–110, 1995.

[5] T. Berghmans, M. Paesmans, and J. J. Body, "A prospective study on hyponatraemia in medical cancer patients: epidemiology, aetiology and differential diagnosis," *Support Care Cancer*, vol. 8, no. 3, pp. 192–197, 2000.

[6] T. I. Huo, H. C. Lin, C. Y. Hsia et al., "The MELD-Na is an independent short- and long-term prognostic predictor for hepatocellular carcinoma: a prospective survey," *Digestive and Liver Disease*, vol. 40, no. 11, pp. 882–889, 2008.

[7] A. J. Feinstein, J. Davis, L. Gonzalez, K. E. Blackwell, E. Abemayor, and A. H. Mendelsohn, "Hyponatremia and perioperative complications in patients with head and neck squamous cell carcinoma," *Head & Neck*, vol. 38, no. S1, pp. E1370–E1374, 2016.

[8] S. Rinaldi, M. Santoni, G. Leoni et al., "The prognostic and predictive role of hyponatremia in patients with advanced non-small cell lung cancer (NSCLC) with bone metastases," *Support Care Cancer*, vol. 27, no. 4, pp. 1255–1261, 2019.

[9] F. A. B. Schutz, W. Xie, F. Donskov et al., "The impact of low serum sodium on treatment outcome of targeted therapy in metastatic renal cell carcinoma: results from the international metastatic renal cell cancer database consortium," *European Urology*, vol. 65, no. 4, pp. 723–730, 2014.

[10] J. Hashimoto, K. Kato, Y. Ito et al., "Phase II feasibility study of preoperative concurrent chemoradiotherapy with cisplatin plus 5-fluorouracil and elective lymph node irradiation for

clinical stage II/III esophageal squamous cell carcinoma," *International Journal of Clinical Oncology*, vol. 24, no. 1, pp. 60–67, 2019.

[11] A. Shimada, H. Takeuchi, K. Fukuda et al., "Hyponatremia in patients with esophageal cancer treated with chemotherapy including cisplatin," *Esophagus*, vol. 15, no. 4, pp. 209–216, 2018.

[12] M. Tahara, N. Fuse, J. Mizusawa et al., "Phase I/II trial of chemoradiotherapy with concurrent S-1 and cisplatin for clinical stage II/III esophageal carcinoma (JCOG 0604)," *Cancer Science*, vol. 106, no. 10, pp. 1414–1420, 2015.

[13] S. M. Doshi, P. Shah, X. Lei, A. Lahoti, and A. K. Salahudeen, "Hyponatremia in hospitalized cancer patients and its impact on clinical outcomes," *American Journal of Kidney Diseases*, vol. 59, no. 2, pp. 222–228, 2012.

[14] A. A. Onitilo, E. Kio, and S. A. R. Doi, "Tumor-related hyponatremia," *Clinical Medicine & Research*, vol. 5, no. 4, pp. 228–237, 2007.

[15] A. Kitchlu and M. H. Rosner, "Hyponatremia in patients with cancer," *Current Opinion in Nephrology and Hypertension*, vol. 28, no. 5, pp. 433–440, 2019.

[16] R. W. Schrier, "Vasopressin and aquaporin 2 in clinical disorders of water homeostasis," *Seminars in Nephrology*, vol. 28, no. 3, pp. 289–296, 2008.

[17] J. H. Kim, J. H. Park, M. Eisenhut, J. W. Yu, and J. I. Shin, "Inflammasome activation by cell volume regulation and inflammation-associated hyponatremia: a vicious cycle," *Medical Hypotheses*, vol. 93, pp. 117–121, 2016.

[18] S. J. Park and J. I. Shin, "Inflammation and hyponatremia: an underrecognized condition ?," *Korean Journal of Pediatrics*, vol. 56, no. 12, pp. 519–522, 2013.

[19] R. Landgraf, I. Neumann, F. Holsboer, and Q. J. Pittman, "Interleukin-1β stimulates both central and peripheral release of vasopressin and oxytocin in the rat," *The European Journal of Neuroscience*, vol. 7, no. 4, pp. 592–598, 1995.

[20] R. M. Swart, E. J. Hoorn, M. G. Betjes, and R. Zietse, "Hyponatremia and inflammation: the emerging role of interleukin-6 in osmoregulation," *Nephron. Physiology*, vol. 118, no. 2, pp. 45–51, 2011.

[21] V. Compan, A. Baroja-Mazo, G. López-Castejón et al., "Cell volume regulation modulates NLRP3 inflammasome activation," *Immunity*, vol. 37, no. 3, pp. 487–500, 2012.

[22] A. Litan and S. A. Langhans, "Cancer as a channelopathy: ion channels and pumps in tumor development and progression," *Frontiers in Cellular Neuroscience*, vol. 9, no. 86, 2015.

[23] S. H. Lin, L. Wang, B. Myles et al., "Propensity score-based comparison of long-term outcomes with 3-dimensional conformal radiotherapy vs intensity-modulated radiotherapy for esophageal cancer," *International Journal of Radiation Oncology • Biology • Physics*, vol. 84, no. 5, pp. 1078–1085, 2012.

[24] A. Ohba, K. Kato, Y. Ito et al., "Chemoradiation therapy with docetaxel in elderly patients with stage II/III esophageal cancer: a phase 2 trial," *Advances in Radiation Oncology*, vol. 1, no. 4, pp. 230–236, 2016.

[25] S. Servagi-Vernat, G. Créhange, F. Bonnetain, C. Mertens, E. Brain, and J. F. Bosset, "Chemoradiation in elderly esophageal cancer patients: rationale and design of a phase I/II multicenter study (OSAGE)," *BMC Cancer*, vol. 17, no. 1, p. 483, 2017.

[26] J. S. Cooper, M. D. Guo, A. Herskovic et al., "Chemoradiotherapy of locally advanced esophageal cancer: long-term follow-up of a prospective randomized trial (RTOG 85-01). Radiation Therapy Oncology Group," *JAMA*, vol. 281, no. 17, pp. 1623–1627, 1999.

[27] Y. Xia, Y. H. Li, Y. Chen et al., "A phase II trial of concurrent chemoradiotherapy with weekly paclitaxel and carboplatin in advanced oesophageal carcinoma," *International Journal of Clinical Oncology*, vol. 23, no. 3, pp. 458–465, 2018.

Hindawi
Journal of Oncology
Volume 2022, Article ID 8628781, 7 pages
https://doi.org/10.1155/2022/8628781

Research Article

Analysis of Serum IgG1 to Predict Progression and Therapeutic Effect in Patients with Multiple Myeloma

Jingping Yin, Jun Qiu, Zheng Zhang, Bin Feng, Jinfang Shi, and Dong Zheng

Center of Clinical Laboratory, The First Affiliated Hospital of Soochow University, Suzhou 215008, Jiangsu, China

Correspondence should be addressed to Dong Zheng; zhengdong1225@outlook.com

Received 4 January 2022; Accepted 26 January 2022; Published 17 March 2022

Academic Editor: Fu Wang

Objective. The correlation between laboratory indicators and clinical treatment effects and the prognosis of multiple myeloma remains poorly understood. Therefore, our study investigated whether serum IgG subclasses could be employed as potential indicators contributed to evaluate the therapeutic effect and prognosis of patients with multiple myeloma. *Patients and Methods*. Records of patients with multiple myeloma were initially diagnosed at the First Affiliated Hospital of Soochow University, China, from August 1, 2017, to February 28, 2020. The assessment abilities of serological indicators for therapeutic effect were evaluated in patients compared with healthy controls. *Results*. In 560 study patients with multiple myeloma, serum IgA, IgG, IgM, κ-LC, and λ-LC increased by15%, 33.04%, 1.96%, 27.50%, and 26.43%, respectively. Further analysis found that IgG1, IgG2, IgG3, and IgG4 were over the upper limit of the reference range with 26.38%, 6.09%, 8.12%, and 4.64%, respectively. κ-LC and λ-LC were found in the urine in 65.13% and 29.70%, respectively. In peripheral blood, the proportion of $CD3^+CD4^+$, $CD3^-CD19^+$ cells, and $CD4^+/CD8^+$ decreased, whereas $CD3^+CD8^+$ cells and $CD16^+/CD56^+$ increased, and the associated cytokines IL-2, IL-4, IL-6, TNF-α, and IFN-γ were upregulated in patients when compared with healthy controls. Furthermore, the serum levels of IgA, IgG, IgG1, IgG2, IgG3, and IgG4 gradually decreased in patients before, during, and after treatment. Similar results were found in serum and urine κ-LC and λ-LC. *Conclusion*. Serum IgG1 level could serve as the potential indicator for evaluating the therapeutic effect for patients with multiple myeloma. κ-LC and λ-LC also have the potential to be prognostic indicators. More studies are warranted to explore these serological indicators for personalized therapy in the future.

1. Introduction

Multiple myeloma (MM) is a common malignant tumor of the blood system characterized by abnormal proliferation of plasma cells [1,2]. Abnormal proliferation of plasma cells or myeloma cells in the bone marrow leads to bone destruction, and excessive secretion of monoclonal immunoglobulin inhibits normal synthesis of polyclonal immunoglobulin, leading to a series of clinical manifestations [1–3]. That is to say, multiple myeloma leads to multiple organ injuries, and patients eventually suffer from bone pain, fracture, renal insufficiency, anemia, bleeding, hypercalcemia, and susceptibility to infection, which are very complex and easy to be misdiagnosed. In recent years, under the application of bortezomib, thalidomide, Relidomide, and other targeted new drugs, overall survival (OS) and progression-free survival (PFS) of patients have been prolonged [4,5]. With the continuous extension of the curative effect and survival period, better biomarkers are needed to evaluate the treatment effect and prognosis of multiple myeloma and to provide better guidance for continuing treatment [6].

Multiple myeloma can be divided into the following eight types according to the increased type of abnormal immunoglobulin: IgG type, IgA type, IgD type, IgM type, IgE type, light chain type, dual clone type, and nonsecreted type, and two types according to the type of light chain: κ type, λ type [7]. However, the correlation among serum IgG, its subclasses, serum and urine κ-light chain (LC), λ-light chain (LC) levels, and the therapeutic effect and prognosis of multiple myeloma was not fully understood. In this study, we retrospectively analyzed 560 cases of hospitalized multiple myeloma patients from August 1, 2017, to February 28,

2020, in our hospital, and explored the potential biomarkers for evaluating the treatment effects of patients with multiple myeloma. Therefore, we hypothesized that total IgG level, levels of IgG subclasses, κ-LC, and λ-LC predict responsiveness to the therapeutic effect of multiple myeloma. To that end, we evaluated serum total IgG level, IgG subclasses, and serum and urine κ-LC and λ-LC in patients with multiple myeloma and healthy controls, and monitored total IgA, IgG, and IgG subclasses, κ-LC, and λ-LC responses to multiple myeloma patients before, during, and after treatment. Therefore, by analyzing the serological tests of multiple myeloma patients as well as the relationship between the examination indicators and the treatment effect, the aim is to find better biomarkers for the evaluation of treatment effects and prognosis of multiple myeloma.

2. Patients and Methods

2.1. Ethics Statement. The study was conducted in accordance with the Declaration of Helsinki and the Ethical Guidelines for Clinical Research. All serological testing and extractions of information from the database were approved by the Ethics Committee of the First Affiliated Hospital of Soochow University and performed in accordance with the relevant guidelines and regulations. All informed consent forms were signed by patients with multiple myeloma and healthy control.

2.2. Study Population and Samples. 560 patients diagnosed with multiple myeloma at the First Affiliated Hospital of Soochow University, China, from August 1, 2017, to February 28, 2020, were prospectively enrolled in this study.

A 5 ml sample of peripheral blood was collected from enrolled patients with multiple myeloma and healthy controls for measurement of serum immunoglobulin and its subclasses, κ-LC and λ-LC, cytokine concentrations, and peripheral blood of patients with multiple myeloma was collected before, during, and after treatment. An additional 5 ml sample of peripheral blood was collected from patients and healthy controls for measurement of the proportion of $CD3^+CD4^+$, $CD3^-CD19^+$, $CD4^+/CD8^+$, $CD3^+CD8^+$, and $CD16^+CD56^+$ cells. A 10 ml sample of urine was collected from enrolled patients with multiple myeloma and healthy controls for measurement of κ-LC and λ-LC, and urine of some patients was collected before, during, and after treatment. The healthy controls were age and sex matched to patients with multiple myeloma.

2.3. Examination of Serum Immunoglobulin and Its Subclasses, κ-LC, λ-LC, Cytokine Concentration, and Urine κ-LC, λ-LC Concentration. Serum from patients with multiple myeloma and from healthy controls was extracted from fresh peripheral blood after centrifugation. Thereafter, serum IgA, IgG, IgM, κ-LC, and λ-LC levels were assessed by an automatic immunology analyzer (Beckman Image 800, CA, USA) following the method of scatter turbidimetry. IgG1, IgG2, IgG3, and IgG4 were detected with SIMENS BN II (Germany) following the method of scatter turbidimetry.

Table 1: Demographic data for 560 patients with multiple myelomas.

Factor	No. of patients	% of patients	Median	Range
Age (y)				
<40	17	3.04		
40–70	483	86.25		
>70	60	10.71		
Median			59	
Range				28–95
Sex				
Male	333	59.46		
Female	227	40.54		

Serum IL-2, IL-4, IL-6, TNF-α, and IFN-γ were measured with ELISA kits (Beyotime Biotechnology, China) according to the manufacturer's instructions. Urine κ-LC and λ-LC concentration were detected with an automatic immunology analyzer (Beckman Image 800, CA, USA) following the method of scatter turbidimetry.

2.4. Assessment of the Proportion of $CD3^+CD4^+$, $CD3^-CD19^+$, CD4+/CD8+, $CD3^+CD8^+$, and $CD16^+CD56^+$ Cells in Peripheral Blood. Peripheral blood from multiple myeloma patients and healthy controls was lysed with red blood cell lysis buffer. Thereafter, the proportion of $CD3^+CD4^+$, $CD3^-CD19^+$, $CD4^+/CD8^+$, $CD3^+CD8^+$, and $CD16^+CD56^+$ cells was analyzed by the BD Multitest™ IMK kit (Becton, Dickinson and Company, New Jersey, USA) using a flow cytometer (Becton, Dickinson and Company, New Jersey, USA) following the manufacturer's instructions.

2.5. Statistical Analysis. The data were presented as the mean ±SD. Each biological indicator was tested three times in this study. The unpaired Student's t-test was used for differences between the two groups. An ANOVA followed by the Newman–Keuls test was employed for multigroup comparisons. P values <0.05 were considered to indicate statistical significance for all statistical tests.

3. Results

3.1. Baseline Characteristics of Patients with Multiple Myeloma. Criteria for the diagnosis of multiple myeloma were fulfilled for 560 patients seen at the First Affiliated Hospital of Soochow University in Suzhou, China, from August 1, 2017, through February 28, 2020. In 560 patients, three percent of patients were younger than 40 years, and 10.71% were 70 years or older (Table 1); the median age was 59 years, and the range was 28–95 years (Table 1). Of these 560 patients, 59.46% were men (Table 1). The serum hemoglobin, creatinine, calcium, cholesterol, and triglyceride values are listed in Table 2. Anemia was present initially in 80.71% of patients, and a serum creatinine level of 73 mg/dL or more in 41.07%. Serum calcium levels were more than 2.52 mg/dL in 5.54% and less than 2.11 mg/dL in 19.11%. The cholesterol and triglyceride levels were increased by 21.96% and 21.79%, respectively.

Table 2: Laboratory test results in 560 patients with multiple myeloma.

	No. of patients	Range	Decreased N (%)	Normal N (%)	Increased N (%)
Hemoglobin (g/dL)	560	130–175	452 (80.71)	108 (19.29)	0
Creatinine (mg/dL)	560	41–73	36 (6.43)	294 (52.50)	230 (41.07)
Calcium (mg/dL)	560	2.11–2.52	107 (19.11)	422 (75.36)	31 (5.54)
Cholesterol (mg/dL)	560	<5.2	—	437 (78.04)	123 (21.96)
Triglyceride (mg/dL)	560	<1.7	—	438 (78.21)	122 (21.79)

Table 3: Concentration of serum monoclonal proteins in patients with multiple myeloma.

	Decreased N (%)	Normal N (%)	Increased N (%)
IgA ($N = 560$; range: 0.82–4.52 g/L)	351 (62.68)	125 (22.32)	84 (15)
IgG ($N = 560$; range: 7.51–15.6 g/L)	204 (36.43)	171 (30.54)	185 (33.04)
IgM ($N = 560$; range: 0.46–3.04 g/L)	381 (68.04)	168 (30.00)	11 (1.96)
IgG1 ($N = 345$; range: 4.05–10.11 mg/ml)	134 (38.84)	120 (34.78)	91 (26.38)
IgG2 ($N = 345$; range: 1.69–7.86 mg/ml)	196 (56.81)	128 (37.10)	21 (6.09)
IgG3 ($N = 345$; range: 0.11–0.85 mg/ml)	119 (34.49)	198 (57.39)	28 (8.12)
IgG4 ($N = 345$; range: 0.03–2.01 mg/ml)	31 (8.99)	298 (86.38)	16 (4.64)

Table 4: Concentration of serum and urine light chains in patients with multiple myeloma.

	Decreased N (%)	Normal N (%)	Increased N (%)
Serum κ-LC ($N = 560$; range: 629–1350 mg/dL)	252 (45.00)	154 (27.50)	154 (27.50)
Serum λ-LC ($N = 560$; range: 313–723 mg/dL)	240 (42.86)	172 (30.71)	148 (26.43)
Urine κ-LC ($N = 543$; range: <1.85 mg/dL)	—	189 (34.87)	353 (65.13)
Urine λ-LC ($N = 543$; range: <5 mg/dL)	—	381 (70.30)	161 (29.70)

3.2. Serum Levels of Immunoglobulin and Its Subclasses in Patients with Multiple Myeloma. To determine the immunoglobulin level in patients with multiple myeloma, we measured serum IgA, IgG, and IgM levels using chemiluminescence immunoassay. We found that serum IgA levels were 4.52 g/L or more in 15% and less than 0.82 g/L in 62.68%; serum IgM levels were more than 3.04 g/L in 1.96% and less than 0.46 g/L up to 68.04% (Table 3). However, serum IgG levels were more than 15.6 g/L in 33.04% and 36.43% were less than 7.51 g/L (Table 3). These results indicated that a higher proportion of patients with multiple myeloma were of the IgG type.

To further analyze IgG subclass levels in patients with multiple myeloma, we detected the serum levels of IgG1, IgG2, IgG3, and IgG4. We found that IgG2, IgG3, and IgG3 increased by 6.09%, 8.12%, and 4.64%, respectively, in patients with multiple myeloma. However, IgG1 was up to 26.38% (Table 3). These results showed that IgG1 was the main type in four IgG subclasses in multiple myeloma.

We also further analyzed the ratio of IgG subclasses and total IgG. The data showed that the IgG2/IgG ratio significantly decreased in patients compared with healthy controls (Table 3). But IgG1/IgG, IgG3/IgG, and IgG4/IgG ratios increased in patients with multiple myeloma compared with healthy controls, especially IgG4 (Table 3).

3.3. Level of κ-LC and λ-LC Increased in Serum and Urine of Patients with Multiple Myeloma. To analyze κ-LC and λ-LC levels in patients with multiple myeloma, we measured the κ-LC and λ-LC concentrations in serum and urine. In 560 patients, our results showed that κ-LC and λ-LC in serum were increased in patients with multiple myeloma by 27.50% and 26.43%; however, decreased by 45.00% and 42.86%, respectively (Table 4). A similar result was found in urine, κ-LC and λ-LC were increased in patients with multiple myeloma, especially κ-LC up to 65.13% (Table 4).

3.4. Proportion of $CD3^+CD4^+$, $CD3^+CD8^+$, $CD3^-CD19^+$, and $CD16^+CD56^+$ Cells and Associated Cytokines Concentration in Peripheral Blood of Patients with Multiple Myeloma. In order to further analyze the possible mechanism, we measured the proportion of $CD3^+CD4^+$, $CD3^+CD8^+$, $CD3^-CD19^+$, and $CD16^+CD56^+$ cells in peripheral blood of patients with multiple myeloma. In 57 patients with multiple myeloma, our results showed that the proportion of $CD3^+CD4^+$ cells and $CD4^+/CD8^+$ significantly decreased in peripheral blood compared with healthy controls (Table 5). Similarly, the proportion of $CD3^-CD19^+$ cells was decreased in most patients compared with healthy controls (Table 5). However, $CD3^+CD8^+$ and $CD16^+CD56^+$ cells, that were CTL cells and NK cells, significantly increased in peripheral blood of patients compared with healthy controls (Table 5).

We also further measured the immune cell-related cytokines in serum of patients with multiple myeloma. In serum of 57 patients, we found that IL-4, IL-6, IFN-γ, and TNF-α significantly increased in multiple myeloma compared with healthy control, especially IL-6 and IFN-γ (Table 6). However, IL-2 also increased in serum with P value <0.0762 (Table 6). In addition, C-reactive protein (CRP)

Table 5: Proportion of immune cells in 57 patients with multiple myeloma compared with healthy controls.

	Healthy control	MM	P value
$CD3^+$ ($N = 57$; range: 61.1–77%)	68.90 ± 4.58	68.93 ± 14.64	<0.99079
$CD3^+CD4^+$ ($N = 57$; range: 25.8–41.6%)	35.31 ± 4.58	28.95 ± 14.10	<0.02259
$CD3^+CD8^+$ ($N = 57$; range: 18.1–29.6%)	24.90 ± 3.25	38.82 ± 16.11	<0.001
$CD4^+/CD8^+$ ($N = 57$; range: 0.9–1.9)	1.41 ± 0.31	0.96 ± 0.74	<0.00290
$CD3^-CD19^+$ ($N = 57$; range: 7.3–18.2%)	11.04 ± 3.21	7.12 ± 8.15	<0.01654
$CD16^+CD56^+$ ($N = 57$; range: 8.1–25.6%)	13.53 ± 4.36	22.86 ± 13.95	<0.001

Table 6: Concentration of serum cytokines in patients with multiple myeloma.

	Healthy control	Multiple myeloma	P value
IL-2 (pg/ml, $N = 57$)	0.60 ± 1.23	2.08 ± 4.38	<0.0762
IL-4 (pg/ml, $N = 57$)	0.44 ± 0.83	2.13 ± 3.92	<0.0226
IL-6 (pg/ml, $N = 57$)	0.38 ± 0.64	10.18 ± 14.67	<0.0005
TNF-α (pg/ml, $N = 57$)	1.52 ± 1.39	4.08 ± 6.88	<0.0268
IFN-γ (pg/ml, $N = 57$)	0.44 ± 1.34	4.06 ± 7.16	<0.0075
CRP (μg/ml, $N = 560$)	3.21 ± 1.81	47.67 ± 66.26	<0.0001

significantly upregulated in serum of patients with multiple myeloma compared with healthy controls (Table 6).

3.5. Level of IgG Subclasses, κ-LC, and λ-LC Decreased in Patients with Multiple Myeloma after Treatment. To evaluate the role of IgA, IgG subclasses, κ-LC, and λ-LC in the treatment of multiple myeloma, we extracted a part of patients with over upper limit of reference range of testing items and analyzed the serum or urine levels of IgA, IgG, IgG1, IgG2, IgG3, and IgG4 and κ-LC and λ-LC in patients with multiple myeloma before, during, and after treatment. Our results showed that the levels of IgG and IgG1 gradually decreased before, during, and after treatment, and especially after treatment, they obviously decreased (Table 7). Similar results were found in IgA, IgG2, IgG3, and IgG4 in the processes of before, during, and after treatment (Table 7).

We also extracted patients with over the upper limit of the reference range and analyzed the serum and urine levels of κ-LC and λ-LC in patients with multiple myeloma before, during, and after treatment. The results showed that the serum levels of κ-LC and λ-LC gradually and significantly decreased before, during, and after treatment (Table 8). Similarly, the levels of κ-LC and λ-LC in urine gradually and significantly decreased before, during, and after treatment, especially after treatment compared with before treatment (Table 8).

Table 7: Concentration of serum monoclonal proteins in patients with multiple myeloma before, during, and after treatment.

	Before treatment	During treatment	After treatment
IgA ($N = 84$)	28.80 ± 23.72	10.80 ± 11.98*	9.90 ± 13.92*
IgG ($N = 185$)	50.69 ± 33.24	17.43 ± 13.16*	13.25 ± 10.19*#
IgG1 ($N = 91$)	37.45 ± 21.30	11.71 ± 6.92*	7.95 ± 3.54*
IgG2 ($N = 21$)	17.11 ± 10.54	9.59 ± 5.45*	7.6 ± 9.01*
IgG3 ($N = 28$)	5.82 ± 7.38	0.84 ± 0.49*	0.66 ± 0.39*
IgG4 ($N = 16$)	35.51 ± 30.32	12.82 ± 18.92*	13.87 ± 7.26*

Compared with the before treatment group, $^*P < 0.05$; compared with the during treatment group, $^\#P < 0.05$.

4. Discussion

In our present study, the age and sex distributions of the 560 patients were similar to those in foreign studies of the 1027 patients with multiple myeloma seen at the Mayo Clinic [8] and a domestic study of the 304 patients with multiple myeloma seen at the Beijing Chaoyang Hospital [9]. However, in the current study, 10.71% of patients were 70 years or older, compared with 38% in the earlier foreign study. The incidence of multiple myeloma is much lower in the elderly population, and the lower percentage of patients 70 years or older in the current series is probably due to regional differences. In addition, some patients may not seek medical treatment due to differences in economic status, health concepts, and medical resources, so there are some differences in age distribution, especially among the elderly. This has yet to be proved. In this study, only 3.04% of patients were younger than 40 years at diagnosis, and this percentage is similar to foreign and domestic studies.

As expected, anemia was a major manifestation of myeloma and was present initially in 80.71% of patients. The mechanism in most patients is inadequate production of red blood cells due to either erythropoietin deficiency from accompanying renal failure or pronounced marrow replacement by myeloma cells [10–12]. The serum creatinine level was increased in 41.07% of our patients. The major causes of renal failure are myeloma kidney and hypercalcemia [13,14]. And dehydration and hyperuricemia are also reasons for renal failure [13–15].

Monoclonal immunoglobulin increases in the serum of patients with multiple myeloma, leading to dysfunction for the synthesis of normal polyclonal immunoglobulin, which makes it is easy to cause infection [16–18]. In the early stages of multiple myeloma, the sensitivity of immunoglobulin quantification is lower, and it is easy to miss the detection. However, in diagnosed patients, the determination of immunoglobulin content is helpful for observing the curative

Table 8: Concentration of serum and urine light chains in patients with multiple myeloma before, during, and after treatment.

	Before treatment	During treatment	After treatment
Serum κ-LC ($N = 74$)	5102.57 ± 5198.35	$1580.39 \pm 1214.76^{*}$	$1169.37 \pm 963.99^{*\dagger}$
Serum λ-LC ($N = 83$)	3488.49 ± 3816.87	$1099.27 \pm 1070.41^{*}$	$761.48 \pm 727.77^{*\dagger}$
Urine κ-LC ($N = 164$)	145.71 ± 526.10	$33.50 \pm 206.75^{*}$	$15.82 \pm 90.29^{*}$
Urine λ-LC ($N = 86$)	656.10 ± 1413.11	$130.30 \pm 473.83^{*}$	$168.07 \pm 648.79^{*}$

Compared with the before treatment group, $^{*}P < 0.05$; compared with the during treatment group, $^{\dagger}P < 0.05$.

effect. In this study, the expression of the IgG type was the highest (33.04%) in patients with multiple myeloma, the expression of the IgA type (15%) was lower than that of the IgG type, and the expression of the IgM type (1.96%) was the lowest, which was consistent with the previous study. The other part of patients with multiple myeloma showed lower IgG, IgA, and IgM, owing to light chain type, nonsecreted type, IgD type, IgE type, etc. Most myeloma cells not only synthesize and secrete a large amount of monoclonal immunoglobulin but also have a imbalanced ratio of light and heavy chains. Serum light chain is one of the higher sensitive indicators for the clonal plasma cells in patients [19–21]. Our results showed that κ-LC and λ-LC significantly increased in the serum and urine of patients with multiple myeloma, consistent with previous studies. Serum and urine levels of light chain have high sensitivity and specificity, which are expected to be helpful for early detection and rapid diagnosis for patients with multiple myeloma via noninvasive detection.

The antitumor immune response of patients with multiple myeloma is dominated by cellular immunity [22]. T cell subsets play an important role in regulating the immune response and maintaining the immune stability in the body. In this study, $CD3^{+}CD4^{+}$ and $CD4^{+}/CD8^{+}$ ratios were significantly reduced, and $CD3^{+}CD8^{+}$ was increased in patients with multiple myeloma at the initial and progressive stages, which was consistent with the previous reports [23]. It can be seen that multiple myeloma patients have abnormal cellular immune regulation, and the immune function is closely related to the disease state. After effective treatment, $CD3^{+}CD4^{+}$, $CD4^{+}/CD8^{+}$ ratio, and $CD3^{+}CD8^{+}$ basically returned to normal. Therefore, by measuring T cell subsets in peripheral blood, the latest trends of the disease can be monitored. B lymphocytes are the major cells in the immune system that produce antibodies, present antigens, and secrete cytokines involved in immune regulation. Our data showed that B cells were significantly lower than healthy control in peripheral blood of patients with multiple myeloma, consistent with other researchers [23]. However, CRP may inhibit the T helper cells function, which would restrain IL-4 production, thereby interfering with polyclonal B cell activation [24]. It had reported that IL-6 production could be induced by TNF-α in a dose-dependent manner in myeloma cells [25]. NK cells can directly kill tumors and virus-infected cells. It plays an important role in the body's immune monitoring and early anti-infection immune process. Our results showed that NK cells were significantly higher than healthy controls in the initial stage, which was consistent with the report of Chan et al. [26]. It indicated that multiple myeloma patients still had the ability of immune self-stabilization in the early stage, and the NK cell function was significantly impaired in the progressive stage. Therefore, multiple myeloma patients have extensive immunodeficiency. Our research data indicate that there are abnormalities of $CD3^{+}CD4^{+}$, $CD3^{+}CD8^{+}$, $CD3^{-}CD19^{+}$, and $CD16^{+}CD56^{+}$ cells in patients with multiple myeloma. Whether these abnormalities are pathogenic factors of multiple myeloma (MM) or the result of the onset of MM. It is still poorly understood and needs to be further explored. In conclusion, lymphocyte subsets and related cytokines play an important role in the development of multiple myeloma, and monitoring these indicators can be used as potential biomarkers for the diagnosis of MM patients and monitoring treatment efficacy.

Several important prognostic factors were identified in our and other researcher's studies [8]. Most of these also have been identified as markers of high-risk disease in other studies [6]; thus, they are reliable and well-validated tools for counseling and patient care decisions. Many of the prognostic factors identified are simple clinical or laboratory variables such as age, hemoglobin, serum calcium, and serum creatinine values, all of which can be easily determined in all patients [27]. Although not analyzed in this study, other studies have shown that high lactate dehydrogenase levels [28], deletion of chromosome 13 [29,30], and circulating plasma cells [31] are other important adverse prognostic factors in multiple myeloma. Our study made interesting findings that IgG, IgG1, IgG2, IgG3, IgG4, κ-LC, and λ-LC, especially IgG1, κ-LC, and λ-LC, showed great changes in the process of treatment, that is, before, during, and after treatment. Therefore, these factors could be considered as prognostic factors, even as potential biomarkers for treatment effects for multiple myeloma.

5. Conclusion

In summary, by analyzing the serological and urine examinations of multiple myeloma patients as well as the correlation between the examination indicators and the treatment effect, we found that IgG1 expression was the highest in patients with multiple myeloma, and IgG1 changed greatly before, during, and after treatment. Therefore, IgG1 has great potential in predicting the progression and therapeutic efficacy of multiple myeloma patients. In this study, we also found that κ-LC and λ-LC, lymphocyte subsets, and related cytokines can be used to evaluate the therapeutic effect and prognosis of multiple myeloma.

This study, however, had some limitations. First, considerable numbers of patients with multiple myeloma did

not detect all test items, so there is not sufficient data to support more accurate conclusions, such as IgG2 ($n = 21$), IgG3 ($n = 28$), and IgG4 ($n = 16$) in this study. Second, the correlation of IgG subclasses with overall survival (OS) and progression-free survival (PFS) was not shown, because there were not enough patients followed up. Therefore, more prospective studies from different medical centers are warranted to further characterize these factors for prediction and evaluation of the treatment effect and prognosis of multiple myeloma. The use of powerful, independent multiple prognostic factors in multiple myeloma has overcome the limitations of the Durie–Salmon staging system, which has been used for almost three decades as a staging and prognostic system for multiple myeloma.

Data Availability

The data used to support the findings of this study are included within the article.

Conflicts of Interest

The authors declare that they have no conflicts of interest.

Authors' Contributions

Jingpin Yin and Jun Qiu contributed equally to this work.

References

[1] K. Brigle and B. Rogers, "Pathobiology and diagnosis of multiple myeloma," *Seminars in Oncology Nursing*, vol. 33, no. 3, pp. 225–236, 2017.

[2] G. Bianchi and N. C. Munshi, "Pathogenesis beyond the cancer clone(s) in multiple myeloma," *Blood*, vol. 125, no. 20, pp. 3049–3058, 2015.

[3] C. Panaroni, A. J. Yee, and N. S. Raje, "Myeloma and bone disease," *Current Osteoporosis Reports*, vol. 15, no. 5, pp. 483–498, 2017.

[4] G. Z. Yang, W. M. Chen, and Y. Wu, "Bortezomib, dexamethasone plus thalidomide for treatment of newly diagnosed multiple myeloma patients with or without renal impairment," *Chinese Journal of Cancer Research*, vol. 25, pp. 155–160, 2013.

[5] J. Chen, H. Liu, L. J. Li et al., "Clinical features and treatment outcome of elderly multiple myeloma patients with impaired renal function," *Journal of Clinical Laboratory Analysis*, vol. 33, Article ID e22888, 2019.

[6] A. Levin, P. Hari, and B. Dhakal, "Novel biomarkers in multiple myeloma," *Translational Research*, vol. 201, pp. 49–59, 2018.

[7] W. Wang, C.-X. Zhang, Z.-L. Li, M. Gong, and Y.-G. Ma, "Detection of intracellular IgD using Flow cytometry could Be a novel and supplementary method to diagnose IgD multiple myeloma," *BMC Cancer*, vol. 18, no. 1, p. 650, 2018.

[8] R. A. Kyle, M. A. Gertz, T. E. Witzig et al., "Review of 1027 patients with newly diagnosed multiple myeloma," *Mayo Clinic Proceedings*, vol. 78, no. 1, pp. 21–33, 2003.

[9] Y. Zhang, X. L. Chen, W. M. Chen, and H. B. Zhou, "Prognostic nomogram for the overall survival of patients with newly diagnosed multiple myeloma," *BioMed Research International*, vol. 2019, Article ID 5652935, 10 pages, 2019.

[10] F. Silvestris, P. Cafforio, M. Tucci, and F. Dammacco, "Negative regulation of erythroblast maturation by Fas-L+/TRAIL+ highly malignant plasma cells: a major pathogenetic mechanism of anemia in multiple myeloma," *Blood*, vol. 99, no. 4, pp. 1305–1313, 2002.

[11] C. A. Baraldi-Junkins, A. C. Beck, and G. Rothstein, "Hematopoiesis and cytokines," *Hematology-Oncology Clinics of North America*, vol. 14, no. 1, pp. 45–61, 2000.

[12] M. Mittelman, "The implications of anemia in multiple myeloma," *Clinical Lymphoma*, vol. 4, no. Suppl 1, pp. S23–S29, 2003.

[13] A. Z. Salahuddin, M. R. Alam, R. M. Hossain et al., "Renal involvement as a presenting feature of multiple myeloma," *Mymensingh Medical Journal*, vol. 28, pp. 527–535, 2019.

[14] A. Hussain, H. F. Almenfi, A. M. Almehdewi, M. S. Hamza, M. S. Bhat, and N. P. Vijayashankar, "Laboratory features of newly diagnosed multiple myeloma patients," *Cureus*, vol. 11, Article ID e4716, 2019.

[15] R. Ryšavá, "Renal failure in multiple myeloma and its treatment. Renální selhání u mnohočetného myelomu a jeho léčba," *Vnitrní Lékarství*, vol. 66, no. 7, pp. 425–431, 2020.

[16] S. V. Rajkumar and S. Kumar, "Multiple myeloma: diagnosis and treatment," *Mayo Clinic Proceedings*, vol. 91, no. 1, pp. 101–119, 2016.

[17] T. Morrison, R. A. Booth, K. Hauff, P. Berardi, and A. Visram, "Laboratory assessment of multiple myeloma," *Advances in Clinical Chemistry*, vol. 89, pp. 1–58, 2019.

[18] S. K. Kumar, N. S. Callander, M. Alsina et al., "Multiple myeloma, version 3.2017, NCCN clinical practice guidelines in oncology," *Journal of the National Comprehensive Cancer Network*, vol. 15, no. 2, pp. 230–269, 2017.

[19] M. Andrei and J. C. Wang, "Cutaneous light chain amyloidosis with multiple myeloma: a concise review," *Hematology/Oncology and Stem Cell Therapy*, vol. 12, no. 2, pp. 71–81, 2019.

[20] H. Y. Ting, P. Sthaneshwar, P. C. Bee, H. Shanmugam, and M. Lim, "Heavy/light chain assay in the monitoring of multiple myeloma," *Pathology*, vol. 51, no. 5, pp. 507–511, 2019.

[21] J. L. J. Heaney, J. P. Campbell, A. E. Griffin et al., "Diagnosis and monitoring for light chain only and oligosecretory myeloma using serum free light chain tests," *British Journal of Haematology*, vol. 178, no. 2, pp. 220–230, 2017.

[22] Y. Kawano, A. M. Roccaro, I. M. Ghobrial, and J. Azzi, "Multiple myeloma and the immune microenvironment," *Current Cancer Drug Targets*, vol. 17, pp. 806–818, 2017.

[23] J. F. San Miguel, M. Gonzale, A. Gascon et al., "Lymphoid subsets and prognostic factors in multiple myeloma cooperative group for the study of monoclonal gammopathies," *British Journal of Haematology*, vol. 80, pp. 305–309, 1992.

[24] Y. Long, C. Xia, Y. Sun et al., "Increased circulating PD-1hiCXCR5- peripheral helper T cells are associated with disease severity of active ulcerative colitis patients," *Immunology Letters*, vol. 233, pp. 2–10, 2021.

[25] C. Lee, J. I. Oh, J. Park et al., "TNF α mediated IL-6 secretion is regulated by JAK/STAT pathway but not by MEK phosphorylation and AKT phosphorylation in U266 multiple myeloma cells," *BioMed Research International*, vol. 2013, Article ID 80135, 8 pages, 2013.

[26] W. C. Chan, L. B. Gu, A. Masih et al., "Large granular lymphocyte proliferation with the natural killer-cell phenotype," *American Journal of Clinical Pathology*, vol. 97, no. 3, pp. 353–358, 1992.

[27] S. V. Rajkumar and P. R. Greipp, "Prognostic factors in multiple myeloma," *Hematology/Oncology Clinics of North America*, vol. 13, no. 6, pp. 1295–1314, 1999.

[28] M. A. Dimopoulos, B. Barlogie, T. L. Smith, and R. Alexanian, "High serum lactate dehydrogenase level as a marker for drug resistance and short survival in multiple myeloma," *Annals of Internal Medicine*, vol. 115, no. 12, pp. 931–935, 1991.

[29] R. Fonseca, D. Harrington, M. M. Oken et al., "Biological and prognostic significance of interphase fluorescence in situ hybridization detection of chromosome 13 abnormalities (delta13) in multiple myeloma: an eastern cooperative oncology group study," *Cancer Research*, vol. 62, pp. 715–720, 2002.

[30] G. Tricot, J. R. Sawyer, S. Jagannath et al., "Unique role of cytogenetics in the prognosis of patients with myeloma receiving high-dose therapy and autotransplants," *Journal of Clinical Oncology*, vol. 15, no. 7, pp. 2659–2666, 1997.

[31] T. Witzig, M. Gertz, J. Lust, R. Kyle, W. O'Fallon, and P. Greipp, "Peripheral blood monoclonal plasma cells as a predictor of survival in patients with multiple myeloma," *Blood*, vol. 88, no. 5, pp. 1780–1787, 1996.

Hindawi
Journal of Oncology
Volume 2022, Article ID 3793318, 14 pages
https://doi.org/10.1155/2022/3793318

Research Article

miR-4731-5p Enhances Apoptosis and Alleviates Epithelial-Mesenchymal Transition through Targeting RPLP0 in Non-Small-Cell Lung Cancer

Chang Chang[1] **and Meilin Xu**[2]

[1]*Department of Pathology, The First Affiliated Hospital, and College of Clinical Medicine of Henan University of Science and Technology, Luoyang 471003, China*
[2]*Department of Pathology, Tianjin Chest Hospital, Tianjin Province 300222, China*

Correspondence should be addressed to Chang Chang; changchangpat@126.com

Received 24 December 2021; Revised 20 January 2022; Accepted 22 January 2022; Published 17 March 2022

Academic Editor: Fu Wang

Background/Aim. MircoRNA-4731-5p (miR-4731-5p) is a new miRNA involved in different human cancers, but its function has not been clarified in non-small-cell lung cancer (NSCLC). The present study attended to resolve the role of miR-4731-5p in NSCLC. *Materials and Methods*. The expression level of miR-4731-5p or ribosomal protein large P0 (RPLP0) and NSCLC clinicopathologic characteristics were analyzed. The binding between miR-4731-5p and RPLP0 was confirmed by TargetScan prediction and luciferase reporter experiment. Also, the probable role of miR-4731-5p in NSCLC via RPLP0 was elaborated by the MTT, western blotting, immunofluorescence, transwell, flow cytometry, and TUNEL assays. Moreover, *in vivo* verification was conducted in xenografted nude mice. *Results*. The level of miR-4731-5p was notably declined *in vivo* and *in vitro*, which was involved in the prognosis of lung cancer patients. The miR-4731-5p mimic could remarkably restrain cell viability, invasion, and the translational expression level of vimentin and e-cadherin, with promoted cell apoptosis in NSCLC, which were notably reversed by RPLP0 overexpression. *Conclusion*. miR-4731-5p/RPLP0 axis might be an underlying therapeutic target for NSCLC.

1. Introduction

Lung cancer has become the dominating cause of death from all kinds of cancers worldwide and is currently the most frequently diagnosed malignancy [1]. It is reported that about 80% of lung cancer is authenticated as non-small-cell lung cancer (NSCLC), including cell carcinoma and adenocarcinoma [2]. The molecularly targeted systemic therapies of NSCLC have significantly improved the outcomes for patients, but the disease control rate and increased overall 5-year survival rate remain poor [3]. Therefore, expounding the pathogenesis of lung cancer is quite necessary and also can contribute to the development of an effective treatment.

A growing body of researches has exhibited differential expression of miRNAs in the development of NSCLC [4–6]. miR-4731-5p is a novel miRNA that has rarely been studied, which is associated with tumor suppression [7], and was able to distinguish tumor stage with high specificity and sensitivity [8], indicating miR-4731 may have a tumor-suppressive activity [7]. Some evidences show that miR-4731-5p suppresses glioma development [9]. Additionally, miR-4731-5p has been exhibited to be down-expressed in several cancers, such as oral lichen planus [10] and glioblastoma [9,11]. Nevertheless, the effect of miR-4731-5p on NSCLC still needs further studies.

The human ribosomal P complex, which contains RPLP0, RPLP1, and RPLP2, accelerates protein synthesis through recruiting translational factors. RPLP0 is a member of the RPLP family and a crucial modulator in the progress of many diseases, including cancers. The overexpression of RPLP0 mRNA is seen in human colorectal and hepatocellular carcinomas [12]. RPLP0 contributes to the onset and

development of gastric cancer [13] and gynecologic tumors [14]. Although the previous study reports that RPLP0 always acts as a reference gene for gene expression studies on NSCLC [15], more and more literature confirm that RPLP0 is differently expressed in lung cancer. Ali et al. [16] show that RPLP0 exhibits low expression stability in the NSCLC cell lines NCI-H A549, NCI-H446, and NCI-H460. Moreover, the level of RPLP0 is demonstrated to be down-regulated in samples from patients with squamous-cell carcinoma compared to that in normal tissues based on the RNA sequencing (RNA-Seq) analysis [17]. Furthermore, our bioinformatics analysis, which predicted that RPLP0 and miR-4731-5p were each other's targets, led us to hypothesize that RPLP0 was silenced by miR-4731-5p.

Thus, the underlying mechanism of miR-4731-5p in NSCLC was illuminated in the present study. The results demonstrated that the level of miR-4731-5p was dramatically diminished in NSCLC tissues. The upregulation of miR-4731-5p may inhibit NSCLC development by directly decreasing the expression of RPLP0.

2. Materials and Methods

2.1. Sample Collection. 35 pairs of NSCLC tissues and relevant normal tissue were acquired from the Tianjin Chest Hospital. All samples were resected during the operation and instantly preserved in liquid nitrogen for the following study. The experiment was in agreement with the ethics committee of the Tianjin Chest Hospital and all participants enrolled in the study offered signed informed consent.

Five NSCLC cell lines, NCI-H1299, NCI-H596, NCI-H1650, HCC827, and A549, and human normal lung epithelial cell (BEAS-2B cell) were bought from the American Type Culture Collection (ATCC, Manassas, VA, USA). Cell lines were sustained in RPMI 1640 medium (Sigma-Aldrich, St. Louis, MO, USA) supplied with 1% streptomycin-penicillin (Sigma-Aldrich) and 10% fetal bovine serum (FBS, Gibco, Rockville, MD, USA) at 37°C with 5% CO_2.

2.2. Cell Transfection. Cells were plated into 6-well plates with an inoculation density of 3×10^6 cells/well and then maintained for 24 h at 37°C with 5% CO_2. When the cells reached 70–80% confluence, 100 nmol/L miR-4731-5p mimic was transfected into the cells through Lipofectamine 3000 (Invitrogen, Carlsbad, CA, USA) based on the operating manual. For the up-regulation of RPLP0 expression, pcDNA3.1 containing the full-length complementary DNA (cDNA) of RPLP0 (5 μg) was used in the NSCLC cells. The cells were gathered for subsequent detection after 48 h of transfection.

2.3. RNA Separation and qRT-PCR Detection. Total RNAs were obtained using TRIzol reagent (Thermo Fisher, CA, USA) based on the instructions. Next, the PrimeScript® RT reagent kit (Takara Bio, Shiga, Japan) was applied to reversely transcribe 1 μg/ml RNA into cDNA. qRT-PCR reactions were conducted with a SYBR Green PCR kit (Takara, Dalian, China) in a CFX96 real-time PCR detection system (Bio-Rad, Hercules, CA, USA). The PCR primer sequences are listed as follows: miR-4731-5p, forward, 5′-GGGGGCCACATGAGT-3′, reverse, 5′-GGTCCAGTTTTTTTTTTTTTTCACA-3′; RPLP0, forward, 5′-TGGCTAGCATGCCCAGGGAAGACAGGGCG-3′, reverse, 5′-CGGAATTCGGTCAAAG AGAC-CAAATCCCATATCC-3′. The PCR amplification condition is listed as follows: 95°C for 10 min, and 95°C for 20 s and 58°C for 60 s of 40 cycles. The data were quantified with the $2^{-\Delta\Delta Ct}$ method.

2.4. Western Blotting. The harvested cells were disrupted through RIPA lysis buffer (Beyotime, Shanghai, China) and cellular proteins were collected via centrifugation. The protein concentration of the lysate was analyzed with the BCA kit (Bio-Rad, Richmond, CA, USA). The protein samples were segregated through 10% SDS-PAGE, and subsequently electroblotted onto PVDF membranes. Then, the membrane sample was sealed with 5% skim milk (Anchor, New Zealand) for 60 min at room temperature, and hatched with the corresponding primary antibodies at 4°C overnight. The primary antibodies supplied in this present study are listed as follows: anti-RPLP0 (1 : 100; ab23750), anti-e-cadherin (1 : 100; ab18103), anti-vimentin (1 : 100; ab59396), anti-Bcl-2 (1 : 1000; ab32167), and anti-Bax (1 : 1000; ab32517; all in Abcam, Cambridge, UK). Then, the appropriate secondary antibodies were supplied and hatched for 1 hour at 20°C. All bands were imaged with Amersham ECL Kit (GE Healthcare, UK).

2.5. MTT Assay. Cells were plated into 96-well plates with an inoculation density of 3×10^3 cells/well and hatched with 10 μl MTT solution (Sigma) at the indicated time for 4 h. Subsequently, the supernatant fluid was abandoned, and each well was appended with 100 μl DMSO to dissolve the crystals. The enzyme-labelling measuring instrument was applied to determine the absorbance at 570 nm, and each individual experiment was repeated for 3 times at least.

2.6. Electronic Microscope Observation. The cells were maintained in 6-well plates with an inoculation density of 1×10^5 cells/ml and then maintained for 24 h to promote the total attachment to the plates' surface. Subsequently, the cells were diverted with the miR-4731-5p mimic or mimic-NC. The cells were imaged by an inverted light microscope (Nikon Corporation, Tokyo, Japan).

2.7. Immunofluorescence Staining. Cells were administrated with vehicle for 24 h. After blocking in phosphate buffer saline (PBS) containing 0.05% BSA, the cells were hatched with primary antibodies overnight at 4°C. Then, the cells were maintained with anti-rabbit immunoglobulin *G* (IgG) coupled to Alexa-Fluor-630 or -488 (2 μg/mL) at room temperature for 60 min. The nuclear component was counterstained with DAPI (Vector Laboratories, Burlingame, CA, USA). The results were imaged under a fluorescence microscope (Carl Zeiss, Thornwood, NY, USA).

2.8. Transwell Assays. Transwell inserts were used to measure the invasion abilities with matrigel. The transwell chamber was loaded with 200 μl of cell suspension with 5×10^5/ml cells. Then, the lower transwell chamber was loaded with DMEM added with FBS (500 μl). The cells were rinsed by PBS buffer after being maintained at 37°C with 5% CO_2 for 36 h. Next, the cells were immobilized with 100% ethanol and stained with 0.1% crystal violet solution. For microscope-based observations, five random fields were chosen to determine the cell numbers.

2.9. Apoptosis Analysis. Cell apoptosis was assessed with the flow cytometry experiment. Briefly, the cells were gathered and rinsed by PBS twice after transfection. Subsequently, 5 μl Annexin V/FITC and propidium iodide (PI) were applied to stain the cells for quarter at room temperature following resuspension by 0.5 ml of bind buffer. The apoptosis of the cells was measured on a FACScan flow cytometer via CellQuest software (BD Biosciences).

2.10. TUNEL. The *in situ* cell death detection kit (Roche, Budapest, Hungary) was utilized to evaluate the TUNEL assay based on the operating manual. The tissue sample was immobilized in 10% formaldehyde solution, and then embedded with paraffin. 5 μm sections were cut and dehydrated in graded concentrations of ethanol, cleared in xylene. Then, the slides were hatched with proteinase K for 20 min at 37°C, blocked with 3% H_2O_2 for 10 min, and fixed with 4% paraformaldehyde. Next, the sections were hatched with the TUNEL reaction mixture for 1 h at 37°C. For the detection of fluorescein-labeled DNA, horseradish peroxidase (HRP)-conjugated antibody was added. The number of TUNEL-positive cells among the total number of cells was counted.

2.11. Luciferase Reporter Experiment. The possible binding between miR-4731-5p and RPLP0 was predicted using the TargetScan website (http://www.targetscan.org/vert_71/). The pmiRGLO vector (Promega, Madison, WI, USA) was interposed with the wild type (WT) and mutant 3′-UTR of RPLP0. The miR-4731-5p-mimics or specified luciferase reporter vectors were transfected into the cells. Luciferase activities were assessed by a dual-luciferase reporter assay system (Promega) after 48 h of transfection.

2.12. In Vivo Assay. Thymus-free nude mice (nu/nu; 8-week-old males) were bought from the Experimental Animal Center of Tianjin Chest Hospital. The mice were housed individually and fed in a temperature-controlled animal room with 12 hours/12 hours light-dark cycle. Animal assays were ratified by the Tianjin Chest Hospital (SYXK Jin 2019–0001). The lentiviral vector with OE- miR-4731-5p or its negative control (OE-NC) acquired from GeneChem (Shanghai, China) was injected into the backs of nude mice subcutaneously. Then, the tumor volume was supervised every 5 d by an electronic vernier caliper when they were visible. The mice were sacrificed with an intraperitoneal injection of sodium pentobarbital (200 mg/kg) after the introduction of tumor cells for 28 days, and also the tumors samples were removed and weighed. The tumor size was quantified based on the formula: volume = $1/2 \times \text{length} \times \text{width}^2$.

2.13. Immunohistochemistry. Immunohistochemistry was performed using the e-cadherin (Abcam) and vimentin antibodies (Abcam). Slides were repaired with sodium citrate buffer (10 mM, pH 6.0) at 94°C for 25 min, and then got back to room temperature. After rinsing, 1% bovine serum albumin (BSA) was utilized to seal the sections for 30 min. Then, the sections were hatched with biotinylated secondary antibody. Restaining with hematoxylin was performed after the slices were washed with PBS for 3×10 min.

2.14. Statistical Analysis. All statistical data were analyzed through the SPSS 20.0 software (IBM, Armonk, New York, USA). The results were shown as mean ± standard deviation (SD). Statistical differences between the two groups were determined by Student's *t*-test, whereas differences among multiple groups were tested by one-way analysis of variance (ANOVA) followed by the *post hoc* Bonferroni test. The survival curve was established by the Kaplan–Meier method and the difference was evaluated with the log-rank test. $p < 0.05$ represents significant difference.

3. Results

3.1. miR-4731-5p Level Was Reduced in NSCLC Cell Lines and Tissues and Related in the Prognosis of NSCLC. The expressions of miR-4731-5p in the NSCLC tissues and five NSCLC cell lines were first examined via qRT-PCR. In comparison with the control group, the relative level of miR-4731-5p was markedly declined in the tissues and cells of NSCLC (Figures 1(a) and 1(b)). Since the expression level of miR-4731-5p in A549 and NCI-H1299 NSCLC cells was obviously diminished relative to that in the other three cell lines, A549 and NCI-H1299 NSCLC cells were selected for the following evaluation. Moreover, the transfection of the miR-4731-5p mimic markedly elevated the level of miR-4731-5p compared with the mimic-NC group in A549 and NCI-H1299 cells (Figures 1(c) and 1(d)). Besides, the interaction between the level of miR-4731-5p and NSCLC clinicopathologic characteristics was examined (Table 1). The expression level of miR-4731-5p was observably related in lymph node metastasis, distance metastasis, and TNM stage, though no statistical difference was indicated between the level of miR-4731-5p and age, gender, smoking, and tumor size. Furthermore, patients with lower expression levels of miR-4731-5p generally showed lymph node metastasis, distance metastasis, and III/IV TNM stage. Altogether, the results clarified that miR-4731-5p was declined in NSCLC tissues and cell lines, which was tightly relevant in the prognosis of NSCLC.

3.2. The Upregulation of miR-4731-5p Reduced Cell Viability, Invasion, and EMT with Elevated Apoptosis in both A549 and NCI-H1299 Cells. To identify the role of miR-4731-5p in the

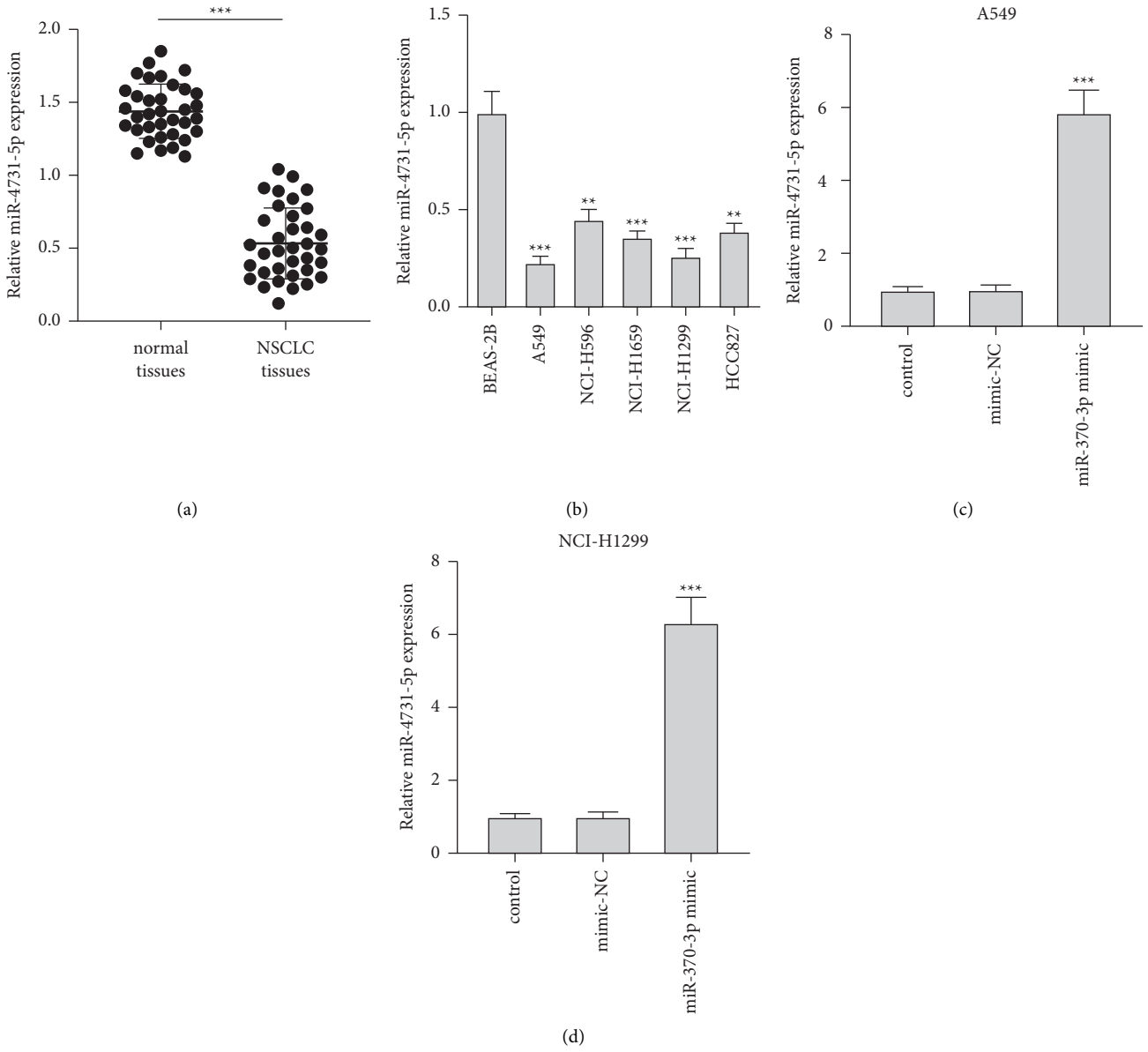

Figure 1: miR-4731-5p is down-expressed in NSCLC tissues and cell lines. (a) The level of miR-4731-5p in NSCLC tissues and normal tissues was measured by qRT-PCR. (b) The level of miR-4731-5p in BEAS-2B and five NSCLC cell lines (A549, NCI-H596, NCI-H1650, NCI-H1299, and HCC82) was assessed by qRT-PCR. (c, d) A549 and NCI-H1299 cells were treated with the miR-4731-5p mimic, and then the level of miR-4731-5p in the two cells was examined by qRT-PCR. $^{**}p < 0.01$ and $^{***}p < 0.001$ relative to the control group.

NSCLC cells, the miR-4731-5p mimic and mimic-NC were diverted into A549 and NCI-H1299 cells separately. The upregulation of miR-4731-5p notably dampened the cell viability of A549 and NCI-H1299 cells relative to the mimic-NC group (Figure 2(a)). Morphological alterations were also discovered. As indicated in Figure 2(b), both A549 and NCI-H1299 cells treated with the miR-4731-5p mimic became sparser with an obvious spindle shape change compared with those in the mimic-NC group. To illustrate the role of miR-4731-5p in EMT, the translational expressions of e-cadherin and vimentin were analyzed via western blot. The miR-4731-5p mimic prominently elevated the expression level of e-cadherin protein with declined translational levels of vimentin both in A549 and NCI-H1299 cells relative to those in the mimic-NC group (Figures 2(c)–2(e)). Moreover, immunofluorescence results verified that the miR-4731-5p mimic memorably attenuated the level of vimentin both in A549 and NCI-H1299 cells (Figure 2(f)). Besides, the invasion ability of A549 and NCI-H1299 cells transfected with the miR-4731-5p-mimic was notably declined relative to that in the mimic-NC group (Figure 2(g)). However, the transfection of the miR-4731-5p-mimic signally promoted the apoptosis rate of both the cells, as shown by an increase in the apoptosis rate (Figure 2(h)), the Bax protein expression level (Figures 2(i)–2(k)), and TUNEL-positive cells (Figure 2(l)), and a diminishment of the Bcl-2 protein expression level (Figures 2(i)–2(k)) compared with those in the mimic-NC group. Therefore, the results elaborated that the

Table 1: Relevance between miR-4731-5p expression and clinicopathologic characteristics in patients with NSCLC.

Characteristics	Cases ($n = 35$)	miR-4731-5p expression		p value
		High ($n = 14$)	Low ($n = 21$)	
Age (years)				
<60	15	5	10	0.728
≥60	20	9	11	
Gender				
Female	18	6	12	0.500
Male	17	8	9	
Smoking				
Yes	18	9	9	0.305
No	17	5	12	
Tumor size (cm)				
<4	12	4	8	0.721
≥4	23	10	13	
Lymph node metastasis				
Yes	20	4	16	0.013*
No	15	10	5	
Distance metastasis				
Yes	17	3	14	0.015*
No	18	11	7	
TNM stage				
I/II	16	11	5	0.002**
III/IV	19	3	16	

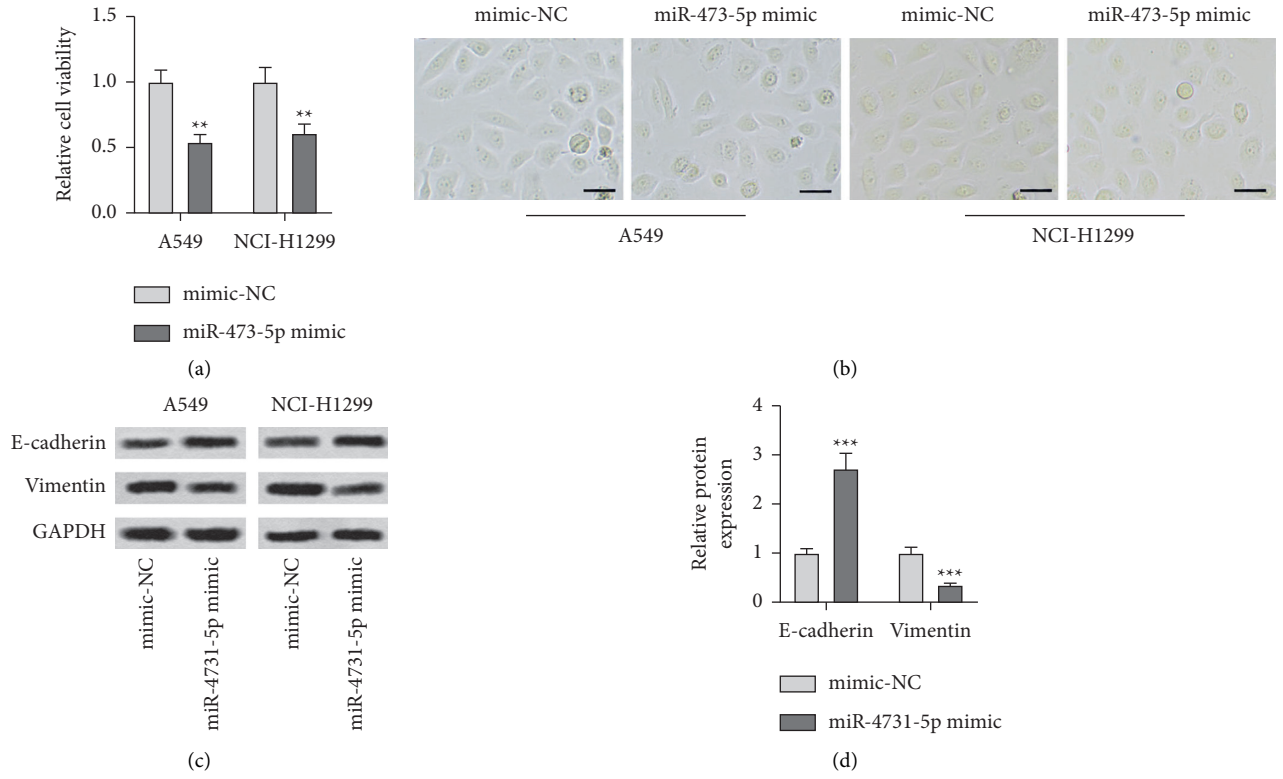

Figure 2: Continued.

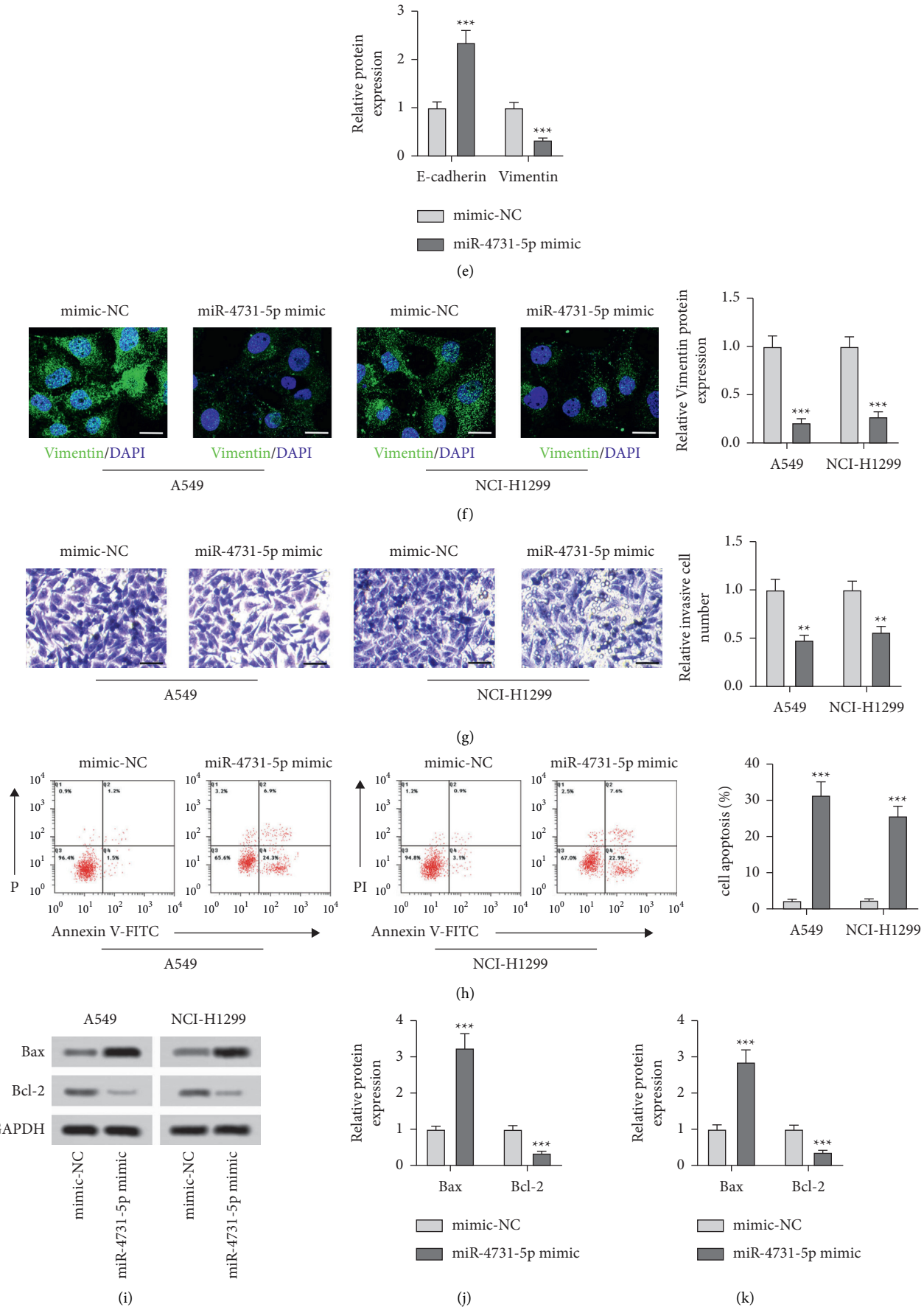

Figure 2: Continued.

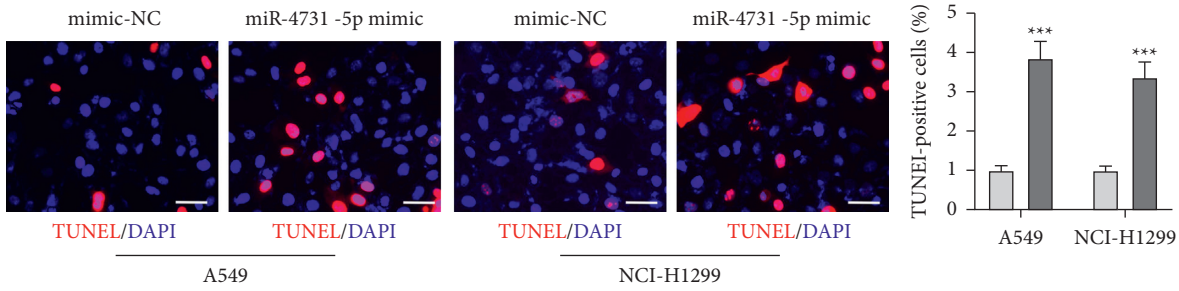

Figure 2: The role of miR-4731-5p in cell viability, invasion, apoptosis, and EMT of the NSCLC cells. (a) The role of the miR-4731-5p mimics in the two cells' viability was analyzed via MTT. (b) The role of the miR-4731-5p mimics in the morphological characteristics of A549 and NCI-H1299 cells was captured by the microscope. Scale bar = 50 μm (c–e) Protein expressions of EMT makers in the two cells with the transfection with miR-4731-5p mimics were measured through the western blot analysis. (f) The effect of the miR-4731-5p mimics on the expression level of vimentin in the two was measured via immunofluorescence staining. Scale bar: 0 μm. (g) The influence of the miR-4731-5p mimics in the invasion of the two cells was measured by the transwell assay. Scale bar = 50 μm. (h) The apoptotic rate was assessed by flow cytometry when miR-4731-5p was overexpressed. (i–k) The expressions of Bax and Bcl-2 in the two cells with the transfection with miR-4731-5p mimics were measured using western blot. (l) The apoptosis of A549 and NCI-H1299 cells with the transfection of miR-4731-5p mimics was assessed by the TUNEL assay. $^{**}p < 0.01$ and $^{***}p < 0.001$ relative to the mimic-NC.

upregulated level of miR-4731-5p repressed the cell viability, invasion, and EMT with increased apoptosis in both A549 and NCI-H1299 cells.

3.3. RPLP0 Directly Targeted to miR-4731-5p. To deeply assess the molecular role of miR-4731-5p in regulating NSCLC, the relative level of RPLP0 in the NSCLC tissues was examined. An increased level of RPLP0 in tissues of NSCLC was observed relative to that in normal tissues (Figure 3(a)). Additionally, in accordance with the results of miR-4731-5p, the level of RPLP0 was also notably related in lymph node metastasis, distance metastasis, and TNM stage, but no statistical difference was found between the expression of RPLP0 and age, gender, smoking, or tumor size. On the contrary, patients with higher expression of RPLP0 usually exhibited distance metastasis, lymph node metastasis, and III/IV TNM stage (Table 2). Besides, the expression level of RPLP0 was negatively involved in the level of miR-4731-5p in NSCLC tissues (Figure 3(b)). The expression of RPLP0 was measured in the five NSCLC cells. The results exhibited that the level of RPLP0 was signally overexpressed in the five NSCLC cell lines relative to that in normal lung cancer cells, among which the level of RPLP0 was higher in A549 and NCI-H1299 cells relative to that in the other three cell lines (Figure 3(c)). The possible binding between miR-4731-5p and RPLP0 was analyzed using the TargetScan (Figure 3(d)). To deeply resolve the relation between miR-4731-5p and RPLP0, the luciferase reporters carrying RPLP0 3'-UTR mutant (RPLP0 3'-UTR mut) or RPLP0 3'-UTR wild type (RPLP0 3'-UTR wt) were constructed. The enhancement of miR-4731-5p obviously declined the luciferase activity of RPLP0 including 3'-UTR wt but not 3'-UTR mut in both the cells (Figures 3(e) and 3(f)). Further findings demonstrated that the miR-4731-5p mimics dramatically decreased the transcriptional and translational expressions of RPLP0 compared with the mimic-NC (Figures 3(g) and 3(h)). Thus, the findings illuminated that RPLP0 was a direct target of miR-4731-5p in the NSCLC cells.

3.4. miR-4731-5p Modulated Cell Viability, Invasion, Apoptosis, and EMT in A549 Cells via Targeting RPLP0. To deeply explore whether miR-4731-5p modulated the development of NSCLC by targeting RPLP0, a cotransfection assay was executed. The repressive role of the miR-4731-5p mimic in the translational level of RPLP0 was significantly antagonized by the cotransfection of the miR-4731-5p mimic and OE-RPLP0 in A549 cells (Figure 4(a)). The MTT assay results indicated that the miR-4731-5p mimic inhibited the cell viability, which could be reversed by OE-RPLP0 (Figure 4(b)). Phase contrast microscopic evaluation further elucidated that A549 cells treated with OE-RPLP0 suppressed the changes caused by the miR-4731-5p mimic (Figure 4(c)). Cotransfection of the miR-4731-5p mimic and OE-RPLP0 markedly diminished the translational level of e-cadherin in A549 cells relative to that in the miR-4731-5p-mimic group. The opposite effect on vimentin was also observed (Figures 4(d) and 4(e)). Immunofluorescence detection displayed that the expression level of vimentin was observably reduced in A549 cells treated with the miR-4731-5p mimic and OE-RPLP0 relative to that in the miR-4731-5p-mimic group (Figure 4(f)). Additionally, the transwell and apoptosis assays revealed decreased cell invasion and increased apoptosis following cotransfection, which was different from the results from the only transfection with the miR-4731-5p mimic (Figures 4(g) and 4(h)). Increased counts of TUNEL-positive cells resulted by the miR-4731-5p mimic were memorably inverted by the cotransfection of the miR-4731-5p mimic and OE-RPLP0 in A549 cells (Figure 4(i)). Besides, after A549 cells were cotreated with the miR-4731-5p mimic and OE-RPLP0, the protein level of Bax was markedly decreased with notably enhanced translational expression of Bcl-2, Wnt1, and Nuc-β-catenin

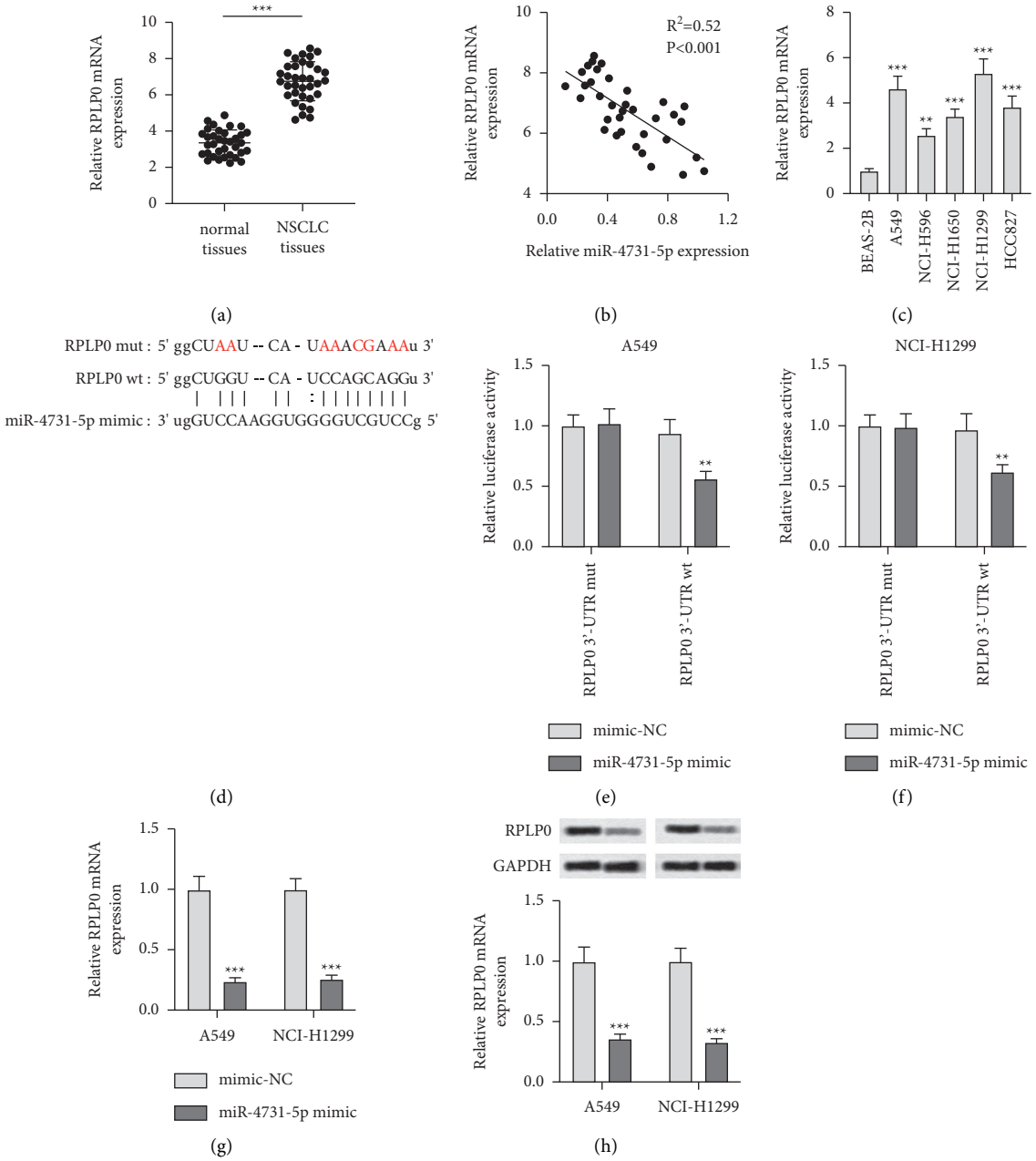

FIGURE 3: RPLP0 is the direct target of miR-4731-5p. (a) The transcriptional level of RPLP0 was examined by qRT-PCR in NSCLC tissues and normal tissues. (b) RPLP0 level was negative correlative to the miR-4731-5p mRNA level. (c) The level of RPLP0 in BEAS-2B and NSCLC cells was assessed via qRT-PCR. (d) RPLP0 was forecasted to be bound by miR-4731-5p according to the TargetScan. (e, f) The effect of the miR-4731-5p-mimic on the luciferase activity of the plasmid RPLP0-3'UTR-wt and RPLP0-3'UTR-mut. (g, h) RPLP0 expression in the two cells with the transfection of the miR-4731-5p-mimics was analyzed via qRT-PCR and western blot experiments. $^{**}p < 0.01$ and $^{***}p < 0.001$ compared to normal tissues, or BEAS-2B, or mimic-NC.

vimentin relative to that in the miR-4731-5p-mimic group (Figures 4(j) and 4(k)). In brief, these results clarified that miR-4731-5p attenuated NSCLC cell growth and invasion with enhanced apoptosis by targeting RPLP0.

3.5. miR-4731-5p Expression Restrained Tumor Growth In Vivo. To investigate whether miR-4731-5p played an analogous antitumor role was determined *in vivo*. The backs of nude mice received lentiviral vector with OE-miR-4731-5p, and a negative control was established as well. As presented in Figures 5(a) and 5(b), the elevation of miR-4731-5p prominently reduced the tumor volume of mice. Also, the upregulation of miR-4731-5p observably reduced the tumor weight of mice (Figure 5(c)); however, no significant effect was found on body weight (Figure 5(d)). The Kaplan–Meier analysis also exhibited that mice with a high level of miR-4731-5p in tumors had longer recurrence-free survival time than the control group

Table 2: Relevance between RPLP0 expression and clinicopathologic characteristics in patients with NSCLC.

Characteristics	Cases ($n = 35$)	RPLP0 expression		p value
		High ($n = 18$)	Low ($n = 17$)	
Age (years)				
<60	15	5	10	0.092
≥60	20	13	7	
Gender				
Female	18	10	8	0.740
Male	17	8	9	
Smoking				
Yes	18	7	11	0.181
No	17	11	6	
Tumor size (cm)				
<4	12	7	5	0.725
≥4	23	11	12	
Lymph node metastasis				
Yes	20	15	5	0.002**
No	15	3	12	
Distance metastasis				
Yes	17	13	4	0.007**
No	18	5	13	
TNM stage				
I/II	16	5	11	0.044*
III/IV	19	13	6	

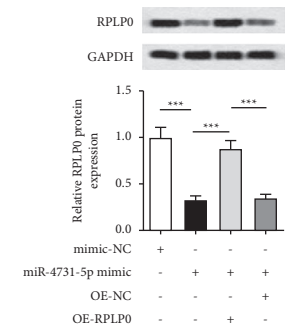

(a)

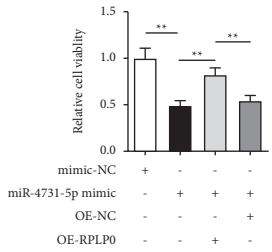

(b)

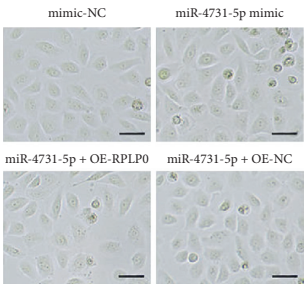

(c)

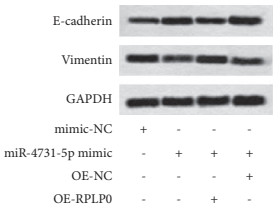

(d)

Figure 4: Continued.

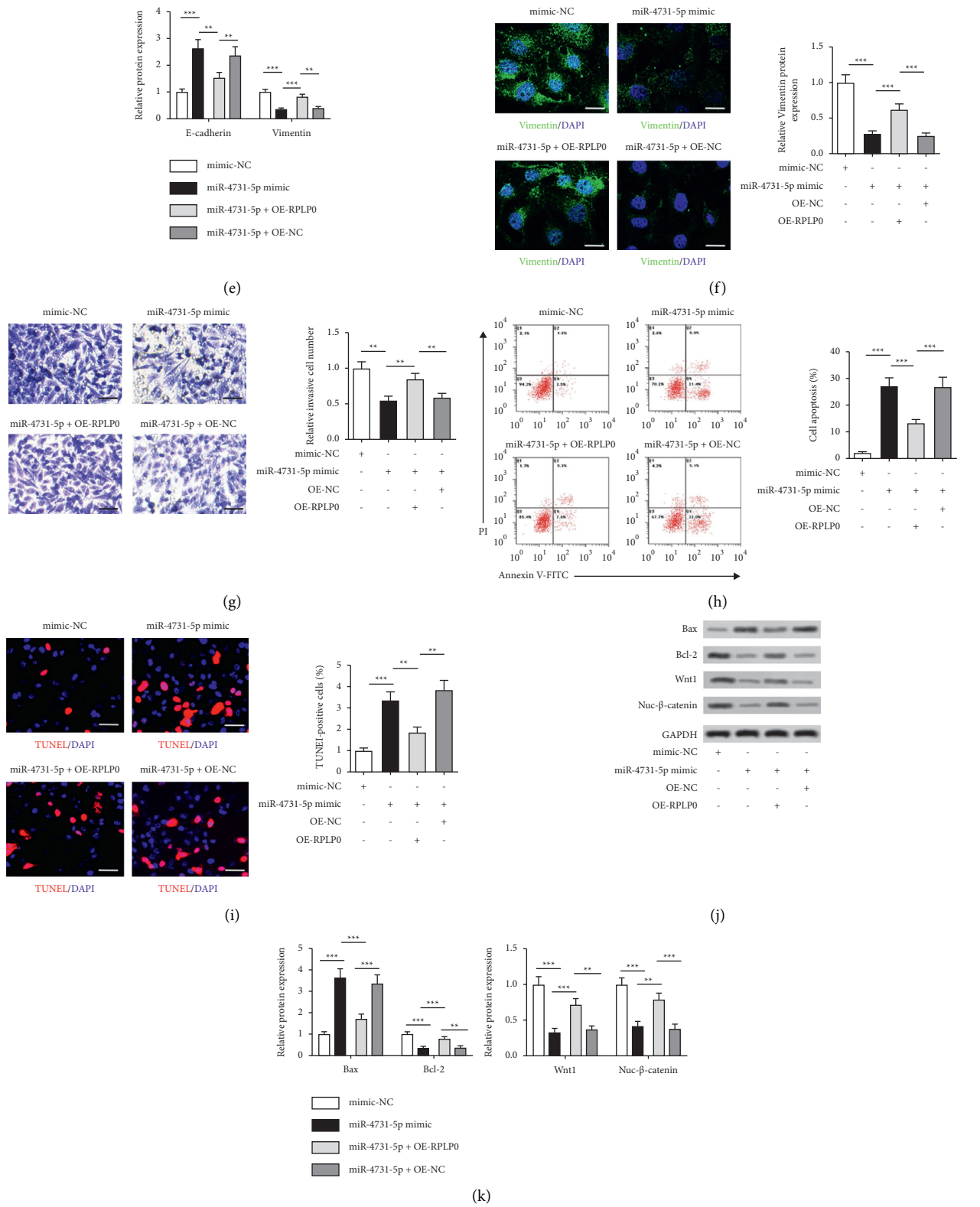

FIGURE 4: miR-4731-5p regulates NSCLC cell viability, invasion, apoptosis, and EMT by targeting RPLP0. (a) RPLP0 protein expression levels in A549 cells were determined through the western blot assay. (b) A549 cells' viability with the transfection of RPLP0 overexpression (OE-RPLP0) was determined using MTT. (c) The morphological characteristics of A549 cells transfected with OE-RPLP0 were captured under a phase-contrast microscope. Scale bar = 50 μm. (d, e) e-cadherin and vimentin translational levels in A549 cells treated with OE-RPLP0 were measured with the western blot assay. (f) The level of vimentin in A549 cells treated with OE-RPLP0 was determined using immunofluorescence staining. Scale bar = 10 μm. (g) Cell invasion in A549 cells with the transfection of OE-RPLP0 was determined using the transwell assay. Scale bar = 50 μm. (h) Cell apoptosis in A549 cells with the transfection of OE-RPLP0 was evaluated by flow cytometry. (i) A549 and NCI-H1299 cells with the transfection of OE-RPLP0 were assessed for apoptosis by the TUNEL assay. (j, k) Protein levels of Bax, Bcl-2, Wnt1, and Nuc-β-catenin in A549 cells with the transfection of OE-RPLP0 were determined by the western blot analysis.

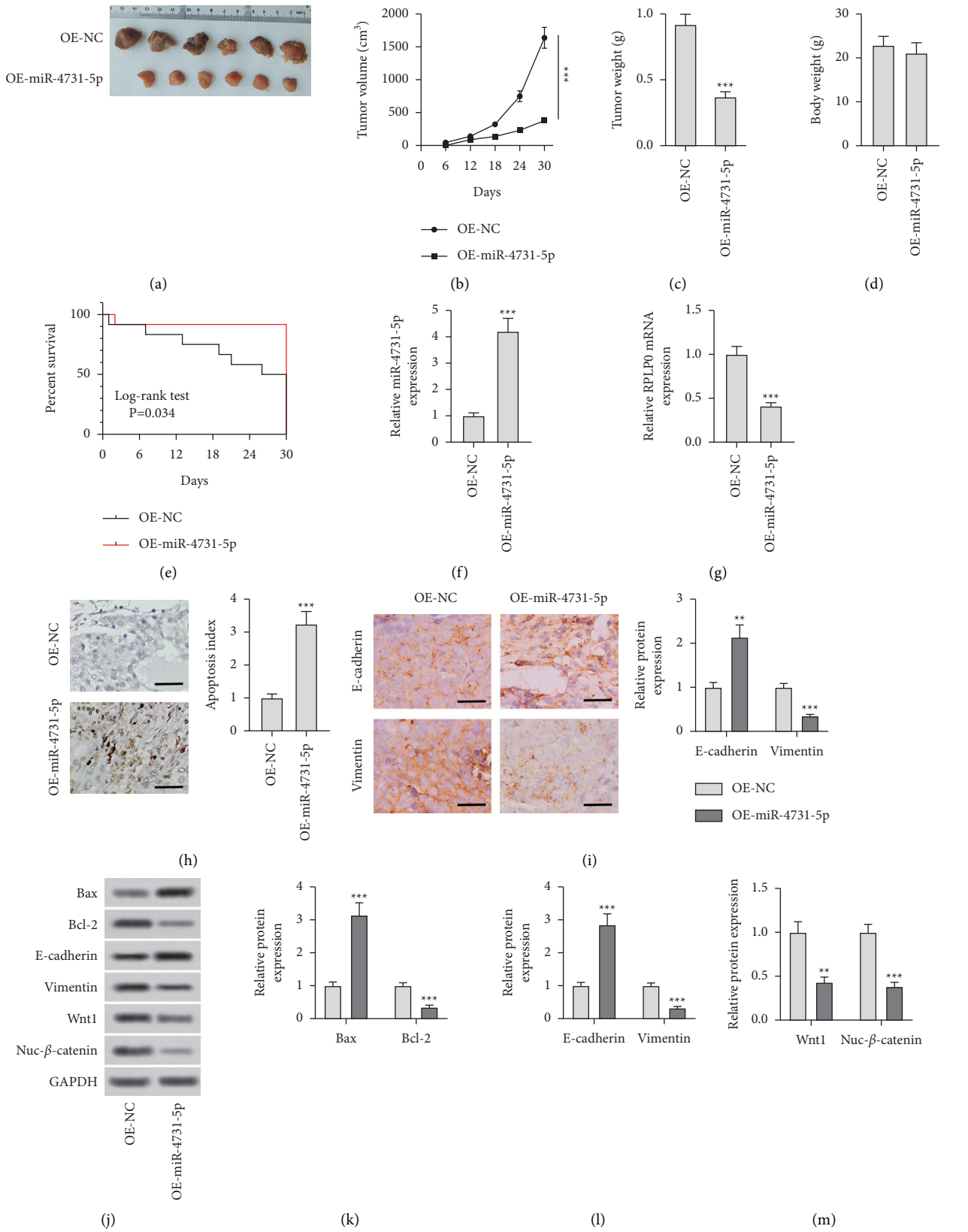

FIGURE 5: miR-4731-5p expression restrained tumor growth *in vivo*. (a) Photographs of the NC and miR-4731-5p overexpression (OE-miR-4731-5p) tumors at day 30. (b) Tumor growth curves were determined according to the tumor volume monitored every 6 days for 30 days. (c) Effects of NC and OE-miR-4731-5p on tumor weight at day 30. (d) Effects of NC and OE-miR-4731-5p on body weight at day 30. (e) The Kaplan–Meier survival analysis (log-rank test) was applied for the analysis of the survival rate of the two groups of mice every 6 days for 30 days. (f, g) The expressions of miR-4731-5p and RPLP0 of different groups in tumor tissues were evaluated by qRT-PCR. (h) Cell apoptosis in tumor tissues was assessed by TUNEL. (i) Bax, Bcl-2, e-cadherin, vimentin, Wnt1, and Nuc-β-catenin expression levels in tumor tissues were examined via western blot. ($n = 6$). $^{***}P < 0.001$ compared with OE-NC.

(Figure 5(e)). An increased level of miR-4731-5p and a decreased level of RPLP0 were indicated in NSCLC tissues relative to those in the adjacent tissues (Figures 5(f) and 5(g)). The TUNEL assay data further revealed that apoptosis was notably elevated in the OE-miR-4731-5p group relative to the control group (Figure 5(h)). The IHC data presented that the level of e-cadherin in NSCLC tissues overexpressing miR-4731-5p was memorably increased relative to that in the control group with an opposite pattern for vimentin (Figure 5(i)), which was consistent with the results of western blotting (Figures 5(j)–5(l)). The translational expression of Bax was significantly elevated following OE-miR-4731-5p treatment in NSCLC tissues with reduced protein levels of Bcl-2, Wnt1, and Nuc-β-catenin (Figures 5(j), 5(k), and 5(m)). Thus, the findings demonstrated that the upregulated level of miR-4731-5p restrained NSCLC tumor growth by suppressing RPLP0 at the mRNA level.

4. Discussion

Lung cancer is a kind of heterogeneous disease derived from the abnormal cells of the respiratory epithelium. MiRNAs play a core role in initiating cancer and its development in different types of malignancies [18]. A large number of evidences have suggested the dysregulation of miRNAs related to a variety of diseases, including lung cancer [19,20]. Extensive miRNAs are dysregulated in NSCLC reported by the high-throughput analysis [21,22]. Therein, miR-4731-5p has been confirmed to be a tumor-suppressed miRNA in melanoma [7] and glioma development [9]. The results of the current study suggested that NSCLC was associated with low expression level of miR-4731-5p, thereby indicating the altered level of miR-4731-5p might be the usual characteristic of NSCLC.

Plenty of studies have shown that miR-4731-5p targets and suppresses the level of oncogenes involved in cancer development, such as cellular proliferation, migration, and apoptosis [23]. The upregulation of miR-4731-5p suppressed the proliferation, migration, and invasion via targeting FOXM1 in breast cancer [24]. miR-4731-5p/E2F2 axis also regulated the progresses of glioma cells [9]. Interference of miR-4731-5p promoted the growth, migration, and invasion of choriocarcinoma by targeting HIF3A as well [25]. In the present study, the level of miR-4731-5p was consistently downregulated both in NSCLC tissues and cells. Plenty of studies have reported that miRNAs exhibited a satisfactory prognostic value in NSCLC [26,27]. Consistent with these findings, patients with a lower expression of miR-4731-5p usually exhibited distance metastasis, lymph node metastasis, and III/IV TNM stage, which indicated that the level of miR-4731-5p was also correlative with the prognosis of lung cancer patients. Moreover, in subsequent transfection assays, A549 and NCI-H1299 treated with the miR-4731-5p mimic exhibited markedly decreased cell viability, invasion, and EMT, as well as strengthened apoptosis as relative to that in the controls. Therefore, these data offered direct evidence of a tumor-suppressive activity of miR-4731-5p against the NSCLC cells, which was tightly correlative in the prognosis of lung cancer.

Previous studies have shown the importance of RPLP protein inhibition, as their downregulation may be critical for the therapy in cancer [28]. Growing evidence has indicated that RPLP proteins are highly regulated in endometrial carcinoma, ovarian cancer, colon carcinoma [14], and other numerous types of cancers [29,30]. Except for the endometrial carcinoma, ovarian cancer, and colon carcinoma [14], RPLP0, as a vital member of the RPLP family, is also upregulated in acute myeloid leukemia [31], clear cell renal cell carcinoma [32], and breast cancer [33]. Moreover, it has been demonstrated that patients with high expressions of RPLP0 are prominently associated with poor prognosis in clear cell renal cell carcinoma [32] and breast cancer [33]. In line with these findings, RPLP0 was also found markedly upregulated in NSCLC cell lines and tissues in our study, and the level of RPLP0 was also related in the prognosis of lung cancer patients. Furthermore, bioinformatics analysis predicted a reciprocity between miR-4731-5p and RPLP0, and the findings displayed that miR-4731-5p directly restrained RPLP0 by interacting with its 3'UTR. The results illustrated that miR-335-5p directly targets RPLP0.

Additionally, previous work has demonstrated that the down-expression of RPLP proteins affected cell growth and cell cycle progression [12]. RPLP0 has been found to regulate cell apoptosis and cycle arrest of cervical tumor cells [34]. The down-regulation of RPLP0 led to G1 arrest of gastric cancer cells [13]. Natalie et al. reported that RPLP0 was stably expressed in melanoma cells [35]. RPLP0 also modulates a variety of cellular functions in neurodegenerative diseases [36]. Overall, these results indicate that RPLP0 made vital contributions to the cell activity in various diseases. Here, we discovered that the over-regulation of miR-4731-5p resulted in the low expression of RPLP0, leading to the retardation of NSCLC cell viability and invasion, and consequently inhibited tumor growth. Epithelial cells can obtain the mesenchymal features during the EMT process [37]. In tumor, EMT is contacted with the progress of tumor beginning, invasion, and metastasis [38–40]. Furthermore, a growing body of research has indicated EMT is correlative with the progress and metastasis of NSCLC [41,42]. In the present study, we discovered that the EMT restraint which was induced by the miR-4731-5p mimic was significantly reversed by OE-RPLP0 in A549 cells. However, there is no relevant reports that describe the antitumor effect of RPLP0 dysregulation modulated by other miRNAs; thus, we discovered a novel target axis that might contribute to the NSCLC treatment in the current study. Taken together, further mechanistic experimentation revealed that RPLP0 contributed to the regulation of cell viability, invasion, EMT, and apoptosis by miR-4731-5p in NSCLC.

It has been shown that animal experiment models are a crucial method for NSCLC studies. Much evidence *in vivo* has demonstrated that the dysregulation of miRNAs plays a role in NSCLC development. For example, miR-367 promotes NSCLC progression *in vivo* [43], overexpression of miR-103 is capable of inhibiting NSCLC growth *in vivo* and promoting mouse survival [44], miR-146a-5p is overexpressed in the NSCLC cell line, and the repressive role of miR-146a-5p in the angiogenesis and tumorigenesis in a tumor model is also found [45]. In the final step, based on our findings, all animal experiments were implemented and finished successfully. *In vivo* tumor growth was suppressed by increasing miR-4731-5p. Besides, the overexpression of

miR-4731-5p promoted apoptosis and inhibited EMT *in vivo*. These *in vitro* effects were confirmed by adopting the nude mice model under *in vivo* conditions.

In short, we discovered that miR-4731-5p and RPLP0 dysregulated NSCLC tissues and cell lines, which are involved in lymph node metastasis, distance metastasis, and III/IV TNM stage, with no relation to age, gender, smoking, or tumor size. Thus, the level of miR-4731-5p and RPLP0 was related in the prognosis of lung cancer patients. Besides, our findings elucidated the mechanistic interaction between miR-4731-5p and RPLP0 in NSCLC. miR-4731-5p-mediated modulation pathway via targeting RPLP0 provides new insights into the therapeutic strategies for NSCLC. Nonetheless, several limitations of the study should be addressed: [1] although NSCLC is greatly sensitive to chemotherapy, it quickly obtains resistance. Only two NSCLC cell lines are utilized in this study, and thus validation in other chemoresistance NSCLC cell lines and clinical specimens is needed in subsequent studies; [2] the results of miR-4731-5P influence on other RPLP family members have been rarely reported. The exact mechanism of RPLP0 regulation of cell viability, invasion, apoptosis, and EMT of NSCLC is still unclear and needs more studies.

Data Availability

The data analyzed and used during the present study are available from the corresponding author on reasonable request.

Conflicts of Interest

The authors declare that they have no conflicts of interest.

Authors' Contributions

All authors approved the final manuscript. Chang was responsible for conceptualization, methodology, software, and data curation, prepared the original draft, and visualized, investigated, and supervised the study. Chang also wrote the manuscript. Meilin Xu validated, reviewed, and edited the manuscript.

Supplementary Materials

Chang et al. showed that the expression of miR-4731-5p was notably declined in NSCLC tissues and cell lines, which was related to the prognosis of lung cancer patients. Mechanically, miR-4731-5p promotes cell apoptosis and alleviates epithelial-mesenchymal transition of non-small-cell lung cancer via targeting RPLP0. (*Supplementary Materials*)

References

[1] J. Ferlay, I. Soerjomataram, R. L. Siegel, L. A. Torre, and A. Jemal, "Global cancer statistics 2018: GLOBOCAN estimates of incidence and mortality worldwide for 36 cancers in 185 countries," *CA: A Cancer Journal for Clinicians*, vol. 68, no. 6, pp. 394–424, 2018.

[2] S. Emma, H. Thomas, G. R. Simon et al., "Molecular pathways and therapeutic targets in lung cancer," *Oncotarget*, vol. 5, no. 6, pp. 1392–1433, 2014.

[3] M. D. Mattes, A. B. Moshchinsky, S. Ahsanuddin et al., "Ratio of lymph node to primary tumor SUV on PET/CT accurately predicts nodal malignancy in non-small-cell lung cancer," *Clinical Lung Cancer*, vol. 16, no. 6, pp. e253–e258, 2015.

[4] J. Cai, L. Fang, Y. Huang et al., "Simultaneous overactivation of Wnt/β-catenin and TGFβ signalling by miR-128-3p confers chemoresistance-associated metastasis in NSCLC," *Nature Communications*, vol. 8, pp. 1–18, Article ID 15870, 2017.

[5] H. Zarredar, K. Ansarin, B. Baradaran et al., "Critical micrornas in lung cancer: recent advances and potential applications," *Anti-Cancer Agents in Medicinal Chemistry*, vol. 18, no. 14, pp. 1991–2005, 2018.

[6] D. Sun, X. Li, M. Ma et al., "The predictive value and potential mechanisms of miRNA-328 and miRNA-378 for brain metastases in operable and advanced non-small-cell lung cancer," *Japanese Journal of Clinical Oncology*, vol. 45, no. 5, pp. 464–473, 2015.

[7] M. S. Stark, L. N. Tom, G. M. Boyle et al., "The "melanoma-enriched" microRNA miR-4731-5p acts as a tumour suppressor," *Oncotarget*, vol. 7, no. 31, pp. 49677–49687, 2016.

[8] M. S. Stark, K. Klein, B. Weide et al., "The prognostic and predictive value of melanoma-related microRNAs using tissue and serum: a microRNA expression analysis," *EBioMedicine*, vol. 2, no. 7, pp. 671–680, 2015.

[9] Z. Yan, W. Zhang, Y. Xiong, Y. Wang, and Z. Li, "Long noncoding RNA FLVCR1-AS1 aggravates biological behaviors of glioma cells via targeting miR-4731-5p/E2F2 axis," *Biochemical and Biophysical Research Communications*, vol. 521, no. 3, pp. 716–720, 2020.

[10] N. Gholizadeh, A. Emami Razavi, H. Mohammadpour, F. Tavakol, and N. Sheykhbahaei, "Association of MAPK and its regulatory miRNAs (603, 4301, 8485, and 4731) with the malignant transformation of oral lichen planus," *Molecular Biology Reports*, vol. 47, no. 2, pp. 1223–1232, 2020.

[11] A. Allahverdi, E. Arefian, M. Soleimani et al., "MicroRNA-4731-5p delivered by AD-mesenchymal stem cells induces cell cycle arrest and apoptosis in glioblastoma," *Journal of Cellular Physiology*, vol. 235, no. 11, pp. 8167–8175, 2020.

[12] A. Artero-Castro, M. Perez-Alea, A. Feliciano et al., "Disruption of the ribosomal P complex leads to stress-induced autophagy," *Autophagy*, vol. 11, no. 9, pp. 1499–1519, 2015.

[13] A. Teller, D. Jechorek, R. Hartig et al., "Dysregulation of apoptotic signaling pathways by interaction of RPLP0 and cathepsin *X*/*Z* in gastric cancer," *Pathology, Research and Practice*, vol. 211, no. 1, pp. 62–70, 2015.

[14] A. Artero-Castro, J. Castellvi, A. García, J. Hernández, S. R. Y. Cajal, and M. E. Lleonart, "Expression of the ribosomal proteins Rplp0, Rplp1, and Rplp2 in gynecologic tumors," *Human Pathology*, vol. 42, no. 2, pp. 194–203, 2011.

[15] P. Gresner, J. Gromadzinska, and W. Wasowicz, "Reference genes for gene expression studies on non-small cell lung cancer," *Acta Biochimica Polonica*, vol. 56, no. 2, pp. 307–316, 2009.

[16] H. Ali, Z. Du, X. Li et al., "Identification of suitable reference genes for gene expression studies using quantitative polymerase chain reaction in lung cancer in vitro," *Molecular Medicine Reports*, vol. 11, no. 5, pp. 3767–3773, 2015.

[17] C. Zhan, Y. Zhang, J. Ma et al., "Identification of reference genes for qRT-PCR in human lung squamous-cell carcinoma by RNA-Seq," *Acta Biochimica et Biophysica Sinica*, vol. 46, no. 4, pp. 330–337, 2014.

[18] M. V. Iorio and C. M. Croce, "Causes and consequences of microRNA dysregulation," *The Cancer Journal*, vol. 18, no. 3, pp. 215–222, 2012.

[19] I. Cristóbal, J. Madoz-Gúrpide, F. Rojo, and J García-Foncillas, "Potential therapeutic value of miR-425-5p in metastatic colorectal cancer," *Journal of Cellular and Molecular Medicine*, vol. 20, no. 11, pp. 2213-2214, 2016.

[20] C.-H. Lin, C.-H. Tsai, C.-T. Yeh et al., "MiR-193a-5p/ERBB2 act as concurrent chemoradiation therapy response indicator of esophageal squamous cell carcinoma," *Oncotarget*, vol. 7, no. 26, pp. 39680–39693, 2016.

[21] L. Petra, B. Thomas, B. Christina et al., "High-throughput qRT-PCR validation of blood microRNAs in non-small cell lung cancer," *Oncotarget*, vol. 7, no. 4, pp. 4611–4623, 2016.

[22] S. Molina-Pinelo, G. Gutiérrez, M. D. Pastor et al., "MicroRNA-dependent regulation of transcription in non-small cell lung cancer," *PLoS One*, vol. 9, no. 3, Article ID e90524, 2014.

[23] S. Lin and R. I. Gregory, "MicroRNA biogenesis pathways in cancer," *Nature Reviews Cancer*, vol. 15, no. 6, pp. 321–333, 2015.

[24] Y. Wang, J. Ma, R. Li, X. Gao, H. Wang, and G. Jiang, "LncRNA TMPO-AS1 serves as a sponge for miR-4731-5p modulating breast cancer progression through FOXM1," *American Journal of Translational Research*, vol. 13, no. 10, pp. 11094–11106, 2021.

[25] Y. Lu, C. Yang, L. Zhang, and J. Ding, "Ropivacaine retards the viability, migration, and invasion of choriocarcinoma cells by regulating the long noncoding RNA OGFRP1/microRNA-4731-5p/HIF3A axis," *Molecular Biotechnology*, 2021.

[26] Q. Ye, J. Putila, R. Raese et al., "Identification of prognostic and chemopredictive microRNAs for non-small-cell lung cancer by integrating SEER-medicare data," *International Journal of Molecular Sciences*, vol. 22, no. 14, pp. 1–28, 2021.

[27] C. Zhou, Z. Chen, L. Zhao et al., "A novel circulating miRNA-based signature for the early diagnosis and prognosis prediction of non-small-cell lung cancer," *Journal of Clinical Laboratory Analysis*, vol. 34, no. 11, Article ID e23505, 2020.

[28] C. Alon, K. Ella, R. Shai, B. A. Nurit, O. Eli, and K. Yitzhak, "Two forms of gonadotropin-releasing hormone (GnRH) are expressed in human breast tissue and overexpressed in breast cancer: a putative mechanism for the antiproliferative effect of GnRH by down-regulation of acidic ribosomal phosphoproteins P1 and P2," *Cancer Research*, vol. 62, no. 4, pp. 1036–1044, 2002.

[29] A. Artero-Castro, H. Kondoh, P. J. Fernández-Marcos, M. Serrano, S. R. y Cajal, and M. E. Lleonart, "Rplp1 bypasses replicative senescence and contributes to transformation," *Experimental Cell Research*, vol. 315, no. 8, pp. 1372–1383, 2009.

[30] W. T. Loging and D. Reisman, "Elevated expression of ribosomal protein genes L37, RPP-1, and S2 in the presence of mutant p53," *Cancer Epidemiology, Biomarkers and Prevention*, vol. 8, no. 11, pp. 1011–1016, 1999.

[31] L. Handschuh, M. Kaźmierczak, M. C. Milewski et al., "Gene expression profiling of acute myeloid leukemia samples from adult patients with AML-M1 and -M2 through boutique microarrays, real-time PCR and droplet digital PCR," *International Journal of Oncology*, vol. 52, no. 3, pp. 656–678, 2018.

[32] Z. Zhu, A. He, L. Lin, C. Xu, T. Cai, and J. Lin, "Biological functions and prognostic value of RNA binding proteins in clear cell renal cell carcinoma," *Journal of Cancer*, vol. 11, no. 22, pp. 6591–6600, 2020.

[33] R. E. McNeill, N. Miller, and M. J. Kerin, "Evaluation and validation of candidate endogenous control genes for real-time quantitative PCR studies of breast cancer," *BMC Molecular Biology*, vol. 8, no. 1, p. 107, 2007.

[34] C.-H. Wang, L.-K. Wang, C.-C. Wu et al., "The ribosomal protein RPLP0 mediates PLAAT4-induced cell cycle arrest and cell apoptosis," *Cell Biochemistry and Biophysics*, vol. 77, no. 3, pp. 253–260, 2019.

[35] N. J. Neubert, C. Soneson, D. Barras et al., "A well-controlled experimental system to study interactions of cytotoxic T lymphocytes with tumor cells," *Frontiers in Immunology*, vol. 7, p. 326, 2016.

[36] H. T. Evans, J. Benetatos, M. V. Roijen, L. G. Bodea, and J. Gtz, "Decreased synthesis of ribosomal proteins in tauopathy revealed by non-canonical amino acid labelling," *The EMBO Journal*, vol. 38, no. 13, Article ID e101174, 2019.

[37] V. Keshamouni, S. Anthwal, R. C. Reddy, D. A. Arenberg, and T. J. Standiford, "Epithelial to mesenchymal transitions in lung tumor progression," *Cancer Research*, vol. 65, no. 1, 2005.

[38] M. Saitoh, "Involvement of partial EMT in cancer progression," *Journal of Biochemistry*, vol. 164, no. 4, pp. 257–264, 2018.

[39] P. Savagner, "Leaving the neighborhood: molecular mechanisms involved during epithelial-mesenchymal transition," *BioEssays*, vol. 23, no. 10, pp. 912–923, 2001.

[40] P. Ievgenia and B. Cédric, "EMT transition states during tumor progression and metastasis," *Trends in Cell Biology*, vol. 29, no. 3, pp. 212–226, 2019.

[41] M. Q. Mahmood, C. Ward, H. K. Muller, S. S. Sohal, and E. H. Walters, "Epithelial mesenchymal transition (EMT) and non-small cell lung cancer (NSCLC): a mutual association with airway disease," *Medical Oncology*, vol. 34, no. 3, p. 45, 2017.

[42] Y. K. Chae, S. Chang, T. Ko et al., "Epithelial-mesenchymal transition (EMT) signature is inversely associated with T-cell infiltration in non-small cell lung cancer (NSCLC)," *Scientific Reports*, vol. 8, no. 1, p. 2918, 2018.

[43] G. Xiao, X. Gao, X. Sun et al., "miR-367 promotes tumor growth by inhibiting FBXW7 in NSCLC," *Oncology Reports*, vol. 38, no. 2, pp. 1190–1198, 2017.

[44] Y. Dong, W. Jian-Jun, L. Jin-Song, and X. Qian-Yu, "MiR-103 Functions as a tumor suppressor by directly targeting programmed cell death 10 in NSCLC," *Oncology Research*, vol. 26, no. 4, pp. 519–528, 2018.

[45] W.-T. Huang, W.-L. Cen, R.-Q. He et al., "Effect of miR-146a-5p on tumor growth in NSCLC using chick chorioallantoic membrane assay and bioinformatics investigation," *Molecular Medicine Reports*, vol. 16, no. 6, pp. 8781–8792, 2017.

Hindawi
Journal of Oncology
Volume 2022, Article ID 1182383, 17 pages
https://doi.org/10.1155/2022/1182383

Research Article

The Detection and Verification of Two Heterogeneous Subgroups and a Risk Model Based on Ferroptosis-Related Genes in Hepatocellular Carcinoma

Jiang Li,[1,2] Haisu Tao,[1] Wenqiang Wang,[1] Jian Li,[1] and Erlei Zhang[1]

[1]*Hepatic Surgery Center, Tongji Hospital, Tongji Medical College, Huazhong University of Science and Technology, No. 1095, Jiefang Avenue, Wuhan 430030, Hubei, China*
[2]*Department of Hepatobiliary Surgery, College of Medicine, First Affiliated Hospital of Shihezi University Medical College, North 2nd Road, Shihezi, Xinjiang Uygur Autonomous Region, China*

Correspondence should be addressed to Erlei Zhang; baiyu19861104@163.com

Received 21 December 2021; Revised 21 January 2022; Accepted 26 January 2022; Published 12 March 2022

Academic Editor: Fu Wang

[#] *Background*. Because of the heterogeneity of hepatocellular carcinoma (HCC) and the complex nature of the tumor microenvironment (TME), the long-term efficacy of therapy continues to be a clinical challenge. It is necessary to classify and refine the appropriate treatment intervention decision-making in this kind of tumor. *Methods*. We used "ConsensusClusterPlus" to establish a stable molecular classification based on the ferroptosis-related genes (FRGs) expression obtained from FerrDb. The clinical features, immune infiltration, DNA damage, and genomic changes of different subclasses were evaluated. The least absolute shrinkage and selection operator regression (LASSO) method and univariate Cox regression were utilized to construct the ferroptosis-related prognosis risk score (FPRS) model, and the association between the FPRS model and HCC molecular characteristics, immune features, and immunotherapy was studied. *Results*. We identified two ferroptosis subclasses, C1 with poor prognosis and a higher proportion of patients in the middle and late stages infected with HBV and HCV, having higher DNA damage including aneuploidy, HRD, fraction altered, and the number of segments, and higher probability of gene mutation and copy number mutation. FPRS model was constructed on the basis of differentially expressed genes (DEGs) between C1 and C2, which showed a higher area under the curve (AUC) in predicting overall survival rate in the training set and independent verification cohort and could reflect the clinical characteristics and response to immunotherapy of different patients, being an independent prognostic factor of HCC. *Conclusion*. Here, we revealed two novel molecular subgroups based on FRGs and develop an FPRS model consisting of six genes that can help predict prognosis and select patients suitable for immunotherapy.

1. Introduction

Primary liver cancer has been reported to be the fifth-highest occurring incidence of cancer in the world, which comprises hepatocellular carcinoma (HCC) (accounting for approximately 75%–85% of all incidents) and intrahepatic cholangiocarcinoma (accounting for approximately 10%–15% of all incidents) and other rare types [1]. As the most prevalent type of primary liver cancer, the treatment of HCC has been restricted by tumor heterogeneity, which greatly limits the progress of individualized therapy [2]. The histological definition of morphological heterogeneity of liver cancer has been modified and refined in the medical community to help clinically choose treatment interventions for patients, but this still does not solve all the problems [3]. Precision medicine has been suggested to add a new perspective to individualized cancer diagnosis and targeted therapy by taking into account the heterogeneity of individual patients [4]. Precision medicine focuses on the importance of accurately classifying heterogeneous diseases into more

accurate subsets with the aid of powerful identification techniques and the incorporation of clinical characteristics. Furthermore, clinicians should come up with more specific diagnostic and therapeutic approaches for the disease subtype in order to optimize the efficacy and ultimately reduce side effects [5].

Iron toxicity is an iron-dependent cell death program, whose primary feature is the accumulation of lethal amounts of lipid-reactive oxygen species in cells [6]. Over the past few years, studies have suggested that the liver is prone to oxidative damage and iron overload is the cause of liver injury as well as the progression of disease in most liver diseases [7]. Therefore, ferroptosis has attracted wide attention in a variety of liver diseases, including HCC, hepatic fibrosis, liver failure, hepatic ischemia-reperfusion injury, and nonalcoholic steatosis [8]. In hepatocyte-specific Trf knockout mice, feeding a diet with high iron increased their vulnerability to liver fibrosis induced by iron death. And ferroptosis suppressants can restore this condition [9]. A study conducted in mice showed that ferroptosis is an inducer of nonalcoholic steatohepatitis, leading to liver injury, immune cell infiltration, and inflammatory response [10]. Ferroptosis also mediates acetaminophen-induced acute liver failure [11]. Multiple studies pointed to the induction of ferroptosis as a possible effective tumor suppressor mechanism and useful for prognosis prediction in HCC [7]. The late first-line therapeutic drug of HCC, sorafenib, has been proved to be a strong inducer of ferroptosis [12]. Sorafenib increased the survival rate of HCC patients to a certain degree, but it may lead to serious harmful impacts and growing resistance characteristics, resulting in a dismal prognosis [13]. Therefore, it is necessary to identify new molecular markers of ferroptosis and downstream signaling pathways, which will aid in the comprehension of the regulatory mechanism of ferroptosis in the physiopathology of HCC.

At present, there are several systems biology methods to identify biomarkers related to the prognosis of HCC and construct gene features. Liang et al. identified a 10-gene signature in the expression profile of iron death related genes by LASSO regression analysis [14]. Liu et al. analyzed m6A methylation related genes and identified five gene markers with poor prognosis [15]. Xu et al. identified 6-gene signature by Cox regression analysis [16]. All three groups of authors tested their gene signature in the internal data set but did not verify the external independent data set, which means that identifying robust lncRNA signature is still a challenge and more queues are needed to verify the signature.

In this research, we collected samples from four databases, identified two distinct ferroptosis-related subclasses in HCC patients based on the expression of 111 FRGs obtained from the FerrDb website, and discussed the clinical, mutation spectrum, and tumor immunological characteristics between ferroptosis subgroups. In addition, the FPRS model was constructed to quantify the survival probability of HCC patients and to predict the response to immunotherapy. Collectively, this FPRS model may be an excellent predictor of HCC and may give insight into the development of innovative possible therapeutic techniques.

2. Materials and Methods

2.1. Acquiring and Preprocessing Sample Data. RNA-Seq data containing 365 samples and valid clinical follow-up information were acquired from TCGA-LIHC (https://portal.gdc.cancer.gov/). In addition, transcriptome data and survival messages from 221 cases of GSE14520 [17] and 115 cases of GSE76427 [18] cohorts were collected from the Gene Expression Omnibus (GEO, https://www.ncbi.nlm.nih.gov/geo/). Similarly, the ICGC-LIRI-JP data set in the HCCDB database was also used for the collection of HCC data, including 212 samples. TCGA-LIHC served as the training set, while the other cohort served as the independent verification set. The whole work flow chart of this study is shown in Figure S1.

2.2. Collection and Unsupervised Clustering of Ferroptosis-Related Genes (FRGs). FerrDb (http://www.zhounan.org/ferrdb) is reported to be the first repository of ferroptosis modulators and indicators, as well as ferroptosis-disease connections, which was manually collated [19]. We got 111 FRGs from this website. Then, the FRGs significantly correlated with the prognosis of HCC patients were selected utilizing univariate Cox analysis. According to the levels of FRGs expression, which is significantly correlated with the prognosis of HCC, the R packet ConsensusClusterPlus [20] was used to classify 365 HCC samples from TCGA-LIHC. And the analysis measured the distance by "Euclidean" and performed 500 times resampling iteration for both algorithms with 80% of probe sets being subsampled to ensure the stability of the clustering.

2.3. Computation of Molecular Features and Immune Cellular Fraction between Subtypes. Genomic Data Commons Data Portal provided somatic mutation profiles identified by VarScan, which were accessible to download [21]. Somatic mutation frequency of more than 5 percent was regarded to be appropriate for comparing values across different subtypes [22]. The "maftools" package [23] of R software was employed to display the mutation spectrum of each subtype. The relative abundance of 22 different immune cells in distinct subgroups in two HCC cohorts was calculated by executing the CIBERSORT algorithm [24]. The stromal, immune, and ESTIMATE scores of each sample were evaluated by ESTIMATE [25] to determine the degree of immune cell infiltration of each subtype.

2.4. Differential Expression Analysis between Molecular Subclasses. The Limma package was employed to identify differentially expressed genes (DEGs) between distinct subgroups in the TCGA-LIHC data set [26]. The genes having an absolute log2 fold change ($|\log FC| > 1.0$, false discovery rate (FDR) < 0.05, and Pvalue < 0.01 were defined as DEGs. The "clusterProfiler" package of *R* [27] was applied to implement the Gene Ontology (GO) and Kyoto Encyclopedia of Genes and Genomes (KEGG) pathways analysis on DEGs between distinct subtypes and the critical value was adjusted as $P < 0.05$.

2.5. Establishment and Evaluation of Ferroptosis-Related Prognosis Risk Score (FPRS) System. Univariate Cox regression analysis and the least absolute shrinkage and selection operator (Lasso) Cox regression analysis were applied to build the prognostic risk model based on DEGs between distinct subtypes, which was performed using R packet (http://www.rstudio.org) "glmnet." The specific formula was as follows: $\mathrm{HPRS} = \Sigma\beta i \times Expi$, where β is the Cox regression coefficient of the corresponding gene, i refers to the prognostic related FRGs, and Exp is the prognostic FRGs expression level. Similarly, the accuracy of FPRS model was verified in two independent validation sets. The cut-off point of FPRS in each cohort was obtained according to R packet "survminer." Patients who were larger than the threshold value were categorized into a high-risk group, and those less than the threshold value were categorized into a low-risk group. The Kaplan–Meier curve was used to display the overall survival (OS) of the sample, and the logarithmic rank test was utilized to determine the statistical difference. The "timeROC" package of R was applied for the generation of receiver operating characteristic (ROC) curve, and the prediction accuracy of the model was examined by calculating the area under the curve (AUC) of one-, three-, and five-year OS.

2.6. The Function of Different FPRS Was Analyzed by Gene Set Enrichment Analysis (GSEA). HALLMARK GSEA was performed to estimate the biological signaling pathways in different risk groups [28]. And single-sample GSEA (ssGSEA) was conducted in the TCGA-LIHC cohort utilizing the "GSVA" package of R to study molecular differences between samples with different FPRS.

2.7. Genomic Correlations with the FPRS. Aneuploidy scores, homologous recombination deficiency (HRD), fraction altered, number of segments, and tumor mutation were derived [29]. The differences in these five indicators between the 2 risk groups were examined by Wilcoxon test. The correlation between FPRS and the above five genomic variables was evaluated by Pearson's correlation analysis.

2.8. Prediction of Response to Different Treatments. Immune checkpoint expression data were obtained from the HisgAtlas database [30] and compared between TCGA-LIHC risk groups. Immunophenoscore (IPS) can be computed in an unbiased way utilizing machine learning algorithms on the basis of 4 primary gene types (immunomodulators, MHC molecules, effector cells, and immunosuppressive cells) that influence immunogenicity [31]. We acquired the IPS of HCC from the TCIA database (https://tcia.at/home) [32] and compared the IPS of the distinct FPRS risk group in TCGA-LIHC to evaluate the responsiveness to immune checkpoint blocking therapy. The Tumor Immune Dysfunction and Exclusion (TIDE, http://tide.dfci.harvard.edu/) algorithm was run in three cohorts to identify the TIDE score difference between the low- and high-risk groups. We employed the pRRophetic algorithm to estimate the response to sorafenib, docetaxel, paclitaxel, and cisplatin identified by the half-maximal inhibitory concentration (IC50) for each TCGA-LIHC sample on the Genomics of Drug Sensitivity in Cancer (GDSC) database.

2.9. Statistical Analysis. All statistical analyses and data visualization were conducted in R (https://www.r-project.org/, version 3.6.3). And all calculated P values were two-tailed; $P < 0.05$ was considered significant.

3. Results

3.1. Two Ferroptosis Clusters in HCC Were Identified by Consensus Clustering Based on FRGs. Univariate Cox regression analysis of 111 FRGs selected from FerrDb showed that 38 FRGs were considerably correlated with the prognosis of HCC patients. According to the expression level of these 38 FRGs (Supplementary Table 1), 365 samples in TCGA-LIHC were clustered (Supplementary Table 2). The cumulative distribution function (CDF) of distinct clustering techniques from $k = 2$ to 9 and the relative variations of the area under CDF curves demonstrated that the area under the CDF chart tended to be stable when $k = 2$ (Figures 1(a) and1(b)). Therefore, HCC was divided into two ferroptosis clusters, namely, C1 and C2 (Figure 1(c)). In the TCGA-LIHC cohort, an obvious difference in prognosis between the two ferroptosis clusters was shown, and the prognosis of C2 was significantly stronger than that of C1 (Figure 1(d)). Survival analysis in ICGC yielded the same results (Figure 1(e)). Heat maps of the expression of 38 prognostic FRGs in two ferroptosis clusters showed that most prognostic FRGs were overexpressed in C1 (Figure 1(f)).

3.2. Association of Ferroptosis Clusters with Clinical Features. Next, the relationship between two ferroptosis clusters and clinicopathological factors was studied. The proportional distribution maps of different clinical bed characteristics are generated. In the TCGA-LIHC cohort, the two ferroptosis clusters did not exhibit any obvious differences in age (age ≤60 and age >60), gender (female and male), life status (alive and dead), M stage (M0 and M1), N stage (N0 and N1), and fibrosis (negative, portal fibrosis, fibrous septa, nodular formation, and cirrhosis) distribution. And the distributions of grade (G1, G2, G3, and G4), AJCC stage (stage I, stage II, stage III, and stage IV), and T stage (T1, T2, T3, and T4), viral etiology (negative, HBV, HCV, and HBV+HCV), and life state (alive and dead) between C1 and C2 in the TCGA-LIHC cohort were significantly different. Among them, C2 samples were often from the AJCC stage, M stage, N stage, T stage, survival patients with low tumor grade and hepatitis C virus (HCV), and hepatitis B virus (HBV) infection (Figure 2(a)). In the ICGC cohort, a significant difference was shown between C1 and C2 only in the proportion of different AJCC stages. In the C1 subtype, stage II and stage III occupy the absolute majority of this subtype in a nearly equal proportion. However, more than half of the samples of the C2 subtype were in stage III. No significant differences

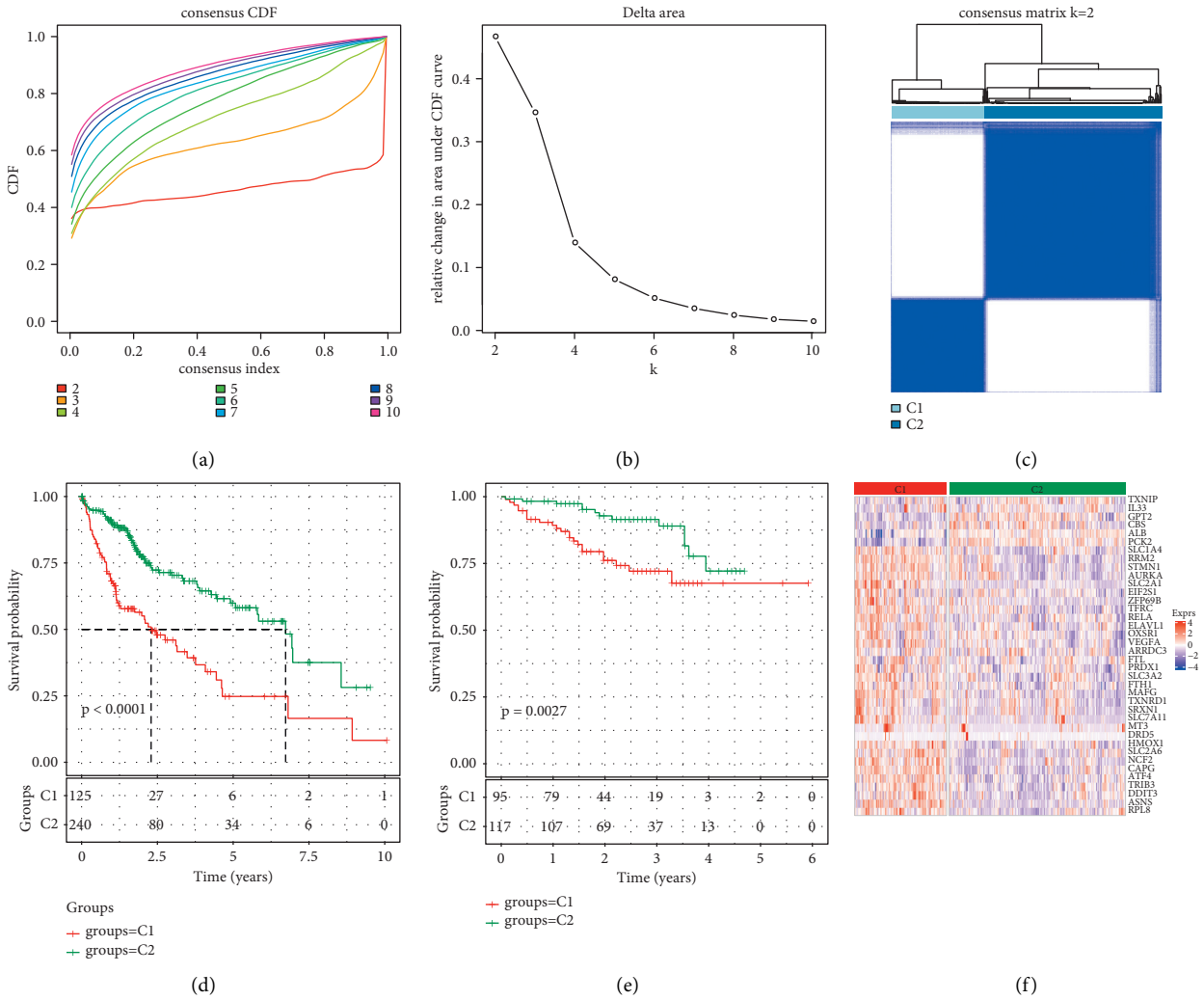

Figure 1: Consensus clustering analysis based on the prognosis on FRGs in HCC. (a) The cumulative distribution function (CDF) of distinct clustering methods from $k = 2$ to 9. (b) The relative alterations of the area under CDF curves with the index from 2 to 9. (c) Clustering heat map of TCGA-LIHC samples with the index $k = 2$. (d) Kaplan–Meier curves for ferroptosis clusters prognosis in TCGA-LIHC cohort. (e) Kaplan–Meier curve of OS between two ferroptosis clusters. (f) The expression heat map of 38 prognostic FRGs in two ferroptosis clusters.

were identified in age, gender, viral etiology, fibrosis, and alcohol consumptions, and smoking between the two subtypes in this cohort (Figure 2(b)).

3.3. Comparisons of the Somatic Variation between Two Ferroptosis Clusters. To further investigate the molecular mechanism behind the classification of ferroptosis subtypes, mutation spectra of two ferroptosis subtypes were analyzed. The ferroptosis subtypes were associated with measures of DNA damage, including aneuploidy, HRD, fraction altered, and the number of segments. Compared with C1, C2 had a lower aneuploidy score, HRD, fraction altered, and the number of segments. Nevertheless, no significant differences were identified in tumor mutation burden (TMB) between C1 and C2 (Figure 3(a)). OncoPrint of gene mutation distribution between C1 and C2 patients showed a significant association between the ferroptosis subtype and somatic mutations. The relative frequency of 20 altered genes in C1 was high. In addition, in terms of copy number variation (CNV), C1 had a higher frequency of copy number amplification and deletion than C2 (Figure 3(b)).

3.4. Differences in Immune-Related Characteristics of Ferroptosis Subtypes. To examine the immune heterogeneity between two ferroptosis subtypes, the immune characteristics of two ferroptosis subtypes were analyzed. The abundance of 22 different kinds of immune cells in TCGA-LIHC and ICGC cohort was computed utilizing the CIBERSORT and compared between groups of ferroptosis subtypes. In the TCGA-LIHC cohort, M0 macrophages, regulatory T cells, helper follicular T cells, and activated memory CD4 T cells were strongly enriched in C1, while the cells significantly enriched in C2 included monocytes,

Figure 2: Correlation of ferroptosis clusters with clinical features. (a) The clinicopathological distribution diagram of two ferroptosis clusters in the TCGA-LIHC cohort, including grade, M stage, sex, N stage, T stage, AJCC, age, viral etiology, fibrosis, and life status. (b) In the ICGC cohort, the age, gender, AJCC stage, viral etiology, fibrosis, alcohol consumptions, and smoking proportion distribution differences between C1 and C2; chi-square test; $^{*}P < 0.05$.

resting memory CD4 T cells, naive B cells, M1and M2 macrophages, and resting mast cells (Figure 4(a)). In the ICGC cohort, activated memory CD4 T cells and M0 macrophages, naive B cells, and resting dendritic cells have significantly different abundances in C1 and C2 (Figure 4(c)). By comprehensive analysis of stromal, immune, and ESTIMATE scores of two ferroptosis subtypes in each cohort, C1 was greatly elevated as opposed to C2 (Figures 4(b) and 4(d)).

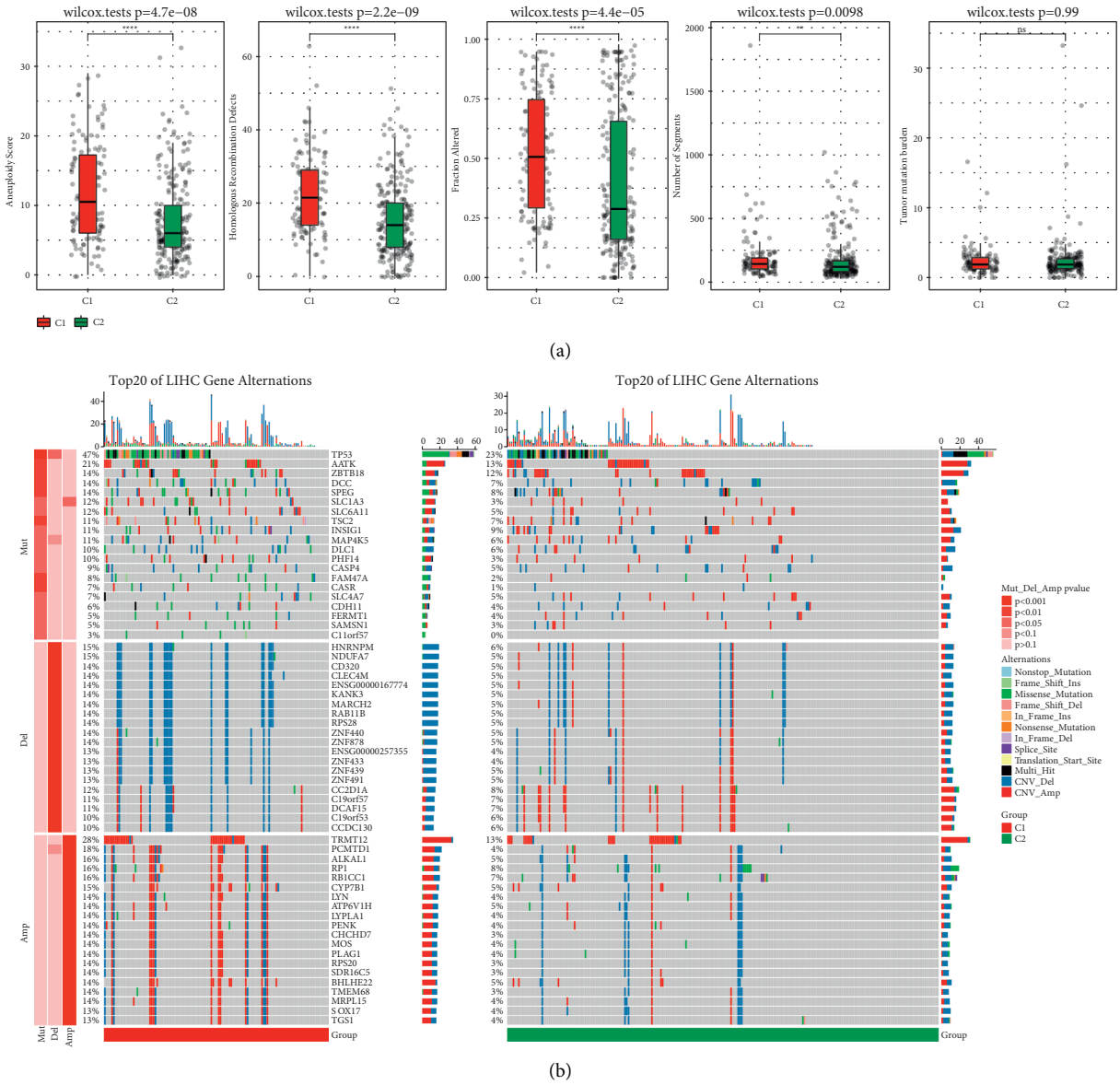

Figure 3: Difference of the somatic variation between two ferroptosis clusters. (a) Relation of DNA damage with ferroptosis subgroups in TCGA-LIHC cohort, including aneuploidy score, HRD, fraction altered, number of segments, and tumor mutation burden; Wilcoxon test. (b) OncoPrint of gene mutation and CNV distribution between C1 and C2 patients. Fisher's test, $^{**}P < 0.01$, and $^{****}P < 0.0001$.

3.5. Identification of Genes Associated with Ferroptosis Phenotype. To identify ferroptosis phenotypes related genes, the differential expression analysis of two ferroptosis subtypes was carried out (FDR <0.05 and | log2FC | > log2 (2)), and 324 upregulated differentially expressed genes (DEGs) and 274 downregulated DEGs were identified for the first time. Among them, the top 5 genes with the highest expression in C1 are SPP1, AFP, PKM, CD24, and MYBL2, and the top 5 genes with the highest expression in C2 are TAT, CYP2A6, SLC10A1, CYP3A4, and HPD. The functional enrichment analysis of the DEGs between the two ferroptosis subtypes was carried out, respectively. In TCGA-LIHC, the top GO terms of DEGs included cell division, immune cell activation, cell migration, and cytokine activity (Figure 5(a)). Moreover, all the pathways generated from KEGG analysis were associated with immune responses (Figure 5(c)). For the ICGC cohort, all DEGs-enriched GO terms and KEGG pathways were correlated with the anabolism of cancer cells (Figures 5(b) and 5(d)). Univariate Cox regression analysis illustrated that 137 genes had prognostic significance in 598 DEGs (Figure 5(e)), which were included in LASSO analysis. The best parameter based on 5-time cross-validation was 13 (Figures 5(f) and 5(g)). The stepAIC in the MASS package reduced the number of genes from 13 to 6 and calculated each gene's risk value in the optimal model as shown in Figure 5(h).

3.6. Generation and Validation of a Risk Scoring Model Based on Six FRGs. The expression and coefficient of 6 FRGs were used to construct the ferroptosis prognosis model, which was used to calculate the risk value of HCC samples and rank them.

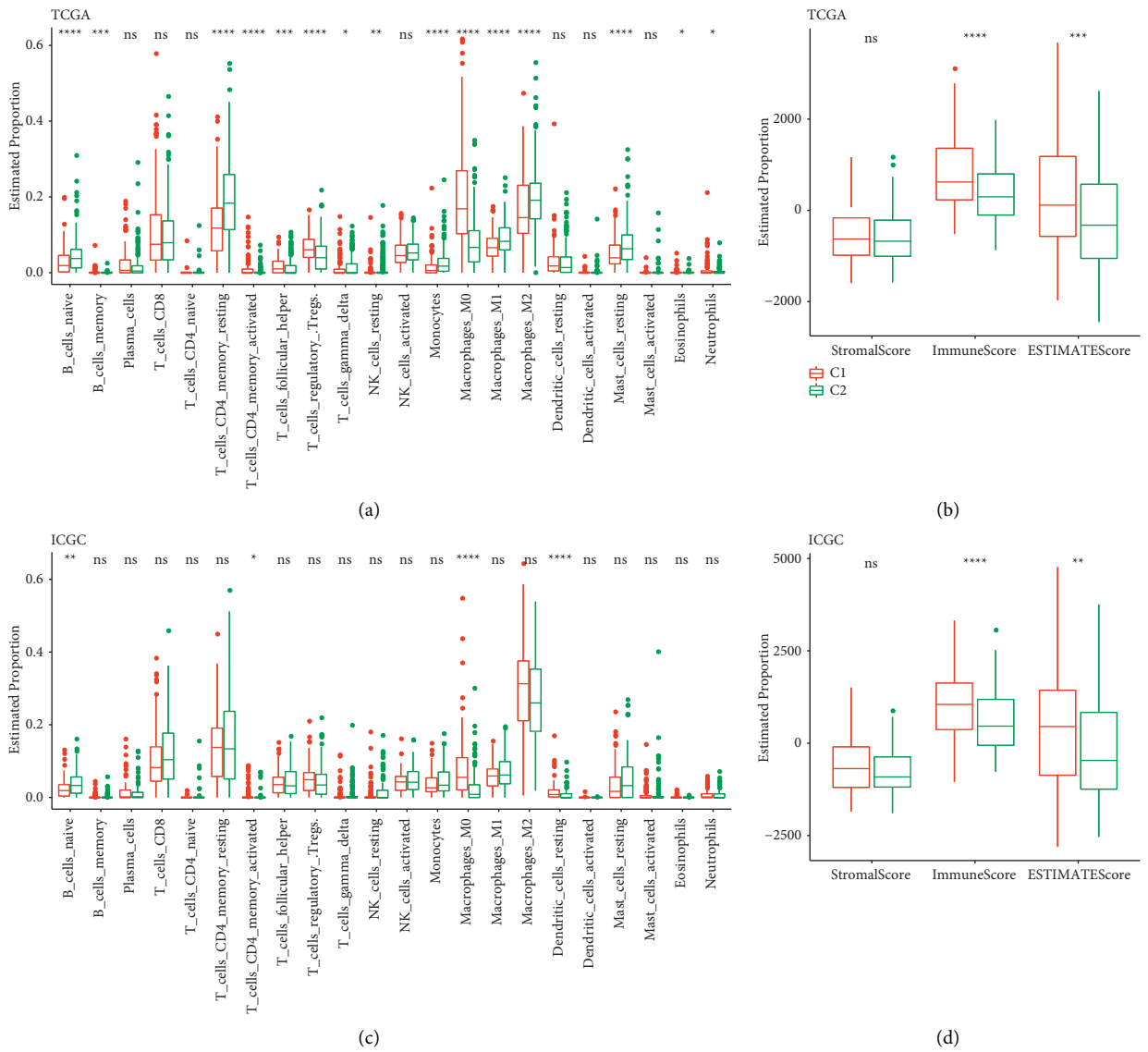

Figure 4: Immune-related features in each ferroptosis subtype. (a) Each immune infiltrating cell abundance of the two ferroptosis subtypes in the TCGA-LIHC cohort. (b) Differences in stromal, immune, and ESTIMATE scores between the two ferroptosis subtypes in the TCGA-LIHC cohort. (c) The abundance of 22 immune infiltrating cells per ferroptosis subtypes in the ICGC cohort. (d) Stromal, immune, and ESTIMATE scores of each ferroptosis subtype in ICGC cohort. $^{*}P < 0.05$; $^{**}P < 0.01$; $^{***}P < 0.001$; $^{****}P < 0.0001$.

According to the cut-off point, 203 samples were classified into the low-FPRS group and 162 samples into the high-FPRS group. The risk plots of TCGA-LIHC illustrated the expression, survival status, and risk values distribution of the 6 FRGs of each HCC patient (Figure 6(a)). The Kaplan–Meier survival curve showed obvious differences in OS among TCGA-LIHC groups (Figure 6(b)). The area under the curve (AUC) for one-, three-, and five-year OS was 0.77, 0.732, and 0.76, respectively (Figure 6(c)). In ICGC and GSE14520 external validation sets, the survival advantage of low-risk samples was considerably greater as opposed to that of high-risk samples (Figures 6(d) and 6(f)). ROC curve showed that the FPRS model can effectively predict one-, three-, and five-year OS of HCC patients in the ICGC cohort and GSE14520 cohorts (Figures 6(e) and 6(g)). Furthermore, we also compared the expression distribution of six FRGs in two molecular subtypes. It can be observed that CDCA8, SPP1, S100A9, EPO, and FTCD are significantly overexpressed in C1 and CFHR3 is significantly overexpressed in C2 (Figure S2(a)). In addition, among the six FRGs, CDCA8, SPP1, S100A9, and EPO were significantly positively correlated with FPRS, and FTCD and CFHR3 were significantly negatively correlated with FPRS (Figure S2(b)). We used the string database to analyze the interaction between the six FRGs. It can be observed that there is no direct interaction between the six FRGs, suggesting that these genes may independently participate in different biological processes (Figure S2(c)).

3.7. The Manifestations of FPRS in Different Clinicopathological Features and Subtypes. When we studied the relationship between FPRS and clinical features, it was

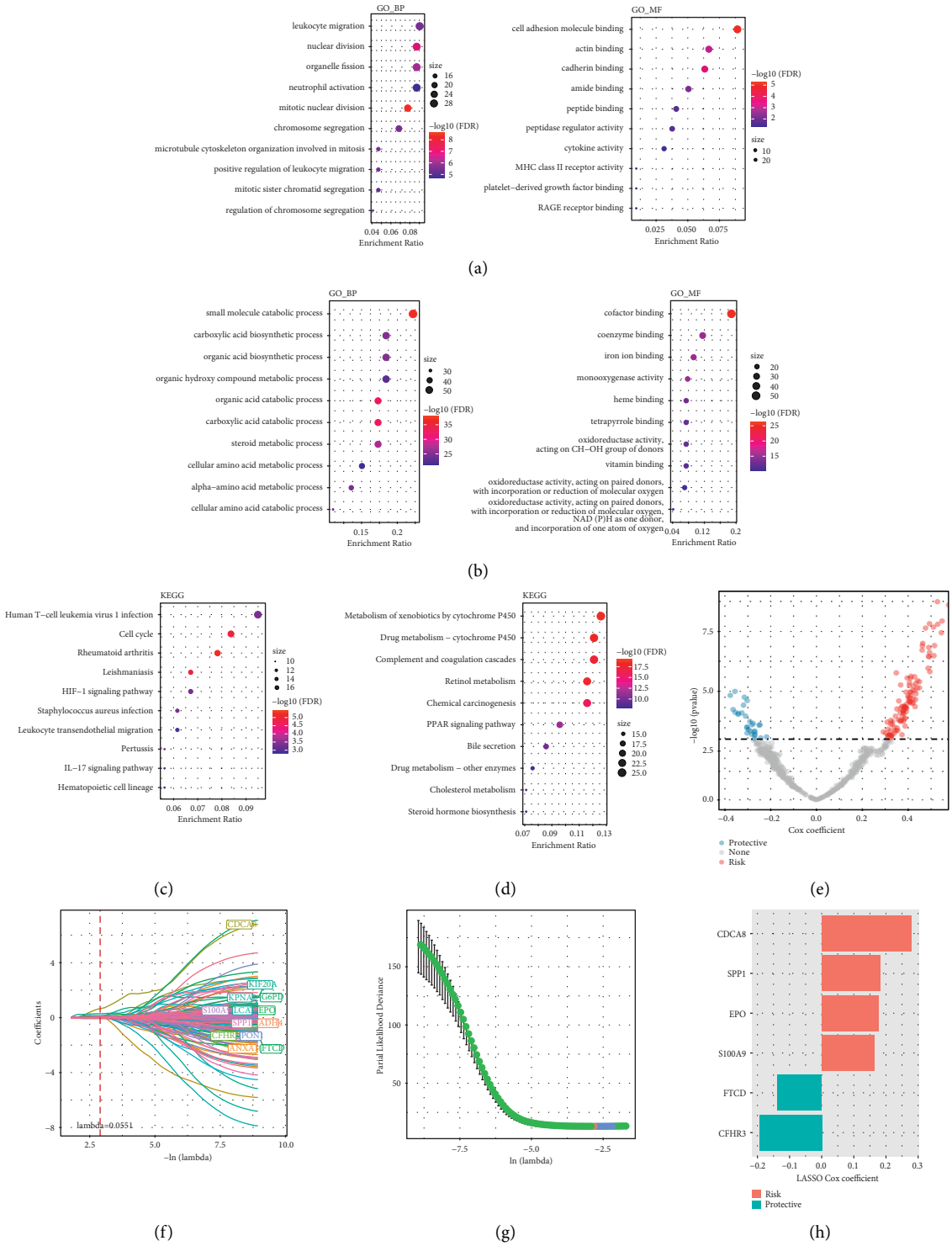

Figure 5: Recognition of genes associated with ferroptosis phenotype. (a) Top 10 GO terms of DEGs between two ferroptosis subtypes in TCGA-LIHC. (b) The KEGG pathways of DEGs between two ferroptosis subtypes in TCGA-LIHC. (c) All DEGs-enriched top 10 GO terms in ICGC cohort. (d) All DEGs-enriched top 10 KEGG pathways in ICGC cohort. (e) Univariate regression between DEGs and HCC prognosis. (f) Distribution of LASSO coefficients of 137 genes with prognostic value. (g) 5-time cross-validation was used to select the best parameters in the model. (h) The coefficient of each gene in the optimal model.

established that the FPRS was associated with pathological characteristics in TCGA-LIHC datasets, including T stage, AJCC stage, grade, viral etiology, and survival status. In addition, the distributions of FPRS were substantially varied between the two molecular subgroups (Figure 7(a)). We found that, in the ICGC cohort, FPRS was significantly correlated with the AJCC stage, life status, and molecular subtypes, but not with age, sex, smoking, viral etiology, and

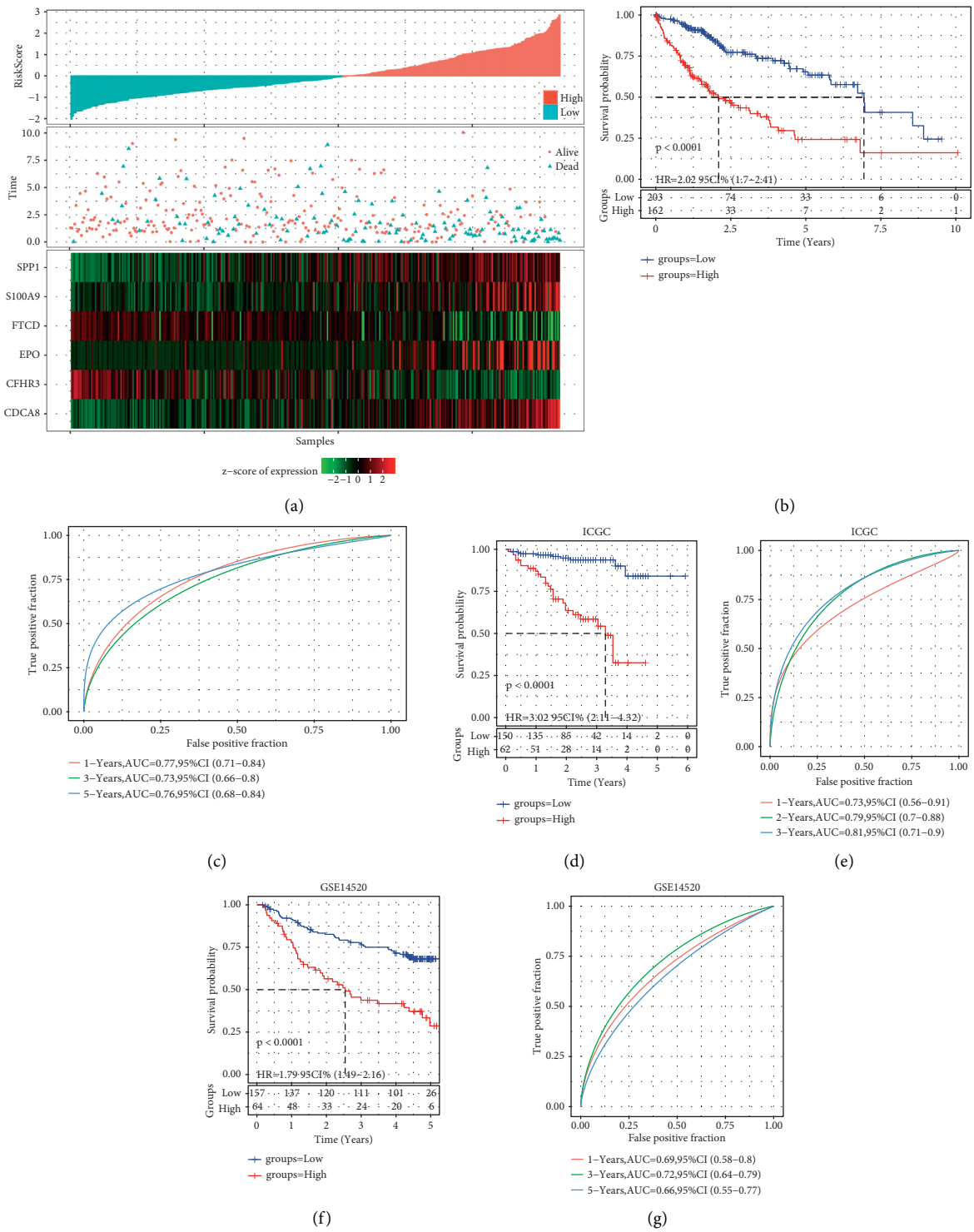

Figure 6: Generation and evaluation of risk scoring models based on six FRGs. (a) The risk plots of TCGA-LIHC showed the expression, survival status, and risk values distribution of the 6 FRGs of each HCC patient. (b) Kaplan–Meier curve for the OS of HCC patients in low- and high-risk groups in the TCGA-LIHC cohort. (c) ROC curves for the predictive significance of risk scores for OS at 1, 3, and 5 years in the TCGA-LIHC cohort. (d) Kaplan–Meier survival analysis between low- and high-risk patients in the ICGC cohort. (e) ROC curve was employed to examine predictive efficacy of the FPRS model over one, three, and five years in the ICGC cohort. (f) Kaplan–Meier curves of the FPRS model for HCC patients in various risk groups in the GSE14520 cohort. (g) Time-dependent ROC curves for the FPRS model in the GSE14520 cohort.

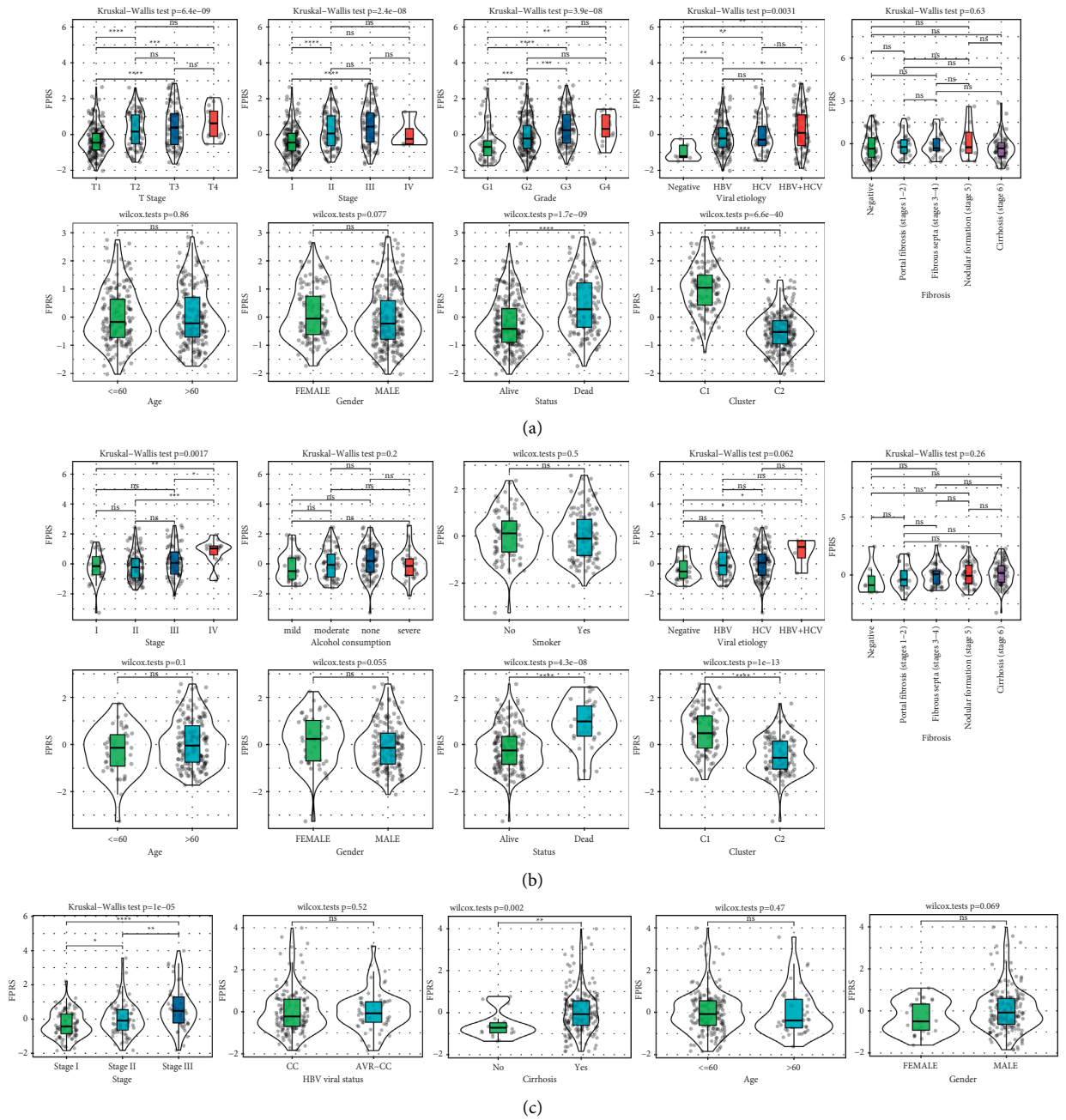

Figure 7: Association between FPRS and clinicopathological characteristics. (a) The violin plot showed the FPRS distributions according to age, gender, AJCC stage, grade, viral etiology, fibrosis, survival state, and molecular subtype in the ICGC cohort. (b) Correlation between FPRS and pathological features of samples in the GSE14520 cohort, including age, gender, AJCC stage, HBV viral status, and cirrhosis. Wilcoxon test was utilized for comparing the two groups, and the Kruskal-Wallis test was utilized for the differences between the two groups. $^{*}P < 0.05$; $^{**}P < 0.01$; $^{***}P < 0.001$; $^{****}P < 0.0001$. (c) The relationship between FPRS and pathological features of samples in the GSE76427 cohort.

fibrosis of HCC patients (Figure 7(b)). In the GSE14520 cohort, FPRS was related to the AJCC stage and cirrhosis (Figure 7(c)).

3.8. Comparison of Molecular and Immune Characteristics Using FPRS. We identified the relationship between FPRS and genomic changes. We found that the two risk groups have significantly different performance on aneuploidy score, HRDs, fraction altered, and the number of segments. High-FPRS samples had significantly higher levels of these DNA damage-related variables (Figure 8(a)). Correlation analysis also illustrated that FPRS had a positive correlation with the score, HRDs, fraction altered, and the number of segments (Figure 8(b)). Furthermore, the overall somatic mutation rate, copy number amplification, and deletion in high-FPRS samples were greatly elevated as opposed to the ones in low-FPRS samples (Figure 8(c)).

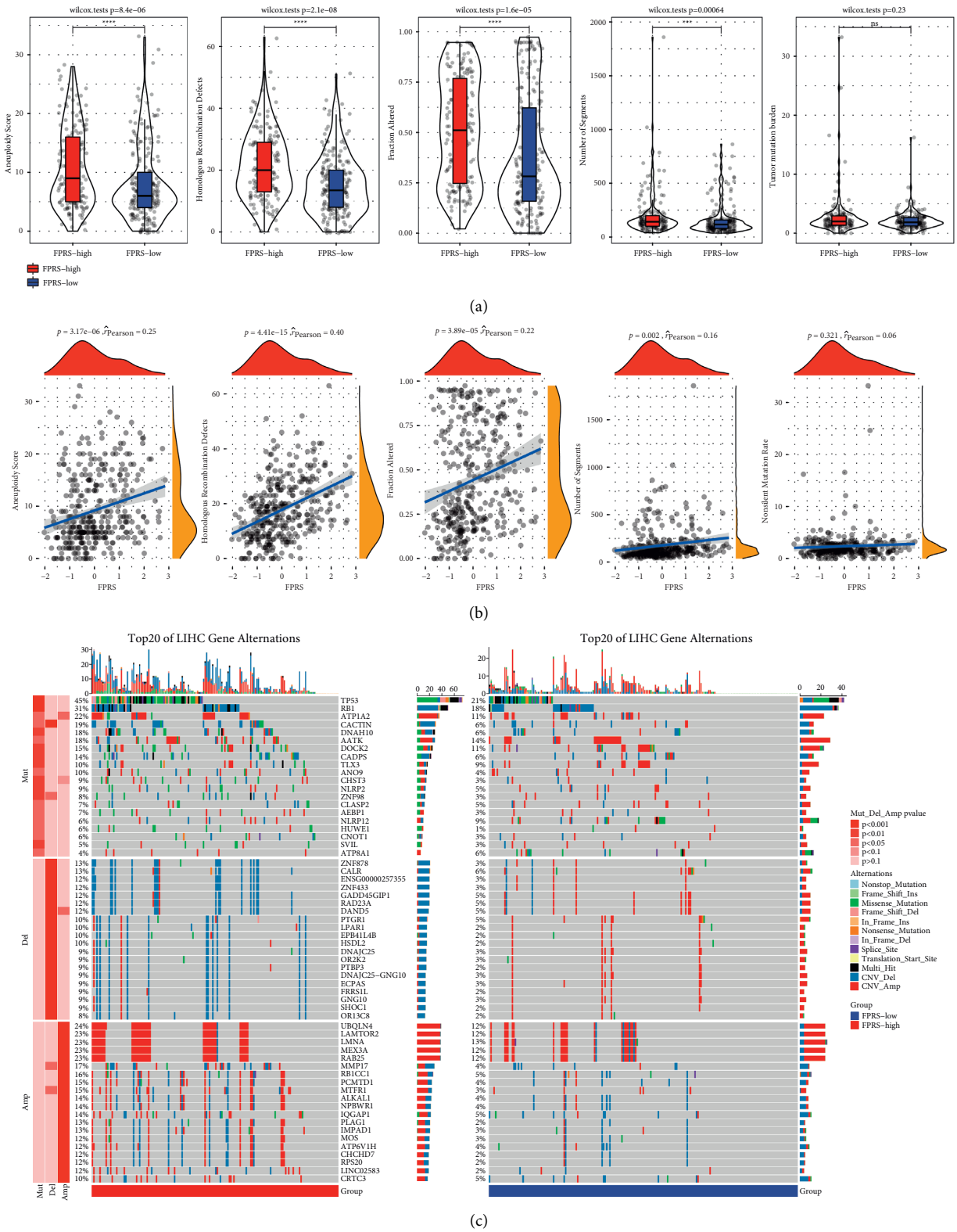

FIGURE 8: Molecular characteristics analysis between the high-FPRS and low-FPRS groups. (a) The difference of DNA damage-related index between high-FPRS and low-FPRS groups; Wilcoxon test. (b) Pearson's correlation analysis of FPRS and DNA damage-related indexes. (c) OncoPrint of somatic mutation and CNV distribution between low-FPRS and high-FPRS groups; Fisher's test; $^{***}P < 0.001$; $^{****}P < 0.0001$.

To further study the immunological differences between distinct FPRS groups, the relative abundance of 22 different kinds of immune cells was computed utilizing CIBERSORT. The results showed that 16 kinds of immune cells showed significantly different estimated proportions in high-FPRS and low-FPRS groups and the proportion of immune cells enriched in the low-FPRS group was higher (Figure 9(a)). The stromal score of the low-FPRS group was greatly elevated in contrast to that of the high-FPRS group, while the immune score was greatly decreased than in high-FPRS group (Figure 9(b)). FPRS was also related to the levels of resting CD4 memory T cell, activated CD 4 memory T cell, neutrophils, regulated T cells, resting dendritic cells, and M0 macrophages (Figure 9(c)). FPRS was closely related to CNVs, DNA damage, and immune characteristics of HCC patients.

3.9. The Application of FPRS in Predicting Immune Chemotherapies. To determine whether FPRS can predict the response of HCC patients to immune checkpoint inhibitor (ICI) therapies, 21 immune checkpoint-related genes were obtained from HisgAtlas database [30] and their expression in high-FPRS and low-FPRS patients was analyzed. 17 immune checkpoint-related genes were found to have differential expression between low- and high-FPRS samples, and the expression level of 17 immune checkpoint-related genes in high-FPRS samples was greater in contrast with that in low-FPRS samples (Figure 10(a)). In addition, the applicability of different FPRS samples to anti-CTLA4 treatment, anti-PD1 treatment, anti-CTLA4, and anti-PD1 combined therapy was compared by IPS. The findings showed that the IPS of the low-FPRS group treated with anti-CTLA4 was relatively higher, indicating that the patients with low FPRS had a better therapeutic effect on anti-CTLA4 (Figure 10(b)). The high-FPRS patient had a greatly elevated TIDE score as opposed to that of the low-FPRS patient in the TCGA-LIHC cohort and ICGC cohort, indicating that a greater trend for immune escape was illustrated by the high-FPRS patient group, which may fail to respond to ICI treatment (Figures 10(c) and 10(d)). It is noteworthy that no significant differences were identified in the TIDE score between low-FPRS and high-FPRS groups in the GSE14520 cohort (Figure 10(e)). In addition, when evaluating the sensitivity of the two FPRS groups to sorafenib, docetaxel, paclitaxel, and cisplatin, we found that patients with high-FPRS had a greater sensitivity to sorafenib, docetaxel, and cisplatin, while patients with low FPRS had a greater sensitivity to paclitaxel (Figure 10(f)).

3.10. FPRS Combined with Clinicopathological Features of Nomogram Improves Prognosis and Survival Prediction. To construct a more effective nomogram model using the FPRS model and other clinicopathological information, multivariate and univariate Cox regression analysis showed that FPRS was an independent prognostic indicator of HCC (Figures 11(a) and11(b)). We established a nomogram including FPRS and several other clinical factors (AJCC stage and T stage) to anticipate OS of HCC patients and observed that FPRS made the greatest contribution to the survival prediction of nomogram (Figure 11(c)). The calibration curve illustrated that the anticipated probabilities of nomogram's one-, three-, and five-year OS were very close to the actually observed probabilities (Figure 11(d)). Decision curve analysis confirmed that the net income of FPRS and nomogram was considerably greater in contrast with that of the extreme curve and showed the strongest predictive ability of OS compared with other clinicopathological features (Figures 11(e) and 11(f)).

4. Discussion

Owing to the variability of HCC and the tumor microenvironment (TME) complexity, determining the long-term effectiveness of HCC continues to be a critical issue in clinical practice [33]. It is necessary to classify and refine the appropriate treatment intervention decision-making in this kind of tumor [34]. In addition, the effectiveness of sorafenib in treating advanced HCC strongly encourages the classification of HCC patients [34]. Several transcriptional group-based classifications were widely accepted in HCC [35–37] but lack genomic analysis. Recent studies have focused on defining different HCC categories based on more detailed biological characteristics to ensure maximum benefit and minimum toxicity for specific treatments [38]. Given the nonnegligible regulatory effect of sorafenib on ferroptosis, we revealed the molecular subclasses of HCC from the perspective of ferroptosis.

Transcriptome, genomic, and clinical data of 912 HCC samples were retrieved from TCGA, ICGC, and GEO. Based on the expression of 111 ferroptosis significantly associated with HCC prognosis, HCC samples from each cohort were separated into two heterogeneous subclasses, with significant differences in OS between the two subclasses. By comparing the clinical, genomic, and immune characteristics between the two subgroups, we recognized that, in C1 with poor prognosis, there were more patients with advanced stage and infection with HBV and HCV, higher rates of DNA damage including aneuploidy, HRD, fraction altered, and the number of segments, and higher probability of gene mutation and copy number variation. To some extent, these results reveal the reason for the poor prognosis of C1, because the TME cell components of HCC are mainly composed of HCC cells, HCC-related fibroblasts, endothelial cells, and immune cells. The TME cell components of HCC are mainly composed of HCC cells, HCC-related fibroblasts, immune cells, and endothelial cells [33]. Among them, immune cells are most often studied, because the infiltration levels of immune cells can largely reflect the applicability of patients to immunotherapy [39]. HCC patients with C1 had higher levels of M0 macrophages, regulatory T cells, helper T cells, and activated memory CD4 T cells infiltration and higher immune score. In C2, there is strong infiltration of resting memory CD4 T cells, naive B cells, monocyte, resting mast cells, and M1and M2 macrophages. Therefore, there was strong heterogeneity between C1 and C2, including clinical, molecular, and immunological features.

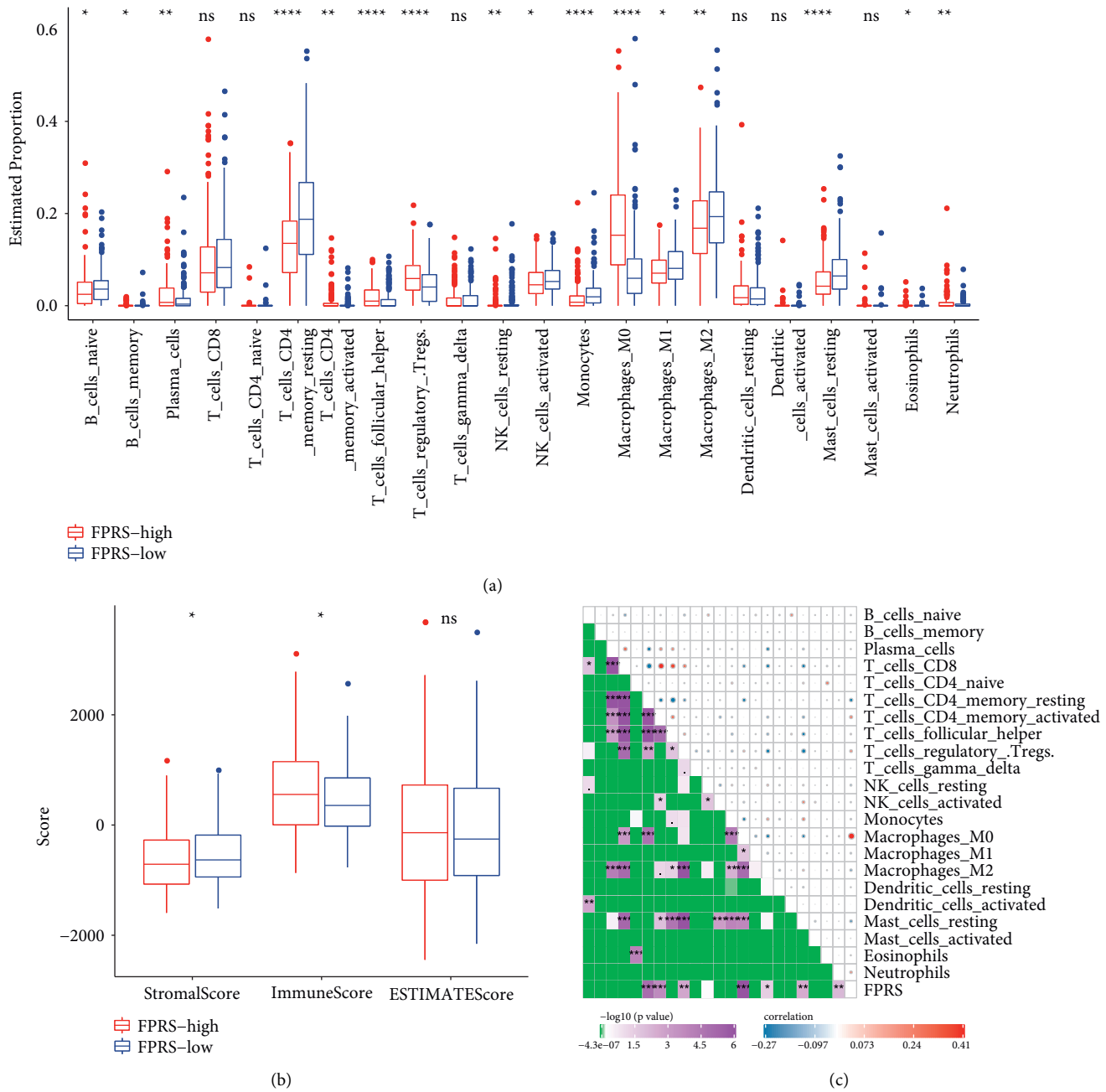

Figure 9: Immunological differences between different FPRS groups. (a) The estimated percentage of 22 different kinds of immune cells between different FPRS groups in the TCGA-LIHC cohort. (b) Difference of stromal, immune, and ESTIMATE scores between low-FPRS and high-FPRS groups. (c) Pearson's correlation analysis between 22 immune cells and FPRS.

Additionally, we developed and validated a prognostic model called FPRS, which is composed of CDCA8, SPP1, EPO, S200A9, FTCD, and CFHR3 in three independent cohorts. It shows considerable effect in predicting the OS probability of HCC samples and can reflect the clinical characteristics of different patients. It is an independent prognostic factor for HCC. FPRS model assigned each sample with a specific risk score, and patients were subdivided into different risk groups according to such score. In line with our expectations, the prognosis of high FPRS was considerably unfavorable in contrast with that of low FPRS. Notably, from the study of Teresa Davoli, we learned that copy number aberration contributed more to immune characteristics than tumor mutation load and the low burden of copy number increase/loss is related to the responsiveness to immunotherapy [40]. Indeed, our results also found that the overall somatic mutation rate, copy number amplification, and deletion in low-FPRS samples were significantly lower than those in high-FPRS samples and low-FPRS samples were more effective in anti-CTLA4

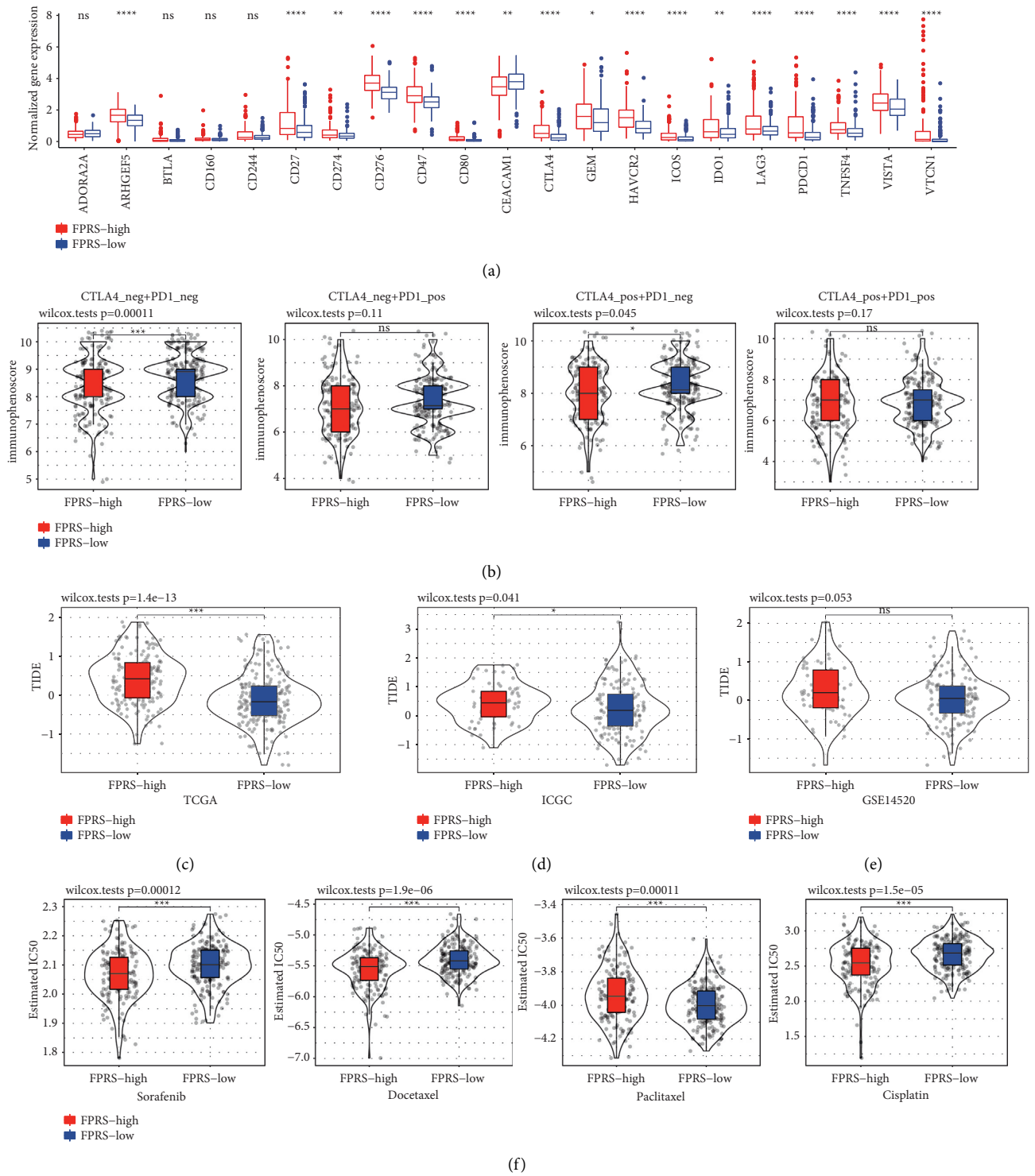

Figure 10: The role of the FPRS model in the prediction of immune/chemotherapeutic benefits. (a) Expression of 21 immune checkpoint-related genes in low-FPRS and high-FPRS patients. (b) The effect of different FPRS samples on IPS of anti-CTLA4 therapy, anti-PD1 therapy, and anti-CTLA4 and anti-PD1 combined therapy. (c) The violin chart illustrated the difference in TIDE scores between high FPRS and low FPRS in the TCGA-LIHC cohort. (d) In the ICGC cohort, the difference of TIDE score between low-FPRS and high-FPRS samples. (e) In the GSE14520 cohort, the performance of TIDE score on high FPRS and low FPRS. (f) Differential chemotherapeutic response between low-FPRS and high-FPRS groups based on IC50 available in the TCGA-LIHC database. Wilcoxon test; $^{*}P < 0.05$; $^{**}P < 0.01$; $^{***}P < 0.001$; $^{****}P < 0.0001$.

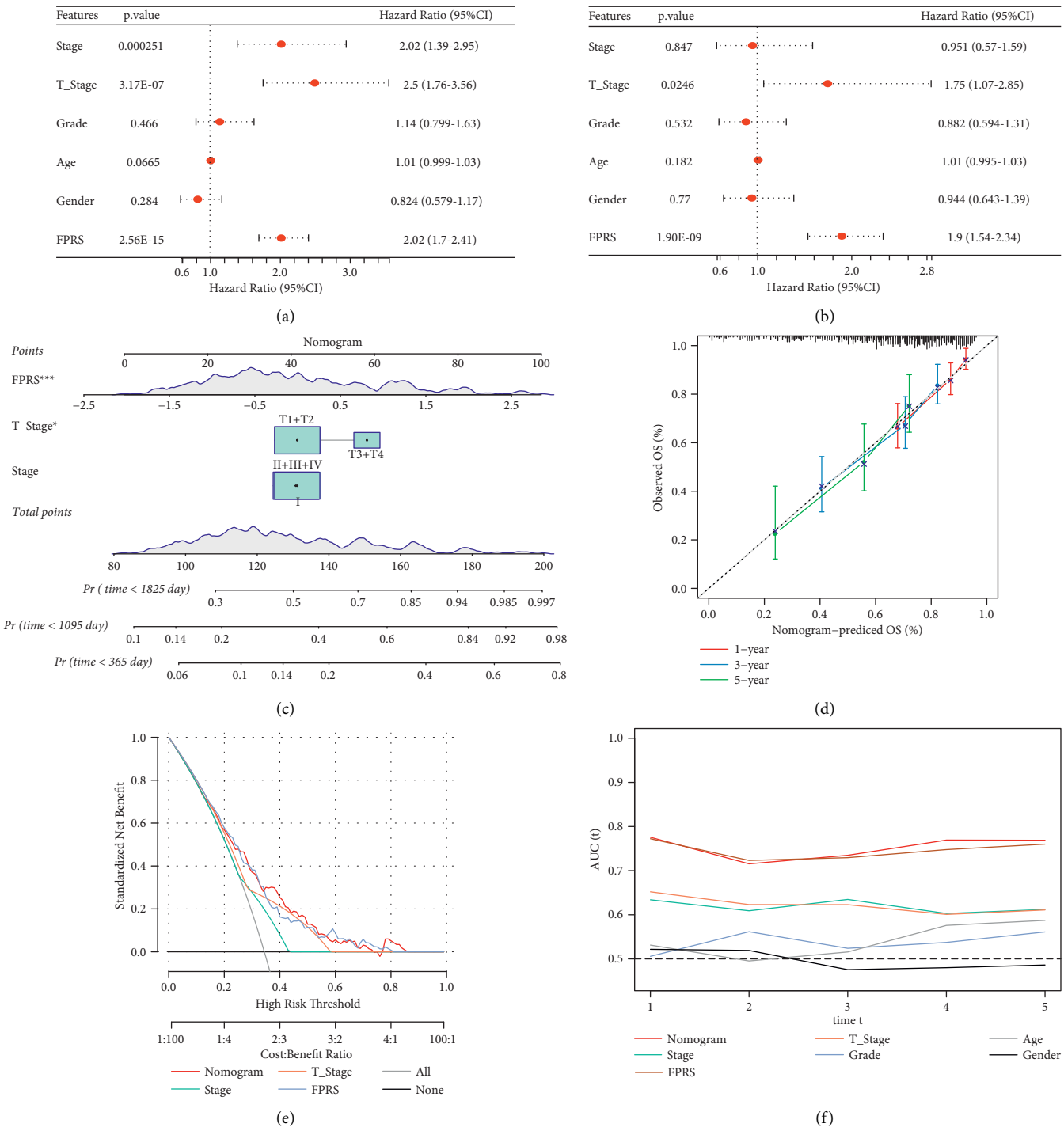

Figure 11: Nomogram of FPRS combined with clinicopathological features. (a) Univariate Cox regression analysis of the clinical variables. (b) Multivariate Cox regression analysis of the prognostic factors. (c) A nomogram based on FPRS and clinical factors was developed to predict the survival rate of HCC patients. Day counts were utilized to determine the survival time. (d) Calibration curve of the nomogram. (e) FPRS and clinical factors are shown in this decision curve analysis diagram. (f) AUC with different clinical variables predicting prognosis.

therapy at immune checkpoints. Moreover, we predicted that patients who have low FPRS had a greater sensitivity to paclitaxel, while patients who have high FPRS had a greater sensitivity to sorafenib, docetaxel, and cisplatin.

In summary, on the one hand, our study revealed two ferroptosis subclasses, which showed heterogeneity in prognosis, clinical characteristics, genetic events, and immune characteristics. On the other hand, a classifier called

the FPRS model has been developed and validated, which may help predict the prognosis and select patients suitable for immunotherapy.

Data Availability

The data used to support the research are included within this manuscript.

Disclosure

Jiang Li and Haisu Tao are the first authors.

Conflicts of Interest

The authors declare that there are no conflicts of interest.

Authors' Contributions

Jiang Li made acquisition of data and drafting the manuscript; Haisu Tao carried out analysis and interpretation of data; Wenqiang Wang helped in acquisition of data; Jian Li performed statistical analysis; Erlei Zhang finished conception and design of the research, as well as revision of manuscript for important intellectual content. Jiang Li and Haisu Tao contributed equally to this research.

Supplementary Materials

Figure S1: work flow chart. Figure S2: expression relationship of 6 FRGs. A: the expression and distribution of 6 genes in two molecular subtypes were different; B: correlation between 6 gene expressions and FPRs; C: protein interaction network among 6 genes. Supplementary Table 1: list of 38 FRGs. Supplementary Table 2: molecular subtypes of each sample in TCGA dataset. (*Supplementary Materials*)

References

[1] H. Sung, J. Ferlay, R. L. Siegel et al., "Global cancer statistics 2020: GLOBOCAN estimates of incidence and mortality worldwide for 36 cancers in 185 countries," *CA: A Cancer Journal for Clinicians*, vol. 71, no. 3, pp. 209–249, 2021.

[2] Y. Wu, Z. Liu, and X. Xu, "Molecular subtyping of hepatocellular carcinoma: a step toward precision medicine," *Cancer Communications*, vol. 40, no. 12, pp. 681–693, 2020.

[3] M. Vacca, M. Di Eusanio, M. Cariello et al., "Integrative miRNA and whole-genome analyses of epicardial adipose tissue in patients with coronary atherosclerosis," *Cardiovascular Research*, vol. 109, no. 2, pp. 228–239, 2016.

[4] J. Fu and H. Wang, "Precision diagnosis and treatment of liver cancer in China," *Cancer Letters*, vol. 412, pp. 283–288, 2018.

[5] Q. Liang, X. Shen, and G. Sun, "Precision medicine: update on diagnosis and therapeutic strategies of hepatocellular carcinoma," *Current Medicinal Chemistry*, vol. 25, no. 17, pp. 1999–2008, 2018.

[6] S. J. Dixon, K. M. Lemberg, M. R. Lamprecht et al., "Ferroptosis: an iron-dependent form of nonapoptotic cell death," *Cell*, vol. 149, no. 5, pp. 1060–1072, 2012.

[7] J. Wu, "Ferroptosis in liver disease: new insights into disease mechanisms," *Cell Death & Disease*, vol. 7, p. 276, 2021.

[8] K. M. Kim, S. S. Cho, and S. H. Ki, "Emerging roles of ferroptosis in liver pathophysiology," *Archives of Pharmacal Research*, vol. 43, no. 10, pp. 985–996, 2020.

[9] Y. Yu, L. Jiang, H. Wang et al., "Hepatic transferrin plays a role in systemic iron homeostasis and liver ferroptosis," *Blood*, vol. 136, no. 6, pp. 726–739, 2020.

[10] S. Tsurusaki, Y. Tsuchiya, T. Koumura et al., "Hepatic ferroptosis plays an important role as the trigger for initiating inflammation in nonalcoholic steatohepatitis," *Cell Death & Disease*, vol. 10, no. 6, p. 449, 2019.

[11] N. Yamada, T. Karasawa, H. Kimura et al., "Ferroptosis driven by radical oxidation of n-6 polyunsaturated fatty acids mediates acetaminophen-induced acute liver failure," *Cell Death & Disease*, vol. 11, no. 2, p. 144, 2020.

[12] E. Lachaier, C Louandre, C Godin et al., "Sorafenib induces ferroptosis in human cancer cell lines originating from different solid tumors," *Anticancer Research*, vol. 34, pp. 6417–6422, 2014.

[13] J. Nie, B. Lin, M. Zhou, L. Wu, and T. Zheng, "Role of ferroptosis in hepatocellular carcinoma," *Journal of Cancer Research and Clinical Oncology*, vol. 144, no. 12, pp. 2329–2337, 2018.

[14] J.-y. Liang, D.-s. Wang, H.-c. Lin et al., "A novel ferroptosis-related gene signature for overall survival prediction in patients with hepatocellular carcinoma," *International Journal of Biological Sciences*, vol. 16, no. 13, pp. 2430–2441, 2020.

[15] J. Liu, G. Sun, S. Pan et al., "The Cancer Genome Atlas (TCGA) based m6A methylation-related genes predict prognosis in hepatocellular carcinoma," *Bioengineered*, vol. 11, no. 1, pp. 759–768, 2020.

[16] G.-M. Liu, H.-D. Zeng, C.-Y. Zhang, and J.-W. Xu, "Identification of a six-gene signature predicting overall survival for hepatocellular carcinoma," *Cancer Cell International*, vol. 19, no. 1, p. 138, 2019.

[17] C. Wang, Y. Liao, W. He et al., "Elafin promotes tumour metastasis and attenuates the anti-metastatic effects of erlotinib via binding to EGFR in hepatocellular carcinoma," *Journal of Experimental & Clinical Cancer Research*, vol. 40, no. 1, p. 113, 2021.

[18] O. V. Grinchuk, S. P. Yenamandra, R. Iyer et al., "Tumor-adjacent tissue co-expression profile analysis reveals pro-oncogenic ribosomal gene signature for prognosis of resectable hepatocellular carcinoma," *Molecular Oncology*, vol. 12, no. 1, pp. 89–113, 2018.

[19] N. Zhou and J. Bao, "FerrDb: a manually curated resource for regulators and markers of ferroptosis and ferroptosis-disease associations," *Database*, vol. 2020, 2020.

[20] M. D. Wilkerson and D. N. Hayes, "ConsensusClusterPlus: a class discovery tool with confidence assessments and item tracking," *Bioinformatics*, vol. 26, no. 12, pp. 1572-1573, 2010.

[21] D. C. Koboldt, Q. Zhang, D. E. Larson et al., "VarScan 2: somatic mutation and copy number alteration discovery in cancer by exome sequencing," *Genome Research*, vol. 22, no. 3, pp. 568–576, 2012.

[22] X. Lyu, G. Li, and Q. Qiao, "Identification of an immune classification for cervical cancer and integrative analysis of multiomics data," *Journal of Translational Medicine*, vol. 19, no. 1, p. 200, 2021.

[23] A. Mayakonda, D.-C. Lin, Y. Assenov, C. Plass, and H. P. Koeffler, "Maftools: efficient and comprehensive analysis of somatic variants in cancer," *Genome Research*, vol. 28, no. 11, pp. 1747–1756, 2018.

[24] A. M. Newman, C. L. Liu, M. R. Green et al., "Robust enumeration of cell subsets from tissue expression profiles," *Nature Methods*, vol. 12, no. 5, pp. 453–457, 2015.

[25] K. Yoshihara, M. Shahmoradgoli, E. Martínez et al., "Inferring tumour purity and stromal and immune cell admixture from expression data," *Nature Communications*, vol. 4, no. 1, p. 2612, 2013.
[26] M. E. Ritchie, B. Phipson, D. Wu et al., "Limma powers differential expression analyses for RNA-sequencing and microarray studies," *Nucleic Acids Research*, vol. 43, no. 7, p. e47, 2015.
[27] G. Yu, L.-G. Wang, Y. Han, and Q.-Y. He, "clusterProfiler: an R package for comparing biological themes among gene clusters," *OMICS: A Journal of Integrative Biology*, vol. 16, no. 5, pp. 284–287, 2012.
[28] A. Liberzon, C. Birger, H. Thorvaldsdóttir, M. Ghandi, J. P. Mesirov, and P. Tamayo, "The molecular signatures database hallmark gene set collection," *Cell Systems*, vol. 1, no. 6, pp. 417–425, 2015.
[29] V. Thorsson, D. L Gibbs, S. D Brown et al., "The immune landscape of cancer," *Immunity*, vol. 48, pp. 812–e14, 2018.
[30] Y. Liu, M. He, D. Wang et al., "HisgAtlas 1.0: a human immunosuppression gene database," *Database*, vol. 2017, 2017.
[31] Q. Xu, H. Xu, R. Deng et al., "Landscape of prognostic m6A RNA methylation regulators in hepatocellular carcinoma to aid immunotherapy," *Frontiers in Cell and Developmental Biology*, vol. 9, Article ID 669145, 2021.
[32] P. Charoentong, F. Finotello, M. Angelova et al., "Pan-cancer immunogenomic analyses reveal genotype-immunophenotype relationships and predictors of response to checkpoint blockade," *Cell Reports*, vol. 18, no. 1, pp. 248–262, 2017.
[33] Q. Chen, A. Z. Chen, G. Jia, J. Li, C. Zheng, and K. Chen, "Molecular imaging of tumor microenvironment to assess the effects of locoregional treatment for hepatocellular carcinoma," *Hepatology Communications*, vol. 5, 2021.
[34] Y. Hoshida, S. Toffanin, A. Lachenmayer, A. Villanueva, B. Minguez, and J. Llovet, "Molecular classification and novel targets in hepatocellular carcinoma: recent advancements," *Seminars in Liver Disease*, vol. 30, no. 01, pp. 035–051, 2010.
[35] J.-S. Lee, I.-S. Chu, J. Heo et al., "Classification and prediction of survival in hepatocellular carcinoma by gene expression profiling," *Hepatology*, vol. 40, no. 3, pp. 667–676, 2004.
[36] Y. Hoshida, S. M. B. Nijman, M. Kobayashi et al., "Integrative transcriptome analysis reveals common molecular subclasses of human hepatocellular carcinoma," *Cancer Research*, vol. 69, no. 18, pp. 7385–7392, 2009.
[37] S. Boyault, D. S. Rickman, A. de Reyniès et al., "Transcriptome classification of HCC is related to gene alterations and to new therapeutic targets," *Hepatology*, vol. 45, no. 1, pp. 42–52, 2007.
[38] O. Yersal and S. Barutca, "Biological subtypes of breast cancer: prognostic and therapeutic implications," *World Journal of Clinical Oncology*, vol. 5, no. 3, pp. 412–424, 2014.
[39] J. M. Pitt, A. Marabelle, A. Eggermont, J.-C. Soria, G. Kroemer, and L. Zitvogel, "Targeting the tumor microenvironment: removing obstruction to anticancer immune responses and immunotherapy," *Annals of Oncology*, vol. 27, no. 8, pp. 1482–1492, 2016.
[40] T. Davoli, H. Uno, E. C. Wooten, and S. J. Elledge, "Tumor aneuploidy correlates with markers of immune evasion and with reduced response to immunotherapy," *Science*, vol. 355, no. 6322, 2017.

Hindawi
Journal of Oncology
Volume 2022, Article ID 2946929, 9 pages
https://doi.org/10.1155/2022/2946929

Research Article

Inhibition of Axl Promotes the Therapeutic Effect of Targeted Inhibition of the PI3K/Akt Pathway in NRAS Mutant Melanoma Cells

Xuejun Gao,[1] Dandan Xue,[1] Jingjing Cheng,[2] Xin Zhang,[3] and Xia Cai[4]

[1]*Department of Thyroid Surgery, Affiliated Hospital of Qingdao University, Qingdao, China*
[2]*Department of Medical Oncology, Affiliated Hospital of Qingdao University, Qingdao, China*
[3]*Department of Neurosurgery, Affiliated Hospital of Qingdao University, Qingdao, China*
[4]*Department of Plastic Surgery, Affiliated Hospital of Qingdao University, Qingdao, China*

Correspondence should be addressed to Xia Cai; caixia@qduhospital.cn

Received 15 December 2021; Accepted 1 February 2022; Published 11 March 2022

Academic Editor: Fu Wang

Melanoma is a malignant tumor produced by highly aggressive and metastatic melanocytes. NRAS mutation is a relatively common mutation in melanoma cells. Mitogen-activated protein kinase (MAPK) signaling pathway and the PI3K/Akt pathway in melanoma cells are relatively common signaling pathways. In this study, we investigated the effect of inhibition of Axl expression on the targeted inhibition of the PI3K/Akt pathway in NRAS-mutant melanoma cells. In this study, immunohistochemistry and western blot methods were used to detect the expression of Axl and Akt proteins in melanoma cells. Axl inhibitor was added, and it detected the inhibitory efficiency of Akt inhibitor in melanoma cells. Finally, a melanoma mouse model was established, and it detected the proliferation and apoptosis of mouse tumor cells induced by Axl inhibitor and Akt inhibitor. The results showed that Axl and Akt were highly expressed in NRAS-mutant melanoma cells, and stimulation of Axl expression could reduce the inhibitory effect of Akt inhibitor on melanoma cells. The addition of Axl inhibitor can synergistically promote the effect of Akt inhibitor, slow down the proliferation of tumor cells, and induce cell apoptosis. According to the experiment in this study, Axl inhibitor combined with Akt inhibitor has a stronger therapeutic effect on melanoma than Akt inhibitor alone.

1. Background

Melanoma is a highly malignant tumor originating from melanocytes. It mostly occurs in the skin but can also be found in the mucous membrane and viscera. Melanoma is highly malignant and can metastasize at an early stage [1]. According to the World Health Organization, about 50,000 people worldwide die of melanoma each year. In recent years, the incidence and mortality of malignant melanoma have been increasing year by year. Compared with other solid tumors, the death age of malignant melanoma is lower [2]. In addition to early surgical resection, malignant melanoma lacks effective treatment and has a poor prognosis. Therefore, the early diagnosis and treatment of malignant melanoma are extremely important. Currently, the treatment of melanoma is mainly divided into two therapeutic mechanisms [3]: (1) targeted therapy: small-molecule inhibitors targeting the mitogen-activated protein kinase (MAPK) signaling pathway; (2) immunotherapy: biological monoclonal antibodies block cytotoxic T lymphocyte-associated antigen-4 (CTLA-4) and programmed cell death protein 1 (PD-1). Both treatments have their own advantages and disadvantages, and molecular targeted therapy is a major research focus. Molecular targeted therapy is a therapeutic method that specifically selects key enzymes involved in the signaling pathway of cell canceration for targeted inhibition according to different types of gene mutations [4]. At present, a variety of targeted inhibitors targeting different signaling pathways have entered preclinical trials [5]. Among them, RAS/MAPK and PI3K/Akt

signaling pathways have been more frequently studied [6], so the development of targeted drugs targeting these two pathways has a broad prospect of clinical application.

Abnormal activation of RAS/RAF/MEK/ERK signaling pathway (MAPK signaling pathway) plays a key role in the occurrence and development of melanoma, and genes related to this pathway are also the main mutation sites of melanoma, especially RAF and RAS genes [7]. Studies have found that 70% of melanomas are associated with BRAF and NRAS gene mutations [8], so there are many studies on BRAF- and NRAS-mutant melanoma. Various small-molecule inhibitors have been extensively studied in BRAF-mutated melanoma cells. For example, the BRAF inhibitor encorafenib can be used in combination with the MEK inhibitor binimetinib to treat advanced $BRAF^{V600E/K}$-mutant melanoma [9]. Cobimetinib combined with vemurafenib in melanoma patients with advanced $BRAF^{V600}$ mutations shows good antitumor activity [10]. The study of NRAS mutation is still under development, so this study selected NRAS mutation melanoma as the research target and studied the use of small-molecule inhibitors for NRAS mutation melanoma.

In melanoma, NRAS is the most common type of mutation in the RAS family, which is commonly seen in congenital pigmented nevi but rarely seen in dysplastic nevi [11]. RAS induces cell proliferation, metastasis, and cell survival through the RAF/MEK/ERK pathway. Therefore, the MAPK pathway plays an important role in the occurrence and progression of NRAS mutated melanoma. Studies have shown that while NRAS activates the downstream MAPK pathway, it also regulates the activation of phosphoinositide 3-kinase-serine/threonine protein kinase B (PI3K-Akt) pathway and thus affects the occurrence of cell apoptosis [12]. Therefore, this study chose MAPK pathway and PI3K/Akt pathway to study melanoma.

In the PI3K/Akt pathway, PI3K is activated by extracellular signals of various cytokine receptors, including tyrosine kinase receptor, nontyrosine kinase receptor, and insulin receptor, which promotes the activation of Akt and further activates a variety of downstream effectors. Akt can affect the adhesion and motor ability of tumor cells by regulating the PI3K/Akt pathway, which is of great significance for the invasion and metastasis of malignant melanoma [13]. Therefore, inhibiting the activity of Akt can inhibit the activity of the PI3K/Akt pathway and then inhibit the proliferation of melanoma. Sanchez-Hernandez et al. [14] found that in the absence of BRAF mutation in melanoma cells, increased phosphorylation of Akt resulted in increased PI3K/Akt pathway activity; inhibition of PI3K/Akt/mTOR pathway activity resulted in increased tumor cell death level. Kuzu OF found that [15], in melanoma cells, Akt inhibition by targeting alone was not obvious, but if targeted together with other enzymes, it could synergistically kill melanoma cells and slow down the growth of tumor cells by 90%. Multiple experiments have shown that BEZ235, an inhibitor of the PI3K/Akt pathway, can effectively inhibit the phosphorylation of Akt and has a good inhibitory effect on the growth of tumor cells in esophageal cancer and glioma cells [16, 17]. In canine melanoma, the combination of BEZ235 and MEK inhibitors effectively reduces the survival rate of melanoma cells and inhibits cell growth [18]. In this experiment, we chose to inhibit the combination of Axl and Akt inhibitors to explore the growth and apoptosis of melanoma cells.

Axl is a tyrosine kinase (RTK), a member of the tumor-associated macrophage (TAM) family. It is composed of Tyro-3, Axl, and Mer [19]. GAS6 and ProS are ligands for TAM. The Axl immunoglobulin-like domain binds to the laminin G-like domains of Gas6 to form the Gas6/Axl complex with high affinity, and the Gas6/Axl complex has a biological activity after translation modification. Axl mediates the proliferation of tumor cells, which is dependent on the MAPK/ERK pathway and involves the activation of PI3K. RAS, Twist, and NF-κB are downstream targets of Axl [20]. Therefore, in melanoma cells, Axl can simultaneously regulate the MAPK pathway and PI3K/Akt pathway, providing a broad research idea for the combination of multiple inhibitors in melanoma. For example, in melanoma, the high expression of Axl makes tumor cells resistant to MAPK pathway inhibitors, and the combination of Axl antibody conjugate and BRAF/MEK inhibitor can synergistically inhibit the growth of tumor cells [21]. Receptor tyrosine kinase (RTK), such as Axl, has great application prospects in melanoma.

Therefore, in this study, melanoma cells with NRAS mutation were selected as the research object, and the activity of Axl was stimulated by Gas6 or the expression of Axl was inhibited by inhibitors, so as to explore the effect of Axl expression on PI3K/Akt pathway and the therapeutic effect of Axl expression on melanoma with NRAS mutation.

2. Materials and Methods

2.1. Cell Culture. Tumor and paracancerous tissues from melanoma patients were collected, cut into 1 mm [3] size, added with trypsin, and digested at 37°C for 10 min. After elution with 10% FBS and centrifugation at 1,000 r/min for 10 min, the supernatant was removed, and then, the precipitation was resuspended with DMEM medium containing FBS. After centrifugation for another 10 min, the precipitates were collected and resuspended with DMEM medium containing FBS. The cell density was adjusted and planted in the culture flask, and the culture medium was changed once in 2D. All the cells and tissues were cultured in an incubator at 37°C and 5% CO_2. Cells in the GAS6-induced group were added with 100 ng/mL recombinant human GAS6 solution and cultured for 12 h.

Human NRAS-mutant melanoma cell line SK-MEL-2 and paracancerous normal tissue HEM were all from the Affiliated Hospital of Qingdao University. The sources of cells used in this study have obtained the informed consent of patients.

2.2. Western Blot Assay. SK-MEL-2 cells or HEM cells were collected, and the total protein was extracted from tissue cells by protein lysate. An appropriate amount of protein was taken and electrophoretically separated with SDS-PAGE adhesive. Cellulose acetate membrane was used for constant pressure membrane transfer, and then, skimmed milk

powder was added to shake at room temperature and sealed for 2 h. After washing with PBS twice, primary antibodies such as rabbit anti-human polyclonal Axl antibody (Abnova Corporation) or rabbit anti-human polyclonal Akt antibody (Abnova Corporation) were added, respectively. They were incubated overnight in a refrigerator at 4°C and washed three times with PBS for 10 minutes each. The second antibody (Abnova Corporation) was added and incubated at room temperature for 2 hours. The PBS was washed three times for 10 minutes each time. Finally, ECL luminescence solution was added for chemiluminescence development, and the western blot fluorescence imager was used to take pictures.

2.3. RT-qPCR. The melanoma cell and tissue were collected, and total RNA was extracted using TRIzol Kit (Thermo Fisher, Shanghai) for reverse transcription. The cDNA expression level obtained by reverse transcription was detected by QRT-PCR. The reaction conditions of qRT-PCR were as follows: pre-denaturation at 95°C for 30 s, 95°C for 5 s, 60°C for 1 min, and a total of 40 cycles. The relative expression levels of target genes were calculated using the $2^{-\triangle\triangle Ct}$ method. The primers sequences were as follows: for Axl, GGCAACCCAGGGAATATCACA (forward) and ACACG AAGGTCTGATGTC CCA (reverse); for Akt, GTGCTGG AGGACAATGACTACGG (forward) and AGCAGCCCTG AAAGCAAGGA (forward); for β-actin, GTCCTGTGG CATCCA CGAAAC (forward) and GCTCCAACCGAC TGCTGTCAG (reverse).

2.4. Immunohistochemical. Melanoma tissue and paracancerous tissue were collected and fixed in paraformaldehyde at room temperature, rinsed with PBS for 3 times, and embedded in paraffin and sectioned. The sections were dewaxed with xylene-ethanol solution, followed by sodium citrate buffer (pH 6.0) for antigen repair, and rinsed with PBS for 3 times. They were put in 30% hydrogen peroxide solution and reacted for 30 minutes in dark at room temperature. They were rinsed with PBS for 3 times. They were blocked with 3% BSA at room temperature for 20 min, then, Axl antibody (Abcam) or Akt antibody (Abcam) was added and incubated overnight in the refrigerator at 4°C. They were rinsed with PBS for 3 times, and HRP-labeled secondary antibody (Abcam) was added at the appropriate concentration and incubated at room temperature for 30 min. They were rinsed with PBS 3 times, 5 minutes each time. DAB chromo-developing solution (Solarbio®, Life Science) was added for staining for 2 min, and sections were rinsed with running water. The hematoxylin solution was redyed for 2 min and rinsed with PBS for 15 min. The slides were dehydrated in ethanol, then, 80% glycerin was added to the slides, and the cover glass was sealed. Finally, microscope observation was performed and photographs were taken (magnification: ×200).

2.5. MTT Assay. Cells to be measured were taken and cultured in a DMEM complete medium for 24 h for synchronous treatment. The cell density was adjusted, and then, the cells were inoculated on 96-well plates for culture. Each group was added with the corresponding drug and cultured for a period of time. After the cells grew for a period of time, 5 mg/mL MTT (Sigma) solution was added to each well and placed in an incubator for culture at 37°C for 4 h. The supernatant was discarded, cleaned once with PBS, and 150 μL DMSO (Sigma) was added to each well. The absorbance OD value at 490 nm was measured with a microplate analyzer (Molecular Devices, Shanghai).

2.6. Flow Cytometry Was Used to Detect the Number of Early-Regulated Deaths. The cells to be tested were placed in the well plate and then cultured with drugs at the condition of 5% CO_2 and 37°C for 24 h. After the trypsin (without EDTA) was added, the cells were washed with PBS for 3 times, centrifuged at 1,500 rpm for 5 min, and the supernatant was removed. The procedure was performed according to the instructions of the Annexin V-FITC/PI Apoptosis Assay Kit (ImmunoChemistry, USA). The cells were resuspended by adding 100 μL × binding buffer, 5 μL FITC-Annexin V, and 10 μL propidium iodide, and reacted at darkroom temperature for 15 min. Then, 400 μL × binding buffer was added, and the apoptosis rate of apoptotic cells was detected by flow cytometry.

2.7. Cell Clone Formation Experiment. Melanoma cells were digested and dispersed with 0.25% trypsin and cultured in a DMEM medium with 10% fetal bovine serum. NVP-BEZ235 (AmyJet Scientific), RXDX-106 (CEP-40783, Selleck), and GAS6 were added into the medium to grow clone cells. The dishes were washed twice with PBS and fixed with paraformaldehyde for 15 minutes. The fixed solution was removed and stained with crystal violet. The stain plate was rinsed with PBS and allowed to dry at room temperature. Images of the Petri dishes were taken under an inverted light microscope.

2.8. Mouse Melanoma Model. Female BALB/c nude mice were purchased from Beijing Vital River Laboratory Animal Technology Co., Ltd. All the animals used in this experiment have been approved by the Ethics Committee of the Affiliated Hospital of Qingdao University. RAS melanoma cell lines were obtained from Tyr: $NRAS^{Q61K}$ transgenic mice, and then, these cell lines were inoculated into the back of female BALB/C nude mice to establish NRAS-mutant melanoma model. Mice were randomly divided into four groups, which were, respectively, injected with normal saline, BEZ235, RXDX-106 (Selleck), and the combination of two drugs. The tumor growth of mice was observed every day. After 28 days, the mice were anesthetized and killed, and the tumor tissue was surgically removed. Then, the mouse melanoma SBcl2 cell line was taken for detection.

2.9. Statistical Analysis. SPSS 25.0 software was used for data analysis in this experiment. The t-test was used for comparison between the two groups, and the results were expressed as mean ± standard deviation ($\bar{x} \pm s$). $p < 0.05$ was

considered statistically significant. The data were processed by GraphPad 8.0 software and presented in the form of charts.

3. Results and Discussion

3.1. Expressions of Axl in NRAS-Mutant Melanoma Tissues and Cell Lines. Previous experiments have shown that Axl is expressed in a variety of cancer cells, but there are few studies on melanoma. In this study, we focused on the role of Axl in melanoma cells in order to adopt more effective treatment methods. First, the expressions of Axl and Akt in melanoma tissues were detected by RT-PCR. Both Axl and Akt were highly expressed in melanoma cells, which were significantly higher than that in normal cells (Figures 1(a) and 1(b)). We further selected NRAS-mutated melanoma tissues and used WB to detect the expressions of Axl and Akt in NRAS-mutated melanoma tissues. The results showed that the expressions of Axl and Akt in NRAS-mutated melanoma tissues were higher than that in paracancerous normal tissues (Figure 1(c)). The expressions of Axl and Akt in melanoma cells were detected by IHC. In most melanoma tissues, the expression of Axl was high in the cytoplasm but lower in the paracancerous tissues than in the melanoma tissues. Akt was highly expressed in both the cytoplasm and nucleus of melanoma cells (Figure 1(d)). These results indicate that both Axl and Akt may promote the growth and proliferation of NRAS-mutated melanoma tissue, and it is speculated that there is a synergistic effect between the two.

3.2. Activation of Axl Reduces the Efficiency of Akt Inhibitor and Promotes Cell Growth. Previous studies have shown that Ras is the downstream target gene of Axl. As a ligand of TAM, GAS6 can activate Axl when combined with Axl and promote the proliferation of tumor cells. Therefore, GAS6 was selected to stimulate melanoma cells, WB was used to detect the phosphorylation level of Axl, and MTT was used to detect the proliferation of melanoma cells after GAS6 stimulation. The results showed that after GAS6 stimulation, the phosphorylation of Axl in cells was significantly increased, and pAxl activity was increased while the expression remained unchanged (Figure 2(a)). We continued to study the effect of Axl on Akt inhibitors. Melanoma cells with NRAS mutation were treated with GAS6 stimulation and Akt inhibitor (BEZ235) for induction culture, respectively, and cell proliferation was detected by cell cloning assay. Compared with the control group, cell proliferation was reduced after the addition of BEZ235. However, after the stimulation of GAS6, cell proliferation was increased and the inhibitory effect of the Akt inhibitor was reduced (Figure 2(b)). This suggests that the activated expression of Axl can reduce the inhibitory efficiency of Akt inhibitors and promote the proliferation of melanoma cells.

3.3. Inhibition of Axl Promotes Apoptosis of NRAS-Mutant Cells Induced by Akt Inhibitors. Since Axl can promote the proliferation of melanoma cells, this study chose to add Axl inhibitors to study the effect of Axl inhibitors on the apoptosis of NRAS-mutant melanoma cells. Axl inhibitor (RXDX-106) and Akt inhibitor (BEZ235) were added into NRAS-mutant melanoma cells, respectively. The activities of phosphorylated Axl, Akt, and apoptosis signaling factor caspase-3 were detected by WB. The results showed (Figure 3(a)) that the activities of pAxl and pAkt decreased after the addition of the corresponding inhibitors, respectively, and the activities of pAxl and pAkt were the lowest in the group with the coinduction culture of the two inhibitors. Compared with the control group, the activity of caspase-3 increased with the addition of inhibitor, and the activity of caspase-3 was the strongest in the group cocultured with RXDX-106 and BEZ235. Cell apoptosis was further detected by flow cytometry. After the addition of inhibitors, the cell apoptosis rate increased, and the cell apoptosis rate was the highest in the group with the addition of two inhibitors (Figure 3(b)). Therefore, inhibition of Axl can synergistically increase the inhibitory effect of the Akt inhibitor and promote cell apoptosis.

3.4. Axl Inhibitors Enhance the Efficacy of PI3K/Akt Pathway Targeted Therapy In Vivo. A mouse model of NRAS-mutated melanoma was established. Axl inhibitor and Akt inhibitor were injected to observe the effects of two inhibitors on the growth and apoptosis of melanoma cells in vivo. First, the IHC was used to examine the expressions of phosphorylated Akt and Axl in the transplanted tumor. The results showed that the addition of RXDX-106 effectively inhibited pAxl, while the addition of BEZ235 effectively inhibited pAkt, and the combination of the two inhibitors further enhanced the inhibition effect. The pAxl and pAkt were the weakest in the RXDX-106 + BEZ235 inhibitor group (Figure 4(a)). Then, cell cloning was used to detect the proliferation of tumor cells in different inhibitory groups. The results showed that compared with the control group, the cell proliferation was significantly decreased in the RXDX-106 and BEZ235 inhibitory groups, and the cell proliferation efficiency was the lowest in the two inhibitor groups (Figure 4(b)). Finally, the apoptosis rate was detected by flow cytometry. With the addition of inhibitors, the apoptosis rate of tumor cells increased. When RXDX-106 and BEZ235 were added at the same time, the cell apoptosis rate was significantly increased (Figure 4(c)). Both RXDX-106 and BEZ235 can effectively inhibit the activity of Axl and Akt and inhibit the growth of melanoma cells. However, the combination of the two inhibitors can more effectively inhibit pAxl and pAkt, and the effect of inhibiting tumor cell proliferation and promoting cell apoptosis is greater than that of one of the inhibitors alone.

4. Discussion

Melanoma is a skin tumor that easily metastasizes and is difficult to treat. Patients with melanoma can be treated by surgery at an early stage, but patients with metastasis are not sensitive to radiotherapy or chemotherapy [22]. This suggests that targeted drugs targeting various enzymes will play an important role. RAS has a high mutation rate in

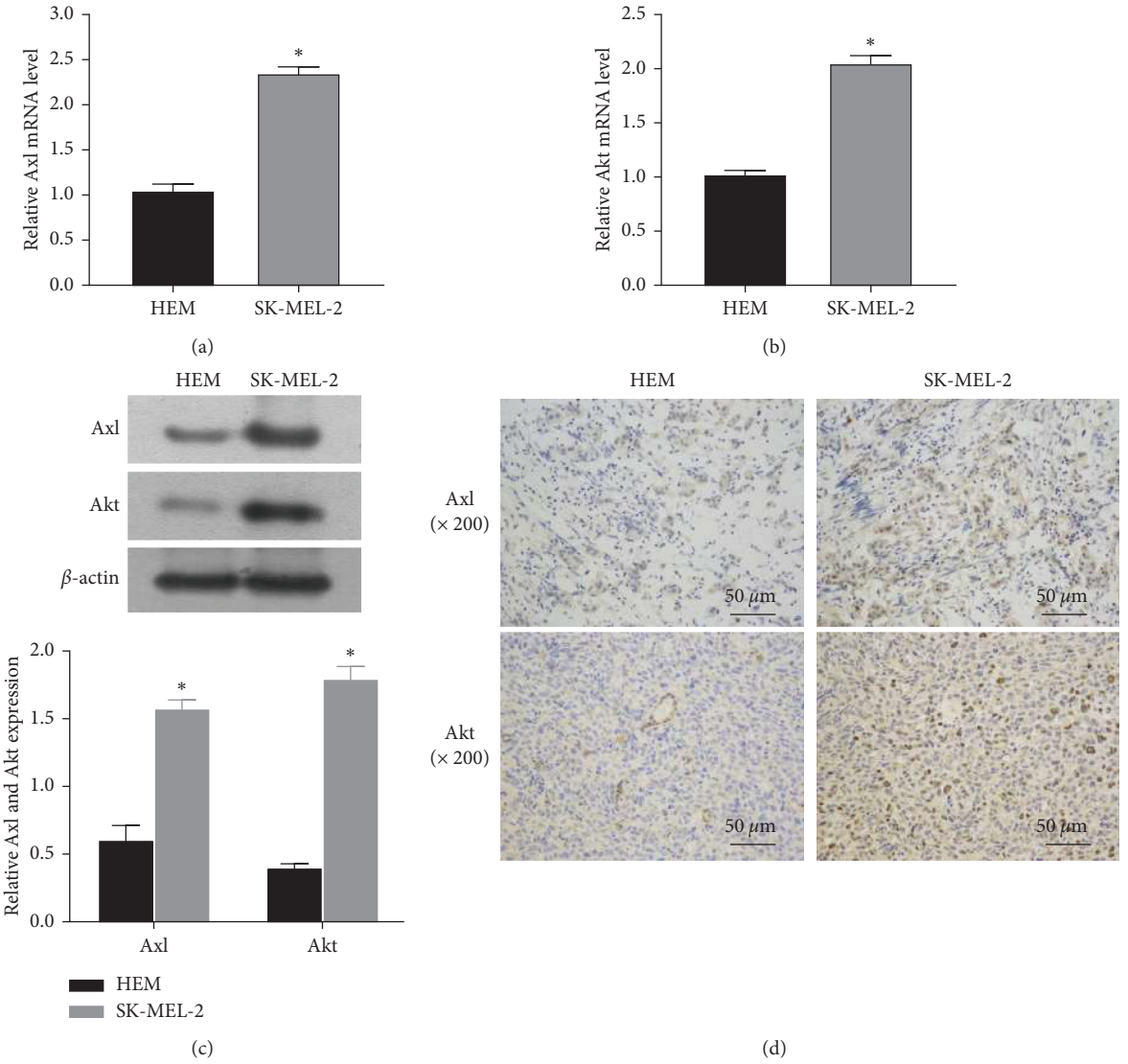

Figure 1: The expressions of Axl and Akt in mutant melanoma cells were detected. (a, b) The expressions of Axl and Akt in mutant melanoma cells were detected by RT-PCR. (c) The expressions of Axl and Akt in melanoma cells were detected by WB. (d) The expressions of Axl and Akt in melanoma tissues were detected by IHC. Compared with the control group, $p < 0.05$, and the difference was statistically significant.

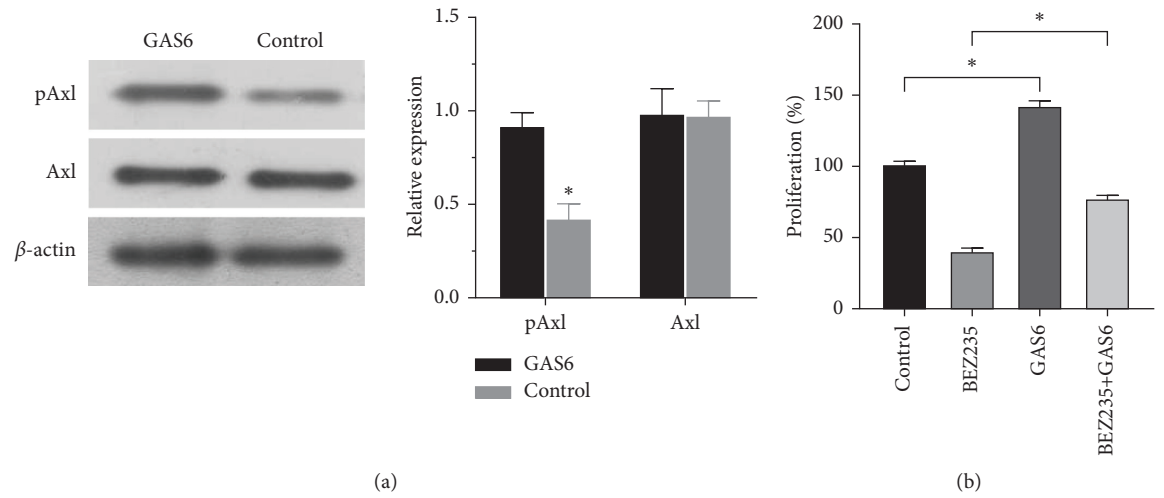

Figure 2: GAS6 stimulated melanoma tissue to detect the effect of Axl activation on the inhibitory efficiency of Akt inhibitor. (a) GAS6 stimulated melanoma tissue, and WB detected Axl activation. (b) Cell proliferation was detected by MTT to determine the effect of Akt inhibitors. Compared with the control group, $p < 0.05$, and the difference was statistically significant.

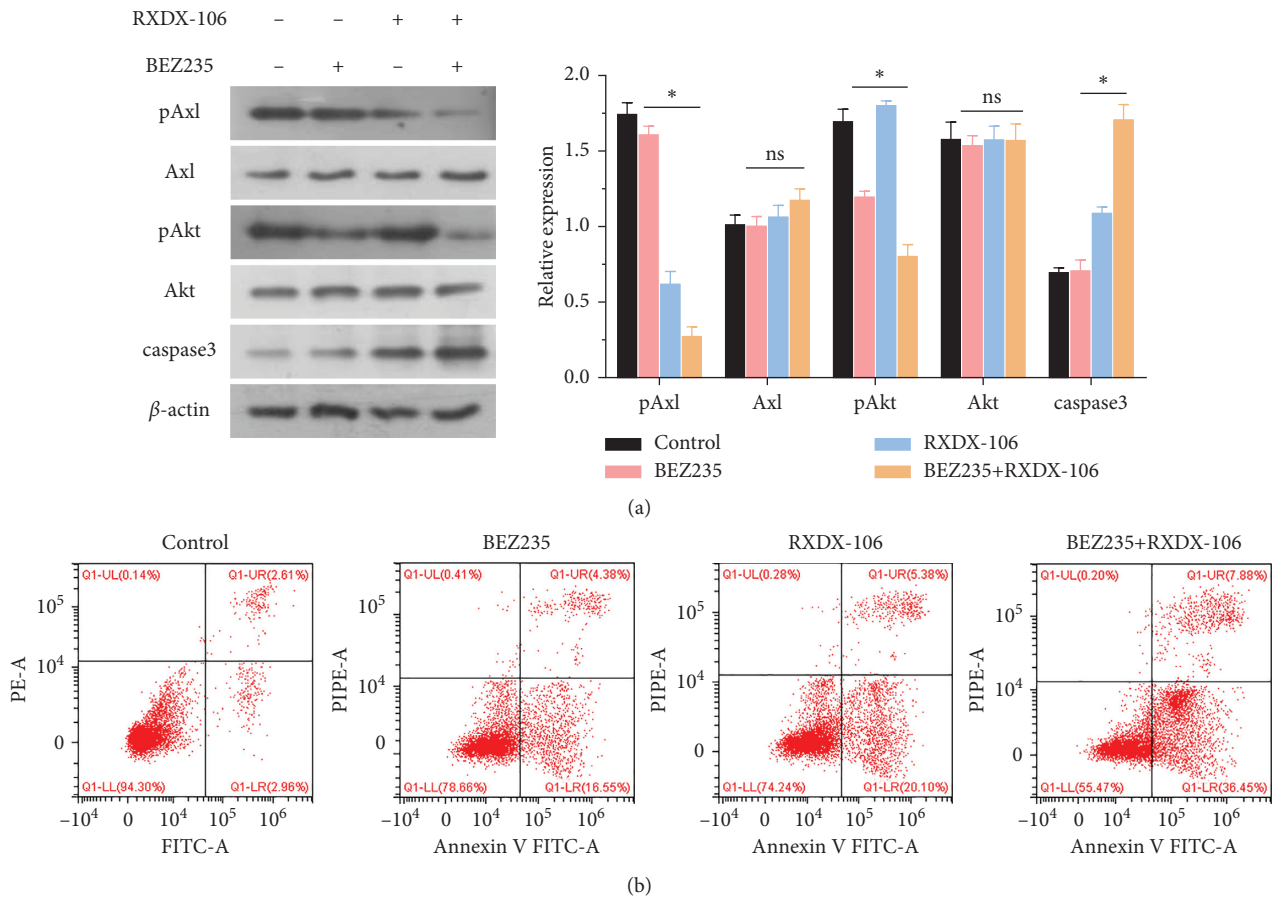

Figure 3: Akt inhibitor BEZ235 was added to determine the apoptotic ability of cells. (a) The phosphorylation activities of Axl and Akt and the activity of apoptotic factor caspase-3 were detected by WB. (b) The apoptosis rate was detected by flow cytometry. Compared with the control group, $p < 0.05$, and the difference was statistically significant.

melanoma, and studies have found that the inactivation of RAS can lead to rapid death of tumor cells and tumor degeneration, [23] and targeted inhibition of NRAS is also an effective treatment method. However, it is a pity that NRAS lacks the binding sites with small-molecule inhibitors, which cannot be directly inhibited. Therefore, for many years, the treatment of melanoma with NRAS mutation has mainly selected targeted inhibition of its related pathway enzyme components. A number of studies have shown that NRAS-mutated melanoma requires the RAS/RAF/MEK/ERK and PI3K/Akt pathways to induce and maintain malignant phenotypes, [24] and the growth of tumor can also be controlled through the interference of this pathway. For example, the MEK inhibitor binimetinib extends survival in melanoma patients with NRAS mutations and is a new treatment option for melanoma patients with NRAS mutations that have failed immunotherapy [25]. Binimetinib, a MEK inhibitor, has shown good efficacy in combination with CDK4 inhibitors [26]. ERK inhibition combined with PI3K/Akt inhibitor is effective in BRAF inhibitor-resistant cell lines and NRAS-mutant cell lines [27].

Therefore, many experiments have shown that in NRAS-mutated melanoma, the combination of multiple groups of inhibitors can effectively inhibit tumor growth. In this study, IHC, WB, and other detection methods were used to prove that Axl and Akt were highly expressed in melanoma cells. Both Axl and PI3K/Akt pathways are involved in the growth of melanoma cells. Activation of Axl by GAS6, MTT, and cell cloning detected an increased proliferation of tumor cells. Compared with the BEZ235 inhibition group, Axl phosphorylation and cell proliferation were increased after Axl activation, and the inhibitory effect was decreased. After the addition of Axl inhibitor, tumor cell apoptosis increased. The combination of BEZ235 and RXDX-106 inhibitor significantly increased the apoptosis rate of melanoma cells. The results showed that the activity of Axl could affect the PI3K/Akt pathway activity. Inhibition of Axl activity can indirectly inhibit the activity of the PI3K/Akt pathway, synergistically promote the effect of PI3K/Akt inhibitor, inhibit the proliferation of tumor cells, and induce cell apoptosis. To further prove the experimental results, a mouse melanoma model was established, and two inhibitors were given to induce culture. The results showed that compared with the other two groups of mice treated with one inhibitor alone, the tumor growth area of the mice cultured with two inhibitor groups was significantly smaller, the tumor growth rate was slowed down, and the cell apoptosis rate was increased. Since both Axl and PI3K/AKT pathways are involved in the development of melanoma with other gene mutations, the combination of Axl inhibitors and PI3K/AKT pathway inhibitors can be

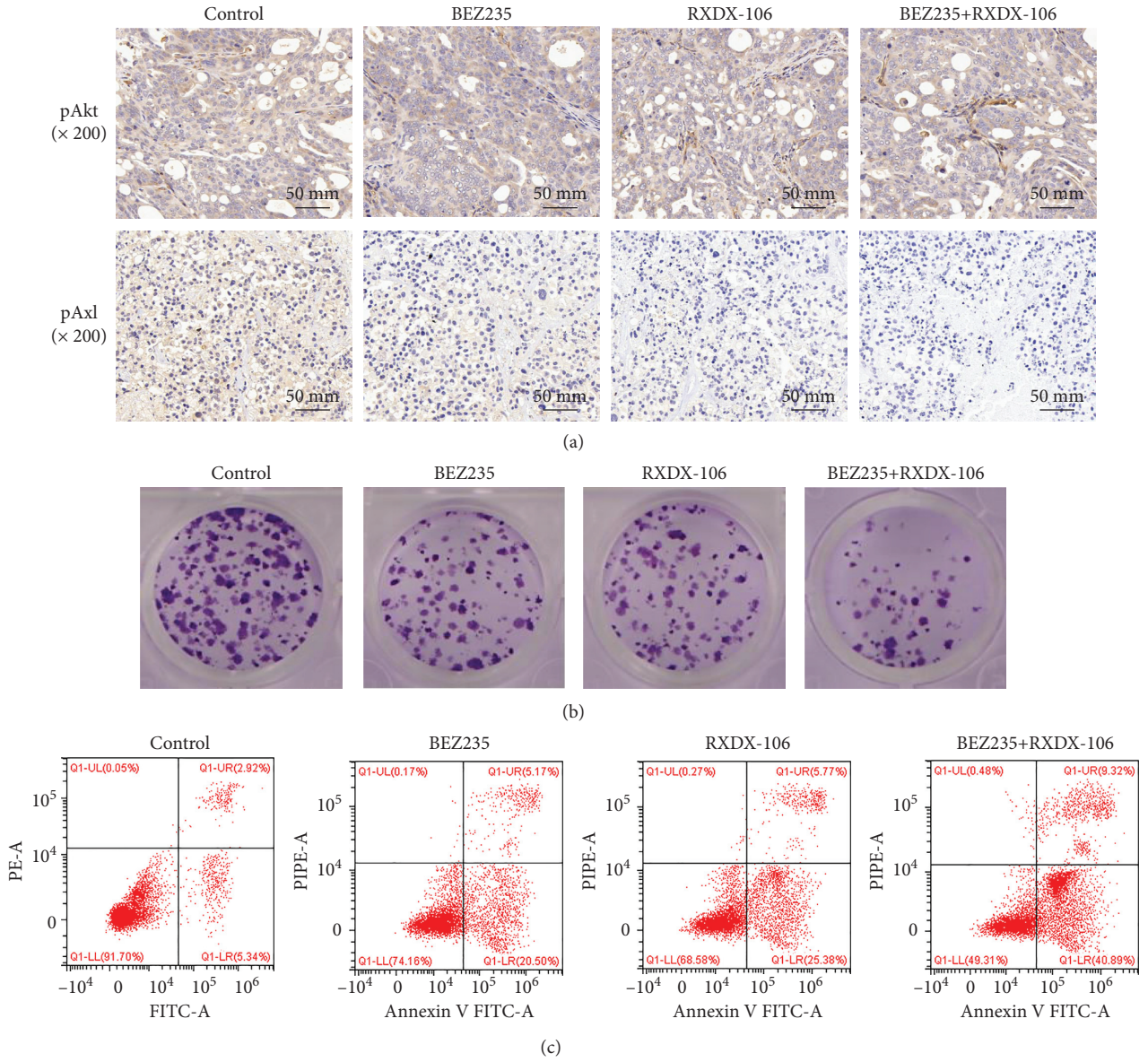

Figure 4: The two inhibitors were used together to determine the growth and apoptosis of tumor cells. (a) The expressions of pAkt and pAxl in mouse transplanted tumors were detected by IHC. (b) Cell cloning was used to examine the proliferation of tumor cells. (c) Apoptosis was detected by flow cytometry.

considered for the treatment of melanoma with other gene mutations in subsequent studies.

In the treatment of melanoma, the combination of a variety of inhibitors is an important part of the research. The use of MEK inhibitors in NRAS-mutated melanoma cells has been extensively studied, and more novel inhibition methods are needed. This experiment verified that Axl inhibitor, when used together with PI3K/Akt pathway inhibitor, can promote the inhibitory effect of PI3K/Akt pathway inhibitor, slow down the growth and proliferation of tumor cells, increase the rate of apoptosis, and increase the research direction of double inhibition. Compared with the abovementioned combination of dual inhibitors in the treatment of melanoma with gene mutation, the therapeutic effect of this study is obvious, and the combination of drugs is better. There are still some limitations in this study. Due to the limited samples, there are only a few melanoma cell lines with NRAS mutations. If more different kinds of melanoma cell lines with NRAS mutation can be used, this study will be enriched. The RTK family has a large number of members, and the next step is to explore more and more effective therapeutic targets based on tyrosine kinase receptors.

Data Availability

The datasets used and/or analyzed during the current study are available from the corresponding author on reasonable request.

Ethical Approval

Ethical approval was obtained for all experimental procedures by the Ethics Committee of the Affiliated Hospital of Qingdao University.

Consent

Verbal informed consent was obtained from the patients for their anonymized information to be published in this article.

Conflicts of Interest

The authors declare that they have no competing interests.

Authors' Contributions

XG and DX contributed equally to this study. XC conceived the study and designed the experiments. XG and DX completed the experiment, analyzed the data, and wrote the manuscript. JC and XZ discussed the results and revised the manuscript.

References

[1] L. M. Duncan, "The classification of cutaneous melanoma," *Hematology-Oncology Clinics of North America*, vol. 23, no. 3, pp. 501–513, 2009.

[2] M. Rastrelli, S. Tropea, C. R. Rossi, and M. Alaibac, "Melanoma: epidemiology, risk factors, pathogenesis, diagnosis and classification," *In Vivo (Athens, Greece)*, vol. 28, no. 6, pp. 1005–1011, 2014.

[3] S. Kakadia, N. Yarlagadda, R. Awad et al., "Mechanisms of resistance to BRAF and MEK inhibitors and clinical update of US food and drug Administration-approved targeted therapy in advanced melanoma," *OncoTargets and Therapy*, vol. 11, pp. 7095–7107, 2018.

[4] A. Hauschild, S. S. Agarwala, U. Trefzer et al., "Results of a phase III, randomized, placebo-controlled study of sorafenib in combination with carboplatin and paclitaxel as second-line treatment in patients with unresectable stage III or stage IV melanoma," *Journal of Clinical Oncology*, vol. 27, no. 17, pp. 2823–2830, 2009.

[5] G. Bollag, P. Hirth, J. Tsai et al., "Clinical efficacy of a RAF inhibitor needs broad target blockade in BRAF-mutant melanoma," *Nature*, vol. 467, no. 7315, pp. 596–599, 2010.

[6] I. Yajima, M. Y. Kumasaka, N. D. Thang et al., "RAS/RAF/MEK/ERK and PI3K/PTEN/AKT signaling in malignant melanoma progression and therapy," *Dermatology Research and Practice*, vol. 2012, Article ID 354191, 5 pages, 2012.

[7] P. A. Ascierto, J. M. Kirkwood, J.-J. Grob et al., "The role of BRAF V600 mutation in melanoma," *Journal of Translational Medicine*, vol. 10, no. 1, p. 85, 2012.

[8] W. H. Conrad, R. D. Swift, T. L. Biechele, R. M. Kulikauskas, R. T. Moon, and A. J. Chien, "Regulating the response to targeted MEK inhibition in melanoma," *Cell Cycle*, vol. 11, no. 20, pp. 3724–3730, 2012.

[9] R. Dummer, P. A. Ascierto, H. J. Gogas et al., "Encorafenib plus binimetinib versus vemurafenib or encorafenib in patients with BRAF mutant melanoma (COLUMBUS): a multicentre, open-label, randomised phase 3 trial," *The Lancet Oncology*, vol. 19, no. 5, pp. 603–615, 2018.

[10] A. Ribas, R. Gonzalez, A. Pavlick et al., "Combination of vemurafenib and cobimetinib in patients with advanced BRAFV600-mutated melanoma: a phase 1b study," *The Lancet Oncology*, vol. 15, no. 9, pp. 954–965, 2014.

[11] H. Tsao, L. Chin, L. A. Garraway, and D. E. Fisher, "Melanoma: from mutations to medicine," *Genes & Development*, vol. 26, no. 11, pp. 1131–1155, 2012.

[12] A. Saei and P. J. A. Eichhorn, "Adaptive responses as mechanisms of resistance to BRAF inhibitors in melanoma," *Cancers*, vol. 11, no. 8, p. 1176, 2019.

[13] N. E. Uko, O. F. Güner, D. F. Matesic, and J. P. Bowen, "Akt pathway inhibitors," *Current Topics in Medicinal Chemistry*, vol. 20, no. 10, pp. 883–900, 2020.

[14] I. Sánchez-Hernández, P. Baquero, L. Calleros, and A. Chiloeches, "Dual inhibition of (V600E) BRAF and the PI3K/AKT/mTOR pathway cooperates to induce apoptosis in melanoma cells through a MEK-independent mechanism," *Cancer Letters*, vol. 314, no. 2, pp. 244–255, 2012.

[15] O. F. Kuzu, R. Gowda, A. Sharma et al., "Improving pharmacological targeting of AKT in melanoma," *Cancer Letters*, vol. 404, pp. 29–36, 2017.

[16] Z. Yu, G. Xie, G. Zhou et al., "NVP-BEZ235, a novel dual PI3K-mTOR inhibitor displays anti-glioma activity and reduces chemoresistance to temozolomide in human glioma cells," *Cancer Letters*, vol. 367, no. 1, pp. 58–68, 2015.

[17] N. Shi, H. Yu, and T. Chen, "Inhibition of esophageal cancer growth through the suppression of PI3K/AKT/mTOR signaling pathway," *OncoTargets and Therapy*, vol. 12, pp. 7637–7647, 2019.

[18] B. R. Wei, H. T. Michael, C. H. C. Halsey et al., "Synergistic targeted inhibition of MEK and dual PI 3K/mTOR diminishes viability and inhibits tumor growth of canine melanoma underscoring its utility as a preclinical model for human mucosal melanoma," *Pigment Cell & Melanoma Research*, vol. 29, no. 6, pp. 643–655, 2016.

[19] V. Davra, S. Kimani, D. Calianese, and R. Birge, "Ligand activation of TAM family receptors-implications for tumor biology and therapeutic response," *Cancers*, vol. 8, no. 12, p. 107, 2016.

[20] W. L. Tam and R. A. Weinberg, "The epigenetics of epithelial-mesenchymal plasticity in cancer," *Nature Medicine*, vol. 19, no. 11, pp. 1438–1449, 2013.

[21] J. Boshuizen, L. A. Koopman, O. Krijgsman et al., "Cooperative targeting of melanoma heterogeneity with an AXL antibody-drug conjugate and BRAF/MEK inhibitors," *Nature Medicine*, vol. 24, no. 2, pp. 203–212, 2018.

[22] K. J. Ransohoff, P. D. Jaju, J. Y. Tang, M. Carbone, S. Leachman, and K. Y. Sarin, "Familial skin cancer syndromes," *Journal of the American Academy of Dermatology*, vol. 74, no. 3, pp. 423–434, 2016.

[23] J. A. Ellerhorst, V. R. Greene, S. Ekmekcioglu et al., "Clinical correlates ofNRASandBRAFMutations in primary human melanoma," *Clinical Cancer Research*, vol. 17, no. 2, pp. 229–235, 2011.

[24] M. Drosten, A. Dhawahir, E. Y. M. Sum et al., "Genetic analysis of Ras signalling pathways in cell proliferation, migration and survival," *The EMBO Journal*, vol. 29, no. 6, pp. 1091–1104, 2010.

[25] R. Dummer, D. Schadendorf, P. A. Ascierto et al., "Binimetinib versus dacarbazine in patients with advanced NRAS-mutant melanoma (NEMO): a multicentre, open-label, randomised, phase 3 trial," *The Lancet Oncology*, vol. 18, no. 4, pp. 435–445, 2017.

[26] A. Forschner, T. Sinnberg, G. Mroz et al., "Case report: combined CDK4/6 and MEK inhibition in refractory CDKN2A and NRAS mutant melanoma," *Frontiers in Oncology*, vol. 11, Article ID 643156, 2021.

[27] M. S. Carlino, J. R. Todd, K. Gowrishankar et al., "Differential activity of MEK and ERK inhibitors in BRAF inhibitor resistant melanoma," *Molecular Oncology*, vol. 8, no. 3, pp. 544–554, 2014.

Hindawi
Journal of Oncology
Volume 2022, Article ID 3370727, 13 pages
https://doi.org/10.1155/2022/3370727

Research Article

Uncovering the Immune Cell Infiltration Landscape in Low-Grade Glioma for Aiding Immunotherapy

Youyuan Yang,[1] Yue Tian,[2] Qing Li,[3] Rui Jiang,[4] and Junfeng Zhang[4]

[1]*Outpatient Department, Sichuan Provincial Military Command of PLA, Chengdu, Sichuan, China*
[2]*Department of General Surgery, Daping Hospital, Army Medical University, Chongqing, China*
[3]*Department of Oncology, Daping Hospital, Army Medical University, Chongqing, China*
[4]*Department of Radiology, The General Hospital of Western Theater Command, Chengdu, Sichuan, China*

Correspondence should be addressed to Junfeng Zhang; zjfbisu@tmmu.edu.cn

Received 20 December 2021; Accepted 21 February 2022; Published 11 March 2022

Academic Editor: Fu Wang

Objective. Low-grade glioma (LGG) mainly threatens the elderly population, with undesirable prognoses. This study uncovered the immune cell infiltration (ICI) landscape in LGG. *Methods*. RNA-seq profiles of LGG were retrieved from TCGA and CGGA databases. CIBERSORTx and ESTIMATE algorithms were employed to characterize the ICI landscape in LGG tissues. Through unsupervised clustering analysis, ICI subtypes were clustered. ICI scores were computed via principal component analysis (PCA). The differences in survival, tumor-infiltrating immune cells, stromal scores, immune scores, immune checkpoint genes, immune activity genes, and tumor mutation burden (TMB) were assessed between high and low ICI score groups. *Results*. Three ICI subtypes were constructed in LGG, with distinct survival outcomes, PD-L1 expression, and infiltration levels of immune cells. Furthermore, ICI scores were developed. Both in TCGA and CGGA datasets, low ICI scores were indicative of undesirable outcomes. High ICI scores were significantly correlated to increased infiltration levels of memory B cells, CD8 T cells, CD4 naïve T cells, T follicular helper cells, macrophages M0, and eosinophils, while low ICI scores were characterized by increased infiltration levels of naïve B cells, plasma cells, CD4 memory resting T cells, Tregs, resting NK cells, macrophages M2, and activated dendritic cells. High ICI scores exhibited correlations with lower immune activity genes and immune checkpoint genes. Furthermore, TMB was distinctly reduced in the high ICI score group. *Conclusion*. The ICI scores may serve as a promising prognostic index and predictive indicator for immunotherapies, extending our understanding of immune microenvironment in LGG.

1. Introduction

Glioma is a common primary intracranial malignancy, which is classified into four grades according to the 2007 WHO classification of tumors: Grades I and II are LGGs, and Grades III and IV are high-grade gliomas [1]. Among them, LGG represents the most common primary brain malignancy [2]. LGG mainly occurs in old people. However, it is predisposed to younger individuals (average age: 41 years old), with mean survival time of approximately seven years [3]. Despite the much progress in neurosurgical resection, chemotherapy, and radiotherapy, it is ineluctable to experience resistance and recurrence [4]. Due to biological behaviors, this malignancy displays considerable heterogeneity. Some subjects experience indolent outcomes, while others develop into high-grade gliomas with undesirable outcomes [5]. Despite the less aggressiveness of LGG, patients usually have varied survival outcomes [6]. Therefore, discovering precisely novel markers to predict patients' prognosis is of importance in current studies.

Immunotherapies have exhibited considerable promise in cancer therapy [7]. Novel immunotherapy has emerged as a promising therapeutic strategy against LGG [8]. Nevertheless, only some patients respond to immunotherapy [9]. The efficacy of immunotherapy is partly affected by tumor microenvironment that contains immune cells as well as stromal cells. Tumor-infiltrating immune cells may affect response to immunotherapies and survival outcomes [10]. Uncovering the relationships between tumor and tumor immune microenvironment is of importance for discovering

prognostic markers, lowering drug resistance, and exploiting novel therapeutic strategies [11]. Therefore, it is of significance to construct ICI subtypes to differentiate LGG patients' prognosis. Herein, this study developed ICI score system to characterize the ICI landscape in LGG, which may accurately predict patients' outcomes as well as responsiveness to immunotherapies.

2. Materials and Methods

2.1. LGG Datasets. RNA-seq data and matched clinical information of LGG patients were retrieved from The Cancer Genome Atlas (TCGA; https://portal.gdc.cancer.gov/) database. After removing samples with survival time of 0, 506 samples were retained as the training set. Furthermore, 596 LGG subjects were obtained from the Chinese Glioma Genome Atlas (CGGA; https://www.cgga.org.cn/), and they were utilized as the validation set. Table 1 lists the clinical information of the two datasets. Fragments per kilobase of transcript per million fragments mapped (FPKM) values were downloaded from TCGA or CGGA database and transformed into transcripts per kilobase million (TPM) values.

2.2. Inferring Tumor-Infiltrating Immune Cells and Stromal Cells. CIBERSORTx algorithm (https://cibersortx.stanford.edu/) was applied to estimate the abundances of immune cells in each LGG sample based on gene expression profiles [12]. The LM22 signatures were employed and permutations were set as 1,000 times. Meanwhile, immune scores and stromal scores were determined to infer the fractions of stromal cells and immune cells in each specimen according to expression data via ESTIMATE algorithm (https://sourceforge.net/projects/estimateproject/) [13].

2.3. Unsupervised Clustering Analysis. Consensus clustering method may provide quantitative evidence for determining the number and membership of possible clusters in a dataset. LGG specimens were clustered utilizing "ConsensusClusterPlus" R package (version 1.58.0) [14]. When $k = 2$ to 9, consensus matrix, consensus cumulative distribution function (CDF), delta area, and tracking plots were constructed to determine the optimal k value. Then, cluster consensus and item consensus were calculated, respectively. Clustering results were validated by principal component analysis (PCA).

2.4. Differential Expression Analysis. Differentially expressed genes (DEGs) with $|\text{fold change (FC)}| > 2$ and adjusted p value < 0.05 were screened among ICI subtypes through applying "limma" R package (version 1.9.6) [13].

2.5. ICI Scores. Unsupervised clustering analysis was applied for categorizing all subjects based on DEGs. Furthermore, DEGs that displayed positive and negative correlations to gene clusters were separately named as ICI gene signatures A and B. To lower the noise or redundant genes, the Boruta algorithm was utilized for performing dimension reduction in the ICI gene signatures A and B. Principal component 1 (PC1) was extracted as the signature score through applying the PCA. According to previous studies [15, 16], the ICI score of each subject was calculated as follows: ICI score = $\sum \text{PC1}_A - \text{PC1}_B$.

Table 1: The clinical characteristics of LGG patients in TCGA and CGGA datasets.

Characteristics	TCGA ($n = 506$)	CGGA ($n = 596$)
Age		
≤50	352	501
>50	154	94
NA	0	1
Gender		
Female	226	251
Male	280	345
IDH		
Mutant	405	416
Wild-type	94	141
NA	7	39
1p19q		
Codel	165	180
Noncodel	337	373
NA	4	43
MGMT		
Methylated	416	287
Unmethylated	86	202
NA	4	107

2.6. Functional Enrichment Analysis. Gene ontology (GO) and Kyoto Encyclopedia of Genes and Genomes (KEGG) enrichment analyses of ICI gene signatures A and B were separately presented via "clusterProfiler" R package (version 2.2.7) [17]. Adjusted p value < 0.05 indicated significant enrichment.

2.7. Gene Set Enrichment Analysis (GSEA). GSEA, a computational method, may be utilized for determining whether a set of genes display differential expression in two biological states [18]. Here, this study employed GSEA to identify differences in KEGG pathways between high and low ICI score groups. Gene set permutations were presented 1000 times. ICI score was set as a phenotype label. Enriched KEGG pathways were screened based on false discovery rate (FDR) < 0.05.

2.8. Tumor Mutation Burden (TMB). TMB was defined as the ratio of total count of variants and the total length of exons [19]. The differences in TMB between high and low ICI score groups were compared by the Wilcoxon rank-sum test. The correlation coefficient between ICI scores and TMB was computed via Spearman analysis.

2.9. Screening Small Molecule Drugs. DEGs with $|\text{FC}| > 2$ and adjusted p value < 0.05 were filtered between high and low ICI score groups utilizing "limma" R package. The two lists

of upregulated and downregulated genes were analyzed through the Connectivity Map (CMap; http://portals.broadinstitute.org/cmap/) database [20]. Small molecular drugs were filtered based on the enrichment value and permutation p value. CMap mode-of-action (MoA) analysis was applied for exploring underlying mechanisms of action.

2.10. Statistical Analysis. Statistical analysis was achieved via R language. Kaplan-Meier curves of overall survival (OS) were presented for LGG patients in different subgroups and the differences were compared by log-rank test. Spearman analysis was employed to determine the correlation coefficients. Kruskal-Wallis test was applied for comparing over two subgroups, while Wilcoxon test was utilized for comparing two subgroups. The X-tile software was employed for classifying patients into high and low ICI groups to lower the computational batch effects. Two-tailed p value < 0.05 indicated statistical significance.

3. Results

3.1. Characterization of ICI Subtypes with Distinct Survival Outcomes in LGG. Here, the CIBERSORTx and ESTIMATE algorithms were employed for determining the infiltration levels of immune cells in LGG tissues. On the basis of 506 LGG specimens plus corresponding ICI profiling, these subjects were classified into three subtypes through the "ConsensusClusterPlus" package (Figures 1(a)–1(c)). PCA results confirmed the distinct classifications into three subtypes: ICI subtype A ($n = 245$), ICI subtype B ($n = 75$), and ICI subtype C ($n = 186$; Figure 1(d)). We further clarified the differences in clinical phenotypes among the three ICI subtypes, as shown in Figure 1(e). Novel immunotherapies have brought hope to LGG patients, but not each patient can respond to such therapies [21]. Since every tumor is different, it is important to investigate how to use the biology behind tumor cells to successfully treat more cancer patients [22]. "Cold" tumors with few T cells are generally less sensitive to immunotherapy [23]. Among the three ICI subtypes, ICI subtype A displayed the lowest infiltration levels of T cells (Figure 1(e)). Moreover, ICI subtype A was in relation with undesirable survival outcomes ($p = 0.007$; Figure 1(f)). This classification pattern was confirmed in the CGGA-LGG dataset (Supplementary Figure 1).

3.2. The Landscape of Tumor Microenvironment Components in the Three ICI Subtypes of LGG. The interactions between tumor-infiltrating immune cells, immune scores, and stromal scores in tumor microenvironment of LGG tissues were analyzed in depth. Figure 2(a) depicts the correlation coefficients between them in tumor microenvironment. We found that activated CD4 memory T cells were strongly positively correlated to plasma cells. Meanwhile, there was a strongly positive correlation between stromal scores and immune scores. ICI subtype B was characterized by increased infiltration levels of plasma cells, CD8 T cells, CD4 memory resting T cells, regulatory T cells (Tregs), macrophages M0, resting dendritic cells, resting mast cells, and neutrophils (Figure 2(b)). ICI subtype C had the features of increased infiltration levels of follicular helper T cells, activated NK cells, monocytes, activated mast cells, and eosinophils. Furthermore, ICI subtype A exhibited the characteristics of elevated macrophage M2 levels, immune scores, and stromal scores. PD-L1, as an immune inhibitory receptor ligand, induces T cell dysfunction as well as apoptosis, thereby suppressing inflammatory responses and promoting tumor immune evasion [24]. Here, the expression of immune checkpoint PD-L1 was evaluated in each ICI subtype. Our results showed that ICI subtype A had the features of an increased PD-L1 expression, while ICI subtype C had the features of decreased PD-L1 expression (Figure 2(c)).

3.3. Identifying ICI Gene Clusters for LGG. This study unraveled potential biological features of the three ICI subtypes. By differential analysis among subtypes, DEGs were determined. Through unsupervised clustering analysis, four ICI gene subtypes were clustered based on these DEGs, called gene clusters A, B, C, and D (Figures 3(a)–3(c)). 231 DEGs that had positive correlations to ICI gene subtypes were called ICI gene signatures A, while 236 DEGs were named as ICI gene signatures B (Supplementary Table 1). The heatmap depicted the clinical features and expression patterns of ICI gene signatures of the four ICI gene clusters (Figure 3(d)). The ICI scores were compared among the gene clusters. We found that gene cluster B was characterized by decreased ICI scores, while gene cluster D had increased ICI scores ($p < 2.2e - 16$; Figure 3(e)).

3.4. Biological Characteristics of ICI-Relevant Gene Signatures. To uncover the biological characteristics of ICI gene signatures A and B, we presented functional enrichment analysis. Our results revealed that ICI gene signatures A were mainly related to signal transduction-related biological processes and pathways such as neurotransmitter transport, synaptic vesicle cycle, vesicle-mediated transport in synapse, modulation of chemical synaptic transmission, regulation of transsynaptic signaling, neurotransmitter secretion, GABAergic synapse, cholinergic synapse, and neuroactive ligand receptor interaction (Figures 4(a) and 4(b)). Meanwhile, ICI gene signatures B were mainly enriched in immune-related pathways such as leukocyte migration, leukocyte cell-cell adhesion, leukocyte proliferation, neutrophil activation, regulation of lymphocyte proliferation, regulation of mononuclear cell proliferation, antigen processing and presentation, complement and coagulation cascades, Toll-like receptor signaling pathway, Th17 cell differentiation, Th1 and Th2 cell differentiation, cytokine-cytokine receptor interaction, and chemokine signaling pathway (Figures 4(c) and 4(d)).

3.5. Development of the ICI Score System for LGG. Based on ICI gene signatures A and B, PCA was presented for computing ICI score of each LGG patient. All patients in the TCGA-LGG dataset were separated into high or low ICI

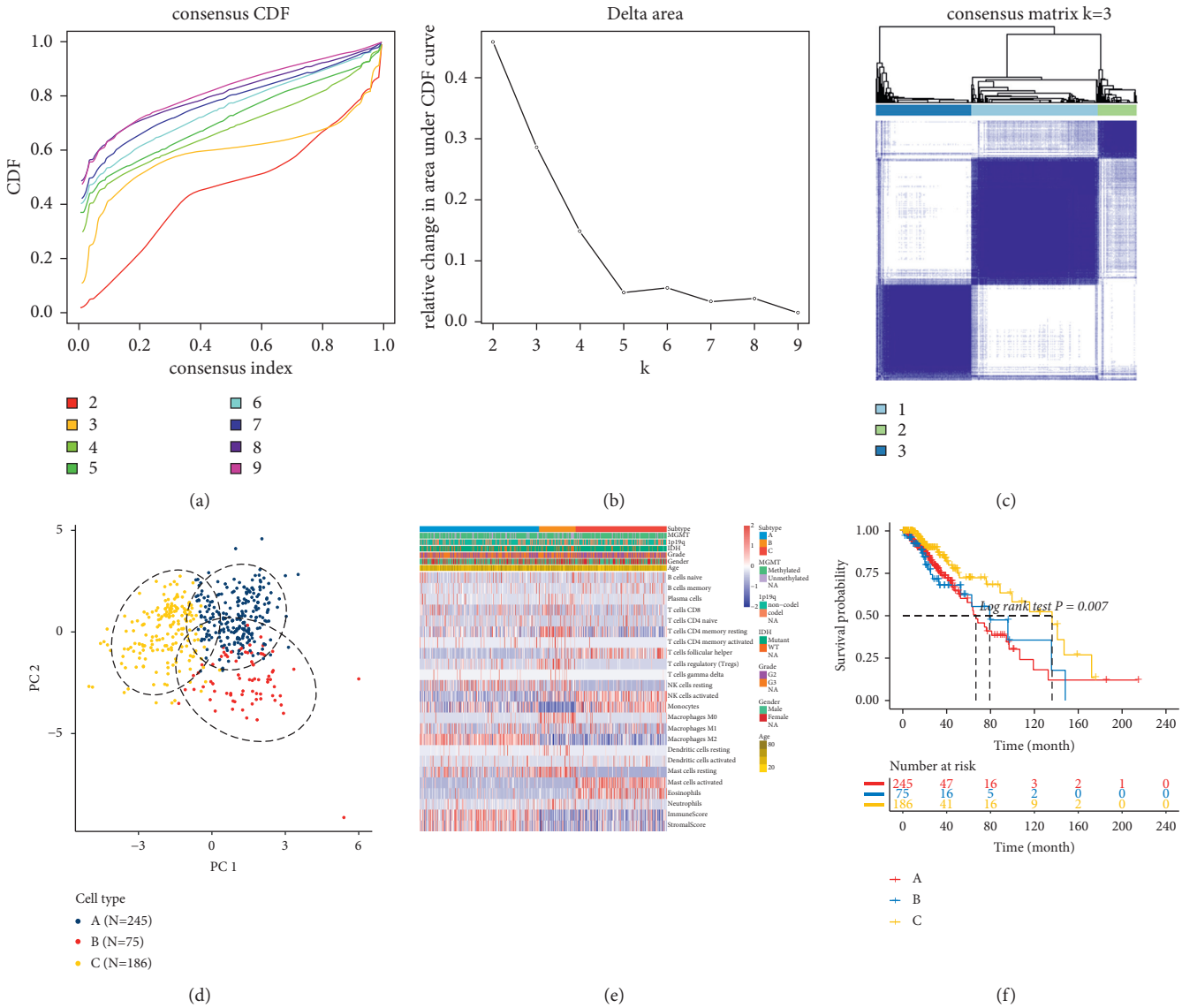

Figure 1: Characterization of ICI subtypes with distinct survival outcomes for LGG in TCGA-LGG dataset. ((a)–(c)) Unsupervised clustering analysis for classifying three ICI subtypes by the "ConsensusClusterPlus" package. (a) Consensus cumulative distribution function graph. (b) Delta area plot. (c) Heatmap for consensus matrix when $k = 3$. (d) PCA plots for the classification patterns of the ICI subtypes. (e) Heatmap of tumor-infiltrating immune cells in different clinical phenotypes and ICI subtypes. (f) Kaplan-Meier curves for OS of LGG patients in the three ICI subtypes.

scores according to the optimal cutoff value. Figure 5(a) depicts the distribution of ICI scores and survival status for patients in the four ICI gene clusters. Patients with low ICI scores exhibited an undesirable prognosis compared to those with high ICI scores in the TCGA-LGG dataset ($p < 0.001$; Figure 5(b)). The prognostic efficiency of the ICI score system was confirmed in the CGGA-LGG dataset ($p < 0.001$; Figure 5(c)). To uncover the biological implications of ICI scores, GSEA was presented. High ICI scores were distinctly correlated to gap junction, neuroactive ligand receptor interaction, and oxidative phosphorylation (Figure 5(d); Supplementary Table 2). Meanwhile, low ICI scores were in relation with apoptosis, B cell receptor signaling pathway, cell adhesion, cytokine-cytokine receptor interaction, JAK STAT signaling pathway, and Notch signaling pathway (Figure 5(e); Supplementary Table 3).

3.6. The Roles of ICI Score in Predicting Response to Immunotherapy. High ICI scores were significantly correlated to increased infiltration levels of memory B cells, CD8 T cells, CD4 naïve T cells, follicular helper T cells, macrophages M0, and eosinophils (Figure 6(a)). Meanwhile, low ICI scores were characterized by increased infiltration levels of naïve B cells, plasma cells, CD4 memory resting T cells, Tregs, resting NK cells, macrophages M2, and activated dendritic cells as well as increased immune scores and stromal scores. We also assessed the differences in the

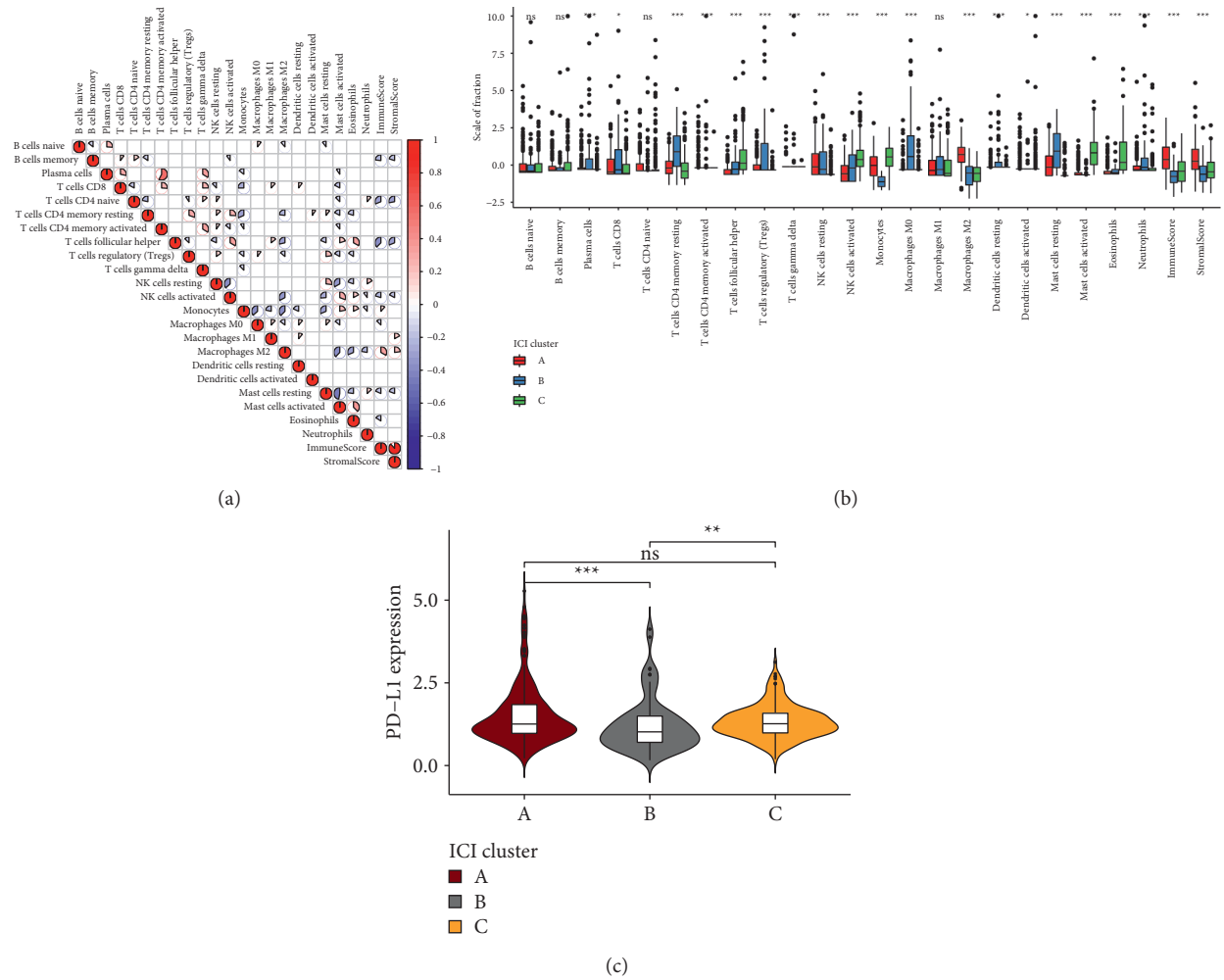

Figure 2: The landscape of tumor microenvironment components in the three ICI subtypes of LGG. (a) Correlations between tumor-infiltrating immune cells, immune scores, and stromal scores in LGG tissues. The more towards red, the greater the positive correlation coefficient; the more towards blue, the greater the negative correlation coefficient. (b) Box plots for the infiltration levels of tumor-infiltrating immune cells in each ICI subtype. (c) Violin plots for the expression of PD-L1 in each ICI subtype. Kruskal-Wallis test, ns: not significant; $^{*}p < 0.05$; $^{**}p < 0.01$; $^{***}p < 0.001$.

expression of immune checkpoint genes and immune activity genes between groups. As shown in Figure 6(b), high ICI scores exhibited correlations with lower immune activity genes including GZMA, TBX2, TNF, PRF1, IFNG, CXCL9, and CXCL10 as well as reduced immune checkpoint genes including LAG3, CD274, IDO1, PDCD1, HAVCR2, and CTLA4. Furthermore, TMB score was distinctly reduced in the high ICI score group compared to the low ICI score group ($p = 0.024$; Figure 6(c)). Spearman analysis demonstrated that ICI scores displayed a significant negative correlation to TMB ($r = -0.15$, $p = 8e - 04$; Figure 6(d)). These data indicated that LGG patients with high ICI scores had lower responses to immunotherapy.

3.7. Potential Small Molecular Drugs Based on ICI Scores. Small molecular drugs were further predicted by employing the CMap database. Firstly, we identified 775 downregulated genes and 366 upregulated genes in high ICI score group compared to low ICI score group (Figure 7(a); Supplementary Table 4). Through the CMap database, underlying small molecular compounds against LGG such as carbarsone, sulfabenzamide, and phenazone were predicted based on downregulated and upregulated genes, listed in Table 2. Furthermore, the potential mechanisms of action were analyzed via MoA. Dopamine receptor antagonist and PPAR receptor agonist were the most shared mechanisms of action (Figure 7(b)).

4. Discussion

LGG displays great heterogeneity at the genetic and molecular levels, affecting the efficacy of immunotherapies [25]. The immune microenvironment of LGG is a complex neuroinflammatory network, involving positive as well as negative immune regulators [26]. This study characterized the ICI landscape and developed ICI score system that may predict survival outcomes as well as the response to immunotherapies, which extended our comprehension about the immune microenvironment of LGG.

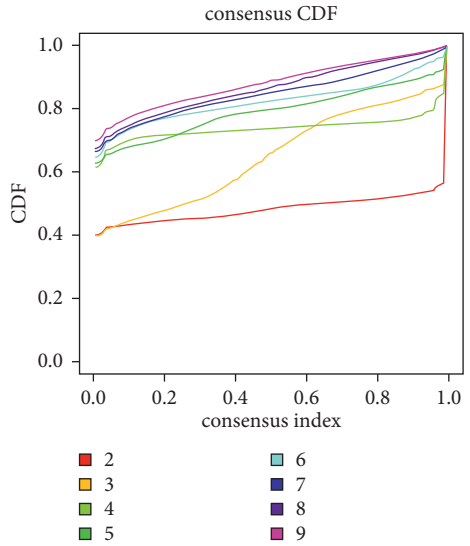

(a)

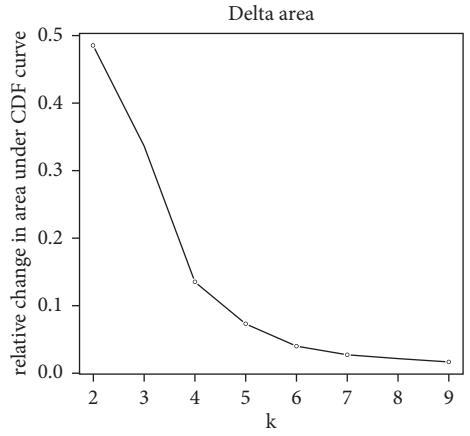

(b)

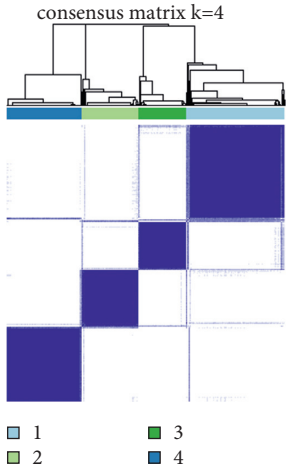

(c)

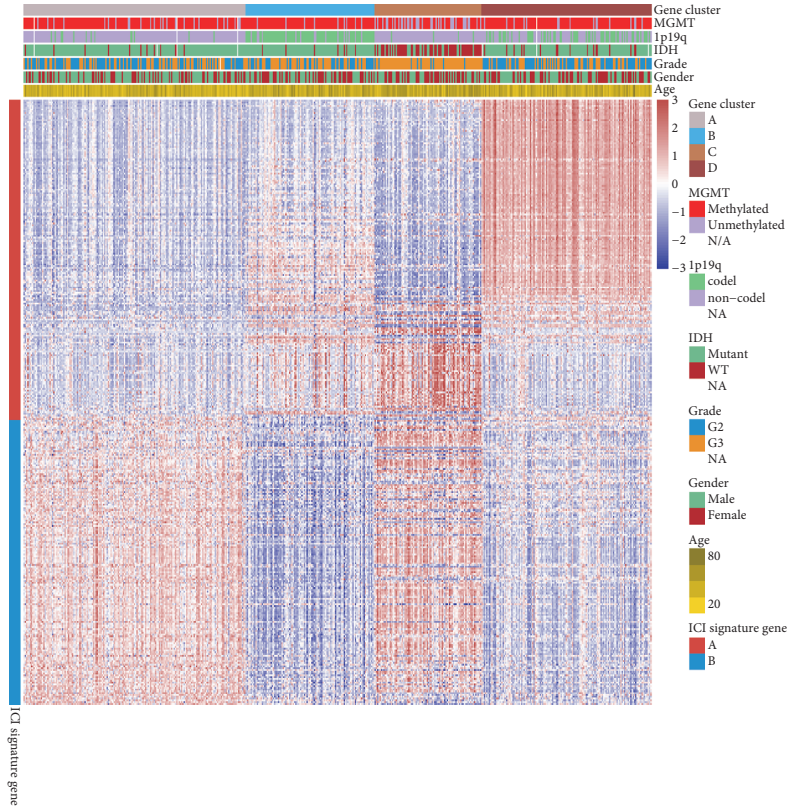

(d)

Figure 3: Continued.

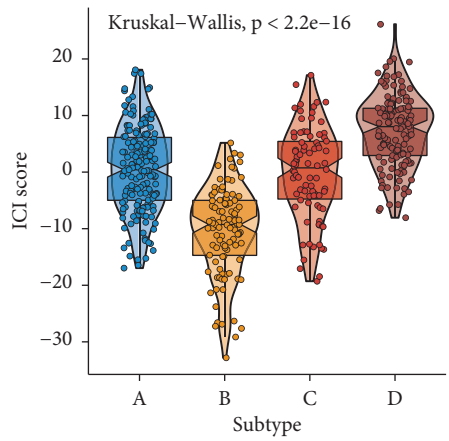

(e)

Figure 3: Construction of ICI gene clusters for LGG. ((a)–(c)) Unsupervised clustering analysis for identifying ICI gene clusters based on DEGs among ICI subtypes. (d) Heatmap for clinical features and expression patterns of ICI gene signatures in each ICI gene cluster. (e) Violin plots for the ICI scores in each ICI gene cluster. Kruskal-Wallis test, $p < 2.2e - 16$.

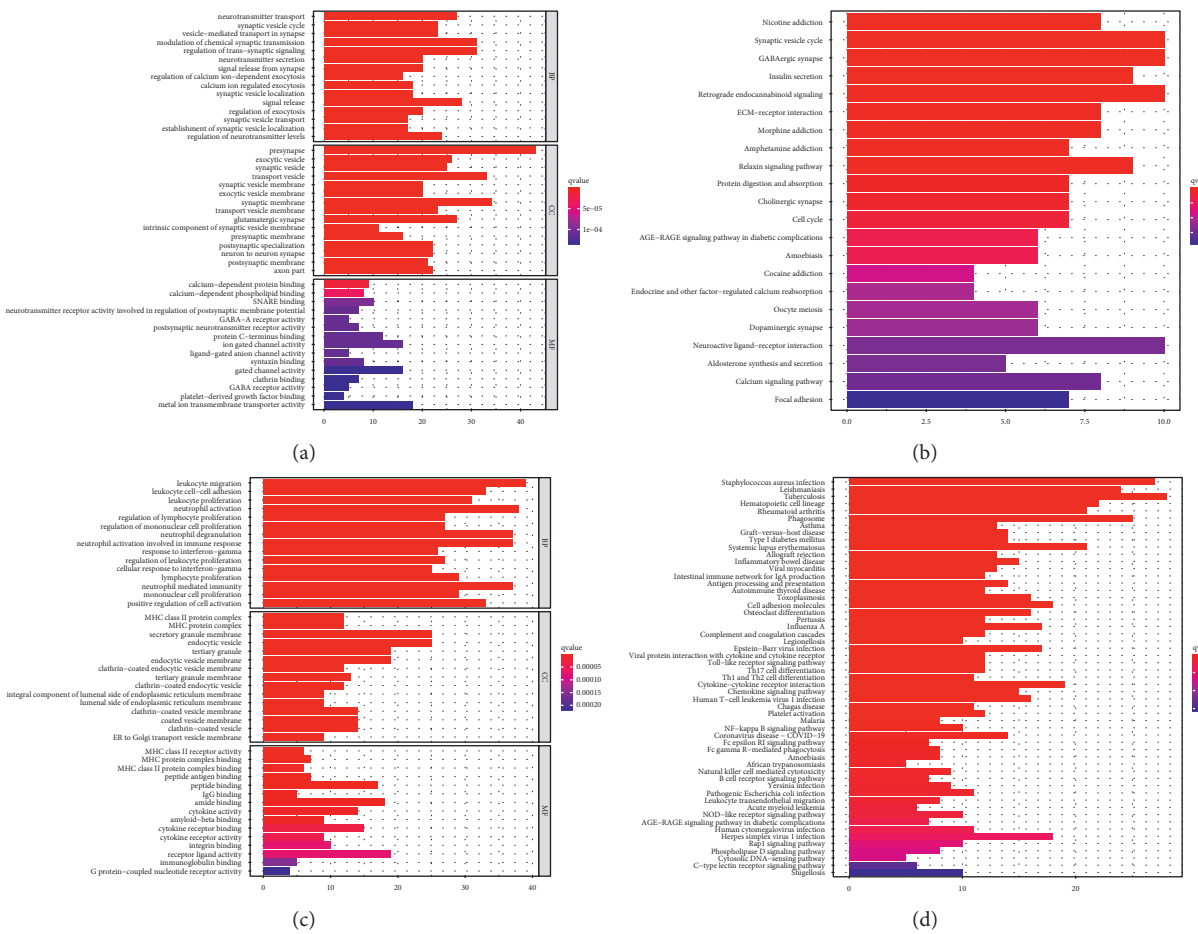

Figure 4: Functional enrichment analysis of ICI gene signatures A and B; GO and KEGG pathway enrichment results of ((a) and (b)) ICI gene signatures A and ((c) and (d)) ICI gene signatures B.

Immunohistochemistry and flow cytometry are two commonly applied methods to detect tumor-infiltrating immune cells, depending on a certain biomarker [27–29]. However, because many marker proteins are expressed in distinct cell types, both are misleading and incomplete [30]. Here, we analyzed the fractions of 22 immune cells, immune

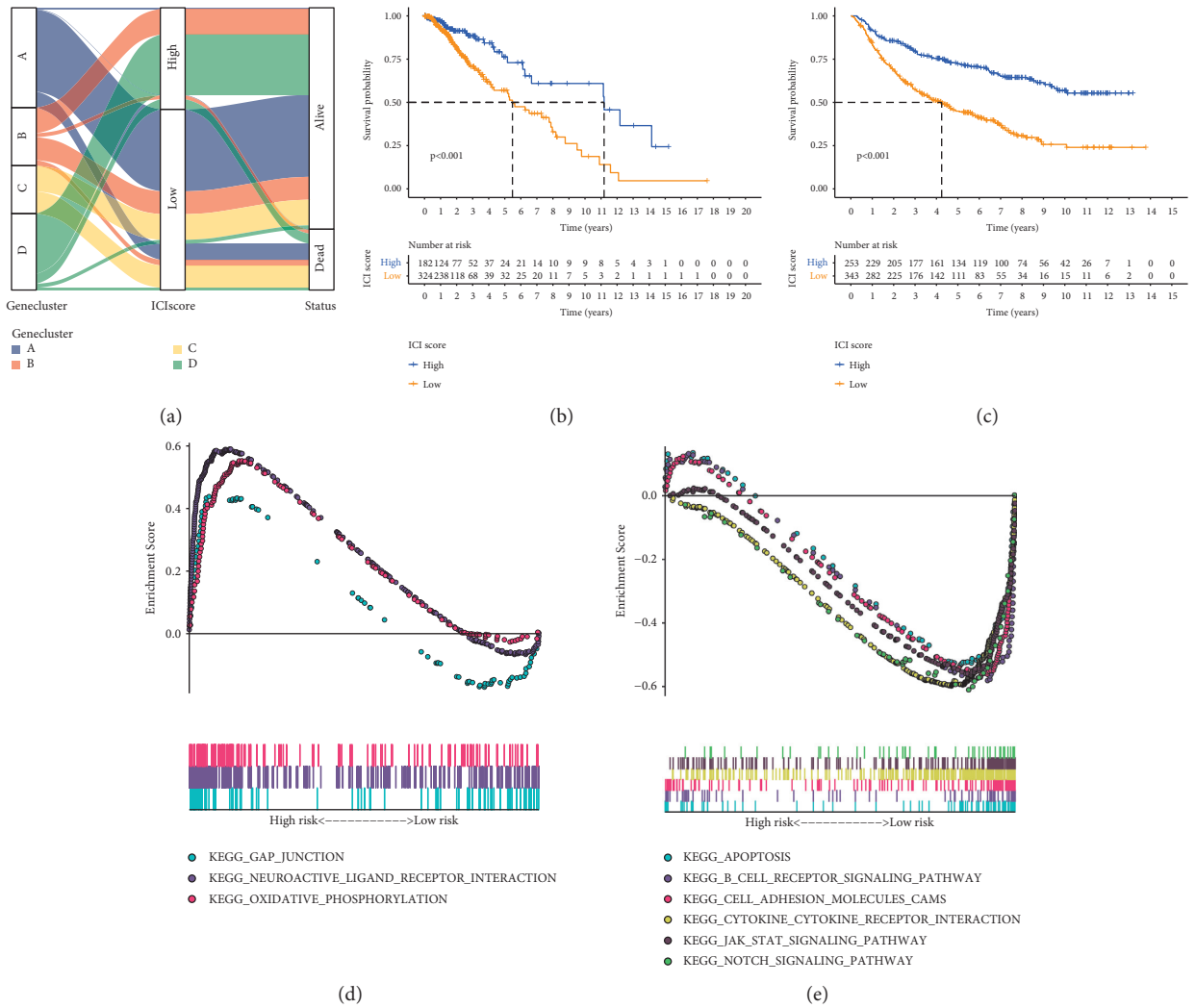

Figure 5: Development of ICI score system for LGG. (a) Alluvial diagram for the distributions of ICI scores and survival status in the four ICI gene clusters. ((b) and (c)) Kaplan-Meier curves of OS for patients with high and low ICI scores in the (b) TCGA-LGG and (c) CGGA-LGG datasets. Log-rank test, $p < 0.001$. ((d) and (e)) GSEA for the enrichment results in (d) high and (e) low ICI score groups.

scores, and stromal scores in LGG tissues by the CIBERSORTx and ESTIMATE algorithms [31]. We found that there was a strongly positive correlation between stromal scores and immune scores. Immune cells and stromal cells are key components in the tumor microenvironment [32], which exert a critical role in LGG progress and survival outcomes [33]. Previously, immune scores and stromal scores exhibited correlations to tumor grade as well as outcomes in LGG [3]. Here, this study characterized three ICI subtypes with distinct survival outcomes and infiltrations of immune cells. ICI subtype B was characterized by increased infiltration levels of plasma cells, CD8 T cells, CD4 memory resting T cells, Tregs, macrophages M0, resting dendritic cells, resting mast cells, and neutrophils. ICI subtype C was featured by increased infiltration levels of follicular helper T cells, activated NK cells, monocytes, activated mast cells, and eosinophils. ICI subtype A exhibited the characteristics of elevated macrophage M2 levels, immune scores, and stromal scores. PD-L1 expression is a critical marker for predicting response to immune checkpoint inhibitor therapy [34]. We found that three ICI subtypes showed correlations to PD-L1 expression, indicating that subjects in the three subtypes could be differentiated to the response to immunotherapy.

This study constructed four ICI gene subtypes. Gene cluster B displayed the features of decreased ICI scores, while gene cluster D had the features of increased ICI scores. We further uncovered the biological characteristics of ICI gene signatures A and B. ICI gene signatures A were mainly related to signal transduction. Malfunction of signal transduction may induce LGG initiation [35]. Moreover, ICI gene signatures B were primarily enriched in immune-related pathways such as Toll-like receptor pathway, chemokine pathway, B cell receptor pathway, and Th1, Th2, and Th17 cell differentiation. ICI score system was developed for prediction of LGG patients' prognosis. Our results showed that patients with low ICI scores exhibited undesirable clinical outcomes, which were confirmed in the CGGA-LGG

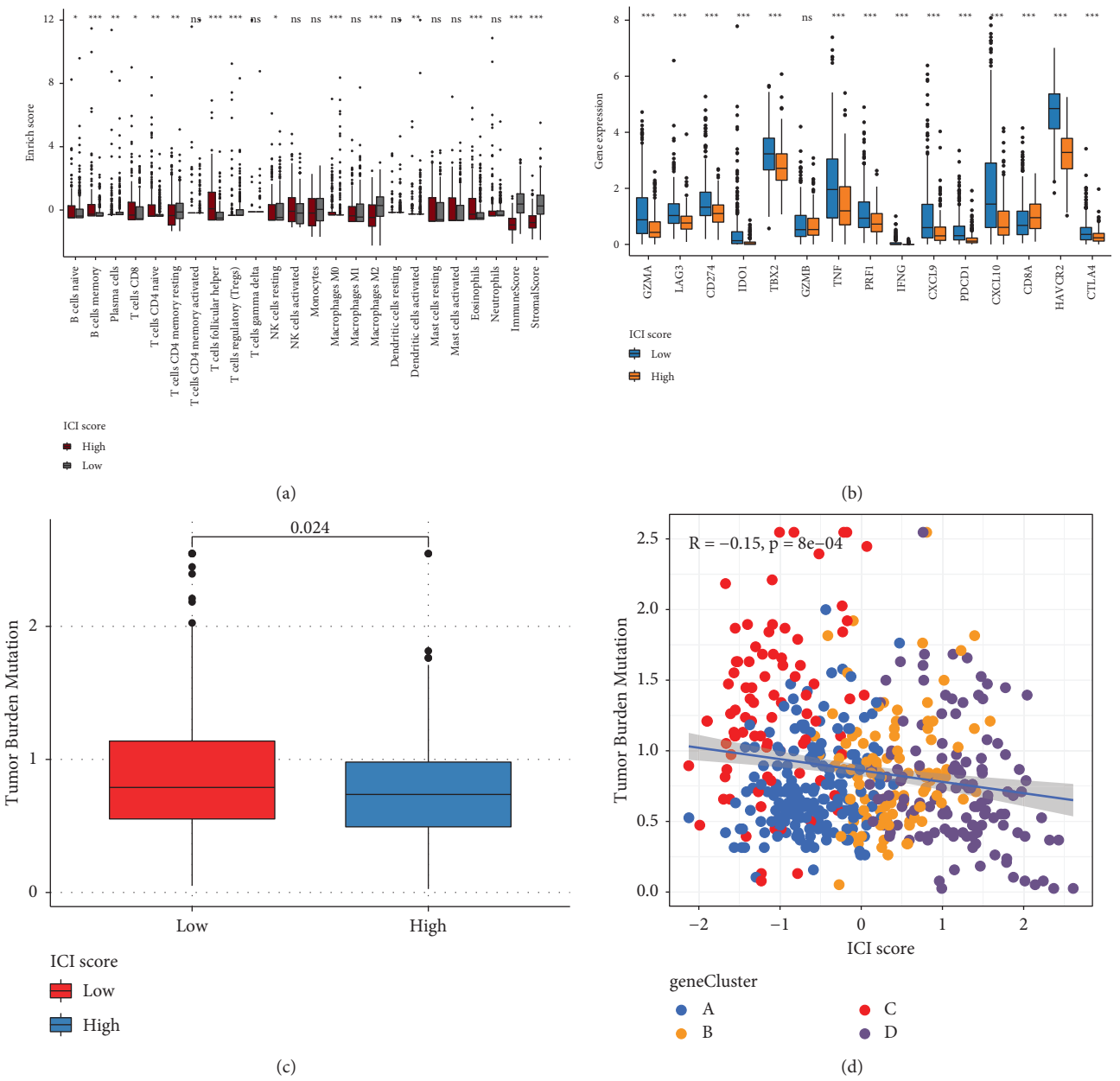

FIGURE 6: Assessment of the roles of ICI score in predicting response to immunotherapy. (a) The correlations between ICI scores and tumor-infiltrating immune cells. (b) The correlations of ICI scores with immune checkpoint genes and immune activity genes. (c) The TMB levels in high and low ICI score groups. (d) Scatter plots for the Spearman correlation between TMB and ICI scores. Wilcoxon test, ns: not significant; $^{*}p < 0.05$; $^{**}p < 0.01$; $^{***}p < 0.001$.

dataset. Thus, this score system could be utilized for predicting LGG patients' prognosis. We further probed into the biological features based on ICI scores. High ICI scores displayed correlations to gap junction, neuroactive ligand receptor interaction, and oxidative phosphorylation. Furthermore, low ICI scores were significantly related to apoptosis, B cell receptor signaling pathway, cell adhesion, cytokine-cytokine receptor interaction, JAK STAT signaling pathway, and Notch signaling pathway. The above pathways may contribute to LGG progression. For example, IFN-γ may activate JAK/STAT pathway by binding to receptor, thereby inducing PD-L1 expression on tumor cells [24]. Several tumor-suppressive factors containing cytokines like TGF-β and IL-10 have been discovered in LGG [36].

Immunotherapies have emerged as promising therapeutic strategies in LGG. Tumor-infiltrating immune cells affect responsiveness to such therapies as well as outcomes. Thus, we further characterized the infiltration levels of tumor-infiltrating immune cells in high and low ICI score LGG samples. High ICI scores exhibited correlations to increased infiltration levels of memory B cells, CD8 T cells, CD4 naïve T cells, follicular helper T cells, macrophages M0, and eosinophils, while low ICI scores were in relation with increased infiltration levels of naïve B cells, plasma cells, CD4 memory resting T cells, Tregs, resting

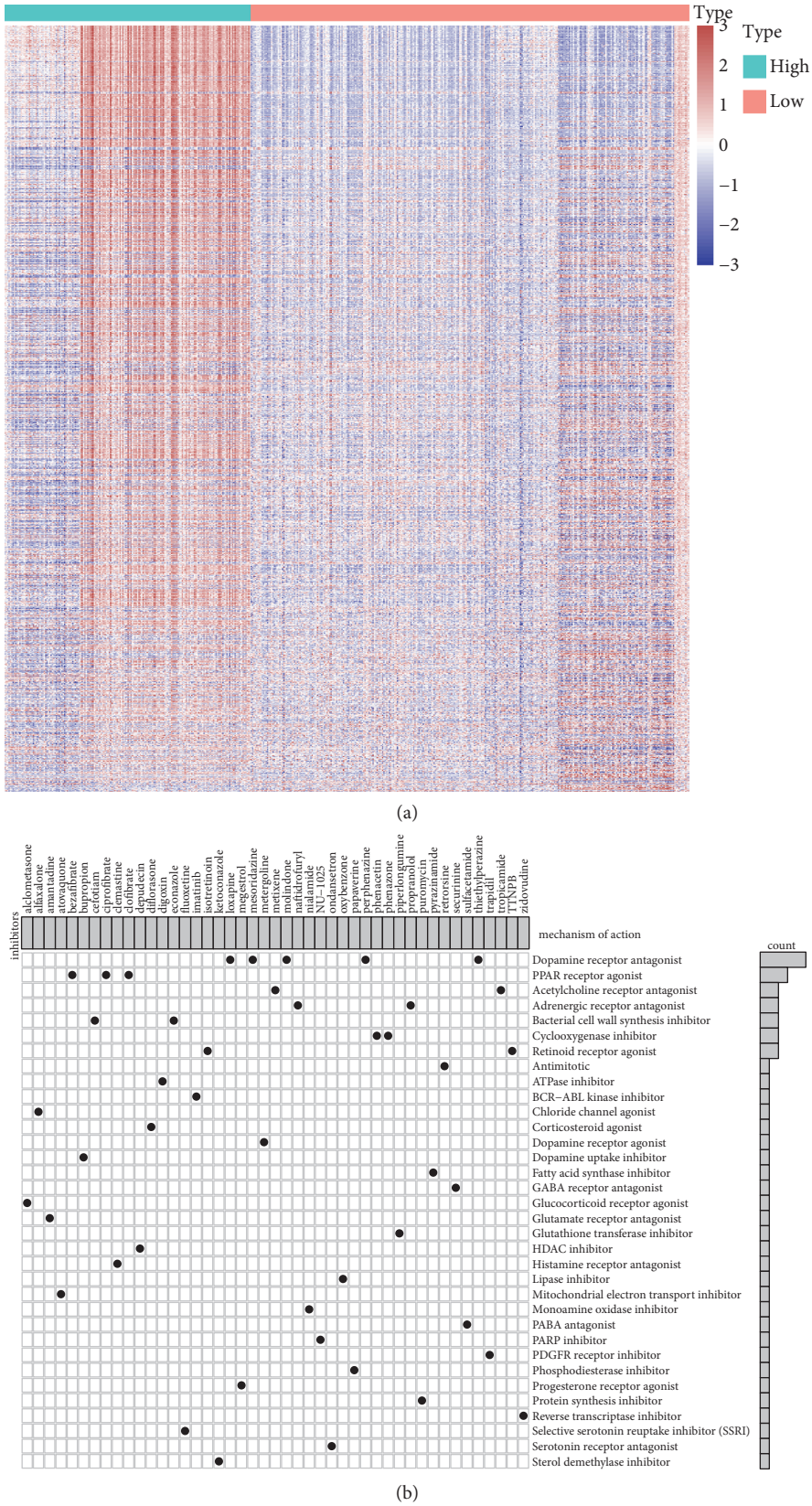

Figure 7: Prediction of potential small molecular drugs based on ICI scores by the CMap database. (a) Heatmap for upregulated genes (red) and downregulated genes (blue) between high and low ICI score groups. (b) Mechanisms of action shared by small molecular compounds.

Table 2: Potential small molecular drugs based on ICI scores through the CMap database.

Rank	CMap name	Mean	n	Enrichment	p	Specificity	Percent nonnull
1	Carbarsone	0.345	4	0.863	0.00048	0	50
2	Sulfabenzamide	0.312	4	0.8	0.00302	0.0072	50
3	Phenazone	−0.359	3	−0.838	0.00853	0.0173	66
4	Prestwick-675	−0.468	4	−0.743	0.00869	0.0928	75
5	Epitiostanol	−0.386	4	−0.712	0.0141	0.0432	50
6	Cinoxacin	−0.5	4	−0.701	0.01675	0.0197	75
7	Econazole	0.508	4	0.7	0.01677	0.1282	75
8	Betulin	0.456	3	0.771	0.02396	0.0127	66
9	Mevalolactone	−0.443	3	−0.77	0.02504	0.0514	66
10	Depudecin	0.391	2	0.887	0.0263	0.0188	50
11	Antazoline	−0.433	4	−0.658	0.03127	0.0315	75
12	16,16-Dimethylprostaglandin E2	−0.388	3	−0.749	0.03219	0.0276	66
13	Naftidrofuryl	−0.3	4	−0.653	0.03428	0.0065	50
14	Metixene	−0.273	4	−0.65	0.03555	0.0615	50
15	Zidovudine	0.281	4	0.644	0.03873	0.0245	50
16	Metergoline	0.336	4	0.638	0.04205	0.1726	50
17	Harmaline	−0.268	4	−0.636	0.04255	0.0353	50

NK cells, macrophages M2, and activated dendritic cells. Furthermore, LGG with low ICI scores had increased immune scores as well as stromal scores. These data reflected the heterogeneity of tumor immune microenvironment between high and low ICI score LGG tissues. Immunotherapies with blockage of immune checkpoints have displayed clinical efficacy in LGG [37]. Here, high ICI scores were characterized by decreased immune activity genes including GZMA, TBX2, TNF, PRF1, IFNG, CXCL9, and CXCL10 as well as reduced immune checkpoint genes including LAG3, CD274, IDO1, PDCD1, HAVCR2, and CTLA4. TMB has been an independent prognostic index for glioma and increased TMB indicates poorer survival outcomes [38]. Furthermore, TMB may predict the response to immune checkpoint inhibitors in advanced cancers [39]. In the high ICI score group, there was a reduced TMB score compared to the low ICI score group. Also, ICI score displayed a negative correlation to TMB score. Hence, LGG patients with high ICI scores might have less response to immunotherapies. Based on DEGs between high and low ICI scores, we predicted several small molecular drugs against LGG such as carbarsone, sulfabenzamide, and phenazone. More experiments should be presented to verify the effects of these compounds on treating LGG in future studies.

However, several limitations should be pointed out. First of all, our conclusion was acquired in public databases. Thus, it is indispensable to verify it through experiments. The clinical significance of ICI score in predicting prognosis and immunotherapy in LGG should be confirmed in the future. Despite these limitations, our study provides clues for the ICI landscape in LGG for aiding immunotherapy.

5. Conclusion

Collectively, this study characterized the ICI landscape in LGG by the CIBERSORTx and ESTIMATE algorithms. Through unsupervised clustering analysis, we established three ICI subtypes and four ICI gene clusters. PCA was applied to develop ICI score system for LGG. Patients with high ICI scores exhibited favorable clinical outcomes but lower sensitivity to immunotherapies. Despite this, this scoring system should be validated in larger LGG cohorts.

Abbreviations

ICI: Immune cell infiltration
LGG: Low-grade glioma
PCA: Principal component analysis
TMB: Tumor mutation burden
CGGA: Chinese Glioma Genome Atlas
CDF: Cumulative distribution function
DEGs: Differentially expressed genes
FC: Fold change
PC1: Principal component 1
GO: Gene ontology
KEGG: Kyoto Encyclopedia of Genes and Genomes
GSEA: Gene set enrichment analysis
CMap: Connectivity Map
MoA: Mode-of-action
OS.: Overall survival.

Data Availability

The data used to support the findings of this study are included within Supplementary Materials.

Conflicts of Interest

The authors declare no conflicts of interest.

Acknowledgments

This work was funded by Foundation of the General Hospital of Western Theater Command (2021-XZYG-C05).

Supplementary Materials

Supplementary Table 1: the list of ICI gene signatures A and B. Supplementary Table 2: GSEA results in high ICI score group. Supplementary Table 3: GSEA results in low ICI score group. Supplementary Table 4: DEGs between high and low ICI score groups. Supplementary Figure 1: validation of the three ICI subtypes for LGG in the CGGA-LGG dataset. (A–C) Unsupervised clustering analysis for validating the classifications of three ICI subtypes. (A) Consensus cumulative distribution function graph. (B) Delta area plot. (C) Heatmap for consensus matrix when $k = 3$. (D) Heatmap of tumor-infiltrating immune cells in different clinical phenotypes and ICI subtypes. (E) PCA plots for confirming the classification patterns of the ICI subtypes. (F) Kaplan-Meier curves for OS of LGG patients in the three ICI subtypes. (*Supplementary Materials*)

References

[1] P. Feng, Z. Li, Y. Li, and Y. Zhang, "Phosphatase and tensin homolog mutation in immune cell infiltration and clinicopathological features of low-grade gliomas," *Frontiers in Molecular Biosciences*, vol. 7, Article ID 562416, 2020.

[2] F. Klemm, R. R. Maas, R. L. Bowman et al., "Interrogation of the microenvironmental landscape in brain tumors reveals disease-specific alterations of immune cells," *Cell*, vol. 181, no. 7, pp. 1643–1660, 2020, e1617.

[3] J. Ni, S. Liu, F. Qi et al., "Screening TCGA database for prognostic genes in lower grade glioma microenvironment," *Annals of Translational Medicine*, vol. 8, no. 5, p. 209, 2020.

[4] H. F. van Thuijl, T. Mazor, B. E. Johnson et al., "Evolution of DNA repair defects during malignant progression of low-grade gliomas after temozolomide treatment," *Acta Neuropathologica*, vol. 129, no. 4, pp. 597–607, 2015.

[5] Y. Tan, S. Zhang, Q. Xiao et al., "Prognostic significance of ARL9 and its methylation in low-grade glioma," *Genomics*, vol. 112, no. 6, pp. 4808–4816, 2020.

[6] C. Han, Y. He, L. Chen et al., "Low expression of APOB mRNA or its hypermethylation predicts favorable overall survival in patients with low-grade glioma," *OncoTargets and Therapy*, vol. 13, pp. 7243–7255, 2020.

[7] R. J. Packer, A. Iavarone, D. T. W. Jones et al., "Implications of new understandings of gliomas in children and adults with NF1: report of a consensus conference," *Neuro-Oncology*, vol. 22, no. 6, pp. 773–784, 2020.

[8] D. A. Reardon, A. Desjardins, J. J. Vredenburgh et al., "Rindopepimut with bevacizumab for patients with relapsed EGFRvIII-expressing glioblastoma (ReACT): results of a double-blind randomized phase II trial," *Clinical Cancer Research*, vol. 26, no. 7, pp. 1586–1594, 2020.

[9] I. Mildenberger, L. Bunse, K. Ochs, and M. Platten, "The promises of immunotherapy in gliomas," *Current Opinion in Neurology*, vol. 30, no. 6, pp. 650–658, 2017.

[10] S. Müller, G. Kohanbash, S. J. Liu et al., "Single-cell profiling of human gliomas reveals macrophage ontogeny as a basis for regional differences in macrophage activation in the tumor microenvironment," *Genome Biology*, vol. 18, p. 234, 2017.

[11] B. Li, E. Severson, J.-C. Pignon et al., "Comprehensive analyses of tumor immunity: implications for cancer immunotherapy," *Genome Biology*, vol. 17, no. 1, p. 174, 2016.

[12] A. M. Newman, C. B. Steen, C. L. Liu et al., "Determining cell type abundance and expression from bulk tissues with digital cytometry," *Nature Biotechnology*, vol. 37, no. 7, pp. 773–782, 2019.

[13] K. Yoshihara, M. Shahmoradgoli, E. Martínez et al., "Inferring tumour purity and stromal and immune cell admixture from expression data," *Nature Communications*, vol. 4, no. 1, Article ID 2612, 2013.

[14] M. D. Wilkerson and D. N. Hayes, "ConsensusClusterPlus: a class discovery tool with confidence assessments and item tracking," *Bioinformatics*, vol. 26, no. 12, pp. 1572-1573, 2010.

[15] B. Zhang, Q. Wu, B. Li, D. Wang, L. Wang, and Y. L. Zhou, "m6A regulator-mediated methylation modification patterns and tumor microenvironment infiltration characterization in gastric cancer," *Molecular Cancer*, vol. 19, no. 1, p. 53, 2020.

[16] Y. Gao, H. Wang, H. Li et al., "Integrated analyses of m1A regulator-mediated modification patterns in tumor microenvironment-infiltrating immune cells in colon cancer," *Oncoimmunology*, vol. 10, no. 1, Article ID 1936758, 2021.

[17] G. Yu, L.-G. Wang, Y. Han, and Q.-Y. He, "clusterProfiler: an R package for comparing biological themes among gene clusters," *OMICS: A Journal of Integrative Biology*, vol. 16, no. 5, pp. 284–287, 2012.

[18] A. Subramanian, P. Tamayo, V. K. Mootha et al., "Gene set enrichment analysis: a knowledge-based approach for interpreting genome-wide expression profiles," *Proceedings of the National Academy of Sciences*, vol. 102, no. 43, pp. 15545–15550, 2005.

[19] T. A. Chan, M. Yarchoan, E. Jaffee et al., "Development of tumor mutation burden as an immunotherapy biomarker: utility for the oncology clinic," *Annals of Oncology*, vol. 30, no. 1, pp. 44–56, 2019.

[20] J. Lamb, E. D. Crawford, D. Peck et al., "The Connectivity Map: using gene-expression signatures to connect small molecules, genes, and disease," *Science*, vol. 313, no. 5795, pp. 1929–1935, 2006.

[21] X. Deng, D. Lin, B. Chen et al., "Development and validation of an IDH1-associated immune prognostic signature for diffuse lower-grade glioma," *Frontiers in Oncology*, vol. 9, Article ID 1310, 2019.

[22] L. Chen, G. Wang, X. Qiao et al., "Downregulated miR-524-5p participates in the tumor microenvironment of ameloblastoma by targeting the interleukin-33 (IL-33)/Suppression of tumorigenicity 2 (ST2) Axis," *Medical Science Monitor : International Medical Journal of Experimental and Clinical Research*, vol. 26, Article ID e921863, 2020.

[23] J. Li, K. T. Byrne, F. Yan et al., "Tumor cell-intrinsic factors underlie heterogeneity of immune cell infiltration and response to immunotherapy," *Immunity*, vol. 49, no. 1, pp. 178–193, 2018, e177.

[24] J. Qian, C. Wang, B. Wang et al., "The IFN-γ/PD-L1 axis between T cells and tumor microenvironment: hints for glioma anti-PD-1/PD-L1 therapy," *Journal of Neuroinflammation*, vol. 15, no. 1, p. 290, 2018.

[25] Y. Xiao, Z. Zhu, J. Li et al., "Expression and prognostic value of long non-coding RNA H19 in glioma via integrated bioinformatics analyses," *Aging*, vol. 12, no. 4, pp. 3407–3430, 2020.

[26] X. Guo, Y. Pan, M. Xiong et al., "Midkine activation of CD8+ T cells establishes a neuron-immune-cancer axis responsible for low-grade glioma growth," *Nature Communications*, vol. 11, no. 1, p. 2177, 2020.

[27] Y. Sun, X. Niu, G. Wang, X. Qiao, L. Chen, and M. Zhong, "A novel lncRNA ENST00000512916 facilitates cell proliferation, migration and cell cycle progression in ameloblastoma," *OncoTargets and Therapy*, vol. 13, pp. 1519–1531, 2020.

[28] X. Niu, B. Huang, X. Qiao, J. Liu, L. Chen, and M. Zhong, "MicroRNA-1-3p suppresses malignant phenotypes of ameloblastoma through down-regulating lysosomal associated membrane protein 2-mediated autophagy," *Frontiers in Medicine*, vol. 8, Article ID 670188, 2021.

[29] X. Wang, G. Cheng, Y. Miao et al., "Piezo type mechanosensitive ion channel component 1 facilitates gastric cancer omentum metastasis," *Journal of Cellular and Molecular Medicine*, vol. 25, no. 4, pp. 2238–2253, 2021.

[30] J. Lu, H. Li, Z. Chen et al., "Identification of 3 subpopulations of tumor-infiltrating immune cells for malignant transformation of low-grade glioma," *Cancer Cell International*, vol. 19, no. 1, p. 265, 2019.

[31] X. Liu, X. Niu, and Z. Qiu, "A five-gene signature based on stromal/immune scores in the tumor microenvironment and its clinical implications for liver cancer," *DNA and Cell Biology*, vol. 39, no. 9, pp. 1621–1638, 2020.

[32] X.-T. Qiu, Y.-C. Song, J. Liu, Z.-M. Wang, X. Niu, and J. He, "Identification of an immune-related gene-based signature to predict prognosis of patients with gastric cancer," *World Journal of Gastrointestinal Oncology*, vol. 12, no. 8, pp. 857–876, 2020.

[33] X. Deng, D. Lin, X. Zhang et al., "Profiles of immune-related genes and immune cell infiltration in the tumor microenvironment of diffuse lower-grade gliomas," *Journal of Cellular Physiology*, vol. 235, no. 10, pp. 7321–7331, 2020.

[34] M. Yarchoan, L. A. Albacker, A. C. Hopkins et al., "PD-L1 expression and tumor mutational burden are independent biomarkers in most cancers," *JCI Insight*, vol. 4, 2019.

[35] R. J. Packer, S. Pfister, E. Bouffet et al., "Pediatric low-grade gliomas: implications of the biologic era," *Neuro-oncology*, vol. 19, pp. 750–761, 2017.

[36] M. H. Robinson, J. Vasquez, A. Kaushal et al., "Subtype and grade-dependent spatial heterogeneity of T-cell infiltration in pediatric glioma," *Journal for Immunotherapy of Cancer*, vol. 8, 2020.

[37] Y. n. Chen, S. q. Hou, R. Jiang, J. l. Sun, C. D. Cheng, and Z. R. Qian, "EZH2 is a potential prognostic predictor of glioma," *Journal of Cellular and Molecular Medicine*, vol. 25, no. 2, pp. 925–936, 2020.

[38] L. Wang, J. Ge, Y. Lan et al., "Tumor mutational burden is associated with poor outcomes in diffuse glioma," *BMC Cancer*, vol. 20, no. 1, p. 213, 2020.

[39] P. Bonaventura, T. Shekarian, V. Alcazer et al., "Cold tumors: a therapeutic challenge for immunotherapy," *Frontiers in Immunology*, vol. 10, Article ID 168, 2019.

Hindawi
Journal of Oncology
Volume 2022, Article ID 8058770, 9 pages
https://doi.org/10.1155/2022/8058770

Research Article

Exosomal LINC01213 Plays a Role in the Transition of Androgen-Dependent Prostate Cancer Cells into Androgen-Independent Manners

Zhuifeng Guo,[1,2] **Xuwei Lu**,[1] **Fan Yang**,[1] **Chang He**,[1] **Liang Qin**,[1] **Ning Yang**,[1] **Conghui Han**,[2,3] **and Jiawen Wu**[1]

[1]*Department of Urology, Minhang Hospital, Fudan University/Minhang Branch, Zhongshan Hospital, Fudan University, Shanghai, China*
[2]*Medical College of Soochow University, Suzhou, Jiangsu Province, China*
[3]*Department of Urology, Xuzhou Central Hospital, Xuzhou, Jiangsu Province, China*

Correspondence should be addressed to Jiawen Wu; kevinwujw@163.com

Received 11 January 2022; Accepted 17 February 2022; Published 10 March 2022

Academic Editor: Fu Wang

Background. Castration-resistant prostate cancer (CRPC), one of the prostate cancers, is a medical conundrum around the world. Some studies have demonstrated that many long noncoding RNAs in exosomes are very important in many types of cancer, including prostate cancer. However, until now, the function of exosomes in the occurrence and development of CRPC has not been reported. *Methods*. In vitro, cell coculture was used in LNCap cells and PC-3 cells, while the isolation and purification of exosomes and the subsequent treatment assays were used in functional studies. In vitro assays were performed to detect the transformation of ADPC cells (androgen-dependent prostate cancer) into AIPC cells (androgen-independent prostate cancer). Subsequently, a lncRNA-sequencing assay was performed to detect different lncRNA expression profiles in ADPC cells cocultured with or without AIPC exosomes. The role of LINC01213 was analysed by a TCGA database after silencing the expression of LINC01213. CCK-8, qRT-PCR, and Western blotting studies were performed to analyse the possible mechanism by which exosomes participate in prostate cancer progression. *Results*. In the coculture system, ADPC cells acquired androgen deprivation tolerance through exosome-mediated intercellular communication. Exosomes secreted by AIPC cells can promote the transformation of ADPC cells into androgen-independent cells in vitro and in vivo. lncRNA sequencing showed that LINC01213 was upregulated in exosomes derived from AIPC cell lines. The rescue experiments were preformed, and the results revealed that most of the functions of LINC01213 were performed by Wnt/β-catenin. *Conclusions*. All the findings showed that exosomes play a key role in CRPC progression by upregulating LINC01213 and activating Wnt/β-catenin signalling.

1. Introduction

Prostate cancer (PCa) is one of the most common malignancies among men in the world [1]. In China, both incidence and death rates from prostate cancer have also increased significantly over the past decade [2]. Although many treatments have been used to treat prostate cancer, such as radical resection and radiotherapy [3], the therapeutic effect is not very satisfactory; most patients eventually revert to castration-resistant prostate cancer (CRPC) [3]. Hence, finding out the pathogenesis of CRPC and further studying its mechanism is the key step to solve this problem, which also is the goal of the research.

Exosomes are extracellular vesicles (EVs) that have been used as a new therapy tool, including drug delivery and antitumor therapy, for a variety of diseases [4]. Almost all cells release exosomes [5], including normal and tumor cells [6, 7]. Exosomes are even found in blood [8], urine [9], and saliva [10]. Exosomes contain not only proteins but also multiple different types of RNA molecules, lncRNAs are included [11], and exosomes also act as messengers between cells that carry messages to each other [5, 12]. The study of

exosomes in prostate cancer is increasing day by day, and the function of exosomes in prostate cancer has been reported by many researchers. It has been shown that lncRNA-p21 is present in exosomes of PCA patients, and this level of lncRNA-p21 may be helpful for improving the diagnosis and prediction of the malignant state in PCA patients [13]. Zhang et al. reported that in prostate cancer, exosomes can activate heme oxygenase-I to affect the progression of prostate cancer [14].

Noncoding long RNA is a new kind of noncoding RNA, which is more than 200 nucleotides (nT) in size and does not encode any protein, and the main reason is that they lack an open reading framework [15–17]. Current studies suggest that lncRNAs can be implicated in various human cancers, and there have been reports of breast cancer [18], lung cancer [19], and gastric cancer [20]. With respect to prostate cancer, there are also related reports, for example, PCA3 and SChLAP1 were reported to be biomarkers for prostate cancer [21–23]. PCGEM1 and PRNCR1 play a key role in androgen-dependent transcription by promoting chromatin cyclization between the AR-binding enhancer and promoter of target gene [24]. In addition, a previous study confirmed that LINC01213 plays an important role in cancers [25, 26]; Until now, the function of LINC01213 is in its infancy of prostate research.

The concept of the tumor microenvironment has been proposed in recent years, and many researchers have focused on the role of tumor microenvironment in the development and progression of tumors, including prostate cancer [27]. Therefore, tumor microenvironment may be involved in the androgen resistance process. We are interested in exosomes that play a key role in cell-cell interactions. The purpose of this study was to investigate the exosomal role of LINC01213 in the transformation of androgen-dependent prostate cancer cells into androgen-independent prostate cancer cells.

2. Materials and Methods

2.1. Cell Culture. The prostate cancer cell lines LNCaP and PC-3 were purchased from the American Type Culture Collection (ATCC; Rockville, MD, USA). RPMI1640 medium was supplemented with 10% fetal bovine serum (FBS, Gibco, Grand Island, NY, USA) and 1% penicillin streptomycin (Gibco). All cells were cultured in 5% CO_2 incubator humidified at 37°C.

2.2. Coculture of LNCAP Cells with PC-3 Cells. LNCaP cells and PC-3 cells were cocultured in the transwell coculture system (0.4 μm transwell insert). LNCaP cells seeded in superior cavity and PC-3 cells were cocultured in inferior cavity for 10 days. When PC-3 cells reached 90% confluence, LNCAP cells were transferred to a new plate.

2.3. Exosomes Isolated by Ultracentrifugation. In order to remove the dead cells, we centrifuged the harvested cultures (300 ml) in 500 g for 30 min and then continued centrifuging in 2000 g for 30 min. After that, the supernatant was collected and centrifuged at 10000 g for 30 min, collected the supernatant again, and centrifuged at 100000 g for 120 min for obtaining exocrine granules. At this step, the pellet was collected and resuspended in PBS.

2.4. lncRNAs Sequencing. We used the miRNeasy kit (Qiagen) to extract total RNA from DHT-treated LNCaP cells. RNA mass was measured by the Agilent Bioanalyzer. Then, according to the published scheme [27], all samples were sequenced with Illumina HiSeq 2000 (read length 100 nT) according to the previous reports [28].

2.5. CCK-8 Determination. Cell proliferation was detected with the CCK-8 kit (Kumamoto Dojindo, Japan). Seed the cells in the 96-well plate at 1000/well density. After 0, 1, 2, 3, and 4 days, 10 L CCK-8 (5 mg/ml) was added to each well and incubated at 37°C for 2 hours. Finally, the cells were measured at 450 nm with an enzyme analyzer (Thermo-Fisher Scientific, Waltham, MA, USA).

2.6. Cell Cycle Assay. The transfected cells were dissolved overnight in precooled ethanol (75%) at 4°C, washed with cold PBS once, and stained with BD, Pharmingen^{TM}, PI/RNase at room temperature for 30 min. Finally, cell cycles (GO/G1, S, and G2) were analysed by flow cytometry (BD Biosciences).

2.7. Tumorigenicity Assay. Male NOD/SCID mice (Shanghai Bikai) aged 4–6 weeks were used to determine their tumorigenicity. The experimental design was approved by the Local Ethics Committee of Minhang Hospital of Fudan University (certificate no.: 2020-032-01K). Before the androgen ablation experiment in vivo, we castrated the mice carefully. After that, two groups of cells were injected into mice; one group cell was treated with PBS, while another one was treated with exosomes. After 40 days, the mice were killed, and the tumors were removed.

2.8. Real-Time Quantitative PCR (qRT-PCR). Total RNA was extracted from cells using TRIzol reagent (15596026, Invitrogen, Carlsbad, CA, USA). For qRT-PCR, the HiScript II first strand cDNA synthesis kit (Vazyme Biotech Co.) was used generate the first station cDNA. Gene expression was detected with SYBR ex Taq premix (RR420A, Takara, Takara, Dalian, China). All PCRs were detected by at least three copies, and the results were standardized by GAPDH, which were calculated using the $2^{-\Delta\Delta CT}$ method. The gene specific primers were designed and synthesized by SprinGen Biotech, and their sequences are given in Supplementary Table S1.

2.9. Small Interfering RNA (siRNA) Transfection. The effective siRNA targeting human LINC01213 was purchased from RiboBio (Guangzhou, China). Lipofectamine 2000 (11668019, Invitrogen, Carlsbad, CA, USA) was used to transfect siRNA, and the final transfection concentration

was 10 nM. Finally, qRT-PCR was used to detect the expression changes.

2.10. Western Blotting. The cells were scraped off with a spatula and then lysed with RIPA buffer which was added with protein inhibitors. The BCA protein assay kit (Beyotime, China) was used to determine the protein concentration. The total protein (30 ug) or exosomes were then isolated by SDS-PAGE gel and transferred to PVDF membrane (1620177, PVDF, BioRad, Hercules, USA). The membranes were sealed in 5% skim milk for 60 min and then treated at 4°C with primary antibodies (PSA, AR, TSG101, HSP70, and Alix) overnight; all primary antibodies dilution ratios are 1–1000. On the second day, the membranes were clear with PBS for 3 times, and the second antibody was then incubated at room temperature for 1 hour. Finally, ELC luminescence was used for measurement the protein bands.

2.11. Statistical Analysis. All experiments were made in triplicate, and the data were analysed using GraphPad Prism 8 (CA, USA) software. All data were expressed as mean ± standard deviation (SD). Student' *t*-test was used to estimate the significance of the difference between the two groups, and one-way analysis of variance (ANOVA) was used to compare the two groups. The statistical significance was $P < 0.05$ $(^{*})$ and $P < 0.01$ $(^{**})$, respectively.

3. Result

3.1. Androgen Deprivation Resistance Induced by Coculture of LNCaP Cells and PC-3 Cells. To investigate trend resistance, we choose two cells for this study: one is LNCaP cell and another is PC-3. First, LNCAP cells and PC-3 cells were cocultured in a transwell system, LNCaP cells were cultured in lower cavity, and PC-3 cells were cultured in upper cavity. After 10 days, we found that AR-responsive genes and EMT marker genes were significantly changed after coculturing; CDK1, CDK2, and GRBE1 were downregulated, and N-cadherin was upregulated, while E-cadherin was downregulated in LNCAP cells (Figures 1(a) and 1(b)). Compared with the normal medium control group, the proliferation of LNCaP cells in the androgen-deficient medium group increased significantly (Figures 1(c) and 1(d)). The results of flow cytometry showed that the S phase was significantly increased in the cocultured group under castration conditions, but there was no significant difference under normal conditions. Western blotting assay was performed to detect the protein level of AR and PSA, and the result showed that both AR and PSA were significantly decreased in the coculture condition (Figures 1(e) and 1(f)).

3.2. Isolation and Identification of Exosomes. Why do LNCaP cells have such a great influence on coculture? We suspected that the exosomes of PC-3 cells played a key role, so the exosomes were isolated from the culture supernatant of PC-3 cells. Transmission electron microscopy showed that the appearance of membrane-limited particles was uniform and ranged from approximately 100 nm. Western blotting of exosomal markers such as Alix, TSG101, and HSP70 showed that the granules had exosomal characteristics and could be separated uniformly (Figures 2(a) and 2(b)).

3.3. Exosomes Derived from AIPC Cells Promote Emasculation Resistance in ADPC Cells. In order to further investigate the role of PC-3 exosomes in the castration resistance of LNCaP cells, we first incubated PC-3 exosomes (50 g/ml) with LNCaP cells, and then, CCK-8 assay and flow cytometry assay were used to detect the proliferation and cell cycles. After incubating PC-3 exosomes, the proliferation of LNCaP cells increased significantly not only in androgen-deprived medium but also in general medium (Figures 3(a) and 3(b)). Similar results occurred in the cell cycles assay; after incubating PC-3 exosomes, the S phase of LNCaP cells increased in both different condition (Figure 3(c)), and the protein levels of PAR and PAR decreased significantly after treated with PC-3 exosomes (Figure 3(d)).

In subsequent studies, animal experiments were performed with intact and castrated NOD/SCID mice. The tumorigenesis data showed that, after treated with PC-3 exosomes, the tumorigenicity of LNCaP cells was significantly higher than that of normal LNCaP cells. It should be noted that normal LNCaP cells cannot form tumors under castration conditions, but some mice injected with the treated LNCaP cells have the ability to form tumors (Figure 3(e)), suggesting that AIPC cells may be induced by androgen secretion.

3.4. LINC01213 May Play a Key Role in AIPC-Derived Exosomes in ADPC Cells. There are many substances in exosomes, such as microRNA, lncRNA, or circRNA. To study the underlying mechanism of exosome-induced castration resistance, we focused on lncRNA. We performed the lncRNA-sequencing assay; a heatmap of the lncRNA expression profiles showed 61 lncRNAs were found to be significantly affected (1.5-fold change), with 52 lncRNAs increased and 9 decreased (Figure 4(a)). KEGG pathway analysis showed that the most affected ncRNAs were those involved in tumor-related pathways, such as the Wnt/-catenin pathway (Supplementary Figure 1).

The first 10 lncRNAs were verified by qRT-PCR. In order to evaluate the role of LINC01213 in prostate cancer, we first analysed the expression of LINC01213 in the TCGA database and found that it was upregulated in prostate cancer. We also found that the expression of LINC01213 correlated with prognosis of prostate cancer, and the higher the expression, the worse the prognosis (Figures 4(c) and 4(d)).

3.5. LINC01213 Inhibits the Growth of ADPC Cells through Wnt/-Catenin Signal Transduction and Partially Reduces Androgen Dependence. In order to study the androgen-dependent effect of LINC01213 on ADPC cells, LINC01213 was downregulated by siRNA, and CCK-8 assay was used to detect the prefoliation again, and the result showed that the prefoliation of LNCaP cells was inhibited under normal

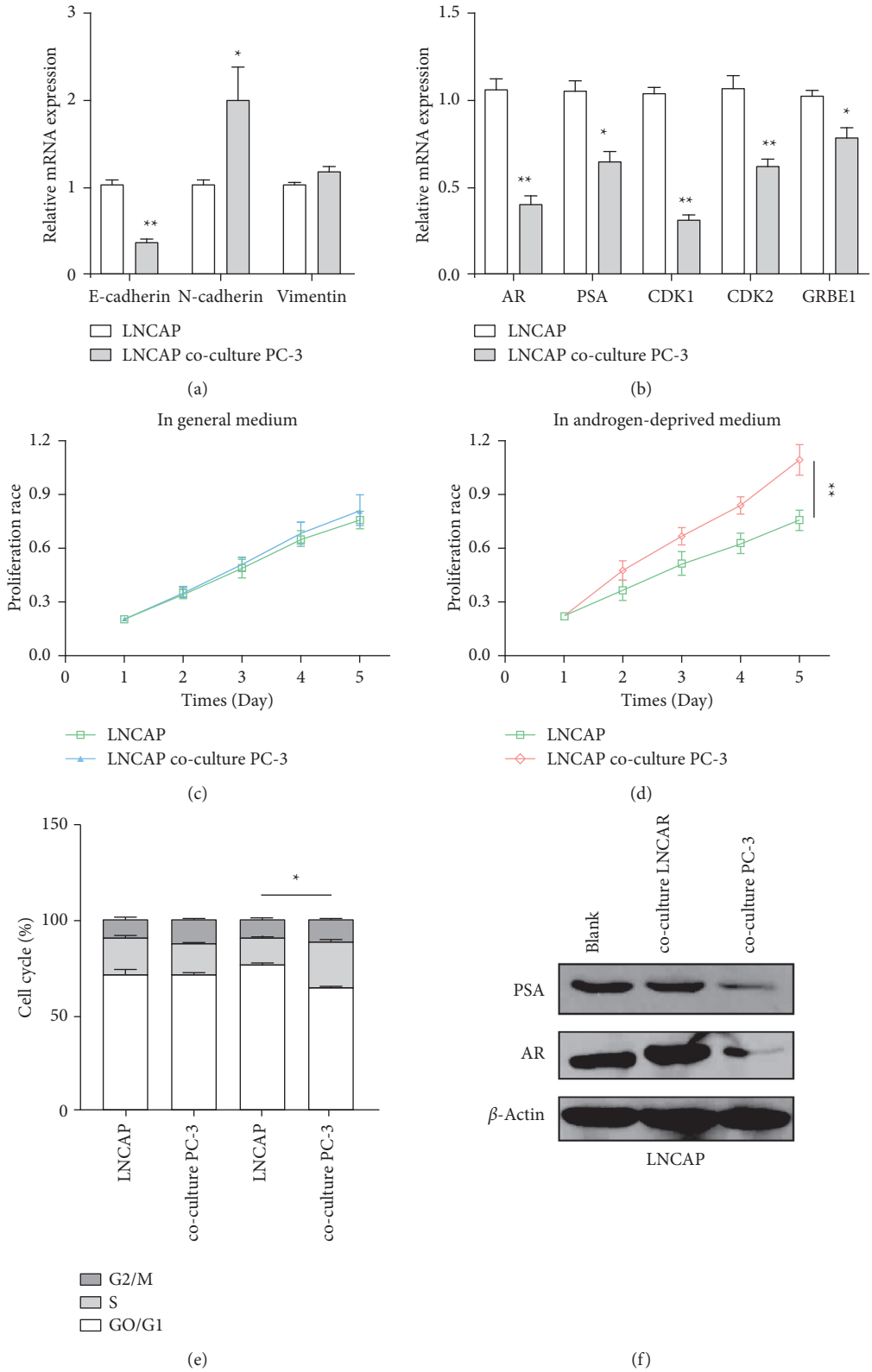

FIGURE 1: The change of resistance of LNCaP cells in coculture with PC-3 cells. (a)-(b) qRT-PCR used to detect the gene level of E-cadherin, N-cadherin, vimentin, AR, PSA, CDK1, CDK2, and GRBE1 after treatment. (c)-(d) CCK-8 used to detect the proliferation of LNCaP cells and PC-3 cells in normal and androgen media. (e) The cell cycle of LNCaP cells and PC-3 cells cocultured on conventional or androgen medium was detected. (f) The protein level of PSA and AR in cocultured LNCAP/PC-3 cells analysed by Western blot. $^{*}P < 0.05$, $^{**}P < 0.01$.

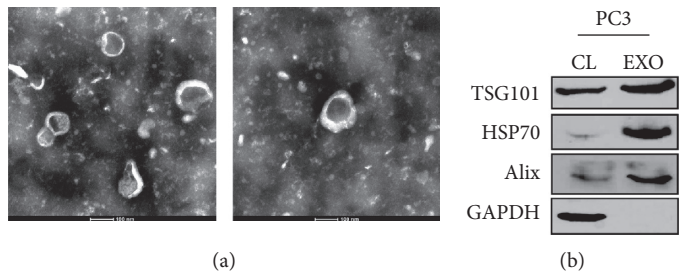

Figure 2: The characterization of isolated exosomes. (a) Exosomes isolated from PC-3 cells identified by electron microscopy. (b) Western blot analysis of exosome markers. CL, cell lysate; EXO, exosome.

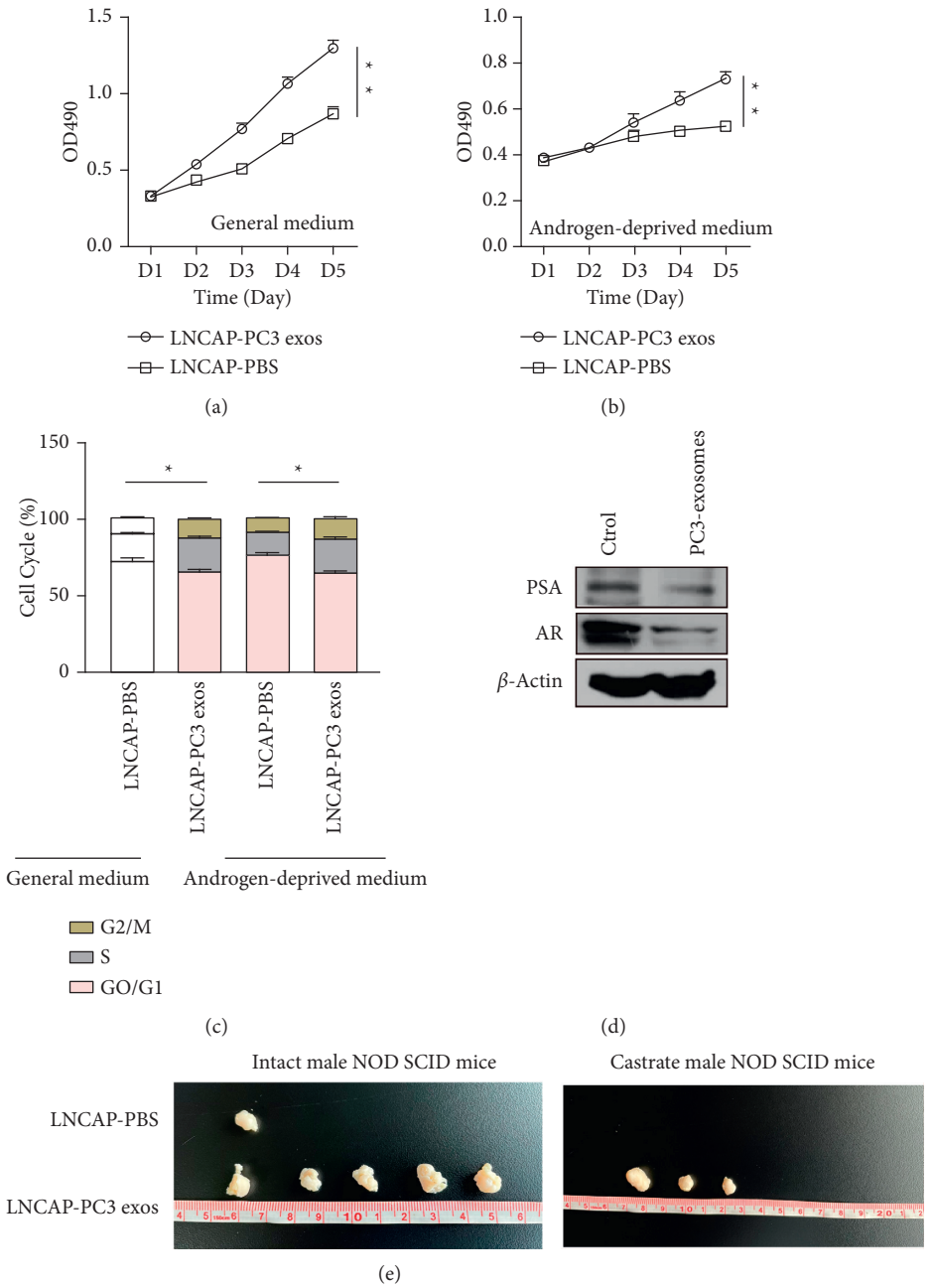

Figure 3: The role of exosomes derived from PC-3 in castration resistance of LNCaP cells. (a)-(b) Proliferation of exosomes-treated LNCaP cells and PC-3 cells in normal and androgen media evaluated with CCK-8. (c) Flow cytometry used to detect the cell cycle of LNCaP cells and PC-3 cells treated with exosomes in the conventional medium and androgen medium. (d) The expression of PSA and AR in PC-3 exocrine analysed by Western blot. (e) Tumorigenesis experiment showing that LNCaP cells cocultured with PC-3 exosomes had stronger tumorigenesis ability, especially under castration condition. $^{*}P < 0.05$, $^{**}P < 0.01$.

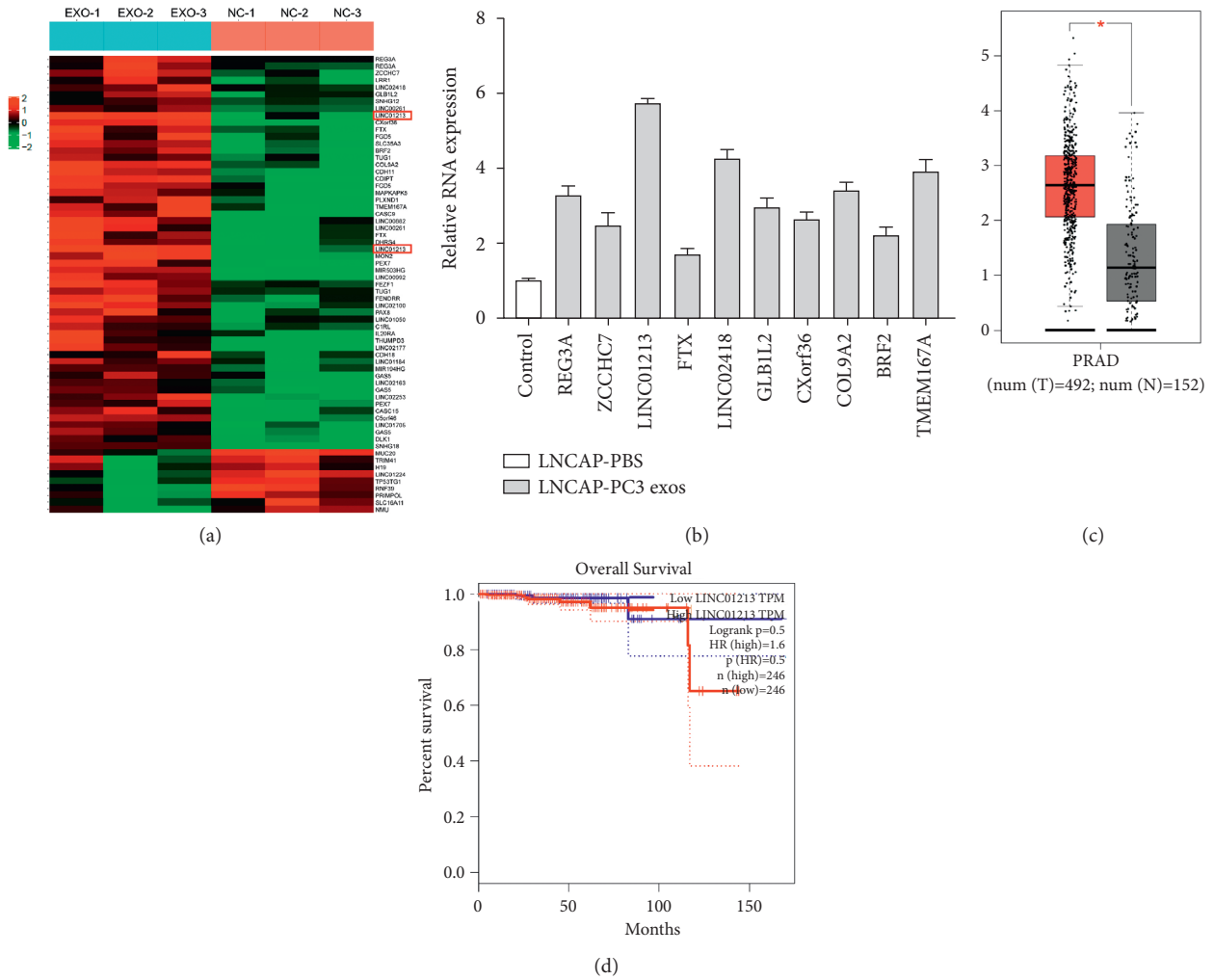

Figure 4: Exosome PC-3 upregulates LINC01213, which may play a key role in prostate cancer. (a) Heatmap showing all differentially expressed ncRNA between LNCaP cells cocultured with PC-3 exosomes and control cells. (b) qRT-PCR analysis confirmed the expression of first 10 lncRNA. (c) LINC01213 levels in 492 PRAD and 152 normal tissues on the GEPIA website. (d) Kaplan–Meier survival analysis (quartile of the two sets of criteria) performed on the prognosis of 246 patients with PAC, which is available on the GEPIA website (the criteria of the two groups were quartile).

conditions (Figure 5(a)), and they cannot proliferate in the absence of androgen (Figure 5(b)). Our results further showed that downregulating LINC01213 in LNCAP cells significantly decreased β-catenin protein levels (Figures 5(c) and 5(d)).

4. Discussion

The development of prostate cancer is a complex process, and the transition from androgen-dependent to androgen-independent is an even more complex process; sometimes, ADPC cells and AIPC cells can coexist in a certain period of time. Therefore, exosomes may play a key role for this transformation. Our results suggest that coculture with PC-3 cells in androgen medium can promote the proliferation of LNCaP cells, but how PC-3 cells endow LNCaP cells with castration resistance is still unclear.

Exosomes are 40–100 nanometre-sized vesicles that are released into the extracellular space from many cell types. In the human body, various body fluids contain these vesicles [5, 29, 30]. Exosomes affect the phenotype of recipient cells through intercellular communication. Until now, there are few studies on exosomes. In recent years, researchers have found that exosomes play multiple roles in many diseases, such as inflammation [31], and there have been many studies on exosomes in cancer, for example, the potential use of exosomes as biomarkers for the diagnosis and treatment of breast cancer [12]. Exosome-mediated miR-200b promotes the proliferation of colorectal cancer [32]. In prostate cancer, Husseini-Behesti et al. reported that prostate cancer-derived excretion promotes proliferation and migration of LNCaP cells [33]. Zhang et al. reported that in prostate cancer, exosomes can activate heme-oxygenase-I to affect the progression of prostate cancer [14]. Nevertheless, there are less reports that focus on function of exosomes in prostate cancer, especially in the transformation. In the current research, our results showed the role of exosomes not only in vitro but also in vivo. The results showed that after treated

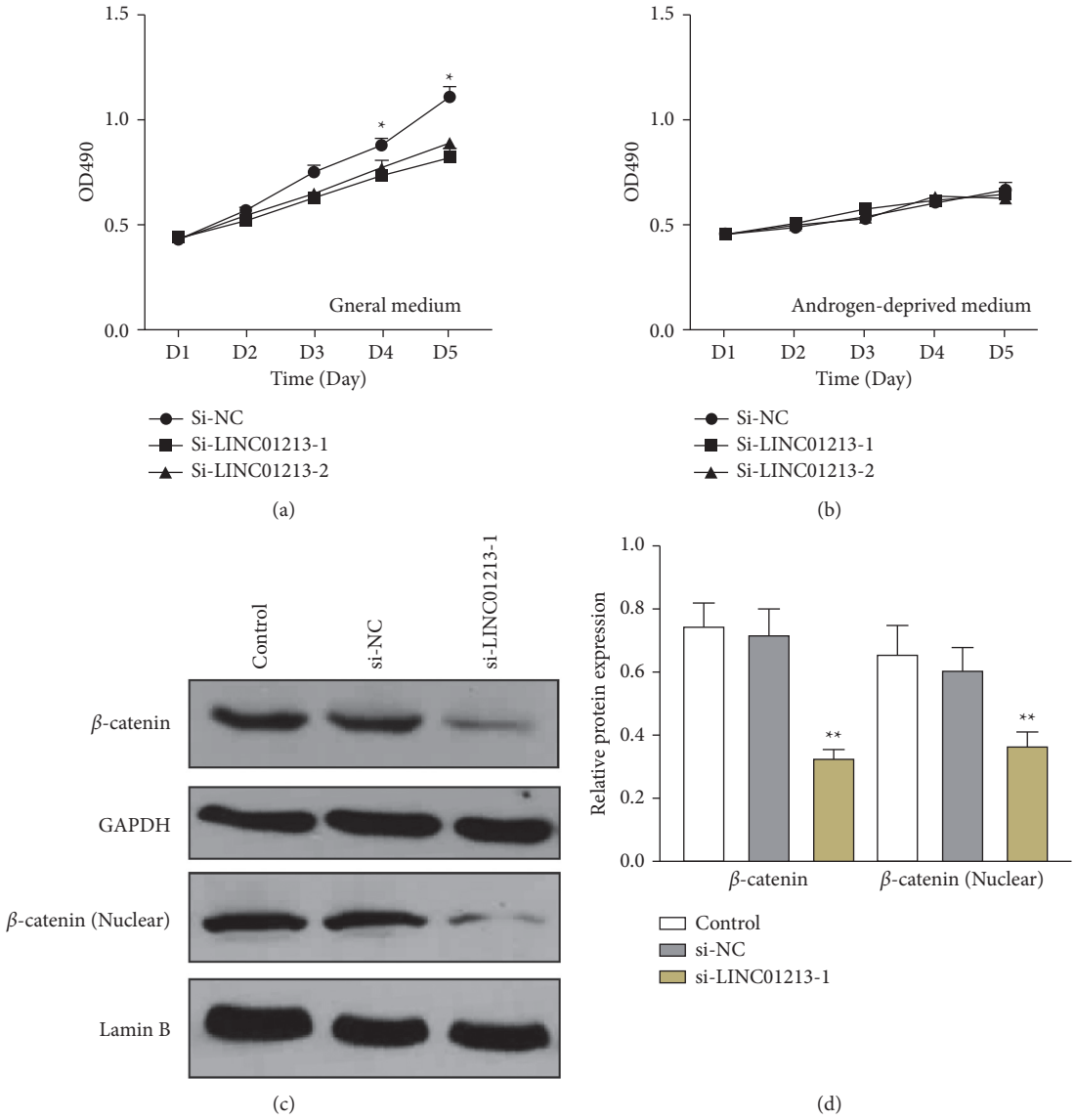

Figure 5: LINC01213 enhances androgen-independent behaviour via Wnt/β-catenin signalling. (a)-(b) Cell growth of si-NC/si-LINC01213 LNCAP cells in conventional and androgen media. (c)-(d) Protein levels of total and nuclear β-catenin in wild-type (control) LNCAP cells and cells transfected with si-NC or si-LINC01213. Data are shown as the mean ± standard deviation (SD) from three independent experiments. $^{*}P < 0.05$, $^{**}P < 0.01$.

with PC-3 exosomes, the tumorigenicity of LNCAP cells was markedly enhanced. Normal LNCAP cells could not grow under castrated conditions, but with the treatment of PC-3 exosomes, cells had tumor-forming ability. These results show that exosomes play a key role in the process of the transformation.

In order to further elucidate the mechanism of castration resistance induced by AIPC exosomes, we used RNA-seq to detect the differential expression of lncRNA in LNCaP cells before and after PC-3 exosomes treatment. The results of KEGG indicated that the differentially expressed lncRNAs are associated with the regulation and cancer-related pathways such as the Wnt/β-catenin pathway.

There are two kinds of ncRNA: short ncRNA and long noncoding RNA (lncRNAs) [34]. lncRNAs have been confirmed to participate in the regulation of tumorigenesis and its progression into tumor suppressor genes or oncogenes [35, 36], including prostate cancer [37]. LINC01213 is a long noncoding intergenic RNA, which has been reported in breast cancer [26]. We found that the expression of LINC01213 was overexpression in prostate cancer. At the same time, upregulation of LINC01213 activated the Wnt/β-catenin pathway. Taken together, our findings suggest that LINC01213 may be a novel therapeutic target for CRPC patients.

To sum up, our study reveals the existence of LINC01213 molecule in exosomes of prostate cancer cells for the first time. Our findings may help to clarify the role of tumor microenvironment in the development of CRPC and provide a new direction for the treatment of CRPC.

Data Availability

The datasets used and/or analysed during the current study are available from the corresponding author upon request.

Consent

All data published here are under consent for publication.

Conflicts of Interest

The authors declare that they have no conflicts of interest.

Authors' Contributions

Zhuifeng Guo and Xuwei Lu contributed equally to this work.

Acknowledgments

The authors thank PR Cai from the Key Laboratory of Whole-Period Monitoring and Precise Intervention of Digestive Cancer (SMHC) for excellent technical assistance. This work was supported by Minhang Hospital, Fudan University (2020MHJC08).

Supplementary Materials

Supplementary Figure 1. KEGG analysis of the differentially expressed lncRNAs. Supplementary Table 1. List of the primer sequences for PCR. (*Supplementary Materials*)

References

[1] F. Martignano, L. Rossi, A. Maugeri et al., "Urinary RNA-based biomarkers for prostate cancer detection," *Clinica Chimica Acta*, vol. 473, pp. 96–105, 2017.

[2] Z. Du, T. Sun, E. Hacisuleyman et al., "Integrative analyses reveal a long noncoding RNA-mediated sponge regulatory network in prostate cancer," *Nature Communications*, vol. 7, Article ID 10982, 2016.

[3] P. Cornford, J. Bellmunt, M. Bolla et al., "EAU-ESTRO-SIOG guidelines on prostate cancer. Part II: treatment of relapsing, metastatic, and castration-resistant prostate cancer," *European Urology*, vol. 71, no. 4, pp. 630–642, 2017.

[4] T. Lener, M. Gimona, L. Aigner et al., "Applying extracellular vesicles based therapeutics in clinical trials-an ISEV position paper," *Journal of Extracellular Vesicles*, vol. 4, Article ID 30087, 2015.

[5] M. Simons and G. Raposo, "Exosomes-vesicular carriers for intercellular communication," *Current Opinion in Cell Biology*, vol. 21, no. 4, pp. 575–581, 2009.

[6] T. Liu, D. E. Mendes, and C. E. Berkman, "Functional prostate-specific membrane antigen is enriched in exosomes from prostate cancer cells," *International Journal of Oncology*, vol. 44, no. 3, pp. 918–922, 2014.

[7] M. C. Boelens, T. J. Wu, B. Y. Nabet et al., "Exosome transfer from stromal to breast cancer cells regulates therapy resistance pathways," *Cell*, vol. 159, no. 3, pp. 499–513, 2014.

[8] M.-P. Caby, D. Lankar, C. Vincendeau-Scherrer, G. Raposo, and C. Bonnerot, "Exosomal-like vesicles are present in human blood plasma," *International Immunology*, vol. 17, no. 7, pp. 879–887, 2005.

[9] T. Pisitkun, R.-F. Shen, and M. A. Knepper, "Identification and proteomic profiling of exosomes in human urine," *Proceedings of the National Academy of Sciences*, vol. 101, no. 36, pp. 13368–13373, 2004.

[10] A. Michael, S. Bajracharya, P. Yuen et al., "Exosomes from human saliva as a source of microRNA biomarkers," *Oral Diseases*, vol. 16, no. 1, pp. 34–38, 2010.

[11] P. Kapranov, G. St Laurent, T. Raz et al., "The majority of total nuclear-encoded non-ribosomal RNA in a human cell is "dark matter" un-annotated RNA," *BMC Biology*, vol. 8, no. 1, p. 149, 2010.

[12] Y. Jia, Y. Chen, Q. Wang et al., "Exosome: emerging biomarker in breast cancer," *Oncotarget*, vol. 8, no. 25, pp. 41717–41733, 2017.

[13] M. Işın, E. Uysaler, E. Özgür et al., "Exosomal lncRNA-p21 levels may help to distinguish prostate cancer from benign disease," *Frontiers in Genetics*, vol. 6, p. 168, 2015.

[14] Y. Zhang, B. Chen, N. Xu et al., "Exosomes promote the transition of androgen-dependent prostate cancer cells into androgen-independent manner through up-regulating the Heme oxygenase-1," *International Journal of Nanomedicine*, vol. 16, pp. 315–327, 2021.

[15] G. Yang, X. Lu, and L. Yuan, "LncRNA: a link between RNA and cancer," *Biochimica et Biophysica Acta (BBA)-Gene Regulatory Mechanisms*, vol. 1839, no. 11, pp. 1097–1109, 2014.

[16] J. Jarroux, A. Morillon, and M. Pinskaya, "History, discovery, and classification of lncRNAs," *Advances in Experimental Medicine & Biology*, vol. 1008, pp. 1–46, 2017.

[17] V. S. Akhade, D. Pal, and C. Kanduri, "Long noncoding RNA: genome organization and mechanism of action," *Advances in Experimental Medicine & Biology*, vol. 1008, pp. 47–74, 2017.

[18] S. Li, J. Hao, Y. Hong, J. Mai, and W. Huang, "Long noncoding RNA NEAT1 promotes the proliferation, migration, and metastasis of human breast-cancer cells by inhibiting miR-146b-5p expression," *Cancer Management and Research*, vol. 12, pp. 6091–6101, 2020.

[19] Y. Pan, L. Liu, Y. Cheng, J. Yu, and Y. Feng, "Amplified LncRNA PVT1 promotes lung cancer proliferation and metastasis by facilitating VEGFC expression," *Biochemistry and Cell Biology*, vol. 98, no. 6, pp. 676–682, 2020.

[20] Q. Wu, J. Ma, J. Wei, W. Meng, Y. Wang, and M. Shi, "lncRNA SNHG11 promotes gastric cancer progression by activating the wnt/β-catenin pathway and oncogenic autophagy," *Molecular Therapy*, vol. 29, no. 3, pp. 1258–1278, 2021.

[21] J. B. de Kok, G. W. Verhaegh, R. W. Roelofs et al., "DD3(PCA3), a very sensitive and specific marker to detect prostate tumors," *Cancer Research*, vol. 62, no. 9, pp. 2695–2698, 2002.

[22] D. A. Sartori and D. W. Chan, "Biomarkers in prostate cancer," *Current Opinion in Oncology*, vol. 26, no. 3, pp. 259–264, 2014.

[23] J. R. Prensner, M. K. Iyer, A. Sahu et al., "The long noncoding RNA SChLAP1 promotes aggressive prostate cancer and antagonizes the SWI/SNF complex," *Nature Genetics*, vol. 45, no. 11, pp. 1392–1398, 2013.

[24] L. Yang, C. Lin, C. Jin et al., "lncRNA-dependent mechanisms of androgen-receptor-regulated gene activation programs," *Nature*, vol. 500, no. 7464, pp. 598–602, 2013.

[25] H. Yan, D. Tan, P. Xie, Z. Liu, and X. Li, "Multiple lncRNAs affect the incidence and development of melanoma," *Zhong Nan Da Xue Xue Bao Yi Xue Ban*, vol. 42, no. 2, pp. 134–138, 2017.

[26] M. Porsch, E. Özdemir, M. Wisniewski et al., "Time resolved gene expression analysis during tamoxifen adaption of MCF-7

cells identifies long non-coding RNAs with prognostic impact," *RNA Biology*, vol. 16, no. 5, pp. 661–674, 2019.

[27] A.-L. Liang, S.-L. Du, B. Zhang et al., "Screening miRNAs associated with resistance gemcitabine from exosomes in A549 lung cancer cells," *Cancer Management and Research*, vol. 11, pp. 6311–6321, 2019.

[28] J. R. Prensner, M. K. Iyer, O. A. Balbin et al., "Transcriptome sequencing across a prostate cancer cohort identifies PCAT-1, an unannotated lincRNA implicated in disease progression," *Nature Biotechnology*, vol. 29, no. 8, pp. 742–749, 2011.

[29] S. Mathivanan, H. Ji, and R. J. Simpson, "Exosomes: extracellular organelles important in intercellular communication," *Journal of Proteomics*, vol. 73, no. 10, pp. 1907–1920, 2010.

[30] J. C. Gross, V. Chaudhary, K. Bartscherer, and M. Boutros, "Active Wnt proteins are secreted on exosomes," *Nature Cell Biology*, vol. 14, no. 10, pp. 1036–1045, 2012.

[31] H. Zhang, L. Wang, C. Li et al., "Exosome-induced regulation in inflammatory bowel disease," *Frontiers in Immunology*, vol. 10, Article ID 1464, 2019.

[32] Z. Zhang, T. Xing, Y. Chen, and J. Xiao, "Exosome-mediated miR-200b promotes colorectal cancer proliferation upon TGF-β1 exposure," *Biomedicine & Pharmacotherapy*, vol. 106, pp. 1135–1143, 2018.

[33] E. Hosseini-Beheshti, W. Choi, L.-B. Weiswald et al., "Exosomes confer pro-survival signals to alter the phenotype of prostate cells in their surrounding environment," *Oncotarget*, vol. 7, no. 12, pp. 14639–14658, 2016.

[34] F. Kopp and J. T. Mendell, "Functional classification and experimental dissection of long noncoding RNAs," *Cell*, vol. 172, no. 3, pp. 393–407, 2018.

[35] H. Cai, Y. Yu, X. Ni et al., "LncRNA LINC00998 inhibits the malignant glioma phenotype via the CBX3-mediated c-Met/Akt/mTOR axis," *Cell Death & Disease*, vol. 11, no. 12, Article ID 1032, 2020.

[36] L. Xu, L. Huan, T. Guo et al., "LncRNA SNHG11 facilitates tumor metastasis by interacting with and stabilizing HIF-1α," *Oncogene*, vol. 39, no. 46, pp. 7005–7018, 2020.

[37] S. Wen, Y. Wei, C. Zen, W. Xiong, Y. Niu, and Y. Zhao, "Long non-coding RNA NEAT1 promotes bone metastasis of prostate cancer through N6-methyladenosine," *Molecular Cancer*, vol. 19, no. 1, p. 171, 2020.

Hindawi
Journal of Oncology
Volume 2022, Article ID 4031403, 11 pages
https://doi.org/10.1155/2022/4031403

Research Article

Circular RNA hsa_circ_0004543 Aggravates Cervical Cancer Development by Sponging MicroRNA hsa-miR-217 to Upregulate Hypoxia-Inducible Factor

Jun Liu,[1] **Yingqiao Liu**,[2] **Yang Zhang**,[1] **Jing Zheng**,[1] **Shuzhen Wang**,[1] **and Guangming Cao**[1]

[1]*Department of Obstetrics and Gynecology, Beijing Chao-Yang Hospital, Capital Medical University, Beijing, China*
[2]*Department of Obstetrics and Gynecology, Lu-He Teaching Hospital, Capital Medical University, Beijing, China*

Correspondence should be addressed to Shuzhen Wang; shuzhenwangw@163.com and Guangming Cao; eaunhk@163.com

Received 1 December 2021; Revised 29 December 2021; Accepted 10 January 2022; Published 9 March 2022

Academic Editor: Guo Chen

Cervical cancer (CC) is the 4th principal source of cancer death in females with 604,000 new patients and 342,000 deaths in 2020 worldwide. It has been extensively shown that circRNAs are involved in regulating CC development. Nevertheless, the function and mechanisms of hsa_circ_0004543 in regulating CC need to be clearly elucidated. Herein, hsa_circ_0004543 expressions were compared between 40 paired paracancerous and cancerous specimens from CC patients and between 6 CC cell lines and a normal human cervical epithelial cell line based on qRT-PCR. Potential complementary binding sites between hsa-miR-217 and hsa_circ_0004543 were predicted using the interactome, while binding sites for the hypoxia-inducible factor-1a (HIF-1a) were predicted by TargetScan. The function and mechanism of hsa_circ_0004543 in the development of CC were estimated by silencing hsa_circ_0004543 with/without hsa-miR-217 or HIF-1a overexpression. The association between gene expressions was evaluated with Pearson's correlation analysis. Molecular mechanisms were explored by ribonucleic acid (RNA) pulldown, dual-luciferase activity, and rescue experimental assays. Our results revealed that the hsa_circ_0004543 expression was considerably increased in CC tissues and cells. Its silencing repressed proliferation and metastasis, while it increased apoptosis of CC cells. The investigation of the mechanism showed that hsa-miR-217 silencing or HIF-1a overexpression rescued hsa_circ_0004543, and silencing inhibited malignant phenotypes of CC cells. hsa_circ_0004543 upregulated the HIF-1α expression by sponging hsa-miR-217 in CC development. Therefore, the hsa_circ_0004543 functioned as a competing endogenous RNA (ceRNA) of hsa-miR-217 to increase CC oncogenesis and metastasis by the upregulation of the HIF-1α expression. Consequently, targeting the hsa_-circ_0004543/hsa-miR-217/HIF-1α axis might be a potential treatment approach for CC.

1. Introduction

Cancer is now commonly acknowledged as a worldwide hazard to international development [1]. The latest United Nations high-level meeting on noncommunicable diseases (NCDs) confirmed this statement and further emphasized the slow development in meeting the 2011 Political Declaration on NCD prevention and control [1]. The lack of sufficient molecular mechanisms to detect new biomarkers for early diagnosis, antidrug development, and clinical outcome prognosis has been recognized as the main problems in reaching these goals. As a result, it is of great significance to discover novel biomarkers in cancers.

As the 4th most commonly diagnosed malignancy, cervical cancer (CC) is the 4th principal source of female cancer deaths, with 604,000 new patients and 342,000 deaths in 2020 worldwide [2, 3].

CC is commonly asymptomatic and may be diagnosed during pelvic examination or routine screening in the early stages, with the symptoms of abnormal or postcoital vaginal bleeding [4]. The presence of large amounts of smelly vaginal discharge may also be a symptom [4, 5]. The triad of flank pain, lower-limb edema, and sciatica indicates pelvic sidewall invasion. The vaginal passage of urine is a bladder invasion symptom of vesicovaginal fistula, whereas the vaginal passage of feces is a rectum invasion symptom of

rectovaginal fistula. Race, age, histological type, grade, stage, location, lymph-node involvement, treatment status, and tumor volume are all the prognostic factors for locally advanced cervical cancers [4–6]. Surgery combined with chemoradiation or chemotherapy is the main management of CC in its early stages.

Despite the fact that diagnostic and therapeutic advances of surgical treatment with concurrent chemoradiotherapy have improved the overall five-year survival to about 70% in advanced CC patients, the metastasis and recurrence of CC still result in a quite poor prognosis with a 5-year overall survival <30% in the majority of regions and countries owing to restricted clinical strategies [3]. Furthermore, almost 30% of patients die from disease relapse or development. Hence, to explore the molecular mechanisms involved in the development and progression of CC [7].

As a newly identified noncoding RNA (ncRNA) class, circular RNAs (circRNAs) are preserved throughout species and are more stable than linear RNAs [8–10]. Increasing evidence implies that circRNAs have the crosstalk capacity with RNA binding proteins to act as sponges of miRNA for regulating downstream gene expression [11]. circRNAs have been reported to be related to CC progression through various mechanisms, where the most important one is serving as a microRNA (miRNA) sponge [12–15]. Consequently, it is essential to find out the abnormal circRNAs and the involved new molecular mechanisms to develop the therapeutic targets for CC management.

hsa_circ_0004543 was significantly increased in CC patient tissues based on circRNA microarray analysis [12]. However, the specific role and related molecular mechanism of hsa_circ_0004543 in CC oncogenesis and metastasis need to be explored further.

Hypoxia-inducible factor-1 α (HIF-1α) is a key responser adapted to cancer hypoxia. HIF-1α signaling activated in hypoxia conditions contributes to cell biology associated with oncogenesis, a key issue restraining the chemotherapy efficiency in various cancer treatment including CC [16, 17]. As a main property of CC [18, 19], hypoxia regulates all steps of cancer metastasis from the initial step to eventually colonizing the target organs [20, 21]. Increased intratumor hypoxia stabilizes and activates HIF-1α, which may activate many metastatic sequences to promote local and distant site cancer recurrence [22, 23]. As a result, targeting hypoxia via diverse methods may decrease extensive cancer-intrinsic metastasis [21, 24].

Moreover, miR-217/HIF-1α/AXL signaling has been reported to be involved in lncRNA-HOTAIR-promoted renal cell carcinoma carcinogenesis, which provides a new target for the diagnosis and treatment of renal cell carcinoma [25].

Therefore, we speculated that hsa_circ_0004543 may stimulate CC development by hsa-miR-217/HIF-1α signaling. Herein, we intend to explore the function and molecular mechanisms of hsa_circ_0004543 in CC oncogenesis and development, thus providing a potential biomarker for better management of CC. After analyzing the expressions of hsa_circ_0004543, hsa-miR-217, and HIF-1α in 40 paired CC and paracancerous tissues with qRT-PCR, which revealed that hsa_circ_0004543 and HIF-1α were increased, while hsa-miR-217 was decreased in tissues of CC patients; hsa_circ_0004543 was further found to increase HIF-1α expression via sponging hsa-miR-217. Thus, this promoted CC oncogenesis and development. These findings may enable the progress of clinical management strategies against CC.

2. Materials and Methods

2.1. Reagents. The following reagents and instruments were used in this study: dual-luciferase reporter assay system (Promega Madison, US), fetal bovine serum (FBS), Dulbecco's modified eagle medium (DMEM) cell culture medium (Gibco, Rockford, US), radio immunoprecipitation assay (RIPA) buffer (Beyotime, Shanghai, China), Matrigel (BD, New Jersey, US), cell counting kit-8 (CCK8) assay kit (Dojindo Corp, Kyushu, Japan), Gene Mutation Kit and SYBR Green Premix Ex Taq™ II (TaKaRa, Dalian, China), Pierce™ Magnetic RNA-Protein Pull-Down kit, Lipofectamine 3000, M-MLV reverse transcriptase kit, miRNA reverse transcriptase kit, TRIzol reagent, and SuperSignal West Dura Extended Duration Substrate (Thermo Fisher Scientific, Inc., Waltham, US). Antibodies were purchased from Santa Cruz (Dallas, US). Propidium iodide and APC-Annexin V were purchased form Sigma-Aldrich (St. Louis, USA). The PsiCHECK™-2 vector was purchased from Promega (Madison, US).

2.2. Patient Specimens, Consents, and Ethics. We collected the cancerous and paracancerous specimens from 40 CC patients during surgical treatment and stored them at -80°C. All patients provided written informed consent. All experimental procedures were approved by the Ethics Committee of the Beijing Chao-Yang Hospital at Capital Medical University.

2.3. Cells and Culture. The Committee on Type Culture Collection of the Chinese Academy of Sciences (Shanghai, China) provided all CC and normal human cervical epithelial (End1/E6E7) cells, which were routinely cultured in DMEM medium containing FBS (10%), penicillin (100 IU/mL), and streptomycin (100 mg/mL) [26].

2.4. Cell Viability Analysis. Cell viability was evaluated using the CCK-8 kit following the manufacturer's guidelines. In brief, 10 μL of CCK-8 reagent was applied to each well of cells cultured in a 96-well plate with an original 2000 cells/well and incubated in the dark for 2 h at 37°C. The optional density (OD) value was determined at a wavelength of 450 nm with a microplate reader (Bio-Rad, Hercules) [27].

2.5. Colony Proliferation Evaluation. Cells were seeded in 6 well plates with 1000 cells/well and incubated for 10 days at 37°C to form colonies, followed by fixation in 4% paraformaldehyde for 10 min and staining in 0.5% crystal violet for 5 min. Colony numbers were determined using the software

ImageJ (National Institutes of Health, Bethesda, MD, USA) and images were acquired with a light microscope (Olympus, Japan) [27].

2.6. Apoptosis Evaluation. Cells washed with precold phosphate buffer solution were fixed and incubated for 15 min with propidium iodide and APC-Annexin V, respectively, in dark conditions at room temperature. Apoptotic cells were then detected using a BD FACSCalibur flow cytometer. Apoptotic rates were determined using Cell Quest software (BDIS, San Jose, USA) [27].

2.7. Invasion and Migration Evaluation. A transwell (24-well, Corning Costar) was applied to evaluate cell invasion (with Matrigel coating) and migration (without Matrigel coating) abilities. In brief, 600 μL of 10% FBS-supplied culture medium was loaded in the lower chamber, and 3×10^5 cells in 200 μl of serum-free medium were loaded in the upper chamber. After being cultured for 24 h (migration assay) or 48 h (invasion assay), the commonly used time points for cell migration and invasion assays to avoid the influence of cell proliferation, the migrated or invaded cells were fixed and stained [27].

2.8. Potential Binding Gene Prediction. Potential hsa_circ_0004543 sponged miRNAs were predicted with the online tool Circular RNA Interactome (https://circinteractome.nia.nih.gov/) [28]. Potential mRNAs binding to hsa-miR-217 were predicted with the TargetScan online tool (http://www.targetscan.org/) [29].

2.9. qRT-PCR Assay. Sangon (Shanghai, China) synthesized the primers. Cells were lysed in Trizol to isolate the total RNA according to the protocols. RNAs were reversely transcribed using the M-MLV reverse transcriptase kit or miRNA reverse transcriptase kit following the accompanying instructions. SYBR Green Premix Ex Taq™ II was mixed with cDNA and specific primers for qRT-PCR assay on a CFX96 TM real-time PCR detection system (Bio-Rad Laboratories, Hercules, USA). Relative gene expressions were calculated using the $2^{-\Delta\Delta Ct}$ method with GAPDH as an internal control for mRNAs and circRNAs, and U6 as an internal control for miRNAs [27, 29].

2.10. Dual-Luciferase Evaluation. Cells cotransfected with hsa-miR-217 mimics or negative control (miR-NC), psiCHECK-2/hsa_circ_0004543 3′-UTR (WT), or psiCHECK-2/hsa_circ_0004543 3′-UTR mutated (MT) plasmid were used for hsa_circ_0004543 activity analysis, while cotransfected with psiCHECK-2/HIF-1A 3′-UTR (WT) or psiCHECK-2/HIF-1A 3′-UTR mutated (MT) plasmid were used for HIF-1A activity analysis using Lipofectamine 3000. The dual-luciferase reporter assay kit was then used following the manufacturer's procedures [26, 29].

2.11. RNA Pull-Down Evaluation. GenePharma (Shanghai, China) provided biotin-labeled hsa_circ_0004543 probes (hsa_circ_0004543) and negative controls (oligoes). PierceTM Magnetic RNA-Protein Pull-Down kit was used for RNA pull-down assay. Briefly, the miRNA binding to hsa_circ_0004543 was determined by qRT-PCR after it was enriched by incubating streptavidin agarose magnetic beads with biotin-labeled hsa_circ_0004543 probes or negative control first, and then with the cell lysates from SiHa or C-4I cells [30].

2.12. Western Blotting Investigation. Total protein was extracted with RIPA lysis buffer. Proteins (25 μg) were used for target protein expression determination based on separation on an 8% SDS-PAGE gel, followed by the transfer on a polyvinylidene fluoride (PVDF) membrane, incubating at 4°C overnight in primary and secondary antibodies for 1 h at RT, and developing with SuperSignal West Dura Extended Duration Substrate after it was washed three times with TBST [26, 27].

2.13. Statistical Assay. SPSS 19.0 (IBM, SPSS, Chicago, US) was used. Tests were conducted with one-way analysis of variance followed by Tukey's post hoc test for multiple groups and Student's *t*-test for two groups. Associations between gene expressions were evaluated with Pearson's correlation assay. $P < 0.05$ was statistically significant.

3. Results

The purpose of the current work was to explore the role and the ceRNA mechanism of hsa_circ_0004543 in regulating CC oncogenesis and metastasis. Based on the bioinformatics analysis and literature review, we hypothesized that hsa_circ_0004543 expression was upregulated in CC cells and tissues, which contributed to increased CC cell viability, colony proliferation, migration, and invasion. It also inhibited cell apoptosis by regulating the hsa-miR-217/HIF-1α axis. Hsa_circ_0004543 levels in human CC tissues and cells were determined with qRT-PCR. Direct binding between hsa-miR-217 and hsa_circ_0004543 or HIF-1a was predicted by the interactome or TargetScan and was verified with a dual-luciferase reporter gene assay with or without RNA pull-down. Aggressive phenotypes of CC cells including cell viability, colony proliferation, apoptosis, migration, and invasion were detected with the CCK-8 assay, colony formation assay, flow cytometry assay, and transwell assay, respectively. The mechanism of hsa_circ_0004543 in CC development was further assessed by silencing hsa_circ_0004543 with/without hsa-miR-217 silencing or HIF-1a overexpression. Associations between gene expressions were evaluated with Pearson's correlation analysis.

3.1. hsa_circ_0004543 Is Upregulated in CC Tissues and Cells. To explore the function of hsa_circ_0004543 in CC oncogenesis and progress, we first collected paired CC and self-matched negative control (NC) paracancerous tissues from

40 CC patients, followed by the analysis of the hsa_circ_0004543 expression by qRT-PCR. The data proved that hsa_circ_0004543 expression was extremely higher in CC tissues versus NC tissues (Figure 1(a)). We also analyzed the hsa_circ_0004543 level in CC cells, and the hsa_circ_0004543 level was significantly higher in CC cells (SiHa, CaSki, C-4I, C-33A, SW756, and HeLa) versus End1/E6E7 cells (Figure 1(b)).

3.2. hsa_circ_0004543 Stimulates CC Growth and Metastasis. To explore the effects of hsa_circ_0004543 on CC malignant phenotypes, silencing RNA (siRNA) specifically targeting hsa_circ_0004543 (si-hsa_circ_0004543) was respectively transfected to two CC cells (SiHa and C-4I) and yielded the highest hsa_circ_0004543 expression for hsa_circ_0004543 knockdown. The results showed that transfecting si-hsa_circ_0004543 in SiHa and C-4I cells produced a significantly reduced hsa_circ_0004543 expression (Figure 2(a)). Viabilities of SiHa and C-4I cells at 0, 24, 48, and 72 h after transfecting si-NC or si-hsa_circ_0004543 were determined with the CCK-8 test. This revealed that hsa_circ_0004543 silencing significantly decreased the viability (OD value) of both SiHa and C-4I cells (Figure 2(b)). The colony proliferation abilities of SiHa and C-4I cells were evaluated with the colony formation assay, which revealed that hsa_circ_0004543 silencing significantly repressed the colony proliferation abilities of both the SiHa and C-4I cells (Figure 2(c)). In the meantime, flow cytometric assays confirmed that apoptosis rates were considerably amplified in SiHa and C-4I cells after hsa_circ_0004543 silencing (Figure 2(d)). Moreover, invasion and migration capabilities of SiHa and C-4I cells were evaluated with a transwell assay, which indicated that hsa_circ_0004543 knockdown significantly repressed CC cell migration (Figure 2(e)) and invasiveness (Figure 2(f)) capabilities.

3.3. hsa_circ_0004543 Sponges hsa-miR-217 in CC Cells to Increase HIF-1α Expression. To explore the molecular mechanism of hsa_circ_0004543 in CC carcinogenesis and development, the potential miRNAs which had complementary binding sites with hsa_circ_0004543 were first predicted based on the use of the Circular RNA Interactome (https://circinteractome.nia.nih.gov/) (Figure 3(a)). This analysis was followed in SiHa and C-4I cells by dual-luciferase reporter activity analysis and RNA pull-down assays, respectively. The luciferase activity of the wild-type hsa_circ_0004543 3′UTR reporter gene in SiHa and C-4I cells was significantly inhibited when hsa-miR-217 was overexpressed with mimics, while the inhibited luciferase activity of the hsa_circ_0004543 3′UTR reporter gene was rescued when the predicted binding sites of hsa_circ_0004543 3′UTR with hsa-miR-217 was mutated (Figure 3(b)). The interaction between hsa_circ_0004543 and hsa-miR-217 in SiHa and C-4I cells was further confirmed by the RNA pulldown, which showed that the hsa_circ_0004543 probe (hsa_circ_0004543) could pulldown more hsa-miR-217 than control oligoes (Figure 3(c)). Moreover, the relationship between hsa_circ_0004543 and hsa-miR-217 was explored based on the determination of the hsa-miR-217 level in CC cells and tissues by qRT-PCR. The data confirmed that the hsa-miR-217 expression was meaningfully decreased in CC cells (SiHa, CaSki, C-4I, C-33A, SW756, and HeLa) compared to normal human cervical epithelial cells (Figure 3(d)) and was considerably declined in CC tissues compared to paired paracancerous normal tissues from 40 local CC patients (Figure 3(e)). Meanwhile, significantly upregulated hsa-miR-217 expression was found in SiHa and C-4I cells after the hsa_circ_0004543 was silenced (Figure 3(f)). Associations between hsa_circ_0004543 and hsa-miR-217 expressions were evaluated further using Pearson's correlation coefficient, which showed that hsa_circ_0004543 level was significantly negatively related to the hsa-miR-217 level in CC tissues from 40 CC patients (Figure 3(g)).

To reveal the ceRNA network trigger by hsa_circ_0004543, potential mRNAs which had complementary binding sites with hsa-miR-217 were first predicted with the online tool TargetScan (http://www.targetscan.org/) (Figure 4(a)), followed by the dual-luciferase reporter activity assay in SiHa and C-4I cells, respectively. The luciferase activity of the wild-type HIF-1a 3′UTR reporter gene was considerably inhibited when hsa-miR-217 was overexpressed using mimics in SiHa and C-4I cells, while inhibited luciferase activity of the HIF-1a 3′UTR reporter gene was rescued when predicted binding sites of HIF-1a 3′UTR with hsa-miR-217 were mutated (Figure 4(b)). Moreover, we investigated whether hsa_circ_0004543 sponges hsa-miR-217 to control HIF-1α level, and HIF-1a expression in CC cells was first detected with qRT-PCR. The data showed that hsa_circ_0004543 silencing in CC cells inhibited HIF-1α expression considerably at both mRNA (Figure 4(c)) and protein (Figure 4(d)) levels, which was partly reversed by the cotransfection of the hsa-miR-217 inhibitor (inh-hsa-miR-217) (Figures 4(c) and 4(d)). Furthermore, the expression of HIF-1a was measured by qRT-PCR in 40 CC patient tissues, which showed that HIF-1a expression was significantly amplified in CC tissues compared with paracancerous normal tissues (Figure 4(c)). Moreover, the association between hsa_circ_0004543 and HIF-1a expressions in 40 CC patient tissues was analyzed using Pearson's correlation analysis. This revealed that the hsa_circ_0004543 level was considerably positively related to HIF-1a expression (Figure 4(d)). These findings suggested that hsa_circ_0004543 stimulated CC oncogenesis and development via sponging hsa-miR-217 induced the upregulation of HIF-1α.

3.4. The hsa-miR-217/hsa-miR-217/HIF-1α Axis Promotes CC Cell Malignant Phenotypes. After being cotransfected using si-NC, si-hsa_circ_0004543, si-hsa_circ_0004543 + inh-hsa-miR-217, or si-hsa_circ_0004543+HIF-1a, viabilities of SiHa and C-4I cells were first determined based on the use of the CCK-8 assay, and the data validated that hsa_circ_0004543 silencing time-dependently decreased OD value (0–72 h) and was partly rescued by hsa-miR-217 silencing or HIF-1a overexpression (Figure 5(a)). Colony proliferation abilities of SiHa and C-4I cells after hsa_circ_0004543 silencing with/

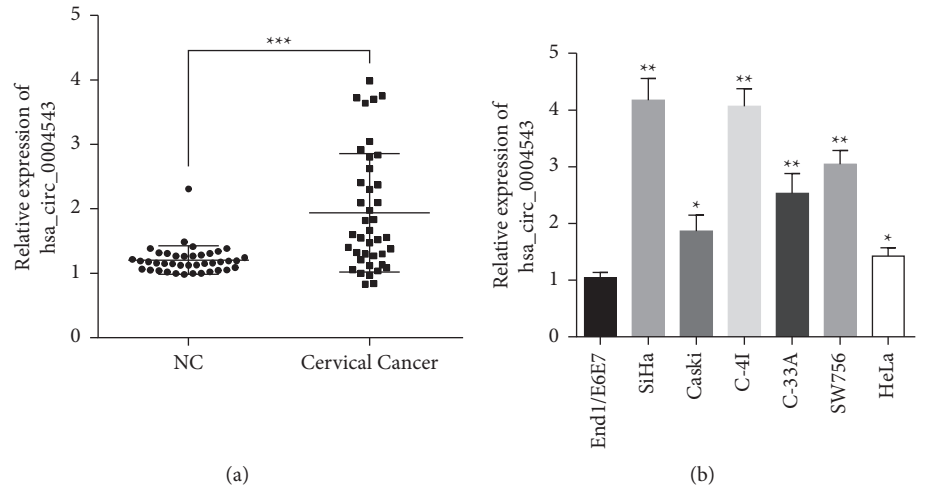

Figure 1: hsa_circ_0004543 was amplified in cervical cancer tissue and cells. hsa_circ_0004543 expression was determined with quantitative reverse transcriptase polymerase chain reaction (qRT-PCR). (a) The hsa_circ_0004543 expression was considerably upregulated in CC patient tissues compared with paired paracancerous normal tissues (NC) ($n = 40$). (b) The hsa_circ_0004543 expression was considerably upregulated in CC cells (SiHa, CaSki, C-4I, C-33A, SW756, and HeLa) compared with End1/E6E7 (normal human cervical epithelial cells) ($^{*}p < 0.05$, $^{**}p < 0.01$, and $^{***}p < 0.001$).

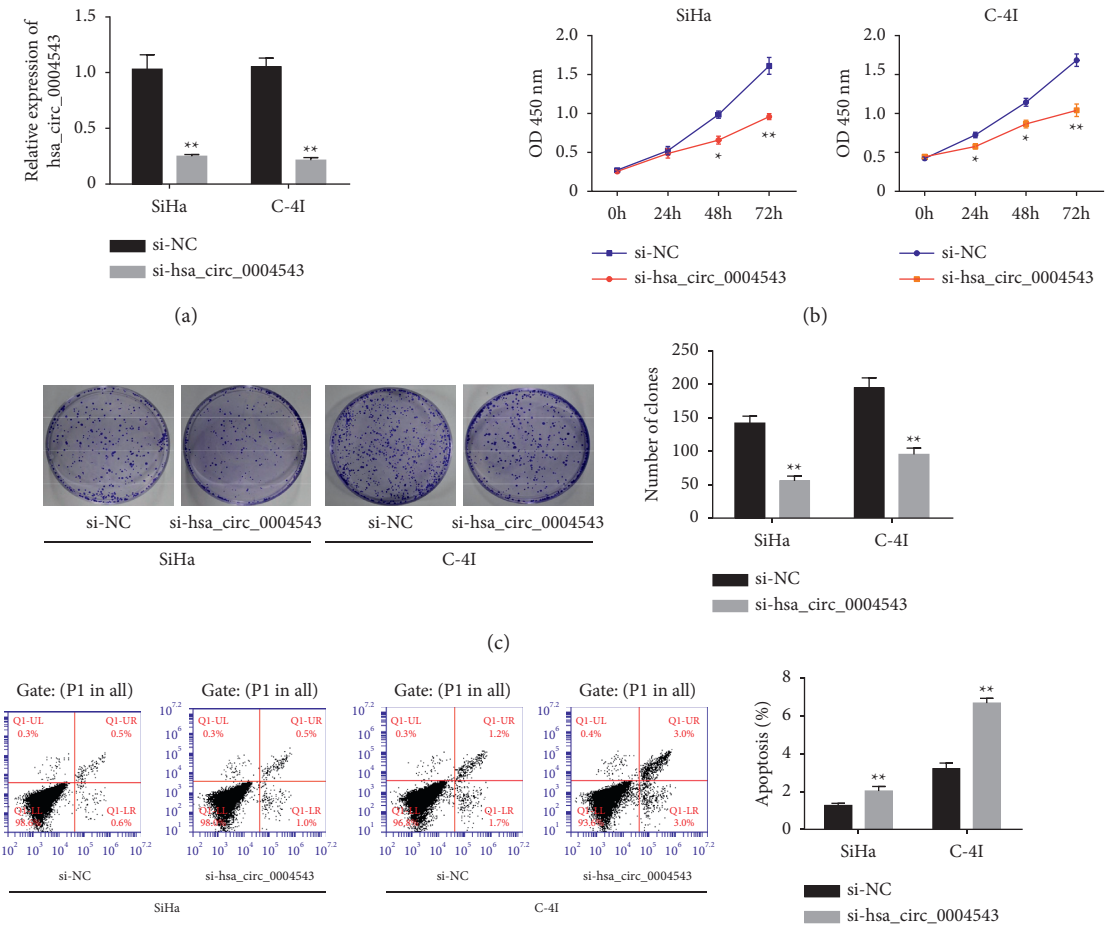

Figure 2: Continued.

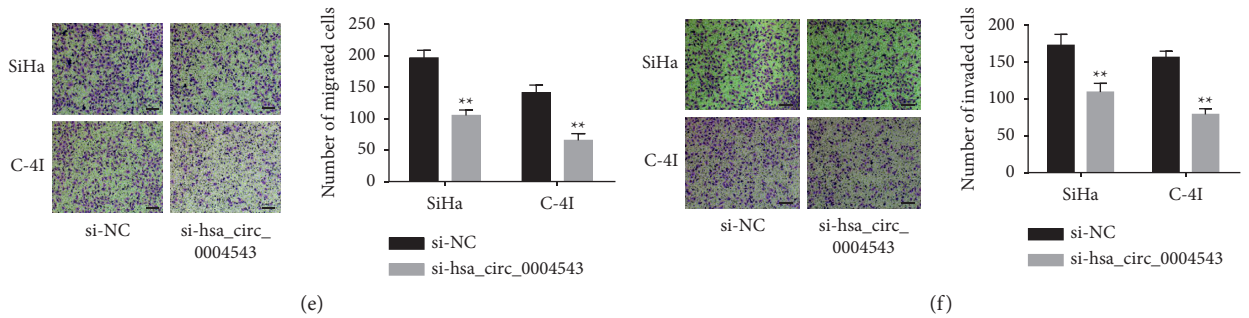

Figure 2: hsa_circ_0004543 silencing inhibited viability, colony formation, migration and invasion, and prompted apoptosis in CC cells. (a) The qRT-PCR assay validated successful hsa_circ_0004543 silencing with si-hsa_circ_0004543 in SiHa and C-4I cells. (b) Viability, (c) colony formation ability, (d) apoptosis, (e) migration capacity, and (f) invasion capacity of SiHa and C-4I cells after they were transfected with si-NC or si-hsa_circ_0004543 ($^{*}p < 0.05$ and $^{**}p < 0.01$).

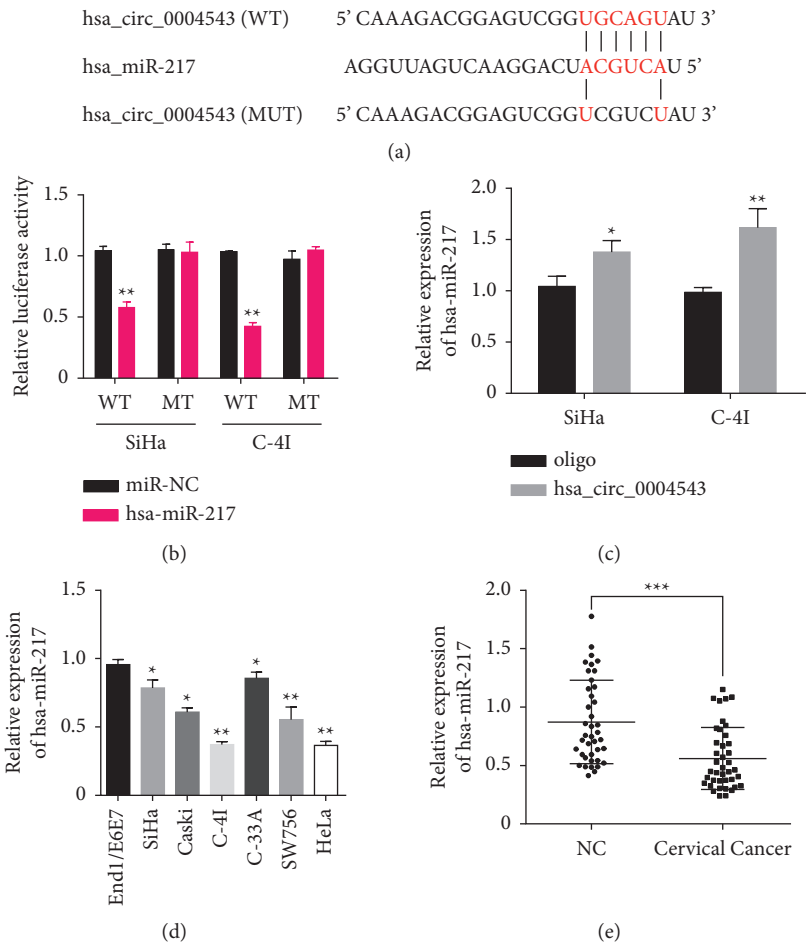

Figure 3: Continued.

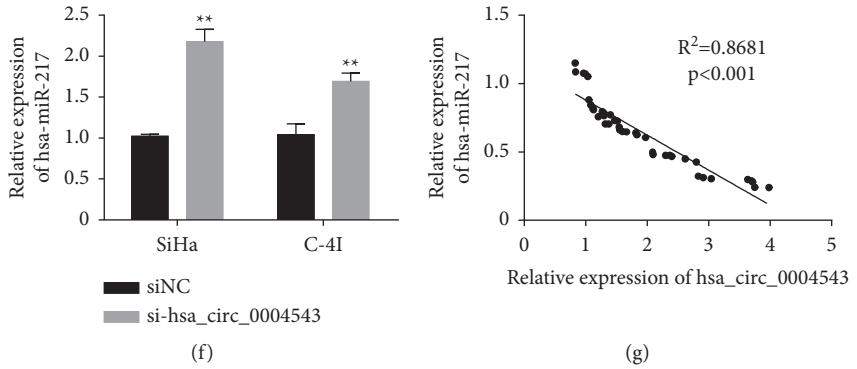

Figure 3: hsa_circ_0004543 was identified to serve as a sponge for hsa-miR-217 in CC cells. (a) Diagram of potential binding sites between hsa-miR-217 and hsa_circ_0004543 (https://circinteractome.nia.nih.gov/) with mutation sites for specific binding assay. (b) Dual-luciferase reporter activity of SiHa and C-4I cells cotransfected by hsa_circ_0004543 3′UTR wild-type or mutated reporter with or without hsa-miR-217 mimics. (c) hsa-miR-217 was pulled down and enriched with biotin-labeled hsa-miR-217 specific probe in CC cell lysates. (d) hsa-miR-217 expression in human CC cells (SiHa, CaSki, C-4I, C-33A, SW756, and HeLa) was significantly downregulated compared with normal human cervical epithelial cells (End1/E6E7). (e) hsa-miR-217 expressions in paired CC and paracancerous (NC) tissues from 40 local CC patients detected by qRT-PCR. (f) hsa-miR-217 expressions in hsa_circ_0004543 silenced SiHa and C-4I cells determined with qRT-PCR. (g) Pearson's correlation analysis of associations between hsa-miR-217 and hsa_circ_0004543 expressions in CC patient tissues ($n = 40$) ($^{*}p < 0.05$, $^{**}p < 0.01$, and $^{***}p < 0.001$).

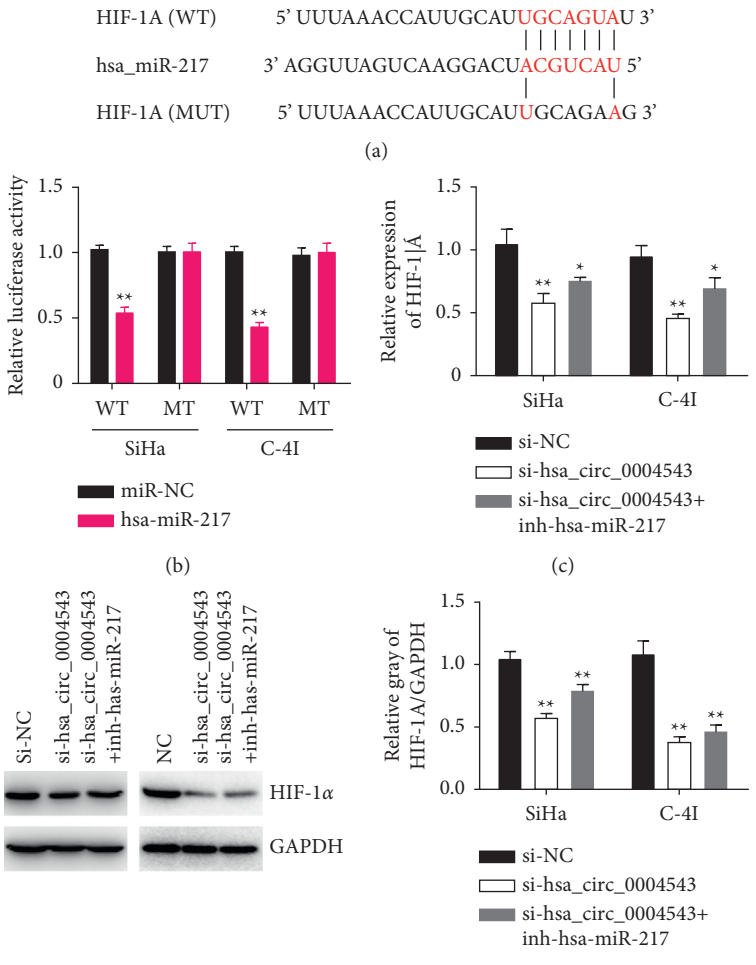

Figure 4: Continued.

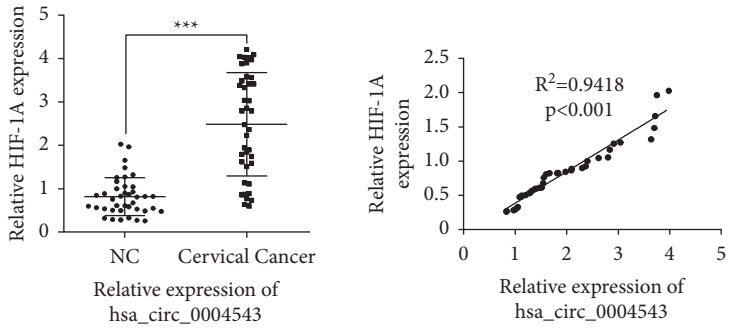

Figure 4: hsa_circ_0004543 increased the hypoxia-inducible factor (HIF-1α) expression by sponging hsa-miR-217 in CC. (a) Diagram of potential binding sites between hsa-miR-217 with HIF-1a (http://www.targetscan.org/) and mutation sites for the specific binding assay. (b) Dual-luciferase activity of SiHa and C-4I cells cotransfected by HIF-1a 3′UTR wild-type (WT) or mutated (MT) reporter with or without hsa-miR-217 mimics. (c) HIF-1a messenger ribonucleic acid (mRNA) expressions in SiHa and C-4I cells after hsa_circ_0004543 silencing (si-hsa_circ_0004543) with or without hsa-miR-217 inhibitor (inh-hsa-miR-217) determined using qRT-PCR. (d) HIF-1α protein expression of SiHa and C-4I cells after hsa_circ_0004543 silencing with or without inh-hsa-miR-217 determined using western blot. (e) Relative HIF-1a expressions in paired CC and paracancerous (NC) tissues determined with qRT-PCR ($n = 40$). (f) Association between HIF-1a and hsa_circ_0004543 expressions in CC patient tissues investigated by Pearson's correlation analysis ($n = 40$) ($^{*}p < 0.05$, $^{**}p < 0.01$, and $^{***}p < 0.001$).

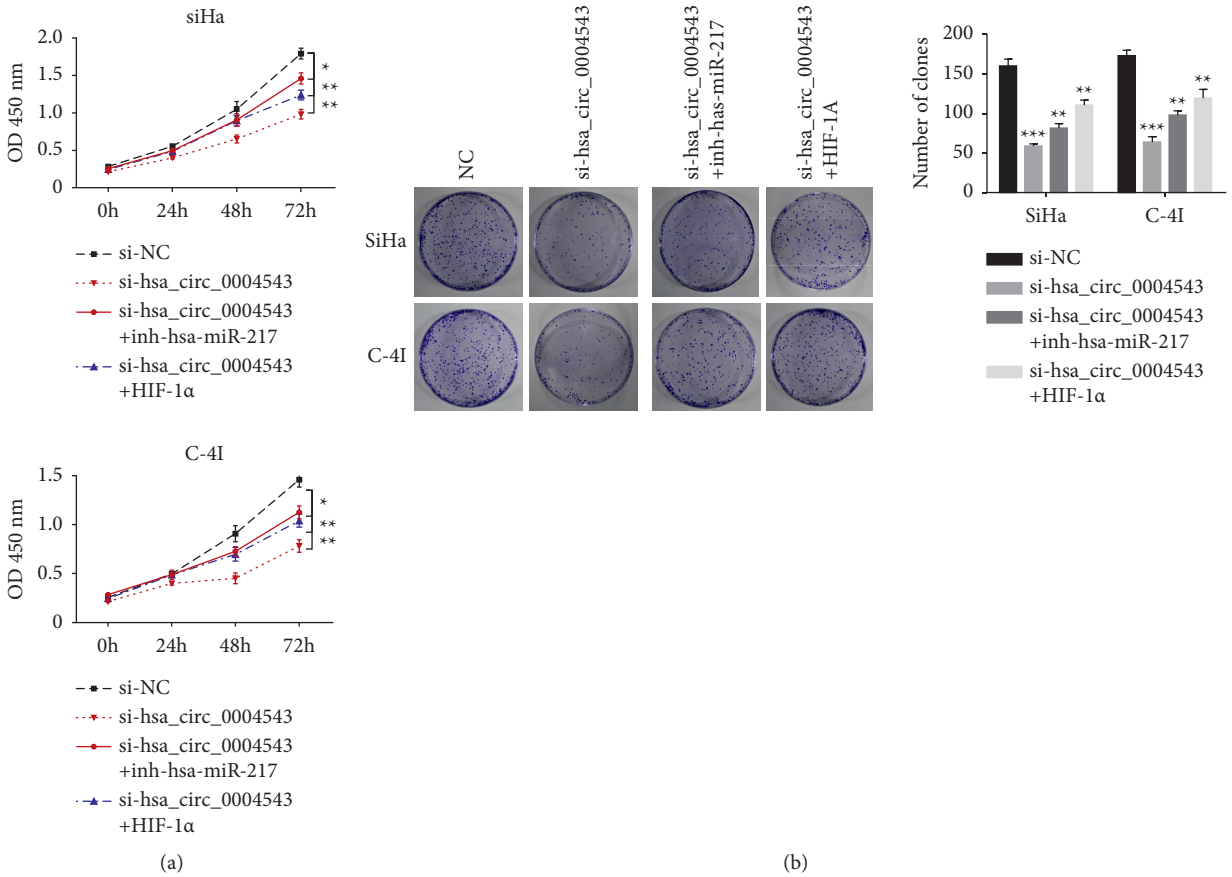

Figure 5: Continued.

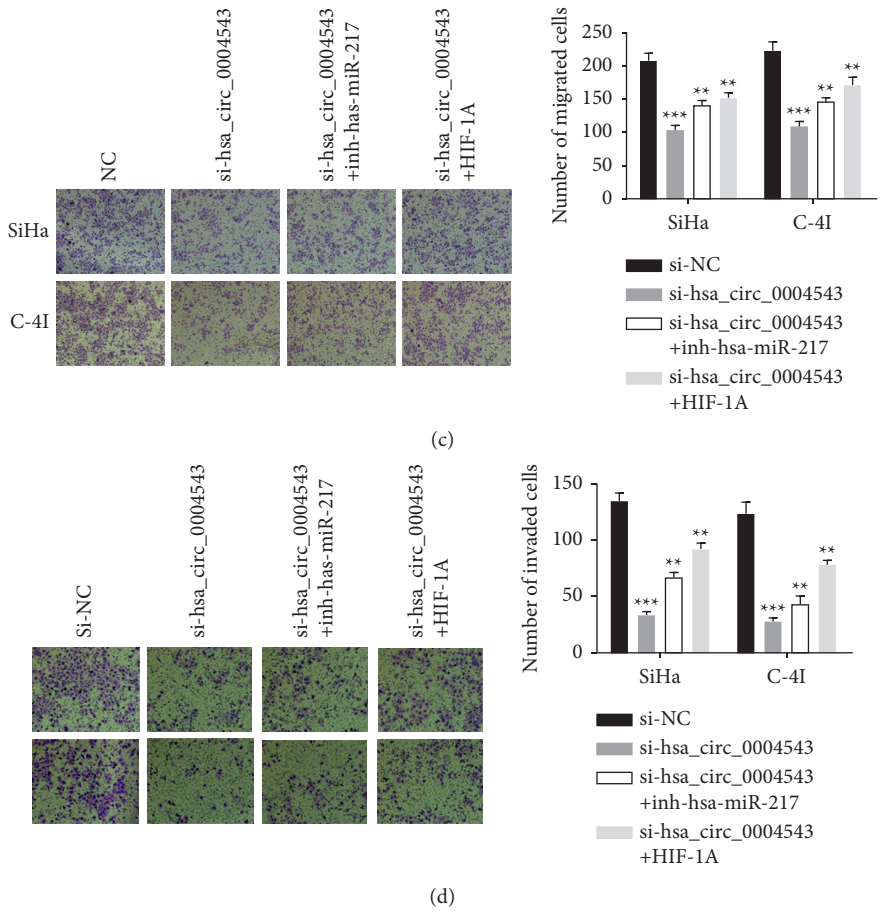

Figure 5: hsa-miR-217 knockdown or HIF-1a overexpression rescued hsa_circ_0004543 silencing inhibited malignant phenotypes in CC cells. (a) Viability of SiHa and C-4I cells after hsa_circ_0004543 silencing with/without inh-hsa-miR-217 or HIF-1a overexpression determined using the CCK-8 assay. (b) Colony proliferation abilities of SiHa and C-4I cells after hsa_circ_0004543 silencing with/without inh-hsa-miR-217 or HIF-1α overexpression determined using colony formation assay. (c) Cell migration capability of SiHa and C-4I cells after hsa_circ_0004543 knockdown with/without inh-hsa-miR-217 or HIF-1a overexpression detected by transwell assay without Matrigel. (d) Cell invasion capability of SiHa and C-4I cells after hsa_circ_0004543 silencing with/without inh-hsa-miR-217 or HIF-1α overexpression detected using transwell assay with Matrigel ($^{*}p < 0.05$; $^{**}p < 0.01$, and $^{***}p < 0.001$).

without inh-hsa-miR-217 or HIF-1a overexpression were detected by the colony formation assay, which showed that hsa_circ_0004543 silencing in SiHa and C-4I cells inhibited colony proliferation abilities (Figure 5(b)), and this inhibitory efficacy was partly rescued by hsa-miR-217 knockdown or HIF-1a overexpression. Finally, cell migration and invasiveness capacities in SiHa and C-4I cells were investigated based on the transwell assay without or with Matrigel. The data showed that hsa_circ_0004543 silencing inhibited both migration (Figure 5(c)) and invasiveness (Figure 5(d)) capabilities, which was partly reversed by hsa-miR-217 knockdown or HIF-1a overexpression. These findings indicated that hsa-miR-217 knockdown or HIF-1a overexpression reversed hsa_circ_0004543 silencing and inhibited malignant phenotypes in CC cells.

4. Discussion

circRNAs are noncoding RNAs that are highly stable in eukaryotic cells. Hsa_circ_0004543 has been newly identified as a significantly upregulated circRNA in CC tissues by circRNA microarray [12]. Nevertheless, its function and clinical implication in malignancy are still unknown. Therefore, we performed a comprehensive investigation of hsa_circ_0004543 in CC oncogenesis and its progression. In this work, we first confirmed a considerably higher hsa_circ_0004543 expression in CC tissues versus paired paracancerous normal tissues from 40 local CC patients, as well as in six different CC cell lines compared with normal human cervical epithelial cells, indicating the potential oncogenic role of hsa_circ_0004543 in CC. Secondly, we revealed that hsa_circ_0004543 silencing in CC cells significantly inhibited cell viability, colony proliferation, migration and invasiveness, and induced apoptosis.

Accumulating evidence has shown that transcriptional regulation between ncRNAs and mRNAs plays an essential function in CC cancer progression, including growth, migration, invasion, and multidrug resistance. As an important class of ncRNAs, miRNAs also play a critical role in regulating cell functions via degradation of target genes, therefore regulating cell proliferation, apoptosis, and metastasis. circRNA may be competitive endogenous RNA (ceRNA) for

miRNAs to regulate expression of downstream targets of mRNAs, and the ceRNA networks are important mechanisms to elucidate the posttranscriptional regulation in CC [26, 31–35]. Therefore, we explored further the ceRNA network mediated by hsa_circ_0004543 in the current study.

We used the online tool Circular RNA Interactome which predicted miRNAs harboring complementary binding sequences with hsa_circ_0004543 and identified the potential candidate of hsa-miR-217. The direct binding between hsa_circ_0004543 and hsa-miR-217 was further confirmed with dual-luciferase reporter activity examination in SiHa and C-4I cells. Meanwhile, hsa-miR-217 was identified to be inhibited in both CC cell lines and tissues, indicating the oncosuppressor role of hsa-miR-217 in CC. Moreover, hsa_circ_0004543 silencing in SiHa and C-4I cells considerably upregulated hsa-miR-217 expression, and Pearson's correlation assay discovered a negative association between hsa-miR-217 with hsa_circ_0004543 expressions in 40 CC patient tissues. These findings suggested that hsa_circ_0004543 directly interacted with hsa-miR-217 to promote the aggressive phenotypes of CC cells.

We used the online tool TargetScan to predict the mRNAs harboring complementary binding sequences with hsa-miR-217 and identified the potential candidate of HIF1A. The direct binding between HIF1A and hsa-miR-217 was further confirmed with a dual-luciferase reporter activity assay in SiHa and C-4I cells. Hypoxia is a typical representative of middle-late stage solid cancers and plays a key role in promoting malignancy cells to adapt to the hypoxia microenvironment in cancer by regulating the HIF transcriptional factors [36]. HIF-1α, encoded by HIF1A, is a commonly expressed HIFα isoform in various cells and the most essential regulator of oxygen homeostasis [37]. HIF-1α changes are associated with the outcomes of patients with various cancers, suggesting its critical role in carcinogenesis [38]. Our advanced investigation revealed that HIF-1a mRNA levels were considerably increased in CC tissues and were positively associated with hsa_circ_0004543. Meanwhile, knockdown of hsa_circ_0004543 considerably inhibited the expression of HIF-1α at both the mRNA and protein levels, and led to reduced viability and colony proliferation ability in CC cells. These effects were partly reversed by inhibiting hsa-miR-217 or overexpressing HIF-1a. Outcomes indicated that HIF-1a directly interacted with hsa-miR-217 via the sponging activity of hsa_circ_0004543 to stimulate CC progression. Hence, hsa_circ_0004543 may function as a ceRNA of hsa-miR-217 to inhibit HIF-1α degradation and thus stimulate the growth and metastasis of CC cells.

In conclusion, our current work showed that the hsa_circ_0004543 level was significantly amplified in CC patients and cells that promoted viability, colony proliferation, migration and invasiveness, and repressed apoptosis by sponging hsa-miR-217 to upregulate the HIF-1α level in CC cells. These changes thus contributed to the CC cell's oncogenesis and progression. Our results emphasized the potential function of hsa_circ_0004543 as a newly identified oncogenic ncRNA and that targeting the hsa_circ_0004543/hsa-miR-217/HIF-1α axis may provide a new therapeutic strategy to treat CC.

Data Availability

The data used to support the findings of this study are included within the article.

Additional Points

(1) circ_0004543 is an oncogenic factor in CC. (2) circ_0004543 acts as a ceRNA of hsa-miR-217 to upregulate HIF-1α. (3) Targeting the hsa_circ_0004543/hsa-miR-217/HIF-1α axis is a potential management strategy for CC.

Conflicts of Interest

The authors declare that they have no conflicts of interest in this study.

Authors' Contributions

Jun Liu and Yingqiao Liu contributed equally to this work.

Acknowledgments

This study was supported by the Key Projects of Sailing Plan of Beijing Medical Administration (no. ZYLX201713).

References

[1] G. B. D. S. C. Collaborators, "The global, regional, and national burden of stomach cancer in 195 countries, 1990-2017: a systematic analysis for the Global Burden of Disease study 2017," *Lancet Gastroenterol Hepatol*, vol. 5, pp. 42–54, 2020.

[2] H. Sung, J. Ferlay, R. L. Siegel, M. Laversanne, I. Soerjomataram, and A. Jemal, "Global cancer statistics 2020: GLOBOCAN estimates of incidence and mortality worldwide for 36 cancers in 185 countries," *CA: A Cancer Journal for Clinicians*, 2021.

[3] C. Allemani, H. K. Weir, H. Carreira et al., "Global surveillance of cancer survival 1995-2009: analysis of individual data for 25 676 887 patients from 279 population-based registries in 67 countries (CONCORD-2)," *The Lancet*, vol. 385, no. 9972, pp. 977–1010, 2015.

[4] S. Stapley and W. Hamilton, "Gynaecological symptoms reported by young women: examining the potential for earlier diagnosis of cervical cancer," *Family Practice*, vol. 28, no. 6, pp. 592–598, 2011.

[5] A. W. Lim, A. J. Ramirez, W. Hamilton, P. Sasieni, J. Patnick, and L. J. Forbes, "Delays in diagnosis of young females with symptomatic cervical cancer in England: an interview-based study," *British Journal of General Practice*, vol. 64, no. 627, pp. e602–e610, 2014.

[6] P. A. Cohen, A. Jhingran, A. Oaknin, and L. Denny, "Cervical cancer," *The Lancet*, vol. 393, no. 10167, pp. 169–182, 2019.

[7] J. Gong, H. Jiang, C. Shu et al., "Integrated analysis of circular RNA-associated ceRNA network in cervical cancer," *Medicine*, vol. 98, no. 34, Article ID e16922, 2019.

[8] J. Salzman, R. E. Chen, M. N. Olsen, P. L. Wang, and P. O. Brown, "Cell-type specific features of circular RNA expression," *PLoS Genetics*, vol. 9, no. 9, Article ID e1003777, 2013.

[9] W. R. Jeck, J. A. Sorrentino, K. Wang et al., "Circular RNAs are abundant, conserved, and associated with ALU repeats," *RNA*, vol. 19, no. 2, pp. 141–157, 2013.

[10] S. Memczak, M. Jens, A. Elefsinioti et al., "Circular RNAs are a large class of animal RNAs with regulatory potency," *Nature*, vol. 495, no. 7441, pp. 333–338, 2013.

[11] Z. Li, C. Huang, C. Bao et al., "Exon-intron circular RNAs regulate transcription in the nucleus," *Nature Structural & Molecular Biology*, vol. 22, no. 3, pp. 256–264, 2015.

[12] Y.-L. Gao, M.-Y. Zhang, B. Xu et al., "Circular RNA expression profiles reveal that hsa_circ_0018289 is up-regulated in cervical cancer and promotes the tumorigenesis," *Oncotarget*, vol. 8, no. 49, pp. 86625–86633, 2017.

[13] J. Zhang, X. Zhao, J. Zhang, X. Zheng, and F. Li, "Circular RNA hsa_circ_0023404 exerts an oncogenic role in cervical cancer through regulating miR-136/TFCP2/YAP pathway," *Biochemical and Biophysical Research Communications*, vol. 501, no. 2, pp. 428–433, 2018.

[14] H. Cai, P. Zhang, M. Xu, L. Yan, N. Liu, and X. Wu, "Circular RNA hsa_circ_0000263 participates in cervical cancer development by regulating target gene of miR-150-5p," *Journal of Cellular Physiology*, vol. 234, no. 7, pp. 11391–11400, 2019.

[15] T. Song, A. Xu, Z. Zhang et al., "CircRNA hsa_circRNA_101996 increases cervical cancer proliferation and invasion through activating TPX2 expression by restraining miR-8075," *Journal of Cellular Physiology*, vol. 234, no. 8, pp. 14296–14305, 2019.

[16] H. Li, Y. Jia, and Y. Wang, "Targeting HIF-1alpha signaling pathway for gastric cancer treatment," *Pharmazie*, vol. 74, pp. 3–7, 2019.

[17] T.-T. Wei, Y.-T. Lin, S.-P. Tang et al., "Metabolic targeting of HIF-1α potentiates the therapeutic efficacy of oxaliplatin in colorectal cancer," *Oncogene*, vol. 39, no. 2, pp. 414–427, 2020.

[18] L. Zhang, S.-T. Huang, Y.-L. Feng et al., "The bidirectional regulation between MYL5 and HIF-1α promotes cervical carcinoma metastasis," *Theranostics*, vol. 7, no. 15, pp. 3768–3780, 2017.

[19] J. A. Bertout, S. A. Patel, and M. C. Simon, "The impact of O2 availability on human cancer," *Nature Reviews Cancer*, vol. 8, no. 12, pp. 967–975, 2008.

[20] E. B. Rankin and A. J. Giaccia, "Hypoxic control of metastasis," *Science*, vol. 352, no. 6282, pp. 175–180, 2016.

[21] X. Lu and Y. Kang, "Hypoxia and hypoxia-inducible factors: master regulators of metastasis," *Clinical Cancer Research*, vol. 16, no. 24, pp. 5928–5935, 2010.

[22] P. Carmeliet and R. K. Jain, "Molecular mechanisms and clinical applications of angiogenesis," *Nature*, vol. 473, no. 7347, pp. 298–307, 2011.

[23] G. L. Semenza, "Hypoxia-inducible factors in physiology and medicine," *Cell*, vol. 148, no. 3, pp. 399–408, 2012.

[24] K. Balamurugan, "HIF-1 at the crossroads of hypoxia, inflammation, and cancer," *International Journal of Cancer*, vol. 138, no. 5, pp. 1058–1066, 2016.

[25] Q. Hong, O. Li, W. Zheng et al., "LncRNA HOTAIR regulates HIF-1α/AXL signaling through inhibition of miR-217 in renal cell carcinoma," *Cell Death & Disease*, vol. 8, no. 5, e2772 pages, 2017.

[26] Q. Gu, W. Hou, L. Shi, H. Liu, Z. Zhu, and W. Ye, "Circular RNA ZNF609 functions as a competing endogenous RNA in regulating E2F transcription factor 6 through competitively binding to microRNA-197-3p to promote the progression of cervical cancer progression," *Bioengineered*, vol. 12, no. 1, pp. 927–936, 2021.

[27] S. Hu, J. Chang, H. Ruan et al., "Cantharidin inhibits osteosarcoma proliferation and metastasis by directly targeting miR-214-3p/DKK3 axis to inactivate β-catenin nuclear translocation and LEF1 translation," *International Journal of Biological Sciences*, vol. 17, no. 10, pp. 2504–2522, 2021.

[28] V. B. O'Leary, J. Smida, M. Matjanovski et al., "The circRNA interactome-innovative hallmarks of the intra- and extracellular radiation response," *Oncotarget*, vol. 8, no. 45, pp. 78397–78409, 2017.

[29] J. Jia, Z. Ouyang, M. Wang et al., "MicroRNA-361-5p slows down gliomas development through regulating UBR5 to elevate ATMIN protein expression," *Cell Death & Disease*, vol. 12, no. 8, p. 746, 2021.

[30] J. Cen, Y. Liang, Y. Huang et al., "Circular RNA circSDHC serves as a sponge for miR-127-3p to promote the proliferation and metastasis of renal cell carcinoma via the CDKN3/E2F1 axis," *Molecular Cancer*, vol. 20, no. 1, p. 19, 2021.

[31] X. Ma, Q. Zhang, J. Du, J. Tang, and B. Tan, "Integrated analysis of ceRNA regulatory network associated with tumor stage in cervical cancer," *Frontiers in Genetics*, vol. 12, Article ID 618753, 2021.

[32] T. Wang, X.-D. Zhang, and K.-Q. Hua, "A ceRNA network of BBOX1-AS1-hsa-miR-125b-5p/hsa-miR-125a-5p-CDKN2A shows prognostic value in cervical cancer," *Taiwanese Journal of Obstetrics & Gynecology*, vol. 60, no. 2, pp. 253–261, 2021.

[33] L. Ding and H. Zhang, "Circ-ATP8A2 promotes cell proliferation and invasion as a ceRNA to target EGFR by sponging miR-433 in cervical cancer," *Gene*, vol. 705, pp. 103–108, 2019.

[34] Y. Wang, L. Wang, W. Wang, and X. Guo, "Overexpression of circular RNA hsa_circ_0001038 promotes cervical cancer cell progression by acting as a ceRNA for miR-337-3p to regulate cyclin-M3 and metastasis-associated in colon cancer 1 expression," *Gene*, vol. 733, Article ID 144273, 2020.

[35] S. Liu, B. Li, Y. Li, and H. Song, "Circular RNA circ_0000228 promotes the malignancy of cervical cancer via microRNA-195-5p/lysyl oxidase-like protein 2 axis," *Bioengineered*, vol. 12, no. 1, pp. 4397–4406, 2021.

[36] G. L. Semenza, "Hypoxia-inducible factor 1 (HIF-1) pathway," *Science's STKE : Signal Transduction Knowledge Environment*, p. cm8, 2007.

[37] G. L. Semenza, "Hydroxylation of HIF-1: oxygen sensing at the molecular level," *Physiology*, vol. 19, no. 4, pp. 176–182, 2004.

[38] W. Yang, J. Ma, W. Zhou et al., "Reciprocal regulations between miRNAs and HIF-1α in human cancers," *Cellular and Molecular Life Sciences*, vol. 76, no. 3, pp. 453–471, 2019.

Hindawi
Journal of Oncology
Volume 2022, Article ID 5694033, 11 pages
https://doi.org/10.1155/2022/5694033

Research Article

Analysis of Stemness and Prognosis of Subtypes in Breast Cancer Using the Transcriptome Sequencing Data

Wei Chen,[1,2,3] Zhipeng Hong,[4] Shaohong Kang,[1,2,3] Xinying Lv,[1,2,3] and Chuangui Song[1,2,3]

[1]*Department of Breast Surgery, Fujian Medical University Union Hospital, Fuzhou, Fujian Province 350001, China*
[2]*Department of General Surgery, Fujian Medical University Union Hospital, Fuzhou, Fujian Province 350001, China*
[3]*Breast Cancer Institute, Fujian Medical University, Fuzhou, Fujian Province 350001, China*
[4]*Affiliated Quanzhou First Hospital of Fujian Medical University, Quanzhou, Fujian Province 362000, China*

Correspondence should be addressed to Chuangui Song; songcg1971@hotmail.com

Received 29 December 2021; Accepted 2 February 2022; Published 9 March 2022

Academic Editor: Fu Wang

The stem characteristics of tumor cells have been proposed in theory very early, and we can use the signature of gene expression to speculate the stemness of tumor cells. However, systematic studies on the stemness of breast cancer as well as breast cancer subtypes, and the relationship between stemness and metastasis and prognosis, are still lacking. In the present research, using the transcriptome data of patients with breast cancer in the TCGA database, a stemness prediction model was utilized to derive the stemness of the patients' tumors. We compared the stemness values among different subtypes and the differences with metastasis. COX regression was employed to evaluate the correlation between stemness value as well as prognosis. Using the Lasso-penalized Cox regression machine learning model, we obtained the gene signature of the basal subtype that is related to stemness and can also predict the prognosis of the patient. Patients can be stratified into two groups of high and low stemness, corresponding to good and poor prognosis. Based on further prediction of tumor infiltration by CIBERSORT and prediction of drug response by a connectivity map, we found that the difference in stemness between these two groups is associated with the activation of tumor-killing immune cells and drug response. Our findings can promote the understanding and research of subtypes of basal breast cancer and provide corresponding molecular markers for clinical detection and therapy.

1. Introduction

According to statistics from global tumor data in 2018, breast cancer has the highest incidence and mortality among women [1]. With the development of science and technology, the ability to identify and diagnose breast cancer has significantly improved, and the past anatomy-based treatment is shifting to diagnosis and treatment through different biological mechanisms. Gene array technology divides breast cancer into different biological subtypes. New systemic drugs have significantly improved survival rates and are expected to enable patients with metastatic tumors to survive longer.

There are five subtypes of breast cancer, LumA, LumB, Basal, HER2, and normal. Among them, LumA and LumB subtypes have many types of mutations in the key genes, and the overall gene mutation rate of Basal and HER2 subtypes is higher than others. Different subtypes have different molecular expression profiles. According to the gene expression in cells, we can diagnose and treat patients accordingly. In terms of relationship with prognosis, Luminal has a better overall prognosis, and HER2 subtype has a worse overall prognosis and will relapse early. The Basal subtype has the worst prognosis. Moreover, as it is triple-negative, the only treatment option is chemotherapy. The normal subtype has a prognosis between Luminal and Basal and is not sensitive to chemotherapy [2].

Stemness, considered as the capacity to self-renew and differentiate from the precursor cells, was initially explored in normal stem cell-related studies, which has the capability to produce all cell types in adult organisms [3]. A significant proportion of genomic, proteomic, epigenomic, and

Table 1: Clinicopathological characteristics in each subtype of breast cancer.

Items	Level	Subtype				
		Basal	Her2	LumA	LumB	Normal
N		183	81	559	208	40
Race (%)	Nonwhite	71 (40.3)	33 (46.5)	82 (15.8)	46 (25.8)	11 (28.2)
	White	105 (59.7)	38 (53.5)	438 (84.2)	132 (74.2)	28 (71.8)
Age (median (IQR))		54.00 (48.00, 62.50)	57.00 (50.00, 64.00)	61.00 (49.00, 69.00)	58.50 (50.00, 68.25)	53.00 (46.00, 62.50)
Pathologic_T (%)	T1	37 (20.3)	17 (21.0)	175 (31.4)	37 (17.8)	11 (27.5)
	T2	121 (66.5)	52 (64.2)	291 (52.2)	135 (64.9)	18 (45.0)
	T3	18 (9.9)	7 (8.6)	74 (13.3)	24 (11.5)	11 (27.5)
	T4	6 (3.3)	5 (6.2)	17 (3.1)	12 (5.8)	0 (0.0)
Pathologic_N (%)	N0	117 (63.9)	29 (37.7)	255 (46.5)	84 (41.2)	21 (53.8)
	N1	46 (25.1)	28 (36.4)	194 (35.4)	77 (37.7)	8 (20.5)
	N2	14 (7.7)	11 (14.3)	56 (10.2)	33 (16.2)	4 (10.3)
	N3	6 (3.3)	9 (11.7)	43 (7.8)	10 (4.9)	6 (15.4)
Pathologic_M (%)	M0	159 (98.1)	70 (95.9)	449 (98.0)	178 (97.3)	33 (97.1)
	M1	3 (1.9)	3 (4.1)	9 (2.0)	5 (2.7)	1 (2.9)
Pathologic_stage (%)	Stage I-II	151 (83.9)	56 (70.9)	410 (75.4)	142 (68.9)	28 (70.0)
	Stage III-IV	29 (16.1)	23 (29.1)	134 (24.6)	64 (31.1)	12 (30.0)
ER_status_by_IHC (%)	Negative	157 (89.2)	47 (62.7)	11 (2.0)	3 (1.5)	14 (37.8)
	Positive	19 (10.8)	28 (37.3)	526 (98.0)	194 (98.5)	23 (62.2)
PR_status_by_IHC (%)	Negative	163 (93.7)	62 (80.5)	54 (10.1)	39 (19.8)	17 (45.9)
	Positive	11 (6.3)	15 (19.5)	480 (89.9)	158 (80.2)	20 (54.1)
HER2_status_by_IHC (%)	Negative	114 (92.7)	13 (20.6)	304 (82.8)	99 (74.4)	20 (87.0)
	Positive	9 (7.3)	50 (79.4)	63 (17.2)	34 (25.6)	3 (13.0)

transcriptomic markers have been shown to be related to cancer stemness in recent years. Over the last ten years, The Cancer Genome Atlas (TCGA) has shed light on the molecular environments of primary tumors by delivering thorough molecular profiles that include epigenomic, transcriptomic, genomic, and (post-translational) proteomic properties [4, 5], as well as clinical and histopathological annotations. The materials generated on the basis of the TCGA data enable us to thoroughly examine the cancer stem in a large sample of breast tumors and their subtypes.

The objective of this study was to perform cell stemness calculations using TCGA breast cancer data and to explore the relationship between cell stemness and prognosis. After subtyping the highly relevant factors, the signatures that can predict prognosis are finally calculated. The biological significance and clinical value of these predicted signatures are analyzed to provide a theoretical basis and reference basis for further research.

2. Materials and Methods

2.1. Collection and Processing of Data

2.1.1. Breast Cancer Data. We acquired breast cancer clinical data through the GDC Data Portal with a total of 1097 valid patients and collected clinical source data as follows: clinical.tsv containing the latest updated prognostic information and the more detailed information was in https://nationwidechildrens.org_clinical_patient_brca.txt.
In addition, molecular subtypes of breast cancer samples were obtained through TCGAbiolinks, and those with complete clinical and subtype information ($n = 1095$) were selected for subsequent integration and analysis (Table 1). Through TCGAbiolinks, the expression data of breast cancer samples including mRNA and lncRNA were obtained.

2.1.2. Stem Cell Data. The Synapse is the portal for the Progenitor Cell Biology Consortium (PCBC), an NHLBI sponsored endeavor to discover and define progenitor cell lineages, to govern the development of stem and progenitor cells into ideal cell fates, and to create innovative ways to resolve certain problems when these cells are transplanted. Stem cell gene expression, methylation, SNV (copy-number variation), and other information are stored on the Synapse database. Synapse provides a variety of interfaces, and researchers can obtain them on the platform through R, Python, and other software and share these data.

2.2. Calculate Sample Stemness Index According to mRNA Expression. Malta et al. [3] developed a prediction model by means of the OCLR algorithm on pluripotent stem cell samples from the PCBC dataset [6, 7] to develop a stemness signature, which was then used to determine the mRNAsi value. There are 11 774 genes in the expression profiles derived from the mRNA expression-based signature. More information on the stemness indices and the flowchart that was used in the present research to produce the aforementioned indices are available on the following website: https://bioinformaticsfmrp.github.io/PanCanStem-Web.
The OCLR algorithm was used to calculate the eigenvector weights for the RNA expression matrix, respectively. The

mRNAsi stem cell index of breast cancer samples was calculated based on the obtained RNA expression data of breast cancer samples and the weights of eigenvectors calculated before. The stemness indices were utilized to stratify the breast cancer samples, which were then employed for the integrative analysis.

2.3. Calculating the Relationship between Breast Cancer Stemness Index and Clinical Features. In order to clarify the correlation between the stem index of breast cancer and the types and metastasis status, we compared mRNAsi of different subtypes (LumA, LumB, Basal, Normal, Her2 subtypes) and metastasis (non-metastasis) status. Assessing mRNAsi differences between groups to see if our calculated breast cancer stem cell index correlates with clinical traits of the disease.

The stemness index was treated as an independent continuous covariate in the present research. Using a three-phase approach, we investigated the correlation between stemness indices and OS in breast cancer. Specifically, we utilized the univariate Cox proportional hazard regression to compute hazard ratios (HRs) for overall survival (OS). Some of the parameters included mRNAsi gender, metastatic status, tumor histology, age, and subgroup. The results of Cox univariate regression showed the clinical indicators of breast cancer associated with the patients' prognosis. In addition, patients were divided into high- and low-risk groups according to their mRNAsi levels, which were obtained utilizing the "cutp" module of the R package "survMisc" (https://cran.r-project.org/web/packages/survMisc) with default settings, and the differences in survival among subjects with elevated mRNAsi and those with reduced mRNAsi were assessed utilizing Kaplan–Meier (K–M) survival plots. Finally, only patients in the Basal subgroup were shown to have a statistically significant survival difference between those with higher mRNAsi and those with lower mRNAsi.

With the aid of the "createDataPartition" module of the R package "caret" (https://cran.r-project.org/web/packages/caret), we were able to divide the Basal subgroup dataset at random into two parts, namely, the 70 percent training set and the 30 percent validation set. We then utilized non-default parameters for the "createDataPartition" module as follows: $P = 0.7$ and list = FALSE. The Chi-square test for categorical variables and Kruskal–Wallis test for continuous variables were utilized to examine the distributions of clinical features across the training set as well as the validation set. In the training set, we divided the gene expression data into mRNA, lncRNA, and performed Cox univariate regression, respectively. Significantly related genes were selected, and then the correlation between their expression and the stem cell index of samples was calculated. Those with correlation coefficients cor >0.2 and correlation test P-value <0.05) were selected as candidate genes.

2.4. Lasso to Build the Best Multivariate COX Model. This step uses machine learning to further filter the candidate lncRNAs and mRNAs, to construct the best gene predicting panel in the Basal subtype. We calculated the lncRNA panel and mRNA panel risk score for each sample based on expression and multiple regression coefficients. The equation for determining risk scores is shown below:

$$\text{Riskscore} = \sum_{i=1}^{n} \beta i^{*} xi. \quad (1)$$

The samples were divided into high index group and low index group according to the risk index (only 2 miRNAs were not screened by Lasso, they were divided into high expression group and low expression group according to their expression levels and drawn, respectively), Kaplan–Meier survival analysis was performed, and survival curves were drawn. Furthermore, based on the risk index of mRNA and lncRNA, ROC curves of three-year, five-year, and ten-year survival periods were drawn. We explored whether the models were accurate predictors based on the area under the curve (AUC) of a time-dependent receiver operating characteristic (ROC) study.

2.5. Assessment of Relationships between Stemness Indices and the Immune Landscape. By means of CIBERSORT (a deconvolution algorithm according to gene expression) (https://cibersort.stanford.edu/) [8], we calculated the relative abundance of the immune cells in the sample that was received. Using ESTIMATE [9], we calculated individual immunity scores to anticipate the level of infiltration of immune cells in each basal sample. The association between mRNAsi and immunological score was also analyzed.

2.6. CMap Predict mRNAsi-Related Drugs. The newly revised CMap (September 2017) [10] is a data-driven and systematic technique for uncovering associations among genes, chemicals, and biological circumstances, to screen for prospective substances that could target pathways associated with breast cancer stemness. Using the CMap database, a sum of 42080 perturbation factors were analyzed and 473647 reference signatures were generated. The CMap workflow consists of querying the CMap reference signature dataset (a LIST of DEGs associated with the biologic state of interest) using a pattern-matching algorithm. The scores fell within the range of −100 to 100. Molecular compounds are ordered on the basis of their proportion to produce the most similar as well as the most opposite compounds. The website https://clue.io provides the CMap data as well as relevant tools. The "lmFit" module of the R package "limma" was utilized to determine the DEGs between the Basal subgroup samples that had elevated mRNAsi and those with reduced mRNAsi on the basis of default settings [11]. A number of genes that had differential expression across Basal subgroup samples with elevated mRNAsi and reduced mRNAsi was compiled, and the topmost 300 genes (150 of which were upmodulated and 150 of which were downmodulated) were chosen for further investigation in the CMap database. Compounds having an enrichment score of ≤−95 were identified as promising chemotherapeutic drugs for the treatment of basal breast cancer.

2.7. Statistical Analysis. In the present research, all statistical analyses were conducted utilizing R (version: 3.4.1) (R Core Team, R Foundation for Statistical Computing, Vienna, Austria). In the case when using the default settings of the R package "gelnet," the OCLR technique was applied successfully [12]. We calculated the P values for the correlations between stemness indices and the immune milieu utilizing Pearson's correlation coefficient tests, followed by multiple testing utilizing the BH technique. Statistical significance was reached when the value of P was less than 0.05.

3. Results

3.1. Breast Cancer Stemness Indices Predicated on mRNA Expression. On the basis of the analysis of the relationship between stemness index and survival of patients, there is an overall significant difference among each subtype ($P = 0.0374$) (Figure 1(a)). We also found the Basal subtype has higher mRNAsi compared with others, and significant different mRNAsi among them ($P < 0.05$). Significant differences were not observed between metastatic (M0) and nonmetastatic (M1) samples, as well as in each subtype of M0 and M1 samples (Figures 1(b)–1(d)). Based on their specific mRNAsi values (ranging from low to high stemness index), we graded the breast cancer samples and searched for correlations with any demographic/molecular/clinical characteristics that were associated with either a higher or lower stemness index (Figure 1(e)).

3.2. Associations between Breast Cancer Stemness Indices and Clinical Outcome. Based on sample survival data, a univariate Cox regression analysis was conducted to test the association between clinical indicators and patients' overall survival (OS). The forest chart is displayed in Figure 2(a). To address the effect of mRNAsi on survival, we did the K–M plots by splitting all patients or each subtype sample into low and high mRNAsi groups (Figures 2(b)–2(g)). The results showed that mRNAsi exhibited a statistically significant impact on OS for Basal patients (HR, 0.32; $P = 0.01$). Then, in basal patients, we conducted cox regression analysis for gene expression and survival. All genes with a significant survival relationship ($P < 0.05$) were subjected to correlation analysis with mRNAsi, and the genes with significant correlation ($|\text{cor}| > 0.2$, $P < 0.05$) were selected for statistical analyses. As a result, we got 2 miRNAs, 111 lncRNAs, and 389 mRNAs (Tables S1–S3).

After the lasso machine learning on candidate 389 mRNA and 111 lncRNA, the mRNA panel (FAM72 C, ZFP36, GRASP, FOSB, SERPINE1, P2RX6), the lncRNA panel (AC104260.1, AC126177.4, LINC02511, DKFZp779M0652, AC025040.1), and the miRNA panel (hsa-mir-143 and hsa-mir-221) for Basal breast cancer were identified. Using univariate (Figures 3(a)–3(c)) and multivariate (Figures 3(d)–3(f)) cox regression beta index analysis, the expression of majority genes in each panel contributed to the prognosis of patients with Basal breast cancer ($P < 0.05$). Combined with gene expression and beta index of multivariate cox regression, we calculated the risk scores (RS) for each sample and then separated them into two groups in each panel, high RS and low RS. Based on the different RS level, three-year, five-year, and ten-year survival ROC curves were drawn for each panel (Figures 4(a)–4(c)). The prediction performance of the prognostic model was evaluated by computing the AUC of the ROC curves. With regard to the mRNA set, the AUCs concerning the 6-mRNA biomarker prognostic model were 0.748, 0.766, and 0.843 for the 3-, 5-, and 10-year survival times (Figure 4(a)). In the lncRNA set, AUCs concerning the 5-lncRNA biomarker prognostic model were 0.755, 0.822 and 0.547 for the 3-, 5-, and 10-year survival times (Figure 4(b)). For the 2 miRNA-based prognostic model, the AUCs were 0.575, 0.568, and 0.618 for the 3-, 5-, and 10-year survival (Figure 4(c)). Then, the K–M plot was produced between low and high-risk score groups. The results showed that the risk model of mRNA, lncRNA, and miRNA panels were all significantly related to the survival of Basal patients (Figures 4(d)–4(f)). Taken together, mRNAsi-related genes were independent factors affecting the prognosis of Basal breast cancer.

3.3. Relationship between Stemness Indices and the Immune Milieu. We evaluated associations between specific kinds of immune cells and mRNAsi in order to better understand the relationships between stemness in Basal patients and the tumor immune milieu in the present study. CIBERSORT was used to calculate the relative abundance of immune cells in each sample based on the expression profile data of the sample (Supplementary Figure S1), and the corresponding immune index of each sample was obtained from ESTIMATE. Combining the relative abundance and immune score of the immune cells of each subtype sample, the relationships between mRNAsi index and immune cell, four immune cell activation status, and immune score in different subtypes were investigated. Out of all other subtypes of breast cancer, Her2 enrichment and Normal subtypes have higher immune activity, while the LumA subtype has lower immune activity. Among them, Basal subtype mRNAsi has a high positive correlation with the activation status of T cells and NK immune cells and a negative correlation with the resting or naive immune cells (Figures 5(a)–5(b)).

3.4. Analysis of the Connectivity Map Reveals New Potential Drugs that Target the Basal Stemness Signature. For the purpose of developing efficacious drugs that can target the pathways correlated with Basal stemness, we utilized mRNA expression signatures to query the connectivity map (CMap) database, followed by the analysis of differential expression in low or high mRNAsi values on breast cancer subgroups. A total of 1,308 potential drugs were obtained, of which the top ten most relevantly positive-regulated drugs were HC toxin, cytochalasin B, dopamine, oxamic acid, cantharidin, dexverapamil, corynanthine, GW-8510, verteporfin, and etofenamate. The top ten most relevantly negative-regulated drugs were 5286656, demecolcine, 2-deoxy-D-glucose, sulindac sulfide, tyrphostin AG-1478, DL-PPMP, 5186324, benzbromarone, BW-B70 C, and topiramate (Figure 5(c)).

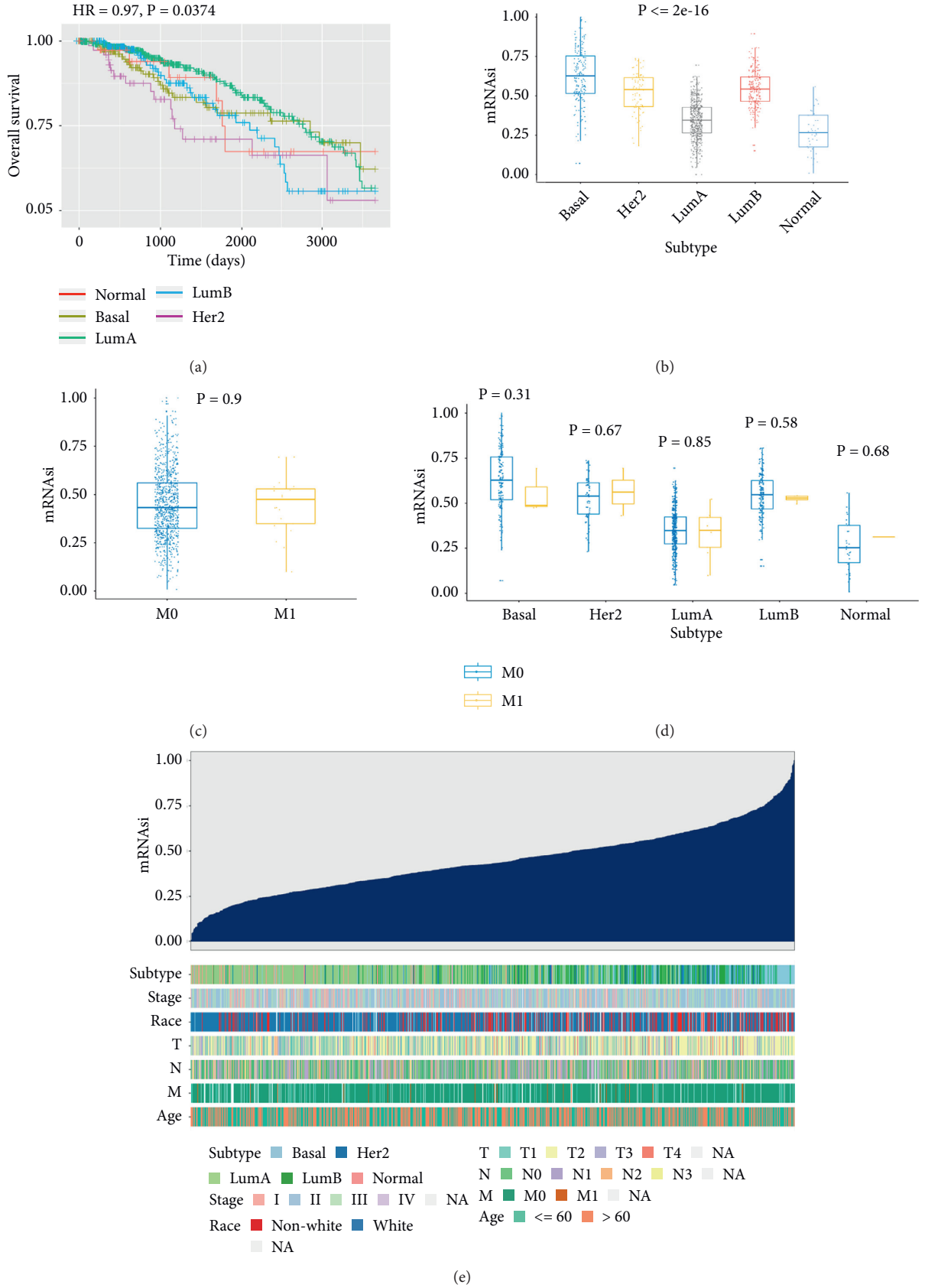

FIGURE 1: Survival for patients in the subtypes and clinical characteristics correlated with the mRNA expression-based stemness index (mRNAsi) in breast cancer. (a) Patients' survival curves in distinct the subtypes for breast cancer. (b) Individual sample boxplots of mRNAsi classified by subtypes. (c) Individual mRNAsi boxplots classified by metastatic status. (d) Individual mRNAsi boxplots for each subtype classified by metastatic state. (e) Summary of the known associations between clinical and molecular characteristics (subtype, stage, race, pathologic TNM stage, and age) and mRNAsi in breast cancer.

Features	Univ_beta	Univ_HR	Univ_95%CI_for HR	Univ_P. value
mRNAsi	0.544	1.723	0.693-4.282	0.241
Age_High	0.531	1.700	1.210-2.391	0.002
Age_Low	-0.531	0.588	0.418-0.827	0.002
Stage_II	-1.132	0.322	0.230-0.451	3.64e-11
Stage_IV	1.014	2.757	1.964-3.872	4.67e-09
Subtype_LumA	-0.425	0.654	0.466-0.916	0.014
Subtype_LumB	0.247	1.281	0.850-1.931	0.237
Subtype_Her2	0.665	1.945	1.154-3.278	0.012
Subtype_Basal	0.075	1.078	0.703-1.653	0.730
Subtype_Normal	0.074	1.077	0.475-2.442	0.859

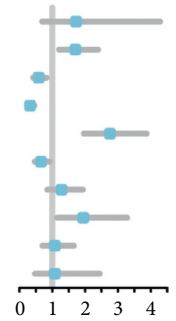

(a)

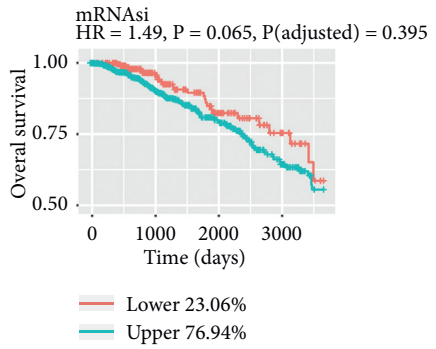

(b)

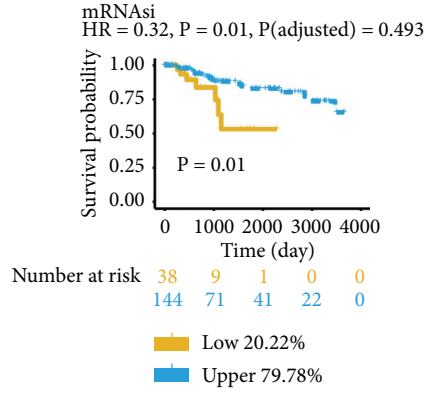

(c)

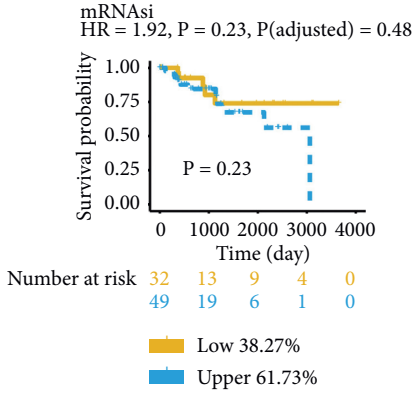

(d)

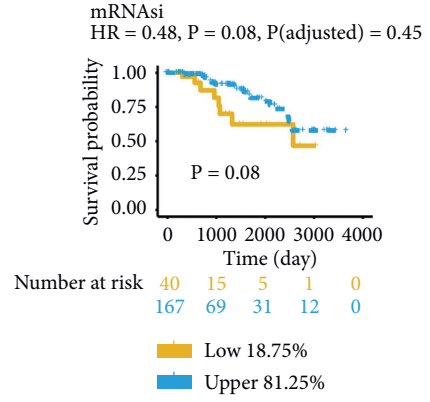

(e)

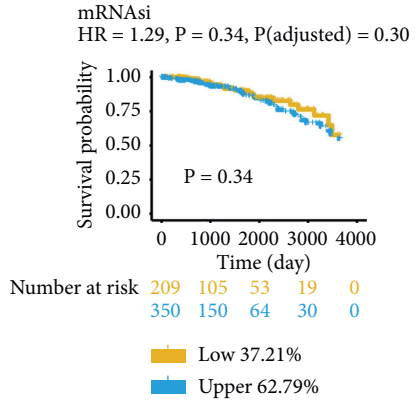

(f)

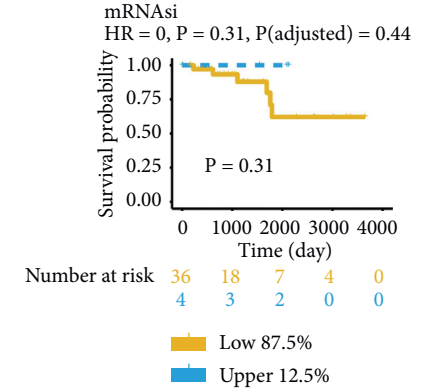

(g)

Figure 2: Association between OS of patients and mRNAsi. The K–M survival curves depict the OS rate for patients with low- and high mRNAsi, classified by the ideal threshold. (a) Cox regression studies of univariate data on clinical and molecular characteristics related to OS in MB patients. (b) K–M curves depicting the OS of all patients in breast cancer having a low or high mRNAsi. (c–g) K–M curves depicting the OS of patients respectively in subtype Basal (c), Her2 (d), LumB (e), LumA (f), and Normal (g).

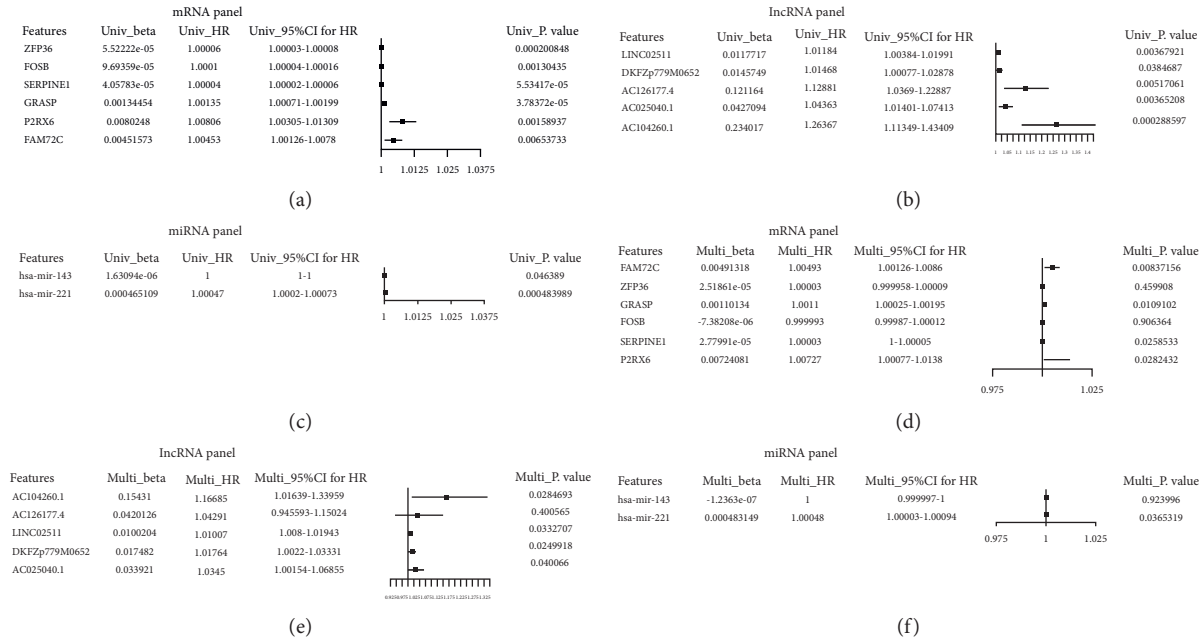

Figure 3: Univariate and multivariate cox regression beta index analysis in mRNA, lncRNA, and miRNA panel. (a–c) Predictive significance of each gene in mRNA, lncRNA, and miRNA panel using univariate cox regression beta index analysis. (d–f) Predictive significance of each gene in mRNA, lncRNA, and miRNA panel using Multivariate cox regression beta index analysis.

4. Discussion

Using a stemness index model-based OCLR machine-learning algorithm, we calculated the stemness index of breast cancer samples in the TCGA database. With the aid of the stemness index, we compared the differences in stemness characteristics of distinct breast cancer subtypes and analyzed the association between breast cancer stemness and patient survival, as well as tumor immune invasion. We found that the stemness of different subtypes is significantly different. Although the survival time of patients within different subtypes is significantly different, we found no substantial association between the stemness index and the overall survival of patients in all breast cancer samples. Stemness also has no significant correlation with the patient's stage or metastasis. Then, we stratified the patients according to the subtype and found that the tumor stemness index in the Basal subtype is relatively high. At the same time, there are two groups of patients with low and high stemness only in the Basal subtype, which have significant differences in overall survival. Patients with high stemness have a longer overall survival, and patients with low stemness have a short overall survival. These suggest that the Basal subtype has higher internal heterogeneity and complexity in tumor stemness than other subtypes.

Stemness refers to cells with the capacity for self-renewal and differentiation, while tumor cells lose their original cellular characteristics during progression and alienate into poorly differentiated and highly proliferating cells, somehow similar to normal stem cells. It is generally believed that these stem cells with elevated stemness have a high likelihood of being migrated to distant organs due to high proliferation and invasion, which will result in an unfavorable prognosis of patients [13, 14]. However, our study found that higher stemness tumors are not as malignant. The breast stemness index of each subtype in breast cancer is not significantly correlated with the presence or absence of distant metastasis of tumors, and the prognosis of patients with high stemness in Basal is better. This is contrary to the oncogenic dedifferentiation in most malignant tumors, which tends to be stem-like. In fact, the association between high dryness and a good prognosis is not identified in all breast tumors. The stemness value of the Basal subtype is relatively high, although we know that the prognosis of patients with basal subtype is usually not good. To be noted, the two groups of high and low stemness we found here are stratified in Basal. This difference between high and low can only suggest that there are different types of Basal subtypes, and the stem cell genes signature could be applied in this classification. Then, we found that this stemness signature is actually related to tumor immune cell infiltration. The prognosis of the patient may be due to the difference in infiltrated immune cells.

With respect to the Basal subtype, we found that the stemness index was substantially correlated with the status of tumor immune infiltration. A strong positive association was observed between the ratio of stemness index and follicular helper T cells, also known as antigen-experienced CD4 + T cells. Moreover, the stemness index was significantly correlated with immune cells participating in tumor killing, such as CD8 + T cells, macrophage M1 type, activated NK, DC, and CD4 + memory T cells, while being negatively correlated with macrophage M2 type and naïve B and CD4 + T cells. This suggests that tumors with a high stemness index tend to trigger activated immune cells infiltration, which has the tumor-killing effect. This result also explains why we found that patients with higher stemness have a

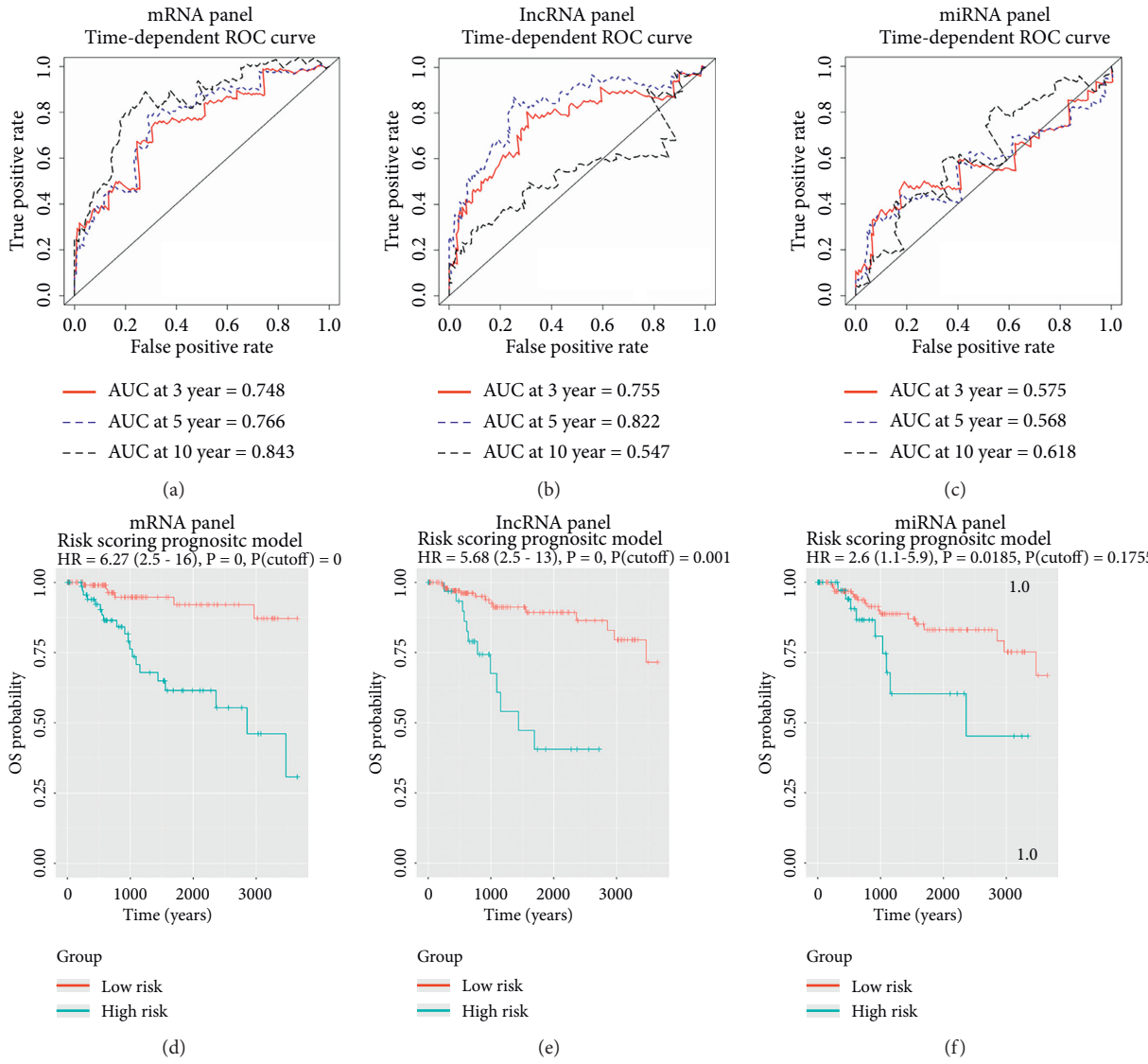

Figure 4: Predictive significance of the mRNA-, lncRNA-, and miRNA-based prognostic model in Basal subgroup patients. (a–c) Time-dependent ROC curves illustrated the prediction power of the mRNA-, lncRNA-, and miRNA-based on the prognostic model in Basal patients. (d–f) K–M curves for Basal patients showed the prediction power of the mRNA-, lncRNA-, and miRNA-based on risk scoring prognostic model.

better prognosis than patients with lower stemness. Our findings show that the differentiation of M1 and M2 is significantly related to the stemness of the tumor. Patients with high tumor stemness have a high proportion of M1 infiltration, long overall survival, and patients with low tumor dryness have a high M2 infiltration ratio and poor prognosis. This is completely in line with the findings of earlier studies on tumor immunity [15–17].

Comparing the two groups of Basal subtypes with high and low stemness, we first identified the related mRNA and lncRNA and then screened and constructed a prognostic model based on 6 mRNA or 5 lncRNA, which can be a very good predictor for the patient's overall survival. It indicates that the expression of genes in this model is related to the tumor's stemness, and it can be associated with patients' prognoses. The clinical examination of these genes may be utilized to anticipate the patients' prognoses. Among these genes, ZFP36 is negatively correlated with drug resistance and proliferation [18]. FOSB is a transcription factor that affects tumor differentiation, proliferation, and metastasis in breast cancer [19]. SERPINE1 affects metastasis by affecting EGFR signaling [20]. To our knowledge, these lncRNAs have not been reported to be associated with breast cancer. The genes identified in these prognostic models can be used as new molecular markers for Basal subtyping of breast cancer.

We used the CMap database to analyze the differentially expressed genes of two groups of patients with high and low stemness whose prognosis is significantly different in the Basal subtype and obtained some drug compounds that can respond to these gene expression changes. Most of these compounds that are positively related to stemness are drugs that inhibit tumor metastasis and progression [21–25],

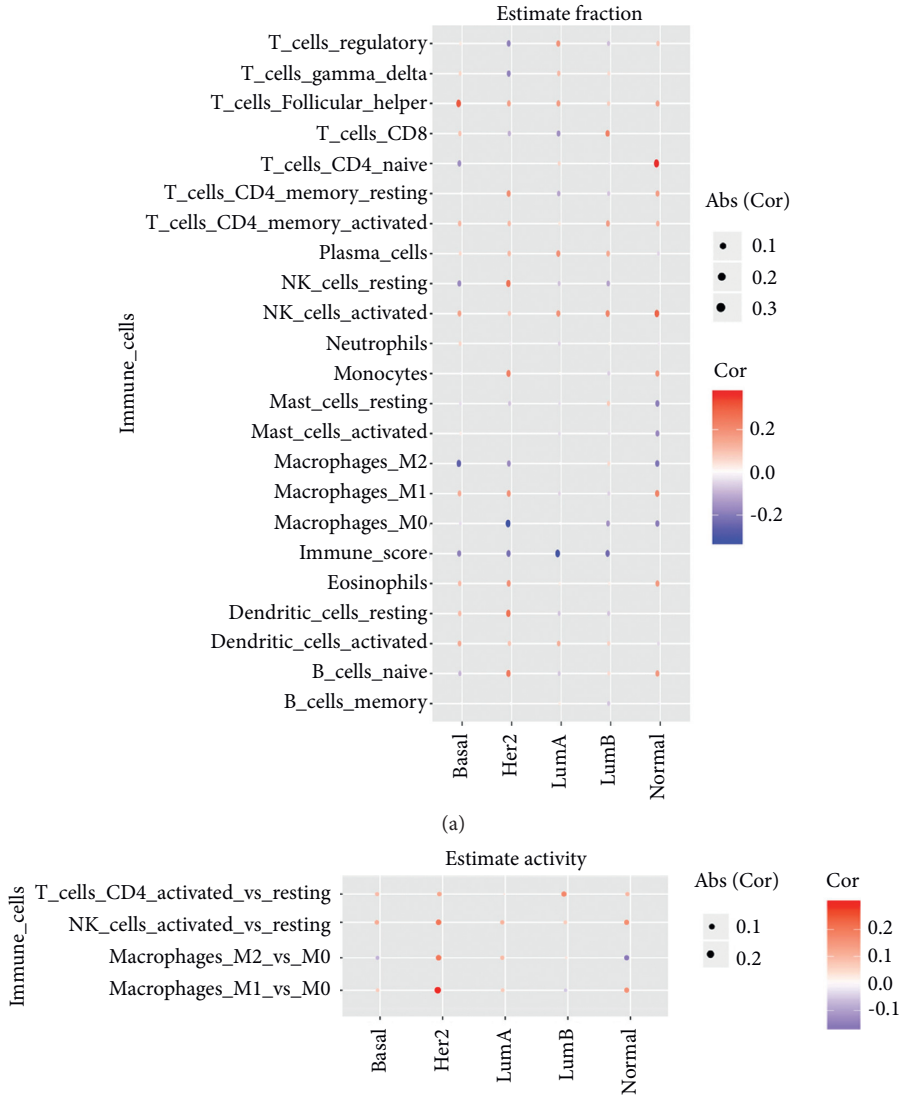

Figure 5: Continued.

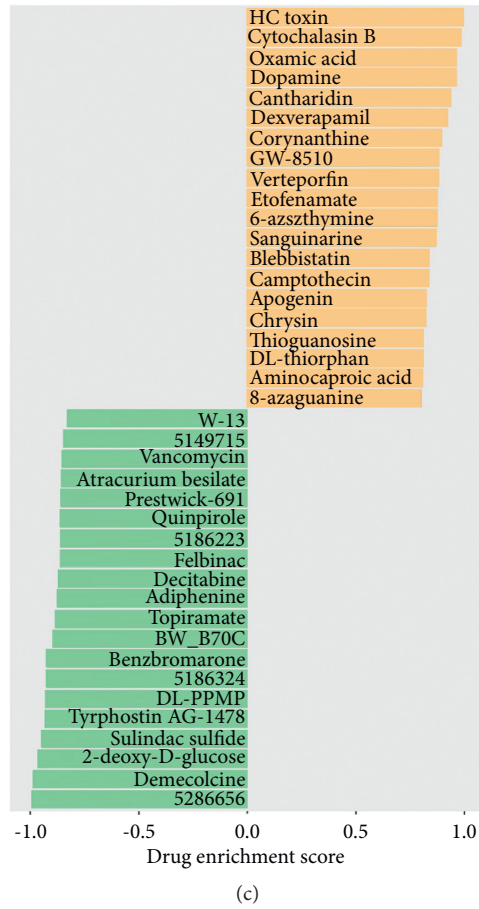

(c)

Figure 5: Relationships between stemness indices and the immune milieu in Basal patients, as well as the enrichment score for each compound (perturbagen) from the CMap for the profile of differently expressed genes in Basal patients with low- and high mRNAsi. (a) Associations between mRNAsi and CIBERSORT estimations of immune cell subgroup proportions are shown in the bar plot. (b) Associations between mRNAsi and estimated immune cell activity are shown in bar plots. Estimated immune cell activity is presented as differences between the proportions of active and resting groups. The correlations are included for macrophages, NK cells, and CD4 + T cells. (c) The top 40 enrichment scores for each chemical (perturbagen) obtained from the CMap.

indicating that these patients with high stemness are under the effective control of tumor metastasis and progression. Compounds that are negatively related to stemness are generally not used for tumor therapy, indicating that patients with low stemness need more effective tumor drug treatment to inhibit tumor progression.

Of course, this study also has some limitations. First, most of the samples in this study are Caucasian and African American (69.3%), so whether our results are also applicable to large sample data of other populations needs more data to support. Second, regarding the genes involved in our prognosis model, we only speculate that the function of these genes is associated with the occurrence and progression of breast cancer, and we need to add more experimental evidence to prove their molecular mechanism. Third, although we can explain why high-stemness tumor tissue has a better prognosis in the perspective of immune infiltration, more single-cell breast cancer data are still needed to confirm that stem-like cells in breast tumor tissues will induce or recruit more activated immune cells.

5. Conclusions

The present research is the first to refine the concept of tumor stem cell index into different subtypes of breast cancer. Among the subtypes, Basal is the one with the most closely related stem cell index and survival. We identified a stratification of Basal subtypes that are not only related to the stemness but also the prognosis and built a 6 mRNA-based or 5 lncRNA-based prognostic models for patients' overall survival. Further tumor immune infiltration and drug analysis confirmed that the two groups have different immune microenvironments and that different tumor drugs should be applied for their treatment. The classification signature in the present research might be used to improve individualized prediction of the prognosis of basal breast cancer and serve as a promising biomarker for basal breast cancer prognosis and responsiveness to differentiation treatments in clinical practice.

Data Availability

The data used to support the findings of this study are included within the article.

Conflicts of Interest

The authors declare that they have no conflicts of interest.

Authors' Contributions

Wei Chen and Zhipeng Hong contributed equally to this work.

Acknowledgments

This study was supported by Fujian Science and Technology Innovation Joint Fund Project, Fujian Province (2019Y9054).

Supplementary Materials

Figure legend S1. The relative abundance of immune cells in each sample based on the expression profile data of the sample was calculated by CIBERSORT. Table S1. Correlation analysis with mRNAsi and miRNAs. Table S2. Correlation analysis with mRNAsi and lncRNAs. Table S3. Correlation analysis with mRNAsi and mRNAs. (*Supplementary Materials*)

References

[1] F. Bray, J. Ferlay, I. Soerjomataram, R. L. Siegel, L. A. Torre, and A. Jemal, "Global cancer statistics 2018: GLOBOCAN estimates of incidence and mortality worldwide for 36 cancers in 185 countries," *CA: A Cancer Journal for Clinicians*, vol. 68, no. 6, pp. 394–424, 2018.

[2] The Cancer Genome Atlas Network, "Comprehensive molecular portraits of human breast tumors," *Nature*, vol. 490, no. 7418, pp. 61–70, 2012.

[3] T. M. Malta, A. Sokolov, A. J. Gentles et al., "Machine learning identifies stemness features associated with oncogenic dedifferentiation," *Cell*, vol. 173, no. 2, pp. 338–354 e15, 2018.

[4] K. A. Hoadley, C. Yau, D. M. Wolf et al., "Multiplatform analysis of 12 cancer types reveals molecular classification within and across tissues of origin," *Cell*, vol. 158, no. 4, pp. 929–944, 2014.

[5] K. Tomczak, P. Czerwińska, and M. Wiznerowicz, "The Cancer Genome Atlas (TCGA): an immeasurable source of knowledge," *Contemporary Oncology*, vol. 19, no. 1A, pp. A68–A77, 2015.

[6] K. Daily, S. J. Ho Sui, L. M. Schriml et al., "Molecular, phenotypic, and sample-associated data to describe pluripotent stem cell lines and derivatives," *Scientific Data*, vol. 4, no. 1, Article ID 170030, 2017.

[7] N. Salomonis, P. J. Dexheimer, L. Omberg et al., "Integrated genomic analysis of diverse induced pluripotent stem cells from the progenitor cell Biology Consortium," *Stem Cell Reports*, vol. 7, no. 1, pp. 110–125, 2016.

[8] A. J. Gentles, A. M. Newman, C. L. Liu et al., "The prognostic landscape of genes and infiltrating immune cells across human cancers," *Nature Medicine*, vol. 21, no. 8, pp. 938–945, 2015.

[9] K. Yoshihara, M. Shahmoradgoli, E. Martínez et al., "Inferring tumour purity and stromal and immune cell admixture from expression data," *Nature Communications*, vol. 4, no. 1, p. 2612, 2013.

[10] A. Subramanian, R. Narayan, S. M. Corsello et al., "A next generation connectivity map: L1000 platform and the first 1,000,000 profiles," *Cell*, vol. 171, no. 6, pp. 1437–e17, 2017.

[11] M. E. Ritchie, B. Phipson, D. Wu et al., "Limma powers differential expression analyses for RNA-sequencing and microarray studies," *Nucleic Acids Research*, vol. 43, no. 7, p. e47, 2015.

[12] A. Sokolov, E. O. Paull, and J. M. Stuart, "ONE-CLASS detection of cell states in tumor subtypes," *Pacific Symposium on Biocomputing. Pacific Symposium on Biocomputing*, vol. 21, pp. 405–416, 2016.

[13] T. Shibue and R. A. Weinberg, "EMT, CSCs, and drug resistance: the mechanistic link and clinical implications," *Nature Reviews Clinical Oncology*, vol. 14, no. 10, pp. 611–629, 2017.

[14] Y. Ge, N. C. Gomez, R. C. Adam et al., "Stem cell lineage infidelity drives wound repair and cancer," *Cell*, vol. 169, no. 4, pp. 636–650 e14, 2017.

[15] T. O. Jensen, H. Schmidt, H. J. Møller et al., "Macrophage markers in serum and tumor have prognostic impact in American Joint Committee on Cancer stage I/II melanoma," *Journal of Clinical Oncology*, vol. 27, no. 20, pp. 3330–3337, 2009.

[16] H. Hu, J.-J. Hang, T. Han, M. Zhuo, F. Jiao, and L.-W. Wang, "The M2 phenotype of tumor-associated macrophages in the stroma confers a poor prognosis in pancreatic cancer," *Tumor Biology*, vol. 37, no. 7, pp. 8657–8664, 2016.

[17] A. Kawachi, H. Yoshida, S. Kitano, Y. Ino, T. Kato, and N. Hiraoka, "Tumor-associated $CD204^{+}$M2 macrophages are unfavorable prognostic indicators in uterine cervical adenocarcinoma," *Cancer Science*, vol. 109, no. 3, pp. 863–870, 2018.

[18] W. Xia, Y. Liu, Y. Du, T. Cheng, X. Hu, and X. Li, "MicroRNA-423 drug resistance and proliferation of breast cancer cells by targeting ZFP36," *OncoTargets and Therapy*, vol. 13, pp. 769–782, 2020.

[19] W.-X. Li, K. He, L. Tang et al., "Comprehensive tissue-specific gene set enrichment analysis and transcription factor analysis of breast cancer by integrating 14 gene expression datasets," *Oncotarget*, vol. 8, no. 4, pp. 6775–6786, 2017.

[20] I. Azimi, R. M. Petersen, E. W. Thompson, S. J. Roberts-Thomson, and G. R. Monteith, "Hypoxia-induced reactive oxygen species mediate N-cadherin and SERPINE1 expression, EGFR signalling and motility in MDA-MB-468 breast cancer cells," *Scientific Reports*, vol. 7, no. 1, Article ID 15140, 2017.

[21] H. Y. Zhao, Y. H. Ren, X. B. Ren, and Y. Wang, "Diprophylline inhibits non-small cell lung cancer A549 cell proliferation and migration, and promotes apoptosis, by downregulating PI3K signaling pathway," *Oncology Letters*, vol. 17, no. 1, pp. 857–862, 2019.

[22] M. Hu, S. Peng, Y. He et al., "Lycorine is a novel inhibitor of the growth and metastasis of hormone-refractory prostate cancer," *Oncotarget*, vol. 6, no. 17, pp. 15348–15361, 2015.

[23] T. Srdic-Rajic, K. Nikolic, M. Cavic et al., "Rilmenidine suppresses proliferation and promotes apoptosis via the mitochondrial pathway in human leukemic K562 cells," *European Journal of Pharmaceutical Sciences*, vol. 81, pp. 172–180, 2016.

[24] C. Kang, S. Dhillon, and E. D. Deeks, "Trifluridine/tipiracil: a review in metastatic gastric cancer," *Drugs*, vol. 79, no. 14, pp. 1583–1590, 2019.

[25] J. Dhami, E. Chang, and S. S. Gambhir, "Withaferin A and its potential role in glioblastoma (GBM)," *Journal of Neuro-Oncology*, vol. 131, no. 2, pp. 201–211, 2017.

Hindawi
Journal of Oncology
Volume 2022, Article ID 7188972, 10 pages
https://doi.org/10.1155/2022/7188972

Research Article

Expression of CD47 in Endometrial Cancer and Its Clinicopathological Significance

Mei Yang,[1,2] **Chunfan Jiang**,[3] **Lin Li**,[2] **Hui Xing**,[2] **and Li Hong**[1]

[1]*Department of Obstetrics and Gynecology, Renmin Hospital of Wuhan University, Wuhan 430060, China*
[2]*Department of Obstetrics and Gynecology, Xiangyang Central Hospital, Affiliated Hospital of Hubei University of Arts and Sciences, Xiangyang 441021, China*
[3]*Department of Pathology, Xiangyang Central Hospital, Affiliated Hospital of Hubei University of Arts and Sciences, Xiangyang 441021, China*

Correspondence should be addressed to Li Hong; dr_hongli@whu.edu.cn

Received 1 December 2021; Revised 11 January 2022; Accepted 31 January 2022; Published 4 March 2022

Academic Editor: Fu Wang

Purpose. To study the prognostic value of CD47 in endometrial carcinoma (EC) and its correlation with clinicopathological variables. *Methods*. Next-generation sequencing data from The Cancer Genome Atlas was analyzed with the Kaplan–Meier curve, Cox's regression model, and ROC curve. A cohort of 544 specimens, including 344 cases of endometrial cancer, 92 cases of endometrial hyperplasia (EH), and 118 cases of normal endometrium (NE), were evaluated with immunohistochemistry and analyzed with statistical methods. *Results*. For TCGA data, CD47 expression in EC was considerably greater than in NE tissues. CD47 expression correlated significantly with age, clinical stage, histological grade, histological type, and menopause status. Kaplan–Meier analysis and Cox's regression model revealed that elevated CD47 expression was positively correlated with a poorer prognosis. ROC curve showed that CD47 had high specificity and sensitivity as an independent prognosis factor. In our cohort, CD47 expression was significantly stronger in EC than in NE. The strongly positive expression of CD47 could be observed in EC, but none was observed in NE. The CD47 expression rate ranked in descending order: atypical endometrium hyperplasia, complex endometrium hyperplasia, and simple endometrium hyperplasia. Atypical endometrium hyperplasia CD47 expression rate was much greater than either simple endometrium hyperplasia or complex endometrium hyperplasia. A substantial connection existed amongst CD47 expression and the clinical stage. Kaplan–Meier survival analysis demonstrated that CD47 expression was connected with overall survival (OS). Univariate analysis instead of the multivariate analysis revealed that CD47 expression was associated significantly with prognosis. *Conclusions*. CD47 is a critical part of the progress of pathogenesis in EC. CD47 expression correlates with multiple clinicopathological variables and is a potential prognostic risk factor.

1. Introduction

Endometrial cancer (EC) is one of the most common female reproductive system malignant tumors with distinct biological behavior. About 634 per 100,000 newly diagnosed cases and 21.8 per 100,000 mortalities in 2017 were claimed by this disease in China [1].

EC is traditionally categorized into two histological types. Type I EC (endometrioid carcinoma) is the most common and is related to estrogen excess, and this type generally belongs to low grade. Type II EC consisting of serous carcinoma, clear cell carcinoma, and others is much more likely to be high grade [2]. EC can be early diagnosed by fractional curettage or endometrial biopsy with the onset symptom of postmenopausal vaginal bleeding. However, about 30% of advanced stage endometrial cancer diagnosed patients do not improve long-term survival even with recommended treatment strategy including surgery, platinum-based chemotherapy, and radiotherapy [3, 4]. The application of CA-125 in clinical practice may be useful in advanced stages and serous carcinoma [5]; however, there is no biomarker with special sensitivity and specificity to predict prognosis and therapeutic effects. Thus, exploring the pathological mechanism and looking for desirable

biomarkers to increase the rate of early diagnosis of EC are the key to ameliorate prognosis.

CD47 is a transmembrane immune-regulatory protein expressed on a variety of cell membranes [6]. This molecule has a ligand to interact with signal regulatory protein alpha (SIRPα) on neutrophils, dendritic cells, macrophages, and T and B lymphocytes to activate various cellular metabolisms, such as nitric oxide, calcium homeostasis, and hydrogen sulfide biosynthesis [7]. The overexpression of CD47 on the aged and superfluous cells initiates the phagocytosis by macrophages to keep the vitality of a healthy cell population. In ovarian carcinoma, breast carcinoma, melanoma, and gastric carcinoma, overexpression of CD47 was found to correlate with poor survival [8–12]. On the contrary, inhibiting CD47 expression could increase the ability of macrophages to eradicate different types of cancer [13]. These exciting experiment results make CD47 a promising new biomarker for cancer therapy and prognosis assessment. Although CD47 has been involved in cancer progression, at the cell level in vitro CD47 was discovered to be a critical part in enhancing cell migration ability, viability, and inhibiting apoptosis in endometrial carcinoma cells via the PI3K_Akt_mTOR Signaling Pathway [14]. Its prognostic value and its correlation with clinicopathological variables in large numbers of endometrial cancer stay vague.

This study explored CD47 expression and available clinical variables from The Cancer Genome Atlas (TCGA) data and also detected CD47 expression in EC, EH, and NE with our collected samples to provide a theoretical basis for screening a potential biomarker to evaluate prognosis and promote new drug development.

2. Materials and Methods

2.1. TCGA Data Analyses. RNAseq data including 552 ECs and 35 adjacent cancer tissues in HTSeq-FPKM (Fragments Per Kilobase Per Million) format and the clinical records were downloaded from TCGA. Some items of the clinical records were incomplete. The RNAseq data in the FPKM format was adapted to the TPM (transcripts per million reads) format and conducted with Log2 conversion before bioinformatics analysis. Preprocession and bioinformatics analysis of the downloaded raw data were conducted using the *R* 3.6.3 software.

2.2. Ethics Approval. The research was conducted following the Helsinki Declaration as well as given approval from the Ethics Committee of Xiangyang Central Hospital (reference number 2021005). Medical data were completely anonymized. Investigators were blinded for all the clinical information during the analyses.

2.3. Case Selection. A group of 544 formalin-fixation paraffin-embedded specimens, containing 344 EC cases, 92 endometrial hyperplasia cases, and 118 normal endometrium cases, were obtained from Xiangyang Central Hospital, Hubei province, from 2006 to 2011 with needed clinical data. All the patients were Han People. The age of endometrial cancer patients was between 29 and 83 years, mean ± SD (55.05 ± 8.70) years; endometrial hyperplasia patients between 29 and 68 years, mean ± SD (45.80 ± 6.22) years; normal endometrium participants between 24 and 57 years, mean ± SD (39.86 ± 8.32) years. EC information on clinicopathological variables was listed in Table 1. EH included 57 cases of simple hyperplasia, 15 cases of complex hyperplasia, and 20 cases of atypical hyperplasia. NE comprised 83 cases of proliferative phase and 35 cases of secretory phase. Two senior pathologists examined all cases individually for a second time to guarantee the diagnosis precision. For EC cases, tissue blocks with abundant carcinoma and adjacent normal endometria were selected.

2.4. Immunohistochemistry. The Ventana Benchmark ULTRA automated staining system (Ventana Medical Systems, Tucson, AZ) CD47 was utilized for immunohistochemical staining implemented with 3 μm thick sections following manufacturer protocol. Mouse monoclonal anti-CD47 antibody (Clone No. 12730, 1 : 100 dilution, Santa Cruz) was the primary antibody used. The reaction was visualized with 3,3′-diaminobenzidine (DAB). Determined EC cases with CD47 strong expression were selected as the positive control. PBS was applied as a negative control in place of the primary antibody. Pictures were scanned with TEKsqray Digital Slide Scanner (Shengqiang Tech Ltd., Shenzhen, China).

2.5. Immunohistochemical Scoring. Positive immunostainings were located on membranes and cytoplasm of cancer cells, and any immunostainings in endothelial, lymphocytic, or desmoplastic tissue were discounted. Scoring of CD47 immunostaining was completed as earlier explained using minor modification [15]. Positive cell intensity and percentage were obtained by counting cancer cells under 400 × magnification from 10 randomly chosen visual fields. The intensity of immunostaining was scored 0, 1, 2, 3, accounting for no signal, weak signal (light yellow), moderate signal (yellowish-brown), and strong signal (brown), individually. Scores of 0–4 for positive cell percentage were 0=<5%, 1 = 5%–25%, 2 = 21%–50%, 3 = 51%–75%, and 4=>75%. The final results for a single case were established by the sum of the two scores: negative (−) 0 or 1 sum, weakly positive (+) 2 or 3 sum, moderately positive (++) 4 or 5 sum, and strongly positive (+++) greater than 6 sum. Two senior pathologists assessed all sections independently. The results were judged by a third pathologist once a disagreement occurred.

2.6. Data Statistics. The correlation amongst CD47 expression and clinicopathological variables was tested by chi-square tests and Fisher exact test. The Kaplan–Meier curve presented the survival probability and was analyzed using the log-rank test. Cox's regression model identified the prognostic risk factors. The specificity and sensitivity of CD47 as an independent prognostic factor were evaluated with the performance of the ROC curve analysis. $P < 0.05$ was deemed statistically significant. Statistical calculation

Table 1: Baseline characteristics of EC patients.

Characteristics	Levels	N (%)
n		344
Age, mean ± SD	29–83	55.05 ± 8.70
Histological type	I	325 (94.5%)
	II	19 (5.5%)
Clinical stage	1	247 (71.8%)
	2	62 (18%)
	3	33 (9.6%)
	4	2 (0.6%)
Histological grade	G1	190 (55.2%)
	G2	96 (27.9%)
	G3	58 (16.9%)
Infiltration depth	<50%	270 (78.5%)
	>50%	74 (21.5%)
P53	Mutant	79 (23%)
	Wild	265 (77%)
Ki67	<50%	268 (77.9%)
	>50%	76 (22.1%)
Lymph node metastasis	Yes	31 (9.0%)
	No	184 (53.5%)
	No lymph node cleaning	129 (37.5%)

was done using the SPSS 23.0 software (IBM, Chicago, IL, USA).

3. Results

3.1. Upregulation of CD47 Expression in EC Using TCGA Data. To explore CD47 expression levels in EC, we analyzed TPM values with Log2 conversion. The expression of CD47 was higher than that of normal endometrial tissues ($p < 0.001$, Figure 1(a)).

3.2. Correlation between CD47 Expression and Clinicopathological Variables Using TCGA Data. CD47 expression correlated significantly with histological grade ($p < 0.001$), histological type ($p < 0.001$), age (≤60 vs. >60, $p < 0.001$), clinical stages (stages I + II vs. stages III + IV, $p = 0.024$), and menopause status ($p = 0.002$, Table 2). There were no significant differences in weight, height, BMI, tumor invasion, and hormones therapy between the low and high CD47 expression group ($p > 0.05$, Table 2).

3.3. The Prognostic Value of CD47 Expression in EC Using TCGA Data. Kaplan–Meier analysis revealed that high CD47 expression was positively correlated with a poorer prognosis (HR = 2.03, CI = 1.31–3.16, $p < 0.001$, Figure 1(b)). Subgroup OS analysis pointed out that patients >60, stages III + IV, serous carcinoma, BMI >30, diabetes, and histological grade G3 combined with the high CD47 expression had a poorer prognosis when weighed against those with the low CD47 expression ($p < 0.01$, Figures 1(c)–(h)).

Univariate regression analysis showed that clinical stage (stages I and II vs. stages III and IV), age (>60 vs. ≤60), histological type (mixed and serous vs. endometrioid), histologic grade (G3 vs. G1 and G2), tumor invasion (≥50 vs. <50), and CD47 (low vs. high) were the factors influencing OS ($p < 0.05$). Multivariate regression analysis revealed that the clinical stage and CD47 were the independent risk factors for EC progression ($p < 0.05$, Table 3).

A ROC curve showed that CD47 could be chosen as a biomarker to foresee EC prognosis with high specificity and sensitivity (AUC = 0.952, CI = 0.927–0.977, Figure 1(i)).

3.4. CD47 Expression in Normal Endometrium and Endometrial Hyperplasia and Endometrial Carcinoma. Two CD47 expression statuses including positivity and strong positivity were set to look for a suitable cut-off value to distinguish a significant difference between groups. CD47 positive and strongly positive expression rates in the endometrial cancer group were considerably greater than the endometrial hyperplasia group and the normal endometrium group ($P < 0.01$). A declining trend of CD47 positive and strongly positive expression rate existed from EC to EH and then to NE. Comparing between the simple hyperplasia group and the complex hyperplasia group, CD47 positive and strongly positive expression rates did not show significant differences; however, comparing between either of the two groups and the atypical hyperplasia group, the positive and strongly positive expression rates showed significant differences ($P < 0.01$). CD47 positive and strongly positive expression did not show significant differences between the proliferation phase group and the secretory phase group ($P > 0.05$, Table 4). Examples of CD47 immunostainings in EC, EH, and NE were represented in Figure 2.

3.5. Relationship between CD47 Expression and Clinicopathological Variables of Endometrial Cancer. CD47 positive and the strongly positive expression rates did not show significant differences in EC types, histological types, histological grade, and Ki67 expression. Significant differences existed among different clinical stages ($P < 0.01$). For infiltration depth, lymph node metastasis, and P53 expression, CD47 positive and strong positive expression rates revealed different results. For CD47 strongly positive expression rates, a significant difference existed among infiltration depth and lymph node metastasis groups; however, there was no significant difference among these two groups for the positive expression rate of CD47 ($P < 0.01$). Comparing between P53 wild-type and mutant type, the CD47 positive expression rate was significantly different ($P < 0.01$); however, there was no significant variation for the strongly positive CD47 expression rate (Table 5).

3.6. Prognosis Analysis. Kaplan–Meier survival analysis demonstrated that endometrial cancer patients with positive CD47 expression had considerably greater mortality than those with no positive CD47 expression ($P < 0.01$). Subgroup Kaplan–Meier survival analysis demonstrated that, in stages III-IV and Ki67 > 50% groups, high CD47 expression correlated significantly with a poorer prognosis ($P < 0.01$, Figure 3).

Univariate analysis showed that age, CD47 expression, clinical stage, histological grade, infiltration, lymph

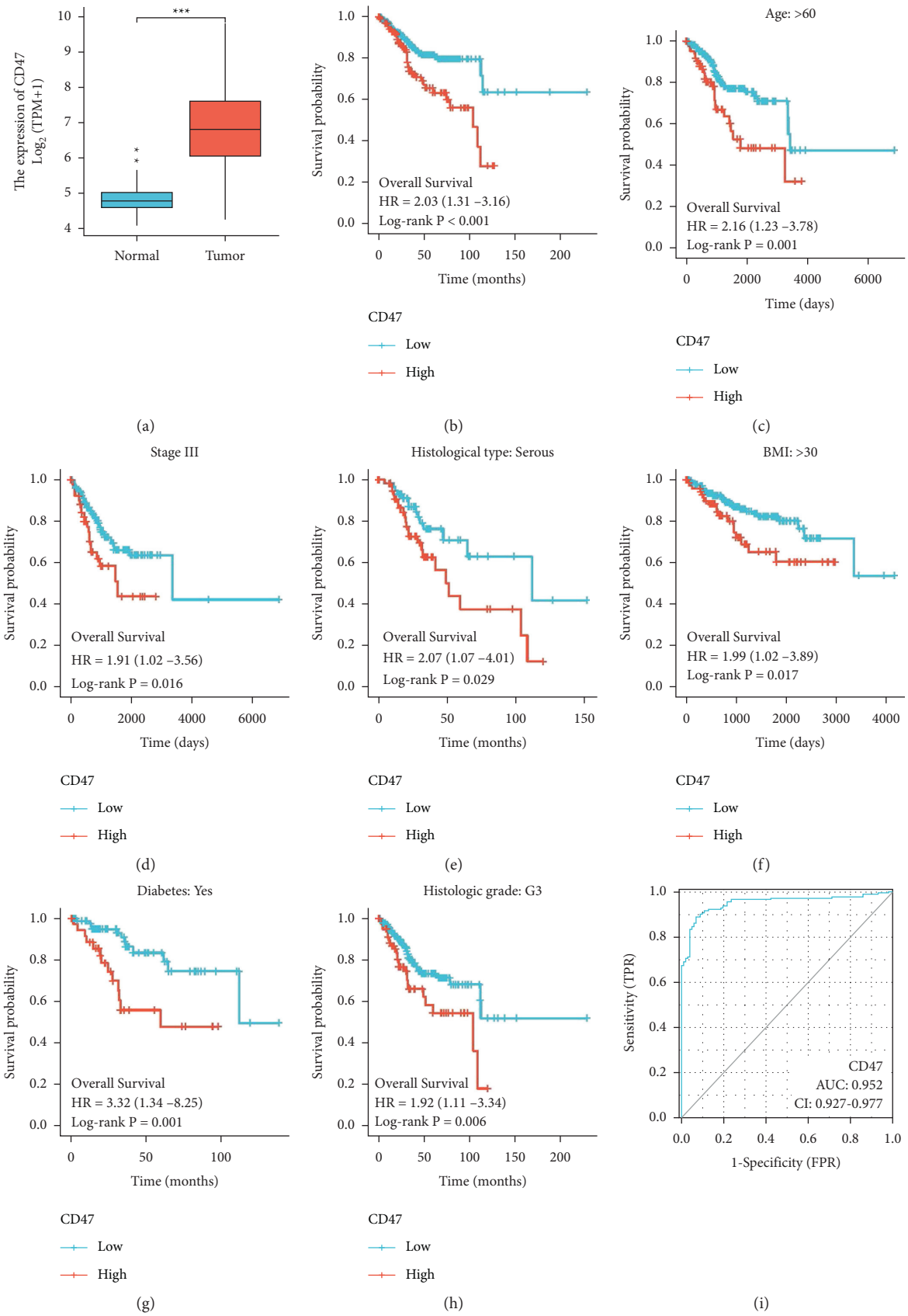

Figure 1: Analysis of CD47 expression and prognosis in EC using TGCA data. (a) CD47 expression differences between NE and EC are shown in the box-and-whisker plot. (b) Overall survival curve. Subgroup survival curve according to age >60: (c) stage III, (d) histological type: serous, (e) BMI >30, (f) diabetes, (g) histological grade: G3, and (h) ROC curve according to CD47 expression (i).

Table 2: CD47 expression in endometrial cancer with different clinicopathological variables using TCGA dada.

Characteristics	Low expression of CD47 (%)	High expression of CD47 (%)	*P* value
n	276	276	
Age, mean ± SD	62.04 ± 11.79	66.12 ± 9.9	
Clinical stage			0.024
Stages I + II	209 (37.8%)	184 (33.3%)	
Stages III + IV	57 (12.1%)	92 (16.7%)	
Age			<0.001
≤60	126 (23%)	80 (14.6%)	
>60	149 (27.1%)	194 (35.3%)	
Weight (Kg)			0.057
≤80	111 (21%)	132 (25%)	
>80	155 (29.4%)	130 (24.6%)	
Height (cm)			0.364
≤160	119 (22.8%)	128 (24.5%)	
>160	145 (27.7%)	131 (25%)	
BMI			0.730
≤30	105 (20.2%)	107 (20.6%)	
>30	158 (30.4%)	149 (28.7%)	
Histological type			<0.001
Endometrioid	245 (44.4%)	165 (29.9%)	
Mixed	9 (1.6%)	15 (2.7%)	
Serous	22 (4%)	96 (17.4%)	
Histologic grade			<0.001
G1	60 (11.1%)	38 (7%)	
G2	73 (13.5%)	47 (8.7%)	
G3	141 (26.1%)	182 (33.6%)	
Tumor invasion (%)			0.882
<50	139 (29.3%)	120 (25.3%)	
≥50	113 (23.8%)	102 (21.5%)	
Menopause status			0.002
Pre	27 (5.3%)	8 (1.6%)	
Peri	11 (2.2%)	6 (1.2%)	
Post	216 (42.7%)	238 (47%)	
Hormones therapy			1.000
No	148 (43%)	149 (43.3%)	
Yes	23 (6.7%)	24 (7%)	

Table 3: Univariate and multivariate analysis of the prognosticators of EC using TCGA data.

Characteristics	Total (n)	Univariate analysis		Multivariate analysis	
		HR (95% CI)	*P* value	HR (95% CI)	*P* value
Clinical stage (stages I and II vs. stages III and IV)	542	3.270 (2.145–4.984)	<0.001	2.671 (1.266–5.637)	<0.001
BMI (>30 vs. ≤30)	519	0.967 (0.636–1.470)	0.876		
Age (>60 vs. ≤60)	549	1.847 (1.160–2.940)	<0.010	1.301 (0.625–2.711)	0.482
Weight (>80 vs. ≤80)	528	1.060 (0.699–1.607)	0.784		
Height (>160 vs. ≤160)	523	1.153 (0.758–1.753)	0.507		
Histological type (mixed and serous vs. endometrioid)	552	2.628 (1.746–3.957)	<0.001	1.620 (0.772–3.402)	0.202
Histologic grade (G3 vs. G1 and G2)	541	3.281 (1.907–5.643)	<0.001	1.344 (0.618–2.923)	0.455
Tumor invasion (%) (≥50 vs. <50)	474	2.813 (1.744–4.535)	<0.001	1.222 (0.603–2.475)	0.578
Menopause status (post vs. pre and peri)	506	1.050 (0.507–2.175)	0.895		
Diabetes (yes vs. no)	451	1.172 (0.731–1.878)	0.510		
Hormones therapy (yes vs. no)	344	0.801 (0.380–1.689)	0.560		
CD47 (low vs. high)	552	1.021 (1.010–1.032)	0.015	1.018 (1.007–1.029)	0.021

node metastasis, and Ki67 index correlated significantly with prognosis ($P < 0.05$). However, only the clinical stage and lymph node metastasis show a significant correlation with prognosis by multivariate analysis ($P < 0.05$, Table 6).

4. Discussion

The immune checkpoint is a type of costimulatory and inhibitory molecule responsible for antigen recognition regulation of T cell receptors (TCR) in the immune response

Table 4: CD47 expression in normal endometrium, endometrial cancer, and endometrial hyperplasia.

Tissue type	Case	-	+	++	+++	Positive cases	Positive rate (%)	Strong positive cases	Strong positive rate (%)
Endometrial cancer	344	85	143	85	31	259	75.29*	116	33.72 *
Endometrial hyperplasia	92	65	23	4	0	27	29.34	4	4.34
Simple hyperplasia	57	49	8	0	0	8	14.04**	0	0
Complex hyperplasia	15	11	4	0	0	4	26.67	0	0
Atypical hyperplasia	20	5	11	4	0	15	75.00	4	20.00
Normal endometrium	118	89	29	0	0	29	24.58	0	0
Proliferative phase	83	66	17	0	0	17	20.48	0	0
Secretory phase	35	23	12	0	0	12	34.29	0	0

Note. * weighed against endometrial hyperplasia group and normal endometrium group, $P < 0.01$; ** weighed against the atypical hyperplasia group, $P < 0.01$.

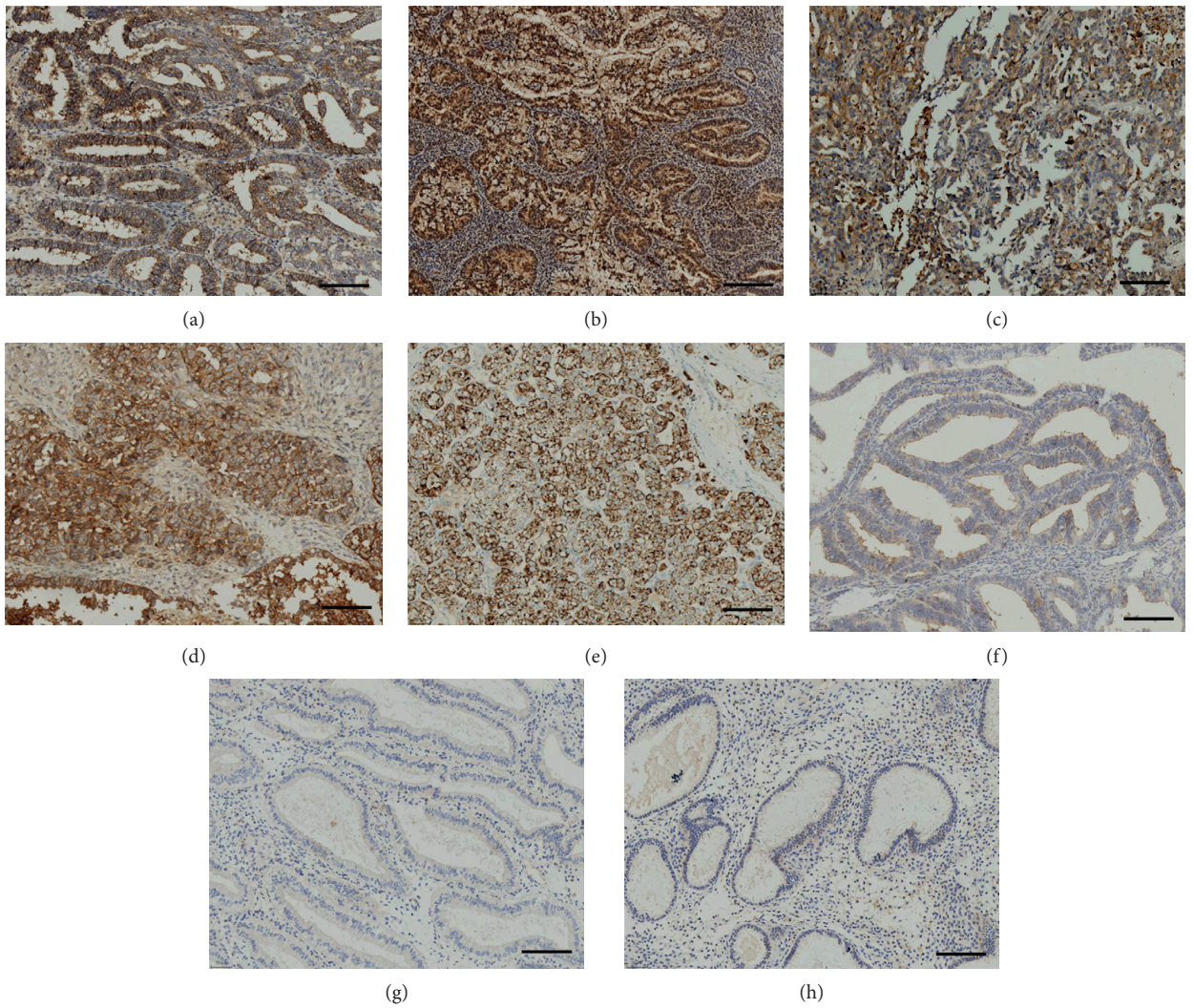

Figure 2: Representative illustrations of the CD47 expression in EC, EH, and NE with immunohistochemistry. (a) G1 endometrioid carcinoma. (b) G2 endometrioid carcinoma. (c) G3 endometrioid carcinoma. (d) Serous carcinoma. (e) Clear cell carcinoma. (f) Atypical endometrial hyperplasia. (g) Proliferation phase endometrium. (h) Secretory phase endometrium. 100X pictures were presented. Scale bars, 300 μm.

process [16]. By dysregulating immune checkpoint-related proteins, cancer cells are able to easily escape immune attacks. Immune checkpoint inhibitors block immune checkpoint-related proteins from binding with their partners and thereby allow the T-cells to kill cancer cells [17]. Nowadays, the most successful example is the development of anti-PD-1/PD-L1 antibodies. Durvalumab, atezolizumab, nivolumab, and pembrolizumab were put into a clinic in

Table 5: CD47 expression in endometrial cancer with different clinicopathological variables.

Features		Cases	Positive cases	Positive rate (%)	Strong positive cases	Strong positive rate (%)	*P* value (positive)	*P* value (strong positive)
EC types	I	321	244	76.01	106	33.02	0.315	0.362
	II	23	15	65.22	10	43.48		
Histological type	Endometrial adenocarcinoma	321	244	76.01	106	33.02	0.335	0.46
	Serous carcinoma	14	10	71.43	7	50.00		
	Clear cell carcinoma	9	5	55.56	3	33.33		
Infiltration depth	<1/2 muscle layer	270	197	72.96	62	22.96	0.068	<0.01
	>1/2 muscle layer	74	62	83.78	36	48.65		
Clinical stage	I	247	171	69.23	51	20.65	<0.01	<0.01
	II	62	58	93.55	39	62.90		
	III + IV	35	30	85.71	26	74.29		
Histological grade	G1	190	146	76.84	60	31.58	0.714	0.265
	G2	96	71	73.96	31	32.29		
	G3	58	42	72.41	25	43.10		
Lymph node metastasis	No	184	134	72.83	50	27.17	0.406	<0.01
	Yes	31	26	83.87	20	64.51		
	No lymph node cleaning	129	99	76.74	46	35.66		
P53	Mutant	79	49	62.03	24	30.38	0.03	0.501
	Wild type	265	210	79.25	92	34.72		
Ki67 proliferation index	>50%	76	56	73.68	27	35.53	0.763	0.784
	<50%	268	203	75.75	89	33.20		

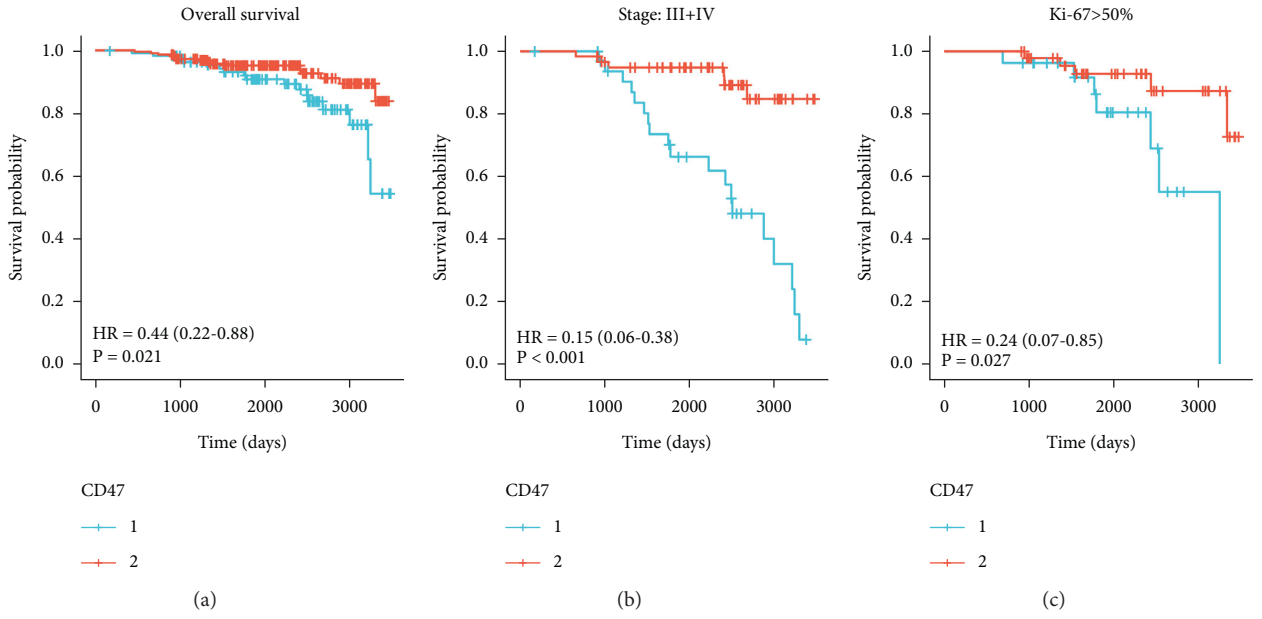

Figure 3: Kaplan–Meier survival analysis of EC patients with various CD47 expression levels. (a) Overall survival curve. (b) Subgroup survival according to stages III + IV. (c) Ki67 > 50%.

succession, and many patients get to benefit from them with gastric cancer, lung cancer, and esophagus cancer [18]. Yet, not all PD-L1-positive cancers react to anti-PD-1/PD-L1 antibodies, and side effects such as rash, diarrhea, and colitis occur in some patients. The success of anti-PD-1/PD-L1 antibody development and its drawback make immune checkpoint a most potential research area, and scientists are still on the hunt for a new target.

CD47 like PD-L1 is widely overexpressed on the membrane of many solid tumors, including triple-negative breast cancer, ovary cancer, bladder cancer, gastric cancer, and so on [8–10, 12, 19]. CD47 overexpression is a useful strategy for solid tumors to escape from immune attack by delivering a "do not eat me" signal to avoid phagocytosis via the binding of SIRPα expressed on phagocytes [6, 7]. Currently, Hu5F9-G4, a humanized anti-CD47 antibody, is

Table 6: Screening of prognosticators in EC patients with univariate and multivariate analysis.

Characteristics	n	HR (95% CI) univariate analysis	*P* value univariate analysis	HR (95% CI) multivariate analysis	*P* value multivariate analysis
Age	344	1.066 (1.026–1.108)	<0.001	1.031 (0.984–1.080)	0.201
CD47 (positive vs. negative)	344	0.438 (0.218–0.881)	0.021	0.754 (0.349–1.630)	0.473
Cancer type (I vs. II)	344	10.275 (5.011–21.070)	<0.001	1.928 (0.629–5.907)	0.251
Clinical stage (I and II vs. III and IV)	344	3.907 (2.714–5.625)	<0.001	2.410 (1.280–4.535)	0.006
Histological grade (G3 vs. G1 and G2)	344	2.491 (1.756–3.532)	<0.001	0.861 (0.463–1.601)	0.636
Infiltration depth (<1/2 vs. >1/2)	344	4.533 (2.250–9.131)	<0.001	0.432 (0.129–1.438)	0.171
P53 (mutant vs. wild type)	344	0.777 (0.349–1.733)	0.538		
Ki67 (>50% vs. <50%)	344	2.244 (1.094–4.603)	0.028	1.218 (0.545–2.719)	0.631
Lymph node metastasis (yes vs. no)	344	13.845 (6.872–27.894)	<0.001	4.675 (1.358–16.096)	0.015

undergoing evaluation in a phase I trial, and it was reported that Hu5F9-G4 could significantly suppress the progression of advanced solid malignancies [20]. It brings a new hope for doctors and patients to treat solid malignancies. Advanced EC patients also need a new medicine in their drug box, and thereby, evaluating the prognostic value of CD47 expression on EC appears very important.

In this study, we first analyzed the TCGA data and discovered that CD47 expression in EC was drastically greater than in normal endometrial tissues. Additional analysis of the relationship amongst CD47 expression and clinicopathological variables demonstrated that CD47 expression correlated significantly with age, clinical stage, histological type, histological grade, and menopause status. Kaplan–Meier analysis revealed that high CD47 expression was positively correlated with a poorer prognosis. Subgroup OS analysis showed that age >60, stages III + IV, serous carcinoma, BMI >30, diabetes, and histological grade G3 combined with the high CD47 expression had a poorer prognosis. Univariate and multivariate analysis indicated that only the clinical stage and CD47 could be the independent risk factors to evaluate the prognosis of EC. A ROC curve showed that CD47 had high specificity and sensitivity as an independent prognosis factor.

Sercan et al. stated that CD47 expression was considerably higher in EC and was associated with histologic grade [21]. However, CD47 expression was not in association with OS and other clinicopathological variables. Sercan's conclusions do not exactly coincide with our observation with TCGA data.

We next analyzed the CD47 expression in our collected cohort. It was discovered that the CD47 expression is considerably stronger in endometrial cancer than in normal endometrium. The strongly positive expression of CD47 could be observed in endometrial cancer, but none was observed in normal endometrium. We also explored the CD47 expression in endometrial hyperplasia. Endometrial hyperplasia could be divided into simple endometrium hyperplasia, complex endometrium hyperplasia, and atypical endometrium hyperplasia. Atypical endometrium hyperplasia is a precancerous lesion. The CD47 expression ranks in descending order, atypical endometrium hyperplasia > complex endometrium hyperplasia > simple endometrium hyperplasia. No significant difference existed between simple endometrial hyperplasia and complex endometrial hyperplasia; however, the atypical endometrium hyperplasia CD47 expression rate was much greater compared to either simple endometrium hyperplasia or complex endometrium hyperplasia. The CD47 expression in precancerous lesions was barely reported in published literature, and our results support that CD47 possibly takes part in oncogenesis and has a critical position in the progression from normal, hyperplasia, and atypia then to EC.

By analyzing our cohort, a significant correlation existed between CD47 expression and the clinical stage. However, the establishment of a significant correlation between infiltration, lymph node metastasis, P53, and CD47 expression depended on the choice of cut-off value (positive or strongly positive). Kaplan–Meier survival analysis demonstrated that CD47 expression was linked with OS. Subgroup Kaplan–Meier survival analysis demonstrated that stages III-IV and Ki67 > 50%, combined with high CD47 expression correlated significantly with a poorer prognosis. Univariate analysis showed that age, CD47 expression, clinical stage, histological grade, infiltration, lymph node metastasis, and Ki67 index correlated significantly with prognosis. However, only the clinical stage and lymph node metastasis show a significant correlation with prognosis by multivariate analysis.

Comparing the results from TCGA data with our cohort, the clinical stage is the most stable prognosticator compared to others with different statistical methods. Routine clinical practices have demonstrated that the clinical stage is a scientific and reasonable prognosticator with overall consideration of infiltration depth, lymph node invasion, and distal metastasis. CD47 showed a significantly different expression in descending order from normal and atypia then to EC. Survival analysis discovered that high CD47 expression had a poorer prognosis. CD47 expression had a significant correlation with several clinicopathological variables especially the clinical stage. Cox's regression model also showed that CD47 had an important prognosis value for EC except for multivariable analysis with our cohort. More serious carcinoma and cases with rare pathological types were included in TCGA data, and to ensure the integrity of clinical data, some cases with incomplete information were not incorporated in our cohort. These data differences may account for the reasons of nonstatistical significance in multivariable analysis with our cohort.

Several studies had reported that the CD47 overexpression is associated with poor prognosis and clinicopathological variables in different cancer patients [8, 9, 11]. Cell and animal studies revealed that downregulation of CD47 significantly suppressed the proliferation and metastasis of cancer cell lines and caused tumor reduction in heterotopic and orthotopic xenograft mouse models [22]. Further researches on molecular mechanisms showed that activated STAT3 pathway by IL-6 upregulated CD47 expression in hepatocellular carcinoma cell lines, and the IL-6-STAT3 axis blockage reduced cancer cells' antiphagocytic ability via downregulation of CD47 expression [23]. Literature of molecular mechanisms on the pathogenesis of EC is rare. PI3K/Akt/mTOR signaling pathway activation via upregulation of CD47 expression enhances cellular viability and migration ability but suppresses endometrial carcinoma cell apoptosis [14]. Blocking the CD47-SIRPa interaction promotes phagocytosis of polarized-M2 macrophages to suppress tumor progression [24]. These experiment results demonstrated that CD47 could be a critical part of the progress of pathogenesis in EC.

Several drawbacks existed in our study. In our cohort, multivariable Cox's regression did not show CD47 correlated with prognosis. We have explored the possible reasons for nonstatistical significance. Multiple clinicopathological variables influence the relationship between CD47 and prognosis. More specimens particularly with rare pathological types should be brought into our study and maybe achieve a possible positive result. A standard cut-off like PD-L1 and HER-2 is important to evaluate immunohistochemistry and predict the relationship between biomarkers and clinicopathological variables [25, 26]. Multiple studies have put forward different cut-offs to evaluate CD47 expression, which brings inconsistent observation results [12, 27, 28]. Further studies need to be performed to validate the practicability of these cut-offs. Clinical data shows that CD47 is an important molecule in the pathogenesis of EC; however, complex molecular mechanism is still unclear. Future studies to determine CD47 details on molecular oncogenesis of endometrial carcinoma are warranted.

5. Conclusion

In conclusion, CD47 could be a critical part of the progress of pathogenesis in EC. CD47 expression correlates with multiple clinicopathological variables and is a potential prognostic risk factor.

Data Availability

The data are available on request to the authors.

Ethical Approval

The study was approved by the Ethics Committee of Xiangyang Central Hospital (Reference no. 2021005).

Conflicts of Interest

The authors declare that they have no conflicts of interest.

Authors' Contributions

LH designed the study. MY and CJ analyzed the data. LL and HX generated the tables and figures. MY and CJ wrote the manuscript. All authors have read and approved the final manuscript. All authors confirmed the authenticity of all the raw data. Mei Yang and Chunfan Jiang contributed equally to this work.

Acknowledgments

The authors acknowledge the excellent technical assistance of Shanghai Er Dong (Xian Tao) Education and Technology Co., Ltd. The study was supported by the National Natural Science Foundation of China (no. 81972449).

References

[1] W. Chen, R. Zheng, P. D. Baade et al., "Cancer statistics in China, 2015," *CA: A Cancer Journal for Clinicians*, vol. 66, no. 2, pp. 115–132, 2016.

[2] R. A. Soslow, C. Tornos, K. J. Park et al., "Endometrial carcinoma diagnosis," *International Journal of Gynecological Pathology*, vol. 38, no. 1, pp. S64–s74, 2019.

[3] R. C. Arend, B. A. Jones, A. Martinez, and P. Goodfellow, "Endometrial cancer: molecular markers and management of advanced stage disease," *Gynecologic Oncology*, vol. 150, no. 3, pp. 569–580, 2018.

[4] R. A. Brooks, G. F. Fleming, R. R. Lastra et al., "Current recommendations and recent progress in endometrial cancer," *CA: A Cancer Journal for Clinicians*, vol. 69, pp. 258–279, 2019.

[5] K. K. Zorn, C. Tian, W. P. McGuire et al., "The prognostic value of pretreatment CA 125 in patients with advanced ovarian carcinoma," *Cancer*, vol. 115, no. 5, pp. 1028–1035, 2009.

[6] S. M. G. Hayat, V. Bianconi, M. Pirro, M. R. Jaafari, M. Hatamipour, and A. Sahebkar, "CD47: role in the immune system and application to cancer therapy," *Cellular Oncology*, vol. 43, no. 1, pp. 19–30, 2020.

[7] D. R. Soto-Pantoja, S. Kaur, and D. D. Roberts, "CD47 signaling pathways controlling cellular differentiation and responses to stress," *Critical Reviews in Biochemistry and Molecular Biology*, vol. 50, no. 3, pp. 212–230, 2015.

[8] K. Yoshida, H. Tsujimoto, K. Matsumura et al., "CD 47 is an adverse prognostic factor and a therapeutic target in gastric cancer," *Cancer Medicine*, vol. 4, no. 9, pp. 1322–1333, 2015.

[9] J. Yuan, X. Shi, C. Chen et al., "High expression of CD47 in triple negative breast cancer is associated with epithelial mesenchymal transition and poor prognosis," *Oncology Letters*, vol. 18, pp. 3249–3255, 2019.

[10] Y. Li, S. Lu, Y. Xu et al., "Overexpression of CD47 predicts poor prognosis and promotes cancer cell invasion in high-grade serous ovarian carcinoma," *American Journal of Tourism Research*, vol. 9, pp. 2901–2910, 2017.

[11] R. Liu, H. Wei, P. Gao et al., "CD47 promotes ovarian cancer progression by inhibiting macrophage phagocytosis," *Oncotarget*, vol. 8, no. 24, pp. 39021–39032, 2017.

[12] W. Fu, J. Li, W. Zhang, and P. Li, "High expression of CD47 predicts adverse prognosis in Chinese patients and suppresses immune response in melanoma," *Biomedicine & Pharmacotherapy*, vol. 93, pp. 1190–1196, 2017.

[13] W. Zhang, Q. Huang, W. Xiao et al., "Advances in anti-tumor treatments targeting the CD47/sirpα Axis," *Frontiers in Immunology*, vol. 11, p. 18, 2020.

[14] Y. Liu, Y. Chang, X. He et al., "CD47 enhances cell viability and migration ability but inhibits apoptosis in endometrial carcinoma cells via the PI3K/Akt/mTOR signaling pathway," *Frontiers Oncology*, vol. 10, Article ID 1525, 2020.

[15] X. Li, Y. Gao, M. Tan et al., "Expression of HE4 in endometrial cancer and its clinical significance," *BioMed Research International*, vol. 2015, pp. 1–8, 2015.

[16] B. Li, H. L. Chan, and P. Chen, "Immune checkpoint inhibitors: basics and challenges," *Current Medicinal Chemistry*, vol. 26, no. 17, pp. 3009–3025, 2019.

[17] L. Galluzzi, J. Humeau, A. Buqué, L. Zitvogel, and G. Kroemer, "Immunostimulation with chemotherapy in the era of immune checkpoint inhibitors," *Nature Reviews Clinical Oncology*, vol. 17, no. 12, pp. 725–741, 2020.

[18] R. K. Vaddepally, P. Kharel, R. Pandey, R. Garje, and A. B. Chandra, "Review of indications of FDA-approved immune checkpoint inhibitors per NCCN guidelines with the level of evidence," *Cancers*, vol. 12, no. 3, p. 738, 2020.

[19] E. Olcucuoglu, M. E. Sirin, and G. Aydog, "Relationship with immunhistochemical staining extent of CD47 and histopathologic features of bladder tumor," *Central European Journal of Urology*, vol. 70, pp. 349–355, 2017.

[20] B. I. Sikic, N. Lakhani, A. Patnaik et al., "First-in-Human, first-in-class phase I trial of the anti-CD47 antibody Hu5F9-G4 in patients with advanced cancers," *Journal of Clinical Oncology*, vol. 37, no. 12, pp. 946–953, 2019.

[21] Ç. Sercan, A. N. Haberal Reyhan, Ö. Özen, and A. Ayhan, "Clinicopathologic and prognostic significance of CD47 expression and tumor-associated macrophages in endometrial carcinoma," *International Journal of Gynecological Pathology*, vol. 2021, 2021.

[22] Z. Xiao, H. Chung, B. Banan et al., "Antibody mediated therapy targeting CD47 inhibits tumor progression of hepatocellular carcinoma," *Cancer Letters*, vol. 360, no. 2, pp. 302–309, 2015.

[23] J. Chen, D.-X. Zheng, X.-J. Yu et al., "Macrophages induce CD47 upregulation via IL-6 and correlate with poor survival in hepatocellular carcinoma patients," *OncoImmunology*, vol. 8, no. 11, Article ID e1652540, 2019.

[24] S. Gu, T. Ni, J. Wang et al., "CD47 blockade inhibits tumor progression through promoting phagocytosis of tumor cells by M2 polarized macrophages in endometrial cancer," *Journal of Immunology Research*, vol. 2018, pp. 1–12, 2018.

[25] J. Yu, X. Wang, F. Teng, and L. Kong, "PD-L1 expression in human cancers and its association with clinical outcomes," *OncoTargets and Therapy*, vol. 9, pp. 5023–5039, 2016.

[26] A. C. Wolff, M. E. H. Hammond, K. H. Allison et al., "Human epidermal growth factor receptor 2 testing in breast cancer: American society of clinical oncology/college of American pathologists clinical practice guideline focused update," *Archives of Pathology & Laboratory Medicine*, vol. 142, no. 11, pp. 1364–1382, 2018.

[27] T. Hu, H. Liu, Z. Liang et al., "Tumor-intrinsic CD47 signal regulates glycolysis and promotes colorectal cancer cell growth and metastasis," *Theranostics*, vol. 10, no. 9, pp. 4056–4072, 2020.

[28] O. Arrieta, A. Aviles Salas, M. Orozco Morales et al., "Association between CD47 expression, clinical characteristics and prognosis in patients with advanced non small cell lung cancer," *Cancer Medicine*, vol. 9, no. 7, pp. 2390–2402, 2020.

Hindawi
Journal of Oncology
Volume 2022, Article ID 8933167, 23 pages
https://doi.org/10.1155/2022/8933167

Research Article

Correlation between Tumor Microenvironment and Immune Subtypes Based on CD8 T Cells Enhancing Personalized Therapy of Gastric Cancer

Jianyu Wu,[1] Yajie Xiao,[2] Weiqi Lu,[1] Zijing Zhang,[1] Haigan Yang,[1] Xiaoli Cui,[2] Dongfang Wu ,[2] and Yuzhong Chen [1]

[1]*No. 2 Surgery Department, The First Affiliated Hospital of Guangzhou University of Traditional Chinese Medicine, Guangzhou 440100, China*
[2]*YuceBio Technology Co., Ltd., Shenzhen 440300, China*

Correspondence should be addressed to Dongfang Wu; wudf@yucebio.com and Yuzhong Chen; cyz1103603@21cn.com

Received 3 December 2021; Accepted 18 January 2022; Published 28 February 2022

Academic Editor: Fu Wang

Background. Immunotherapy is a promising therapy for metastatic gastric cancer (GC) patients. However, the component of tumor microenvironment (TME) is a pivotal factor hindering immunotherapy outcome. CD8 T cells suppress tumor progression. This study developed an immune subtyping system and a prognostic model for guiding personalized therapy of GC patients. *Methods*. Marker genes related to CD8 T cells were identified by weighted correlation network analysis (WGCNA). Consensus clustering was used to develop immune subtypes. Univariate Cox regression analysis was performed to screen prognostic genes. Functional analysis (KEGG and GO annotation) and gene set enrichment analysis were applied. *Results*. Based on marker genes related to CD8 T cells, we identified three immune subtypes (IC1, IC2, and IC3) with distinct prognosis and differential TME. In IC3, CD8 T cell function was impaired by high activation of CXCR4/CXCL12 axis, and impaired T cell function predicted high response to immune checkpoint blockade. IC1 was sensitive to chemotherapeutic drugs but showed low response to immunotherapy. We also developed an 8-gene prognostic signature with robust performance to stratify GC patients into high-risk and low-risk groups. *Conclusions*. This study identified three immune subtypes and a prognostic signature, and both were effective in direct personalized therapy for GC patients. The correlation between TME and immunotherapy was further characterized from a new perspective.

1. Introduction

Although the incidence and mortality of gastric cancer (GC) have declined over the past decades, GC is still the leading cause of cancer death [1]. The discovery and application of curative modalities for GC treatment increased the 5-year overall survival (OS) rate from 18.8% to 28.0% according to the statistics of the Surveillance, Epidemiology, and End Results (SEER) program [2]. However, a large number of metastatic patients still face the difficulties of seeking an effective therapy. Currently, immunotherapy targeting immune checkpoints seems a promising strategy for treating advanced gastric cancer [3].

Tumor microenvironment (TME) is highly associated with tumor cell proliferation, invasion, migration, and immunotherapy outcome [4, 5]. To a large extent, infiltration of different types of immune cells is decisive of the prognosis of immunotherapy [6]. An extensive immunogenomic analysis on pan-cancer performed with The Cancer Genome Atlas (TCGA) identified 6 immune subtypes, and GC can be classified into 5 immune subtypes [7]. The pancaner study further characterized the critical role of TME to drive personalized cancer immunotherapy. Focusing on tumor immune infiltration in gastric cancer, Zhou et al. developed two immune subtypes (Immune Activation Subtype and Immunosuppressive Subtype), which were

predicted to have different responses to different immunotherapies [8].

A link between increased levels of cytotoxic CD8 T cells and strong antitumor effects has been discovered in many cancer types such as breast cancer [9], glioblastoma, cervical cancer [10, 11], and gastric cancer [12]. In the TME, receptors of PD-L1 and CD80 expressed by tumor cells or tumor-related immune cells can interact with PD-1 and CTLA-4 expressed by CD8 T cells, respectively, to impair CD8 T cell function [13, 14]. These interactions may be the potential targets for immunotherapy [15, 16]. Current studies also proved that anti-PD-1/PD-L1 and anti-CTLA-4 inhibitors can suppress cancer cell proliferation [17]. Clinical trial of anti-PD-1 antibody combined with apatinib revealed a positive outcome in advanced GC patients [18]. Immune infiltration of CD8 T cells plays a pivotal role in inhibiting cancer cell progression, and its function is closely correlated with TME. In addition, immune response activated by targeted immunotherapy is highly related to the status of infiltrated CD8 T cells and TME [19].

The current study focused on CD8 T cells and examined the role of CD8 T cells in immunotherapy. Integrative bioinformatics analysis identified genes related to CD8 T cells, based on which three immune subtypes with distinct prognosis were determined. A link between immune subtypes and personalized therapy such as immunotherapy was comprehensively described in the study. Furthermore, we constructed an 8-gene prognostic signature to predict the outcomes of GC patients and guide immunotherapy.

2. Materials and Methods

2.1. Data Information and Study Design. GC samples and expression data of immune cells were obtained from public databases. TCGA-STAD dataset was downloaded from TCGA (https://portal.gdc.cancer.gov/). GSE26942 [20], GSE66229 [20], and GSE84437 [21] datasets containing GC samples were downloaded from Gene Expression Omnibus (GEO, https://www.ncbi.nlm.nih.gov/geo/). Expression data of immune cells was obtained from GEO, including GSE13906 [22], GSE23371 [23], GSE27291 [24], GSE27838 [25], GSE28490 [26], GSE28726 [27], GSE37750 [28], GSE39889 [29], GSE42058 [30], GSE49910 [31], GSE59237 [32], GSE6863 [33], and GSE8059 [34] (Supplementary Table S1). GSE78220 [35] contains the immunotherapy data of metastatic melanoma patients. IMvigor210 [36] dataset was from https://research-pub.gene.com/IMvigor210CoreBiologies. The workflow of this study is shown in Figure 1.

2.2. Data Preprocessing. Of TCGA-STAD dataset, samples without survival status, survival time, or follow-up data were excluded. Using R software package hgu133plus2.db to convert Ensembl ID to gene symbol, genes with relative expression level <1 in over 50% samples were excluded. The median of expression was selected when one gene had more than one gene symbol. In this way, 353 samples were included in TCGA-STAD dataset (Supplementary Table S2). Of GC samples in GSE cohort, normal samples, and samples without survival status, survival time or follow-up data were excluded. Genes in probes were converted to gene symbol. Finally, 826 samples were included in the GSE cohort (Supplementary Table S2).

The RMA procedure in affy package [37] was used process raw data of Affymetrix GeneChip data for GSE cohort. Then, batch effect among different batches was removed using the function "removeBatchEffect" in limma R package [38]. The principle component analysis (PCA) was applied to display the expression data before and after the removal of batch effect. No difference was observed in TCGA-STAD datasets and immune cell datasets after removing the batch effect (Supplementary Figures S1 and S2).

2.3. Weighted Correlation Network Analysis (WGCNA). WGCNA was applied to identify coexpression gene modules from immune cell data, and to construct weight coexpression networks [39]. Pearson correlation coefficients between genes were calculated. The optimal power of soft threshold (β) was confirmed, according to the coefficient between log (k) and log ($p(k)$). For a scale-free network, the coefficient between log (k) and log ($p(k)$) up to 0.85 was selected. Then, expression matrix was converted to adjacent matrix and topological overlap matrix (TOM). Using average-linkage hierarchical clustering, genes were clustered with at least 100 genes in one gene module based on hybrid dynamic shear tree and TOM. Gene modules were further clustered according to the eigengenes of each module under the criteria of height = 0.25, deepSplit = 2, minModuleSize = 150.

2.4. Gene Enrichment Analysis. R package of clusterProfiler (v3.14.0) was employed to annotate Kyoto Encyclopedia of Genes and Genomes (KEGG) pathways and gene ontology (GO) terms of marker genes related to CD8 T cells [40]. CIBERSORT [41] (https://cibersort.stanford.edu/) was used to calculate the enrichment score of 22 types of immune cells. GSVA R package was applied for single sample gene set enrichment analysis (ssGSEA) to analyze the relation between risk score and KEGG pathways [42].

2.5. Identification of Immune Subtypes Based on CD8 T Cells. Marker genes related to CD8 T cells were identified by WGCNA. Univariate Cox regression analysis screened genes related to prognosis from TCGA-STAD dataset and GSE cohort. The intersected genes between the two datasets were selected for consensus clustering in TCGA-STAD dataset. ConsensusClusterPlus R package was applied to perform unsupervised consensus clustering [43]. The optimal cluster number $k = 3$ was confirmed by cumulative distribution function (CDF) and the relative change in area under CDF curve. Kaplan-Meier survival analysis was performed to verify the effectiveness of classification. GSE cohort was used to validate the robustness of classification.

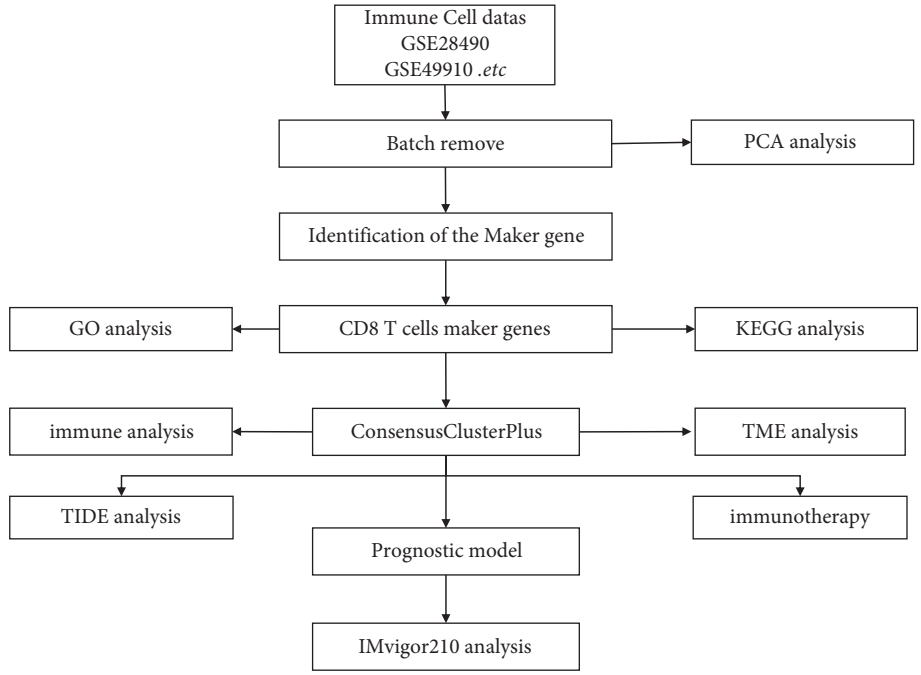

Figure 1: The flow chart of developing immune subtypes and prognostic genes based on genes related to CD8 T cells.

2.6. The Relation between Immune Subtypes and Personalized Therapy. TIDE (https://tide.dfci.harvard.edu/) was used to predict the potential correlation between immune subtypes and immune response. Higher TIDE score integrating T cell dysfunction and T cell exclusion was positively related to the possibility of immune escape. GSE78220 dataset containing anti-PD-1 immunotherapy data of melanoma patients was used for submap analysis on TCGA-STAD samples. Lower p value represented a higher similarity of treatment outcomes among samples. Bonferroni-correction was performed to correct p value. In addition, estimated IC50 of chemotherapeutic drugs including cisplatin, cyclopamine, and rapamycin was analyzed in different immune subtypes. Lower estimated IC50 represented higher drug sensitivity.

2.7. Construction of a Prognostic Model. A total of 826 samples in GSE cohort were randomly divided into training group and test group at a ratio of 8 : 2 for 100 times. The most ideal training group and test group were selected under two conditions: (1) similar proportion of gender and survival status in two groups; (2) close number of binary classification samples after clustering expression profiles. Finally, 659 samples in the training group and 165 samples in the test group were confirmed, and no statistical difference was observed between the two groups (*Chi*-square test, $p > 0.05$, Supplementary Table S3). TCGA-STAD dataset was an independent validation group.

Survival R package of "coxph function" was conducted for univariate Cox regression analysis in the training group. Differentially expressed genes with coefficients were screened under $p < 0.05$. Least absolute shrinkage and selection operator (LASSO) regression analysis in the glmnet package [44] and step Akaike information criterion (stepAIC) in the MASS package [45] were employed to optimize the prognostic model defined as: risk score = gene 1 expression $*$ coefficient 1 + gene 2 expression $*$ coefficient $2 + \ldots +$ gene n expression $*$ coefficient n. Risk score was converted to z-score, and z-score = 0 was the cut-off for stratifying samples into high-risk and low-risk groups. Receiver operating characteristic (ROC) curve and Kaplan-Meier survival curve were used to assess the prognostic model.

2.8. Statistics Analysis. All the statistics analyses were performed in R (v3.6.2). $p < 0.05$ was considered as a statistical significance. All statistics methods were shown in figure legends.

3. Results

3.1. Identification of Marker Genes Related to CD8 T Cells. We first extracted marker genes associated with CD8 T cells. To this end, WGCNA was used to analyze expression profiles of immune cells and identify coexpressed gene modules. Hierarchical clustering analysis classified a number of immune-related genes into various branches (Figure 2(a)). For ensuring a scale-free topology nature, the Pearson correlation coefficient between log (k) and log ($p(k)$) should reach 0.85. Therefore, $\beta = 8$ where β represents power of soft threshold selected (Figure 2(b)). Based on the soft threshold and correlation coefficient between genes, a topological overlap matrix was built, and a series of gene modules were identified. Finally, after merging adjacent modules according to eigengenes, 14 coexpressed gene modules were determined (Figure 2(c)). These 14 gene modules were differently associated with various types of immune cells;

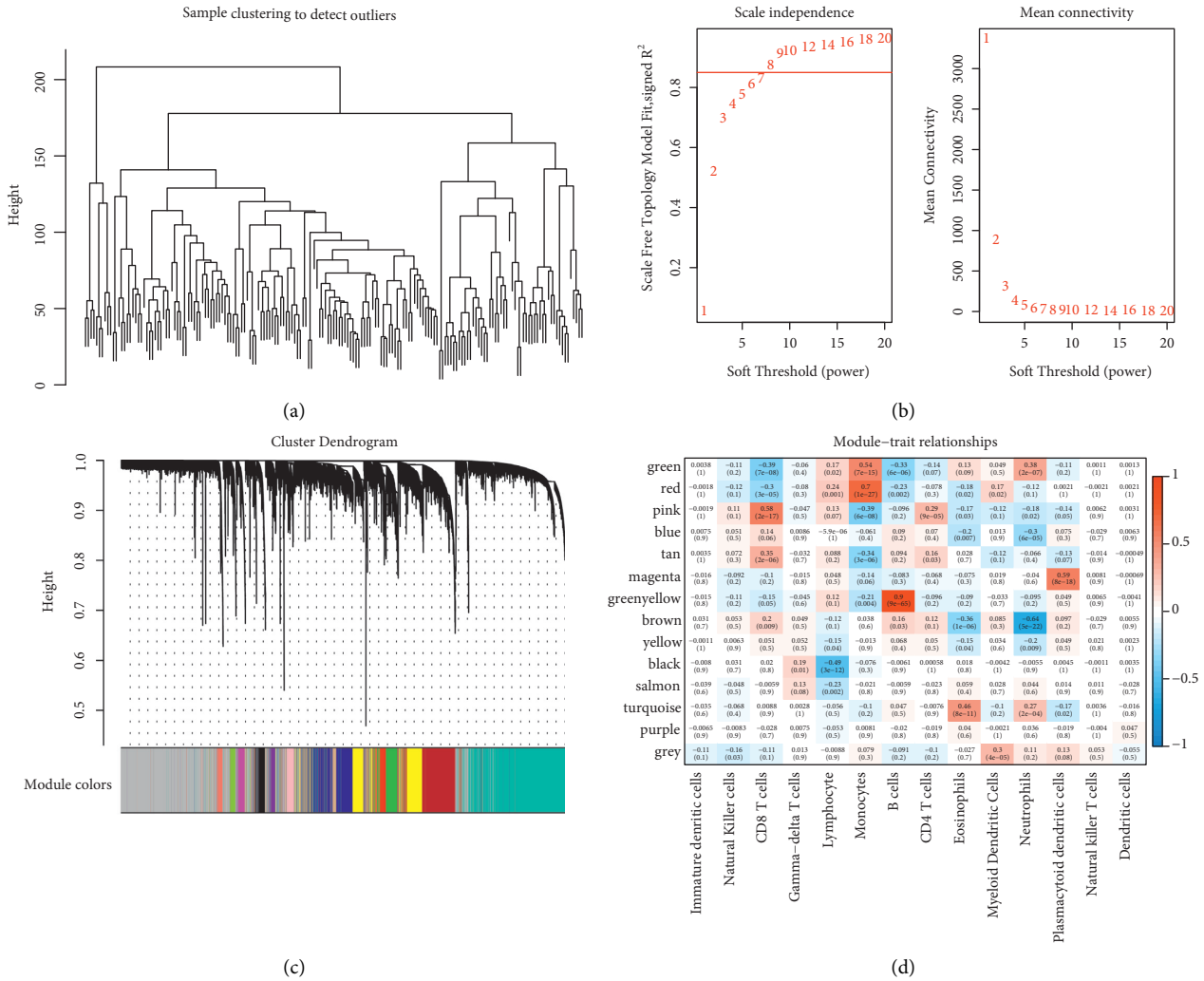

Figure 2: WGCNA for identifying marker genes related to CD8 T cells from immune cell datasets. (a) Hierarchical clustering tree based on 179 expression profiles in immune cells datasets. (b) Confirmation of soft threshold (power) by scale independence and mean connectivity. (c) Identification of 14 gene modules with different colors from clustering dendrogram. Grey represents gene clusters that cannot merge with others. (d) Pearson correlation rank analysis between 14 gene modules and 14 types of immune cells.

here, pink module with 446 genes was found to be closely associated with CD8 T cells (coefficient = 0.58, $p = 2e - 17$, Figure 2(d)).

KEGG and GO analysis on 446 CD8 T cells-related genes demonstrated a strong relation between these genes and immune function. The number of annotated terms of biological process, cellular component, and molecular function were 284, 46, and 26 ($p < 0.05$), respectively, and the top 10 terms were listed (Figures 3(a)–3(c)). These genes were closely involved in T cell receptor signaling pathway, antigen receptor-mediated signaling pathway, T cell differentiation, immune response-activating cell surface receptor signaling pathway, lymphocyte differentiation, etc. KEGG analysis annotated 33 pathways significantly correlated with these genes including multiple immune-related pathways, such as primary immunodeficiency, Th1 and Th2 cell differentiation, T cell receptor signaling pathway, Th17 cell differentiation, and natural killer cell mediated cytotoxicity (Figure 3(d)).

3.2. Construction of CD8 T Cells-Related Immune Subtypes. After 446 marker genes of CD8 T cells were extracted, CD8 T cells-related immune subtypes were constructed. By using univariate Cox regression analysis, 45 and 127 genes associated with GC prognosis were identified from TCGA-STAD dataset and GSE cohort, respectively. The intersection of two sets displayed a total of 28 genes, with 3 genes positively correlated with overall survival (OS) and 25 genes related to a worse OS ($p < 0.05$, Figure 4(a)). According to the expression of 28 genes, we conducted consensus clustering on 353 samples from TCGA-STAD dataset. CDF curve showed the highest relative change in area under CDF curve when cluster number $k = 3$, suggesting that the optimal cluster number was 3 (Figure 4(b), Supplementary Table S4). Consensus matrix classified 353 samples into three immune subtypes of IC1, IC2, and IC3 (IC, immune cluster; Figure 4(c)). Survival analysis revealed the distinct OS among the three subtypes with the optimal OS in IC1 and the worst OS in IC3 ($p = 0.035$, Figure 4(d)). Likewise, we

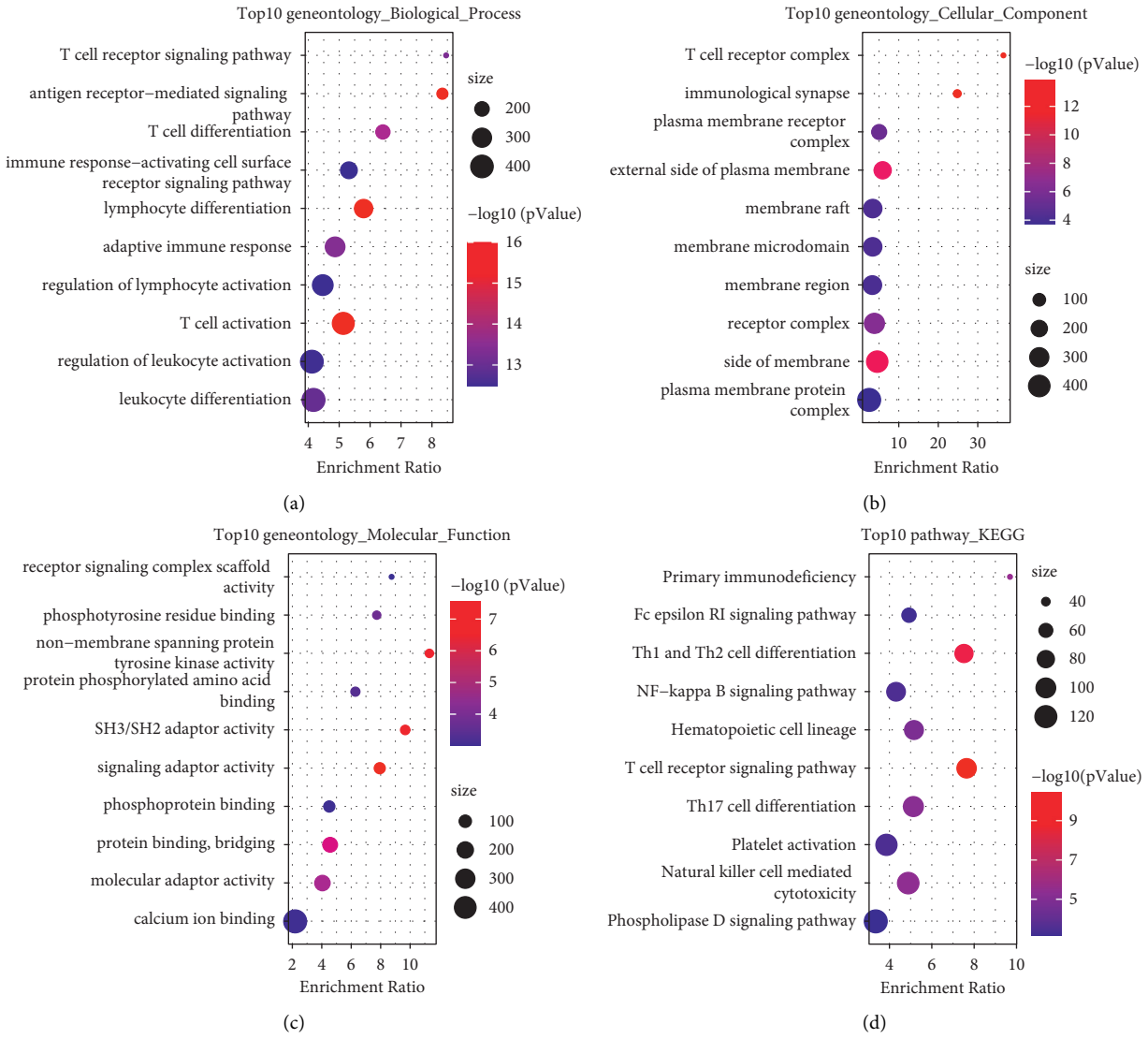

Figure 3: Go function and KEGG analysis of 446 genes related to CD8 T cells. (a–d) The top 10 enriched terms annotated in biological process (a), cellular component (b), molecular function (c), and KEGG pathways (d). Size means the enriched gene numbers.

observed the same results in GSE cohort ($p < 0.0001$, Figure 4(e)), indicating that this immune subtyping system was valid in different datasets.

3.3. The Distribution of Immune Subtypes in Clinical Features. To analyze if there was a relation between immune subtypes and clinical features, we analyzed the distribution of three subtypes in different clinical features including survival status, T stage, N stage, M stage, stage I to IV, age, and gender. The results showed that three subtypes were differentially distributed in survival status, T stage, stages I to IV, and age; however, no difference was shown in N stage, M stage, and gender (Figure 5). The proportion of deceased samples in IC3 was higher than IC1 ($p < 0.05$, Figure 5(a)), which was consistent with the worse OS of IC3. As for T stage, IC1 had the highest proportion of T1, while IC3 had the highest proportion of T4 $p < 0.05$, Figure 5(b)), showing that T stage was tightly correlated with immune subtypes. The proportion of stage I from IC1 to IC3 was decreasing ($p < 0.05$, Figure 5(e)), which may be one of the reasons contributing to the optimal prognosis of IC1 and the worst prognosis of IC3. Interestingly, age ≤65 consisted of the majority in IC3, which was opposite to IC1 and IC2 ($p < 0.05$, Figure 5(f)).

3.4. The Correlation between Immune Subtypes and Tumor Mutation Burden. We calculated the tumor mutation burden (TMB) of each sample in TCGA-STAD dataset using mutect2 software. Distinct TMB was shown in three immune subtypes, with the highest TMB in IC1 and the lowest TMB in IC3 ($p = 2.6e - 8$, Figure 6(a)). Consistently, IC1 had the most numbers of mutated genes, while IC3 had the least ($p = 1.8e - 10$, Figure 6(b)). Furthermore, 10031 genes were screened with a mutation frequency up to 3%; here, 1636 genes were found to be significantly mutated using *Chi*-square test ($p < 0.05$). The mutation patterns of the top 15

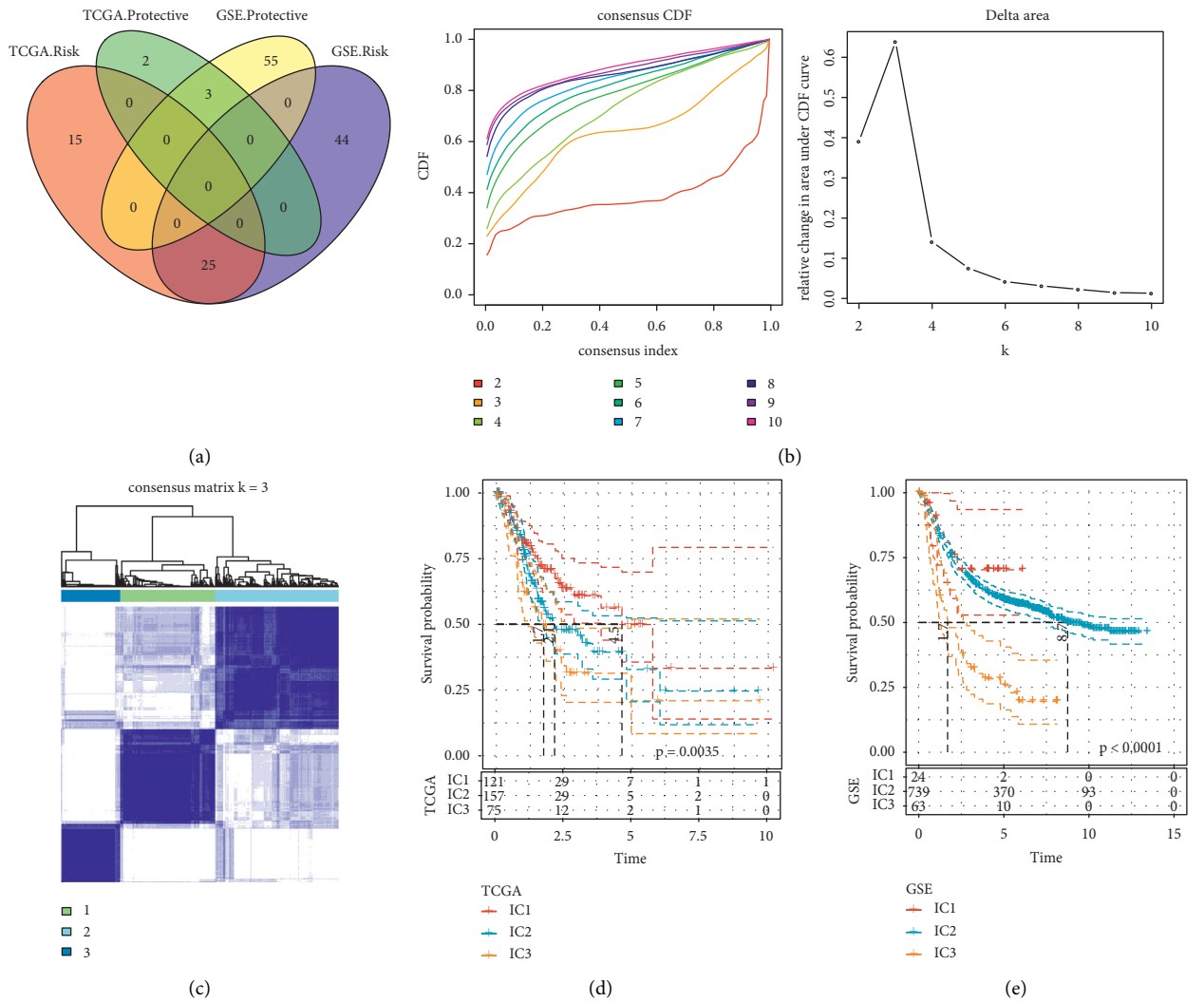

Figure 4: Construction of an immune subtyping system. (a) The Venn plot of genes related to prognosis screened from TCGA-STAD dataset and GSE cohort. Risk represents the negative correlation between gene expression and prognosis. Protective represents the positive correlation between them. (b) Cluster numbers k from 2 to 10 were analyzed to select the optimal number according to CDF and relative change in area under CDF curve. (c) The consensus matrix when $k = 3$. (d, e) Kaplan-Meier survival curve of three immune subtypes in TCGA-STAD dataset (d) and GSE cohort (e). Log-rank test was performed.

mutated genes were displayed in Figure 6(c). The proportion of TP53 mutations accounted for 37%, and other highly mutated genes such as MUC16, LRP1B, and ARID1A were reported to be closely associated with various cancers.

3.5. Differential Expression of Chemokines and Immune Checkpoints among Immune Subtypes. Chemokines play a pivotal role in determining TME by recruiting and orchestrating immune cells, which can elicit or inhibit antitumoral responses. Through binding with chemokine receptors, chemokines promote tumor proliferation, tumor angiogenesis, and migration. Therefore, we assessed the expression of 41 chemokines and 18 chemokine receptors of three immune subtypes and observed that 28 out of 41 chemokines and 11 out of 18 chemokines receptors were differentially expressed among the three subtypes, and that the majority of them were higher-expressed in IC3 (Figures 7(a) and 7(b)), which may lead to a distinct TME. As chemokines are critical for tumor angiogenesis that is necessary for tumor proliferation and migration, we also evaluated the angiogenesis score of each sample in TCGA-STAD dataset according to a series of genes related to angiogenesis [46]. Significant difference was observed among three subtypes that the angiogenesis score was the lowest in IC1 but the highest in IC3, which was consistent with their prognosis (Figures 7(c) and 4(d)). Immune checkpoints are responsible for transducing signals between immune cells; thereby, they can regulate cytokine secretion in response to TME. We obtained 47 genes related to immune checkpoints from previous research [47] and analyzed their expression of each sample. The result showed that 25 out of 47 genes were differentially expressed among IC1,

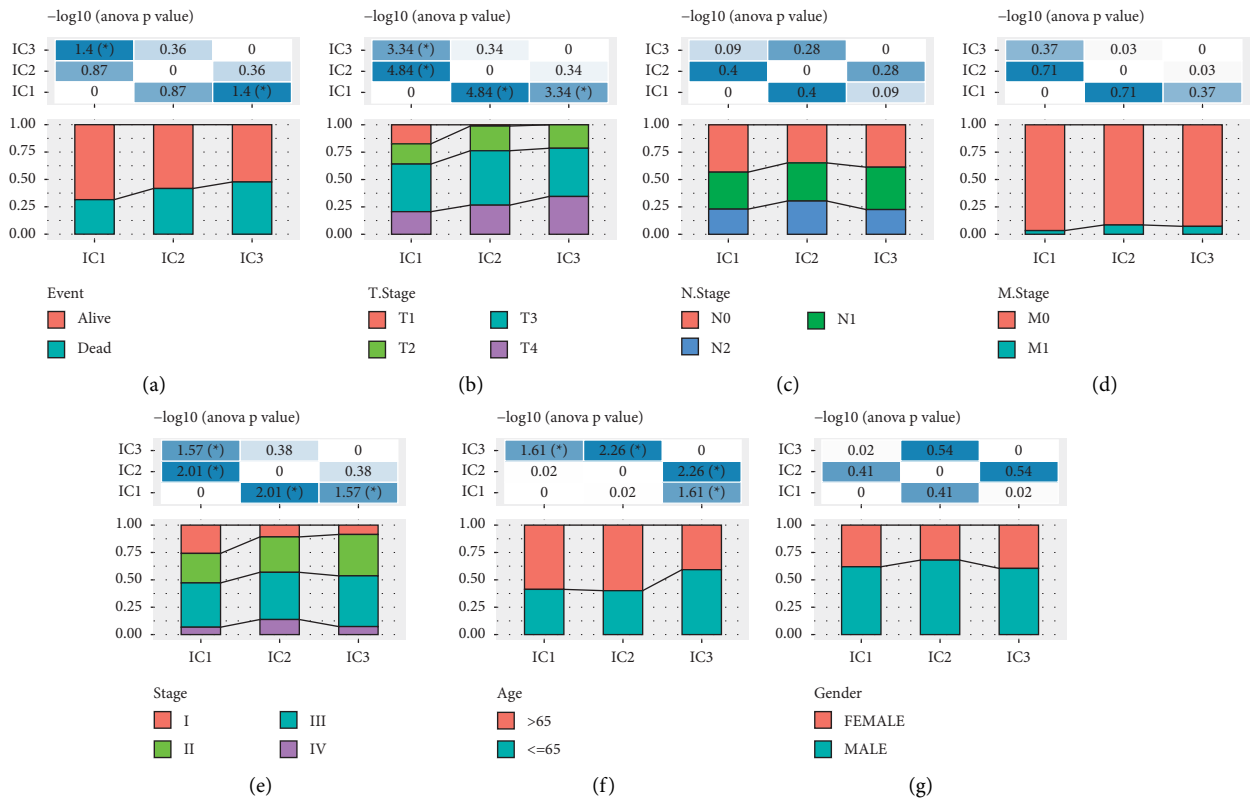

FIGURE 5: The relation between immune subtypes and clinical features, including survival status (a), T stage (b), N stage (c), M stage (d), stage I to IV (e), age (f) and gender (g).

IC2, and IC3 (Figure 7(d)), suggesting that these 25 genes related to immune checkpoints were closely involved in contributing to different TMEs.

3.6. Differential Enrichment of Immune Cells and Oncogenic Pathways among Immune Subtypes. As the expression of chemokines and genes related to immune checkpoints varied in three immune subtypes, we further analyzed the distribution of immune cells and activity of tumor-related pathways. CIBERSORT was employed to calculate enrichment score of 22 types of immune cells. Among these immune cells, CD8 T cells, resting memory CD4 T cells, M0 macrophages, and M2 macrophages were apparently higher enriched than others, and 8 immune cells were differentially enriched in three subtypes, including naive B cells, activated memory CD4 T cells, helper follicular T cells, resting NK cells, monocytes, M0 macrophages, M2 macrophages, and resting dendritic cells (Figures 8(a) and 8(b)). Activated memory CD4 T cells were highly enriched in IC1, enabling more active antitumor response, although no difference of enrichment of CD8 T cells was observed in the three subtypes. A low proportion of M0 macrophages and a high proportion of M2 macrophages were found in IC3, which could explain the increased number of tumor-associated macrophages (TAMs). IC3 had the highest immune score than IC1 and IC2, which may result from a high expression of chemokines and chemokine receptors in IC3 (Figures 8(d), 7(a) and 8(b)).

In addition, we evaluated the enrichment of 10 oncogenic pathways in the three subtypes [48], and all pathways were differentially enriched in the three subtypes (Figure 8(c)). Noticeably, IC3 was significantly higher-enriched than IC1 and IC2 in the most pathways, including Hippo signaling pathway, Notch signaling pathway, PI3K signaling pathway, TGF-β signaling pathway, RAS signaling pathway, and WNT signaling pathway ($p < 0.0001$, Figure 8(c)).

According to various aspects of analysis, the three immune subtypes presented significant difference and correlation in prognosis, TME, and oncogenic pathways, demonstrating the effectiveness of this immune subtyping system. Compared with the previous immune subtypes in a pan-cancer research [7], a close relation was also discovered. The pan-cancer research divided gastric cancer into five immune subtypes (C1, C2, C3, C4, and C6) with different OS, and the distribution of five subtypes was assessed in IC1, IC2, and IC3 (Figure 8(e)). C2 subtype with favorable OS consisted of a high proportion of IC1 and a low proportion of IC3. C3 subtype with worse OS than C2 was densely gathered in IC3, and C6 subtype with the worst OS only presented in IC1 and IC2 (Figure 8(e) and Supplementary Figure S3). The results further proved that our immune subtyping system was solid and reliable in predicting gastric cancer prognosis.

3.7. Immune Escape and T Cell Function Analyzed by TIDE. Next, we analyzed whether there was a difference among IC1, IC2, and IC3 on their immune response using TIDE

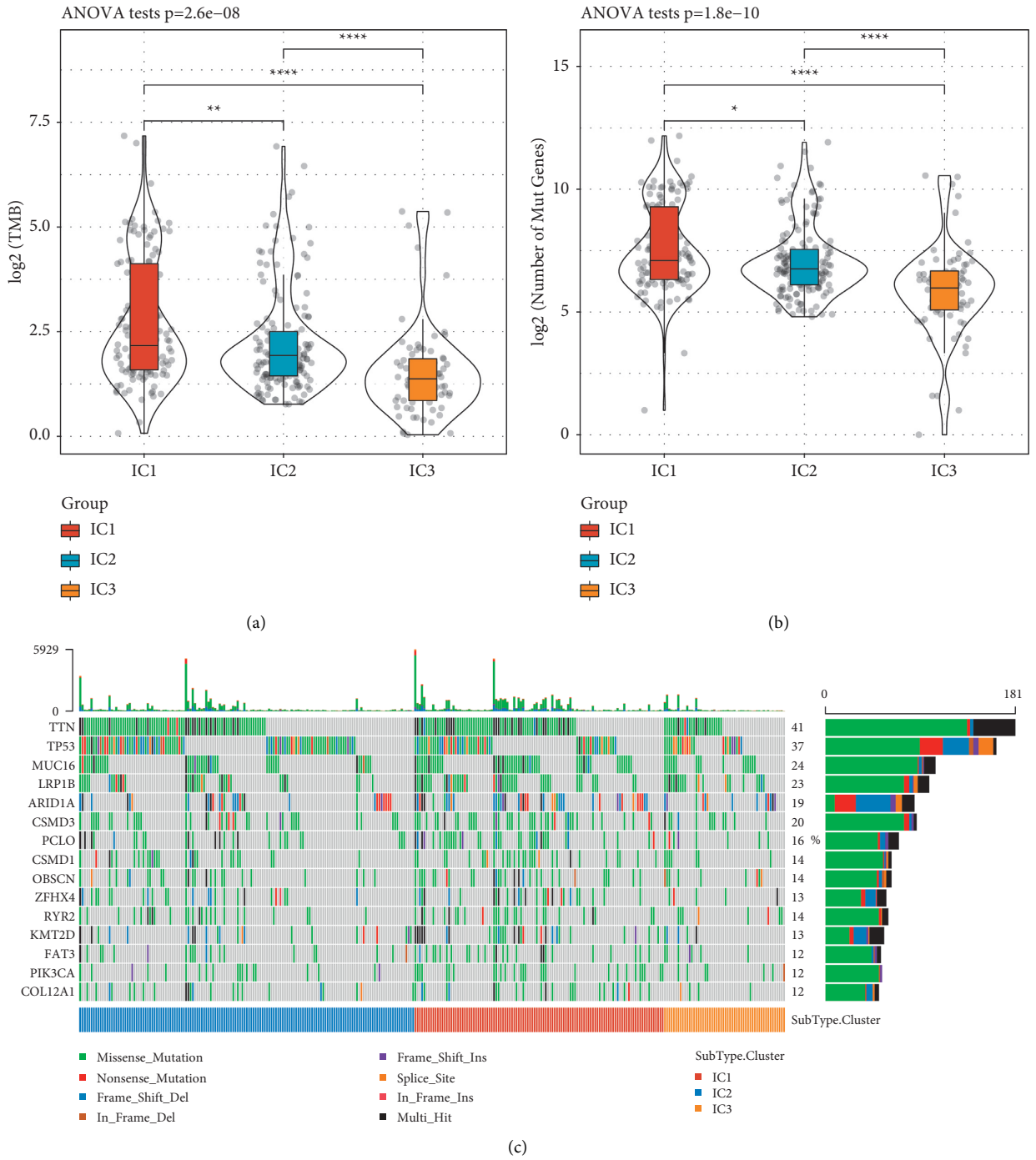

Figure 6: TMB and mutation patterns in TCGA-STAD dataset. ((a) and (b)) TMB (a) and number of mutated genes (b) of three immune subtypes. ANOVA was performed. (c) Mutation patterns of the top 15 genes in three immune subtypes. 8 types of mutations were presented including missense, nonsense, frame-shift deletions or insertions, in-frame deletions or insertions, splice site mutations, and different combinations of multiple genetic mutations (multi-hit). $^{*}p < 0.05$, $^{**}p < 0.01$, $^{****}p < 0.0001$.

methodology [49]. In TCGA-STAD dataset, IC1 had the lowest TIDE score, and IC3 had the highest (Figure 9(a)), indicating a high possibility of immune escape in IC1. The function of T cells is an important factor that can directly affect the immune response against tumor cells. Therefore, we also analyzed the manifestation of T cell function from the aspects of dysfunction and exclusion. IC1 showed the lowest score of both T cell dysfunction and exclusion, while IC3 had the highest score of the two (Figures 9(b) and 9(c)), suggesting impaired function of T cells to kill tumor cells in IC3. The similar results were also found in GSE cohort (Figures 9(d)–9(f)).

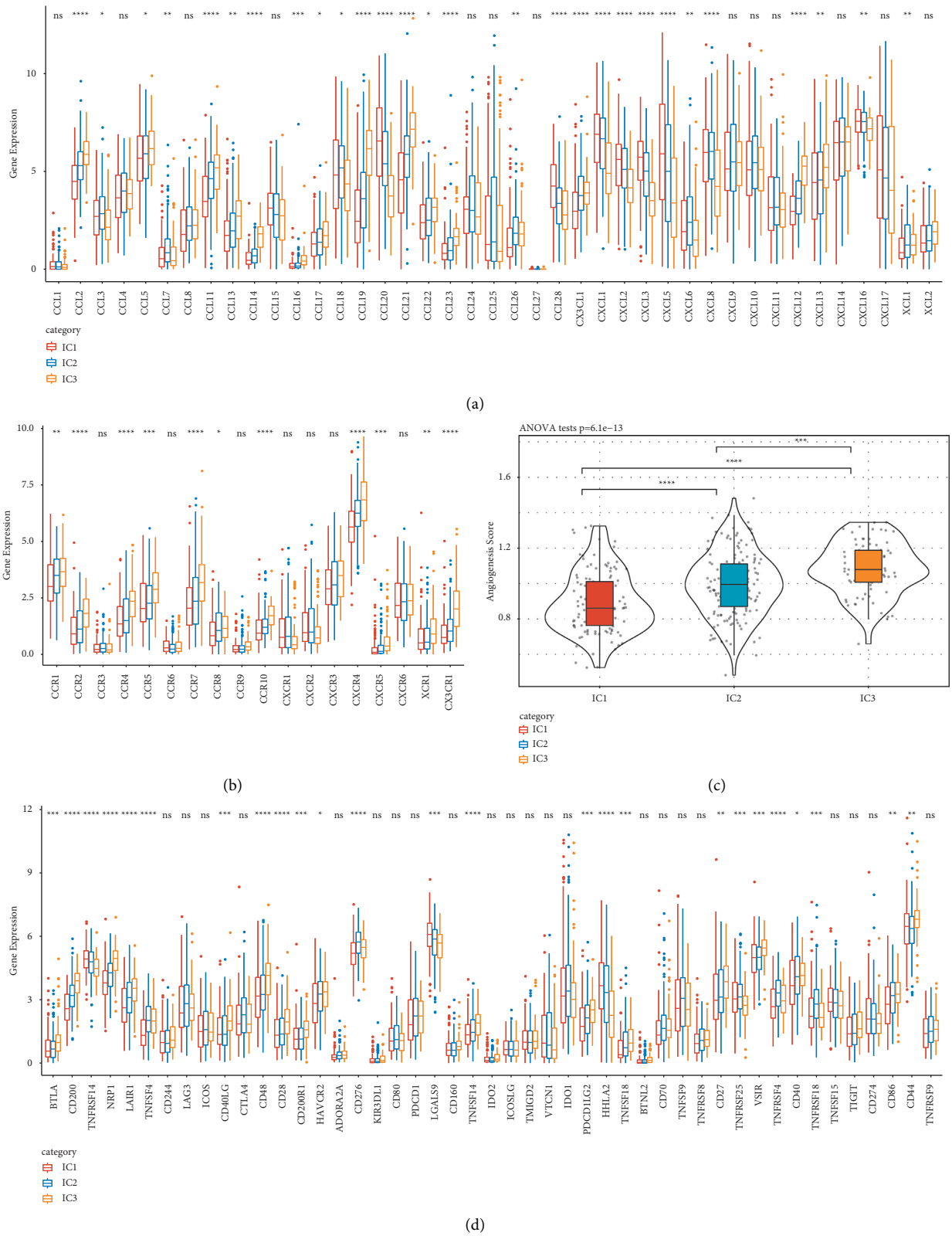

FIGURE 7: Expression of chemokines, chemokine receptors and genes related to immune checkpoints in TCGA-STAD dataset. ((a) and (b)) Expression of 41 chemokines (a) and 18 chemokine receptors (b) in three subtypes. (c) Differential angiogenesis score among three subtypes. (d) Expression of 47 genes related to immune checkpoints in three subtypes. ANOVA was performed. $^{*}p < 0.05$, $^{**}p < 0.01$, $^{**}p < 0.001$, $^{****}p < 0.0001$.

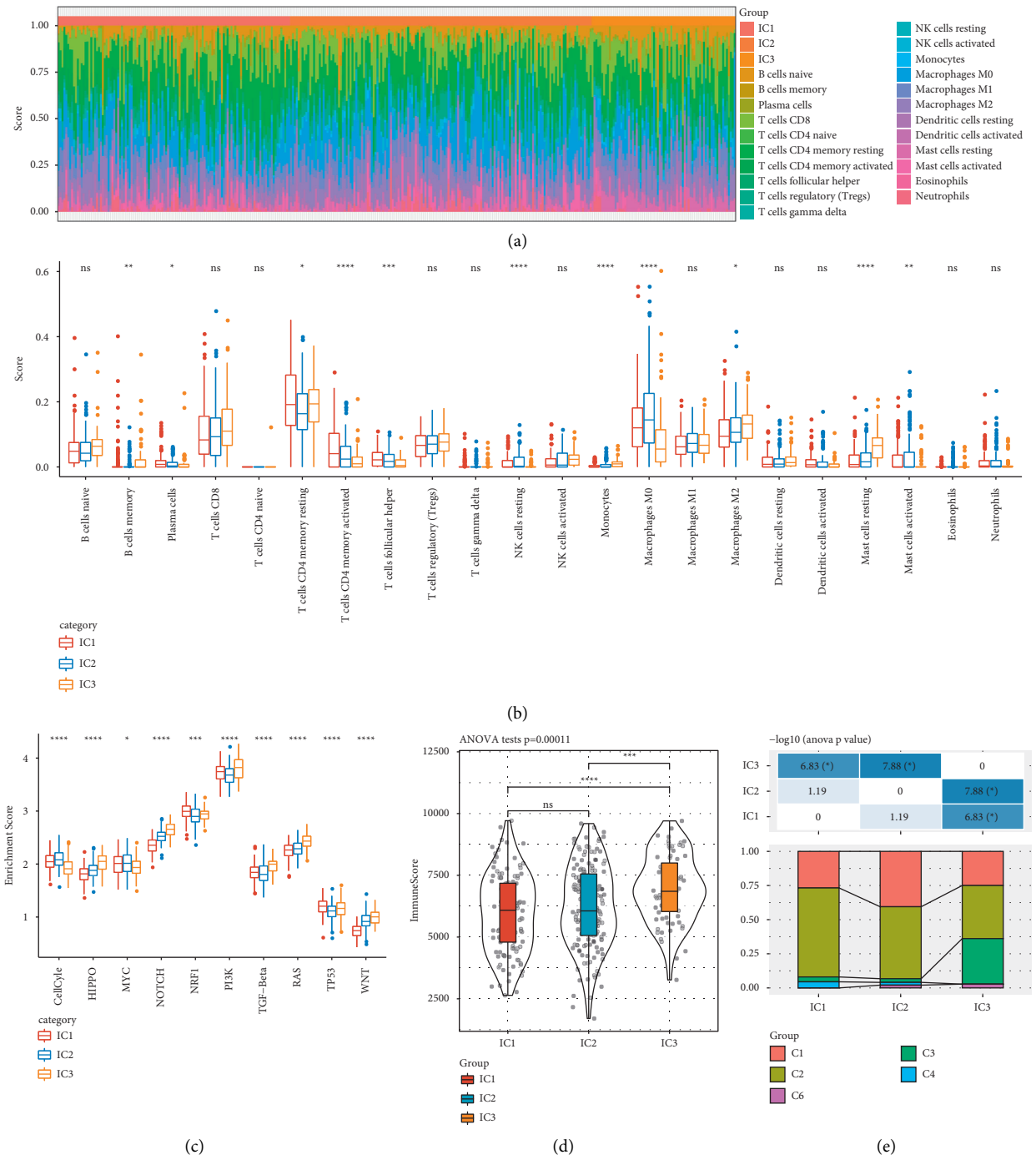

Figure 8: Immune features of three immune subtypes in TCGA-STAD dataset. (a) The heatmap presenting the distribution of 22 immune cells. (b) Comparison of enrichment score of 22 immune cells among three subtypes. (c) The enrichment of 10 oncogenic pathways in three subtypes. (d) Total immune score of three subtypes. (e) The distribution of pan-cancer immune subtypes in three subtypes. ANOVA was performed. ns, no significance. $^{*}p < 0.05$, $^{**}p < 0.01$, $^{**}p < 0.001$, $^{****}p < 0.0001$.

3.8. Differential Sensitivity of Three Immune Subtypes to PD-1 Inhibitor and Chemotherapeutic Drugs. Anti-PD-1/PD-L1 therapy using PD-1/PD-L1 inhibitors to active or reactive immune response to tumor cells is one of the most promising immunotherapies for treating many cancer types. We performed submap analysis to compare the similarity of TME between samples treated by anti-PD-1 inhibitor in GSE78220 dataset and three immune subtypes. High similarity with a low p value indicated a high efficacy of anti-PD-1 therapy. IC3 was shown to be not sensitive to anti-PD-1 therapy in both TCGA-STAD dataset and GSE cohort (Bonferroni-corrected $p = 0.001$, Figures 10(a) and 10(b)). However, IC1 and IC2 showed different responses to anti-PD-1 therapy in two datasets. Furthermore, we also

examined the response to chemotherapeutic drugs by calculating estimated IC50. Lower IC50 was indicative of a higher drug sensitivity and possibly a more favorable outcome. In TCGA-STAD dataset, IC1 displayed the lowest estimated IC50 of all three drugs (cisplatin, cyclopamine, and rapamycin), indicating that IC1 had the highest sensitivity to these drugs (Figures 10(c)–10(e)); however, IC3 could only limitedly benefit from the treatment of these drugs. Simultaneously, consistent results were observed in GSE cohort (Figures 10(f)–10(h)).

3.9. Construction of a Prognostic Model Based on Marker Genes Related to CD8 T Cells. Although the immune subtyping system can stratify GC patients into three subtypes with distinct prognosis and can largely guide chemotherapy and immunotherapy, it is not effective in predicting the treatment outcomes of GC patients. Based on the genes related to CD8 T cells, we constructed a prognostic model with the least number of genes to simply and efficiently predict prognosis. To this end, GSE cohort was randomly divided into training group and test group (Supplementary Table S3), with TCGA-STAD dataset as an independent validation group.

Within the training group, we screened 107 differentially expressed genes related to OS using univariate Cox regression analysis ($p < 0.05$). Then, LASSO regression analysis was conducted to compress the model and reduce number of genes. The coefficient of each gene was close to zero with the increasing value of lambda (Supplementary Figure S4A). 10-fold cross validation was applied to construct model with different lambda, and the confidential interval of different lambda was calculated (Supplementary Figure S4B). When lambda = 0.0671, the optimal model consisting a total of 12 genes was developed (Supplementary Figure S4). Then, we applied stepAIC to further optimize the model, and finally an 8-gene prognostic model was constructed as follows:

$$\begin{aligned}\text{Risk score} = {} & 0.358 * \text{FBLN5} + 0.307 * \text{ENPP5} \\ & - 0.665 * \text{KLHDC4} - 0.620 * \text{CD160} \\ & + 0.890 * \text{ZNF578} + 0.751 * \text{LBH} \\ & - 0.864 * \text{KLRD1} + 0.215 * \text{TCEAL2}.\end{aligned} \quad (1)$$

The risk score of each sample was counted using the 8-gene signature, and risk score was converted to z-score. Each sample was classified into low-risk and high-risk groups by the cutting of z-score = 0. In the training group, 327 samples and 332 samples were classified into high-risk and low-risk groups, respectively, with the high-risk group showing more deceased samples (Figure 11(a)). ZNF578, TCEAL2, LBH, FBLN5, and ENPP5 were highly expressed in high-risk group, while KLHDC4, KLRD1, and CD160 were low-expressed in low-risk group (Figure 11(a)). ROC analysis manifested the reliability of the classification that AUC of 1-year, 3-year, and 5-year was 0.60, 0.68, and 0.70, respectively (Figure 11(b)). Survival curve revealed the significantly distinct OS between two groups, with a better prognosis in low-risk group ($p < 0.0001$, Figure 11(c)). Risk score could be an independent factor to efficiently predict prognosis (HR = 1.62, 95% CI = 1.47–1.79, Figure 11(c)). We therefore assessed the prognostic model in the test group. 165 samples were stratified into high-risk and low-risk groups with distinct OS ($p < 0.0001$, Supplementary Figure S5). The robustness of the prognostic model was also validated in TCGA-STAD dataset, and 353 samples were classified into low-risk and high-risk groups with differential OS ($p = 0.002$, Supplementary Figure S6). In addition, we also analyzed the expression differences of these eight genes between cancer and adjacent samples. We can observe that most of these genes have significant expression differences, such as KLHDC4, ZNF578, LBH, and KLRD1 that are significantly overexpressed in tumor samples and tceal2 that is significantly underexpressed in adjacent samples (Supplementary Figure S7A). Further, we observed the expression differences of these genes in three molecular subtypes; FBLN5, LBH, and TCEAL2 were specifically highly expressed in IC3, and KLHDC4 was specifically low expressed in IC3 (Supplementary Figure S7B). The above results indicated that the 8-gene signature was effective in GC prognosis prediction.

3.10. Risk Score was Associated with Clinical Features and Immune Subtypes. Then, we analyzed the relation between risk score and clinical features including T, N, M stage, stages I to IV, gender, and age and found that low risk score was presented in T1, N0, M0 stage, and stage I with clinically mild progression (Figures 12(a)–12(d)). Especially, significantly differential risk score was distributed in T stage ($p = 0.00021$), stages I to IV ($p = 0.00054$). However, gender and age were not the factors affecting risk score (Figures 12(e) and 12(f)). Notably, a strong correlation was observed between risk score and immune subtypes, where IC1 had the lowest risk score and IC3 showed the highest risk score ($p = 5.8e - 27$, Figure 12(g)). These results further demonstrated the viability of the prognostic signature. Moreover, hazard ratio of clinical features and risk type was assessed with univariate and multivariate Cox regression analysis using TCGA-STAD dataset. Risk type was significantly associated with overall survival, with HR = 1.66 (95% CI = 1.18–2.32, $p = 0.003$) and HR = 1.52 (95% CI = 1.05 –2.19, $p = 0.025$) in univariate and multivariate Cox regression analysis, respectively (Figure 13). Moreover, age and M stage were also risk factors, with HR >1, which could be included to delineate nomogram together with risk score.

3.11. The Correlation between Risk Score and KEGG Pathways. To further examine whether risk score and functional pathways were correlated, ssGSEA was performed to calculate enrichment score of each sample in TCGA-STAD dataset, followed by correlation analysis between enrichment score in functional pathways and risk score using Pearson correlation analysis. |Correlation coefficient| ≥0.4 was set as a cut-off to screen the functional pathways closely associated with risk score. 64 KEGG pathways, including 18 pathways negatively correlated with risk score and 46 pathways positively correlated with risk score, were

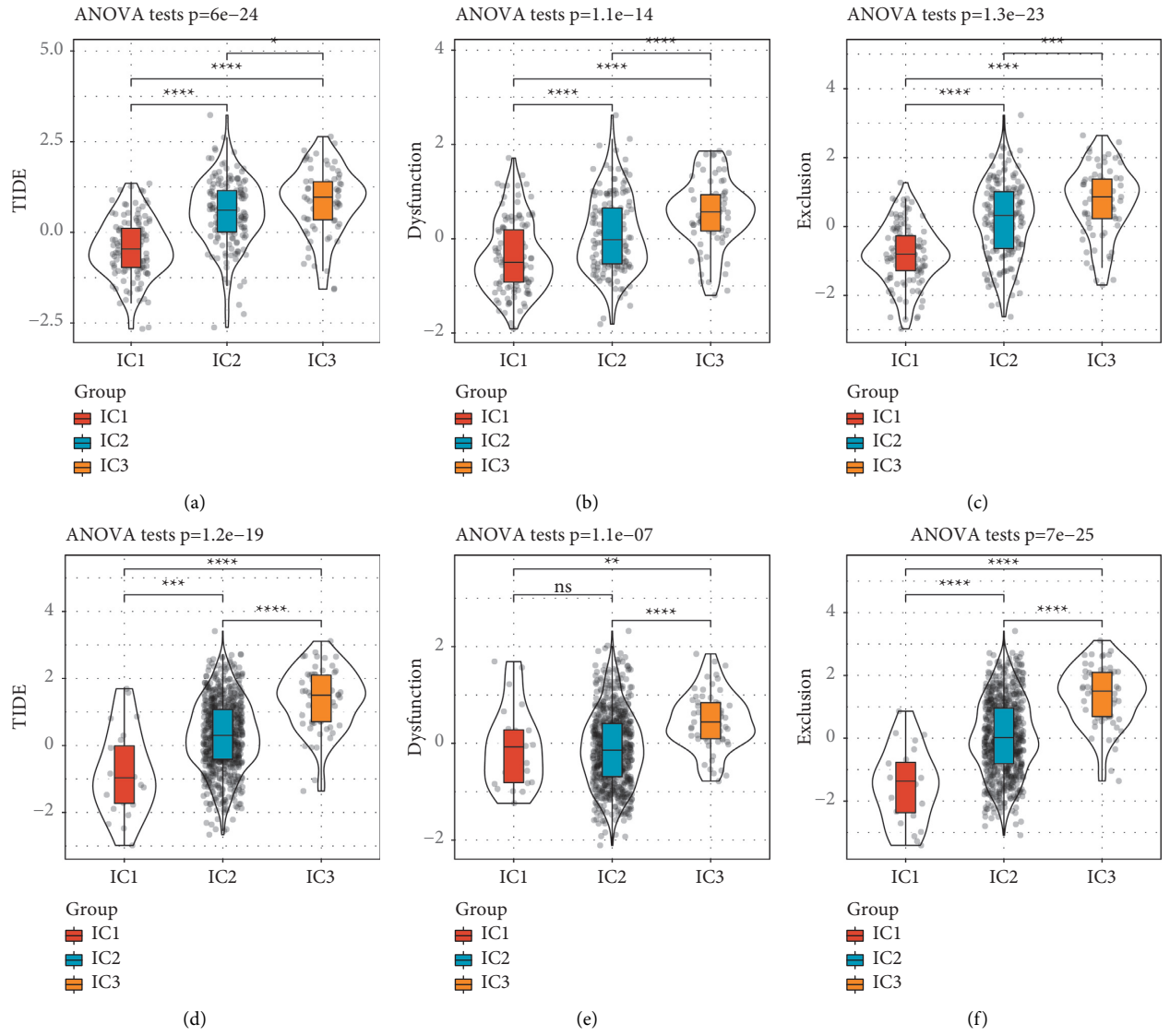

Figure 9: TIDE analysis for predicting the efficacy of immunotherapy in different subtypes. (a–c) TIDE score (a), T cell dysfunction score (b), and T cell exclusion score (c) of samples in TCGA-STAD dataset. (d–f) TIDE score (d), T cell dysfunction score (e), and T cell exclusion score (f) of samples in GSE cohort. ANOVA was performed. ns, no significance. $^{*}p < 0.05$, $^{**}p < 0.01$, $^{**}p < 0.001$, $^{****}p < 0.0001$.

identified (Figure 14(a)). Pathways related to cell cycle, DNA replication, and DNA repair were greatly enriched in the samples with low risk score, while tumor-related pathways, such as VEGF signaling pathway, NOTCH signaling pathway, TGF-β signaling pathway, WNT signaling pathway, and MAPK signaling pathway, were highly enriched in the samples with high risk score (Figure 14(b)). The strong correlation between high risk score and high enrichment of oncogenic pathways showed that the 8 prognostic genes may be closely involved in promoting tumor progression through activating or regulating oncogenic pathways.

3.12. Construction of a Nomogram to Predict Prognosis. To more precisely predict overall survival, we constructed a nomogram combining three risk factors (risk score, M stage, and age). Each risk factor corresponds to a point according to clinical information, and the total points correspond to the predicted death possibility in 1-, 3-, and 5-year (Figure 15(a)). The predicted OS was corrected by the observed OS (Figure 15(b)). Decision curve analysis (DCA) was performed to evaluate the effectiveness of the nomogram. As a result, nomogram was more advantageous to predict prognosis than risk score only (Figure 15(c)).

3.13. Prognostic Significance of Risk Score in Immunotherapy. We further examined whether the 8-gene signature was associated with the efficacy of immunotherapy. Imvigor210 dataset containing metastatic urothelial carcinoma patients treated by anti-PD-L1 immunotherapy was used in the following analysis. Kaplan-Meier survival curve showed a more favorable OS in low-risk group ($p < 0.0001$, Figure 16(a)). In comparison to neoantigen (NEO) and

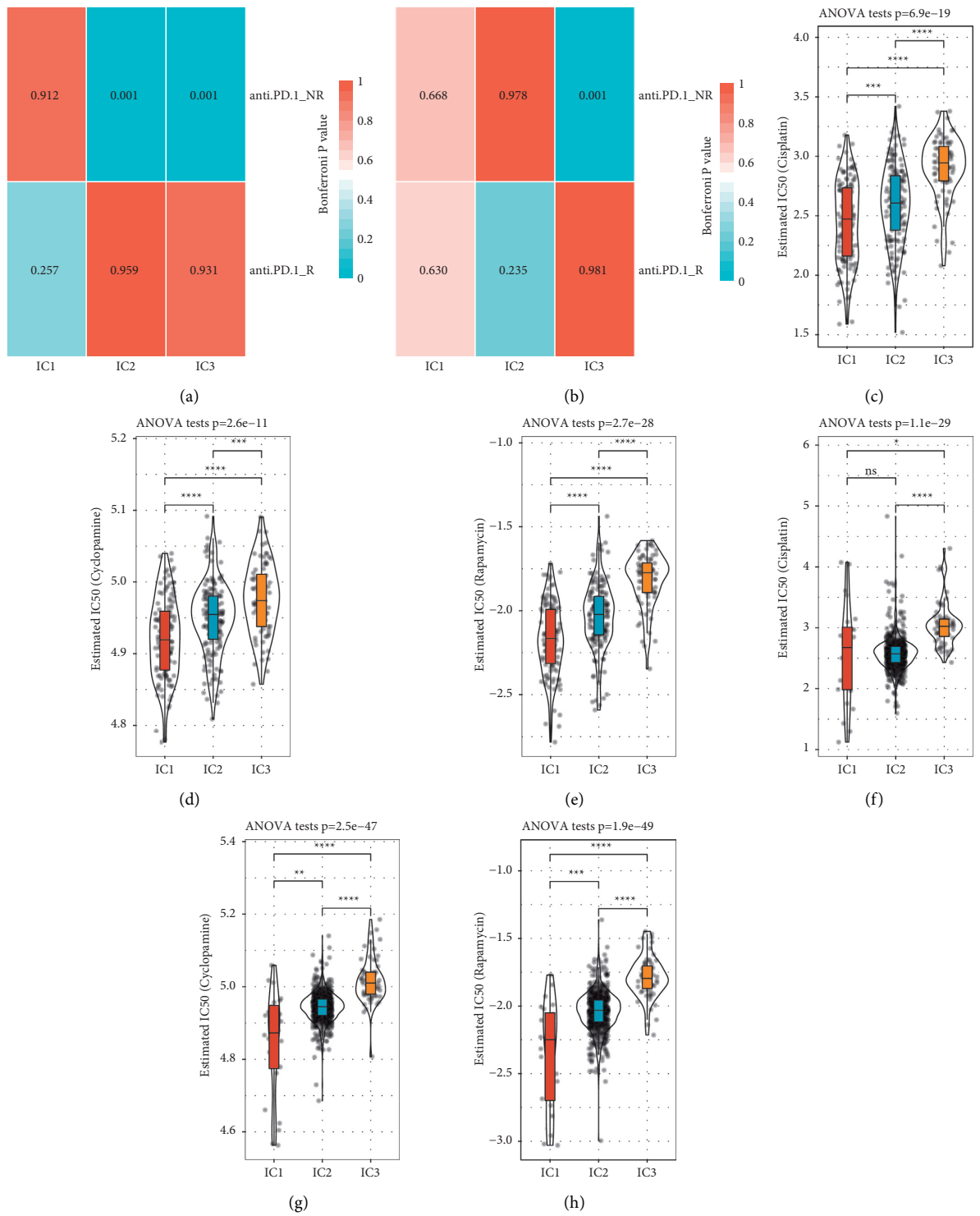

Figure 10: Different responses to immunotherapy and chemotherapy among three immune subtypes. ((a, b)) Submap analysis between GSE78220 and TCGA-STAD dataset (a), GSE78220 and GSE cohort (b). Bonferroni correction was applied to correct (p) value. Anti-PD-1_NR and anti-PD-1_R groups represent nonresponsive and responsive to anti-PD-1 therapy respectively. (c–e) Estimated IC50 of cisplatin (c), cyclopamine (d) and rapamycin (e) in TCGA-STAD dataset. (f–h) Estimated IC50 of cisplatin (f), cyclopamine (g) and rapamycin (h) in GSE cohort. ANOVA was performed. ns, no significance. $^{*}p < 0.05$, $^{**}p < 0.01$, $^{**}p < 0.001$, $^{****}p < 0.0001$.

TMB, risk score with an AUC of 0.83 (95% CI = 0.67–1.00, Figure 16(b)) was the most effective when predicting prognosis. Between high-risk and low-risk groups, differential responses to immunotherapy were detected, where the proportion of complete response (CR) and stable disease (SD) was found to be significantly higher in low-risk

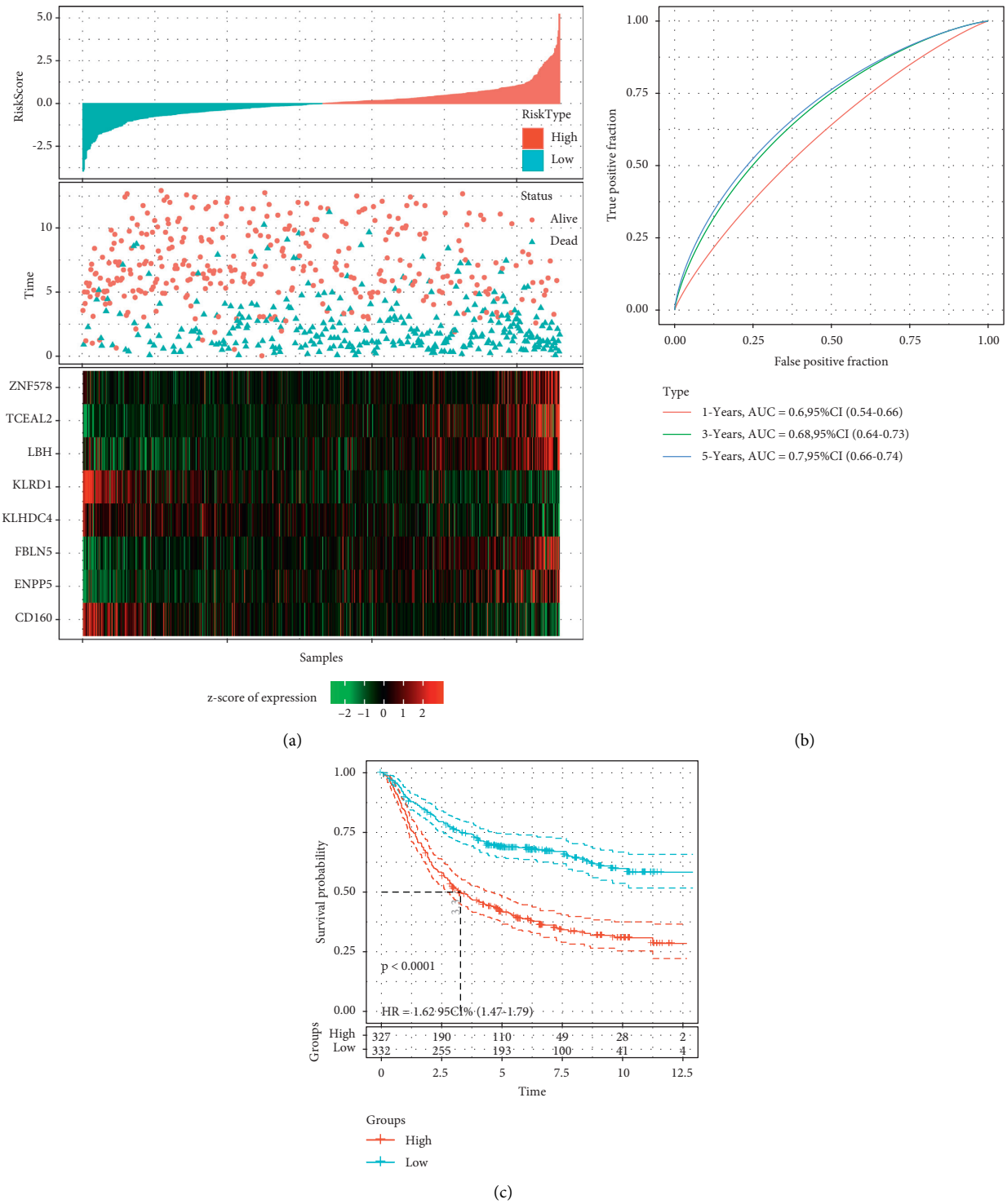

Figure 11: Assessment of the prognostic model in the training group. (a) The distribution of high-risk and low-risk groups, and the expression of 8 prognostic genes corresponding to risk score. (b) ROC analysis and AUC of 1-year, 3-year and 5-year OS predicted by the 8-gene signature. (c) Kaplan-Meier survival curve of high-risk and low-risk groups. Log-rank test was performed.

group ($p < 0.05$, Figure 16(c)). In the relation to immune infiltration, risk score was negatively related to many types of immune cells such as CD8 T cells, cytotoxic lymphocytes, B lineage, and NK cells, while NEO and TMB were not obviously correlated with these immune cells (Figure 16(d)). Moreover, lower risk score was related to higher NEO and TMB, suggesting that patients with higher NEO and TMB could benefit much more from anti-PD-L1 therapy.

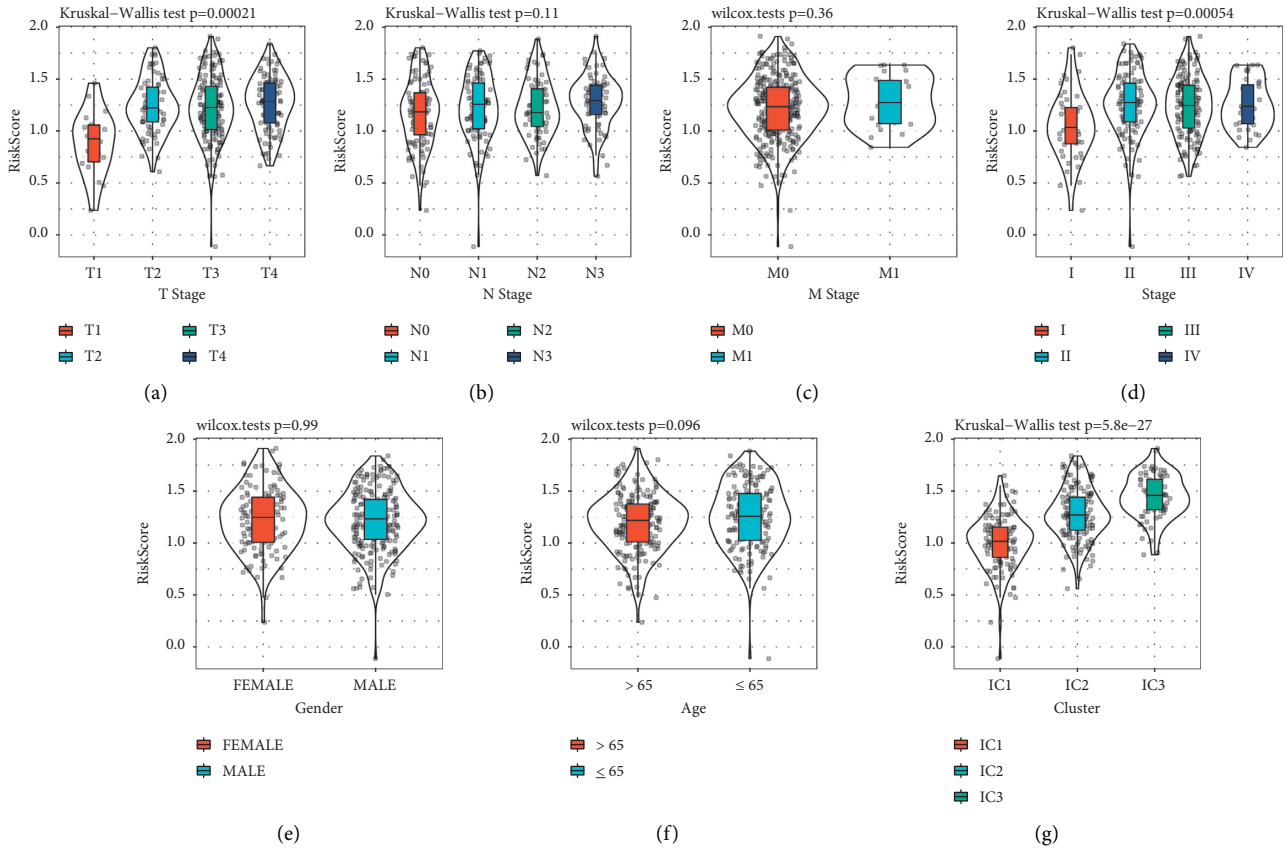

Figure 12: The relation of risk score to T stage (a), N stage (b), M stage (c), stage I to IV (d), gender (e), age (f) and immune subtypes (g). Wilcoxon test was performed.

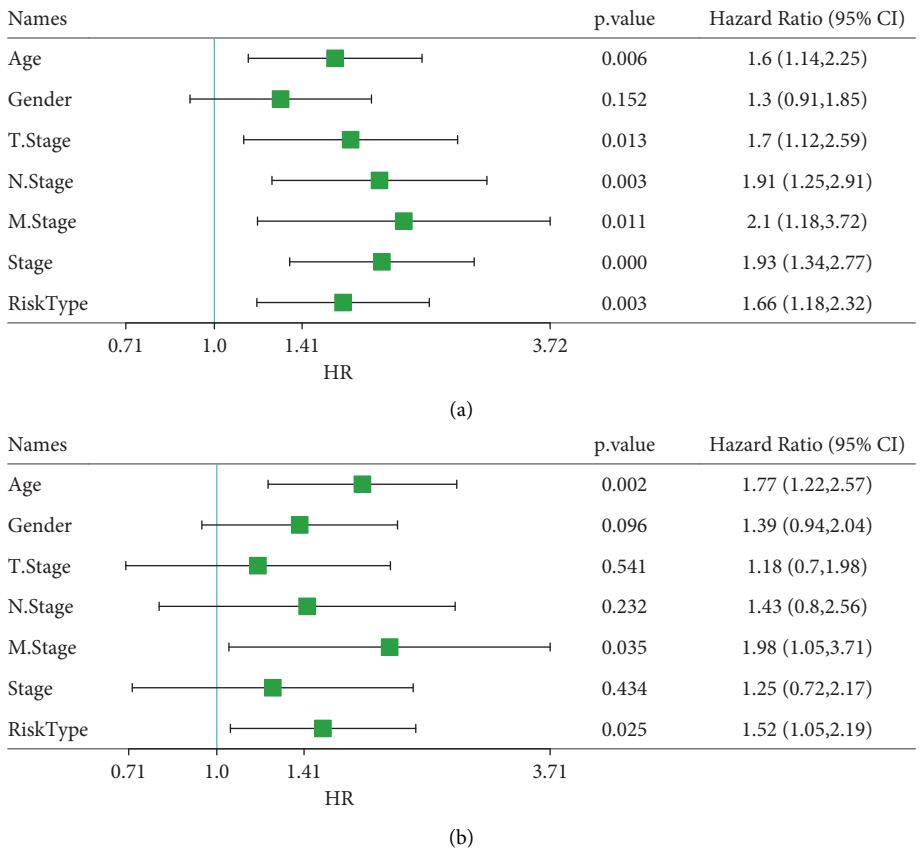

Figure 13: Univariate (a) and multivariate (b) Cox regression analysis between potential risk factors and prognosis.

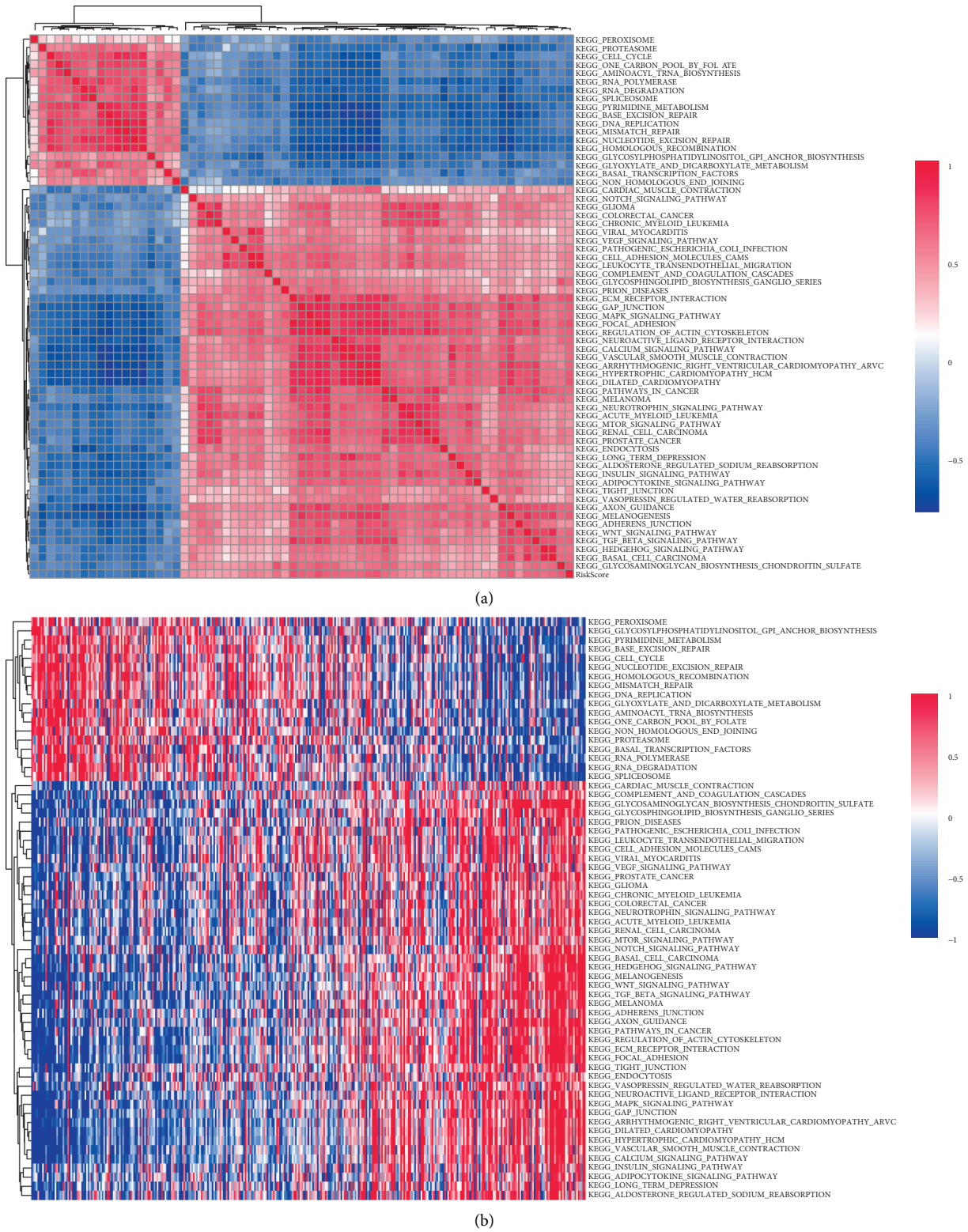

Figure 14: The relation between risk score and KEGG pathways. (a) 64 KEGG pathways related to risk score identified by Pearson correlation analysis. |correlation coefficient| >0.4. (b) The relation between enrichment of pathways and risk score. Horizontal axis represents the increasing risk score from left to right. Red means positive correlation and blue means negative correlation.

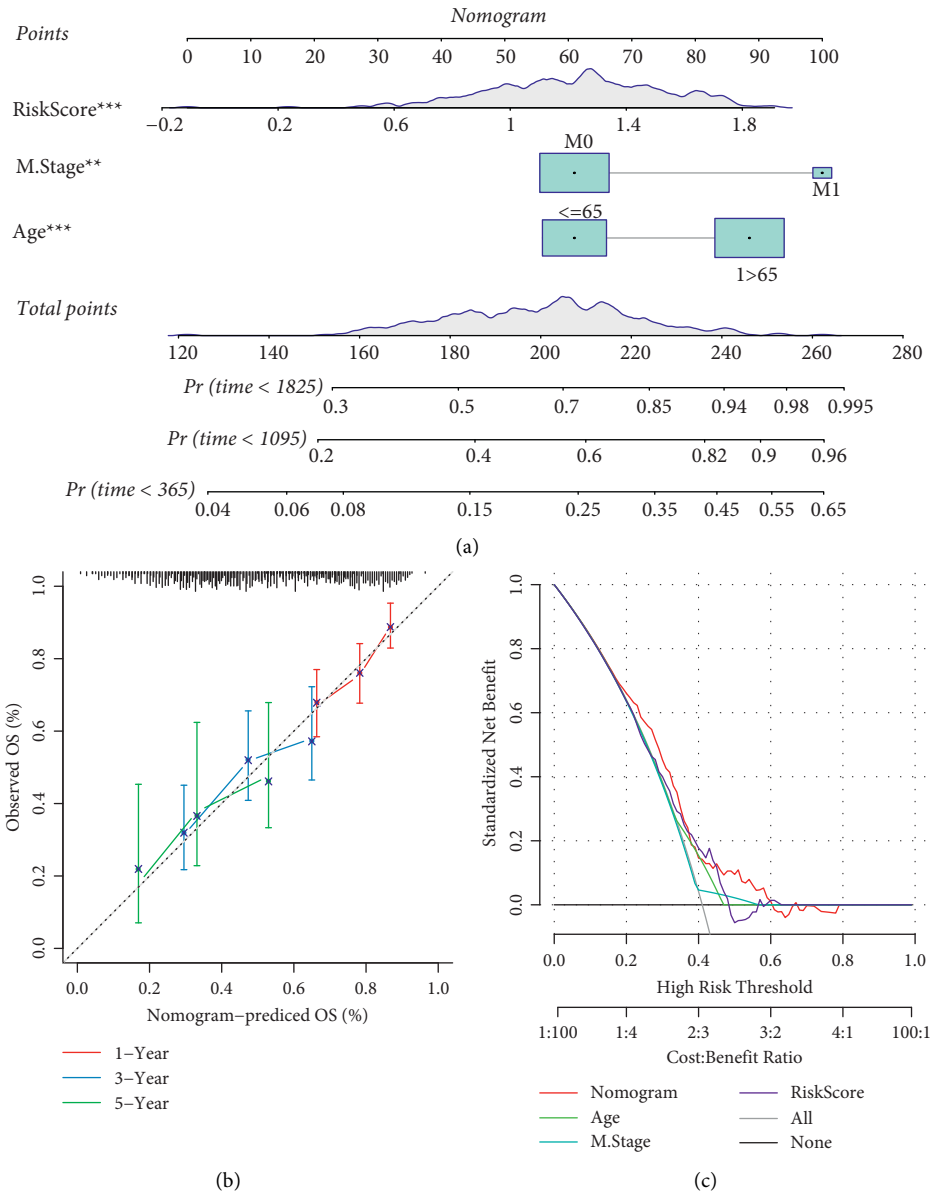

FIGURE 15: Visualization of the prognostic model. (a) A nomogram based on risk score, M stage and age for predicting overall survival. (b) The correction plot of 1-year, 3-year and 5-year OS predicted by the nomogram. (c) DCA curve of nomogram, age, M stage and risk score.

In addition, we analyzed the risk score in different kinds of groups, including treatment response, immune cells, tumor cells, and immune phenotype. CR patients had the lowest risk score among CR, PD, PR, and SD patients (Figure 17(a)). Previous study divided immune cells (IC) and tumor cells (TC) into three groups, according to the percentage of PD-L1 positive cells: IC0/TC0 (<1%), IC1/TC1 (≥1% but <5%) and IC2+/TC2+ (≥5%) [50]. The result showed that IC2+ and TC2+ group had the lowest risk score (Figures 17(b) and 17(c)), indicating that patients showing TME enriched with PD-L1-positive cells could be treated by anti-PD-L1 therapy. In terms of three immune phenotypes (desert, excluded, and inflamed), inflamed phenotype has been reported to be actively responsible to immunotherapy, which was consistent with the present result that inflamed group had the lowest risk score ($p < 0.0001$, Figure 17(d)). These analyses demonstrated that the prognostic signature was robust to predict outcomes for patients who have undergone immunotherapy.

4. Discussion

The antitumor effects of cytotoxic CD8 T cells rely on CD8 T cell differentiation and its infiltration in tumor site but can be suppressed by cytokines and chemokines secreted from tumor cells and immune cells in TME. It has been demonstrated that the inhibition of PD-1/PD-L1 can activate the function of cytotoxic CD8 T cells, thereby suppressing tumor proliferation. However, the anti-PD-1/PD-L1 therapy is only effective to certain cancer patients due to differential TME of patients. Therefore, an effective molecular subtyping system is strongly needed to characterize TME and status of CD8

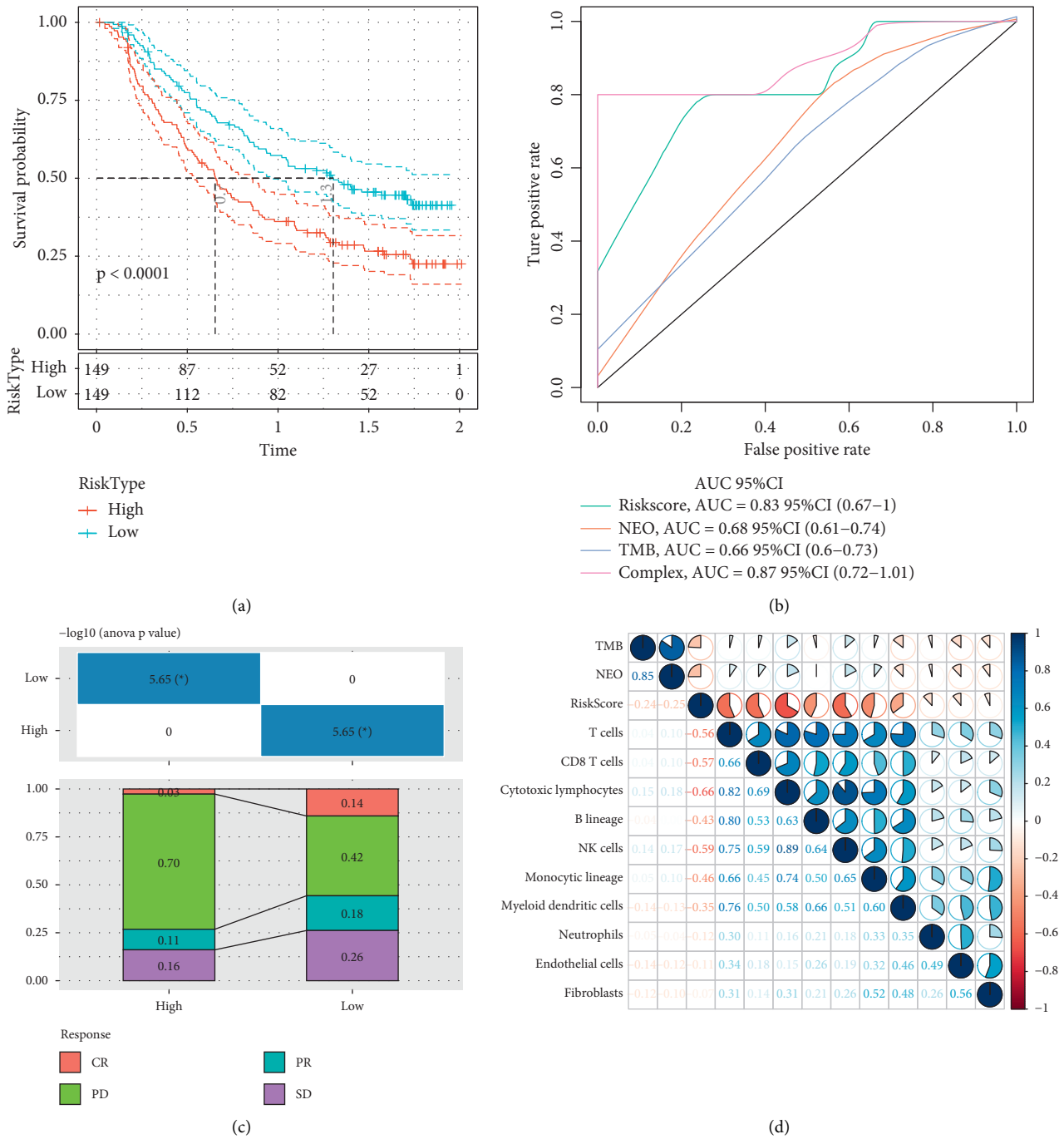

FIGURE 16: The application of the 8-gene prognostic signature in Imvigor210 dataset with patients treated by anti-PD-L1 inhibitors. (a) Kaplan-Meier survival curve of high-risk and low-risk groups. Log-rank test was performed. (b) ROC analysis of risk score, NEO and TMB in predicting prognosis. (c) The distribution of CR, PD, PR, SD patients in high-risk and low-risk groups. ANOVA was performed. (d) Pearson correlation analysis between risk score and TMB, NEO, and immune infiltration. Blue represents positive correlation and red represents negative correlation.

T cells, so as to predict the outcomes of immunotherapy. Although previous studies have developed various types of molecular subtypes for gastric cancer [7, 51], none of them focuses on CD8 T cells. In the present study, we constructed three immune subtypes (IC1, IC2, and IC3) based on marker genes related to CD8 T cells and fully characterized the tight relation among immune subtypes, TME, oncogenic pathways, chemotherapy, and immunotherapy.

Chemokines play a critical role in facilitating the migration of immune cells to tumor site and can also modulate tumor cell metastasis and growth [52]. Differential expression of chemokines and chemokine receptors was shown

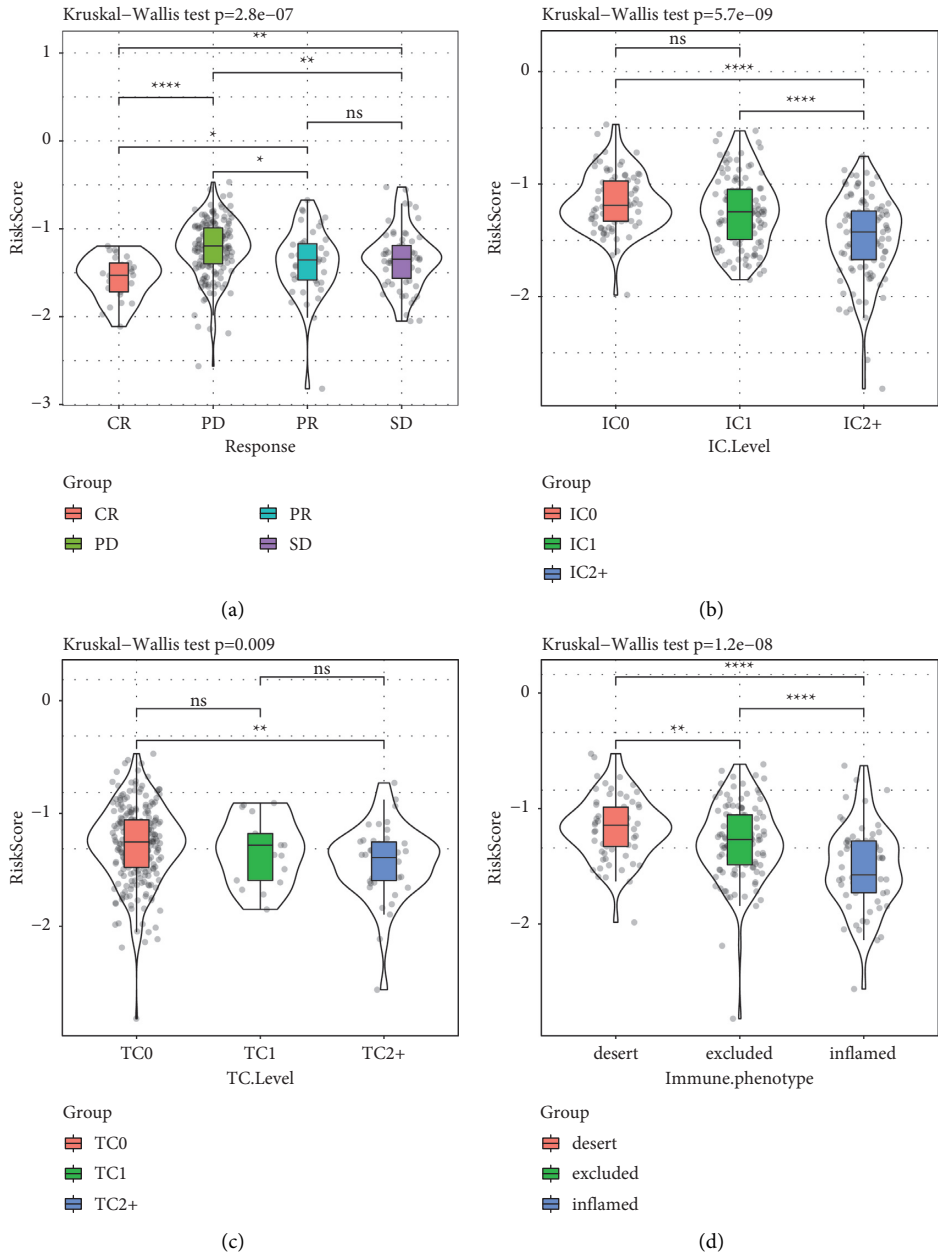

Figure 17: The relation of risk score to response treated by anti-PD-L1 (a), PD-L1-postive immune cells (b), PD-L1-postive tumor cells (c), and immune phenotypes (d). IC2+ represents IC2/IC3 and TC2+ represents TC2/TC3. Kruskal-Wallis test was performed. ns, no significance. $^{*}p < 0.05$, $^{**}p < 0.01$, $^{**}p < 0.001$, $^{****}p < 0.0001$. IC, immune cell. TC, tumor cell.

in three immune subtypes, which may explain the distinct OS outcomes of the three. CCL2, CCL5, CCL17, and CCL22 can induce immunosuppressive cell migration through their interactions with their receptors of CCR2, CCR5, and CCR4 in macrophages and regulatory T cells [53]. High expression of CCL2, CCL5, CCL17, and CCL22 and their receptors were observed in IC3 (Figure 7), which was related to a poor prognosis of IC3. CXCR4 can direct the migration of CD8 T cells and NK cells to tumor sites [54] but can also impede the infiltration of T cells to tumor cells through CXCL12 [55]. Pharmacological studies targeting CXCR4/CXCL12 axis demonstrated that CXCR4 antagonist releases T cells from CXCL12-rich stroma and increases T cell infiltration to tumor sites [55–57]. Moreover, CXCL12 can induce epithelial-mesenchymal transition (EMT) and gastric cancer metastasis possibly through the interaction between MET proto-oncogene (c-MET) and CXCR4 [58]. Among three immune subtypes, the expression tendency of CXCL12 was corresponding with CXCR4 expression, and IC3 had the highest expression level of them, which was consistent with its poor outcome. In addition, previous studies discovered that low expression of CXCL8 is associated with unfavorable prognosis in gastric cancer [59, 60], and the same phenomenon is also observed in the present study. These

observations proved that our immune subtyping system based on CD8 T cells was reliable.

Immune checkpoint blockade, such as inhibiting PD-1/PD-L1 axis, is a promising immunotherapy for the management of metastatic cancer patients. PD-1 expressed by CD8 T cells can interact with its ligand PD-L1 expressed by immune cells or tumor cells in TME, leading to T cell exhaustion and apoptosis, which refers to immune escape [61]. TIDE analysis revealed that IC3 had the highest score of T cell exhaustion and exclusion, indicating its impaired T cell function and poor prognosis (Figure 9). High expression of CXCL12 and CXCR4 was the possible reason for promoting the interaction between PD-1 and PD-L1, further triggering T cell dysfunction. In other words, high immune escape score of IC3 probably resulted from the activation of CXCL12/CXCR4 and PD-1/PD-L1 axis. Various immune checkpoint inhibitors have been examined in cancer patients; however, only around 20% of patients can obtain long-term benefits [3]. Our immune subtyping system could guide a better personalized therapy to GC patients.

The three immune subtypes manifested differential enrichment in oncogenic pathways, especially cell cycle, HIPPO, NOTCH, PI3K, TGF-β, RAS, and WNT signaling pathways. Apart from cell cycle pathway, activation of remained pathways is closely related to poor prognosis of cancer patients. Some inhibitors targeting HIPPO, NOTCH, PI3K, TGF-β, and WNT signaling pathways have been applied in clinical trials [62–65]. High enrichment of PI3K signaling pathway in GC samples, especially in IC3, may be a potential target for effective targeted drug therapy for GC patients. As for chemotherapeutic drugs, the subtyping system can also provide a direction for their clinical use; here, IC1 was found to be the most sensitive to cisplatin, cyclopamine, and rapamycin (Figures 10(c)–10(h)).

To further evaluate the clinical outcomes of GC patients, we developed an 8-gene prognostic signature and constructed a nomogram with an easy application in clinical practice. The signature can calculate the risk score of each patient and clearly stratify the patients into high-risk and low-risk groups with distinctly different prognosis. Functional analysis demonstrated that the risk score was closely associated with oncogenic pathways, such as cell cycle, NOTCH, WNT, and TGF-β signaling pathways (Figure 14). Furthermore, the signature also exhibited robust performance in screening metastatic urothelial carcinoma patients treated by anti-PD-1 (Figures 16(a)–16(c)). As for the relation between risk score and immune infiltration, high infiltration of CD8 T cells, cytotoxic lymphocytes, and NK cells is negatively correlated with risk score (Figure 16(d)), suggesting that immune infiltration was a critical factor of prognosis of patients who received anti-PD-1 therapy. Consistent with previous studies, in this study, patients with immune-desert phenotype had poor outcome of immunotherapy, while those with immune-inflamed phenotype can benefit much from immunotherapy [66] (Figure 17(d)).

By an integrated analysis on functional pathways, TME, immune response, immunotherapy, etc., we comprehensively characterized the links among them and demonstrated the reliability of the immune subtyping system. This subtyping system based on CD8 T cells together with the prognostic signature has demonstrated its applicability in clinical practice.

5. Conclusion

In conclusion, based on genes related to CD8 T cells, we developed three immune subtypes and an 8-gene prognostic signature to guide personalized therapy for GC patients. Three immune subtypes manifested differential responses to chemotherapy and immunotherapy. The prognostic signature can predict whether GC patients can benefit from immunotherapy.

Abbreviations

AIC: Akaike information criterion
AUC: Area under ROC curve
CDF: Cumulative distribution function
c-MET: MET proto-oncogene
CR: Complete response
DCA: Decision curve analysis
EMT: Epithelial-mesenchymal transition
GC: Gastric cancer
GEO: Gene expression omnibus
GO: Gene ontology
HR: Hazard ratio
IC: Immune cluster
IC50: The biochemical half maximal inhibitory concentration
KEGG: Kyoto encyclopedia of genes and genomes
LASSO: Least absolute shrinkage and selection operator
NEO: Neoantigen
OS: Overall survival
PCA: Principle component analysis
PD: Progressive disease
PD-1: Programmed cell death protein 1
PD-L1: Programmed cell death ligand 1
PR: Partial response
ROC: Receiver operating characteristic
SD: Stable disease
SEER: The surveillance, epidemiology, and end results
ssGSEA: Single sample gene set enrichment analysis
TAMs: Tumor-associated macrophages
TCGA: The cancer genome atlas
TMB: Tumor mutation burden
TME: Tumor microenvironment
TOM: Topological overlap matrix
WGCNA: Weighted correlation network analysis.

Data Availability

The data used to support the findings of this study are included within the article.

Conflicts of Interest

The authors declare that they have no competing interest.

Authors' Contributions

Jianyu Wu and Yajie Xiao equally contributed to this study. All authors made a significant contribution to the work reported, whether that is in the conception, study design, execution, acquisition of data, analysis and interpretation, or in all these areas; took part in drafting and revising or critically reviewing the article; gave final approval of the version to be published; have agreed on the journal to which the article has been submitted; and agree to be accountable for all aspects of the work.

Acknowledgments

The authors did not receive specific funding.

Supplementary Materials

Supplementary Figure S1. Elimination of batch effects for GSE cohort. (A) The PCA result before eliminating batch effects. (B) The PCA result after eliminating batch effects. Supplementary Figure S2. Elimination of batch effects for immune cell datasets. (A) The PCA result before eliminating batch effects. (B) The PCA result after eliminating batch effects. Supplementary Figure S3. Kaplan-Meier survival curve of C1, C2, C3, C4, and C6 immune subtypes reported in the previous study. Log-rank test was performed. Supplementary Figure S4. LASSO regression analysis for optimizing the model. (A) The coefficients of each variate (gene) change with different lambda values. The red dotted line represents when lambda = 0.0671, the model was the optimal. (B) Confidential interval under different lambda values. The red dot represents the site of the optimal lambda. Supplementary Figure S5. Assessment of the prognostic model in the test group. (A) The distribution of high-risk and low-risk groups, and the expression of 8 prognostic genes corresponding to risk score. (B) ROC analysis and AUC of 1-year, 3-year and 5-year OS predicted by the 8-gene signature. (C) Kaplan-Meier survival curve of high-risk and low-risk groups. Log-rank test was performed. Supplementary Figure S6. Validation of the prognostic model in TCGA-STAD dataset. (A) The distribution of high-risk and low-risk groups, and the expression of 8 prognostic genes corresponding to risk score. (B) ROC analysis and AUC of 1-year, 3-year and 5-year OS predicted by the 8-gene signature. (C) Kaplan-Meier survival curve of high-risk and low-risk groups. Log-rank test was performed. Supplementary Figure S7. The expression difference of 8 genes. (A) Expression difference of 8 genes in cancer and adjacent cancer. (B) Expression difference of 8 genes in three molecular subtypes. Supplementary Table S1. Sample information of each data set. Supplementary Table S2. The clinical information of TCGA-STAD dataset and GSE cohort. Supplementary Table S3. The information of training group and test group. Supplementary Table S4. Molecular subtypes of TCGA samples. (*Supplementary Materials*)

References

[1] P. Rawla and A. Barsouk, "Epidemiology of gastric cancer: global trends, risk factors and prevention," *Gastroenterology Review*, vol. 14, no. 1, pp. 26–38, 2019.

[2] A. P. Thrift and H. B. El-Serag, "Burden of gastric cancer," *Clinical Gastroenterology and Hepatology*, vol. 18, no. 3, pp. 534–542, 2020.

[3] C. Coutzac, S. Pernot, N. Chaput, and A. Zaanan, "Immunotherapy in advanced gastric cancer, is it the future?" *Critical Reviews in Oncology/Hematology*, vol. 133, pp. 25–32, 2019.

[4] M. Wang, J. Zhao, L. Zhang et al., "Role of tumor microenvironment in tumorigenesis," *Journal of Cancer*, vol. 8, no. 5, pp. 761–773, 2017.

[5] M. Najafi, N. H. Goradel, B. Farhood et al., "Tumor microenvironment: interactions and therapy," *Journal of Cellular Physiology*, vol. 234, no. 5, pp. 5700–5721, 2019.

[6] T. Wu and Y. Dai, "Tumor microenvironment and therapeutic response," *Cancer Letters*, vol. 387, pp. 61–68, 2017.

[7] V. Thorsson, D. L. Gibbs, S. D. Brown et al., "The immune landscape of cancer," *Immunity*, vol. 48, no. 4, pp. 812–830.e814, 2018.

[8] Y.-J. Zhou, G.-Q. Zhu, X.-F. Lu et al., "Identification and validation of tumour microenvironment-based immune molecular subgroups for gastric cancer: immunotherapeutic implications," *Cancer Immunology, Immunotherapy*, vol. 69, no. 6, pp. 1057–1069, 2020.

[9] H. R. Ali, E. Provenzano, S.-J. Dawson et al., "Association between CD8+ T-cell infiltration and breast cancer survival in 12 439 patients," *Annals of Oncology*, vol. 25, no. 8, pp. 1536–1543, 2014.

[10] P. S. Kim and R. Ahmed, "Features of responding T cells in cancer and chronic infection," *Current Opinion in Immunology*, vol. 22, no. 2, pp. 223–230, 2010.

[11] J. Kmiecik, A. Poli, N. H. C. Brons et al., "Elevated CD3+ and CD8+ tumor-infiltrating immune cells correlate with prolonged survival in glioblastoma patients despite integrated immunosuppressive mechanisms in the tumor microenvironment and at the systemic level," *Journal of Neuroimmunology*, vol. 264, no. 1-2, pp. 71–83, 2013.

[12] Y. Wang, C. Zhu, W. Song, J. Li, G. Zhao, and H. Cao, "PD-L1 expression and CD8(+) T cell infiltration predict a favorable prognosis in advanced gastric cancer," *Journal of Immunology Research*, vol. 2018, Article ID 4180517, 10 pages, 2018.

[13] V. R. Juneja, K. A. McGuire, R. T. Manguso et al., "PD-L1 on tumor cells is sufficient for immune evasion in immunogenic tumors and inhibits CD8 T cell cytotoxicity," *Journal of Experimental Medicine*, vol. 214, no. 4, pp. 895–904, 2017.

[14] S. Chikuma, "CTLA-4, an essential immune-checkpoint for T-cell activation," *Current Topics in Microbiology and Immunology*, vol. 410, pp. 99–126, 2017.

[15] B. Rowshanravan, N. Halliday, and D. M. Sansom, "CTLA-4: a moving target in immunotherapy," *Blood*, vol. 131, no. 1, pp. 58–67, 2018.

[16] A. Salmaninejad, S. F. Valilou, A. G. Shabgah et al., "PD-1/PD-L1 pathway: basic biology and role in cancer immunotherapy," *Journal of Cellular Physiology*, vol. 234, no. 10, pp. 16824–16837, 2019.

[17] B. Wang, L. Qin, M. Ren, and H. Sun, "Effects of combination of anti-CTLA-4 and anti-PD-1 on gastric cancer cells proliferation, apoptosis and metastasis," *Cellular Physiology and Biochemistry*, vol. 49, no. 1, pp. 260–270, 2018.

[18] J. Xu, Y. Zhang, R. Jia et al., "Anti-PD-1 antibody SHR-1210 combined with apatinib for advanced hepatocellular carcinoma, gastric, or esophagogastric junction cancer: an open-label, dose escalation and expansion study," *Clinical Cancer Research*, vol. 25, no. 2, pp. 515–523, 2019.

[19] T. Frankel, M. P. Lanfranca, and W. Zou, "The role of tumor microenvironment in cancer immunotherapy," *Advances in Experimental Medicine and Biology*, vol. 1036, pp. 51–64, 2017.

[20] S. C. Oh, B. H. Sohn, J.-H. Cheong et al., "Clinical and genomic landscape of gastric cancer with a mesenchymal phenotype," *Nature Communications*, vol. 9, no. 1, p. 1777, 2018.

[21] S.-J. Yoon, J. Park, Y. Shin et al., "Deconvolution of diffuse gastric cancer and the suppression of CD34 on the BALB/c nude mice model," *BMC Cancer*, vol. 20, no. 1, p. 314, 2020.

[22] Y. Zhang, J. H. Ohyashiki, N. Shimizu, and K. Ohyashiki, "Aberrant expression of NK cell receptors in Epstein-Barr virus-positive$\gamma\delta$T-cell lymphoproliferative disorders," *Hematology*, vol. 15, no. 1, pp. 43–47, 2010.

[23] B. J. Jansen, I. E. Sama, D. Eleveld-Trancikova et al., "MicroRNA genes preferentially expressed in dendritic cells contain sites for conserved transcription factor binding motifs in their promoters," *BMC Genomics*, vol. 12, no. 1, p. 330, 2011.

[24] M. Tosolini, F. Pont, D. Bétous et al., "Human monocyte recognition of adenosine-based cyclic dinucleotides unveils the A2a Galphas protein-coupled receptor tonic inhibition of mitochondrially induced cell death," *Molecular and Cellular Biology*, vol. 35, no. 2, pp. 479–495, 2015.

[25] T. K. Garg, S. M. Szmania, J. A. Khan et al., "Highly activated and expanded natural killer cells for multiple myeloma immunotherapy," *Haematologica*, vol. 97, no. 9, pp. 1348–1356, 2012.

[26] F. Allantaz, D. T. Cheng, T. Bergauer et al., "Expression profiling of human immune cell subsets identifies miRNA-mRNA regulatory relationships correlated with cell type specific expression," *PLoS One*, vol. 7, no. 1, Article ID e29979, 2012.

[27] M. G. Constantinides, D. Picard, A. K. Savage, and A. Bendelac, "A naive-like population of human CD1d-restricted T cells expressing intermediate levels of promyelocytic leukemia zinc finger," *The Journal of Immunology*, vol. 187, no. 1, pp. 309–315, 2011.

[28] L. L. Aung, A. Brooks, S. A. Greenberg, M. L. Rosenberg, S. Dhib-Jalbut, and K. E. Balashov, "Multiple sclerosis-linked and interferon-beta-regulated gene expression in plasmacytoid dendritic cells," *Journal of Neuroimmunology*, vol. 250, no. 1-2, pp. 99–105, 2012.

[29] K. C. Malcolm, E. M. Nichols, S. M. Caceres et al., "Mycobacterium abscessus induces a limited pattern of neutrophil activation that promotes pathogen survival," *PLoS One*, vol. 8, no. 2, Article ID e57402, 2013.

[30] L. H. Nagy, I. Grishina, M. Macal et al., "Chronic HIV infection enhances the responsiveness of antigen presenting cells to commensal Lactobacillus," *PLoS One*, vol. 8, no. 8, Article ID e72789, 2013.

[31] N. A. Mabbott, J. Baillie, H. Brown, T. C. Freeman, and D. A. Hume, "An expression atlas of human primary cells: inference of gene function from coexpression networks," *BMC Genomics*, vol. 14, no. 1, p. 632, 2013.

[32] C. Martínez-Cingolani, M. Grandclaudon, M. Jeanmougin, M. Jouve, R. Zollinger, and V. Soumelis, "Human blood BDCA-1 dendritic cells differentiate into Langerhans-like cells with thymic stromal lymphopoietin and TGF-β," *Blood*, vol. 124, no. 15, pp. 2411–2420, 2014.

[33] A. Ricciardi, A. R. Elia, P. Cappello et al., "Transcriptome of hypoxic immature dendritic cells: modulation of chemokine/receptor expression," *Molecular Cancer Research*, vol. 6, no. 2, pp. 175–185, 2008.

[34] K. Dybkaer, J. Iqbal, G. Zhou et al., "Genome wide transcriptional analysis of resting and IL2 activated human natural killer cells: gene expression signatures indicative of novel molecular signaling pathways," *BMC Genomics*, vol. 8, no. 1, p. 230, 2007.

[35] W. Hugo, J. M. Zaretsky, L. Sun et al., "Genomic and transcriptomic features of response to anti-PD-1 therapy in metastatic melanoma," *Cell*, vol. 165, no. 1, pp. 35–44, 2016.

[36] N. Vander Velde, A. Guerin, R. Ionescu-Ittu et al., "Comparative effectiveness of non-cisplatin first-line therapies for metastatic urothelial carcinoma: phase 2 IMvigor210 study versus US patients treated in the veterans health administration," *European Urology Oncology*, vol. 2, no. 1, pp. 12–20, 2019.

[37] L. Gautier, L. Cope, B. M. Bolstad, and R. A. Irizarry, "Affy--analysis of affymetrix genechip data at the probe level," *Bioinformatics*, vol. 20, no. 3, pp. 307–315, 2004.

[38] I. Diboun, L. Wernisch, C. A. Orengo, and M. Koltzenburg, "Microarray analysis after RNA amplification can detect pronounced differences in gene expression using limma," *BMC Genomics*, vol. 7, no. 1, p. 252, 2006.

[39] P. Langfelder and S. Horvath, "WGCNA: an R package for weighted correlation network analysis," *BMC Bioinformatics*, vol. 9, no. 1, p. 559, 2008.

[40] G. Yu, L.-G. Wang, Y. Han, and Q.-Y. He, "ClusterProfiler: an R package for comparing biological themes among gene clusters," *OMICS: A Journal of Integrative Biology*, vol. 16, no. 5, pp. 284–287, 2012.

[41] B. Chen, M. S. Khodadoust, C. L. Liu, A. M. Newman, and A. A. Alizadeh, "Profiling tumor infiltrating immune cells with CIBERSORT," *Methods in Molecular Biology*, vol. 1711, pp. 243–259, 2018.

[42] S. Hänzelmann, R. Castelo, and J. Guinney, "GSVA: gene set variation analysis for microarray and RNA-seq data," *BMC Bioinformatics*, vol. 14, no. 1, p. 7, 2013.

[43] M. D. Wilkerson and D. N. Hayes, "ConsensusClusterPlus: a class discovery tool with confidence assessments and item tracking," *Bioinformatics*, vol. 26, no. 12, pp. 1572-1573, 2010.

[44] T. Hastie and J. Qian, *Glmnet Vignette*, pp. 1–30, Stanford University, Stanford, CA, USA, 2016.

[45] B. Ripley, B. Venables, D. M. Bates et al., "Package "mass"," *Cran R*, vol. 538, pp. 113–120, 2013.

[46] M. Masiero, F. C. Simões, H. D. Han et al., "A core human primary tumor angiogenesis signature identifies the endothelial orphan receptor ELTD1 as a key regulator of angiogenesis," *Cancer Cell*, vol. 24, no. 2, pp. 229–241, 2013.

[47] L. Danilova, W. J. Ho, Q. Zhu et al., "Programmed cell death ligand-1 (PD-L1) and CD8 expression profiling identify an immunologic subtype of pancreatic ductal adenocarcinomas with favorable survival," *Cancer Immunology Research*, vol. 7, no. 6, pp. 886–895, 2019.

[48] F. Sanchez-Vega, M. Mina, J. Armenia et al., "Oncogenic signaling pathways in the cancer Genome atlas," *Cell*, vol. 173, no. 2, pp. 321–337.e310, 2018.

[49] P. Jiang, S. Gu, D. Pan et al., "Signatures of T cell dysfunction and exclusion predict cancer immunotherapy response," *Nature Medicine*, vol. 24, no. 10, pp. 1550–1558, 2018.

[50] J. E. Rosenberg, J. Hoffman-Censits, T. Powles et al., "Atezolizumab in patients with locally advanced and metastatic urothelial carcinoma who have progressed following treatment with platinum-based chemotherapy: a single-arm, multicentre, phase 2 trial," *Lancet (London, England)*, vol. 387, no. 10031, pp. 1909–1920, 2016.

[51] Cancer Genome Atlas Research Network, "Comprehensive molecular characterization of gastric adenocarcinoma," *Nature*, vol. 513, no. 7517, pp. 202–209, 2014.

[52] M. T. Chow and A. D. Luster, "Chemokines in cancer," *Cancer Immunology Research*, vol. 2, no. 12, pp. 1125–1131, 2014.

[53] K. Kohli, V. G. Pillarisetty, and T. S. Kim, "Key chemokines direct migration of immune cells in solid tumors," *Cancer Gene Therapy*, vol. 29, 2021.

[54] M. Goedhart, S. Gessel, R. van der Voort et al., "CXCR4, but not CXCR3, drives CD8(+) T-cell entry into and migration through the murine bone marrow," *European Journal of Immunology*, vol. 49, no. 4, pp. 576–589, 2019.

[55] Y. D. Seo, X. Jiang, K. M. Sullivan et al., "Mobilization of CD8+ T cells via CXCR4 blockade facilitates PD-1 checkpoint therapy in human pancreatic cancer," *Clinical Cancer Research*, vol. 25, no. 13, pp. 3934–3945, 2019.

[56] C. Feig, J. O. Jones, M. Kraman et al., "Targeting CXCL12 from FAP-expressing carcinoma-associated fibroblasts synergizes with anti-PD-L1 immunotherapy in pancreatic cancer," *Proceedings of the National Academy of Sciences*, vol. 110, no. 50, pp. 20212–20217, 2013.

[57] B. Bockorny, V. Semenisty, T. Macarulla et al., "BL-8040, a CXCR4 antagonist, in combination with pembrolizumab and chemotherapy for pancreatic cancer: the COMBAT trial," *Nature Medicine*, vol. 26, no. 6, pp. 878–885, 2020.

[58] Y. Cheng, Y. Song, J. Qu et al., "The chemokine receptor CXCR4 and c-MET cooperatively promote epithelial-mesenchymal transition in gastric cancer cells," *Translational oncology*, vol. 11, no. 2, pp. 487–497, 2018.

[59] U. M. Raja, G. Gopal, S. Shirley, A. S. Ramakrishnan, and T. Rajkumar, "Immunohistochemical expression and localization of cytokines/chemokines/growth factors in gastric cancer," *Cytokine*, vol. 89, pp. 82–90, 2017.

[60] P. Yan, Y. He, K. Xie, S. Kong, and W. Zhao, "In silico analyses for potential key genes associated with gastric cancer," *PeerJ*, vol. 6, Article ID e6092, 2018.

[61] G. L. Beatty and W. L. Gladney, "Immune escape mechanisms as a guide for cancer immunotherapy," *Clinical Cancer Research*, vol. 21, no. 4, pp. 687–692, 2015.

[62] H. W. Park and K.-L. Guan, "Regulation of the Hippo pathway and implications for anticancer drug development," *Trends in Pharmacological Sciences*, vol. 34, no. 10, pp. 581–589, 2013.

[63] N. Takebe, D. Nguyen, and S. X. Yang, "Targeting notch signaling pathway in cancer: clinical development advances and challenges," *Pharmacology & Therapeutics*, vol. 141, no. 2, pp. 140–149, 2014.

[64] J. T. Buijs, K. R. Stayrook, and T. A. Guise, "The role of TGF-β in bone metastasis: novel therapeutic perspectives," *BoneKEy Reports*, vol. 1, no. 6, p. 96, 2012.

[65] S. G. Pai, B. A. Carneiro, J. M. Mota et al., "Wnt/beta-catenin pathway: modulating anticancer immune response," *Journal of Hematology & Oncology*, vol. 10, no. 1, p. 101, 2017.

[66] M. Binnewies, E. W. Roberts, K. Kersten et al., "Understanding the tumor immune microenvironment (TIME) for effective therapy," *Nature Medicine*, vol. 24, no. 5, pp. 541–550, 2018.

Hindawi
Journal of Oncology
Volume 2022, Article ID 4097428, 11 pages
https://doi.org/10.1155/2022/4097428

Research Article

Comprehensive Analysis of Prognostic Value and Immune Infiltration of MMP12 in Esophageal Squamous Cell Carcinoma

Jing-tao Mao,[1] Qiang Lu,[2] Peng-yu Jing,[2] Zi-liang Li,[1] Xiao-qi Yang,[1] Ji-peng Zhang,[2] and Zhe Li[3]

[1]*Department of Thoracic Surgery, Shaanxi Provincial Sengong Hospital, Xi'an, Shaanxi 710300, China*
[2]*Department of Thoracic Surgery, Tangdu Hospital, The Air Force Military Medical University, Xi'an, Shaanxi 710038, China*
[3]*Department of Thoracic Surgery, The Ninth Hospital of Xi' an, Xi'an, Shaanxi 710054, China*

Correspondence should be addressed to Zhe Li; lizhe197906@163.com

Received 16 January 2022; Revised 6 February 2022; Accepted 9 February 2022; Published 27 February 2022

Academic Editor: Fu Wang

Esophageal squamous cell carcinoma (ESCC) is a typical neoplastic disease and a frequent cause of death in China. The prognosis of most ESCC patients is still poor. Previous studies demonstrated that MMP12 is involved in tumor metastasis. However, its clinical significance and association with cancer immunity remained largely unclear. In this study, we first analyzed the expressing pattern of MMPs in ESCC from TCGA datasets and found that several MMPs expression was distinctly increased in ESCC. However, only MMP12 expression was associated with five-year survival of ESCC patients. Then, we focused on MMP12 and found its high expression was positively related to advanced clinical stages of ESCC specimens. KEGG assays revealed MMP12 may influence the activity of several tumor-related pathways, such as the Toll-like receptor signaling pathway, TNF signaling pathway, and IL-17 signaling pathway. Then, we sought to determine whether MMP12 expressions were related to immune cell infiltration in ESCC. We observed that increased MMP12 levels were positively associated with the infiltration levels of mast cells activated and macrophages M0. However, eosinophils, B cells naïve, and mast cells resting exhibited an opposite result. Finally, we showed that knockdown of MMP12 suppressed the proliferation of ESCC cells. Overall, our findings proved that high expression of MMP12 may be a novel and valuable prognostic factor in ESCC.

1. Introduction

Esophageal squamous cell carcinoma (ESCC) remains the most prevailing histological subtype of esophageal cancer in developing nations or regions, such as China and Iran [1]. Among many types of clinical features associated with ESCC progression, distant metastases remain the critical element for unfavorable survivals [2]. Although the significant progresses have been achieved in the effective treatments of ESCC by the use of chemoradiotherapy and surgery in recent years, the 5-year survival rate remains <40% [3, 4]. Consequently, it is urgent to comprehend the genetic and molecular mechanism of ESCC to develop potential diagnostic therapy and treatment on ESCC.

As a family of zinc-dependent proteolytic enzymes, the matrix metalloproteinases (MMPs) are able to degrade the extracellular matrix and basement membrane [5]. More and more studies have demonstrated the positive effects of MMPs on the tumor grow, neoangiogenesis, migration, and metastasis [6, 7]. In the past two decades, several suppressors of MMPs have been developed in many types of tumors [8, 9]. However, although in vitro and in vivo experiments are very beneficial, the clinical experiments failed due to the lack of susceptibility and serious adverse reactions. Many researchers have analyzed the possible reason, and several MMPs which exhibit tumor-suppressor functions may be the most important one [10, 11]. With the developments of understating the potential function of MMPs in tumor progression, the sensitive narrow-spectrum MMPs inhibitors were currently being developed. In addition, some studies have reported the dysregulation of MMPs and their association with clinical outcome in several types of tumors [12–14].

In recent years, the effect of MMP12 has been verified in tumors. For example, MMP12 was highly expressed in adamantinomatous craniopharyngioma, while its knockdown inhibited the proliferation and attack of adamantinomatous craniopharyngioma cells [15]. Lin et al. reported that MMP12 was overexpressed in cervical cancer cells, and its silence clearly inhibited cell migration and invasion both in vitro and in vivo [16]. High expressions of MMP12 were related to the prognosis of several types of tumors, such as hepatocellular carcinoma and cutaneous melanoma [17, 18]. However, the expression and function of MMP12 in ESCC were rarely reported.

This study is to sort out the clinical significance of MMP12 on ESCC and its contribution to cancer immunity.

2. Methods and Materials

2.1. Data Collection from the TCGA Database. The data of RNA transcriptome and the corresponding clinicopathological and survival for patients were obtained from the Cancer Genome Atlas (TCGA, https://cancergenome.nih.gov/). All assays were carried out based on the publication guidelines of TCGA. 160 ESCC samples and 11 nontumor samples were enrolled in this study.

2.2. Cell Culture and Transfection. Het-1A and ESCC cell lines (KYSE30, EC-1, Eca109 and EC9706) were bought from the Shanghai Institute of Biochemistry and Cell Biology (Shanghai, China). The cells were cultured in RPMI-1640 medium supplemented with 10% fetal bovine serum (FBS) (Gibco BRL, USA) and maintained in a humidified incubator at 37°C with 5% CO_2.

MMP12 small interfering RNA (si-MMP12) and the corresponding control RNA (si-NC) were purchased from Jinlai Biology (Beijing, China). Lipofectamine 3000 was applied for cellular transfection.

2.3. Identification of Differently Expressed MMPs. "Limma" package of R was applied to sort out the differently expressed MMPs between ESCC specimens and nontumor specimens. The keys with $|\log FC| \geq 1$ and p value <0.05 were defined as significant cutoff points. In addition, gene annotation and its data files of the differently expressed MMPs were collected through R software.

2.4. Prognosis-Related MMPs Screening. We constructed the Kaplan–Meier plots of MMPs in the TCGA dataset to comprehend the overall survival (OS) and verified it by log-rank tests.

2.5. Screening of Dysregulated Genes and GO and KEGG Pathway Assays. We carried out GO and KEGG pathway assays on the dysregulated genes between high MMP12 expression group and low MMP12 expression group: GO assays included molecular function (MF), cell component (CC), and biological process (BP). KEGG (http://www.genome.jp/) was a novel method for exploring the related regulatory pathways involved in gene functions. ClusterProfiler package was applied for GO and KEGG pathway assays, while GOplot package was applied for cluster assays [19]. Besides, it was thought to grind a significant difference when both the p value and q value were less than 0.05 only.

2.6. Assessment of Immune Infiltration. As a deconvolution algorithm, CIBERSORT applied the expressions of 547 tag genes to define the structure of immune cells in specimens. Hence, the associated proportion of 22 infiltrating immune cells was examined by the use of CIBERSORT in all samples from TCGA datasets. $P < 0.05$ was deem as statistically valuable.

2.7. Quantitative Real-Time PCR. RNA was isolated using TRIzol (Invitrogen, Pudong, Shanghai, China) following the manufacture's protocols. A Transcript RT kit (Vazyme, Nanjing, Jiangsu, China) was applied to compound the first strand cDNA. Real-time RT-PCR was performed to detect the expression of CRNDE using the One-Step SYBR PrimeScript RT-PCR Kit (Takara). GADPH was used as endogenous controls. The relative expressions were calculated using the $2^{-\Delta\Delta Ct}$ method.

2.8. CCK-8 Assays. Cellular proliferation was examined applying the Cell Counting Kit-8 (Beyotime, Haidian, China). Cells were seeded into 48-well plates at 3×10^3 cells/well cell concentration. Then, 15 μL CCK-8 solution was added to each well. At a wavelength of 450 nm for each well, the absorbance was examined.

2.9. Statistical Analysis. We adopted R (version 3.6.0) to conduct statistical analyses. The Wilcox test was applied to determine the dysregulated genes and infiltrative immune cells. We obtain the survival curves by the Kaplan–Meier method and compared by the log-rank test. P value <0.05 was considered statistically significant.

3. Results

3.1. Identification of the Dysregulated MMPs in ESCC. To screen the dysregulated MMPs in ESCC, we analyzed TCGA datasets using Limma and edgeR packages. The dysregulated MMPs were shown in heat map (Figure 1(a)). We noticed that the behaviors of MMP12 were distinctly enhanced on ESCC specimens comparing to nontumor specimens, including MMP1 (Figure 1(b)), MMP3 (Figure 1(c)), MMP7 (Figure 1(d)), MMP8 (Figure 1(e)), MMP9 (Figure 1(f)), MMP13 (Figure 1(g)), MMP10 (Figure 1(h)), MMP11 (Figure 1(i)), MMP12 (Figure 1(j)), MMP14 (Figure 1(k)), MMP17 (Figure 1(l)), and MMP20 (Figure 1(m)).

3.2. The Survival-Related MMPs in ESCC. Then, we performed Kaplan–Meier methods to screen survival-related MMPs in ESCC. Only high MMP12 expression was associated with a short overall survival of ESCC patients (Figure 2(a)). For other MMPs, the results indicated no

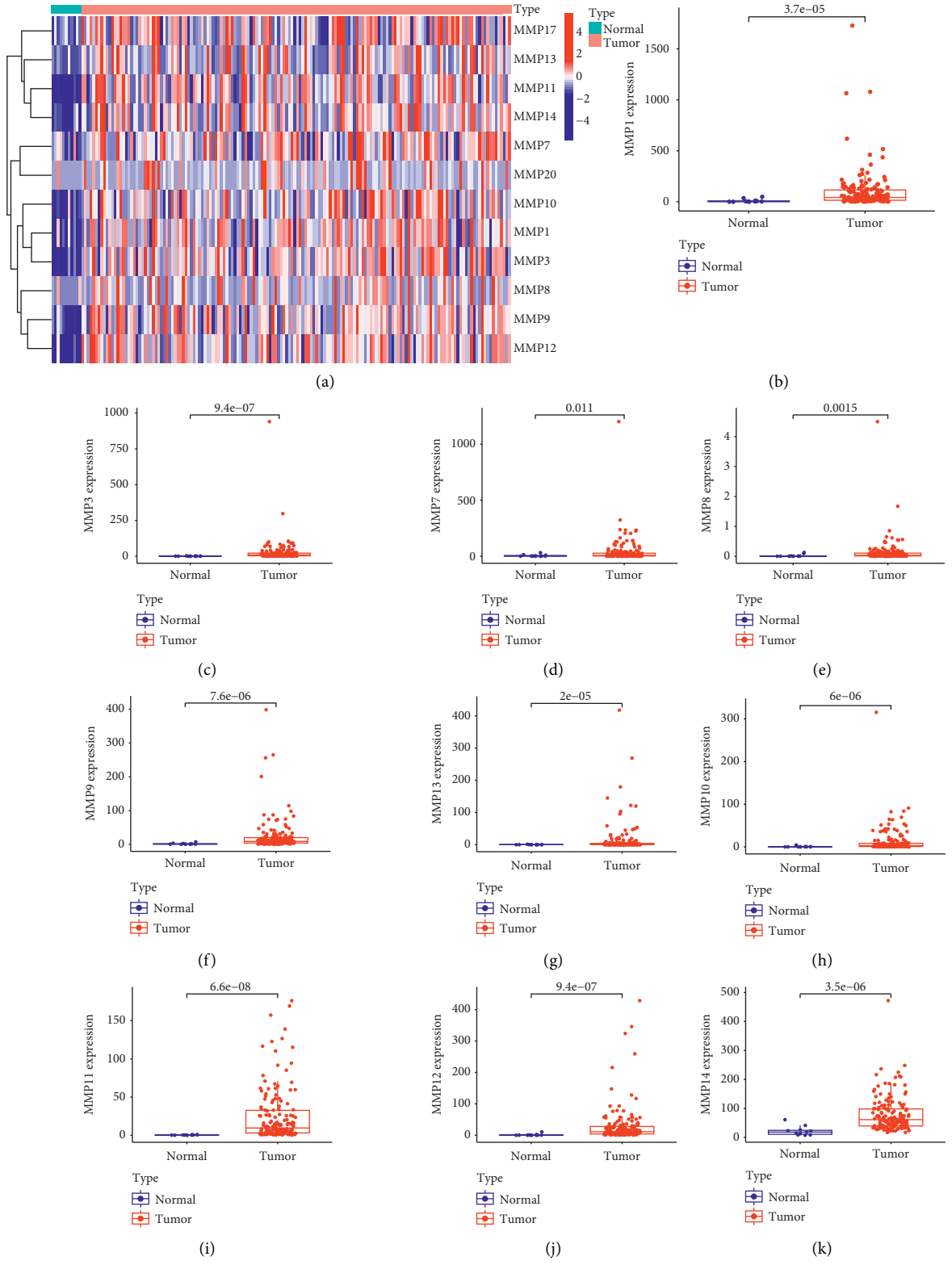

Figure 1: Continued.

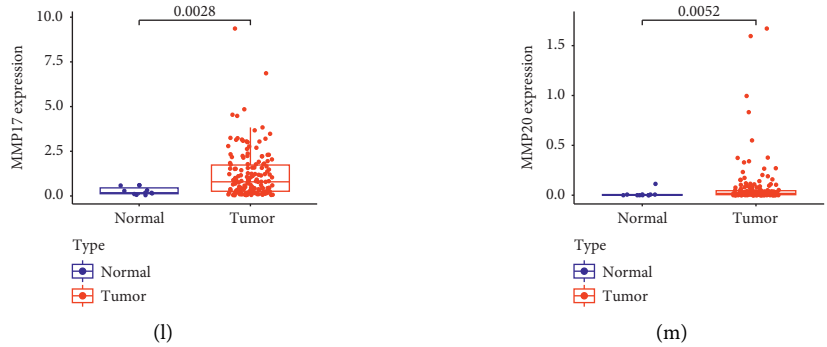

Figure 1: Identification of the dysregulated MMPs in ESCC. (a) Hierarchical clustering analysis of differently expressed MMPs in ESCC and normal tissues. (b)–(m) An increased expression of (b) MMP1, (c) MMP3, (d) MMP7, (e) MMP8, (f) MMP9, (g) MMP13, (h) MMP10, (i) MMP11, (j) MMP12, (k) MMP14, (l) MMP17, and (m) MMP20 observed in ESCC specimens compared with nontumor specimens.

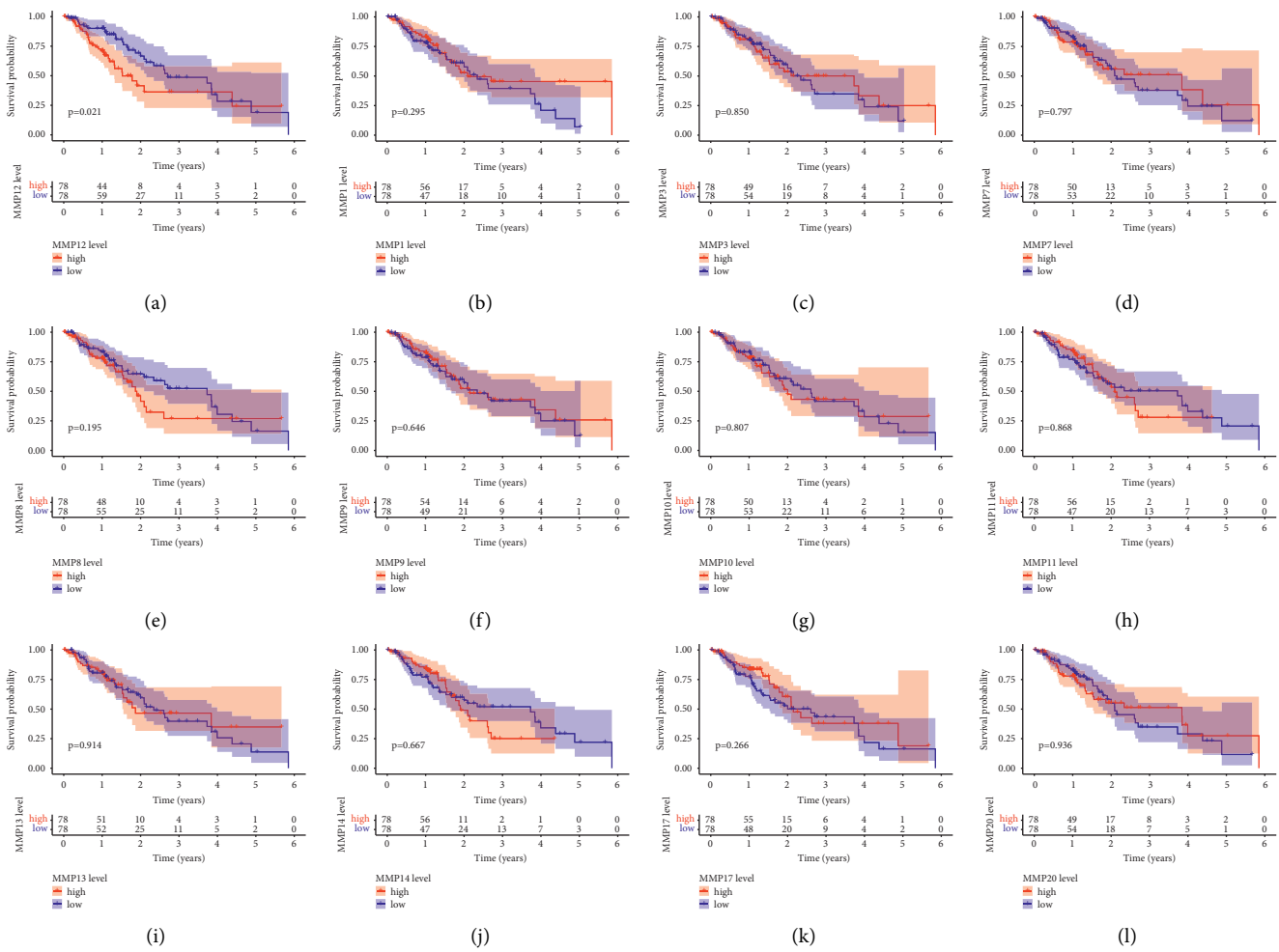

Figure 2: Identification of survival-related MMPs. (a) Survival analysis for MMP12 in ESCC. Patient with high MMP12 expression showed a shorter overall survival of ESCC patients. (b)–(l) Survival analysis for (b) MMP1, (c) MMP3, (d) MMP7, (e) MMP8, (f) MMP9, (g) MMP10, (h) MMP11, (i) MMP13, (j) MMP14, (k) MMP17, and (l) MMP20 in ESCC. According to median expression of MMPs, the patients were classified into high-level and low-level groups.

obvious difference in the survival rate between patients with high MMPs and low ones (Figures 2(b)–2(l)). Thus, our attention focused on MMP12.

3.3. Correlation between MMP12 Behaviors and Clinical Trials in ESCC Patients. We further examined the associations between MMP12 patients' clinical features and the

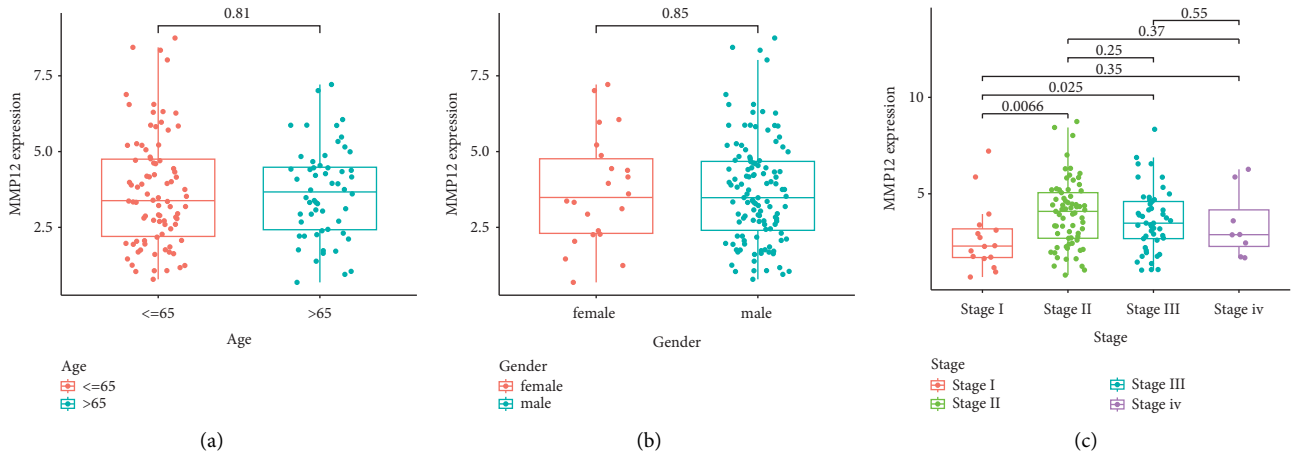

FIGURE 3: The relationship between MMP12 and clinical features. (a) Age ($p = 0.81$). (b) Gender ($p = 0.85$). (c) Clinical phase ($p < 0.05$).

MMP12 expressions and concluded that MMP12 expressions were not associated with age ($p = 0.81$, Figure 3(a)) and gender ($p = 0.85$, Figure 3(b)). However, we observed that the expressions of MMP12 in ESCC were distinctly linked to stage (Figure 3(c)).

3.4. Functional Enrichment Analysis of Genes That Were Coexpressed with MMP12. To explore the biological function of MMP12 in ESCC, we divided all ESCC specimens into two (high and low) based on the mean expression of MMP12 in all ESCC samples. A total of 15 differently expressed genes between low and high MMP12 expression groups were screened. Next, 15 genes were chosen to perform GO and KEGG analyses using the ClusterProfiler R package. The results showed that MMP12-associated dysregulated genes were mainly involved in processes like the collagen catabolic process, extracellular matrix disassembly, collagen-containing, blood microparticle, metalloendopeptidase activity, and chemokine activity (Figure 4(a)). Meanwhile, KEGG pathway analysis showed that pathways were significantly enriched (Figure 4(b)) including the relaxin signaling pathway, Toll-like receptor signaling pathway, TNF signaling pathway, IL-17 signaling pathway, and transcriptional misregulation in cancer [20–22].

3.5. Distribution of Tumor-Infiltrating Immune Cells. We explored the pattern of immune cells by the use of the CIBERSORT method. Its composition on ESCC samples and the associations among immune cells are shown in Figures 5(a) and 5(b), respectively. However, we found that there were no significant differences in the levels of tumor-infiltrating immune cells between tumor and nontumor specimens (Figures 6(a) and 6(b)). Several studies had proved that immune cells might serve as independent indicators of survivals and immunotherapy efficacies in ESCC [23, 24]. Then, we needed to finalize whether MMP12 behaviors were associated with immune cells. Importantly, we observed that the levels of MMP12 were in positive association with the infiltrated levels of mast cells activated (Figure 7(a)) and macrophages M0 (Figure 7(b)). However, eosinophils (Figure 7(c)), B cells naïve (Figure 7(d)), and mast cells resting (Figure 7(e)) exhibited an opposite result.

3.6. The Oncogenic Roles of MMP12 in ESCC Progression. To demonstrate the expression of MMP12 in ESCC, we performed RT-PCR using four ESCC cell lines and observed that MMP12 expression was distinctly increased in four ESCC cell lines compared with Het-1A cells (Figure 8(a)). Given that Eca109 and EC-1 exhibited a relatively higher level among four ESCC cells, we chose them for further study. We used loss-of-function experiments to explore the possible effects of MMP12 in ESCC. The interference efficiencies of siRNA are shown in Figure 8(b), suggesting that siRNA efficiently decreased MMP12 expressions. CCK-8 assays revealed that Eca109 and EC-1 proliferation was distinctly suppressed when silencing MMP12 (Figures 8(c) and 8(d)).

4. Discussion

The research for effective molecular markers for diagnosis and prognosis of ESCC is very important for prognosis of patients [25]. In the last decade, more and more tumor-related genes have been well studied. For instance, as a main RNA N6-adenosine methyltransferase, METTL3 was highly expressed in gastric cancer. Clinical assays disclosed that overexpression of METTL3 predicted a poor outcome of gastric cancer patients [26]. Hu et al. outlined that HIF-1α was distinctly enhanced on ESCC and was in line with metastasis, recurrence, and poor prognosis. Functionally, knockdown of HIF-1α suppressed the metastasis of ESCC cells via targeting SP1 [27]. These findings encouraged us to further identify functional genes involved in ESCC progression.

MMPs are commonly expressed in normal specimens [5]. It has been demonstrated that the expressions and activities exhibited an increased trend during inflammation and tumor progression [28, 29]. In this study, we analyzed the expressing pattern of MMPs in ESCC specimens based

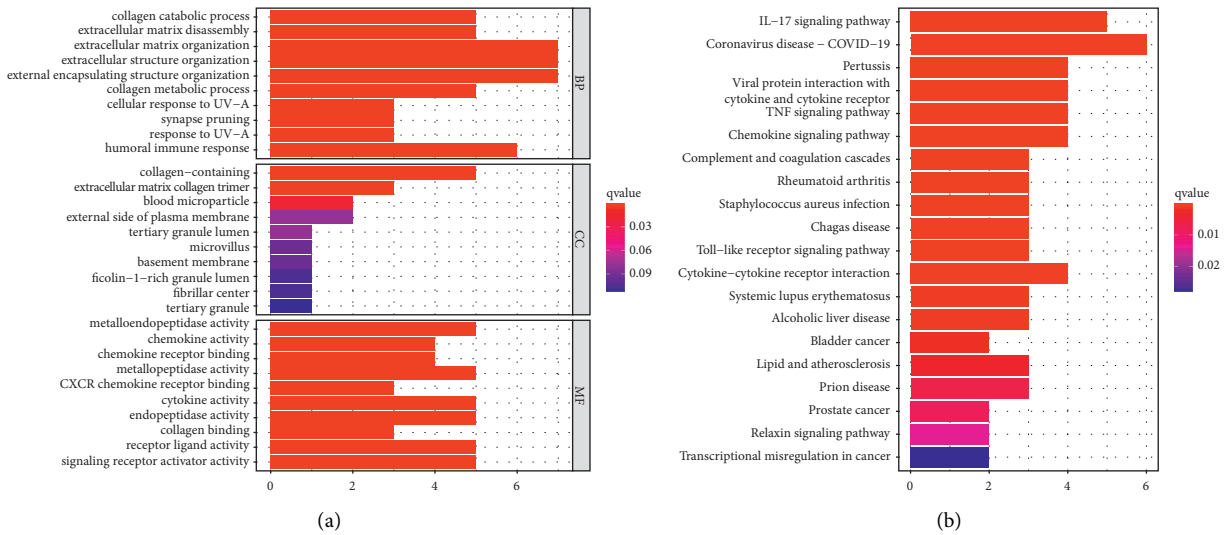

Figure 4: Functional enrichment analysis of the dysregulated genes in low and high MMP12 expression groups. (a) The enriched GO annotation included the biological process, cellular component, and molecular function. (b) Dotplot of the KEGG signal pathway.

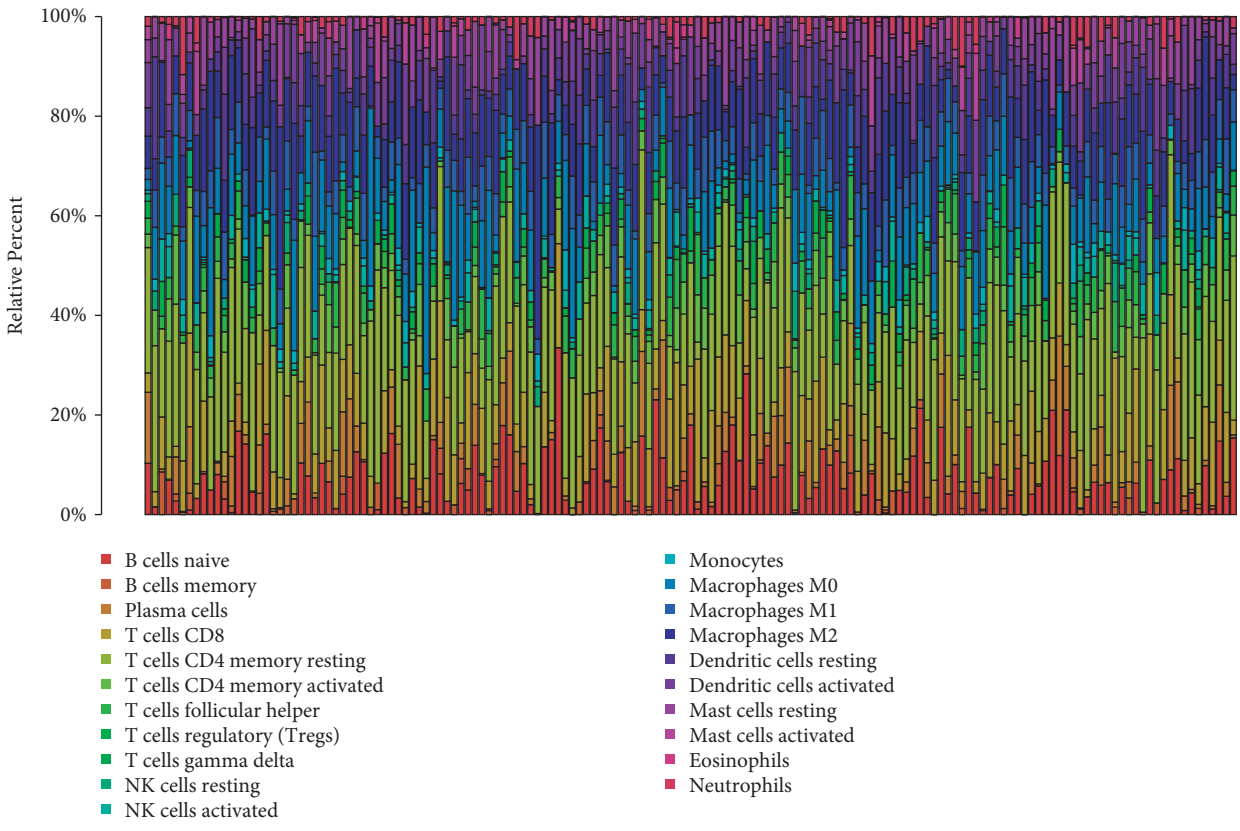

(a)

Figure 5: Continued.

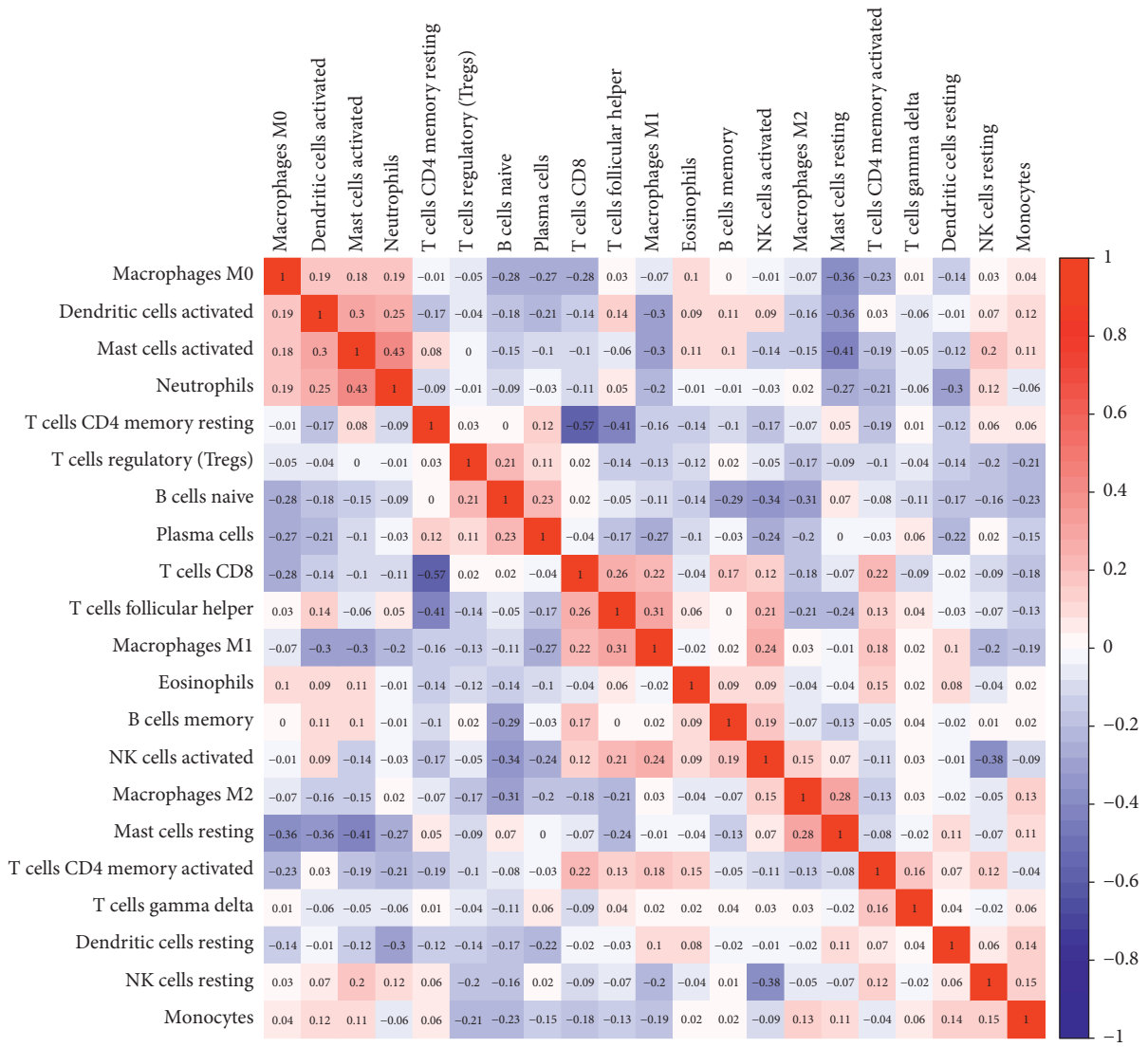

(b)

Figure 5: (a), (b) The proportion of the 22 immune cells detected by the CIBERSORT algorithm.

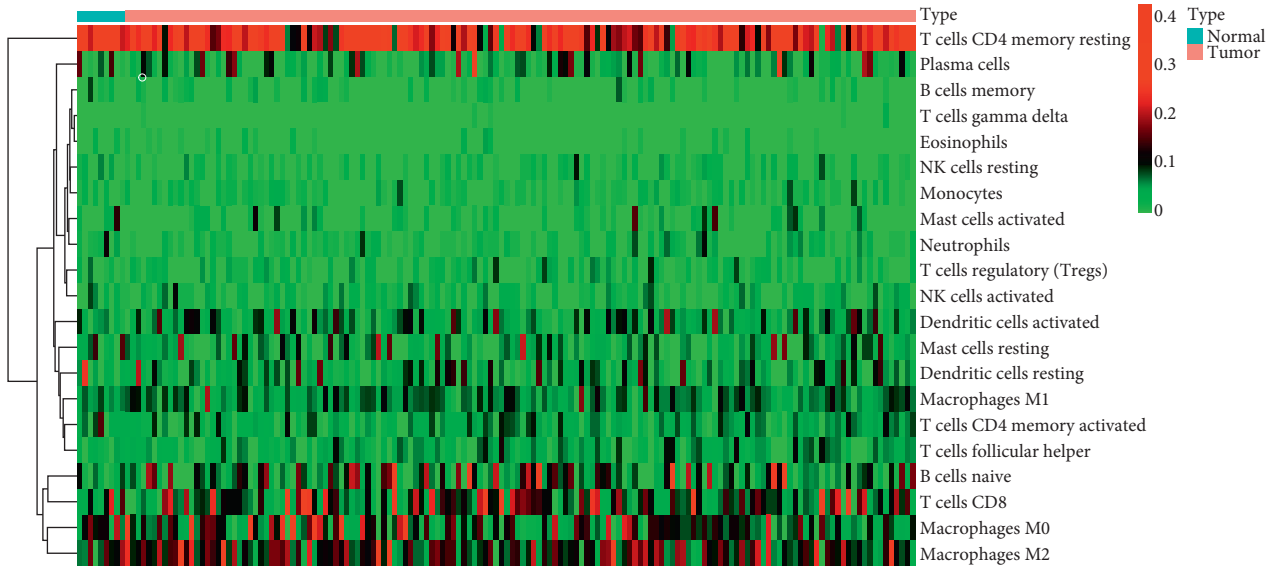

(a)

Figure 6: Continued.

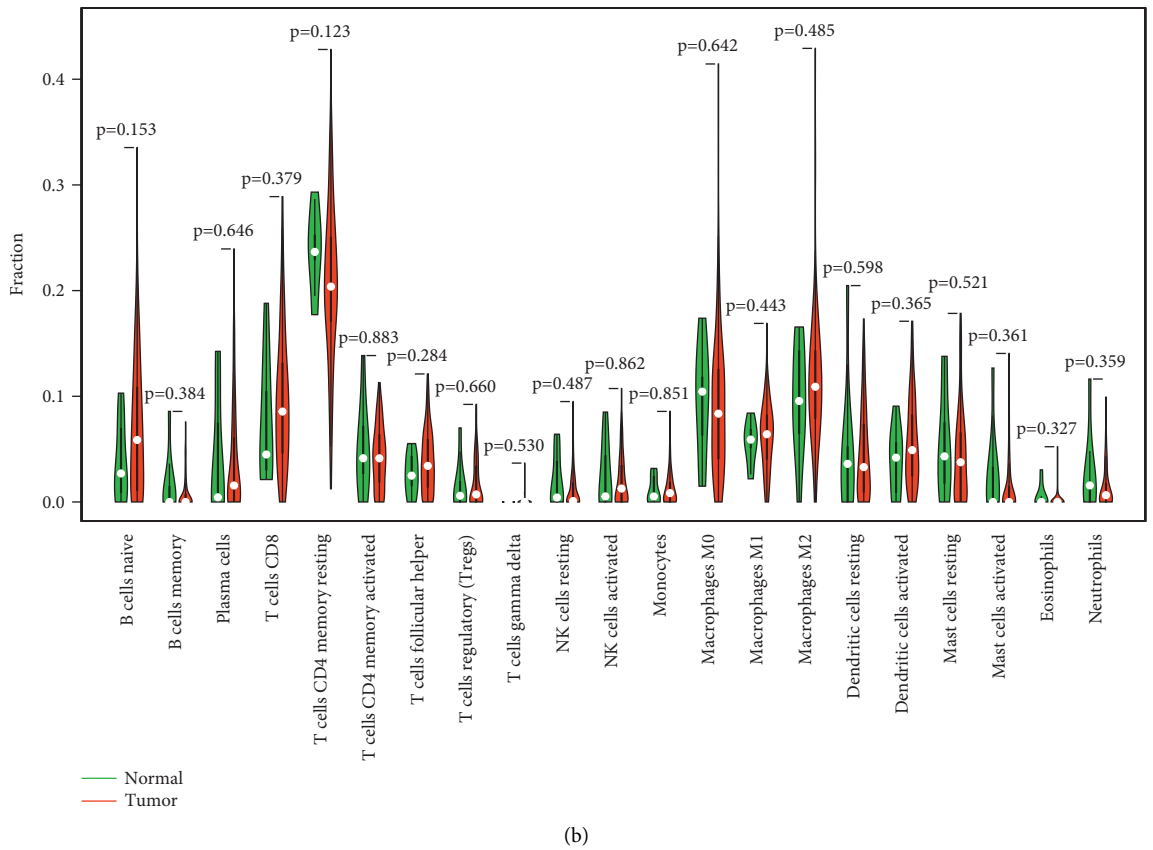

(b)

Figure 6: Analysis of the levels of 22 TIICs and its correlations in ESCC specimens and 11 normal cases. (a) Heatmaps indicated the expressing pattern of the immune cell between ESCC specimens and nontumor specimens. (b) The differences in the structure of TIICs between normal tissue and ESCC tissues.

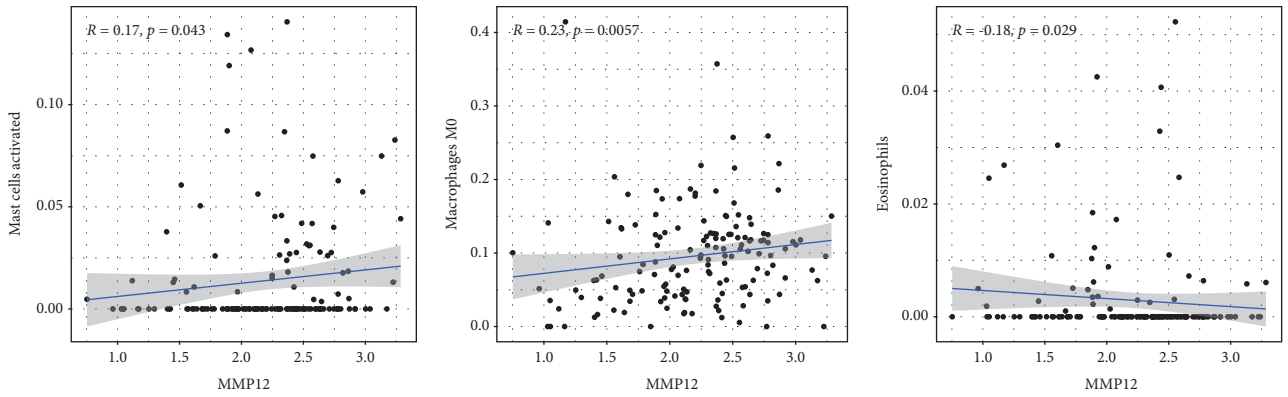

(a) (b) (c)

Figure 7: Continued.

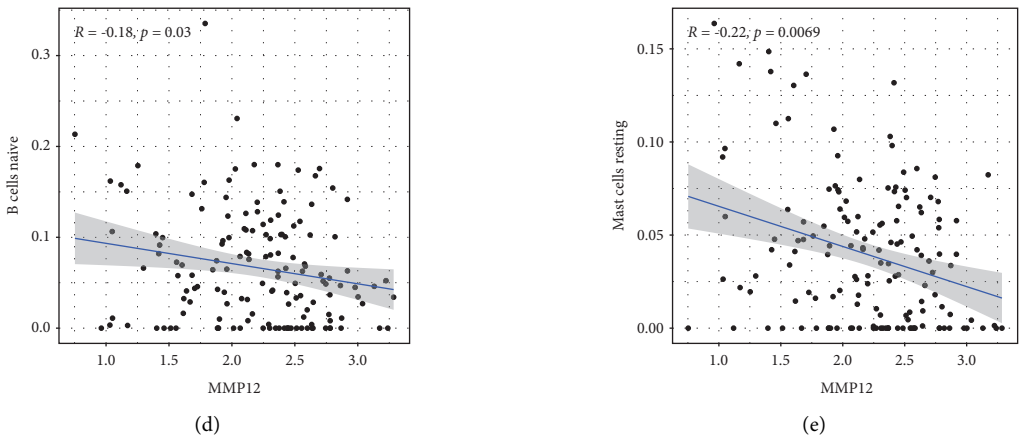

Figure 7: The correlation between MMP12 and immune infiltration level in ESCC. (a), (b) A positive association between MMP12 behaviors and the levels of macrophages M0 and mast cells activated was observed. (c)–(e) A negative association between MMP12 expression and the levels of B cells naïve, eosinophils, and mast cells resting was observed.

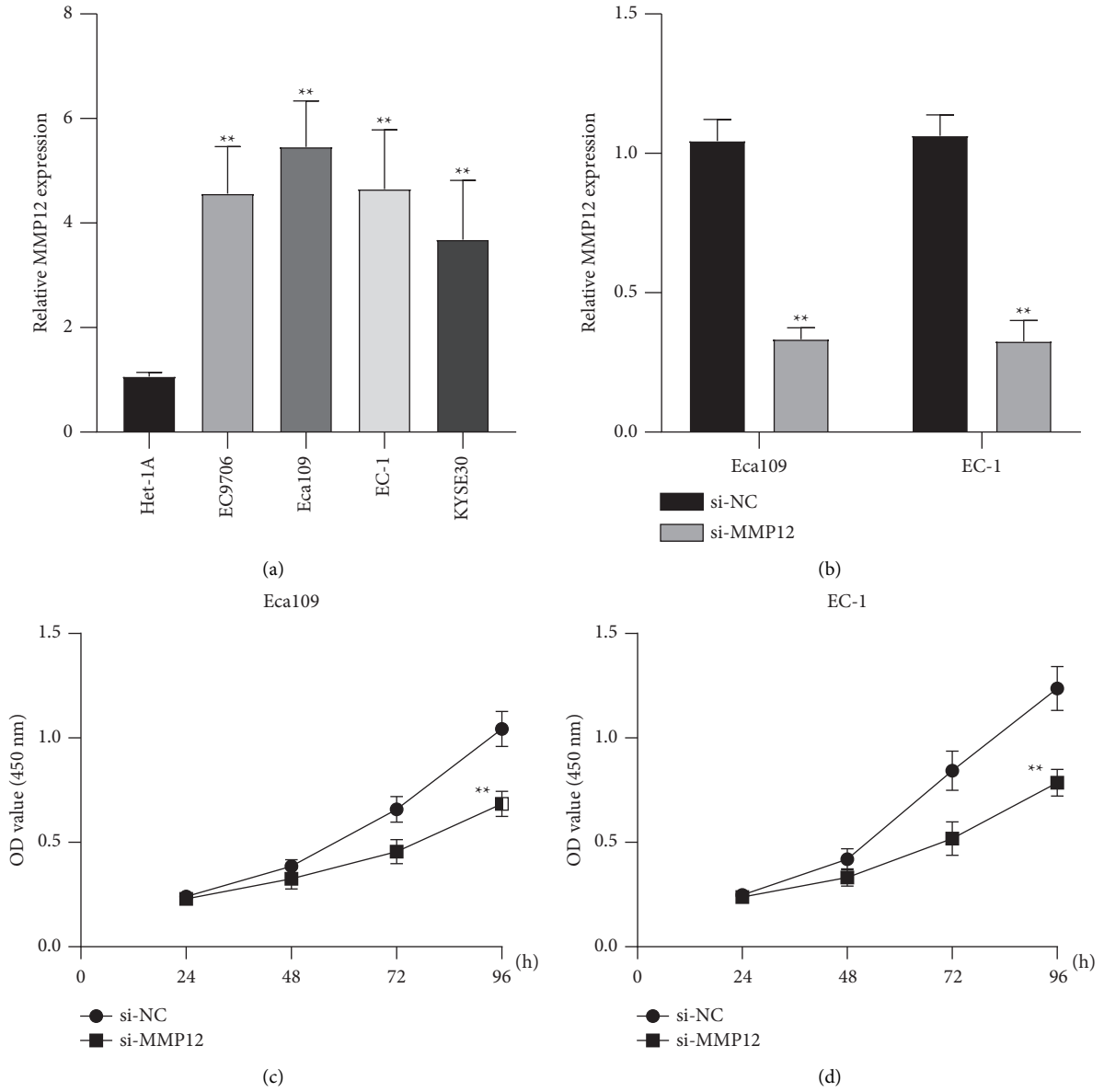

Figure 8: Knockdown of MMP12 suppressed the proliferation of ESCC cells. (a) RT-PCR for the expression of MMP12 in ESCC cell lines. (b) The expression of MMP12 decreased in Eca109 and EC-1 cells transfected with si-MMP12. (c), (d) CCK-8 assay indicated that OD values of Eca109 and EC-1 cells significantly decreased when transfected with si-MMP12. $^{**}P < 0.01$.

on TCGA datasets and identified 12 dysregulated MMPs in ESCC, including MMP1, MMP12, MMP20, MMP17, MMP14, MMP11, MMP10, MMP13, MMP9, MMP8, MMP7, and MMP3. Among the above genes, only MMP12 was associated with five-year survival of ESCC patients, and its high expression was also associated with advanced clinical stages in ESCC specimens. To explore the possible function of MMP12 in ESCC progression, we performed KEGG assays, which revealed that the genes associated with MMP12 were mainly enriched in several tumor-related pathways including PI3K-Akt signaling, estrogen signaling, and relaxin signaling [30–32]. Moreover, we also proved that knockdown of MMP12 distinctly suppressed the proliferation of ESCC cells. Besides, the effect of MMP12 has been reported in several tumors. For instance, MMP12 was highly expressed in lung adenocarcinoma, and its knockdown distinctly inhibited the growth and invasion of lung adenocarcinoma cells [33]. In hepatocellular carcinoma, high MMP12 expression predicted a poor prognosis. Importantly, the prognostic value of MMP12 was also demonstrated in 93 patients, which was consistent with our findings [34]. Thus, together with previous findings, these results indicated MMP12 as a novel prognostic biomarker for ESCC patients.

Several antibodies targeting immune checkpoints for the treatments of ESCC were approved by the FDA for the sake of its efficacy [35, 36]. Biomarkers would be tremendously valuable in improving therapeutic decision making in ESCC [37]. In this study, we elaborated on the impact of MMP12 on the immune systems. However, we did not observe a distinct different of the level of immune cells between ESCC specimens and nontumor specimens. Then, we needed to figure out whether MMP12 expression was related to immune cell on ESCC and observed that upregulated MMP12 was positively in line with the infiltration levels of macrophages M0 and mast cells activated. In addition, downregulated MMP12 was negatively correlated with the infiltration of B cells naïve, eosinophils, and mast cells resting. Our findings provided evidence that MMP12 may be a potential immunotherapeutic object for ESCC.

There are some limitations in our study. The first one is the limited sample size that needs to be improved. The second one is the lack of the exploration of mechanisms underpinning MMP12-medicated tumor immunity and the prognostic values of immune signatures. The third one is that examining the biomarkers in the serum/plasma samples might help monitor the therapy response in real-time.

5. Conclusion

We identified several dysregulated MMPs in ESCC, and their function needed to be further studied. We provided clinical evidence that MMP12 was highly expressed in ESCC and can serve as an independent prognostic marker for survival in ESCC. Our conclusion is that MMP12 might play a role in controlling the tumor immune microenvironments. Additional investigation is required to confirm the findings before the clinical application of MMP12.

Data Availability

The analyzed datasets generated during the study are available from the corresponding author upon request.

Disclosure

Jing-tao Mao, Qiang Lu, and Peng-yu Jing are the co-first authors.

Conflicts of Interest

The authors declare that they have no conflicts of interest.

Authors' Contributions

Jing-tao Mao, Qiang Lu, and Peng-yu Jing contributed equally to this work.

Acknowledgments

This work was supported by the Youth Program of the National Natural Science Foundation of China (82002422).

References

[1] A. Pennathur, M. K. Gibson, B. A. Jobe, and J. D. Luketich, "Oesophageal carcinoma," *Lancet*, vol. 381, no. 9864, pp. 400–412, 2013.

[2] C. C. Abnet, M. Arnold, and W.-Q. Wei, "Epidemiology of esophageal squamous cell carcinoma," *Gastroenterology*, vol. 154, no. 2, pp. 360–373, 2018.

[3] Z. W. Reichenbach, M. G. Murray, R. Saxena et al., "Clinical and translational advances in esophageal squamous cell carcinoma," *Advances in Cancer Research*, vol. 144, pp. 95–135, 2019.

[4] M. di Pietro, M. I. Canto, and R. C. Fitzgerald, "Endoscopic management of early adenocarcinoma and squamous cell carcinoma of the esophagus: screening, diagnosis, and therapy," *Gastroenterology*, vol. 154, no. 2, pp. 421–436, 2018.

[5] C. Kapoor, S. Vaidya, V. Wadhwan, G. Kaur, Hitesh, and A. Pathak, "Seesaw of matrix metalloproteinases (MMPs)," *Journal of Cancer Research and Therapeutics*, vol. 12, no. 1, pp. 28–35, 2016.

[6] E.-S. E. Mehana, A. F. Khafaga, and S. S. El-Blehi, "The role of matrix metalloproteinases in osteoarthritis pathogenesis: an updated review," *Life Sciences*, vol. 234, Article ID 116786, 2019.

[7] K. Kessenbrock, V. Plaks, and Z. Werb, "Matrix metalloproteinases: regulators of the tumor microenvironment," *Cell*, vol. 141, no. 1, pp. 52–67, 2010.

[8] J. Gonzalez-Molina, S. Gramolelli, Z. Liao, J. W. Carlson, P. M. Ojala, and K. Lehti, "MMP14 in sarcoma: a regulator of tumor microenvironment communication in connective tissues," *Cells*, vol. 8, no. 9, 2019.

[9] C. Joseph, M. Alsaleem, N. Orah et al., "Elevated MMP9 expression in breast cancer is a predictor of shorter patient survival," *Breast Cancer Research and Treatment*, vol. 182, no. 2, pp. 267–282, 2020.

[10] C. Lombard, J. Saulnier, and J. Wallach, "Assays of matrix metalloproteinases (MMPs) activities: a review," *Biochimie*, vol. 87, no. 3-4, pp. 265–272, 2005.

[11] M. Egeblad and Z. Werb, "New functions for the matrix metalloproteinases in cancer progression," *Nature Reviews Cancer*, vol. 2, no. 3, pp. 161–174, 2002.

[12] C. Böckelman, I. Beilmann-Lehtonen, T. Kaprio et al., "Serum MMP-8 and TIMP-1 predict prognosis in colorectal cancer," *BMC Cancer*, vol. 18, no. 1, p. 679, 2018.

[13] J. Ren, J. Liu, and X. Sui, "Correlation of COX-2 and MMP-13 expressions with gastric cancer and their effects on prognosis," *Journal of B.U.ON.: Official Journal of the Balkan Union of Oncology*, vol. 23, pp. 665–671, 2018.

[14] X. Gou, H. Chen, F. Jin et al., "Expressions of CD147, MMP-2 and MMP-9 in laryngeal carcinoma and its correlation with poor prognosis," *Pathology and Oncology Research*, vol. 20, no. 2, pp. 475–481, 2014.

[15] M. Li, L. Zhou, S. Li et al., "MMP12 is a potential therapeutic target for Adamantinomatous craniopharyngioma: conclusions from bioinformatics analysis and in vitro experiments," *Oncology Letters*, vol. 22, no. 1, p. 536, 2021.

[16] C.-L. Lin, T.-H. Ying, S.-F. Yang et al., "MTA2 silencing attenuates the metastatic potential of cervical cancer cells by inhibiting AP1-mediated MMP12 expression via the ASK1/MEK3/p38/YB1 axis," *Cell Death & Disease*, vol. 12, no. 5, p. 451, 2021.

[17] H. Gao, X. Zhou, H. Li et al., "Role of matrix metallopeptidase 12 in the development of hepatocellular carcinoma," *Journal of Investigative Surgery*, vol. 34, no. 4, pp. 366–372, 2021.

[18] Z. Zhang, S. Zhu, Y. Yang, X. Ma, and S. Guo, "Matrix metalloproteinase-12 expression is increased in cutaneous melanoma and associated with tumor aggressiveness," *Tumor Biology*, vol. 36, no. 11, pp. 8593–8600, 2015.

[19] G. Yu, L.-G. Wang, Y. Han, and Q.-Y. He, "clusterProfiler: an R package for comparing biological themes among gene clusters," *OMICS: A Journal of Integrative Biology*, vol. 16, no. 5, pp. 284–287, 2012.

[20] G. Chen and D. V. Goeddel, "TNF-R1 signaling: a beautiful pathway," *Science*, vol. 296, no. 5573, pp. 1634-1635, 2002.

[21] M. J. McGeachy, D. J. Cua, and S. L. Gaffen, "The IL-17 family of cytokines in health and disease," *Immunity*, vol. 50, no. 4, pp. 892–906, 2019.

[22] K.-H. Lim and L. M. Staudt, "Toll-like receptor signaling," *Cold Spring Harbor Perspectives in Biology*, vol. 5, no. 1, Article ID a011247, 2013.

[23] R. L. Sabado, S. Balan, and N. Bhardwaj, "Dendritic cell-based immunotherapy," *Cell Research*, vol. 27, no. 1, pp. 74–95, 2017.

[24] B. J. Laidlaw, J. E. Craft, and S. M. Kaech, "The multifaceted role of CD4+ T cells in CD8+ T cell memory," *Nature Reviews Immunology*, vol. 16, no. 2, pp. 102–111, 2016.

[25] Y.-M. Yang, P. Hong, W. W. Xu, Q.-Y. He, and B. Li, "Advances in targeted therapy for esophageal cancer," *Signal Transduction and Targeted Therapy*, vol. 5, no. 1, p. 229, 2020.

[26] B. Yue, C. Song, L. Yang et al., "METTL3-mediated N6-methyladenosine modification is critical for epithelial-mesenchymal transition and metastasis of gastric cancer," *Molecular Cancer*, vol. 18, no. 1, p. 142, 2019.

[27] X. Zhao, Y. P. Tang, C. Y. Wang, J. X. Wu, and F. Ye, "Prognostic values of STAT3 and HIF-1α in esophageal squamous cell carcinoma," *European Review for Medical and Pharmacological Sciences*, vol. 23, no. 8, pp. 3351–3357, 2019.

[28] G. Gonzalez-Avila, B. Sommer, A. A. García-Hernández, and C. Ramos, "Matrix metalloproteinases' role in tumor microenvironment," *Advances in Experimental Medicine & Biology*, vol. 1245, pp. 97–131, 2020.

[29] J. Xiong and H. Gao, "Matrix metalloproteases-responsive nanomaterials for tumor targeting diagnosis and treatment," *Journal of Microencapsulation*, vol. 34, no. 5, pp. 440–453, 2017.

[30] M. Martini, M. C. De Santis, L. Braccini, F. Gulluni, and E. Hirsch, "PI3K/AKT signaling pathway and cancer: an updated review," *Annals of Medicine*, vol. 46, no. 6, pp. 372–383, 2014.

[31] E. Kulkoyluoglu-Cotul, A. Arca, and Z. Madak-Erdogan, "Crosstalk between estrogen signaling and breast cancer metabolism," *Trends in Endocrinology and Metabolism*, vol. 30, no. 1, pp. 25–38, 2019.

[32] T. Thanasupawat, A. Glogowska, S. Nivedita-Krishnan, B. Wilson, T. Klonisch, and S. Hombach-Klonisch, "Emerging roles for the relaxin/RXFP1 system in cancer therapy," *Molecular and Cellular Endocrinology*, vol. 487, pp. 85–93, 2019.

[33] F.-Z. Lv, J.-L. Wang, Y. Wu, H.-F. Chen, and X.-Y. Shen, "Knockdown of MMP12 inhibits the growth and invasion of lung adenocarcinoma cells," *International Journal of Immunopathology & Pharmacology*, vol. 28, no. 1, pp. 77–84, 2015.

[34] M. K. He, Y. Le, Y. F. Zhang et al., "Matrix metalloproteinase 12 expression is associated with tumor FOXP3(+) regulatory T cell infiltration and poor prognosis in hepatocellular carcinoma," *Oncology Letters*, vol. 16, pp. 475–482, 2018.

[35] Y. Zheng, Z. Chen, Y. Han et al., "Immune suppressive landscape in the human esophageal squamous cell carcinoma microenvironment," *Nature Communications*, vol. 11, no. 1, p. 6268, 2020.

[36] J. Yang, X. Liu, S. Cao, X. Dong, S. Rao, and K. Cai, "Understanding esophageal cancer: the challenges and opportunities for the next decade," *Frontiers in Oncology*, vol. 10, p. 1727, 2020.

[37] G. Terrero and A. C. Lockhart, "Role of immunotherapy in advanced gastroesophageal cancer," *Current Oncology Reports*, vol. 22, no. 11, p. 112, 2020.

Hindawi
Journal of Oncology
Volume 2022, Article ID 1476038, 13 pages
https://doi.org/10.1155/2022/1476038

Research Article

The Meta-Analysis of Bevacizumab Combined with Platinum-Based Treatment of Malignant Pleural Effusions by Thoracic Perfusion

Bairu Shen, Minghua Tan, Zhengyu Wang, Changshan Song, Hui Hu, Shunfu Deng, and Yuxin Yang

Department of Thoracic Surgery, Foshan Clinical Medical School of Guangzhou University of Chinese Medicine, Guangzhou, Guangdong, China

Correspondence should be addressed to Bairu Shen; bairushen@yeah.net

Received 8 December 2021; Accepted 31 January 2022; Published 25 February 2022

Academic Editor: Fu Wang

Objective. To evaluate the safety of bevacizumab combined with platinum-based thoracic perfusion for treating lung cancer-related malignant pleural effusion (MPE) through meta-analysis. *Methods*. The CNKI, PubMed, Cochrane Library, Embase, Chinese Science and Technology Journal Database (VIP), and Wanfang Databases were searched for randomized controlled trials (RCTs) of bevacizumab combined with platinum-based thoracic perfusion for the treatment of MPE. The references included in the articles were manually searched for additional studies. A meta-analysis of the RCTs was conducted using the RevMan 5.3 application. *Results*. A total of 8 studies involving 540 patients (271 cases in the test group and 269 cases in the control group) were included in the meta-analysis. The test group had a significantly greater risk of elevated blood pressure as well as a higher rate of complete remission (CR) compared to the control group ($P < 0.05$). In contrast, the incidence of partial remission (PR) was only slightly higher in the test group ($P > 0.05$), and the risks of leukopenia, vomiting or nausea, rhinorrhea, diarrhea, gastrointestinal bleeding or hemoptysis, proteinuria, abnormal kidney and liver function, arrhythmia, and rashes were not significantly different between the test and control groups ($P > 0.05$). *Conclusion*. Bevacizumab combined with platinum-based thoracic perfusion can achieve CR of MPE in patients with advanced lung cancer without significantly increasing the risk of adverse effects. The rate of PR was similar for the combination treatment and platinum-based infusion.

1. Introduction

The presence of malignant pleural effusion (MPE) in patients with advanced lung cancer is mainly due to cancer cell infiltration or metastasis into the pleura. The molecular basis of MPE pathogenesis is not completely clear, although overexpression of immune-related factors and vascular permeability regulators has been implicated [1]. MPE seriously affects the quality of life, and the median survival of lung cancer patients with MPE is about six months [2, 3]. Currently, advanced lung cancer complicated with MPE is primarily treated with systemic drug therapy and local treatment of the chest cavity. Intraluminal drainage combined with intraluminal injection is the most common local treatment modality; selecting an effective intracavitary can increase therapeutic efficacy with fewer complications [4–7]. Combined intrathoracic perfusion therapy is also an effective treatment modality for MPE, and several studies have reported better outcomes and lower drug toxicity with this approach. However, there are also reports of potential side effects of local perfusion, especially when two groups of drugs are combined. Since the pleural absorption kinetics of drugs differ significantly compared to that of intravenous administration, there are concerns regarding the safety of two-drug perfusion therapy. We conducted a meta-analysis to analyze the safety and efficacy of the combination of bevacizumab and platinum-based thoracic infusion in the treatment of lung cancer-associated MPE.

2. Data and Methods

2.1. Case Exclusion Standards and Inclusion

2.1.1. Study Type. This is a published Phase III RCT.

2.1.2. Study Subjects. Patients with pathologically or cytologically confirmed advanced non-small-cell lung cancer (NSCLC) or small-cell lung cancer (SCLC)-associated MPE.

2.1.3. Interventions. The RCT group was treated with bevacizumab in combination with platinum-based thoracic perfusion, and the control group was treated with platinum-based thoracic perfusion alone.

2.1.4. Outcome Indicators. Efficacy evaluation: the efficacy was determined according to the WHO evaluation criteria [8]. Complete remission (CR) was defined as the disappearance of pleural effusion for over four weeks, partial remission (PR) as the significant reduction in the volume of pleural fluid by at least 50% for over four weeks, no significant remission (NC) as less than 50% reduction in pleural fluid or no significant change, and progressive disease (PD) as a significant increase in pleural fluid volume and worsening of symptoms after treatment [8]. The patients in each treatment and dosage group were monitored for adverse reactions according to the National Cancer Institute-Common Toxicity Criteria (NCI-CTC) [8].

2.1.5. Exclusion Criteria. (1) Phase I and II RCT studies, (2) reviews or case-control studies, and non-RCT studies such as retrospective cohort studies, (3) concurrent radiotherapy as first-line therapy, (5) incomplete data and unclear study indices, and (6) published in languages other than English and Chinese [9].

2.2. Literature Search Strategy. The Wanfang databases, Cochrane Library, Embase, CNKI, PubMed, and VIP databases were systematically searched for RCTs conducted on the safety and efficacy of bevacizumab in combination with platinum for treating lung cancer-related MPE. The search was limited to articles published till December 31, 2019. The keywords used for searching articles published in English included Bevacizumab, Avastin, lung cancer, cisplatin, and carboplatin, whereas the search terms for Chinese literature included Bevacizumab, Avastin, lung cancer, MPE, cisplatin, and carboplatin. The search terms for interventions ("cisplatin or carboplatin," "Bevacizumab or Avastin," "thoracic perfusion," "thoracic perfusion," "Bevacizumab or Avastin") were combined with related diseases ("lung cancer and MPE," "lung cancer and MPE") using Boolean logic. The references included in each study were manually retrieved to expand the search. In addition, the ProQuest and CNKI platforms were also screened to collect abstracts of dissertations or scientific conferences. Journals in relevant specialized fields were supplemented with manual or other searches to avoid missing relevant literature [9].

2.3. Literature Screening and Data Extraction. The literature was reviewed independently by two researchers, and the decision to include any study was made on the basis of the review results. In case of any disagreement, a third researcher was consulted, and the final decision was made through a joint discussion among all three reviewers. The data were extracted from the studies by two researchers independently and cross-checked. Any inconsistencies in the data were resolved by discussing them with a third researcher. The following data were included in the meta-analysis: (i) writer ranking, (ii) publication year, (iii) country of publication, (iv) histological type, (v) the total number of studies, (vi) median age, (vii) treatment regimen, (viii) number of evaluable indicators, and (ix) outcome indicators such as treatment efficacy and complications [9].

2.4. Risk of Bias Assessment. The risk of bias was evaluated by applying the Bias Assessment Tool's Cochrane Risk, which includes (i) random sequence generation (selective bias), (ii) allocation concealment (selective bias), (iii) implementation of blinding (implementation bias), (iv) blinded assessment results (measurement bias), (v) completeness of data (missing visit bias), (vi) selective reporting (reporting bias), and (vii) other bias (issues that could clearly lead to a risk of bias, e.g., apparent benefit and early discontinuation of the trial). The risk of bias was classified as low, unclear, and high [9].

2.5. Statistical Analysis. Meta-analysis was conducted using the RevMan 5.3 application, with a relative risk (OR) as the outcome. The results were presented using 95% confidence intervals (95% CI), and $P < 0.05$ was set as a statistically significant difference. The heterogeneity between the included studies was analyzed using the Q test and quantified using the I^2 index. The fixed-effects model was used in case of low heterogeneity ($P > 0.05$, $I^2 < 40\%$) [9]; otherwise, the random-effects model was applied.

2.6. Evaluation of Publication Bias. Publication bias was assessed based on the symmetry of outcome indicators using a funnel plot. A symmetrical funnel plot indicated a lack of any publication bias, whereas an asymmetrical plot suggested publication bias [7].

3. Results

3.1. Preliminary Literature Screening Results. A total of 316 articles were initially screened, including 40 from PubMed, 168 from Embase, 44 from the Cochrane Library, 22 from CNKI, 24 from the Wanfang database, and 18 from VIP. Eight studies were finally included after excluding duplicate or ineligible literature, including seven studies on combined cisplatin perfusion [8, 10–15] and one on combined carboplatin perfusion [16], involving a total of 540 patients (271 cases in the trial group and 269 cases in the control group). The details are summarized in Figure 1.

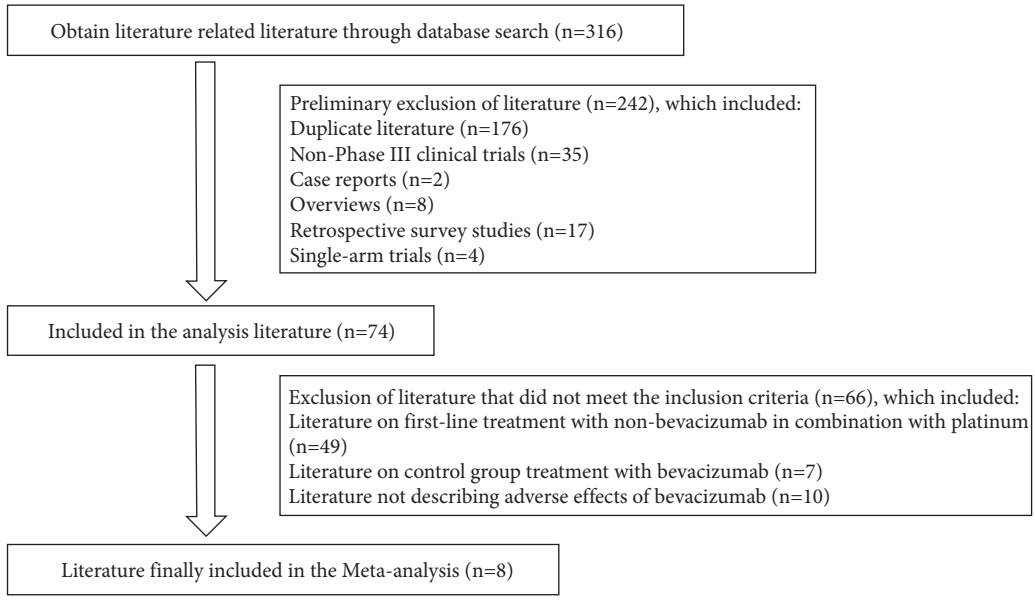

Figure 1: Preliminary literature screening results.

3.2. Basic Characteristics of the Included Studies. Six of the included studies had been conducted on NSCLC patients and two on lung cancer patients. All patients were treated with thoracic perfusion. Bevacizumab and cisplatin perfusion were used in eight studies, and bevacizumab and carboplatin perfusion in one study, with cisplatin or carboplatin as the control group. The administered dosage of bevacizumab was 200 mg/dose in one study, 300 mg/dose in two studies, and 5 mg/kg in 6 studies (Table 1). In six studies, MPE was diagnosed by ultrasound, whereas two did not specify whether the diagnostic modality was CT or ultrasound. Nevertheless, the same diagnostic modality was used to compare pre- and posttreatment status in all studies.

3.3. Risk of Bias Assessment. All eight studies showed a low risk of bias. The risk percentages of individual biases in each study are shown in Figure 2. The overall risk of individual biases is summarized in Figure 3.

3.4. Results of Meta-Analysis

3.4.1. Rate of PR. All studies included in the meta-analysis (271 cases in the trial group and 269 cases in the control group) reported PR. Due to low heterogeneity between the studies ($P = 0.52$, $I^2 = 0$), meta-analysis was conducted using the fixed-effects model. The rate of PR was higher in the trial group compared to the control group, albeit not statistically significant (OR = 1.11, 95% CI: 0.78–1.57, $P > 0.05$). The data are summarized in Figures 4 and 5.

3.4.2. Rate of CR. All studies included in the meta-analysis (271 cases in the trial group and 269 cases in the control group) reported CR. Statistical heterogeneity between the studies was significant ($P = 0.06$, $I^2 = 49\%$), which warranted the random-effects model. The rate of CR was significantly higher in the test group compared to the control group (OR = 3.10, 95% CI: 1.68–5.71, $P < 0.05$). The data are shown in Figures 6 and 7.

3.4.3. Risk of Leukopenia. Six studies, including 194 patients in the trial group and 194 patients in the control group, reported leucopenia. Statistical heterogeneity between the studies was low ($P = 0.94$, $I^2 = 0$), and the fixed-effects model was used. The risk of leukopenia was lower in the test group compared to the control group, although the difference was not statistically significant (OR = 0.88, 95% CI: 0.56–1.40, $P > 0.05$). The data are shown in Figures 8 and 9.

3.4.4. Risk of Nausea and Vomiting. All studies reported the frequency of nausea and vomiting in the test and control groups. Statistical heterogeneity between the studies was low ($P = 0.52$, $I^2 = 0$), and the fixed-effects model was used. The test group had a slightly lower risk of nausea compared to the control group (OR = 0.72, 95% CI: 1.48–1.07, $P > 0.05$). The data are shown in Figures 10 and 11.

3.4.5. Risk of Diarrhea. Diarrhea was reported in four studies that included 123 patients in the trial group and 119 patients in the control group. The fixed-effects model was used due to the low statistical heterogeneity between the studies ($P = 0.84$, $I^2 = 0$). The risk of diarrhea was higher in the test group compared to the control group, albeit without statistical significance (OR = 1.24, 95% CI: 0.62–2.52, $P > 0.05$). The data are shown in Figures 12 and 13.

3.4.6. Risk of Nosebleeds, Hemoptysis, or Gastrointestinal Bleeding. Five studies reported the frequency of nasal bleeding, hemoptysis, or gastrointestinal bleeding among 134 patients in the trial group and 132 patients in the control

Table 1: Basic characteristics of the included studies.

Inclusion in studies	Country	Type of pathology	Staging	Total number of cases	Number of cases in each group		Gender (male/female)	Number of treatment lines	Interventions		Evaluation indicators
					Experimental group	Control group			Experimental group	Control group	
Nan Du 2013	China	Non-small-cell lung cancer	IV	70	36	34	39/32	First-line treatment	Cisplatin (60 mg) + bevacizumab (300 mg) dissolved in saline 20 ml by intrathoracic infusion, every 2 weeks, at least two courses of treatment	Cisplatin (60 mg) dissolved in saline 20 ml for intrathoracic instillation	①, ②, ③, ④, ⑤, ⑥, ⑦, ⑧
Liu X.-T. 2017	China	Non-small-cell lung cancer	IV	98	49	49	54/44	First-line treatment	Bevacizumab (5 mg/kg) + cisplatin (45 mg/m^2) was dissolved in 20 mg of 0.9% sodium chloride and injected intrathoracically through a central venous catheter once/week for 3 weeks	Cisplatin (45 mg/m^2) dissolved in 20 mg 0.9% sodium chloride for intravenous injection	①, ②, ④, ⑨, ⑩,
Jiang M. 2018	China	Non-small-cell lung cancer	IV	52	24	28	33/19	First-line treatment	Bevacizumab (5 mg/kg) + saline (20 mL) was administered once every 7 days via central venous catheter by thoracic infusion for 3 consecutive doses	Carboplatin injection (300 mg) + saline (50 mL) via central venous catheter for thoracic infusion	①, ②, ③, ④, ⑥, ⑦, ⑧, ⑨,
Ang Bing 2018	China	Non-small-cell lung cancer	IV	27	14	13	15/12	First-line treatment	Bevacizumab (200 mg) + cisplatin (60 mg/m^2) by intrathoracic infusion, d1, 2 times/week for 3 weeks	Cisplatin (60 mg/m^2) by intrathoracic infusion	①, ②, ③, ④, ⑤, ⑥, ⑦, ⑧
Qu B. 2015	China	Non-small-cell lung cancer	IV	63	32	31	36/27	First-line treatment	Bevacizumab (5 mg/kg) + cisplatin (40 mg/m^2) by intrathoracic infusion, 1 time/week, 3 cycles	Cisplatin (40 mg/m^2) by intrathoracic infusion	(①, ②, ③, ④, ⑤, ⑥, ⑦, ⑧
Lin F. H. 2016	China	Non-small-cell lung cancer	IV	94	47	47	50/44	First-line treatment	Bevacizumab (5 mg/kg) + cisplatin (45 mg/m^2), dissolved in 20 ml of saline and injected into the chest cavity through a central venous catheter once a week for 3 weeks	Cisplatin (45 mg/m^2) dissolved in 20 ml saline for intrathoracic instillation	①, ②, ③, ④, ⑨, ⑩, ⑪
Xue D. F. 2017	China	Non-small-cell lung cancer	IV	82	41	41	47/35	First-line treatment	Bevacizumab (5 mg/kg) + cisplatin (60 mg) by intrathoracic infusion, once a week for 3 weeks	Cisplatin (60 mg) by intrathoracic infusion	(①, ②, ③, ④, ⑤
Chen L. 2015	China	Non-small-cell lung cancer	IV	54	28	26	27/17	First-line treatment	Bevacizumab, (5 mg/kg) + cisplatin (75 mg/m^2) by intrathoracic infusion, divided into 2 cycles of 21 d each	Cisplatin (75 mg/m^2) by intrathoracic infusion	①, ②, ④, ⑦, ⑧, ⑩

Note. ① CR, complete remission; ② PR, partial remission; ③ leukopenia; ④ nausea and vomiting; ⑤ diarrhea; ⑥ rhinorrhea; hemoptysis or gastrointestinal bleeding; ⑦ elevated blood pressure; ⑧ proteinuria; ⑨ abnormal liver and kidney function; ⑩ heart rate disorders; ⑪ skin rash.

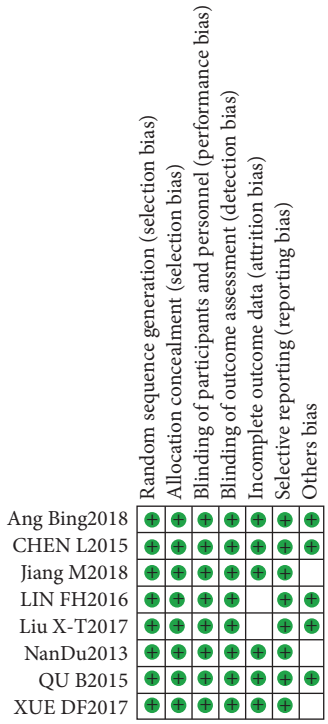

Figure 2: Risk of single-item bias in the included literature.

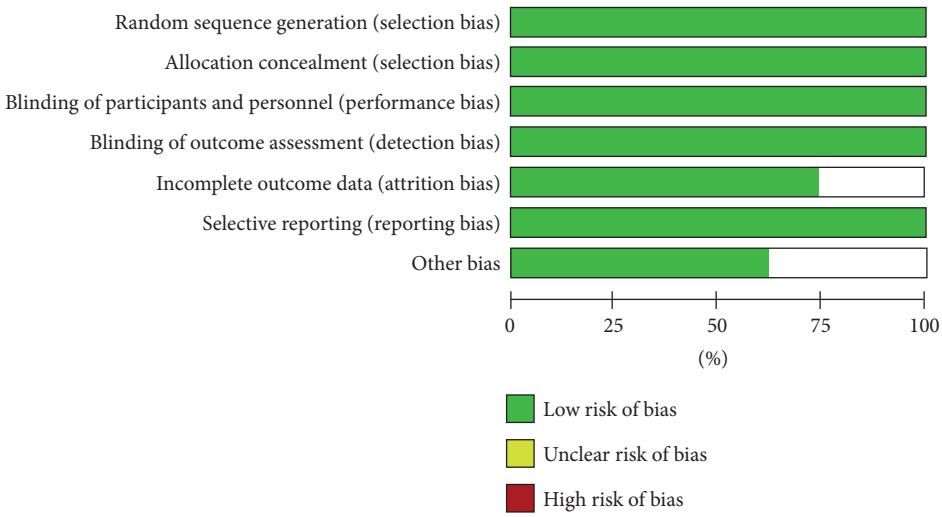

Figure 3: Overall risk of individual biases.

group. An increased risk of these events was observed in the trial group compared to the control group using the fixed-effects model ($P = 0.82$, $I^2 = 0$), although the difference was not statistically significant (OR = 4.01, 95% CI: 0.43–37.44, $P > 0.05$). The data are shown in Figures 14 and 15.

3.4.7. Risk of Elevated Blood Pressure. Five studies, including 134 patients in the trial group and 132 patients in the control group, reported elevated blood pressure. Statistical heterogeneity between the studies was low ($P = 0.66$, $I^2 = 0$), and the fixed-effects model was used. The risk of high blood pressure was significantly higher in the test group compared to the control group (OR = 3.46, 95% CI: 1.43–8.36, $P < 0.05$). The data are shown in Figures 16 and 17.

3.4.8. Risk of Proteinuria. Four studies, including 106 patients in the trial group and 106 patients in the control group, reported proteinuria. Statistical heterogeneity between the studies was low ($P = 0.94$, $I^2 = 0$), and the fixed-effects model was used. The risk of proteinuria was higher in the test group compared to the control group, albeit not statistically significant (OR = 3.60, 95% CI:

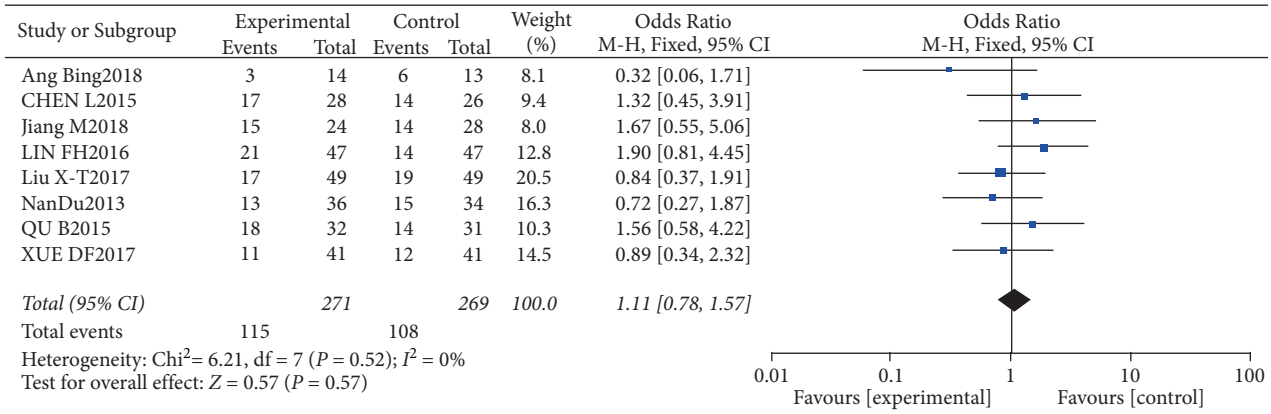

Figure 4: PR analysis.

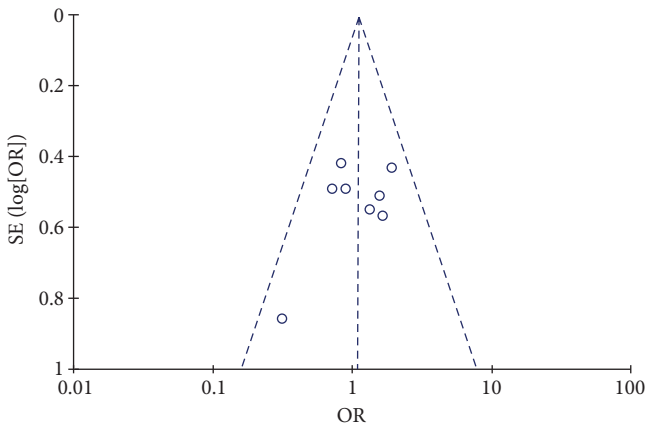

Figure 5: Results of funnel plot.

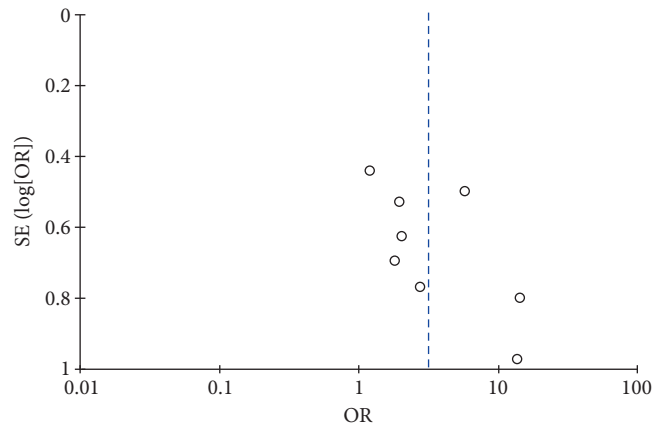

Figure 7: Results of funnel plots.

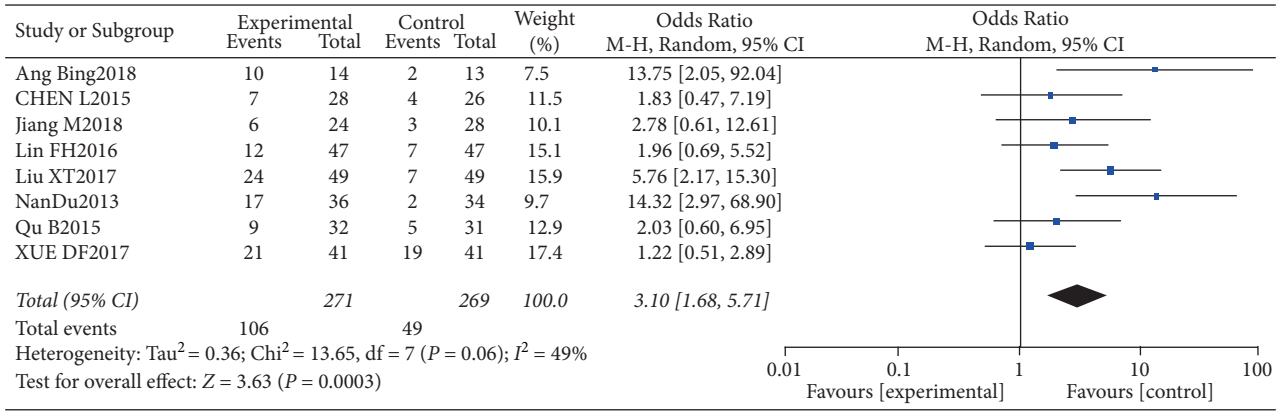

Figure 6: Results of CR analysis.

0.86–15.11, $P > 0.05$). The data are shown in Figures 18 and 19.

3.4.9. Incidence of Kidney and Liver Dysfunction. Three studies, including 120 patients in the trial group and 124 patients in the control group, reported abnormal liver and kidney function. The fixed-effects model was used on account of the low heterogeneity between the studies ($P = 0.54$, $I^2 = 0$). The patients in the test group showed a slightly lower risk of aberrant kidney and liver function compared to the control group (OR = 0.67, 95% CI: 0.33–1.35, $P > 0.05$). The data are shown in Figures 20 and 21.

3.4.10. Risk of Arrhythmia. Three studies, including 124 patients in the trial group and 122 patients in the control group, reported arrhythmia. Statistical heterogeneity between the studies was low ($P = 0.87$, $I^2 = 0$), and the fixed-effects

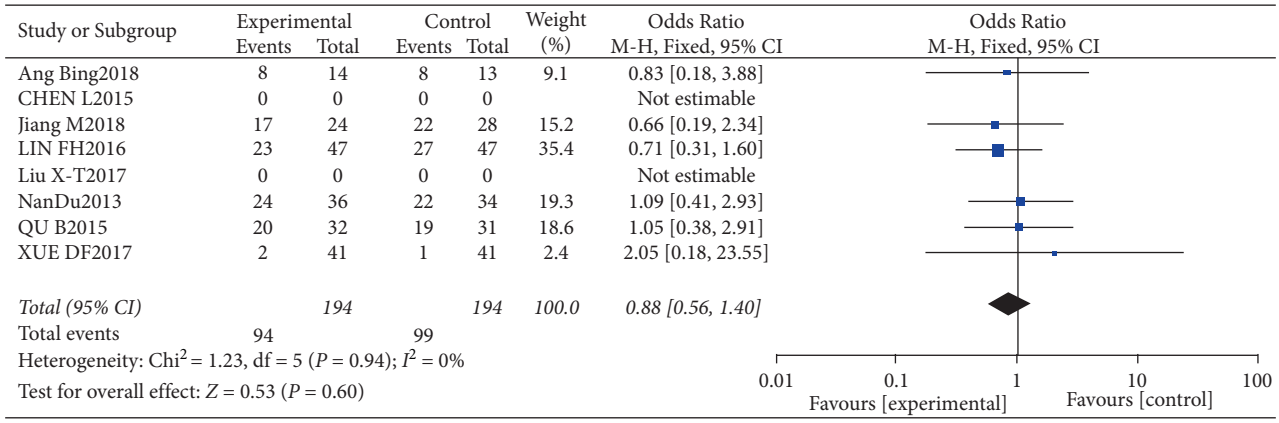

Figure 8: Results of leukopenia analysis.

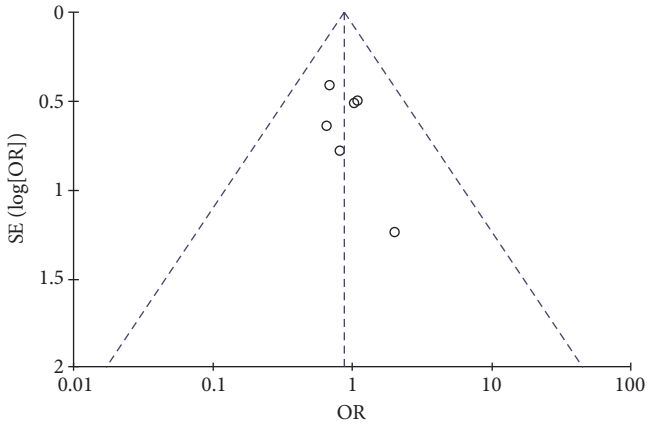

Figure 9: Results of funnel plots included in the literature.

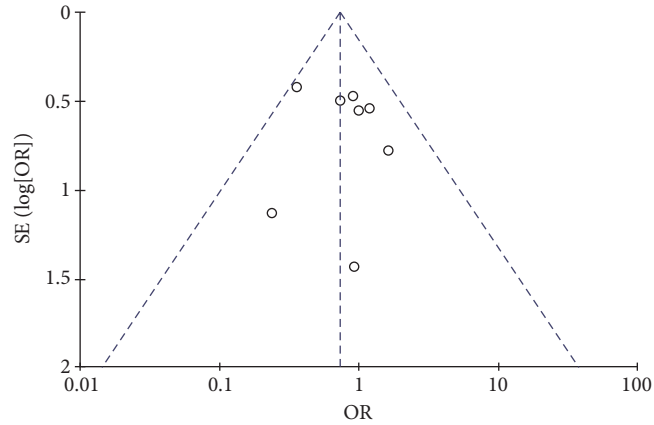

Figure 11: Results of funnel plots.

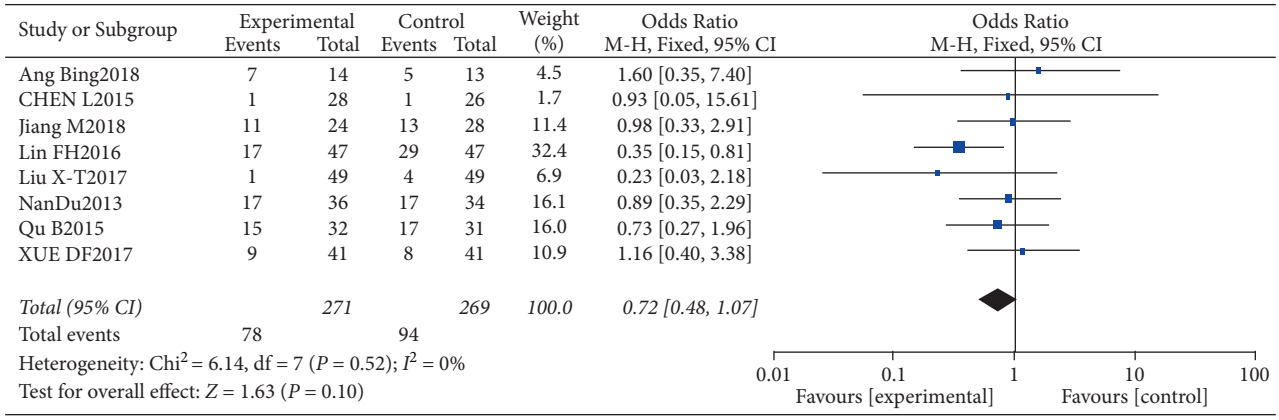

Figure 10: Results of nausea and vomiting analysis.

model was used. The risk of arrhythmia was slightly lower in the test group compared to the control group (OR = 0.75, 95% CI: 0.35–1.58, $P > 0.05$). The data are shown in Figures 22 and 23.

3.4.11. Risk of Rashes. Two studies, including 96 patients in the trial group and 96 patients in the control group, reported an incidence of rashes. Since the statistical heterogeneity between the studies was significant ($P = 0.20$, $I^2 = 40\%$), the random-effects model was used. Patients in the test group were at a slightly higher risk of developing rashes compared to the control group (OR = 0.56, 95% CI: 0.15–2.13, $P > 0.05$). The data are shown in Figures 24 and 25.

4. Discussion

MPE is a frequent complication of intestinal cancers, breast cancer, pleural mesothelioma, etc., and the highest incidence

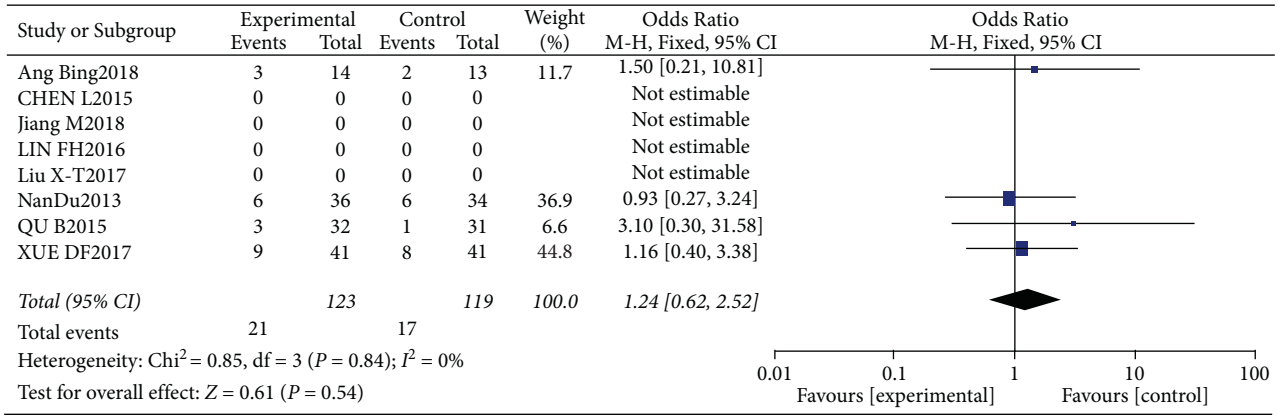

Figure 12: Results of diarrhea analysis.

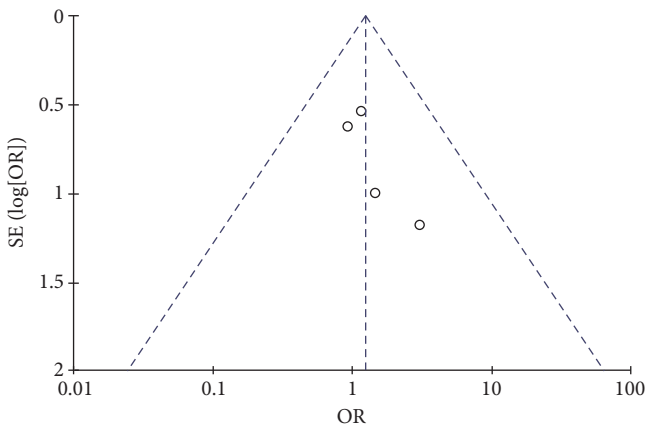

Figure 13: Results of funnel plots.

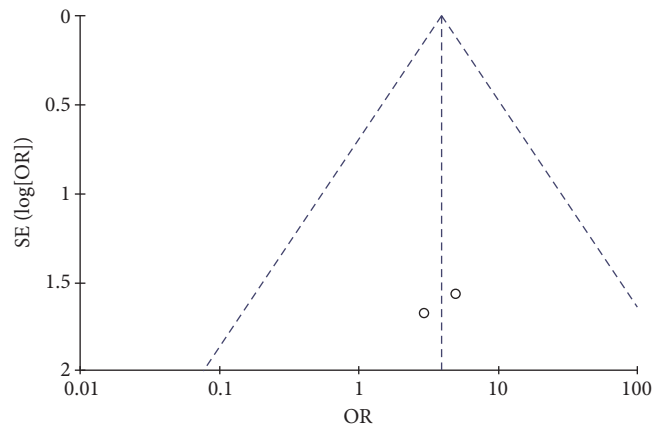

Figure 15: Results of funnel plots.

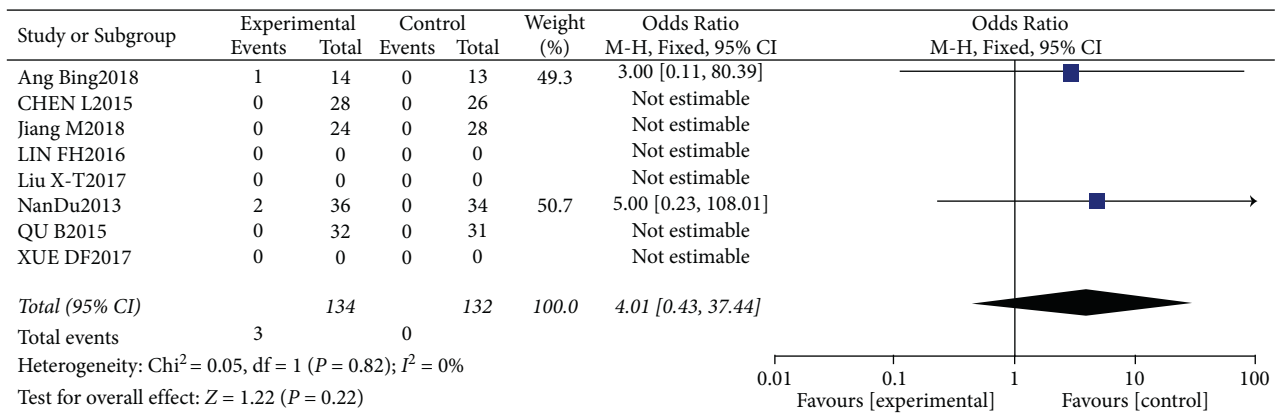

Figure 14: Results of the analysis of nosebleeds, hemoptysis, or gastrointestinal bleeding.

is observed in lung cancer patients (about 35%) [17]. The pathogenesis of MPE is complex. The key factors include lymphatic vessel obstruction, vascular endothelial cell damage, and increased vascular permeability, in addition to the decrease in plasma colloid osmotic pressure due to hypoproteinemia. However, the mechanisms through which tumor cells induce vascular damage are unclear.

Vascular endothelial growth factor (VEGF) promotes tumor neovascularization by increasing fibrinase production, which lyses the basement membrane and interstitial fibers of blood vessels, thereby encouraging the growth of new vessels. In addition, VEGF also participates in the formation of pleural effusion by malignant tumor cells [18–21]. Chen et al. found that VEGF competitively binds to receptors on endothelial cells and activates the mitogen-activated protein kinase signaling pathway, which induces their differentiation and promotes the formation of intercellular gaps, thereby increasing vascular permeability [22–26]. Li et al. reported

Study or Subgroup	Experimental Events	Experimental Total	Control Events	Control Total	Weight (%)	Odds Ratio M-H, Fixed, 95% CI
Ang Bing2018	2	14	1	13	14.9	2.00 [0.16, 25.11]
CHEN L2015	2	28	2	26	32.2	0.92 [0.12, 7.08]
Jiang M2018	4	24	1	28	12.9	5.40 [0.56, 52.08]
LIN FH2016	0	0	0	0		Not estimable
Liu X-T2017	0	0	0	0		Not estimable
NanDu2013	9	36	2	34	25.8	5.33 [1.06, 26.83]
QU B2015	5	32	1	31	14.3	5.56 [0.61, 50.60]
XUE DF2017	0	0	0	0		Not estimable
Total (95% CI)		*134*		*132*	*100.0*	*3.46 [1.43, 8.36]*
Total events	22		7			

Heterogeneity: $Chi^2 = 2.40$, df = 4 ($P = 0.66$); $I^2 = 0\%$

Test for overall effect: $Z = 2.76$ ($P = 0.006$)

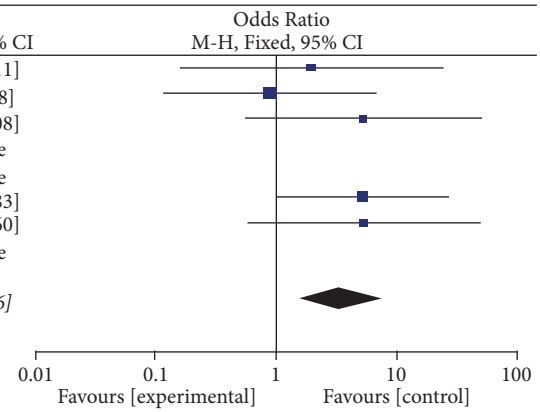

Figure 16: Results of the analysis of blood pressure elevation.

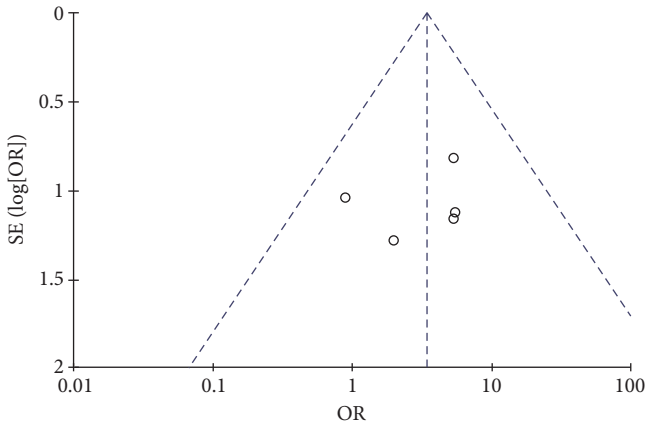

Figure 17: Results of funnel plots.

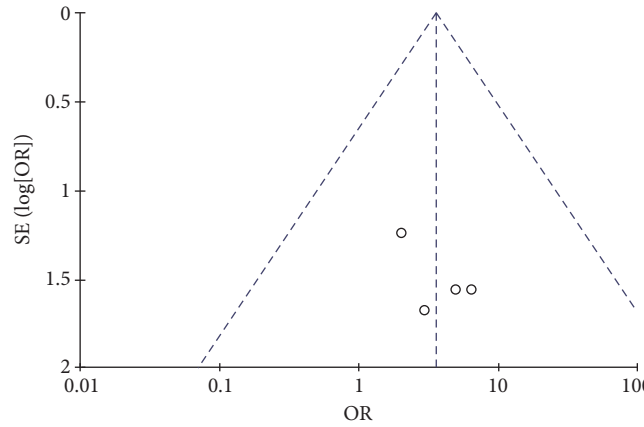

Figure 19: Results of funnel plots.

Study or Subgroup	Experimental Events	Experimental Total	Control Events	Control Total	Weight (%)	Odds Ratio M-H, Fixed, 95% CI
Ang Bing2018	1	14	0	13	20.1	3.00 [0.11, 80.39]
CHEN L2015	0	0	0	0		Not estimable
Jiang M2018	2	24	0	28	18.0	6.33 [0.29, 138.67]
Lin FH2016	0	0	0	0		Not estimable
Liu X-T2017	0	0	0	0		Not estimable
NanDu2013	2	36	0	34	20.7	5.00 [0.23, 108.01]
Qu B2015	2	32	1	31	41.2	2.00 [0.17, 23.25]
XUE DF2017	0	0	0	0		Not estimable
Total (95% CI)		*106*		*106*	*100.0*	*3.60 [0.86, 15.11]*
Total events	7		1			

Heterogeneity: $Chi^2 = 0.41$, df = 3 ($P = 0.94$); $I^2 = 0\%$

Test for overall effect: $Z = 1.75$ ($P = 0.08$)

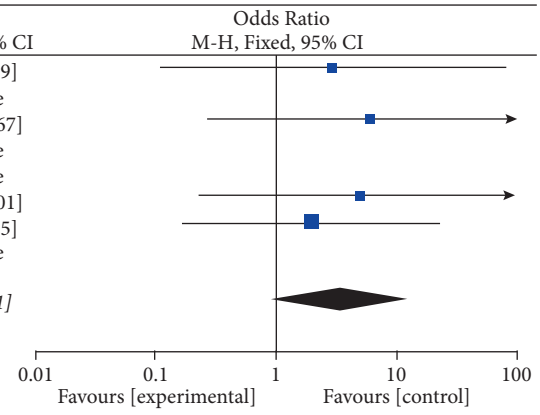

Figure 18: Results of proteinuria.

that the significant increase in VEGF expression in MPE could distinguish the latter from benign pleural effusion, and treatment with bevacizumab led to VEGF blockade [6]. Therefore, VEGF is a key factor in MPE production and a predictive factor of its therapeutic regression.

MPE is routinely treated by thoracic infusion of chemotherapeutic drugs such as cisplatin, carboplatin, lopressor, and oxaliplatin, all of which are associated with systemic or local side effects and require multiple perfusions. Local perfusion of platinum drugs into the pleural cavity can alleviate MPE by directly killing the tumor cells and indirectly promoting the adhesion between the two layers of the pleura, which in turn inhibits MPE production. Although cisplatin and carboplatin have different pharmacokinetic characteristics, there is no significant difference in their therapeutic effects when administered intravenously. Studies comparing

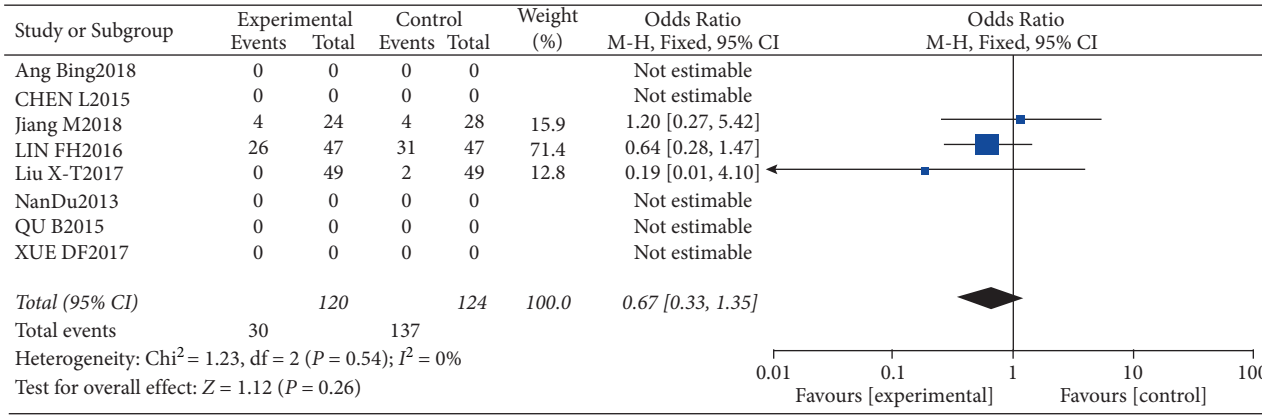

Figure 20: Results of the analysis of kidney and liver dysfunction.

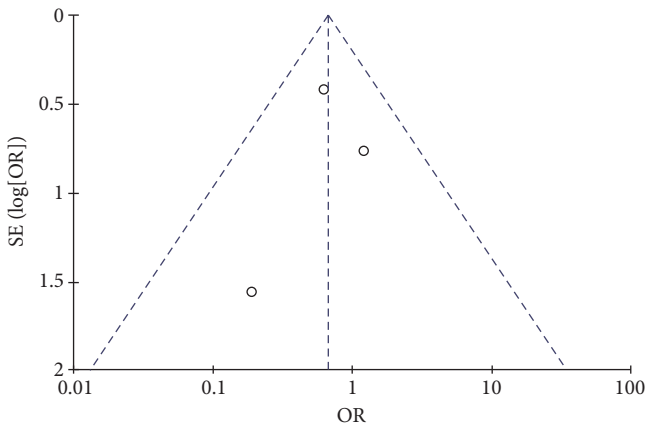

Figure 21: Results of funnel plots.

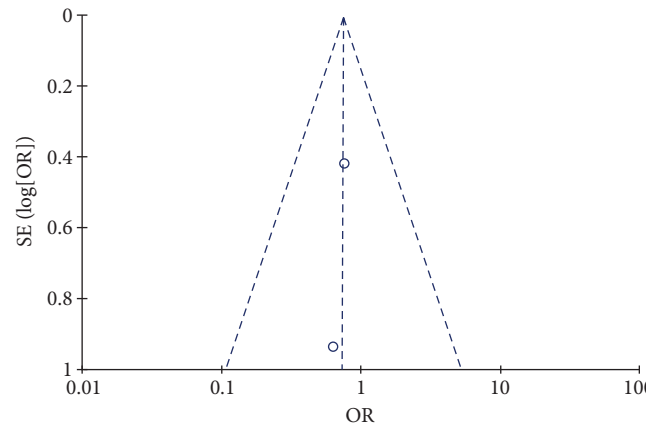

Figure 23: Results of funnel plots.

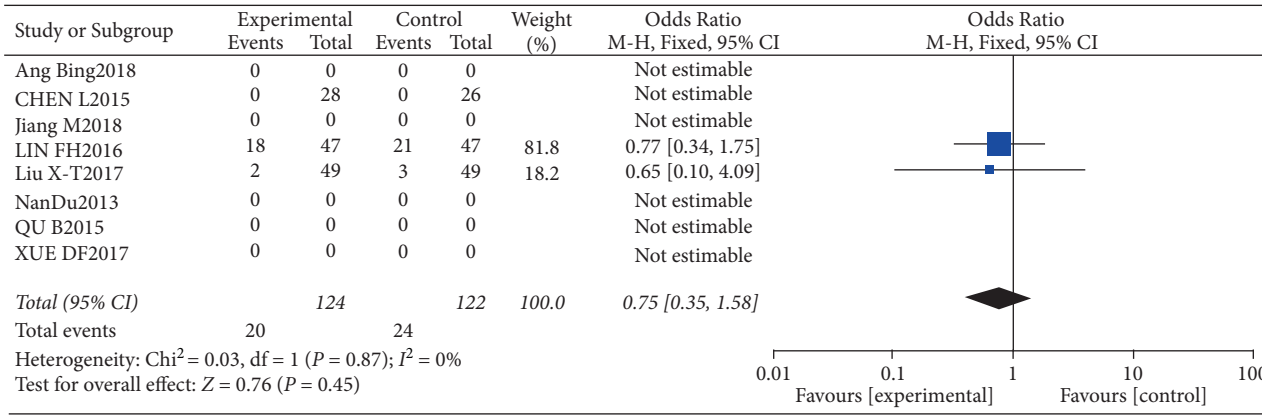

Figure 22: Results of arrhythmia.

the effects of the intrathoracic/intrapleural instillation of cisplatin or carboplatin are limited. Xi et al. did not detect any significant difference between the therapeutic efficiency of intrathoracically instilled cisplatin and carboplatin. Xiaoyan et al. found that the therapeutic efficacy of cisplatin administered by pleural perfusion is only 50–60% [27], whereas Liang et al. reported 73.3% efficacy of similarly administered lobaplatin [28]. Therefore, local perfusion of platinum drugs is routinely combined with thymidine, Conrad injection, thermal perfusion therapy, interleukins, targeted drugs, etc., for treating MPE, and the combination therapies are superior to individual perfusion schemes in terms of efficacy and side effects. Lu et al. conducted a meta-analysis of eight RCTs, including a total of 328 patients, and found that thoracic perfusion of thymidine and oxaliplatin achieved greater efficacy against MPE compared to oxaliplatin alone, along with fewer side effects [29]. The majority of the studies included in the present meta-analysis showed

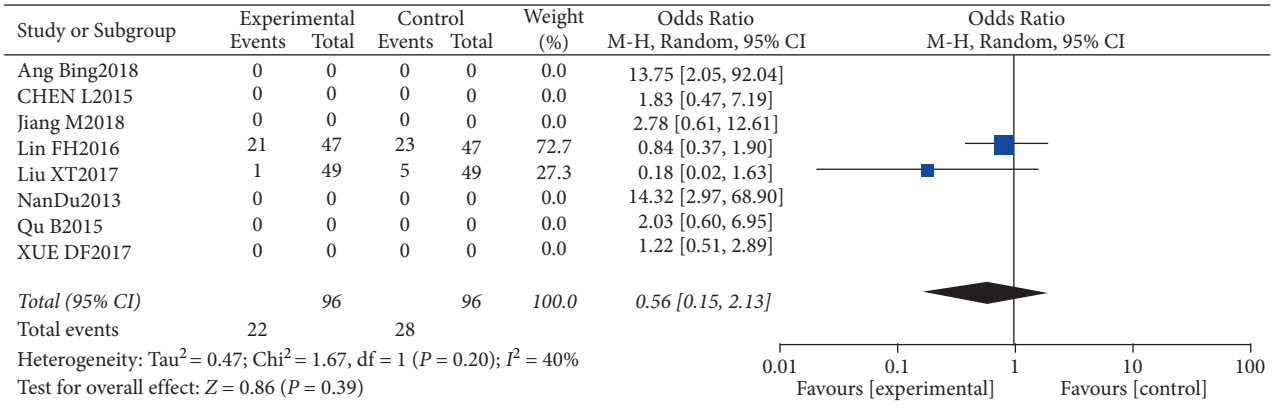

Figure 24: Results of rash analysis.

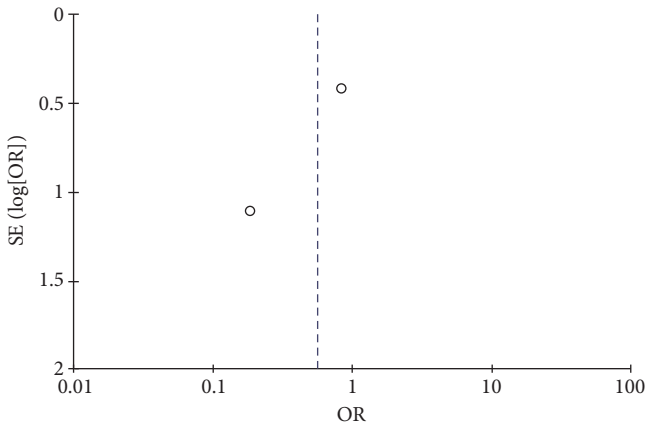

Figure 25: Results of funnel plots.

that bevacizumab combined with platinum drugs was more effective than the individual drugs, albeit with a trend towards increased side effects compared to carboplatin alone. Nevertheless, it cannot yet be assumed that the dual drug combination increased the risk of adverse effects. Previous studies have also shown that the secondary increase in blood pressure due to bevacizumab is manageable and does not cause serious secondary damage.

Since VEGF is also essential for maintaining normal vascular endothelial cell function, blocking the VEGF signaling pathway can lead to endothelial dysfunction and hypertension. Several studies have shown that bevacizumab increases the risk of hypertension [30–32]. Therefore, blood pressure ≥150/95 mmHg before or during initial treatment warrants anti-hypertensive intervention and reevaluation of bevacizumab treatment after at least two weeks [33]. Amlodipine is recommended as the first choice for patients taking anti-hypertensive medications [33]. In addition, blood pressure measurement is recommended for patients prior to each administration of bevacizumab. Another concern of intrathoracic perfusion therapy is the extravasation of the perfused drugs into the subcutaneous tissues. Although it is a very rare occurrence, it is still necessary to verify the location of the intrathoracic tube before each infusion. Most studies included in this meta-analysis emphasized the need for multiple position changes after perfusion therapy to reduce the risk of drug extravasation and promote drug absorption.

To summarize, thoracic perfusion of bevacizumab combined with platinum-based drugs improves the survival and clinical outcomes of lung cancer patients with MPE without significantly increasing the risk of complications. However, the impact of this regimen on the long-term survival of MPE patients still needs to be further validated in a multicenter prospective study on a larger cohort.

The limitation of this meta-analysis is that we compared the effects of the combination treatment with carboplatin or cisplatin but not with bevacizumab due to the lack of data on bevacizumab as the control group. Therefore, more prospective studies should be done to analyze the difference between single-drug perfusion and multiple-drug perfusion therapy or between single-drug perfusion and thoracic fever perfusion. Recent meta-analyses suggest that intravenous and intrathoracic administration of bevacizumab have the same efficacy, whereas our data indicate that chest infusion has greater therapeutic benefit.

5. Conclusion

Bevacizumab combined with platinum-based thoracic perfusion can achieve CR of MPE in patients with advanced lung cancer without significantly increasing the risk of adverse effects. The rate of PR was similar for the combination treatment and platinum-based infusion.

Data Availability

All data generated and analyzed in this study are included in this published article and are available upon request.

Ethical Approval

All experimental data were collected and collated with the approval of the hospital ethics committee.

Conflicts of Interest

All authors declare that they have no conflicts of interest.

Authors' Contributions

Bairu Shen conceived, designed, and was responsible for the specific conduct of the research project and wrote the paper. Changshan Song directed the study implementation and reviewed a draft of the paper. Minghua Tan, Zhenyu Wang and Hui Hu assisted with the statistical analysis of the study data. Yuxin Yang and Shunfu Deng assisted with data collection. All authors approved the final manuscript.

Acknowledgments

The authors greatly appreciate the support and guidance of President and Professor Xiaodong Zhao over the years and are grateful to the hospital for providing information and media support.

References

[1] S.-D. Lu and Z. Sheng, "Changes in serum and pleural effusion tumor marker levels in patients with lung cancer and malignant pleural effusion and their differential diagnostic value for benign and malignant pleural effusion," *Journal of Practical Cardiopulmonary Vascular Disease*, vol. 9, pp. 38–42, 2018.

[2] Z. Zhang, X. Cheng, and Y. Hu, "Clinical effects of Bevacizumab combined with chemotherapy in the treatment of malignant pleural effusion in non-small cell lung cancer," *Journal of Practical Cancer*, vol. 7, pp. 1155–1157, 2018.

[3] H. E. Davies and Y. C. G. Lee, "Management of malignant pleural effusions," *Current Opinion in Pulmonary Medicine*, vol. 19, no. 4, pp. 374–379, 2013.

[4] F. Xie, F. Zhou, Y. R. Chen, D. S. Zhang, Y. Y. Shun, and L. Nie, "Analysis of the efficacy of thoracic thermal perfusion chemotherapy for lung cancer with malignant pleural effusion," *Journal of Clinical Internal Medicine*, vol. 10, pp. 708-709, 2017.

[5] D.-D. Cao, M. Xu, Z.-M. Jiang, Y. Y. Zhang, and W. Ge, "Systematic evaluation of the efficacy of intrathoracic injection of element in the treatment of malignant pleural effusion in lung cancer," *Modern Oncology Medicine*, vol. 2, pp. 223–229, 2018.

[6] K. A. Li, Z. F. Hao, H. P. Chen, P. T. Miao, and J. L. Cu, "Effect of intracavitary injection of Bevacizumab combined with oxaliplatin in the treatment of malignant pleural effusion in lung cancer," *Guangdong Medicine*, vol. 40, no. 23, pp. 3327–3330, 2019.

[7] B. R. Shen, C. S. Song, X. H. Wu, S. T. Zhou, and S. Zhu, "Effect of ultrasound-guided radiofrequency ablation combined with targeted thoracic perfusion on the efficacy and survival quality of malignant pleural effusion in lung cancer," *Journal of Clinical Surgery*, vol. 29, no. 4, pp. 363–366, 2021.

[8] B. Ang, L. Wu, and C. Zhou, "Clinical efficacy of Bevacizumab combined with cisplatin in the treatment of malignant pleural fluid in lung cancer," *Chinese Journal of Oncology Biotherapy*, vol. 25, no. 11, pp. 1176–1179, 2018.

[9] L. L. Zheng, M. Y. Yuan, T. Jiang, and T. Yuan, "Meta-analysis of the safety of Bevacizumab in combination with chemotherapy/EGFR-TKI for advanced lung cancer," *Journal of Pharmacoepidemiology*, vol. 27, no. 3, pp. 145–152, 2018.

[10] N. Du, X. Li, F. Li et al., "Intrapleural combination therapy with bevacizumab and cisplatin for non-small cell lung cancer-mediated malignant pleural effusion," *Oncology Reports*, vol. 29, no. 6, pp. 2332–2340, 2013.

[11] X.-T. Liu, C.-M. Zhao, and L.-H. Zhang, "Effectiveness of Bevacizumab combined with cisplatin in the treatment of patients with malignant pleural effusion in non-small cell lung cancer," *Medical Equipment*, vol. 31, no. 6, pp. 125-126, 2018.

[12] C. Lei and S. Xia, "Effectiveness and safety of Bevacizumab combined with cisplatin in the treatment of malignant pleural effusion in non-small cell lung cancer," *Journal of Shanghai Jiaotong University*, vol. 35, no. 8, pp. 1194–1198, 2015.

[13] B. Qu, W. Jiang, and C. Zhou, "Clinical study of Bevacizumab combined with cisplatin in the treatment of malignant pleural effusion in non-small cell lung cancer," *Journal of China Medical University*, vol. 44, no. 7, pp. 648–652, 2015.

[14] F. H. Lin, W. P. Su, and R. W. Jin, "Clinical study of Bevacizumab combined with cisplatin in the treatment of malignant pleural effusion in non-small cell lung cancer," *Journal of Clinical Military Medicine*, vol. 44, no. 7, pp. 698–700, 2016.

[15] D. F. Xue and X. J. Zhao, "Study on the therapeutic effect of Bevacizumab combined with cisplatin on non-small cell lung cancer pleural effusion," *China Journal of Medicine*, vol. 19, no. 4, pp. 377-378, 2017.

[16] M. Jiang, F. Chi, and R. Wu, "Clinical study of Bevacizumab combined with carboplatin in the treatment of malignant pleural effusion in non-small cell lung cancer," *Journal of Clinical Pulmonology*, vol. 22, no. 5, pp. 813–816, 2017.

[17] X. Song, D. Chen, J. Guo, L. Kong, H. Wang, and Z. Wang, "Better efficacy of intrapleural infusion of Bevacizumab with pemetrexed for malignant pleural effusion mediated from nonsquamous non-small cell lung cancer," *OncoTargets and Therapy*, vol. 11, pp. 8421–8426, 2018.

[18] M. Bradshaw, A. Mansfield, and T. Peikert, "The role of vascular endothelial growth factor in the pathogenesis, diagnosis and treatment of malignant pleural effusion," *Current Oncology Reports*, vol. 15, no. 3, pp. 207–216, 2013.

[19] E. A. Lieser, G. A. Croghan, W. K. Nevala, M. J. Bradshaw, S. N. Markovic, and A. S. Mansfield, "Up-regulation of proangiogenic factors and establishment of tolerance in malignant pleural effusions," *Lung Cancer*, vol. 1, pp. 63–68, 2013.

[20] I. Gkiozos, S. Tsagouli, A. Charpidou et al., "Levels of vascular endothelial growth factor in serum and pleural fluid are independent predictors of survival in advanced non-small-cell lung cancer: results of a prospective study," *Anticancer Research*, vol. 2, pp. 1129–1137, 2015.

[21] E. Fafliora 1, C. Hatzoglou, K. I. Gourgoulianis, and S. G. Zarogiannis, "Systematic review and meta-analysis of vascular endothelial growth factor as a biomarker for malignant pleural effusions," *Physics Reports*, vol. 4, no. 24, Article ID e12978, 2016.

[22] C. Y. Chen, Y. L. Chang, J. Y. Shih et al., "Thymidylate synthase and dihydrofolate reductase expression in non-small cell lung carcinoma: the association with treatment efficacy of pemetrexed," *Lung Cancer*, vol. 74, no. 1, pp. 132–138, 2011.

[23] Y. Ding, J. R. Zhou, P. Shuai, C. F. Liao, Y. Wang, and X. L. Yuan, "Value of VEGF, EGFR and CD40 assays in identifying benign and malignant pleural effusions," *China Pharmaceutical Herald*, vol. 16, no. 20, pp. 141–144, 2019.

[24] Y. Y. Zhu, H. M. Wu, and R. Y. Liu, "Diagnostic values of sVEGFR—1 and endostatin in malignant pleural effusions in patients with lung cancer," *Clinical Laboratory*, vol. 63, no. 9, pp. 1371–1378, 2017.

[25] M. M. P. Acencio, J. Puka, V. A. Alvarenga et al., "Intrapleural targeted therapies (anti-VEGF and anti-EGFR) in the model

of malignant pleural effusion," *Oncotarget*, vol. 8, no. 62, pp. 105093–105102, 2017.

[26] Y. Duzkopru, Z. Oruf, M. A. Kaplan et al., "The importance of serum and pleural fluid level of vascular endothelial growth factor (VEGF) and VEGF fluid/serum ratio in the differential diagnosis of malignant mesothelioma -related pleural effusion," *Contemporary Oncology*, vol. 21, no. 3, pp. 213–217, 2017.

[27] X. Hu, F. Du, X. Dong, and L. Xu, "Clinical study of raltitrexed combined with cisplatin intraperitoneal thermal perfusion for the treatment of malignant ascites," *Basic and Clinical Oncology*, vol. 30, no. 2, pp. 114–117, 2017.

[28] X. T. Liang, G. P. Ma, and X. E. P. Gao, "Clinical efficacy analysis of oxaliplatin combined with thymidine in the treatment of malignant pleural effusion in lung cancer," *Hebei Medicine*, vol. 2, no. 13, pp. 1994–1996, 2015.

[29] H. Lu, B. Zhao, and Y. Liu, "Meta-analysis of thymidine combined with oxaliplatin by thoracic infusion in the treatment of lung cancer combined with malignant pleural effusion," *Journal of Guangxi Medical University*, vol. 36, no. 1, pp. 36–41, 2019.

[30] Y. S. Wu, L. Shui, D. Shen, and X. P. Chen, "Bevacizumab combined with chemotherapy for ovarian cancer: an updated systematic review and meta-analysis of randomized controlled trials," *Oncotarget*, vol. 8, no. 6, pp. 10703–10713, 2017.

[31] T. Botrel, L. Clark, L. Paladini, and O. A. C. Clark, "Efficacy and safety of Bevacizumab plus chemotherapy compared to chemotherapy alone in previously untreated advanced or metastatic colorectal cancer: a systematic review and meta-analysis," *BMC Cancer*, vol. 16, p. 677, 2016.

[32] S. P. Lee, H. C. Hsu, Y. J. Tai et al., "Bevacizumab dose affects the severity of adverse events in gynecologic malignancies," *Frontiers in Pharmacology*, vol. 10, p. 426, 2019.

[33] C. Plummer, A. Michael, G. Shaikh et al., "Expert recommendations on the management of hypertension in patients with ovarian and cervical cancer receiving Bevacizumab in the UK," *British Journal of Cancer*, vol. 121, no. 2, pp. 109–116, 2019.

Hindawi
Journal of Oncology
Volume 2022, Article ID 2174758, 7 pages
https://doi.org/10.1155/2022/2174758

Research Article

SIRT6 Promotes the Progression of Prostate Cancer via Regulating the Wnt/β-Catenin Signaling Pathway

Xian Zhang,[1] Rong Chen,[2] Li-De Song,[2] Ling-Fei Zhu ,[2] and Jian-Fei Zhan [2]

[1]*Department of Urology Surgery, The Wenzhou Central Hospital, The Dingli Clinical College of Wenzhou Medical University, Wenzhou, Zhejiang, China*
[2]*Department of Urology Surgery, The People's Hospital of Zhuji, Shao Xing, Zhejiang, China*

Correspondence should be addressed to Ling-Fei Zhu; 343017336@qq.com and Jian-Fei Zhan; zhss9118@aliyun.com

Received 15 January 2022; Revised 29 January 2022; Accepted 8 February 2022; Published 25 February 2022

Academic Editor: Fu Wang

Sirtuin 6 (SIRT6), a DNA repair-related gene, has undergone an extremely thorough study for its involvement in the development of many different cancers. The objective of our study was to explore the function and mechanism of SIRT6-induced regulation of prostate cancer (PCa). RT-PCR was performed to validate the levels of SIRT6 in PCa cell lines. Cell proliferation, migration, and invasion of cells with SIRT6 knockdown were assessed using CCK-8 assay, colony formation assay, wound-healing assay, and transwell assay. Western blot was applied to assess the related proteins. We found that SIRT6 expression was distinctly upregulated in PCa specimens and cells. Loss-of-functional assays revealed that SIRT6 silence suppressed the proliferation and metastasis of PCa cells. Mechanistic studies revealed that SIRT6 silence inhibited Wnt/β-catenin signaling and EMT progress. Overall, the study confirmed the upregulation of SIRT6 in patients with PCa and its association with the progression. SIRT6 promoted PCa progression by regulating Wnt/β-catenin signaling, providing a promising biomarker and treatment approach for preventing PCa.

1. Introduction

Prostate cancer (PCa) is one of the most common malignancies in elderly males around the world [1]. The incidence rates are increasing over the last two decades. The clinical outcome of many patients with PCa has achieved a positive situation after the application of early surgical excisions [2]. However, a poor prognosis was frequently observed in patients with advanced stages or unresectable tumors [3]. In addition, neoadjuvant chemotherapy and surgery are necessary for the improvement of long-term survivals [4, 5]. Although plenty of effort has been made to improve the treatment efficiency of PCa, the potential mechanisms involved in PCa progression have limited the development of effective treatments.

Sirtuin 6 (SIRT6) is a nicotinamide adenine dinucleotide (NAD+)-dependent histone deacetylase which has been confirmed to remove acetyl groups from histone 3 lysine 9 and histone 3 lysine 56 motifs [6, 7]. More and more evidence have demonstrated that histone deacetylase exhibited multiple effects, such as inhibition of suppression of cellular transformation, maintenance of genome stability, and glucose homeostasis [8, 9]. As a multifunctional nuclear protein, the functions of SIRT6 are complex. It has been demonstrated that SIRT6 exhibited a regulatory effect in several biological progressions, including bone disorders, inflammation, diabetes, heart and liver diseases, neurodegenerative, glucose metabolism, longevity, genome stability, and various tumors [10, 11]. Besides, several research studies have reported that SIRT6 plays an important role in DNA damage, repair, and mutagenesis [12, 13]. In recent years, more and more studies have reported the distinct dysregulation of SIRT6 in many types of tumors [14, 15]. However, the expressing pattern of SIRT6 exhibited a different trend based on the types of tumors. In pancreatic cancer, SIRT6 expression was distinctly decreased and its overexpression suppressed tumor metastasis [16].

However, SIRT6 was found to be overexpressed in diffuse large B-cell lymphoma and promote the proliferation and invasion of tumor cells via mediating PI3K/Akt signaling [17]. The potential function of SIRT6 in PCa remained largely unclear.

In this research, we aimed to examine the expression of SIRT6 in PCa patients, investigate its possible functions, and characterize molecular mechanisms involved in SIRT6 roles in PCa progression. Our findings provided a novel perspective therapeutic target of SIRT6 in PCa.

1.1. Patients and Methods

1.1.1. Cell Transfection. A panel of PCa cell lines including PC-3, 22RV1, and DU145 cells and a human normal prostate cell line (WPMY) were all obtained from BeNa Company (Suzhou, Jiangsu, China) and maintained in RPMI-1640 media (Beikai, Changsha, Hunan, China) with 10% FBS. Besides, TransEasy transfection reagent kits (Fujiyin, Chengdu, Sichuan, China) were then applied to perform the cell transfection in accordance with the kits' protocols. The siRNAs (si-NC and si-SIRT6) were purchased from JiMa Biological Corporation (Suzhou, Jiangsu, China).

1.1.2. Real-Time PCR. TRIzol reagents (Qianchen, Pudong, Shanghai, China) were employed to extract total RNAs. The first-strand cDNA synthesis was carried out with a High-Fidelity 1st Strand cDNA synthesis kit (Agilent, Chaoyang, Beijing, China), and the qRT-PCR analysis for SIRT6 detection was carried out by the use of SYBR-Green Real-Time Mix kits (Shenggong, Songjiang, Shanghai, China). The expressing values of SIRT6 were normalized to GAPDH and calculated using the $2^{-\triangle\triangle Ct}$ method. The PCR primers were designed as follows: SIRT6 forward, 5′-CCCACGGAG TCTGGACCAT-3′ and reverse, 5′-CTCTGCCAGTTTGT CCCTG-3′ and GAPDH forward, 5′-CTGGGCTACACTG GCACC-3′ and reverse, 5′-AAGTGGTCGTTGAGGGC AATG-3′.

1.1.3. Cell Viability Detection. The cell viability was assessed by CCK-8 assays. In short, 2000 PC-3 or DU145 cells after treatment with si-NC were seeded in 96-well plates per well. After culturing for 48 h, 72 h, and 96 h, the cells were treated with CCK8 reagents (10 μl; BOSTER, Wuhan, Hubei, China). Then, the absorbance at 450 nm at the indicated time point was evaluated by a microreader.

1.1.4. Colony Formation Assay. Briefly, PC-3 or DU145 cells after treatment with si-NC were plated into 6-well plates at a density of 500 cells per well. Cells were then cultured for about 2 weeks. Then, paraformaldehyde (4%) (Sigma, Yangfu, Shanghai, China) and crystal violet (0.1%) (Solarbio, Tongzhou, Beijing, China) were applied to fix and stain the cell colonies, respectively. Finally, the cell colonies were observed using a microscope (XHC-BV1; DongFangHuaCe, Chaoyang, Beijing, China).

1.1.5. Wound-Healing Assay. In short, PC-3 or DU145 cells were treated with si-NC. Then, cells were planted into 12-well plates and continued to be cultured until 100% cell confluence. A pipette tip (200 μl) was then employed to generate a wound field. After that, the cells were washed and observed by a microscope at 0 h and 48 h (XHC-BV1; DongFangHuaCe, Chaoyang, Beijing, China).

1.2. Transwell Assay. Cellular invasion was evaluated by transwell invasion assays using Corning Costar transwell inserts (Lianshuo Biotech, Qingpu, Shanghai, China). First, the upper chambers of the transwell inserts were treated with Matrigel. Then, PC-3 or DU145 cells after treatment with si-NC were resuspended in serum-free media and then planted into the upper chambers of the inserts. In addition, the lower chambers were loaded with a medium containing 15% FBS. After 24 h, the invaded cells in the lower chamber were fixed in 4% paraformaldehyde and stained with 0.1% crystal violet. Finally, these cells were observed and photographed under an inverted microscope (XHC-BV1; DongFangHuaCe, Chaoyang, Beijing, China).

1.3. Western Blot. In brief, the PC-3 or DU145 cells were lysed using a cell lysates extraction kit (X-Y Bioscience, Minhang, Shanghai, China), and the lysates were quantified by a BCA kit (Jingke Chemical Technology, Jinshan, Shanghai, China). Subsequently, 20 μg of the protein sample was fractionated by 10% SDS-PAGE, which was then transferred to PVDF membranes (Millipore, Bedford, Massachusetts, USA). Proteins were blocked by 5% skim milk and then were examined by corresponding antibodies using a super-enhanced ECL detection kit (Servicebio, Wuhan, Hubei, China). The primary antibodies against β-catenin, cyclin D1, and c-myc were purchased from Wuhan BOSTER Co., Ltd. (Wuhan, Hubei, China).

1.4. Statistical Analysis. Data analysis was performed using SPSS 19.0 statistical software (SPSS, Chicago, IL, USA). The Student's t-test was applied to two-group analysis. A value of $p < 0.05$ was considered to indicate statistical significance.

2. Results

2.1. Upregulation of SIRT6 in PCa Tissues and Cell Lines. To explore the possible function of SIRT6 in PCa, we searched "GEPIA", which can be used to analyze the expressions of various genes in tumors based on TCGA data sets [18], finding that SIRT6 expression was distinctly upregulated in PCa specimens compared with normal specimens ($p < 0.01$, Figure 1(a)). Moreover, the levels of SIRT6 in three PCa cell lines were also higher than those in WPMY-1 (Figure 1(b)). In addition, survival assays revealed that high SIRT6 expression was associated with a shorter overall survival of PCa patients (Figure 1(c)). Overall, our findings revealed SIRT6 as a possible regulator in the progression of PCa.

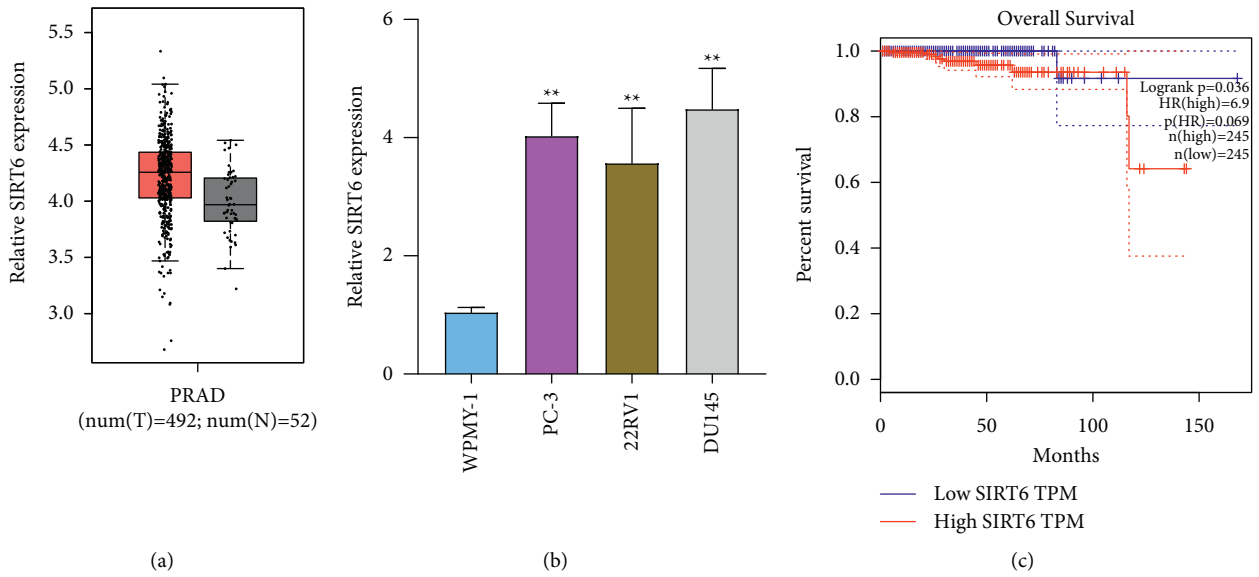

Figure 1: SIRT6 was upregulated in PCa specimens and cell lines. (a) GEPIA was used to analyze the expression of SIRT6 in PCa specimens ($n = 492$) and nontumor specimens ($n = 52$) based on TCGA data sets. (b) qPCR detected the relative SIRT6 levels in PCa cells. (c) Survival value of SIRT6 expression in PCa patients based on TCGA data sets. $^{**}p < 0.01$.

2.2. Overexpression of SIRT6 Contributed to the Inhibition of Cellular Proliferation in PCa Cells. Because SIRT6 was lowly expressed in PCa, we next conducted gain-of-function studies using si-NC transfection to examine the functions of SIRT6 in PCa. The results of qPCR suggested the distinct overexpression of SIRT6 in PC-3 or DU145 cells (Figure 2(a)). CCK8 assays were then carried out to evaluate the potential biological roles of SIRT6 in PCa cell proliferation. After transfecting si-SIRT6, the cellular growth of PCa cells was significantly decreased at 72 h and 96 h (Figures 2(b) and 2(c)). In addition, the colony formation assays demonstrated that the silence of SIRT6 distinctly suppressed the clonogenic abilities of PCa cells (Figures 2(d) and 2(e)).

2.3. Effects of SIRT6 on the Migration and Invasion of PCa Cells. To further explore the roles of SIRT6 in the migration and invasiveness of PCa cells, we conducted wound healing and transwell invasion assays using PC-3 or DU145 cells after treatment of si-SIRT6. The data of wound healing assays validated that knockdown of SIRT6 dramatically suppressed the width of wounded areas (Figure 3(a)). Furthermore, with the downregulation of SIRT6, the invasive capability of PCa cells was notably reduced when they were assessed by transwell invasion assays (Figure 3(b)). In addition, to elucidate the mechanisms of SIRT6 on cell metastasis, we carried out Western blot analysis to evaluate the levels of N-cadherin and vimentin which were involved in epithelial-mesenchymal transition. The data demonstrated that silence of SIRT6 led to obvious decline of N-cadherin and vimentin protein levels in PCa cells (Figures 3(c) and 3(d)). Collectively, these data provided evidence that SIRT6 served as an important regulator in modulating the migration and invasion of PCa cells.

2.4. Depression of SIRT6 Impeded the Activation of Wnt/β-Catenin Signaling in PCa Cells. We next aimed to ascertain the detailed mechanisms by which SIRT6 orchestrated cellular ability. Wnt/β-catenin signaling, a well-known signaling which was closely associated with the functional regulation of multiple cancers, was investigated in the following experiments [19]. Hence, Western blot assays were utilized to evaluate the protein levels of molecules involved in Wnt/β-catenin signaling. The results indicated that the protein levels of c-myc, cyclin D1, and β-catenin were remarkably decreased in PC-3 and DU145 cells (Figures 4(a) and 4(b)). Overall, these data revealed that the activation of Wnt/β-catenin signaling was suppressed by SIRT6 knockdown in PCa cells, and our above results implied that SIRT6 modulated the development and progression of PCa via affecting Wnt/β-catenin signaling.

3. Discussion

To date, many PCa patients with advanced stages have an unfavorable clinical outcome because of limited chemotherapy and the antibiotic drugs [20]. Thus, the identification of novel therapeutic targets is very important for the clinical outcome of PCa patients. Here, our group observed that SIRT6 expression was distinctly increased in PCa specimens compared with nontumor specimens. Then, the knockdown of SIRT6 was shown to suppress the proliferation, migration, and invasion of PCa cells, indicating its oncogenic roles in PCa progression. Previously, several studies reported the dysregulation of SIRT6 in several types of tumors [16, 21]. For instance, SIRT6 was shown to be lowly expressed in colorectal cancer stem cells, and its overexpression suppressed the cell proliferation, colony formation, and induced G0/G1 phase arrest in colorectal cancer stem cells via regulating CDC25A [22]. However,

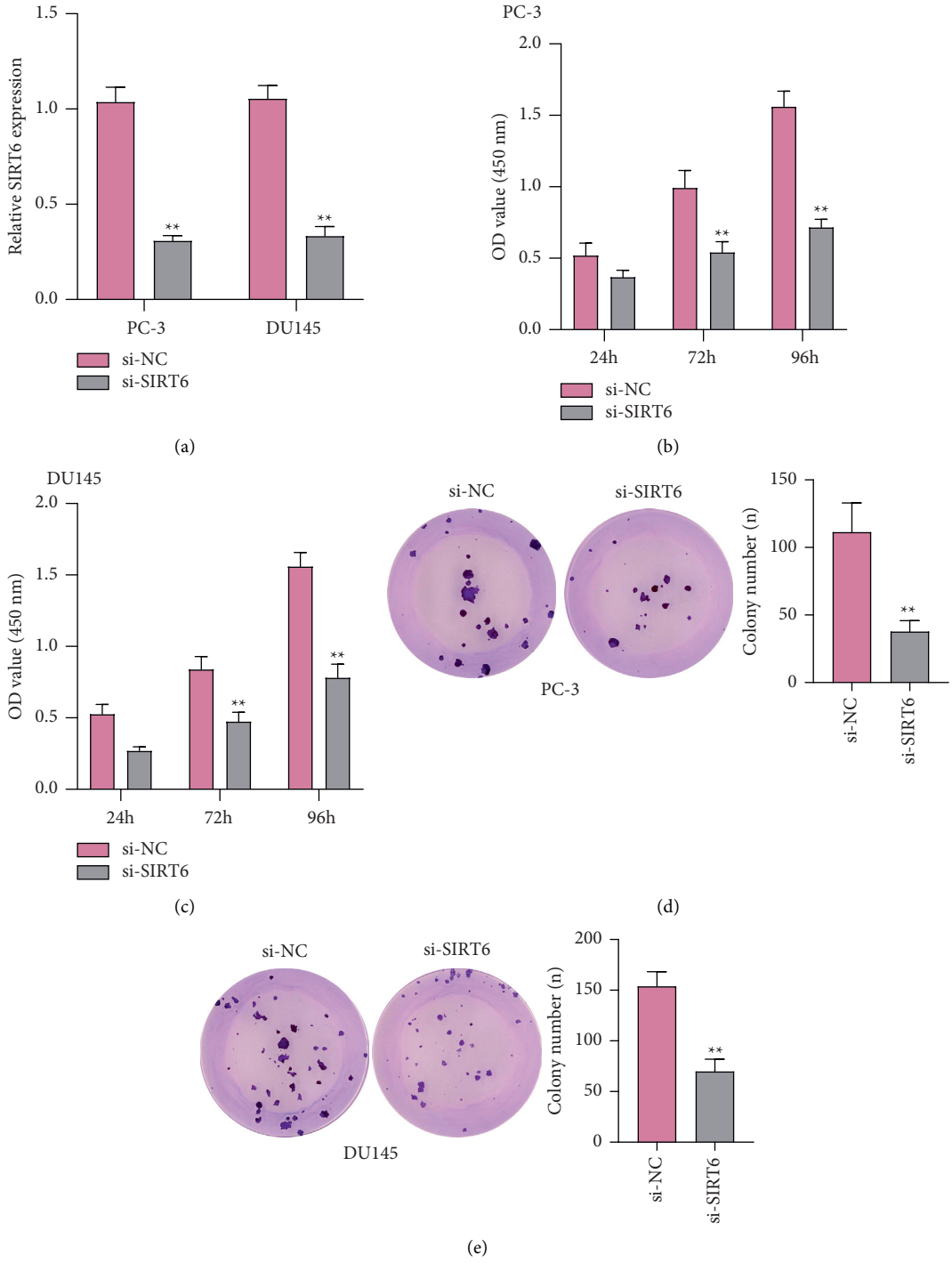

Figure 2: Knockdown of SIRT6 suppressed the proliferation of PC-3 or DU145 cells. (a) qPCR assays detected the expression levels of SIRT6 in PCa cells after transfected with si-SIRT6 or si-NC. (b, c) CCK-8 assays evaluated the cellular growth after treatment with si-SIRT6 or si-NC at 48 h, 72 h, and 96 h. (d and e) Colony formation assays assessed the effects of SIRT6 knockdown on the clonogenic capacity of PCa cells. $^{**}p < 0.01$.

high levels of SIRT6 were observed in diffuse large B-cell lymphoma, and its overexpression promoted the metastasizing capacity of tumor cells and drug resistance of diffuse large B-cell lymphoma by mediating PI3K/Akt signaling [17]. These findings suggested a different role of SIRT6 based on the types of tumors. Our findings indicated SIRT6 as an oncogene, which was not consistent with its function in breast cancer and lung cancer [23, 24].

Epithelial-mesenchymal transition (EMT) is a process in which epithelial cells acquire mesenchymal features [25]. It has been demonstrated that EMT is involved in cancer progression, metastatic competency, and problems of drug

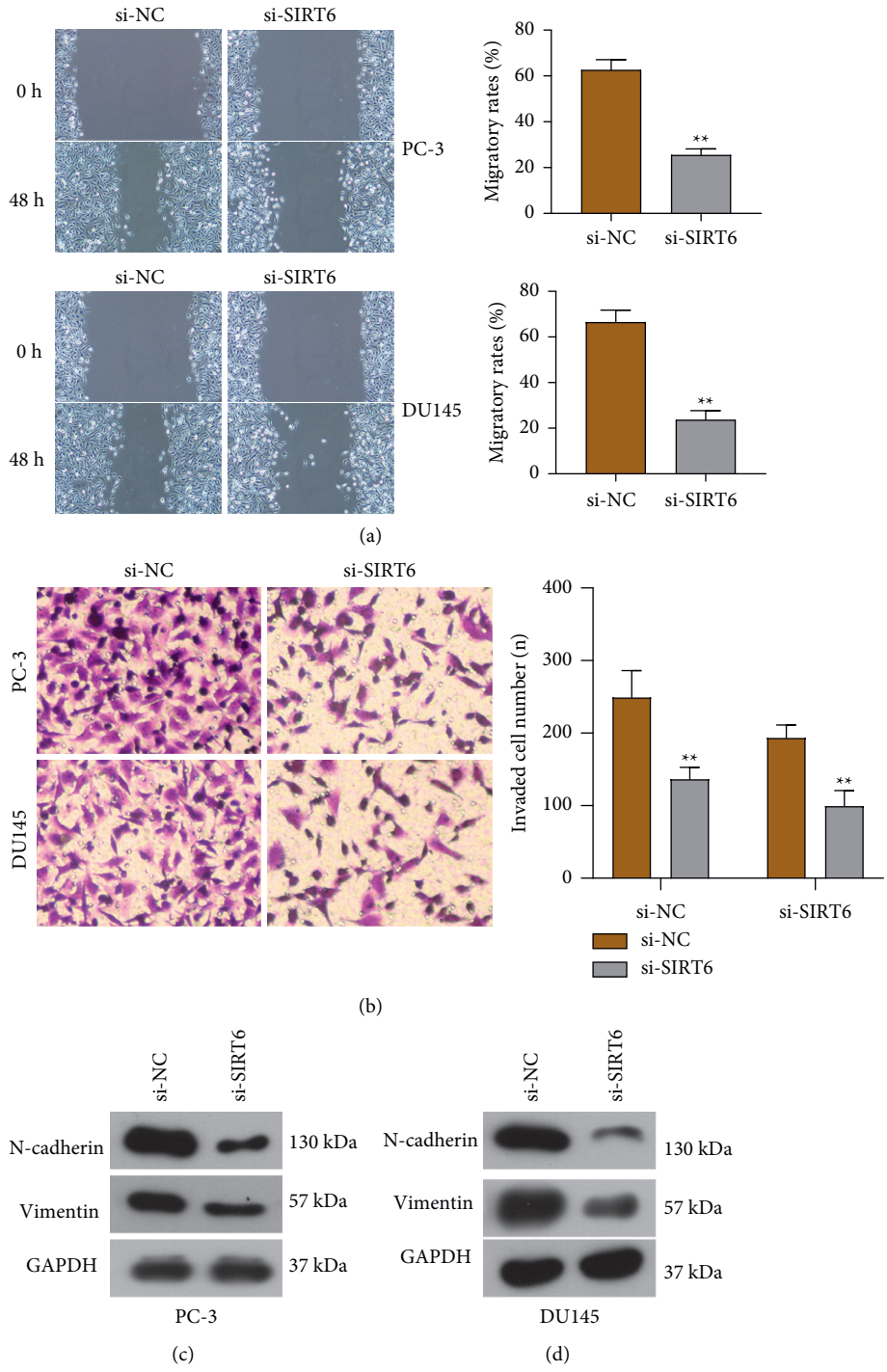

Figure 3: Knockdown of SIRT6 impaired the invasion and migration of PCa cells. (a) Migration was inhibited in PCa cells when transfecting with si-NC or si-SIRT6. (b) Transfection of si-SIRT6 reduced the invasion of PCa cells. (c, d) Western blot measured the protein expressions of N-cadherin and vimentin. The relative optical density of the protein bands was analyzed by Image J software (NIH, Bethesda, MD, USA). $^{*}p < 0.05$; $^{**}p < 0.01$.

resistance [26, 27]. In recent years, more and more studies have shown that some tumor-related genes displayed their oncogenic or antioncogenic functions on tumor progression via modulating the EMT pathway [28, 29]. In this study, we also observed that SIRT6 knockdown distinctly suppressed EMT progress. Previously, SIRT6 was reported to promote an aggressive phenotype and the EMT in papillary thyroid cancer, which was consistent with our findings [30]. However, more experiments were needed to further explore the possible effects of SIRT6 on EMT progress.

Wnt/β-catenin signaling is evolutionarily conserved and required for embryonic development and tissue homeostasis

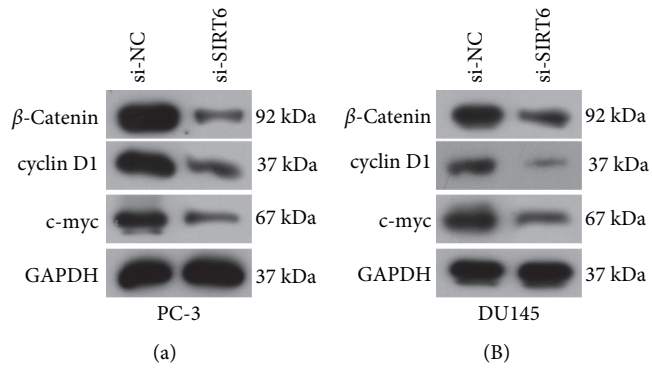

Figure 4: The activity of Wnt/β-catenin signaling in PCa cells was depressed by SIRT6 silence. The protein levels of c-myc, cyclin D1, and β-Catenin in PC-3 (a) and DU145 (B) cells were decreased after SIRT6 silence.

[31]. Wnt/β-catenin signaling is frequently reported to participate in the development and progressions of various types of tumors [32, 33]. This signaling pathway is highly conserved throughout evolution, and it is important in intercellular communication [34]. Growing evidence indicate that enhancing Wnt/β-catenin signaling elements' expression, like receptors and downstream targets, is important in overcoming drug resistance and the reversal of the EMT phenotype [35, 36]. In this study, PCa cells were transduced with si-SIRT6, and we found that the protein level of c-myc, cyclin D1, and β-Catenin were remarkably decreased, suggesting this pathway was inversely modulated by SIRT6 in PCa cells. Thus, our findings indicated that silence of SIRT6 suppressed PCa progression via modulating Wnt/β-catenin signaling.

4. Conclusions

Our findings provided novel evidence that SIRT6 was highly expressed in PCa and promoted the proliferation and metastasis of PCa cells. Mechanistically, SIRT6 silence suppressed the activity of Wnt/β-catenin signaling. Together, our findings suggested that SIRT6 could become a novel prognostic biomarker and potential therapeutic target in PCa.

Data Availability

The data sets generated during and/or analyzed during the current study are available from the corresponding author upon reasonable request.

Conflicts of Interest

The authors declare no conflicts of interest in this work.

Authors' Contributions

Xian Zhang and Jian-fei Zhan performed the study and wrote the paper. Xian Zhang, Rong Chen, and Li-de Song performed the data processing and statistics. Xian Zhang, Ling-fei Zhu, and Jian-fei Zhan designed the study and revised the paper. All authors contributed to the article and approved the submitted version.

Acknowledgments

This work was supported by the Science and Technology Program of Zhuji City, China (No. 2019YW036).

References

[1] G. Attard, C. Parker, R. A. Eeles et al., "Prostate cancer," *The Lancet*, vol. 387, no. 10013, pp. 70–82, 2016.

[2] M. S. Litwin and H.-J. Tan, "The diagnosis and treatment of prostate cancer," *JAMA*, vol. 317, no. 24, pp. 2532–2542, 2017.

[3] T. Gourdin, "Recent progress in treating advanced prostate cancer," *Current Opinion in Oncology*, vol. 32, no. 3, pp. 210–215, 2020.

[4] K. Komura, C. J. Sweeney, T. Inamoto, N. Ibuki, H. Azuma, and P. W. Kantoff, "Current treatment strategies for advanced prostate cancer," *International Journal of Urology*, vol. 25, no. 3, pp. 220–231, 2018.

[5] E. M. Sebesta and C. B. Anderson, "The surgical management of prostate cancer," *Seminars in Oncology*, vol. 44, no. 5, pp. 347–357, 2017.

[6] J. Kuang, L. Chen, Q. Tang, J. Zhang, Y. Li, and J. He, "The role of Sirt6 in obesity and diabetes," *Frontiers in Physiology*, vol. 9, p. 135, 2018.

[7] S. Kugel and R. Mostoslavsky, "Chromatin and beyond: the multitasking roles for SIRT6," *Trends in Biochemical Sciences*, vol. 39, no. 2, pp. 72–81, 2014.

[8] L. Tasselli, W. Zheng, and K. F. Chua, "SIRT6: novel mechanisms and links to aging and disease," *Trends in Endocrinology and Metabolism*, vol. 28, no. 3, pp. 168–185, 2017.

[9] N. D'Onofrio, L. Servillo, and M. L. Balestrieri, "SIRT1 and SIRT6 signaling pathways in cardiovascular disease protection," *Antioxidants and Redox Signaling*, vol. 28, no. 8, pp. 711–732, 2018.

[10] J. W. Nicholatos, A. B. Francisco, C. A. Bender et al., "Nicotine promotes neuron survival and partially protects from Parkinson's disease by suppressing SIRT6," *Acta neuropathologica communications*, vol. 6, no. 1, p. 120, 2018.

[11] M. Van Meter, V. Gorbunova, and A. Seluanov, "SIRT6: a promising target for cancer prevention and therapy," *Advances in Experimental Medicine and Biology*, vol. 818, pp. 181–196, 2014.

[12] X. Tian, D. Firsanov, Z. Zhang et al., "SIRT6 is responsible for more efficient DNA double-strand break repair in long-lived species," *Cell*, vol. 177, no. 3, pp. 622–638, 2019.

[13] T. Hou, Z. Cao, J. Zhang et al., "SIRT6 coordinates with CHD4 to promote chromatin relaxation and DNA repair," *Nucleic Acids Research*, vol. 48, no. 6, pp. 2982–3000, 2020.

[14] M. Vitiello, A. Zullo, L. Servillo et al., "Multiple pathways of SIRT6 at the crossroads in the control of longevity, cancer, and cardiovascular diseases," *Ageing Research Reviews*, vol. 35, pp. 301–311, 2017.

[15] M. Cai, Z. Hu, L. Han, and R. Guo, "MicroRNA-572/hMOF/Sirt6 regulates the progression of ovarian cancer," *Cell Cycle*, vol. 19, no. 19, pp. 2509–2518, 2020.

[16] S. Kugel, C. Sebastián, J. Fitamant et al., "SIRT6 suppresses pancreatic cancer through control of Lin28b," *Cell*, vol. 165, no. 6, pp. 1401–1415, 2016.

[17] J. Yang, Y. Li, Y. Zhang et al., "Sirt6 promotes tumorigenesis and drug resistance of diffuse large B-cell lymphoma by mediating PI3K/Akt signaling," *Journal of Experimental & Clinical Cancer Research*, vol. 39, no. 1, p. 142, 2020.

[18] Z. Tang, C. Li, B. Kang, G. Gao, C. Li, and Z. Zhang, "GEPIA: a web server for cancer and normal gene expression profiling and interactive analyses," *Nucleic Acids Research*, vol. 45, no. W1, pp. W98–w102, 2017.

[19] Y. Zhang and X. Wang, "Targeting the Wnt/β-catenin signaling pathway in cancer," *Journal of Hematology & Oncology*, vol. 13, no. 1, p. 165, 2020.

[20] M. Y. Teo, D. E. Rathkopf, and P. Kantoff, "Treatment of advanced prostate cancer," *Annual Review of Medicine*, vol. 70, no. 1, pp. 479–499, 2019.

[21] W. Zheng, L. Tasselli, T. M. Li, and K. F. Chua, "Mammalian SIRT6 represses invasive cancer cell phenotypes through ATP citrate lyase (ACLY)-Dependent histone acetylation," *Genes*, vol. 12, no. 9, 2021.

[22] W. Liu, M. Wu, H. Du, X. Shi, T. Zhang, and J. Li, "SIRT6 inhibits colorectal cancer stem cell proliferation by targeting CDC25A," *Oncology Letters*, vol. 15, no. 4, pp. 5368–5374, 2018.

[23] L. Ruan, J. Chen, L. Ruan, T. Yang, and P. Wang, "MicroRNA-186 suppresses lung cancer progression by targeting SIRT6," *Cancer Biomarkers*, vol. 21, no. 2, pp. 415–423, 2018.

[24] P. Becherini, I. Caffa, F. Piacente et al., "SIRT6 enhances oxidative phosphorylation in breast cancer and promotes mammary tumorigenesis in mice," *Cancer & Metabolism*, vol. 9, no. 1, p. 6, 2021.

[25] M. Singh, N. Yelle, C. Venugopal, and S. K. Singh, "EMT: mechanisms and therapeutic implications," *Pharmacology & Therapeutics*, vol. 182, pp. 80–94, 2018.

[26] N. M. Aiello and Y. Kang, "Context-dependent EMT programs in cancer metastasis," *Journal of Experimental Medicine*, vol. 216, no. 5, pp. 1016–1026, 2019.

[27] M. Suarez-Carmona, J. Lesage, D. Cataldo, and C. Gilles, "EMT and inflammation: inseparable actors of cancer progression," *Molecular oncology*, vol. 11, no. 7, pp. 805–823, 2017.

[28] S. Tian, P. Peng, J. Li et al., "SERPINH1 regulates EMT and gastric cancer metastasis via the Wnt/β-catenin signaling pathway," *Aging*, vol. 12, no. 4, pp. 3574–3593, 2020.

[29] J. Wang, H. He, Q. Jiang, Y. Wang, and S. Jia, "CBX6 promotes HCC metastasis via transcription factors snail/zeb1-mediated EMT mechanism," *OncoTargets and Therapy*, vol. 13, pp. 12489–12500, 2020.

[30] Z. Yang, R. Huang, X. Wei, W. Yu, Z. Min, and M. Ye, "The SIRT6-autophagy-warburg effect Axis in papillary thyroid cancer," *Frontiers in Oncology*, vol. 10, p. 1265, 2020.

[31] L. Brunt and S. Scholpp, "The function of endocytosis in Wnt signaling," *Cellular and Molecular Life Sciences*, vol. 75, no. 5, pp. 785–795, 2018.

[32] D. J. Flanagan, E. Vincan, and T. J. Phesse, "Wnt signaling in cancer: not a binary ON:OFF switch," *Cancer Research*, vol. 79, no. 23, pp. 5901–5906, 2019.

[33] J. Harb, P.-J. Lin, and J. Hao, "Recent development of Wnt signaling pathway inhibitors for cancer therapeutics," *Current Oncology Reports*, vol. 21, no. 2, p. 12, 2019.

[34] H. Clevers, "Wnt/β-Catenin signaling in development and disease," *Cell*, vol. 127, no. 3, pp. 469–480, 2006.

[35] S. He and S. Tang, "WNT/β-catenin signaling in the development of liver cancers," *Biomedicine & Pharmacotherapy*, vol. 132, p. 110851, 2020.

[36] S. G. Pai, B. A. Carneiro, J. M. Mota et al., "Wnt/beta-catenin pathway: modulating anticancer immune response," *Journal of Hematology & Oncology*, vol. 10, no. 1, p. 101, 2017.

Hindawi
Journal of Oncology
Volume 2022, Article ID 3507436, 10 pages
https://doi.org/10.1155/2022/3507436

Research Article

Prognostic Significance of PTTG1 and Its Methylation in Lung Adenocarcinoma

Lu Bai,[1,2] Li-Hong Li,[2] Jing Liang,[1] and En-Xiao Li[1]

[1]*Department of Medical Oncology, The First Affiliated Hospital of Xi'an Jiaotong University, Xi'an, Shaanxi, China*
[2]*Department of Geriatric Respiration, Xi'an No. 1 Hospital, Xi'an, Shaanxi, China*

Correspondence should be addressed to Jing Liang; doctorjing55121@163.com and En-Xiao Li; doclienxiao@sina.com

Received 20 December 2021; Revised 10 January 2022; Accepted 12 January 2022; Published 24 February 2022

Academic Editor: Fu Wang

Pituitary tumor-transforming gene-1 (PTTG1), one type of DNA repair-related gene, has been reported to be dysregulated in several tumors and serve as a tumor promotor. Previously, the oncogenic roles of PTTG1 were also reported in lung adenocarcinoma (LUAD). However, the prognostic values of PTTG1 in LUAD and the possible mechanism of its dysregulation have not been clarified. We analyzed TCGA datasets and reported that PTTG1 expression showed a distinct increase within LUAD specimens in comparison with nontumor specimens. Further survival study revealed that patients containing a great PTTG1 level had noticeably less overall survival and progression-free survival as compared with patients containing a low PTTG1 level. Multivariate analyses confirmed that PTTG1 expression was a factor of prognosis that is independent in terms of LUAD patients. Besides, PTTG1 methylation had a negative regulation on PTTG1, so PTTG1 had a high expressing level in LUAD tissues. However, the relation between hypermethylation and overall survival was not demonstrated using TCGA datasets. In addition, we observed that LUAD specimens with advanced stages exhibited a higher level of PTTG1. Finally, the dysregulated genes related to PTTG1 expression were screened, and KEGG assays revealed that the above genes were involved in the p53 signaling pathway, indicating the possible regulatory function of PTTG1 in the p53 signaling pathway. Overall, our findings suggest that PTTG1 may serve as an efficient clinical biomarker and a therapeutic target for patients suffering from LUAD.

1. Introduction

Lung carcinoma has been recognized as a highly common malignant tumor worldwide [1]. Lung carcinoma turns out to be the first main factor causing people in China's urban regions to die [2]. Lung adenocarcinoma (LUAD) refers to the commonest among lung carcinoma and has become a popularly aggressive carcinoma [3]. Though LUAD treatment and diagnosis using surgical methods and/or adjuvant chemotherapy have greatly progressed, patients impacted still have poor prognostic results since over 80% patients impacted have the advanced-stage diagnosis [4, 5]. Accordingly, probable prognosis factors should be explored according to survivors for gaining more insights into LUAD malignancy and developing alternatives to treat various subgroups of patients with LUAD.

Pituitary tumor-transforming gene-1 (PTTG1), a ubiquitously expressed factor of transcription, is proven with the overexpression within several types of tumors, including lung carcinoma, ovarian carcinoma, prostate carcinoma, and breast carcinoma [6–8]. In recent years, growing evidence has shown that PTTG1 exhibits regulatory functions in the progression of angiogenesis, DNA damage repair, programmed cell death, and differentiation [9, 10]. In addition, it has also been confirmed that the dysregulation of PTTG1 was related to the abilities of proliferation and metastasis. For instance, PTTG1 expression was distinctly increased in cholangiocarcinoma, and its knockdown suppressed tumor growth via modulating the pathway of MAPK signaling [11]. PTTG1 was also shown with an ability of promoting the invasion of migration of LUAD cells, and its levels were regulated by miR-186, implying a possible role for PTTG1 in LUAD [12]. In addition, the prognostic values of PTTG1 were also reported. However, the studies are limited, and the possible mechanism of PTTG1 dysregulation has not been clarified.

DNA methylation, frequently occurring at CpG dinucleotides, is demonstrated to be related to clinical progression of patients suffering from LUAD, such as TP53 status, carcinoma status, WHO grade, and clinical stages [13, 14]. In recent years, several studies have demonstrated the positive relation between the pattern of single gene and methylation state [15, 16]. However, the specific clinical significance of the methylated markers in LUAD subtypes and the complex role of DNA methylation remained largely unclear, which needed to be further demonstrated in clinical cohorts of patients suffering from LUAD. This paper aimed at exploring the expressing pattern of PTTG1 within patients suffering from LUAD. An analysis was conducted on the relation of PTTG1 DNA methylation and PTTG1 expression within the LUAD dataset of TCGA datasets. Finally, we examined the prognostic significance of PTTG1 expression in LUAD patients and its DNA methylation.

2. Materials and Methods

2.1. Raw Data. Transcriptome RNA-seq data of 59 normal samples and 526 tumor samples were downloaded from TCGA database (https://portal.gdc.carcinoma.gov/) with level 3. The following samples were excluded: (1) "0" gene expression value and (2) insufficient survival information. A total of 513 patients with LUAD with the corresponding clinical characteristics were enrolled in this paper. Then, we downloaded the methylation profiles of patients with LUAD from TCGA database via UCSC Xena (https://xena.ucsc.edu/).

2.2. Relation Assays of PTTG1 Expressions and Methylation of CpG Sites. The relations of PTTG1 expressions with the methylation of CpG sites in different regions of the PTTG1 gene were studied by the use of Pearson's relation tests. The relations of PTTG1 expressions with the methylation of each CpG site were examined.

2.3. Relation of PTTG1 CpG Sites with the Characteristics of LUAD. The clinical characteristics of patients suffering from LUAD were extracted, including patients' age, clinical stage, and sex. PTTG1 CpG sites at which methylation states were distinctly related to OS were applied to study their relation with clinical characteristics of LUAD.

2.4. GO and KEGG Enrichment Analyses of the Differentially Expressed Genes. Patients with LUAD from TCGA datasets were initially divided into two groups (high and low). The dysregulated genes between the two groups were selected with $p < 0.05$. To study potential biological processes (BP), cellular components (CC), molecular functions (MF), and pathways of the differentially expressed genes, we performed GO and KEGG assays by the use of the "clusterProfiler" package in R with a statistical threshold of $p < 0.05$ [17].

2.5. Statistical Analysis. All statistical analyses were based on R language 3.6.1 version. With the use of Fisher's exact test or Pearson chi-squared test, an investigation was conducted on the relation of PTTG1 and clinical feature variables. Kaplan–Meier methods with log-rank tests were applied to determine the overall survival (OS) and progression-free survival (PFS). Significant variables in univariate models were further analyzed by multivariate assays for the identification of independent prognosis factors. $p \leq 0.05$ was considered to indicate a statistically significant difference.

3. Results

3.1. The Distinct Upregulation of PTTG1 in LUAD and Its Prognostic Value. To delve into the potential function of PTTG1 in LUAD, we analyzed TCGA datasets and found that PTTG1 expression was distinctly increased in LUAD specimens in comparison with nontumor lung specimens (Figure 1(a)). We also performed survival assays which revealed that patients with high PTTG1 expression exhibited a shorter OS ($p < 0.001$, Figure 1(b)) and PFS ($p < 0.024$, Figure 1(c)) as compared with those with low PTTG1 expression. The predictive performance of PTTG1 expression for OS was assessed according to time-dependent ROC curves, and the area under the curve (AUC) reached 0.618 at 1 year, 0.609 at 3 years, and 0.601 at 5 years (Figure 1(d)). Moreover, the results of univariate assays revealed that PTTG1 expression and clinical stage were related to OS of patients suffering from LUAD (Figure 2(a)). Further results by multivariate analyses confirmed that PTTG1 expression (HR = 1.302, 95% CI: 1.122–1.510, $p < 0.001$) as well as stage (HR = 1.619, 95% CI: 1.408–1.861, $p < 0.001$) was an independent prognosis factor for the patients with LUAD (Figure 2(b)). Overall, our findings suggested that PTTG1 was an overexpressed gene in LUAD and predicted a poor prognosis of patients suffering from LUAD.

3.2. The Relation of DNA Methylation with PTTG1 and Its Survival Analysis. Then, we analyzed the level of methylation sites of PTTG1. The distribution of 8 PTTG1 CpG sites is clearly exhibited in Figure 3(a). In addition, a strong negative relation between PTTG1 expressions and PTTG1 DNA methylation was found (Figure 3(b)). Then, Pearson's relation assays were conducted to screen the PTTG1 CpG sites involved in PTTG1 mRNA expressions. We observed that methylation of cg19619065, cg21784134, cg2302444, cg26775866, and cg09468767 was negatively related to the expressions of PTTG1 (Figures 3(c)–3(g)). However, methylation of cg12430567, cg00116688, and cg27185377 was not related to the expression of PTTG1 (Figures 3(h)–3(j)). On the contrary, to explore the prognostic value of methylation of CpG sites, we performed Kaplan–Meier methods and observed that all CpG sites were not related to OS of patients suffering from LUAD from TCGA datasets (Figure 4). However, patients with high methylation of cg12430567 achieved a shorter PFS as compared with those with low methylation of cg12430567 (Figure 5(a)). Other CpG sites showed no relation with PFS of patients suffering from LUAD (Figures 5(b) and 5(c)). The chi-square test was performed for investigating the specific relation of PTTG1 expression and PTTG1 methylation with several clinical characteristics. As shown in Tables S1 and S2, the expression of PTTG1 was closely related to N stage, clinical stage, and PTTG1 methylation. The

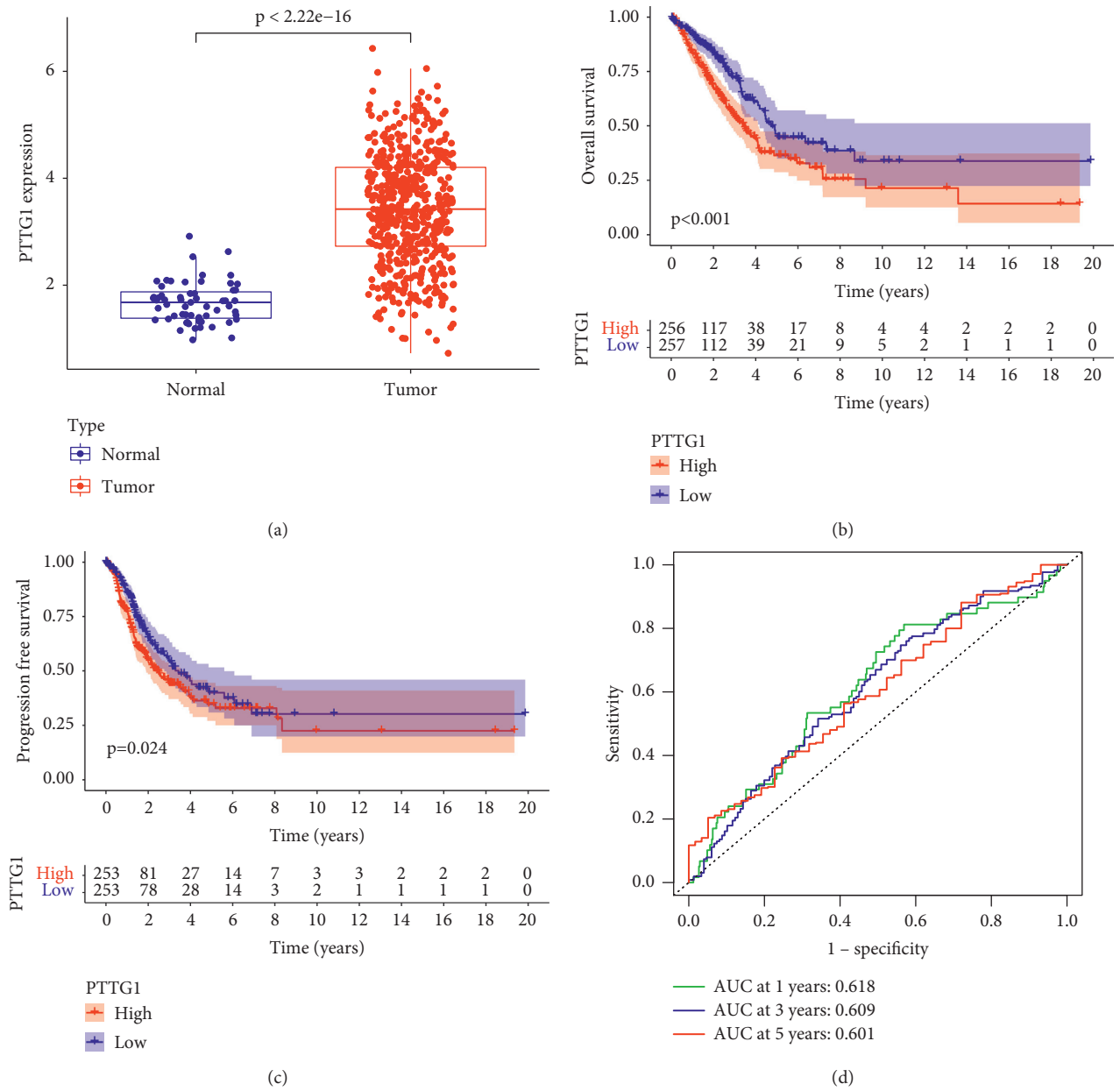

Figure 1: The distinct upregulation of PTTG1 in LUAD patients and its prognostic value. (a) The expression of PTTG1 in LUAD specimens and normal lung specimens from TCGA datasets. (b, c) The overall survival and progression-free survival of LUAD patients based on the expression of PTTG1 in all samples. (d) ROC curve was used to predict the value of PTTG1 expression in predicting the survival of LUAD patients.

relation between PTTG1 expression and clinical characteristics is also shown in Figures 6(a)–6(f), and the relation between PTTG1 methylation and clinical characteristics is shown in Figures 6(g)–6(l). Our results indicated that the levels of PTTG1 were modulated by methylation. However, the prognostic value of most CpG sites of PTTG1 was also confirmed.

3.3. Functional Analyses of the Dysregulated Genes in TCGA Cohort. For a clarification of the functional effect of PTTG1 on LUAD, we divided all patients suffering from LUAD into two groups (high and low) based on the mean expression of PTTG1. Then, we screened the dysregulated genes between samples containing high PTTG1 expression and samples with low PTTG1 expression. The dysregulated genes are presented in Table S3. Subsequently, we performed GO assays using the "clusterProfiler" R package and found that, in the BP group, the dysregulated genes were primarily involved in the regulation of mitotic sister chromatid separation, cytoskeleton organization involved in mitosis, nuclear division, mitotic nuclear division, chromosome segregation, and sister chromatid segregation. In the CC, the dysregulated genes were mainly involved in condensed chromosome kinetochore,

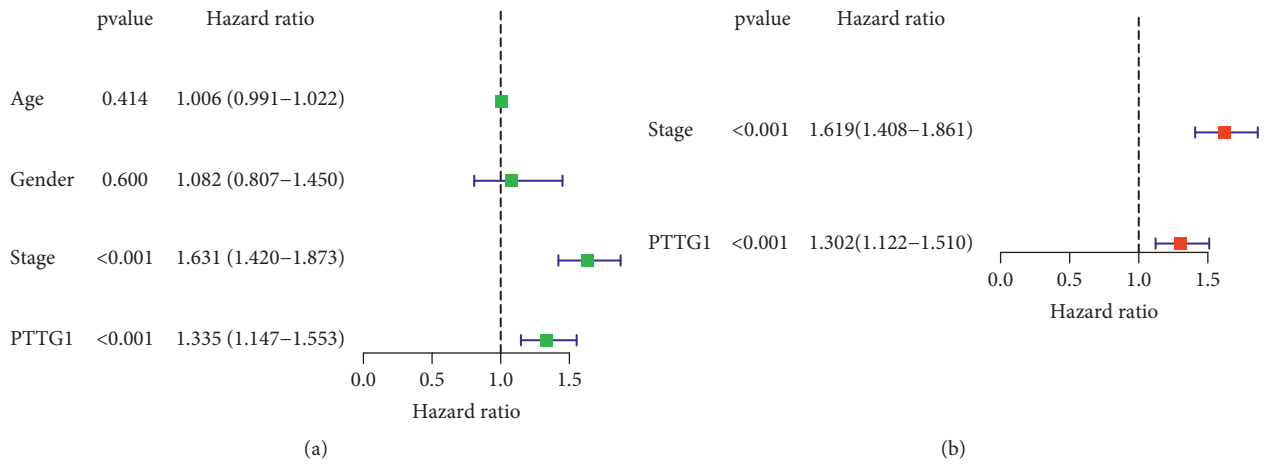

Figure 2: Univariate (a) and multivariate (b) independent prognosis analyses of clinical parameters and PTTG1 expression.

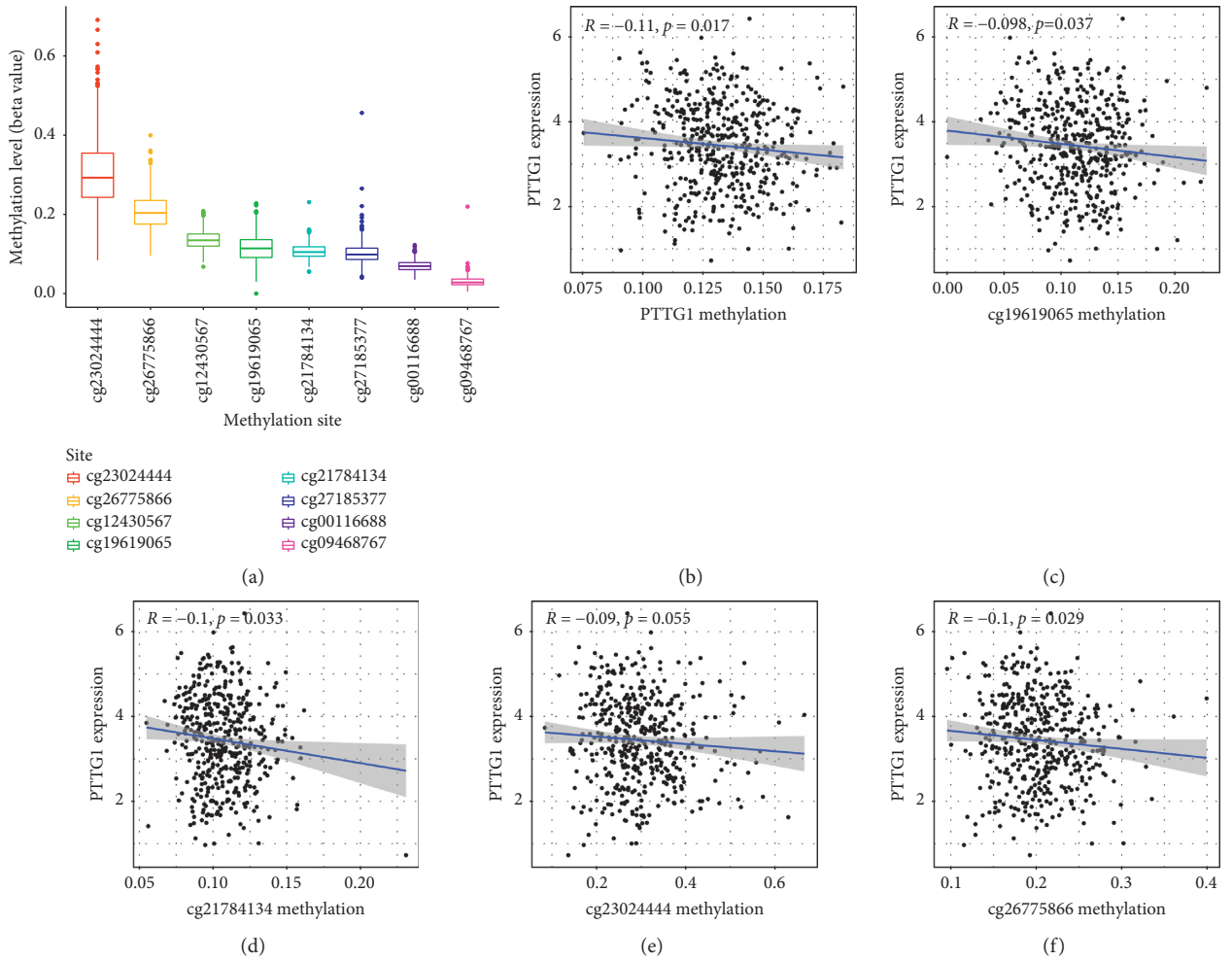

Figure 3: Continued.

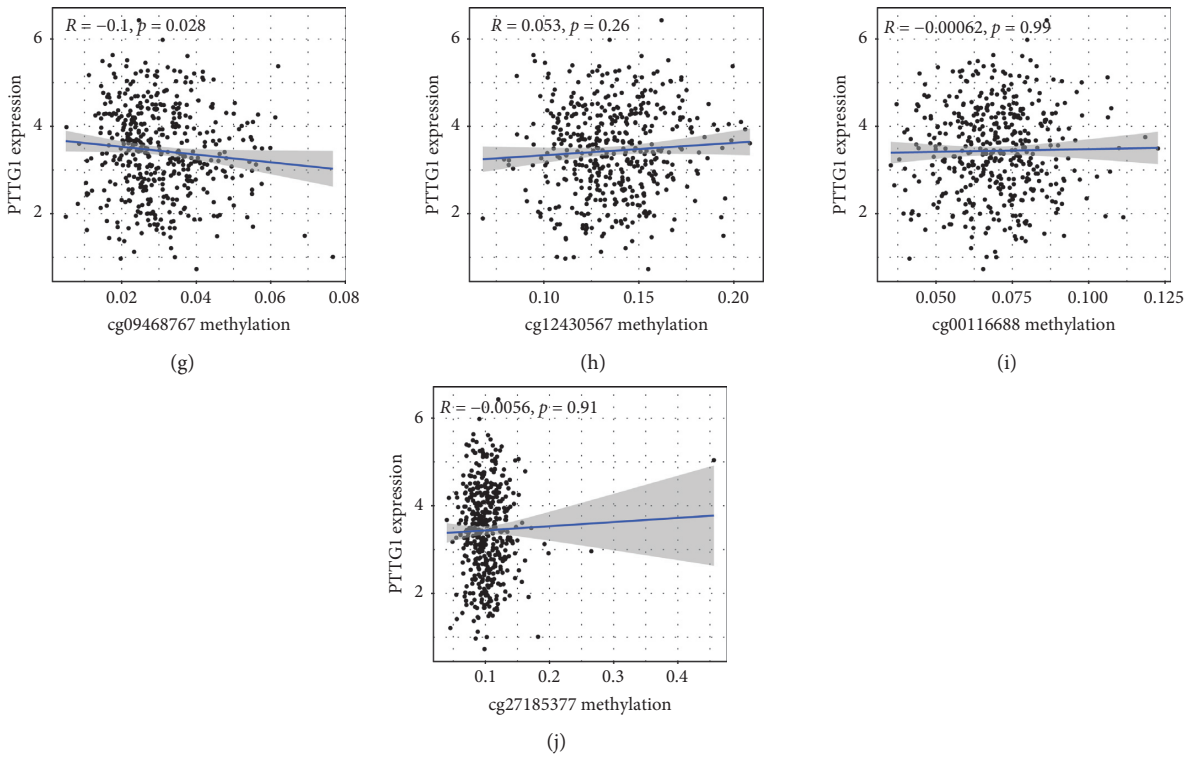

Figure 3: The associations between PTTG1 expressions and methylation of several sites. (a) Histogram of the methylation level in eight methylation sites. (b) The expressions of PTTG1 were negatively modulated by PTTG1 DNA methylation. (c–j) Correlation analysis of PTTG1 with the methylation of (c) cg19619065, (d) cg21784134, (e) cg2302444, (f) cg26775866, (g) cg09468767, (h) cg12430567, (i) cg00116688, and (j) cg27185377.

kinetochore, centromeric region, condensed chromosome, spindle, chromosomal region, midbody, and mitotic spindle. In the MF group, the dysregulated genes were mainly involved in microtubule binding, tubulin binding, motor activity, microtubule motor activity, water channel activity, water transmembrane transporter activity, histone kinase activity, and aspartic-type endopeptidase activity (Figure 7(a)). KEGG analysis showed that the dysregulated genes are mainly enriched in cell cycle, oocyte meiosis, progesterone-mediated oocyte maturation, cellular senescence, and p53 signaling pathway (Figure 7(b)). Our findings suggested that PTTG1 expression was related to progression of LUAD.

4. Discussion

New strategies for treatment in terms of LUAD are increasingly designed, which consist of immunotherapy, gene therapy, and molecular targeted therapy [18, 19]. Nevertheless, there were not any satisfactory therapeutic results, and a low survival rate of LUAD has been achieved. New therapeutic and prognostic methods aiming to optimize the outcome of LUAD patients require an overall insight into the molecular mechanism of tumor initiation and progression [20, 21]. Recently, DNA repair-related genes emerge as a novel gene regulator class in various malignancies [22, 23].

As a DNA repair-related gene, the expression and function of PTTG1 have been reported in several tumors. For instance, PTTG1 expression was distinctly increased in glioma, and its knockdown suppressed cell angiogenesis and metastasis in glioma cells [24]. A previous study reported that PTTG1, an overexpressed gene in seminoma tumor, promoted the migration and invasion of tumor cells via activation of MMP-2 [25]. In addition, the prognostic values of PTTG1 were also reported in several tumors, such as breast carcinoma and prostate carcinoma [8, 26]. According to the findings above, PTTG1 is an oncogene in the above tumors. Importantly, Li et al. also reported that PTTG1 was highly expressed in lung carcinoma, and its knockdown distinctly suppressed the invasion and migration of lung carcinoma cells. In their cohort, they also reported upregulation of PTTG1 was related to poor prognosis of patients with lung carcinoma [12]. However, the sample size was small in their cohort. In this paper, we analyzed TGCA datasets and also confirmed that expressions of PTTG1 were distinctly increased in LUAD specimens. Survival assays revealed that patients with high PTTG1 expression showed a shorter OS and PFS as compared with those with low PTTG1 expression. More importantly, in a multivariate Cox model, PTTG1 expression was reported as a poor prognosis factor that is independent in terms of 5-year OS. Clinical stage has been considered to be a very important prognostic factor for LUAD patients, which was also further demonstrated in this study. Thus, whether PTTG1 expression may be associated with clinical stages of LUAD patients needed to be further explored. Overall, our findings suggested PTTG as a novel biomarker for LUAD.

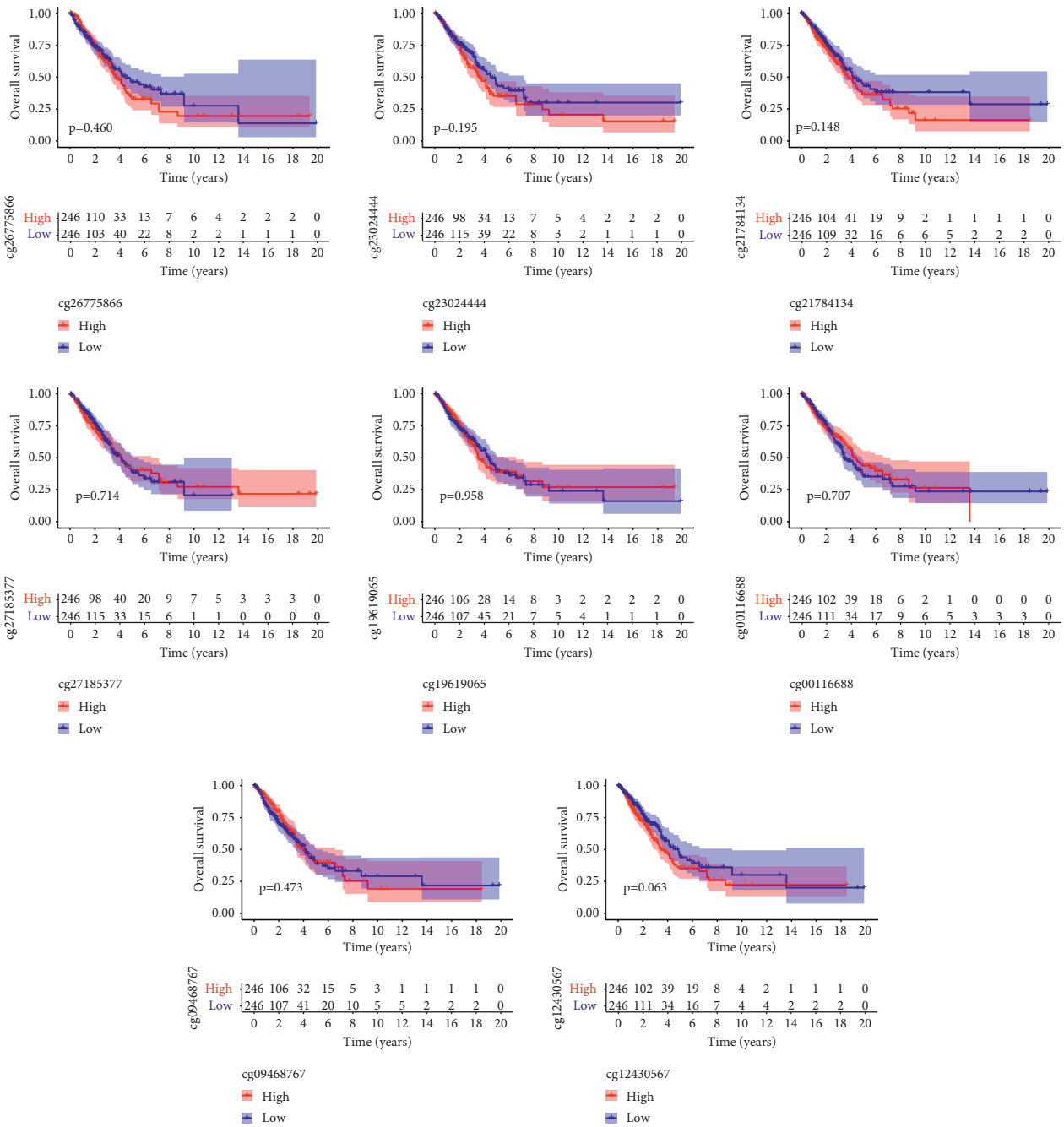

Figure 4: The survival assays of methylation of CpG sites in LUAD patients using Kaplan–Meier methods.

Increasing evidence proved that the dysregulation of DNA methylation significantly impacts the developments and progressions of LUAD [27, 28]. Our group firstly examined if the PTTG1 methylation state could have an effect on PTTG1 expressions by the use of Pearson's coefficients. A potent negative relation of PTTG1 methylation and PTTG1 expressions was found in LUAD tissues. Such a negative relation could effectively account for the high LUAD expression within LUAD tissues. Subsequently, we further screened the specific CpG sites. It is noteworthy that nearly all the CpG sites with the exception of cg27185377 and cg00116688 were obviously related to PTTG1 expressions. In previous studies, the relationship of specific gene expression and its DNA methylation had a range (weak to moderate), and rare genes under the significant regulation by DNA methylation had been found [29, 30]. Furthermore, the prognosis value of PTTG1 DNA methylation and 8 selected CpG sites was explored, and we found that the levels of PTTG1 methylation were not related to the OS and PFS in patients suffering from LUAD. Only cg12430567 was related to OS and patients suffering from LUAD. Our findings suggested PTTG1 was negatively regulated by PTTG1 methylation. However, more experiments were needed to

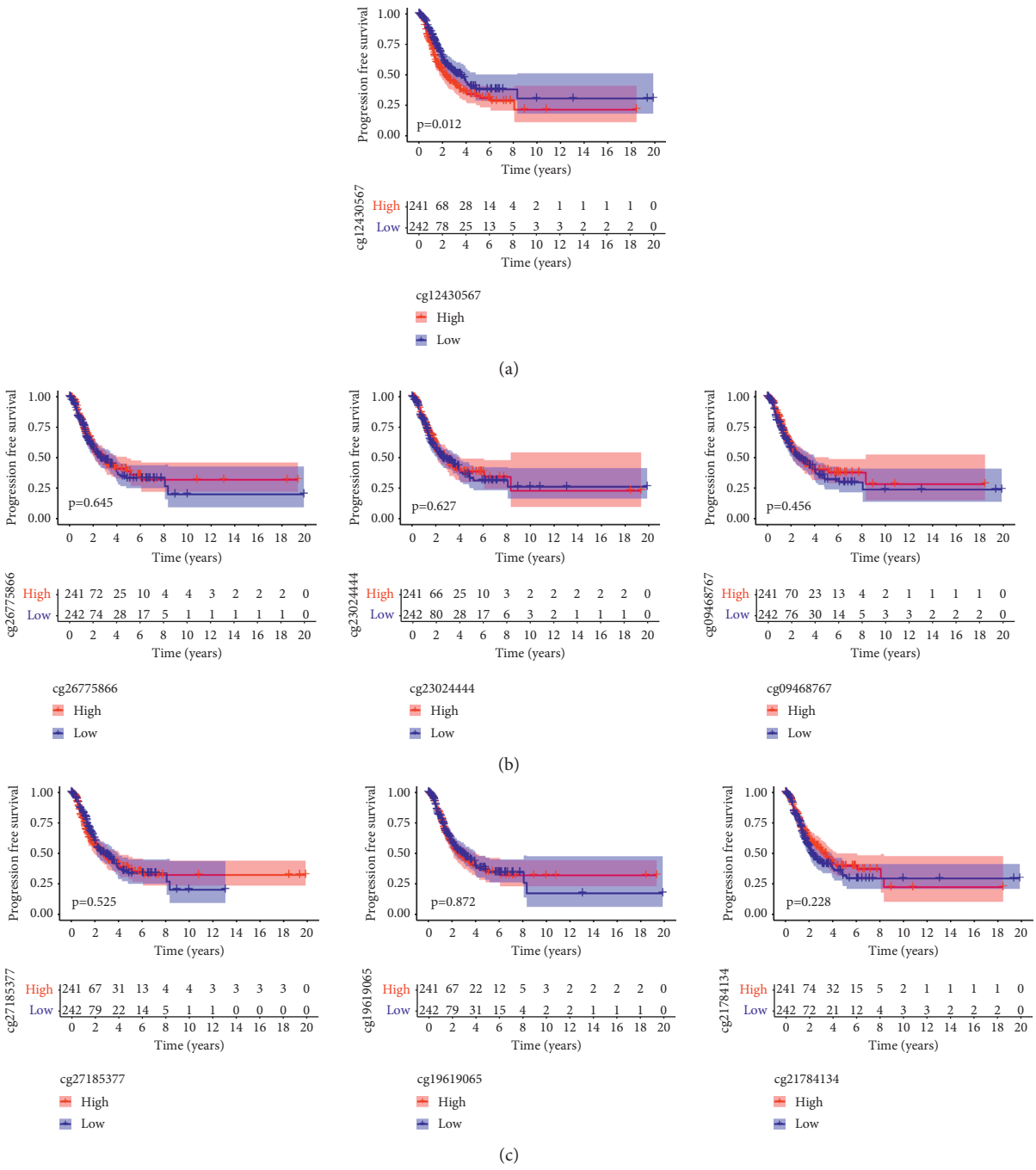

Figure 5: (a) The 5-year progression-free survival rate of LUAD patients with high levels of cg12430567 was distinctly lower than that of those patients with low levels of cg12430567. (b, c) Kaplan–Meier plots of overall survival in patients with LUAD and with low and high levels of methylation sites.

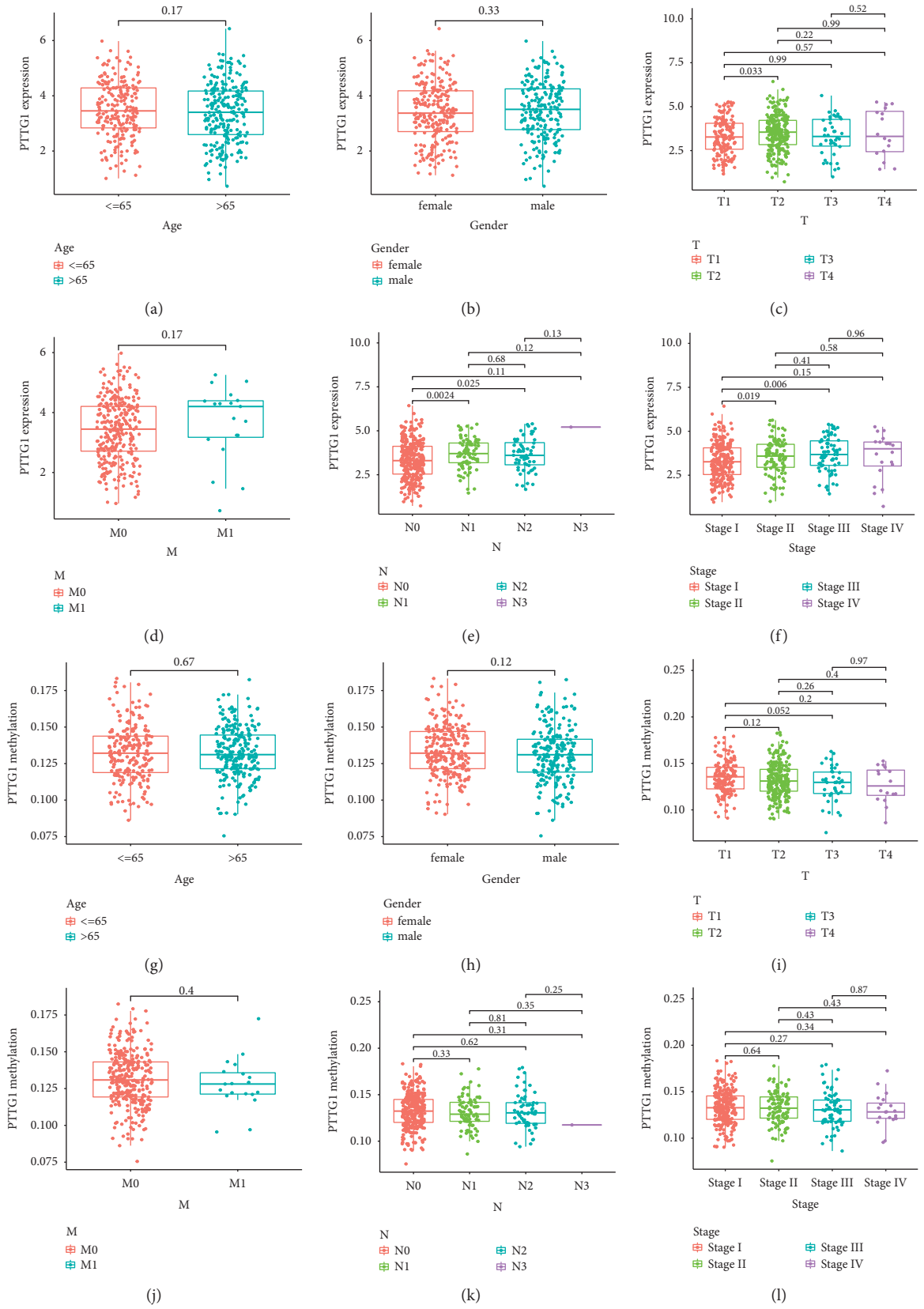

Figure 6: Correlation between PTTG1 expression/methylation and clinicopathologic features in TCGA datasets. (a) Age and PTTG1 expression. (b) Gender and PTTG1 expression. (c) T stage and PTTG1 expression. (d) M stage and PTTG1 expression. (e) N stage and PTTG1 expression. (f) TMN stage and PTTG1 expression. (g) Age and PTTG1 methylation. (h) Gender and PTTG1 methylation. (i) T stage and PTTG1 methylation. (j) M stage and PTTG1 methylation. (k) N stage and PTTG1 methylation. (l) TMN stage and PTTG1 methylation.

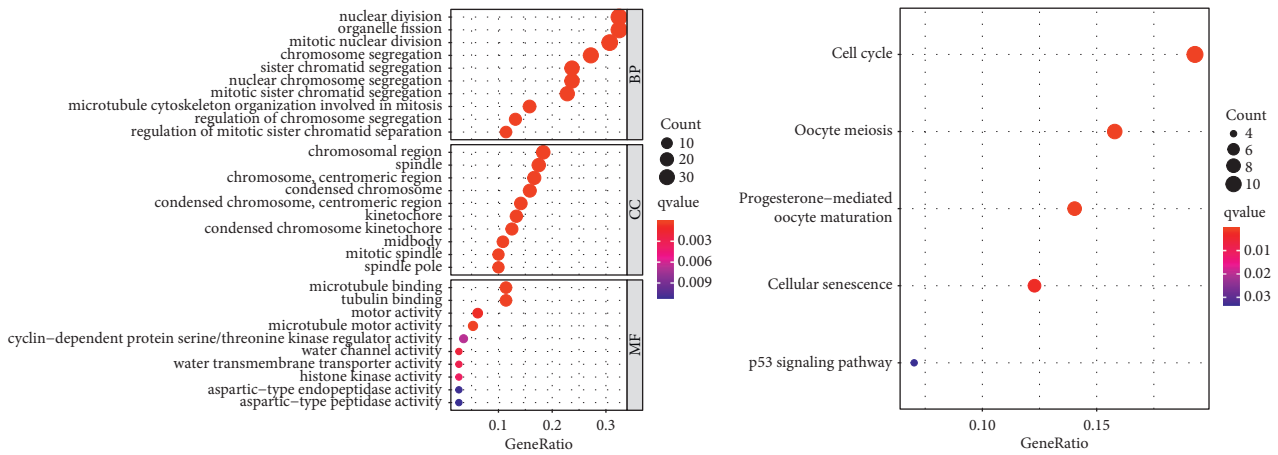

(a) (b)

Figure 7: GO (a) and KEGG (b) enrichment analyses of genes associated with PTTG1 expression.

further demonstrate the prognostic value of the PTTG1 methylation state.

There were several limitations in this research. Firstly, the sample size was relatively small, and more clinical experiments were necessary to demonstrate our findings. Secondly, we did not perform in vitro and in vivo experiments to study the potential function of PTTG1 in LUAD progression. Finally, we did not explore the downstream factors which PTTG1 modulated.

5. Conclusion

This paper identified PTTG1 hypermethylation state as a prognosis factor in LUAD. Methylation of cg12430567 was related to the survival of patients suffering from LUAD. Our findings indicated the effects of PTTG1 methylation on the pathogenesis of LUAD and provided new targeting genes for predicting the clinical outcomes of patients suffering from LUAD.

Data Availability

The data used to support the findings of this study are available from the corresponding authors upon request.

Conflicts of Interest

All the authors declare no conflicts of interest.

Authors' Contributions

Lu Bai, Jing Liang, and En-Xiao Li designed this study. Lu Bai and Li-Hong Li analyzed the data and wrote the original manuscript. All authors read and approved the final manuscript.

Acknowledgments

This study was supported by the Project of Health and Family Planning Commission of Shaanxi Province (no. 2018D028).

Supplementary Materials

Table S1: correlation between PTTG1 expression and clinicopathologic features in TCGA database. Table S2: correlation between PTTG1 methylation and clinicopathologic features in TCGA database. Table S3: the dysregulated genes between the high PTTG1 expression group and low PTTG1 expression group. (*Supplementary Materials*)

References

[1] F. R. Hirsch, G. V. Scagliotti, J. L. Mulshine et al., "Lung cancer: current therapies and new targeted treatments," *The Lancet*, vol. 389, no. 10066, pp. 299–311, 2017.

[2] M. Cao and W. Chen, "Epidemiology of lung cancer in China," *Thoracic cancer*, vol. 10, no. 1, pp. 3–7, 2019.

[3] T. V. Denisenko, I. N. Budkevich, and B. Zhivotovsky, "Cell death-based treatment of lung adenocarcinoma," *Cell Death & Disease*, vol. 9, no. 2, p. 117, 2018.

[4] K. C. Arbour and G. J. Riely, "Systemic therapy for locally advanced and metastatic non-small cell lung cancer: a review," *JAMA*, vol. 322, no. 8, pp. 764–774, 2019.

[5] S. K. Thakur, D. P. Singh, and J. Choudhary, "Lung cancer identification: a review on detection and classification," *Cancer and Metastasis Reviews*, vol. 39, no. 3, pp. 989–998, 2020.

[6] W.-H. Li, L. Chang, Y.-X. Xia et al., "Knockdown of PTTG1 inhibits the growth and invasion of lung adenocarcinoma cells through regulation of TGFB1/SMAD3 signaling," *International Journal of Immunopathology and Pharmacology*, vol. 28, no. 1, pp. 45–52, 2015.

[7] S. Parte, I. Virant-Klun, M. Patankar, S. K. Batra, A. Straughn, and S. S. Kakar, "PTTG1: a unique regulator of stem/cancer stem cells in the ovary and ovarian cancer," *Stem Cell Reviews and Reports*, vol. 15, no. 6, pp. 866–879, 2019.

[8] C. Fraune, S. Yehorov, A. M. Luebke et al., "Upregulation of PTTG1 is associated with poor prognosis in prostate cancer," *Pathology International*, vol. 70, no. 7, pp. 441–451, 2020.

[9] Y. Tong and T. Eigler, "Transcriptional targets for pituitary tumor-transforming gene-1," *Journal of Molecular Endocrinology*, vol. 43, no. 5, pp. 179–185, 2009.

[10] C. P. Tanase, M. Neagu, and R. Albulescu, "Key signaling molecules in pituitary tumors," *Expert Review of Molecular Diagnostics*, vol. 9, no. 8, pp. 859–877, 2009.

[11] Z. G. Hu, C. W. Zheng, H. Z. Su et al., "MicroRNA-329-mediated PTTG1 downregulation inactivates the MAPK signaling pathway to suppress cell proliferation and tumor growth in cholangiocarcinoma," *Journal of Cellular Biochemistry*, vol. 120, no. 6, pp. 9964–9978, 2019.

[12] H. Li, C. Yin, B. Zhang et al., "PTTG1 promotes migration and invasion of human non-small cell lung cancer cells and is modulated by miR-186," *Carcinogenesis*, vol. 34, no. 9, pp. 2145–2155, 2013.

[13] L. D. Moore, T. Le, and G. Fan, "DNA methylation and its basic function," *Neuropsychopharmacology*, vol. 38, no. 1, pp. 23–38, 2013.

[14] S. Horvath and K. Raj, "DNA methylation-based biomarkers and the epigenetic clock theory of ageing," *Nature Reviews Genetics*, vol. 19, no. 6, pp. 371–384, 2018.

[15] X. Hao, H. Luo, M. Krawczyk et al., "DNA methylation markers for diagnosis and prognosis of common cancers," *Proceedings of the National Academy of Sciences*, vol. 114, no. 28, pp. 7414–7419, 2017.

[16] C.-C. Sun, W. Zhu, S.-J. Li et al., "FOXC1-mediated LINC00301 facilitates tumor progression and triggers an immune-suppressing microenvironment in non-small cell lung cancer by regulating the HIF1α pathway," *Genome Medicine*, vol. 12, no. 1, p. 77, 2020.

[17] G. Yu, L.-G. Wang, Y. Han, and Q.-Y. He, "Clusterprofiler: an R package for comparing biological themes among gene clusters," *OMICS: A Journal of Integrative Biology*, vol. 16, no. 5, pp. 284–287, 2012.

[18] M. Duruisseaux and M. Esteller, "Lung cancer epigenetics: from knowledge to applications," *Seminars in Cancer Biology*, vol. 51, pp. 116–128, 2018.

[19] F. Oberndorfer and L. Müllauer, "Molecular pathology of lung cancer: current status and perspectives," *Current Opinion in Oncology*, vol. 30, no. 2, pp. 69–76, 2018.

[20] F. Wu, L. Wang, and C. Zhou, "Lung cancer in China: current and prospect," *Current Opinion in Oncology*, vol. 33, no. 1, pp. 40–46, 2021.

[21] T. Nagano, M. Tachihara, and Y. Nishimura, "Molecular mechanisms and targeted therapies including immunotherapy for non-small cell lung cancer," *Current Cancer Drug Targets*, vol. 19, no. 8, pp. 595–630, 2019.

[22] E. Gatzidou, C. Michailidi, S. Tseleni-Balafouta, and S. Theocharis, "An epitome of DNA repair related genes and mechanisms in thyroid carcinoma," *Cancer Letters*, vol. 290, no. 2, pp. 139–147, 2010.

[23] A. Minias, A. Brzostek, and J. Dziadek, "Targeting DNA repair systems in antitubercular drug development," *Current Medicinal Chemistry*, vol. 26, no. 8, pp. 1494–1505, 2019.

[24] L. Cui, T. Ren, H. Zhao et al., "Suppression of PTTG1 inhibits cell angiogenesis, migration and invasion in glioma cells," *Medical Oncology*, vol. 37, no. 8, p. 73, 2020.

[25] E. Teveroni, F. Di Nicuolo, G. Bianchetti et al., "Nuclear localization of PTTG1 promotes migration and invasion of seminoma tumor through activation of MMP-2," *Cancers*, vol. 13, 2021.

[26] C. Meng, Y. Zou, W. Hong, C. Bao, and X. Jia, "Estrogen-regulated PTTG1 promotes breast cancer progression by regulating cyclin kinase expression," *Molecular Medicine*, vol. 26, no. 1, p. 33, 2020.

[27] A. Koch, S. C. Joosten, Z. Feng et al., "Analysis of DNA methylation in cancer: location revisited," *Nature Reviews Clinical Oncology*, vol. 15, no. 7, pp. 459–466, 2018.

[28] M. Vaid and J. Floros, "Surfactant protein DNA methylation: a new entrant in the field of lung cancer diagnostics? (review)," *Oncology Reports*, vol. 21, pp. 3–11, 2009.

[29] P. A. Jones, "Functions of DNA methylation: islands, start sites, gene bodies and beyond," *Nature Reviews Genetics*, vol. 13, no. 7, pp. 484–492, 2012.

[30] O. Bogdanović and R. Lister, "DNA methylation and the preservation of cell identity," *Current Opinion in Genetics & Development*, vol. 46, pp. 9–14, 2017.

Hindawi
Journal of Oncology
Volume 2022, Article ID 6548644, 12 pages
https://doi.org/10.1155/2022/6548644

Research Article

QPRT Acts as an Independent Prognostic Factor in Invasive Breast Cancer

Lili Zhou, Lin Mu, Wenyan Jiang, and Qi Yang

Department of Radiology, First Hospital of Jilin University, Changchun, Jilin 130031, China

Correspondence should be addressed to Qi Yang; yangqi_tt@jlu.edu.cn

Received 8 November 2021; Accepted 22 December 2021; Published 24 February 2022

Academic Editor: Guo Chen

Background. Quinolinic acid phosphoribosyltransferase (QPRT) is a rate-limiting enzyme that encodes the uronic acid pathway, which is involved in cell cycle progression and cancer cell metabolism. Some studies have demonstrated the progrowth effect of QPRT on breast cancer (BRCA) tumour cells, but its mechanism of action requires further exploration. *Methods*. We investigated the expression of QPRT and the prognosis of patients with different tumours by performing a pan-cancer analysis of QPRT. Prognostic values for overall survival (OS) were determined using uni- and multivariate Cox proportional hazard analyses. The prognostic survival of patients with a different pathological staging of BRCA and with QPRT high and low expression was also analysed. We also explored the relevant pathways by which QPRT affected BRCA tumorigenesis by gene set enrichment analysis (GSEA) and western blotting. The impact of QPRT on the PI3K/Akt pathway was also evaluated. *Results*. Pan-cancer analysis revealed significant QPRT expression in pan-cancer and correlated with prognosis in most tumour patients. QPRT was also highly expressed in BRCA when patients had poor prognoses, and its expression was associated with different pathological BRCA subtypes. GSEA revealed an association between BRCA progression and the cell cycle and the phosphatidylinositol 3-kinase (PI3K)/Akt signalling pathway, and this association was confirmed by western blotting. *Conclusion*. QPRT is highly expressed in breast cancer and particularly in HER2 breast cancer. Upregulated QPRT expression is an independent predictor of breast cancer prognosis and promotes breast cancer progression by activating the PI3K/Akt signalling pathway.

1. Introduction

As of 2020, invasive breast cancer (BRCA) (2.26 million cases) remains one of the most commonly diagnosed cancer types worldwide [1] and is the leading cause of cancer death in women aged 20–59 years [2]. Currently, standard screening methods for BRCA include mammography, magnetic resonance imaging (MRI), computed tomography (CT), and biopsy [3]. Despite significant advances in diagnostic tools and treatment strategies, BRCA continues to rise in prevalence and affects approximately one in twenty countries worldwide [4], with higher rates in developed countries [5]. BRCA is classified, based on differences in gene expression patterns, into five major categories, luminal A, luminal B, HER2 overexpression, basal_like, and normal_like, with HER2 overexpressing breast tumours having the poorest prognosis [6]. BRCA is metastatic cancer and can spread to distant organs, such as the bone, liver, and lung, a condition that is often incurable, whereas early diagnosed BRCA generally has a better prognosis and survival rate [7]. The 5-year survival rate of patients with stage I BRCA can be as high as 100%, while in patients with stage IV BRCA, it decreases to 26% [8].

In BRCA cells, a reduction in cellular levels of nicotinamide adenine dinucleotide (NAD+) may induce apoptosis [9]. NAD+ is a critical coenzyme involved in the redox reactions of cancer cell metabolic pathways [10] and plays a role in DNA repair, gene transcription regulation, the cell cycle, apoptosis, metabolism, and other biological processes [11]. The production of NAD+ is promoted by the activity of quinolinate phosphoribosyltransferase (QPRT), the rate-limiting enzyme encoding the kynurenic pathway, via catabolism tryptophan. QPRT is upregulated in cancer cells, and this upregulation is resistant to inhibitors of nicotinamide phosphoribosyltransferase (NAMPT) [12], the rate-limiting enzyme of the NAD + salvage pathway [13]. Studies have shown that high expression of NAMPT is related to the

aggressive biological characteristics of BRCA [14] and can regulate the PI3K-AKT signalling pathway and promote tumour cell proliferation [15]. Similarly, QPRT expression has shown great relevance to the migration and invasive ability of BRCA cancer cells [16], and tumour xenograft assays have demonstrated the growth-promoting effect of QPRT overexpression in BRCA tumour cells [17].

The mechanism of action of QPRT on BRCA onset and progression has not been adequately studied. Therefore, the present study aimed to analyse the impact of QPRT on the expression and prognosis of BRCA tumours. The biological functions and pathways of QPRT were studied through gene set enrichment analysis (GSEA), the relationship between QPRT and signalling pathways was established by western blot analysis, and the mechanism of QPRT effects on breast cancer progression was determined.

2. Materials and Methods

2.1. Data Sources and Processing. Data were obtained from The Cancer Genome Atlas (TCGA) dataset, Cancer Cell Line Encyclopedia (CCLE), and Genotype-Tissue Expression (GTEx) dataset, including clinical information data and gene expression matrices for normal tissues, tumour tissues, and tumour cell lines. In total, 33 tumour samples were obtained from the TCGA dataset, RNA sequencing data for 21 tumour cell lines were obtained from the CCLE dataset, and expression profile data were obtained for 27 cancer and paracancer tissues by integrating the TCGA and GTEx datasets. The expression matrices of GSE46563 and GSE59246 were obtained from the GEO database (https://www.ncbi.nlm.nih.gov/geo/). GSE46563 contains 75 HER− and 19 HER+ samples, and GSE59246 contains a total of 50 HER− and 19 HER+ samples.

2.2. Analysis of QPRT Expression and Survival in Each Tumour. The Kruskal–Wallis test was used to analyse differences in tumour tissues and normal tissues. Survival analysis was performed using the R survival package, and the disease-specific survival (DFS) between QPRT expression and patients with different tumours was examined using one-way Cox risk proportional regression analysis, with data expressed as forest plots. Kaplan–Meier (KM) analysis was used to test the association between QPRT and survival among patients with different tumours. A value of $P < 0.05$ was considered statistically significant.

2.3. Expression and Survival Analysis of QPRT in BRCA. The differences in QPRT expressions in different pathological subtypes of BRCA were analysed using the R package Limma. The log-rank test was used to test the survival differences between the high and low QPRT expression groups, and KM curves were plotted to show the overall survival (OS) and progression-free survival (PFS) of different pathological staging. Univariate and multifactorial Cox risk proportional regression analyses were performed to compare the relationship between QPRT expression and each clinicopathological feature with breast cancer survival for BRCA. The R package "RMS" was also used to plot nomograms for 1, 3, and 5 year survival rates.

2.4. Immunohistochemistry (IHC) to Detect Protein Expression. Immunohistochemical staining results of QPRT protein in breast cancer tumor tissues and normal tissues were compared using human Protein Atlas (HPA) database.

2.5. Functional and Pathway Enrichment Analyses. Based on the median expression of QPRT in breast cancer for high and low expression groups, gene ontology (GO) and Kyoto Encyclopedia of Genes and Genomes (KEGG) functional and pathway enrichment analyses were performed using the R package clusterProfiler. GSEA was used to demonstrate the activation or repression of biological pathways mediated by QPRT expression [18] and was performed using the R package clusterProfiler to search for potential biological mechanisms of QPRT in breast cancer. Biological pathway enrichment of high and low QPRT expressions was analysed using the Reactome gene sets in GSEA.

2.6. Cell Culture and Transfection. Human breast cancer MDA-MB-231 cell line (ATCC® HTB-26™) was cultured in Dulbecco's Modified Eagle Medium (DMEM-high glucose, 01-052-1A, Biological Industries, Beit HaEmek, Israel) containing 5% FBS (04-001-1A, Biological Industries, Beit HaEmek, Israel) and 4 mM glutamic acid base, incubated at 37°C in a humidified atmosphere of 5% CO_2. Lentivirus vector is constructed (objective: HBLV-h-QPRT-ZsGreen-PURO, control: HBLV-h-ZsGreen-PURO), plasmid extraction kit (DP117, TIANGEN BIOTECH CO., LTD, China) was used to extract the plasmids, and 293T cells were co-transfected with Lipofectamine 3000 kit (L3000001, Thermo, USA). After infection, MDA-MB-231 cells were infected with the virus supernatant. After infection, the fusion rate of cells reached 80–90%, the cells were transferred to petri dishes, and 0.5 μg/mL puromycin was added to screen positive cells under pressure. When the fluorescence rate and survival rate of cells were better than 95%, cell lines with stable expression were obtained.

2.7. Western Blotting (WB). Cells were lysed in RIPA buffer (50 mM Tris-HCl, pH 7.4, 150 mM NaCl, 1% sodium deoxycholate, 1% NP-40, 0.1% SDS, 100 mM PMSF, 1 mM pepstatin A, and 1 mM E64). The released proteins were separated on an 8–12% SDS polyacrylamide gel, transferred to a PVDF membrane (IPFL00010, Millipore, Burlington, MA, USA), and treated with a primary antibody. The specific primary antibodies are as follows: QPRT (ab171944, rabbit monoclonal antibody, dilution 1 : 1000), Akt (ab8805, rabbit polyclonal antibody, dilution 1 : 500), P-Akt (ab38449, rabbit polyclonal antibody, dilution 1 : 500), PI3K (ab32089, rabbit monoclonal antibody, dilution 1 : 1000), P-PI3K (ab278545, rabbit monoclonal antibody, 0.5 μg/ml), MDM2 (ab16895, mouse monoclonal antibody, used at an assay-dependent concentration), P-MDM2 (ab170880, rabbit monoclonal antibody, dilution 1 : 50000), and β-actin (ab8226, mouse monoclonal antibody, 1 μg/ml). Then the primary antibody was incubated at 4°C overnight, and the TBST buffer (100 mM TrIS-HCl, pH 7.5, 150 mM NaCl) was oscillated and washed for 3 times, 5 minutes each time. The second antibody was incubated at room temperature for 1 h, and

the film was washed 3 times with TBST oscillation for 5 minutes each time. After the membrane was incubated with TMB substrate for 1 minute, the membrane was soaked in developing solution until the strip was clear and cleaned with tap water. Then the membrane was fixed with fixing solution, and the imaging was observed with a gel imaging analysis system (XR+, Bio-RAD Laboratories, China).

2.8. Statistical Analysis. Statistical analysis was carried out using SPSS software (version 20.0, SPSS Inc., Chicago, IL, USA). Data were expressed as mean ± SD. Student's *t*-test was employed to determine p values. The χ^2 test and Fisher's exact test were employed to assess the association between factors. Survival curves were created by the Kaplan–Meier method and compared by the log-rank tests. Multivariate survival analysis was conducted with the multivariate Cox proportional hazard regression model. Significant difference was recognized at $P < 0.05$.

3. Results

3.1. QPRT Was Significantly Expressed in Most Tumour Tissues. Analysis of the CCLE dataset showed that QPRT was significantly expressed in all 21 tumour cell lines (Figure 1(a)). Integration of data in TCGA and GTEx revealed upregulation of QPRT expression in 16 tumours, including BRCA, COAD, and GBM, and downregulation in 10 tumours, including CHOL, KICH, and KIRP, among 27 tumour types.

3.2. QPRT Was Associated with the Prognosis of Certain Tumours. High QPRT expression was significantly associated with poor OS prognosis in patients with BRCA, KIRP, LGG, SKCM, and UVM, and the relationship between high and low QPRT expressions and patients with each tumour was further confirmed using KM curves (Figures 2(a) and 2(b)). To avoid the impact of nontumour death during follow-up, the relationship between QPRT expression levels and prognostic DSS (disease-specific survival) was analysed, and QPRT was found to be prognostically significant only with BRCA, KIRP, LGG, and READ tumours (Figure 2(c)). QPRT was hypothesized to be a prognostic marker for tumour DSS based on the KM curve (Figure 2(d)).

3.3. QPRT Expression Was Significantly Associated with Different Pathological Staging of BRCA. QPRT expression was significantly correlated with poor prognosis in BRCA patients, and QPRT expression was significantly higher in BRCA tumour tissues than in normal tissues (Figure 3(a)). Subsequent analysis of expression in different pathological subtypes of BRCA revealed significant differences in QPRT expression in all pathological subtypes, with the highest expression in the HER2 type (Figure 3(b)). The data analysis in the two validation sets (GSE46563 and GSE59246) revealed a significant differential expression of QPRT in HER2 breast cancer (Figures 3(c) and 3(d)). The immunohistochemical results (Figure 3(e)) showed that QPRT was localized in the cytoplasm, cell membrane, and nucleus and showed a positive expression in pathological breast cancer tissues but not in normal tissues.

3.4. The Prognosis of BRCA Was Significantly Associated with Many Factors. Survival analysis showed that breast cancer patients with low QPRT expression had higher OS and PFS than those with high expression (Figures 4(a) and 4(b)). Survival analysis of different pathological staging of BRCA also showed that the median survival time was significantly longer in basal-like and HER2-enriched than in luminal A, luminal B, and normal-like (Figure 4(c)). In addition, high QPRT expression was significantly associated with the prognosis of breast cancer patients with different pTNM stages (Figure 4(e)).

We also developed a prognostic model for BRCA to assess the impact of each factor on survival. In univariate survival analyses, BRCA cases with high QPRT expression had a poor OS. In Cox risk proportional regression analysis, after adapting for age, grade, tumour size, and subtype, QPRT was still an independent prognostic factor for OS (Figures 5(a) and 5(b)). Columnar tables were established to predict the prognostic survival of breast cancer patients at 1, 3, and 5 years, and the ROC curves showed that the 1-year (AUC = 0.695, 95% CI: 0.599–0.791) survival prediction model was the best model (Figures 5(c) and 5(d)).

3.5. QPRT May Be Involved in BRCA Progression through the PI3K/Akt Signalling Pathway. Enrichment analysis revealed (Figures 6(a) and 6(b)) that oxygenation levels and the development of the reproductive system were the most significant biological functions; the PI3K-Akt signalling pathway was the most significant KEGG pathway; some of the related functions and pathways are listed in Table 1. Subsequent GSEA showed that the oestrogen signalling pathway and cell cycle were the most significant KEGG pathways and that the cell cycle and mitosis were the most significantly related biological processes in the Reactome gene set (Figures 6(c) and 6(d)).

3.6. QPRT Activated the PI3K/Akt Signalling Pathway in Breast Cancer Cells. We confirmed the influence of QPRT on the PI3K/Akt signalling pathway by western blotting (Figure 7). Phosphorylation and protein levels of P-PI3K (ab278545) and P-Akt (ab38449) were significantly increased in MDA-MB-231 cells with foreign expression of QPRT. We also evaluated the PI3K/Akt downstream protein kinase P-MDM2 (ab170880) and found a significant enhancement of its phosphorylation and protein levels. These results indicate that QPRT may promote breast cancer progression through the PI3K/Akt pathway.

4. Discussion

Cancer is a significant factor affecting the health and longevity of people worldwide, with nearly 20 million new cancer cases and nearly 10 million deaths reported worldwide in 2020 [19]. Pan-cancer analysis can identify the similarities and differences in the tumour genomes and provide helpful information for cancer diagnosis and treatment [20]. In the present study, we evaluated the efficacy of QPRT for pan-cancer analysis. QPRT is significantly expressed in most tumours, and its expression is related to prognosis. Among them, the expression of QPRT has a prominent effect on the prognosis of breast cancer patients.

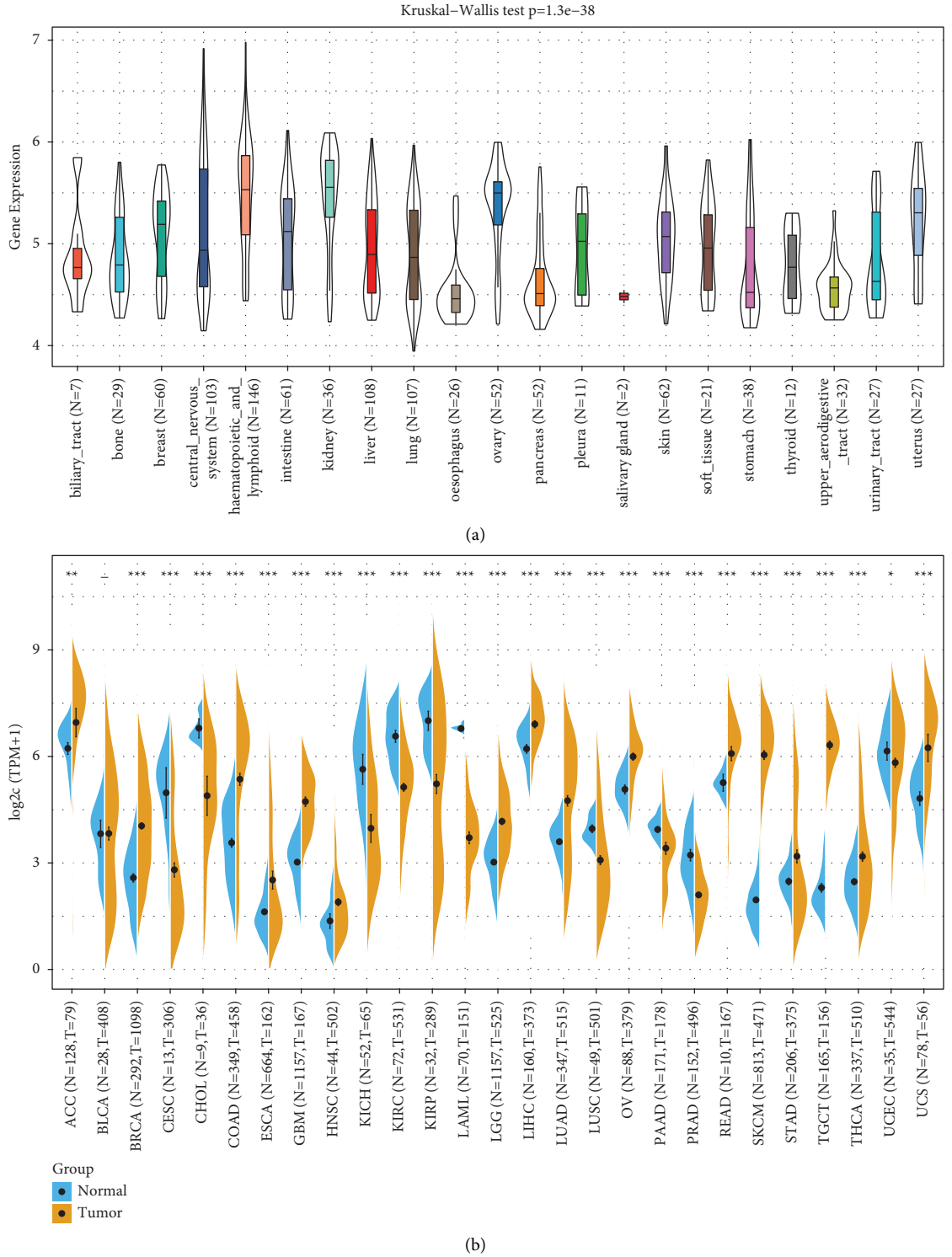

Figure 1: Expression levels of QPRT in different tumours: (a) QPRT expression in the CCLE dataset, total 21 tumour cell lines; (b) QPRT expression in the integrated GTEx and TCGA dataset, total 27 tumors. $^{*}P < 0.01$, $^{**}P < 0.001$, and $^{***}P < 0.0001$.

Because of the strong relationship found for QPRT in breast cancer, this study mainly analysed the relationship between QPRT and breast cancer. The TCGA dataset as the test set revealed significant QPRT expression in breast cancer, especially HER2 breast cancer. These results were reproduced in two GEO validation sets. A study screening for prognosis-related candidate genes in breast cancer showed that QPRT expression was significantly associated with prognosis in breast cancer patients [21]. The analysis in the present study shows that QPRT is an independent prognostic factor of breast cancer and is related to different pathological subtypes.

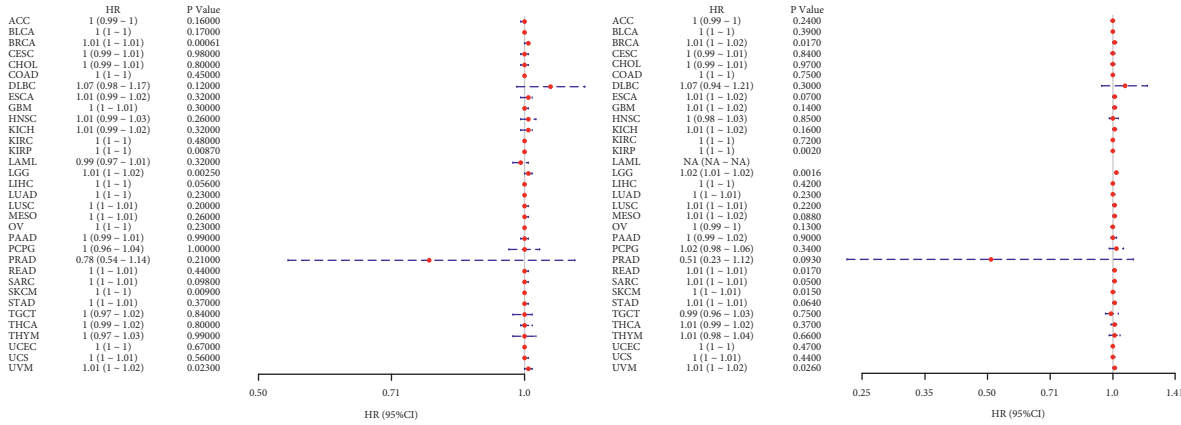

Figure 2: Continued.

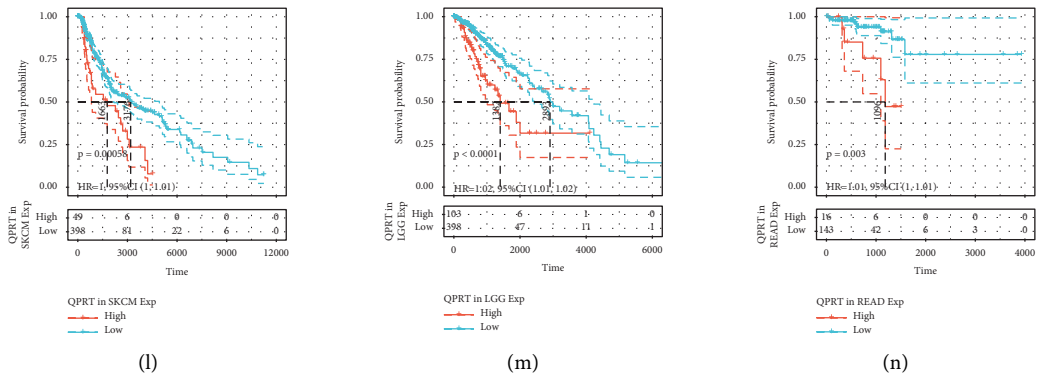

(l) (m) (n)

Figure 2: OS and DSS of high and low expressions of QPRT in each tumour: (a) forest plot of OS of QPRT in each tumour; (b) forest plot of DSS of QPRT in each tumour; (c–g) KM survival curve to show the OS of patients with high and low QPRT expressions in different tumors; (h–n) KM survival curve to show the DSS of patients with high and low QPRT expressions in different tumors.

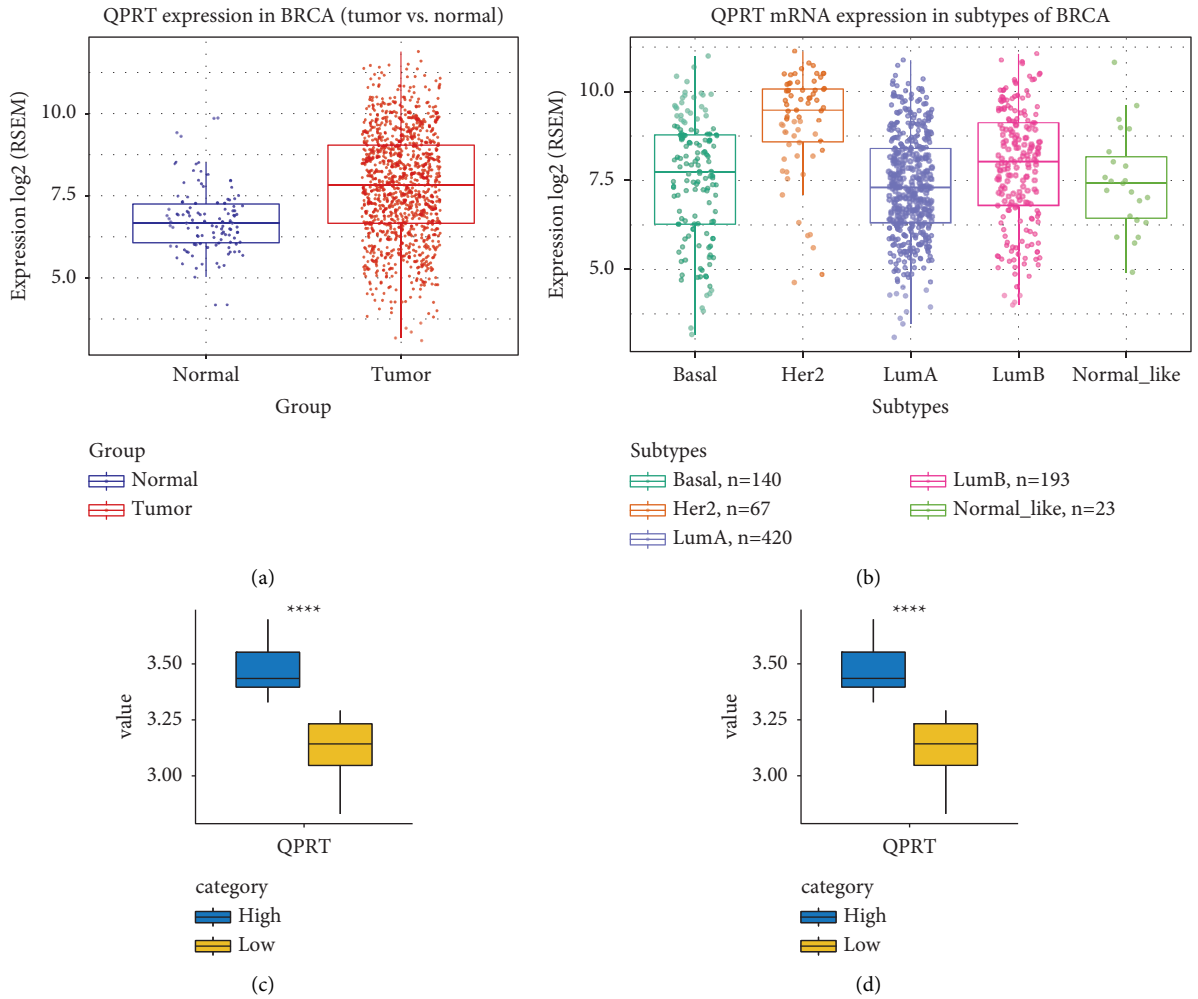

(a) (b) (c) (d)

Figure 3: Continued.

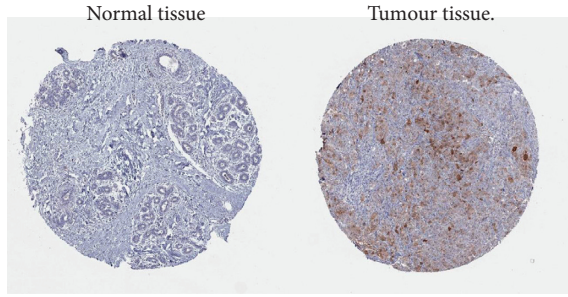

(e)

Figure 3: The expression of QPRT in BRCA: (a) differential expression of QPRT in BRCA tumour tissues and normal tissues; (b) expression of QPRT in different pathological staging of BRCA; ((c), (d)) the high and low expression distribution of QPRT in HER2 breast cancer, the data come from GSE46563 and GSE59246, respectively; (e) breast cancer immunohistochemical map.

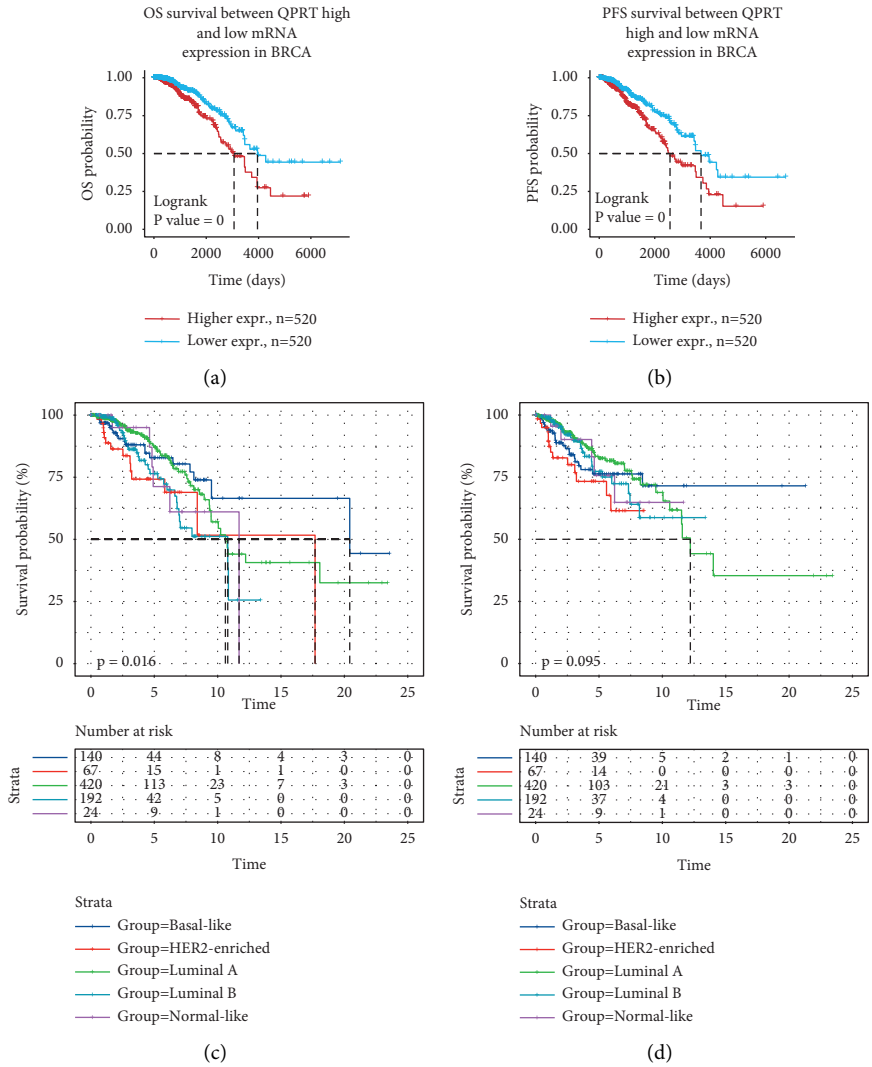

Figure 4: Continued.

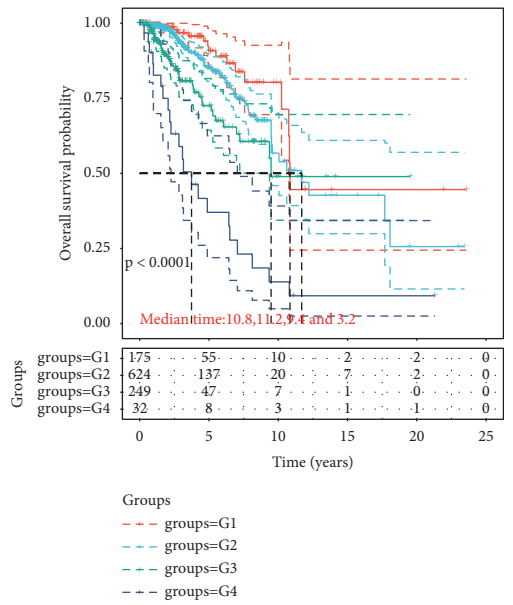

(e)

Figure 4: Prognostic relationship between QPRT and BRCA: (a) the relationship between high and low QPRT expressions and OS of BRCA by KM survival analysis; (b) the relationship between high and low QPRT expressions and PFS of BRCA by KM survival analysis; (c) the relationship between QPRT and OS of different pathological staging of BRCA; (d) the relationship between QPRT and PFS of different pathological staging of BRCA; (e) the relationship between QPRT and OS of different pTNM staging of BRCA.

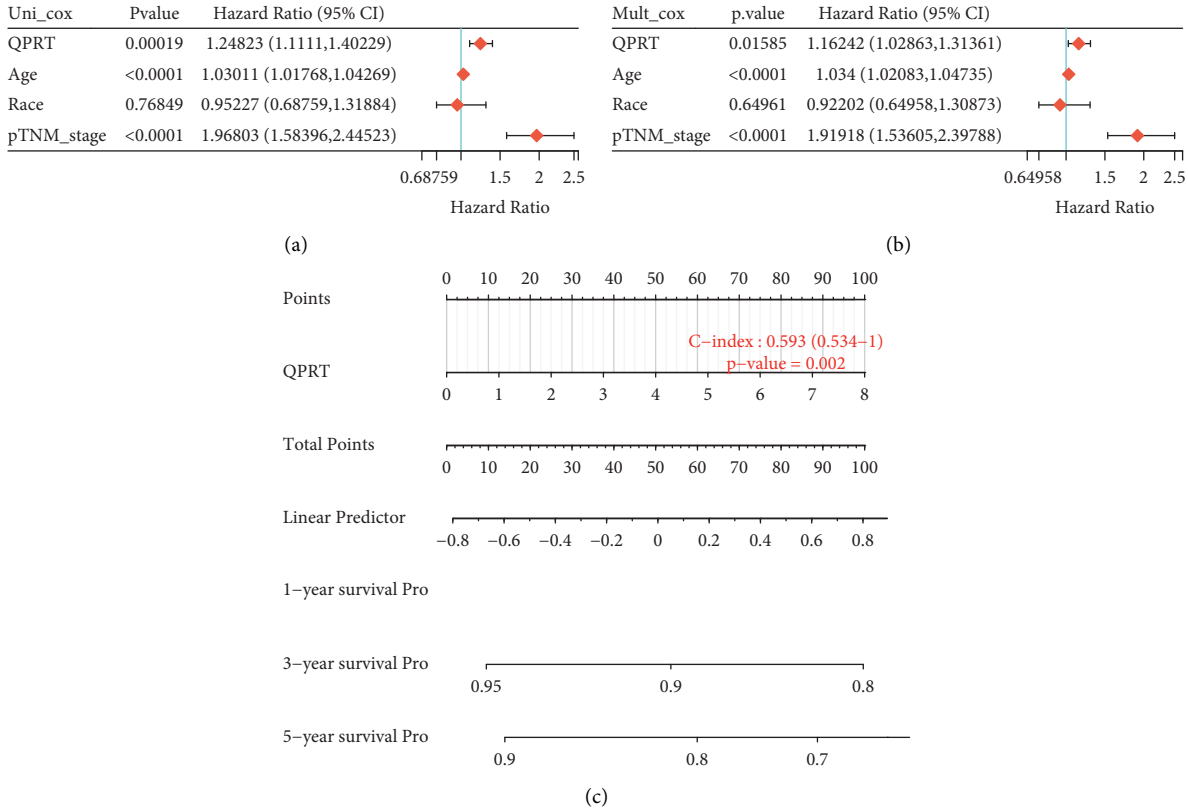

Figure 5: Continued.

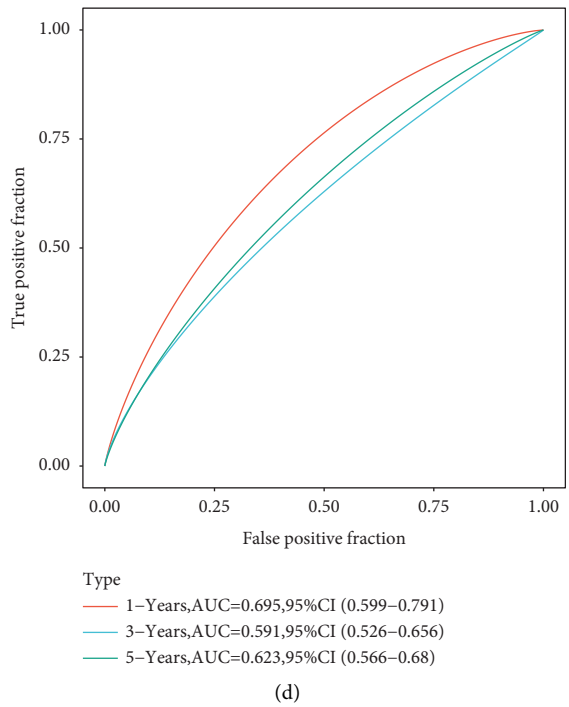

(d)

Figure 5: Prognosis of the BRCA prediction column line graph: (a) single-factor Cox regression analysis of the risk relationship of BRCA with age, race, and pTNM; (b) multifactor Cox regression analysis of the risk relationship of BRCA with age, race, and pTNM; (c) column line graphs for predicting the overall survival of BRCA patients at 1, 3, and 5 years; (d) ROC curve graphs for overall survival at 1, 3, and 5 years.

In breast cancer, HER2 gene amplification can lead to the proliferation of specific aggressive breast cells, and HER2 expression has been identified as an independent factor for the poor prognosis of breast cancer patients [22]. Targeted therapy is one of the treatments aimed at improving the survival rate of HER2-positive breast cancer patients, but the selection of targeted genes still needs further study [23].

QPRT catalyses the production of nicotinic acid mononucleotide (NMN), which in turn promotes the synthesis of nicotinamide adenine dinucleotide (NAD+), which plays a crucial role in cell survival [24]. Zhang et al. used in vivo and in vitro experiments to confirm that QPRT promotes growth, migration, and invasion of breast cancer and inhibits cell apoptosis [17]. Liu et al. also provided strong evidence that upregulation of QPRT promotes breast cancer progression [16]. Earlier work indicated that QPRT might have an antiapoptotic function (Ullmark et al., 2017). Furthermore, QPRT was identified as a potential prognosis biomarker of BC [21]. However, whether QPRT is an independent prognostic factor in invasive breast cancer and the mechanisms by which QPRT may contribute to invasive breast cancer remain undefined. Thus, the present study was based on this previous research and aimed to explore the mechanism underlying promoting breast cancer progression by QPRT.

QPRT overexpression is known to activate the PI3K/Akt signalling pathway in cancer cells [25], but this has not been proven in breast cancer. The GSEA results presented here showed that QPRT expression was related to the PI3K/Akt signalling pathway, and western blot analysis showed that overexpression of QPRT can increase the phosphorylation levels of PI3K and Akt, indicating that QPRT and the PI3K/Akt signalling pathway may have a positive feedback effect in breast cancer.

Phosphoinositide 3-kinase (PI3K) can integrate signals from growth factors, cytokines, and other extracellular stimuli, and the modification of this pathway is closely related to the pathogenesis of cancer [26, 27]. Protein kinase B (PKB, also known as Akt) is an essential mediator of the PI3K pathway and the signalling endpoint of various growth factors and cytokines [28]. The PI3K/Akt signalling pathway is one of the phosphatidylinositol signalling systems involved in tumorigenesis, cell growth, proliferation, metabolism, survival, and apoptosis [29]. The PI3K/Akt signalling pathway is activated in various cancers and has been proven to be one of the most important signalling pathways in cancer development [30]. The PI3K/Akt signalling pathway has attracted increasing attention in breast cancer research as activating this pathway can promote breast cancer cell proliferation, inhibit apoptosis [31], and modulate cell invasion [16]. Human epidermal growth factor receptor-2 (HER2) is involved in the development of breast cancer through the PI3K/Akt/mTOR pathway [27], and the PI3K/Akt/mTOR pathway is an important pathway involved in chemoresistance and survival of triple-negative breast cancer (TNBC) [32]. However, the current study also had some limitations. This research was based on microarray data

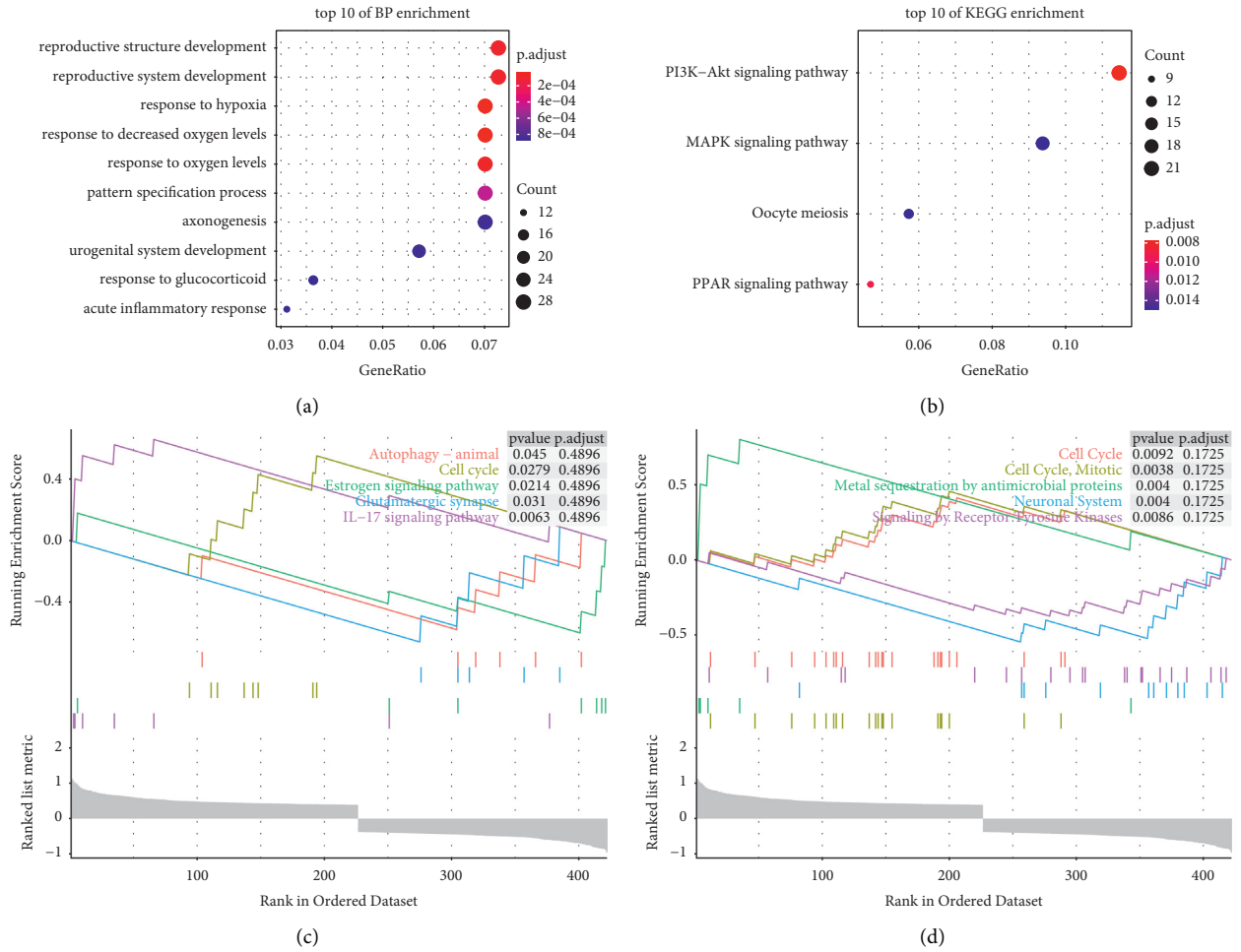

Figure 6: BRCA whole gene enrichment analysis: (a) enrichment of GO function in QPRT expression; (b) enrichment of KEGG function in QPRT expression; (c) enrichment of the KEGG pathway in GSEA with high and low QPRT expressions; (d) enrichment of biological processes in the Reactome gene set with high and low QPRT expressions. $P < 0.05$ is statistically significant.

Table 1: The most significant GO biofunction and KEGG pathways in the enrichment analysis.

Class	Function/pathway	*p* value	*p*. adjust	*q*-value
BP	Response to hypoxia	7.92E-09	3.08E-05	2.57E-05
	Response to decreased oxygen levels	1.50E-08	3.08E-05	2.57E-05
	Response to oxygen levels	5.54E-08	7.58E-05	6.32E-05
	Reproductive structure development	9.59E-08	9.10E-05	7.58E-05
	Reproductive system development	1.11E-07	9.10E-05	7.58E-05
	Pattern specification process	6.59E-07	0.000450942	0.00037565
	Urogenital system development	1.52E-06	0.000852121	0.000709846
	Axonogenesis	1.66E-06	0.000852121	0.000709846
	Response to glucocorticoid	2.04E-06	0.000874411	0.000728415
	Acute inflammatory response	2.34E-06	0.000874411	0.000728415
KEGG	PI3K-Akt signalling pathway	3.00E-05	0.007825176	0.007132445
	PPAR signalling pathway	7.00E-05	0.009139327	0.00833026
	MAPK signalling pathway	0.000198423	0.014943102	0.01362025
	Oocyte meiosis	0.000229013	0.014943102	0.01362025

analysis. The samples from the datasets were insufficient and without cancer stage information, and data from biological samples carried out no confirmation. Consequently, large-scale, potential, and widespread clinical examinations are required to confirm our results. It was necessary to obtain a single gene to profile QPRT expression in BRCA. The mechanism of QPRT needs further findings through in vivo and in vitro models.

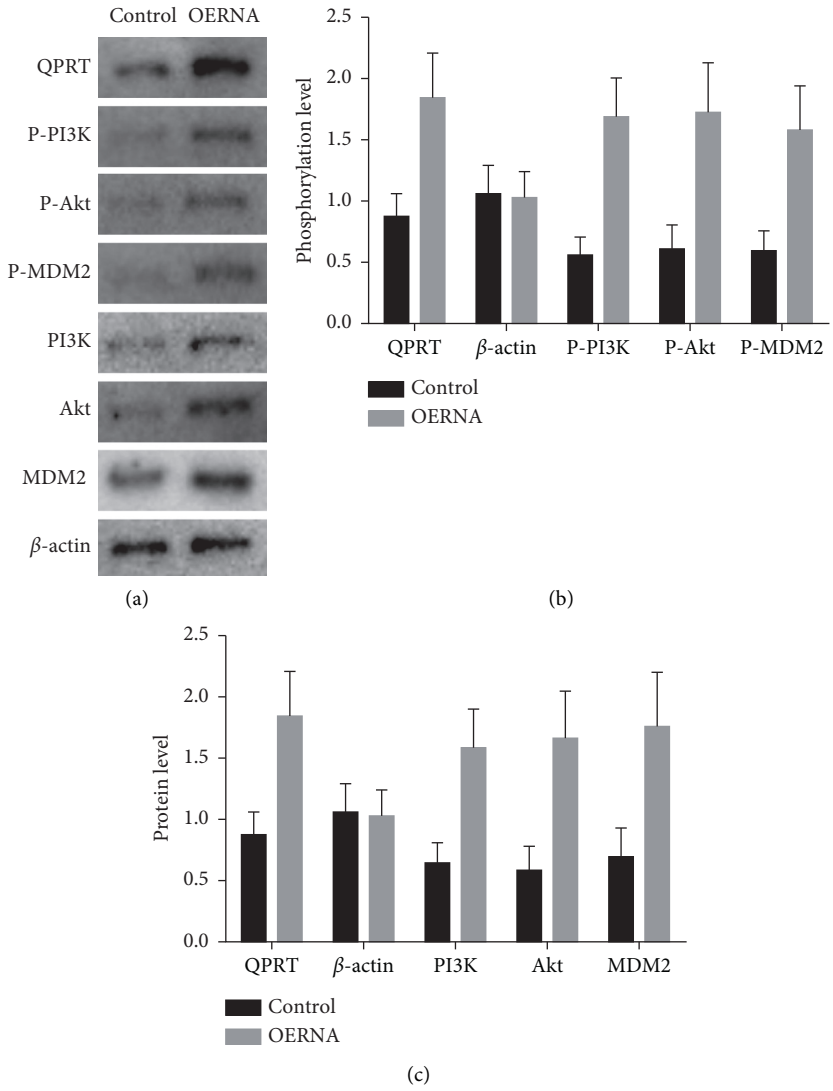

Figure 7: QPRT overexpression induces phosphorylation of PI3K/Akt-related signalling pathways: (a) western blot; (b) phosphorylation levels of different signalling pathways; (c) protein levels of different signalling pathways.

5. Conclusions

Collectively, our results here support a vital role for QPRT in breast cancer and indicate that its upregulation is related to the poor prognosis of patients with BRCA. Subsequently, in vitro experimental results show that QPRT upregulation may affect breast cancer progression by activating the PI3K/Akt signalling pathway. The current study implies that QPRT may therefore be a novel specific therapeutic target for breast cancer treatment.

Data Availability

The data used to support the findings of this study are available from the corresponding author upon request.

Conflicts of Interest

The authors declare that they have no conflicts of interest.

Acknowledgments

This work was supported by the Finance Department of Jilin Province under grant no. JLSWSRCZX2020-069, Jilin Provincial Key Laboratory of Medical Imaging and Big Data under grant no. 20200601003JC, and Radiology and Technology Innovation Center of Jilin Province under grant no. 20190902016TC.

References

[1] J. Ferlay, M. Colombet, I. Soerjomataram et al., "Cancer statistics for the year 2020: an overview," *International Journal of Cancer*, vol. 149, 2021.

[2] R. L. Siegel, K. D. Miller, and A. Jemal, "Cancer statistics, 2020," *CA: A Cancer Journal for Clinicians*, vol. 70, no. 1, pp. 7–30, 2020.

[3] L. Wang, "Early diagnosis of breast cancer," *Sensors*, vol. 17, no. 7, Article ID 1572, 2017.

[4] K. L. Britt, J. Cuzick, and K.-A. Phillips, "Key steps for effective breast cancer prevention," *Nature Reviews Cancer*, vol. 20, no. 8, pp. 417–436, 2020.

[5] Z. Momenimovahed and H. Salehiniya, "Epidemiological characteristics of and risk factors for breast cancer in the world," *Breast Cancer: Targets and Therapy*, vol. 11, pp. 151–164, 2019.

[6] X. Dai, T. Li, Z. Bai et al., "Breast cancer intrinsic subtype classification, clinical use and future trends," *American journal of cancer research*, vol. 5, no. 10, pp. 2929–2943, 2015.

[7] Y.-S. Sun, Z. Zhao, Z.-N. Yang et al., "Risk factors and preventions of breast cancer," *International Journal of Biological Sciences*, vol. 13, no. 11, pp. 1387–1397, 2017.

[8] K. D. Miller, L. Nogueira, A. B. Mariotto et al., "Cancer treatment and survivorship statistics, 2019," *CA: A Cancer Journal for Clinicians*, vol. 69, no. 5, pp. 363–385, 2019.

[9] Z. B. Pour, M. Nourbakhsh, K. Mousavizadeh, Z. Madjd, S. S. Ghorbanhosseini, and Z. Abdolvahabi, "Up-regulation of miR-381 inhibits NAD+ salvage pathway and promotes apoptosis in breast cancer cells," *EXCLI journal*, vol. 18, Article ID 683, 2019.

[10] M. Vora, J. Ansari, R. M. Shanti et al., "Increased nicotinamide phosphoribosyltransferase in rhabdomyosarcomas and leiomyosarcomas compared to skeletal and smooth muscle tissue," *Anticancer Research*, vol. 36, no. 2, pp. 503–507, 2016.

[11] R. Xu, Z. Yuan, L. Yang, L. Li, D. Li, and C. Lv, "Inhibition of NAMPT decreases cell growth and enhances susceptibility to oxidative stress," *Oncology Reports*, vol. 38, no. 3, pp. 1767–1773, 2017.

[12] J. Guo, L. T. Lam, K. L. Longenecker et al., "Identification of novel resistance mechanisms to NAMPT inhibition via the de novo NAD+ biosynthesis pathway and NAMPT mutation," *Biochemical and Biophysical Research Communications*, vol. 491, no. 3, pp. 681–686, 2017.

[13] A. A. Pramono, G. M. Rather, H. Herman, K. Lestari, and J. R. Bertino, "NAD- and NADPH-contributing enzymes as therapeutic targets in cancer: an overview," *Biomolecules*, vol. 10, no. 3, Article ID 358, 2020.

[14] Y.-C. Lee, Y.-H. Yang, J.-H. Su, H.-L. Chang, M.-F. Hou, and S.-S. F. Yuan, "High visfatin expression in breast cancer tissue is associated with poor survival," *Cancer Epidemiology Biomarkers & Prevention*, vol. 20, no. 9, pp. 1892–1901, 2011.

[15] C. Ji, R. Cong, Y. Wang et al., "Relationship between NAMPT/PBEF/visfatin and prognosis of patients with malignant tumors: a systematic review and meta-analysis," *Annals of Translational Medicine*, vol. 7, no. 23, Article ID 785, 2019.

[16] C.-L. Liu, S.-P. Cheng, M.-J. Chen, C.-H. Lin, S.-N. Chen, and Y.-H. Kuo, "Quinolinate phosphoribosyltransferase promotes invasiveness of breast cancer through myosin light chain phosphorylation," *Frontiers in Endocrinology*, vol. 11, Article ID 1124, 2021.

[17] Z. Yue, J. Shusheng, S. Hongtao et al., "Silencing DSCAM-AS1 suppresses the growth and invasion of ER-positive breast cancer cells by downregulating both DCTPP1 and QPRT," *Aging*, vol. 12, no. 14, pp. 14754–14774, 2020.

[18] Y. Zhang, D. J. Topham, J. Thakar, and X. Qiu, "FUNNEL-GSEA: FUNctioNal ELastic-net regression in time-course gene set enrichment analysis," *Bioinformatics*, vol. 33, no. 13, pp. 1944–1952, 2017.

[19] H. Sung, J. Ferlay, R. L. Siegel et al., "Global cancer statistics 2020: GLOBOCAN estimates of incidence and mortality worldwide for 36 cancers in 185 countries," *CA: A Cancer Journal for Clinicians*, vol. 71, no. 3, pp. 209–249, 2021.

[20] D. He, X. Zhang, and J. Tu, "Diagnostic significance and carcinogenic mechanism of pan-cancer gene POU5F1 in liver hepatocellular carcinoma," *Cancer medicine*, vol. 9, no. 23, pp. 8782–8800, 2020.

[21] Y.-H. Xu, J.-L. Deng, L.-P. Wang et al., "Identification of candidate genes associated with breast cancer prognosis," *DNA and Cell Biology*, vol. 39, no. 7, pp. 1205–1227, 2020.

[22] J. Wang and B. Xu, "Targeted therapeutic options and future perspectives for HER2-positive breast cancer," *Signal transduction and targeted therapy*, vol. 4, no. 1, pp. 34–22, 2019.

[23] K. Goutsouliak, J. Veeraraghavan, V. Sethunath et al., "Towards personalized treatment for early stage HER2-positive breast cancer," *Nature Reviews Clinical Oncology*, vol. 17, no. 4, pp. 233–250, 2020.

[24] H. S. Youn, T. G. Kim, M. K. Kim et al., "Structural insights into the quaternary catalytic mechanism of hexameric human quinolinate phosphoribosyltransferase, a key enzyme in de novo NAD biosynthesis," *Scientific Reports*, vol. 6, no. 1, Article ID 19681, 2016.

[25] Y. C. Niu, J. Tong, X. F. Shi, and T. Zhang, "MicroRNA-654-3p enhances cisplatin sensitivity by targeting QPRT and inhibiting the PI3K/AKT signaling pathway in ovarian cancer cells," *Experimental and Therapeutic Medicine*, vol. 20, no. 2, pp. 1467–1479, 2020.

[26] S. Noorolyai, N. Shajari, E. Baghbani, S. Sadreddini, and B. Baradaran, "The relation between PI3K/AKT signalling pathway and cancer," *Gene*, vol. 698, pp. 120–128, 2019.

[27] M. A. Ortega, O. Fraile-Martínez, Á. Asúnsolo, J. Buján, N. García-Honduvilla, and S. Coca, "Signal transduction pathways in breast cancer: the important role of PI3K/Akt/mTOR," *Journal of oncology*, vol. 2020, 2020.

[28] C. De Marco, C. Laudanna, N. Rinaldo et al., "Specific gene expression signatures induced by the multiple oncogenic alterations that occur within the PTEN/PI3K/AKT pathway in lung cancer," *PLoS One*, vol. 12, no. 6, Article ID e0178865, 2017.

[29] H. Zhang, Y. Z. Pan, M. Cheung et al., "LAMB3 mediates apoptotic, proliferative, invasive, and metastatic behaviors in pancreatic cancer by regulating the PI3K/Akt signaling pathway," *Cell Death & Disease*, vol. 10, no. 3, pp. 230–314, 2019.

[30] N. Jiang, Q. Dai, X. Su, J. Fu, X. Feng, and J. Peng, "Role of PI3K/AKT pathway in cancer: the framework of malignant behavior," *Molecular Biology Reports*, vol. 47, no. 6, pp. 4587–4629, 2020.

[31] Z. Gholinejad, N. kheiripour, M. Nourbakhsh et al., "Extracellular NAMPT/Visfatin induces proliferation through ERK1/2 and AKT and inhibits apoptosis in breast cancer cells," *Peptides*, vol. 92, pp. 9–15, 2017.

[32] M. A. Khan, V. K. Jain, M. Rizwanullah, J. Ahmad, and K. Jain, "PI3K/AKT/mTOR pathway inhibitors in triple-negative breast cancer: a review on drug discovery and future challenges," *Drug Discovery Today*, vol. 24, no. 11, pp. 2181–2191, 2019.

Hindawi
Journal of Oncology
Volume 2022, Article ID 5758601, 17 pages
https://doi.org/10.1155/2022/5758601

Research Article

Comprehensive Analysis of HOX Family Members as Novel Diagnostic and Prognostic Markers for Hepatocellular Carcinoma

Zhipeng Jin,[1] **Dongxu Sun**,[1] **Mengying Song**,[2] **Wenjing Zhu**,[3] **Huayuan Liu**,[1] **Jianping Wang**,[1] **and Guangjun Shi**[1]

[1]*Department of Hepatobiliary Surgery, Qingdao Municipal Hospital, Qingdao, China*
[2]*Department of Operation Room, Cancer Hospital of China Medical University, Shenyang, China*
[3]*Clinical Research Center, Qingdao Municipal Hospital, Qingdao, China*

Correspondence should be addressed to Guangjun Shi; sgjzp@hotmail.com

Received 17 December 2021; Revised 26 January 2022; Accepted 29 January 2022; Published 23 February 2022

Academic Editor: Fu Wang

Background. The homeobox (HOX) gene family has been found to be involved in human cancers. However, its involvement in hepatocellular carcinoma (HCC) has not been well documented. Here, we comprehensively evaluated the role of HOXs in HCC. *Methods*. RNA sequencing profile of TCGA-LIHC and LIRI-JP were obtained from the Cancer Genome Atlas (TCGA) and the International Cancer Genome Consortium (ICGC), respectively. Data of TCGA-LIHC methylation were downloaded from UCSC Xena. Genetic alteration data for the TCGA samples was obtained from cBioPortal and GSCA. The diagnostic efficiency was assessed using ROC curves. The prognostic significance was evaluated by the Kaplan–Meier method and Cox regression analysis. Subsequent functional analysis was performed through the clusterProfiler package. ssGSEA, ESTIMATE, and TIDE algorithms were employed to explore the relationship between HOXs and the HCC microenvironment. Finally, pRRophetic package and NCI-60 cancerous cell lines were applied to estimate anticancer drug sensitivity. *Results*. The mRNA levels of HOXs in HCC tissues were higher than those of noncancerous tissues and were correlated with poor overall survival (OS). HOXA6, C6, D9, D10, and D13 could serve as independent risk factors for OS. Further functional analysis revealed that these five HOXs regulate the cell proliferation, cell cycle, immune response, and microenvironment composition of HCC. In addition, the aberrant expression and methylation of HOXs is of great value in the diagnosis of HCC. *Conclusion*. HOXs play crucial roles in HCC and could serve as potential markers for HCC diagnosis and prognosis.

1. Introduction

Hepatocellular carcinoma is an important cause of human cancer-related deaths worldwide, and its incidence continues to rise [1]. Meanwhile, it is also one of the cancers with the worst prognosis. According to statistics, the median survival time of advanced cases is only 2-3 years [2]. Surgery is the most important treatment for early HCC. However, due to the lack of specific symptoms, patients miss the best opportunity for surgery [1]. Posthepatic resection recurrence is another considerable challenge. Even in patients with early HCC, the 5-year recurrence rate was close to 70% [3]. The high recurrence rate and poor curative effect are related to the complicated pathogenesis of HCC, as various networks of molecules and signaling pathways are involved in its occurrence and development [4]. Therefore, the discovery of new molecules involved in HCC progression and the identification of new diagnostic markers and therapeutic targets is critically important for improving HCC patients' prognosis.

The HOX genes share a DNA sequence called "homeobox" which consists of a 120-base pair and encodes a polypeptide consisting of 61 amino acids, known as a homeodomain [5].

For the first time, HOX genes were found to be involved in the embryogenesis of *Drosophila melanogaster* [6]. Notably, structural and developmental variations were observed in mutant *D. melanogaster*, such as the replacement of antennae with legs. These anomalies, caused by mutations, are called "homeotic" transformations. In 1921, geneticists proposed the existence of genes that specifically regulate these transformations [7]. Seventy years later, the protein structures of such genes were identified in humans, and termed "homeotic" or "HOX" genes [8, 9]. The discovery of the HOX gene is crucial to understanding the genetic control mechanisms of embryonic development. In mammals, diverse HOX members control the development of different parts of the body [10].

Thirty-nine HOXs were identified in the human genome, located on chromosomes 2, 7, 12, and 17, and divided it them into four gene clusters (A, B, C, and D, respectively). Each cluster was also divided into 13 paralog groups. Each gene cluster contains from 9 to 11 members (Figure S1) [11]. Over the past century, many studies found that HOXs were closely related to human cancers [12–15]. Meanwhile, the aberrant methylation of HOX genes was also identified as a characteristic of cancers [16]. All these findings have shown the potential of HOXs as biomarkers for human cancers.

In HCC, the abnormal expression of few HOX members was established to be involved in disease progression [17, 18]. However, the significance of most HOX members is still not clear. Here, we integrally analyzed the genomic data of HOXs in HCC, and assessed their diagnostic and prognostic value.

2. Materials and Methods

The flowchart of this study is presented in Figure 1.

2.1. Datasets Sources and Processing. The RNA-seq (FPKM format) and clinical data of TCGA-LIHC were downloaded from the GDC Data Portal (https://portal.gdc.cancer.gov/). The RNA-seq (FPKM) of LIRI-JP was downloaded from ICGC Data Portal (https://dcc.icgc.org/). The limma package [19] in R software was applied to identify HOX genes differentially expressed between cancerous tissues and adjacent noncancerous tissues. The threshold was set as $|\log2 \text{ Fold Change}| > 1.5$ and a P value < 0.05. The methylation data for TCGA-LIHC was downloaded from the University of California, Santa Cruz (UCSC; Santa Cruz, CA, USA) Xena data portal (https://xena.ucsc.edu/). The beta values from the same sample but from different vials/portions/analytes/aliquotes were averaged, whereas the beta values from different samples were combined into a genomic matrix. The Corrplot [20] package in R software was used to evaluate the correlation between the gene expression or the methylation levels of the CpG sites and the corresponding gene expression.

2.2. Assessment of Genetic Alterations in HOX Genes. cBioPortal is an interactive open-source platform that provides large scale cancer genomics data sets (https://www.cBioPortal.org/) [21]. We obtained the genomic data of samples in TCGA-LIHC (Firehose Legacy), including mutations, putative copy-number alterations from GISTIC, and mRNA expression z-Scores (RNASeq V2 RSEM) with a z-score threshold ± 2.0. All samples were divided into two groups. The altered group included 59 samples with mutations or CNA, whereas the unaltered group consisted of 301 samples without mutations or CNA. Then, the differences in the overall survival and disease-free statuses (since initial treatment) between the two groups were analyzed using K–M survival analysis.

Gene Set Cancer Analysis (GSCA) is an integrated database for the analysis of cancer genomics (http://bioinfo.life.hust.edu.cn/GSCA/#/) [22]. We obtained the details of the SNV and CNV of HOX family genes in TCGA-LIHC from the GSCA database. The mutation data showed seven types of deleterious mutations. The CNV data were processed through GISTICS2.0. Based on the GISTIC score, CNV was divided into four categories.

2.3. PPI Network and Functional Enrichment Analysis. The genes coexpressed with HOX genes in TCGA-LIHC were collected from the UALCAN database (https://ualcan.path.uab.edu/) [23]. A correlation coefficient ≥0.4 was considered to indicate a significant correlation. Based on genes significantly correlated with HOXs, we constructed a PPI network using STRING v.10.0b (https://string-db.org/) [24]. Next, we screened the hub genes and visualized the STRING results using Cytoscape v3.8.0 (https://cytoscape.org/cy3.html) [25]. Then, the clusterProfiler package [26] in R was employed to identify the Gene Ontology (GO) terms (including cellular component, biological process, and molecular function) and Kyoto Encyclopedia of Genes and Genomes (KEGG) pathways that were enriched by hub genes and to visualize the results.

2.4. Relationship between HOXs and HCC Microenvironment. The abundance of 24 immune cell types was predicted by calculating the single-sample gene set enrichment analysis (ssGSEA) scores based on the gene set signatures of each type of the immune cells through ImmuCellAI (http://bioinfo.life.hust.edu.cn/ImmuCellAI/#!/) [27]. Further, we obtained bubble plots presenting the correlation between the mRNA expression of the HOX genes and the estimated abundance of immune cells from the GSCA database. Then, the ssGSEA scores of 13 immune functions of each HCC sample were quantified using the GSVA package [28] in R software.

Afterwards, the stromal cell levels in HCC tissues were estimated using the ESTIMATE algorithm, which analyzes the composition of the microenvironment and calculates the tumor purity based on the gene expression data [29].

2.5. Role of HOXC6 in Immune-Checkpoint Inhibitor Treatment. First, the correlation of HOXC6 with two types of immune-checkpoint inhibitor treatment response-related biomarkers, immune-checkpoint genes, and tumor mutation burden (TMB) was evaluated. Gene expression and

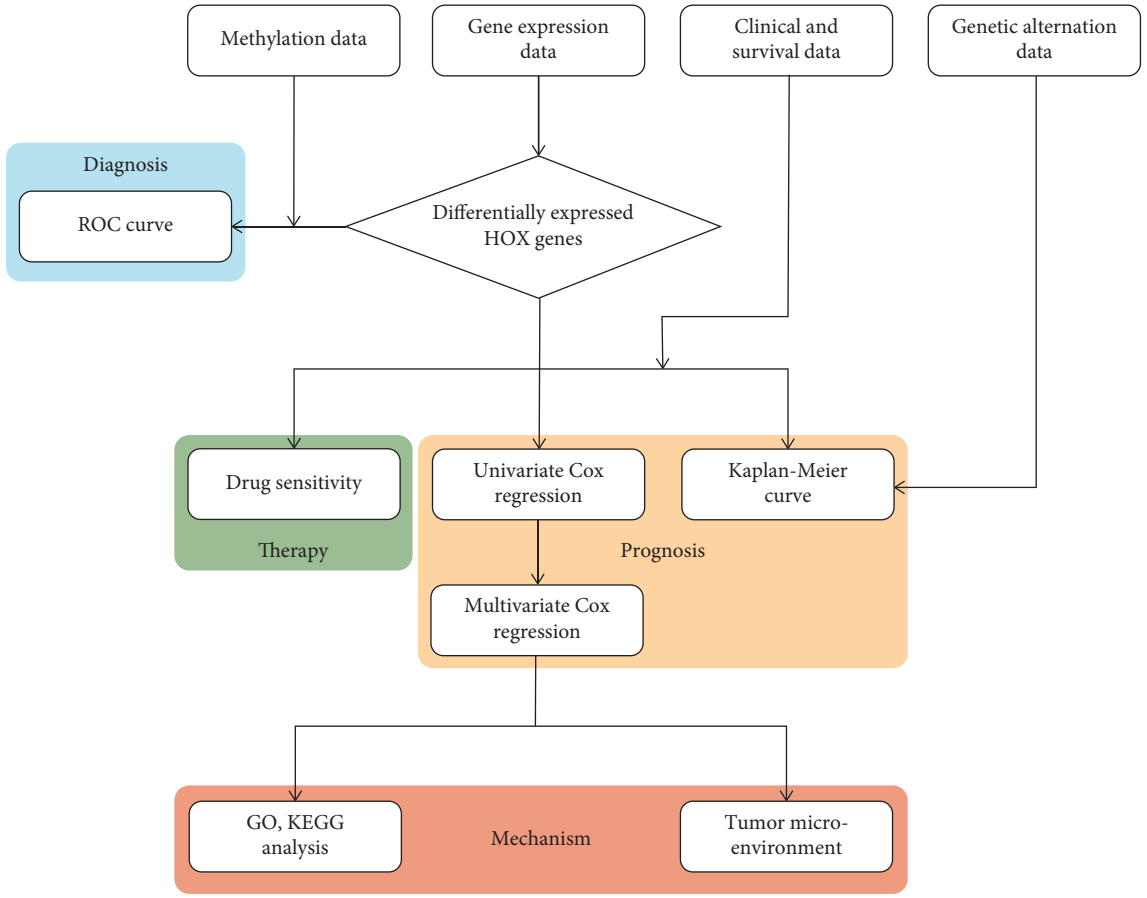

Figure 1: Flowchart of the present research.

somatic mutation data were obtained from TCGA-LIHC, and TMB was calculated based on the somatic mutation data collected.

Then, the Tumor Immune Dysfunction and Exclusion (TIDE) algorithm (http://tide.dfci.harvard.edu/login/) [30] was applied to predict the response to anti-PD-1 and anti-CTLA4 treatment.

2.6. Anticancer Drug Sensitivity Prediction. We analyzed the relationship between HOX genes expression and anticancer drugs sensitivity by estimating the half-maximal inhibitory concentration (IC50). The IC50 of sorafenib in each HCC sample was predicted using the pRRophetic package [31] in R.

The NCI-60 human cancer cell line panel [32] was previously used by cancer investigators and the NCI Developmental Therapeutics Program (DTP) to discover novel anticancer drugs [33]. We obtained data of the RNA-seq/composite expression and the compound activity (average z score) of DTP NCI-60 from CellMiner v2.6 (https://discover.nci.nih.gov/cellminer/home.do) [34].

2.7. Statistical Analysis. Statistical analyses were conducted in R software (version 4.0.2). Wilcoxon rank-sum test was used to analyze the differences between the two subgroups. Then, the Kaplan–Meier method and the log-rank test were utilized to analyze the differences in the survival between the groups of patients. The best cut-off values of the groups were determined using the survminer package in R. Moreover, independent prognostic analysis was conducted via Cox proportional hazards models. We factored gender, age, tumor stage, and tumor differentiation into confounding factors and excluded patients with multiple sets of expression data, missing expression data, or without the aforementioned clinical information. Pearson correlation test was employed to measure the correlation between variables. Receiver operating characteristic curves were established to evaluate the diagnostic values of HOXs, and the pROC package was used to quantify the area under the curve (AUC). In all statistical analyses, a P value <0.05 was considered statistically significant.

3. Results

3.1. Increased HOX Family Genes Expression in HCC. We first compared the transcriptional expression of HOXs in 374 HCC and 50 noncancerous samples from TCGA-LIHC (Figure 2(a)). The result showed that the mRNA levels of HOXs were generally higher in HCC. Then, we analyzed the differences between 243 HCC and 202 noncancerous samples from the LIRI-JP cohort. Similar to our previous result, the mRNA levels of the HOX family members in HCC

were generally higher than those in the noncancerous samples, except for HOXB4. A total number of 25 members (Figure 2(b)); HOXA3, 6-7, 9-11, 13, HOXB8-9, 13, HOXC5-6, 8-11, 13, HOXD1, 3-4, 8-11, and D13 were significantly upregulated ($|\log2\ FC| > 1.5$, $P < 0.05$) in the two cohorts (Figures 2(c) and 2(d)) (Table S1).

Altogether, the expression of HOX genes was generally increased in the HCC tissues, suggesting that they may play important roles in HCC.

3.2. Methylation Patterns of HOX Genes in HCC. We first analyzed the correlation between the methylation levels of different CpG sites in the promoters of the HOX genes and the corresponding expression of the HOX genes based on the data of the TCGA-LIHC cohort (Figure S2). A total number of 5 CpG sites showed a significant negative correlation ($r < -0.3$) between the methylation level and the corresponding gene expression (Figure 3(a)). Then, we analyzed the differences in their methylation levels between HCC samples and noncancerous samples (Figure 3(b)). We found that the methylation levels of cg20712820 in HCC were significantly lower than those in the noncancerous samples. Conversely, the methylation levels of cg06397837 and cg07083464 in HCC were significantly higher than those in the adjacent noncancerous samples. These data suggested that these three CpG sites may be closely associated with HCC.

3.3. Diagnostic Value of HOXs in HCC. First, the diagnostic value of HOX genes expression was assessed by performing ROC curve analysis based on the expression data collected from the TCGA and ICGC databases (Figures 4(a) and 4(b)). We established that a total number of five HOX members (HOXA10, 13, D1, 3, and D4) had superior predictive power (AUC >0.8) in both cohorts. Among them, the AUC of HOXA13 was higher than 0.9 (0.91 and 0.92, respectively).

Next, we also assessed the diagnostic value of three differentially methylated CpG sites (Figure 4(c)). We detected a correlation between the methylation of cg20712820 and cg07083464 and HCC incidence (AUCs of 0.74 and 0.79, correspondingly).

The above data suggested that the expression of HOXA10, 13, D1, 3, and D4 could serve as potential markers for the diagnosis of HCC, especially HOXA13. Besides, the methylation levels of cg20712820_HOXA3 and cg07083464_HOXA13 also had moderate value for the identification of HCC.

3.4. Prognostic Value of HOXs in HCC. The clinical characteristics of all HCC patients included in our survival analysis are displayed in Table 1. First, the prognostic value of the HOX family members was evaluated using the K–M method. As can be observed in Figure 5(a), the high expression of HOXA3, 6, 9-11, 13, B8-9, 13, C6, 8-11, 13, D3, 8-10, and D13 was related to poor OS. Moreover, the results of the Cox regression model revealed that the elevated expression of HOXA6, 9, B8, C6, 8, D9-10, and D13 was significantly associated with unfavorable OS (Figure 5(b)). Five of them (HOXA6, C6, D9-10, and D13) were independent risk factors (Figure 5(c)). These results indicated that HOXA6, C6, D9-10, and D13 could serve as markers for predicting the prognosis of HCC patients.

3.5. Genetic Alterations of HOXs in HCC Patients. To further explore the role of HOX family in HCC patients, we assessed the genetic alterations of the HOX members. We first analyzed the mutation, CNA, and the expression data of TCGA-LIHC using the cBioPortal. The genetic alterations percentages of HOXs in HCC varied from 1.9% to 8% (Figure 6(a)). We next obtained the details of CNV and the mutations of HOXs from the GSCA database. We established that heterozygous amplification was the main type of CNV (Figure 6(b)), and missense mutations constituted the largest proportion of the mutations (Figure 6(c)). Moreover, the results of the K–M analysis obtained by using the cBioPortal showed poor OS and DFS in cases with mutations and CNV of HOX genes (Figures 6(d) and 6(e)).

In conclusion, the genetic alterations of HOXs in HCC patients were also associated with poor prognosis.

3.6. Functional Enrichment Analysis of Prognosis-Related HOXs. To further explore the mechanism by which the five HOXs influence HCC patients' prognosis, we first obtained the genes that were significantly correlated ($|r| \geq 0.4$) with these HOXs in TCGA-LIHC from the UALCAN database. Then, STRING analysis was conducted to construct a PPI network, and Cytoscape was applied to screen the hub genes. As can be seen in Figure 7(a), there were 145 genes in the core network. The gene (CDK1) with the darkest red color and the largest node size had the highest degree in the network. Then, GO and KEGG enrichment analysis were performed to understand the potential function of the hub genes (Table S2, S3). The top 30 enriched categories of each GO group are depicted in Figures 7(b)–7(d). The KEGG pathways are illustrated in Figure 7(e). These results revealed that the hub genes were involved mainly in cell proliferation, cell cycle regulation, and immune response.

3.7. Relationship between the Five Prognosis-Related HOX Genes and the Tumor Microenvironment. To further explore the roles of the five HOXs in tumor microenvironment (TME), we first used the GSCA database to analyze the correlation between the expression levels of these HOXs and the estimated abundance of 24 immune cell types (Figure 8(a)). We found that the five HOXs were associated with a number of immune cell types. Then we used the ssGSEA algorithm to analyze the effect of the five HOX genes on immune functions (Figure 8(b)). All HCC samples were divided into two groups based on the median HOXs expression level. The HCC samples with high HOXA6 expression had lower scores of their cytolytic

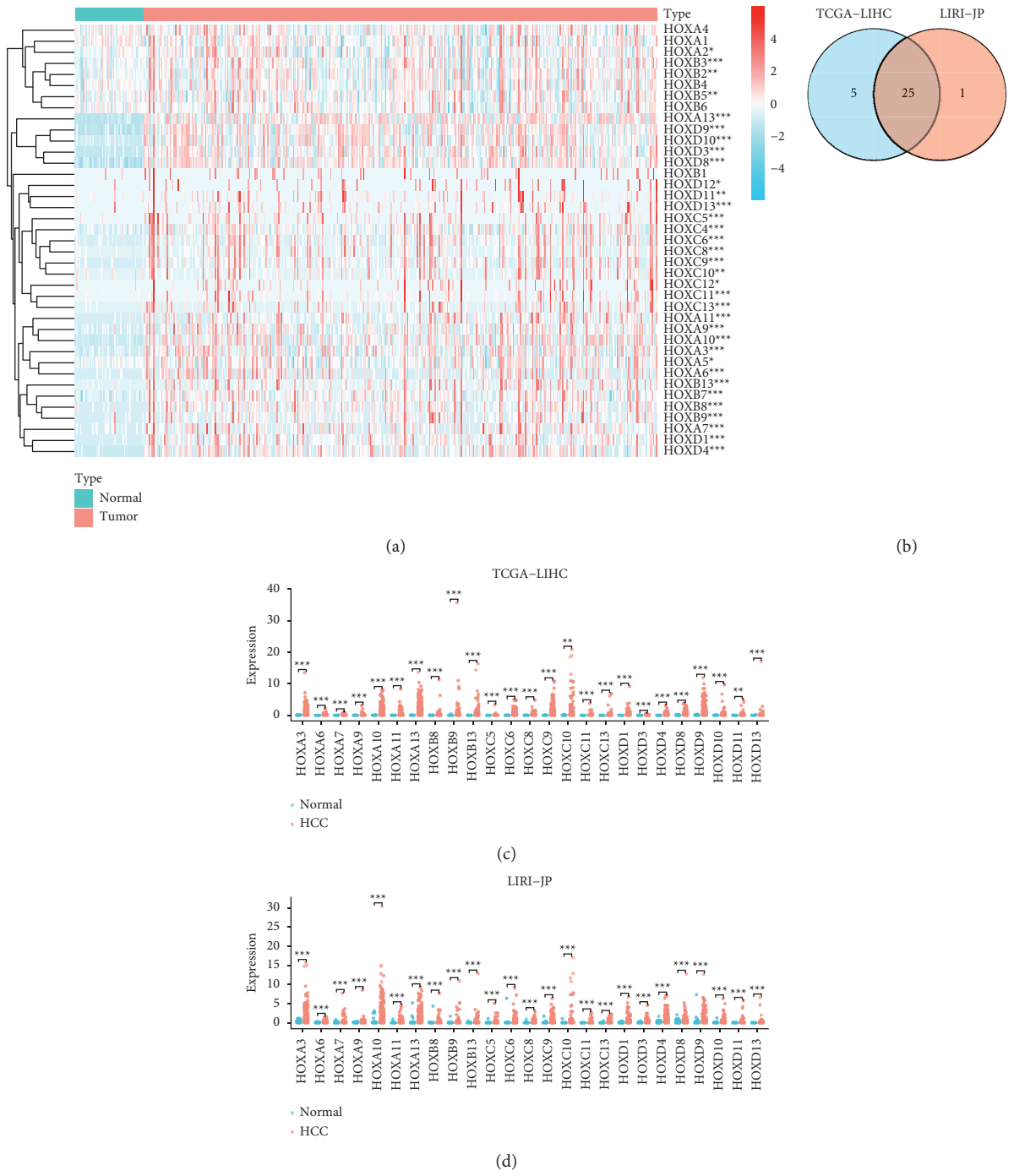

Figure 2: Expression profile of HOXs in HCC. (a) Heatmap of HOX family genes expression in TCGA-LIHC; (b) venn diagram of differentially expressed HOX genes in two HCC cohorts; (c) expression of 25 DEGs in TCGA-LIHC; (d) Expression of 25 DEGs in LIRI-JP. ($^{*}P < 0.05$, $^{**}P < 0.01$, and $^{***}P < 0.001$).

activity. In contrast, the samples with high HOXC6 expression showed higher scores in multiple immune functions, such as check point, but obtained lower scores in the type II IFN response. Meanwhile, the scores of CCR, APC costimulation, and parainflammation of the groups with high expression of HOXD9 and HOXD10 were lower than those in the groups with low expression of these two HOXs. The samples with high expression of HOXD10 and HOXD13 had lower scores in both IFN response types. In addition, the higher expression of HOXD9 was also associated with a lower score of type II IFN response but a higher score of MHC class I.

Further, using the ESTIMATE algorithm, we also explored the association of the five HOXs with stromal cells, another important component of TME. As visible in Figure 8(c), the stromal scores in the tissues with high

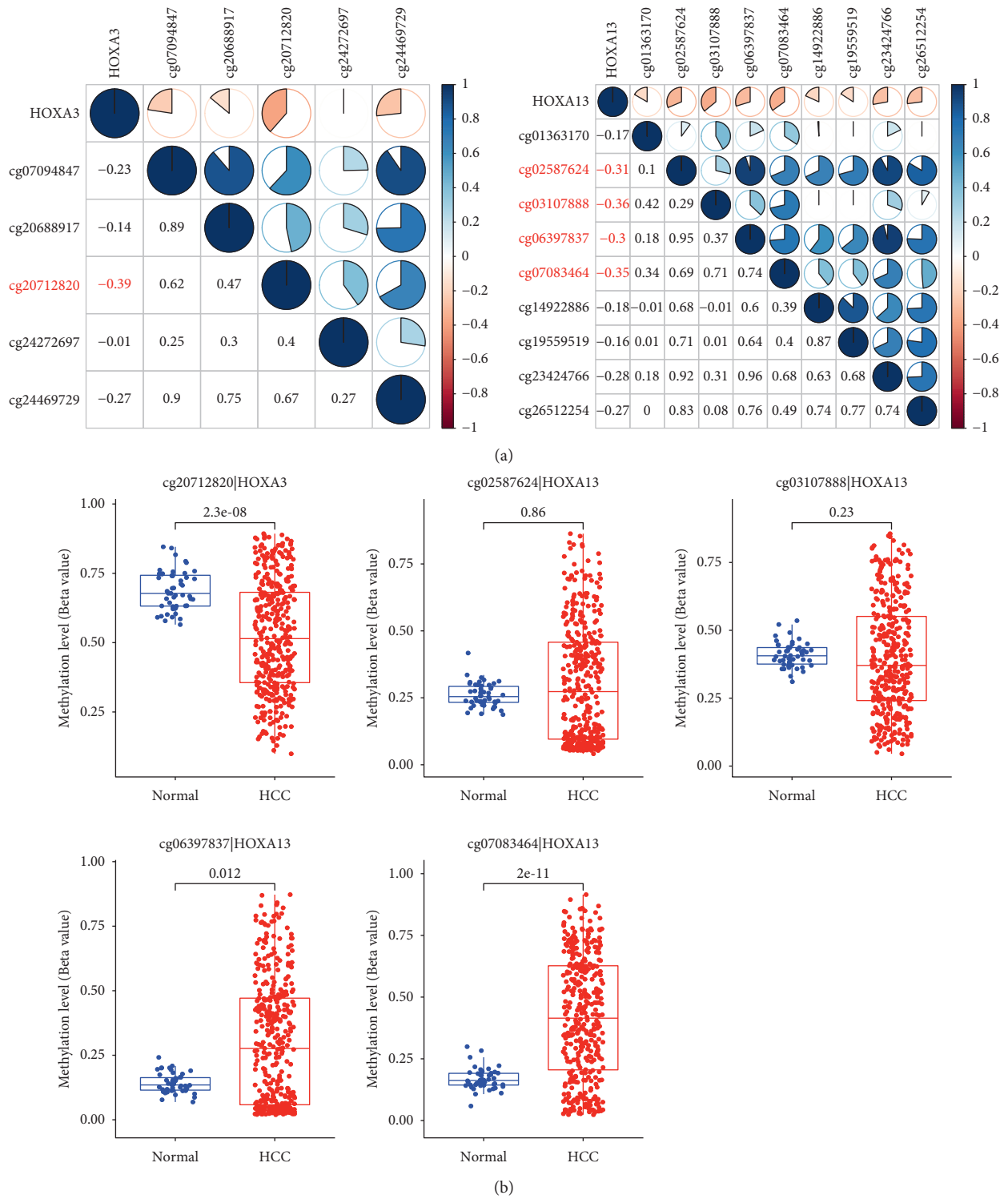

Figure 3: Methylation patterns of HOX genes in TCGA-LIHC. (a) Correlation between the methylation and expression of HOX genes. The methylation levels of 5 CpG sites were negatively correlated with the expression of the corresponding HOX gene ($r < -0.3$); (b) differences in the methylation levels of 5 CpG sites in HCC and noncancerous tissues. Three of the five CpG sites were differentially methylated positions between HCC and noncancerous tissues.

HOXC6 expression were higher than those in the tissues with low HOXC6 expression. However, the results of HOXD9 and HOXD10 were opposite to those of HOXC6. The further KM analysis showed that the patients with higher stromal scores had better overall survival (Figure 8(d)).

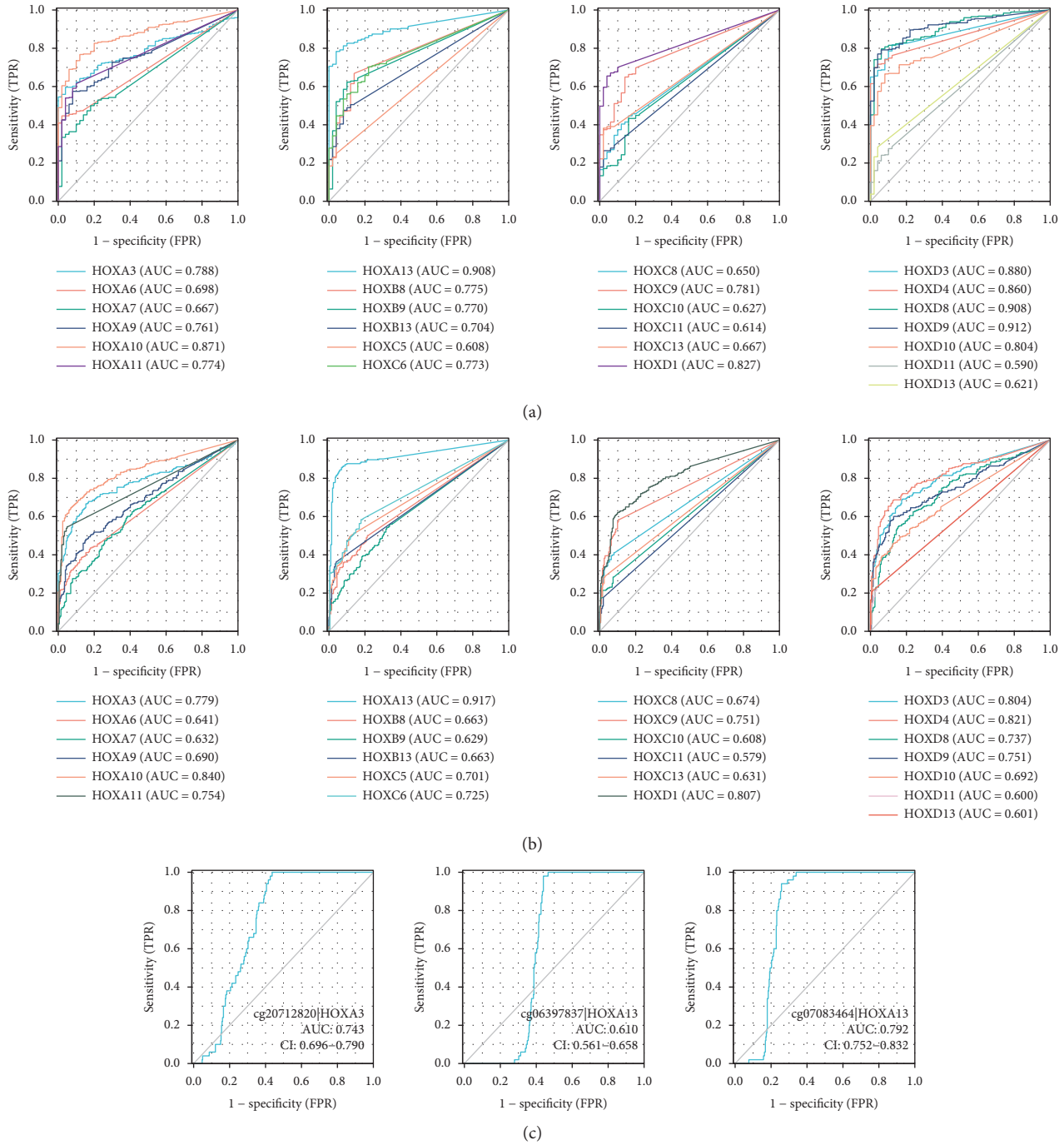

Figure 4: Diagnostic value of HOXs in HCC. ROC curves of HOX genes expression in TCGA-LIHC (a) and LIRI-JP (b); ROC curves of the methylation levels of three differentially methylated CpG sites in TCGA-LIHC (c). AUC: area under the curve.

Taken together, the role of the five prognosis-related HOXs in HCC may be achieved in part by influencing the compositions and functions of TME.

3.8. Relationship between HOXC6 and Immune-Checkpoint Inhibitor Therapy. To elucidate the relationship between HOXC6 and immune checkpoint, we first investigated the expression differences of 46 immune-checkpoint genes between tissues with low and high HOXC6 expression. As can be seen in Figure 9(a), the median expression level of most immune-checkpoint genes was higher in the tissues with high HOXC6 expression than in those with low. Then, we measured the correlation between the expression of HOXC6 and immune checkpoints (Figure 9(b)). Our results evidenced that the expression of 25 genes was correlated with HOXC6 expression. Among them, PDCD1LG2 ($r = 0.32$), CD70 ($r = 0.52$), TNFRSF8 ($r = 0.37$), and CD276

Table 1: Clinical characteristics of the HCC patients.

Characteristic	Type	*N*	Proportion (%)
Age	≤65	232	62.70
	>65	138	37.30
Gender	Male	249	67.30
	Female	121	32.70
Histologic grade	G1-2	232	62.70
	G3-4	133	35.95
	Unknown	5	1.35
Pathologic stage	Stage I-II	256	69.19
	Stage III-IV	90	24.32
	Unknown	24	6.49
Vital status	Dead	130	35.14
	Alive	240	64.86

($r = 0.35$) were closely correlated with the expression level of HOXC6. It should be noted that the expression of PD-1 (PDCD1) had little correlation ($r = 0.13$) with the expression of HOXC6, and CTLA4 expression was independent of HOXC6 expression. Meanwhile, the Pearson correlation coefficient between PD-L1 (CD274) expression and HOXC6 expression was 0.23.

Then, TIDE algorithm was employed to predict the clinical response to anti-PD1 and anti-CTLA4 treatments. The TIDE score in HCC samples with high HOXC6 expression was higher than that in tissues with low HOXC6 expression (Figure 9(c)). However, HOXC6 expression was independent of TMB.

In conclusion, the high expression of HOXC6 in HCC might suggest poor outcome of anti-PD1 and anti-CTLA4 therapy. However, some other checkpoint genes, such as CD70, were associated with HOXC6, suggesting that HOXC6 might be a potential marker for therapy targeting these immune checkpoints in HCC.

3.9. Correlation between HOXs and Anticancer Drug Sensitivity. In the past decade, sorafenib has been the only systemic agent with proven clinical efficacy for patients with advanced HCC [35]. We first compared the estimated IC50 of sorafenib in tissues with low and high expression of HOX genes. As shown in Figure 10(a), tissues with high HOXA6, B9, C5, 8, 10, and D1 expression were less sensitive to sorafenib.

Then, the NCI-60 cancerous cell lines were used to measure the correlation between HOXs expression and the sensitivity to 218 FDA approved anticancer drugs. The expression of HOXC9, D10, and D11 were positively correlated with the IC50 of lenvatinib (Figure 10(b)), which was the first new drug approved for advanced stage HCC in the first-line setting in over 10 years [36]. Meanwhile, there were also significant correlations between the IC50 values of many drugs and the expression of HOX genes (Table S4).

Taken together, the expression of HOXs may be associated with the efficacy of many anticancer drugs, which might be another factor affecting the prognosis of cancer patients.

4. Discussion

The HOX genes were discovered in the human body at the end of the 20th century, and have attracted widespread attention since then [8, 9]. Apart from their well-known roles in embryogenesis, for over 20 years, the links between HOX genes and human cancer have been comprehensively investigated. Accumulating evidence has shown the role of HOXs in many cancers [12–15]. However, the significance of most HOX members in HCC has remained unclear. To address this scientific gap, we conducted the present study, which is the first to comprehensively analyze the role of HOXs in HCC using multiple bioinformatics algorithms. We found that the increased mRNA levels of HOX genes in HCC were associated with poor prognosis. Among them, HOXA6, C6, D9, D10, and D13 were identified as independent risk factors. Functional analysis suggested that cell proliferation, cell cycle, and microenvironment regulation might be the main mechanisms of the involvement of these five HOXs in HCC development. Meanwhile, multiple HOX members (such as A13) showed excellent diagnostic value in HCC.

A previous study showed that the transcription of HOXs was silent in adult noncancerous liver tissues, whereas the expression levels of most HOXs in HCC were increased [37]. Moreover, in almost all HCC samples analyzed in another study, the mRNA content of HOXA13 in HCC tissues was over 100 times higher than that in normal liver tissues, strongly suggesting that HOXA13 was closely related to HCC [38]. In our study, the HOXA13 expression fold change was 191 in TCGA cohort and 161 in ICGC cohort after outliers' removal. Our results on the expression of HOX genes in HCC were consistent with those of previous studies. Abnormal methylation of HOX genes was also evidenced to be characteristic for some human cancers [16]. However, the published reports on the significance of methylation of HOXs in HCC are scarce. The hypothesis that HOXD3 was upregulated in HCC by methylation modification was proposed [39]. Here, we identified five CpG sites that might regulate the expression of corresponding HOX genes. Among them, the hypomethylation of cg20712820_HOXA3 and the hypermethylation of cg07083464_HOXA13 were closely related to HCC. Therefore, further research of these two CpG sites may be conducive to better understanding the role of HOXs in HCC.

Several studies have elucidated the clinical significance of these five HOXs in some cancers. HOXA6 was found to be associated with the proliferation, apoptosis, migration and invasion of CRC [40]. In ccRCC, HOXA6 inhibited cell proliferation and induced cell apoptosis by the suppression of the PI3K/AKT signaling pathway [41]. Our present results also suggested that HOXA6 may affect the proliferation and apoptosis of HCC. In an earlier investigation, the increased HOXC6 expression promoted the proliferation of HCC and reduced the sensitivity to 5-FU [42]. Meanwhile, HOXC6 promoted the invasion of HCC cells by driving EMT [43]. In addition, HOXD9 enhanced EMT and cell metastasis in HCC by ZEB1 regulation [44]. The HOXD10/RHOC/UPAR/MMPs pathway is related to the migration and

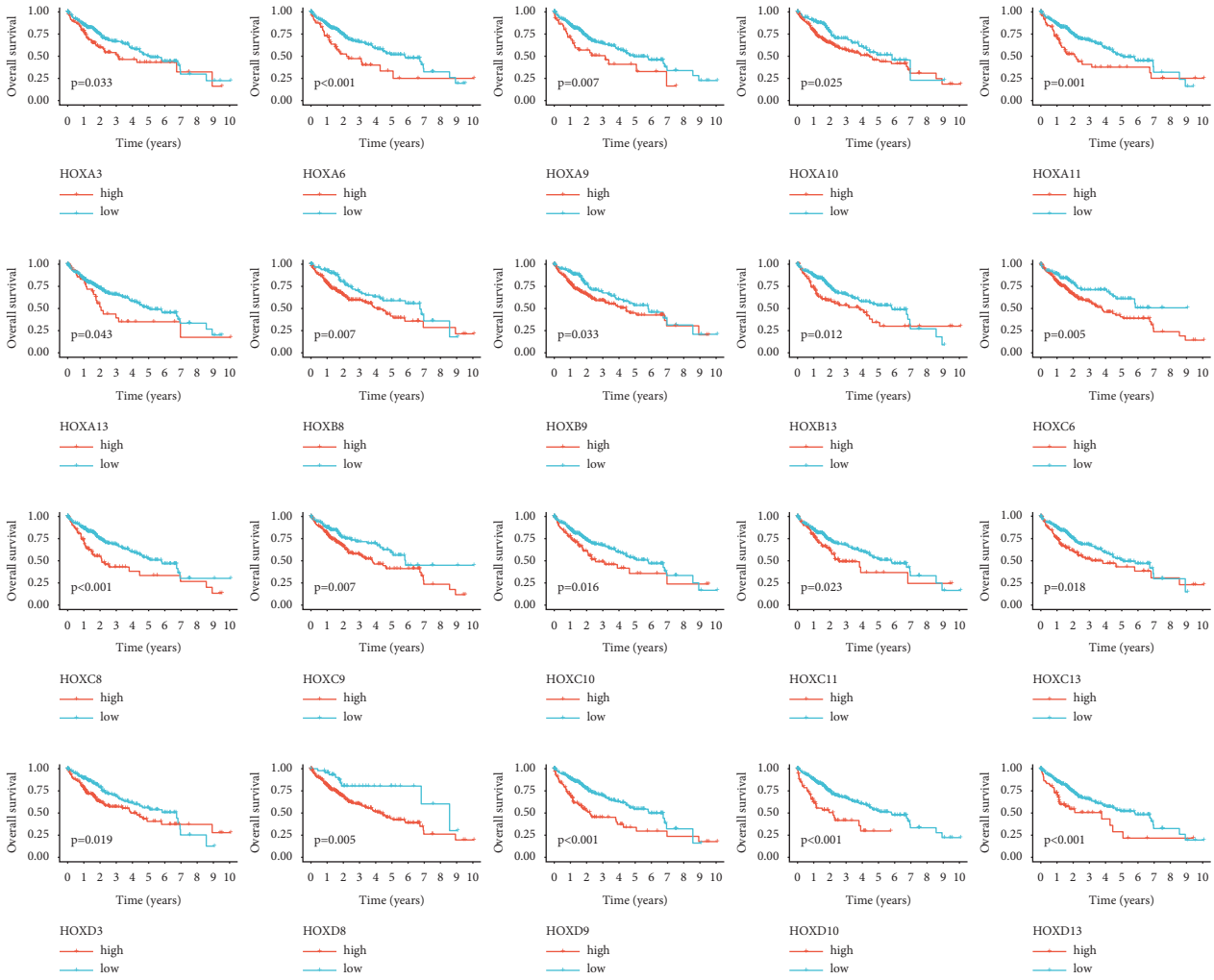

(a)

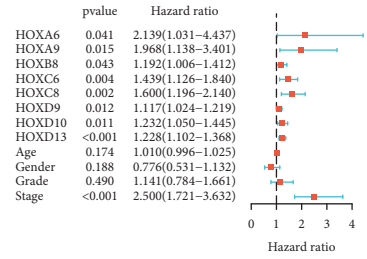

(b)

Figure 5: Continued.

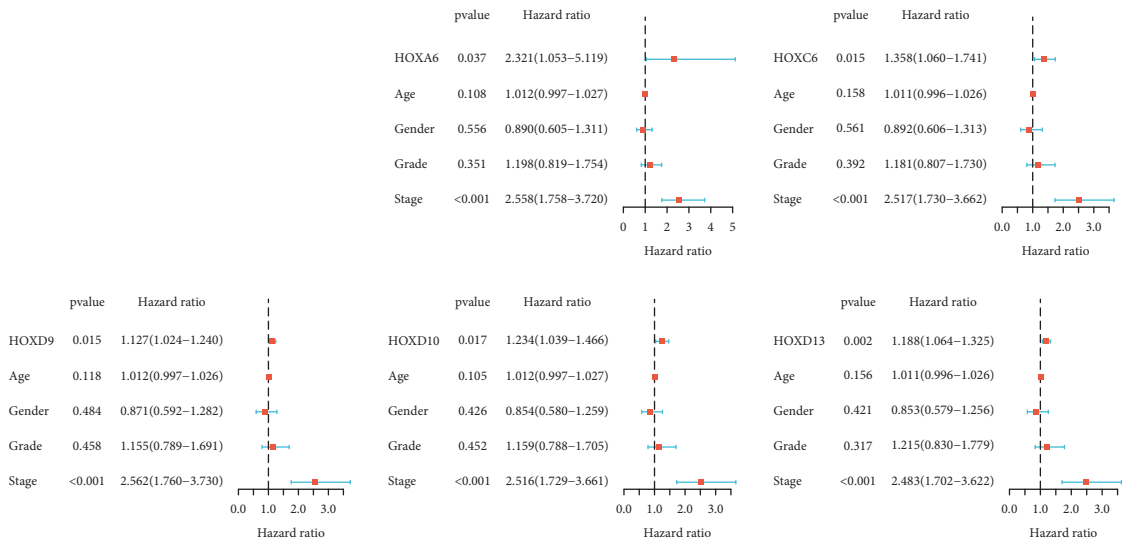

(c)

Figure 5: Prognostic value of HOXs in HCC. (a) K–M analysis for OS of patients stratified by HOX genes expression; (b) univariate Cox analysis; (c) multivariate Cox analysis of HOX family genes and clinical factors.

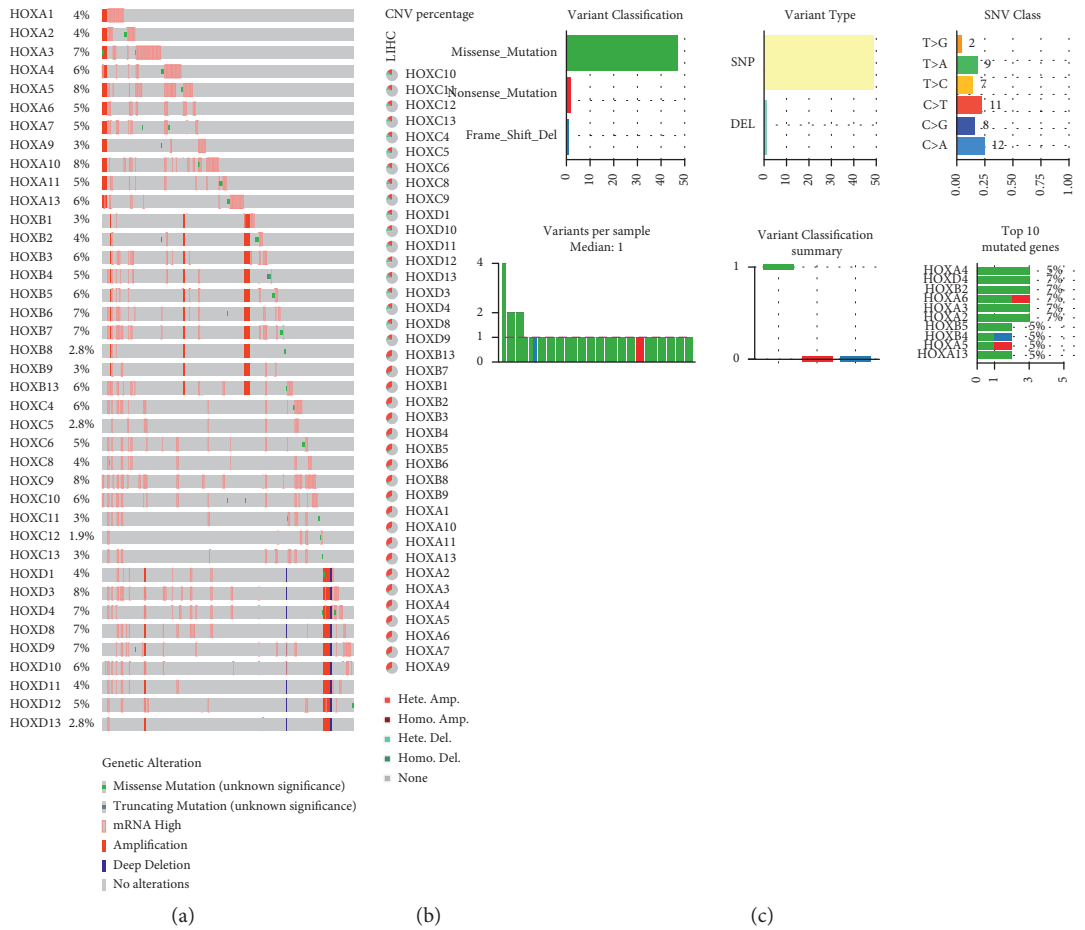

(a) (b) (c)

Figure 6: Continued.

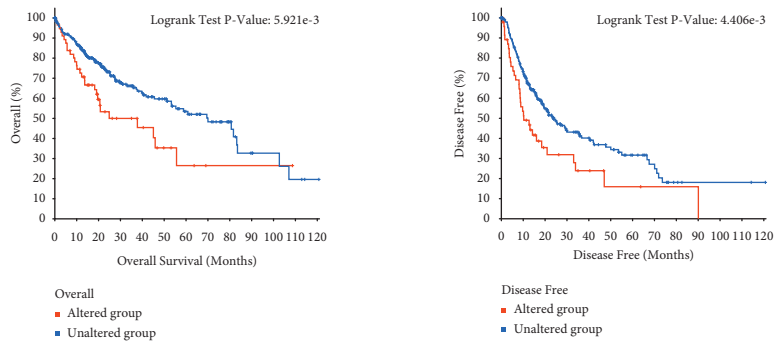

(d) (e)

Figure 6: Genetic alterations of HOXs in TCGA-LIHC. (a) The genetic alteration rate of HOXs; (b) the constitute of CNV of HOXs; (c) the details of SNV of HOXs; (d, e) Differences in OS and DFS between patients with CNV or SNV and patients without CNV or SNV.

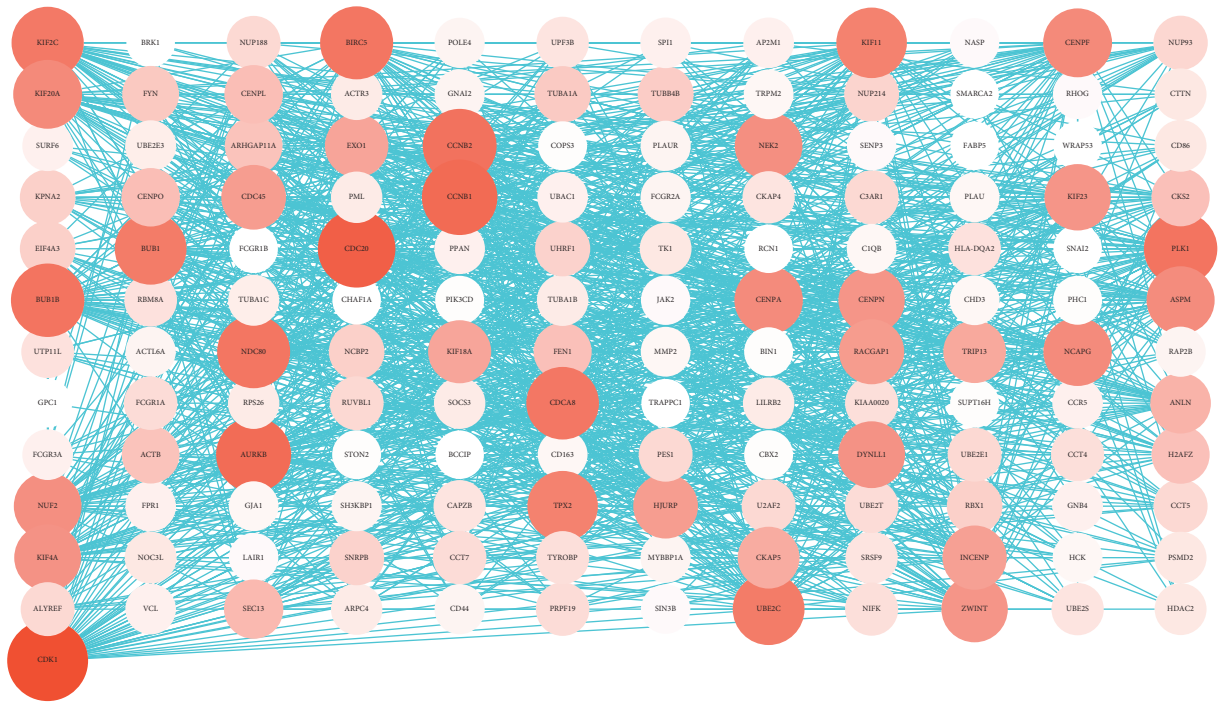

(a)

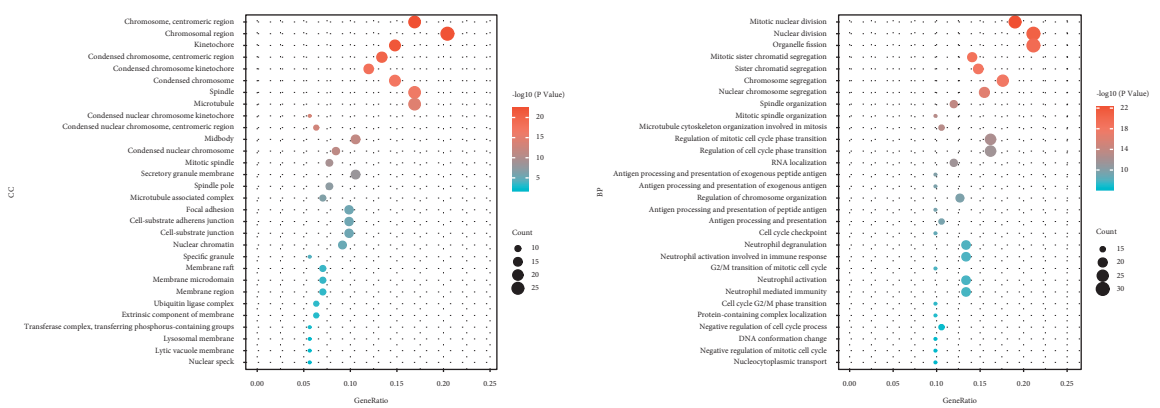

(b) (c)

Figure 7: Continued.

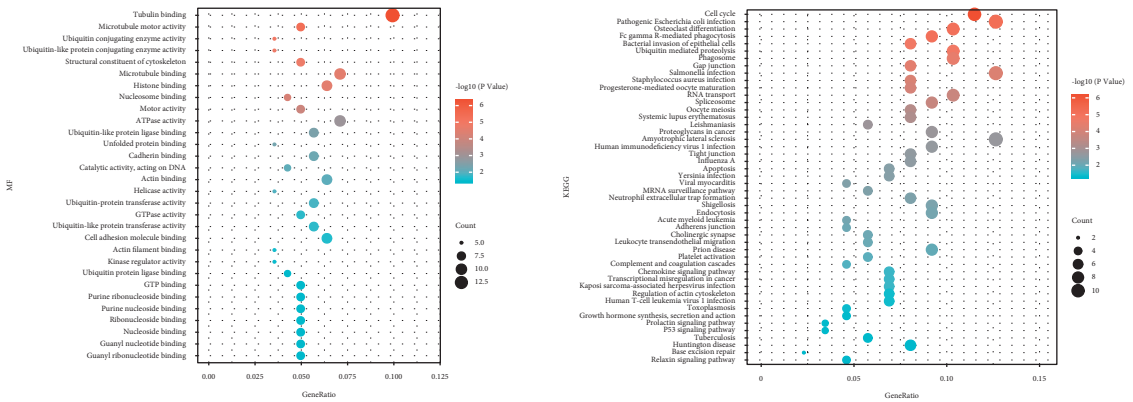

(d) (e)

Figure 7: Functional analysis of the five prognosis-related HOXs. (a) PPI network of hub genes in coexpression network; (b) cellular components; (c) biological process; (d) molecular function; (e) KEGG pathways.

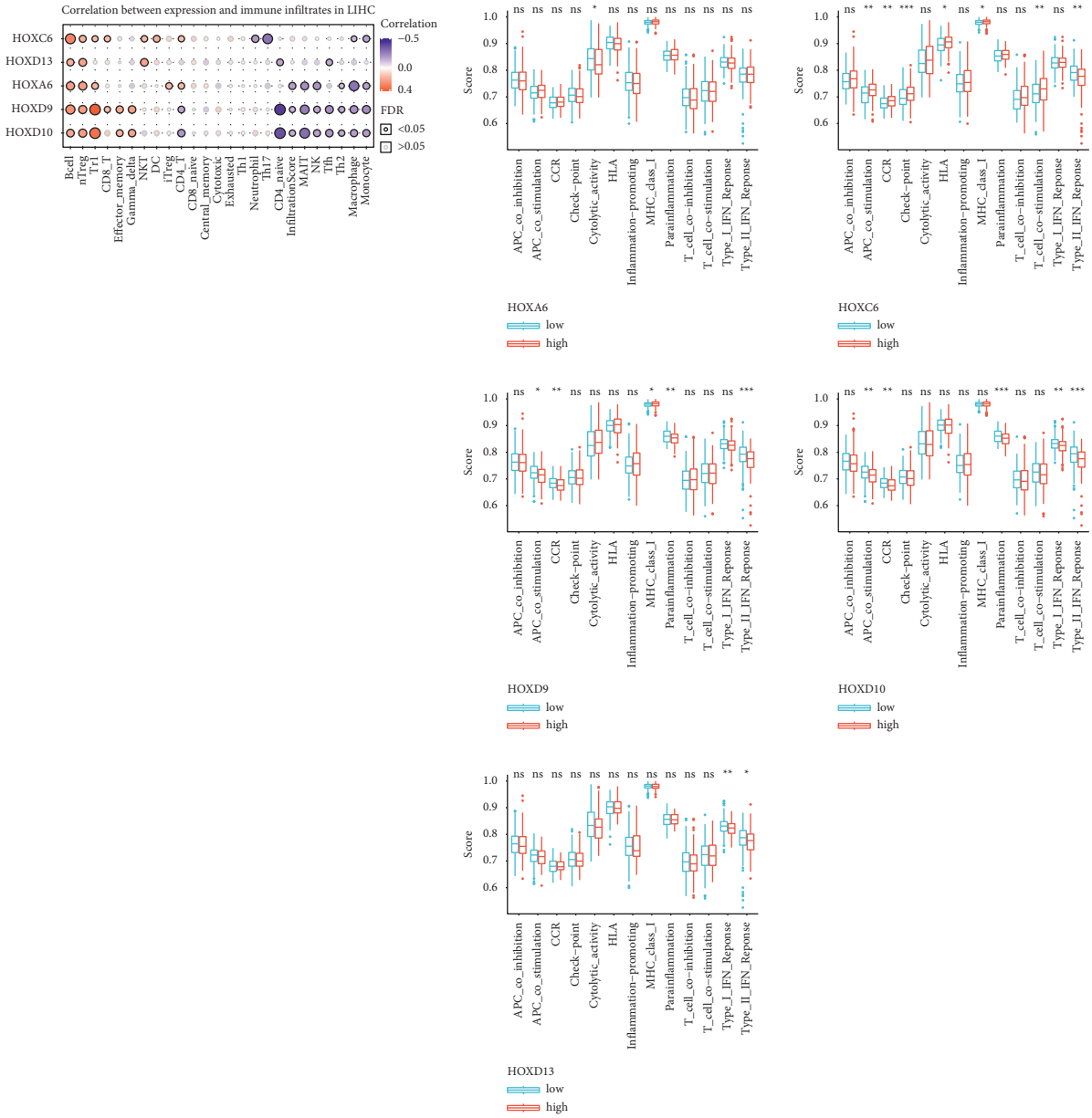

(a) (b)

Figure 8: Continued.

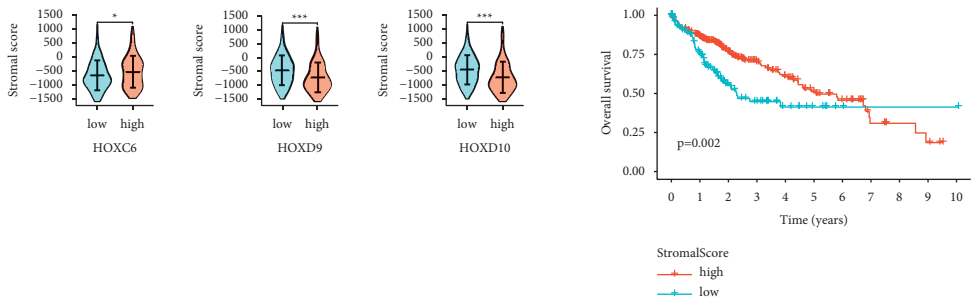

(c) (d)

Figure 8: Relationship between the five prognosis-related HOX genes and the tumor microenvironment. (a) Correlation between HOXs expression and the abundance of immune cells. The bubble size correlates with FDR; (b) differences in the ssGSEA scores of the immune functions between the tissues with different expression levels of HOXs; (c) differences in the stromal scores between the tissues with different expression levels of HOXs; (d) K–M result for the OS of the patients stratified by the stromal score. (ns: no statistical significance, $^{*}P < 0.05$, $^{**}P < 0.01$, and $^{***}P < 0.001$).

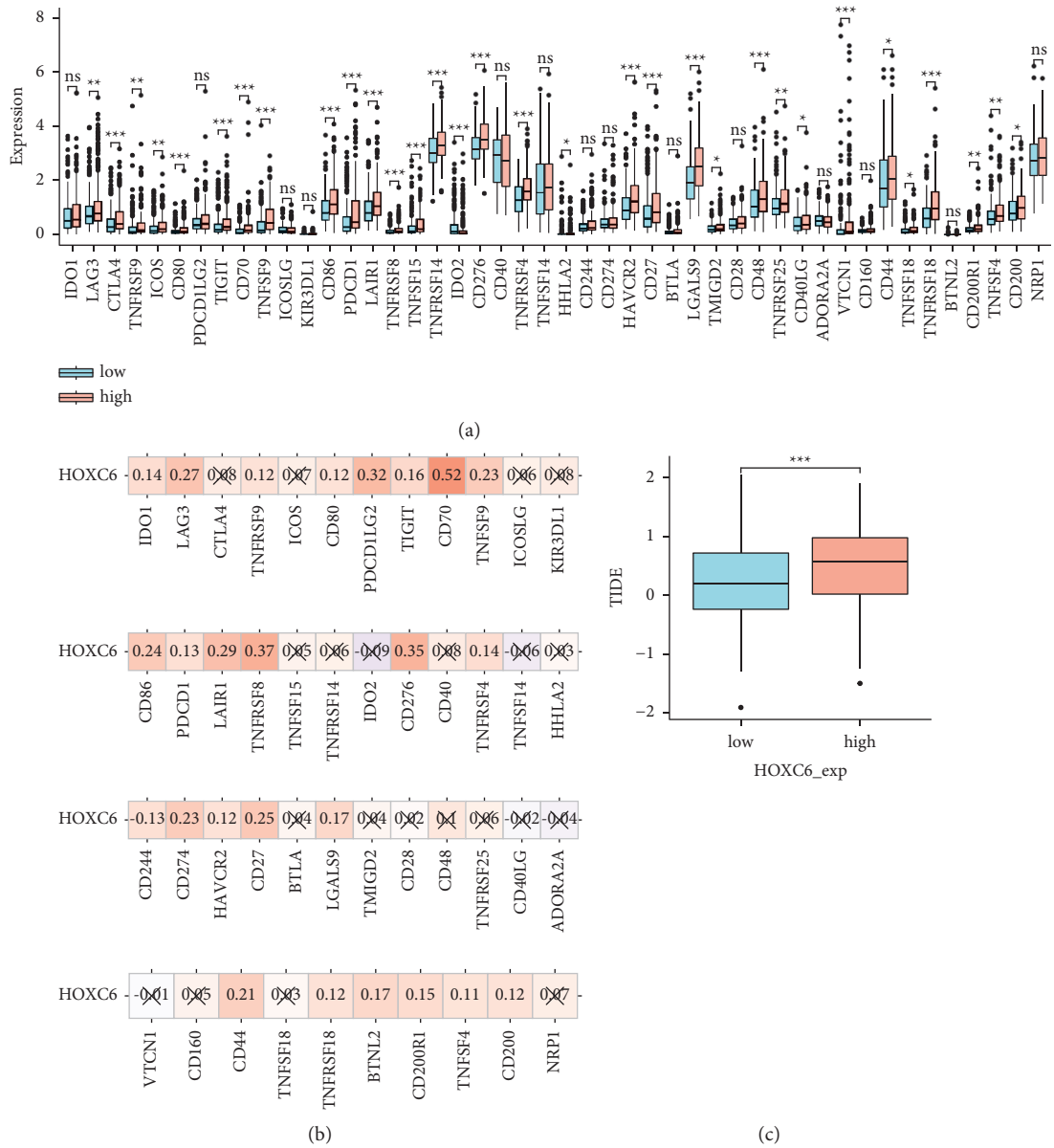

Figure 9: Relationship between HOXC6 and ICIs therapy. (a) Differences in the immune-checkpoint genes expression between HCC tissues with different expression levels of HOXC6; (b) correlation between the HOXC6 expression and the immune-checkpoint genes expression in TCGA-LIHC. The cross mark indicates $P \geq 0.05$; (c) differences in the TIDE score between the tissues with different expression levels of HOXC6 (ns: no statistical significance, $^{*}P < 0.05$, $^{**}P < 0.01$, and $^{***}P < 0.001$).

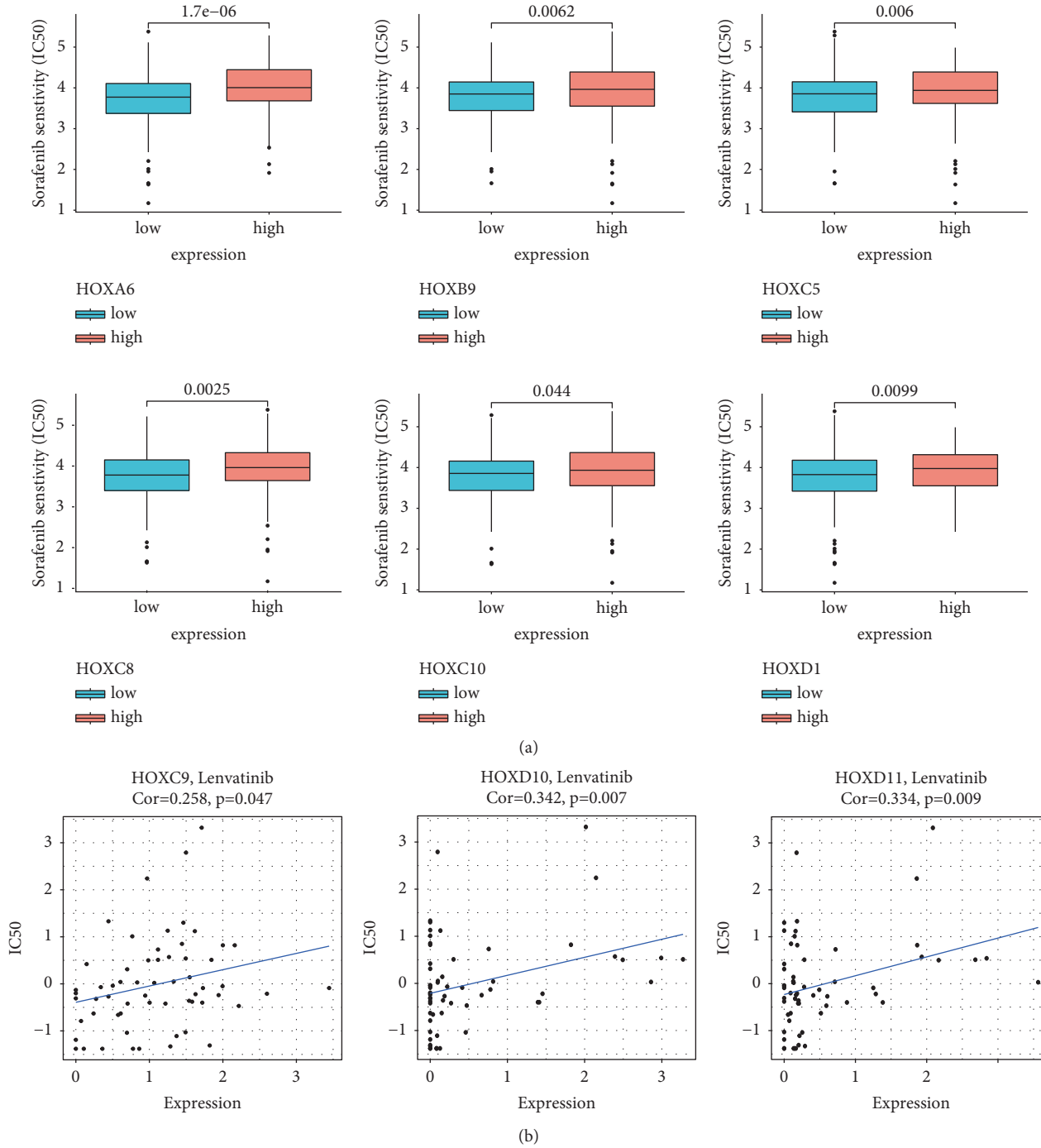

Figure 10: Relationship between the HOXs expression and anticancer drug sensitivity. (a) Differences in the estimated IC50 of sorafenib between HCC tissues with different expression levels of HOXs; (b) correlation between the HOXs expression and IC50 of lenvatinib in NCI-60 cancerous cell lines.

invasion of HCC [45]. The aforementioned *in vitro* experiments have evidenced that these HOXs are involved in the progression of HCC. We also confirmed the effect of HOXs on the clinical outcomes of HCC patients by analysis of large-sample follow-up data. Notably, the drug sensitivity data of the present study suggested that HOX genes may have guiding significance in the treatment of HCC and even pan-cancer.

The disturbance of various components of TME also contributes to the malignant features of HCC [46]. As one of the main components of TME, the abundance of immune cells, especially T cells, is closely associated with tumor progression [47]. Tregs are the major immunosuppressive and anti-inflammatory cells that can inhibit the T-cell response through IL-17 and IL-6 activities, leading to T-cell exhaustion and immune escape [48, 49]. NK cells were found

to be the main antitumor cells in the liver [50]. NKT cells can directly kill tumor cells by recognizing the CD1d antigen or by activating NK cells, and the number of NKT cells is positively correlated with OS and RFS of HCC patients [51, 52]. Here, we also focused our attention on some crucial immune response processes. Cytolytic activity (CYT) reflects the ability of cytotoxic T cells and NK cells to lyse tumor cells [53]. A recent study found that higher CYT values in HCC indicate greater immunogenicity and more favorable TME, which leads to better prognosis [54]. This might be a mechanism by which HOXA6 expression is associated with poor prognosis. The absence of the costimulatory molecules renders tumors invisible to the immune system, whereas inhibitory molecules protect tumors from effective T cells [55]. Chemokines are the bridge between inflammation and tumor, and control several aspects of tumor biology, such as immune infiltration, angiogenesis, proliferation and migration [56]. IFN response plays crucial roles in promoting host antitumor immunity and is considered to be pivotal components in the cancer-elimination phase of the cancer immunosurveillance [57]. The expression of HLA is related to tumor immune escape, and it is considered to act as a tumor suppressor [58]. It can be inferred that these HOX genes may be regulators of TME that influence the patient's clinical outcome by their effects on antitumor immunity. Nevertheless, the mechanisms through which they shape the TME remains to be further explored.

Certain limitations of our study are to be acknowledged. First, we analyzed the expression of the HOX family genes only at the mRNA level. Thus, it is necessary to further investigate the role of HOXs at the protein level. Second, our results on the molecular mechanism of HOXs need to be verified by further experiments. We will focus on addressing these issues in future studies.

5. Conclusions

In conclusion, HOX genes expression was generally upregulated and correlated with poor prognosis in HCC. HOXA6, C6, D9-10, and D13 are independent risk factors that might affect patients' prognosis through multiple pathways. The transcription and methylation characteristics of HOXs also had excellent diagnostic efficacy. Therefore, the HOX family genes might play important roles in the occurrence and development of HCC and thus could be exploited as effective biomarkers for HCC diagnosis and prognosis.

Data Availability

The data of this study were collected from the TCGA and ICGC databases.

Conflicts of Interest

The authors declare that they have no conflicts of interest.

Authors' Contributions

Zhipeng Jin and Dongxu Sun contributed equally to this work. Zhipeng Jin, Dongxu Sun, and Mengying Song designed the research. Zhipeng Jin, Dongxu Sun, Mengying Song, Huayuan Liu, and Jianping Wang collected and analyzed the data. Zhipeng Jin and Dongxu Sun carried out the research and wrote the manuscript. Wenjing Zhu and Guangjun Shi reviewed the manuscript. Guangjun Shi supervised the study. All authors have read and approved the final version of the manuscript.

Acknowledgments

This work was supported by the Key R&D Program of Shandong Province (no. 2018GSF118057). The authors express their gratitude to TCGA and ICGC databases for providing raw research data, as well as to the developers of the bioinformatic websites and algorithms employed in our study.

Supplementary Materials

Figure S1: genomic organization of human HOX genes. Figure S2: Pearson's correlation between the methylation and expression of HOX genes in TCGA-LIHC. Table S1: results of differential expression analysis of HOX genes. Table S2: results of the GO analysis. Table S3: results of the KEGG analysis. Table S4: Pearson's correlation between HOX genes expression and IC50 of anticancer drugs in NCI-60 cell lines. (*Supplementary Materials*)

References

[1] J. M. Llovet, R. K. Kelley, A. Villanueva et al., "Hepatocellular carcinoma," *Nature Reviews Disease Primers*, vol. 7, no. 1, 2021.

[2] J. D. Yang, P. Hainaut, G. J. Gores, A. Amadou, A. Plymoth, and L. R. Roberts, "A global view of hepatocellular carcinoma: trends, risk, prevention and management," *Nature Reviews Gastroenterology & Hepatology*, vol. 16, no. 10, pp. 589–604, 2019.

[3] S. Roayaie, K. Obeidat, C. Sposito et al., "Resection of hepatocellular cancer ≤2 cm: results from two Western centers," *Hepatology*, vol. 57, no. 4, pp. 1426–1435, 2013.

[4] J. M. Llovet, R. Montal, D. Sia, and R. S. Finn, "Molecular therapies and precision medicine for hepatocellular carcinoma," *Nature Reviews Clinical Oncology*, vol. 15, no. 10, pp. 599–616, 2018.

[5] M. Billeter, Y.-q. Qian, G. Otting, M. Mu¨ller, W. J. Gehring, and K. Wu¨thrich, "Determination of the three-dimensional structure of theAntennapedia homeodomain fromDrosophila in solution by1H nuclear magnetic resonance spectroscopy," *Journal of Molecular Biology*, vol. 214, no. 1, pp. 183–197, 1990.

[6] E. B. Lewis, "A gene complex controlling segmentation in Drosophila," *Nature*, vol. 276, no. 5688, pp. 565–570, 1978.

[7] C. B. Bridges, "Genetical and cytological proof of non-disjunction of the fourth chromosome of *Drosophila melanogaster*," *Proceedings of the National Academy of Sciences*, vol. 7, no. 7, pp. 186–192, 1921.

[8] J. Nourse, J. D. Mellentin, N. Galili et al., "Chromosomal translocation t (1;19) results in synthesis of a homeobox fusion mRNA that codes for a potential chimeric transcription factor," *Cell*, vol. 60, no. 4, pp. 535–545, 1990.

[9] M. P. Kamps, C. Murre, X.-h. Sun, and D. Baltimore, "A new homeobox gene contributes the DNA binding domain of the t

(1;19) translocation protein in pre-B ALL," *Cell*, vol. 60, no. 4, pp. 547–555, 1990.

[10] A. Graham, N. Papalopulu, and R. Krumlauf, "The murine and Drosophila homeobox gene complexes have common features of organization and expression," *Cell*, vol. 57, no. 3, pp. 367–378, 1989.

[11] F. H. Ruddle, J. L. Bartels, K. L. Bentley, C. Kappen, M. T. Murtha, and J. W. Pendleton, "Evolution of hox genes," *Annual Review of Genetics*, vol. 28, no. 1, pp. 423–442, 1994.

[12] S. Bhatlekar, J. Z. Fields, and B. M. Boman, "HOX genes and their role in the development of human cancers," *Journal of Molecular Medicine (Berlin)*, vol. 92, no. 8, pp. 811–823, 2014.

[13] A. Paço, S. Aparecida de Bessa Garcia, J. Leitão Castro, A. R. Costa-Pinto, and R. Freitas, "Roles of the HOX proteins in cancer invasion and metastasis," *Cancers*, vol. 13, no. 1, p. 10, 2020.

[14] S. Bhatlekar, J. Z. Fields, and B. M. Boman, "Role of HOX genes in stem cell differentiation and cancer," *Stem Cells International*, vol. 2018, Article ID 3569493, 15 pages, 2018.

[15] B. Li, Q. Huang, and G.-H. Wei, "The role of HOX transcription factors in cancer predisposition and progression," *Cancers*, vol. 11, no. 4, p. 528, 2019.

[16] A. Paço, S. A. de Bessa Garcia, and R. Freitas, "Methylation in *HOX* clusters and its applications in cancer therapy," *Cells*, vol. 9, no. 7, p. 1613, 2020.

[17] Y. Dang, J. Chen, W. Feng et al., "Interleukin 1β-mediated HOXC10 overexpression promotes hepatocellular carcinoma metastasis by upregulating PDPK1 and VASP," *Theranostics*, vol. 10, no. 8, pp. 3833–3848, 2020.

[18] L. Quagliata, M. S. Matter, S. Piscuoglio et al., "Long noncoding RNA HOTTIP/HOXA13 expression is associated with disease progression and predicts outcome in hepatocellular carcinoma patients," *Hepatology*, vol. 59, no. 3, pp. 911–923, 2014.

[19] M. E. Ritchie, B. Phipson, D. Wu et al., "Limma powers differential expression analyses for RNA-sequencing and microarray studies," *Nucleic Acids Research*, vol. 43, no. 7, p. e47, 2015.

[20] T. Wei and V. Simko, "R Package "corrplot": visualization of a correlation matrix (version 0.84)," 2017.

[21] E. Cerami, J. Gao, U. Dogrusoz et al., "The cBio cancer genomics portal: an open platform for exploring multidimensional cancer genomics data: figure 1," *Cancer Discovery*, vol. 2, no. 5, pp. 401–404, 2012.

[22] C.-J. Liu, F.-F. Hu, M.-X. Xia, L. Han, Q. Zhang, and A.-Y. Guo, "GSCALite: a web server for gene set cancer analysis," *Bioinformatics*, vol. 34, no. 21, pp. 3771-3772, 2018.

[23] D. S. Chandrashekar, B. Bashel, S. A. H. Balasubramanya et al., "UALCAN: a portal for facilitating tumor subgroup gene expression and survival analyses," *Neoplasia*, vol. 19, no. 8, pp. 649–658, 2017.

[24] D. Szklarczyk, A. L. Gable, K. C. Nastou et al., "The STRING database in 2021: customizable protein-protein networks, and functional characterization of user-uploaded gene/measurement sets," *Nucleic Acids Research*, vol. 49, no. D1, pp. D605–D612, 2021.

[25] G. Su, J. H. Morris, B. Demchak, and G. D. Bader, "Biological network exploration with cytoscape 3," *Current Protocols in Bioinformatics*, vol. 47, no. 1, pp. 8.13.1–8.13.24, 2014.

[26] G. Yu, L.-G. Wang, Y. Han, and Q.-Y. He, "clusterProfiler: an R package for comparing biological themes among gene clusters," *OMICS: A Journal of Integrative Biology*, vol. 16, no. 5, pp. 284–287, 2012.

[27] Y. R. Miao, Q. Zhang, Q. Lei et al., "ImmuCellAI: a unique method for comprehensive T-cell subsets abundance prediction and its application in cancer immunotherapy," *Advanced Science*, vol. 7, no. 7, Article ID 1902880, 2020.

[28] S. Hänzelmann, R. Castelo, and J. Guinney, "GSVA: gene set variation analysis for microarray and RNA-seq data," *BMC Bioinformatics*, vol. 14, no. 1, 2013.

[29] K. Yoshihara, M. Shahmoradgoli, E. Martínez et al., "Inferring tumour purity and stromal and immune cell admixture from expression data," *Nature Communications*, vol. 4, no. 1, p. 2612, 2013.

[30] P. Jiang, S. Gu, D. Pan et al., "Signatures of T cell dysfunction and exclusion predict cancer immunotherapy response," *Nature Medicine*, vol. 24, no. 10, pp. 1550–1558, 2018.

[31] P. Geeleher, N. Cox, and R. S. Huang, "pRRophetic: an R package for prediction of clinical chemotherapeutic response from tumor gene expression levels," *PLoS One*, vol. 9, no. 9, Article ID e107468, 2014.

[32] R. H. Shoemaker, "The NCI60 human tumour cell line anticancer drug screen," *Nature Reviews Cancer*, vol. 6, no. 10, pp. 813–823, 2006.

[33] J. N. Weinstein, "Cell lines battle cancer," *Nature*, vol. 483, no. 7391, pp. 544-545, 2012.

[34] W. C. Reinhold, M. Sunshine, H. Liu et al., "CellMiner: a web-based suite of genomic and pharmacologic tools to explore transcript and drug patterns in the NCI-60 cell line set," *Cancer Research*, vol. 72, no. 14, pp. 3499–3511, 2012.

[35] S. Faivre, L. Rimassa, and R. S. Finn, "Molecular therapies for HCC: looking outside the box," *Journal of Hepatology*, vol. 72, no. 2, pp. 342–352, 2020.

[36] M. Kudo, R. S. Finn, S. Qin et al., "Lenvatinib versus sorafenib in first-line treatment of patients with unresectable hepatocellular carcinoma: a randomised phase 3 non-inferiority trial," *The Lancet*, vol. 391, no. 10126, pp. 1163–1173, 2018.

[37] M. Kanai, J. Hamada, M. Takada et al., "Aberrant expressions of HOX genes in colorectal and hepatocellular carcinomas," *Oncology Reports*, vol. 23, no. 3, pp. 843–851, 2010.

[38] C. Cillo, G. Schiavo, M. Cantile et al., "The HOX gene network in hepatocellular carcinoma," *International Journal of Cancer*, vol. 129, no. 11, pp. 2577–2587, 2011.

[39] Y. Yang, L. Zhao, B. Huang et al., "A new approach to evaluating aberrant DNA methylation profiles in hepatocellular carcinoma as potential biomarkers," *Scientific Reports*, vol. 7, no. 1, Article ID 46533, 2017.

[40] S. Wu, F. Wu, and Z. Jiang, "Effect of HOXA6 on the proliferation, apoptosis, migration and invasion of colorectal cancer cells," *International Journal of Oncology*, vol. 52, no. 6, pp. 2093–2100, 2018.

[41] F. Wu, S. Wu, H. Tong, W. He, and X. Gou, "HOXA6 inhibits cell proliferation and induces apoptosis by suppressing the PI3K/Akt signaling pathway in clear cell renal cell carcinoma," *International Journal of Oncology*, vol. 54, no. 6, pp. 2095–2105, 2019.

[42] C. J. Sui, F. Xu, W. F. Shen et al., "MicroRNA-147 suppresses human hepatocellular carcinoma proliferation migration and chemosensitivity by inhibiting HOXC6," *American journal of cancer research*, vol. 6, no. 12, pp. 2787–2798, 2016.

[43] P.-D. Li, P. Chen, X. Peng, C. Ma, W.-J. Zhang, and X.-F. Dai, "HOXC6 predicts invasion and poor survival in hepatocellular carcinoma by driving epithelial-mesenchymal transition," *Aging*, vol. 10, no. 1, pp. 115–130, 2018.

[44] X. Lv, L. Li, L. Lv et al., "HOXD9 promotes epithelial-mesenchymal transition and cancer metastasis by ZEB1

regulation in hepatocellular carcinoma," *Journal of Experimental & Clinical Cancer Research*, vol. 34, no. 1, p. 133, 2015.

[45] C.-g. Liao, L.-m. Kong, P. Zhou et al., "miR-10b is overexpressed in hepatocellular carcinoma and promotes cell proliferation, migration and invasion through RhoC, uPAR and MMPs," *Journal of Translational Medicine*, vol. 12, no. 1, p. 234, 2014.

[46] V. Hernandez–Gea, S. Toffanin, S. L. Friedman, and J. M. Llovet, "Role of the microenvironment in the pathogenesis and treatment of hepatocellular carcinoma," *Gastroenterology*, vol. 144, no. 3, pp. 512–527, 2013.

[47] T. F. Greten, X. W. Wang, and F. Korangy, "Current concepts of immune based treatments for patients with HCC: from basic science to novel treatment approaches," *Gut*, vol. 64, no. 5, pp. 842–848, 2015.

[48] H. Zhang, Z. Jiang, and L. Zhang, "Dual effect of T helper cell 17 (Th17) and regulatory T cell (Treg) in liver pathological process: from occurrence to end stage of disease," *International Immunopharmacology*, vol. 69, pp. 50–59, 2019.

[49] Y. Kondo and T. Shimosegawa, "Significant roles of regulatory T cells and myeloid derived suppressor cells in hepatitis B virus persistent infection and hepatitis B virus-related HCCs," *International Journal of Molecular Sciences*, vol. 16, no. 2, pp. 3307–3322, 2015.

[50] G. F. Sonnenberg and M. R. Hepworth, "Functional interactions between innate lymphoid cells and adaptive immunity," *Nature Reviews Immunology*, vol. 19, no. 10, pp. 599–613, 2019.

[51] E. Vivier, S. Ugolini, D. Blaise, C. Chabannon, and L. Brossay, "Targeting natural killer cells and natural killer T cells in cancer," *Nature Reviews Immunology*, vol. 12, no. 4, pp. 239–252, 2012.

[52] Y.-S. Xiao, Q. Gao, X.-N. Xu et al., "Combination of intratumoral invariant natural killer T cells and interferon-gamma is associated with prognosis of hepatocellular carcinoma after curative resection," *PLoS One*, vol. 8, no. 8, Article ID e70345, 2013.

[53] M. S. Rooney, S. A. Shukla, C. J. Wu, G. Getz, and N. Hacohen, "Molecular and genetic properties of tumors associated with local immune cytolytic activity," *Cell*, vol. 160, no. 1-2, pp. 48–61, 2015.

[54] H. Takahashi, T. Kawaguchi, L. Yan et al., "Immune cytolytic activity for comprehensive understanding of immune landscape in hepatocellular carcinoma," *Cancers*, vol. 12, no. 5, p. 1221, 2020.

[55] X. Zang and J. P. Allison, "The B7 family and cancer therapy: costimulation and coinhibition," *Clinical Cancer Research*, vol. 13, no. 18, pp. 5271–5279, 2007.

[56] E. M. Borroni, B. Savino, R. Bonecchi, and M. Locati, "Chemokines sound the alarmin: the role of atypical chemokine in inflammation and cancer," *Seminars in Immunology*, vol. 38, pp. 63–71, 2018.

[57] G. P. Dunn, C. M. Koebel, and R. D. Schreiber, "Interferons, immunity and cancer immunoediting," *Nature Reviews Immunology*, vol. 6, no. 11, pp. 836–848, 2006.

[58] E. Pujadas and C. Cordon-Cardo, "The human leukocyte antigen as a candidate tumor suppressor," *Cancer Cell*, vol. 39, no. 5, pp. 586–589, 2021.

Hindawi
Journal of Oncology
Volume 2022, Article ID 1459636, 11 pages
https://doi.org/10.1155/2022/1459636

Research Article

Ai-Tong-An-Gao-Ji and Fisetin Inhibit Tumor Cell Growth in Rat CIBP Models by Inhibiting the AKT/HIF-1α Signaling Pathway

Jing Wang, Zonglang Lai, Xin Zhou, Song Na, Liufan Zhang, and Jun Cheng

Department of Oncology, Chongqing Hospital of Traditional Chinese Medicine, Chongqing 400021, China

Correspondence should be addressed to Jun Cheng; chengjunnn@outlook.com

Received 16 November 2021; Revised 29 December 2021; Accepted 12 January 2022; Published 16 February 2022

Academic Editor: Guo Chen

Background. Ai-Tong-An-Gao-Ji (ATAGJ) has been extensively applied for acute bone cancer pain treatment with a satisfactory efficacy, while the specific mechanisms remain unclear and require further investigation. *Methods*. Overlapped genes of ATAGJ and CIBP obtained from SwissTargetPrediction website and GeneCards database were presented as a Venn diagram. A network diagram of drug-component-target was further established using the Cytoscape 3.6.0 software. The effect of fisetin on Walker 256 cell proliferation was observed by clone formation assay and EDU assay, and the interaction between fisetin and AKT was revealed using the immunoprecipitation assay. Effects of fisetin on AKT/HIF-1α signaling pathway in Walker 256 cells were ultimately detected using Western blot and qPCR assays. *Results*. The key component fisetin and core target gene AKT were sorted out using the drug-component-target network with a binding energy between fisetin and AKT less than −5 kcal/mol. Clone formation assay and EDU assay showed that fisetin substantially suppressed the proliferation of Walker 256 cells. Immunoprecipitation assay results revealed that the combination of fisetin and AKT decreased the level of AKT/HIF-1α signaling pathway of Walker 256 cells. *Conclusions*. The fisetin of ATAGJ can markedly suppress Walker 256 cells, and the mechanisms may be intimately associated with the combination of fisetin and AKT. Furthermore, fisetin decreased the level of p-AKT and inhibited the expression of the AKT/HIF-1α signaling pathway.

1. Introduction

As the treatment techniques for cancers advance, the five-year survival rate of cancer patients has been substantially improved. However, cancer-induced bone pain (CIBP) is ongoing and bothers the patients seriously, which greatly reduces their quality of life [1, 2]. Numerous studies have revealed that 55% of cancer patients and 66% of patients with advanced, metastatic, or terminal disease fall victim to CIBP [3].

CIBP represents the most common form of pain in cancer patients. About two-thirds of advanced cancer patients have a propensity to bone metastasis, which is reckoned to be a frequently encountered cause of cancer pain [4–6]. Currently, most strategies for CIBP treatment focuses on opioids, radiation therapy, and chemotherapy [7]. Unfortunately, the administration of opioids causes serious side effects, which often attenuates the therapeutic effect and the quality of life for cancer patients. A bunch of treatment methods based on traditional Chinese medicine including internal administration of decoction, external application, and acupuncture has achieved satisfactory clinical effects for cancer pain treatment. These therapeutic methods have the advantages of quick onset, safety, nontoxic side effects, and easy acceptance by patients [8, 9].

ATAGJ acts as effective preparation for CIBP management, and the main components of ATAGJ consist of borneol, spina gleditsiae, pillworm, faeces trogopterori, resina draconis, and semen strychni. The compound fisetin was contained in the spina gleditsiae, and it has been proved to play a role in antitumor by inhibiting tumor cell proliferation, inducing apoptosis, and mediating tumor cell migration [10–13].

Hypoxia-inducible factor-1α (HIF-1α) is a transcription factor at an extensive presence in mammals and humans under low oxygen levels. It responds to hypoxic tissue cells

by elevating the expression of hypoxia-inducible genes, which represents the key link of adaptation to hypoxia. HIF-1α protein is highly expressed in most tumor tissues and the corresponding metastases. AKT pathway is a regulatory pathway of HIF-1α. AKT mainly regulates the changes of HIF-1α proteins [14–16].

We predicted active ingredients and related targets of cancer pain using the ointment in a network pharmacological approach. The targets of active ingredients and the target genes of CIBP were overlapped to identify core targets; GO analysis and KEGG pathway enrichment were subsequently conducted. The main components and core targets were selected for molecular docking. Additionally, whether fisetin acted on the proliferation and migration of Walker 256 cells were investigated by cloning, EDU, and transwell experiments, and the effects of fisetin on the AKT/HIF-1α signaling pathway Walker 256 cells were investigated by Western blot and qPCR assays.

2. Methods

2.1. Experimental Herbal Formulation. ATAGJ consists of borneol (BP), spina gleditsiae (ZJC), pillworm (SF), faeces trogopterori (WLZ), resina draconis (XJ), and semen strychni (MQZ). The ATAGJ administration dosage included low (10 g/d), medium (20 g/d), and high (30 g/d) doses. Female SD rats were employed as the laboratory animals and they were randomly classified into 5 groups: a sham group, a model group, a low dose ATAGJ group, a medium dose ATAGJ group, and a high dose ATAGJ group, with 10 rats in each group. The modeling procedures were described as follows: Walker 256 breast cancer cell lines were selected as the model cells. The rats were anesthetized with 0.3% sodium pentobarbital (1 ml/100 g). The white patellar ligament was exposed on the skin. The upper part of the tibia inferior to the white patellar ligament of the right hind limb was perforated. After the penetration into the bone marrow cavity, 4 μL Walker 256 cell suspension at a concentration of 4×10^4 cells/mL was injected into the model group. The rats were administered with low (10 g/day), medium (20 g/day), and high doses (30 g/day) of ATAGJ for 10 h and lasted for 14 d.

2.2. Cell Culture and Treatment. The Walker 256 breast cancer cell line was selected using 89% high glucose medium containing various amino acids and glucose (H-DMEM, High glucose Dulbecco's Modified Eagle Medium) + 10% fetal bovine serum (FBS) + 1% penicillin/streptomycin (P/S) [17].

Culture conditions were set at 37°C, 95% air, and 5% carbon dioxide. These cells were treated with fisetin (10 μM, 20 μM, and 30 μM) and Cisplatin (5 μM) in the positive control group for 24 h.

2.3. Network Pharmacology Analysis. Based on the principle of network pharmacology, the main components and targets of ATAGJ were predicted. The active ingredients of ATAGJ (BP, ZJC, SF, WLZ, XJ, and MQZ) were detected from the TCMSP website (https://tcmspw.com/tcmsp.php). Related targets were predicted and exported from the SwissTargetPrediction website. Human CIBP related genes were collected from the gene disease database, a PPI protein interaction network diagram was constructed using String, and the diagram network of drug-component-target was established using the Cytoscape 3.6.0 software. GO analysis and KEGG pathway enrichment were performed on 92 targets by Cytoscape ClueGO, and enrichment analysis results were visualized ultimately.

2.4. Molecular Docking. The 3D structure of fisetin was initially obtained from the TMMSP website. Meanwhile, the 3D structures of the key targets AKT and VEGFA were collected from the Protein Data Bank (https://www.rcsb.org/pdb). The AutoDock 4.2.6 software was used to hydrogenate the receptor protein and to calculate the charge treatment. The molecular docking between the receptor protein and the ligand small molecule was subsequently carried out by AutoDock Vina 1.1.2. The confirmation was obtained by docking and the binding energy was scored. The best binding energy was obtained and analyzed. PyMOL was used to visualize the interaction between the receptor protein and the ligand small molecule.

2.5. Paw Withdrawal Threshold (PWT). The PWT of rats in each group was assessed every 7 days. During the process, the rats were put into a plexiglass cage equipped with a metal screen at the bottom for 5 min. The central skin of the hind paw at the molding side of the rats was vertically stimulated with Von Frey cilia mechanical stimulation probe so that the cilia were bent to the point where the rats had a paw constriction reflex. If there was no paw constriction reflex, a more intense cilia mechanical stimulation probe was replaced. Starting from 0.6 g, the stimulation of each intensity was 5 times and the mechanical stimulation interval was 15 s. The minimum ciliate stimulation probe strength was recorded as PWT with an upper limit of 15.0 g when 3 paw constriction reflexes occurred in the 5 tests [18].

2.6. Transwell Assay. The Transwell assay was performed to evaluate the capability of cell invasion. Cells of 6×10^4 were initially followed by a cycle of washing with PBS and resuspended in 200 ml of serum-free medium. The upper Transwell chamber was precoated with Matrigel before the cells were supplemented. Simultaneously, the lower chamber was supplemented with a medium containing 10% FBS for incubation in 5% CO_2 at 37°C for 24 h, followed by the addition of 4% paraformaldehyde (PFA) for fixation 15 min and stained for 3 min using crystal violet. Quantification was ultimately carried out using Axio Imager A2.

2.7. Clone Formation Assay. Cells at 1×10^3 were planted in each well of 6-well plates and cultured at 37°C 5% CO_2 for 14 d. The medium was refreshed every 3 days. Following two cycles of washing of the cell colonies using PBS, the cells were fixed with 4% paraformaldehyde for 30 min before

being stained with 0.1% crystal violet for 20 min. Cell clone was triplicated three times.

2.8. EdU Assay. To perform the EdU assay, Walker 256 cells were inoculated into a 24-well plate. Following the instructions of the EdU kit, 2 × EdU reaction solution was prepared and added to a 24-well plate. Following incubation in the reaction solution for 2 h in the dark, the cells were fixed at room temperature for 20 min with 4% paraformaldehyde and added with 500 μL 0.3% Triton X-100. PBS was subsequently added for rinsing 3 times when the reaction lasted 10 min at room temperature. AZIDE 555-Click reaction solution was subsequently prepared, 200 μL of the solution was added to each well, and followed by incubation in the dark at room temperature for 30 min. The reaction solution was removed after three cycles of washing with PBS, and the nucleus was restained by Hoechst and then followed by the immunofluorescence technique.

2.9. Coimmunoprecipitation Assay. The kit used for biotin labeling fisetin was EZ-Link TM Biotin-LC-Hydrazide (Thermo Scientific). All procedures were carried out according to the operating instructions. The biotin-labeled fisetin was inoculated into Walker 256 cell suspension, and the cells were collected by centrifugation after 24 h of culture. Precooled coimmunoprecipitation assay A buffer was added. Cells were collected and centrifuged. The beads were washed twice with PBS, protein A agarose beads were added and centrifuged. Rabbit antibody was supplemented, and the antigen-antibody mixture was slowly shaken at 4°C overnight. Protein A agarose beads were subsequently added and shaken slowly at 4°C overnight. The agarose bead-antigen antibody complex was ultimately centrifuged, and electrophoresis was performed.

2.10. Western Blot Assay. Cells were collected and cleaved with immunoprecipitation assay lysate. After centrifugation at 13,000 rpm 4°C for 20 min, the supernatant was collected, and the total protein was separated utilizing 10% SDS-PAGE. Then the protein was transferred to a PVDF membrane, sealed with skimmed milk at room temperature for 1 h, and TBST was used to wash 3 times. Primary antibody was added for incubation at 4°C overnight, and second antibody was supplemented for incubation on the next day for 1 h. Finally, ECL color development was performed. The primary antibodies were listed below: anti-AKT, anti-p-AKT, anti-HIF-1α, anti-VEGF, and β-actin antibodies were from Cell Signaling Technology (Shanghai, China).

2.11. qPCR Assay. Total RNA was extracted using a Trizol reagent. Retranscription of the first cDNA strand was conducted using a Prime Scr immunoprecipitation assay kit [19]. When determining the relative expression level of genes, the reaction system and procedures of qPCR followed the instructions of the TB Green Premix TaqII. Relative expression levels of genes were measured and then calculated using $2^{-\Delta\Delta CT}$ algorithm methods.

2.12. Statistical Analysis. All data from the experiments were expressed as the mean ± standard deviation (SD). Student's *t*-tests were adopted for pairwise comparison and one-way analysis of variance (ANOVA) was for multiple group comparison. Statistical analysis was conducted using GraphPad Prism 7.0 software (LaJolla, CA, USA) and the differences were significant at P values < 0.05.

3. Results

3.1. GO and KEGG Analysis of CIBP Treated by ATAGJ. ATAGJ has been proved to be effective for CIBP through long-term clinical trials in this group. ATAGJ is composed of BP, ZJC, SF, WLZ, XJ, and MQZ. To investigate the effects of ATAGJ on CIBP, we first identified the active components and related targets of ATAGJ. There were 332 targets in ATAGJ, 198 targets in CIBP, and 28 overlapped targets (Figures 1(a) and 1(b)). To elucidate the function of ATAGJ targets and the role of potential targets in the signaling pathways, we analyzed the 28 targets utilizing GO and KEGG analysis and visualized the results of enrichment analysis. GO enrichment analysis revealed that the effects on eux transmembrane transporter activity, ATPase-coupled xenobiotic transmembrane transporter activity, NADPH as one donor, and incorporation of one atom of oxygen were more significant in biological processes. The effects of monooxygenase activity, nuclear receptor activity, positive regulation of phospholipase C activity in molecular function were more significant (Figures 1(c) and 1(d)). The results of the KEGG pathway analysis indicated that the 28 potential targets of ATAGJ for CIBP were positively related to the HIF-1α signaling pathway. Next, we verified the effect of ATAGJ on the HIF-1α signaling pathway (Figure 1(e)).

3.2. Component-Target Network Mapping and Molecular Docking in ATAGJ Treatment of CIBP. A network diagram of PPI protein interaction (Figure 2(a)) was construed via the String platform. We found that fisetin was one of the key components of ATAGJ, and AKT1 and VEGFA were the core target genes with high degree values (Figure 2(b)). The results showed that fisetin, AKT, and VEGFA were less than −5 kcal/mol. The amino acid residues ALA-5, ILE-6, and Glu-49 of AKT and fisetin formed hydrogen bond interaction and hydrophobic interaction with amino acid residues VAL-4, LYS-30, LEU-28, ILE-36, ARG48, and TYR38. The amino acid residues VAL-216, LYS-48, SER-50, and CYS-51 of VEGFA and fisetin formed hydrogen bond interaction and hydrophobic interaction with amino acid residues ILE-215, MET-197, TYR-165, and PRO-49. Molecular docking results showed that fisetin, the key component of ATAGJ, might affect CIBP by regulating AKT or VEGFA (Figures 2(c) and 2(d)). The KEGG pathway analysis revealed that the HIF-1α signaling pathway might play a pivotal role in treating CIBP following ATAGJ administration, and the AKT pathway was the regulatory pathway of

Figure 1: GO and KEGG pathway enrichment analysis; (a) Venn diagram of intersection gene between ATAGJ and bone cancer pain target; (b) gene venn diagram of intersection between borneol (BP), spina gleditsiae (ZJC), pillworm (SF), faeces trogopterori (WLZ), resina draconis (XJ) and semen strychni (MQZ), and bone cancer pain target. (c, d) Bubble diagrams of biological process and molecular function via GO analysis. The *Y* axis on the left is the name of the GO channel, and the *X* axis is the *P* value. The larger the circle is, the more genes are compared. The darker the color is, the more genes are compared. (e) KEGG pathway enrichment analysis circle diagram, the right side of the outermost layer is the names of the signaling pathways, and the left side is the genes. The left inner circle represents the significant *P* values of the pathways of the corresponding genes.

HIF-1α. Therefore, we suspected whether ATAGJ and fisetin could regulate the HIF-1α signaling pathway by combining AKT.

3.3. ATAGJ Alleviates CIBP in Rats by AKT/HIF-1α Signaling Pathway. Despite ATAGJ produced satisfactory clinical efficacy in patients with CIBP, its specific mechanism has not

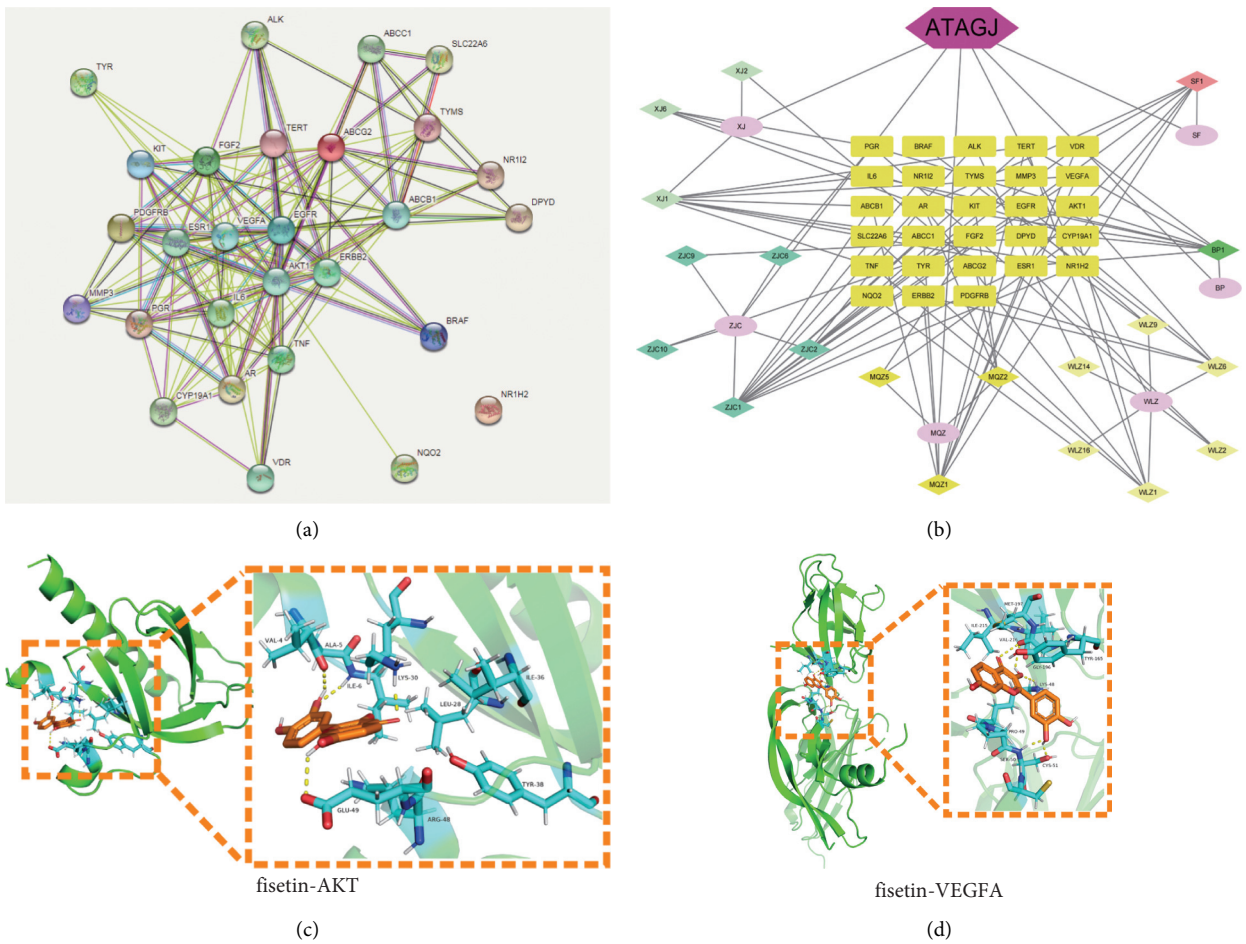

Figure 2: The key components and core targets of ATAGJ in treating bone cancer pain were analyzed by network pharmacology: (a) interaction analysis of 28 proteins; (b) drug-component-target gene network diagram. ATAGJ refers to compound MQZ, BP, ZJC, SF, WLZ, and XJ. MQZ refers to the borneol, spina gleditsiae, pillworm, faeces trogopterori, resina draconis, and semen strychni; (c) molecular docking between fisetin and AKT; (d) molecular docking between fisetin and VEGFA.

been defined yet. We analyzed CIBP in patients with possible AKT/HIF-1α signaling pathway regulation by ATAGJ in a network pharmacology approach. To figure out the molecular mechanism of ATAGJ affecting CIBP treatment, the SD rats were selected and divided into a sham group, a model group, a low dose ATAGJ group, a medium dose ATAGJ group, and a high dose ATAGJ group. At 9 a.m., ATAGJ was applied at low (10 g/d), medium (20 g/d), and high (30 g/d) doses, respectively, for 10 h and lasted for 14 d. The PWT of the model group was markedly lower than that of the sham group at day 7 ($P < 0.01$), which indicated that the pain threshold was decreased and the CIBP model was constructed successfully. No significant difference was exhibited between both groups ($P > 0.05$), which indicated that ATAGJ could substantially increase PWT and improve the pain threshold of the rats (Figure 3(a)). The effects of ATAGJ on the AKT/HIF-1α signaling pathway were subsequently detected using Western blot experiments, which suggested that the levels of p-AKT, HIF-1α, and VEGF were elevated markedly in the model group compared with the sham group ($P < 0.01$). The levels of p-AKT, HIF-1α, and VEGF decreased largely when compared with the model group ($P < 0.01$) (Figures 3(b) and 3(c)). The results of qPCR suggested that the levels of HIF-1α and VEGF rose substantially in the model group in contrast to those of the sham group ($P < 0.01$). Compared with the model group, the levels of HIF-1α and VEGF decreased significantly ($P < 0.01$) (Figure 3(d)).

3.4. ATAGJ's Monomer Fisetin Inhibits Tumor Growth. Fisetin was regarded as the key component (with the most connections) of ATAGJ through network pharmacology analysis. It is a compound derived from natural plants and characterized by a wide range of pharmacological effects. To investigate whether ATAGJ monomer fisetin affected the proliferation of Walker 256 cells, we classified Walker 256 cells into a control group, a cisplatin group, a low dose fisetin group, a medium dose fisetin group, and a high dose fisetin group. Walker 256 cells were treated with fisetin (10 μM, 20 μM, and 30 μM) and Cisplatin (5 μM) in the positive control group for 24 h.

The results of the colony formation assay showed that the cisplatin group could apparently inhibit the proliferation of

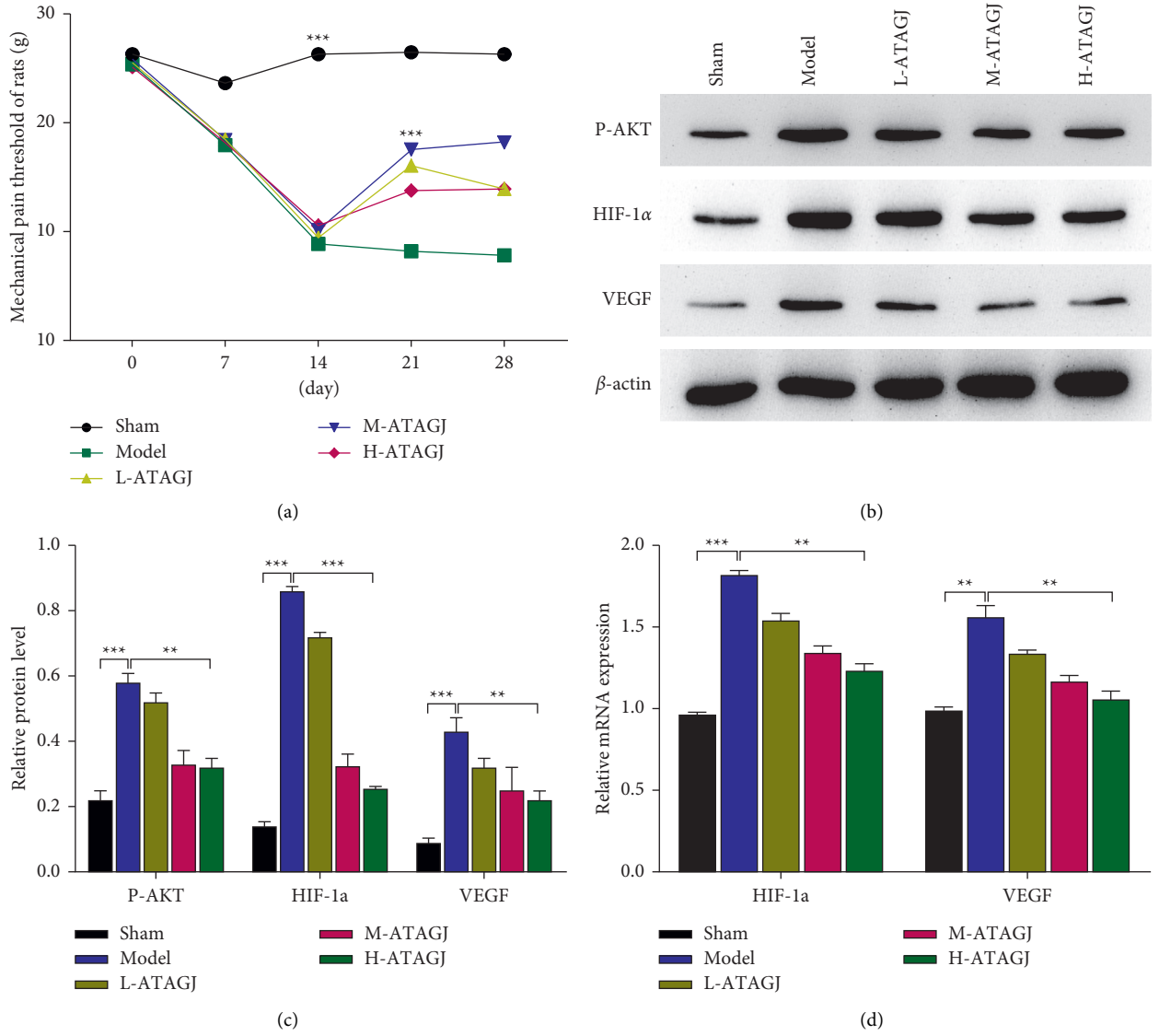

FIGURE 3: ATAGJ affects AKT/HIF-1α signaling pathway in CIBP rats; (a) mechanical pain threshold of rats in all groups; (b, c) western blot detection of protein expressions of p-Akt, HIF-1α, and VEGF. β-actin expression was regarded as an internal control. (d) qRT-PCR detection of mRNA expression levels of the indicated genes. Student's t-tests (two groups) or one-way ANOVA was employed and followed by Tukey's tests (more than two groups) ($n \geq 3$). $^{*}P < 0.05$, $^{**}P < 0.01$, and $^{***}P < 0.001$.

Walker 256 cells in both medium and high dose fisetin groups ($P < 0.01$) (Figures 4(a) and 4(b)). Further detection on the effects of fisetin was performed to identify the migration ability of Walker 256 cells by the Transwell experiment, indicating that the cisplatin group could substantially inhibit the migration of Walker 256 cells in both low and high dose fisetin groups ($P < 0.01$) (Figures 4(c) and 4(d)). Meanwhile, EDU experiment results showed that the cisplatin group could significantly inhibit the proliferation of Walker 256 cells in medium and high dose fisetin groups ($P < 0.01$) (Figures 4(e) and 4(f)).

3.5. ATAGJ Monomer Fisetin Inhibits Tumor Growth via AKT/HIF-1α Signaling Pathway. Through network pharmacology, we found that AKT1 and VEGFA were the core target genes with a high degree. KEGG pathway analysis showed that the HIF-1α signaling pathway might be of great importance in the treatment of CIBP by ATAGJ, and the AKT pathway was the regulatory pathway of HIF-1α. The results of molecular docking indicated that fisetin might regulate the HIF-1α signaling pathway by binding to AKT. To verify the relationship between fisetin and AKT1, we labeled fisetin with biotin to investigate whether this monomer could bind to AKT1. Co-IP results indicated that fisetin could be combined with AKT1 (Figure 5(a)). To investigate whether fisetin inhibited tumor growth through the AKT/HIF-1α signaling pathway, we found that fisetin could significantly reduce the levels of p-AKT, HIF-1α, and VEGF ($P < 0.01$) (Figure 5(b)). Meanwhile, fisetin was indicated to substantially decrease the levels of HIF-1α and VEGFR ($P < 0.01$) (Figures 5(c) and 5(d)).

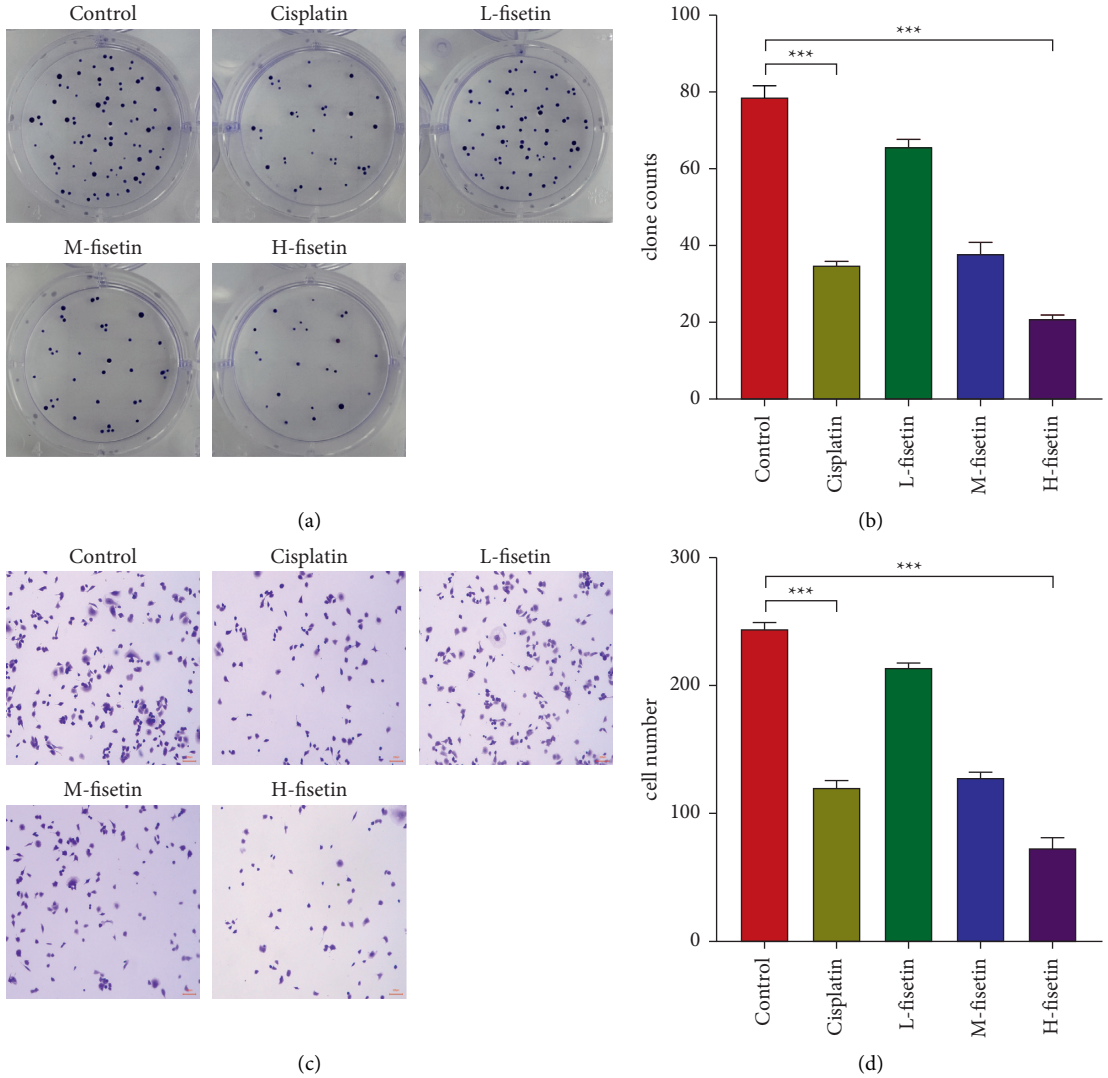

Figure 4: Continued.

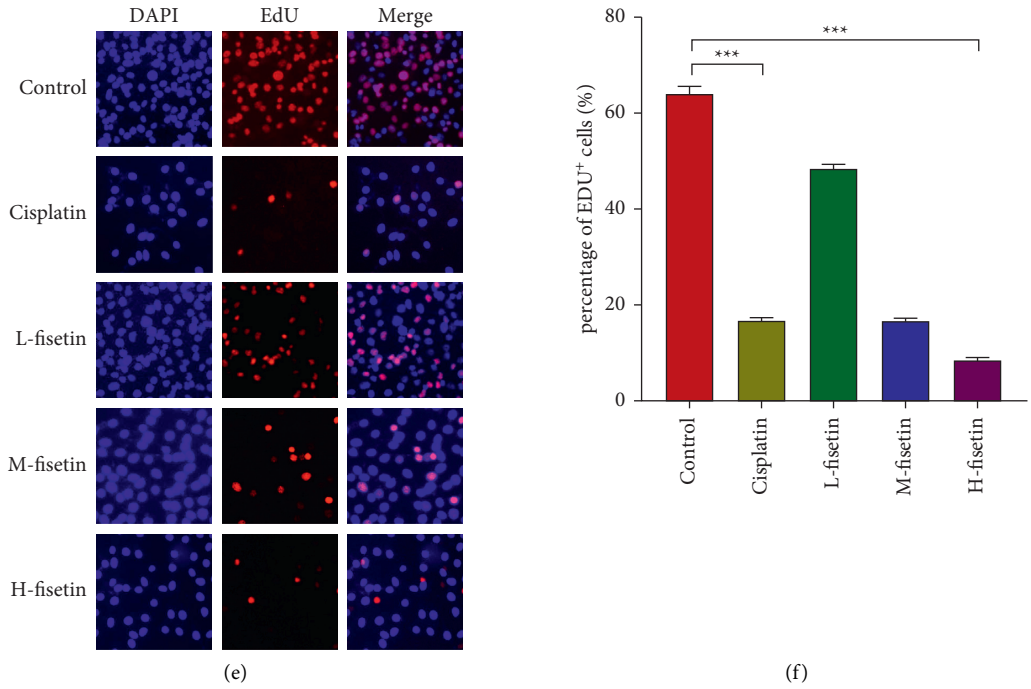

Figure 4: Fisetin affects tumor cell proliferation; (a) colony formation assay of each group of cells; (b) quantification of several colonies in Figure 4(a); (c) transwell experiment of cells in each group; (d) quantification of several cells in Figure 4(c); (e) EDU experiment of each group; (f) quantification of EDU$^+$ cells in Figure 4(e). We divided the Walker 256 cells into a control group, cisplatin group, low dose fisetin group, medium dose fisetin group, and a high dose fisetin group. Walker 256 cells were treated with fisetin (10 μM, 20 μM, and 30 μM) and cisplatin (5 μM) in the positive control group for 24 h Student's t-tests (two groups) or one-way ANOVA was employed and followed by Tukey's tests (more than two groups) ($n \geq 3$). $^*P < 0.05$, $^{**}P < 0.01$, $^{***}P < 0.001$.

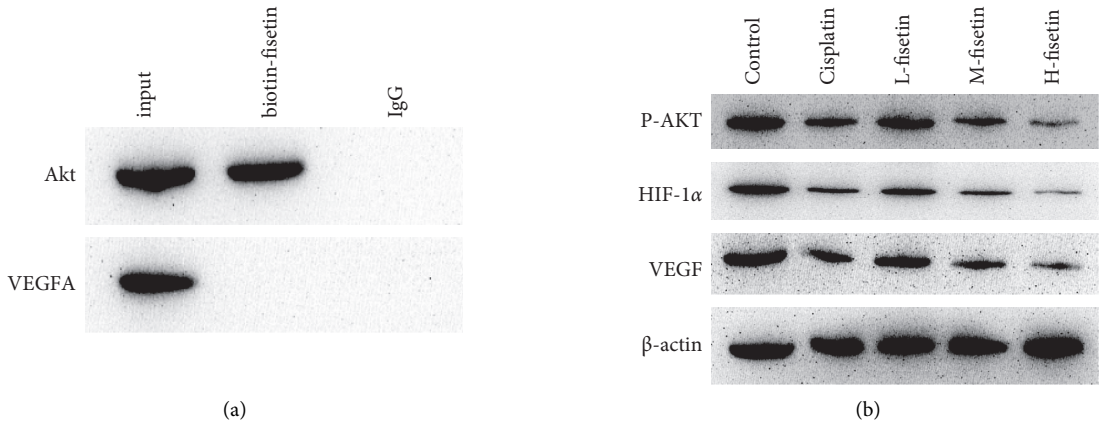

Figure 5: Continued.

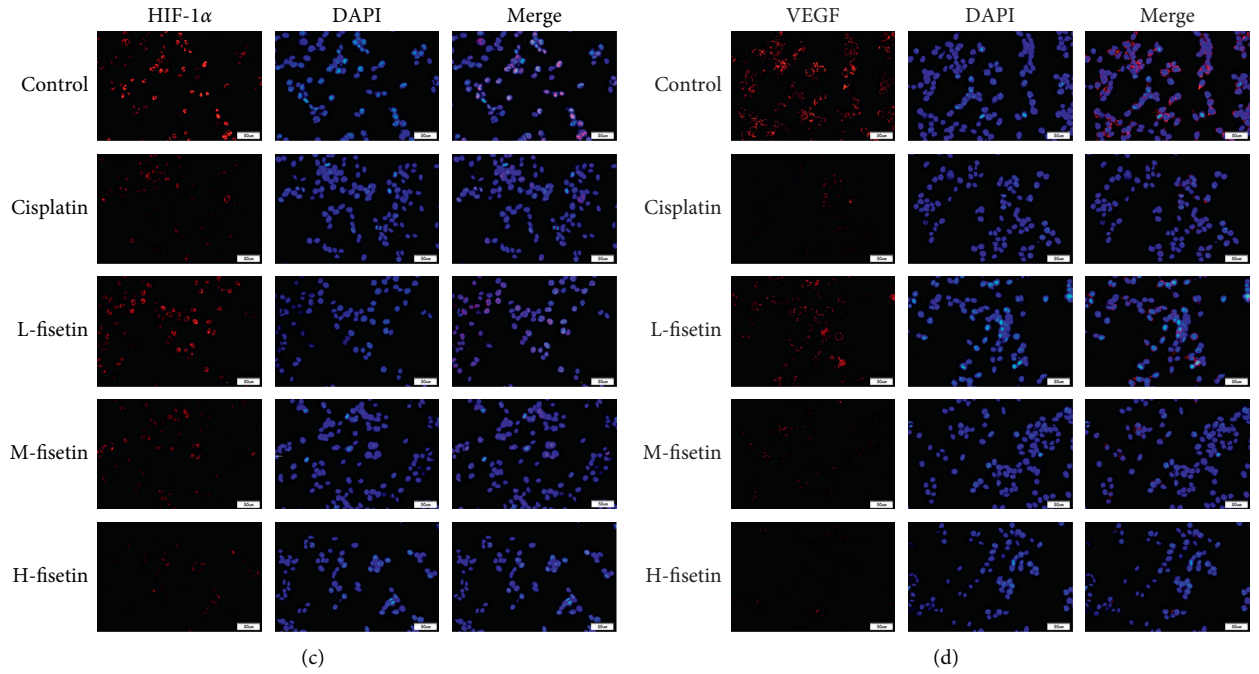

FIGURE 5: Fisetin affects the Akt/HIF-1α signaling pathway in tumor cells. (a) Coimmunoprecipitation assay showed fisetin-AKT interactions in Walker 256 cells. (b) Protein expressions of p-Akt, HIF-1α, and VEGF. (c, d) HIF-1α and VEGF were detected by immunofluorescence assay. Red represented HIF-1α and VEGF. Blue represented DAPI.

4. Discussion

Cancer pain has been well-recognized as one of the common complications suffered by patients with a range of cancers, occurring approximately 25% for the first time [20]. The incidence of pain in advanced cancer patients can reach up to 60~80%, and 1/3 of the patients suffer from ongoing severe pain. At present, most therapeutic methods preferred by western medicine in treating cancerous pain mainly include analgesic drugs, nerve block, primary lesion surgery, and chemoradiotherapy [9]. The treatment principles of drug analgesia are mainly based on the "third-order ladder" recommended by WHO [21]. Despite some effects that have been achieved in clinical practice, adverse reactions including gastrointestinal reaction, constipation, vertigo, respiratory depression, and mental disorder are also present [22]. It is, therefore, an urgent need to find a satisfactory therapy that can win the confidence of cancer pain patients.

ATAGJ functions as an effective therapeutic option for CIBP relief and pain management. Its main components consist of borneol, spina gleditsiae, pillworm, faeces trogopterori, resina draconis, and semen strychni. Spina gleditsiae contains the compound fisetin, which represents a kind of yellow bioactive pigment [23]. The molecular formula of fisetin is $C_{15}H_{10}O_6$, with a molar mass of 286.2363 g/mol and a density of 1.688 g/mL. It is soluble in ethanol, acetone, acetic acid, and hydroxide base solution [24, 25]. In general, some pain inducing mediators including tumor cells and inflammatory cells are reckoned to be involved in the occurrence and development of CIBP. Also, continuous activation of osteoclasts is considered to be related to this pain. Furthermore, tumor expansion on the nerve compression and damage is also a source of pain [26]. Tumors are not highly dominated by sensory neurons. However, rapid tumor growth has a propensity to bind to and damage nerves, resulting in mechanical damage, compression, ischemia, or direct proteolysis. As the proliferation of tumor cells, they first compress then destroy the hematopoietic cells that normally make up the bone marrow and the sensory fibers that normally dominate the bone marrow and mineralized bone [1].

We initially identified the active components and related targets of ATAGJ by network pharmacology. And the GO analysis and KEGG pathway analysis were performed using the Cytoscape ClueGO plugin. The findings of the KEGG pathways revealed that the 28 potential targets of ATAGJ treatment for CIBP were mainly correlated to the HIF-1α signaling pathway. HIF-1α was the core regulator of inducing hypoxia gene and intracellular oxygen environment repair, which could regulate cell growth, proliferation, migration, inflammation, and apoptosis. High expression of HIF-1α protein was indicated in most tumor tissues and their metastatic sites [14–24, 27–29]. Then Zhang et al. reported that CIBP was alleviated through inhibiting the HIF-1α/vascular endothelial growth factor signaling pathway [30]. Therefore, we concluded that ATAGJ might reduce CIBP by inhibiting the expression of HIF-1α. We then validated the hypothesis by constructing a CIBP model of rats. The mechanical pain thresholds of the low, middle, and high dose ATAGJ groups were higher than that of the model group at day 21 ($P < 0.01$). No significant difference was exhibited between both groups ($P > 0.05$), which indicated that ATAGJ had a satisfactory effect on reducing CIBP.

Furthermore, we observed that the expression levels of p-AKT, HIF-1α, and VEGF were markedly elevated in the model group instead of sham group ($P < 0.01$). Compared with the model group, those of p-AKT, HIF-1α, and VEGF decreased greatly in H-ATAGJ treatment group ($P < 0.01$). The results suggested that ATAGJ could reduce CIBP in rats by reducing AKT/HIF-1α signaling pathway. We visualized the drugs, components, and targets using the Cytoscape 3.6 software and found that fisetin was the key component in ATAGJ (with the most connections). It indicated that the fisetin group could markedly inhibit the proliferation of Walker 256 cells in both low and high dose fisetin groups ($P < 0.01$). Further, we analyzed whether fisetin acted on the migration of Walker 256 cells by the Transwell experiment. Significant inhibition of the fisetin group on the migration of Walker 256 cells was revealed in medium and high dose fisetin groups ($P < 0.01$). Concomitantly, the EDU experiment indicated that the fisetin group could markedly inhibit the proliferation of Walker 256 cells in medium and high dose fisetin groups ($P < 0.01$). The previously described results indicated that fisetin could greatly suppress the proliferation and metastasis of tumor cells.

AKT1 and VEGFA are the core target genes with high degree scores. The results of molecular docking indicated that fisetin, AKT, and VEGFA were less than −5 kcal/mol. We, therefore, speculated that fisetin might affect CIBP by regulating AKT or VEGFA. We then labeled fisetin with biotin to investigate whether it could bond to AKT1. Co-IP results revealed that fisetin could be combined with AKT1. From this, we hypothesized fisetin could regulate the HIF-1α signaling pathway by binding to AKT. In addition, we found that fisetin could significantly reduce the levels of HIF-1α, p-AKT, and VEGF ($P < 0.01$). This suggested that fisetin inhibited the AKT/HIF-1α signaling pathway in tumor cells by binding to AKT.

5. Conclusion

We initially predicted the potential targets and pathways of ATAGJ for CIBP management using a network pharmacology approach. The clone formation and proliferation of Walker 256 cells were detected after fisetin treatment. Furthermore, experiments were performed to detect the AKT/HIF-1α signal pathway expression in CIBP rats and Walker 256 cells. The molecular docking and IP experiments verify the binding of fisetin and AKT. The results demonstrated the effect of ATAGJ in CIBP rats and the key component fisetin could suppress Walker 256 cells proliferation and downregulate the expressions levels of HIF-1α, p-AKT, and VEGF through targeting AKT.

Data Availability

The data used to support the findings of this study are included within the article.

Disclosure

Wang Jing and Lai are co-first authors.

Conflicts of Interest

The authors declare that they have no conflicts of interest.

Authors' Contributions

Wang Jing and Lai Zonglang contribute equally to this paper. WJ conceived the project, planned the experiments, and analyzed and interpreted the data. Lai ZL performed in vitro experiments and wrote the paper. All authors contributed to and approved the final manuscript.

Acknowledgments

This work was supported by Special Project for Performance Incentive and Guidance of Scientific Research Institutions in Chongqing (no. cstc2019jxj1130021).

References

[1] X. C. Zhu, J. L. Zhang, C. T. Ge et al., "Advances in cancer pain from bone metastasis," *Drug Design, Development and Therapy*, vol. 9, pp. 4239–4245, 2015.

[2] M. Lucchesi, G. Lanzetta, A. Antonuzzo et al., "Developing drugs in cancer-related bone pain," *Critical Reviews in Oncology*, vol. 119, pp. 66–74, 2017.

[3] M. H. J. van den Beuken-van Everdingen, L. M. J. Hochstenbach, E. A. J. Joosten, V. C. G. Tjan-Heijnen, and D. J. A. Janssen, "Update on prevalence of pain in patients with cancer: systematic review and meta-analysis," *Journal of Pain and Symptom Management*, vol. 51, no. 6, pp. 1070–1090, Article ID e1079, 2016.

[4] S. Buga and J. E. Sarria, "The management of pain in metastatic bone disease," *Cancer Control*, vol. 19, no. 2, pp. 154–166, 2012.

[5] C. F. Jehn, I. J. Diel, F. Overkamp et al., "Management of metastatic bone disease algorithms for diagnostics and treatment," *Anticancer Research*, vol. 36, no. 6, pp. 2631–2637, 2016.

[6] T. A. Guise, W. M. Kozlow, A. Heras-Herzig, S. S. Padalecki, J. J. Yin, and J. M. Chirgwin, "Molecular mechanisms of breast cancer metastases to bone," *Clinical Breast Cancer*, vol. 5, no. 2, pp. S46–S53, 2005.

[7] F. D. Yao, J. Q. Yang, Y. C. Huang et al., "Antinociceptive effects of Ginsenoside Rb1 in a rat model of cancer-induced bone pain," *Experimental and Therapeutic Medicine*, vol. 17, no. 5, pp. 3859–3866, 2019.

[8] P. W. Mantyh, D. R. Clohisy, M. Koltzenburg, and S. P. Hunt, "Molecular mechanisms of cancer pain," *Nature Reviews Cancer*, vol. 2, no. 3, pp. 201–209, 2002.

[9] M. Fallon, R. Giusti, F. Aielli et al., "Management of cancer pain in adult patients: ESMO Clinical Practice Guidelines," *Annals of Oncology*, vol. 29, pp. iv166–iv191, 2018.

[10] D. N. Syed, F. Afaq, N. Maddodi et al., "Inhibition of human melanoma cell growth by the dietary flavonoid fisetin is associated with disruption of wnt/β-catenin signaling and decreased mitf levels," *Journal of Investigative Dermatology*, vol. 131, no. 6, pp. 1291–1299, 2011.

[11] S.-J. Chiu, H. H. Tseng, C. W. Peng, W. S. Chen, and S. J. Chiu, "Dietary flavonoid fisetin targets caspase-3-deficient human breast cancer MCF-7 cells by induction of caspase-7-associated apoptosis and inhibition of autophagy," *International Journal of Oncology*, vol. 40, no. 2, pp. 469–478, 2012.

[12] N. Ravichandran, G. Suresh, B. Ramesh, R. Manikandan, Y. W. Choi, and G. Vijaiyan Siva, "Fisetin modulates mitochondrial enzymes and apoptotic signals in benzo(a)pyrene-induced lung cancer," *Molecular and Cellular Biochemistry*, vol. 390, no. 1-2, pp. 225–234, 2014.

[13] V. M. Adhami, D. N. Syed, N. Khan, and H. Mukhtar, "Dietary flavonoid fisetin: a novel dual inhibitor of PI3K/Akt and mTOR for prostate cancer management," *Biochemical Pharmacology*, vol. 84, no. 10, pp. 1277–1281, 2012.

[14] Z. Zhang, L. Yao, J. Yang, Z. Wang, and G. Du, "PI3K/Akt and HIF-1 signaling pathway in hypoxia-ischemia (Review)," *Molecular Medicine Reports*, vol. 18, no. 4, pp. 3547–3554, 2018.

[15] A. Pezzuto and E. Carico, "Role of HIF-1 in cancer progression: novel insights. A review," *Current Molecular Medicine*, vol. 18, no. 6, pp. 343–351, 2019.

[16] S. Noorolyai, N. Shajari, E. Baghbani, S. Sadreddini, and B. Baradaran, "The relation between PI3K/AKT signalling pathway and cancer," *Gene*, vol. 698, pp. 120–128, 2019.

[17] W. N. I. Z. Wan Mohamad Zain, J. Bowen, E. Bateman, and D. Keefe, "Cytotoxic effects of the dual ErbB tyrosine kinase inhibitor, lapatinib, on walker 256 rat breast tumour and IEC-6 rat normal small intestinal cell lines," *Biomedicines*, vol. 8, no. 1, Article ID 2, 2019.

[18] B. Yang, Z. Zhang, Z. Yang et al., "Chanling gao attenuates bone cancer pain in rats by the IKKβ/NF-κB signaling pathway," *Frontiers in Pharmacology*, vol. 11, Article ID 525, 2020.

[19] M. Zhang, J. Wei, H. Shan et al., "Calreticulin-STAT3 signaling pathway modulates mitochondrial function in a rat model of furazolidone-induced dilated cardiomyopathy," *PLoS One*, vol. 8, no. 6, Article ID e66779, 2013.

[20] R. Adam, M. de Bruin, C. D. Burton, C. M. Bond, M. Giatsi Clausen, and P. Murchie, "What are the current challenges of managing cancer pain and could digital technologies help?" *BMJ Supportive & Palliative Care*, vol. 8, no. 2, pp. 204–212, 2018.

[21] E. Bruera and R. L. Fainsinger, "Pharmacologic treatment of cancer pain," *New England Journal of Medicine*, vol. 336, no. 13, pp. 962-963, 1997.

[22] A. W. Oosten, W. H. Oldenmenger, R. H. J. Mathijssen, and C. C. D. van der Rijt, "A systematic review of prospective studies reporting adverse events of commonly used opioids for cancer-related pain: a call for the use of standardized outcome measures," *The Journal of Pain*, vol. 16, no. 10, pp. 935–946, 2015.

[23] Z.-J. Zhang, W.-Y. Wu, J.-J. Hou et al., "Active constituents and mechanisms of Respiratory Detox Shot, a traditional Chinese medicine prescription, for COVID-19 control and prevention: network-molecular docking-LC-MSE analysis," *Journal of Integrative Medicine*, vol. 18, no. 3, pp. 229–241, 2020.

[24] D. Kashyap, V. K. Garg, H. S. Tuli et al., "Fisetin and quercetin: promising flavonoids with chemopreventive potential," *Biomolecules*, vol. 9, no. 5, Article ID 174, 2019.

[25] G. Grynkiewicz and O. M. Demchuk, "New perspectives for fisetin," *Frontiers of Chemistry*, vol. 7, Article ID 697, 2019.

[26] A. N. Khan, H. E. Jacobsen, J. Khan et al., "Inflammatory biomarkers of low back pain and disc degeneration: a review," *Annals of the New York Academy of Sciences*, vol. 1410, no. 1, pp. 68–84, 2017.

[27] G. N. Masoud and W. Li, "HIF-1α pathway: role, regulation and intervention for cancer therapy," *Acta Pharmaceutica Sinica B*, vol. 5, no. 5, pp. 378–389, 2015.

[28] F. Duan, C. Mei, L. Yang et al., "Vitamin K2 promotes PI3K/AKT/HIF-1α-mediated glycolysis that leads to AMPK-dependent autophagic cell death in bladder cancer cells," *Scientific Reports*, vol. 10, no. 1, Article ID 7714, 2020.

[29] F. Agani and B.-H. Jiang, "Oxygen-independent regulation of HIF-1: novel involvement of PI3K/AKT/mTOR pathway in cancer," *Current Cancer Drug Targets*, vol. 13, no. 3, pp. 245–251, 2013.

[30] Z. Zhang, M. Deng, J. Huang et al., "Microglial annexin A3 downregulation alleviates bone cancer-induced pain through inhibiting the Hif-1α/vascular endothelial growth factor signaling pathway," *Pain*, vol. 161, no. 12, pp. 2750–2762, 2020.

Hindawi
Journal of Oncology
Volume 2022, Article ID 1183173, 18 pages
https://doi.org/10.1155/2022/1183173

Research Article

Development of a Novel Immune Subtyping System Expanded with Immune Landscape and an 11-Gene Signature for Predicting Prostate Cancer Survival

Nan Li,[1,2,3] Kai Yu,[4] Zhong Lin,[5] and Dingyuan Zeng[3,6]

[1]*Reproductive Medicine Center, Liuzhou Maternity and Child Health Care Hospital, Liuzhou 545001, China*
[2]*Guangxi Health Commission Key Laboratory of Birth Cohort Study in Pregnant Women of Advanced Age, Liuzhou 545001, China*
[3]*Affiliated Maternity Hospital and Affiliated Children's Hospital of Guangxi University of Science and Technology, Liuzhou 545001, China*
[4]*College of Animal Science and Technology, Guangxi University, Nanning 530004, China*
[5]*The Guangxi Zhuang Autonomous Region Reproducitve Hospital, Nanning 530021, China*
[6]*The Department of Obstetrics and Gynecology, Liuzhou Maternity and Child Health Care Hospital, Liuzhou 545001, China*

Correspondence should be addressed to Zhong Lin; zhonglin_submit@163.com and Dingyuan Zeng; zdy13607723199@163.com

Received 6 December 2021; Revised 11 January 2022; Accepted 17 January 2022; Published 16 February 2022

Academic Editor: Fu Wang

Background. Nearly half of patients with prostate cancer will develop metastasis. Immunotherapy is currently a promising strategy for treating metastatic prostate cancer. This study aimed to construct an immune subtyping system and provide a more comprehensive understanding of tumor microenvironment. *Methods*. Data were downloaded from TCGA database and cBioPortal database. Consensus clustering was used to identify immune subtypes. Immune features were scored by ESTIMATE and CIBERSORT. Efficacy of different subtypes in immunotherapy was predicted by TIDE tool. Immune landscape was delineated through "monocle." Coexpressed gene modules were identified by weighted correlation network analysis. Univariate Cox regression analysis and LASSO analysis were applied to construct a prognostic model. *Results*. Four immune subtypes (IS1 to IS4) were identified. Prognosis, mutation patterns, expression of immune genes, immune biomarkers, immunohistochemical biomarkers, and prediction efficacy of immunotherapy were significantly different among four immune subtypes. Five coexpressed gene modules were identified and an 11-gene prognostic model was constructed based on the modules. *Conclusions*. The study developed a novel immune subtyping system and an 11-gene prognostic model of prostate cancer, which could guide personalized treatment and immunotherapy for patients with prostate cancer.

1. Introduction

Prostate cancer (PCa) is a commonly diagnosed male malignancy, which accounted for 10% of cancer-caused deaths [1]. Traditional therapies such as androgen depravation therapy (ADT), radiotherapy, and radical prostatectomy are usually applied treatment options for PCa patients, but not all patients will develop a positive prognosis. Over 40% of PCa patients with prostatectomy will experience disease recurrence [2]. ADT is the mainstay of managing metastatic PCa, despite an initial active response during the treatment, metastatic castration resistant prostate cancer (mCRPC) still occurs to a majority of patients [3].

Immunotherapy has been greatly improved in treating various cancers in the last decades, especially in the management of renal cell carcinoma, melanoma, and lung cancer [4–6]. Particularly, immune checkpoint inhibitors have been reported to possess impressive efficacy. However, only a

small number of PCa show positive response to immunotherapy. Evidence proved that tumor microenvironment (TME) plays an essential role in each process of tumorigenesis, driving the outcome of prognosis [7]. The different components of TME can result in differential efficacy of immunotherapy. Although biomarkers have been widely explored to predict PCa prognosis [8–10], a guide tool for predicting the response of immunotherapy has not been developed.

In the present study, we aimed to comprehensively characterize an immune signature for PCa. We proposed a novel molecular subtyping system based on immune genes to predict the efficacy of immunotherapy. An immune landscape was delineated to complementary the immune subtyping system, and a prognostic model was constructed to predict the overall survival (OS) of PCa patients. Analysis was performed according to workflow diagram (Supplementary Figure S1).

2. Materials and Methods

2.1. Data Acquisition. TCGA-PRAD dataset including RNA-Seq and CNV data was downloaded from TCGA database (https://portal.gdc.cancer.gov/). MSKCC-PRAD dataset (MSKCC, Cancer Cell 2010) was downloaded from cBioPortal database (https://www.cbioportal.org/). TCGA-PRAD and MSKCC-PRAD were defined as training dataset and validation dataset, respectively. A total of 1989 immune-related genes including immune cell-specific genes, genes of costimulatory and coinhibitory molecules, genes of cytokines and cytokine receptors, genes for antigen processing and presentation, and other immune-related genes (Supplementary Table S1) were collected by extensively reviewing previous studies. In the below strategies, we followed the methods of Xia et al. [11].

2.2. Data Preprocessing. In TCGA-PRAD dataset, samples without survival data were excluded, while those whose transcripts per million (TPM) = 0 were in more than 50% samples were excluded. Ensembl gene ID was transferred to gene symbol. 495 samples and 20088 genes in TCGA-PRAD dataset were retained (Supplementary Table S2). In MSKCC-PRAD dataset, samples without survival data and probes without value were also excluded. Probes were matched to gene symbol, but one probe mapped to multiple genes was excluded. Median value of expression data was calculated if multiple probes mapped to one gene. Finally, 63 samples and 22486 genes were included in this study (Supplementary Table S3).

2.3. Identification of Immune Subtypes. ConsensusClusterPlus R package was performed to cluster immune-related genes from TCGA-PRAD dataset [12]. Partitioning around medoids (PAM) algorithm and Canberra distance was employed in consensus clustering. 80% of the total samples in TCGA-PRAD dataset were included in each time of bootstrap, which was implemented for 500 times. Groups (k) were set from 2 to 10, and the most optimized clusters were determined by cumulative distribution function (CDF) curve and consensus CDF. Kaplan–Meier survival curve and log-rank test were used to evaluate the performance of the immune subtyping system.

2.4. Immune Landscape of PCa. Monocle is an unsupervised algorithm and has been previously used to reduce dimensionality and construct a two-dimensional landscape [13]. The algorithm of Monocle represented the expression data of each sample as a point in a high-dimensional Euclidean space, allowing each sample to be casted as a point in the two-dimensional graph. Finally, a tree structure manifesting the immune features of each sample was established by Monocle.

2.5. Identification of Coexpressed Gene Modules. Weighted correlation network analysis (WGCNA) R package was performed to identify immune-related gene modules [14]. The most optimized cluster was defined with a condition of the negative relation between $\log(k)$ and $\log(p(k))$, $R^2 > 0.85$, and soft threshold (power) = 12. Topological overlap matrix (TOM) was established based on adjacency matrix. We applied average-linkage hierarchical clustering and dynamic branch cutting to identify co-expression modules that contained at least 30 genes.

2.6. Gene Enrichment Analysis. Single sample gene set enrichment analysis (ssGSEA) in the GSVA R package was implemented to score immune cells [15]. ANOVA was performed to assess the relation between immune subtypes and 56 types of immune-related biomarkers [16]. Enriched biological processes in gene ontology (GO) terms of six immune-related gene modules were annotated by David (v6.8) [17].

2.7. Identification of Prognostic Model. Univariate Cox regression analysis was conducted to identify gene modules and prognostic genes significantly correlated with OS in TCGA-PRAD dataset. Least absolute shrinkage and selection operator (LASSO) regression in the glmnet R package and stepAIC in the MASS R package were applied to reduce the quantity of prognostic genes and optimize the prognostic model [18, 19]. Risk score was defined as coefficient 1 $*$ gene 1 expression + coefficient 2 $*$ gene 2 expression + $\cdots$ + coefficient n $*$ gene n expression. Kaplan–Meier survival curve and log-rank test were used to evaluate the model performance.

3. Results

3.1. Construction and Validation of Immune Subtypes of Prostate Cancer. Gene expression profiles of 1909 immune-related genes in TCGA-PRAD dataset were extracted initially. After conducting univariate Cox regression analysis, a total of 534 immune-related genes were found to be significantly associated with OS. Gene expression profiles of

these 534 genes were then used to determine molecular subtypes. According to the algorithm of consensus clustering, the optimal cluster was defined by cluster numbers (k) from 2 to 10. The most stable cluster when $k = 4$ (Figures 1(a) and 1(b)) was delineated by CDF and CDF delta area curves, and four immune subtypes (IS, IS1 to IS4) were constructed (Figure 1(c)). Survival analysis revealed that the four immune subtypes varied in OS; specifically, IS4 group had the favorable prognosis, while IS1 group had the worst prognosis ($p < 0.0001$, Figure 1(d)). Moreover, we also described the distribution of four immune subtypes in the conventional TNM staging system within TCGA-PRAD dataset. The analysis showed that the proportion of IS4 group decreased from T1 to T4, N0 to N1, and M0 to M1, while the proportion of IS1 group increased oppositely, which was consistent with the tendency of disease progression (Figures 1(e)–1(g)). In addition, a significant difference of distribution of immune subtypes was also observed between age <60 and age ≥60 groups (Figure 1(h)). To further verify the robustness of this immune subtyping system, another independent dataset, MKSCC-PRAD dataset, was classified into four groups. Similarly, significant difference was shown within four immune subtypes, and IS4 group still showed the best OS (Figure 1(i)).

3.2. Tumor Mutation Burden and Mutation Patterns of Four Immune Subtypes. In TCGA-PRAD dataset, mutect2 software was employed to calculate tumor mutation burden (TMB). IS4 group showed the lowest TMB and number of mutated genes when compared with other groups ($p < 0.001$, Figures 2(a) and 2(b)). We further assessed the mutation patterns of each group. Copy number alternations, especially deletions, were the majority mutations in all groups (Figure 2(c)). Reasonably, IS1 group comprised the largest amount of mutations, and IS4 group had the least mutations. The top 10 mutated genes were TP53, ACAP1, AP3B1, NXPE4, CHRNA6, APC, AP1G1, ALX4, NCOR2, and TIAM2. The mutation frequencies of TP53, NXPE4, and CHRNA6 were the highest in IS1 group, while ACAP1, AP3B1, APC, AP1G, 1NCOR2, and ADPRM genes showed the most mutations in IS2 group ($p < 0.001$). Interestingly, the frequencies of copy number variations of BTNL2, AGPAT1, APOM, ATP6V1G2-DDX39B, C6orf136, CCDC154, and CFB genes were greatly higher than other groups ($p < 0.001$).

3.3. Differential Expression of Chemokines, Chemokine Receptors, and Immune Checkpoints among Four Immune Subtypes. Chemokines together with cytokines play a critical role in TME. Chemokine receptors secreted by tumor cells are involved in tumor proliferation and metastasis and can serve as biomarkers of immunotherapy. Therefore, we evaluated the expression of chemokines and chemokine receptors and compared in the four immune subtypes. In TCGA-PRAD dataset, a total of 39 types of chemokines were expressed; noticeably, the expression level of each gene varied significantly among four immune subtypes ($p < 0.01$, Figure 3(a)), and the expression of chemokine receptors was also differential among the four groups ($p < 0.01$, Figure 3(b)). In MKSCC-PRAD dataset, 38 out of 41 chemokines expressed differentially, and the expression of chemokine receptors was differential among the four groups ($p < 0.05$, Figures 3(c) and 3(d)). Furthermore, the expression level of immune checkpoints was calculated. Among 47 immune checkpoints, 46 genes expressed differentially in TCGA-PRAD dataset, and 40 genes expressed differentially in MKSCC-PRAD dataset ($p < 0.05$, Figures 3(e) and 3(f)). These results supported the fact that the expression of chemokines, chemokine receptors, and immune checkpoints was different among IS1, IS2, IS3, and IS4 groups.

3.4. Differential Expression of PCa Immunohistochemical Biomarkers. Immunohistochemistry is commonly used in biopsy, and prostate-specific antigen (PSA) is one of the most popularly performed tests in PCa. To examine whether there was a correlation between immune subtypes and PCa immunohistochemical biomarkers, we incorporated a series of biomarkers currently used from Abcam website (https://www.abcam.cn/cancer/). In both TCGA-PRAD and MKSCC-PRAD datasets, significant expression difference of biomarkers among IS1, IS2, IS3, and IS4 groups was detected. There was no difference of FOLH1 and ERG in MKSCC-PRAD dataset, but the remaining biomarkers were all differentially expressed among the four groups (Figure 4).

3.5. Immune Features of Four Immune Subtypes. To investigate whether there was immune heterogeneity among the four immune subtypes, ESTIMATE and CIBERSORT tools were applied to score the samples in TCGA-PRAD and MKSCC-PRAD datasets. The enrichment score of the two datasets significantly varied among the four immune subtypes (Figures 5(a)–5(d)). In TCGA-PRAD dataset, IS1 group had the highest ESTIMATE score, but IS2 group had the lowest ESTIMATE score ($p < 0.0001$, Figure 5(a)). In MKSCC-PRAD dataset, IS2 group had the highest ESTIMATE score, but IS3 group had the lowest ESTIMATE score ($p < 0.0001$, Figure 5(c)). 22 types of immune cells were scored by CIBERSORT tool. In the two datasets, IS4 group exhibited a high enrichment score in plasma cells, macrophages M0, and resting mast cells, while IS1 group showed a high score in CD8+ T cells and regulatory T cells ($p < 0.0001$, Figures 5(b) and 5(d)).

A pan-cancer research classified cancers into six immune subtypes C1 to C6 based on IFN-γ, TGF-β, macrophage, lymphocyte, and wound healing, and PCa was stratified into C1 to C4 four groups [16]. Reasoning that the same TCGA-PRAD dataset was used, a comparison between C1 to C4 groups and IS1 to IS4 groups was conducted in this study. A significant difference of C1 to C4 distribution was observed from IS1 to IS4 groups. C2 group mostly accumulated in IS1 group, and a majority of C1 and C4 groups were in IS2 group ($p < 0.05$, Figure 5(e)). Moreover, we evaluated the correlation between IS1 to IS4 groups and immune biomarkers from the literature [16]. A total of 56 immune biomarkers were included, and 38 of them had differential enrichment score among the four immune

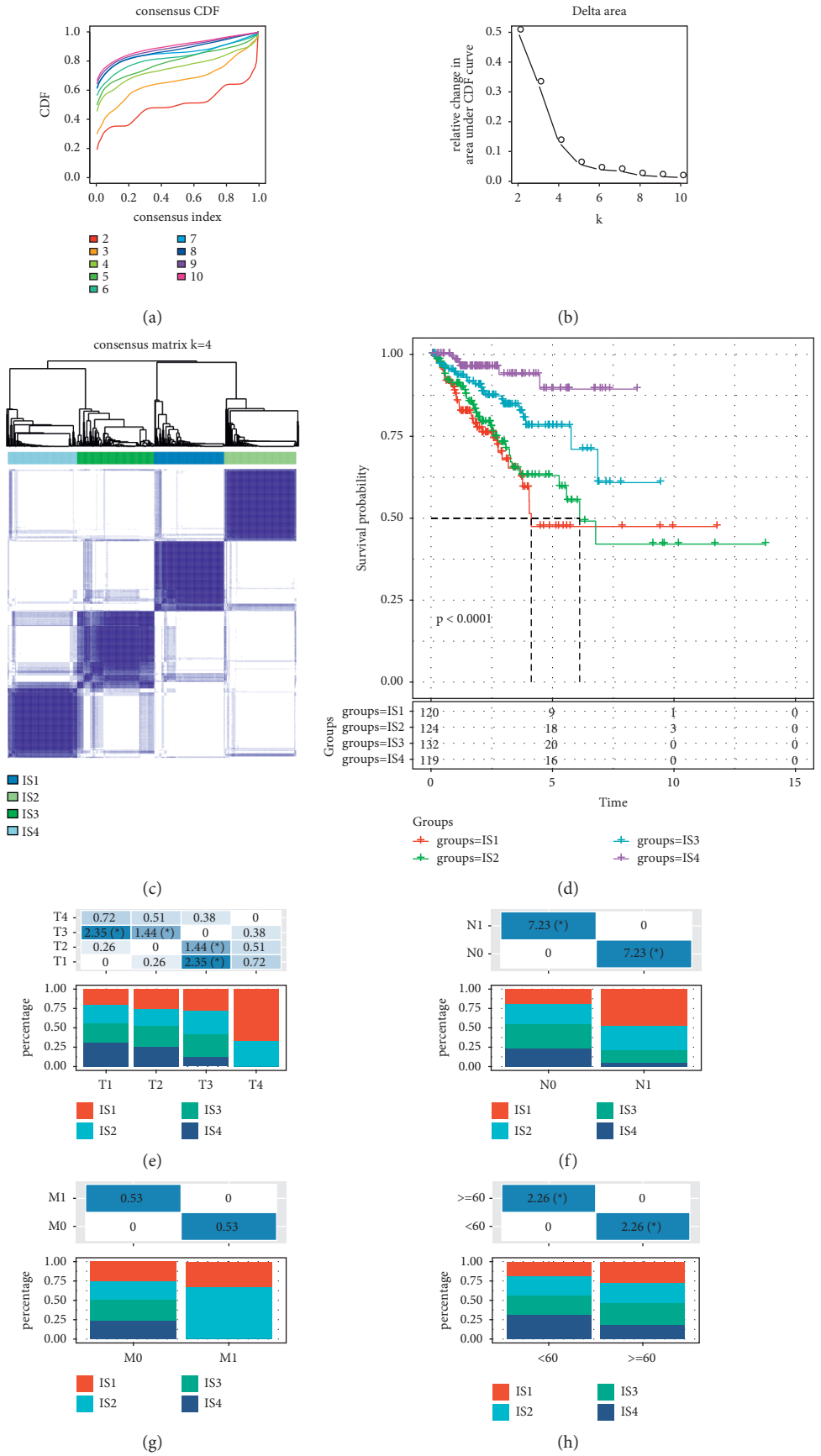

Figure 1: Continued.

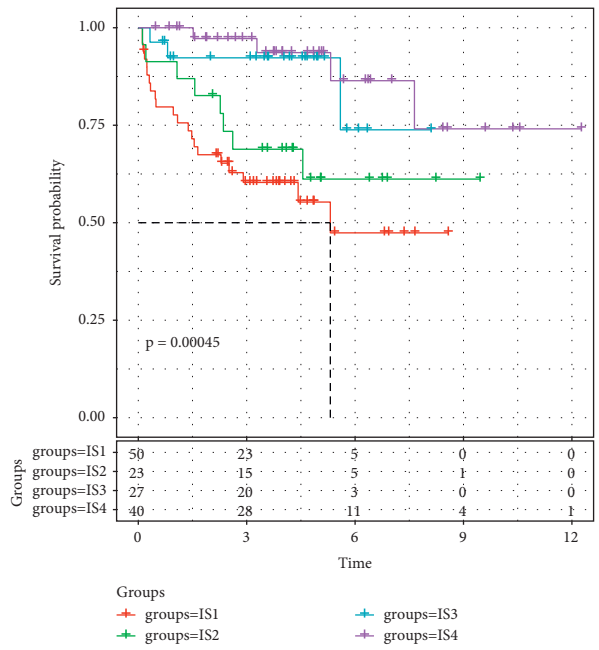

(i)

Figure 1: Four immune subtypes of PCa and its relation with clinical features. (a) CDF curve containing cluster numbers k from 2 to 10. (b) CDF delta area curve with $k = 2$ to 10. (c) The consensus matrix when $k = 4$. (d) Kaplan–Meier survival curve of four immune subtypes within TCGA-PRAD dataset. (e-g) The distribution of four immune subtypes in clinical features including T stage (e), N stage (f), M stage (g), and age (h). ANOVA was performed. (i) Kaplan–Meier survival curve of four immune subtypes within MKSCC-PRAD dataset. Log-rank test was performed $^{*}p < 0.05$.

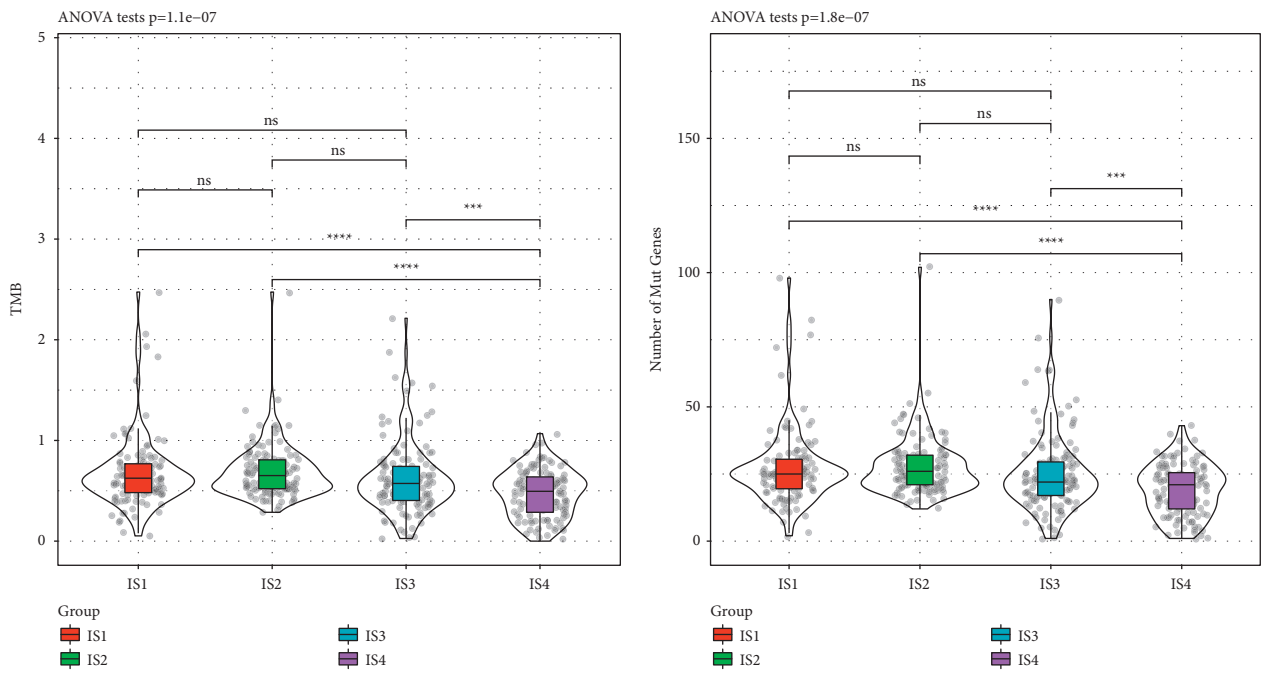

(a) (b)

Figure 2: Continued.

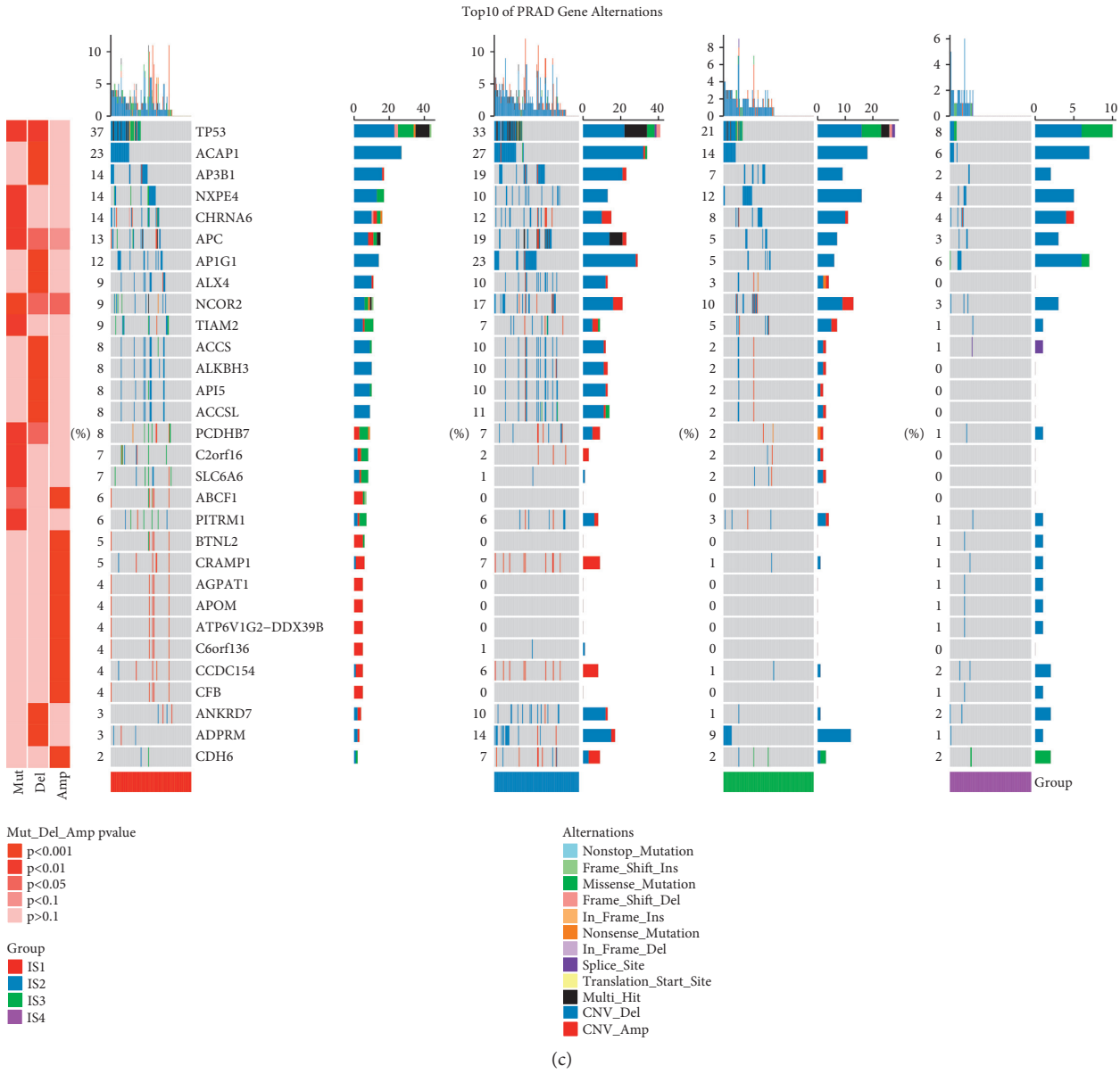

(c)

Figure 2: Mutation analysis in TCGA-PRAD dataset. The distribution of TMB (a) and number of mutated genes (b) in four immune subtypes. ANOVA was performed. (c) Mutation patterns and 12 types of variations in four groups. Fisher's exact test was used *** $p < 0.001$, **** $p < 0.001$.

subtypes (FDR < 0.01, $p < 0.05$, Figure 5(f)). A majority of immune biomarkers were enriched in IS1 group, especially leukocyte fraction, macrophage regulation, lymphocyte infiltration, IFN-γ response, TCR Shannon, TCR richness, dendritic cells and lymphocytes; however, these biomarker were less enriched in IS2 group ($p < 0.01$, Figure 5(f)).

3.6. The Differential Performance of Immunotherapy within Four Immune Subtypes. We then analyzed the immunotherapeutic performance of IS1 to IS4 using TIDE software (http://tide.dfci.harvard.edu/). A higher TIDE score represents higher possibility of immune escape, indicating less benefit from immunotherapy. IS1 and IS3 groups showed higher TIDE score than IS2 and IS4 groups, indicating lower effectiveness of immunotherapy of IS1 and IS3 groups ($p = 6.5e - 12$, Figure 6(a)). In addition, we also calculated the scores of T cell dysfunction and T cell exclusion, as shown in Figures 6(b) and 6(c), respectively. T cell dysfunction was the strongest in IS1 group, and this was correlated with unfavorable survival, although its T cell exclusion score was the lowest. Immune response was significantly different among these immune subtypes, showing the worst immunotherapeutic efficacy in IS3 group and the optimal immune response in IS2 group (Figure 6(d)).

3.7. An Immune Landscape of PCa and an Extension for Immune Subtyping System. To further examine the immune features and subtypes of PCa, we applied a reduced

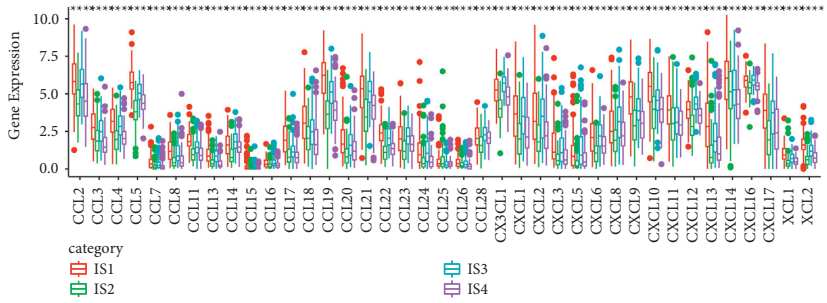

(a)

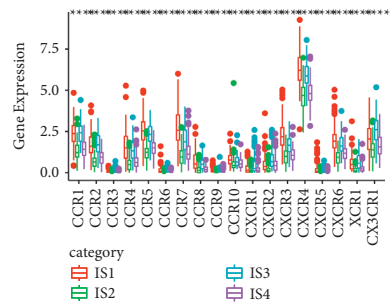

(b)

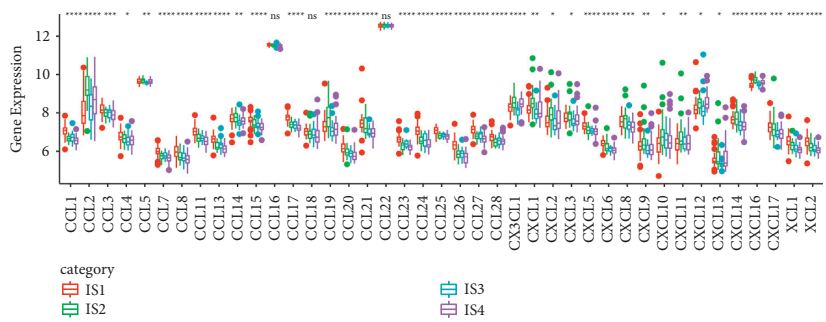

(c)

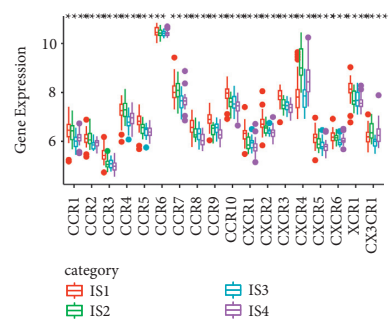

(d)

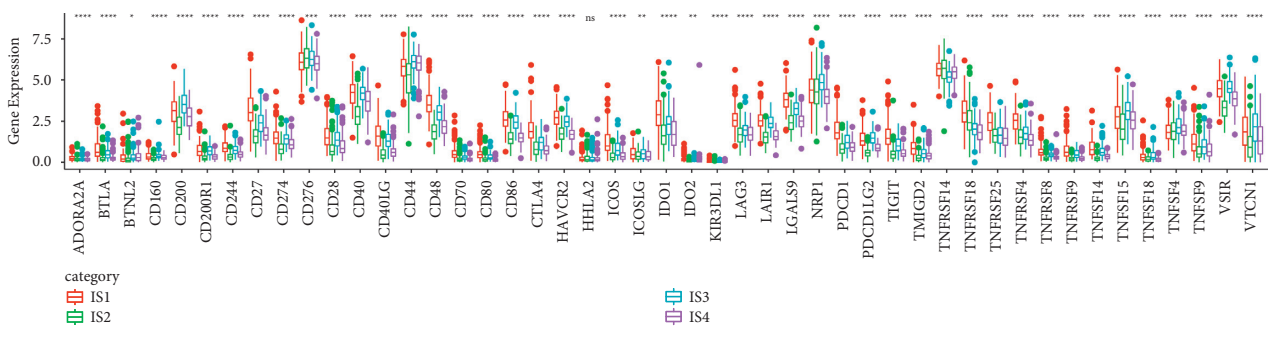

(e)

Figure 3: Continued.

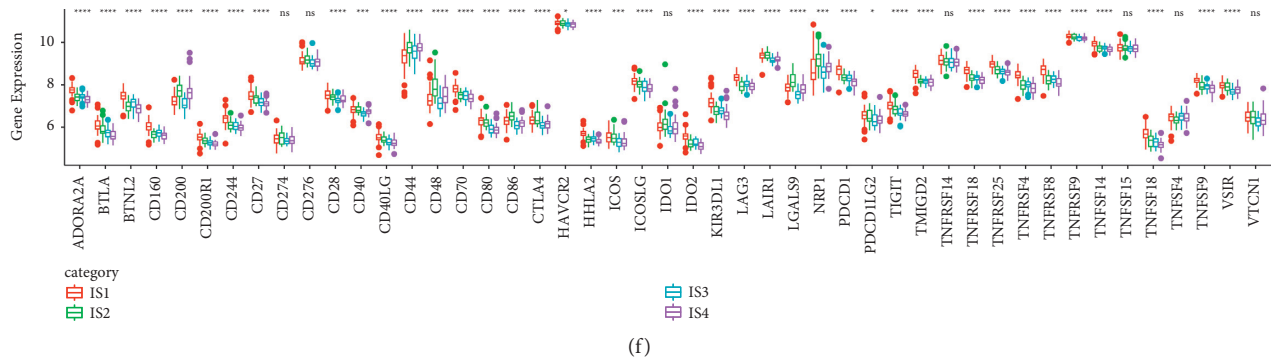

(f)

Figure 3: The differential expression of chemokines, chemokine receptors, and immune checkpoints among four immune subtypes. (a-b) The expression of chemokines (a) and chemokine receptors (b) in TCGA-PRAD dataset. (c-d) The expression of chemokines (c) and chemokine receptors (d) in MKSCC-PRAD dataset. (e-f) The expression of total 47 immune checkpoints in TCGA-PRAD dataset (e) and MKSCC-PRAD dataset (f). ANOVA was performed. $^{*}p < 0.05$, $^{**}p < 0.01$, and $^{***}p < 0.001$. ns: no significance.

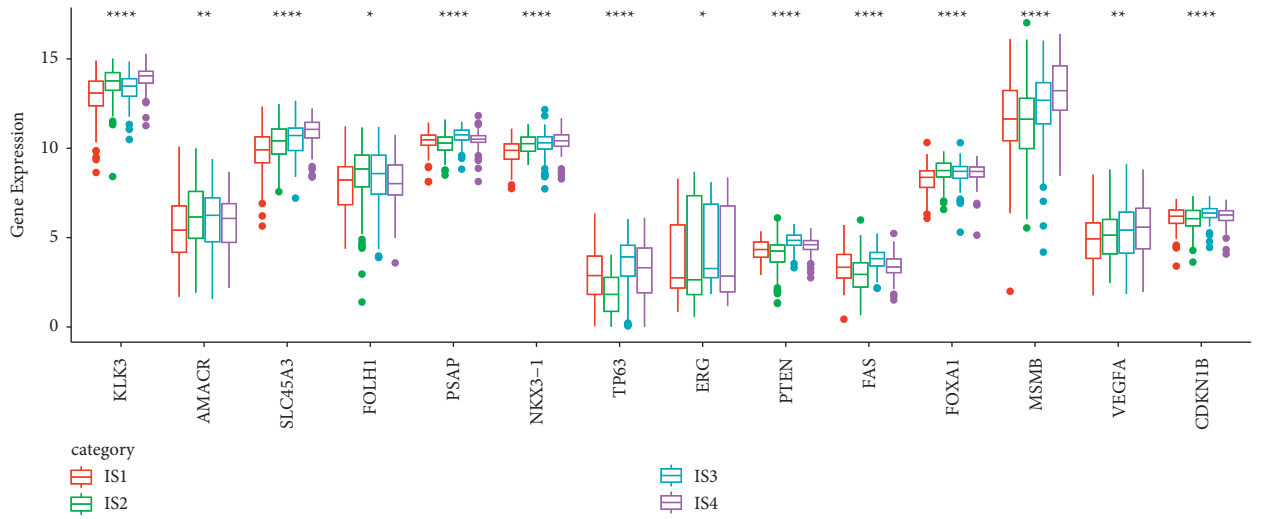

(a)

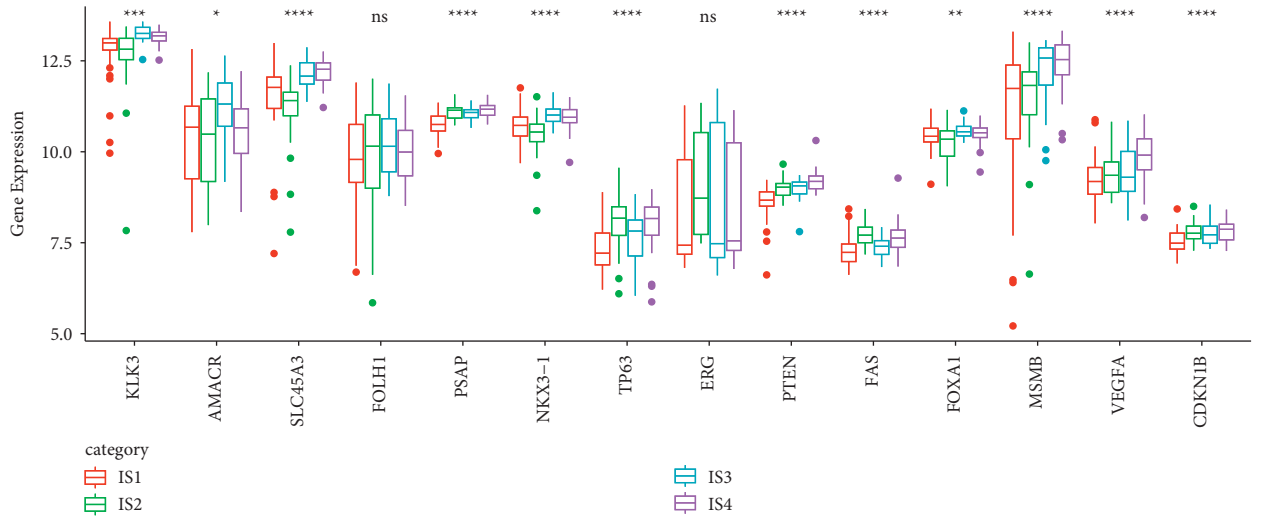

(b)

Figure 4: The differential expression of PCa immunohistochemical biomarkers in TCGA-PRAD dataset (a) and MKSCC-PRAD dataset (b). ANOVA was performed. $^{*}p < 0.05$, $^{**}p < 0.01$, $^{***}p < 0.001$, and $^{****}p < 0.0001$. ns: no significance.

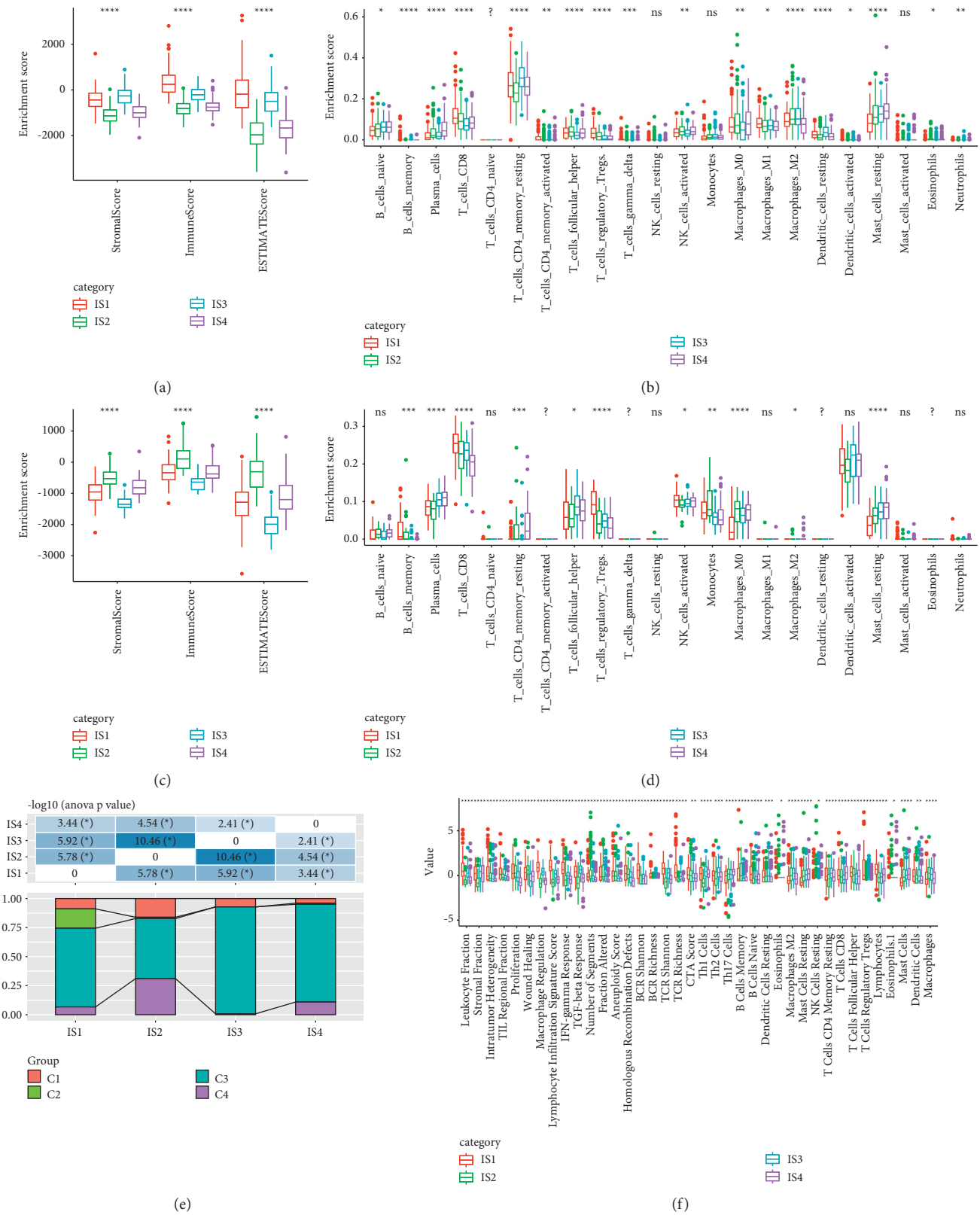

FIGURE 5: Differential immune features of immune subtypes. (a-b) Immune features of four immune subtypes scored by ESTIMATE (a) and CIBERSORT (b) tools in TCGA-PRAD dataset. (c-d) Immune features of four immune subtypes scored by ESTIMATE (c) and CIBERSORT (d) tools in MKSCC-PRAD dataset. (e) The distribution of C1 to C4 groups in IS1 to IS4 groups. (f) 38 immune biomarkers significantly varied in IS1 to IS4 groups. ANOVA was performed. $^{*}p < 0.05$, $^{**}p < 0.01$, $^{***}p < 0.001$, and $^{****}p < 0.0001$. ns: no significance. $^{?}$Low expression cannot be calculated.

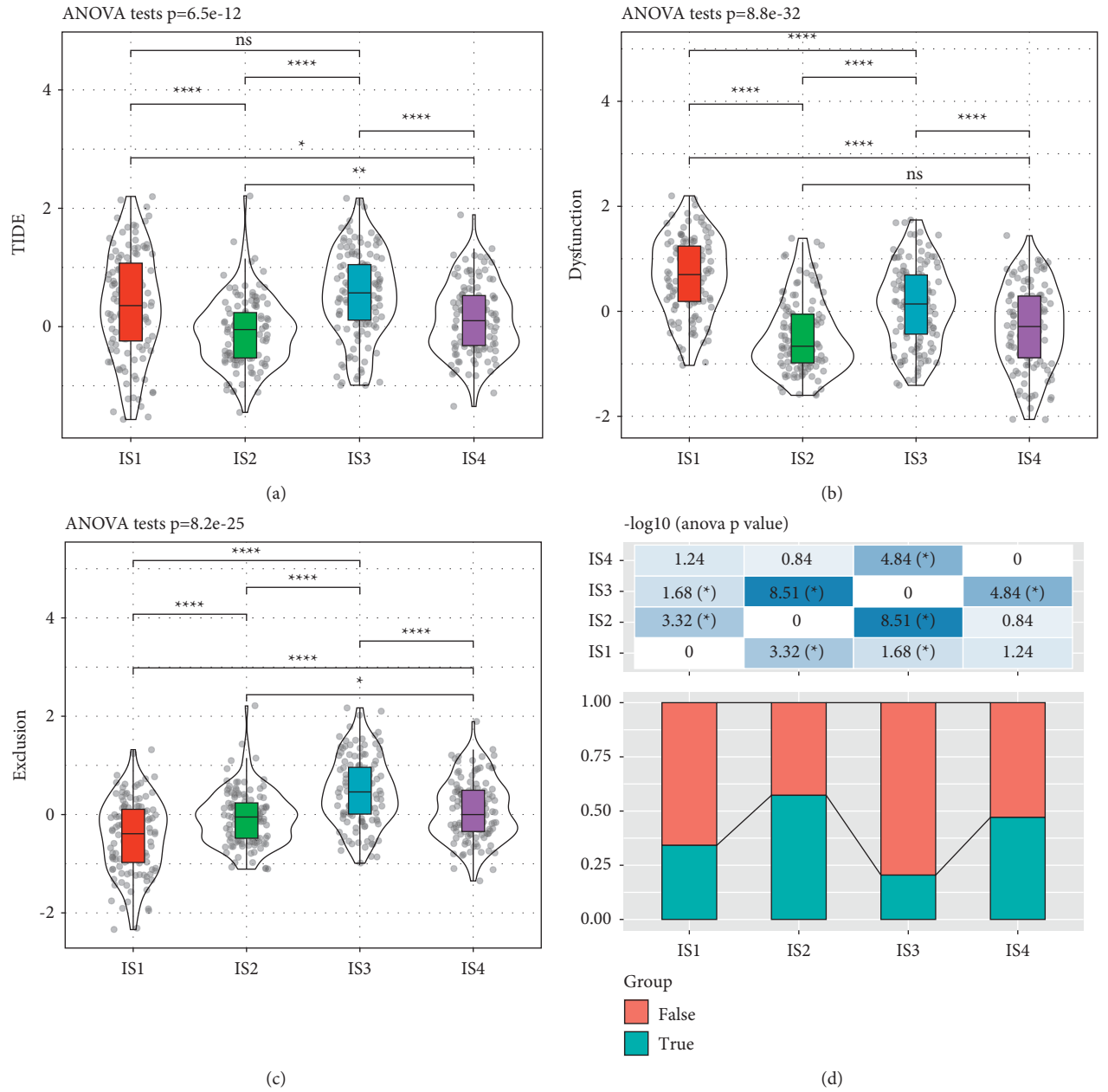

Figure 6: Prediction of immunotherapeutic efficacy among four immune subtypes. (a) Immune response scored by TIDE. (b-c) The performance of T cell dysfunction (b) and T cell exclusion (c) in four groups. (d) Prediction of immunotherapeutic efficacy in four groups. True and false represents the positive and negative immune response to immunotherapy, respectively. ANOVA was performed. $^{*}p < 0.05$, $^{**}p < 0.01$, $^{***}p < 0.001$, and $^{****}p < 0.0001$. ns: no significance.

dimensional method where each sample was casted as a point in a two-dimensional space in a latent tree structure. Component 1 and component 2 were two independent immune-related gene sets generated by principle component analysis. An immune landscape of PCa was constructed, and four immune subtypes were labeled with different colors (Figure 7(a)). Next, we assessed the correlation between two components and immune biomarkers. Component 1 was found to be negatively related to leukocyte fraction, macrophage regulation, lymphocyte infiltration signature score, TGF-β response, TCR Shannon, and TCR richness, which was consistent with the previous result ($|R| > 0.5$, $p < 0.001$, Figures 7(b) and 5(f)). Component 2 was significantly associated with wound healing, T cells follicular helper, IFN-gamma response, and T cells CD4 memory resting ($p < 0.001$, Figure 7(c)). According to the immune landscape, IS1 and IS3 groups could be further subdivided into IS1A and IS1B, IS3A and IS3B. The immune features of subgroups showed subtle difference between two groups scored by CIBERSORT, and differential enrichment score was calculated by ESTIMATE (Figure 7(d)). Additionally, survival analysis revealed that three branches of the tree structure showed differences in OS

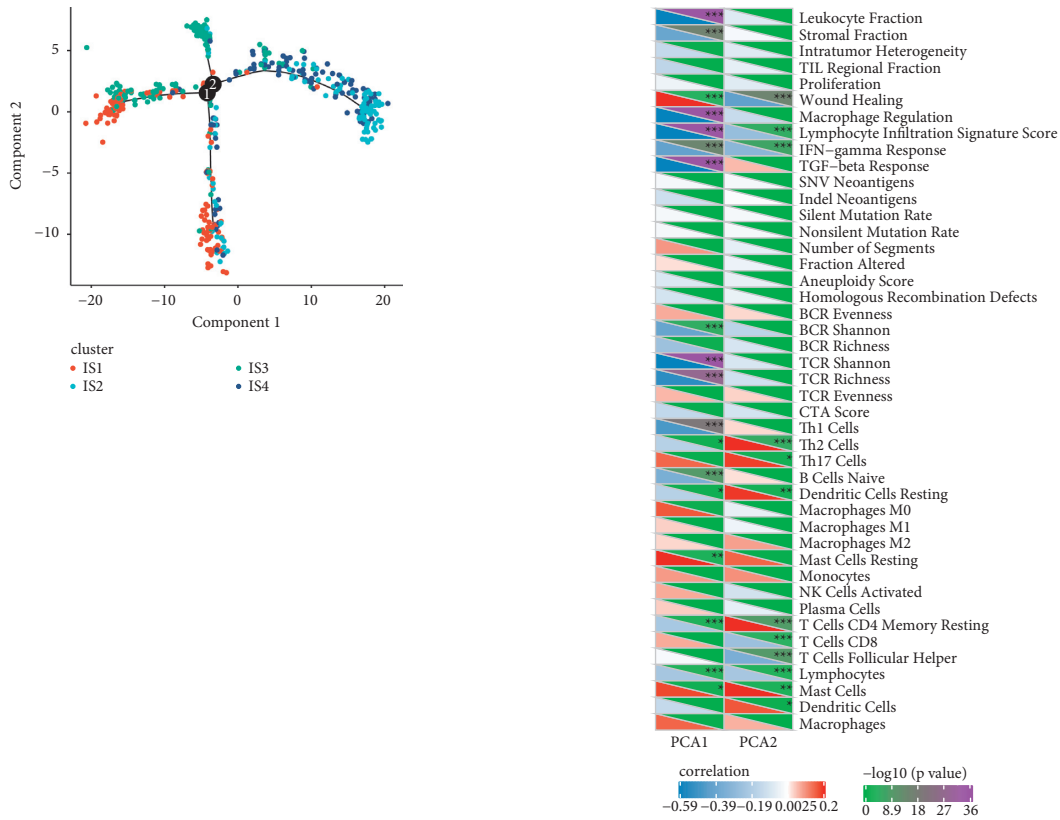

Figure 7: Continued.

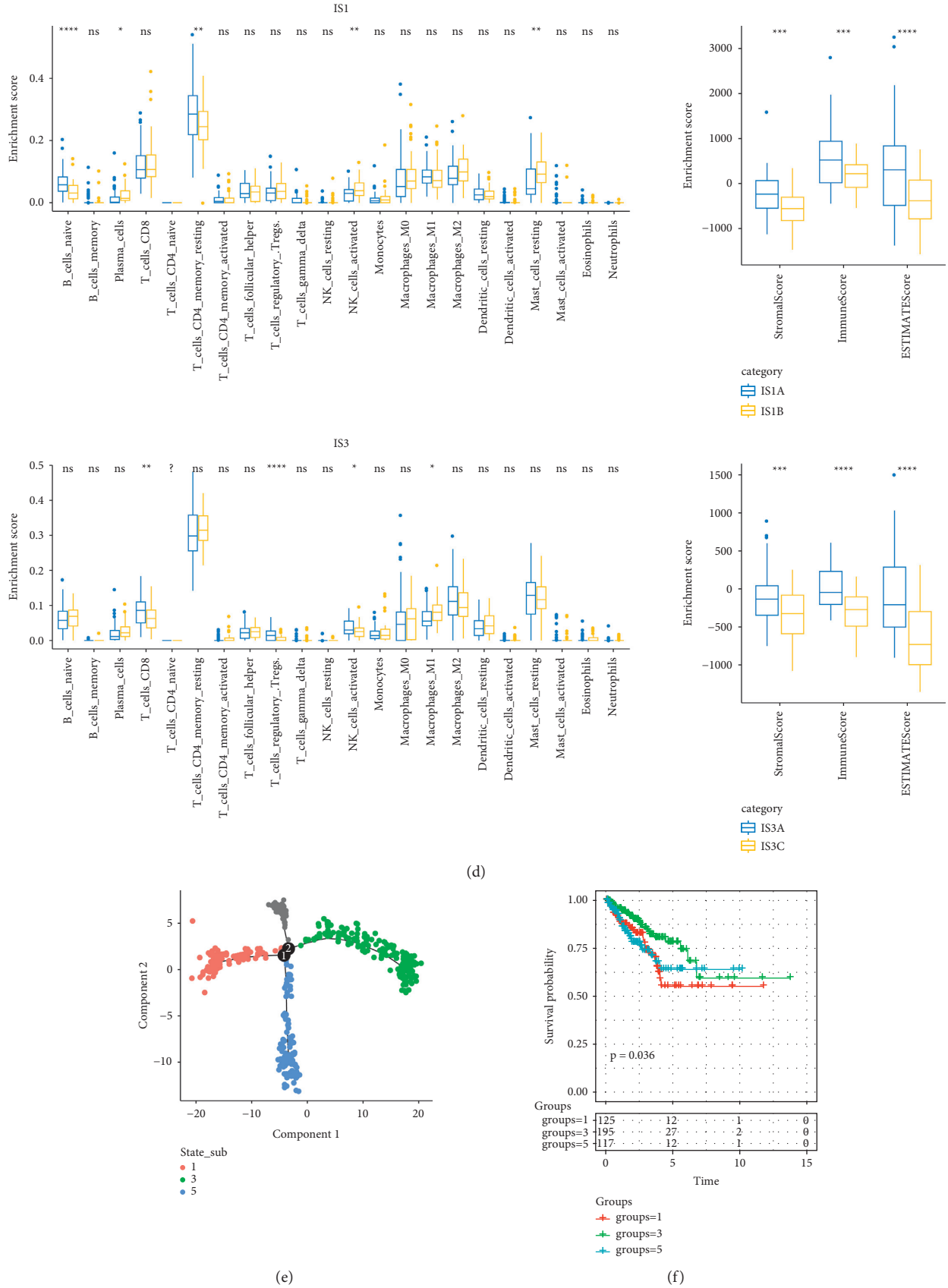

FIGURE 7: Construction of immune landscape within TCGA-PRAD dataset. (a) The distribution of four immune subtypes in the immune landscape. (b) The relation between component 1 (PCA1), component 2 (PCA2), and immune biomarkers. (c) Subdivision of IS1 and IS3 groups. (d) Immune features of IS1A and IS1B, IS3A, and IS3B scored by ESTIMATE and CIBERSORT tools. (e) Immune landscape grouped by branches 1, 3, and 5. (f) Kaplan–Meier survival curve of groups 1, 3, and 5. Log-rank test was performed. $^{*}p < 0.05$, $^{**}p < 0.01$, $^{***}p < 0.001$, and $^{****}p < 0.0001$. ns: no significance.

($p = 0.036$), indicating that this immune landscape was reliable and effective in further supplementary the immune subtypes (Figures 7(e) and 7(f)).

3.8. Identification of Coexpressed Gene Modules Based on Immune-Related Genes. We also identified coexpressed gene modules to further explore immune-related genes by WGCNA. Under the condition of the negative relation between $\log(k)$ and $\log(p(k))$, $R^2 > 0.85$ and soft threshold (power) = 12 were defined to meet a scale-free network (Figures 8(a) and 8(b)). Using average-linkage hierarchical clustering and dynamic branch cutting, co-expression modules containing at least 30 genes in each module were identified. Modules with close distance were then merged, and five modules were identified when height = 0.3, deepSplit = 4, and minModuleSize = 30 (Figure 8(c)). Finally, 1905 immune-related genes were classified into five modules colored as turquoise, grey, green-yellow, blue, and black (Figure 8(d), Supplementary Table S4). In each module, all eigengenes varied significantly within four immune subtypes, which supported the effectiveness of the immune subtyping system ($p < 0.0001$, Figure 8(e)). Furthermore, close relation between modules and immune subtypes was demonstrated. IS1 and IS3 groups were positively related to modules, especially to the black and blue modules, while IS2 and IS4 were negatively correlated with the modules (Figure 8(f)). However, clinical features including age, T, N, and M stages were not tightly associated with modules. The scatter diagram demonstrated close association of black module with IS3 group (coefficient = 0.82, $p < 0.0001$) and blue module with IS1 group (coefficient = 0.58, $p < 0.0001$) (Figures 8(g) and 8(h)).

3.9. Function of Coexpressed Gene Modules and Screening of Prognostic Genes. Gene set enrichment analysis was conducted to determine enriched biological processes of blue and black modules. The results showed that blue module was largely enriched to biological processes such as T cell activation, regulation of lymphocyte activation, and leukocyte proliferation, and it was negatively correlated with component 1 ($R = -0.816$, $p < 0.0001$, Figures 9(a) and 9(b)). For black module, biological processes of extracellular structure organization and extracellular matrix organization were enriched, and the module was also negatively correlated with component 1 ($R = -0.736$, $p < 0.0001$, Figures 9(c) and 9(d)).

Genes closely related to prognosis were screened, and a total of 243 genes with $R > 0.85$ were detected from the blue and black modules. LASSO regression analysis was applied to construct a prognostic model. When lambda = 016636511, the model was optimal, and 17 genes were identified. To further simply the model, we conducted Akaike information criterion to reach a high fitting degree through including the minimum amount of genes. Finally, based on FGD2, IL2RG, LRMP, NCF1, VAV1, ZNF831, COL5A1, EBF1, PCDH18, PLXND1, and PTGIS, an 11-gene prognostic model was defined as follows.

$$\begin{aligned}\text{Risk Score} = {} & 0.4463861 * \text{FGD2} - 0.3572187 * \text{IL2RG} - 0.5703754 \\ & * \text{LRMP} * 0.5567643 * \text{NCF1} + 0.5364159 * \text{VAV1} - 0.3522158 * \\ & \text{ZNF831} + 0.6454266 * \text{COLA1} - 0.4826737 * \text{EBF1} - 0.5881331 * \\ & \text{PCDH18} + 0.4988597 * \text{PLXNDI} - 0.4001723 * \text{PTGIS}.\end{aligned} \tag{1}$$

The risk score of each sample in TCGA-PRAD and MKSCC-PRAD datasets was calculated and converted to z-score, which was then used to divide the samples that were divided into high-risk or low-risk group. The result showed that OS in low-risk group was higher than high-risk group in both datasets ($p < 0.001$, Figures 9(e) and 9(f)). In addition, we compared the expression differences of these 11 genes in cancer and adjacent samples and observed that FGD2, LRMP, VAV1, EBF1, PCDH18, and PTGIS were significantly underexpressed in tumor samples (Supplementary Figure S2A). Further, we analyzed the relationship between these 11 genes and immune infiltration and observed that these genes were significantly related to multiple immune infiltrating cells, especially with T_ cells_ CD4_ memory_ Resting and dendritic_ cells_ Resting showed a significant positive correlation (Supplementary Figure S2B). The correlation analysis of immune checkpoint genes showed that ZNF831, VAV1, NCF1, LRMP, IL2RG, and FGD2 showed a significant positive correlation with a variety of immune checkpoint genes (Supplementary Figure S2C). Further, we mapped these 11 genes to the string database to analyze the interaction between these genes. It can be observed that there is little direct interaction between these genes, but more indirect interaction, suggesting that these genes may play different roles in different time and space (Supplementary Figure S2D).

4. Discussion

For mCRPC patients, immunotherapy is now the only available treatment. Sipuleucel-T, which is the only cancer vaccine approved by Food and Drug Administration (FDA) in treating mCRPC, was a significant improvement in mCRPC treatment [20, 21]. Extended OS was observed in the sipuleucel-T trials with tolerated adverse effects [21, 22]. According to a large-scale research on mCRPC patients, only approximately 10% could benefit from sipuleucel-T, indicating the limitation of the cancer vaccine in wide application [23]. Immune checkpoint inhibitors against PD-1, PD-L1, and CTLA-4 have found to be able to prolong the OS

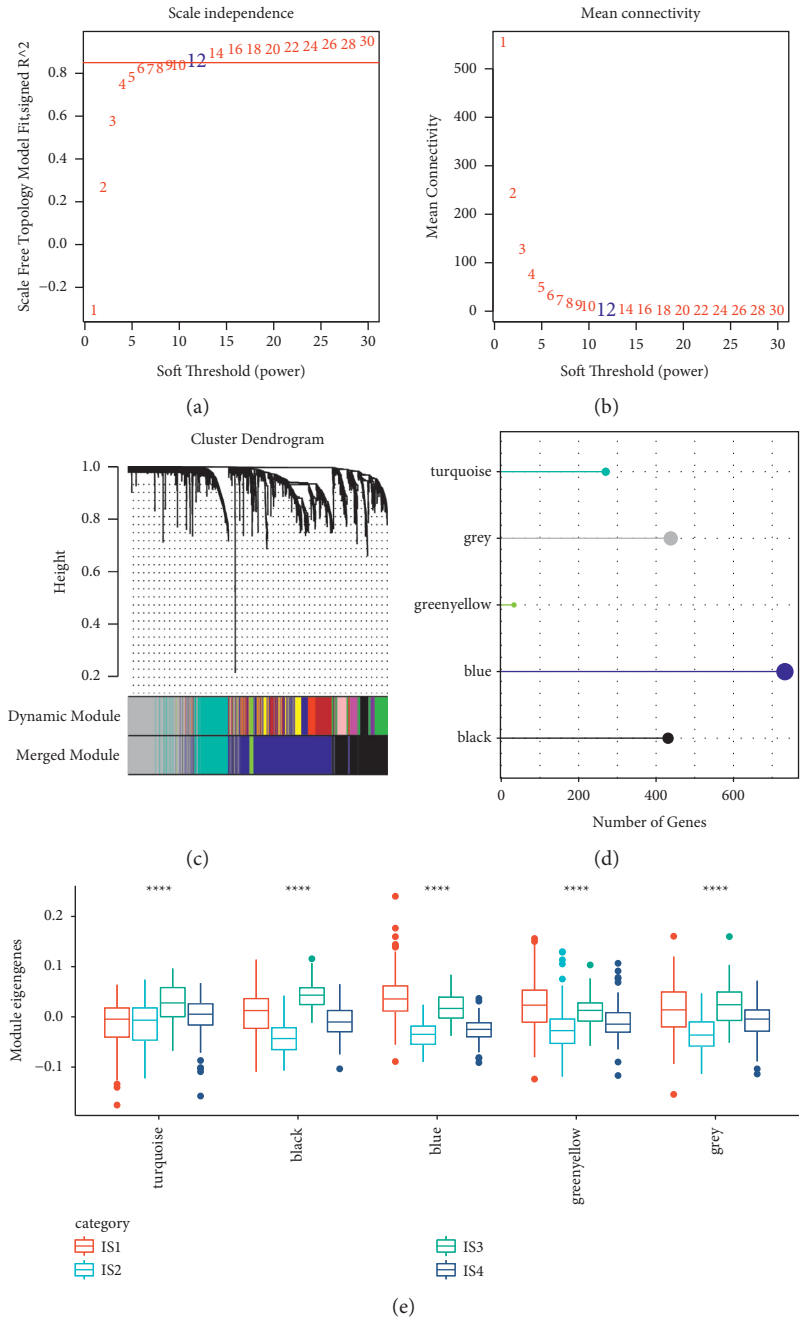

Figure 8: Continued.

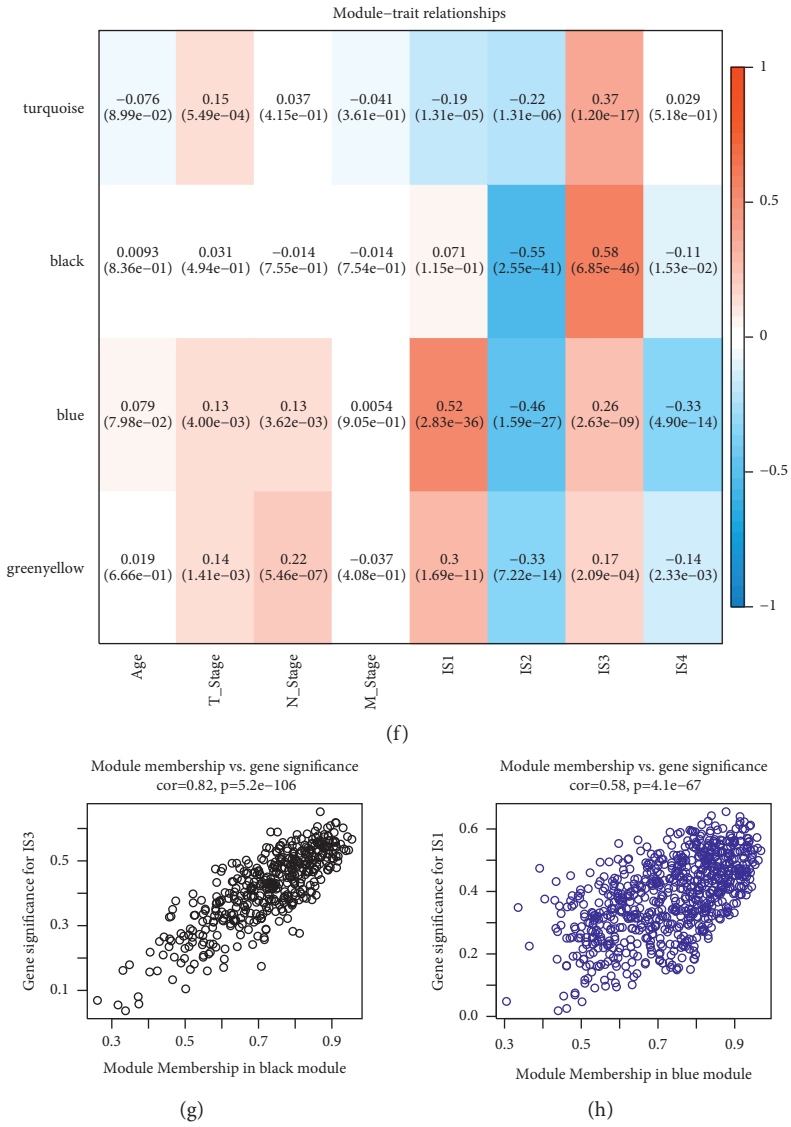

Figure 8: Identification of coexpressed gene modules. (a-b) Analysis of the scale-free fit index (a) and mean connectivity (b) for various soft-thresholding powers. (c) Cluster dendrogram and merged modules when soft-thresholding powers = 12. (d) Five modules colored with turquoise, grey, green-yellow, blue, and black. (e) Eigengenes of four immune subtypes groups by modules. (f) The correlation between modules and clinical features, immune subtypes. Positive correlation and negative correlation were colored with red and blue, respectively. (g-h) Scatter diagram of the relation between black module and IS3 group (g), blue module and IS1 group (h).$^{****}p < 0.0001$.

of mCRPC patients. However, the efficacy of current monoclonal antibodies is not satisfactory, and new clinical trials of updated strategies are still ongoing [24]. To some extent, immunotherapy of PCa is still far from mature. Evidence revealed that TME is of great importance for tumor progression and can suppress or stimulate the efficacy of immunotherapy [25]. Therefore, a comprehensive understanding of the TME of Pca plays a critical role in guiding immunotherapy.

In the current study, we explored an immune subtyping system that has not been reported before. Based on immune-related gene expression profiles of TCGA-PRAD dataset, a unique molecular subtyping system was generated through substantial informatics analysis. All patients could be classified into four immune subtypes (IS1 to IS4). The OS was different among the groups, with the optimal prognosis in IS4 group and the worst prognosis in IS1 group. The proportion of IS1 group in the TNM staging system was consistent with the progressing stages. In addition, IS1 group had the highest mutation frequency, especially increased copy numbers. The different mutation patterns may explain the differential component of TME.

Immune infiltration is a pivotal component of TME and represents the immune signatures of cancers. Chemokines are a family of chemotactic cytokines that can regulate the positioning and expression of immune cells [26, 27]. As chemokines and chemokine receptors are responsible for cancer metastasis, they have also been considered to be the possible targets of cancer immunotherapy [28]. The expression of chemokines and

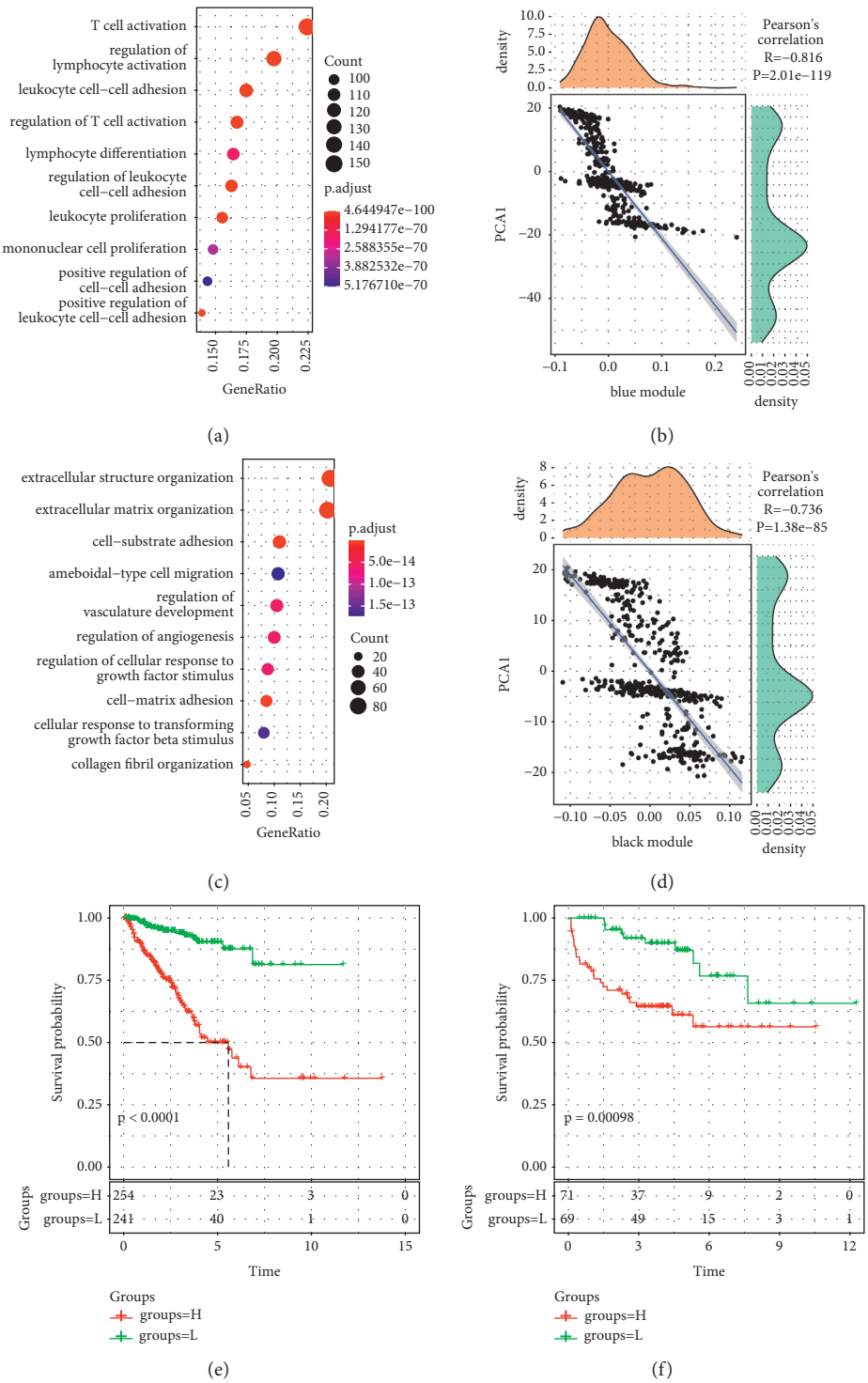

FIGURE 9: Functional analysis of blue and black modules, and survival analysis of two datasets. (a) Top 10 enriched biological processes in blue module. (b) Pearson's correlation between blue module and component 1. (c) Top 10 enriched biological processes in black module. (d) Pearson's correlation between black module and component 1. (e-f) Kaplan–Meier survival curve in TCGA-PRAD (e) and MKSCC-PRAD (f) datasets. H: high risk. L: low risk. Log-rank test was performed.

chemokine receptors in PCa was evaluated in our study. Differential expression was observed among the four immune subtypes, indicating that expression patterns of chemokines and chemokine receptors may result in different outcomes of PCa development.

According to the previous researches, tumors can be divided into three infiltration patterns (immune-inflamed or immune-active ('hot'), immune-excluded, and immune-deserted ('cold')) in terms of the components of TME [29, 30]. PCa has been stratified into immune-desert pattern

and is inactively responsive to immunotherapy [31]; therefore, only a small number of patients can benefit from the immunotherapy. To ascertain whether the infiltration pattern would be different among the four immune subtypes, we assessed 56 immune biomarkers and scored their enrichment. The expression of immune biomarkers varied in four immune subtypes. The results showed that according to the enrichment level of leukocyte fraction, stromal fraction, TIL regional fraction proliferation, macrophage regulation, IFN-γ response, TCR richness, CD8+ T cells, and TGF-β response, IS1 group was classified into immune-excluded pattern and IS2 group was immune-desert pattern. Furthermore, TIDE analysis also revealed that patients in IS2 and IS4 groups were more suitable to receive immunotherapy than those in IS1 and IS3 groups. The specific stratification of infiltration patterns and efficacy prediction of immunotherapy can provide a guidance for personalized immunotherapy.

By introducing a graph-learning landscape, IS1 and IS3 groups were further subdivided. The enrichment of immune biomarkers was significantly different in the subdivisions. The immune landscape of PCa supplemented the immune subtyping system and visualized the immune signatures, providing a better understanding of the tumor microenvironment. In addition, co-expression gene modules were constructed, and 11 prognostic genes were identified from the models. The 11-gene prognostic model can predict the prognosis and further facilitate personalized treatment of PCa.

5. Conclusion

In conclusion, we defined a new molecular subtyping system based on immune-related genes. PCa patients were classified into four immune subtypes and showed significant difference in prognosis, immune signatures, response of immunotherapy, and infiltration patterns. An immune landscape of PCa was generated and helps further understand the TME. This novel immune subtyping system can be a guidance in the development of immunotherapy and personalized treatment of PCa patients.

Abbreviations

ADT: Androgen depravation therapy
CDF: Cumulative distribution function
CNV: Copy number variants
CTLA-4: Cytotoxic T-lymphocyte-associated protein 4
ESTIMATE: Estimation of STromal and Immune cells in MAlignant Tumours using Expression data
FDA: Food and Drug Administration
IS: Immune subtypes
LASSO: Least absolute shrinkage and selection operator
MCRPC: Metastatic castration-resistant prostate cancer
OS: Overall survival
PAM: Partitioning around medoids
PCa: Prostate cancer
PD-1: Programmed cell death protein 1
PD-L1: Programmed cell death ligand 1
PSA: Prostate-specific antigen
SsGSEA: Single-sample gene set enrichment analysis
TCGA: The Cancer Genome Atlas
TGF: Transforming growth factor
TIDE: Tumor immune dysfunction and exclusion
TIL: Tumor-infiltrating lymphocyte
TMB: Tumor mutation burden
TME: Tumor microenvironment
TOM: Topological overlap matrix
TPM: Transcripts per million
WGCNA: Weighted correlation network analysis.

Data Availability

The data used to support the findings of this study are included within the article.

Conflicts of Interest

The authors declare that they have no conflicts of interest regarding the publication of this paper.

Authors' Contributions

Zhong Lin and Dingyuan Zeng contributed equally to this article.

Supplementary Materials

Supplementary Figure S1. Work flow chart. *Supplementary Figure S2*. Expression and interaction analysis of 11 genes. (A) Differential expression of 11 genes in cancer and adjacent tissues. (B) Correlation between 11 genes and immune infiltrating cells. (C) Correlation analysis between the expression of 11 genes and immune checkpoint genes. (D) Interaction between 11 genes. *Supplementary Table S1*. Immune related genes list. *Supplementary Table S2*. Clinical information of TCGA-PRAD dataset. *Supplementary Table S3*. Clinical information of MKSCC-PRAD dataset. *Supplementary Table S4*. Information of co-expression module corresponding to each gene. (*Supplementary Materials*)

References

[1] H. Sung, J. Ferley, R. L. Siegel et al., "Global cancer statistics 2020: GLOBOCAN estimates of incidence and mortality worldwide for 36 cancers in 185 countries," *CA: A Cancer Journal for Clinicians*, vol. 71, 2021.

[2] M. R. Cooperberg and P. R. Carroll, "Trends in management for patients with localized prostate cancer, 1990–2013," *JAMA*, vol. 314, no. 1, pp. 80–82, 2015.

[3] M. Tucci, G. V. Scagliotti, and F. Vignani, "Metastatic castration-resistant prostate cancer: time for innovation," *Future Oncology*, vol. 11, no. 1, pp. 91–106, 2015.

[4] M. Santoni, F. Massari, V. Di Nunno et al., "Immunotherapy in renal cell carcinoma: latest evidence and clinical implications," *Drugs In Context*, vol. 7, Article ID 212528, 2018.

[5] S. A. Weiss, J. D. Wolchok, and M. Sznol, "Immunotherapy of melanoma: facts and hopes," *Clinical Cancer Research*, vol. 25, no. 17, pp. 5191–5201, 2019.

[6] D. B. Doroshow, M. F. Sanmamed, K. Hastings et al., "Immunotherapy in non-small cell lung cancer: facts and hopes," *Clinical Cancer Research*, vol. 25, no. 15, pp. 4592–4602, 2019.

[7] M. Wang, J. Zhao, L. Zhang et al., "Role of tumor microenvironment in tumorigenesis," *Journal of Cancer*, vol. 8, no. 5, pp. 761–773, 2017.

[8] S. Saini, "PSA and beyond: alternative prostate cancer biomarkers," *Cellular Oncology*, vol. 39, no. 2, pp. 97–106, 2016.

[9] S. Hatakeyama, T. Yoneyama, Y. Tobisawa, and C. Ohyama, "Recent progress and perspectives on prostate cancer biomarkers," *International Journal of Clinical Oncology*, vol. 22, no. 2, pp. 214–221, 2017.

[10] L. Fabris, Y. Ceder, A. M. Chinnaiyan et al., "The potential of MicroRNAs as prostate cancer biomarkers," *European Urology*, vol. 70, no. 2, pp. 312–322, 2016.

[11] F. Xia, Z. Yu, A. Deng, and G. Gao, "Identification of molecular subtyping system and four-gene prognostic signature with immune-related genes for uveal melanoma," *Experimental Biology and Medicine (Maywood, N. J.)*, vol. 247, no. 3, pp. 246–262, 2021.

[12] M. D. Wilkerson and D. N. Hayes, "ConsensusClusterPlus: a class discovery tool with confidence assessments and item tracking," *Bioinformatics*, vol. 26, no. 12, pp. 1572-1573, 2010.

[13] C. Trapnell, D. Cacchiarelli, J. Grimsby et al., "The dynamics and regulators of cell fate decisions are revealed by pseudotemporal ordering of single cells," *Nature Biotechnology*, vol. 32, no. 4, pp. 381–386, 2014.

[14] P. Langfelder and S. Horvath, "WGCNA: an R package for weighted correlation network analysis," *BMC Bioinformatics*, vol. 9, no. 1, p. 559, 2008.

[15] S. Hänzelmann, R. Castelo, and J. Guinney, "GSVA: gene set variation analysis for microarray and RNA-seq data," *BMC Bioinformatics*, vol. 14, p. 7, 2013.

[16] V. Thorsson, D. L. Gibbs, S. D. Brown et al., "The immune landscape of cancer," *Immunity*, vol. 48, no. 4, pp. e14–e814, 2018.

[17] X. Jiao, B. T. Sherman, D. W. Huang et al., "DAVID-WS: a stateful web service to facilitate gene/protein list analysis," *Bioinformatics*, vol. 28, no. 13, pp. 1805-1806, 2012.

[18] T. Hastie and J. Qian, *Glmnet Vignette*, pp. 1–30, 2014, Retrieved June 9(2016).

[19] B. Ripley, *Package 'Mass'. Cran R*, pp. 113–120, 2013.

[20] E. J. Small, P. F. Schellhammer, C. S. Higano et al., "Placebo-controlled phase III trial of immunologic therapy with sipuleucel-T (APC8015) in patients with metastatic, asymptomatic hormone refractory prostate cancer," *Journal of Clinical Oncology*, vol. 24, no. 19, pp. 3089–3094, 2006.

[21] P. W. Kantoff, C. S. Higano, N. D. Shore et al., IMPACT Study Investigators, "Sipuleucel-T immunotherapy for castration-resistant prostate cancer," *New England Journal of Medicine*, vol. 363, no. 5, pp. 411–422, 2010.

[22] P. F. Schellhammer, G. Chodak, J. B. Whitmore, R. Sims, M. W. Frohlich, and P. W. Kantoff, "Lower baseline prostate-specific antigen is associated with a greater overall survival benefit from sipuleucel-T in the Immunotherapy for Prostate Adenocarcinoma Treatment (IMPACT) trial," *Urology*, vol. 81, no. 6, pp. 1297–1302, 2013.

[23] M. E. V. Caram, R. Ross, P. Lin, and B. Mukherjee, "Factors associated with use of sipuleucel-T to treat patients with advanced prostate cancer," *JAMA Network Open*, vol. 2, no. 4, Article ID e192589, 2019.

[24] A. Rizzo, "Is there a role for immunotherapy in prostate cancer?" *Cells*, vol. 9, no. 9, 2020.

[25] H. Tang, J. Qiao, and Y.-X. Fu, "Immunotherapy and tumor microenvironment," *Cancer Letters*, vol. 370, no. 1, pp. 85–90, 2016.

[26] J. W. Griffith, C. L. Sokol, and A. D. Luster, "Chemokines and chemokine receptors: positioning cells for host defense and immunity," *Annual Review of Immunology*, vol. 32, no. 1, pp. 659–702, 2014.

[27] E. Marcuzzi, R. Angioni, B. Molon, and B. Calì, "Chemokines and chemokine receptors: orchestrating tumor metastasization," *International Journal of Molecular Sciences*, vol. 20, no. 1, 2018.

[28] V. Mollica Poeta, M. Massara, A. Capucetti, and R. Bonecchi, "Chemokines and chemokine receptors: new targets for cancer immunotherapy," *Frontiers in Immunology*, vol. 10, p. 379, 2019.

[29] J. N. Kather, M Suarez-Carmona, P Charoentong et al., "Topography of cancer-associated immune cells in human solid tumors," *Elife*, vol. 7, 2018.

[30] T. Turan, D. Kannan, M. Patel et al., "Immune oncology, immune responsiveness and the theory of everything," *Journal for Immunotherapy of Cancer*, vol. 6, no. 1, p. 50, 2018.

[31] P. Thienger and M. A. Rubin, "Prostate cancer hijacks the microenvironment," *Nature Cell Biology*, vol. 23, no. 1, pp. 3–5, 2021.

Hindawi
Journal of Oncology
Volume 2022, Article ID 8423173, 17 pages
https://doi.org/10.1155/2022/8423173

Research Article

Pan-Cancer Analysis of Microfibrillar-Associated Protein 2 (MFAP2) Based on Bioinformatics and qPCR Verification

Zhilei Qiu,[1] Miao Xin,[2] Chenyang Wang,[3] Yueli Zhu,[4] Qingnuan Kong,[5] and Zhijun Liu[1]

[1]*Department of Urology, Qingdao Municipal Hospital, Qingdao, Shandong 266071, China*
[2]*Department of Anesthesiology, Qingdao Municipal Hospital, Qingdao, Shandong 266071, China*
[3]*Qingdao University, Qingdao, Shandong 266071, China*
[4]*Department of Radiology, Qingdao Municipal Hospital, Qingdao, Shandong 266071, China*
[5]*Department of Pathology, Qingdao Municipal Hospital, Qingdao, Shandong 266071, China*

Correspondence should be addressed to Zhijun Liu; zhijunliu2@outlook.com

Received 3 November 2021; Revised 24 December 2021; Accepted 30 December 2021; Published 15 February 2022

Academic Editor: Guo Chen

MFAP2 has been reported to play an oncogenic role in several types of human cancers. However, the expression profile of MFAP2 in various cancers and its impact on prognosis and immune infiltration remain unclear. In this study, the mRNA expression and protein expression of MFAP2 in normal tissues, tumor cell lines, and 33 malignant tumor tissues were analyzed comprehensively using Genotype-Tissue Expression (GTEx), Cancer Cell Line Encyclopedia (CCLE), and The Cancer Genome Atlas (TCGA), Oncomine and UALCAN databases, and the expression of MFAP2 in different grades and stages of cancers was assessed using Gene Expression Profiling Interactive Analysis 2 (GEPIA2) and Tumor and Immune System Interaction Database (TISIDB). In general, MFAP2 showed distinct expression in most tumor and normal tissues, closely associated with higher tumor grade, higher tumor stage, and poor survival in multiple cancers. A search of the UALCAN database and the cBioPortal database revealed that this difference in mRNA level expression could be partly attributed to abnormal DNA methylation and mutations at the genomic level. In addition, MFAP2 expression was also associated with tumor mutation burden, microsatellite instability, and neoantigens in different cancer types. More importantly, the TIMER and TISIDB databases also showed that MFAP2 levels were significantly correlated with immune infiltration abundance and immune-related gene markers, as well as ESTIMATE scores. By qPCR, MFAP2 expression was validated in four kinds of tumor tissue samples. The present study combined several databases and performed a pan-cancer analysis of the expression profile, methylation, and mutation for MFAP2 and its implications for prognosis and immune infiltration, suggesting that MFAP2 could contribute to malignant properties of many tumors. MFAP2 may be an important biomarker with prognostic value and has the potential to be a target for tumor immunotherapy.

1. Introduction

Immunotherapy is considered to be a promising treatment for cancers [1]. However, due to the heterogeneity of tumors, only 10–20% of the population can benefit from current immunotherapy [2, 3]. For example, anti-CTLA4 has poor clinical efficacy in gastric cancer [4]. Anti-PD-1 and anti-PD-L1 have shown partial response in progressive colorectal cancer [5]. With the development of high-throughput sequencing technologies, abundant data are available to the public, such as TCGA database containing transcriptome data for 33 tumors. It is possible and necessary to perform pan-cancer analyses of genes and to assess their correlation with clinical prognosis and immune infiltration [6]. New biomarkers are urgently needed to predict prognosis and to find new immune-related therapeutic targets.

MFAP2 consists of a 183-amino-acid protein with 2 domains [7]. MFAP2 exists in two forms. One is extracellular MFAP2, which is a protein binding to fibrin, collagen VI, tropoelastin, deproteinized, and biglycan14. The other is intracellular protein, which is a functional protein upregulating downstream genes related to cell adhesion, movement, and matrix remodeling. In the last decade, aberrant expression of MFAP2 was found in various malignant

tumors. MFAP2 is overexpressed in melanoma with its capacity of manipulating EMT-related proteins and Wnt/β-catenin pathway to enhance melanoma invasion and migration ability [8]. Upregulation of MFAP2 in gastric carcinoma has been found, in which MFAP2 accelerates cancer cell migration via MFAP2/integrin $\alpha5\beta1$/FAK/ERK pathway [9, 10]. The ability of MFAP2 in activating TGF-β/SMAD2/3 pathway in gastric carcinoma has also been reported, and this activation accelerates the transformation of gastric carcinoma from an epithelial cell phenotype to a mesenchymal phenotype [11]. Previous studies have pointed out that MFAP2 possesses a hyperaffinity to TGF-β superfamily member in adipose tissue [12–14].

However, there are no pan-cancer studies on the relationship between MFAP2 and various cancers. Here, we retrieved multiple databases, GTEx, CCLE, Oncomine, TCGA, UALCAN, GEPIA2, and TISIDB, to analyze MFAP2 expression in pan-cancer and its relationship with prognosis. In addition, we explored the relationship between MFAP2 expression and gene mutations, promoter methylation, tumor neoantigens, tumor mutation burden (TMB), microsatellite instability (MSI), mismatch repair (MMR) genes, and immune infiltration. Our results suggested that aberrant expression of MFAP2 was associated with its altered promoter methylation, affected immune infiltration in the tumor microenvironment, and also acted as a prognostic risk factor for a variety of cancers. This study was expected to provide a theoretical basis for gaining insight into the role of MFAP2 in tumor immunotherapy.

2. Materials and Methods

2.1. Gene Expression Analysis. We downloaded the normalized pan-cancer datasets TCGA and GTEx from the UCSC database, extracted the expression data of MFAP2 gene in each sample, and further transformed each expression value as log2(x+1). The MFAP2 expression in 33 cancers was obtained. In addition, data of each tumor cell line were also downloaded from the CCLE database and analyzed the expression levels of MFAP2 in 21 tumor cell lines. Data analysis was performed using RStudio version 1.1.456 (RStudio Inc., USA) and the *R* package ggpubr. Moreover, the expression levels of MFAP2 gene in different cancers were identified in the Oncomine database [15], with the thresholds of p-value = 0.05, fold change = 2, and gene rank = ALL. MFAP2 protein expression was investigated in UALCAN database, providing us a platform for protein expression analysis of Clinical Proteomics Cancer Analysis Alliance dataset [16]. Finally, we explored MFAP2 expression in different pathological stages and grades of TCGA tumors via GEPIA2 and TISIDB databases.

2.2. Prognostic Analysis. We first analyzed the relationship between MFAP2 expression in the 33 tumors and overall survival (OS) using TCGA data and visualized it with forest plots using univariate Cox regression analysis. Kaplan–Meier curves were further plotted to show the prognostic significance of MFAP2. Considering the possibility of non-tumor-related deaths during follow-up, we analyzed the relationship between MFAP2 expression and disease-specific survival (DSS), disease-free interval (DFI), and progression-free interval (PFI) in the 33 TCGA tumors.

2.3. Genetic Changes Analysis. On the website cBioPortal [17], we selected "TCGA Pan Cancer Atlas Studies" datasets. The mutations and copy number of MFAP2 were investigated, and MFAP2 mutation sites were displayed in schematic and 3D structure maps.

The TMB and MSI scores of all samples were determined from the somatic mutation data downloaded from TCGA, and the correlation between MFAP2 expression and TMB and MSI was assessed using Spearman's rank correlation coefficient. The number of tumor neoantigens in each tumor sample was counted and its relationship with MFAP2 expression was analyzed. Moreover, TCGA expression profile data were used to analyze the expression of MMR genes, including MutL homologous gene (MLH1), MutS homologous gene (MSH2), MSH6, increased separation after meiosis (PMS2), and epithelial cell adhesion molecule (EPCAM) in different tumors. The correlation between MFAP2 and MMR genes was visualized in a heat map using the Reshape2 and *R* ColorBrewer packages.

2.4. DNA Methylation Analysis. The UALCAN database was used to show the methylation levels of MFAP2 in different tumors and corresponding normal tissues. In addition, we analyzed the correlation between MFAP2 expression and the expression of the four methyltransferases, including DNMT1, DNMT2, DNMT3A, and DNMT3B.

2.5. Immune Infiltration Analysis. We used TISIDB database, and TIMER, microenvironment cell populations (MCP)-counter and XCELL algorithms to explore the relationship between MFAP2 expression and immune infiltration in all TCGA tumors. We analyzed the stromal, immune, and ESTIMATE scores of each tumor sample using the ESTIMATE package and visualized the relationship between these scores and MFAP2 expression using scatter plots. In addition, we investigated the correlation of MFAP2 expression with monocyte and macrophage biomarkers using the TIMER database. Furthermore, we performed Spearman correlation analysis of MFAP2 and immune-related genes, including immunoinhibitors, immunostimulators, major histocompatibility complex (MHC) genes, chemokines, chemokine receptors, and immune checkpoints molecules. All data obtained were finally visualized in heat maps or scatter plots.

2.6. Tumor Tissue Collection. BLCA, BRCA, HNSC, and KICH tissues and normal tissues were collected from 5 patients, respectively. They were stored immediately in liquid nitrogen and kept at -80 °C. The study was approved by the Ethics Committee of the Qingdao Municipal

Hospital of Shandong province and conducted following the Declaration of Helsinki.

2.7. Quantitative Real-Time Polymerase Chain Reaction (qPCR). Total RNA was extracted from tissues using TRIzol reagent (Invitrogen, Thermo Fisher Scientific, Shanghai, China) and reverse-transcribed into cDNA using cDNA Reverse Transcription Kit (Applied Biosystems, Foster City, CA, USA). qPCR was performed using SYBR Premix Ex Taq II kit (RR820 A, TaKaRa, Dalian, China), with GAPDH as an internal reference. The relative expression of MFAP2 was calculated using the $2^{-\Delta\Delta Ct}$ method. The primers used are listed in Table 1.

2.8. Statistical Analysis. The data were analyzed using *R* 4.0.2 software and GraphPad 9.0.0 and expressed as mean ± SD. Differences were analyzed by *t*-test, with *p* values less than 0.05 considered statistically significant.

3. Results

3.1. MFAP2 Expression across Cancers. We first examined the expression levels of MFAP2 in normal tissues via the GTEx dataset. As shown in Figure 1(a), MFAP2 expression levels were the highest in cervix uteri tissues and the lowest in blood and bone marrow tissues. Also, the basal levels of MFAP2 expression in various tumor cell lines were assessed. As shown in Figure 1(b), MFAP2 was expressed at the highest level in bone cell lines and the lowest level in haematopoietic and lymphoid cell lines.

To determine the differential expression of MFAP2, the Oncomine database was used to analyze MFAP2 mRNA levels in different tumors and corresponding normal tissues. This analysis showed that, compared to normal tissues, MFAP2 expression was higher in bladder cancer, brain and central nervous system (CNS) cancer, breast cancer, colorectal cancer, esophageal cancer, gastric cancer, head and neck cancer, lymphoma, melanoma, myeloma, ovarian cancer, pancreatic cancer, and sarcoma. In some datasets of liver cancer and prostate cancer, no difference in expression was observed. In addition, MFAP2 expression was ambiguous in kidney cancer, leukemia, and lung cancer datasets; see Figure 2(a). Table 2 summarizes the details of MFAP2 expression in various cancers. To further assess the expression of MFAP2 in human cancers, we integrated transcriptomic data from all tumors in TCGA and GTEx. MFAP2 expression obtained from data in TCGA database and integrated data in the GTEx plus TCGA databases are shown in Figure 2(b) and Figure 2(c), respectively. Taking into account individual differences, we further assessed MFAP2 expression in paired samples Figure 2(d). The results showed that MFAP2 was significantly higher in BLCA, BRCA, CHOL, COAD, ESCA, HNSC, LIHC, LUAD, LUSC, READ, STAD, THCA, and UCEC than in adjacent normal tissues and significantly lower in KICH, KIRC, KIRP, and PRAD than in adjacent normal tissues. There was no MFAP2 expression difference in PAAD, which may be due to the small sample size. Moreover, MFAP2 protein expression was elevated in breast cancer, colon cancer, and lung adenocarcinoma and reduced in clear cell renal cell carcinoma; see Figure 2(e).

Table 1: PCR primers.

MFAP2	Forward(5′-3′)	CGCCGTGTGTACGTCATTAAC
	Reverse(5′-3′)	CCATCACGCCACATTTGGA
GAPDH	Forward(5′-3′)	TGCCATGTAGACCCCTTGAAG
	Reverse(5′-3′)	ATGGTACATGACAAGGTGCGG

Based on further analysis of the relationship between MFAP2 mRNA expression levels and cancer stage or grade, the results suggested that MFAP2 was positively correlated with the advanced BLCA stage in both GEPIA2 and TISIDB (see Figures 3(a) and 3(b)), and the TISIDB database of MFAP2 was positively correlated with the advanced CESC, KIRC, LGG, and LIHC grades (see Figure 3(c)).

3.2. MFAP2 Prognostic Value across Cancers. To investigate the relationship between MFAP2 expression levels and prognosis in terms of DFI, DSS, OS, and PFI, we depicted forest plots for each cancer (Figure 4). COX proportional risk model analysis showed that high expression of MFAP2 was associated with poor DFI for ACC, BRCA, CESC, CHOL, OV, and PAAD (Figure 4(a)), with poor DSS for ACC, BRCA, CESC, CHOL, KIRC, LGG, LIHC, and SARC (Figure 4(b)), with poor OS for ACC, BRCA, CESC, KIRC, LGG, LIHC, and SARC (Figure 4(c)), and poor PFI for ACC, BLCA, BRCA, CESC, KICH, KIRC, LGG, and SARC (Figure 4(d)). Interestingly, MFAP2 expression levels in UVM correlated with better DSS, OS, and PFI.

3.3. MFAP2 Mutation Profile. Genomic mutations are strongly associated with tumorigenesis. So, we used cBioPortal database to analyze the genomic alterations of MFAP2 in the TCGA pan-cancer datasets, consisting of 10,967 samples from 32 studies. The results showed that cholangiocarcinoma patients with deep deletion as the only mutation type had the highest frequency of MFAP2 alterations, exceeding 5%. In addition, amplification was the only type of MFAP2 mutation in the uterine carcinosarcoma samples, with a mutation frequency of over 3% (Figure 5(a)). Figure 5(b) shows that between amino acids 0 and 183, a total of 29 MFAP2 mutation sites, including 27 missense and 2 splices, were detected, with missense being the predominant type of DNA alteration. Of these, F157 L in the ShKr protein domain was the most frequent mutant site, detected in 2 cases of endometrial carcinoma. Moreover, the MFAP2 mutant sites were further demonstrated in the 3D structure as shown in Figure 5(c). Additionally, we found that MFAP2 expression was independent of mutations (Figure 5(d)) and independent of DNA copy variation Figure (5(e)).

3.4. MFAP2 Aberrant DNA Methylation. The genomic alteration analysis suggested that altered MFAP2 expression might not be due to genetic variation. We then examined epigenetic disorders of MFAP2 in cancers. As shown in Figure 6(a), we found that 4 tumors with high MFAP2

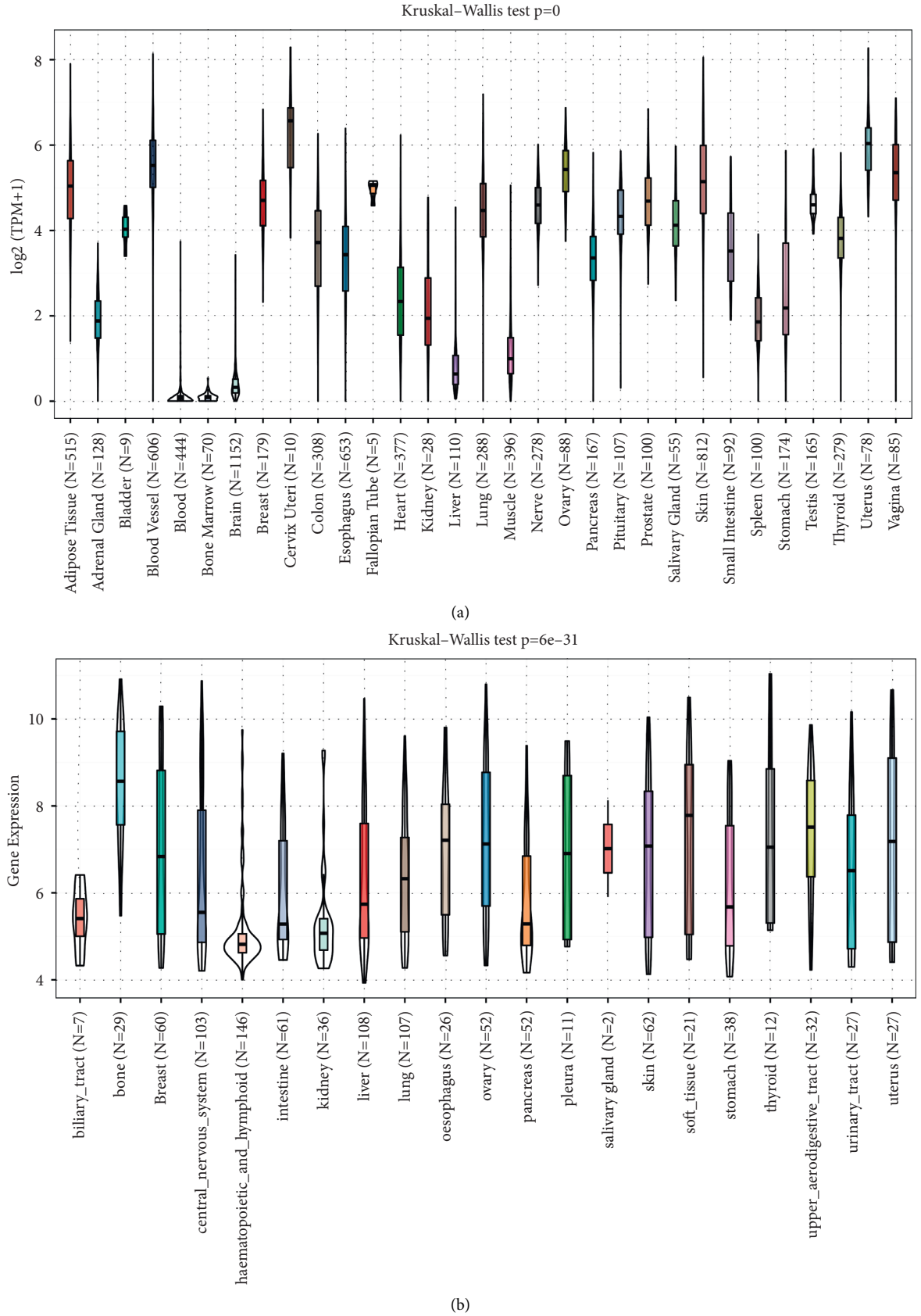

Figure 1: MFAP2 basal level. (a) MFAP2 expression in normal tissues obtained from GTEx database. (b) MFAP2 expression in tumor cell lines obtained from CCLE database.

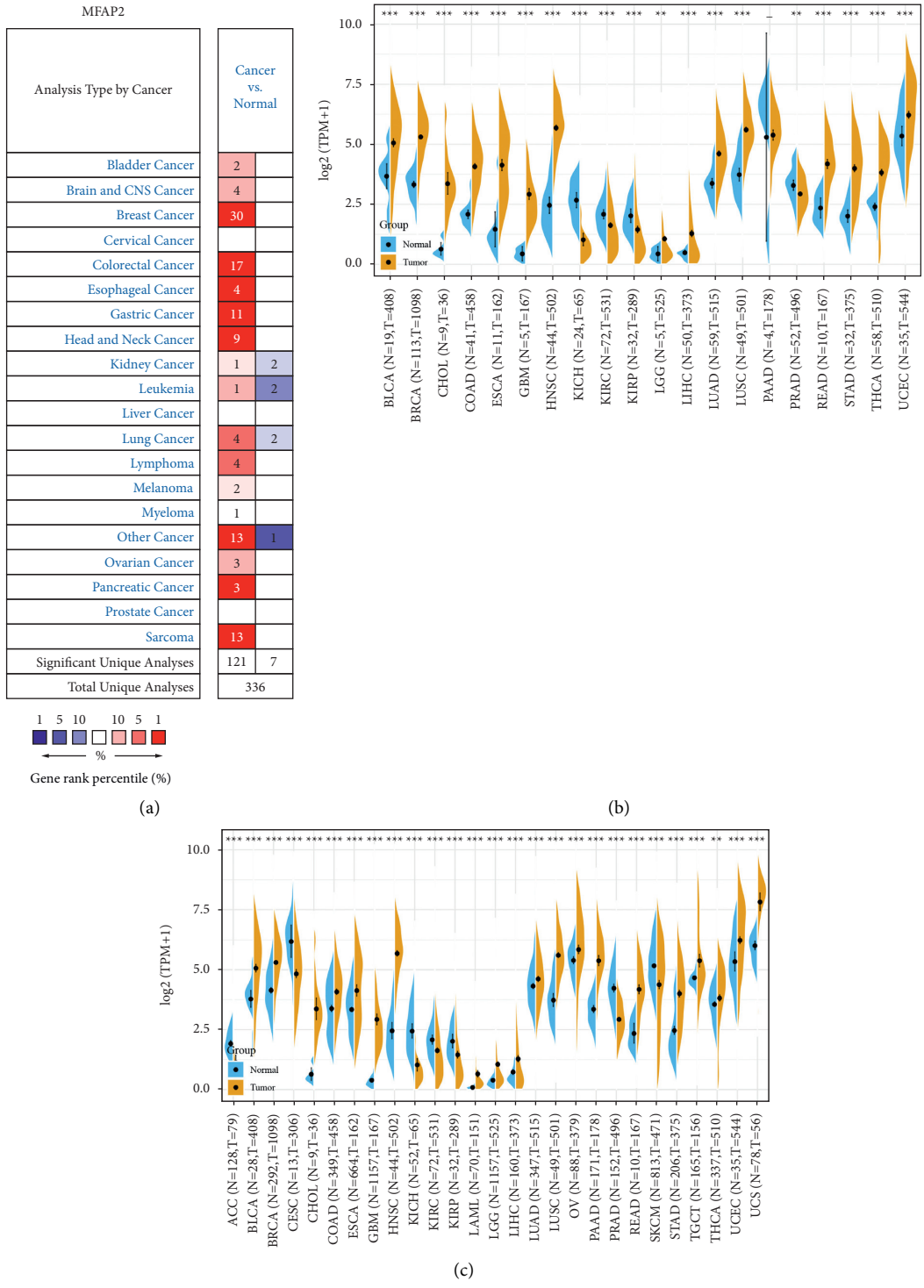

Figure 2: Continued.

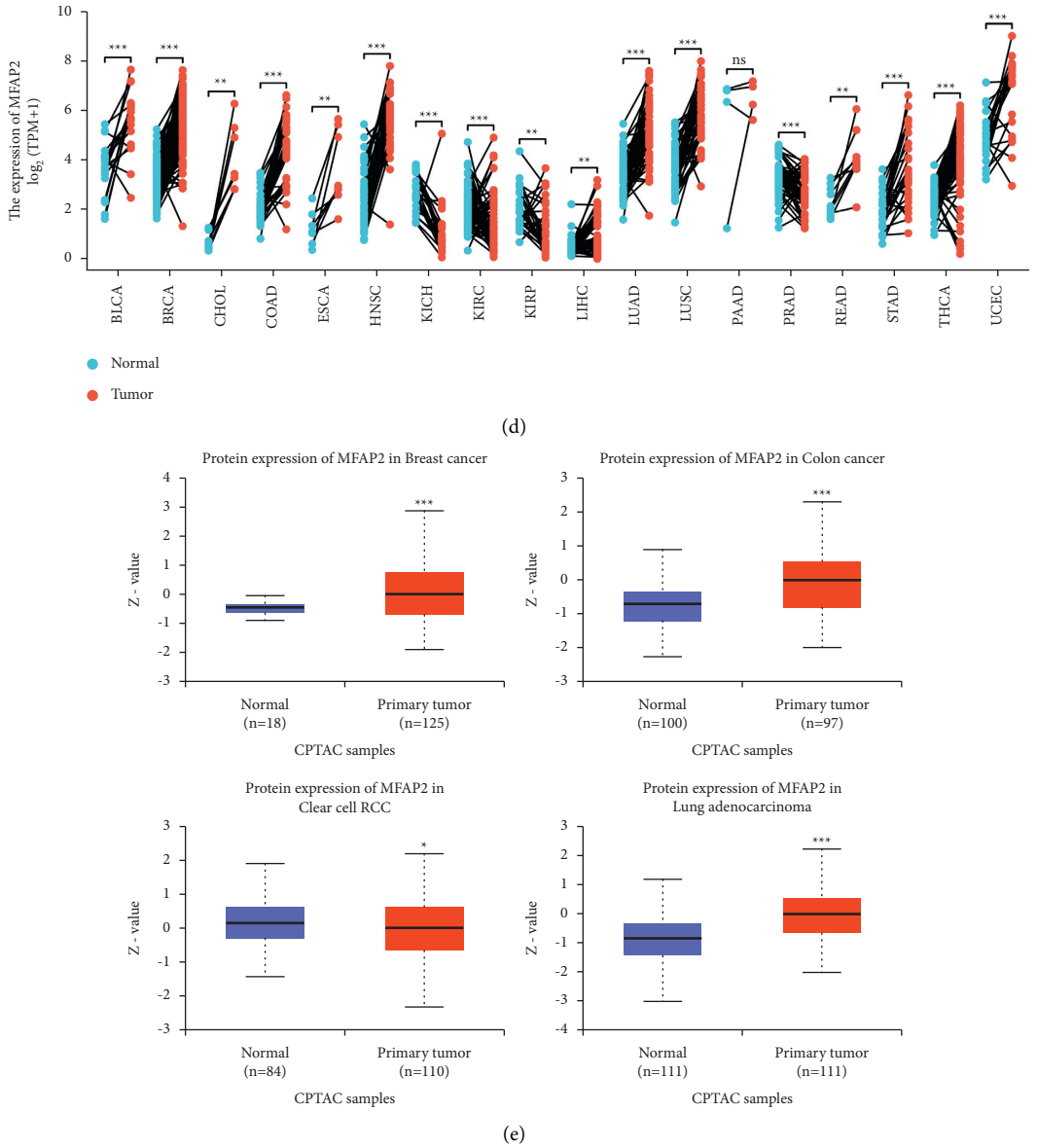

Figure 2: MFAP2 expression landscape in various human cancers. (a) MFAP2 mRNA expression change showed in Oncomine database. (b) MFAP2 mRNA expression levels in tumor tissues and adjacent tissues from TCGA database. (c) MFAP2 mRNA expression levels determined by TCGA database and GTEx database. (d) MFAP2 mRNA expression levels in matched tissues determined by TCGA database. (e) MFAP2 protein expression levels showed in UALCAN database. $^{*}p < 0.05$, $^{**}p < 0.01$, and $^{***}p < 0.001$.

expression, including BLCA, BRCA, COAD, and UCEC, exhibited reduced DNA methylation levels of MFAP2. Methylation level of MFAP2 was reduced in KIRP, which could not explain the reduced MFAP2 mRNA expression. In addition, two tumors with low MFAP2 expression, including KIRC and PRAD, exhibited elevated DNA methylation levels of MFAP2. Methylation level of MFAP2 was elevated in LIHC and LUAD, which could not explain the elevated MFAP2 mRNA expression. Then, we assessed the relationship between MFAP2 expression and the four methyltransferases, including DNMT1, DNMT2, DNMT3A, and DNMT3B. As shown in Figure 6(b), MFAP2 expression was positively correlated with some of the four methyltransferases in the vast majority of the 33 tumors.

3.5. Tumor Neoantigen, TMB, MSI, and MMRs. Tumor neoantigens are new abnormal proteins encoded by mutated genes in tumor cells, acting as antigens to activate T cells. Here we counted the number of neoantigens for each tumor sample separately and analyzed the relationship between MFAP2 expression and antigens number. The results showed that MFAP2 expression was negatively correlated with tumor neoantigen in UCEC (Figure 7(a)). TMB, usually measured as the number of somatic nonsynonymous mutations occurring in an average of 1 Mb bases in the coding region of the exonic region, reflects the number of mutations contained in tumor cells [18]. Spearman's rank correlation analysis showed that MFAP2 expression was positively correlated with TMB in COAD, STAD, and UCEC, while it was negatively correlated

Table 2: MFAP2 expression in cancers versus normal tissue in Oncomine database.

Cancer	Cancer type	*P*-value	Fold change	Rank (%)	Sample	Reference (PMID)
Bladder	Infiltrating bladder urothelial carcinoma	1.51E−7	2.327	7%	157	16432078
Bladder	Infiltrating bladder urothelial carcinoma	6.46E−5	3.192	10%	60	15173019
Breast cancer	Invasive ductal breast carcinoma	6.80E−5	4.265	1%	30	17389037
Breast cancer	Invasive ductal breast carcinoma	8.43E−13	3.700	1%	64	15034139
Breast cancer	Lobular breast carcinoma	3.33E−7	3.496	2%	64	15034139
Breast cancer	Ductal breast carcinoma in situ stroma	5.81E−5	2.882	2%	66	19187537
Breast cancer	Tubular breast carcinoma	3.32E−27	2.390	2%	2,136	22522925
Breast cancer	Invasive ductal and invasive lobular breast carcinoma	3.47E−23	2.001	5%	2,136	22522925
Breast cancer	Medullary breast carcinoma	4.21E−8	2.057	8%	2,136	22522925
Breast cancer	Ductal breast carcinoma	6.05E−6	4.753	5%	47	16473279
Colorectal cancer	Colon mucinous adenocarcinoma	4.97E−8	4.413	1%	105	17615082
Colorectal cancer	Cecum adenocarcinoma	3.86E−8	3.135	2%	105	17615082
Colorectal cancer	Rectosigmoid adenocarcinoma	5.22E−6	3.630	2%	105	17615082
Colorectal cancer	Colon adenocarcinoma	2.69E−8	3.485	4%	105	17615082
Colorectal cancer	Colorectal carcinoma	4.42E−12	4.475	1%	105	20957034
Colorectal cancer	Colon carcinoma	3.04E−10	3.539	2%	40	20957034
Colorectal cancer	Colon carcinoma epithelia	5.76E−7	2.270	6%	40	20957034
Colorectal cancer	Rectal adenocarcinoma	1.12E−28	4.306	2%	130	20725992
Esophageal cancer	Esophageal squamous cell carcinoma	7.35E−25	3.246	1%	106	21385931
Esophageal cancer	Esophageal squamous cell carcinoma	3.44E−8	5.112	2%	34	20955586
Gastric cancer	Gastric cancer	5.99E−7	6.107	1%	27	21132402
Gastric cancer	Gastric adenocarcinoma	6.48E−5	2.238	1%	90	21447720
Gastric cancer	Diffuse gastric adenocarcinoma	7.33E−8	2.562	1%	90	21447720
Gastric cancer	Gastric intestinal type adenocarcinoma	6.67E−6	2.656	1%	90	21447720
Gastric cancer	Gastric cancer	1.29E−8	3.563	1%	160	20965966
Gastric cancer	Diffuse gastric adenocarcinoma	1.12E−6	3.264	2%	132	12925757
Gastric cancer	Gastric mixed adenocarcinoma	1.09E−5	4.778	2%	132	12925757
Gastric cancer	Gastric intestinal type adenocarcinoma	4.03E−13	2.947	3%	132	12925757
Gastric cancer	Gastric intestinal type adenocarcinoma	7.03E−12	6.968	2%	69	19081245
Gastric cancer	Gastric mixed adenocarcinoma	1.69E−5	8.780	3%	69	19081245
Head and neck cancer	Head and neck squamous cell carcinoma	1.82E−16	4.913	1%	38	14676830
Head and neck cancer	Salivary gland adenoid cystic carcinoma	2.54E−8	3.510	1%	22	12368205
Head and neck cancer	Head and neck squamous cell carcinoma	8.79E−14	6.381	1%	54	14729608
Head and neck cancer	Oral cavity squamous cell carcinoma epithelia	7.56E−5	2.097	2%	20	15381369
Head and neck cancer	Oral cavity squamous cell carcinoma	1.17E−15	2.621	2%	79	21853135
Head and neck cancer	Tongue carcinoma	2.45E−5	2.754	6%	84	17510386
Lung cancer	Lung adenocarcinoma	2.63E−9	2.443	5%	156	20421987
Lung cancer	Squamous cell lung carcinoma	6.20E−8	2.845	9%	156	20421987
Other cancer	Yolk sac tumor, NOS	3.64E−11	6.521	1%	107	16424014
Other cancer	Mixed germ cell tumor, NOS	4.87E−16	4.189	1%	107	16424014
Other cancer	Teratoma, NOS	5.23E−8	5.705	4%	107	16424014
Other cancer	Uterine corpus leiomyoma	2.49E−10	3.321	1%	77	19622772
Other cancer	Skin basal cell carcinoma	1.65E−7	8.119	1%	87	18442402
Other cancer	Malignant fibrous histiocytoma	1.30E−6	10.342	2%	54	15994966
Other cancer	Pleural malignant mesothelioma	1.63E−5	5.298	3%	54	15920167
Ovarian cancer	Ovarian carcinoma	3.52E−8	3.330	9%	195	18593951
Pancreatic cancer	Pancreatic ductal adenocarcinoma	5.17E−17	4.117	1%	78	19260470
Sarcoma	Dedifferentiated liposarcoma	3.74E−16	6.514	1%	158	20601955
Sarcoma	Myxofibrosarcoma	6.33E−11	4.627	3%	158	20601955
Sarcoma	Pleomorphic liposarcoma	4.94E−8	3.568	3%	158	20601955
Sarcoma	Myxoid/Round cell liposarcoma	4.77E−9	2.956	5%	158	20601955
Sarcoma	Malignant fibrous histiocytoma	1.30E−6	10.342	2%	54	15994966
Sarcoma	Fibrosarcoma	7.42E−6	13.669	2%	54	15994966

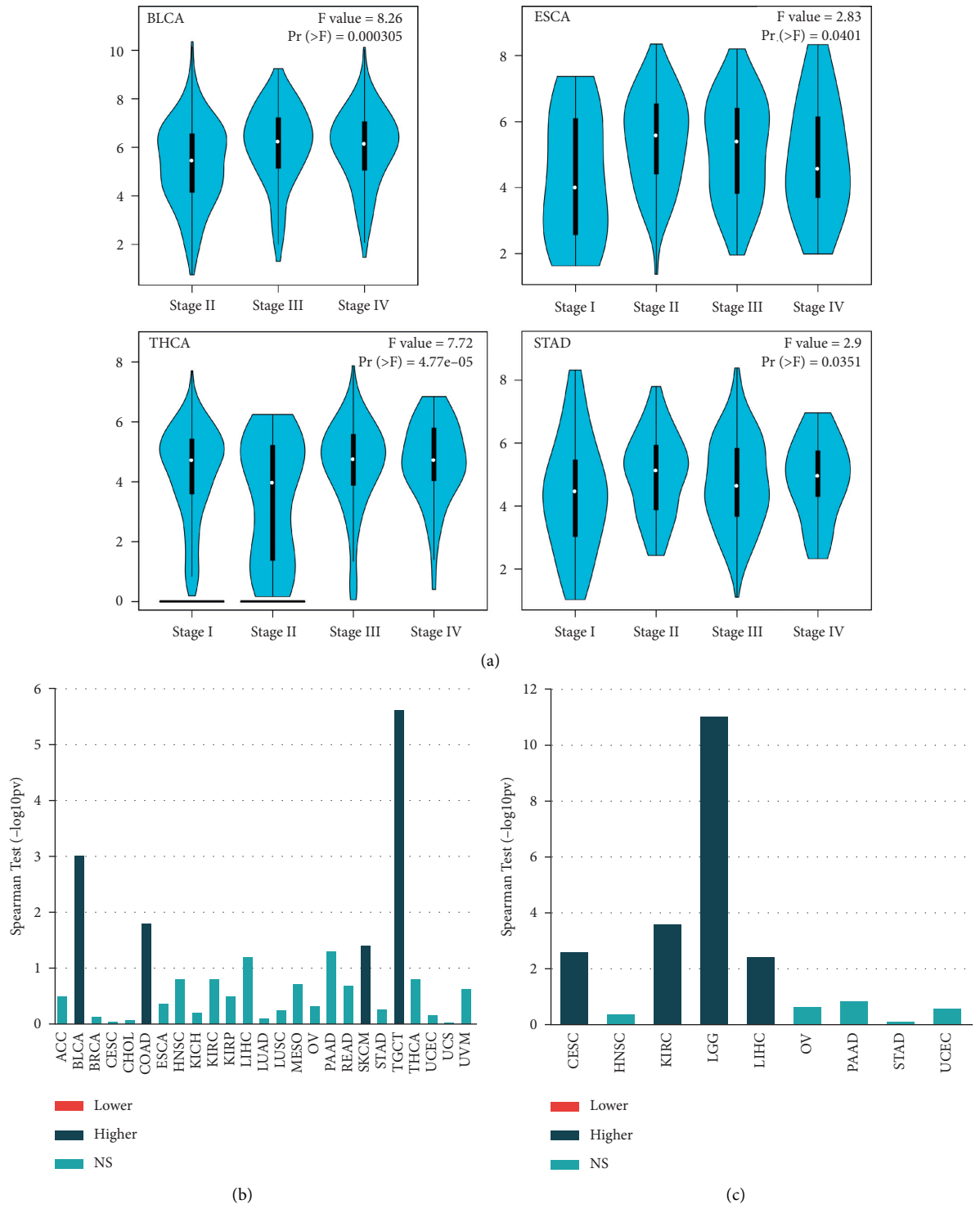

Figure 3: Correlation analysis of MFAP2 expression and clinicopathologic features across various cancers. (a) MFAP2 expression in main pathological stages based on GEPIA2 database. (b) MFAP2 expression in main pathological stages based on TISIDB database. (c) MFAP2 expression in main pathological grades based on TISIDB database.

with TMB in DLBC, LGG, PRAD, SARC, SKCM, and THCA as shown in Figure 7(b). MSI refers to the length change of microsatellites due to insertion or deletion of a repeat unit in a tumor compared to normal tissue, producing a new microsatellite allele [19]. Using Spearman rank correlation analysis, MFAP2 expression was positively correlated with TMB in COAD, LGG, MESO, and STAD, while it was negatively correlated with TMB in BLCA, BRCA, HNSC, LIHC, READ, SARC, SKCM, THCA, and THYM (Figure 7(c)). MSI and high TMB may result from MMR deficiency [20]. As shown

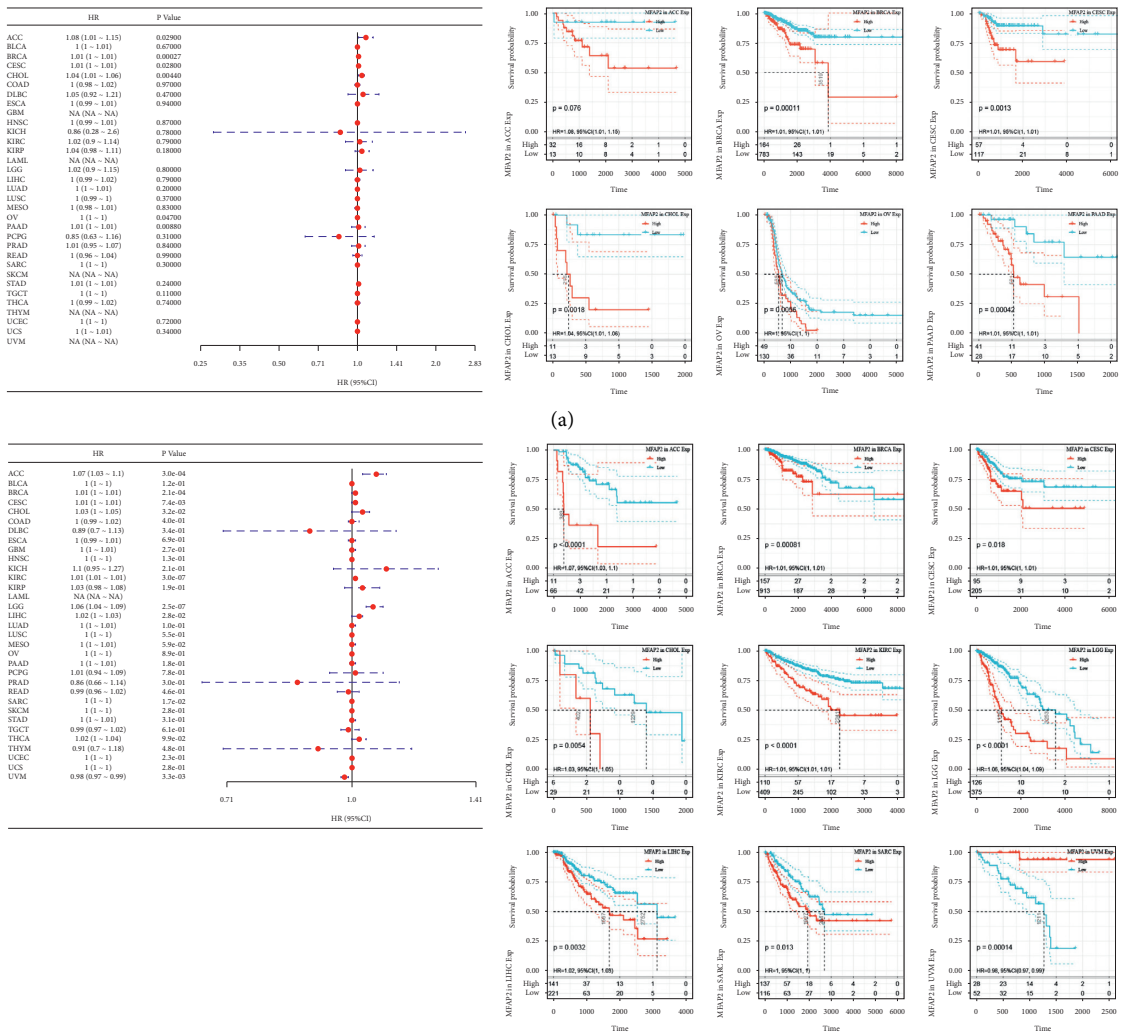

(a)

(b)

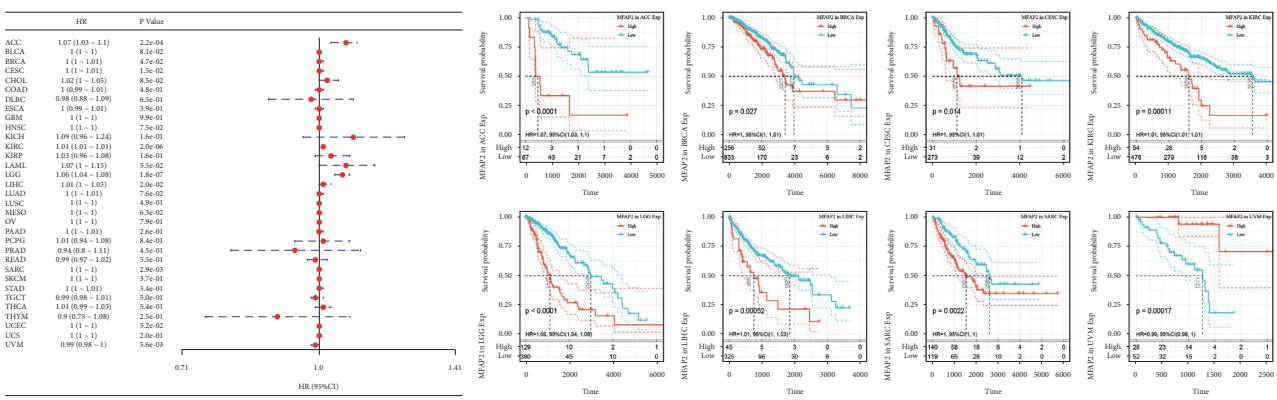

(c)

Figure 4: Continued.

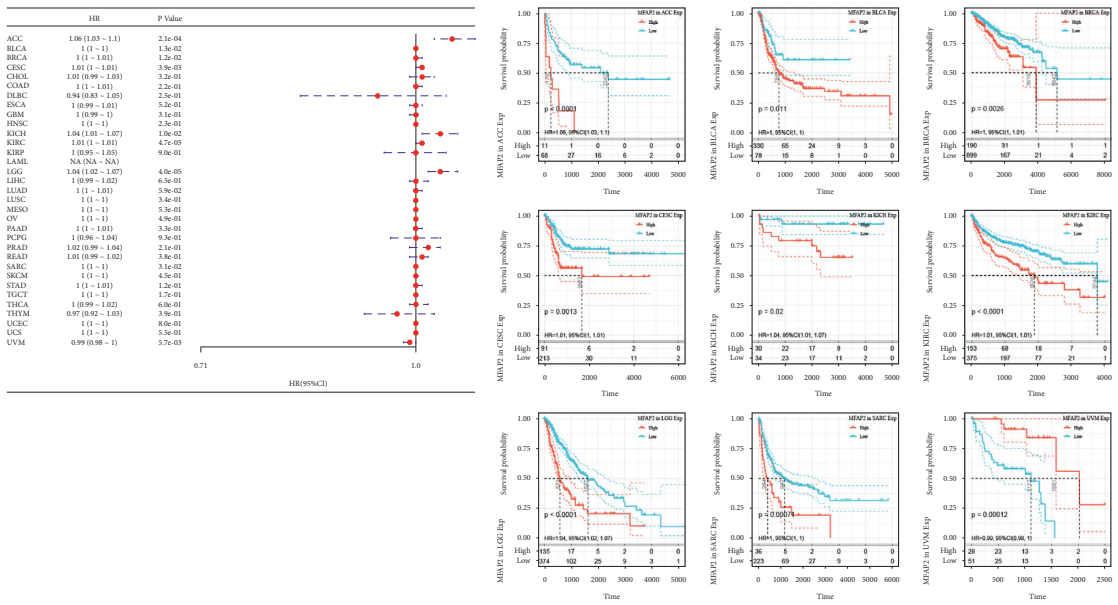

(d)

Figure 4: Forest plots and Kaplan–Meier analysis of the association between MFAP2 expression and (a) DFI, (b) DSS, (c) OS, and (d) PFI.

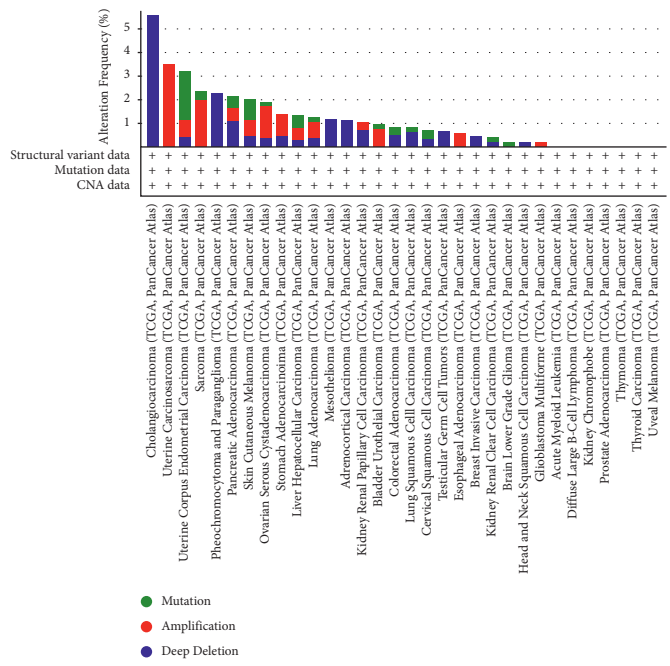

(a)

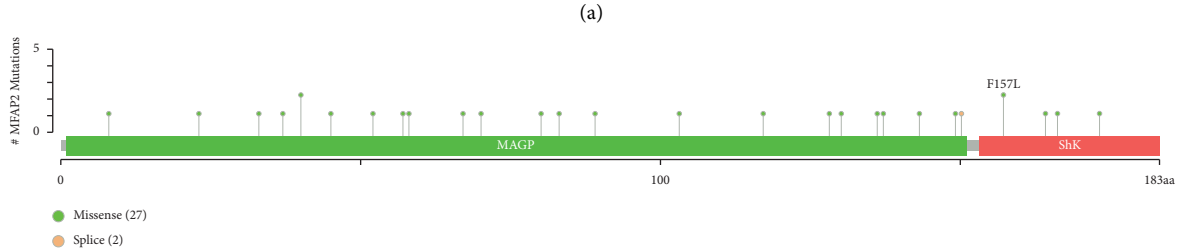

(b)

Figure 5: Continued.

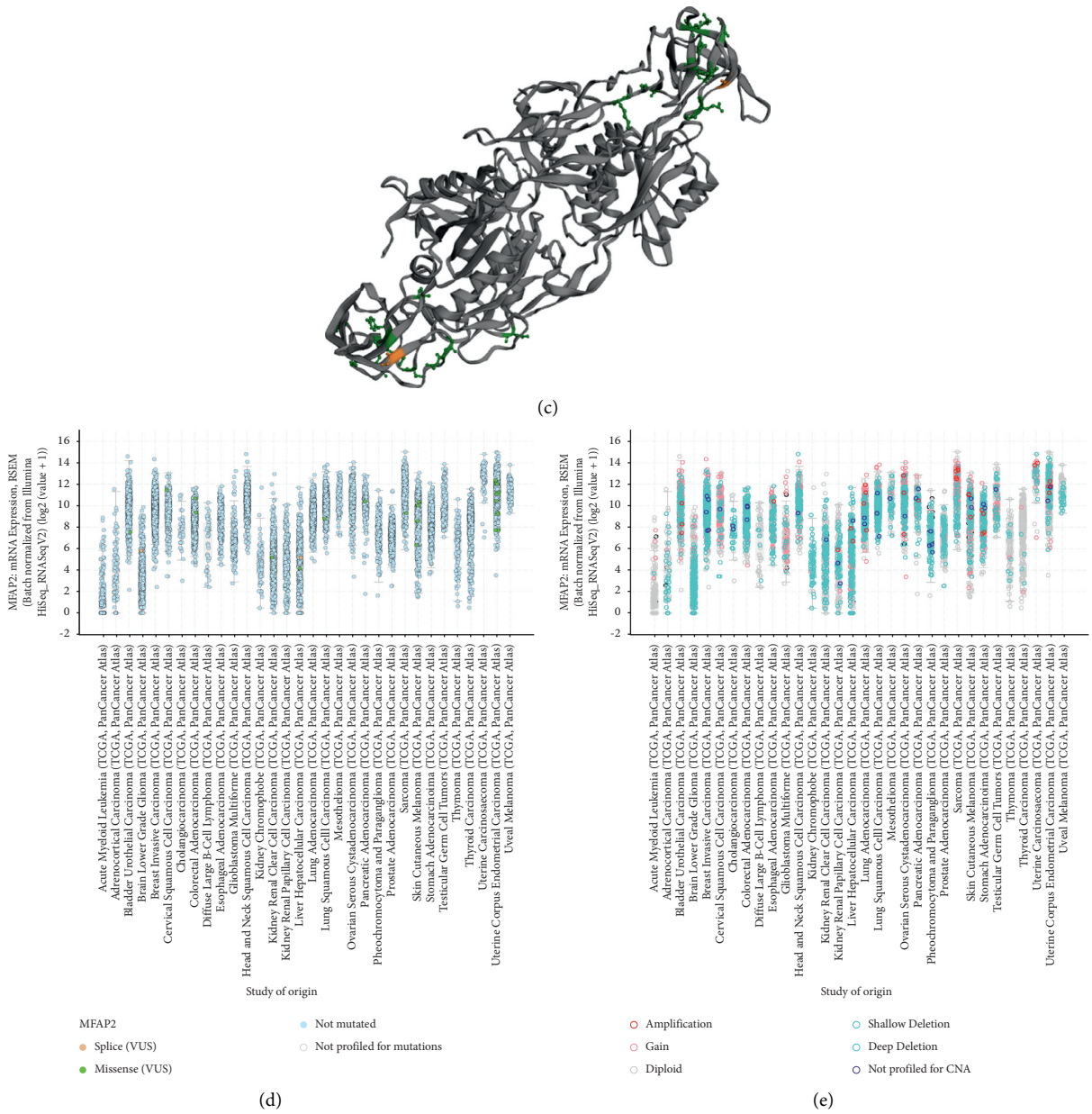

Figure 5: Mutation features of MFAP2 in TCGA pan-cancer panel according to cBioPortal tool. (a) The mutation frequency distribution. (b) The mutation sites distribution across protein domains. (c) The 3D structure of MFAP2. (d) The relevance of mutations and MFAP2 expression. (e) The relevance of DNA copy variation and MFAP2 expression.

in Figure 7(d), MFAP2 expression was positively correlated with MLH1, MSH2, MSH6, PMS2, and EPCAM in a variety of tumors, while it was negatively correlated with EPCAM in GBM, LGG, and THYM.

3.6. Immune Infiltration Analysis. Tumor-infiltrating lymphocytes, an essential part of the tumor microenvironment, play an essential role in carcinogenesis [21, 22]. Therefore, we analyzed the interaction of MFAP2 with various immune cell infiltration in multiple TCGA cancers by searching TIMER and TISIDB databases or by MCP and XCELL algorithms. In TIMER database, it turned out that, in BLCA, BRCA, and LGG, MFAP2 expression correlated most strongly with the immune infiltration level, with a significant positive correlation with the infiltration levels of B cells, CD4+ T cells, CD8+ T cells, dendritic cells, macrophages, and neutrophils (Figure 8(a)). The detailed correlation in each type of cancer is shown in Supplementary Figure 1. In addition, other algorithms were also performed to assess the correlation. The correlation of MFAP2 expression with immune infiltration in cancers was also analyzed in TISIDB database (Figure 8(b)). MCP analysis (Figure 8(c)) and xCell analysis (Figure 8(d)) were also performed to analyze the correlation, separately. Interestingly, we found that the expression levels of most monocytes, TAMs, M1, and M2

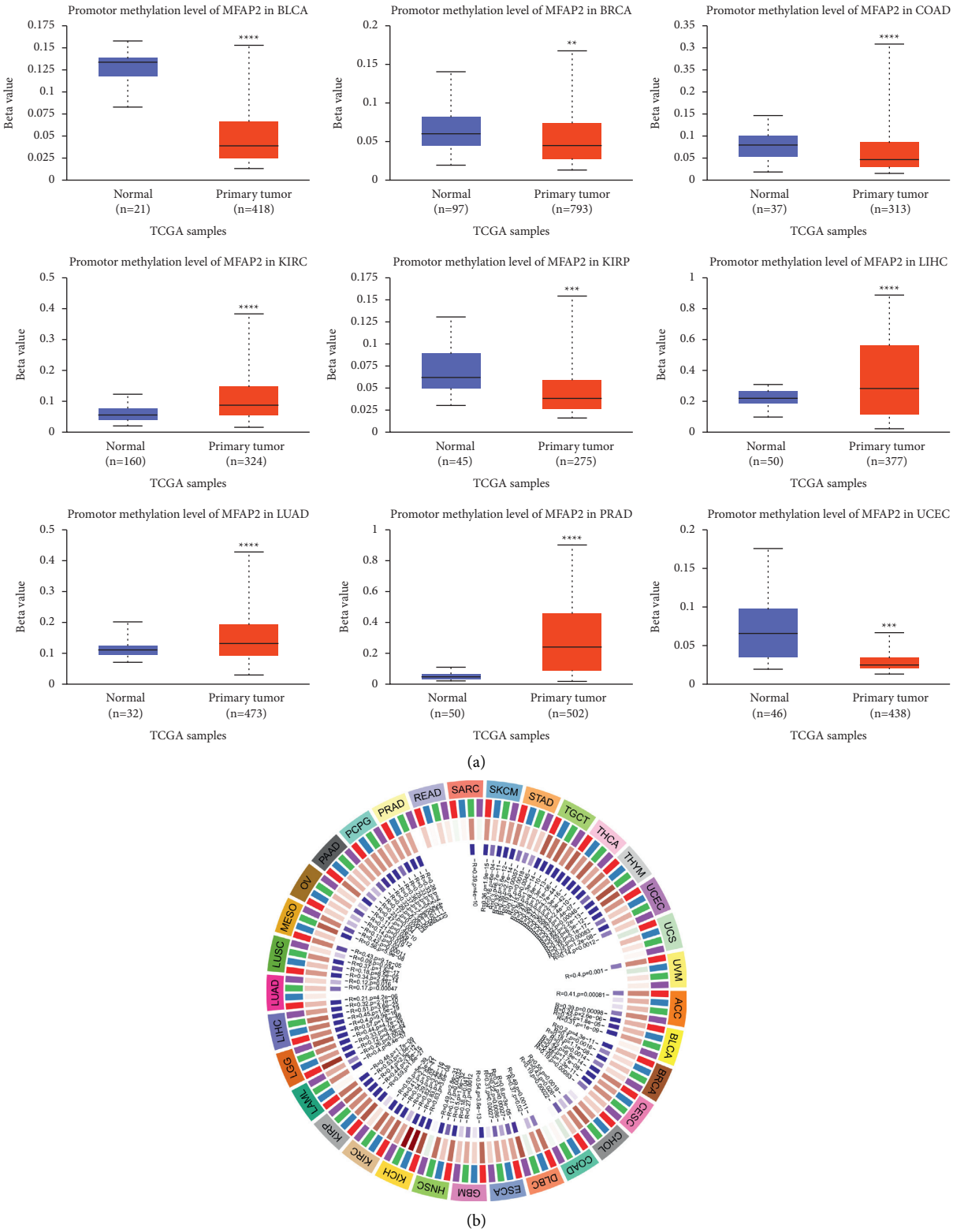

FIGURE 6: DNA methylation aberration (a) and association with four methyltransferases (b) of MFAP2 in pan-cancer analysis, with DNMT1 in red, DNMT2 in blue, DNMT3A in green, and DNMT3B in purple. $^{**}p < 0.01$, $^{***}p < 0.001$, and $^{****}p < 0.001$.

macrophage markers positively correlated with MFAP2 expression levels in BLCA, COAD, ESCA, HNSC-HPV-, KICH, LGG, LIHC, PAAD, PRAD, READ, STAD, THCA, and THYM (Figure 8(e)), suggesting that MFAP2 might regulate macrophage polarization in the aforementioned tumors.

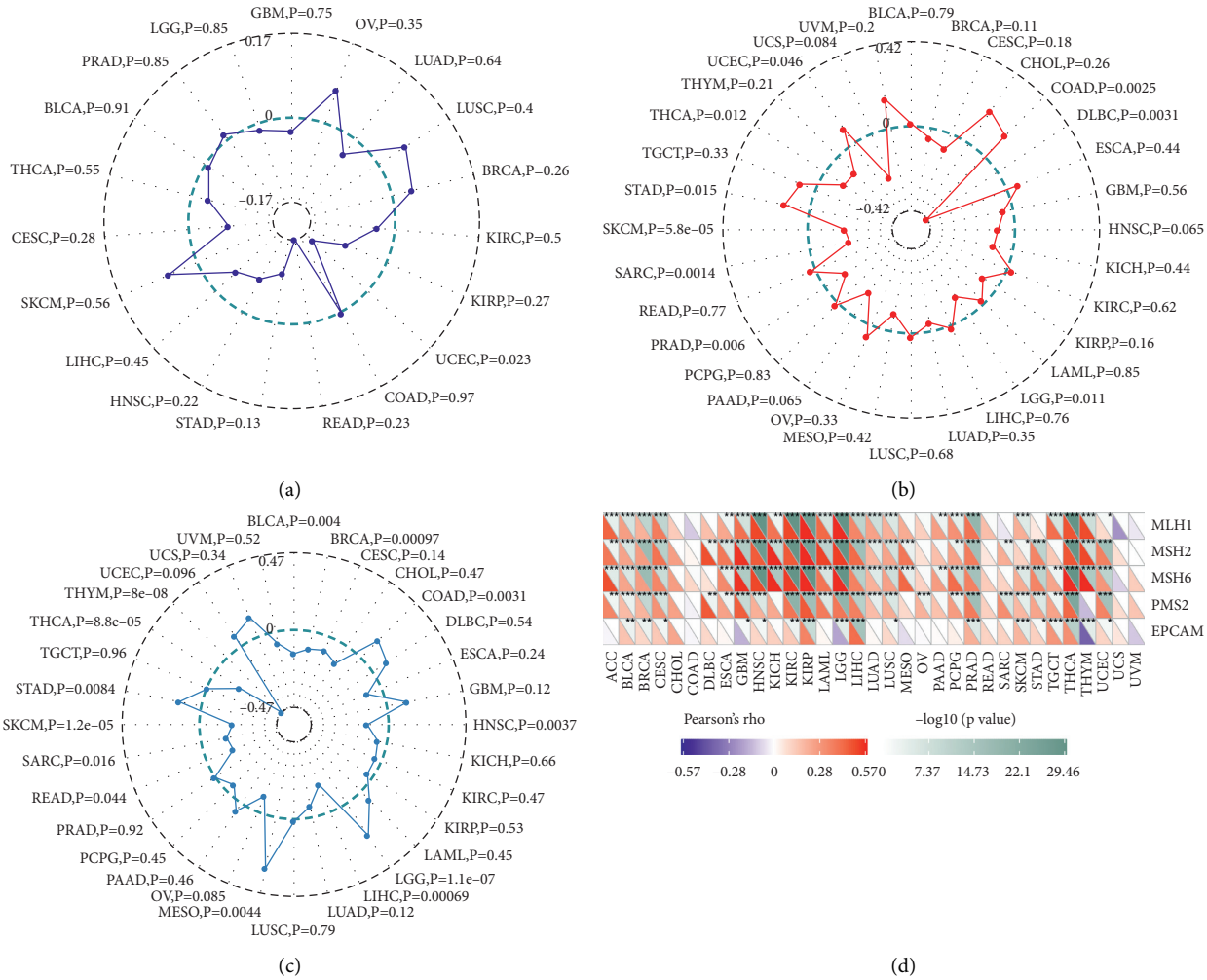

Figure 7: Correlation between MFAP2 expression and the tumor neoantigens (a), TMB (b), MSI (c), and MMRs (d) across cancers. $^{*}p < 0.05$, $^{**}p < 0.01$, and $^{***}p < 0.001$.

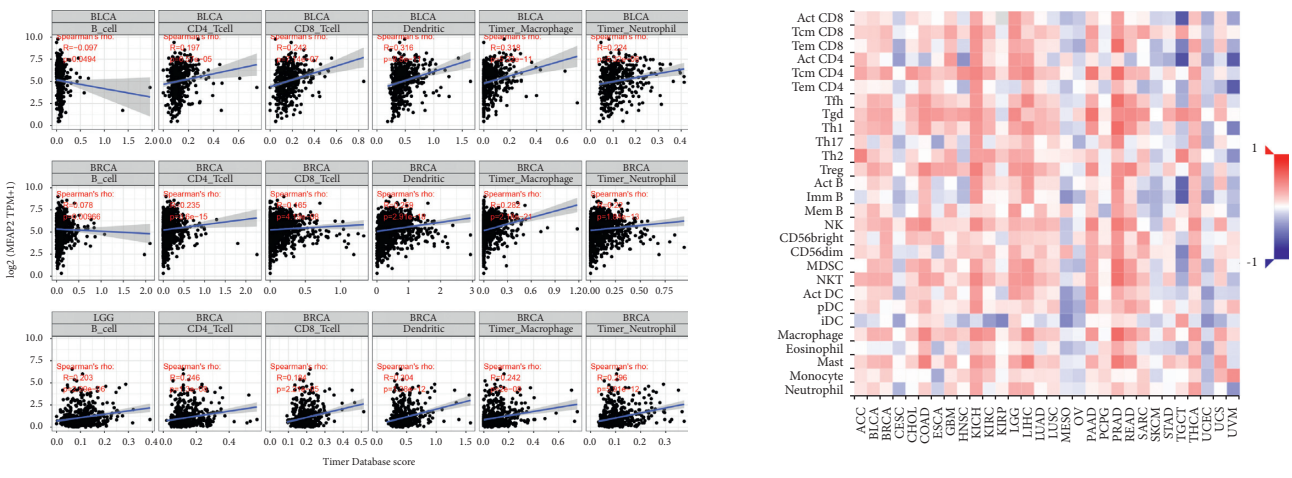

Figure 8: Continued.

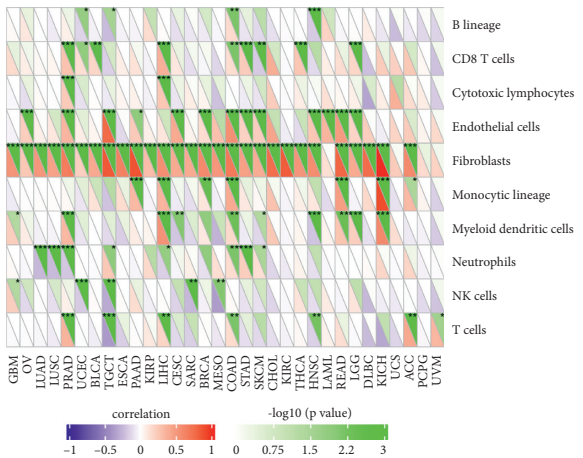

(c)

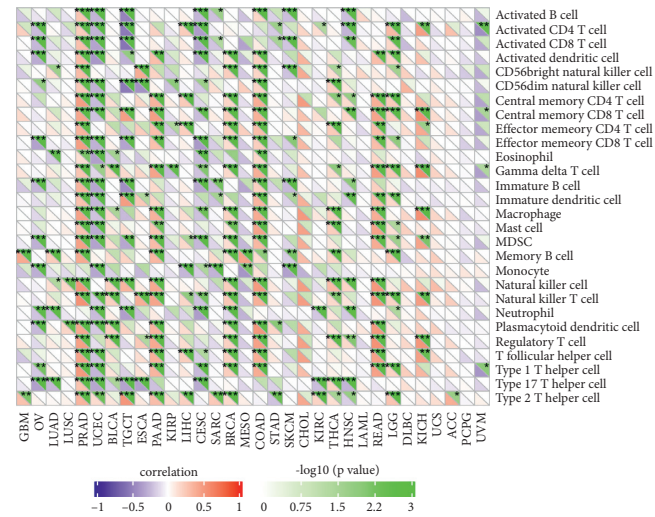

(d)

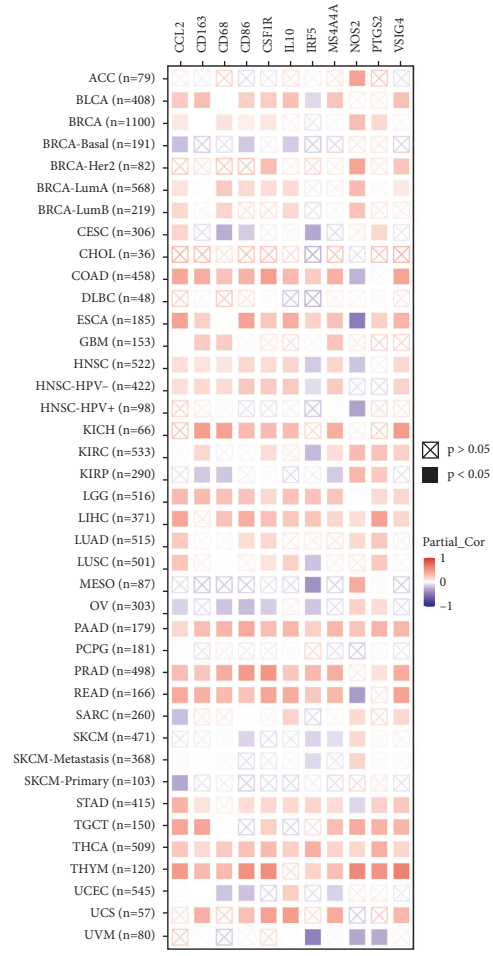

(e)

Figure 8: Correlation of MFAP2 expression with immune infiltration in cancers shown in TIMER database (a), TISIDB database (b), MCP analysis (c), and xCell analysis (d). TIMER database showed the correlation of MFAP2 expression with macrophage polarization in cancers, manifested by monocyte markers (CD86 and CSF1R), TAM markers (CCL2, CD68, and IL10), M1 macrophage markers (NOS2, IRF5, and PTGS2), and M2 macrophage markers (CD163, VSIG4, and MS4A4A) (e). $^{*}p < 0.05$, $^{**}p < 0.01$, and $^{***}p < 0.001$.

An increasing number of reports have indicated an important role of the tumor immune microenvironment in tumor development [23, 24]. We analyzed the immune and stromal scores of each tumor sample using the *R* package ESTIMATE to observe the relationship between MFAP2 expression in 33 tumors and the StromalScore, ImmuneScore, and ESTIMATEScore (Supplementary Figure 2).

MFAP2 expression in BLCA, BRCA, HNSC, and KICH tissues was shown by qPCR.

The expression of MFAP2 was finally examined by qPCR in BLCA, BRCA, HNSC, and KICH tissue samples and the corresponding normal tissue samples. As a result, qPCR showed that MFAP2 expression was significantly lower in KICH tissues than in normal tissues, while it was significantly higher in the other three tumors (Figure 9).

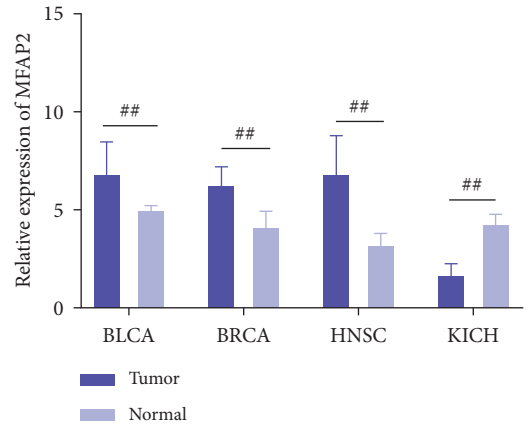

Figure 9: MFAP2 expression was detected in BLCA, BRCA, HNSC, and KICH by qPCR. $^{*}p < 0.05$, $^{**}p < 0.01$, $^{***}p < 0.001$, and $^{\#\#}p < 0.01$.

4. Discussion

MFAP2 is an essential component of extracellular elastic microfibers, which interacts with and affects fibrin. It is also the constitutive protein of most vertebrate microfibrils [25]. A representative feature of MFAP2 is its capacity to work with TGF-β family growth factors, Notch, and Notch ligands, as well as a variety of elastins [26]. Mutations of MFAP2 gene may indicate thrombosis, thoracic aneurysms, metabolic diseases, and osteopenia in humans [27]. Studies have shown that MFAP2 is highly expressed in gastric cancer tissues, and its high expression is significantly related to the overall and disease-free survival of patients with gastric cancer [7]. Furthermore, MFAP2 is found to be a possible player in TGF-β/SMAD2/3 signaling pathway activation to advance proliferation, migration, invasion, and epithelial-mesenchymal transition of gastric cancer cells [11]. A previous study pointed out that MFAP2 is a novel microRNA-29 target, and miR-29/MFAP2/integrinα5β1/FAK/ERK1/2 might be an important carcinogenic pathway in gastric cancer progression [10]. Another study has also indicated the relevance of MFAP2 in hepatic carcinoma, whereby MFAP2 overexpression in hepatic carcinoma is associated with cancer staging, poor OS, and disease-specific survival [9, 26]. An in vitro experiment showed that downregulation of MFAP2 inhibited the proliferation and migration levels of liver cancer cells. Moreover, the transcription factors, DNA methyltransferases, and immune factors in liver cancer might interact with MFAP2 and accelerate tumor progression [27].

In this study, we found that MFAP2 exhibited different expression levels in different tissues and cells. The analysis based on Oncomine, TCGA, GTEx, and UALCAN databases revealed that MFAP2 mRNA and protein were aberrantly expressed in a variety of tumors. However, this aberrant expression was not associated with gene mutations and was influenced to some extent by its promoter methylation. Moreover, the expression of MFAP2 was significantly correlated with the pathological stage, grade, and prognosis of many cancers, suggesting that MFAP2 played an oncogene role in many tumors. In addition, MFAP2 expression was also correlated with DNA methyltransferases, TMB, MSI, and MMR-related genes. Aberrant DNA methylation is frequently seen during cancer progression [28]. MMR is an intracellular MMR mechanism, where the loss of function of key genes may lead to irreparable DNA replication errors and ultimately higher somatic mutations [29]. The correlation between MFAP2 and gene mutations further suggested its importance in tumorigenesis, although such mutations did not produce tumor neoantigens in most cancers.

Combining multiple algorithms, we found that MFAP2 was closely related to the immune infiltration profile in tumor tissue, affecting not only the proportion of immune cells but also the expression levels of many immune-related genes, including immune checkpoints. Among these, a type I transmembrane protein CD276 [30], recently identified as a promising target for tumor immunotherapy [31], is notable. Numerous studies have revealed that CD276 is overexpressed in a variety of tumors, including leukemia [32], breast cancer [33], prostate cancer [34], and other tumors, with expression levels strongly correlating with poor patient prognosis, and presumably involved in tumor immune evasion. In addition, CD276 has been shown to promote lactate production by promoting hexokinase 2 expression, thereby promoting glycolysis and drug resistance [35]. CD276 also could lead to increased NF-κB activity and elevated VEGF expression, further promoting tumor-associated angiogenesis and tumor invasion [36]. Despite unclear underlying mechanisms, the correlation between MFAP2 and CD276 in a variety of tumors suggests that MFAP2 is a promising target for tumor immunotherapy. In the next study, we intend to further verify the effect of MFAP2 on tumor cell proliferation, migration, and invasion and explore the molecular regulation mechanism.

5. Conclusion

In summary, our first pan-cancer analysis of MFAP2 suggested that MFAP2 could affect clinical prognosis in various cancers and immune cell infiltration, which deepened the understanding of the MFAP2 role in tumorigenesis.

Data Availability

The datasets used and/or analyzed during the current study are available from the corresponding author.

Conflicts of Interest

The authors declare that they have no competing interests.

Supplementary Materials

Supplementary Figure 1: correlation of MFAP2 expression with immune infiltration level in diverse kinds of cancers in TIMER database. Supplementary Figure 2: StromalScore (a), ImmuneScore (b), and ESTIMATEScore (c) were analyzed to estimate the correlation of MFAP2 expression with the proportion of immune and stroma in cancers. (*Supplementary Materials*)

References

[1] M. Abbott and Y. Ustoyev, "Cancer and the immune system: the history and background of immunotherapy," *Seminars in Oncology Nursing*, vol. 35, no. 5, Article ID 150923, 2019.

[2] R. Grosser, L. Cherkassky, N. Chintala, and P. S. Adusumilli, "Combination immunotherapy with CAR T cells and checkpoint blockade for the treatment of solid tumors," *Cancer Cell*, vol. 36, no. 5, pp. 471–482, 2019.

[3] C. E. Rudd, "A new perspective in cancer immunotherapy: PD-1 on myeloid cells takes center stage in orchestrating immune checkpoint blockade," *Science Immunology*, vol. 5, no. 43, p. 5, 2020.

[4] C. Ralph, E. Elkord, D. J. Burt et al., "Modulation of lymphocyte regulation for cancer therapy: a phase II trial of tremelimumab in advanced gastric and esophageal adenocarcinoma," *Clinical Cancer Research*, vol. 16, no. 5, pp. 1662–1672, 2010.

[5] M. J. Overman, R. McDermott, J. L. Leach et al., "Nivolumab in patients with metastatic DNA mismatch repair-deficient or microsatellite instability-high colorectal cancer (CheckMate 142): an open-label, multicentre, phase 2 study," *The Lancet Oncology*, vol. 18, no. 9, pp. 1182–1191, 2017.

[6] X. Cheng, X. Wang, K. Nie et al., "Systematic pan-cancer analysis identifies TREM2 as an immunological and prognostic biomarker," *Frontiers in Immunology*, vol. 12, Article ID 646523, 2021.

[7] Z. Shan, "Genome-scale Analysis identified NID2, SPARC, and MFAP2 as prognosis markers of overall survival in gastric cancer," *Medical Science Monitor*, Article ID e929558, 27 pages, 2021.

[8] Z. Chen, "Microfibril-Associated Protein 2 (MFAP2) Potentiates invasion and migration of melanoma by EMT and wnt/beta-catenin pathway," *Medical Science Monitor*, Article ID e923808, 26 pages, 2020.

[9] S. Y. Dong, H. Chen, L. Z. Lin et al., "MFAP2 is a potential diagnostic and prognostic biomarker that correlates with the progression of papillary thyroid cancer," *Cancer Management and Research*, vol. 12, pp. 12557–12567, 2020.

[10] L.-w. Yao, L.-l. Wu, L.-h. Zhang et al., "MFAP2 is overexpressed in gastric cancer and promotes motility via the MFAP2/integrin $\alpha 5\beta 1$/FAK/ERK pathway," *Oncogenesis*, vol. 9, no. 2, 17 pages, 2020.

[11] J.-K. Wang, W.-J. Wang, H.-Y. Cai et al., "MFAP2 promotes epithelial–mesenchymal transition in gastric cancer cells by activating TGF-β/SMAD2/3 signaling pathway," *OncoTargets and Therapy*, vol. 11, pp. 4001–4017, 2018.

[12] C. S. Craft, T. A. Pietka, T. Schappe et al., "The extracellular matrix protein MAGP1 supports thermogenesis and protects against obesity and diabetes through regulation of TGF-β," *Diabetes*, vol. 63, no. 6, pp. 1920–1932, 2014.

[13] S. E. Turecamo, T. A. Walji, T. J. Broekelmann et al., "Contribution of metabolic disease to bone fragility in MAGP1-deficient mice," *Matrix Biology*, vol. 67, pp. 1–14, 2018.

[14] T. A. Walji, S. E. Turecamo, A. C. Sanchez et al., "Marrow adipose tissue expansion coincides with insulin resistance in MAGP1-deficient mice," *Frontiers in Endocrinology*, vol. 787 pages, 2016.

[15] D. R. Rhodes, S. Kalyana-Sundaram, V. Mahavisno et al., "Oncomine 3.0: genes, pathways, and networks in a collection of 18,000 cancer gene expression profiles," *Neoplasia*, vol. 9, no. 2, pp. 166–180, 2007.

[16] F. Chen, D. S. Chandrashekar, S. Varambally, and C. J. Creighton, "Pan-cancer molecular subtypes revealed by mass-spectrometry-based proteomic characterization of more than 500 human cancers," *Nature Communications*, vol. 10, no. 1, 5679 pages, 2019.

[17] E. Cerami, J. Gao, U. Dogrusoz et al., "The cBio cancer genomics portal: an open platform for exploring multidimensional cancer genomics data," *Cancer Discovery*, vol. 2, no. 5, pp. 401–404, 2012.

[18] B. B. Campbell, N. Light, D. Fabrizio et al., "Comprehensive analysis of hypermutation in human cancer," *Cell*, vol. 171, no. 5, pp. 1042–1056, 2017.

[19] I. Cortes-Ciriano, S. Lee, W.-Y. Park, T.-M. Kim, and P. J. Park, "A molecular portrait of microsatellite instability across multiple cancers," *Nature Communications*, vol. 8, no. 1, Article ID 15180, 2017.

[20] A. Georgiadis, J. N. Durham, L. A. Keefer et al., "Noninvasive detection of microsatellite instability and high tumor mutation burden in cancer patients treated with PD-1 blockade," *Clinical Cancer Research*, vol. 25, no. 23, pp. 7024–7034, 2019.

[21] P. Domingues, M. González-Tablas, Á. Otero et al., "Tumor infiltrating immune cells in gliomas and meningiomas," *Brain, Behavior, and Immunity*, vol. 53, pp. 1–15, 2016.

[22] H. Ohtani, "Focus on TILs: prognostic significance of tumor infiltrating lymphocytes in human colorectal cancer," *Cancer Immunity*, vol. 7, p. 4, 2007.

[23] J. M. Pitt, A. Marabelle, A. Eggermont, J.-C. Soria, G. Kroemer, and L. Zitvogel, "Targeting the tumor microenvironment: removing obstruction to anticancer immune responses and immunotherapy," *Annals of Oncology*, vol. 27, no. 8, pp. 1482–1492, 2016.

[24] H. Locy, S. de Mey, W. de Mey, M. De Ridder, K. Thielemans, and S. K. Maenhout, "Immunomodulation of the tumor microenvironment: turn foe into friend," *Frontiers in Immunology*, vol. 92909 pages, 2018.

[25] S. Zhu, L. Ye, S. Bennett, H. Xu, D. He, and J. Xu, "Molecular structure and function of microfibrillar-associated proteins in skeletal and metabolic disorders and cancers," *Journal of Cellular Physiology*, vol. 236, no. 1, pp. 41–48, 2021.

[26] D. P. C. Considine, G. Jia, X. Shu et al., "Genetically predicted circulating protein biomarkers and ovarian cancer risk," *Gynecologic Oncology*, vol. 160, no. 2, pp. 506–513, 2021.

[27] X. Zhu, Y Cheng, F Wu et al., "MFAP2 promotes the proliferation of cancer cells and is associated with a poor prognosis in hepatocellular carcinoma," *Technology in Cancer*

Research & Treatment, vol. 19, Article ID 1533033820977524, 2020.

[28] A. Mehdi and S. A. Rabbani, "Role of Methylation in Pro- and Anti-cancer Immunity," *Cancers*, vol. 13, no. 3, 2021.

[29] T. A. Kunkel and D. A. Erie, "DNA mismatch repair," *Annual Review of Biochemistry*, vol. 74, no. 1, pp. 681–710, 2005.

[30] E. Picarda, K. C. Ohaegbulam, and X. Zang, "Molecular pathways: targeting B7-H3 (CD276) for human cancer immunotherapy," *Clinical Cancer Research*, vol. 22, no. 14, pp. 3425–3431, 2016.

[31] F. Kontos, T. Michelakos, T. Kurokawa et al., "B7-H3: an attractive target for antibody-based immunotherapy," *Clinical Cancer Research*, vol. 27, no. 5, pp. 1227–1235, 2021.

[32] Y. Hu, X. Lv, Y. Wu et al., "Expression of costimulatory molecule B7-H3 and its prognostic implications in human acute leukemia," *Hematology*, vol. 20, no. 4, pp. 187–195, 2015.

[33] R. Bam, P. S. Lown, L. A. Stern et al., "Efficacy of affibody-based ultrasound molecular imaging of vascular B7-H3 for breast cancer detection," *Clinical Cancer Research*, vol. 26, no. 9, pp. 2140–2150, 2020.

[34] S. Bonk, P. Tasdelen, M. Kluth et al., "High B7-H3 expression is linked to increased risk of prostate cancer progression," *Pathology International*, vol. 70, no. 10, pp. 733–742, 2020.

[35] T. Shi, Y. Ma, L. Cao et al., "B7-H3 promotes aerobic glycolysis and chemoresistance in colorectal cancer cells by regulating HK2," *Cell Death & Disease*, vol. 10, no. 4, 308 pages, 2019.

[36] R. Wang, Y. Ma, S. Zhan et al., "B7-H3 promotes colorectal cancer angiogenesis through activating the NF-κB pathway to induce VEGFA expression," *Cell Death & Disease*, vol. 11, no. 1, 55 pages, 2020.

Hindawi
Journal of Oncology
Volume 2022, Article ID 4407541, 17 pages
https://doi.org/10.1155/2022/4407541

Research Article

Comprehensive Network Analysis Identified SIRT7, NTRK2, and CHI3L1 as New Potential Markers for Intervertebral Disc Degeneration

Haoxi Li,[1] **Wenhao Li**,[1] **Li Zhang**,[2] **Jicheng He**,[1] **Lin Tang**,[1] **Zhuhai Li**,[1] **Feng Chen**,[1] **Qie Fan**,[1] **and Jianxun Wei**[1]

[1]*Department of Spine Surgery, The People's Hospital of Guangxi Zhuang Autonomous Region, Nanning 530021, China*
[2]*Department of Pathology, The Third People's Hospital of Guangxi Zhuang Autonomous Region, Nanning 530021, China*

Correspondence should be addressed to Haoxi Li; volvoxc-90@163.com, Qie Fan; fanqie2331@163.com, and Jianxun Wei; jxwei1972@163.com

Received 23 November 2021; Revised 28 December 2021; Accepted 31 December 2021; Published 12 February 2022

Academic Editor: Fu Wang

Intervertebral disc degeneration (IDD) is considered the basis of serious clinical symptoms, especially for low back pain (LBP). Therefore, it is essential to explore the regulatory role and diagnostic performance of dysregulated genes and potential drugs in IDD. Through WGCNA co-expression analysis, 36 co-expression modules were obtained. Among them, MidnightBlue and Red modules were the most related to IDD. Functional enrichment analysis showed that the Red module was mainly related to neutrophil activation and regulation of cytokine-mediated signaling pathway and apoptosis, whereas the MidnightBlue module was mainly related to extracellular matrix organization, bone development, extracellular matrix, extracellular matrix component, and other extracellular matrices. Furthermore, 356 genes highly related to the module were screened to construct a protein interaction network. Network degree distribution analysis showed that the known IDD-related genes had a higher degree of distribution. Enrichment analysis demonstrated that these genes were enriched in MAPK_SIGNALING_PATHWAY (FDR = 0.012), CHEMOKINE_SIGNALING_PATHWAY, and some other pathways. By constructing a disease-gene interaction network, three disease-specific genes were finally identified. Through combining with the drug-target gene interaction network, two potential therapeutic drugs, entrectinib and larotrectinib, were determined. Finally, based on these genes, the diagnostic model in the training dataset, test dataset, and verification dataset all showed a high diagnostic performance. The findings of this study contributed to the diagnosis of IDD and personalized treatment of IDD.

1. Introduction

Low back pain (LBP) is a multifactor disease, with intervertebral disc degeneration (IDD) as a main causal factor [1]. The aging of process intervertebral disc [2] will lead to the degeneration of vertebral disc (IVD), resulting in nerve symptoms including LBP [3]; 80% of the world population was reported to suffer from LBP, which could even cause the loss of labor in severe cases [4, 5]. Due to the lack of a clear understanding of the pathological mechanism of IDD, treatment or delay of IDD seems to be ineffective. With the aging of the population, the incidence of IDD-induced LBP is further increasing, pointing to the need of exploring the pathological mechanism of IDD.

Large-scale gene expression studies showed that many coding genes are differentially expressed in IDD, and some of them play an important role in IDD [6, 7]. For example, the expression of the inflammation-associated autocrine factor CHI3L1, a tissue specific in nucleus pulposus (NP), is significantly upregulated during denaturation, and this protects IDD by promoting the Akt3 signaling pathway [8]. With the development of genetic and proteomic tools, our understanding of genetic disorders in IDD has greatly improved. Targeted dissonant gene therapy strategies

developed encouraging results from animal models of IDD [9]. The novel lentiviral vector expressing CHOP shRNA effectively inhibits the apoptosis of rat annulus fibrosus (AF) cells by silencing the expression of CHOP [10].

In recent years, more and more bioinformatics research has been carried out on disc repair, and some effective analysis results have been obtained. For example, bioinformatic analyses identified CCND1, GATA3, TNFSF11, LEF1, and DKK1 were related to degenerative disc diseases [11]. Based on bioinformatics analysis, LOC102555094 might be demethylated by ZFP217, activating FTO, and LOC102555094/miR-431/GSK-3β/Wnt played a crucial role in IDD [12]. Jinwen Zhu et al. identified several lncRNA/circRNA-miRNA-mRNA interaction axes (MALAT1/hsa_circRNA_102348-hsa-miR-185-5p- TGFB1/FOS, MALAT1-hsa-miR-155-5p-HIF1A, hsa_circRNA_102399-hsa-miR-302a-3p-HIF1A, MALAT1-hsa-miR-519d-3p-MAPK1, and hsa_circRNA_100086-hsa-miR-509-3p-MAPK1), which may be crucial for the treatment of IDD [13].

The purpose of this study was to investigate the potential function of mRNA expression in IDD based on RNA expression profiles from IDD patients. We systematically analyzed mRNA expression profiles between IDD and healthy patients. In addition, we developed a novel algorithm for identifying mRNAs during IDD progression to determine mRNA biomarkers for IDD diagnosis and prognosis.

2. Results

2.1. Identification of IDD-Related Gene Modules. Methodology consisted of data collection, batch effect removal, co-expression module identification, and enrichment analysis, followed by protein network construction, network feature selection, and classifier construction and verification. The workflow is shown in Figure 1. The datasets GSE56081 and GSE124272 were obtained from GEO, and the data were standardized and re-annotated on the chip. To include more sample sizes, the GSE56081 and GSE124272 expression profile datasets were merged, and finally, we obtained the expression profiles of 12296 genes. The overall gene expression in the GSE56081 dataset was higher than that in the GSE124272 dataset, and there is a batch effect (Figure 2(a)), which was removed using the R software package SVA to obtain a new expression profile. As the new profile showed consistent distribution among the datasets (Figure 2(b)), this suggested that the expression profile without batch effects was qualified for further data analysis. The abnormal gene expression modules in IDD were analyzed by applying the R software package WGCNA to analyze IDD-related co-expression modules based on gene expression profiles. In this study, the power of $\beta = 7$ ($R2 > 0.85$ without scale) was the soft threshold to ensure the scale-free network (Figure 2(c) and 2(d)). A total of 36 modules were identified (Figure 2(e)). The correlation between diseases and modules was determined. Firstly, the Pearson correlation coefficient between the feature vectors of each module and the occurrence of diseases was calculated (Figure 2(f)). Further analysis on the distribution difference of the feature vectors of the significantly related modules in IDD and the control group showed that the feature vector distribution of the disease group in LightPink4, MidnightBlue, and Red modules was remarkably higher than that of the healthy group, whereas the feature vector distribution of the LightCyan1 module in the disease group was significantly lower than that of the healthy group (Figure 2(g)). Based on these two methods, LightPink4, MidnightBlue, Red, and LightCyan1 modules, which were found to be closely related to the occurrence of IDD, were determined as the key modules of IDD in this study.

2.2. Functional Involvement of IDD-Related Modules. To better understand the functional involvement of the four disease-related modules, IDD-related genes were first obtained from the DisGeNET [14]. The intersection of gene sets and IDD-related regulatory genes in the four IDD-related modules was analyzed (Figure 3(a)). We found that the genes in Red and MidnightBlue modules showed significant intersection with IDD-related regulatory genes ($P < 0.05$), suggesting that the genes in Red and MidnightBlue modules were biologically correlated with IDD. GO functional enrichment analysis was performed on the Red and MidnightBlue modules. The Red module was enriched to 20 GO biological processes, which are mainly related to neutrophil activation and regulation of cytokine-mediated signaling pathway and apoptosis, and to another 23 cellular components that mainly involved cellular outer membrane and cell adhesion (Figure 3(b)). Similarly, the MidnightBlue module was enriched to a large number of GO terms but most significantly to 10 biological processes, which mainly included extracellular matrix organization, bone development, and other biological processes (Figure 3(c)). The top 10 cellular components contained extracellular matrix, extracellular matrix component, and other components related to extracellular matrix (Figure 3(d)). In addition, the MidnightBlue module was also enriched in many molecular functions, such as receptor regulator activity and extracellular matrix structural constituent (Figure 3(e)). Previous reports indicated that pro-inflammatory cytokines, immune cells secretion, and cytokines regulate extracellular matrix in the intervertebral disc-abnormal modification enzymes, causing an imbalance between metabolic enzymes and anabolic enzymes, which will lead to widespread back, neck and back pain [15]. These results suggested genes in the Red and MidnightBlue modules shared a strong biological correlation with IDD.

2.3. Construction of IDD-Specific Protein Interaction Network. To identify new IDD-related genes, the gene sets in the Red and MidnightBlue modules were selected, and the Pearson correlations between the genes in the modules and the feature vectors of the modules were calculated, respectively. A total of 855 genes with a correlation greater than 0.7 were selected, and the expression table of these genes was further calculated to determine the AUC of IDD. We obtained a total of 356 genes with AUC higher than 0.8 and mapped these 356 genes to the STRING database [16] (https://string-db.org/). From here, 533 interaction data involving 252 genes were collected to construct an IDD-specific protein interaction network. In the network, a few genes were linked

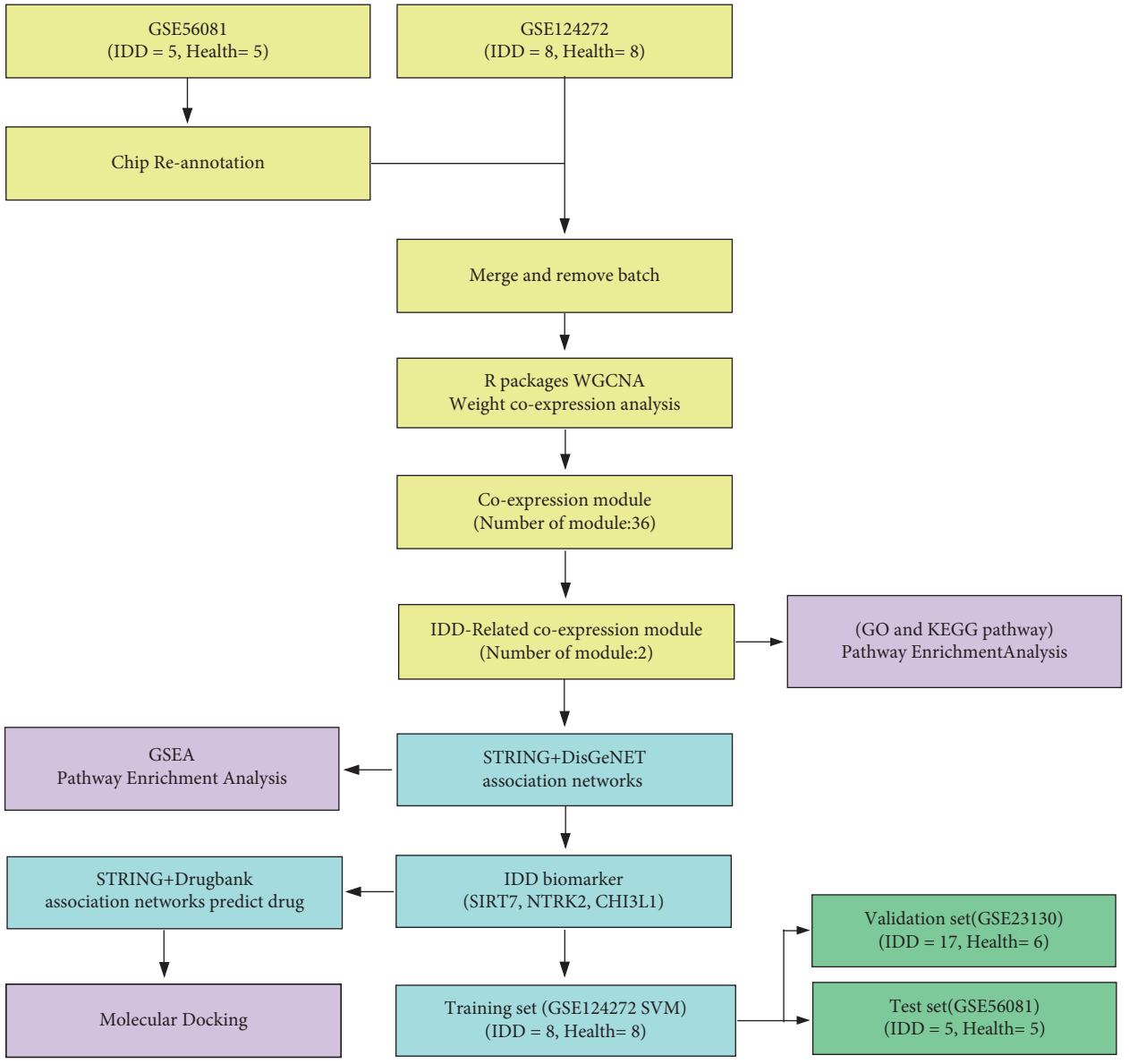

Figure 1: Workflow chart.

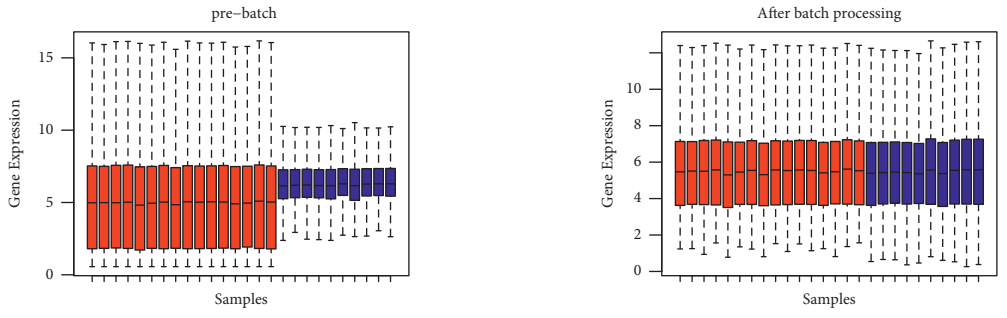

(a) (b)

Figure 2: Continued.

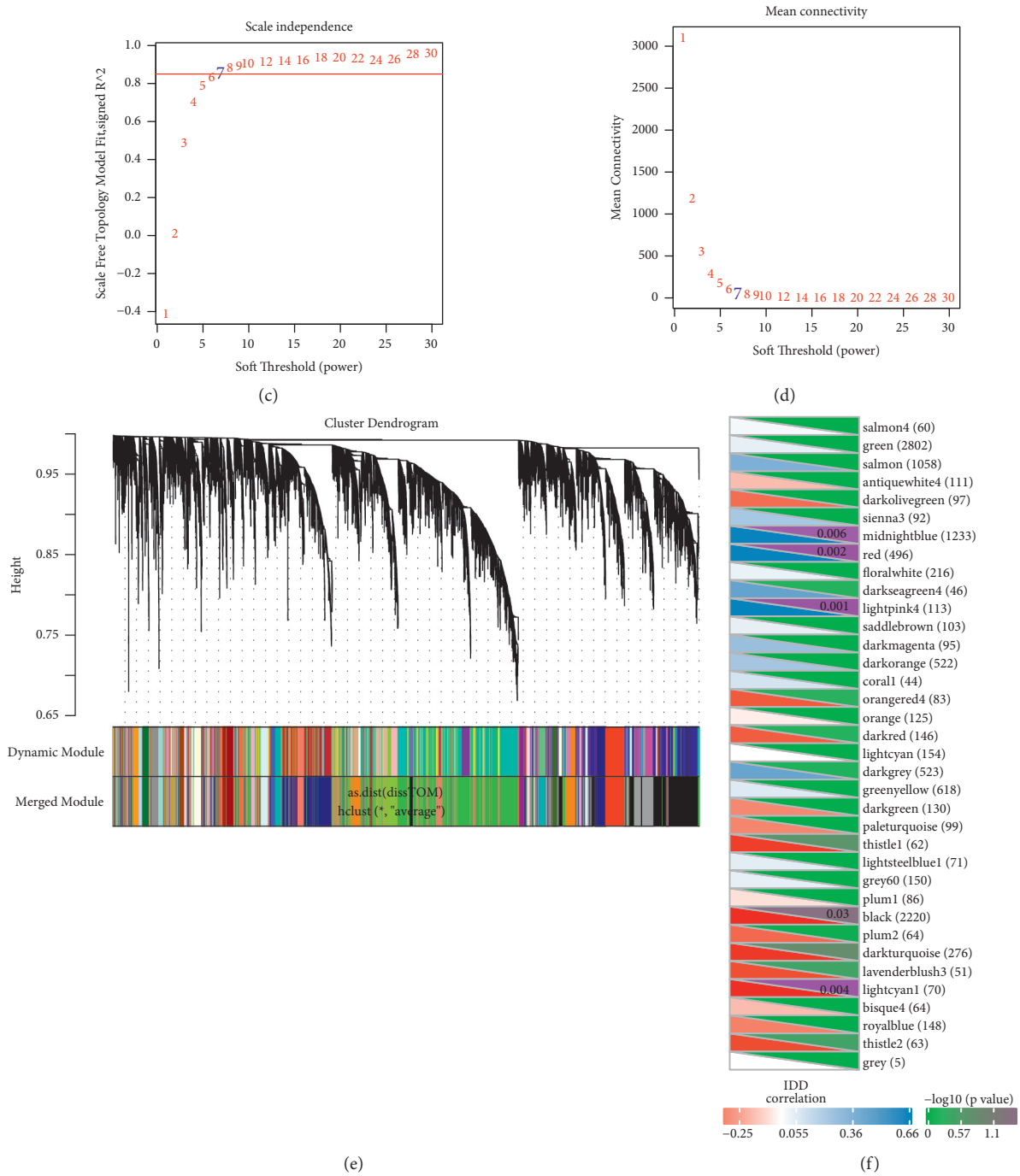

Figure 2: Continued.

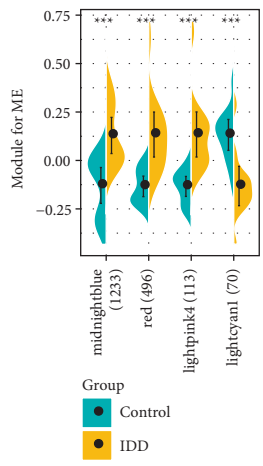

(g)

Figure 2: Identification of IDD-related modules. (a) Expression distribution in each sample in the combined dataset of GSE56081 and GSE124272. Blue is the GSE56081 dataset sample, Red is the GSE124272 dataset sample. (b) Expression distribution in each sample in GSE56081 and GSE124272 datasets after removing batch effect, Blue is the GSE56081 dataset sample, Red is the GSE124272 dataset sample. (c) Analysis of the scale-free fit index for various soft-thresholding powers (β). (d) Analysis of the mean connectivity for various soft-thresholding powers. (e) Dendrogram of all expressed genes clustered based on a dissimilarity measure (1-TOM). (f) The correlation between co-expression module and IDD, where the upper right corner represents significant P value, and the lower left corner represents correlation coefficient, $^{*}p < 0.05$, $^{**}p < 0.01$, and $^{***}p < 0.001$. The number in parentheses is the number of genes in the module. (g) The difference distribution of the feature vectors of modules that are significantly related to IDD in IDD and the control group.

by a large number of other genes, and many genes only interacted with a few genes (Figure 4(a)), and among these genes, MAPK1 was relatively the genes with the largest interaction with other genes in the network. The p38 MAPK signaling pathway plays an important role in many inflammatory and metabolic changes during disc degeneration [17]. The degree distribution in the network was analyzed (Figure 4(b)), and it has been found that the majority of nodes had degrees around 1 and a few nodes were above 10, showing a median law distribution, which is consistent with the characteristics of biological networks. There were 9 known IDD-regulated genes in the network, and most of these genes had a large degree ranking, suggesting that a larger node degree in the IDD-specific protein interaction network is more closely related to IDD (Figure 4(c)). The degree of nodes in the network was used as rank for GSEA function enrichment analysis, and these genes were found to be significantly enriched into 5 KEGG pathways (Figure 4(d)–4(h)), which were MAPK_SIGNALING_Pathway (FDR = 0.012) and CHEMOKINE_SIGNALING_Pathway (FDR = 0.024).

2.4. Key Genes of IDD Were Mined and Identified. Considering the significance of IDD-specific protein networks, we introduced all IDDRGs into the network. The interaction relationships between two IDDRGs and between two IDDPPIG were obtained from the STRING database to construct a new IDD regulation network, which contained 435 nodes and 4362 pieces of interaction information, and there were 194 IDDRGs (Figure 5(a)). We found that the degree of IDDRG in the network was significantly higher than that of IDDPIG. The enrichment significance of each IDDPPIG gene by IDDRG was calculated, and the results demonstrated that a total of 168 IDDPPIG genes (69.7%) were significantly enriched by IDDRG with a $P < 0.05$, suggesting that a large number of IDDPPIG genes in the network were indirectly or interrelated with IDDRG. The network characteristics of IDDRG and IDDPPIG were further systematically compared, and it was observed that the average shortest path between each IDDPPIG and IDDRG was significantly ($p = 1E - 16$) shorter than the average shortest path between other IDDPPIGs (Figure 5(b)), indicating that there was a closer interaction relationship between IDDPPIG and IDDRG. The multiples of the average shortest path from an IDDPPIG gene to an IDDRG and the average shortest path from each IDDPPIG gene to other IDDPPIG were calculated, and we found that most of them were between 0.8 and 0.85, which was lower than that of the random network (Figure 5(c)). After analyzing the degree distribution of each IDDPPIG in the network, it is observed that the average degree was higher than that of the random network (Figure 5(d)). In addition, we also found a higher proportion of IDDRG interacting with IDDPPIG gene than that in the random network (Figure 5(e)).

Based on the above results, IDDRG with a significantly high interaction ratio and IDDPPIG with both significantly low multiple of shortest path and high degree of distribution were selected as a new potential key gene of IDD. Here, we obtained three genes (Table 1).

2.5. Potential Drugs and Drug Targets of Key IDD Genes. To further determine the potential drug targets of key IDD genes, following Wang et al. [18], we determined the network distance between these 3 key genes and 5490 drugs on DrugBank (Figure 6(a)), and found that the distance

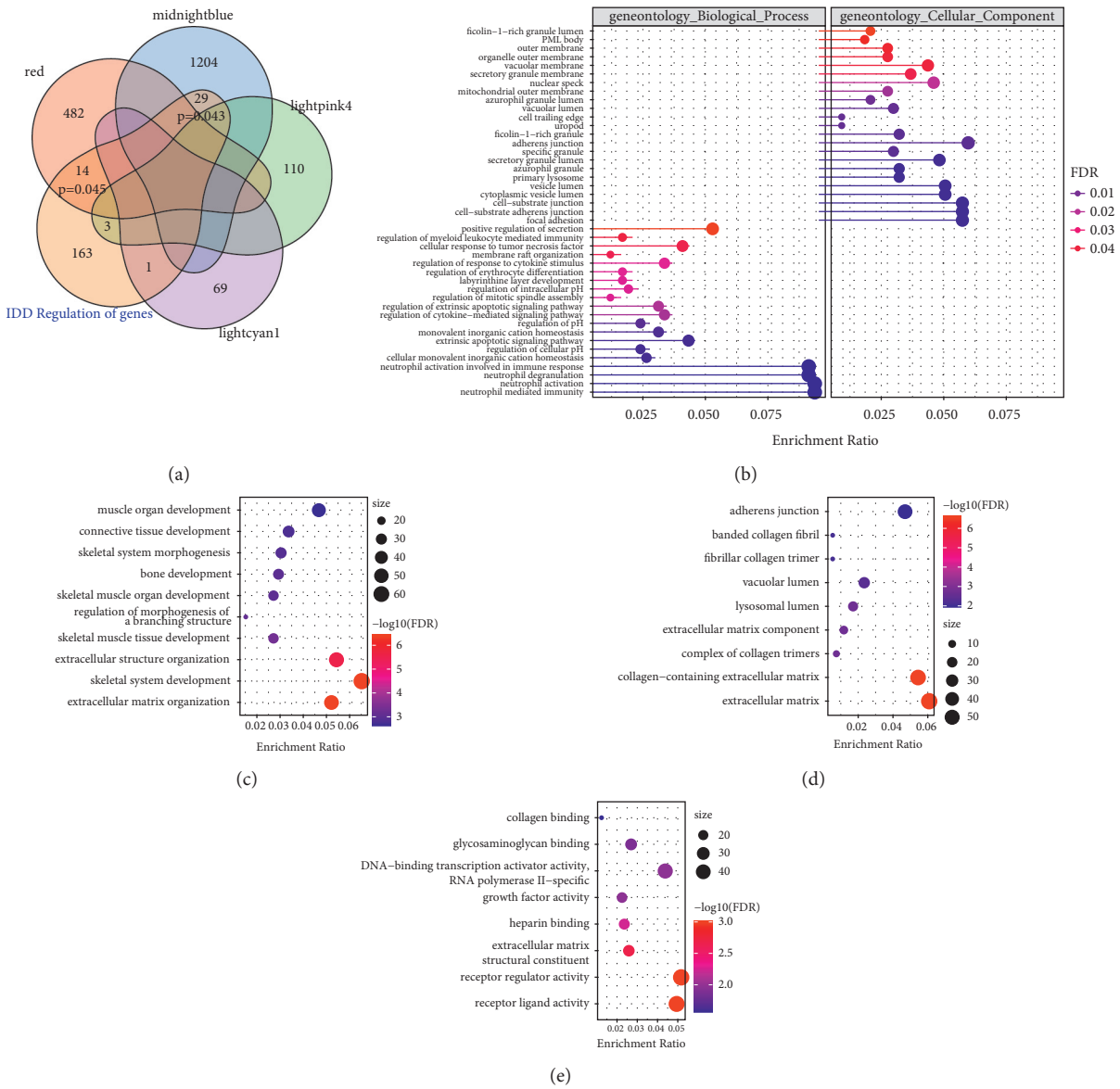

FIGURE 3: Functional analysis of IDD-related modules. (a) Winn diagram of intersection between genes in four IDD-related modules and known regulatory genes of IDD. (b) GO Biological Process and Cellular Component enriched by genes in the Red module. (c) The most significant 10 bcCellular components enriched by the MidnightBlue module. (c) The most significant 10 molecular functions enriched in the MidnightBlue module. The dot size in the figure represents the number of module genes enriched in term. Color denotes significance FDR.

between the three key genes and the drug was shorter than that of the random background. A total of two drugs were determined according to a global FDR < 0.05 (Table 2). Subsequently, the relationship between these two drugs and the three key IDD genes (SIRT7, NTRK2, CHI3L1) was further analyzed by molecular docking methods (Figure 6(b)). When drugs DB11986 and DB14723 were combined with CHI3L1 protein, both drugs could well bind to the active site of the protein and carried −9.7 kcal/mol and 10.0 kcal/mol, respectively. Such a high docking score indicated that these two molecules may have potential biological activity against CHI3L1 protein. When the two drugs bound to NTRK2 protein, the docking score was significantly reduced to −8.6 kcal/mol and −7.9 kcal/mol, respectively, though both of them bound to the active site. The drug DB11986 could be extended from the other side of the active site due to the molecular structure of the additive farm, but DB14723 was all embedded into NTRK2 protein for its relatively small molecular structure. Interestingly, when drugs DB11986 and DB14723 interacted with SIRT7 protein, the docking scores of the two drugs were significantly different. Among them, the docking score of DB11986 for SIRT7 was −9.5 kcal/mol, whereas that of DB14723 for SIRT7 was −7.9 kcal/mol. Such a significant difference also indicated that there may also be potential differences in the activity of these two drugs against SIRT7 protein. These results suggest that the different binding affinities of the two drugs to the three proteins could indicate the potential differences in interaction and biological activity.

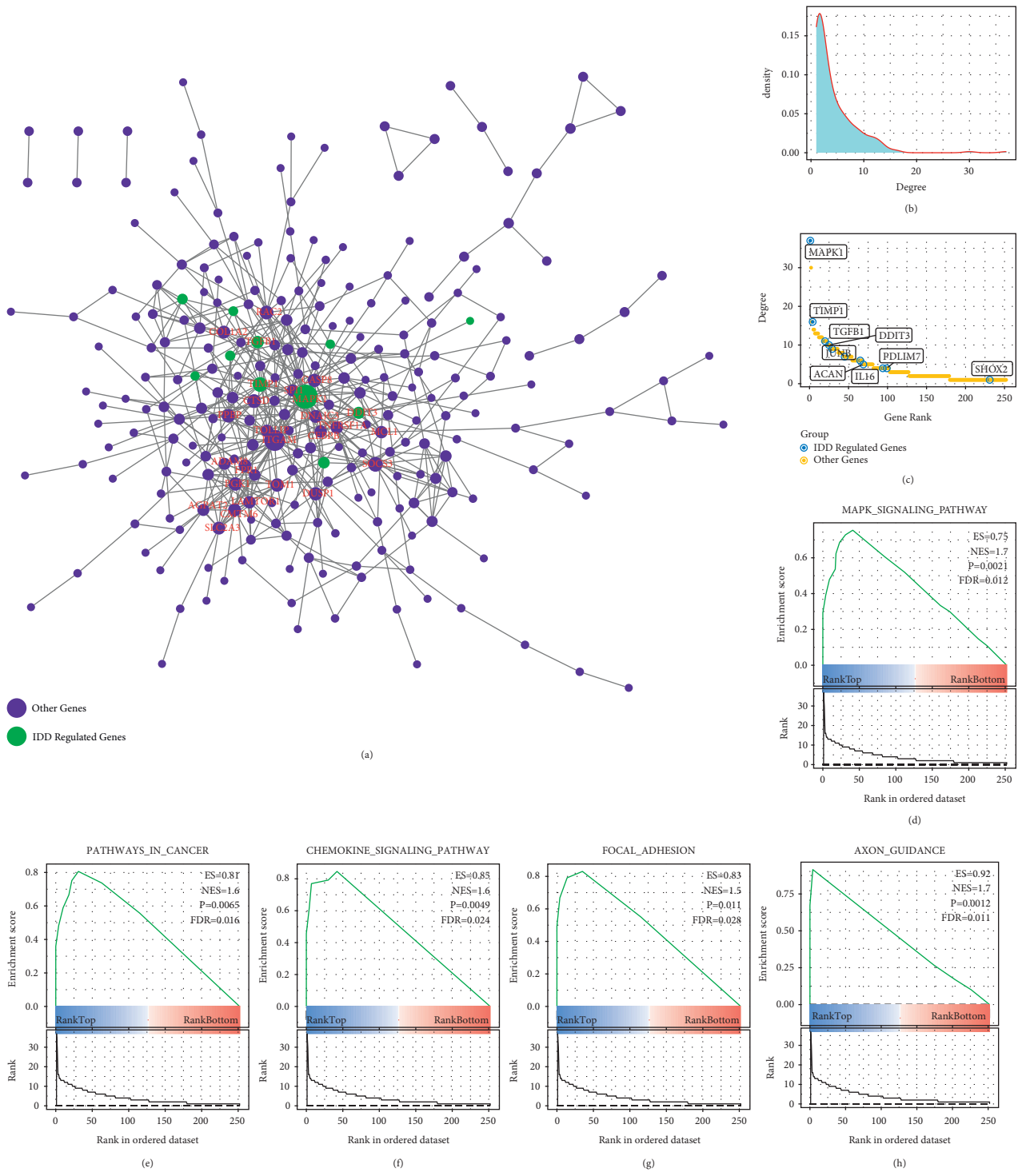

Figure 4: Analysis of IDD-specific protein interaction networks. (a) IDD-specific protein interaction networks. (b) Degree distribution of the network. (c) Degree rank of each node in the network, marked as IDDRG; D-H: the KEGG pathway is enriched by ranked GSEAs in the network.

2.6. Identification and Validation of IDD Biomarker. Markers related to IDD were further determined based on three disease-specific genes, we used GSE124272 as the training set, GSE56081 as the test set, and GSE23130 and GSE150408 as the external validation set. SIRT7, NTRK2, and CHI3L1 served as features in the training dataset to obtain their corresponding expression profiles. The heat map of expression profiles in each dataset demonstrated that SIRT7, NTRK2, and CHI3L1 were all highly expressed in the IDD group in different datasets (Figure 7(a)). After analyzing the expressions of the three genes in different datasets, we found that SIRT7 and NTRK2 genes were significantly

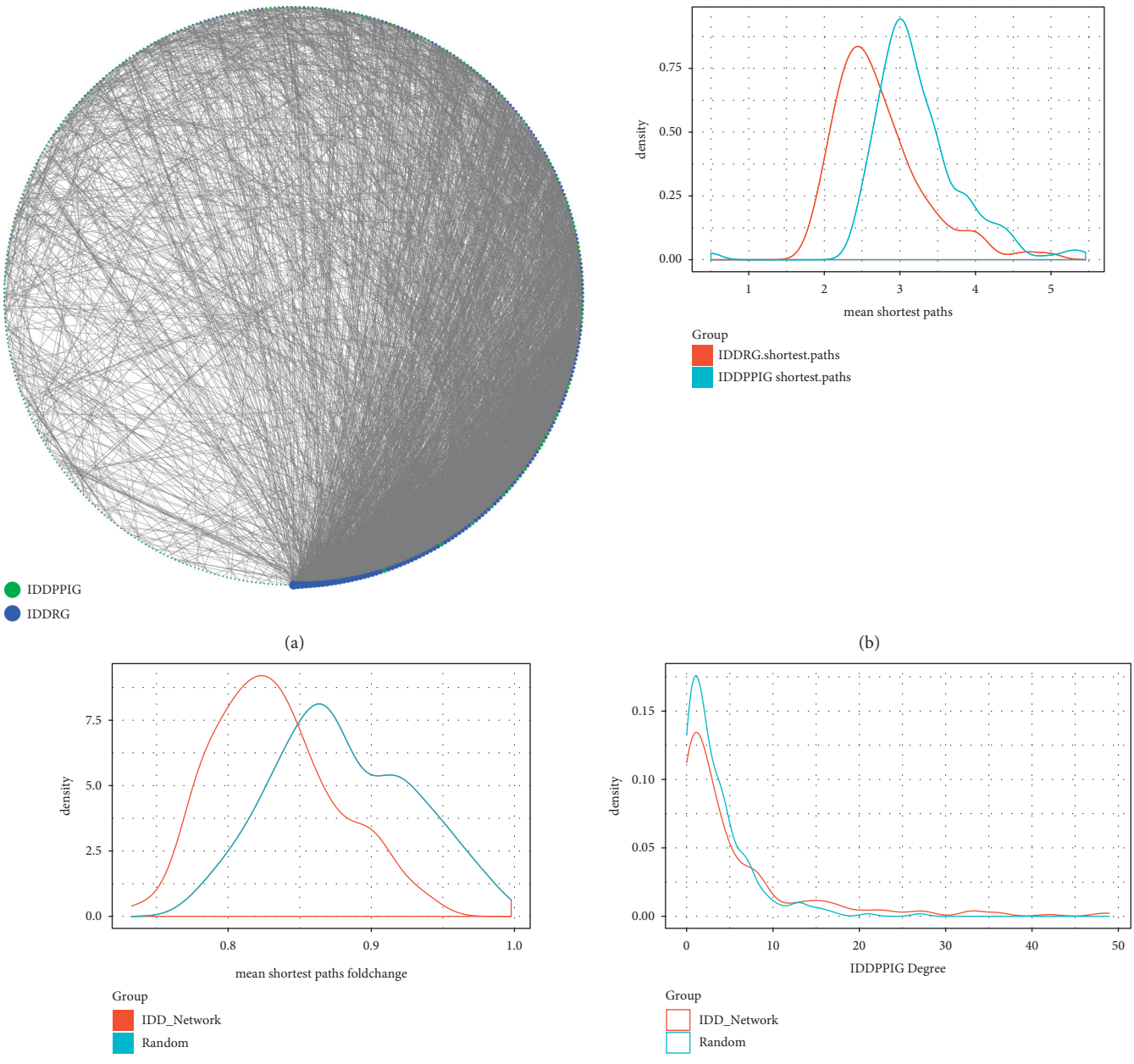

Figure 5: Continued.

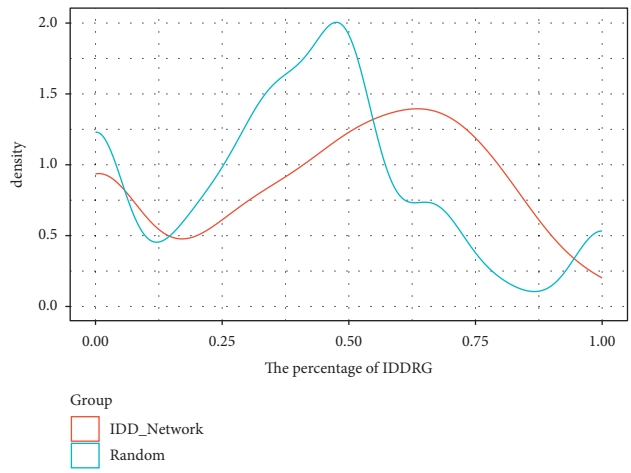

(e)

Figure 5: Integrated analysis of IDD-specific protein network and IDD-regulated gene network. (a) Interaction network of IDDRG and IDDPPIG. (b) The average shortest path distribution between IDDPPIG and IDDRG and other IDDPPIG in the network. (c) Distribution of the average shortest path multiples between IDDPPIG and IDDRG and other IDDPPIG in the network. (d) Degree distribution of IDDPPIG in the network. (e) IDDRG Proportion Distribution of IDDRG Interaction in the Network.

Table 1: Network characteristics of 3 key genes.

Symbol	IDDRG Count	IDDRG Count p value	IDDRG ratio	IDDRG ratio p value	Shortest ratio	Shortest Ratio_p value	IDDRG enrichment p value
SIRT7	16	0.000609	0.94	0.024	0.76	0.01	4.93E-28
NTRK2	21	3.04E-06	0.87	0.041	0.77	0.015	5.33E-35
CHI3L1	18	8.84E-05	0.86	0.048	0.76	0.01	9.30E-30

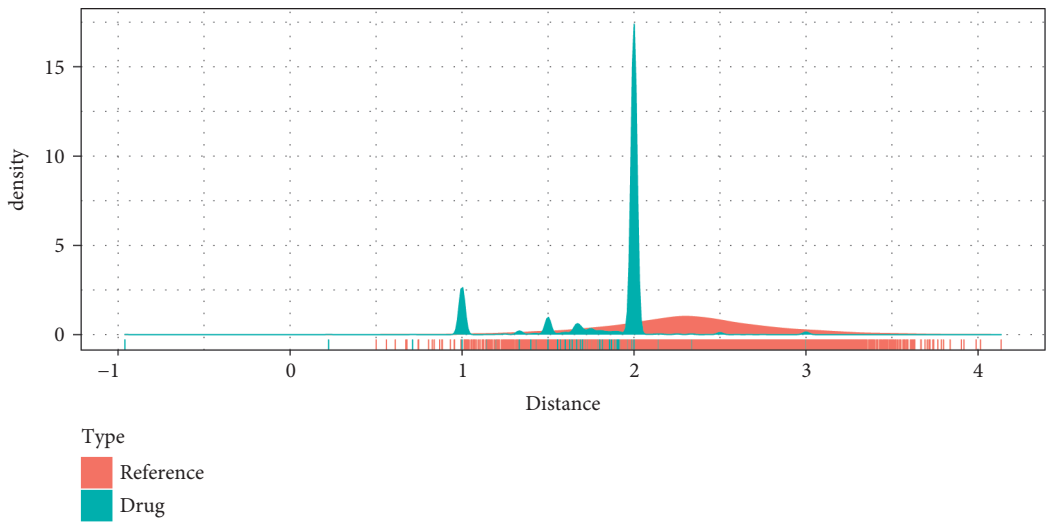

(a)

Figure 6: Continued.

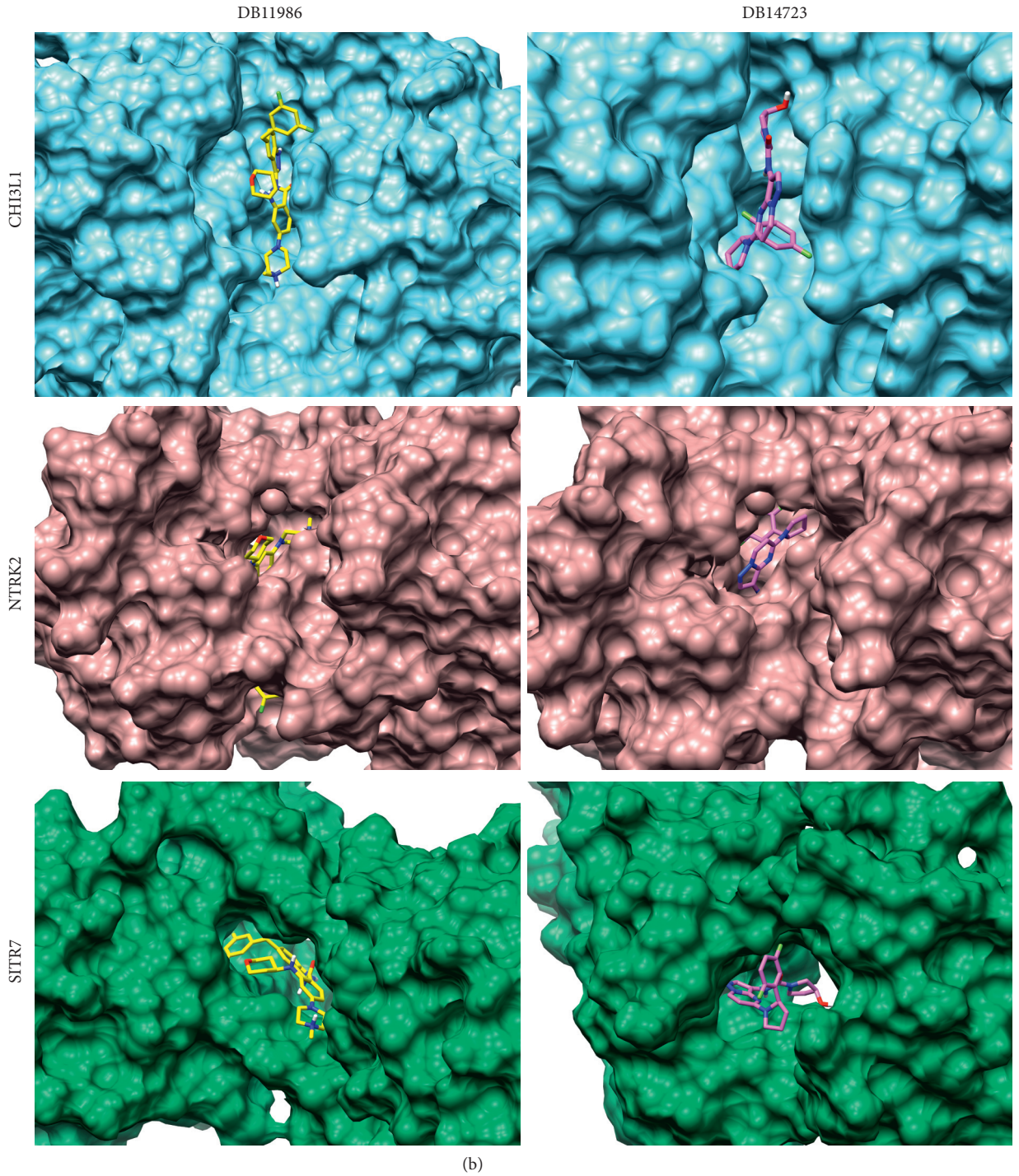

Figure 6: Potential drugs and drug-target analysis of key IDD genes. (a) The distribution of network-regulated distance between drug and disease key genes. (b) Interaction results of drugs DB11986 and DB14723 with CHI3L1, NTRK2, and SIRT7 proteins. Among them, CHI3L1 protein was added sky blue surface, NTRK2 protein was added rosy brown surface, and SIRT7 protein was added sea green surface. The drug DB11986 was displayed as yellow, and DB14723 was displayed as orchid.

overexpressed in GSE124272 (Figure 7(b)), that NTRK2 and CHI3L1 were significantly highly expressed in GSE56081 dataset (Figure 7(c)), that SIRT7 and CHI3L1 were significantly highly expressed in GSE23130 dataset (Figure 7(d)), and that SIRT7 and NTRK2 were significantly highly expressed in GSE150408 dataset (Figure 7(e)). Also, we added experimental validation, specifically, we collected tissues from five early IDD patients (III) and five advanced IDD patients (V) from The Third People's Hospital of Nanning and evaluated the expression differences of SIRT7, NTRK2, and CHI3L1 using RT-PCR, and as expected, they had a trend of higher expression in advanced IDD patients,

Table 2: Potential drugs for key genes.

Drug_id	Drug name	Distances	P value	FDR
DB11986	Entrectinib	0.2238934	5.219693e-06	2.865090e-02
DB14723	Larotrectinib	-0.9601777	2.416713e-12	1.326775e-08

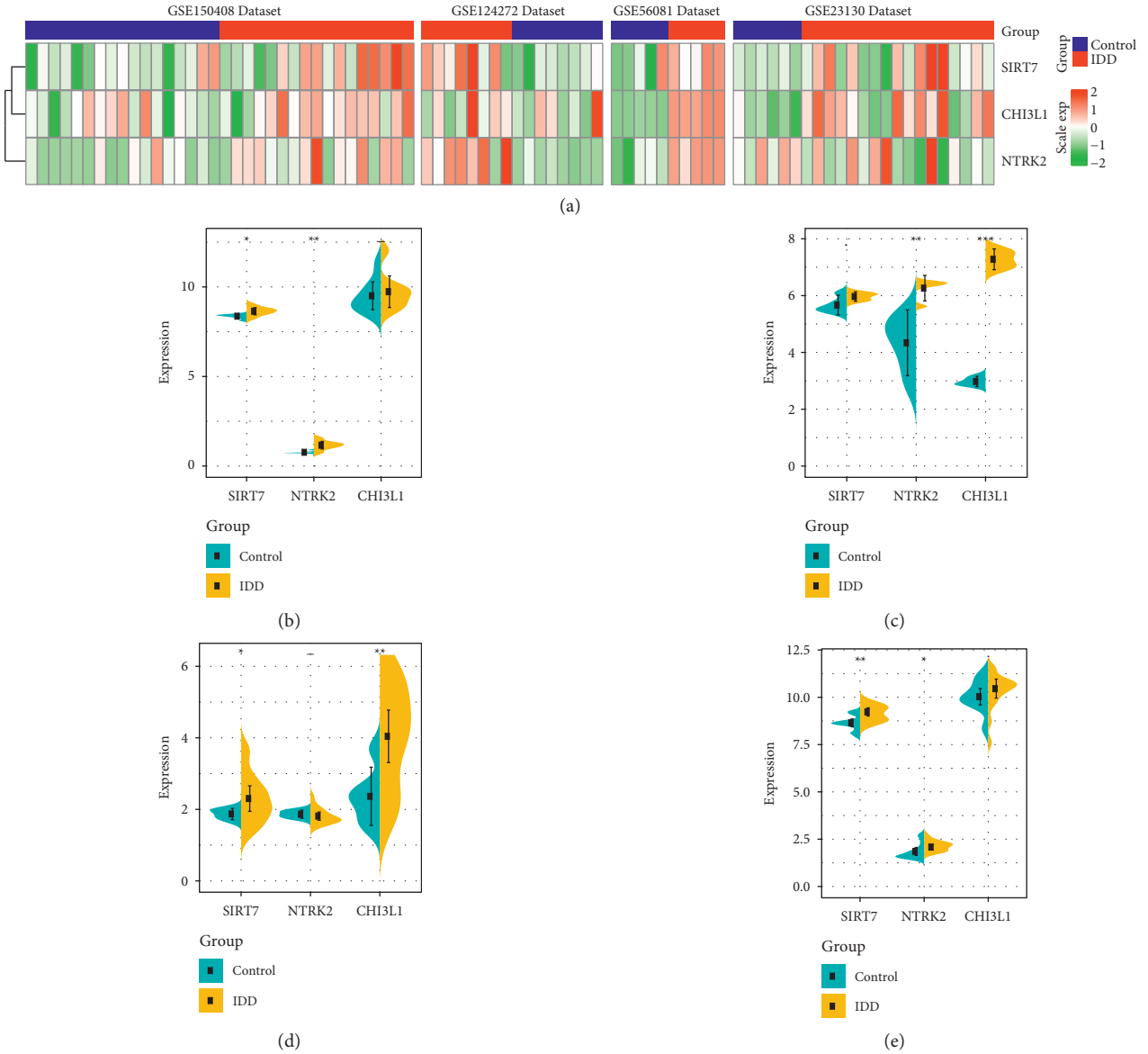

Figure 7: Continued.

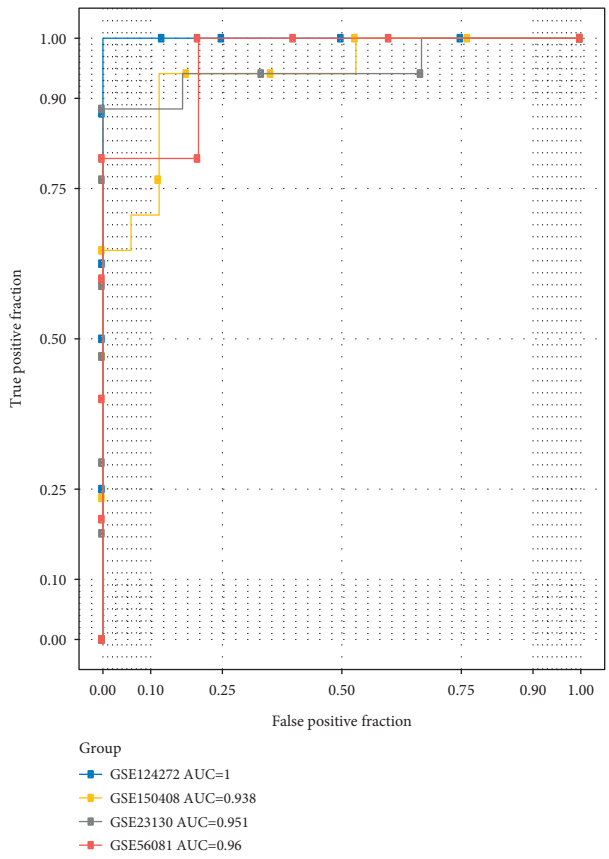

(f)

Figure 7: Identification and validation of IDD biomarker. (a) Heatmaps of expression profiles of SIRT7, NTRK2, CHI3L1 genes in the training set, test set, GSE150408 Dataset, and validation set. (b) Differential distribution of SIRT7, NTRK2, CHI3L1 genes in the GSE124272 dataset. (c) Differential distribution of SIRT7, NTRK2, CHI3L1 genes in the GSE56081 dataset. (d) Differential distribution of SIRT7, NTRK2, CHI3L1 genes in the GSE23130 dataset. (e) Differential distribution of SIRT7, NTRK2, CHI3L1 genes in the GSE150408 dataset. (f) Classification of ROC curve of the lncRNA diagnostic model in four datasets.

with CHI3L1 and NTRK2 having a significant expression difference (Supplementary Figure S1). These findings suggested that the expression of a single gene in different datasets was easily disturbed by other factors. Therefore, we used the three genes as a panel to construct a SVM classification model. Tenfold cross-validation was used to test the model, and the classification accuracy was 100%, as all the 16 samples were correctly classified in the training dataset. The sensitivity of the model to IDD was 100%, the specificity was 100%, and the area under ROC curve (AUC) was 1.0. When using the GSE56081 dataset for verification, 9 out of 10 samples were correctly classified, with a classification accuracy of 90%, a model sensitivity to IDD of 80%, a specificity of 100%, and an area under ROC curve of 0.96. The GSE23130 dataset was further used for verification and accurately classified 19 samples out of 23, with a classification accuracy of 83.6%, a sensitivity of the model to IDD of 50%, a specificity of 94%, and area under ROC curve of 0.95. The GSE150408 dataset was further used for verification and accurately classified 27 samples out of 34, with a classification accuracy of 88.2%, a sensitivity of the model to IDD of 70.6%, a specificity of 79.4%, and an area under ROC curve of 0.94 (Figure 7(f)). These results indicated that the diagnostic prediction model based on SIRT7, NTRK2, and CHI3L1 could effectively distinguish IDD patients from control population; therefore, these genes could serve as reliable biomarkers for specific diagnosis of IDD.

3. Discussion

Low back pain (LBP) caused by intervertebral disc degeneration (IDD) is the most common musculoskeletal system disease [19]. IDD is the result of the interaction of many factors, including abnormal pressure load, inflammatory factors, cell aging, and related signal pathways, but the final result is the imbalance of extracellular matrix synthesis and catabolism [20]. In this study, the gene expression patterns between IDD and healthy samples were systematically analyzed, and two disease-related gene modules were identified by the weighted co-expression method. These genes were mainly enriched in neutrophil activation and regulation of cytokine-mediated signaling pathways, and extracellular matrix-related multiple biological pathways, suggesting that these modular genes have a strong biological correlation with IDD. Based on this, we constructed a protein interaction network and observed high-degree nodes with known

IDD, and found that a higher correlation of related genes. Finally, IDD-related genes were introduced to establish a disease-specific network. Through the analysis of network topology, SIRT7, NTRK2, and CHI3L1 were finally identified as new IDD-specific genes, and these genes were significantly highly expressed in IDD samples.

Sirtuin 7 (SIRT7), which is a nicotinamide adenine dinucleotide (NAD+)-dependent histone deacetylase, is mainly located in the nucleus. SIRT7 is involved in a variety of cellular processes, including aging, DNA repair, tumorigenesis, and metabolism [21, 22]. SIRT7 is proven to be an important regulator of cartilage homeostasis and is involved in the development of OA [23]. SIRT7 expression is significantly downregulated in OA articular cartilage, which is consistent with autophagy gene expression; moreover, loss of SIRT7 accelerates type II collagen catabolism [24]. Neurotrophic receptor tyrosine kinase 2 (NTRK2) is a member of the neurotrophic receptor kinase (NTRK) family and a membrane-bound receptor. When neurotrophic proteins bind, members of the NTRK family and MAPK pathways are phosphorylated and give out signal through NTRK2, leading to cell differentiation. Jinhuai Hu et al. reported that NTRK2 is an oncogene, and its overexpression partially reverses the inhibitory effect of miR-22 on tumor proliferation and invasion [25]. Inflammation-related autocrine factor CHI3L1, which is tissue-specific and significantly upregulated during denaturation, protects IDD by promoting the Akt3 signaling pathway [8]. CHI3L1 can be expressed by a variety of cells, including chondrocytes, smooth muscle cells, and osteosarcoma cells, but its function is usually related to inflammation and tissue remodeling [26–28]. According to current studies, SIRT7 and NTRK2 have not been previously reported in IDD. The current study is the first to reveal the involvement of these two genes may be involved in the occurrence and development of IDD.

Entrectinib is an effective oral tyrosine kinase inhibitor of TrkA, TrkB, and TrkC (encoded by the genes neurotrophic tyrosine receptor kinase (NTRK) 1, 2, and 3, respectively). In a clinical study of 25 patients who had various malignancies containing NTRK, ROS1, or ALK gene fuses and received an effective dose of entrectinib, an overall response rate of 79% with significant tumor regression in all NTRK-altered tumors (including ETv6: NTRK3 translocation) [29] was observed. Larotrectinib is a selective inhibitor of neurotrophin receptor kinase (NTRK) and can be used to treat solid tumors carrying NTRK gene fusion [30, 31]. David S Hong et al. showed that among 159 patients with TRK fusion-positive cancer who received larotrectinib, 121 out of 153 evaluable patients showed an objective response (79%, 95% CI 72–85), and 24 (16%) showed a complete response (16%) [32]. As NTRK2 was confirmed as a prognostic gene for IDD in this study, we speculated that entrectinib and larotrectinib may relieve IDD through NTRK2.

Although we analyzed and verified the abnormal expression and functional role of genes in IDD from multiple data coalitions using bioinformatics techniques, some limitations of this study should be noted. Firstly, the sample lacked some clinical follow-up information; thus, we failed to consider factors such as the presence of other patient health conditions. Secondly, the results obtained only by bioinformatics analysis were insufficient, which required further experimental validation. Therefore, further genetic and experimental studies with larger sample sizes and experimental validation are needed.

4. Conclusion

In conclusion, in this study, we systematically analyzed the gene expression patterns in IDD and conducted a large-scale genome-wide study on the RNA expression profile to identify two gene modules closely related to IDD. Three new IDD-specific genes have been found for IDD through disease-association network mining, and the three genes were involved in a variety of important biological pathways. At the same time, we also discovered that entrectinib and larotrectinib may be effective in the treatment of IDD, which provides a target and reference for clinicians and biological experimentalists.

5. Materials and Methods

5.1. RNA Expression Profile. All gene expression profiles of human intervertebral disc degeneration were retrieved from the Gene Expression Omnibus (GEO) database (https://www.ncbi.nlm.nih.gov/geo/), and 4 datasets with a sample size of no less than 10, namely, GSE56081 [33], GSE124272 [34], GSE23130 [7], and GSE150408, were selected. Among them, there were 10 samples in GSE56081, including 5 samples from patients with IDD and 5 samples from the nucleus pulposus of normal control. The platform was Arraystar Human lncRNA microarray V2.0 (Agilent_033010 Probe Name version). The GSE124272 dataset contained of 8 IDD samples and 8 control samples on the Agilent-072363 SurePrint G3 Human GEV3 8×60 K Microarray 039494. The GSE23130 dataset contained a total of 23 samples on Affymetrix Human X3P Array.

The GSE56081 dataset is a lncRNA chip platform. The probe sequence of the GSE56081 dataset was aligned to the genome (GRCh38.p13, https://ftp.ebi.ac.uk/pub/databases/gencode/Gencode_human/release_39/gencode.v39.primary_assembly.annotation.gff3.gz) through the method of chip re-annotation to determine the transcript ID mapped by the probe. Each transcript cluster was assigned to Ensembl gene ID to obtain the matching relationship between probe and gene to acquire gene expression profile.

The specific process is as follows:

(1) The matrix files expressing the sequence tags were downloaded to obtain the nucleic acid sequences of these probes.

(2) The nucleic acid sequences of these probes were matched to the human genome library (ENCODE database, version 38, https://www.gencodegenes.org/human/) using SeqMap software [35]. The library requires sequence matches and no mismatches, and the corresponding chromosomal positions of the probes were obtained.

(3) A total of 19873 re-annotated mRNA probes were obtained by simultaneously removing the presence of multiple matching probes.

Finally, for all the expression profiles, the probe was mapped to the gene, and when multiple probes were mapped to the same gene, the median value was taken as the expression value of the gene. To enlarge the sample size of the dataset, we combined the GSE56081 and GSE124272 datasets, combat function of R software package SVA [36] was used to remove the batch effect to obtain a new expression profile, and the GSE23130 dataset served as an external independent verification queue.

5.2. Weighted Co-Expression Network Analysis. After merging the datasets of GSE56081 and GSE124272 and removing the batch effect, the weighted co-expression module was constructed using the gene expression profile. Specifically, the RNA expression data profile of the genes was used to examine whether the samples and genes were qualified. Then, we used the WGCNA [37] package in R to construct a scale-free co-expression network for the genes. The Pearson's correlation matrices and average linkage method were performed for pairwise. Then, a weighted adjacency matrix was constructed using a power function $A_{mn} = |C_{mn}|^{\beta}$ (C_{mn} = Pearson's correlation between gene m and gene n; A_{mn} = adjacency between gene m and gene n). β, which is a soft-thresholding parameter, emphasizes strong correlations between gene and indicates weak correlations. After determining the power of β, the adjacency was transformed into a topological overlap matrix (TOM) for measuring the network connectivity of a gene, which was defined as the ratio of sum of its adjacency to all other genes, and then, the corresponding dissimilarity (1-TOM) was calculated. To classify genes with similar expression profiles into gene modules, average linkage hierarchical clustering was performed according to the TOM-based dissimilarity measured with a minimum size (gene group) of 30 for the gene dendrogram. To further analyze the module, we calculated the dissimilarity of module eigen gene, determined a cut line for module dendrogram, and merged some modules.

5.3. Identification of Co-Expression Modules Associated with IDD. We defined the module related to the occurrence of IDD as the IDD Module. Specifically, the correlation between ME and IDD features was calculated to identify the relevant modules with significance $P < 0.05$. Further analysis on the distribution differences of each module's feature vectors in IDD and control group was performed to select the modules with significant FDR < 0.05. Also, we obtained known IDD-related gene (IDDRG) sets from the DisGeNET [14] database, analyzed the intersection of genes and IDDRGs in each Module, evaluated the enrichment significance of IDDRG by hypergeometric test, and selected the modules with significantly rich IDDRGs as the final IDD Module.

5.4. Functional Enrichment Analyses. Gene Ontology (GO) and Kyoto Encyclopedia of Genes and Genomes (KEGG) pathway enrichment analysis was performed using the R package clusterProfiler [38] for screening genes associated with the IDD Module, so as to identify over-represented GO terms in three categories (biological processes, molecular function, and cellular component) and KEGG pathway. For both analyses, a FDR of <0.05 was considered to denote statistical significance.

5.5. Construction of IDD-Related Protein Interaction Network. In the IDD Module, the correlation between the genes in the Module and the feature vectors of the Module was calculated to select gene set with the correlation coefficient greater than 0.7. The classification performance of each gene expression in IDD and control group was further analyzed, and the gene set with AUC greater than 0.8 was determined as the final core gene set of IDD Module. These gene sets were mapped to the STRING v11.0 [16] database to obtain the interaction data among these genes, and an IDD-related protein interaction network (IDDPPI) was established. Visual analysis was performed using cytoscope [39], and the degree of nodes in the protein interaction network was used as the rank. GSEA [40] enrichment analysis was employed to obtain significantly enriched KEGG pathways to evaluate network function.

5.6. Construction of IDDRG-IDDPPI-Related Network. The genes in IDDRG and IDDPPI (IDDPPIG) were mapped to the STING V11.0 [16] database to construct a protein interaction network. The degree distribution of each IDDPPIG and IDDRG in the network was further analyzed. The significance of each IDDPPIG enriched by IDDRG and the proportion of IDDPPIG gene interaction were calculated using a hypergeometric test to analyze the network characteristics of IDDPPIG and IDDRG, and the average shortest path between two IDDPPIG or between IDDPPIG and IDDRG was compared. The multiple relationship distribution of the average shortest path between two IDDPPIG genes and between an IDDRG and an IDDPPIG gene was calculated. Based on the above characteristics, the random perturbation method was used to establish a random network as the background, and the significant genes were selected as the new key genes of IDD (IDDG).

5.7. IDDG and Drug-Target Network Construction. To examine the potential drug effects of IDDG, the relationship between drugs and drug-target genes was obtained from DrugBank v5.1.7 database [41], and a total of 16196 drug-gene interaction data were identified. These drug-target genes and IDDG genes were mapped to the STRING V11.0 [16] database to obtain gene interaction information, and a drug-gene-IDDG network was constructed. As previously described by Wang et al. [18], the shortest path of drugs to IDDG was calculated for identifying potentially related drugs to IDDG.

Specifically, we calculated the proximity of the drug to IDDG. In this case, we can give S, the IDD-related gene set IDDG; D, the degree of IDD-related gene set nodes in PPI; and T, drug-target gene collection. Distance D (s, t) is the shortest path between s node and T node (where $S \in S$ is IDD-related gene; $T \in T$ is drug-target gene), and the calculation method is as follows:

$$d(S,T) = \frac{1}{|T|}\sum_{t\in T}\min_{s\in S}(d(s,t)+\omega), \tag{1}$$

where ω is the weight of the target gene. If the target gene is a gene in the IDD-related gene set, the calculation method is $\omega = -\ln(D+1)$; otherwise, $\omega = 0$.

We generated the simulated reference distance distribution corresponding to the drug. To put it simply, a group of protein nodes were randomly selected in the network as the simulated drug target, and the number of nodes was the same as the target size (denoted as R). Next, the distances $d(S, R)$ between these simulated drug targets (representing the simulated drug) and DMEGs were calculated. After 1000 random repeats, the simulated reference distributions were generated. At the same time, the mean and standard deviation of the μd (S, R) and σd (S, R) reference distributions and the corresponding actual observed distances were converted into standardized scores, that is, proximity Z:

$$z(S,T) = \frac{d(S,T) - \mu_{d(S,R)}}{\sigma_{d(S,R)}}. \tag{2}$$

Finally, the shortest path to IDDG was significantly higher for the drug than for the background drug according to the simulated reference distance distribution. The degree of binding between IDDG and drugs was evaluated by molecular docking.

5.8. Establishment of IDD Diagnostic Prediction Model and Evaluation of Model Prediction Performance. IDDG was used to construct a diagnostic prediction model based on support vector machine (SVM) classification [42] to predict the IDD and control samples. SVM, which is a supervised machine learning algorithm model, analyzes data, and identifies patterns. A SVM creates a hyperplane, in high or infinite dimensions, and can be used for classification and regression. Given a set of training samples in which each marker belongs to two classes, an SVM training algorithm builds a model that assigns new instances to one class or another, making it an improbabilistic binary linear classification.

In this study, GSE124272 was the training set, GSE56081 was the test set, and GSE23130 was the external verification set. The model was constructed in the training dataset, and the classification ability of the model was verified by the tenfold cross-validation method. The established model was then used to predict the samples in the test set and validation dataset. The predictive ability of the model was evaluated using area under the ROC curve (AUC), and the sensitivity and specificity of the model for IDD prediction were analyzed.

5.9. Statistical Analysis. Ggplot2 of R software was used for visualization, and heatmap was used to draw heat maps. Fisher's exact test was used for multigroup comparison, and significance was defined as $P < 0.05$. The Benjamini method was used for multiple test correction to obtain FDR. All of these analyses are performed in R 3.4.3.

Data Availability

The data that support the findings of this study are available from the corresponding author upon reasonable request.

Conflicts of Interest

The authors declare that they have no conflicts of interest.

Authors' Contributions

Haoxi Li and Qie Fan conceived and designed the study; Wenhao Li, Li Zhang, and Jianxun Wei acquired the data. Jicheng He analyzed and interpreted the data; Lin Tang, Zhuhai Li, and Feng Chen statistically analyzed the study; Haoxi Li drafted the manuscript; and Qie Fan revised the manuscript for intellectual content. Haoxi Li and Wenhao Li contributed equally to this work.

Supplementary Materials

Figure S1. The mRNA expression differences of SIRT7, NTRK2, and CHI3L1 early IDD patients (III) and advanced IDD patients (V). (*Supplementary Materials*)

Acknowledgments

This study was approved by Youth Fund Project of People's Hospital of Guangxi Zhuang Autonomous Region (YXQNRC 2018-2) and Guangxi Science and Technology Planning Project (Guike AD21220134).

References

[1] C.-J. Zheng and J. Chen, "Disc degeneration implies low back pain," *Theoretical Biology and Medical Modelling*, vol. 12, no. 1, p. 24, 2015.

[2] F. Wang, F. Cai, R. Shi, X.-H. Wang, and X.-T. Wu, "Aging and age related stresses: a senescence mechanism of intervertebral disc degeneration," *Osteoarthritis and Cartilage*, vol. 24, no. 3, pp. 398–408, 2016.

[3] S. Mohanty and C. L. Dahia, "Defects in intervertebral disc and spine during development, degeneration, and pain: new research directions for disc regeneration and therapy," *Wiley interdisciplinary reviews. Developmental biology*, vol. 8, p. e343, 2019.

[4] D. Hoy, L. March, P. Brooks et al., "The global burden of low back pain: estimates from the Global Burden of Disease 2010 study," *Annals of the Rheumatic Diseases*, vol. 73, no. 6, pp. 968–974, 2014.

[5] F. Balagué, A. F. Mannion, F. Pellisé, and C. Cedraschi, "Non-specific low back pain," *The Lancet*, vol. 379, no. 9814, pp. 482–491, 2012.

[6] H. E. Gruber, G. L. Hoelscher, J. A. Ingram, S. Bethea, N. Zinchenko, and E. N. Hanley Jr, "Variations in aggrecan

localization and gene expression patterns characterize increasing stages of human intervertebral disk degeneration," *Experimental and Molecular Pathology*, vol. 91, no. 2, pp. 534–539, 2011.

[7] H. E. Gruber, G. L. Hoelscher, J. A. Ingram, and E. N. Hanley Jr, "Genome-wide analysis of pain-, nerve- and neurotrophin -related gene expression in the degenerating human annulus," *Molecular Pain*, vol. 8, p. 63, 2012.

[8] Z. Fang, J. Zhao, W. Xie, Q. Sun, H. Wang, and B. Qiao, "LncRNA UCA1 promotes proliferation and cisplatin resistance of oral squamous cell carcinoma by sunppressing miR-184 expression," *Cancer Medicine*, vol. 6, no. 12, pp. 2897–2908, 2017.

[9] T. Suzuki, K. Nishida, K. Kakutani et al., "Sustained long-term RNA interference in nucleus pulposus cells in vivo mediated by unmodified small interfering RNA," *European Spine Journal*, vol. 18, no. 2, pp. 263–270, 2009.

[10] Y.-H. Zhang, C.-Q. Zhao, L.-S. Jiang, and L.-Y. Dai, "Lentiviral shRNA silencing of CHOP inhibits apoptosis induced by cyclic stretch in rat annular cells and attenuates disc degeneration in the rats," *Apoptosis*, vol. 16, no. 6, pp. 594–605, 2011.

[11] Q. Yan, Q. Xiao, J. Ge et al., "Bioinformatics-based research on key genes and pathways of intervertebral disc degeneration," *Cartilage*, vol. 13, 2020.

[12] X. Wang, N. Chen, Z. Du et al., "Bioinformatics analysis integrating metabolomics of m6A RNA microarray in intervertebral disc degeneration," *Epigenomics*, vol. 12, no. 16, pp. 1419–1441, 2020.

[13] J. Zhu, X. Zhang, W. Gao, H. Hu, X. Wang, and D. Hao, "lncRNA/circRNA-miRNA-mRNA ceRNA network in lumbar intervertebral disc degeneration," *Molecular Medicine Reports*, vol. 20, pp. 3160–3174, 2019.

[14] J. Piñero, J. M. Ramírez-Anguita, J. Saüch-Pitarch et al., "The DisGeNET knowledge platform for disease genomics: 2019 update," *Nucleic Acids Research*, vol. 48, pp. D845–D855, 2020.

[15] M. H. Hwang, K. S. Kim, C. M. Yoo et al., "Photobiomodulation on human annulus fibrosus cells during the intervertebral disk degeneration: extracellular matrix-modifying enzymes," *Lasers in Medical Science*, vol. 31, no. 4, pp. 767–777, 2016.

[16] D. Szklarczyk, A. L. Gable, D. Lyon et al., "STRING v11: protein-protein association networks with increased coverage, supporting functional discovery in genome-wide experimental datasets," *Nucleic Acids Research*, vol. 47, no. D1, pp. D607–D613, 2019.

[17] C.-C. Niu, L.-J. Yuan, L.-H. Chen et al., "Beneficial effects of hyperbaric oxygen on human degenerated intervertebral disk cells via suppression of IL-1β and p38 MAPK signal," *Journal of Orthopaedic Research*, vol. 29, no. 1, pp. 14–19, 2011.

[18] Y. Peng, M. Yuan, J. Xin, X. Liu, and J. Wang, "Screening novel drug candidates for Alzheimer's disease by an integrated network and transcriptome analysis," *Bioinformatics*, vol. 36, no. 17, pp. 4626–4632, 2020.

[19] A. N. Khan, H. E. Jacobsen, J. Khan et al., "Inflammatory biomarkers of low back pain and disc degeneration: a review," *Annals of the New York Academy of Sciences*, vol. 1410, no. 1, pp. 68–84, 2017.

[20] J. Dowdell, M. Erwin, T. Choma, A. Vaccaro, J. Iatridis, and S. K. Cho, "Intervertebral disk degeneration and repair," *Neurosurgery*, vol. 80, no. 3S, pp. S46–s54, 2017.

[21] D. Wu, Y. Li, K. S. Zhu, H. Wang, and W.-G. Zhu, "Advances in cellular characterization of the sirtuin isoform, SIRT7," *Frontiers in Endocrinology*, vol. 9, p. 652, 2018.

[22] T. Finkel, C.-X. Deng, and R. Mostoslavsky, "Recent progress in the biology and physiology of sirtuins," *Nature*, vol. 460, no. 7255, pp. 587–591, 2009.

[23] W. Korogi, T. Yoshizawa, M. F. Karim et al., "SIRT7 is an important regulator of cartilage homeostasis and osteoarthritis development," *Biochemical and Biophysical Research Communications*, vol. 496, no. 3, 2018.

[24] S. Y. Wu, Y. C. Du, and C. F. Yue, "Sirt7 protects chondrocytes degeneration in osteoarthritis via autophagy activation," *European Review for Medical and Pharmacological Sciences*, vol. 24, pp. 9246–9255, 2020.

[25] J. Hu, Y. Huang, Y. Wu et al., "NTRK2 is an oncogene and associated with microRNA-22 regulation in human gastric cancer cell lines," *Tumor Biology*, vol. 37, no. 11, pp. 15115–15123, 2016.

[26] C. Deutschmann, D. Roggenbuck, and P. Schierack, "The loss of tolerance to CHI3L1 - a putative role in inflammatory bowel disease?" *Clinical Immunology*, vol. 199, pp. 12–17, 2019.

[27] K. Huang and L. Wu, "YKL-40: a potential biomarker for osteoarthritis," *Journal of International Medical Research*, vol. 37, no. 1, pp. 18–24, 2009.

[28] D. H. Lee, K. C. Kim, C. J. Hwang et al., "Decreased lung tumor development in SwAPP mice through the down-regulation of CHI3L1 and STAT 3 activity via the upregulation of miRNA342-3p," *Molecular Therapy-Nucleic Acids*, vol. 16, pp. 63–72, 2019.

[29] D. Sigal, M. Tartar, M. Xavier et al., "Activity of entrectinib in a patient with the first reported NTRK fusion in neuroendocrine cancer," *Journal of the National Comprehensive Cancer Network*, vol. 15, no. 11, pp. 1317–1322, 2017.

[30] T. W. Laetsch, S. G. DuBois, L. Mascarenhas et al., "Larotrectinib for paediatric solid tumours harbouring NTRK gene fusions: phase 1 results from a multicentre, open-label, phase 1/2 study," *The Lancet Oncology*, vol. 19, no. 5, pp. 705–714, 2019.

[31] L. J. Scott, "Larotrectinib: first global approval," *Drugs*, vol. 79, no. 2, pp. 201–206, 2019.

[32] D. S. Hong, S. G. DuBois, S. Kummar et al., "Larotrectinib in patients with TRK fusion-positive solid tumours: a pooled analysis of three phase 1/2 clinical trials," *The Lancet Oncology*, vol. 21, no. 4, pp. 531–540, 2020.

[33] Z.-Y. Wan, F. Song, Z. Sun et al., "Aberrantly expressed long noncoding RNAs in human intervertebral disc degeneration: a microarray related study," *Arthritis Research and Therapy*, vol. 16, no. 5, p. 465, 2014.

[34] Y. Wang, G. Dai, L. Li et al., "Transcriptome signatures reveal candidate key genes in the whole blood of patients with lumbar disc prolapse," *Experimental and Therapeutic Medicine*, vol. 18, pp. 4591–4602, 2019.

[35] H. Jiang and W. H. Wong, "SeqMap: mapping massive amount of oligonucleotides to the genome," *Bioinformatics*, vol. 24, no. 20, pp. 2395-2396, 2008.

[36] J. T. Leek, W. E. Johnson, H. S. Parker, A. E. Jaffe, and J. D. Storey, "The sva package for removing batch effects and other unwanted variation in high-throughput experiments," *Bioinformatics*, vol. 28, no. 6, pp. 882-883, 2012.

[37] P. Langfelder and S. Horvath, "WGCNA: an R package for weighted correlation network analysis," *BMC Bioinformatics*, vol. 9, no. 1, p. 559, 2008.

[38] G. Yu, L.-G. Wang, Y. Han, and Q.-Y. He, "clusterProfiler: an R package for comparing biological themes among gene

clusters," *OMICS: A Journal of Integrative Biology*, vol. 16, no. 5, pp. 284–287, 2012.

[39] M. E. Smoot, K. Ono, J. Ruscheinski, P.-L. Wang, and T. Ideker, "Cytoscape 2.8: new features for data integration and network visualization," *Bioinformatics*, vol. 27, no. 3, pp. 431-432, 2011.

[40] A. Subramanian, H. Kuehn, J. Gould, P. Tamayo, and J. P. Mesirov, "GSEA-P: a desktop application for gene set enrichment analysis," *Bioinformatics*, vol. 23, no. 23, pp. 3251–3253, 2007.

[41] D. S. Wishart, Y. D. Feunang, A. C. Guo et al., "DrugBank 5.0: a major update to the DrugBank database for 2018," *Nucleic Acids Research*, vol. 46, no. D1, pp. D1074–D1082, 2018.

[42] H. Sanz, C. Valim, E. Vegas, J. M. Oller, and F. Reverter, "SVM-RFE: selection and visualization of the most relevant features through non-linear kernels," *BMC Bioinformatics*, vol. 19, no. 1, p. 432, 2018.

Hindawi
Journal of Oncology
Volume 2022, Article ID 7945077, 17 pages
https://doi.org/10.1155/2022/7945077

Research Article

System Analysis of Adaptor-Related Protein Complex 1 Subunit Mu 2 (AP1M2) on Malignant Tumors: A Pan-Cancer Analysis

Yuanxue Yi,[1,2] Qiufang Zhang,[3] Youfeng Shen,[1] Yueyi Gao,[1,4] Xiaohong Fan,[1] Sini Chen,[1] Xin Ye,[2] and Jian Xu [1,4]

[1]*Chongqing Precision Medical Industry Technology Research Institute, Chongqing 400000, China*
[2]*Chongqing D.A. Medical Laboratory, Chongqing 400000, China*
[3]*Hangzhou D.A. Medical Laboratory, Hangzhou 310030, China*
[4]*College of Laboratory Medicine, Chongqing Medical University, Chongqing 400000, China*

Correspondence should be addressed to Jian Xu; jianxuuu@outlook.com

Received 16 November 2021; Revised 24 December 2021; Accepted 28 December 2021; Published 10 February 2022

Academic Editor: Fu Wang

Objective. To identify new tumor marker genes available for early tumor screening, differentially expressed gene profiles of multiple tumors were compared using Genotype-Tissue Expression (GTEx), Cancer Cell Line Encyclopedia (CCLE), and The Cancer Genome Atlas (TCGA) databases. As AP1M2 was highly and differentially expressed in invasive breast carcinoma, the purpose of this study was to explore the association of AP1M2 gene with the survival, immune invasion, and tumor neoantigens of patients on a pan-cancer basis. *Methods*. The expression and distribution of AP1M2 gene in tumor tissues and the corresponding normal control tissues were analyzed using the pan-cancer databases GTEx, CCLE, and TCGA. Kaplan-Meyer survival plots and proportional hazards model (COX) were employed to evaluate actions of AP1M2 on the clinical prognosis of tumor patients. Subsequently, the association of AP1M2 expression with immune invasion in different tumor types was explored. Simultaneously, the investigation of the interrelationship of AP1M2 and tumor neoantigens of the immune system, unstable microsatellite, DNA repair genes, and DNA methyltransferases were explored, and the mutation frequency of AP1M2 gene in diverse tumors was studied. Several tumor types were analyzed using gene-set enrichment analysis (GSEA). *Results*. AP1M2 was abundantly expressed in a wide range of cancers, and its expression level was positively correlated with the outcome of tumor victims. Through a study on AP1M2 action on clinical prognosis and immune infiltration in tumor patients, AP1M2 expression in breast-infiltrating carcinoma was found to be highly associated with patients' overall survival and infiltration levels of macrophages, dendritic cells, T cells (CD4+ and CD8+), and B cells. Also, AP1M2 expression was positively correlated with tumor immune neoantigens and microsatellite instability in breast invasive carcinoma. The effect of AP1M2 on tumors was analyzed by GSEA, and findings demonstrated that AP1M2 expression levels in most tumors influenced the activation of tumor-associated pathways and immune-associated pathways. *Conclusions*. These findings suggest that AP1M2 expression levels are significantly correlated to patients' outcomes and levels of immune infiltration in most cancer types, including T cells (CD8+ and CD4+), macrophages, neutrophils, and dendritic cells (DCs), particularly in breast cancer. The results indicate that AP1M2 may influence the tumor environment of invasive breast cancer patients and it may be a target contributing to early screening and treatment for breast cancer, helping improve the efficiency of early screening and overall survival rate in invasive breast cancer patients.

1. Introduction

AP1M2 belongs to the adhesive protein-associated adaptor protein complex 1 that functions in the anti-Golgi network (TGN) and protein sorting in the endothelium. The adaptor-related protein complex has been characterized by mediating the recruitment of adhesive proteins to membranes and the recognition of sorting signals within the cytoplasmic tail of transmembrane cargo molecules. AP1M2 is phylogenetically conserved and expressed in all cell types detected, from yeast to mammals. Meanwhile, it is homologous in a variety of eukaryotes [1].

As little research has been made on the correlation between AP1M2 expression levels and tumorigenesis development, this study initiated a pan-cancer analysis of AP1M2 using databases TCGA, GTEx, and CCLE. Several influencing factors such as gene expression, survival status, genetic alterations, immune infiltration, and associated cellular pathways were analyzed. Meanwhile, the role of AP1M2, possible molecular mechanisms of AP1M2 in different tumor pathogeneses, and clinical outcomes were simultaneously investigated. We found that AP1M2 expression could affect survival prognosis, immune infiltration, and tumor load, as well as methylation in tumors, especially BRCA.

This research currently revealed that AP1M2 expression level in BRCA was positively associated with genetic differences, immune system, DNA methyltransferase, tumor mutational load, and microsatellite instability. This gene has the potential to be a promising target for early screening and even BRCA treatment, which can benefit patients with efficient early screening of invasive breast cancer with improved overall survival.

2. Materials and Methods

2.1. Transcriptional Data Acquisition. First, we detected expression levels of genes in 31 tissues using the GTEx dataset (https://commonfund.nih.gov/GTEx/), and further, we analyzed the gene expression levels in 31 tissues from the CCLE database (https://portals.broad.institute.org/ccle/), which was downloaded for each tumor cell line and the expression levels of 21 tissues were determined following tissue origin. mRNA data in 31 tumor samples were then obtained from the TCGA database (https://www.cancer.gov/about-nci/organization/ccg/research/structural-genomics/tcga) [2]. Data were ultimately obtained, and differences were compared by Kruskal–Wallis tests.

2.2. Differential Gene Expression Analysis. Subsequently, differences of AP1M2 gene expression in the tumor samples and the corresponding normal control tissues were to be determined. We downloaded TCGA Pan-Cancer and GTEx datasets from the UCSC Xena database (https://xena.ucsc.edu/). We obtained the expression difference of AP1M2 from the TCGA database of both tumor tissues and corresponding normal control tissues in 20 tumor samples. Considering limited normal tissue samples in TCGA, we synthesized normal tissue data from GTEx database and TCGA tumor tissues to determine expression differences of 27 tumors. The significance of the difference at threshold $P < 0.05$ was calculated using RStudio version 1.1.456 (RStudio Inc, USA).

2.3. Survival Analysis at a Pan-Cancer Level. This work assessed interrelationship between AP1M2 expression level and 33 tumor prognoses in the TCGA cohort, and univariate COX regression analyses for disease-free interval (DFI), overall survival (OS), progression-free interval (PFI), and disease-specific survival (DSS) were conducted taking into account the possible presence of nontumor mortality factors during follow-up. The threshold of Cox was $P < 0.05$. A summary forest plot was generated utilizing R package forest plot [3]. Tumors with significant correlations in the regression analysis were selected, and the samples were grouped into two at high or low expressions, referring to a median AP1M2 expression level. Hypothesis testing was performed using a log-rank test, and $P < 0.05$ was used as a threshold to calculate significant differences in survival. In addition, a correlation assessment was carried out between AP1M2 expression levels and TNM stages.

2.4. Relationship between AP1M2 Expression Levels and Immunity. The existence of tumor-infiltrating lymphocytes in the tumor microenvironment correlates with the improvement of outcomes and therapeutic results for different types of cancer [4]. Further investigation on whether AP1M2 expression in diverse tumors would interact with immune infiltration. It was, therefore, that we employed CIBERSORT of R package to calculate the relative proportional relationship of immunocytes in multiple tumors [5]. Their levels of immune infiltration were assessed using ESTIMATE of R package, including the immune and stromal scores of 33 tumor cell samples in the tumor microenvironment in the TCGA cohort [6]. The association between AP1M2 and the previously described indicators was analyzed using Spearman correlation analysis.

A total of 47 immune checkpoint genes were collected, and their association of expression with AP1M2 gene expression was analyzed using Spearman correlation analysis. The correlation heatmap was then created employing the R package heatmap.

2.5. Relationship between AP1M2 and Immune Neoantigens, Tumor Mutational Burden (TMB), and Microsatellite Instability (MSI). Tumor neoantigens can be recognized by specific cells and encoded by mutated genes. They are mostly generated by new abnormal proteins, such as point mutation, deletion mutation, and gene fusion, and vary from those in normal cells. These proteins are enzymatically cleaved into peptide fragments and presented via DC cells to T cells as antigens. In this process, T cells can be induced to mature and activate, and characterized by tumor neoantigen-specific, thereby enabling the activated T cells to proliferate [7]. Herein, the number of neoantigens contained in tumor samples was calculated, and the results were analyzed to investigate whether there exists a correlation between AP1M2 expression levels and immune neoantigens using a Spearman correlation method [8].

TMB refers to the total number of detected somatic mutations (nonsynonymous mutations) occurring in an average 1 Mb base in the coding or exon region of malignant cell genome. It is also briefly expressed as entire nonsynonymous mutations. Meanwhile, the types of TMB mutations usually consist of single nucleotide variants (SNVs) and small insertions or deletions (Indel) [9]. In this research, the estimates of TMB in an individual tumor sample were presented separately. Spearman's rank

correlation coefficient was ultimately adopted to analyze the interrelationship of the AP1M2 expression level and TMB.

MSI represents Indel of a repeat unit in malignancies, resulting in somatic alteration in the microsatellite length when compared to normal tissues. Emerging microsatellite alleles represent one phenomenon of heredity or biological inheritance [10]. PreMSIm, an R package, was utilized to predict MSI following gene expression profiles of 33 cancers, and the interrelation analysis of both gene expressions and MSI was analyzed utilizing Spearman rank correlation coefficient [11].

2.6. Mutation Patterns of AP1M2 in TCGA Database. The mutation details of the previously described 33 malignant tumors were downloaded from TCGA. All changes that AP1M2 developed in the tumor specimens were analyzed subsequently. Maftools, an R package, was subsequently utilized to visualize the tumors with the most AP1M2 mutations [12].

2.7. Correlation of AP1M2 Expression Levels with DNA Methyltransferases (DNMT) and Mismatch Repair (MMR) Genes. MMR is a mechanism of mismatch repair occurred intracellularly; the function depletion of key genes leads to irreparable DNA replication mistakes, which in turn results in higher somatic mutations. Therefore, whether AP1M2 could influence five MMR genes (MLH1, MSH2, MSH6, PMS2, and EPCAM mutations) was assessed using TCGA expression profiles.

DNA methylation also represents a mechanism that regulates relevant gene expression free from changing DNA sequences. This action mechanism enables to control of expressions of genes, resulting in chromatin structure alternation, changes in DNA conformation, and DNA stability, as well as interactions of DNA with proteins. DNA methylation is catalyzed by the action of DNA methyltransferases, and methyl groups can be added at $5'$ carbon position of the cytosine ring. Thus, this study elucidated the correlation of expressions between genes and four methyltransferases (DNMT1, DNMT2, DNMT3A, and DNMT3B).

2.8. GSEA Analysis of Patients with Pancytopenia in TCGA. To further clarify whether AP1M2 gene expression influences tumors and in light of gene expression levels, we divided the samples into two experimental groups: a high expression group and a low expression group. KEGG enrichment analysis and signature pathways were performed in both groups using GSEA [13]. The enrichment and signature pathways of KEGG analysis were subsequently analyzed for both of the experimental groups. The c5 curated signatures were collected from the MSigDB database (https://www.gsea-msigdb.org/gsea/msigdb/collections.jsp) [9]. KEGG and HALLMARK terms and conditions were concomitantly defined in both high and low AP1M2 expression groups. FDR <0.05 was utilized to determine the significance of pathway enrichment results.

3. Results

3.1. Gene Expression Analysis Data. We analyzed differences in gene expression between cancer and paracancer in each cancer sample obtained from the TCGA database (Figure 1(c)) in READ ($P < 0.05$), BLCA, COAD ($P < 0.01$), BRCA, CHOL, LIHC, LUAD, LUSC, PRAD, STAD ($P < 0.001$), THCA, and UCEC ($P < 0.001$), while AP1M2 expression levels in GBM, LGG ($P < 0.05$), KICH, KIRC, and KIRP ($P < 0.001$) were elevated compared with those in the normal control group (control tissues). The levels were lower than those of the relevant control normal tissues.

Evaluation of AP1M2 expression differences in LAML, OV, ACC, CESC, TGCT, and UCS was conducted after normal tissues from the GTEx dataset were set as control. Figure 1(d) indicated highly expressed AP1M2 in CESC, OV, TGCT, and UCS ($P < 0.001$) compared with the tissues of the relevant control normal group, whereas AP1M2 was poorly expressed in LAML ($P < 0.001$) compared with those of the relevant control normal group. Unluckily, we failed to discover any significant differences in AP1M2 expression levels between ACC and its control normal.

Furthermore, the Kruskal–Wallis test showed significant differences in AP1M2 expression levels between organs (Figures 1(a) and 1(b)).

3.2. Survival Analysis Data. We investigated the interrelationship of AP1M2 expression levels and the survival prognosis in several types of tumor patients. The association of expression levels with prognostic OS (overall survival time in days) in 33 tumors from TCGA was identified using gene expression profile data, one-way survival analysis, and forest plots in 33 tumors as shown in Figure 2(a). Meanwhile, significant tumors BRCA ($P = 0.015$), SARC ($P = 0.0064$), and SKCM ($P = 0.0067$) were selected for prognostic KM curves. Following the expression levels of AP1M2, cancer cases were categorized into high and low expression groups, between which their correlation between AP1M2 expression and patient prognosis of different cancer types was studied using databases TCGA and GEO. As presented in Figure 2(b), highly expressed AP1M2 linked to poorer prognosis in BRCA ($P = 0.039$, HR = 1, 95% CI = 1) and SKCM ($P = 0.0015$, HR = 1.02, 95% CI = 1.01–1.04).

Meanwhile, considering the presence of nontumor death factor during the follow-up period, the correlation between the gene expression of 33 tumors and the prognostic DSS in TCGA was initially analyzed (Figure 3(a)). The significant tumor SARC ($P = 0.0023$) was selected according to the expression level of AP1M2, and the cancer samples were grouped into high and low expression experimental groups for prognostic KM curves. The results failed to reveal any positive correlated features between AP1M2 expression and DSS in SARC (Figure 3(b)) ($P = 0.063$, HR = 1, 95% CI = 1).

Next, the same procedures were carried out to explore whether there existed correlations between gene expressions and prognostic DFI (Figure 4(a)) and PFI (Figure 5(a)) in 33 tumors of TCGA. There were significant correlation in ACC ($P = 0.048$), CESC ($P = 0.01$), TGCT ($P = 0.013$) and ACC

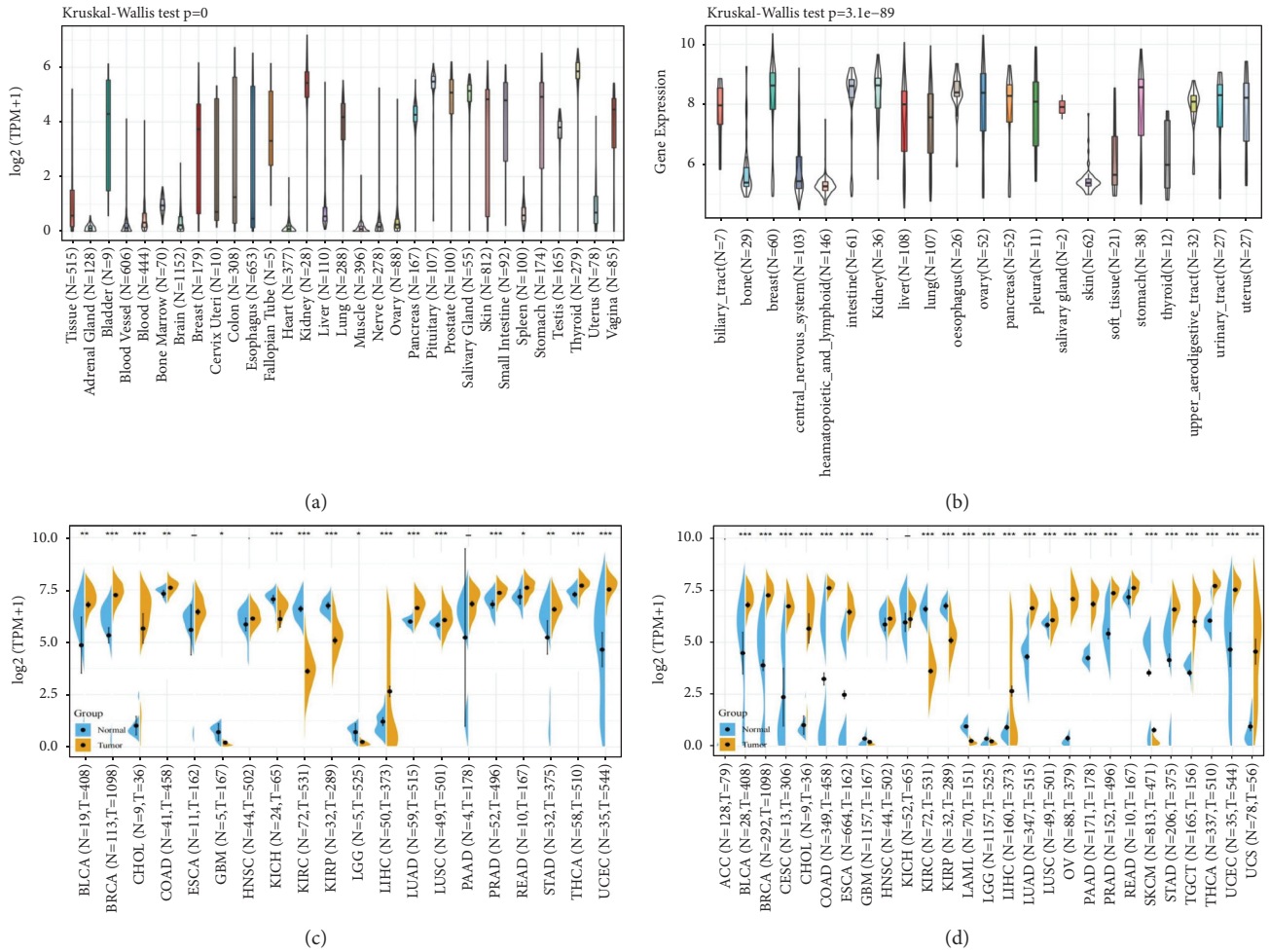

Figure 1: AP1M2 expression level in 31 normal tissues across (a) GTEx dataset and (b) CCLE database. The differences in gene expression between cancer and paracancerous in individual tumor samples obtained from the (c) TCGA database and (d) GTEx datasets.

($P = 0.046$), HNSC ($P = 0.015$), MESO ($P = 0.036$), PCPG ($P = 0.00053$), and SARC ($P = 0.0023$), and two high and low expression groups were divided in light of the AP1M2 levels for prognostic KM curves. As shown in Figure 4(b), the DFI survival analysis revealed that there was an association of higher AP1M2 expression with poorer prognosis in CESC ($P = 0.013$, HR = 1.01, 95% CI = 1–1.01) and TGCT ($P = 0.004$, HR = 0.01, 95% CI = 1–1.01). As shown in Figure 5(b), the same propensity of PFI survival analysis was revealed as that of the previously described conditions that highly expressed AP1M2 corresponded to poorer prognosis in ACC ($P < 0.0001$, HR = 1.88, 95% CI = 1.01–3.51), HNSC ($P = 0.0011$, HR = 1, 95% CI = 1–1.01), and MESO ($P = 0.035$, HR = 1.01, 95% CI = 1–1.02).

3.3. Association of Gene Expression with Immunity Infiltration Levels. Tumor-infiltrating lymphocytes consist of cells invading cancer tissues, and they function as independent biomarkers for the prediction of anterior lymph node status and efficacy of cancer treatment [14]. We investigated whether this gene expression linked to immune invasion in different cancer types and figured out that AP1M2 expression levels were positively correlated with the levels of B-cell infiltration in 14 cancers, CD4+ T cell infiltration in 17 cancers, CD8+ T cells in 16 cancers, macrophages in 19 cancers, neutrophils in 19 cancers, and dendritic cells in 19 cancers. The three most significantly correlated tumors BLCA, BRCA, and COAD were selected (Figure 6). AP1M2 expression levels in BLCA, BRCA, and COAD (all $P < 0.0001$) were all significantly and negatively related to B cells, T cells (CD4+ and CD8+), macrophages, neutrophils, and DC.

Numerous researchers have demonstrated that the tumor immune microenvironment determines the occurrence and development of a wide variety of tumors [15]. Following the visualization of the interrelationships between gene expression and scores of the immune system, stromal, and ESTIMATE in the 33 reported tumors, we selected three tumors with the most significant relationship in each score (Figure 7). AP1M2 levels were more significant in PAAD (RS = −0.556, PS < 0.0001, RI = -0.517, PI < 0.001) and BRCA (RS = −0.341, PS = $2.89e-31$, RI = −0.385, PI = $3.24e-40$). PRAD (RS = −0.46, PS = $2.28e-27$, RI = −0.401, PI = $1.24e-20$) was negatively correlated between the

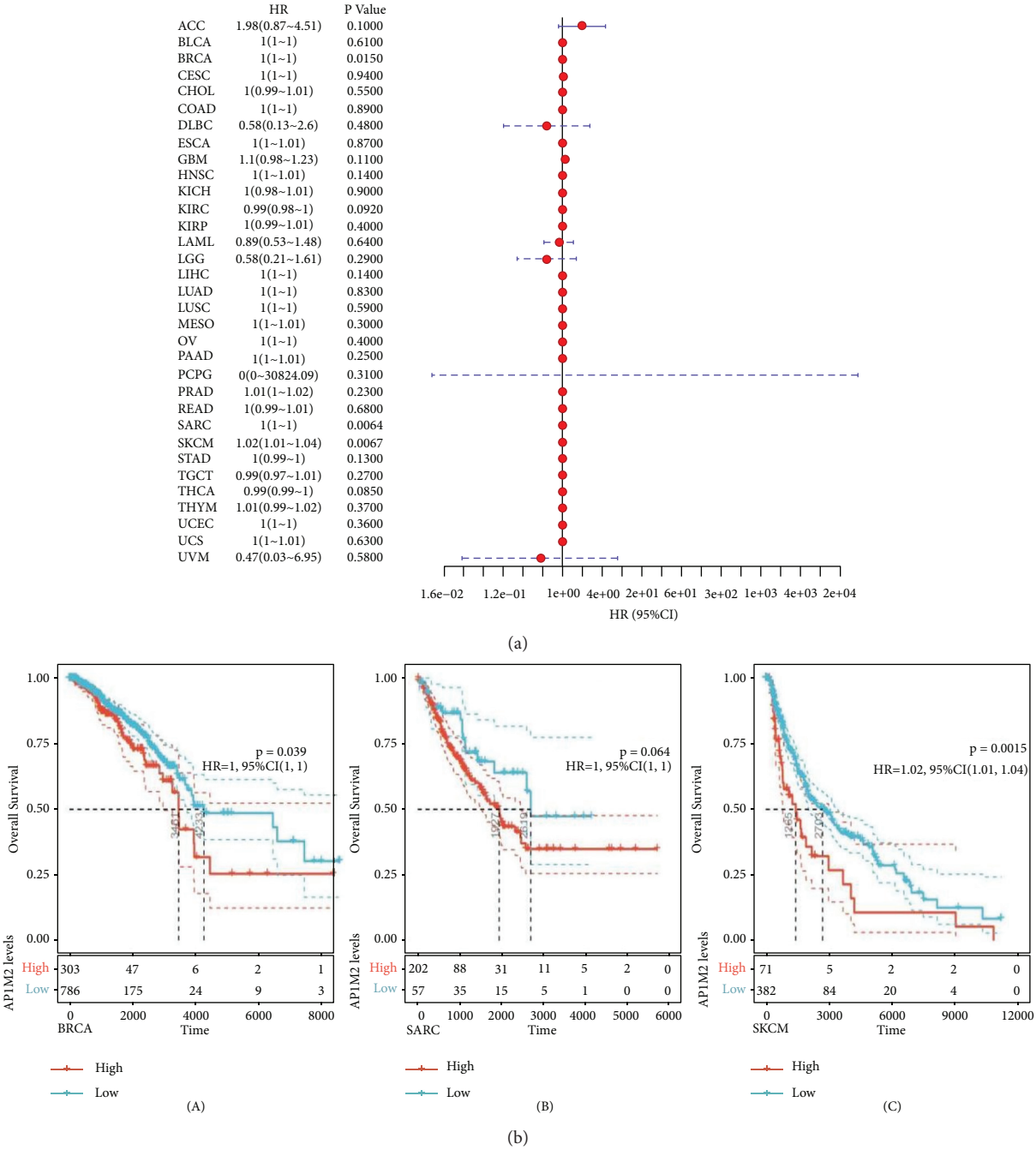

Figure 2: The relationship between expression and OS (overall survival time in days) in 33 tumors of TCGA. (a) The results of univariate COX regression analysis was presented via forest plot. (b) Alog-rank test was used to calculate the significance of survival differences with a threshold of $P < 0.05$, and the results were presented via Kaplan–Meier survival curves comparing survival rates of low and high expressions of AP1M2 in tumors.

expression levels in PRAD ($RS = -0.46$, $PS = 2.28e-27$, $RI = -0.401$, $PI = 1.24e-20$) and the stromal and immune scores. However, as for LUAD ($R = -0.374$, $P < 0.0001$), PAAD ($R = -0.564$, $P < 0.0001$), and BRCA ($R = -0.409$, $P = 1.41e-45$), AP1M2 gene expression level had a negative correlation with composite scores.

Under normal conditions, immune cells can recognize tumor cells and remove them from the tumor microenvironment [16]. Tumor immunotherapy has been recognized in medicine by reactivating and maintaining the tumor immune cycle to suppress and eliminate immune cells as a way to repair the body's normal antitumor immune response. The current widely applied immune checkpoints are inhibitors of monoclonal antibody-based immune checkpoints and small molecules, antibody therapeutics, and cancer treatment vaccines, as well as cytotherapy [17]. As shown in Figure 8, the horizontal coordinate indicates the 33 selected tumors and the vertical coordinate indicates the

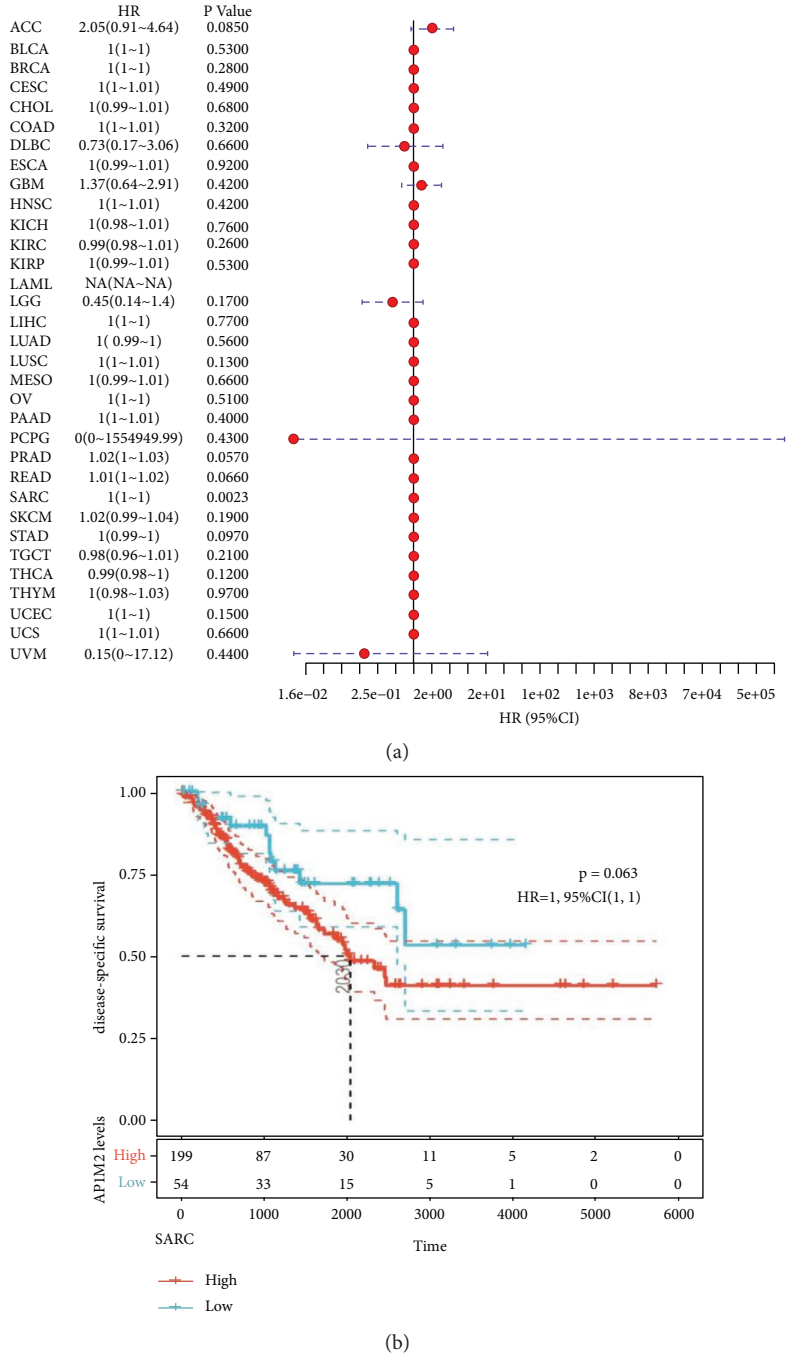

Figure 3: The relationship between expression and DFS (disease-specific survival) in 33 tumors of TCGA. (a) The results of univariate COX regression analysis were presented via forest plot. (b) A log-rank test was used to calculate the significance of survival differences with a threshold of $P < 0.05$, and the results were presented via Kaplan–Meier survival curves comparing the survival rates of low and high expression of AP1M2.

relevant immune checkpoints, where *indicates correlation ($P < 0.05$), **indicates high correlation ($P < 0.01$), and ***indicates significant correlation ($P < 0.001$). Higher AP1M2 expression indicated poorer prognosis of tumor patients by the survival analysis of BRCA, while AP1M2 expression levels were negatively correlated with B cells, T cells (CD4+ and CD8+), macrophages, neutrophils, DC infiltration, and scores of the immune system, stromal, and composites via immune analysis. These results suggested a specific role of AP1M2 in the prognostic analysis and immune infiltration in BRCA. According to Figure 6, the immune checkpoint genes were positively associated with BRCA immunity including BTLA, CD200, NRP1, LAIR1, TNFSF4, CD244, LAG3, ICOS, CD40LG, CTLA4, CD48, CD28, CD200R1, HAVCR2, CD80, LGALS9, CD160, TNFSF14, TMIGD2, PDCD1LG2, HHLA2, TNFSF18,

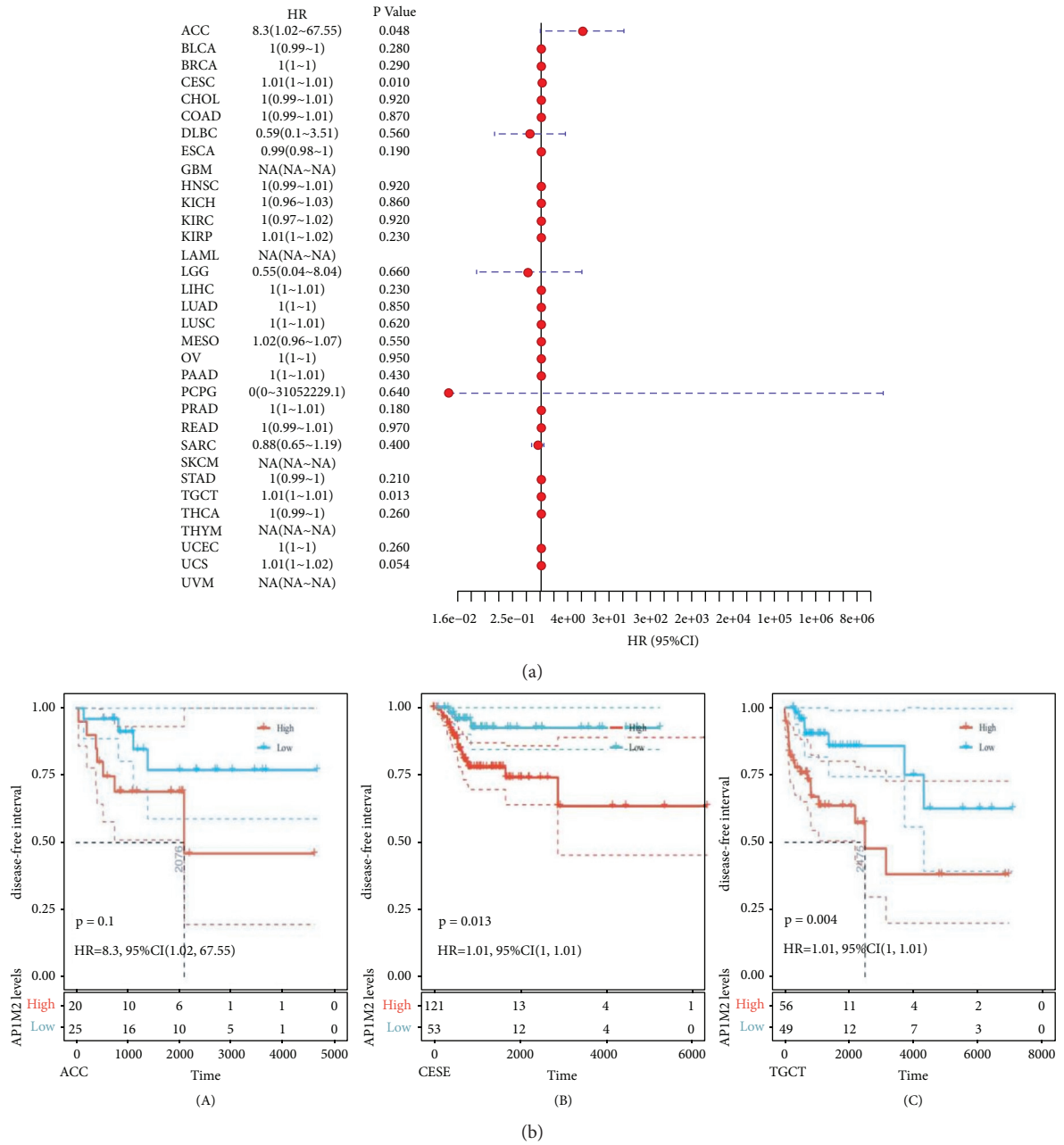

Figure 4: The relationship between expression and DFI (disease-free interval) in 33 tumors of TCGA. (a) The results of univariate COX regression analysis were presented via forest plot. (b) A log-rank test was used to calculate the significance of survival differences with a threshold of $P < 0.05$, and the results were presented via Kaplan–Meier survival curves comparing the survival rates of low and high expression of AP1M2 in tumors.

CD70, TNFSF9, TNFRSF8, CD27, VSIR, TNFRSF4, CD40, TNFRSF18, TIGIT, CD274, CD86, and TNFRSF9.

3.4. Relationship between Gene Expression and Immune Neoantigens, TMB, and MSI. Neoantigen vaccines can be designed and synthesized using strong immunogenicity and heterogeneity of tumor neoantigens according to the tumor cell mutations, which will benefit patients with a satisfactory therapeutic effect after immunization [18]. By counting the neoantigen quantity of every sample tumor, we subsequently studied whether there was any association with AP1M2 expression. As shown in Figure 9, the expression levels of AP1M2 in UCEC ($R = 0.131$, $P < 0.0404$), PRAD ($R = 0.123$, $P < 0.0476$), HNSC ($R = 0.17$, $P < 0.0045$), and STAD ($R = 0.316$, $P = 6.08e - 07$) showed a link to the number of neoantigens.

As TMB predicts favorable responses to immune checkpoint inhibitors, mutated cell count can be calculated from the tumors applying Spearman rank correlation coefficient. Meanwhile, its association with gene expression was also analyzed, as shown in Figure 10(a). The results were

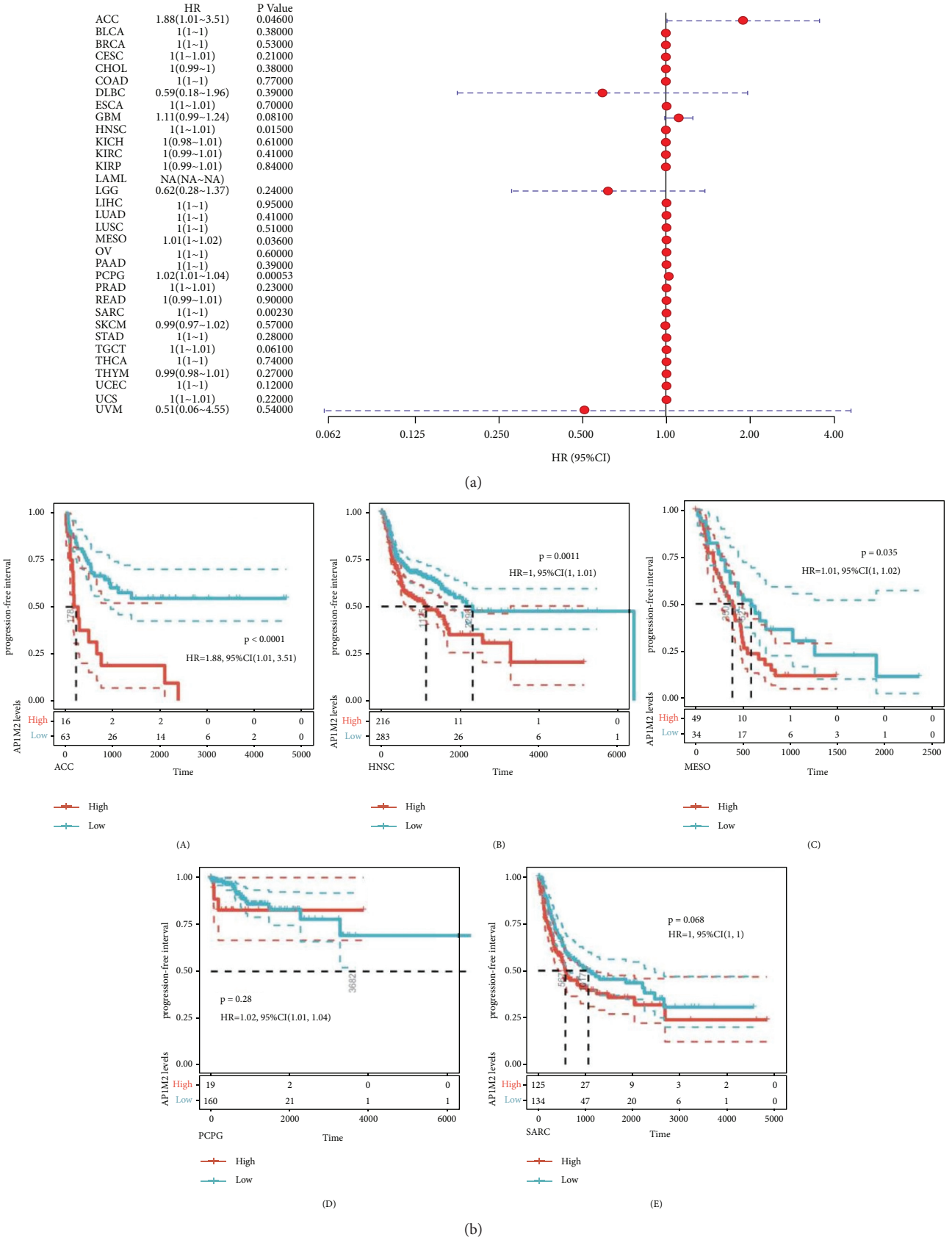

Figure 5: The relationship between expression and PFI (progression-free interval) in 33 tumors of TCGA. (a) The results of univariate COX regression analysis were presented via forest plot. (b) A log-rank test was used to calculate the significance of survival differences with a threshold of $P < 0.05$, and the results were presented via Kaplan–Meier survival curves comparing the survival rates of low and high expression of AP1M2 in tumors.

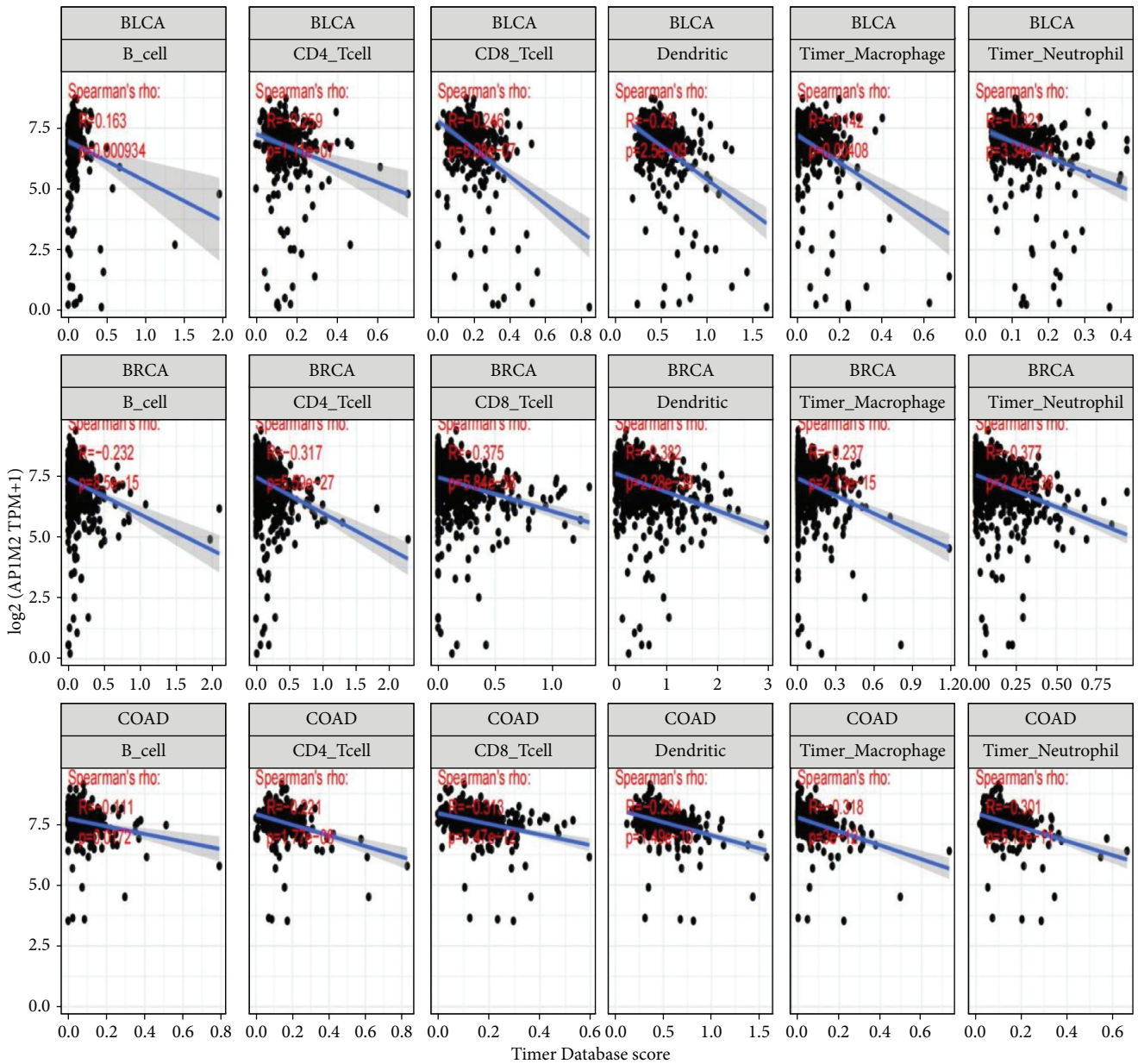

Figure 6: We used the CIBERSORT method in the R package to calculate the relative proportional relationship of immune cells in multiple tumors. The three most significantly correlated tumors BLCA, BRCA, and COAD were selected.

as follows: the AP1M2 gene expression level in BRCA ($P = 9.5e - 05$) was significantly and negatively correlated with TMB, whereas those expression levels revealed in BLCA ($P = 0.015$), ESCA ($P = 1.4e - 06$), HNSC ($P = 3.2e - 05$), LIHC ($P = 0.03$), PAAD ($P = 5.5e - 07$), STAD ($P = 4.8e - 10$), THYM ($P = 0.0017$), and UCEC (0.0022) were positively correlated with TMB. Among them, AP1M2 levels in STAD, PAAD, and ESCA were most significantly related to TMB.

Whether gene expression and MSI had a connection was subsequently verified applying Spearman rank correlation coefficient (Figure 10(b)). The results indicated that the AP1M2 gene expression levels in DLBC ($P = 0.012$), ESCA ($P = 0.0065$), GBM ($P = 0.012$), HNSC ($P = 0.00012$), STAD ($P = 6.7e - 05$), and TGCT ($P = 0.0023$) were positively correlated with MSI, whereas those in the UCS ($P = 0.0034$) and READ ($P = 0.00012$) were negatively correlated with MSI.

3.5. Mutation Patterns of Genes in TCGA Tumor Samples. Mutated AP1M2 was further analyzed following data collection of the 33 tumors through the TCGA database. As shown in Figure 11, mutations of AP1M2 only occurred in BLCA, BRCA, CESC, COAD, GBM, LUAD, LUSC, OV, SARC, SKCM, and UCEC after observation. Among them, the top three tumors with the highest AP1M2 mutation rates were UCEC (3.77%), COAD (1.5%), and SKCM

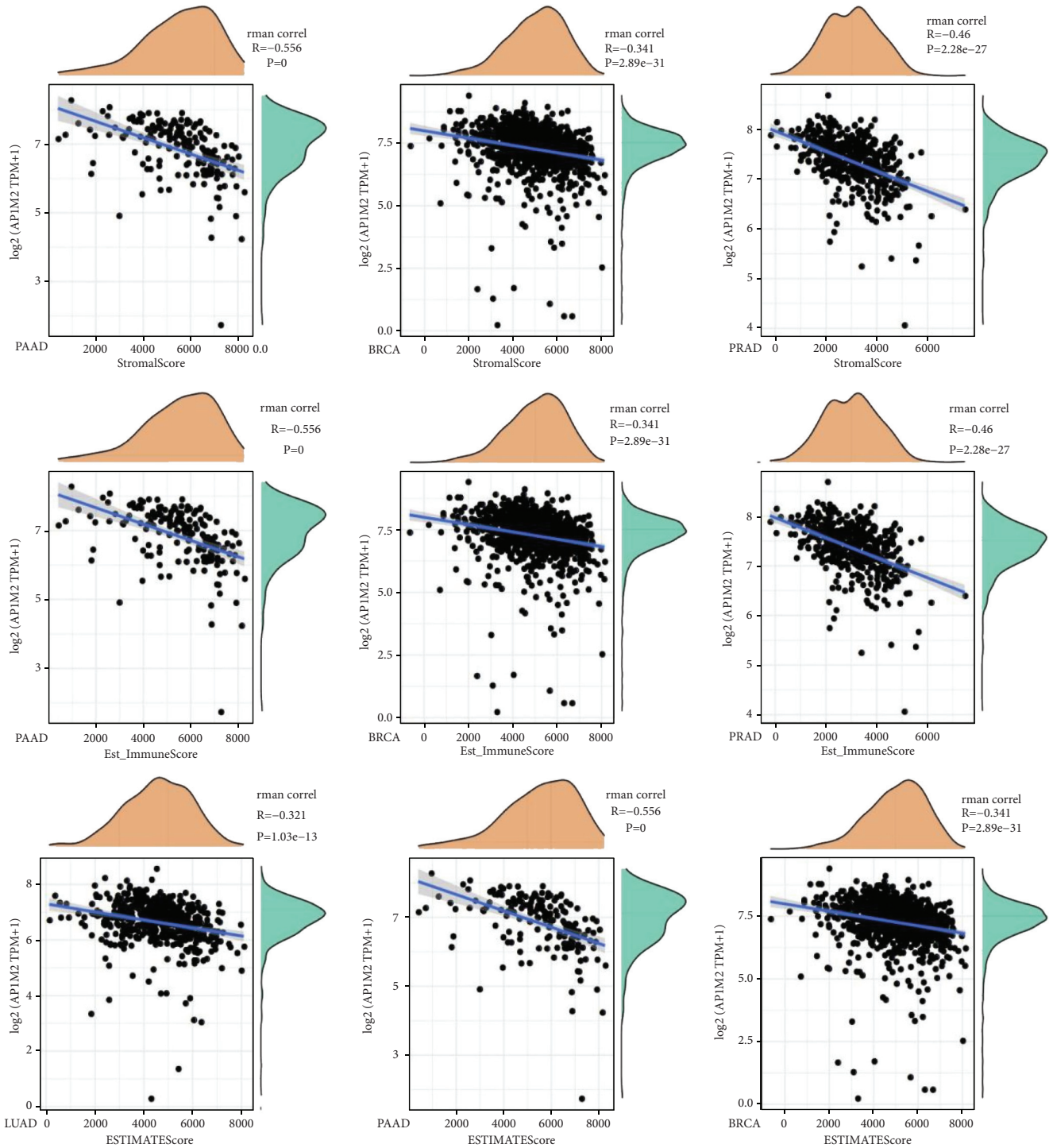

Figure 7: Correlation of AP1M2 expression with the immune score, ESTIMATE score, and stromal score in PAAD, BRCA, PRAD, and LUAD.

(1.07%), indicating that AP1M2 was rarely mutated in most tumors.

3.6. Gene Expression TCGA Tumor Samples concerning DNA MMR and Methyltransferases. In light of the TCGA expression profile data, we subsequently assessed the interrelationship between mutations of the five MMR genes MLH1, MSH2, MSH6, PMS2, and EPCAM and gene expressions (Figure 12(a)). The results revealed that AP1M2 expression levels were significantly correlated with the five MMR genes in CESC, HNSC, LUAD, PRAD, SKCM, and THCA.

We simultaneously analyzed the visualization of expression correlation between AP1M2 and the previously described four methyltransferases (DNMT1: red, DNMT2:

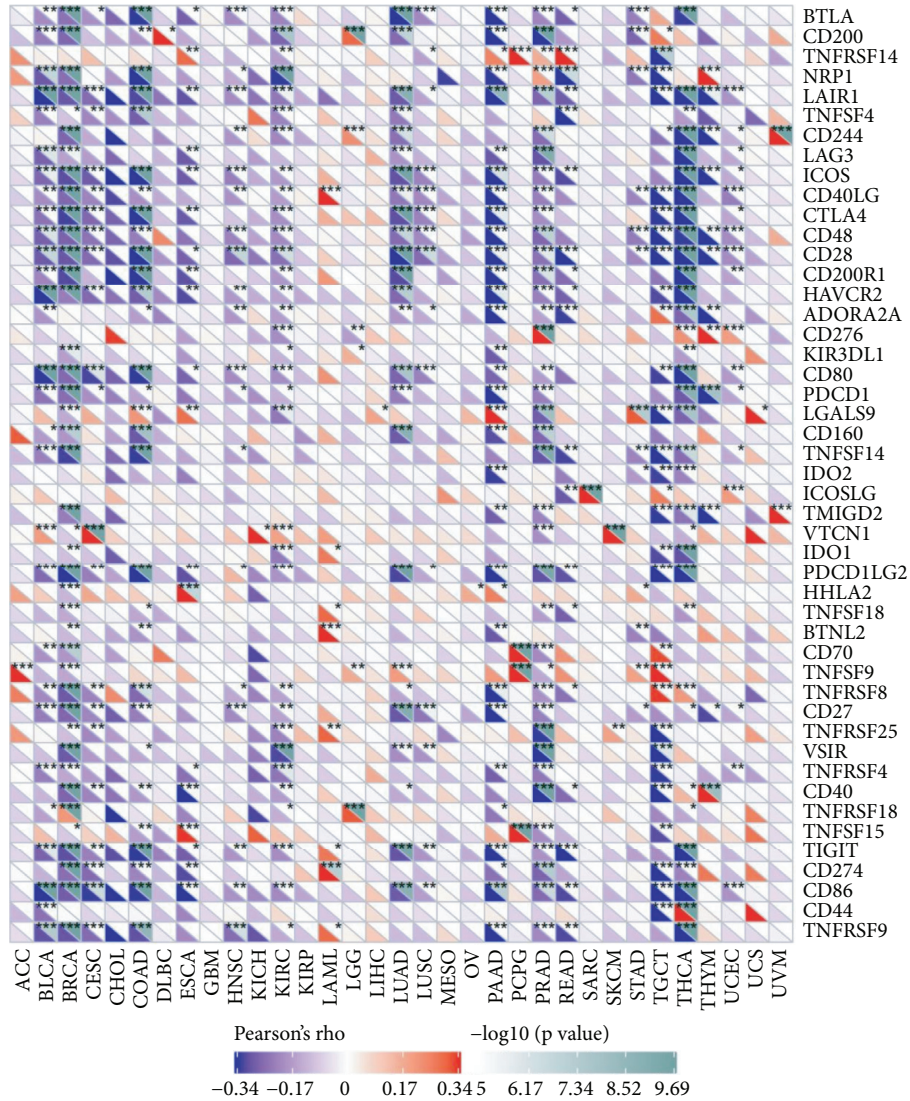

Figure 8: The relationship between AP1M2 and the expression of immune checkpoint genes is presented via heatmap. The horizontal coordinate indicates the 33 selected tumors, and the vertical coordinate indicates the relevant immune checkpoints, where *indicates correlation ($P < 0.05$), **indicates high correlation ($P < 0.01$), and ***indicates significant correlation ($P < 0.001$).

blue, DNMT3A: green, and DNMT3B: purple) (Figure 12(b)). The results indicated that expression levels of UCEC, BRCA, CESC, COAD, KIRC, LGG, LUAD, PRAD, TGCT, THCA, and PCPG, AP1M2 were substantially correlated with the four genes, with AP1M2 expression levels in TGCT ($R = 0.38$, $P = 3.3e-06$) being the most significantly correlated.

3.7. GSEA Analysis. We employed two groups of tumor specimens to verify actions of gene expression on tumors: a high and a low expression groups in accordance with gene expression. GSEA was employed for KEGG enrichment and HALLMARK pathway analysis in both expression groups. Subsequently, three pathways were selected, which presented the most significant GSEA results (Figure 13). KEGG pathway analysis in Figure 13 exhibited that high expression of AP1M2 mainly activated PEROXISOME (ES = −0.58, NES = −2, $P = 0.0019$, FDR = 0.072), ARGININE_AND_PROLINE_METABOLISM (ES = −0.56, NES = −2, $P < 0.001$, FDR = 0.039), and PYRIMIDINE_METABOLISM (ES = −0.58, NES = −2, $P < 0.001$, FDR = 0.036), while poorly expressed AP1M2 mainly activated AUTOIMMUNE_THYROID_DISEASE (ES = 0.68, NES = 1.9, $P = 0.0098$, FDR = 0.031), HEMATOPOIETIC_CELL_LINEAGE (ES = 0.61, NES = 1.9, $P = 0.0097$, FDR = 0.029), INTESTINAL_IMMUNE_NETWORK_FOR_IGA_PRODUCTION (ES = 0.74, NES = 2, $P = 0.0019$, FDR = 0.03), and CYTOKINE_CYTOKINE_RECEPTOR_INTERACTION (ES = 0.54, NES = 2, $P = 0.004$, FDR = 0.026). In the HALLMARK pathway, the highly expressed AP1M2 mainly activated PEROXISOME (ES = −0.57, NES = −2.2, $P = 0$, FDR = $9e-04$), CHOLESTEROL_HOMEOSTASIS

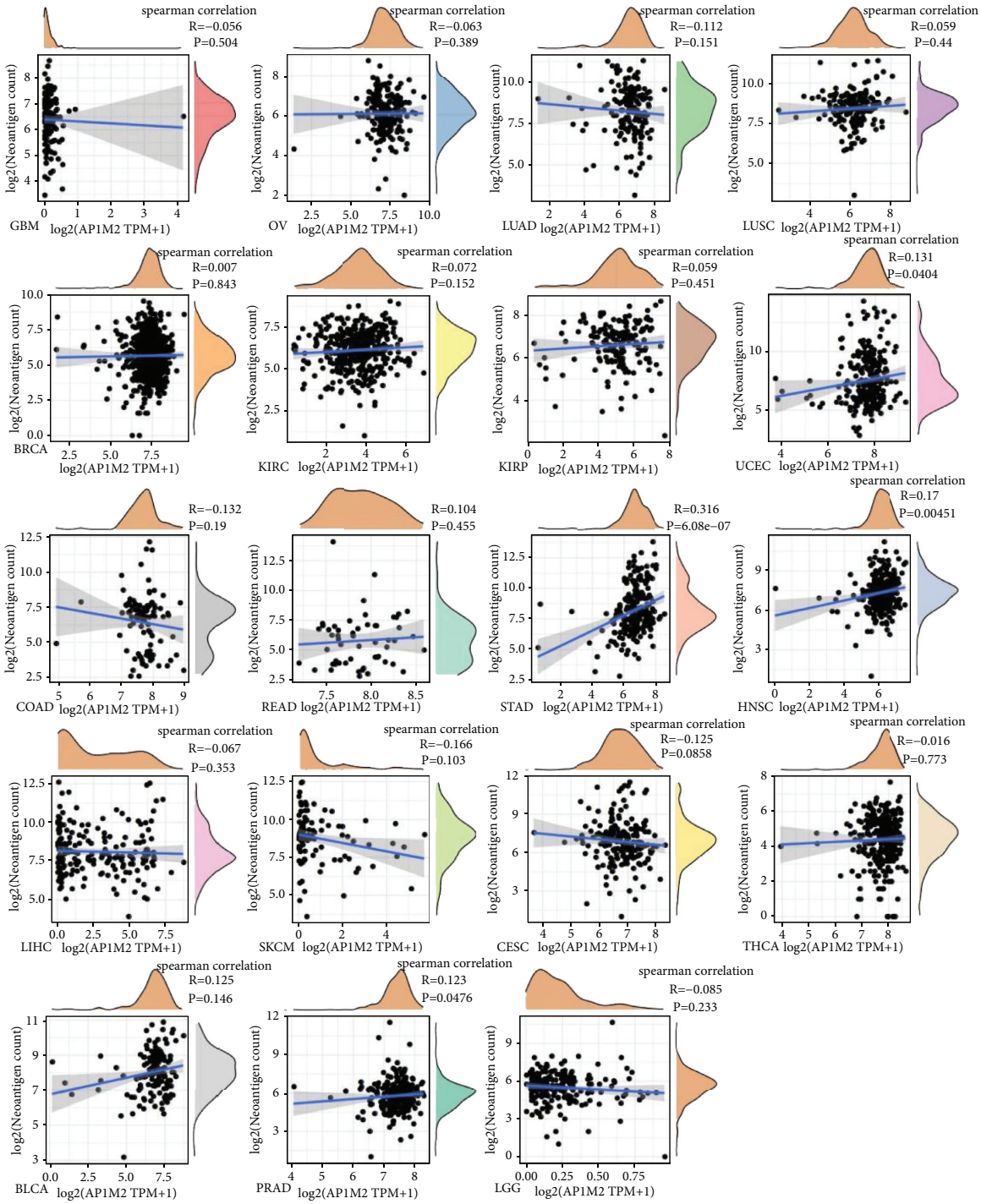

Figure 9: Correlation of AP1M2 expression with neoantigens.

(ES = −0.57, NES = −2, P = 0.002, FDR = 0.013), and FATTY_ACID_METABOLISM (ES = −0.54, NES = −2, P = 0.0021, FDR = 0.011), whereas poorly expressed AP1M2 mainly activated IL6_JAK_STAT3_SIGNALING (ES = 0.49, NES = 1.6, P = 0.069, FDR = 0.12), KRAS_SIGNALING_UP (ES = 0.43, NES = 1.7, P = 0.02, FDR = 0.066), INFLAMMATORY_RESPONS (ES = 0.5, NES = 1.8, P = 0.027, FDR = 0.059), and ALLOGRAFT_REJECTION (ES = 0.62, NES = 2, P = 0.015, FDR = 0.028).

4. Discussion

Being one of the most densely populated countries, China has achieved remarkable progress in the improvement of people's health over the last several decades. As the population ages, China's burden of cancer expenses keeps growing [19]. Meanwhile, since the outbreak of the novel coronavirus pandemic in 2019, several studies have demonstrated that individuals under a high risk of COVID-19

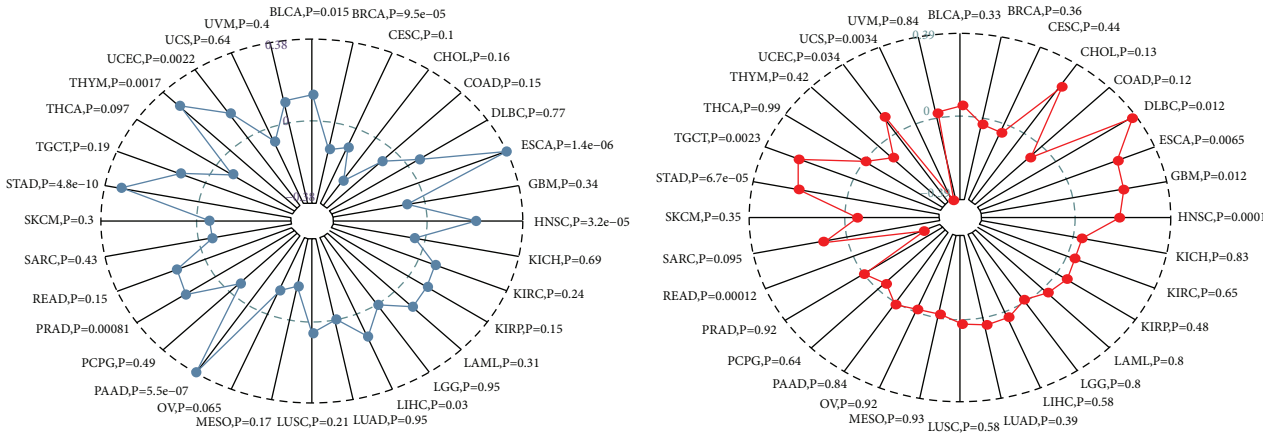

Figure 10: Correlation between AP1M2 and TMB (a) and microsatellite instability (b).

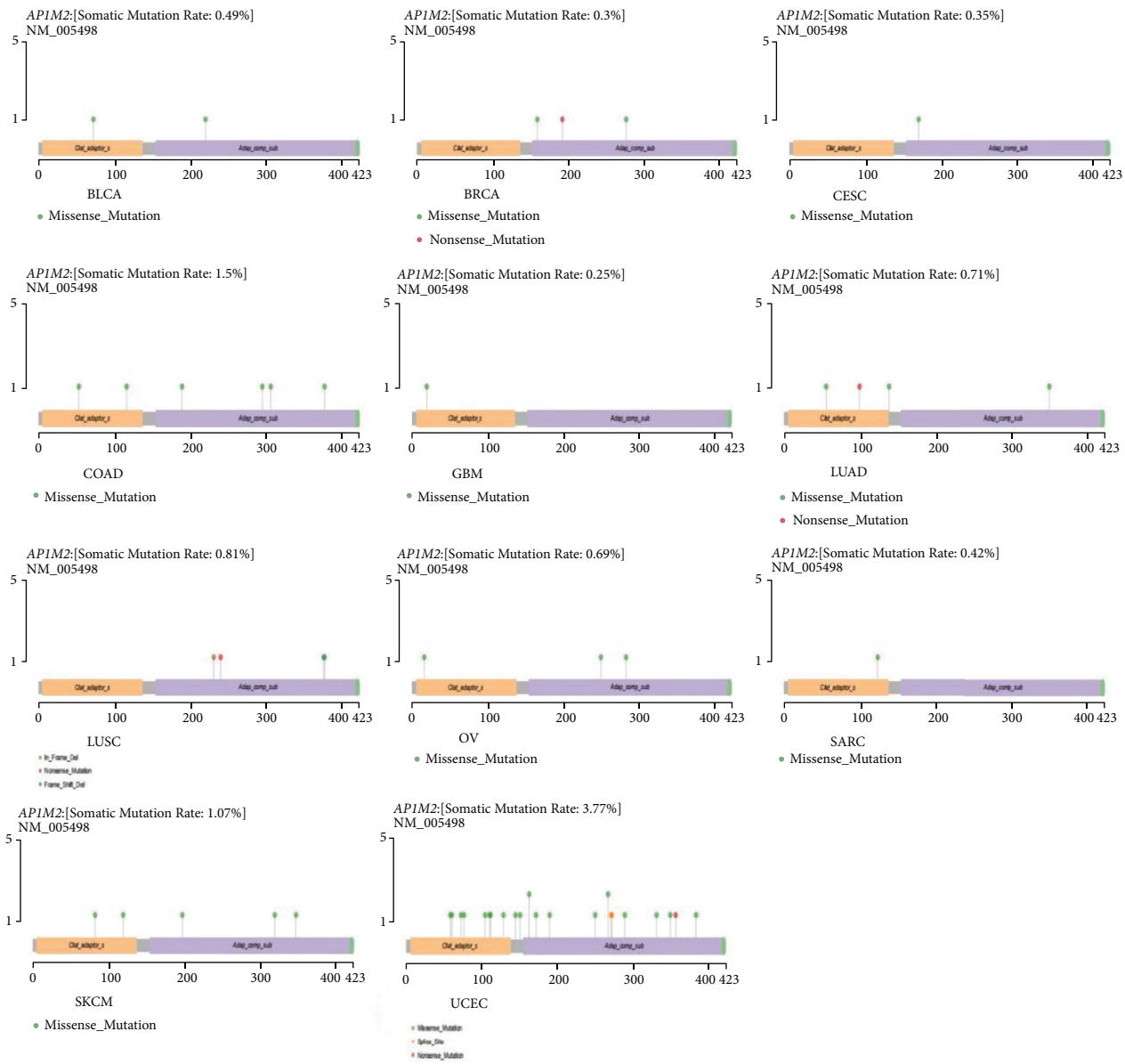

Figure 11: AP1M2 gene mutation patterns in several tumors.

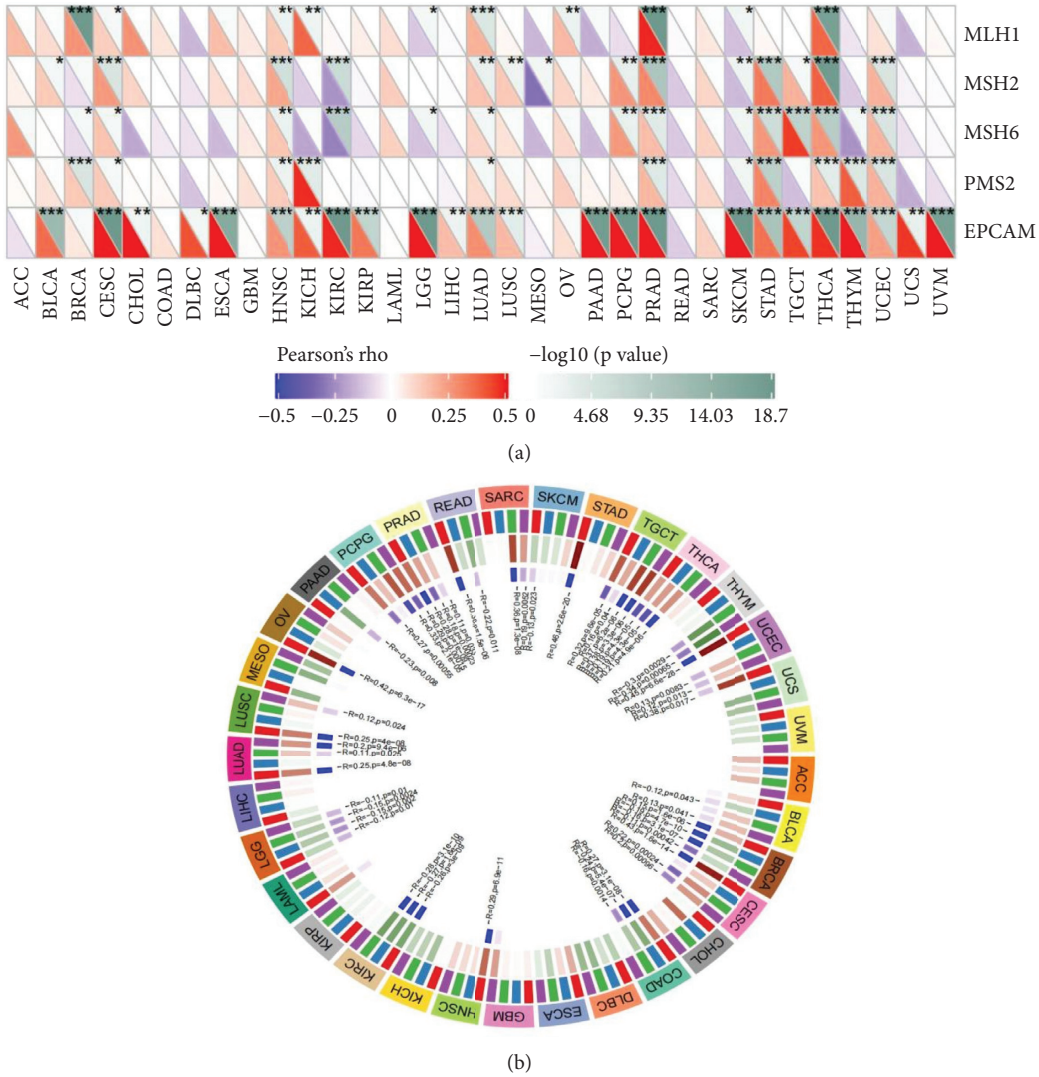

Figure 12: The relationship between AP1M2 expression level and (a) mismatch repair genes and (b) DNA methyltransferase. $^{*}P < 0.05$, $^{*}P < 0.01$; $^{***}P < 0.001$.

include cancer patients who are immunosuppressed throughout the body [20].

Through literature retrieval, little literature on AP1M2 pan-cancer analysis of the overall tumor has been found. Therefore, based on data from TCGA, CCLE, UCSC Xena, and GTEx databases, as well as gene expression, gene variants, methylation, immune infiltration, and enrichment analysis, a comprehensive exploration was conducted on AP1M2 gene from the 33 different tumor types in the TCGA cohort. The findings indicated that the AP1M2 expression level exhibited a positive link to the prognosis and immune aspects of several different tumors, especially breast-infiltrating carcinomas. Hence, AP1M2 may be applied as a screening indicator and therapeutic target for multiple tumors in the future.

AP1M2 expression differences were revealed simultaneously among various cancers and normal control, which indicated that AP1M2 was highly expressed and significant in breast cancer, liver cancer, lung cancer, bile duct cancer, prostate cancer, gastric cancer, thyroid cancer, and common genital tumors compared to normal tissues. Conversely, some datasets also showed that AP1M2 was poorly expressed in kidney cancer and acute myeloid leukemia compared to normal tissues in the control group. AP1M2, also known as Mu-2, has been shown that Mu-2-related death-inducing gene (MuD) is a 490-amino-acid protein belonging to the medium subunit family of adaptin protein (AP), which can independently induce cancer cell death in association with adhesive protein-mediated endocytosis found in the Mu-2 subunit of the articulation protein [21]. Therefore, AP1M2 may also possess the function of inducing cancer cell death. However, such speculation is inconsistent with gene expression analysis and survival analysis, and more investigations remain indispensable to reveal actions and mechanisms of AP1M2 among a range of cancer types.

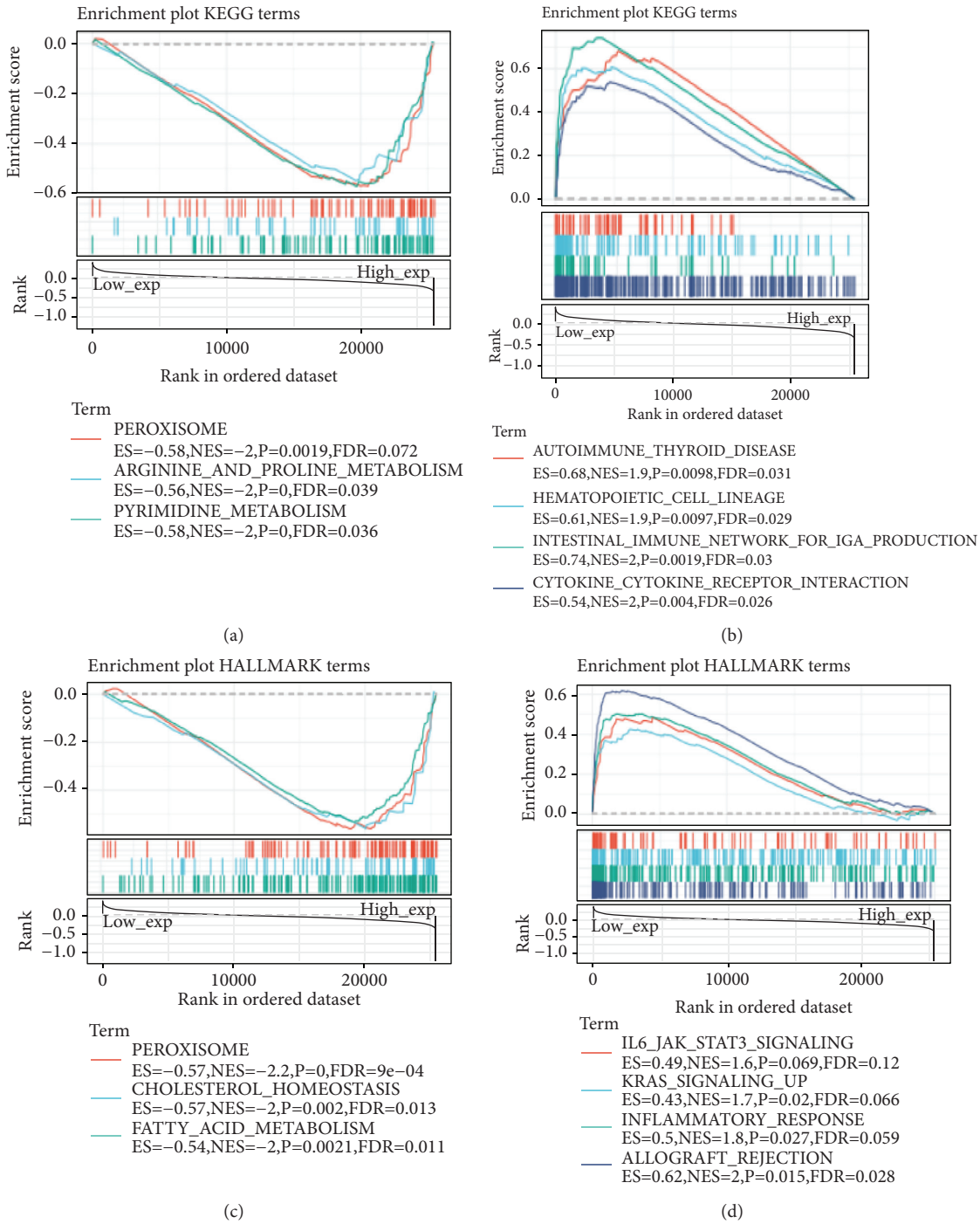

Figure 13: The result of GSEA.

Following the analysis of AP1M2 expression levels and immunity, we found that AP1M2 expression in BRCA was negatively associated not only with B cells, CD4+ T cells, CD8+ T cells, macrophages, neutrophils, and DC (Figure 4), but also with scores of the immune system, stromal, and composite in ESTIMATE analysis (Figure 5). The occurrence and progress of a tumor are complicated, and the processes in which cancer cells interact with microenvironment and immune system influence tumorigenesis and progression [22]. Furthermore, immunocytes have a pivotal secondary role in maintaining tissue integrity and normal functions by eliminating pathogens in different states of homeostasis, infection, and noninfectious disturbances of the body and have an impact on the clinical outcome of tumors [23]. In addition, it has been shown that immune scores in RBCA at either a high or moderate level can lead to improved disease-free survival or OS [24]. Hence, the

association of increased AP1M2 expression levels with poor prognosis in BRCA patients may be related to the fact that AP1M2 expression suppresses immunocyte infiltration into tumor microenvironment and decreased immune score.

In BRCA, the AP1M2 expression level was significantly and negatively related to most immune checkpoints except TNFRSF18 (Figure 6). Immune checkpoints represent multiple inhibitions and stimulation pathways for immunocytes to maintain their immunologic tolerance and adjust corresponding immune responses to dangerous physical signals [25]. Immune checkpoint blockade can either retard or suppress evasion of tumor cells and slow down tumor growth. Through inquiring literature, we found that high expression levels of CTLA-4 and TIGIT were associated with a good prognosis of BRCA [26]. Figure 6 presented that AP1M2 levels were correlated with both CTLA-4 and TIGIT.

Several investigations have revealed that TMB is critical for cancer development and progression, and cancer patients with high TMB levels responded more strongly to immunotherapy than low TMB level patients, which is also associated with cancer prognosis [27–29]. However, through the analysis of AP1M2 expression levels and TMB (Figure 7), AP1M2 expression levels in BRCA were significantly negatively correlated with TMB. Thus, increased AP1M2 expression levels may lead to lower TMB in patients, which might be less sensitive to immunotherapy.

In addition, a positive correlation was revealed between AP1M2 expression and MMR and DNA methyltransferases in BRCA. Taken together, AP1M2 may be used as a prognostic predictor or a therapeutic target of BRCA for immunotherapy in clinical settings for the improvement of patients' prognosis and survival rates. In future research, we plan to use gene editing methods to overexpress or knock out AP1M2 in tumor cells and animal models to verify the function and molecular regulation mechanism of AP1M2. Through these studies, it is expected that the clinical application potential of AP1M2 will be further explored.

Data Availability

The data used to support the findings of this study are included within the article.

Disclosure

Yuanxue Yi and Qiufang Zhang are first authors.

Conflicts of Interest

The authors declare that they have no conflicts of interest.

Authors' Contributions

Yuanxue Yi and Qiufang Zhang contributed equally to this article.

Acknowledgments

This work was supported by Chongqing Science and Health Joint Chinese Medicine Research Project (2019ZDXM034) and Chongqing Natural Science Foundation (cstc2021jcyj-bsh0146).

References

[1] F. Nakatsu, T. Kadohira, D. J. Gilbert et al., "Genomic structure and chromosome mapping of the genes encoding clathrin-associated adaptor medium chains μ1A (Ap1m1) and μ1B (Ap1m2)," *Cytogenetic and Genome Research*, vol. 87, no. 1-2, pp. 53–58, 1999.

[2] J. Liu, T. Lichtenberg, K. A. Hoadley et al., "An integrated TCGA pan-cancer clinical data resource to drive high-quality survival outcome analytics," *Cell*, vol. 173, pp. 400–e11, 2018.

[3] C. J. Ryan, M. R. Smith, J. S. de Bono et al., "Abiraterone in metastatic prostate cancer without previous chemotherapy," *New England Journal of Medicine*, vol. 368, no. 2, pp. 138–148, 2013.

[4] E. J. de Ruiter, M. L. Ooft, L. A. Devriese, and S. M. Willems, "The prognostic role of tumor infiltrating T-lymphocytes in squamous cell carcinoma of the head and neck: a systematic review and meta-analysis," *OncoImmunology*, vol. 6, no. 11, Article ID e1356148, 2017.

[5] B. Chen, M. S. Khodadoust, C. L. Liu, A. M. Newman, and A. A. Alizadeh, "Profiling tumor infiltrating immune cells with CIBERSORT," *Methods in Molecular Biology*, vol. 1711, pp. 243–259, 2018.

[6] K. Yoshihara, M. Shahmoradgoli, E. Martínez et al., "Inferring tumour purity and stromal and immune cell admixture from expression data," *Nature Communications*, vol. 4, no. 1, p. 2612, 2013.

[7] R. M. Srivastava, T. A. Purohit, and T. A. Chan, "Diverse neoantigens and the development of cancer therapies," *Seminars in Radiation Oncology*, vol. 30, no. 2, pp. 113–128, 2020.

[8] S. Boegel, J. C. Castle, J. Kodysh, T. O'Donnell, and A. Rubinsteyn, "Bioinformatic methods for cancer neoantigen prediction," *Progress in Molecular Biology and Translational Science*, vol. 164, pp. 25–60, 2019.

[9] J. Song, J. Han, F. Liu et al., "Systematic analysis of coronavirus disease 2019 (COVID-19) receptor ACE2 in malignant tumors: pan-cancer analysis," *Frontiers in Molecular Biosciences*, vol. 7, Article ID 569414, 2020.

[10] R. Bonneville, M. A. Krook, E. A. Kautto et al., "Landscape of microsatellite instability across 39 cancer types," *JCO Precision Oncology*, vol. 1, 2017.

[11] L. Li, Q. Feng, and X. Wang, "PreMSIm: an R package for predicting microsatellite instability from the expression profiling of a gene panel in cancer," *Computational and Structural Biotechnology Journal*, vol. 18, pp. 668–675, 2020.

[12] L. Yin, L. Xiao, Y. Gao et al., "Comparative bioinformatical analysis of pancreatic head cancer and pancreatic body/tail cancer," *Medical Oncology*, vol. 37, no. 5, p. 46, 2020.

[13] A. Subramanian, P. Tamayo, V. K. Mootha et al., "Gene set enrichment analysis: a knowledge-based approach for interpreting genome-wide expression profiles," *Proceedings of the National Academy of Sciences*, vol. 102, no. 43, pp. 15545–15550, 2005.

[14] M. Yusuf, J. Gaskins, S. Mandish et al., "Tumor infiltrating lymphocyte grade in merkel cell carcinoma: relationships with clinical factors and independent prognostic value," *Acta Oncologica*, vol. 59, no. 12, pp. 1409–1415, 2020.

[15] D. Dai, L. Liu, H. Huang et al., "Nomograms to predict the density of tumor-infiltrating lymphocytes in patients with

high-grade serous ovarian cancer," *Frontiers in Oncology*, vol. 11, Article ID 590414, 2021.

[16] F. Massari, M. Santoni, C. Ciccarese, and D. Santini, "The immunocheckpoints in modern oncology: the next 15 years," *Expert Opinion on Biological Therapy*, vol. 15, no. 7, pp. 917–921, 2015.

[17] L. Danilova, W. J. Ho, Q. Zhu et al., "Programmed cell death ligand-1 (PD-L1) and CD8 expression profiling identify an immunologic subtype of pancreatic ductal adenocarcinomas with favorable survival," *Cancer Immunology Research*, vol. 7, no. 6, pp. 886–895, 2019.

[18] L. Li, S. P. Goedegebuure, and W. E. Gillanders, "Preclinical and clinical development of neoantigen vaccines," *Annals of Oncology: Official Journal of the European Society for Medical Oncology*, vol. 28, p. xii11, 2017.

[19] D. Sun, H. Li, M. Cao et al., "Cancer burden in China: trends, risk factors and prevention," *Cancer Biology and Medicine*, vol. 17, no. 4, pp. 879–895, 2020.

[20] S. Yang, Y. Zhang, J. Cai, and Z. Wang, "Clinical characteristics of COVID-19 after gynecologic oncology surgery in three women: a retrospective review of medical records," *The Oncologist*, vol. 25, no. 6, pp. e982–e985, 2020.

[21] M. Muthu, S. Chun, J. Gopal et al., "The mudeng augmentation: a genesis in anti-cancer therapy?" *International Journal of Molecular Sciences*, vol. 21, 2020.

[22] D. S. Chen and I. Mellman, "Elements of cancer immunity and the cancer-immune set point," *Nature*, vol. 541, no. 7637, pp. 321–330, 2017.

[23] S. Sui, X. An, C. Xu et al., "An immune cell infiltration-based immune score model predicts prognosis and chemotherapy effects in breast cancer," *Theranostics*, vol. 10, no. 26, pp. 11938–11949, 2020.

[24] J. Wang, Y. Li, W. Fu et al., "Prognostic nomogram based on immune scores for breast cancer patients," *Cancer Medicine*, vol. 8, no. 11, pp. 5214–5222, 2019.

[25] D. M. Pardoll, "The blockade of immune checkpoints in cancer immunotherapy," *Nature Reviews Cancer*, vol. 12, no. 4, pp. 252–264, 2012.

[26] J. Fang, F. Chen, D. Liu, F. Gu, Z. Chen, and Y. Wang, "Prognostic value of immune checkpoint molecules in breast cancer," *Bioscience Reports*, vol. 40, 2020.

[27] T. A. Chan, M. Yarchoan, E. Jaffee et al., "Development of tumor mutation burden as an immunotherapy biomarker: utility for the oncology clinic," *Annals of Oncology*, vol. 30, no. 1, pp. 44–56, 2019.

[28] X. Wang and M. Li, "Correlate tumor mutation burden with immune signatures in human cancers," *BMC Immunology*, vol. 20, no. 1, p. 4, 2019.

[29] V. Endris, I. Buchhalter, M. Allgäuer et al., "Measurement of tumor mutational burden (TMB) in routine molecular diagnostics: in silico and real-life analysis of three larger gene panels," *International Journal of Cancer*, vol. 144, pp. 2303–2312, 2019.

Hindawi
Journal of Oncology
Volume 2022, Article ID 6080049, 11 pages
https://doi.org/10.1155/2022/6080049

Research Article

A Ferroptosis-Related lncRNA Model to Enhance the Predicted Value of Cervical Cancer

Zhaojing Jiang,[1] **Jingyu Li**,[2] **Wenqing Feng**,[3] **Yujie Sun**,[3] **and Junguo Bu**[4]

[1]*Department of Radiotherapy, Zhujiang Hospital, Southern Medical University, Guangzhou, China*
[2]*Department of Pathology, Zhujiang Hospital, Southern Medical University, Guangzhou, China*
[3]*Department of Oncology, Zhujiang Hospital, Southern Medical University, Guangzhou, China*
[4]*Department of Oncology, Guangdong Second Provincial General Hospital, Guangzhou, China*

Correspondence should be addressed to Junguo Bu; flkd007@smu.edu.cn

Received 21 December 2021; Revised 12 January 2022; Accepted 17 January 2022; Published 8 February 2022

Academic Editor: Fu Wang

Background. Cervical cancer (CC) is a common gynecological malignant tumor. Ferroptosis is a new type of programmed cell death, which plays a crucial part in cancer. However, current knowledge regarding ferroptosis-related long noncoding RNAs (lncRNAs) in CC is still limited. Therefore, our aim is to identify ferroptosis-related lncRNAs, build a steady prediction model, and improve the prediction value of CC. *Methods*. We obtained RNA expression and ferroptosis-related gene data of female CC patients from TCGA and FerrDb databases, respectively. Then, the ferroptosis-related lncRNAs were obtained by the limma R package and Cytoscape 3.7.1. We constructed the prediction model by Cox regression analysis. Finally, the prediction model was verified by the median risk score, Kaplan–Meier analysis, the time-dependent receiver operating characteristic (ROC) curve, clinical features, and immunoinfiltration analysis. *Results*. We acquired 1393 ferroptosis-related lncRNAs. The ferroptosis-related lncRNA signature was obtained by multivariate Cox regression analysis, and the patients were divided into a high-risk group and a low-risk group. The prognosis of the high-risk group was worse than that of the low-risk group. We found that the risk score can be used as an independent prognostic index by multivariate Cox regression analysis. The area under the time-dependent ROC curve reached 0.847 at 1 year, 0.906 at 2 years, 0.807 at 3 years, and 0.724 at 5 years in the training cohort. Principal component analysis showed that the diffusion directions of the two groups were different. Gene set enrichment analysis indicated that lncRNAs of two groups may be involved in tumorigenesis. Further analysis showed that high-risk groups were related to immune-related pathways. Ferroptosis-related lncRNAs are related to the proportion of tumor-infiltrating immune cells in CC. *Conclusion*. We have constructed a ferroptosis-related lncRNA prediction model. The prognostic model had important clinical significance, including improving the predictive value and guiding the individualized treatment of CC patients.

1. Introduction

Cervical cancer (CC) is a serious threat to women's health [1]. Many people around the world die of this cancer every year [2]. Human papillomavirus (HPV) infection is an essential factor for developing CC [3]. The incidence of CC has dropped by 40% to 50% in recent years, due to the wide application of early cervical cancer screening and advances in surgical, radiotherapy, and chemotherapy treatments [4]. Although the popularity of the HPV vaccine has reduced the number and mortality of CC patients, many women still suffer from CC [5, 6]. Therefore, it is imperative to find an ideal clinical model or accurate prognostic biomarkers that instruct the treatment of CC.

In the past few decades, the research on ferroptosis of tumors has increased rapidly. Different from apoptosis and autophagy, this is a new mode of nonapoptotic cell death that relies on the accumulation of reactive oxygen species (ROS) in an iron-dependent manner [7]. At present, many studies have shown that ferroptosis plays a vital role in mediating tumor development and drug resistance [8]. Ubellacker et al. [9] reported that melanoma cells in lymph have a higher ability to metastasize due to their resistance to ferroptosis. In tumor treatment, chemotherapy can induce

ferroptosis of cancer cells, resulting in increase in the survival time of cancer patients [10]. Different from normal cells, cancer cells rely too much on iron for cell proliferation [11]. This evidence suggested that ferroptosis has a different effect on cancer. In fact, targeting the tumor ferroptosis pathway is a new antitumor mechanism, which opens up a new therapeutic for the treatment of cancer [12].

Long-chain noncoding RNA (lncRNA) is an RNA with no or limited protein coding ability, whose length is about 200 bp to more than 100 kb [13]. lncRNAs participate in multiple biological regulatory processes, such as tumor occurrence, development, and metastasis [14]. One recent study revealed that lncRNA suppresses ferroptosis by acting as a competitive endogenous RNA (ceRNA) [15]. In a related study, lncRNA GABPB1 may be a key molecule for ferroptosis in hepatoma cells [16]. However, there are few studies to systematically evaluate the characteristics of ferroptosis-related lncRNAs and their relationship with the overall survival (OS) of CC patients.

In this research, we first established the prognostic multi-lncRNA signature of ferroptosis-related lncRNA based on Cancer Genome Atlas (TCGA) and FerrDb databases. Moreover, we discussed the effect of the novel ferroptosis-related lncRNA signature in immune response during CC prognosis. Our study provides a new gene signature for the prognosis prediction of CC patients and offers an important basis for the future study of the relationship between iron ferroptosis-related lncRNA and immunity in CC.

2. Methods

2.1. Collection and Preprocessing of Raw Data. The transcriptome profiling data including the RNA sequencing data of 309 samples (CC patients: 306; control groups: 3) and corresponding clinical data were obtained from the TCGA database (https://portal.gdc.cancer.gov/). The expression profiling matrix of both encoding gene and lncRNA was extracted with Perl. Ferroptosis-related genes were identified from the FerrDb database [17] (https://www.zhounan.org/ferrdb/). The clinicopathological data of CC patients were collected, including survival status, stage, TMN, grade, and survival time.

2.2. Data Processing of lncRNAs and Ferroptosis-Related Genes. The correlation test between ferroptosis-related mRNAs and lncRNAs was performed with Cor.test in R software (corFilter = 0.4; pvalueFilter = 0.01). Finally, the coexpression network of prognostic ferroptosis-related genes and lncRNAs was drawn by the Cytoscape software.

2.3. Construction of Prognostic Ferroptosis-Related lncRNAs Signature. We first used the survival "*R*" package (version: 3.2.1) for Cox regression analysis to construct survival prognostic characteristics. Then we selected lncRNA with significant statistical significance in univariate Cox regression for multivariate Cox regression. Finally, the risk score of patients was calculated according to the normalized expression level of each gene and the corresponding regression coefficient in the model. The formula = $e^{\text{sum (each gene's expression} \times \text{corresponding coefficient)}}$. CC patients were divided into the high-risk group and the low-risk group based on the median value of the risk scores.

2.4. Prognostic and Independent Analysis. We used Kaplan–Meier survival curves to distinguish the difference in overall survival (OS) between the different risk groups. In addition, we also used different R packages to construct K-M survival curve and analyze the ROC curve. Finally, we used the method of independent analysis to verify the independence of the model, such as stage and TNM.

2.5. The Predictive Nomogram. The gene set enrichment analysis (GSEA) was performed with GSEA 4.0.1 for investigating the potential mechanisms involved in the high-risk and low-risk groups. We considered $p < 0.05$ as statistically significant. We constructed a nomogram with prognostic characteristics to predict OS in CC patients at 1, 2, 3 and 5 years. Finally, the "prcomp" function of "stats" R package is used for principal component analysis (PCA).

2.6. Immunoinfiltration Analysis. We calculated the relative proportion of tumor infiltrating immune cells using the CIBERSORT algorithm to understand the infiltrating immune cells in the CC microenvironment associated with multi-lncRNA signature. Then we used the Wilcoxon test to compare the composition fraction of infiltrating immune cells between two different risk groups. Finally, we used Pearson correlation analysis to find out the relationship between lncRNA and significantly infiltrating immune cells.

2.7. Statistical Analysis. The R software was used for survival, Cox regression, and PCA analyses. We used the "survival R" and "surviviner R" packages for Kaplan–Meier analysis. Moreover, we validate the prediction model by using the "survival R," "surviviner R," "survival ROC R," "pheatmap R," and "ggpubr" software packages. GSEA was used to analyze the function of two risk groups of lncRNAs. When the p value <0.05, the difference was statistically significant.

3. Result

3.1. Identification of Ferroptosis-Related lncRNA in CC. Our flow-process diagram is shown in Figure 1. We constructed a coexpression network of lncRNA and ferroptosis-related genes through the "limma package" of R studio and Cytoscape 3.7.1 to obtain ferroptosis-related lncRNA (Figure 2(a)). The lncRNA whose expression level was significantly correlated with one or more of the 211 ferroptosis-related genes, with the correlation coefficient $|R^2| > 0.4$ at $p < 0.01$, was considered a ferroptosis-related lncRNA. Finally, 1393 ferroptosis-related lncRNAs were identified, with 1346 ferroptosis-related lncRNAs positively

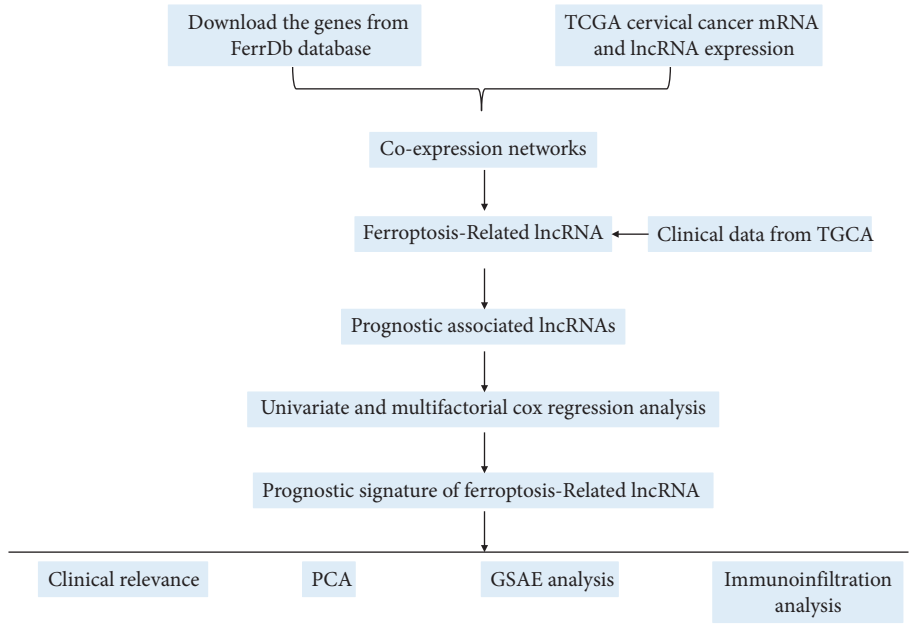

Figure 1: The flow-process diagram of the study.

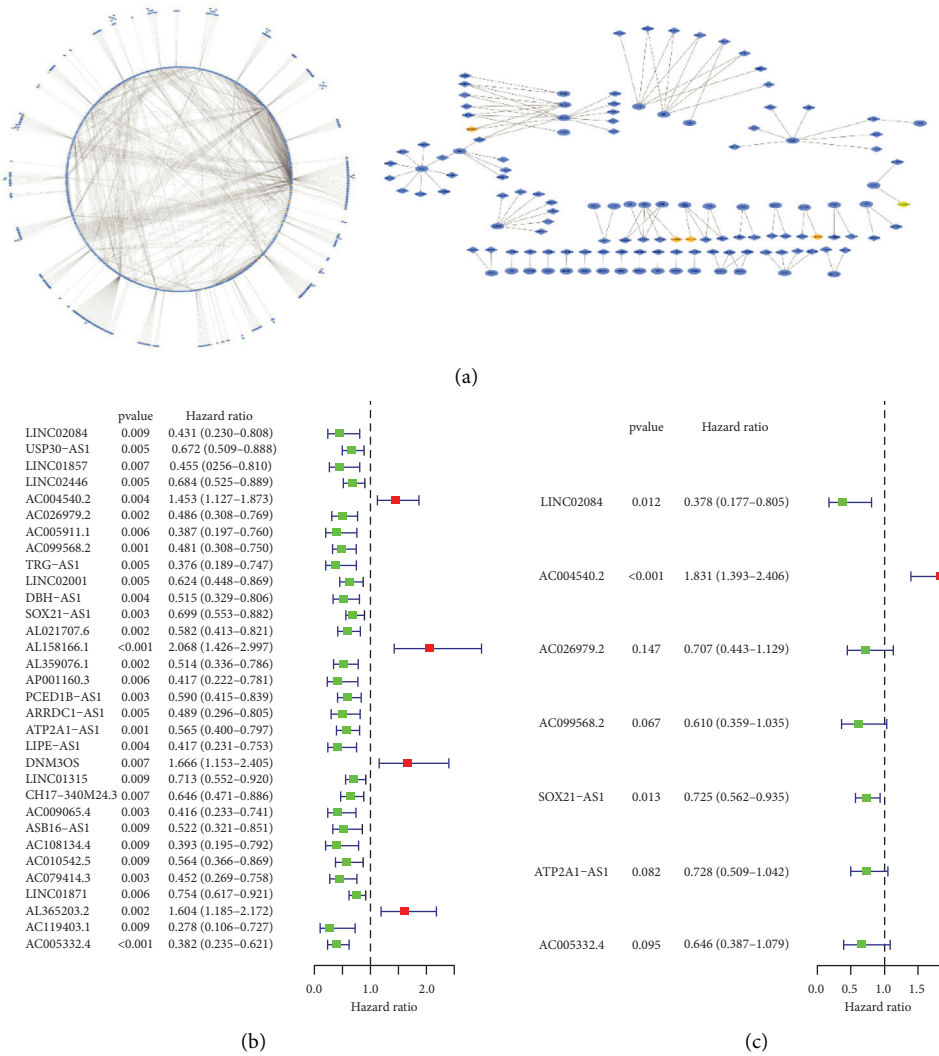

Figure 2: The coexpression network and Cox regression analysis result. (a) The network of ferroptosis genes and lncRNAs. (b) The forest plot of univariate Cox regression confirmed 32 ferroptosis-related lncRNAs. (c) The forest plot of multivariate Cox regression confirmed 7 ferroptosis-related lncRNAs.

correlated and 47 ferroptosis-related lncRNAs negatively correlated with CC.

3.2. Construction and Validation of the Ferroptosis-Related lncRNA Feature of CC. We first determine the prediction model based on univariate Cox regression analysis, and there were 32 lncRNAs related to ferroptosis in the prediction model (Figure 2(b)). Then these lncRNAs are included in the multivariate COX analysis (Figure 2(c)). Finally, there were 7 ferroptosis-related lncRNAs (LINC02084, AC004540.2, AC026979.2, AC099568.2, SOX21-AS1, ATP2A1-AS1, and AC005332.4) that can be considered an alone prognostic factor for CC. On the basis of the median risk score, all samples were allocated to a high-risk group ($n = 136$) and a low-risk group ($n = 137$). According to Kaplan–Meier analysis, poorer overall survival was associated with high-risk lncRNA expression ($p = 6.706e - 07$, Figure 3(a)). The mortality of CC patients in the low-risk group was lower than that in the high-risk group (Figure 3(b)). The heatmap showed that the expression of lncRNAs (SOX21-AS1, AC026979.2, ATP2A1-AS1, AC099568.2, and AC005332.4) was significantly upregulated in the low-risk group, while the lncRNAs (LINC02084 and AC004540.2) were downregulated in the low-risk group compared to the high-risk group (Figure 3(c)). The predictive performance of OS risk score was evaluated by the time-dependent ROC curve, and the area under the curve (AUC) was 0.769 in 1 year, 0.849 in 2 years, and 0.776 in 3 years (Figure 3(d)). These results suggested that ferroptosis-related lncRNAs were a major risk factor for CC patients.

3.3. Independent Analysis of Prognostic Model and Other Clinical Variables. Based on the predictive model, we used Cox regression to analyze the clinical feature of CC. There were significant differences in risk score, pathological T staging, and stage related to overall survival by univariate independent prognostic analysis ($p < 0.05$, Figure 4(a)). The risk score can be used as an independent forecast of CC in the multivariate Cox regression analysis (Figure 4(b)). Overall, the independent prognostic analysis of single factor and multiple factors showed that the predictive model is an independent predictive element. Multi-index ROC curve analysis compared the AUC values of the risk prognosis model and the clinical indicator prognosis model, which expressed that the AUC values of the risk score for 1-year, 2-year, 3-year, and 5-year survival are 0.847, 0.906, 0.807, and 0.724, respectively, and the areas are all maximum (Figure 4(c)). In addition, the hierarchical analysis was used to determine the independence of the prediction model (Figures 5(a) and 5(b)). For stage, AC099568.2 was significantly upregulated in the early stage of CC, whereas gradually downregulated as cancer metastasized ($p < 0.001$). For pathological T phase, AC005332.4 and AC099568.2 were statistically significant ($p < 0.05$), and the expression of AC099568.2 decreased with the progression of the T phase. These results revealed that the signature of ferroptosis-related lncRNAs can be used as a model for predicting CC.

3.4. Gene Set Enrichment Analyses. To determine the difference between the diverse groups in lncRNA based on the model, we performed a PCA (Figure 6). Our results demonstrated that the two groups of patients spread in different directions. And the model lncRNAs divided CC patients into two specific parts, indicating that the prognostic status of CC patients in the two groups is very different. Furthermore, we performed GSEA on the two groups to find the possible biological function of the model of CC (Figure 7). GSEA revealed that ferroptosis-related lncRNA prognostic models mainly regulated immune- and cancer-related pathways, such as DNA replication, primary immunodeficiency, ERBB signaling pathway, pathways in cancer, the intestinal immune network for IGA production, and BETA signaling pathway. These results suggested that these related biological pathways play an important role in the carcinogenesis of CC.

3.5. The Immune Cell Infiltration Landscape in CC. We used the CIBERSORT algorithm to analyze the connection between ferroptosis-related lncRNAs and antitumor immune. The results reasonably showed that there was a significant difference in the proportion of tumor infiltrating immune cells between the low- and high-risk groups (Figure 8(a)). We constructed a violin chart to compare the difference in immune cell infiltration between the low- and high-risk groups. The result displayed that there were significant differences in B cells native ($p = 0.003$), T cells CD8 ($p < 0.001$), T cells CD4 memory activated ($p = 0.018$), macrophage M0 ($p = 0.024$), and macrophage M2 ($p = 0.025$) between the two groups (Figure 8(b)). The correlation matrix of the proportion of all cancer infiltrating immune cells is shown in Figure 8(c). These results demonstrated that there were differences in immune-related genes between the high-risk group and the low-risk group, which may partly explain the significant difference in prognosis between subgroups.

4. Discussion

In the world, two-thirds of CC patients are still diagnosed as advanced. Although they have been treated with a variety of methods, they have lost the chance of radical cure [18]. In recent years, ferroptosis can help remove defective cells, which has become a new treatment method for tumors [19]. Moreover, lncRNAs have a profound influence in the occurrence and change of cancer [20]. Meanwhile, the importance of ferroptosis-related lncRNA in cancer development and treatment is increasingly recognized [21]. Zhou et al. certified that a risk model of ferroptosis-related lncRNA signature helped to predict immune infiltration, immunotherapeutic outcomes, and chemotherapy sensitivity in bladder cancer [22]. However, to our knowledge, there are few studies on the prognosis of ferroptosis-associated lncRNAs in CC. Therefore, in this study, we first constructed a coexpression network of lncRNA and ferroptosis-related genes and identified 1393 ferroptosis-related lncRNA. Then, we created a new prediction model integrating 7 ferroptosis-associated lncRNAs by univariate

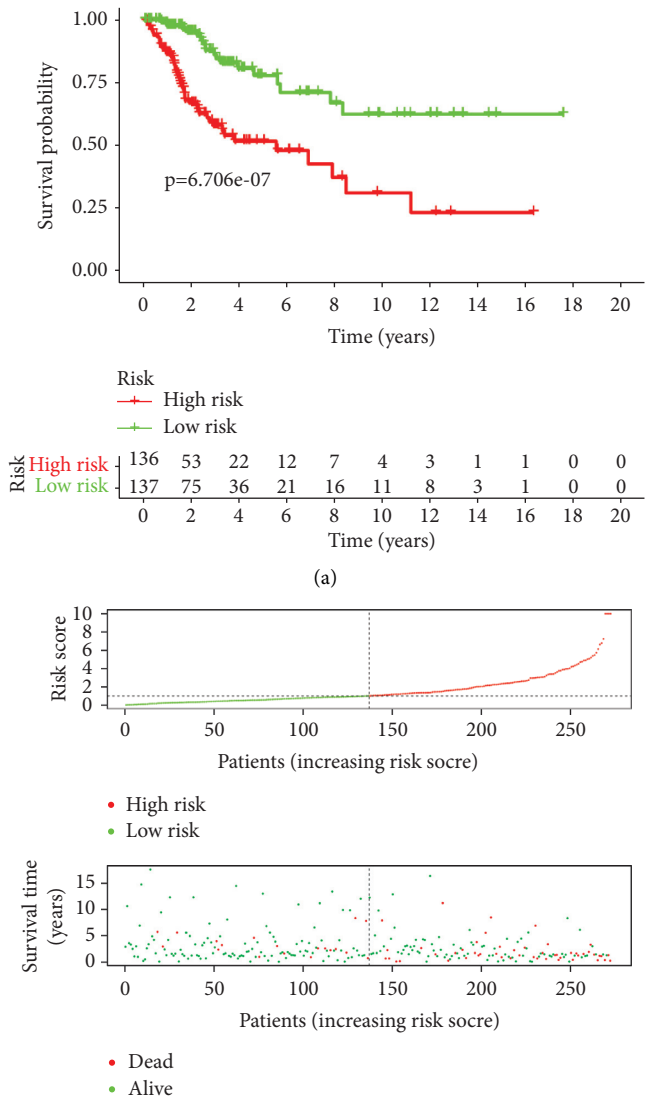

Figure 3: Continued.

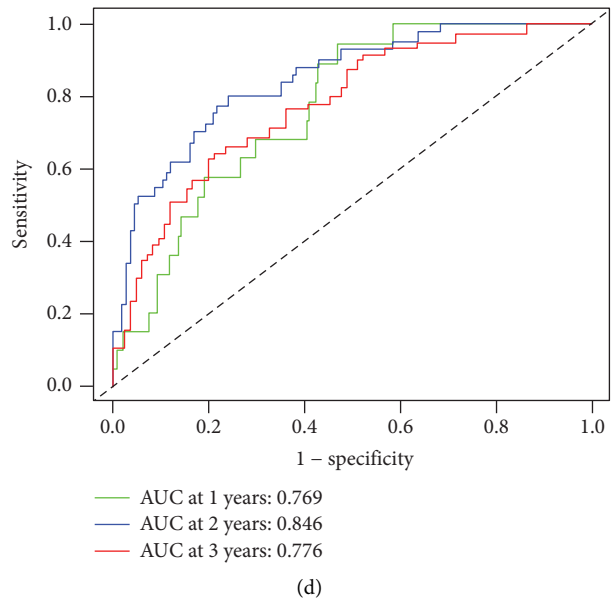

(d)

Figure 3: Prognostic analysis of the ferroptosis-related lncRNAs feature. (a) Kaplan–Meier curve of the patients in the high-risk and low-risk groups. (b) The rank of calculated risk score. (c) Heatmap of expression of 7 ferroptosis-related lncRNAs. (d) Time-dependent ROC curve analysis.

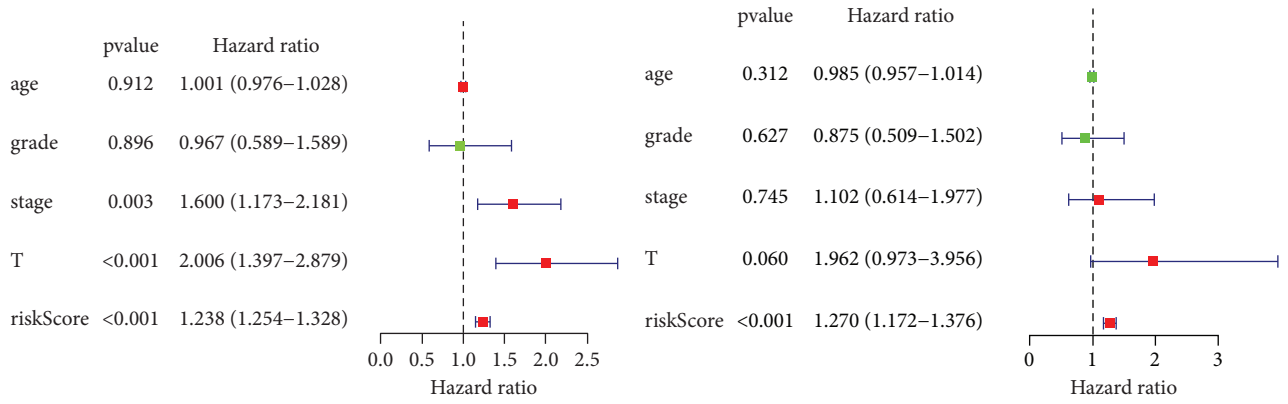

(a) (b)

Figure 4: Continued.

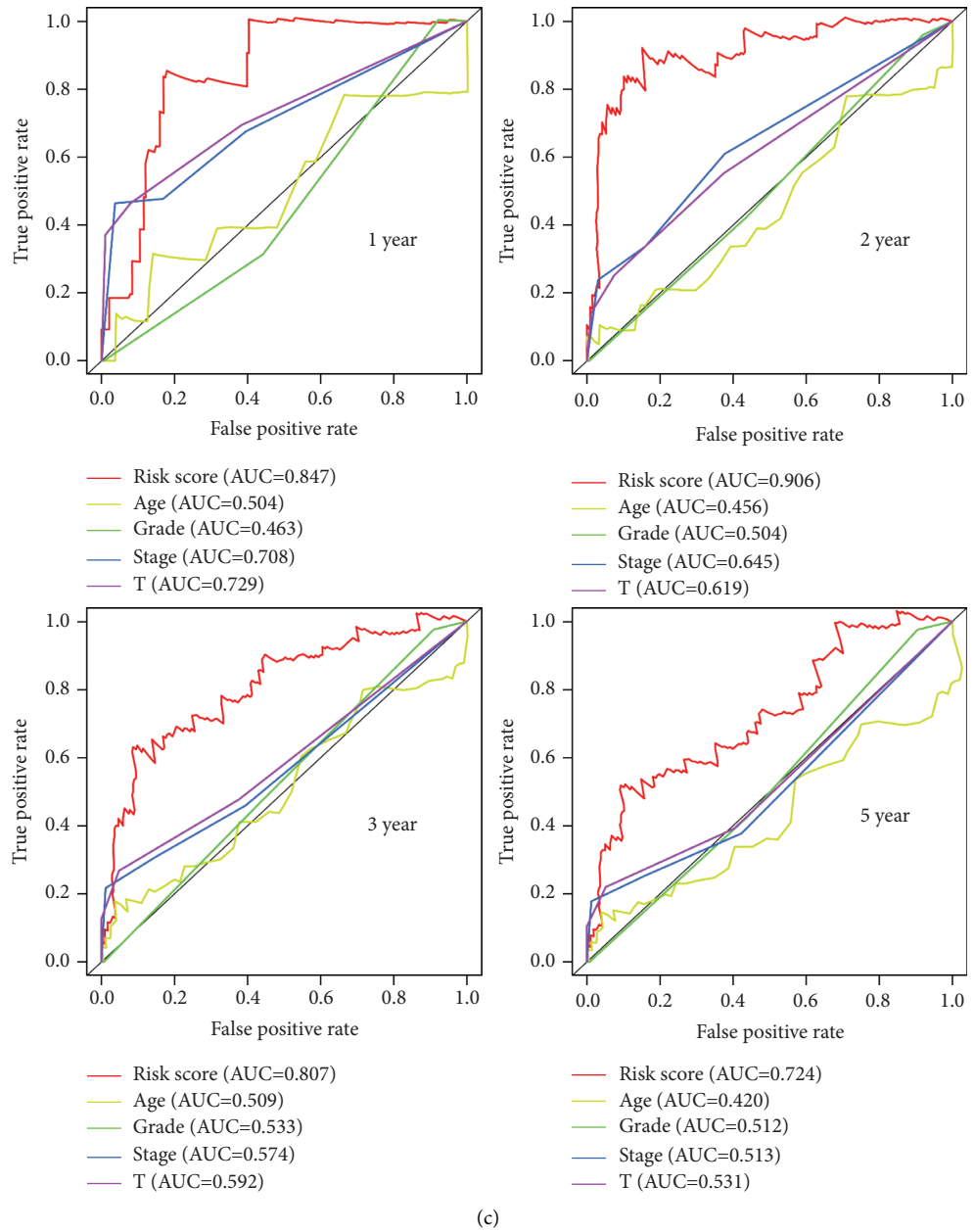

(c)

Figure 4: The clinicopathological characteristics. (a) The forest plot of univariate Cox regression. (b) The forest plot of multivariate Cox regression. (c) Multi-index ROC curve analysis compares the AUC value of the risk prognosis model and the clinical index prognosis model.

Cox regression and multivariate Cox analysis, which was then validated to perform well in an external dataset. The PCA result divided patients with different risk scores into two categories. The GSEA indicated that ferroptosis-associated lncRNAs regulated immune- and cancer-related pathways. Finally, the immune cell infiltration of the low-risk group and high-risk group was compared, high-risk group decreased levels of T cell CD8 and macrophage M2 and increased levels of B cells native, T cells CD4 memory activated, and macrophage M0 compared with the low-risk group.

Ferroptosis has been shown to be involved in cancer [23]. However, lncRNA may inhibit ferroptosis in cancer through the function of ceRNA [15]. In our research, we showed a coexpression network of ferroptosis-lncRNA, which proved that there is a regulatory relationship between lncRNA and ferroptosis-related genes. Combining this feature, we have built a prognostic model for CC. In our study, the K-M survival curve indicated that our prediction model is closely related to CC patients. In our results, the AUC values were 0.847 at 1 year, 0.906 at 2 years, 0.807 at 3 years, and 0.724 at 5 years. However, similar to this prognostic model, other researchers' AUC values were smaller than ours [24], which proved that the predictive ability of our model is relatively good. In addition, from the perspective of the cancer stage and pathological stage, AC099568.2 always was the most obvious lncRNA, indicating that the molecule is critical to the prognosis of CC. Ma

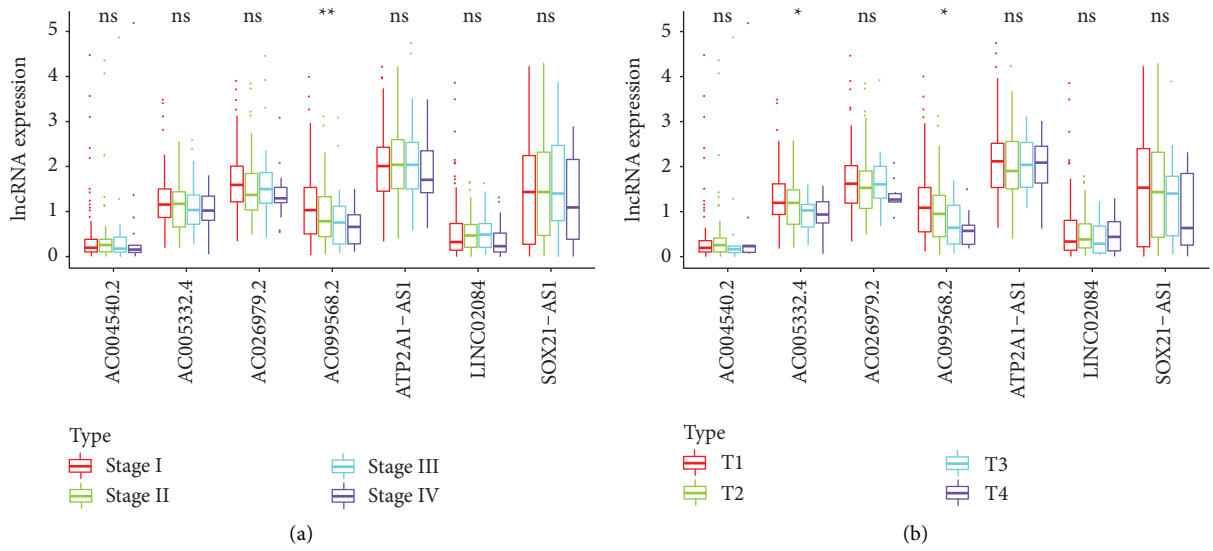

Figure 5: Independent prognostic value of the ferroptosis-related lncRNAs feature. (a) Stratification analyses of stage. (b) Stratification analyses of T stage.

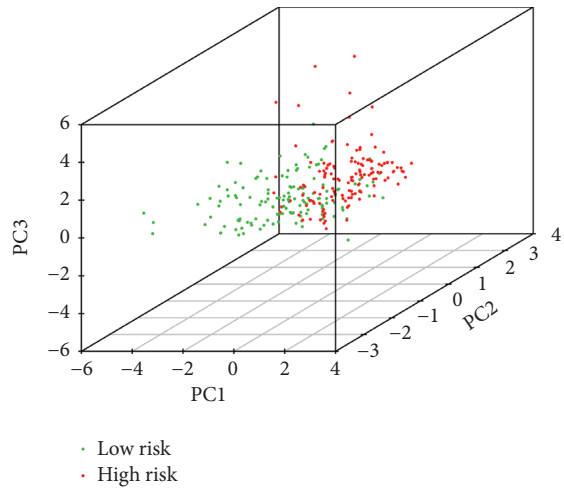

Figure 6: PCA.

et al. [25] reported that immune-related lncRNA signature was an independent prognostic factor for breast cancer and was closely related to clinicopathological features, indicating that this model is a very good prognostic tool for breast cancer. Moreover, similar to our research method, by constructing the prognostic 13-lncRNA signature of hepatocellular carcinoma and verifying it externally, it is proved that the model can be used to predict and diagnose the prognosis of hepatocellular carcinoma [26]. Compared with other studies [27], comprehensive analysis shows that our prognostic model is very reliable. These results manifested that the prognostic model can improve the prognostic ability of CC.

We have demonstrated that our model of ferroptosis-related lncRNAs can enhance the prognosis of CC. Next, we analyzed the biological functions of this prediction model through GSEA. GSEA revealed that ferroptosis-related lncRNAs were involved in the pathways of "primary immunodeficiency," "DNA replication," "ERBB signaling pathway," "pathways in cancer," "intestinal immune network for IGA production," and "BETA signaling pathway." DNA replication is crucial for tumorigenesis. Macheret and Halazonetis showed that DNA replication can drive cancer progression [28]. Moreover, Wang illustrated many cancers are related to overexpression or mutation of the ERBB receptor [29]. Low expression of ferroptosis-related genes is associated with poor prognosis of cancer and defective immune cell infiltration [30]. However, other studies reported that patients with high risk scores in model showed greater adaptive immunity [25]. In our study, the model showed "primary immunodeficiency," which makes patients prone to frequent infection and malignant tumor [31]. Although the two models involve different functions, they all implied that these prognostic models had good predictive ability and played an important role in cancer immunotherapy. The above results proved that the

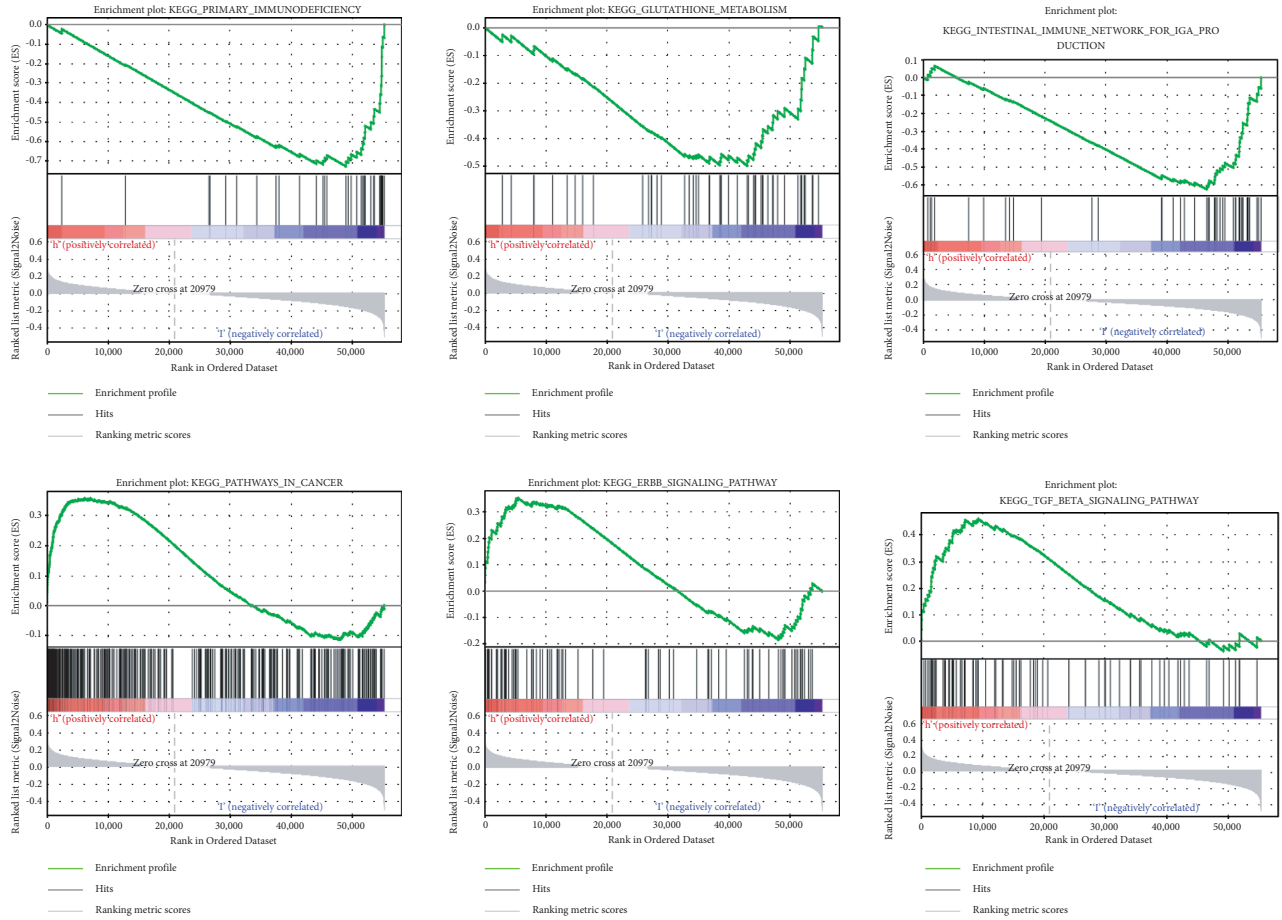

Figure 7: GSEA for the high-risk and low-risk groups.

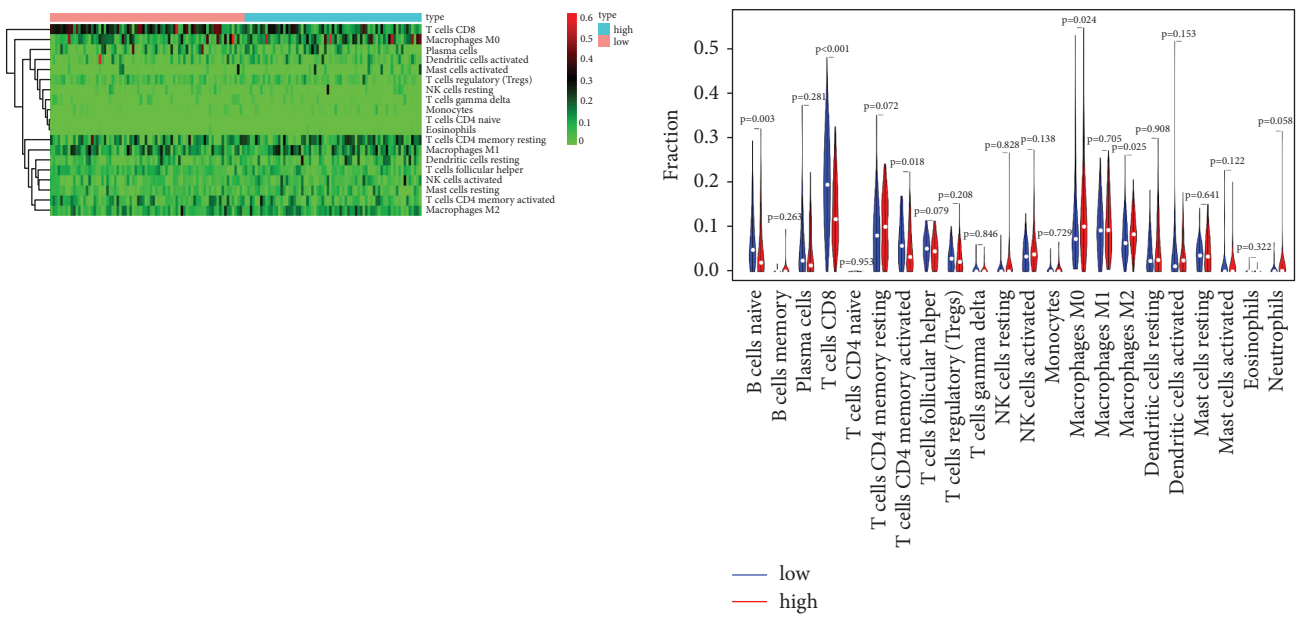

(a) (b)

Figure 8: Continued.

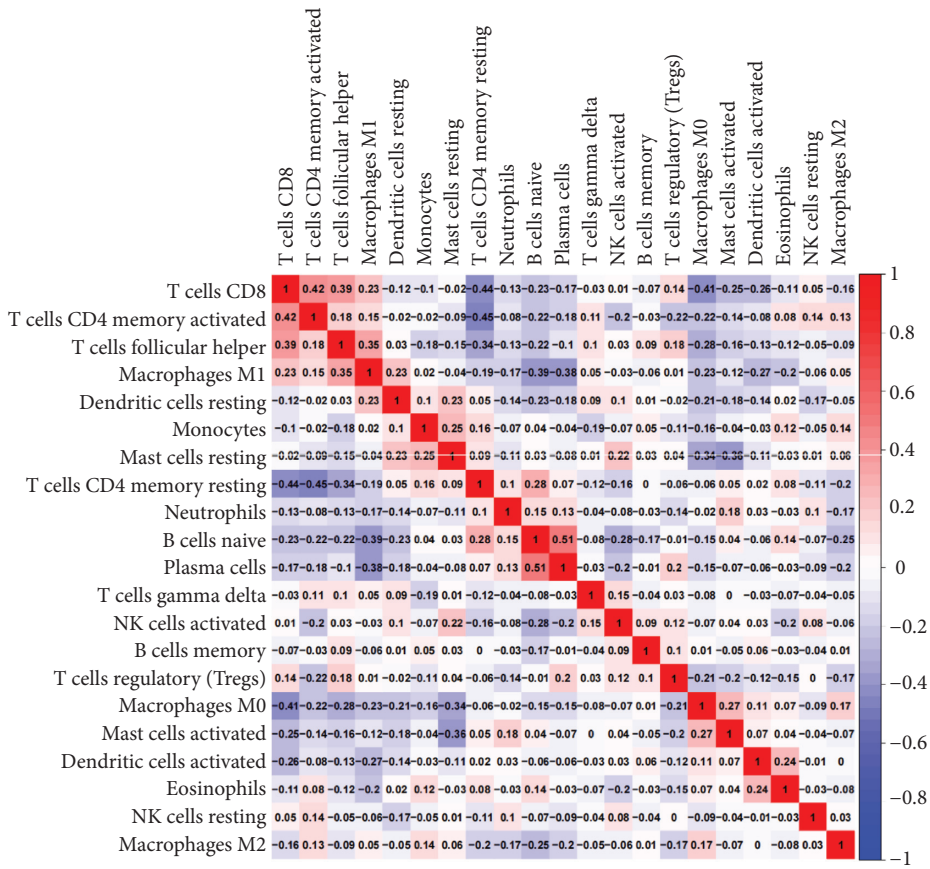

(c)

Figure 8: Comparison of 22 immune cell infiltration levels between the high-risk and low-risk groups. (a) Heatmap. (b) Violin plot. (c) Correlation matrix of immune cell proportions.

predictive signature is related to not only tumorigenesis, but also correlative immune response.

Many studies have reported there is a relationship between lymphocyte infiltration and prognosis [32]. For example, the degree of lymphocytic infiltration in the primary tumor is positively correlated with the presence or absence of metastasis [33]. Therefore, we calculated the rate of immune cell infiltration in both risk groups. Different from the low-risk group, T cells CD8 and macrophage M2 cells were significantly reduced in the high-risk group. The main function of CD8 cells is to induce tumor cell death [34]. Besides, B cells native, T cells CD4 memory activated, and macrophage M0 cells were significantly increased in the high-risk group, which were generally used to defend against external aggressions [35]. Therefore, we considered that ferroptosis-related lncRNA is closely correlated with the proportion of tumor-infiltrating immunocytes in CC, and low-risk groups have more effective immune status than high-risk groups.

5. Conclusion

In summary, we have discovered a novel 7 ferroptosis-related lncRNA signature as a potential prognostic tool for CC patients. It is closely related to the tumor status, risk value, and OS. The signature offers a new insight into ferroptosis-related lncRNAs in CC and recognizes possible biomarkers for prognosis and immunological therapy.

Data Availability

The data used to support the findings of this study are available from the corresponding author upon request.

Conflicts of Interest

The authors declare that there are no conflicts of interest regarding the publication of this article.

Authors' Contributions

Zhaojing Jiang was involved in original draft preparation. Jingyu Li carried out data curation. Wenqing Feng and Yujie Sun reviewed and edited the manuscript. Junguo Bu contributed to project administration. All the authors commented and approved the text.

Acknowledgments

The present research was supported by President Foundation of Zhujiang Hospital, Southern Medical University (no. yzjj2019qn08).

References

[1] X. Ding, X. Jia, C. Wang, J. Xu, S.-J. Gao, and C. Lu, "A DHX9-lncRNA-MDM2 interaction regulates cell invasion and angiogenesis of cervical cancer," *Cell Death & Differentiation*, vol. 26, no. 9, pp. 1750–1765, 2019.

[2] A. Hoeben, J. Polak, L. Van De Voorde, F. Hoebers, H. I. Grabsch, and J. de Vos-Geelen, "Cervical esophageal cancer: a gap in cancer knowledge," *Annals of Oncology*, vol. 27, no. 9, pp. 1664–1674, 2016.

[3] N. Muñoz, F. X. Bosch, S. de Sanjosé et al., "Epidemiologic classification of human papillomavirus types associated with cervical cancer," *New England Journal of Medicine*, vol. 348, no. 6, pp. 518–527, 2003.

[4] C. J. L. M. Meijer and P. J. F. Snijders, "Screening comes of age and treatment progress continues," *Nature Reviews Clinical Oncology*, vol. 11, no. 2, pp. 77-78, 2014.

[5] G. Hancock, K. Hellner, and L. Dorrell, "Therapeutic HPV vaccines," *Best Practice & Research Clinical Obstetrics & Gynaecology*, vol. 47, pp. 59–72, 2018.

[6] N. D. Fleming, M. Frumovitz, K. M. Schmeler et al., "Significance of lymph node ratio in defining risk category in node-positive early stage cervical cancer," *Gynecologic Oncology*, vol. 136, no. 1, pp. 48–53, 2015.

[7] L. Huang, D. B. McClatchy, P. Maher et al., "Intracellular amyloid toxicity induces oxytosis/ferroptosis regulated cell death," *Cell Death & Disease*, vol. 11, no. 10, p. 828, 2020.

[8] J. Guo, B. Xu, Q. Han et al., "Ferroptosis: a novel anti-tumor action for cisplatin," *Cancer Research and Treatment*, vol. 50, no. 2, pp. 445–460, 2018.

[9] J. M. Ubellacker, A. Tasdogan, V. Ramesh et al., "Lymph protects metastasizing melanoma cells from ferroptosis," *Nature*, vol. 585, no. 7823, pp. 113–118, 2020.

[10] G. Lei, Y. Zhang, P. Koppula et al., "The role of ferroptosis in ionizing radiation-induced cell death and tumor suppression," *Cell Research*, vol. 30, no. 2, pp. 146–162, 2020.

[11] D. H. Manz, N. L. Blanchette, B. T. Paul, F. M. Torti, and S. V. Torti, "Iron and cancer: recent insights," *Annals of the New York Academy of Sciences*, vol. 1368, no. 1, pp. 149–161, 2016.

[12] W. Wang, M. Green, J. E. Choi et al., "CD8+ T cells regulate tumour ferroptosis during cancer immunotherapy," *Nature*, vol. 569, no. 7755, pp. 270–274, 2019.

[13] S. Jathar, V. Kumar, J. Srivastava, and V. Tripathi, "Technological developments in lncRNA biology," *Advances in Experimental Medicine & Biology*, vol. 1008, pp. 283–323, 2017.

[14] R. A. Gupta, N. Shah, K. C. Wang et al., "Long non-coding RNA HOTAIR reprograms chromatin state to promote cancer metastasis," *Nature*, vol. 464, no. 7291, pp. 1071–1076, 2010.

[15] M. Wang, C. Mao, L. Ouyang et al., "Long noncoding RNA LINC00336 inhibits ferroptosis in lung cancer by functioning as a competing endogenous RNA," *Cell Death & Differentiation*, vol. 26, no. 11, pp. 2329–2343, 2019.

[16] W. Qi, Z. Li, L. Xia et al., "LncRNA GABPB1-AS1 and GABPB1 regulate oxidative stress during erastin-induced ferroptosis in HepG2 hepatocellular carcinoma cells," *Scientific Reports*, vol. 9, no. 1, p. 16185, 2019.

[17] N. Zhou and J. Bao, "FerrDb: a manually curated resource for regulators and markers of ferroptosis and ferroptosis-disease associations," *Database*, vol. 2020, Article ID baaa021, 2020.

[18] G. Marquina, A. Manzano, and A. Casado, "Targeted agents in cervical cancer: beyond bevacizumab," *Current Oncology Reports*, vol. 20, no. 5, p. 40, 2018.

[19] Y. Tang, C. Li, Y.-J. Zhang, and Z.-H. Wu, "Ferroptosis-related long non-coding RNA signature predicts the prognosis of head and neck squamous cell carcinoma," *International Journal of Biological Sciences*, vol. 17, no. 3, pp. 702–711, 2021.

[20] M. Mohebi, S. Ghafouri-Fard, M. H. Modarressi et al., "Expression analysis of vimentin and the related lncRNA network in breast cancer," *Experimental and Molecular Pathology*, vol. 115, Article ID 104439, 2020.

[21] J. Pan, X. Zhang, X. Fang, and Z. Xin, "Construction on of a ferroptosis-related lncRNA-based model to improve the prognostic evaluation of gastric cancer patients based on bioinformatics," *Frontiers in Genetics*, vol. 12, Article ID 739470, 2021.

[22] R. Zhou, J. Liang, H. Tian, Q. Chen, C. Yang, and C. Liu, "Development of a ferroptosis-related lncRNA signature to predict the prognosis and immune landscape of bladder cancer," *Disease Markers*, vol. 2021, Article ID 1031906, 22 pages, 2021.

[23] T. Xu, W. Ding, X. Ji et al., "Molecular mechanisms of ferroptosis and its role in cancer therapy," *Journal of Cellular and Molecular Medicine*, vol. 23, no. 8, pp. 4900–4912, 2019.

[24] L. Chen, G. Ma, P. Wang et al., "Establishment and verification of prognostic model for gastric cancer based on autophagy-related genes," *American Journal of Cancer Research*, vol. 11, no. 4, pp. 1335–1346, 2021.

[25] W. Ma, F. Zhao, X. Yu et al., "Immune-related lncRNAs as predictors of survival in breast cancer: a prognostic signature," *Journal of Translational Medicine*, vol. 18, no. 1, p. 442, 2020.

[26] X. Zhang, J. Yu, J. Hu et al., "13-lncRNAs signature to improve diagnostic and prognostic prediction of hepatocellular carcinoma," *Combinatorial Chemistry & High Throughput Screening*, vol. 24, no. 5, pp. 656–667, 2021.

[27] Z. Li, D. Wang, and H. Yin, "A seven immune-related lncRNA signature predicts the survival of patients with colon adenocarcinoma," *American Journal of Tourism Research*, vol. 12, no. 11, pp. 7060–7078, 2020.

[28] M. Macheret and T. D. Halazonetis, "DNA replication stress as a hallmark of cancer," *Annual Review of Pathology: Mechanisms of Disease*, vol. 10, no. 1, pp. 425–448, 2015.

[29] Z. Wang, "ErbB receptors and cancer," *Methods in Molecular Biology*, vol. 1652, pp. 3–35, 2017.

[30] Y. Mou, J. Wu, Y. Zhang, O. Abdihamid, C. Duan, and B. Li, "Low expression of ferritinophagy-related NCOA4 gene in relation to unfavorable outcome and defective immune cells infiltration in clear cell renal carcinoma," *BMC Cancer*, vol. 21, no. 1, p. 18, 2021.

[31] R. Kebudi, A. Kiykim, and M. K. Sahin, "Primary immunodeficiency and cancer in children; a review of the literature," *Current Pediatric Reviews*, vol. 15, no. 4, pp. 245–250, 2019.

[32] W. C. Maccarty, "Longevity in cancer: a study of 293 cases," *Annals of Surgery*, vol. 76, no. 1, pp. 9–12, 1922.

[33] G. Husby, P. M. Hoagland, R. G. Strickland, and R. C. Williams Jr, "Tissue T and B cell infiltration of primary and metastatic cancer," *Journal of Clinical Investigation*, vol. 57, no. 6, pp. 1471–1482, 1976.

[34] A. N. Henning, R. Roychoudhuri, and N. P. Restifo, "Epigenetic control of CD8+ T cell differentiation," *Nature Reviews Immunology*, vol. 18, no. 5, pp. 340–356, 2018.

[35] Y. Xia, X.-T. He, X.-Y. Xu, B.-M. Tian, Y. An, and F.-M. Chen, "Exosomes derived from M0, M1 and M2 macrophages exert distinct influences on the proliferation and differentiation of mesenchymal stem cells," *PeerJ*, vol. 8, Article ID e8970, 2020.

Hindawi
Journal of Oncology
Volume 2022, Article ID 9282557, 6 pages
https://doi.org/10.1155/2022/9282557

Research Article

Single Nucleotide Polymorphism of Genes Associated with Metabolic Fatty Liver Disease

Tong Mu,[1] **Linrui Peng**,[1] **Xinglei Xie**,[1] **He He**,[2] **Qing Shao**,[1] **Xiran Wang**,[3] **and Yuwei Zhang**[1]

[1]*Department of Endocrinology and Metabolism, West China Hospital, Sichuan University, Chengdu 610041, China*
[2]*Department of Clinical Laboratory, West China Hospital, Sichuan University, Chengdu 610041, China*
[3]*Department of Preventive Medicine, Sichuan University, Chengdu 610041, China*

Correspondence should be addressed to Yuwei Zhang; doczhangyuwei@sina.com

Received 22 November 2021; Revised 5 January 2022; Accepted 13 January 2022; Published 3 February 2022

Academic Editor: Guo Chen

Aims. The present study aimed to reveal the relationship between single nucleotide polymorphism (SNP) of PNPLA3, TM6SF2, MBOAT7, GATAD2A, and STAT3 genes and metabolism-related fatty liver disease (MAFLD), so as to provide a research basis for further exploring the diagnosis and treatment of diseases at the molecular level. *Methods*. A total of 564 patients were included in the physical examination center of Xinjiang Karamay People's Hospital. They were divided into an MAFLD case group and a healthy control group. The whole blood DNA of each sample was extracted by a whole blood genomic DNA extraction kit, and the genotypes of PNPLA3 rs738409, MBOAT7 rs64173, STAT3 rs744166, TM6SF2 rs58542926, and GATAD2A rs4808199 were performed; after adjusting for confounding factors, the additive model, dominant model, and recessive model of each gene were analyzed by multivariate logistic regression. *Results*. The CC genotype of the PNPLA3 gene rs738409 and the TT genotype of the MBOAT7 gene rs64173 are risk factors in the occurrence of MAFLD. The AA genotype of the STAT3 gene rs744166 is a protective factor of MAFLD, while TM6SF2 rs58542926 and GATAD2A rs4808199 show no significant correlation with MAFLD.

1. Introduction

Metabolism-related fatty liver disease (MAFLD) is a clinicopathological syndrome characterized by diffuse hepatocyte steatosis and lipid storage without excessive drinking history. It may lead to a series of diseases, including steatohepatitis, liver fibrosis, and liver cirrhosis [1], which is a chronic metabolic disease seriously endangering human health. Clinically, the gold standard for the diagnosis of MAFLD is liver biopsy, which has a certain risk. For example, liver puncture may lead to bleeding at the puncture point, bleeding in the abdominal cavity, damage to the surrounding tissues and organs, causing liver injury, bile fistula, intrahepatic arteriovenous fistula, intrahepatic infection, abdominal infection, and puncture to the lungs causing pneumothorax. Therefore, it is particularly important to deeply explore the pathophysiological process of exploring and finding out possible biomarkers for the diagnosis of MAFLD.

MAFLD is a metabolic liver injury closely related to genetic susceptibility, which is related to single nucleotide polymorphisms at multiple related gene loci. Single nucleotide polymorphism (SNP) refers to the DNA sequence polymorphism caused by the change of a single nucleotide at the genomic level, mostly the conversion or transversion of a single base. MALFD is associated with multiple endogenous gene polymorphisms. A current study involving a large sample of European populations is based on genome-wide association analysis (GWAS) and identified five MAFLD susceptibility loci, which are located at or near GCKR, tr1b1, mau2/TM6SF2, ApoE, and PNPLA3, respectively [2]. However, we found that the correlation between TM6SF2 and PNPLA3 gene polymorphisms and MAFLD in the Chinese population is not consistent with that in the European and American populations. In addition to the abovementioned five loci, studies have found MBOAT7, STAT3, and GATAD2A gene polymorphisms may be

related to the liver lipid metabolism pathway [3–7]. However, there is no study on the correlation between these gene polymorphisms and MALFD in the Chinese population. Therefore, we selected the gene encoding patatin such as phospholipase domain protein 3 (PNPLA3) rs738409, transmembrane 6 superfamily 2 gene (TM6SF2) rs58542926, membrane bound o-acyltransferase domain 7 gene (MBOAT7) rs64173, signal transduction activating transcription factor-3 gene (STAT3) rs744166, and nuclear small body weight plastic deacetylase gene (GATAD2A) rs4808199, to explore the relationship between these gene loci and MAFLD.

The incidence rate of MAFLD in China's Xinjiang area is much higher than that of Han nationality due to its unique genetic background and special lifestyle [8]. Therefore, we intend to take the Karamay minority population in Xinjiang, China as the research object to explore the relationship between single nucleotide polymorphisms of PNPLA3, TM6SF2, MBOAT7, GATAD2A, and STAT3 genes and metabolic fatty liver, and to explore the mechanism of the abovementioned gene loci affecting the occurrence and development of MAFLD, so as to provide a basis for early diagnosis and individualized early prevention, and a research basis for further exploring the diagnosis and treatment of diseases at the molecular level in the modern medical model.

2. Methods

2.1. Subjects and Clinical Criteria. 564 patients were divided into two groups: the case group and the healthy control group. They are all 28–67 years old and have lived in the Karamay area for more than 10 years. The case group was the patients with MAFLD in Karamay City, Xinjiang, whose weight was stable three months before the start of the study and did not take liver protective drugs and were diagnosed as MAFLD according to imaging examination or pathological biopsy. On the other hand, the control group consisted of normal people without abnormalities in imaging and hematology. The age, sex, nationality, and region of the control group were matched with those of the case group. The exclusion criteria were as follows: history of excessive drinking (alcohol consumption equivalent to more than 30 g/*D* for men and more than 20 g/*D* for women), specific liver diseases (such as genotype 3 HCV infection, autoimmune hepatitis, and hepatolenticular degeneration), drug effects (such as tamoxifen, amiodarone, sodium valproate, methotrexate, and glucocorticoid), total parenteral nutrition, inflammatory bowel disease, celiac disease, hypothyroidism, Cushing's syndrome, β-lipoprotein deficiency, lipoatrophy, diabetes, and so on. Next, data were collected, including general information (such as name, nationality, age, gender, height, weight, BMI, smoking history, drinking history, medication history, and past medical history), biochemical indicators (such as fasting blood glucose, triglyceride, cholesterol, high-density lipoprotein, low-density lipoprotein, aspartate aminotransferase, alanine aminotransferase, direct bilirubin, indirect bilirubin, albumin, and uric acid), and liver B-ultrasound results.

The severity of hepatotoxicity was classified according to the WHO toxicity classification standards (Grade 1 (mild), ALT < 2.5 ULN; Grade 2 (mild), ALT 2.5–5 ULN; Grade 3 (moderate), ALT 5–10 ULN; and Grade 4 (severe), ALT > 10 ULN) [9], and different clinical patterns were categorized into hepatocellular, cholestatic, and mixed liver injury based on the *R* value, where $R = (\text{ALT/ULN})/(\text{ALP/ULN})$ (ALP, alkaline phosphatase) [10].

2.1.1. Genomic DNA Extraction and Genotyping. A whole blood genomic DNA extraction kit was used to extract whole blood DNA. Primer3 online, Oligo, GeneMapper, SHEsis, and other software were used to design PCR amplification primers and the single-base extension primers for the polymorphic sites to be tested. Multiplex PCR technology and single-base extension technology were combined for genotyping detection.

2.1.2. Statistical Analysis. Unless stated otherwise, all statistical analyses were performed with SPSS 20.0 (SPSS, Munich, Germany) or GraphPad Prism 5.0 (GraphPad Software Inc., CA, USA). Quantitative data were expressed as medians and ranges. Exact tests were performed to check the consistency of genotyping results with Hardy–Weinberg equilibrium (HWE). Under the additive, dominant, and recessive genetic models, linear regression was used to analyze the correlation between each gene locus and MAFLD. All models were adjusted for confounding factors.

3. Results

3.1. Demographical and Clinical Data. Among the 282 ATLI cases, a total of 110 (39.0%) ATLI cases had Grade 1 (mild) hepatotoxicity, 107 (37.9%) had Grade 2 (mild) hepatotoxicity, 46 (16.3%) had Grade 3 (moderate) hepatotoxicity, and 19 (6.8%) had Grade 4 (severe) hepatotoxicity. There were no significant differences in the baseline characteristics of the two groups except for weight, BMI, and triglycerides (Table 1).

3.2. Genotype Analysis. Hardy–Weinberg equilibrium tests demonstrated no significant deviation from the expected values for the five tagSNPs among the controls (rs738409, $\chi^2 = 1.137$, $P = 0.478$; rs641738, $\chi^2 = 0.340$, $P = 0.286$; rsrs744166, $\chi^2 = 0.938$, $P = 0.130$; rs58542926, $\chi^2 = 0.503$, $P = 0.560$; and rsrs4808199, $\chi^2 = 0.013$, $P = 0.338$) (Table 2).

3.3. Gene Single Nucleotide Polymorphism and MAFLD. After correcting for potential confounding factors, conditional logistic regression analysis (Table 3) showed that patients carrying the CC genotype at rs738409 in PNPLA3 were at a higher risk of MAFLD than those with the GG and GC genotypes (adjusted OR = 1.402, 95% CI: 1.026–2.239, $P = 0.033$), and significant differences were also found under the recessive ($P = 0.016$) and additive models ($P = 0.046$). The TT genotype of MBOAT7 rs64173 was a risk factor in the occurrence of MAFLD ($P = 0.02$), while the AA genotype of

Table 1: Characteristics of patients in MAFLD cases and controls.

Characteristic	MAFLD cases ($n = 282$)	Controls ($n = 282$)	P value
Gender (male/female)	145/137	142/140	—
Age (y)	47.8 ± 19.1	47.7 ± 19.0	0.868
Weight (kg)	57.3 ± 10.6	55.8 ± 10.0	0.004
BMI (kg/m^2)	24.83 (18.61–30.47)	20.12 (18.51–23.80)	0.018
Glycosylated hemoglobin (%)	5.6 (4.6–8.1)	5.3 (4.0–6.0)	0.067
ALT (U/L)	19.0 (7.0–79.0)	16.0 (5.0–31.0)	0.090
AST (U/L)	22.0 (10.0–82.0)	20.0 (17.0–27.0)	0.053
Triglycerides (mmol/L)	1.79 (0.66–5.38)	1.09 (0.38–1.60)	0.048
Cholesterol (mmol/L)	3.31 (1.69–8.33)	2.82 (0.87–4.78)	0.749
Low-density lipoprotein (mmol/L)	2.96 (0.99–7.17)	2.51 (0.19–3.19)	0.690

Table 2: Information on five tagSNPs.

Gene	tagSNPs	Chromosome position	Base change	HWE P value
PNPLA3	rs738409	35777618	$G > C$	0.478
MBOAT7	rs641738	45782513	$C > T$	0.286
STAT3	rs744166	11307603	$G > A$	0.130
TM6SF2	rs58542926	55786873	$C > T$	0.560
GATAD2A	rs4808199	69743760	$G > A$	0.338

Table 3: Genotypes distribution in two groups and the risks of MAFLD.

Gene	tagSNPs	Cases ($n = 282$)		Controls ($n = 282$)		OR (95% CI)	P value	Model	OR (95% CI)	P value
		n	%	n	%					
PNPLA3	rs738409 ($G > C$)									
	GG	56	19.9	68	24.1	1.000		Dom	1.160 (0.824–1.615)	0.424
	GC	152	53.9	161	57.1	1.006 (0.713–1.447)	0.859	Rec	1.492 (1.080–2.066)	0.016
	CC	74	26.2	53	18.8	1.402 (1.026–2.239)	0.033	Add	1.232 (1.003–1.504)	0.046
MBOAT7	rs64173 ($C > T$)									
	CC	53	18.8	64	22.7	1.000		Dom	1.018 (0.778–1.459)	0.848
	CT	159	56.4	167	59.2	1.003 (0.742–1.359)	0.979	Rec	1.398 (1.053–1.692)	0.032
	TT	70	24.8	51	18.1	1.299 (0.933–1.748)	0.040	Add	1.038 (0.856–1.259)	0.061
STAT3	rs744166 ($G > A$)									
	GG	55	19.5	69	24.5	1.000		Dom	1.193 (0.957–1.491)	0.398
	GA	150	53.2	159	56.4	1.223 (0.842–1.573)	0.947	Rec	0.682 (0.372–1.195)	0.019
	AA	77	27.3	54	19.1	0.738 (0.469–1.201)	0.026	Add	1.004 (0.894–1.356)	0.059
TM6SF2	rs58542926 ($C > T$)									
	CC	60	21.3	71	25.2	1.000		Dom	0.973 (0.765–1.320)	0.883
	CT	155	54.9	146	51.8	1.005 (0.782–1.392)	0.969	Rec	0.915 (0.657–1.280)	0.615
	TT	67	23.8	65	23.0	0.928 (0.631–1.336)	0.655	Add	0.952 (0.792–1.169)	0.699
GATAD2A	rs4808199 ($G > A$)									
	AA	54	19.1	42	14.9	1.000		Dom	1.042 (0.769–1.415)	0.789
	AG	164	58.2	162	57.4	0.980 (0.719–1.364)	0.957	Rec	1.687 (0.734–3.897)	0.217
	GG	64	22.7	78	27.7	1.678 (0.719–3.883)	0.218	Add	1.088 (0.836–1.416)	0.536

STAT3 rs744166 can serve as a protective factor in the occurrence of MAFLD ($P = 0.016$). TM6SF2 and GATAD2 had no significant correlation with the occurrence of MAFLD. However, no other significant differences in the genotypes of the remaining genes were observed between patients and healthy controls.

3.4. Subgroup Analysis. According to the extended subgroup analysis of liver injury severity, risk related tagSNP-PNPLA3 rs738409 was still a risk factor in Grade 1 and Grade 2 (mild) cases under implicit and additive models (or = 1.614, $P = 0.009$; or = 1.279, $P = 0.038$), but there was no correlation in Grade 3 and Grade 4 (moderate and severe) cases ($P > 0.05$) (Table 4).

4. Discussion

As a common chronic disease, the pathogenesis of metabolism-related fatty liver disease has not been clearly determined. Current studies mostly believe that it is the result of multiple factors such as polygenic genetic variation and the environment. In a European population study of 423252 people, the researchers constructed a polygenic risk score (GRS) related to metabolism-related fatty liver disease. It was found that a higher GRS can significantly amplify the risk of MAFLD for

Table 4: Subgroup analysis among different severity of hepatotoxicity with different genetic models.

Genes	tagSNPs	Model	Grade 4 and 3 ($n = 65$) OR (95% CI)	P value	Grade 2 and 1 ($n = 217$) OR (95% CI)	P value
PNPLA3	rs738409 ($G > C$)					
	GG	Dom	1.198 (0.482–2.479)	0.683	1.121 (0.685–1.633)	0.507
	GC	Rec	1.052 (0.581–1.876)	0.749	1.614 (1.156–2.506)	0.009
	CC	Add	1.079 (0.754–1.732)	0.738	1.279 (1.010–1.628)	0.038
MBOAT7	rs64173 ($C > T$)					
	CC	Dom	0.796(0.373–1.919)	0.683	0.787 (0.463–1.349)	0.298
	CT	Rec	–	–	2.013 (0.115–5.97)	0.654
	TT	Add	0.861 (0.392–1.896)	0.687	0.830 (0.519–1.316)	0.438
STAT3	rs744166 ($G > A$)					
	GG	Dom	1.417 (0.812–2.389)	0.221	1.219 (0.891–1.672)	0.229
	GA	Rec	0.827 (0.355–1.863)	0.675	1.464 (0.862–2.483)	0.150
	AA	Add	1.152 (0.891–1.810)	0.488	1.217 (0.961–1.533)	0.135
TM6SF2	rs58542926 ($C > T$)					
	CC	Dom	1.011 (0.524–1.838)	0.921	0.885 (0.629–1.252)	0.518
	CT	Rec	0.787 (0.376–1.632)	0.528	1.062 (0.729–1.537)	0.886
	TT	Add	0.954 (0.662–1.399)	0.792	0.973 (0.772–1.219)	0.769
GATAD2A	rs4808199 ($G > A$)					
	AA	Dom	0.618 (0.345–1.096)	0.095	1.215 (0.885–1.669)	0.266
	AG	Rec	1.122 (0.519–2.481)	0.789	1.090 (0.712–1.683)	0.693
	GG	Add	0.816 (0.540–1.226)	0.316	1.125 (0.896–1.387)	0.392

liver-related diseases, and the risk is further amplified with age [11]. This suggests that there is a close correlation between metabolism-related fatty liver disease and endogenous genes.

With the upgrading of gene screening methods and the development of human genome projects, whole genome scanning (GWAS) is widely used in the related gene screening of MAFLD, promoting the diagnosis of diseases, the development of new drugs, and the exploration of new therapies. Among them, single nucleotide polymorphism, that is, the study of single nucleotide substitution in the genome, plays an increasingly important role in gene mapping and association analysis of complex diseases. The latest genome-wide analysis results show that in 770180 case-control studies, researchers have identified five MAFLD susceptibility loci through genome-wide meta-analysis, which are located in GCKR, tr1b1, mau2/TM6SF2, and ApoE, respectively, and PNPLA3 [2]. However, the correlation between TM6SF2 and PNPLA3 gene polymorphisms and MAFLD in the Chinese population is different from that in the European population. According to a study of 1200 Chinese people, the CC genotype of PNPLA3 rs738409 is a risk factor for MAFLD ($P = 0.046$) [12], while the GC genotype is more prone to MAFLD than the CC genotype in the European population [3, 13]. We know that most of the more than 100 loci identified by GWAS are found in the European population, while the weight of different loci is different in various ethnic groups [14]. Therefore, the correlation between TM6SF2 and PNPLA3 gene polymorphisms and MAFLD still needs to be improved in the Chinese population with the help of a lot of evidence-based medical evidence.

In our study, taking fatty liver as the dependent variable and adjusting body weight, BMI, and other factors, multivariate logistic analysis was carried out on the additive model, dominant model, and recessive model of each gene. The CC gene of PNPLA3 is a risk factor in the occurrence of MAFLD, and the TT gene of MBOAT7 carries out the same job. The AA gene of STAT3 is a risk factor in the occurrence of MAFLD, while TM6SF2 and GATAD2A have no significant correlation with the occurrence of fatty liver.

Based on the abovementioned results, our study shows that PNPLA3, MBOAT7, and STAT3 affect the occurrence and development of MAFLD. The PNPLA3 gene mutation is associated with increased transaminase activity, which can promote the progression of liver fibrosis and steatosis [15–17]. MBOAT7 can catalyze the desaturation of the second acyl chain of phospholipids and transfer polyunsaturated fatty acids [18]. STAT3 plays a key role in the process of leptin resistance, and high leptin levels may be related to the increase of nonalcoholic fatty liver disease [19]. In addition, STAT3 is downregulated in atherosclerotic lesions of ApoE -/- mice. Its forced overexpression can reduce inflammation, lipid accumulation, and vascular smooth muscle cell proliferation, indicating that it has atherosclerotic protective function [20]. TM6SF2 and GATAD2A are also related to MAFLD in foreign studies [21, 22], but they are not related in our study of Xinjiang ethnic minorities.

The PNPLA3 gene is a member of the non-Ca2 + − dependent patatin like phospholipase family on chromosome 22 [23]. The protein encoded by the PNPLA3 gene is a nonsecretory protein adiponutrin composed of 481 amino acids. It is a four times transmembrane protein, which mainly exists on the cell membrane and cytoplasmic lipid droplets [24]. PNPLA3 is a genetic variation highly related to the occurrence and development of MAFLD. Studies have shown that GG homozygous variants in European populations increase the risk of HCC associated with MAFLD by 10 times [25]. Interestingly, PNPLA3 carriers have a

significantly increased risk of cirrhosis and hepatocellular carcinoma, independent of the tendency to steatosis. This indicates that PNPLA3 is directly involved in the process of fiber formation and carcinogenesis [26].

In 2015, MBOAT7rs641738 was first found to be closely associated with metabolic cirrhosis in a European study including 1148 patients with metabolic cirrhosis and 922 healthy controls. Researchers from the European Dallas Research Center genotyped MBOAT7rs641738 in 1149 patients who underwent liver biopsy. The results showed that the MBOAT7rs641738 polymorphism was associated with liver fat content, and patients with *T* allele were at greater risk of serious liver injury and fibrosis. In individuals with a site mutation, the expression of MBOAT7 was downregulated at mRNA and protein levels, and the levels of phosphatidylinositol in hepatocytes and circulating blood were also changed [27]. Researchers from Italy found that carrying the MBOAT7 T allele is an independent risk factor for MAFLD related liver cancer [28]. Contrary to the abovementioned population studies, the study from Taiwan children in China detected the MBOAT7rs641738 gene polymorphism in 831 obese MAFLD children aged 7~15. The results showed that the MBOAT7rs641738 gene polymorphism was associated with steatohepatitis, insulin resistance, and blood lipid levels. There was no significant correlation between liver enzyme levels and serum CK18 levels [29]. The results of this study showed that TT genotype at the MBOAT7rs641738 locus increased the risk of MAFLD, which was consistent with the data of the European population.

In our study, STAT3 gene polymorphism was associated with MAFLD. The activation of STAT3 eventually leads to cytokine signal inhibitor-3 (SOCS-3) playing a feedback inhibitory role by weakening the OBRb signal and plays a key role in leptin resistance in part by binding tyr985 [30]. Leptin is considered to be an antitear hormone, which can protect nonadipose tissues including the liver, from fat accumulation and fat toxicity. However, in the state of insulin resistance, including obesity, it is not only high and thin. The protective effect of leptinemia seems to be limited, and hyperleptinemia may have adverse effects, thus promoting insulin resistance, hepatic steatosis, inflammation, fibrosis, and carcinogenesis.

In summary, MAFLD is a complex disease related to genetic, environmental, and metabolic stress. Its pathogenesis is affected by many factors, such as genetics, environment, immunity, nutrition, and so on [31, 32]. By affecting lipid metabolism, inflammatory response, insulin resistance, oxidative stress, liver fibrosis and other processes, gene polymorphism, and epigenetics can regulate the susceptibility and progression of MAFLD [33]. Gene polymorphism provides ideas for the early diagnosis and targeted therapy of MAFLD and provides a theoretical basis for the creation and secondary development of new drugs.

Data Availability

The datasets used and/or analyzed during the current study are available from the corresponding author on reasonable request.

Consent

Patients have provided informed consent for the publication of the case.

Conflicts of Interest

The authors declare that they have no conflicts of interest.

Acknowledgments

This work was supported by the Contract for special project of scientific and technological cooperation and exchange in Karamay (2018hz004a).

References

[1] P. Bedossa, "Pathology of non-alcoholic fatty liver disease," *Liver International*, vol. 37, no. 1, pp. 85–89, 2017.

[2] N. Ghodsian, E. Abner, C. A. Emdin et al., "Electronic health record-based genome-wide meta-analysis provides new insights on the genetic architecture of non-alcoholic fatty liver disease," *SSRN Electronic Journal*, vol. 2, 2021.

[3] S. Romeo, J. Kozlitina, C. Xing et al., "Genetic variation in PNPLA3 confers susceptibility to nonalcoholic fatty liver disease," *Nature Genetics*, vol. 40, no. 12, pp. 1461–1465, 2008.

[4] G. Dai, P. Liu, X. Li, X. Zhou, and S. He, "Association between PNPLA3rs738409 polymorphism and nonalcoholic fatty liver disease(NAFLD) susceptibility and severity," *Medicine(Baltimore)*, vol. 98, Article ID e14324, 2019.

[5] M. Eslam, L. Valenti, and S. Romeo, "Genetics and epigenetics of NAFLD and NASH: clinical impact," *Journal of Hepatology*, vol. 68, no. 2, pp. 268–279, 2018.

[6] J. Del Campo, R. Gallego-Durán, P. Gallego, and L. Grande, "Genetic and epigenetic regulation in nonalcoholic fatty liver disease (NAFLD)," *International Journal of Molecular Sciences*, vol. 19, no. 3, p. 911, 2018.

[7] K. H. Jung, W. Yoo, H. L. Stevenson et al., "Multifunctional effects of a small-molecule STAT3 inhibitor on NASH and hepatocellular carcinoma in mice," *Clinical Cancer Research*, vol. 23, no. 18, pp. 5537–5546, 2017.

[8] D. Jiang, H. Zhiyi, X. Cailan et al., "Prevalence and influencing factors of non obese fatty liver," *Journal of clinical hepatobiliary diseases*, vol. 37, no. 11, p. 5, 2021.

[9] WHO, *TheUse of the WHO-UMC System for Standardized Case Causality Assessment* WHO, Uppsala, Sweden, 2005.

[10] C. Bénichou, "Criteria of drug-induced liver disorders. Report of aninternational consensus meeting," *Journal of Hepatology*, vol. 11, no. 2, pp. 272–276, 1990.

[11] Z. Liu, C. Suo, O. Shi et al., "The health impact of MAFLD, a novel disease cluster of NAFLD, is amplified by the integrated effect of fatty liver disease related genetic variants," *Clinical Gastroenterology and Hepatology*, vol. 20, 2020.

[12] N. Baoshuo, "Effect of PNPLA3 on lipid metabolism of hepatocytes and hepatoma cells," *Journal of practical Hepatology*, vol. 2, pp. 300–304, 2020.

[13] L. Shang and D. G. Mashek, "The underpinnings of PNPLA3-mediated fatty liver emerge," *Hepatology*, vol. 71, pp. 375–377, 2020.

[14] D. Paola, R. Stefano, and V. Luca, "Genetic factors in the pathogenesis of nonalcoholic fatty liver and steatohepatitis," *BioMed Research International*, vol. 2015, Article ID 460190, 2015.

[15] F. N. Mazzini, F. Cook, J. Gounarides et al., "Plasma and stool metabolomics to identify microbiota derived-biomarkers of metabolic dysfunction-associated fatty liver disease: effect of PNPLA3 genotype," *Metabolomics*, vol. 17, no. 7, pp. 1–13, 2021.

[16] Y. C. Lin, C. C. Wu, and Y. H. Ni, "New perspectives on genetic prediction for pediatric metabolic associated fatty liver disease," *Frontiers in Pediatrics*, vol. 8, 2020.

[17] Y.-L. Liu, G. L. Patman, J. B. S. Leathart et al., "Carriage of the PNPLA3 rs738409 C >G polymorphism confers an increased risk of non-alcoholic fatty liver disease associated hepatocellular carcinoma," *Journal of Hepatology*, vol. 61, no. 1, pp. 75–81, 2014.

[18] R. M. Mancina, P. Dongiovanni, S. Petta et al., "The MBOAT7-TMC4 variant rs641738 increases risk of nonalcoholic fatty liver disease in individuals of European descent," *Gastroenterology*, vol. 150, no. 5, pp. 1219–1230, 2016.

[19] S. A. Polyzos, J. Kountouras, C. Zavos, and G. Deretzi, "The potential adverse role of leptin resistance in nonalcoholic fatty liver disease: a hypothesis based on critical review of the literature," *Journal of Clinical Gastroenterology*, vol. 45, no. 1, pp. 50–54, 2011.

[20] N. K. Saxena, D. Sharma, X. Ding et al., "Concomitant activation ofthe JAK/STAT, PI3K/AK,and ERK signaling is involved in leptin-mediated promotion of invasion and migration of hepatocellular carcinoma cells," *Cancer Research*, vol. 67, no. 6, pp. 2497–2507, 2007.

[21] J. Kozlitina, E. Smagris, S. Stender et al., "Exome-wide association study identifies a TM6SF2 variant that confers susceptibility to nonalcoholic fatty liver disease," *Nature Genetics*, vol. 46, 2014.

[22] E. A. O'Hare, R. Yang, L. M. Yerges-Armstrong et al., "TM6SF2 rs58542926 impacts lipid processing in liver and small intestine," *Hepatology*, vol. 65, 2017.

[23] M. Hoekstra, Z. Li, J. K. Kruijt, M. V. Eck, T. J. Berkel, and J. Kuiper, "The expression level of non-alcoholic fatty liver disease-related gene PNPLA3 in hepatocytes is highly influenced by hepatic lipid status," *Journal of Hepatology*, vol. 52, no. 2, pp. 244–251, 2010.

[24] S. Sookoian and C. Pirola, "PNPLA3,the triacylglycerol synthesis/hydrolysis/storage dilemma, and nonalcoholic fatty liver disease," *World Journal of Gastroenterology*, vol. 18, 2012.

[25] E. Scorletti, A. L. West, L. Bhatia et al., "Treating liver fat and serum triglyceride levels in NAFLD, effects of PNPLA3 and TM6SF2 genotypes: Results from the WELCOME trial," *Journal of Hepatology*, vol. 63, 2015.

[26] J. P. Mann and Q. M. Anstee, "NAFLD: PNPLA3 and obesity: a synergistic relationship in NAFLD," *Nature Reviews Gastroenterology & Hepatology*, vol. 14, pp. 506-507, 2017.

[27] S. Buch, F. Stickel, E. Trépo et al., "A genome-wide association study confirms PNPLA3 and identifies TM6SF2 and MBOAT7 as risk loci for alcohol-related cirrhosis," *Nature Genetics*, vol. 47, no. 12, pp. 1443–1448, 2015.

[28] P. K. Luukkonen, Y. Zhou, T. Hyötyläinen et al., "The MBOAT7 variant rs641738 alters hepatic phosphatidylinositols and increases severity of non-alcoholic fatty liver disease in humans," *Journal of Hepatology*, vol. 65, no. 6, pp. 1263–1265, 2016.

[29] B. Donati, P. Dongiovanni, S. Romeo et al., "MBOAT7 rs641738 variant and hepatocellular carcinoma in non-cirrhotic individuals," *Scientific Reports*, vol. 7, no. 1, p. 4492, 2017.

[30] B. Laura, C. S. Di, G. Francesca et al., "Targeting a phospho-STAT3-miRNAs pathway improves vesicular hepatic steatosis in an in vitro and in vivo model," *Scentific Reports*, vol. 8, no. 1, 2018.

[31] J. Voisey and C. P Morris, "SNP technologies for drug discovery: a current review," *Current Drug Discovery Technologies*, vol. 5, pp. 230–5, 2008.

[32] N. Chalasani, Z. Younossi, J. E. Lavine et al., "The diagnosis and management of non-alcoholic fatty liver disease: practice guideline by the American association for the study of liver diseases, American college of gastroenterology, and the American gastroenterological association," *Hepatology*, vol. 55, no. 6, pp. 2005–2023, 2012.

[33] A. Naik, R. Košir, and D. Rozman, "Genomic aspects of NAFLD pathogenesis," *Genomics*, vol. 102, no. 2, pp. 84–95, 2013.

Hindawi
Journal of Oncology
Volume 2022, Article ID 2559258, 23 pages
https://doi.org/10.1155/2022/2559258

Research Article

Inflammation-Related Gene Signature: An Individualized Risk Prediction Model for Kidney Renal Clear Cell Carcinoma

Ze Zhang,[1] Yan-Yan Wei,[1] Qiong-Mei Guo,[1] Chang-Hao Zhou,[1] Nan Li,[2] Jin-Fang Wu,[2] Ya-Ting Li,[3] Wei-Wei Gao ,[1] and Hui-Li Li [1]

[1]*Department of Anesthesiology, The First Hospital of Hebei Medical University, Shijiazhuang, Hebei, China*
[2]*Department of Operating Room, The First Hospital of Hebei Medical University, Shijiazhuang, Hebei, China*
[3]*Pharmacy Intravenous Admixture Services, The First Hospital of Hebei Medical University, Shijiazhuang, Hebei, China*

Correspondence should be addressed to Wei-Wei Gao; gaoweiwei@hebmu.edu.cn and Hui-Li Li; 413732827@qq.com

Received 23 November 2021; Revised 21 December 2021; Accepted 22 December 2021; Published 31 January 2022

Academic Editor: Fu Wang

Background. There is much evidence that confirms the inextricable link between inflammation and malignancy. Inflammation-related regulators were involved in the progression of kidney renal clear cell carcinoma (KIRC). However, the predictive role of single gene biomarkers is inadequate, and more accurate prognostic models are necessary. We undertook the current research to construct a robust inflammation-related gene signature that could stratify patients with KIRC. *Methods*. The transcriptome sequencing data along with clinicopathologic information of KIRC were obtained from TCGA. A list of inflammation-related genes was acquired from the Molecular Signatures Database. Using the RNA-seq and survival time data from the TCGA training cohort, an inflammation-related gene signature was built using bioinformatic methods, and its performance in predicting patient prognosis was assessed by Kaplan–Meier and ROC curve analyses. Furthermore, we explored the association of risk score with immune score, stromal score, tumor immune-infiltrating cells (TIICs), immunosuppressive molecules, m6A regulators, and autophagy-related biomarkers. *Results*. Herein, nine inflammation-related hub genes (ROS1, PLAUR, ACVR2A, KLF6, GABBR1, APLNR, SPHK1, PDPN, and ADORA2B) were determined and used to build a predictive model. All sets, including training set, four testing sets, and the entire TCGA group, were divided into two groups (low and high risk), and Kaplan–Meier curves all showed an adverse prognosis for patients in the high-risk group. ESTIMATE algorithm revealed a higher immune score in the high-risk subgroup. CIBERSORT algorithm illustrated that the high-risk group showed higher-level immune infiltrates. Furthermore, LAG3, TIGIT, and CTLA4 were overexpressed in the high-risk subgroup and positively associated with risk scores. Moreover, except for METTL3 and ALKBH5, the other m6A regulators decreased in the high-risk subgroup. *Conclusions*. In conclusion, a novel inflammation-related gene signature comprehensively constructed in the current study may help stratify patients with KIRC.

1. Introduction

Kidney renal clear cell carcinoma (KIRC) is the most lethal urological tumor and its incidence and mortality are increasing yearly [1]. Radical surgery is the preferred treatment of limited renal clear cell carcinoma. Then, 20–40% of patients in the early stages eventually develop metastatic KIRC. Moreover, approximately 30% of patients with renal clear cell carcinoma have a metastasis initial diagnosis due to insidious onset [2]. Unlike other advanced malignancies, advanced renal clear cell carcinoma is resistant to conventional radiotherapy, and although the advent of targeted drugs such as tyrosine kinase and mTOR pathway inhibitors has enhanced the long-term survivals for several patients, the clinical outcome for most patients remains poor due to the presence of toxic side effects and the emergence of drug resistance [3, 4].

The link between cancer and inflammation has been explored extensively since it was discovered in the 19th century. Several lines of evidence suggest that tumors usually occur in the site of chronic inflammation and inflammatory cells exist in the biopsy of tumor [5]. Researchers found that

inflammation mediators and cellular effects are essential components of the local tumor environment [6]. In several types of cancer, inflammation exists prior to the development of malignant changes. In contrast, carcinogenic changes in other types of cancer can induce an inflammatory microenvironment and promote tumor progress [7]. Whatever its origin, the inflammation in the tumor microenvironment has many tumorigenesis effects. It not only accelerates tumor progression by promoting the proliferation, angiogenesis, and metastasis, but also disrupts adaptive immune responses and makes tumor cells tolerant to hormones and chemotherapy drugs. This cancer-related inflammatory molecular pathway is now being uncovered [8]. Balkwill et al. [9] have revealed that the invasion ability of neoplastic cells is increased in the presence of inflammatory cytokines. Tan et al. [10] have shown that inflammation-related genes might serve as important prognostic biomarkers for assessing recurrence risk (GADD45G) and death (CARD9, CIITA, and NCF2) in patients with KIRC. At present, some therapeutic drugs for inflammatory cytokines are being developed and tested in clinical practice [11], suggesting that targeting inflammation-related genes is a promising cancer therapy.

As mentioned above, targeting inflammation-related biomarkers may be a promising novel choice for tumor treatment. A large number of inflammation-related regulators are associated with the KIRC progression; however, cancer is a disease caused by the combined involvement of multiple genes and pathways. Given the limitations of a single biomarker, we screened multiple inflammation-related genes for prognostic relevance and constructed a gene signature for risk stratification and prognostic assessment of patients. Herein, we aim to develop an inflammation-related lncRNA model to predict the survival outcomes of patient with KIRC. We used the TCGA database to develop and validated the individualized prognostic signature for KIRC based on inflammation-related genes. Combined with the inflammation-related genes with clinical variables, we construct a comprehensive gene model that could assess the prognosis of patients with KIRC.

2. Materials and Methods

2.1. Data Collection. RNA-Seq gene expression data for KIRC was downloaded from the TCGA database (https://portal.gdc.cancer.gov/), called TCGA-KIRC. The reads per map per million base pairs (FPKM) counts and fragment counts per thousand transcripts were downloaded for further analysis. We finally obtained RNA sequencing data from 530 patients with complete clinical information and their clinicopathological data.

2.2. Identification of Differentially Expressed Inflammation-Related Genes (DE-IFRGs). A comprehensive list of inflammation-related genes (IFRGs) was retrieved from the hallmark gene sets from the Molecular Signatures Database v7.4 (http://www.gsea-msigdb.org/gsea/msigdb/index.jsp), which consists of 200 IFRGs. The "limma" *R* package and the Wilcoxon test method were used to identify the DE-IFRGs with an adjusted $P < 0.05$ between KIRC and adjacent normal renal tissues. The "pheatmap" *R* package was employed to visualize the degree range of differences in the TCGA-KIRC datasets.

2.3. Gene Ontology (GO) and Kyoto Encyclopedia of Genes and Genomes (KEGG). To reveal the potential biological functions and underlying action mechanisms of DE-IFRGs, we conducted the GO and KEGG analyses applying the "clusterProfiler" *R* package [12]. Functional enrichment items were considered as "functional" when the false discovery rate (FDR) <0.05.

2.4. Building and Verifying a Prognostic Inflammation-Related Gene Signature. According to the ratio of 6 : 1 : 1 : 1 : 1, all patients were randomly randomized into five cohorts, including training set ($n = 320$), testing-1 set ($n = 53$), testing-2 set ($n = 52$), testing-3 ($n = 52$), and testing-4 set ($n = 53$). Firstly, using the data from the training set, prognosis-related DE-IFRGs were selected by the univariate Cox analysis ($P < 0.001$). Then, we further reduce the amount of genes using the LASSO regression analysis to prevent overfitting. Finally, multivariate assays were conducted to identify the hub IFRGs and build a prognostic signature. We then calculate the risk score for each KIRC patient using the following formula: exp gene 1 * β gene 1 + exp gene 2 * β gene 2 + exp gene 3 * β gene 3 + . . . exp gene n * β gene n. Furthermore, patients in all sets as well as the entire TCGA set were classified into low- and high-risk subgroups according to the median risk score of the training set. Then, survival assays were conducted. ROC assays were utilized to measure the predictive capability of the prognostic model.

2.5. Evaluation of the Risk Signature. Uni- and multivariate Cox regression analyses were conducted to select the independent prognostic factors. Besides, the associations between risk scores and clinical features of patients were studied. Then, we construct a nomogram consisting of independent prognostic factors to predict the OS of KIRC patients. Calibration curve was employed to compare the differences between predicted OS and actual OS. In addition, we compared the differences in the ability of risk model as well as clinicopathological variables to assess patient prognosis.

2.6. Functional Enrichment Analysis. Differentially expressed genes (DEGs) between the high- and low-risk subgroups were identified using the "limma" *R* package. Genes with $|\log2FC| \geq 1$, FDR <0.05 were considered differentially expressed. Then, GO and KEGG assays based on these DEGs were carried out applying the "clusterProfiler" *R* package [12].

2.7. Evaluation of the Tumor Microenvironment (TME) and Tumor Infiltrated Immune Cells (TIICs). The ESTIMATE algorithm was used to evaluate scores representative of the relative proportion of immune and stromal cells. Furthermore, we further compared the difference of immune and stromal scores between high- and low-risk subgroups by the Wilcoxon test. Additionally, to analyze the relationships between risk score and TIICs, the content of TIICs was calculated using the CIBERSORT algorithm (http://cibersort.stanford.edu/).

2.8. Association of Risk Score with Immunosuppressive Molecule, m6A Regulators, and Autophagy-Related Biomarkers. Considering immune checkpoint inhibitors (ICIs) were clinically employed to treat KIRC, we evaluated the association between risk score with ICI-related regulators. m6A regulators and autophagy-related biomarkers were closely related to cancer progression; we thus evaluated the correlation between risk score and m6A regulators as well as autophagy-related biomarkers.

2.9. Statistical Analysis. All statistical analyses were carried out using *R* (version 3.6.1). Univariate, LASSO, and multivariate assays were used to select the prognostic genes and develop a gene signature. The Kaplan–Meier analysis was applied to show the survival difference. ROC assays were applied to estimate the predictive performance of the risk model. The independent prognostic factors were determined applying multivariate assays. Wilcoxon's test and Pearson's correlation methods were utilized to evaluate the association of risk score with TME, TIICs, ICI-related regulators, m6A regulators, and autophagy-related biomarkers. *P*-value <0.05 was considered statistically significant.

3. Results

3.1. Data Preparation. The detailed workflow flowchart of this study is listed in Figure 1. The transcriptome profiles and clinical information of 530 patients with KIRC were publicly downloaded from the TCGA database. We then randomly divided all patients into the training set ($n = 320$), testing-1 set ($n = 53$), testing-2 set ($n = 52$), testing-3 ($n = 52$), and testing-4 set ($n = 53$). Data from the training set was used to choose prognosis-related hub IFRGs and construct a risk signature. Simultaneously, data from testing-1, testing-2, testing-3, and testing-4 sets as well as the entire group was utilized to demonstrate the capability of the risk score.

3.2. Identification of DE-IFRGs. The "limma" *R* package was employed to screen the differentially expressed DE-IFRGs between KIRC samples and normal renal specimens. Herein, 177 dysregulated genes were identified, of which 46 were downregulated, and 131 were upregulated (Figure 2(a)). Figure 2(b) shows the top ten up- and downregulated IFRGs in KIRC. Additionally, we calculate the Pearson coefficients DE-IFRGs, and Figure 2(c) showed a strongly correlated DE-IFRGs association map (cor > 0.8 and $P < 0.05$), of which the strongest correlations were found between CXCL11 and CXCL10, LTA and LCK, and MSR1 and C3AR1 (Figures 2(d)–2(f)).

3.3. Functional Enrichment Analysis of DE-IFRGs. Functional enrichment analysis of these DE-IFRGs was conducted using the "clusterProfiler" *R* package. As revealed in Figure 3(a), the significantly enriched BP terms were response to molecule of bacterial origin, response to lipopolysaccharide, and positive regulation of cytokine production; in terms of CC, DE-IFRGs were mainly involved in positive regulation of cytokine production, secretory granule membrane, and membrane raft; as for MF, DE-IFRGs were mainly involved in receptor-ligand activity, cytokine receptor binding, and cytokine activity. Figure 3(b) showed the three significantly enriched GO terms and relevant DE-IFRGs involved in them. Additionally, the top 10 KEGG pathways were TNF signaling, lipid and atherosclerosis, JAK-STAT signaling, chemokine signaling pathway, Influenza A, Toll-like receptor signaling pathway, and inflammatory bowel disease (Figure 3(c)). Figure 3(d) displays the three significantly enriched signaling pathways and related DE-IFRGs involved in these pathways.

3.4. Construction and Validation of a Risk Signature Based on Prognosis-Related IFRGs. Using univariate Cox regression analysis, 20 prognosis-related IFRGs were identified ($P < 0.001$) (Table 1). Subsequently, the least absolute Lasso regression analysis was employed to prevent the overfitting and determine the most important prognosis-related IFRGs in KIRC (Figures 4(a) and 4(b)). Then, stepwise multivariate assays were applied to build a gene signature. Eventually, nine hub IFRGs (ROS1, PLAUR, ACVR2A, KLF6, GABBR1, APLNR, SPHK1, PDPN, and ADORA2B) were used to construct the gene signature (Figure 4(c)). Based on regression coefficients (Table 2), we calculated the risk score for each patient using the following formula: risk score = (1.069 * ROS1) + (0.339 * PLAUR) + (−0.720 * ACVR2A) + (−0.198 * KLF6) + (0.600 * GABBR1) + (−0.164 * APLNR) + (−0.386 * SPHK1) + (0.183 * PDPN) + (0.472 * ADORA2B). As exhibited in Figures 5(a) and 5(b), ROS1, PLAUR, GABBR1, SPHK1, and PDPN were overexpressed in the high-risk subgroup, whereas ACVR2A, KLF6, and APLNR were distinctly decreased in the high-risk subgroup. However, no difference was found in ADORA2B. Moreover, our group observed that overexpression of ROS1 and PLAUR indicated worse overall survival (Figures 5(c) and 5(d)). The downregulation of ACVR2A and KLF6 predicted a poor prognosis of patients (Figures 5(e) and 5(f)). Increased expression of GABBR1 was associated with a shorter OS (Figure 5(g)). Low APLNR expression predicted a shorter OS (Figure 5(h)). Increased expression of SPHK1 and PDPN suggested worse prognosis (Figures 5(i) and 5(j)). Also, no difference was found in ADORA2B (Figure 5(k)). Furthermore, using the cBioPortal database, we explored the genetic mutations of 9 hub IFRGs, and results were shown in Figure 5(l). Subsequently, 320 patients in the training set were stratified into the low- and high-risk subgroups based on the median risk score

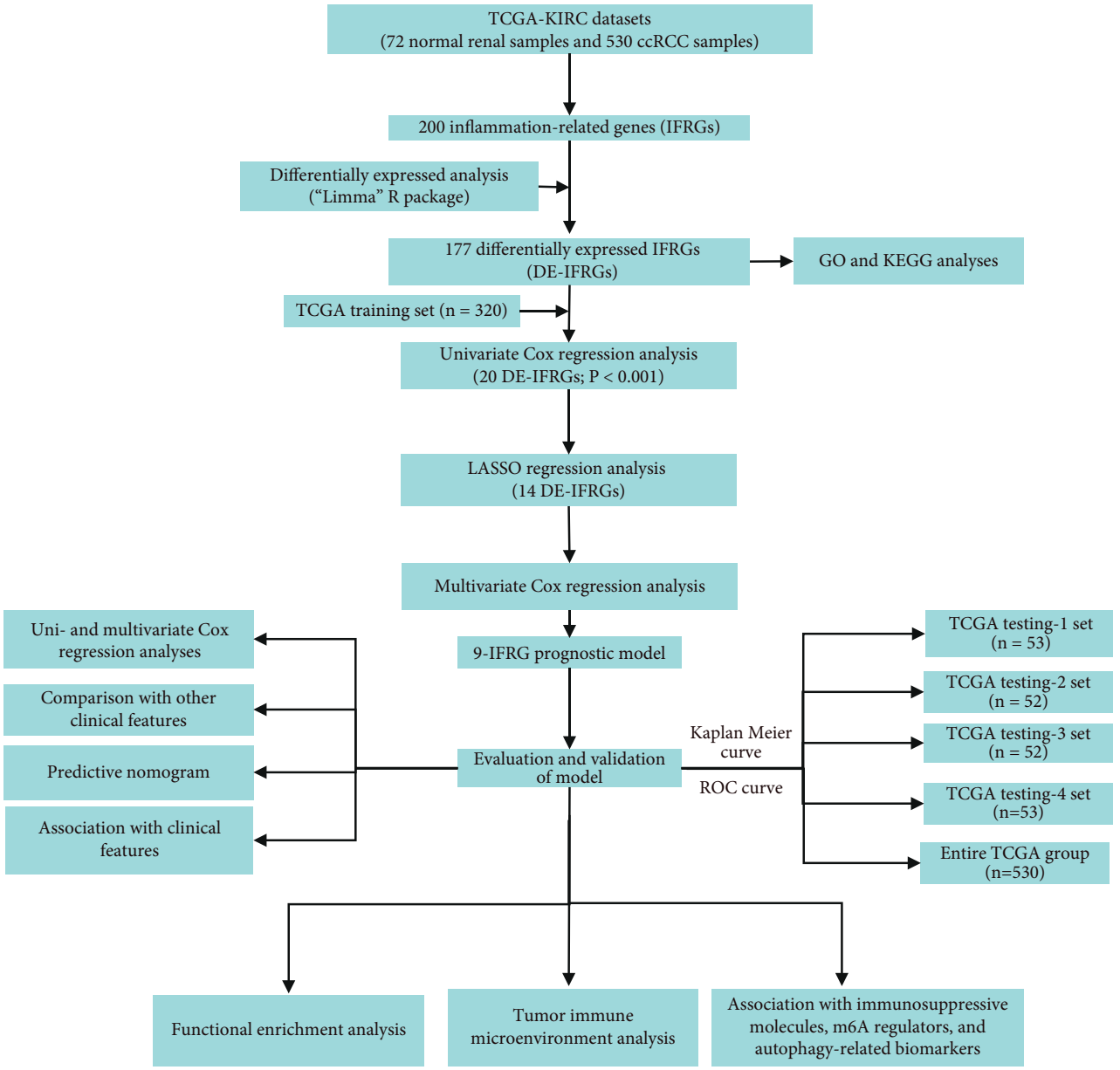

Figure 1: The flowchart describes the gene signature of KIRC established in this study and its comprehensive analysis.

value. Kaplan–Meier curves showed that high-risk patients showed poorer OS by comparison with low-risk patients ($P < 0.001$) (Figure 6(a)). ROC assays were utilized to evaluate the prognostic performance of the gene signature, and results showed that the area under the ROC curve for 1-year, 3-year, and 5-year OS was 0.766, 0.721, and 0.751 (Figure 6(b)). The survival status and the expressions of 9-IFRGs in the training cohort were presented in –. To verify the predictive performance of the gene model, patients in the testing-1 cohort, testing-2 cohort, testing-3 cohort, testing-4 cohort, and the entire group were classified as high- and low-risk subgroups. The Kaplan–Meier survival curve showed a significantly good OS in the low-risk group (Figures 7(a)–7(e)). The AUC of the gene signature in the testing-1 cohort for 1-year, 3-year, and 5-year OS is also shown in Figures 7(f)–7(j).

3.5. Independent Prognostic Analysis, Correlation of Risk Score with Clinical Features, and Construction of a Nomogram. By coupling with the risk model and clinicopathological features, we identified the risk score (HR = 1.023, $P < 0.001$) as a factor of overall survival for KIRC using uni- and multivariate Cox regression analyses (Figures 8(a) and 8(b)). Besides, we showed that elevated risk score was notably correlated with higher histological grade ($P < 0.05$, Figure 8(c)), advanced clinical stage ($P < 0.05$, Figure 8(d)), and T stage ($P < 0.05$, Figure 8(e)), suggesting that risk score was positively correlated with tumor progression. Moreover, we used the independent prognostic factors to establish a prognostic nomogram (Figure 8(f)), and calibration curves showed that the nomogram performed well at predicting 1-, 3-, and 5-year OS in KIRC patients (Figures 8(g)–8(i)), indicating the robust predictive ability of the prognostic

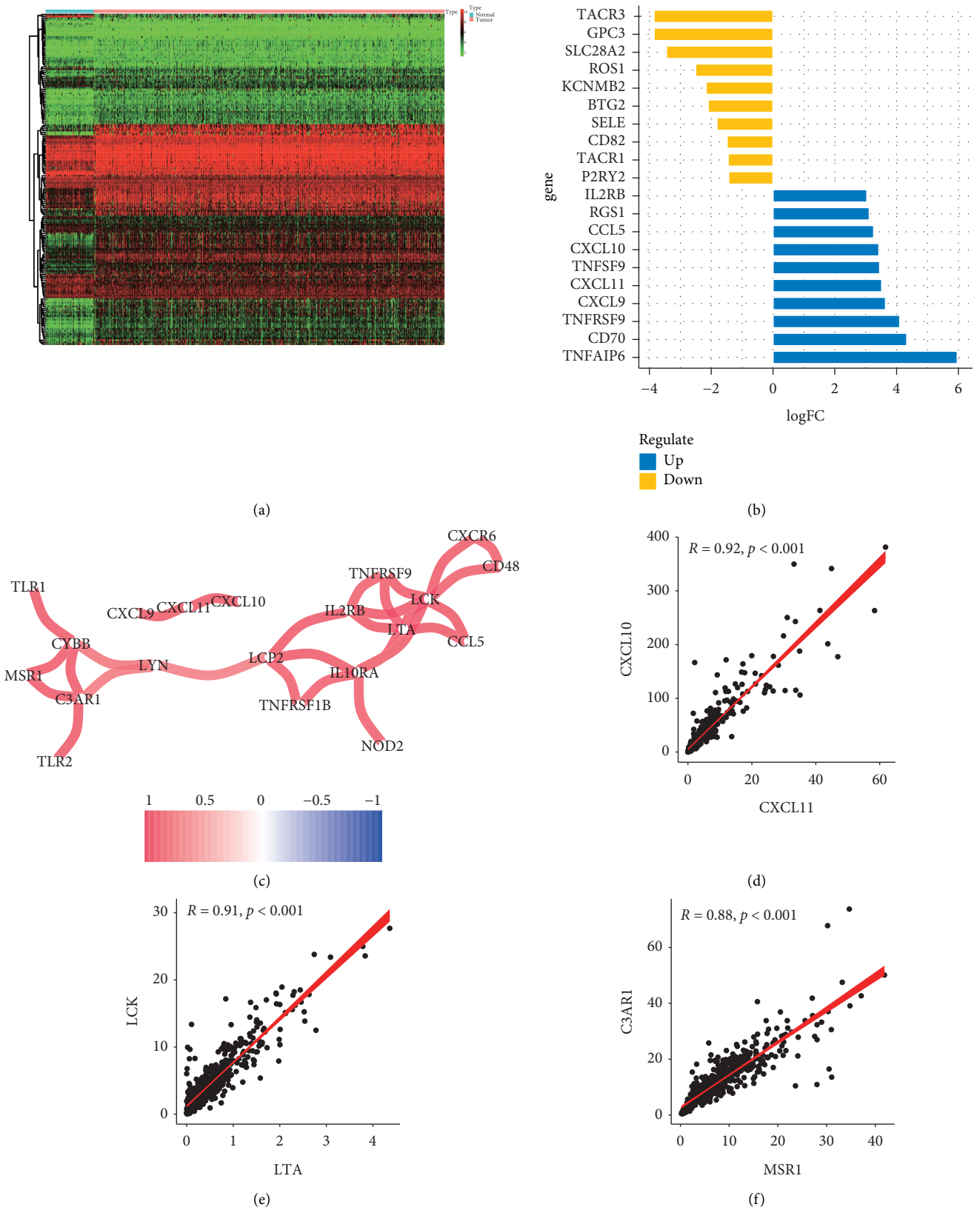

Figure 2: Identification of differentially expressed inflammation-related genes (DE-IFRGs) between normal tissues and KIRC tissues. (a) The heat map of DE-IFRGs. (b) The top ten upregulated and downregulated PRGs. (c) Correlation network between DE-IFRGs (Pearson's coefficient >0.8). (d–f) The strongest correlations were found between CXCL11 and CXCL10, LTA and LCK, and MSR1 and C3AR1.

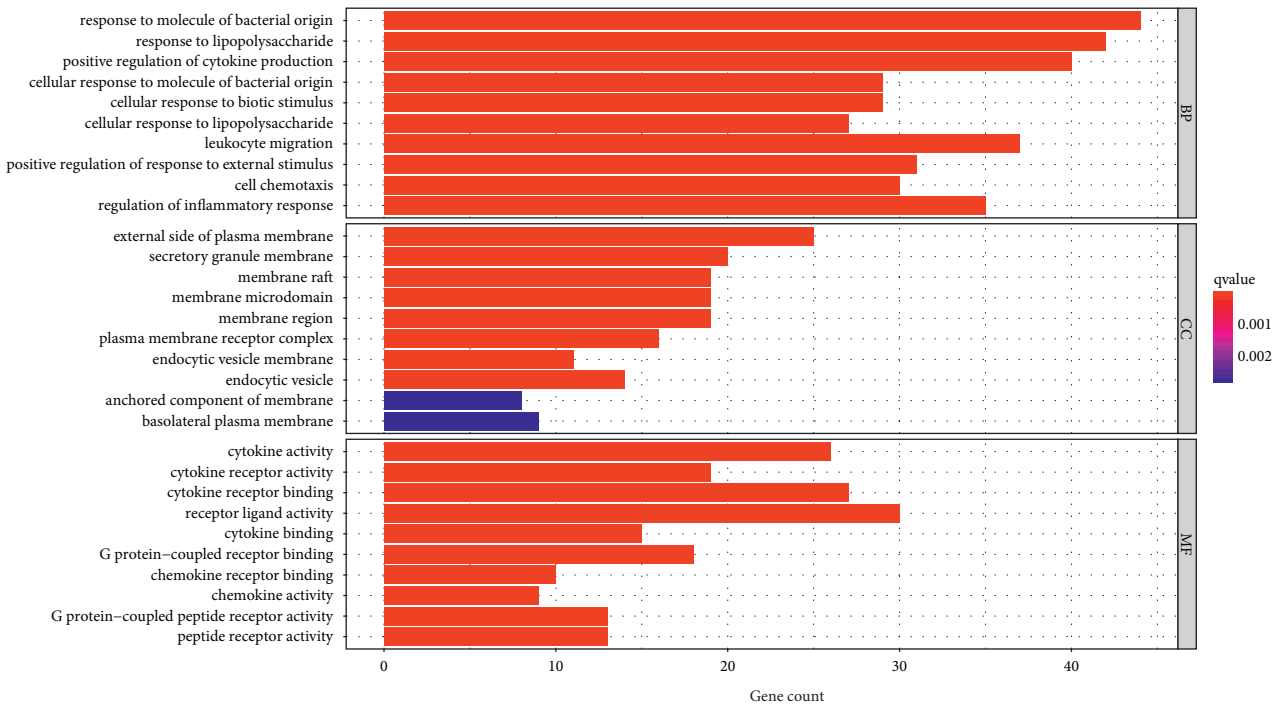

(a)

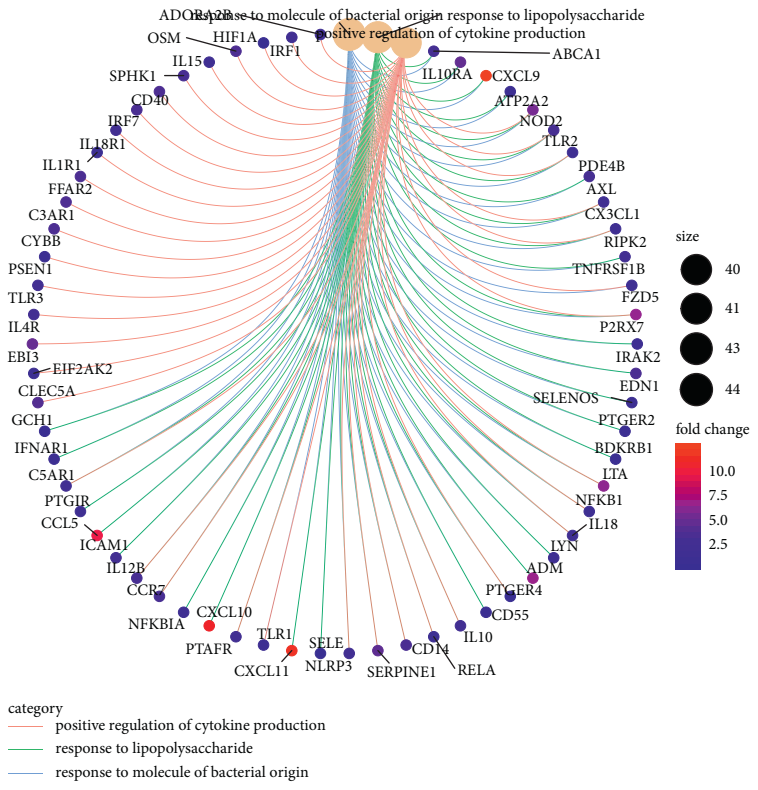

(b)

Figure 3: Continued.

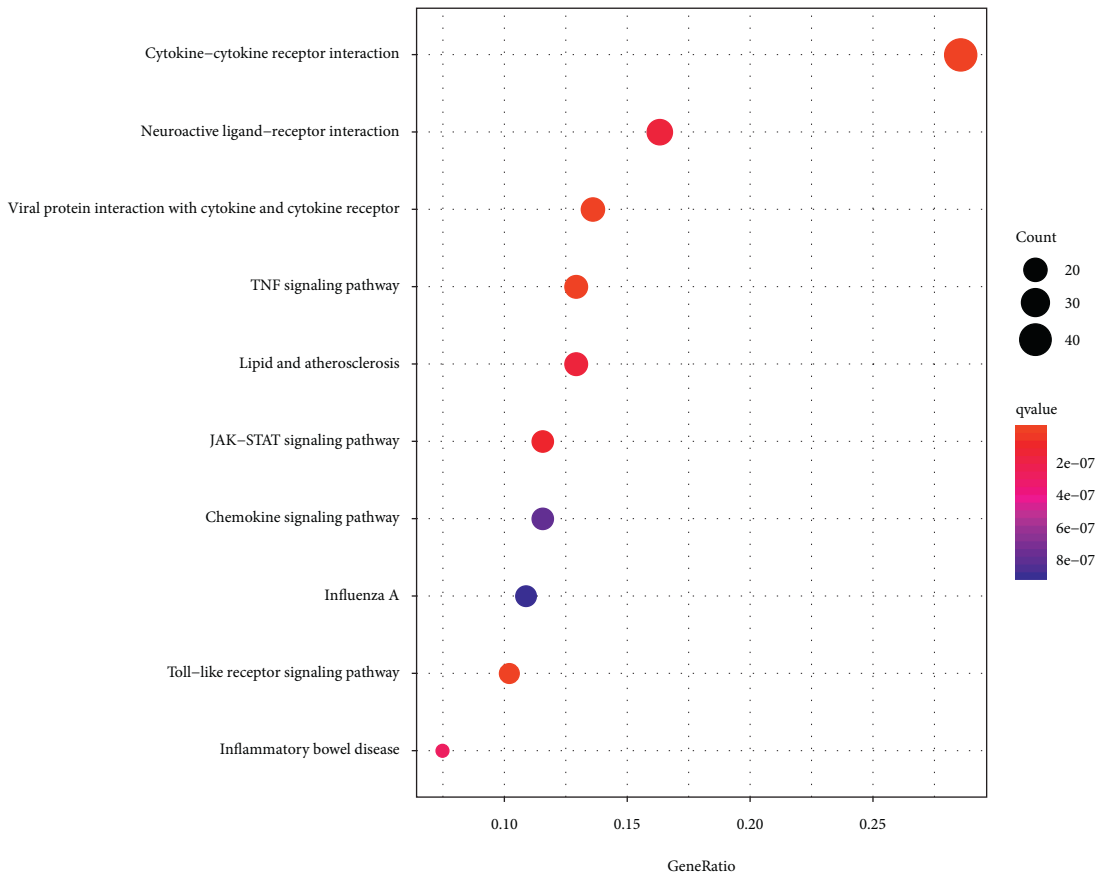

(c)

Figure 3: Continued.

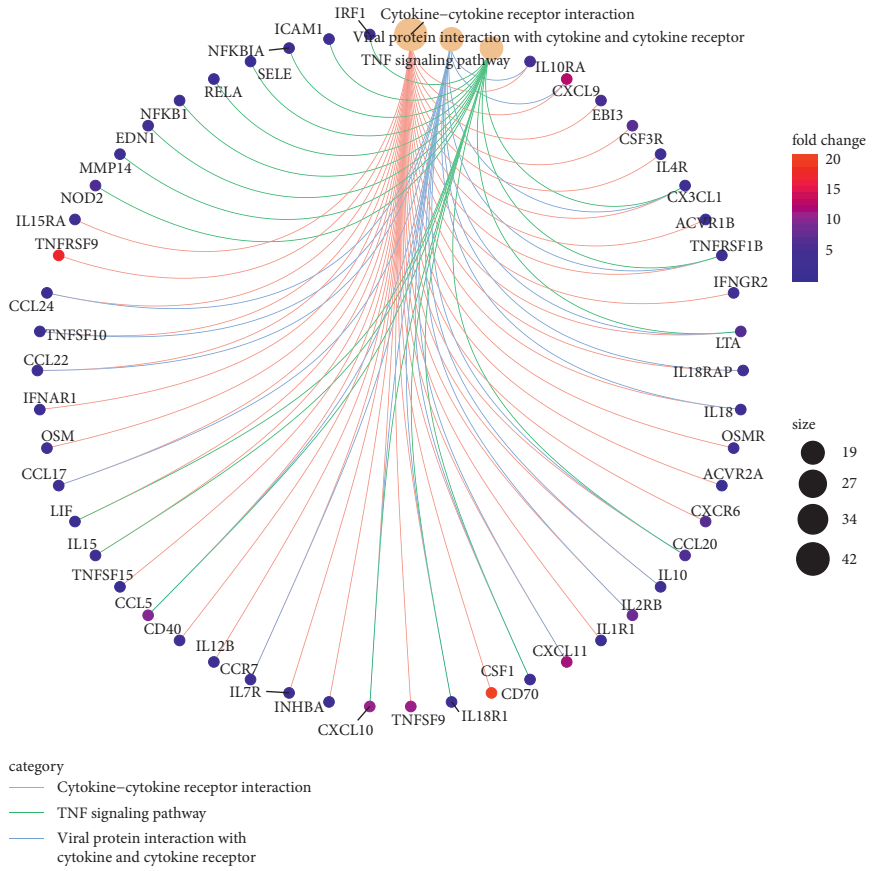

(d)

Figure 3: Functional enrichment analysis of DE-IFRGs. (a) GO enrichment analysis of DE-IFRGs. (b) Enriched GO enrichment terms and corresponding DE-IFRGs. (c) KEGG signaling pathway analysis of DE-IFRGs. (d) Enriched cancer-related pathways and corresponding DE-IFRGs.

Table 1: Univariate Cox regression analysis for identification of prognosis-related IFRGs in the training dataset.

IFRGs, inflammation-related genes				
ID	HR	HR.95L	HR.95H	*P*-value
CD82	1.411	1.154	1.725	7.904*E*−04
SLC4A4	0.770	0.663	0.895	6.653*E*−04
F3	1.298	1.117	1.509	6.529*E*−04
SGMS2	0.627	0.482	0.817	5.291*E*−04
NOD2	1.844	1.316	2.585	3.817*E*−04
TIMP1	1.384	1.161	1.651	2.931*E*−04
RIPK2	1.883	1.340	2.645	2.632*E*−04
BEST1	2.144	1.430	3.216	2.252*E*−04
KLF6	0.683	0.558	0.836	2.213*E*−04
APLNR	0.741	0.634	0.867	1.817*E*−04
ACVR2A	0.405	0.253	0.649	1.742*E*−04
ADRM1	2.553	1.567	4.160	1.677*E*−04
SPHK1	1.639	1.296	2.072	3.751*E*−05
CX3CL1	0.671	0.556	0.811	3.541*E*−05
PDPN	1.545	1.259	1.897	3.089*E*−05
GABBR1	1.690	1.326	2.154	2.226*E*−05
ADORA2B	2.236	1.550	3.227	1.695*E*−05
CALCRL	0.681	0.572	0.810	1.506*E*−05
ROS1	3.007	1.877	4.817	4.677*E*−06
PLAUR	1.812	1.456	2.256	1.032*E*−07

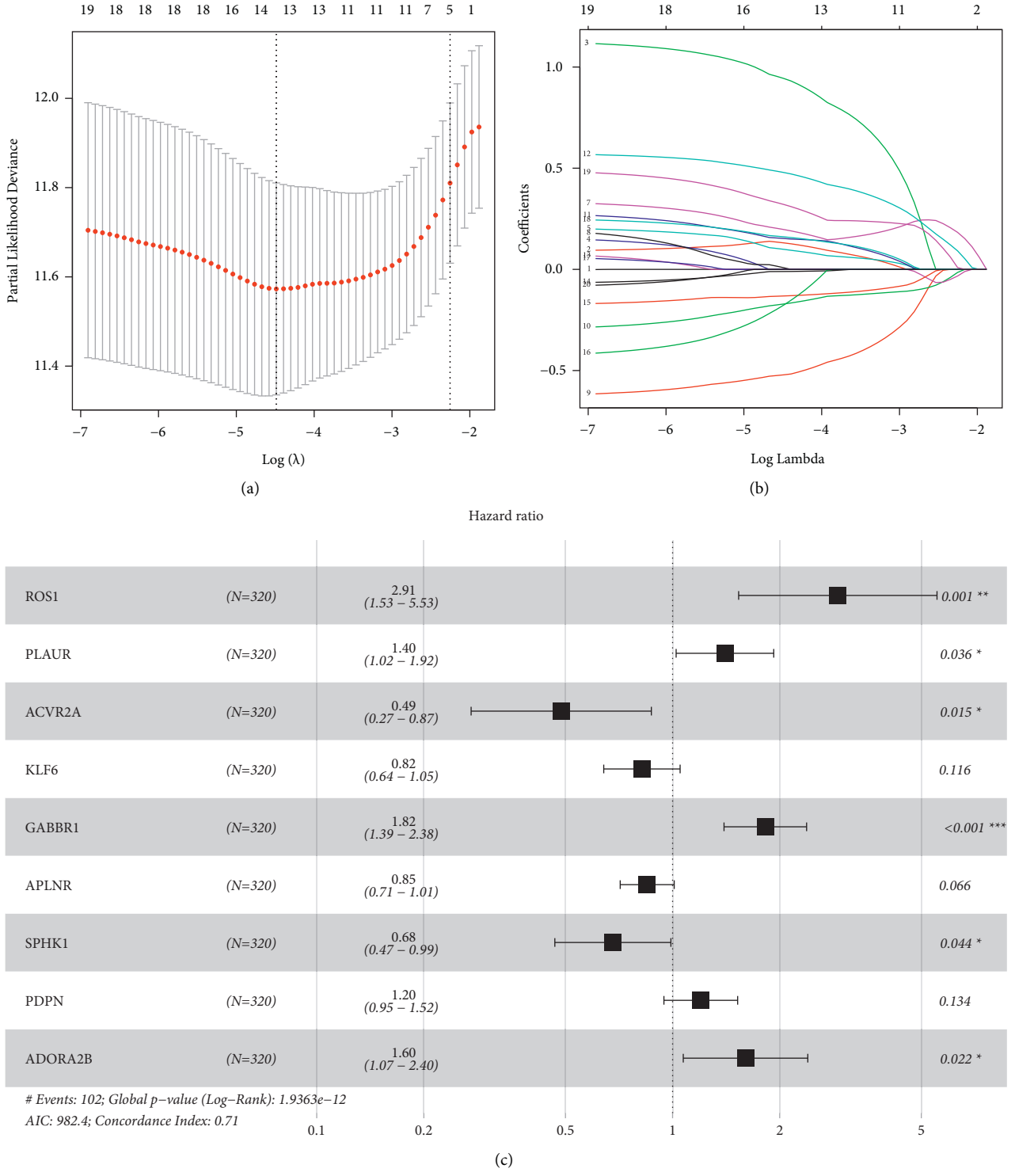

Figure 4: Identification of a 9-gene risk signature for overall survival by multivariate Cox regression analysis. (a) The minimum number corresponds to the covariates. (b) The changing trajectory of each independent variable. (c) Nine prognosis-associated hub IFRGs were identified by further multivariate Cox regression analysis.

nomogram. Additionally, we found that risk score had the largest AUC compared with other clinical variables in predicting 5-year OS of KIRC (Figure 8(j)), suggesting that risk score has advantages over other clinical traits in estimating 5-year OS of KIRC.

3.6. Functional Enrichment Analyses. To illustrate the underlying action mechanisms related with the 9-IFRG signature-derived risk model, a total of 1,771 DEGs were identified between high- and low-risk subgroups. Figures 9(a) and 9(b) shows the heat map and volcano map

Table 2: 9 prognosis-associated hub PRGs identified by multivariate Cox regression analysis.

IFRGs, inflammation-related genes					
ID	coef	HR	HR.95L	HR.95H	*P*-value
ROS1	1.069	2.913	1.533	5.535	$1.092E-03$
PLAUR	0.339	1.403	1.023	1.924	$3.553E-02$
ACVR2A	−0.720	0.487	0.272	0.872	$1.546E-02$
KLF6	−0.198	0.820	0.641	1.050	$1.156E-01$
GABBR1	0.600	1.822	1.395	2.380	$1.073E-05$
APLNR	−0.164	0.849	0.713	1.011	$6.565E-02$
SPHK1	−0.386	0.679	0.467	0.989	$4.367E-02$
PDPN	0.183	1.200	0.945	1.524	$1.337E-01$
ADORA2B	0.472	1.603	1.072	2.399	$2.165E-02$

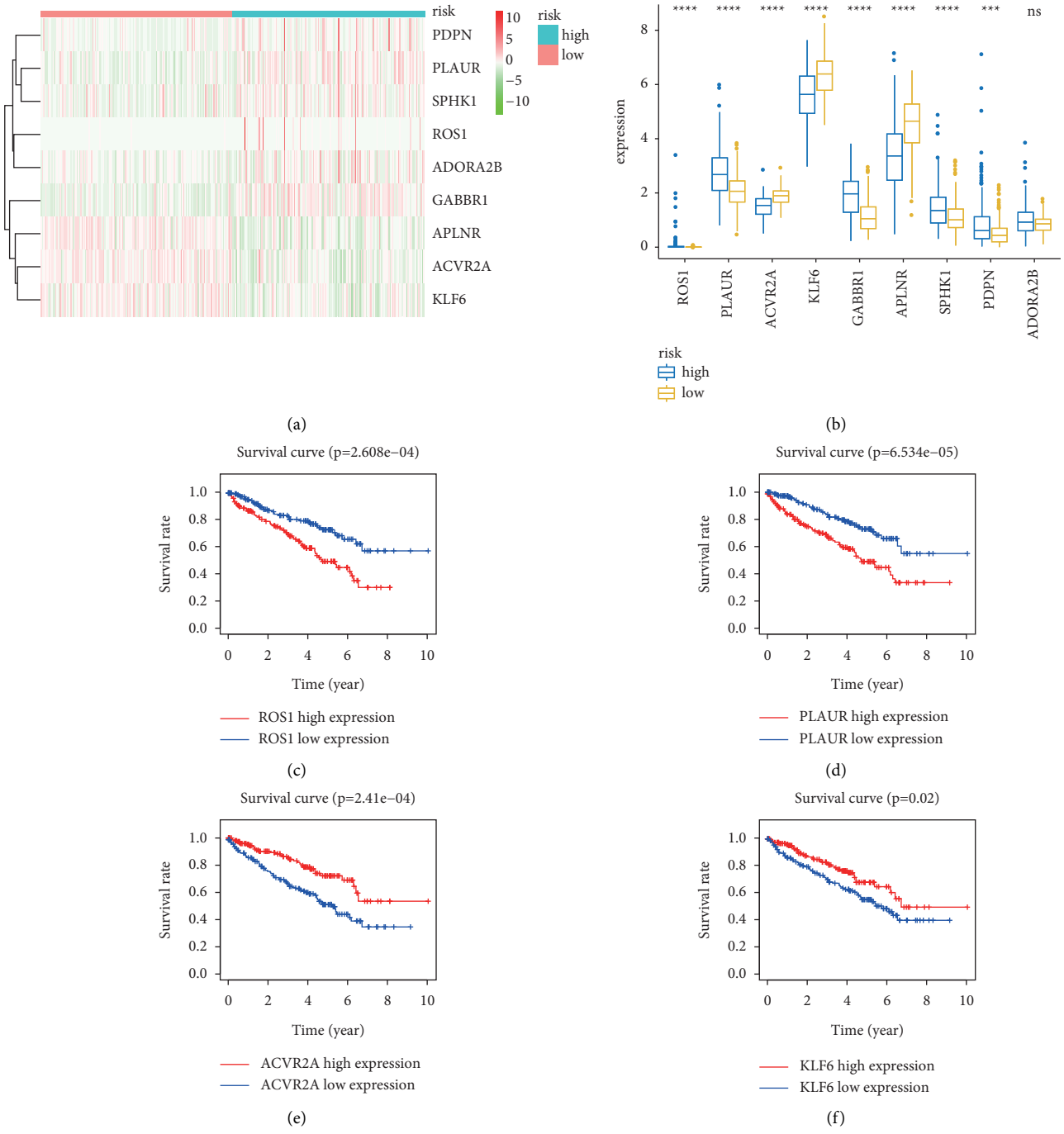

Figure 5: Continued.

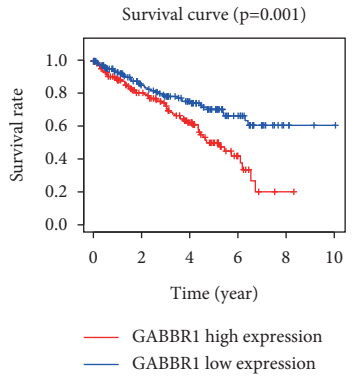

(g)

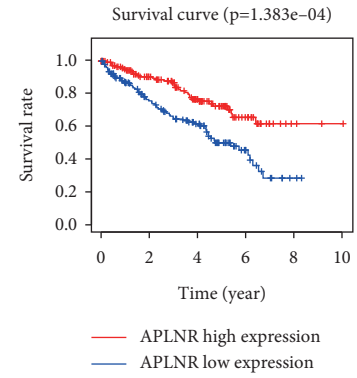

(h)

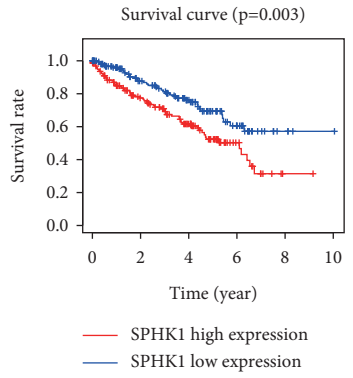

(i)

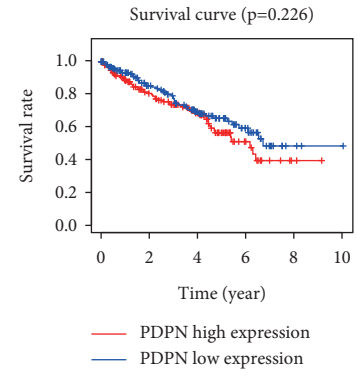

(j)

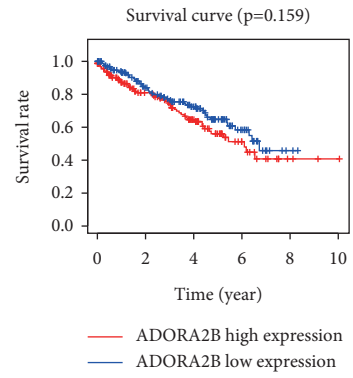

(k)

Figure 5: Continued.

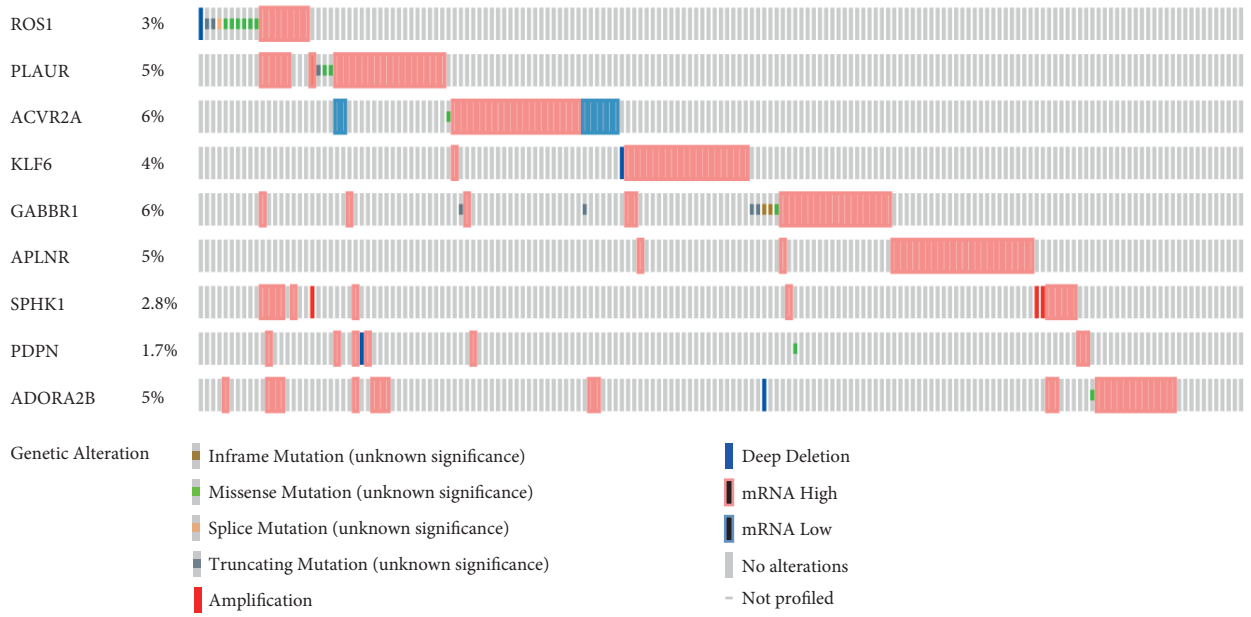

(l)

Figure 5: Comprehensive analysis of nine prognosis-associated hub IFRGs. (a) Heat map of expression of nine hub IFRGs between high and low risk subgroups (***$P < 0.001$). (b) Differential expression of nine hub IFRGs between high- and low-risk subgroups. (c–k) The Kaplan–Meier curves of ROS1, PLAUR, ACVR2A, KLF6, GABBR1, APLNR, SPHK1, PDPN, and ADORA2B, respectively. (l) Genetic alteration of nine hub IFRGs in KIRC patients.

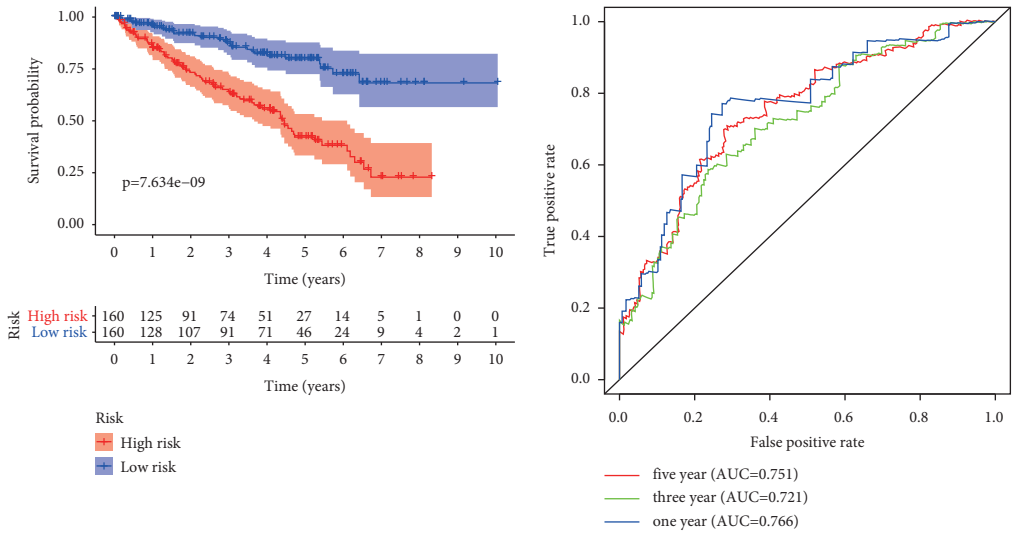

(a) (b)

Figure 6: Continued.

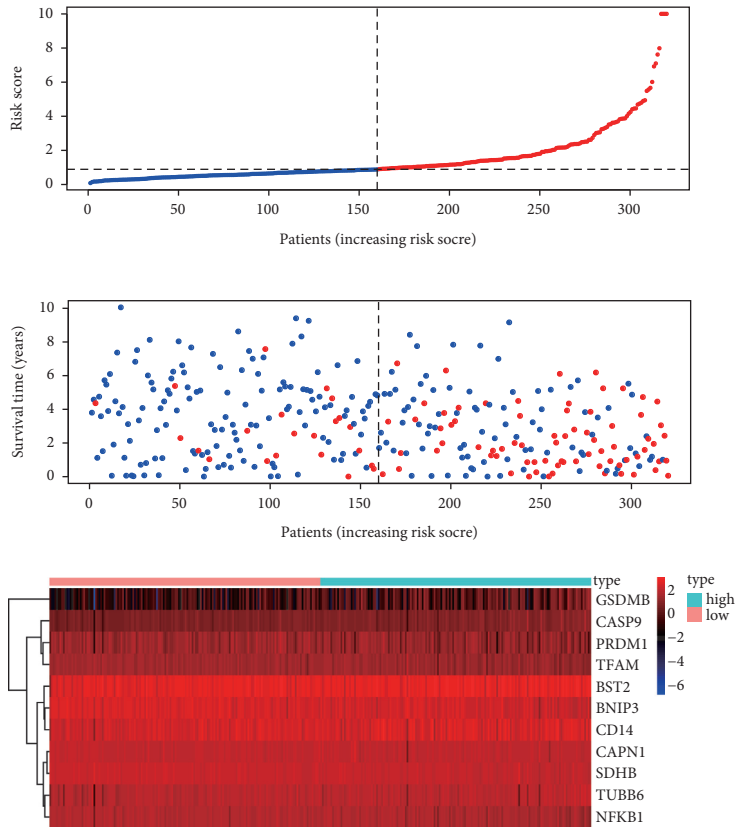

(c)

Figure 6: Development of the prognostic signature based on nine hub IFRGs. (a) Survival curve for low- and high-risk subgroups in the TCGA training cohort. (b) Time-dependent ROC curve of the 9-IFRG prognostic risk signature. (c) Relationships among the risk score (upper), survival status of patients (middle), and the expressing pattern of the genes (bottom).

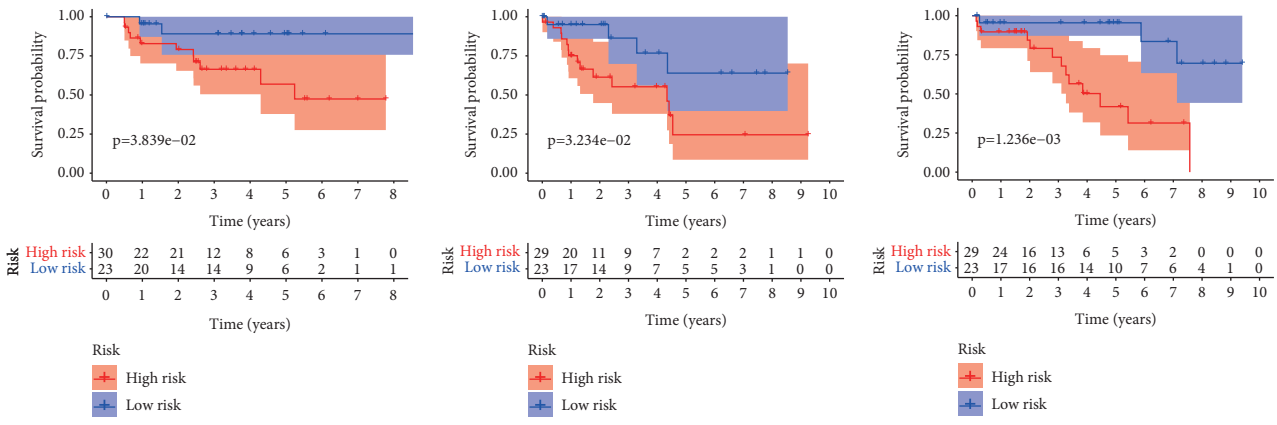

(a) (b) (c)

Figure 7: Continued.

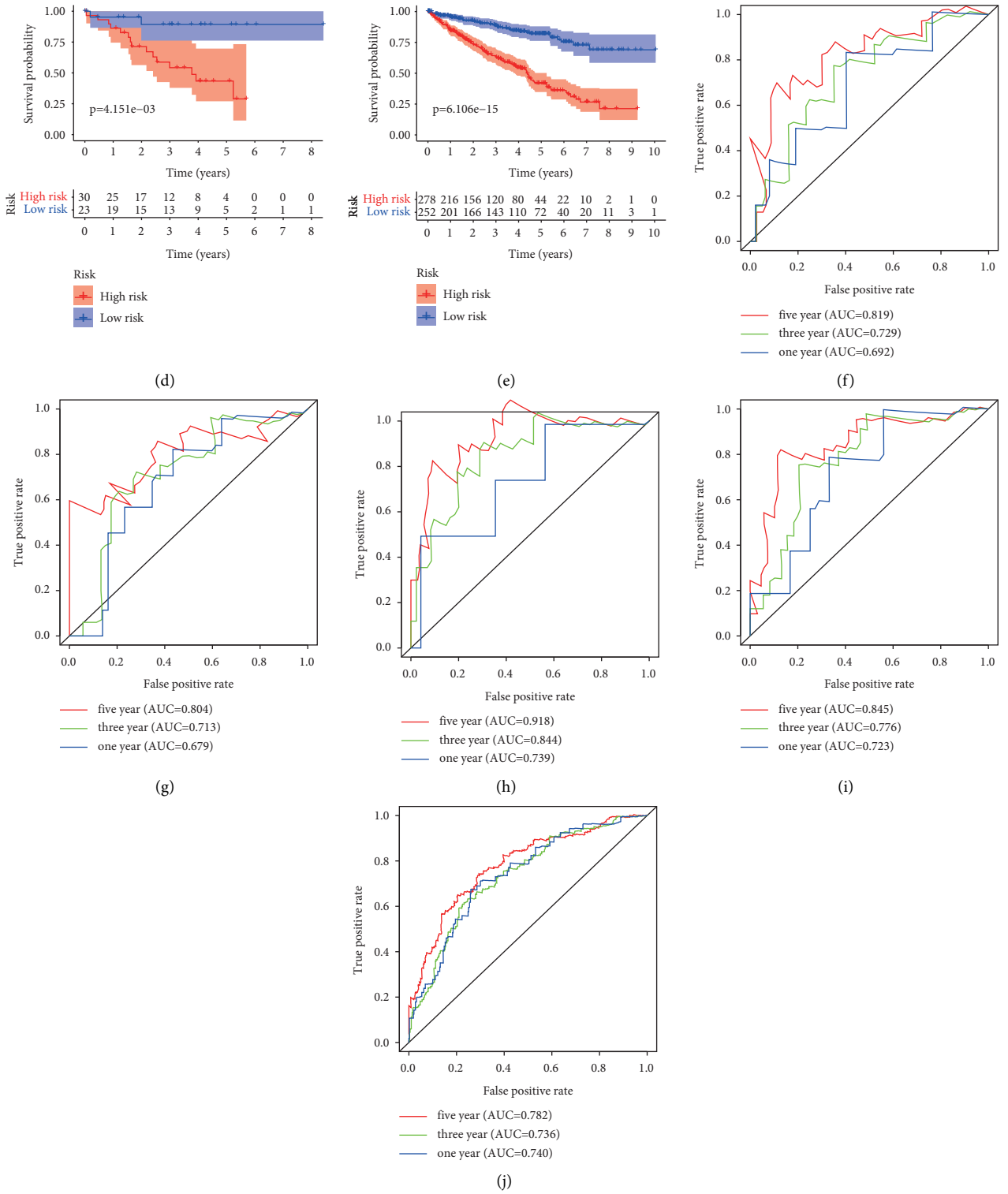

Figure 7: Validation of the prognostic signature based on nine inflammation-related genes in different cohorts. (a–e) Survival assays of the 9-IFRG prognostic signature in the testing-1 cohort, testing-2 cohort, testing-3 cohort, testing-4 cohort, and the entire group, respectively. (f–j) Time-dependent ROC curves of the 9-IFRG prognostic risk signature in the four cohorts.

of DEGs, respectively. As illustrated in Figure 9(c), concerning biological processes, DEGs were significantly enriched in the modulation of negative regulation of hydrolase activity; with regard to cellular components, DEGs were significantly involved in the collagen-containing extracellular matrix, presynapse, and synaptic membrane; in point of molecular functions, DEGs were noticeably involved in receptor-ligand activity, passive transmembrane

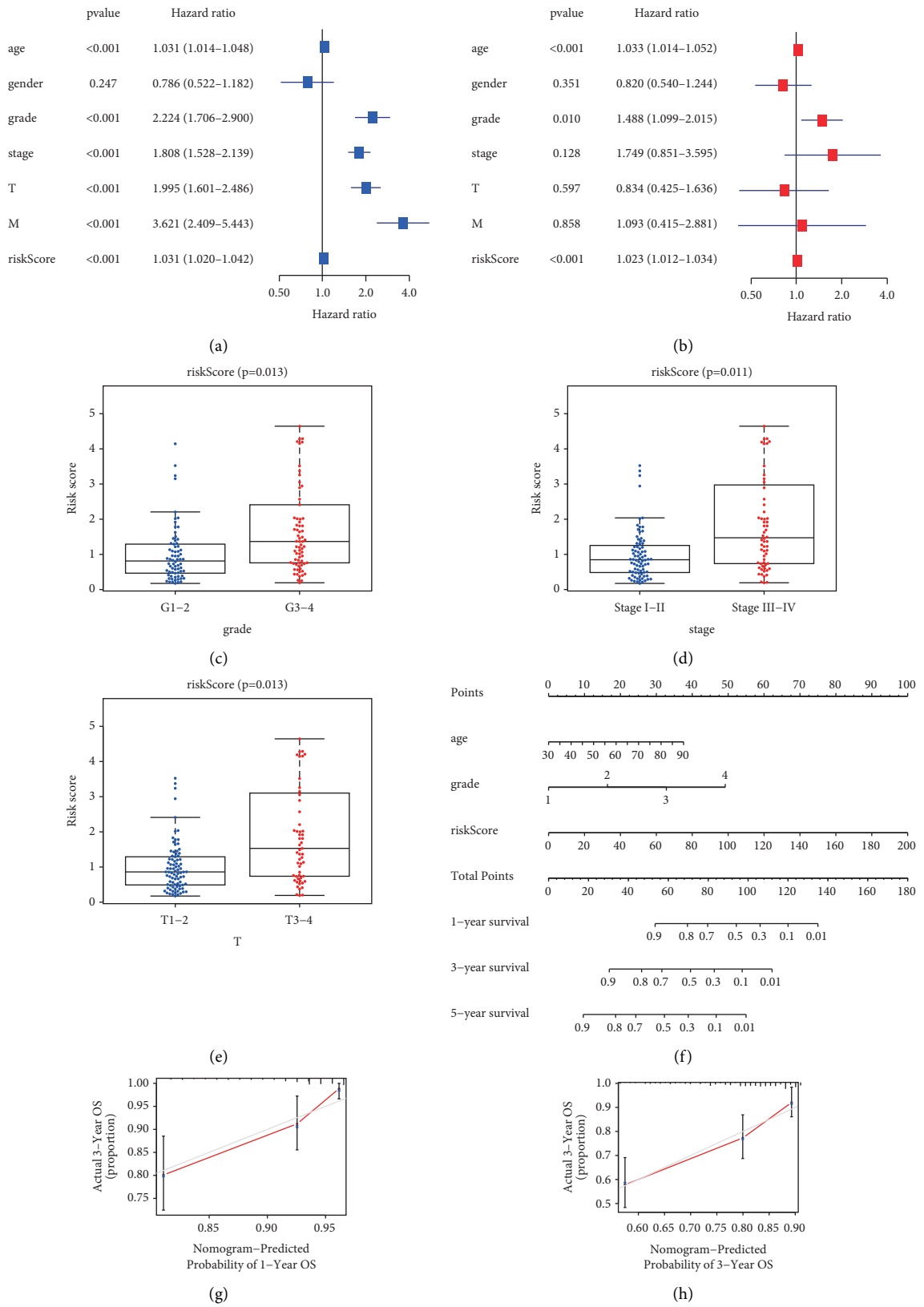

Figure 8: Continued.

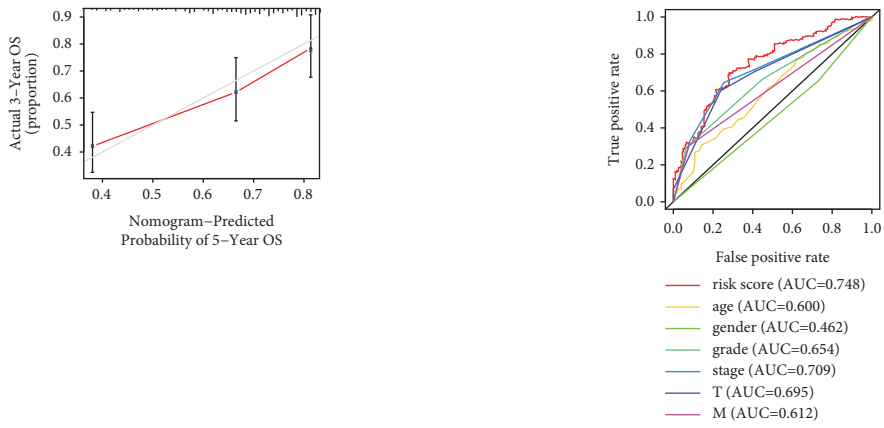

(i) (j)

FIGURE 8: Independent prognostic analysis and construction of nomogram. (a) Univariate Cox regression assays were used to explore the prognostic value of risk score and other clinical features in KIRC. (b) Multivariate Cox regression assays were applied to demonstrate whether risk score and other clinical features could be an independent marker for KIRC patients. (c–e) An elevated risk score was significantly correlated with higher histological grade, advanced clinical stage, and T stage. (f) A nomogram consisting of independent clinical features for predicting 1-, 3-, and 5-year OS of KIRC. (g–i) Calibration curves of 1-year, 3-year, and 5-year OS of KIRC. (j) ROC curves for the superiority of the gene signature.

transporter activity, and channel activity. DEGs were mainly enriched in phototransduction, linoleic acid metabolism, cholesterol metabolism, arachidonic acid metabolism, IL-17 signaling pathway, and protein digestion and absorption (Figure 9(d)).

3.7. Association of Risk Score with TME. Immune and stromal cells are crucial constituents of the immune microenvironment. In this current study, the contributions of stromal and immune cells to KIRC were estimated by the ESTIMATE algorithm. The results signified that immune score was crucially higher in the high-risk group (Figure 10(a)); however, no difference was found for the stromal score (Figure 10(b)). Additionally, we applied the CIBERSORT algorithm to compare the differences in each type of immune infiltrating cells. Figure 10(c) showed the proportion of 21 immune cells in each sample. Figure 10(d) illustrates the correlations between infiltrated immune cells in the tumor. Figure 10(e) shows the heat map of the 21 immune cell proportions. Moreover, Figure 10(f) shows the relationship between risk score with different immune cells, and we found that the high-risk group showed higher-level immune infiltrates of M0 macrophages, regulatory T cells (Tregs), follicular helper T cells, plasma cells, and memory B cells.

3.8. Association of Risk Score with Immunosuppressive Molecules, m6A Regulators, and Autophagy-Related Biomarkers. Then, we estimated the association between immunosuppressive molecules and risk score. Figure 11(a) shows the heat map of common immunosuppressive molecules in high- and low-risk subgroups. Furthermore, as illustrated in Figure 11(b), patients with high-risk score expressed higher levels of LAG-3, ICOS, CTLA4, PDCD1, CD27, and TIGIT, whereas HAVCR2 was overexpressed in patients with the low-risk score. Correlation analysis confirmed that LAG-3 (cor = 0.15, Figure 11(c)), TIGIT (cor = 0.11, Figure 11(d)), and CTLA4 (cor = 0.21, Figure 11(e)) were positively associated with the risk score, whereas no difference was found for ICOS, PDCD1, CD27, and HAVCR2 (Figures 11(f)–11(i)). Together, these results indicate that LAG-3, TIGIT, and CTLA4 were positively associated with the risk score. Recent evidence indicated the vital role of m6A mRNA methylation in reducing the antitumor response of CD8 + T cells and promoting anti-PD-1 drug resistance. We thus assess the relationship between risk score and m6A regulators. Figure 12(a) shows the heat map of common m6A regulators in high- and low-risk subgroups. Additionally, we discovered that most of the m6A regulators were significantly decreased in the high-risk subgroup except for METTL3 (Figure 12(b)). The results indicate that high-risk subgroup patients may be more suitable for immunotherapy with emerging checkpoint inhibitors. Growing researches have revealed a key role for autophagic pathways and proteins in immunity and inflammation. We thus explore the association of autophagy-related genes with risk score, and we found that several autophagy-related genes have a significant link with risk score (Figure 13(a)), and the top three relevant autophagy-related genes are DKK1 (Figure 13(b)), SNAI2 (Figure 13(c)), and AREG (Figure 13(d)).

4. Discussion

In this work, we constructed an inflammation-related gene feature and evaluated its predictive capability in predicting OS of KIRC patients. Then, we studied the potential functions and signaling pathways closely related to risk score and further explored the association between risk score with

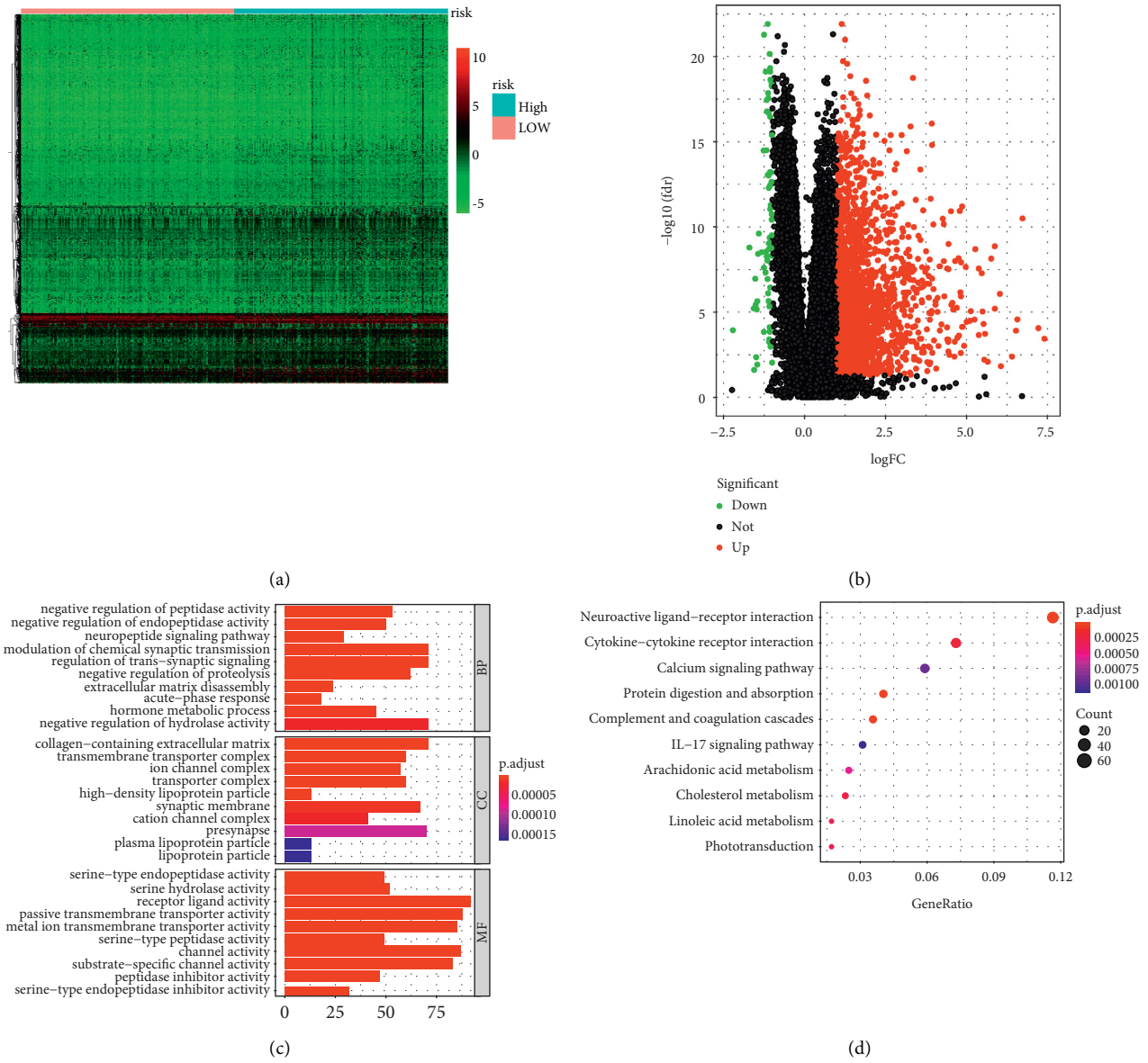

Figure 9: Functional assays of DEGs between high- and low-risk subgroups. (a) Heat map of DEGs between high- and low-risk subgroups. (b) Volcano map of DEGs between high- and low-risk subgroups. (c) Significantly enriched GO enrichment terms. (d) KEGG signaling pathway analysis.

immune microenvironment, immunosuppressive molecules, m6A regulators, and autophagy-related biomarkers. Here, nine hub IFRGs (ROS1, PLAUR, ACVR2A, KLF6, GABBR1, APLNR, SPHK1, PDPN, and ADORA2B) were selected by bioinformatics and used to construct 9-IFRG risk signature successfully. Afterwards, we found that gene signature performed well in the training set, testing-1 set, testing-2 set, testing-3 set, testing-4, and the entire TCGA group. Specifically, the higher the risk score of patients is, the worse the overall survival rate is. ROC curve also confirms the robust predictive performance of the risk model. Additionally, by combining the risk model with the clinicopathological features of patients, we found that the 9-IFRG gene model can independently predict the OS of patients with KIRC. Further investigation indicated that the nomogram performed well at predicting 1-, 3-, and 5-year OS in KIRC patients. Furthermore, we found that the risk score was significantly associated with cancer progression in KIRC patients. Moreover, compared to other clinical variables, the risk score had the highest predictive performance of prognosis. To sum up, we constructed a powerful 9-IFRG risk signature and an effective nomogram for KIRC risk stratification and overall survival prediction.

Of the nine hub IFRGs (ROS1, PLAUR, ACVR2A, KLF6, GABBR1, APLNR, SPHK1, PDPN, and ADORA2B) we identified, some are associated with cancer progression. The protooncogene ROS1 encodes a tyrosine kinase receptor that has an essential physiological role in humans. Studies have shown that somatic chromosomal fusions involving ROS1 generate chimerical tumor proteins that can cause various

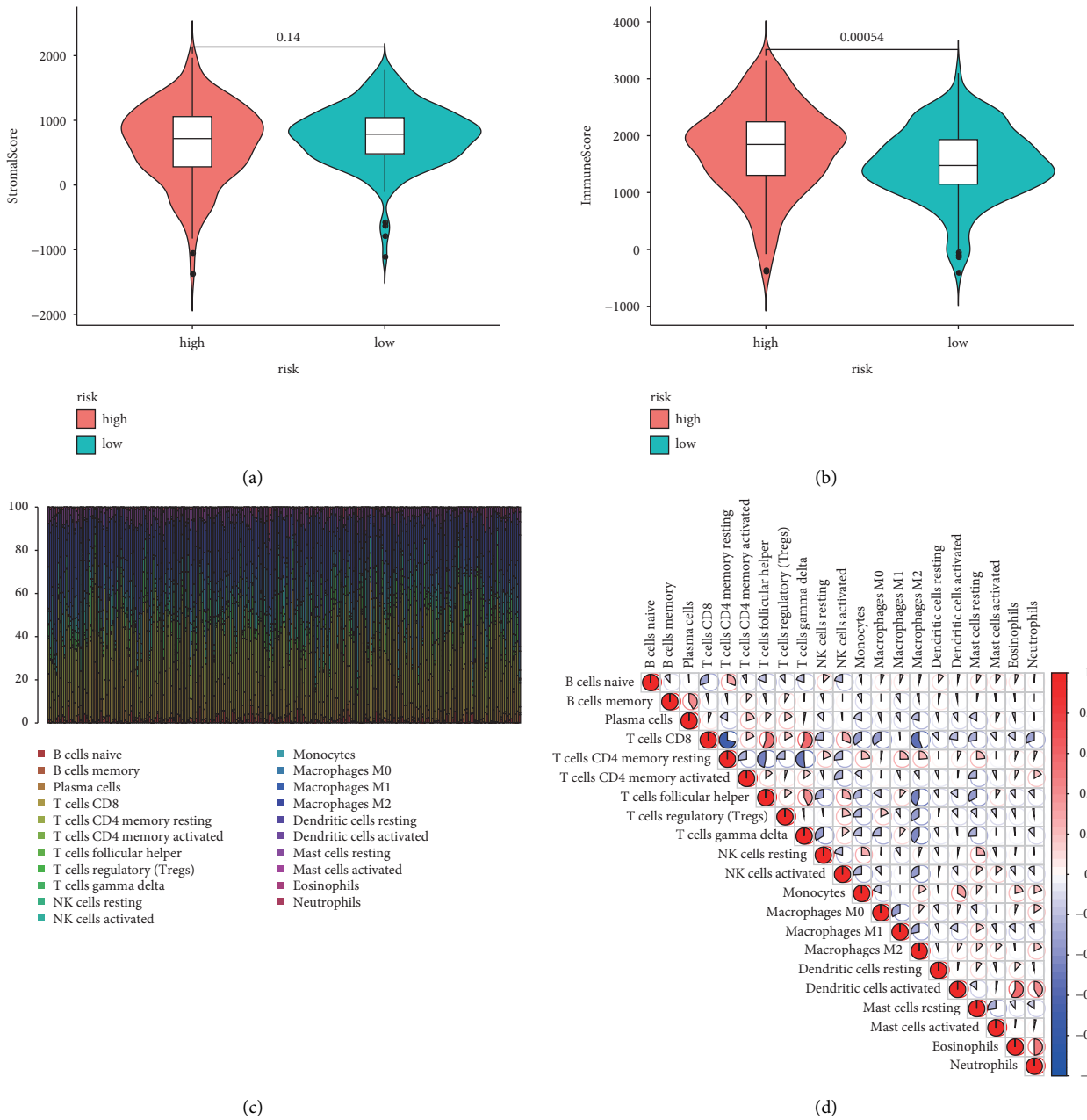

Figure 10: Continued.

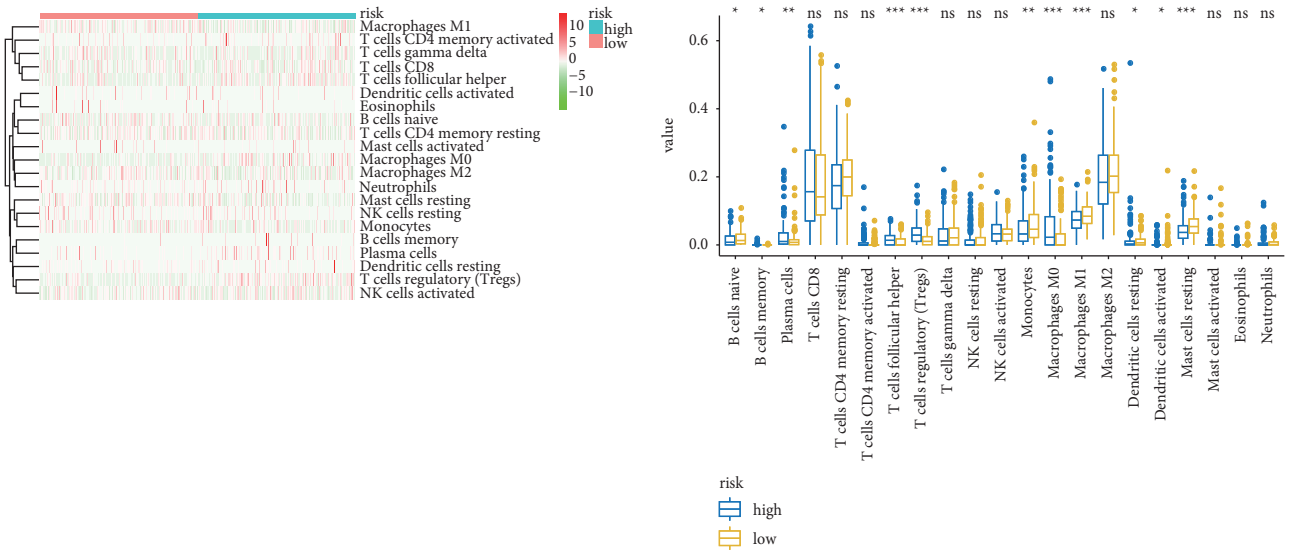

(e) (f)

Figure 10: Association of risk score with tumor immune microenvironment in KIRC. (a) Differences in stromal score between high- and low-risk subgroups. (b) Differences in immune score between high- and low-risk subgroups. (c) Relative proportion of immune infiltration in KIRC. (d) Correlation between tumor-infiltrating immune cells. (e) The heatmap exhibited the infiltrating difference of immune cells in two groups. (f) Barplot showed the ratio differentiation of 21 kinds of immune cells.

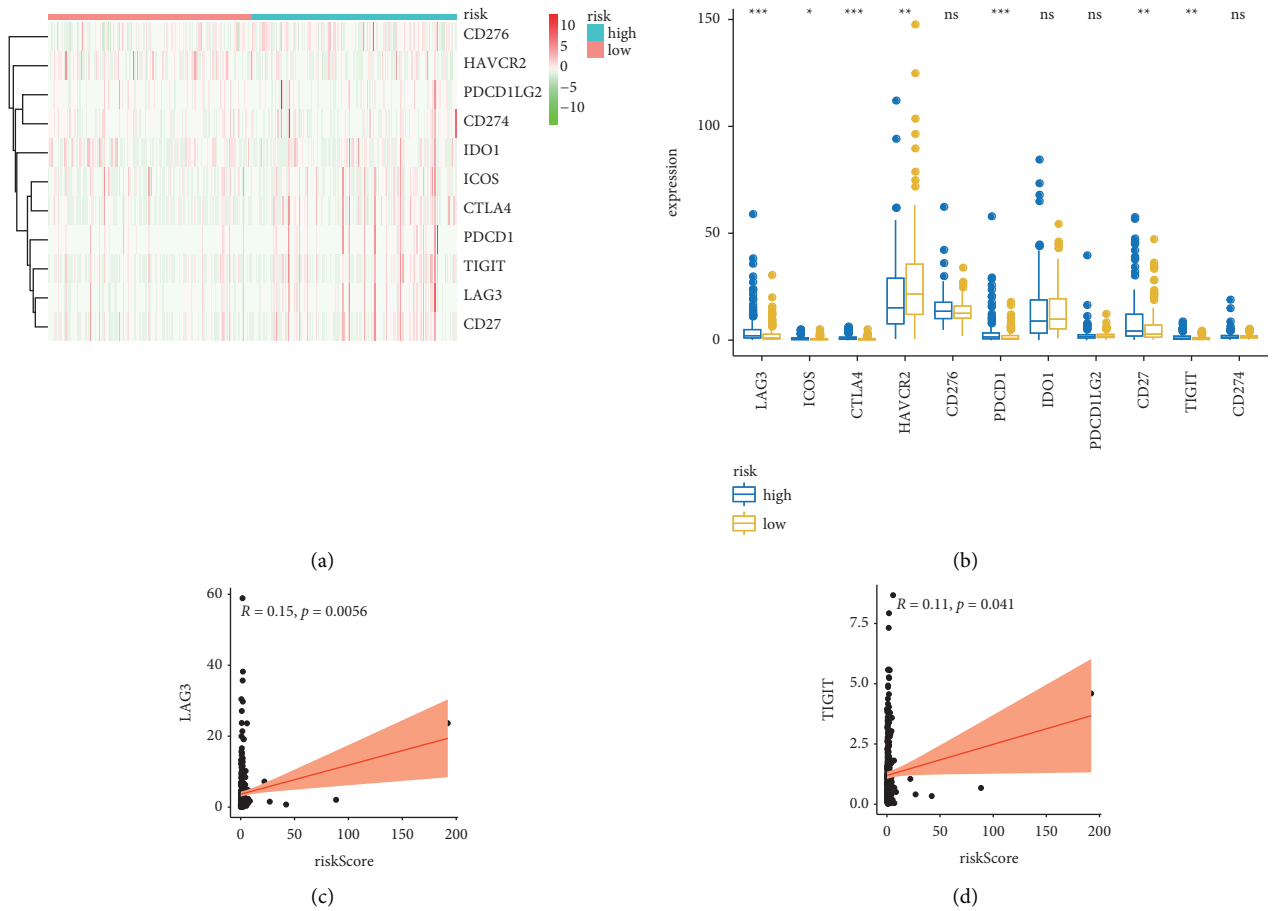

(a) (b)

(c) (d)

Figure 11: Continued.

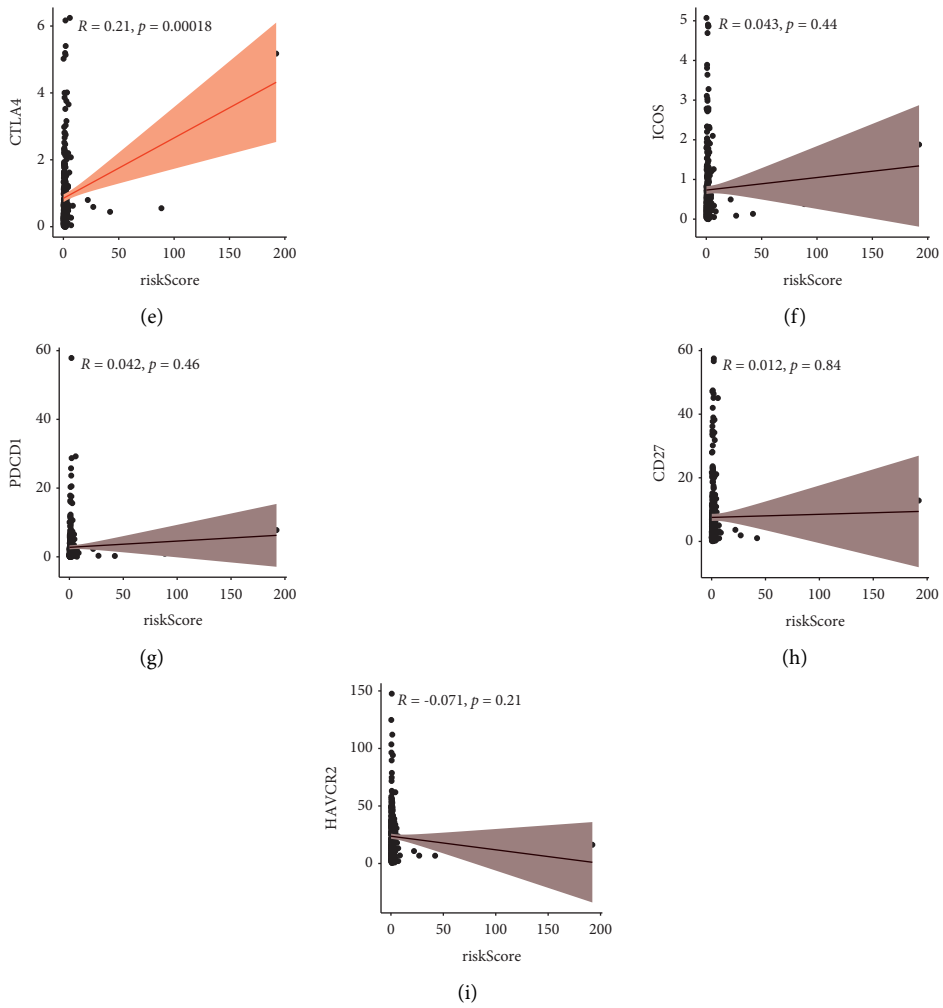

Figure 11: Differences in immunosuppressive molecule expression between high- and low-risk subgroups. (a) The heatmap exhibited the immunosuppressive molecules in two groups. (b) Barplot showed the immunosuppressive molecules between KIRC specimens with low- or high-risk subgroups relative to the median of risk score. (c–i) Association of LAG-3, TIGIT, CTLA4, ICOS, PDCD1, CD27, and HAVCR2 with the risk score.

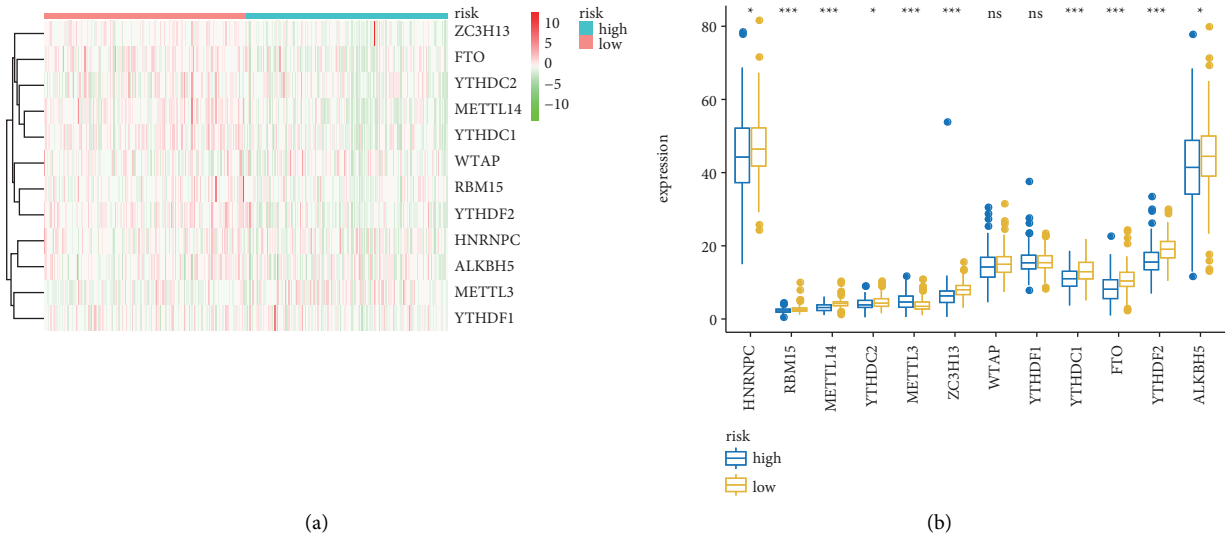

Figure 12: Association of risk score with m6A regulators in KIRC. (a) The heatmap exhibited the immunosuppressive molecules in two groups. (b) Barplot showed the m6A regulators between KIRC specimens with low- or high-risk subgroups.

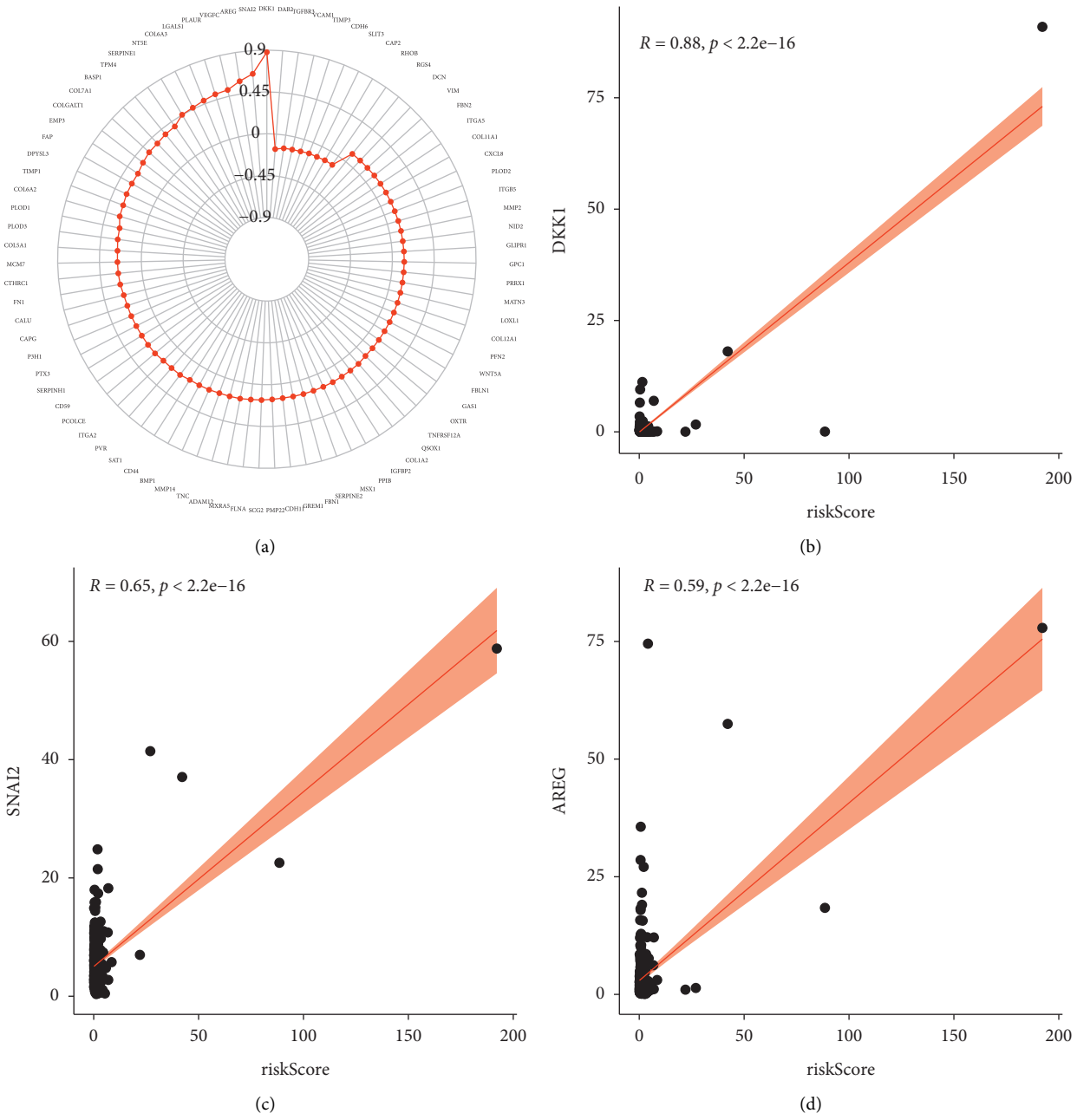

Figure 13: Association of risk score with autophagy-related genes in KIRC. (a) Autophagy-related genes significantly associated with risk score. (b–d) The top three autophagy-related genes associated with risk score are DKK1, SNAI2, and AREG.

cancers [13]. In inflammatory myofibroblastic tumors, ROS1 expression predicts ROS1 gene rearrangement [14]. PLAUR, also known as u-PAR, is an essential molecule in modulating cell surface fibrinogen activation and plays a vital role in many healthy and pathological processes [15]. Abnormal PLAUR disorders played a key role in the progression and metastasis of human colon cancer [16]. Moreover, PLAUR impacted colorectal liver metastases by influencing the protein hydrolytic activity and inflammation of the tumor microenvironment in colorectal cancer. Consequently, the colorectal liver metastases [17] ACVR2A is a ligand for activin A protein and is closely associated with polyarthrosis syndrome, protointestinal embryogenesis, and spermatogenesis [18]. Emerging evidence indicated that ACVR2A is involved in many cancer-related signaling pathways, such as the PEDF-induced signaling, the TFG-β signaling, or signaling pathways regulating stem cell pluripotency [19]. KLF6 is a transcription factor of the zinc finger family and modulates lipid homeostasis in KIRC [20]. Additionally, KLF6 had been found to promote the expression and function of proinflammatory genes by inhibiting miR-223 expression in macrophages [21]. GABBR1, also known as GABABR1, is a 7-transmembrane receptor. In colorectal cancer, decreased GABBR1 fosters the proliferation and

invasion; overexpression of GABBR1 has the opposite [22]. APLNR is also a seven-transmembrane G protein-coupled receptor that is universally present in diverse tissues. In osteosarcoma, elevated APLNR expression promotes proliferation and invasion [23]. SPHK1 is a biologically active metabolite of sphingosine that is involved in various tumor progression by enhancing cell proliferation and motility. Currently, drugs targeting SPHK1 are now being progressively validated in clinical trials [24]. Type I integral membrane glycoprotein encoded by PDPN is widely distributed in human tissues. In breast tumor-infiltrating immune cells, PDPN was found highly expressed in tumor-associated macrophages (TAMs), and the latter spurs local stromal remodeling and promotes vascular growth and lymphatic infiltration [25]. ADORA2B is a member of the G protein-coupled receptor superfamily and encodes an adenosine receptor. A recent report indicates that hypoxia-inducible factor 1-dependent expression of ADORA2B facilitates breast cancer stem cell enrichment [26]. The above reports confirmed the role of 9 hub IFRGs in carcinogenesis. However, whether ROS1, PLAUR, ACVR2A, KLF6, GABBR1, APLNR, SPHK1, PDPN, and ADORA2B affect the clinical outcome of KIRC patients via modulating the process of inflammation requires to be further elaborated, and there are few relevant studies.

To elucidate the functional roles associated with the risk score, the DEGs between the high-risk and low-risk subgroups were identified and used to perform functional enrichment analysis. Intriguingly, we noticed that DEGs are involved in several tumor-related signaling pathways. These signaling pathways are all in connection with the regulation of tumor immunity. Through the interaction between chemokines or cytokines and their receptors, different subsets of immune cells are recruited into the tumor microenvironment, causing these populations having a differential impact on tumor progression and treatment outcome [27]. In gastric cancer, elevated intratumoral mast cells resulted in immune suppression via modulating TNF-α-PD-L1 pathway [28]. The JAK-STAT signaling pathway is involved in tumor cell recognition and tumor-driven immune escape and plays a role in almost all immune regulatory processes [29]. Toll-like receptor signaling pathway is a classical immune signaling pathway that plays an irreplaceable role in modulating tumor immunity and cancer progression [30]. In addition, we found that the high-risk group had a higher immune score. With regard to immune infiltrating cells, we found that high-risk group showed higher level immune infiltrates. Among them, regulatory T cells (Tregs) play crucial roles in keeping self-tolerance and immune homeostasis. However, in some cases, they promote tumor progression by inhibiting the effective antitumor response [31]. The low-risk group showed higher level immune infiltrates. Among them, M1 macrophage types are thought to be key factors in antitumorigenesis, production of proinflammatory cytokines, and promotion of T-cell immunity. Furthermore, the study suggested that LAG-3, CTLA4, and TIGIT were highly expressed in the high-risk subgroup and also positively associated with risk score, indicating that the high-risk group is in a more immunosuppressed state by comparison with the low-risk group, but also means that patients of high-risk subgroup may benefit more from immune checkpoint inhibitors. N6-methyladenosine (m6A) RNA methylation plays a crucial role in the tumor immune microenvironment cancer development. A recent study indicates that downregulated m6A-related genes predict unfavorable outcomes in gastric cancer [32]. We assess the association of m6A regulators with risk score, and we found that most of the m6A regulators were significantly decreased in the high-risk subgroup. Autophagy is an essential homeostatic process by which cells decompose their components. Recent studies have uncovered a key role for autophagic pathways and proteins in immunity and inflammation. We thus evaluate the association of autophagy-related genes and the risk score, and results indicate that many autophagy-related genes were significantly correlated with risk scores, particularly the DKK1, SNAI2, and AREG.

5. Conclusion

Collectively, our study constructs and validates a robust 9-IFRG risk signature, which may be to the advantage of risk classification and prognosis prediction in KIRC patients. However, there are still some restrictions that should not be overlooked. Our results are mainly derived from bioinformatic analysis; clinical samples and cellular experiments are required to prove our findings; in addition, our analysis discovered that inflammation-related genes might influence renal clear cell carcinoma progression through several mechanisms; nevertheless, further in vivo and in vitro experiments are needed to explore the exact biological roles.

Data Availability

The datasets used and/or analyzed during the present study are available from the corresponding author upon reasonable request.

Conflicts of Interest

The authors declare that they have no conflicts of interest regarding the publication of this paper.

Authors' Contributions

Ze Zhang and Yan-Yan Wei contributed equally to this work.

Acknowledgments

This study was supported by grants from Hebei Provincial Health Commission (no. 20190442).

References

[1] J. J. Hsieh, M. P. Purdue, S. Signoretti et al., "Renal cell carcinoma," *Nature Reviews Disease Primers*, vol. 3, no. 1, p. 17009, 2017.

[2] M. M. Wolf, W. Kimryn Rathmell, and K. E. Beckermann, "Modeling clear cell renal cell carcinoma and therapeutic implications," *Oncogene*, vol. 39, pp. 3413–3426, 2020.

[3] M. B. Atkins and N. M. Tannir, "Current and emerging therapies for first-line treatment of metastatic clear cell renal cell carcinoma," *Cancer Treatment Reviews*, vol. 70, pp. 127–137, 2018.

[4] E. Jonasch, J. Gao, and W. K. Rathmell, "Renal cell carcinoma," *BMJ*, vol. 349, no. nov10 11, Article ID g4797, 2014.

[5] C. I. Diakos, K. A. Charles, D. C. McMillan, and S. J. Clarke, "Cancer-related inflammation and treatment effectiveness," *The Lancet Oncology*, vol. 15, no. 11, pp. e493–e503, 2014.

[6] A. Mantovani, P. Allavena, A. Sica, and F. Balkwill, "Cancer-related inflammation," *Nature*, vol. 454, no. 7203, pp. 436–444, 2008.

[7] C.-P. Liao, R. C. Booker, J.-P. Brosseau et al., "Contributions of inflammation and tumor microenvironment to neurofibroma tumorigenesis," *Journal of Clinical Investigation*, vol. 128, no. 7, pp. 2848–2861, 2018.

[8] E. Elinav, R. Nowarski, C. A. Thaiss, B. Hu, C. Jin, and R. A. Flavell, "Inflammation-induced cancer: crosstalk between tumours, immune cells and microorganisms," *Nature Reviews Cancer*, vol. 13, no. 11, pp. 759–771, 2013.

[9] F. Balkwill, K. A. Charles, and A. Mantovani, "Smoldering and polarized inflammation in the initiation and promotion of malignant disease," *Cancer Cell*, vol. 7, no. 3, pp. 211–217, 2005.

[10] W. Tan, M. A. T. Hildebrandt, X. Pu et al., "Role of inflammatory related gene expression in clear cell renal cell carcinoma development and clinical outcomes," *The Journal of Urology*, vol. 186, no. 5, pp. 2071–2077, 2011.

[11] S. M. Crusz and F. R. Balkwill, "Inflammation and cancer: advances and new agents," *Nature Reviews Clinical Oncology*, vol. 12, no. 10, pp. 584–596, 2015.

[12] G. Yu, L.-G. Wang, Y. Han, and Q.-Y. He, "clusterProfiler: an R package for comparing biological themes among gene clusters," *OMICS: A Journal of Integrative Biology*, vol. 16, no. 5, pp. 284–287, 2012.

[13] A. Drilon and C. Jenkins, *ROS1-dependent cancers - biology, diagnostics and therapeutics*, vol. 18, pp. 35–55, 2021.

[14] J. L. Hornick, L. M. Sholl, P. Dal Cin, M. A. Childress, and C. M. Lovly, "Expression of ROS1 predicts ROS1 gene rearrangement in inflammatory myofibroblastic tumors," *Modern Pathology*, vol. 28, no. 5, pp. 732–739, 2015.

[15] A. D. Børglum, A. Byskov, P. Ragno et al., "Assignment of the urokinase-type plasminogen activator receptor gene (PLAUR) to chromosome 19q13.1-q13.2," *The American Journal of Human Genetics*, vol. 50, pp. 492–497, 1992.

[16] D. Li, P. Wei, Z. Peng et al., "The critical role of dysregulated FOXM1-PLAUR signaling in human colon cancer progression and metastasis," *Clinical Cancer Research*, vol. 19, no. 1, pp. 62–72, 2013.

[17] R. L. Eefsen, L. Engelholm, W. Alpizar-Alpizar et al., "Inflammation and uPAR-expression in colorectal liver metastases in relation to growth pattern and neo-adjuvant therapy," *Cancer Microenvironment*, vol. 8, no. 2, pp. 93–100, 2015.

[18] A. Dillenburg, G. Ireland, R. K. Holloway et al., "Activin receptors regulate the oligodendrocyte lineage in health and disease," *Acta Neuropathologica*, vol. 135, no. 6, pp. 887–906, 2018.

[19] M. Dean, D. A. Davis, and J. E. Burdette, "Activin A stimulates migration of the fallopian tube epithelium, an origin of high-grade serous ovarian cancer, through non-canonical signaling," *Cancer Letters*, vol. 391, pp. 114–124, 2017.

[20] S. E. Syafruddin, P. Rodrigues, E. Vojtasova et al., "A KLF6-driven transcriptional network links lipid homeostasis and tumour growth in renal carcinoma," *Nature Communications*, vol. 10, no. 1, p. 1152, 2019.

[21] G.-D. Kim, H. P. Ng, N. Patel, and G. H. Mahabeleshwar, "Kruppel-like factor 6 and miR-223 signaling axis regulates macrophage-mediated inflammation," *The FASEB Journal*, vol. 33, no. 10, pp. 10902–10915, 2019.

[22] Y. Longqiu, L. Pengcheng, F. Xuejie, and Z. Peng, "A mi RNA s panel promotes the proliferation and invasion of colorectal cancer cells by targeting GABBR 1," *Cancer Medicine*, vol. 5, no. 8, pp. 2022–2031, 2016.

[23] L. Cui, J.-Y. Zhang, Z.-P. Ren, H.-J. Zhao, and G.-S. Li, "APLNR promotes the progression of osteosarcoma by stimulating cell proliferation and invasion," *Anti-Cancer Drugs*, vol. 30, no. 9, pp. 940–947, 2019.

[24] P. C. Hart, T. Chiyoda, X. Liu et al., "SPHK1 is a novel target of metformin in ovarian cancer," *Molecular Cancer Research*, vol. 17, no. 4, pp. 870–881, 2019.

[25] P. Bieniasz-Krzywiec, R. Martín-Pérez, M. Ehling et al., "Podoplanin-expressing macrophages promote lymphangiogenesis and lymphoinvasion in breast cancer," *Cell Metabolism*, vol. 30, no. 5, pp. 917–936, 2019.

[26] J. Lan, H. Lu, D. Samanta, S. Salman, Y. Lu, and G. L. Semenza, "Hypoxia-inducible factor 1-dependent expression of adenosine receptor 2B promotes breast cancer stem cell enrichment," *Proceedings of the National Academy of Sciences*, vol. 115, no. 41, pp. E9640–e9648, 2018.

[27] N. Nagarsheth, M. S. Wicha, and W. Zou, "Chemokines in the cancer microenvironment and their relevance in cancer immunotherapy," *Nature Reviews Immunology*, vol. 17, no. 9, pp. 559–572, 2017.

[28] Y. Lv, Y. Zhao, X. Wang et al., "Increased intratumoral mast cells foster immune suppression and gastric cancer progression through TNF-α-PD-L1 pathway," *Journal for ImmunoTherapy of Cancer*, vol. 7, no. 1, p. 54, 2019.

[29] K. L. Owen, N. K. Brockwell, and B. S. Parker, "JAK-STAT signaling: a double-edged sword of immune regulation and cancer progression," *Cancers*, vol. 11, 2019.

[30] Y. Xu, C. Jagannath, X.-D. Liu, A. Sharafkhaneh, K. E. Kolodziejska, and N. T. Eissa, "Toll-like receptor 4 is a sensor for autophagy associated with innate immunity," *Immunity*, vol. 27, no. 1, pp. 135–144, 2007.

[31] Y. Takeuchi and H. Nishikawa, "Roles of regulatory T cells in cancer immunity," *International Immunology*, vol. 28, no. 8, pp. 401–409, 2016.

[32] C. Zhang, M. Zhang, S. Ge et al., "Reduced m6A modification predicts malignant phenotypes and augmented Wnt/PI3K-Akt signaling in gastric cancer," *Cancer Medicine*, vol. 8, no. 10, pp. 4766–4781, 2019.

Hindawi
Journal of Oncology
Volume 2022, Article ID 2647825, 17 pages
https://doi.org/10.1155/2022/2647825

Research Article

SERPINE1 Overexpression Promotes Malignant Progression and Poor Prognosis of Gastric Cancer

Shujia Chen,[1] Yuqiao Li,[2] Yinghui Zhu,[1] Jiayue Fei,[1] Liaoyuan Song,[1] Guoyan Sun,[1] Lianyi Guo ,[1] and Xiaofei Li [1]

[1]*Department of Gastroenterology, The First Affiliated Hospital of Jinzhou Medical University, Jinzhou 121001, China*
[2]*Tianjin Medical University, Tianjin, China*

Correspondence should be addressed to Lianyi Guo; guoly@jzmu.edu.cn and Xiaofei Li; doctorlixiaofei@163.com

Received 25 November 2021; Revised 29 December 2021; Accepted 7 January 2022; Published 29 January 2022

Academic Editor: Fu Wang

The serine protease inhibitor clade E member 1 (SERPINE1) is a major inhibitor of tissue plasminogen activator and urokinase, and has been implicated in the development and progression of a variety of tumors. In this study, mRNA microarray and TCGA database were used to comprehensively analyze the upregulation of SERPINE1 in gastric cancer (GC) tissues compared with the normal stomach tissues. Kaplan-Meier results confirmed that patients with high SERPINE1 expression exhibited worse overall survival and disease-free survival. In addition, cell proliferation, cell scratches, transwell migration and invasion assay showed that SERPINE1 knockdown inhibited the proliferation, migration and invasion of GC ells. Western blot showed that the expression of VEGF and IL-6 was significantly upregulated after overexpression of SERPINE1. Meanwhile, SERPINE1 was positively correlated with the level of immune infiltration using the online analysis tools TISIDB and TIMER. And SERPINE1 expression increased with the increase of malignancy of GC which were detected by Immunohistochemistry. Finally, tumorigenesis experiments in nude mice further demonstrated that SERPINE1 could promote the occurrence and development of GC, while deletion of SERPINE1 inhibited the progression of GC. In summary, SERPINE1 was highly expressed in GC tissues, and SERPINE1 was helpful for differential diagnosis of pathological grade of gastric mucosal lesions. SERPINE1 might regulate the expression of VEGF and IL-6 through the VEGF signaling pathway and JAK-STAT3 inflammatory signaling pathway, thus ultimately affecting the invasion and migration of GC cells.

1. Introduction

As one of the most common cancers in the world, gastric cancer (GC) is the first malignant tumor of digestive tract, which seriously threatens human life and health. It was reported that GC ranked fifth in the number of new cases among all cancers in 2020, and was also the fourth most common cause of cancer-related death [1]. In general, GC can be diagnosed by endoscopic pathological tissue biopsy [2]. Currently, the main treatment methods for GC include surgery, radiotherapy, chemotherapy and targeted therapy, etc., but the above treatment effects are not ideal, the recurrence rate of GC is still high and the prognosis is very poor [3]. This is mainly due to the uncertainty of histopathological behavior and metastasis characteristics of early GC, so the early diagnosis rate of GC is low (about 10%). Most GC is already in the middle and late stages when diagnosed, while the 5-year survival rate of late GC is about 20% [4]. Therefore, it is very important to explore new biomarkers and therapeutic targets for GC.

Serine protease inhibitor clade E member 1 (SERPINE1) is a member of the Serine protease inhibitor family and a key modulator of the plasminogen/plasminase system [5]. SERPINE1 is a single-chain, non-glycosylated polypeptide chain containing 400 amino acids with a molecular weight of 50 kDa [6]. This gene encodes a member of the serine protease inhibitor (Serpin) superfamily, which is a major inhibitor of tissue plasminogen activator (TPA) and urokinase (UPA) [7]. SERPINE1 protein is composed of 379 amino acids and is mainly synthesized and secreted by

platelets, megakaryocytes, hepatocytes, adipocytes, smooth muscle cells and vascular endothelial cells [8]. In addition, SERPINE1 is associated with a variety of diseases and activities *in vivo*, including cardiovascular diseases, inflammation, cancer, metabolic disorders, aging, tissue fibrosis, etc [9].

Previous studies showed that SERPINE1 had focused on its effect on thrombosis in humans [10]. Using high-throughput sequencing technology, SERPINE1 was found to be significantly overexpressed in a variety of tumor tissues [11]. It has been reported that SERPINE1 can be used as a proliferation regulator of glioblastoma, and its high expression can promote the proliferation and invasion of glioma cells [12]. Enhanced SERPINE1 activity promotes metastasis of melanoma [13], and high SERPINE1 expression is a potential marker of poor prognosis of breast cancer [14]. Other SERPINE1-related tumors include ovarian cancer, renal clear cell carcinoma, etc. [15, 16].

In recent years, SERPINE1 has been found to be involved in immune cell infiltration, which plays a role in the remodeling of colon cancer microenvironment and immune cell infiltration [17]. SERPINE1 can affect immune cell infiltration in the microenvironment of diffuse low-grade glioma and has independent prognostic value [12]. Currently, SERPINE1's abnormal tumor-promoting function in cancer progression and metastasis has become a consensus. Previous literature have indicated that SERPINE1 had pro-angiogenic, growth and migration stimulation and anti-apoptotic activity, all of which were targeted at promoting tumor growth, cancer cell survival and metastasis [18]. SERPINE1 has been proven to be the most reliable biological and prognostic marker for a variety of cancers, including breast cancer [19–21], ovarian cancer [22], bladder cancer [23, 24], colon cancer [25], kidney cancer [26] and non-small cell lung cancer [27].

In this study, we used data from The Cancer Genome Atlas (TCGA) database to evaluate SERPINE1 expression and verified it in the Gene Expression Omnibus (GEO) database (GSE118916, GSE66229 and GSE13911). Gene Set Enrichment Analysis (GSEA) signaling pathway was used to analyze the biological pathways involved in the pathogenesis of GC regulated by SERPINE1. In addition, we also observed the effects of SERPINE1 on GC cell proliferation, invasion and migration, and subcutaneous tumorigenesis in nude mice. We may discover a novel prognostic biomarker and a potential molecular mechanism affecting the prognosis of GC.

2. Materials and Methods

2.1. Sample Sources and Clinical Data. From 2018 to 2020, a total of 8 GC tissues were collected from the First Affiliated Hospital of Jinzhou Medical University for paraffin embedding. Written informed consent was obtained from all participants. This study was approved by the Ethics Committee of the First Affiliated Hospital of Jinzhou Medical University (KYLL 202119). None of the patients received radiation and chemotherapy before surgery. All sections were evaluated by the pathologist and a definitive diagnosis was made.

2.2. Data Collection. Three datasets (GSE118916, GSE66229 and GSE13911) were obtained from the GEO database (https://www.ncbi.cn) of the National Center for Biotechnology Information. The two sets of raw data were integrated using multi-array averaging and SVA software package preprocessing and removal of batch effect. Using $p < 0.05$ and $|\log FC| \geq 1$ or as a critical value and crossed the genetic variations of intersection, the R programming language limma package was applied to compare GC tissue with normal tissue samples from TCGA database to identified the differentially expressed genes (DEGs).

2.3. UALCAN Database. Possible subgroup analysis UALCAN (http://ualcan.path.uab.edu/cgi-bin/ualcan-res.pl) is an effective cancer data on-line analysis and mining site, mainly based on the TCGA related cancer database, UALCAN database allowed relevant biomarker identification, gene expression profile analysis, survival analysis, etc. [28]. We used it to analyze the relationship between SERPINE1 expression and clinicopathological variables.

2.4. Gene Set Enrichment Analysis (GSEA). Molecular signatures database (http://software.broadinstitute org/gsea/msigdb) available to be gene sets for this [29]. GSEA was used to evaluate the relationship between SERPINE1 expression and signaling pathways.

2.5. SERPINE1 Positioning Tool. SERPINE1 mRNA expression in human body and its positioning in the cells could be obtained by human proteins chart spectrum (https://www.proteinatlas.org/).

2.6. Immunocorrelation Analysis Tool. TISIDB (http://cis.hku.hk/TISIDB/index.php), a portal for tumor-immune system interaction, integrates series of heterogeneous data for further study of the correlation between SERPINE1 and the expression of immune regulator of Spearman [30]. TIMER2.0 (http://timer.cistrome.org/) as the network server update, analyze and visualize tumor immune with its connected other tumor molecular and clinical features. TIMER provides a reliable assessment of immune invasion levels and helps to discover associations among immune invasion, gene expression, mutation, and survival characteristics in the TCGA cohort. It can be said that the TIMER2.0 web server provides comprehensive analysis and visualization of tumor-infiltrating immune cells [31].

2.7. Cell Culture and Transfection. BGC-823 and MKN-28 cell lines were cultured in complete medium supplemented with 10% fetal bovine serum (FBS; Gibco, USA) and 1% penicillin and streptomycin. The cells were cultured in an incubator at 37°C and 5% CO_2.

Small interfering RNA for SERPINE1 (si-SERPINE1) and Control siRNA (si-NC), SERPINE1 overexpression plasmid (oe-SERPINE1) and Control plasmid (vector) were synthesized by Hongxin Company. All cell transfection was

performed using Lipofectamine 2000 (Sigma, USA). The obtained cells were used for data study 48 h after transfection.

2.8. RT-qPCR. Total RNA was extracted from the transfected cells with TRIzol reagent (Invitrogen, USA) and was then transcribed into cDNA according to the reverse transcription kit instructions (Promega, USA). Subsequently, the quantitative PCR was performed with SYBR Green RT-PCR kit (Takara, Japan) according to the manufacturer's protocol. The relative expression of SERPINE1 was performed using the 2-ΔΔCT method. And GAPDH was used as an internal reference. The primer sequences were shown in Table 1.

2.9. Cell Proliferation Assay. BGC-823 and MKN-28 cells were transfected, and cells were added into a 6-well plate containing 10% CCK-8 complete medium at 37°C for 30–60 min. And liquid discoloration was observed by naked eyes. The absorbance value at OD450 nm was measured at 0, 24, 48 and 72 h after all the holes in the test plate have no color change or no orange yellow substance is formed. All the above experiments need to be carried out three times.

2.10. Cell Scratch Test. The cells were transfected in 6-well plates. After the cells were observed to be full of holes, a straight line was drawn in the center of the holes with appropriate strength with 20 μL pipette tip. After the line was drawn, the cells were left standing for 30 min, and the time was recorded. The scratch distance was observed and photographed at 24 h and 48 h. Finally, the scratch distance was analyzed. The above experiments were in triplicate.

2.11. Transwell Migration and Invasion Experiment. In transwell migration assay, the transfection cells were centrifuged and suspended, and then added into the upper layer of transwell cell. Meanwhile, 600 μL complete medium containing 20% FBS was added into the lower chamber. The cells were placed in the cell culture box for incubation for 24 h. The cells were then fixed, washed and stained. Finally, the stained cells were counted under the microscope, and the average value was taken and photographed.

In transwell invasion assay, based on the migration experiment, the matrigel was extracted and precoated with the upper chamber. The other steps referred to the migration assay.

2.12. Western Blot. Cells were lysed with cell lysis buffer And the total protein was extracted. Next, 20 μg total protein was separated by 10% SDS-PAGE gel and then transferred to the polyvinylidene fluoride (PVDF) membranes. The membrane was sealed with 5% skimmed milk at room temperature for 1 h. According to the instructions of primary antibody (all purchased from Bode biological company), the membrane was incubated with Anti-IL-6 antibody (product No. pb0061, 1 : 500 dilution), anti Serpine1 antibody (product No. a00637-1, 1 : 1000 dilution), anti VEGF antibody (product No. a00623, 1 : 500 dilution) and β-Actin (product No. ba0426, diluted 1 : 1000) overnight at 4°C. Then, the horseradish peroxidase (HRP) labeled secondary antibody (product No. ab7090, diluted 1 : 1000, purchased from Abcam company) was diluted with secondary antibody diluent according to the instructions, and incubated at room temperature for 1 h. After incubation, the film was developed using a chemiluminescence substrate. Grayscale analysis was performed using ImageJ software (version 1.50b; National Institutes of Health).

Table 1: RT-qPCR primer sequence.

Primer name	Primer sequence
GAPDH-F	TCAAGATCATCAGCAATGCC
GAPDH-R	CGATACCAAAGTTATCATGGA
SERPINE1-F	TTCAAGATTGATGACAAGGGC
SERPINE1-R	CTCATCCTTGTTCCATGGC

2.13. Immunohistochemical Analysis. Paraffin blocks of GC tissue were processed into 5 μm thick sections. SERPINE1 expression was detected by streptavidin-peroxidase (SP) assay. Gastric tissue sections expressing SERPINE1 were used as positive control and phosphate buffer was used instead of antibody as negative control. Each section was analyzed in parallel with the positive and negative control sections. Polyclonal antibodies against SERPINE1 (Abcam, Cambridge, UK; 1 : 75) to evaluate the expression and clinical significance of SERPINE1 in GC. The staining procedure was performed using the SP kit. The presence of strong particle staining in the cell membrane and cytoplasm is considered SERPINE1 positive. Staining cells were classified according to color intensity using the following scoring system: no pigment (0 points), light yellow (1 points), brown-yellow (2 points), and dark brown (3 points). The percentage of stained cells in the microscopic field was classified as <5% (0 points), 5%–25% (1 point), 26%–50% (2 points), 51%–75% (3 points), and >75% (4 points). Multiply the number of stained cells by the percentage of stained cells to obtain the following final scores: 0–2 points (−), 3–4 points (+), 5–8 points (++), and 9–12 points (+++). A score of 3–12 is considered positive, and a score of 5–12 is considered highly positive. Each tissue section was independently evaluated by two observers to minimize errors.

2.14. Subcutaneous Tumorigenesis in Nude Mice. Twelve male nude mice (6 weeks old, 19.8 ± 1.7 g) were fed at 23°C, 55% humidity, 12 hours of time/dark cycle and sufficient food and water. Add the previously obtained 15×10^6 cells were resuspended and injected subcutaneously into 12 nude mice (4 in each group). The tumor size was checked regularly to monitor the tumor growth. After the study, the cervical spine was severed, the mice were killed, and the tumor was separated subcutaneously for follow-up evaluation. The animal experiment was approved by the animal ethics committee of the First Affiliated Hospital of Jinzhou Medical University.

2.15. Statistical Analysis. R (v.3.5.1) and GraphPad Prism 7 software were used for statistical analysis. Continuous data comparison between the two groups was performed by independent *t* test, and classified data was performed by chi-square test. The prognostic value of SERPINE1 expression in GC was evaluated according to overall survival (OS) and disease-free survival (DFS) by Kaplan-Meier analysis. $p < 0.05$ was considered statistically significant.

3. Result

3.1. Screening of DEGs. After pretreatment and removal of batch effect, DEG (GSE13911, GSE118916 and GSE66229) was analyzed by limma software package. According to $|\log FC| \geq 1$, the volcano map showed the up-regulated genes marked in red and the down-regulated genes marked in green (Figures 1(a)–1(c)). Taking the intersection with DEGs in the three datasets and TCGA database, total of 44 DEGs were finally identified (Figure 1(d)). After screening, it was found that SERPINE1 gene was differentially expressed in GC and normal tissues.

3.2. Relationship of SERPINE1 Expression with Prognostic Clinicopathological Variables in GC. In order to clarify the role of SERPINE1 expression in predicting the prognosis of GC, Kaplan Meier was used for survival analysis. Figure 2(a) showed that patients with high expression of SERPINE1 had shorter DFS than those with low expression ($p = 0.005$). At the same time, GC patients with high expression of SERPINE1 exhibit worse OS than those with low expression ($p < 0.05$) (Figure 2(b)).

The relationship between SERPINE1 expression and clinicopathological variables was analyzed through the UALCAN database. The subgroup analysis results showed that SERPINE1 expression in patients with GC was related to race, age, tumor grade and individual cancer stage (Figures 2(c)–2(f)).

3.3. GSEA Identified SERPINE1 Related Signal Pathways. Based on MSigDB enrichment analysis, GSEA results showed that there were significant differences between SERPINE1 high expression group and low expression group. In the SERPINE1 high expression group, the eight most significantly enriched signal pathways were cytokine cytokine receptor interaction, extracellular matrix receptor interaction, focal adhesion, hypertrophic obstructive cardiomyopathy, JAK-STAT3 signal pathway, MAPK signal pathway, and cancer pathway (Figures 3(a)–3(i)).

3.4. SERPINE1 Promoted the Growth of GC Cells in Vitro. In order to locate SERPINE1 in cells, we used human protein Atlas database to locate SERPINE1 in cells. The results showed that SERPINE1 was localized in the cytoplasm in U2-OS and U-251 cell lines (Supplementary Figure 1).

We knocked down and overexpressed SERPINE1 in GC cells for subsequent experiments to clarify the role of SERPINE1 in the occurrence and development of GC. Human GC cell lines BGC-823 and MKN-28 were transfected with si-SERPINE1 or oe-SERPINE1. The results in Figures 4(a)–4(d) confirmed that oe-SERPINE1 significantly upregulated the expression of SERPINE1 in GC cells. And si-SERPINE1 could significantly inhibit SERPINE1 expression. CCK-8 assay results showed that Serpine1 knockdown suppressed the proliferation of BGC-823 and MKN-28 cells (Figure 5(a)). Moreover, the results of scratch test and Transwell assay showed that downregulation of SERPINE1 (si-SERPINE1 group) could significantly inhibit the migration and invasion ability of BGC-823 and MKN-28 cells (Figures 5(b)–5(d)). However, the results of Serpine1 overexpression group were just opposite to those of Serpine1 knockdown group (Figures 6(a)–6(d)).

3.5. SERPINE1 Promoted the Expression of VEGF and JAK-STAT3 Pathway Related Proteins. Previous studies have shown that VEGF and IL-6 were highly expressed in GC and promoted the occurrence and development of GC by promoting angiogenesis and maintaining continuous uncontrollable inflammatory response [31]. Here, we analyzed the relationship between SERPINE1 expression and VEGF and IL-6 to explore the possible mechanism in GC. When SERPINE1 was knocked down in MKN-28 cells, the results showed that the expression of SERPINE1 decreased. At the same time, the expression of VEGF and IL-6 in si-SERPINE1 group was significantly lower ($p < 0.05$) (Figures 7(a) and 7(b)). However, when SERPINE1 expression was upregulated (oe-SERPINE1 group), the expression of VEGF and IL-6 was significantly increased (Figures 7(a) and 7(b)).

3.6. SERPINE1 Expression Was Related to the Immune System. Previous studies have shown that the immune system was significantly related to the development of tumor. Therefore, we further explored whether SERPINE1 has an effect on immune factors. We found that SERPINE1 was significantly correlated with ENTPD1, CXCL12, IL10, KDR, TGFB1, PDCD1LG2, CCL2, CCL3 and CXCL5 ($p < 0.001$) (Figure 8).

Using the TIMER database to evaluate the relationship between the expression of SERPINE1 and the level of immune infiltration, we found that after purity adjustment, SERPINE1 was highly expressed in cells, macrophages, dendritic cells and neutrophils in the high immune infiltration group (supplementary Figures 2(a), 2(c), 2(e), 2(g)). Copy number variation of SERPINE1 was significantly correlated with CD8 + T cells, dendritic cells, and neutrophils ($p < 0.05$), but not macrophages ($p > 0.05$) (supplementary Figures 1(b), 1(d), 1(f), 1(h)). The above results suggest that SERPINE1 was related to the infiltration of immune cells, and SERPINE1 might be involved in the recruitment of immune cells.

3.7. Immunohistochemical Verification of the Expression of SERPINE1 and Ki67 in GC Lesions. Because the expression of SERPINE1 and Ki-67 was directly proportional to the staining, through the comparative analysis of

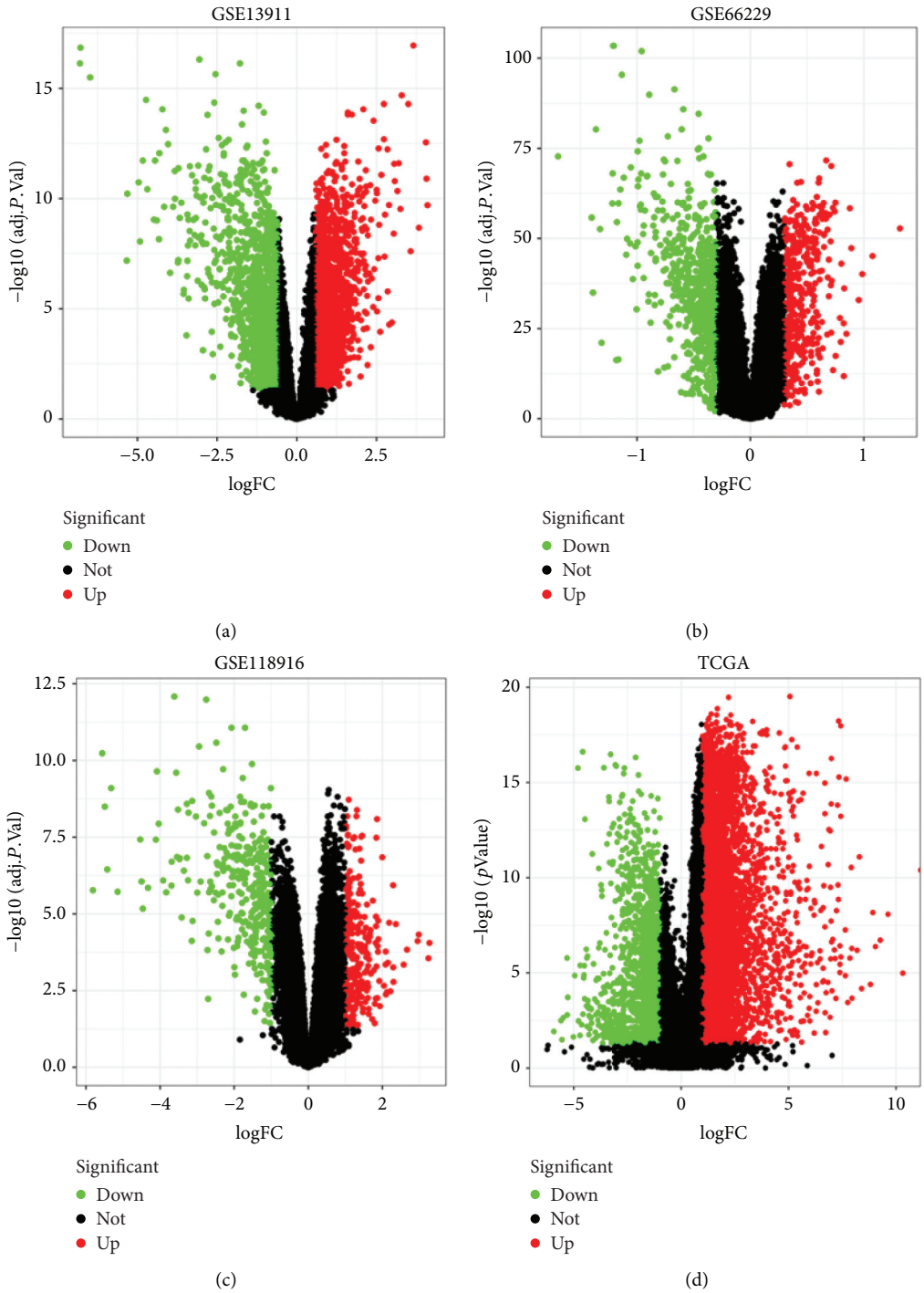

Figure 1: Continued.

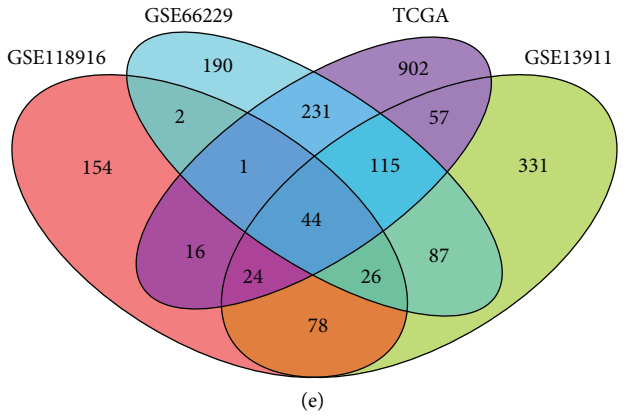

(e)

Figure 1: Differentially expressed genes between gastric cancer and normal tissues. (a-c): volcanic map of differentially expressed genes in GSE13911 (a), GSE66229 (b), GSE118916 (c) and TCGA (d) database. (e) Venn diagram distribution of differentially expressed genes.

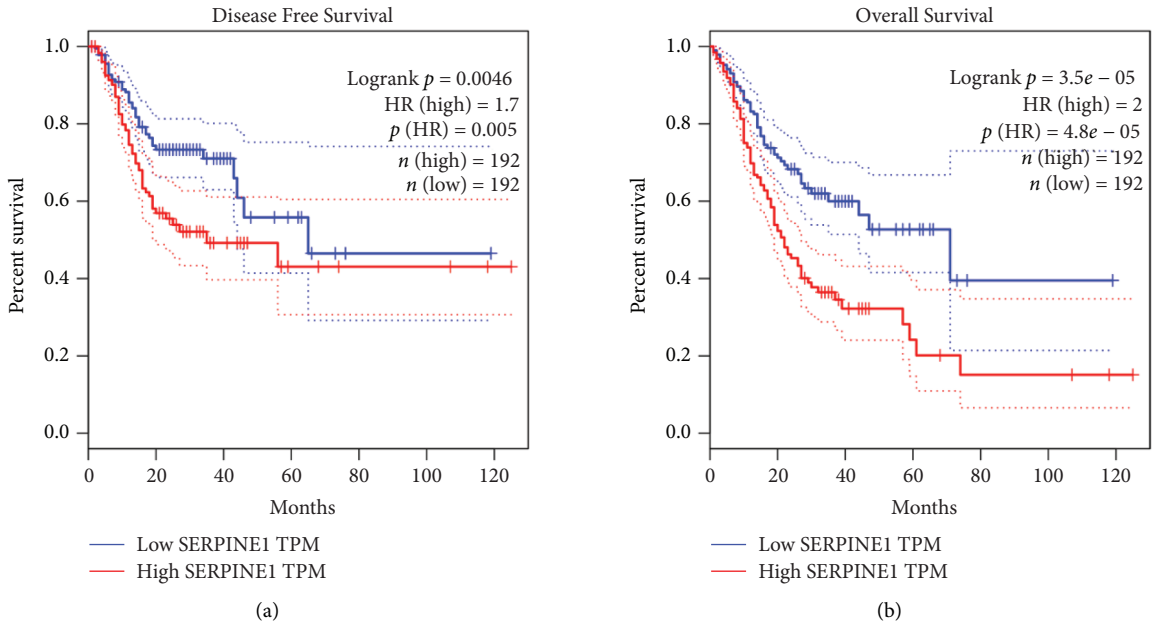

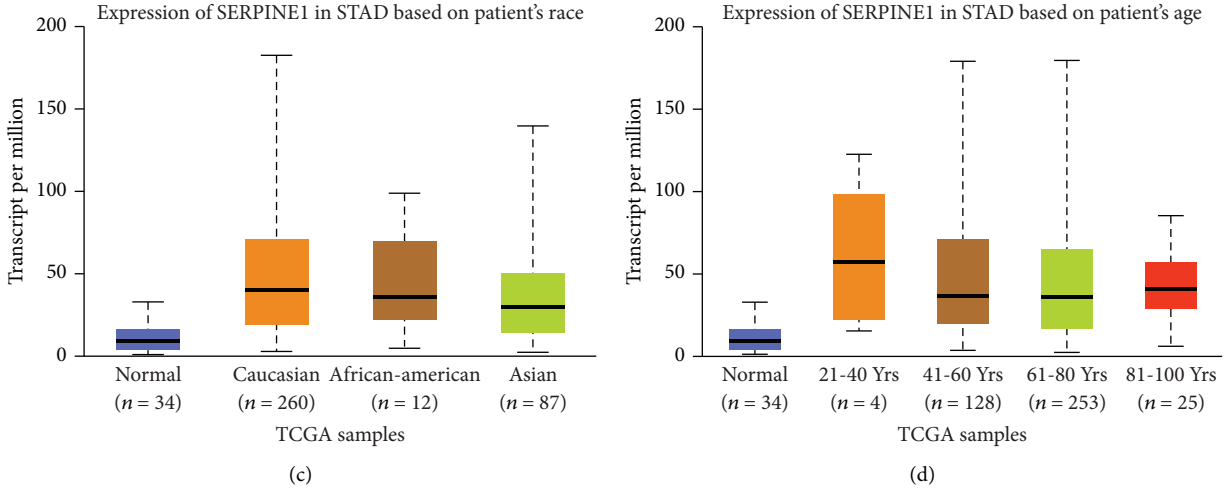

Figure 2: Continued.

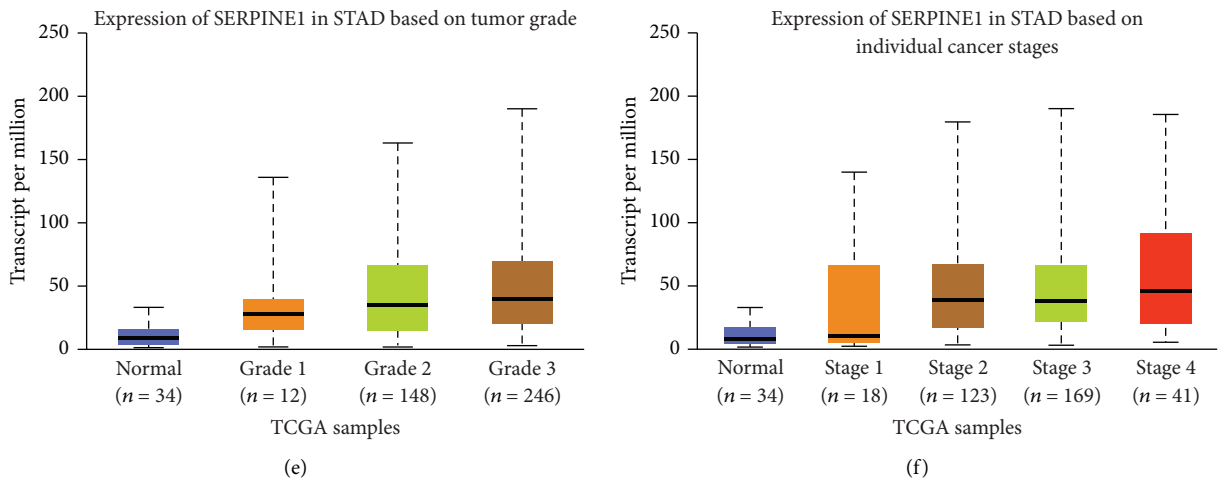

Figure 2: The value of SERPINE1 in the prognosis of gastric cancer and its relationship with clinicopathological features. (a-b) Patients with higher SERPINE1 expression had worse disease-free survival (a) and overall survival (b). (c-f) The expression of SERPINE1 in patients with gastric cancer was related to their race (c), age (d), tumor grade (e) and cancer stage (f).

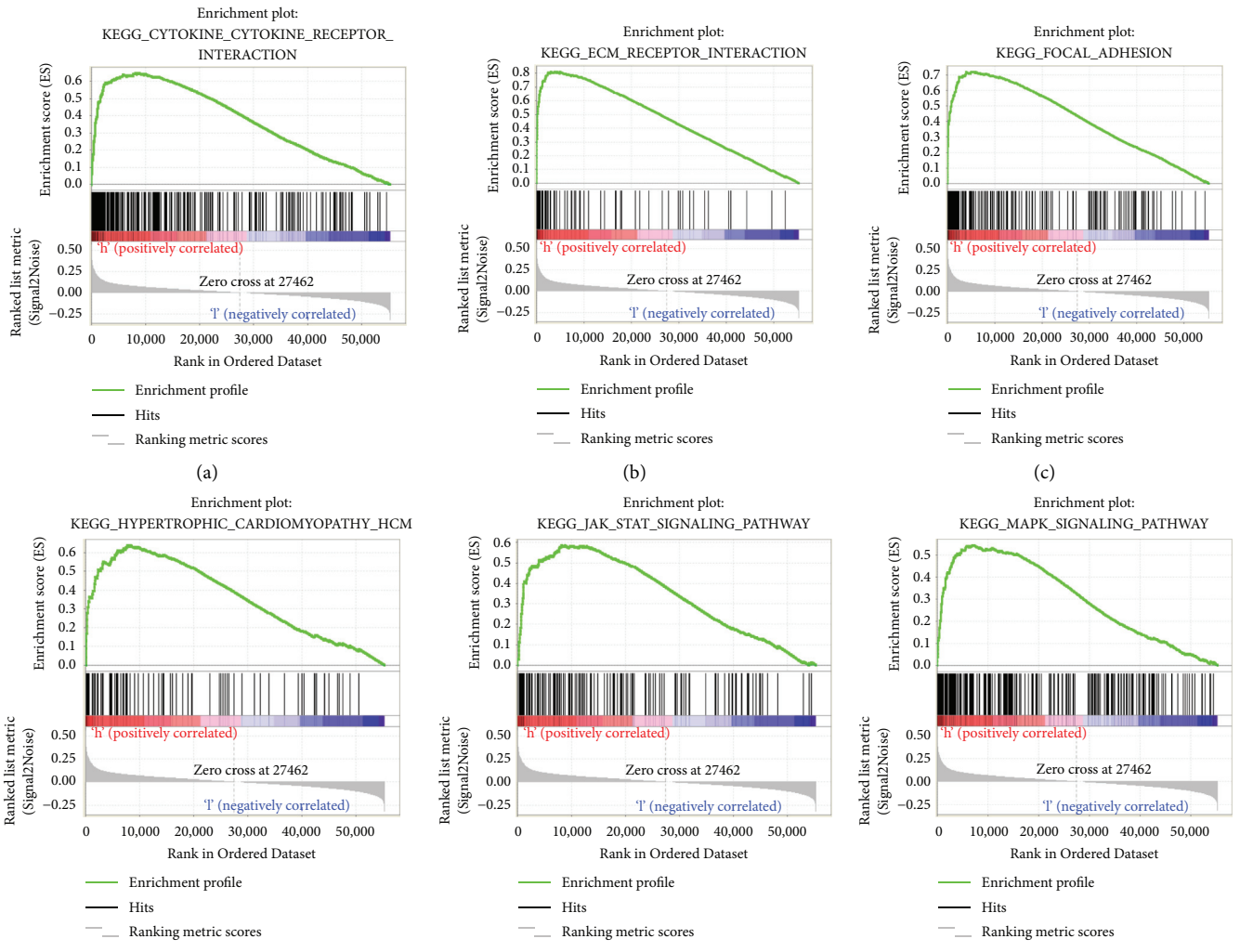

Figure 3: Continued.

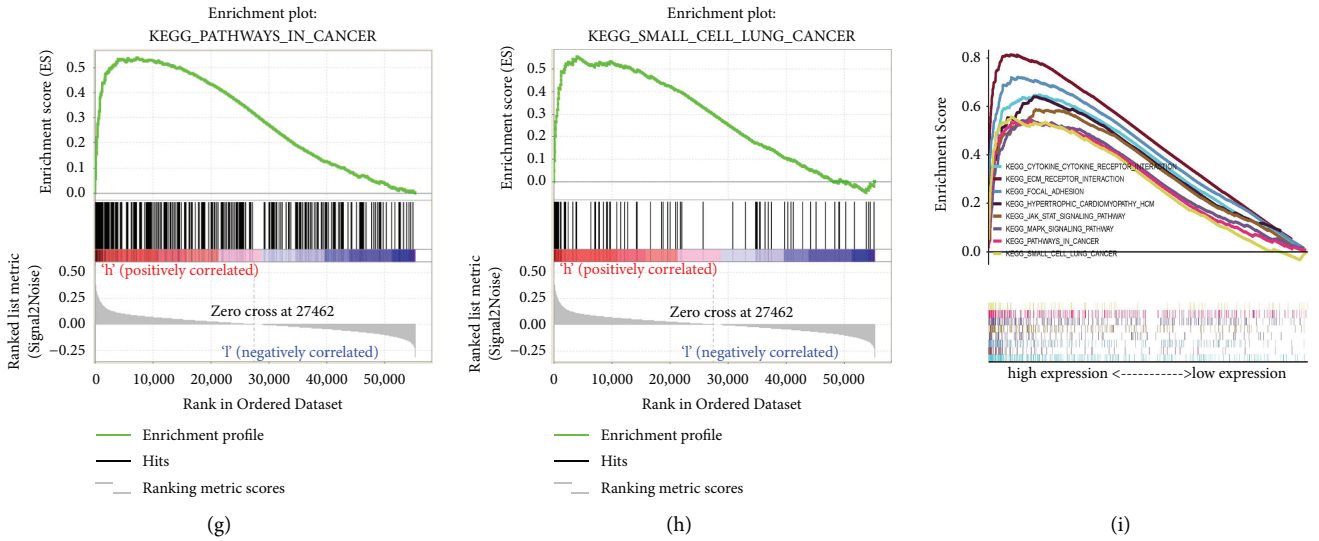

Figure 3: SERPINE1 enrichment analysis diagram based on GSEA. GSEA analysis showed that the high expression of SERPINE1 was mainly concentrated in (a) the interaction between cytokines and cytokine receptors, (b) the interaction between extracellular matrix receptors, (c) focal adhesion, (d) hypertrophic obstructive cardiomyopathy, (e) JAK/STAT signal pathway, (f) MAPK signal pathway, (g) cancer pathway and (h) small cell lung cancer signal. (i) The enrichment Score of the pathway. NES, normalized enrichment fraction, concentration fraction; FDR, false discovery rate.

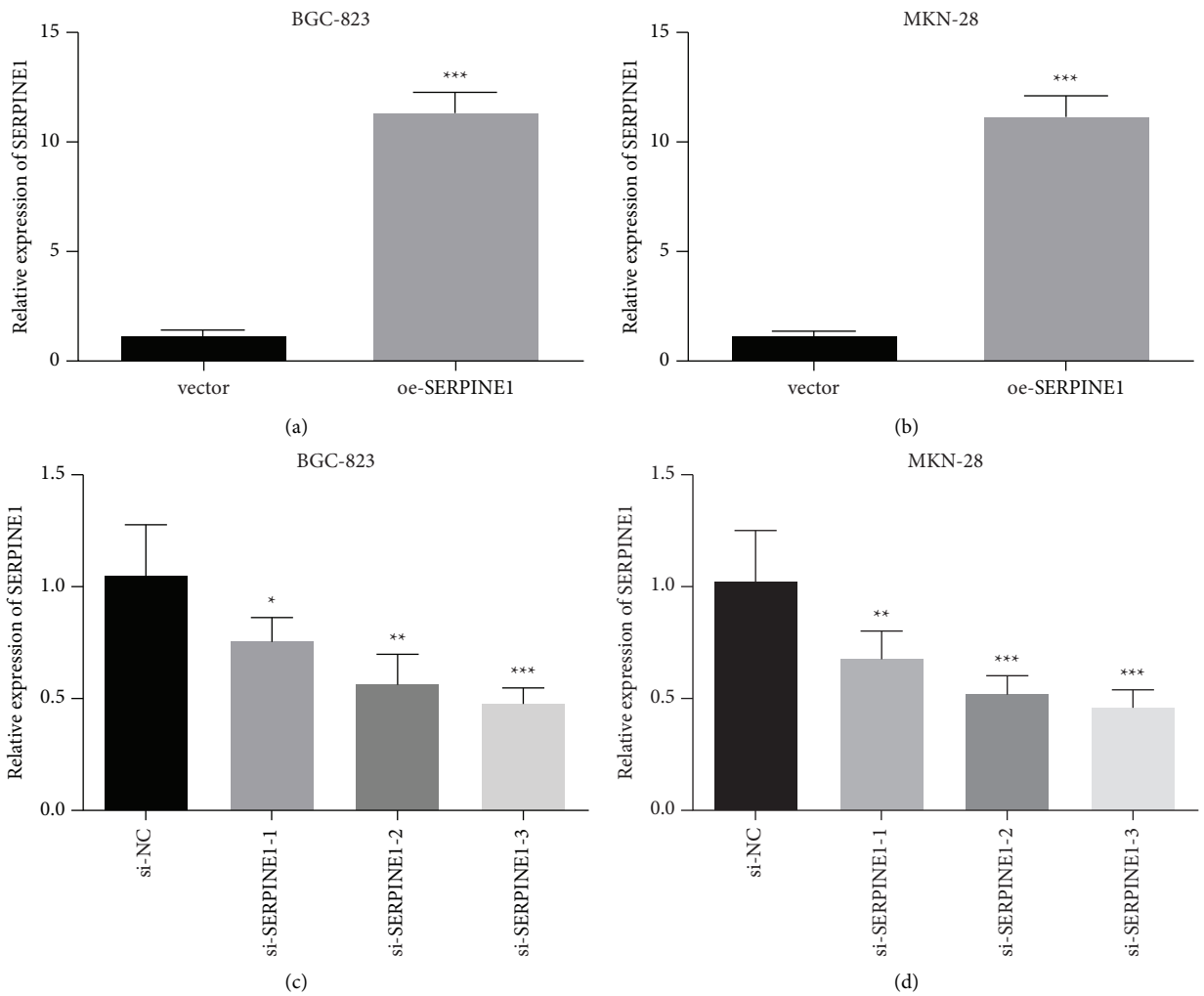

Figure 4: Establishment of SERPINE1 knockdown and overexpression cell model. The overexpression efficiency of SERPINE1 (a-b) and the knockdown of efficiency of SERPINE1 (c-d) in BGC-823 and MKN-28 cells were evaluated by RT-qPCR. $^{*}p < 0.05$, $^{**}p < 0.05$, $^{***}p < 0.001$.

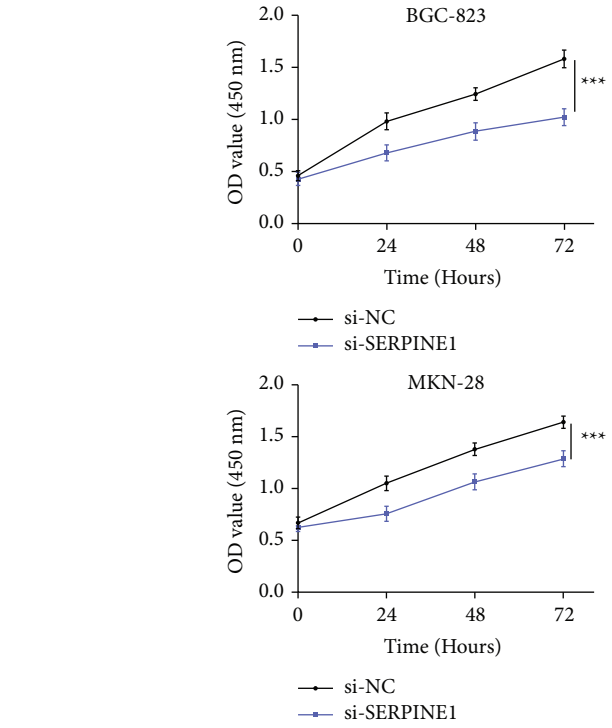

(a)

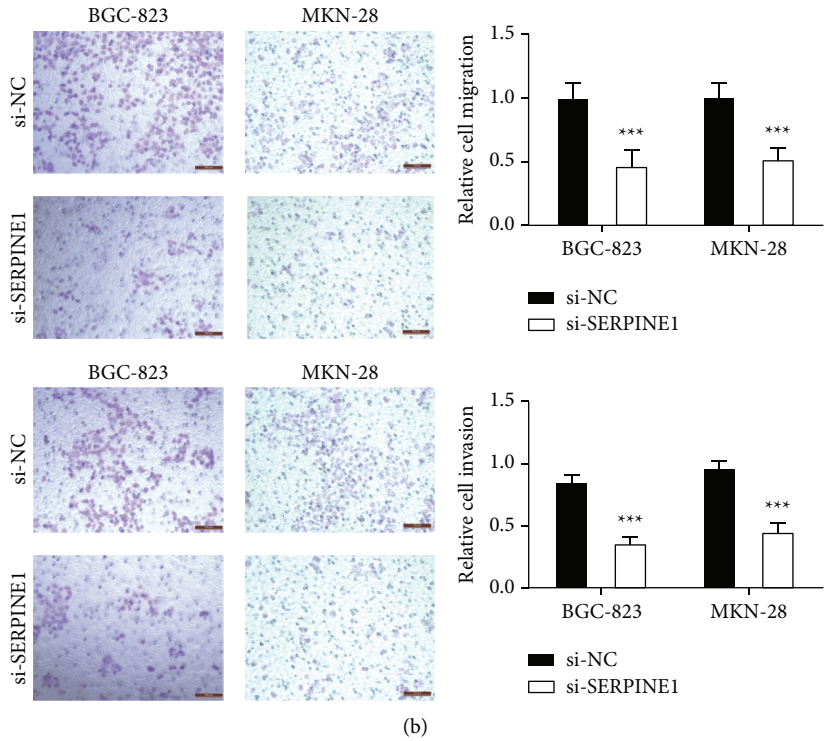

(b)

Figure 5: Continued.

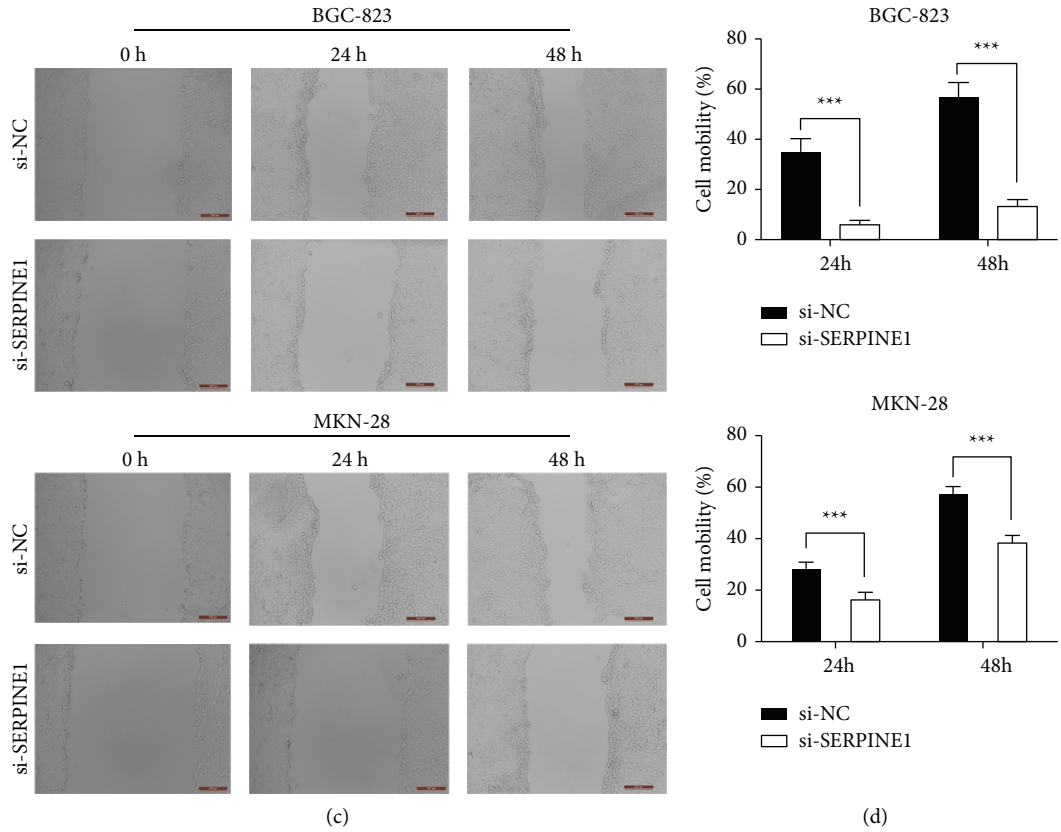

Figure 5: Knockdown of SERPINE1 inhibited the proliferation, migration and invasion of gastric cancer cells. (a) The proliferation of BGC-823 and MKN-28 cells was detected by CCK8 assay. (b) BGC-823 and MKN-28 cells migration and invasion were measured by Transwell assay. (c-d) Scratch test was performed to detect the cell mobility. $^{***}p < 0.001$.

immunohistochemical results, we found that the expression of SERPINE1 and Ki-67 in poorly differentiated GC group was significantly higher than that in highly differentiated group. With the progress of pathological severity, the staining degree gradually deepened, and the staining degree of low differentiation group was significantly higher than that of medium and high differentiation group (Figures 9(a) and 9(b)).

3.8. SERPINE1 Promoted the Growth of GC in Vivo. Further, we analyzed the effect of SERPINE1 expression on GC growth *in vivo*. Compared with NC group, the tumor volume of SERPINE1 knockout group ($114.9 \pm 14.04\,mm^3$) was significantly smaller. However, the tumor volume in the overexpression group ($531.6 \pm 64.55\,mm^3$) was the largest among the three groups, ($p < 0.001$) (Figures 9(c) and 9(d)).

4. Discussion

GC has a high mortality rate, which is nowthought to be associated with extensive invasion and metastasis [32]. Tumor metastasis is the result of many factors, and the process is more complex, including cancer cells entering the blood, invading lymph nodes, transiting through the tumor microenvironment, aggregating and secondary tissues, etc. Cancer cell migration plays an important role in the process of tumor metastasis, but the specific mechanism has not been determined and needs further studied [31], p. 2.

SERPINE1 protein can quickly inhibit the formation of plasmin. Based on its effect on fibrinolytic function, SERPINE1 is involved in chronic inflammation, tumor metastasis, tissue fibrosis and other pathological processes involving heart and lung, kidney, breast and other organs, and has a wide range of biological activities. According to previous studies, SERPINE1 is related to immune cell infiltration, which plays a role in the remodeling of colon cancer microenvironment and immune cell infiltration; SERPINE1 can affect the immune cell infiltration in diffuse low-grade glioma microenvironment and has independent prognostic value.

In this study, we comprehensively analyzed GC and normal tissues through mRNA microarray and TCGA database, and obtained the DEGs. For the relationship between SERPINE1 expression and clinicopathological variables, subgroup analysis showed that SERPINE1 expression in GC patients was related to race, age, tumor grade and individual cancer stage. Kaplan-Meier method was used to evaluates the prognosis by analyzing OS, and it is clear that SERPINE1 can be used as an independent prognostic factor of GC. SERPINE1 is located by HPA database; the effects of SERPINE1 on the proliferation, invasion and migration of

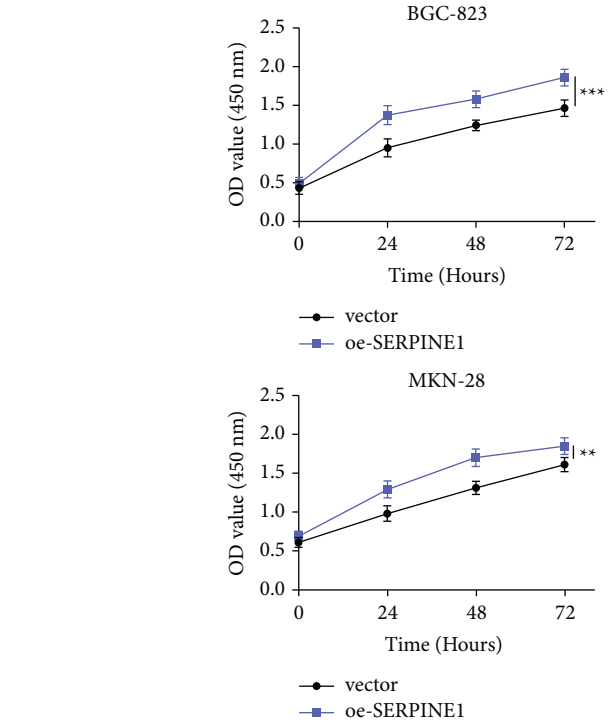

(a)

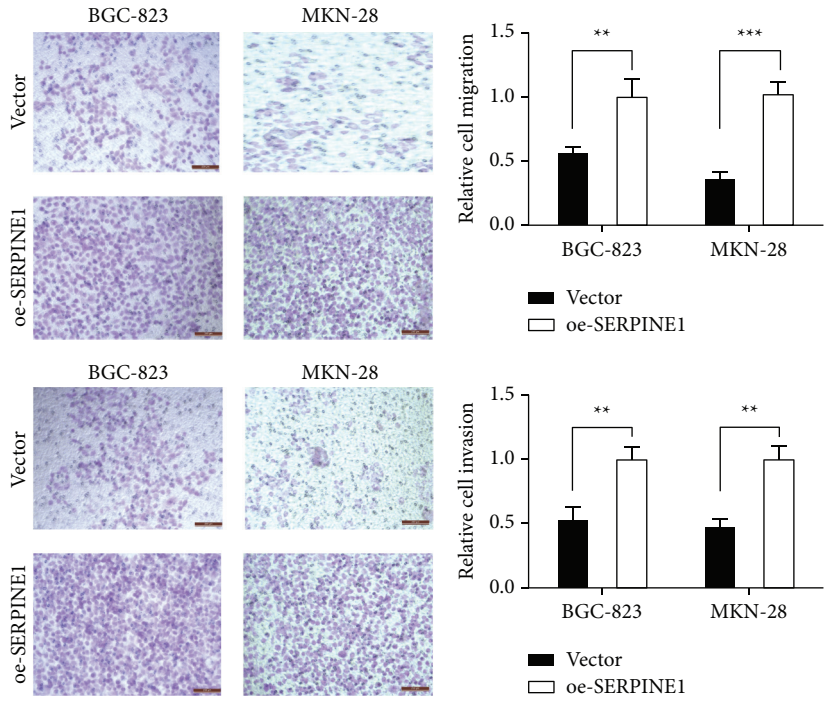

(b)

Figure 6: Continued.

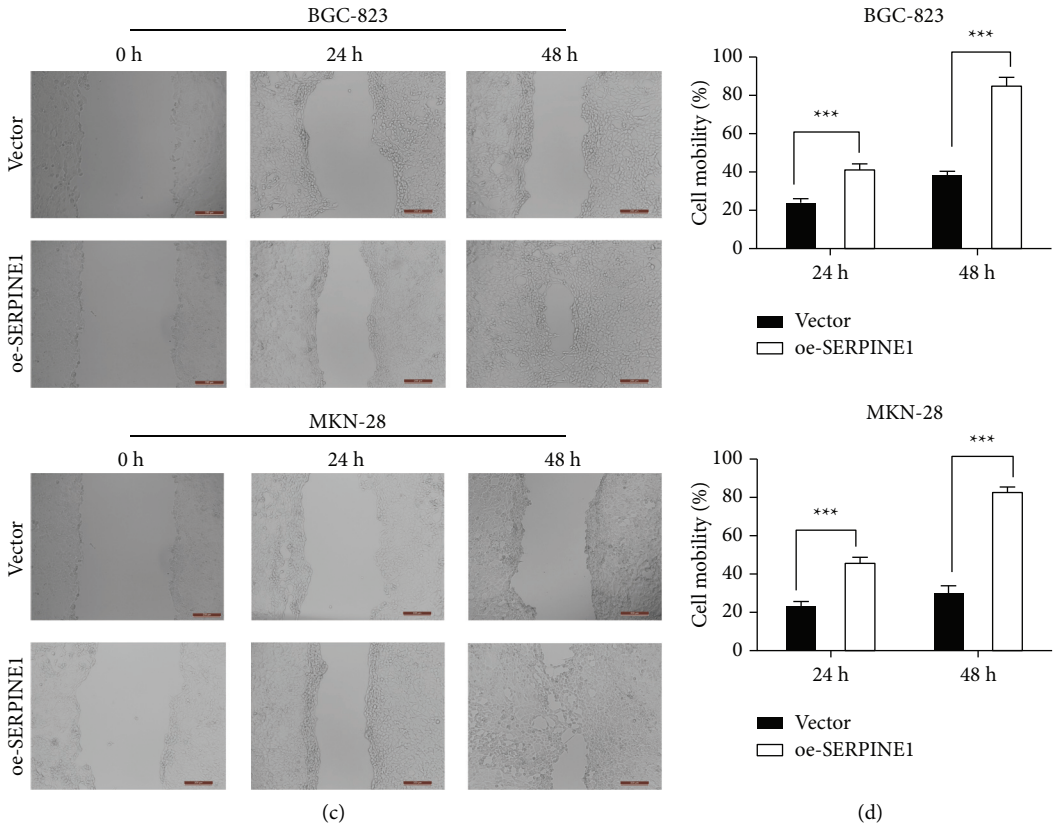

Figure 6: SERPINE1 overexpression promoted the proliferation, migration and invasion of gastric cancer cells. (a) The proliferation of BGC-823 and MKN-28 cells was detected by CCK8 assay. (b) BGC-823 and MKN-28 cells migration and invasion were measured by Transwell assay. (c-d) Scratch test was performed to detect the cell mobility. $^{**}p < 0.05$; $^{***}p < 0.001$.

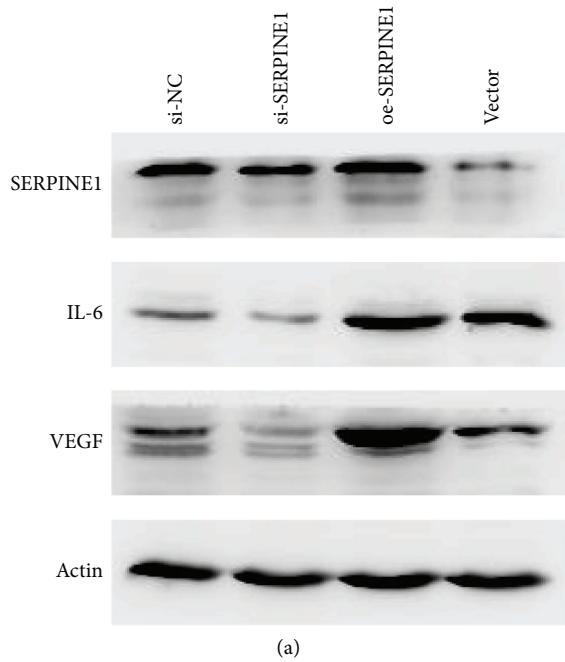

Figure 7: Continued.

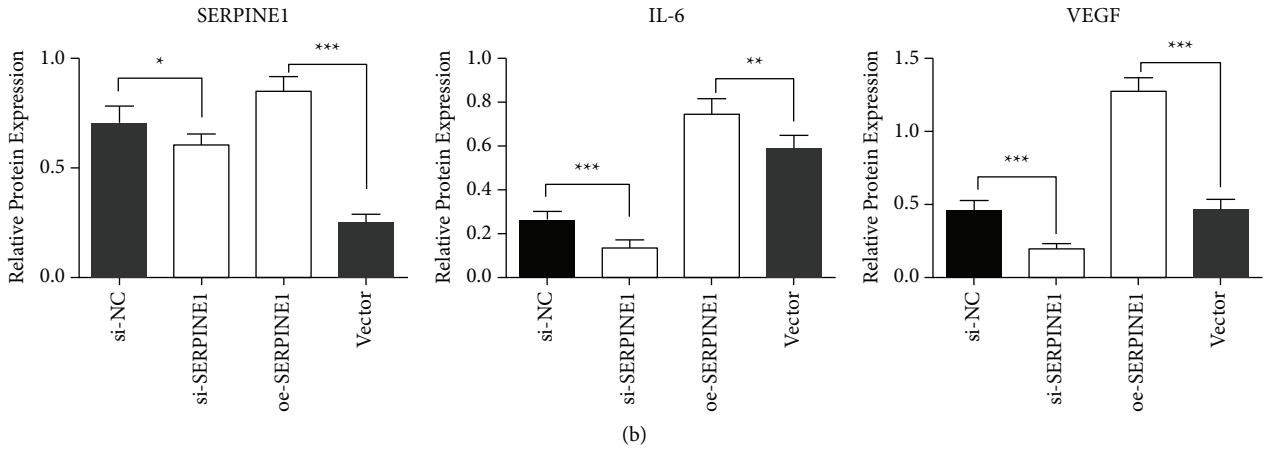

Figure 7: SERPINE1 promoted the expression of VEGF and JAK-STAT3 pathway related proteins. (a) The expression bands of SERPINE1, VEGF, and IL-6 in MKN-28 cells were detected by Western blot. (b) Gray scale analysis of SERPINE1, VEGF and IL-6 protein expression bands. $^{*}p < 0.05$; $^{**}p < 0.01$; $^{***}p < 0.001$.

GC cells were studied by cell proliferation experiment, cell scratch experiment, Transwell migration and invasion experiment and protein imprinting method. The results of TISIDB website analysis showed that SERPINE1 could affect immune regulation, and the results of TIMER analysis showed that the expression of SERPINE1 was positively correlated with immune infiltration; through immunohistochemical detection of the expression of SERPINE1 in different pathological stages and grades of mucoid lesions, we found that the expression of SERPINE1 was positively correlated with the occurrence of GC, indicating that SERPINE1 may promote GC. Finally, the above results were verified by nude mouse tumorigenesis experiment to further illustrate the effect of SERPINE1 on the progression of GC.

Previous studies showed that the high expression of SERPINE1 was significantly associated with the poor prognosis of various cancers including colon cancer, non-small cell lung cancer, ovarian cancer and breast cancer [33–35]. We believe that this situation may be closely related to SERPINE1's ability to maintain proliferation signal, promote tumor cell migration and anti-tumor cell apoptosis. Studies have shown that SERPINE1 can stimulate growth activity, up regulate cyclin D3/CDK4/6 and advance the cell cycle from G1 phase to S phase. SERPINE1 has the functions of anti-fibrinolysis, regulating cell adhesion and uPA/uPAR, and can indirectly regulate the growth of tumor cells [36]. Anti-fibrinolysis enables SERPINE1 to maintain thrombin activity and activate receptor (PAR) through thrombin and protease of tumor cells. SERPINE1 can inhibit the adhesion between tumor cells and vitronectin, and then stimulate the migration of tumor cells to other extracellular matrix substrates, such as fibronectin [37]. SERPINE1 can inhibit the binding of urokinase to urokinase type plasminogen activator receptor and further inhibit the excessive degradation of extracellular matrix proteins necessary for cell adhesion and migration [38]. At the same time, inhibiting the adhesion of tumor cells to vitronectin also makes SERPINE1 have pro-apoptotic and anti-apoptotic effects [18]. SERPINE1 can stimulate apoptosis by promoting cell separation. However, when cells separate and migrate to other extracellular matrix proteins, SERPINE1 can play a role in resisting apoptosis. SERPINE1 can inhibit caspase 3 in cells and resist tumor cell apoptosis induced by chemotherapy [39]. SERPINE1 can inhibit the cleavage of FasL and its abscission by plasmin on the cell surface outside the cell, and avoid FasL mediated and chemotherapy-induced apoptosis [40, 41]. In addition, SERPINE1 can induce c-Jun/ERK signal to up regulate anti apoptotic protein through interaction with LRP-1 [18].

Targeting SERPINE1 may have significant beneficial effects in combination with various biological effects of SERPINE1 and its effects on various pathological processes. At present, some selective PAI-1 inhibitors have been listed, including insulin sensitizers and angiotensin-converting enzyme inhibitors, and antisense oligonucleotides have been proved to reduce the synthesis or secretion of SERPINE1. Although some of these molecules are *in vitro*. It has been proved to be an effective SERPINE1 inhibitor in vivo and in vivo, but no SERPINE1 inhibitor has been approved for human treatment [9]. Therefore, it is necessary to further study the mechanism of action of SERPINE1 and its targeted drugs.

SERPINE1 is involved in the occurrence and development of a variety of cancers. High expression of SERPINE1 can promote the proliferation, invasion and migration of tumor cells. Our study found that high expression of SERPINE1 in GC can promote the proliferation, invasion and metastasis of GC cells, and is related to the epithelial mesenchymal transformation of GC cells. Therefore, SERPINE1 can be used as a new biomarker and therapeutic target of GC, provide new candidate drugs for the treatment of GC.

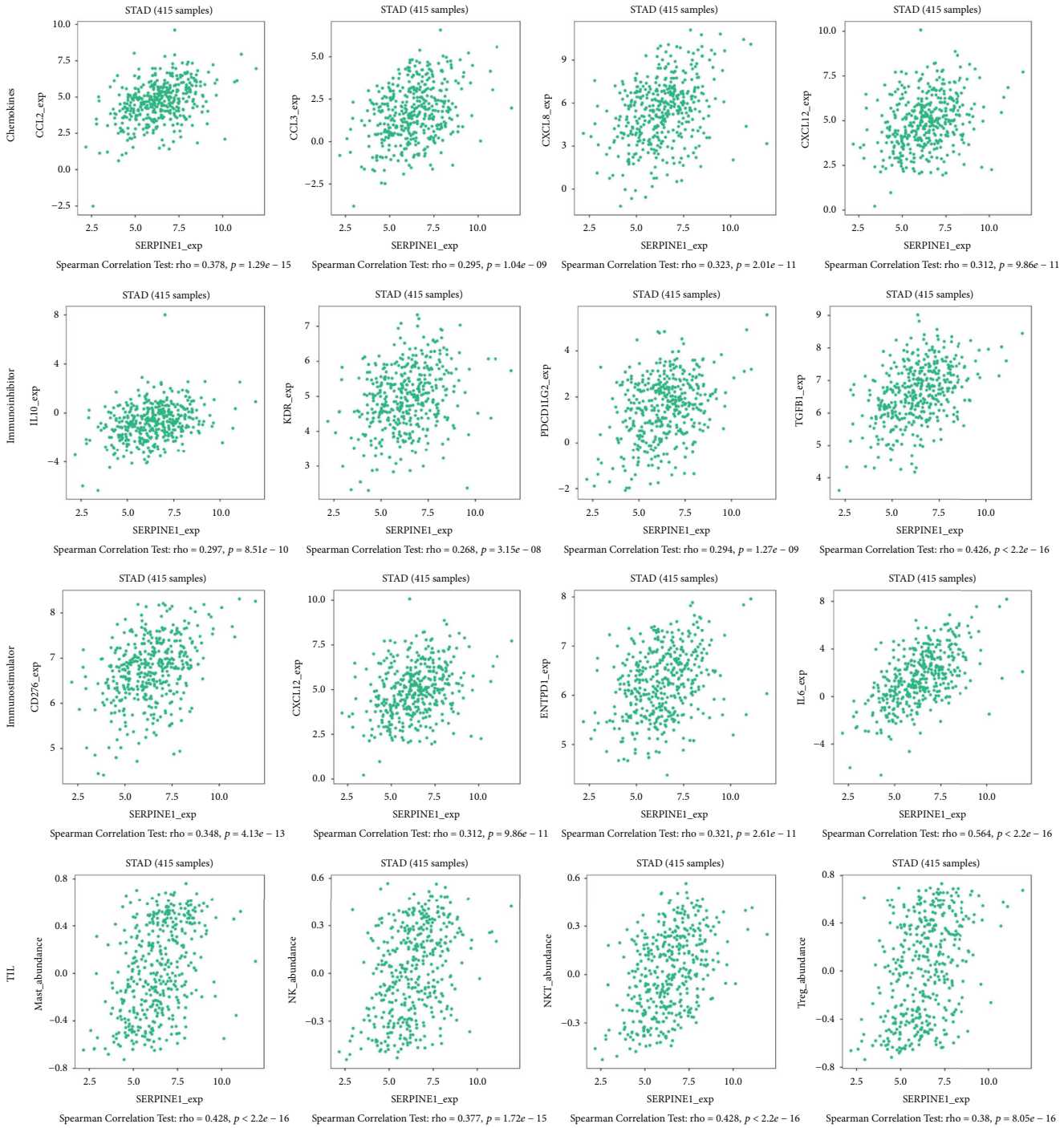

Figure 8: The expression of SERPINE1 is related to the immune system. SERPINE1 was significantly correlated with ENTPD1, CXCL12, IL10, KDR, TGFB1, PDCD1LG2, CCL2, CCL3 and CXCL5 ($p < 0.001$).

At present, our research still has some limitations, such as some data are from public databases, unable to evaluate the quality and accuracy of data, small clinical sample size, certain errors in the process of data collection, and the evaluation of the direct action mechanism of SERPINE1 in GC may not be detailed enough,

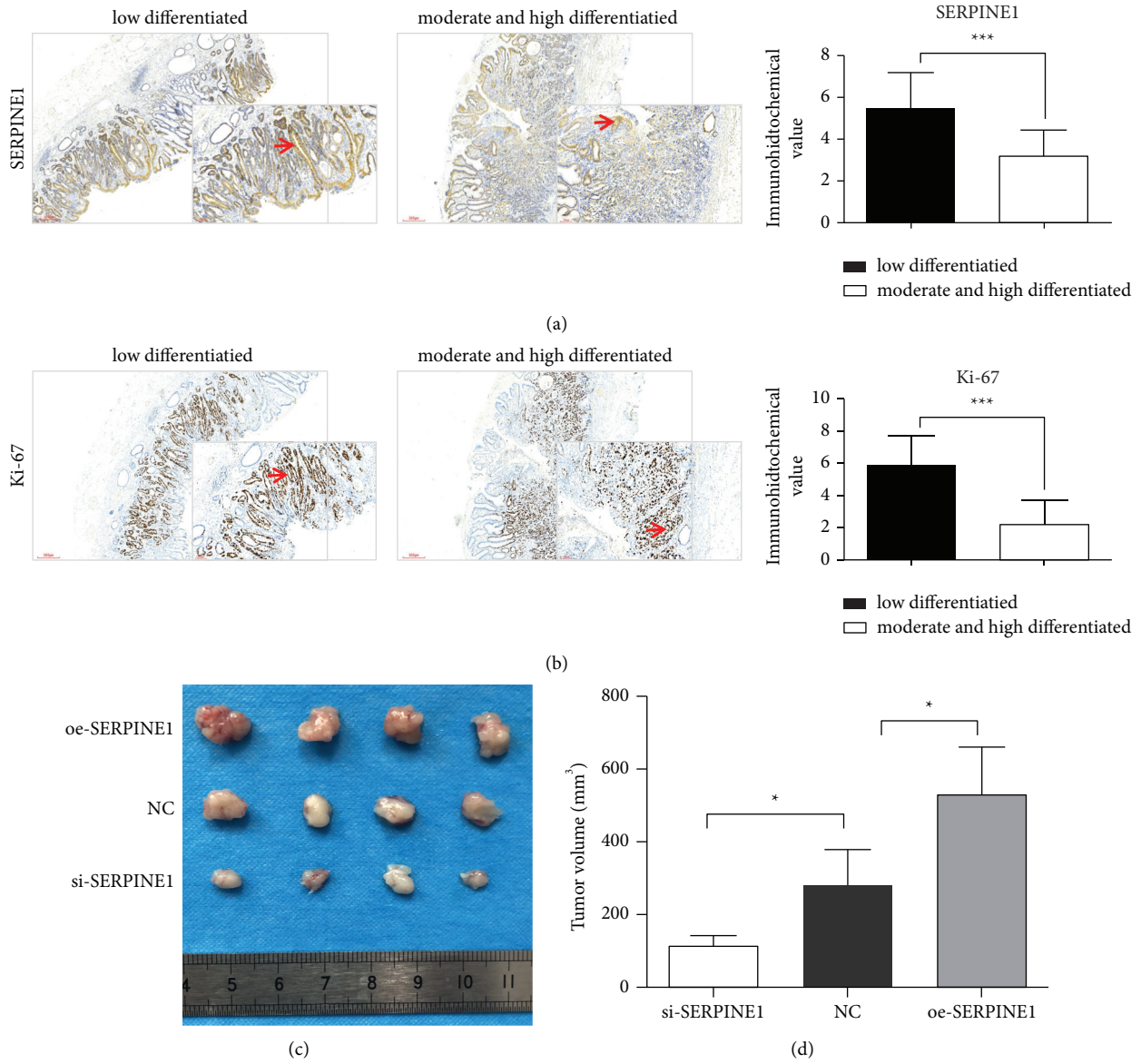

FIGURE 9: Effect of SERPINE1 on the tumorigenic ability of GC cells *in vivo*. (a-b) immunohistochemical staining representative images (Scare bar = 300 μm; Magnification: 40 x) and local enlarged images (Scare bar = 100 μm; Magnification: 100 x) of SERPINE1 (a) and Ki-67 (b) in gastric cancer tissues. (c) Image of representative tumors excised from mice. (d) The tumor volume was quantified. * $p < 0.05$; * * * $p < 0.001$.

which need to be discussed in the follow-up study improvement.

5. Conclusion

SERPINE1 was highly expressed in GC and closely related to the low overall survival rate. Silencing SERPINE1 significantly inhibited the proliferation, invasion and metastasis of GC cells. SERPINE1 expression was related to GC angiogenesis and tumor inflammatory microenvironment. Moreover, SERPINE1 might regulate the expression of VEGF and IL-6 through VEGF signal pathway and JAK-STAT3 inflammatory signal pathway. Finally, it affects the invasion and migration ability of GC cells.

Data Availability

All data and materials used in the production of this work will be available on request.

Ethical Approval

No specific ethical approval required for the production of this review article.

Consent

All contributors give consent for unrestricted publication of this work.

Conflicts of Interest

The authors have declared that there are no conflicts of interest.

Authors' Contributions

Shujia Chen and Yuqiao Li These authors contributed equally to this work. All authors contributed to the design of this study.

Acknowledgments

No specific acknowledgements. This research work was supported by Scientific research fund project of Liaoning Provincial Department of education in 2020 (JYTQN2020031).

Supplementary Materials

Supplementary Figure 1. Localization of serpine1 in cells. SERPINE1 was localized in the cytoplasm in U2-OS and U-251 mg cell lines. Scare bar = 20 μm. Supplementary Figure 2. Relationship between SERPINE1 expression and the degree of immune cell infiltration. SERPINE1 expression was positively correlated with CD8 + T cell (A), macrophage (C), dendritic cell (E) and neutrophil (G) infiltration in gastric cancer. The violin diagram example from the "scna module" shows the difference in the estimation of immune cell infiltration level between tumors with different SERPINE1 gene sacn status in gastric cancer. SERPINE1 copy number variation affects the infiltration levels of CD8 + T cells (B), macrophage (D), dendritic cells (F) and neutrophils (H) in gastric cancer. (*Supplementary Materials*)

References

[1] "Global cancer statistics 2020: GLOBOCAN estimates of incidence and mortality worldwide for 36 cancers in 185 countries-sung-2021," 2021, https://acsjournals.onlinelibrary.wiley.com/doi/10.3322/caac.21660.

[2] "Updates on management of gastric cancer," 2021, https://link.springer.com/article/10.1007/s11912-019-0820-4.

[3] L. Necula, L. Matei, D. Dragu et al., "Recent advances in gastric cancer early diagnosis," *World Journal of Gastroenterology*, vol. 25, no. 17, pp. 2029–2044, 2019.

[4] N. Coburn, R. Cosby, L. Klein et al., "Staging and surgical approaches in gastric cancer: a systematic review," *Cancer Treatment Reviews*, vol. 63, pp. 104–115, 2018.

[5] A. P. J. Declerck and A. Gils, "Three decades of research on plasminogen activator inhibitor-1: a multifaceted serpin," *Seminars in Thrombosis and Hemostasis*, vol. 39, no. 04, pp. 356–364, 2013.

[6] "uPA/uPAR and SERPINE1 in head and neck cancer: role in tumor resistance, metastasis, prognosis and therapy," 2021, https://www.ncbi.nlm.nih.gov/pmc/articles/PMC5302994/.

[7] J. Huang, M. Sabater-Lleal, F. W. Asselbergs et al., "Genome-wide association study for circulating levels of PAI-1 provides novel insights into its regulation," *Blood*, vol. 120, no. 24, pp. 4873–4881, 2012.

[8] "Research progress on the SERPINE1 protein and chronic inflammatory diseases of the upper respiratory tract: a literature review-FullText-international archives of allergy and immunology-karger publishers," 2021, https://www.karger.com/Article/FullText/516195.

[9] "A narrative review on plasminogen activator inhibitor-1 and its (Patho)Physiological role: to target or not to target?," 2021, https://www.ncbi.nlm.nih.gov/pmc/articles/PMC7962805/.

[10] S. Li, X. Wei, J. He, X. Tian, S. Yuan, and L. Sun, "Plasminogen activator inhibitor-1 in cancer research," *Biomedicine & Pharmacotherapy*, vol. 105, pp. 83–94, 2018.

[11] X. Huang, F. Zhang, D. He et al., "Immune-related gene SERPINE1 is a novel biomarker for diffuse lower-grade gliomas via large-scale Analysis," *Frontiers in Oncology*, vol. 11, 2021.

[12] F. Seker, A. Cingoz, İ. Sur-Erdem et al., "Identification of SERPINE1 as a regulator of glioblastoma cell dispersal with transcriptome profiling," *Cancers*, vol. 11, no. 11, pp. 1651–11, 2019.

[13] G. S. Hanekom, H. M. Stubbings, and S. H. Kidson, "The active fraction of plasmatic plasminogen activator inhibitor type 1 as a possible indicator of increased risk for metastatic melanoma," *Cancer Detection and Prevention*, vol. 26, no. 1, pp. 50–59, 2002.

[14] "Plasma plasminogen activator inhibitor-1 (PAI-1) levels in breast cancer – relationship with clinical outcome | anticancer research," 2021, https://ar.iiarjournals.org/content/34/3/1153.long.

[15] Y. Peng, H. Kajiyama, H. Yuan et al., "PAI-1 secreted from metastatic ovarian cancer cells triggers the tumor-promoting role of the mesothelium in a feedback loop to accelerate peritoneal dissemination," *Cancer Letters*, vol. 442, pp. 181–192, 2019.

[16] "Prognostic and therapeutic implications of extracellular matrix associated gene signature in renal clear cell carcinoma," 2021, https://www.ncbi.nlm.nih.gov/pmc/articles/PMC8026590/.

[17] S. Wang, L. Pang, Z. Liu, and X. Meng, "SERPINE1 associated with remodeling of the tumor microenvironment in colon cancer progression: a novel therapeutic target," *BMC Cancer*, vol. 21, no. 1, 2021.

[18] R. D. Balsara and V. A. Ploplis, "Plasminogen activator inhibitor-1: the double-edged sword in apoptosis," *Thrombosis & Haemostasis*, vol. 100, no. 6, pp. 1029–1036, 2008.

[19] M. Jevrić, I. Z. Matić, A. Krivokuća et al., "Association of uPA and PAI-1 tumor levels and 4G/5G variants of PAI-1 gene with disease outcome in luminal HER2-negative node-negative breast cancer patients treated with adjuvant endocrine therapy," *BMC Cancer*, vol. 19, no. 1, 2019.

[20] M. J. Duffy, N. O'Donovan, E. McDermott, and J. Crown, "Validated biomarkers: the key to precision treatment in patients with breast cancer," *The Breast*, vol. 29, pp. 192–201, 2016.

[21] R. Gauger, A. Willems, M. Kiechle, V. Magdolen, M. Schmitt, and N. Harbeck, "Urokinase-type plasminogen activator (uPA) and its inhibitor PAI-1: novel tumor-derived factors with a high prognostic and predictive impact in breast cancer," *Thrombosis and Haemostasis*, vol. 91, no. 03, pp. 450–456, 2004.

[22] E. Nakatsuka, K. Sawada, K. Nakamura et al., "Plasminogen activator inhibitor-1 is an independent prognostic factor of ovarian cancer and IMD-4482, a novel plasminogen activator inhibitor-1 inhibitor, inhibits ovarian cancer peritoneal dissemination," *Oncotarget*, vol. 8, no. 52, pp. 89887–89902, 2017.

[23] O. T. M. Chan, H. Furuya, I. Pagano et al., "Association of MMP-2, RB and PAI-1 with decreased recurrence-free

survival and overall survival in bladder cancer patients," *Oncotarget*, vol. 8, no. 59, pp. 99707–99721, 2017.

[24] "Prognostic impact of plasminogen activator inhibitor type 1 expression in bladder cancer-becker-2010-cancer-Wiley Online Library," 2021, https://acsjournals.onlinelibrary.wiley.com/doi/10.1002/cncr.25326.

[25] "Plasminogen activator inhibitor-1 as a potential marker for the malignancy of colorectal cancer," 2021, https://www.ncbi.nlm.nih.gov/pmc/articles/PMC2361636/.

[26] "Type 1 plasminogen activator inhibitor (PAI-1) in clear cell renal cell carcinoma (CCRCC) and its impact on angiogenesis, progression and patient survival after radical nephrectomy," 2021, https://www.ncbi.nlm.nih.gov/pmc/articles/PMC3002359/.

[27] G. Sotiropoulos, M. Kotopouli, I. Karampela et al., "Circulating plasminogen activator inhibitor-1 activity: a biomarker for resectable non-small cell lung cancer?" *J BUON*, vol. 24, no. 3, pp. 943–954, 2019.

[28] D. S. Chandrashekar, B. Bashel, S. A. H. Balasubramanya et al., "UALCAN: a portal for facilitating tumor subgroup gene expression and survival analyses," *Neoplasia*, vol. 19, no. 8, pp. 649–658, 2017.

[29] A. Subramanian, P. Tamayo, V. K. Mootha et al., "Gene set enrichment analysis: a knowledge-based approach for interpreting genome-wide expression profiles," *Proceedings of the National Academy of Sciences*, vol. 102, no. 43, pp. 15545–15550, 2005.

[30] "TISIDB: an integrated repository portal for tumor–immune system interactions | Bioinformatics | Oxford Academic," 2021, https://academic.oup.com/bioinformatics/article/35/20/4200/5418799.

[31] R. Xie, J. Liu, X. Yu et al., "ANXA2 silencing inhibits proliferation, invasion, and migration in gastric cancer cells," *Journal of Oncology*, vol. 2019, pp. 1–13, 2019.

[32] "Identification of potential key genes associated with the pathogenesis and prognosis of gastric cancer based on integrated bioinformatics analysis," 2021, https://www.ncbi.nlm.nih.gov/pmc/articles/PMC6056647/.

[33] M. Schmitt, N. Harbeck, N. Brünner et al., "Cancer therapy trials employing level-of-evidence-1 disease forecast cancer biomarkers uPA and its inhibitor PAI-1," *Expert Review of Molecular Diagnostics*, vol. 11, no. 6, pp. 617–634, 2011.

[34] M. Niki, T. Yokoi, T. Kurata, and S. Nomura, "New prognostic biomarkers and therapeutic effect of bevacizumab for patients with non-small-cell lung cancer," *Lung Cancer: Targets and Therapy*, vol. 8, pp. 91–99, 2017.

[35] "PAI-1 leads to G1-phase cell cycle progression through cyclin D3/CDK4/6 up-regulation," 2021, https://www.ncbi.nlm.nih.gov/pmc/articles/PMC4064567/.

[36] T. A. McEachron, F. C. Church, and N. Mackman, "Regulation of thrombin-induced plasminogen activator inhibitor-1 in 4T1 murine breast cancer cells," *Blood Coagulation & Fibrinolysis*, vol. 22, no. 7, pp. 576–582, 2011.

[37] T. D. Brooks, J. Slomp, P. H. A. Quax et al., "Antibodies to PAI-1 alter the invasive and migratory properties of human tumour cells in vitro," *Clinical and Experimental Metastasis*, vol. 18, no. 6, pp. 445–453, 2000.

[38] "Co-expression of urokinase, urokinase receptor and PAI-1 is necessary for optimum invasiveness of cultured lung cancer cells-liu-1995-international Journal of Cancer-wiley Online Library," 2021, https://onlinelibrary.wiley.com/doi/abs/10.1002/ijc.2910600413?sid=nlm%3Apubmed.

[39] U. A. Lademann and M. U. Rømer, "Regulation of programmed cell death by plasminogen activator inhibitor type 1 (PAI-1)," *Thrombosis & Haemostasis*, vol. 100, no. 6, pp. 1041–1046, 2008.

[40] H. Fang, V. R. Placencio, and Y. A. DeClerck, "Protumorigenic activity of plasminogen activator inhibitor-1 through an antiapoptotic function," *Journal of the National Cancer Institute*, vol. 104, no. 19, pp. 1470–1484, 2012.

[41] M. Valiente, A. C. Obenauf, X. Jin et al., "Serpins promote cancer cell survival and vascular co-option in brain metastasis," *Cell*, vol. 156, no. 5, pp. 1002–1016, 2014.

Hindawi
Journal of Oncology
Volume 2022, Article ID 4552445, 9 pages
https://doi.org/10.1155/2022/4552445

Research Article

A Novel Nomogram Combining Alternative Splicing Events and Clinical Factors for Prognosis Prediction in Head and Neck Squamous Cell Carcinoma

Jun Jiang,[1] Li Niu,[1] Ming-Xia Zhang,[1] Hao Wang,[1] Jia-Qi Xie,[2] and Guo-Ping Sun [3]

[1]*Department of Radiation Oncology, The First Affiliated Hospital of Anhui Medical University, Hefei, Anhui, China*
[2]*Department of Cancer Center, Drum Tower Hospital of Nanjing University, Nanjing, Jiangsu, China*
[3]*Department of Medical Oncology, The First Affiliated Hospital of Anhui Medical University, Hefei, Anhui, China*

Correspondence should be addressed to Guo-Ping Sun; sungp@ahmu.edu.cn

Received 14 December 2021; Revised 4 January 2022; Accepted 7 January 2022; Published 22 January 2022

Academic Editor: Fu Wang

Due to limitations of sensitive biomarkers, the clinical prognosis of patients with head and neck squamous cell carcinoma (HNSCC) remains poor. Alternative splicing (AS) is the basis of both transcriptome and proteome richness, so more and more evidence indicates an important relationship between AS and tumor progression. The aim of this study was to offer a comprehensive analysis on AS events and then investigate its potentials as a new biomarker for patients with squamous cell carcinoma of the head and neck. In this study, univariate assays were conducted to examine the prognosis-associated AS events, and we screened 4068 survival-related AS events in 2573 genes. Then, the AS events related to survival were further determined and analyzed using LASSO regression and multivariate assays, and an eleven-AS signature was developed. Kaplan–Meier assays indicated patients with high-risk scores exhibited a shorter OS than those with low-risk scores. Multivariate assays further demonstrated that the signature's risk score was independent of HNSCC survivals. Meanwhile, we analyzed the clinical association of AS-based prognostic signature in HNSCC patients and observed that tumor specimens with advanced stages and grades exhibited a high risk score. In addition, the results of survival nomogram revealed that predicted outcomes and actual outcomes were highly consistent. Overall, our group showed an eleven-AS signature of HNSCC, which could be regarded as a separate prognostic factor.

1. Introduction

Head and neck squamous cell carcinoma (HNSCC) is the most common malignant tumor of the epidermis of the head and neck, involving multiple anatomical sites, such as the lip, oral cavity, pharynx (nasopharynx, oropharynx, and hypopharynx), and larynx, and more than 600,000 new cases are reported every year [1, 2]. Despite the distinct developments in molecular mechanisms and biological studies, the long-term survivals of patients with HNSCC remain poor [3]. Thus, a suitable choice for different patients using radical treatments or conservative treatments is necessary. In the last twenty years, the prediction of clinical outcome of HNSCC patients was mainly based on the TNM staging system [4]. In addition, differentiation grade is also applied as a critical predictor. However, these systems cannot satisfy clinical requirements.

Alternative splicing (AS) is considered to be a critical impetus for the production of different types of proteins [5]. In eukaryotic cells, it is the basis for the other regulatory mechanisms involved in gene functions. A wealth of supporting evidence has indicated that transcripts >95% of human multiexon-containing genes experience AS [6]. Importantly, based on the different types of specimen, a variable expression was observed in most genes [7]. It has been confirmed that there are seven major patterns of AS events, including mutually exclusive exons (MEs), alternate terminator (AT), alternate promoter (AP), alternate acceptor site (AA), alternate donor site (AD), and retained intron (RI), as well as exon skip (ES) [8, 9]. The dysregulation

of AS events could result in multiple pathological processes, especially tumor progression and chemotherapy resistance. Splicing factors (SFs) exhibited a critical role in the progression of various tumors induced by AS [10, 11]. More importantly, the potential of AS events used as novel biomarkers for diagnosis and prognosis attracts more and more attention [12, 13]. On the other hand, targeting AS events may be developed as novel therapeutic targets for tumor patients.

The clinical data from TCGA datasets made the analysis of AS in cancers possible. Recently, a large number of studies have performed comprehensive analysis based on TCGA splicing data in several types of tumors [14, 15]. However, there are very few reports on the correlation between AS events and the clinical outcomes of HNSCC patients. In this study, a comprehensive analysis was performed by using TCGA datasets to discuss the prognostic value of AS events in patients with HNSCC. Our findings may contribute to the developments of novel biomarkers for tumor patients.

2. Materials and Methods

2.1. Data Acquisition and Processing. There were 546 samples in FPKM data of TCGA RNA-Seq that were downloaded from the UCSC Cancer Browser (https://xenabrowser.net/datapages/), and a total of 528 patients were followed up. The alternative splicing data of the TCGA HNSCC cohort were downloaded from the TCGASpliceSeq database (https://bioinformatics.mdanderson.org/TCGASpliceSeq/). The same TCGA ID was applied to confirm the data of AS events.

2.2. Quantification of Splicing Events. Percent Spliced In (PSI) values were calculated in all samples. The PSI values (>0 and <100%) represented the percentage of gene mRNA transcripts that contain a specific exon or splice. Here, an AS event whose PSI value was larger than 75% was included for further assays. The AS events were exhibited by the use of three elements.

2.3. Identification of AS Events Related to Survival. For the survival assays, our group just finally enrolled these patients who had AS event data and clinical follow-up. In addition, HNSCC patients whose survival time <1 month were excluded. After excluding AS events with SD <0.01, univariate assays were conducted to examine the associations between each AS event and overall survival in HNSCC patients. Then, the correlation between AS events and genes was visualized by the use of UpSet [16].

2.4. Prognostic Model Construction. To screen the final AS events for prognostic model, the OS-related AS events were analyzed by using lasso analysis. Then, multivariate assays were applied to analyze the results of lasso analysis via the forward stepwise methods. Subsequently, by the use of each prognostic model, we calculated risk scores, and the median risk score was applied to divide all patients into two groups. The predictive accuracy of the prognostic models was demonstrated using dynamic time-dependent ROC curves and K–M survival assays. To realize the abovementioned assays, we used timeROC package, survivalROC package, and the survminer package.

2.5. AS-Clinicopathological Nomogram. To further explore the prognostic value of the prognostic model, univariate assays were applied to analyze the clinicopathological variables described above with the prognostic models. Then, a nomogram was developed by the use of the abovementioned results with a distinct p value to examine the patients' individual survival possibilities. Finally, corresponding calibration curves were plotted, which were further used to calculate the C-index and validate and quantify the scoring system's discrimination capability.

2.6. Statistical Analysis. We used R (v.3.6.1, R Core Team, Boston, MA, USA) for the abovementioned data analysis.

3. Results

3.1. Details of AS Events. By analyzing TCGA datasets, we showed 42849 AS events of 10123 genes in all samples. Figure 1 exhibited the detailed information of the seven categories of AS events. We observed that a single gene could possess some different AS patterns.

3.2. Identification of the OS-Associated AS Events. Univariate assays were performed, and 4068 OS-related AS events were *screened* in 2573 genes. Of the OS-related AS events, 276 OS-related RIs were found in 235 genes, 14 OS-related MEs in 9 genes, 608 OS-related ESs in 519 genes, 522 OS-related ATs in 292 genes, 588 OS-related APs in 358 genes, 140 OS-related ADs in 133 genes, and 169 OS-related AAs in 166 genes (Figure 2). The distribution of the OS-related AS events was shown by the use of a volcano plot (Figure 3(a)). The 20 most distinct OS-related AAs (Figure 3(b)), ADs (Figure 3(c)), APs (Figure 3(d)), ATs (Figure 3(e)), ESs (Figure 3(f)), MEs (Figure 3(g)), and RIs (Figure 3(h)) were shown using a bubble chart.

3.3. Distinction and Evaluation of AS-Based Prognostic Signature for HNSCC. Then, a prognostic model for HNSCC patients was developed based on the abovementioned results. For avoiding overfitting, the Lasso plot and the Lambda plot were conducted (Figures 4(a) and 4(b)). Finally, 11 OS-SEs were screened for further multivariate assays. The heat map revealed that SH3KBP1|88643|AP and ZFYVE20|63554|ES might have positive effects on HNSCC,

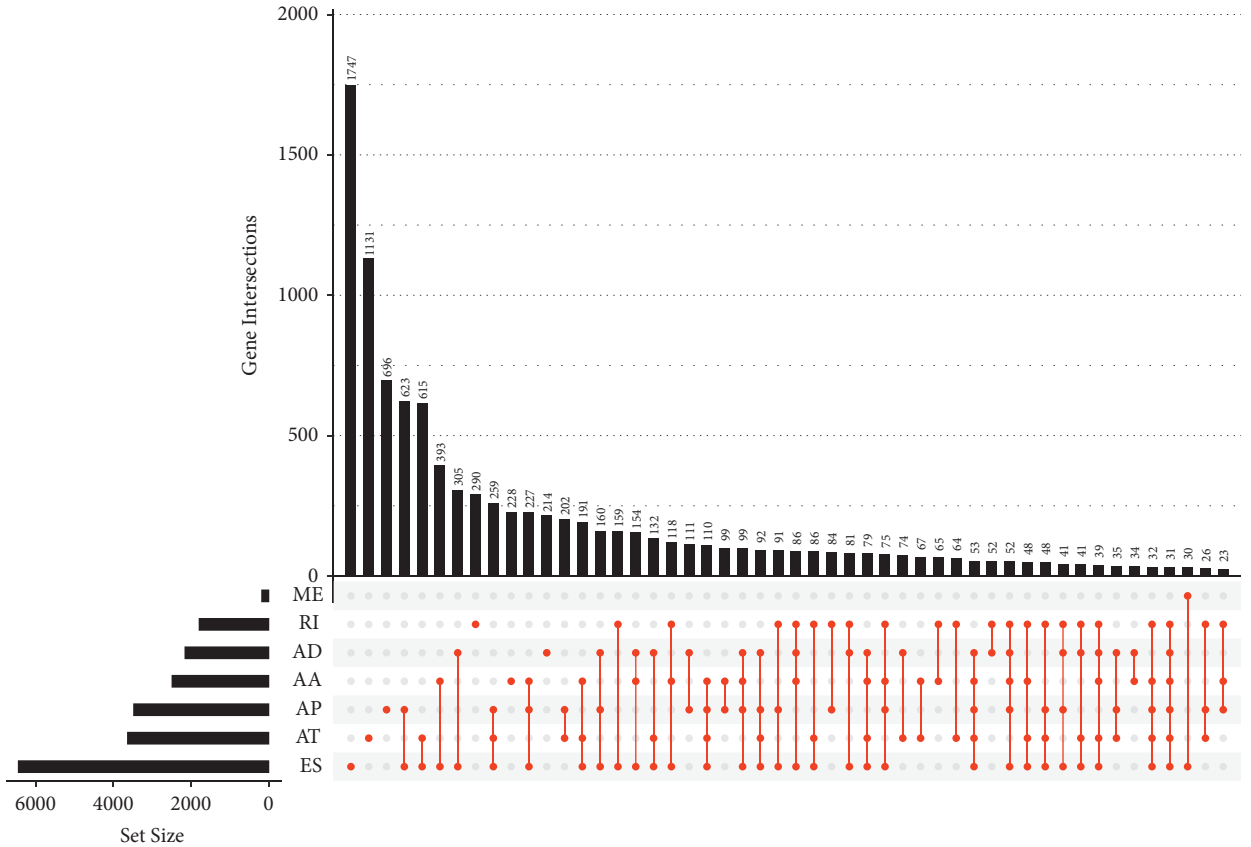

Figure 1: The upset plot of gene interactions among the seven types of AS events in HNSCC samples.

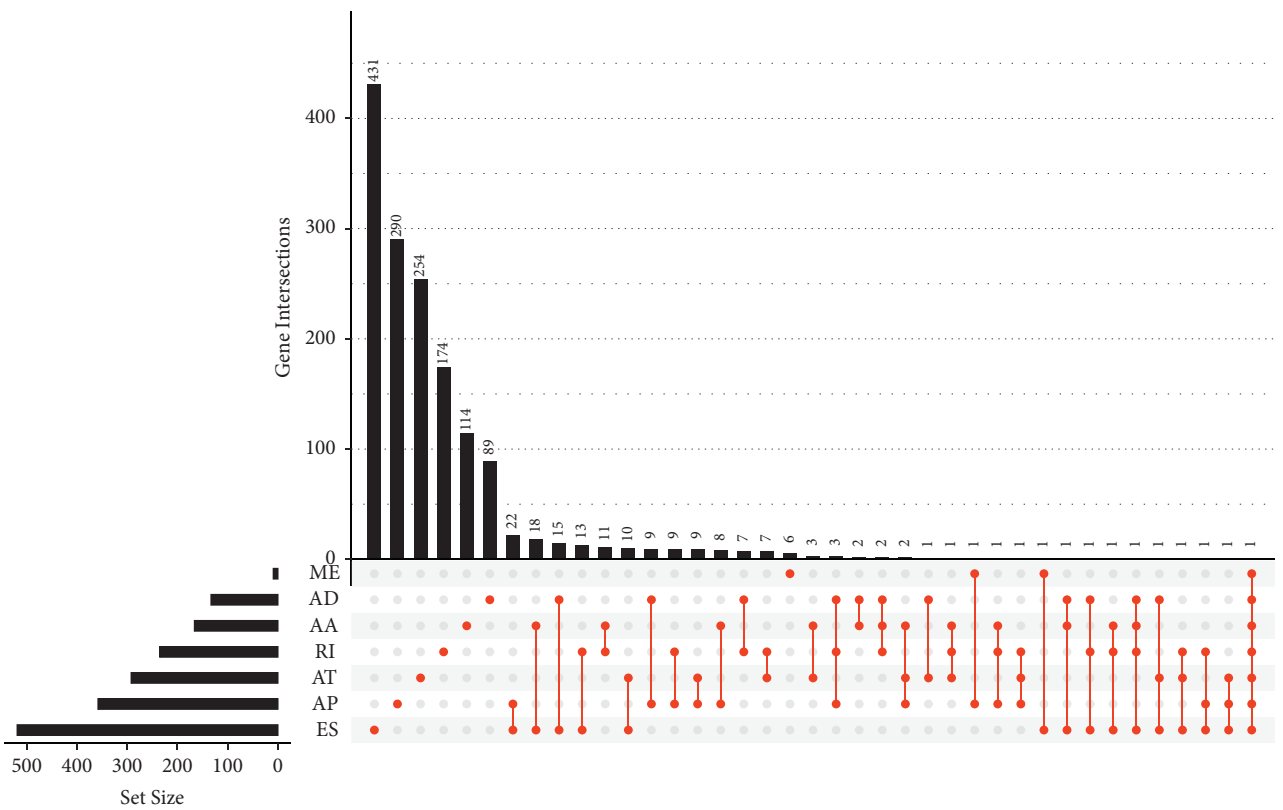

Figure 2: The upset plot of gene interactions based on the survival-associated AS events.

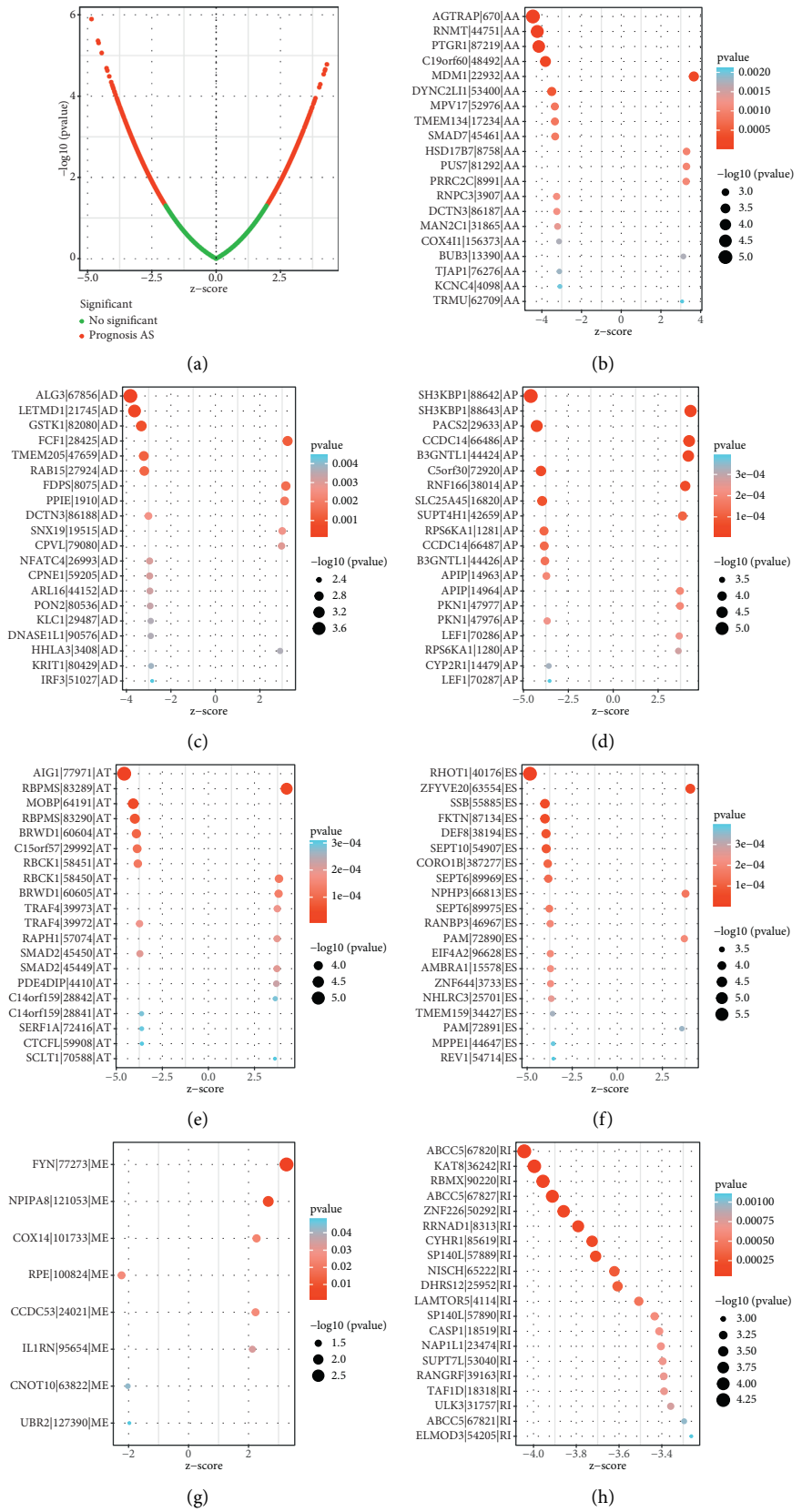

Figure 3: The survival-associated AS events. (a) Survival-related AS events were displayed by the use of a volcano plot. (b–h) The most distinct prognosis-related AA, AD, AP, AT, ES, ME, and RI in TCGA HNSCC datasets.

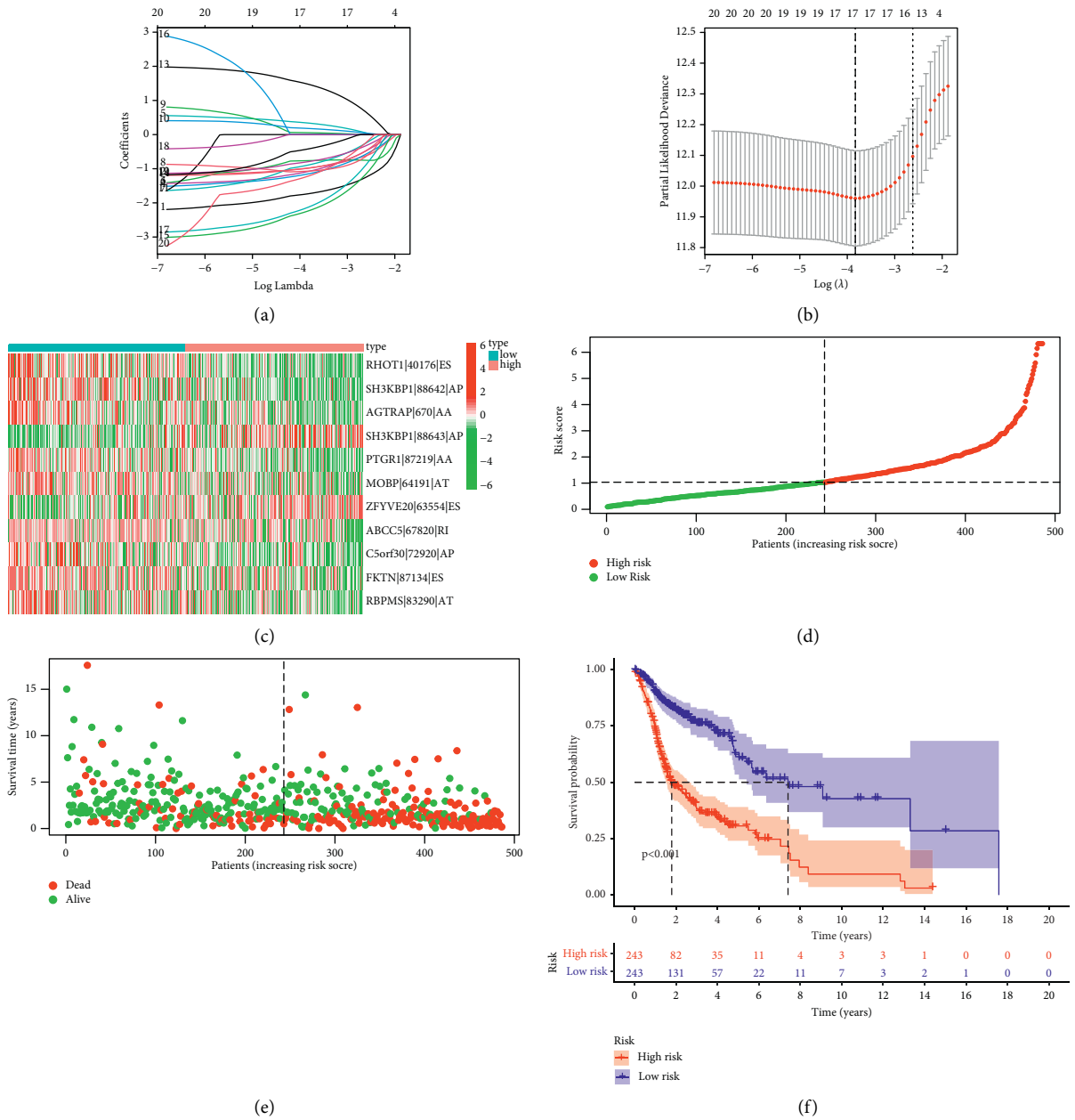

Figure 4: Evaluation of the performance of AS-based prognostic signature in TCGA datasets. (a) LASSO coefficient profiles. (b) LASSO deviance profiles. (c) Distribution of the AS events shown by a heat map in the TCGA dataset. (d) Distribution of risk score. (e) The survival status and duration of HNSCC patients. (f) Kaplan–Meier assays of AS-based prognostic signature in HNSCC patients.

while AGTRAP|670|AA, SH3KBP1|88642|AP, RHOT1|40176|ES, PTGR1|87219|AA, MOBP|64191|AT, ABCC5|67820|RI, C5orf30|72920|AP, FKTN|87134|ES, and RBPMS|83290|AT exhibited a contrary effect (Figure 4(c)). The specimens with lower risk scores exhibited a lower risk of mortality, which were shown using the risk curve and scatterplot (Figures 4(d) and 4(e)). Then, survival assays revealed that high-risk patients showed a shorter OS than low-risk ones (Figure 4(f)). To further demonstrate the independent roles of the risk score, we performed univariate and multivariate assays and demonstrated that the system was a well-predicting model (Figures 5(a) and 5(b)). Moreover, combined with clinical variables, AUC curve analysis was performed on 1-, 2-, and 3-year OS, and the AUC value obtained by risk characteristics was the highest (Figures 5(c) and 5(d)). On the other hand, we also analyzed the clinical association of the prognostic signature based on AS in HNSCC patients, and the clinical information is shown in Figures 6(a)–6(g). Importantly, we observed that tumor specimens with advanced stages and grades exhibited a high risk score (Figures 6(c)–6(e) and 6(g)). Finally, our group constructed a prognostic nomogram using clinicopathological stage and risk score for the prediction of the clinical outcome of HNSCC patients (Figure 7(a)). The

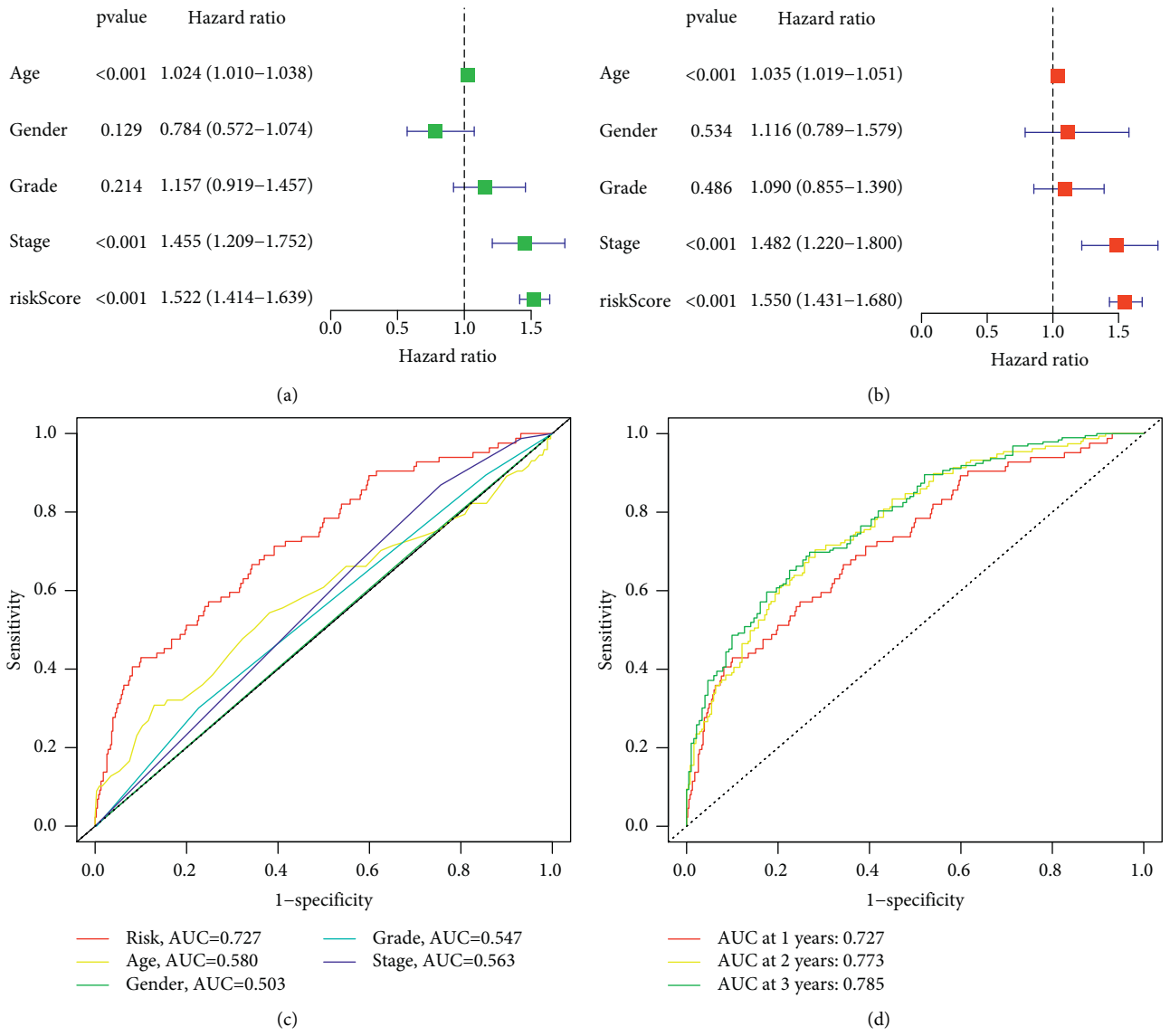

Figure 5: The prognostic values of AS-based prognostic signature in TCGA datasets. (a) Univariate and (b) multivariate assays in AS-based prognostic signature. (c) AUC for predicting one-year survival with different clinical features. (d) The diagnostic value of AS-based prognostic signature in predicting 1-, 2-, and 3-year survival.

results of calibration curves exhibited an approximate diagonal, suggesting strong abilities in predicting the clinical outcome for 1-year OS using our system (Figure 7(b)).

4. Discussion

HNSCC remains a healthy challenge for many countries [17]. In recent years, multimodal treatments, including surgery, chemotherapy, and radiation, have improved substantially [18]. However, there was no significant increase in 5-year overall survival (OS) and no significant reduction in mortality. Identification of novel sensitive biomarkers is very important for the improvements of clinical outcome of HNSCC patients [19]. In recent years, more and more evidence indicated that misregulation of AS may result in splicing defects that are related to multiple pathological conditions including different categories of cancers, and AS events may work as potential molecular markers during the cancer diagnosis and treatment process [20, 21]. However, there are few effective prognostic biomarkers based on AS events, which may provide crucial insights into the pathobiology of HNSCC based on AS events.

In this study, many OS-related AS events were screened by using TCGA datasets. Moreover, based on the above-mentioned AS events, we developed a prognostic signature that can be used to divide HNSCC patients into groups with high and low risks. Importantly, we observed that high-risk patients were correlated with a short OS. Moreover, multivariate analyses indicated that our model could be a separate prognostic factor for overall survival of HNSCC. To further explore its clinical value, we developed a nomogram model using our system and several clinical features.

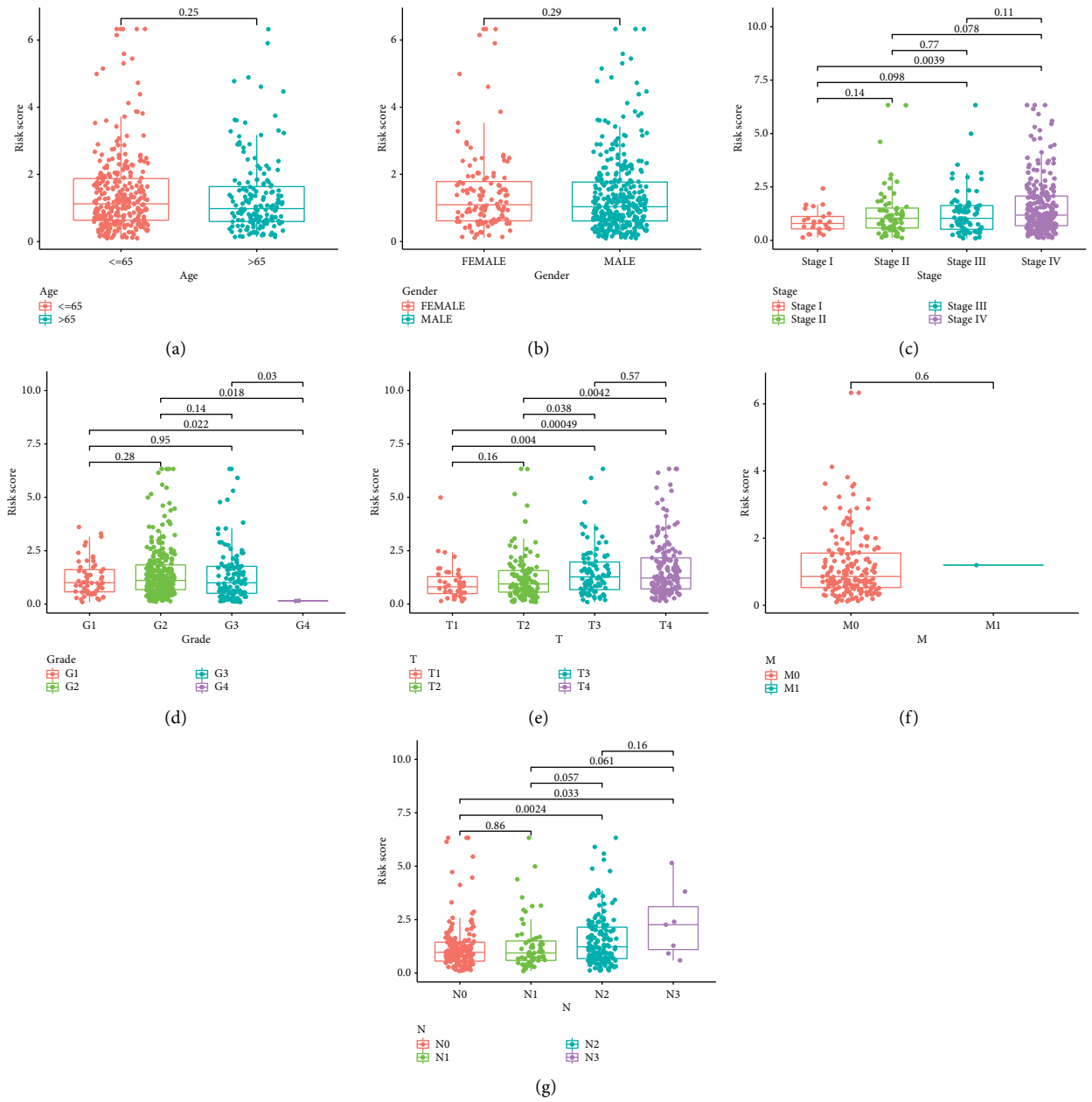

FIGURE 6: Relationship between risk score and clinical features. Distribution of risk score in (a) age, (b) gender, (c) stage, (d) grade, (e) T classification, (f) M classification, and (g) N classification.

Importantly, the results were significant, and a strong agreement was observed. Previously, several studies have reported the prognostic value of novel models based on alternative splicing events in several types of tumors. For instance, Xie et al. developed a splicing prognostic model using AS events, which showed satisfactory predictive efficacy for the GBM patients' survival, indicating the important clinical value of AS events for the developments of novel biomarkers [22]. In uveal melanoma, 1014 AS events were recognized as prognostic AS ones in total, and a robust prognostic prediction model containing seven AS events revealed a great promise for the prediction of overall survival of patients with uveal melanoma [23]. However, the related studies in HNSCC patients were rarely reported. Our findings provided HNSCC patients with a robust prognostic signature based on AS.

However, this study has the following limitations. Firstly, we just used TCGA datasets to confirm our findings. No cross validation was applied to demonstrate our findings. Other cohorts and in vitro and in vivo assays are needed to further demonstrate this signature in the future. Secondly, it was hard to develop a suitable system by the clinical application of the AS-based prognostic signature. The high cost of sequencing chip made it hard to detect the expressions of AS events for most HNSCC patients. Thirdly, we got many AS event-related genes, but the regulation relationships

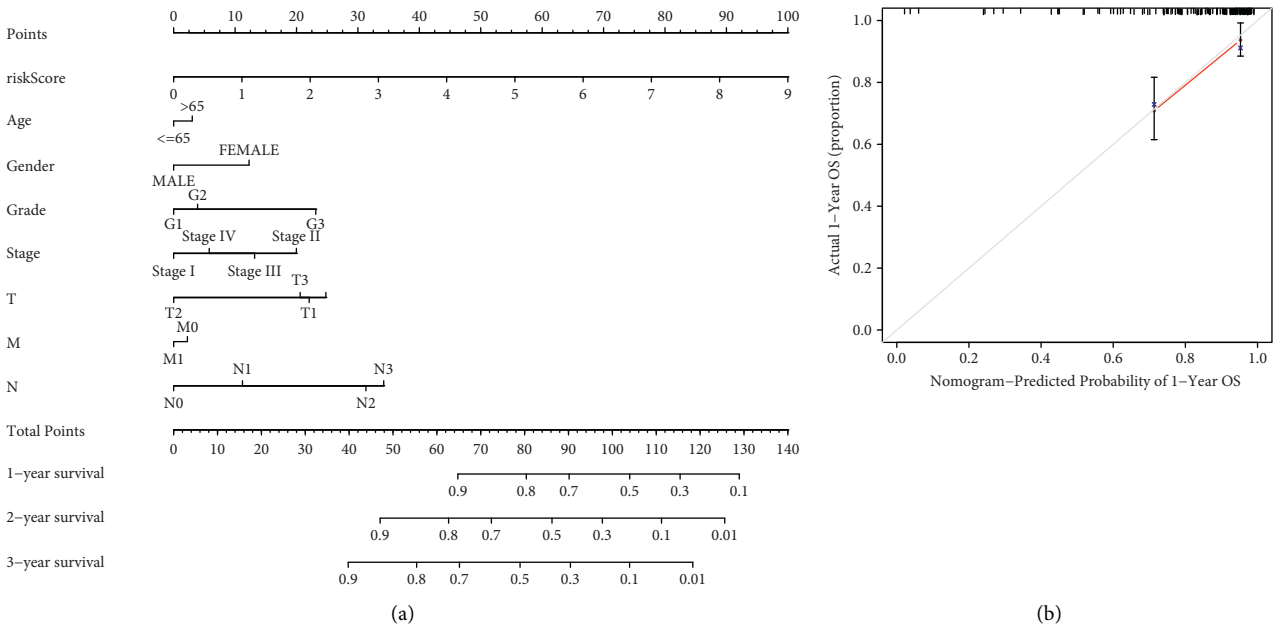

FIGURE 7: A quantitative method to predict HNSCC patients' probability of 1-, 3-, and 5-year OS. (a) Nomogram was assembled by signature and clinical stages for the prediction of HNSCC patients' survivals. (b) One-year nomogram calibration curves.

among themselves and other genes were not clear. Advanced bioinformatics is needed to reveal the regulation relationship.

5. Conclusions

A comprehensive analysis was conducted to AS events related to overall prognostic in HNSCC, and a prognostic model was built to convincingly forecast HNSCC patients' long-term survival outcomes. These findings may contribute to ongoing efforts to develop therapeutic targets for patients with HNSCC.

Data Availability

The analysed datasets generated during the study are available from the corresponding author on reasonable request.

Conflicts of Interest

The authors declare no conflicts of interest regarding the publication of this article.

Authors' Contributions

Jun Jiang and Guo-ping Sun conceptualized the study, Jun Jiang and Li Niu formulated the methodology, Ming-xia Zhang conducted investigation, Jun Jiang, Hao Wang, and Jia-qi Xie performed visualization, Guo-ping Sun supervised the work, and Jun Jiang wrote the original draft of the manuscript.

Acknowledgments

This project was funded by the grant of the China International Medical Foundation (CIMF, Z-2014-06-17357).

References

[1] D. E. Johnson, B. Burtness, C. R. Leemans, V. W. Y. Lui, J. E. Bauman, and J. R. Grandis, "Head and neck squamous cell carcinoma," *Nature Reviews Disease Primers*, vol. 6, no. 1, p. 92, 2020.

[2] K. Jung, M. Narwal, S. Y. Min, B. Keam, and H. Kang, "Squamous cell carcinoma of head and neck: what internists should know," *The Korean Journal of Internal Medicine*, vol. 35, no. 5, pp. 1031–1044, 2020.

[3] J. Moskovitz, J. Moy, and R. L. Ferris, "Immunotherapy for head and neck squamous cell carcinoma," *Current Oncology Reports*, vol. 20, no. 2, p. 22, 2018.

[4] J. D. McDermott and D. W. Bowles, "Epidemiology of head and neck squamous cell carcinomas: impact on staging and prevention strategies," *Current Treatment Options in Oncology*, vol. 20, no. 5, p. 43, 2019.

[5] J. Ule and B. J. Blencowe, "Alternative splicing regulatory networks: functions, mechanisms, and evolution," *Molecular Cell*, vol. 76, no. 2, pp. 329–345, 2019.

[6] F. E. Baralle and J. Giudice, "Alternative splicing as a regulator of development and tissue identity," *Nature Reviews Molecular Cell Biology*, vol. 18, no. 7, pp. 437–451, 2017.

[7] E. Bowler and S. Oltean, "Alternative splicing in angiogenesis," *International Journal of Molecular Sciences*, vol. 20, no. 9, 2019.

[8] O. Kelemen, P. Convertini, Z. Zhang et al., "Function of alternative splicing," *Gene*, vol. 514, no. 1, pp. 1–30, 2013.

[9] L. M. Urbanski, N. Leclair, and O. Anczuków, "Alternative-splicing defects in cancer: splicing regulators and their downstream targets, guiding the way to novel cancer

therapeutics," *Wiley Interdisciplinary Reviews. RNA*, vol. 9, no. 4, Article ID e1476, 2018.

[10] S. Cherry and K. W. Lynch, "Alternative splicing and cancer: insights, opportunities, and challenges from an expanding view of the transcriptome," *Genes & Development*, vol. 34, no. 15-16, pp. 1005–1016, 2020.

[11] A. R. Farina, L. Cappabianca, M. Sebastiano, V. Zelli, S. Guadagni, and A. R. Mackay, "Hypoxia-induced alternative splicing: the 11th hallmark of cancer," *Journal of Experimental & Clinical Cancer Research*, vol. 39, no. 1, p. 110, 2020.

[12] D. Zhao, C. Zhang, M. Jiang et al., "Survival-associated alternative splicing signatures in non-small cell lung cancer," *Aging*, vol. 12, no. 7, pp. 5878–5893, 2020.

[13] B. Rahmutulla, K. Matsushita, and F. Nomura, "Alternative splicing of DNA damage response genes and gastrointestinal cancers," *World Journal of Gastroenterology*, vol. 20, no. 46, pp. 17305–17313, 2014.

[14] A. Kahles, K. V. Lehmann, N. C. Toussaint et al., "Comprehensive analysis of alternative splicing across tumors from 8,705 patients," *Cancer Cell*, vol. 34, no. 2, pp. 211–224.e216, 2018.

[15] Z. Guo, H. Zhu, W. Xu et al., "Alternative splicing related genetic variants contribute to bladder cancer risk," *Molecular Carcinogenesis*, vol. 59, no. 8, pp. 923–929, 2020.

[16] A. Lex, N. Gehlenborg, H. Strobelt, R. Vuillemot, and H. Pfister, "UpSet: visualization of intersecting sets," *IEEE Transactions on Visualization and Computer Graphics*, vol. 20, no. 12, pp. 1983–1992, 2014.

[17] C. R. Leemans, P. J. F. Snijders, and R. H. Brakenhoff, "The molecular landscape of head and neck cancer," *Nature Reviews Cancer*, vol. 18, no. 5, pp. 269–282, 2018.

[18] B. Solomon, R. J. Young, and D. Rischin, "Head and neck squamous cell carcinoma: genomics and emerging biomarkers for immunomodulatory cancer treatments," *Seminars in Cancer Biology*, vol. 52, no. Pt 2, pp. 228–240, 2018.

[19] N. Kitamura, S. Sento, Y. Yoshizawa, E. Sasabe, Y. Kudo, and T. Yamamoto, "Current trends and future prospects of molecular targeted therapy in head and neck squamous cell carcinoma," *International Journal of Molecular Sciences*, vol. 22, no. 1, 2020.

[20] S. C. Bonnal, I. López-Oreja, and J. Valcárcel, "Roles and mechanisms of alternative splicing in cancer-implications for care," *Nature Reviews Clinical Oncology*, vol. 17, no. 8, pp. 457–474, 2020.

[21] L. Prochazka, R. Tesarik, and J. Turanek, "Regulation of alternative splicing of CD44 in cancer," *Cellular Signalling*, vol. 26, no. 10, pp. 2234–2239, 2014.

[22] Z. C. Xie, H. Y. Wu, Y. W. Dang, and G. Chen, "Role of alternative splicing signatures in the prognosis of glioblastoma," *Cancer Medicine*, vol. 8, no. 18, pp. 7623–7636, 2019.

[23] Q. Wan, X. Sang, L. Jin, and Z. Wang, "Alternative splicing events as indicators for the prognosis of uveal melanoma," *Genes*, vol. 11, no. 2, 2020.

Hindawi
Journal of Oncology
Volume 2022, Article ID 5490461, 14 pages
https://doi.org/10.1155/2022/5490461

Research Article

Identification of Molecular Subtypes and Potential Small-Molecule Drugs for Esophagus Cancer Treatment Based on m^{6}A Regulators

Jianjun Li,[1] Hongbo Zhu,[2] Qiao Yang,[3] Hua Xiao,[4] Haibiao Wu,[3] Zhe Fang,[3] Wenjun Li,[3] and Manbo Cai[3]

[1]*Department of Urinary Surgery, The Second Affiliated Hospital, Hengyang Medical School, University of South China, Hengyang City, Hunan Province, 421001, China*
[2]*Department of Medical Oncology, The First Affiliated Hospital, Hengyang Medical School, University of South China, Hengyang City, Hunan Province, 421001, China*
[3]*Department of Oncology Radiotherapy, The First Affiliated Hospital, Hengyang Medical School, University of South China, Hengyang City, Hunan Province, 421001, China*
[4]*Department of Endoscopy Center, The First Affiliated Hospital, Hengyang Medical School, University of South China, Hengyang City, Hunan Province, 421001, China*

Correspondence should be addressed to Manbo Cai; caimanbo@nhfyyy.com

Received 14 November 2021; Revised 7 December 2021; Accepted 13 December 2021; Published 13 January 2022

Academic Editor: Fu Wang

Background. Esophagus cancer (ESCA) is the sixth most frequent cancer in males, with 5-year overall survival of 15%–25%. RNA modifications function critically in cancer progression, and m^{6}A regulators are associated with ESCA prognosis. This study further revealed correlations between m^{6}A and ESCA development. *Methods*. Univariate Cox regression analysis and consensus clustering were applied to determine molecular subtypes. Functional pathways and gene ontology terms were enriched by gene set enrichment analysis. Protein-protein interaction (PPI) analysis on differentially expressed genes (DEGs) was conducted for hub gene screening. Public drug databases were employed to study the interactions between hub genes and small molecules. *Results*. Three molecular subtypes related to ESCA prognosis were determined. Based on multiple analyses among molecular subtypes, 146 DEGs were screened, and a PPT network of 15 hub genes was visualized. Finally, 8 potential small-molecule drugs (BMS-754807, gefitinib, neratinib, zuclopenthixol, puromycin, sulfasalazine, and imatinib) were identified for treating ESCA. *Conclusions*. This study applied a new approach to analyzing the relation between m^{6}A and ESCA prognosis, providing a reference for exploring potential targets and drugs for ESCA treatment.

1. Introduction

Esophagus cancer (ESCA) is the sixth leading cancer with 3.1% incidence and 5.5% mortality worldwide [1]. Males tend to have a higher incidence (4.2%) and mortality (6.8%) than females, mainly due to differences in the smoking and drinking habits between two genders. The major risk factors of ESCA include race, gender, alcohol, tobacco, obesity, gastroesophageal reflux disease (GRED), diet of low fruits and vegetables, and so on [2]. The 5-year overall survival (OS) of the cancer is about 15% to 25%, and poor treatment outcomes are closely associated with late diagnosis and metastasis [3].

In the recent decades, the development of molecular and sequencing technology has deepened the understanding of the genetic causes of ESCA. For example, CCND1, CDK4/CDK6, and MDM2 genes involved in cell cycle are overexpressed in ESCA patients [4]. High expression of epidermal growth factor receptor (EGFR) is associated with worse prognosis and late clinical stage; therefore EGFR expression could serve as a prognostic biomarker [5, 6]. More importantly, epigenetic factors such as DNA or RNA

methylation, histone modifications, and loss of genome imprinting show strong correlation with tumor progression [7–9]. These epigenetic alternations can regulate downstream or upstream gene expression through silencing or activating regulatory factors, resulting in aberrant gene expressions associated with tumor development.

RNA modifications in transcripts are the most commonly detected epigenetic alternation. N^6-methyladenosine (m^6A) accounts for a majority of RNA modifications under the control of methyltransferases (writers), binding proteins (readers), and demethylases (erasers) [10]. Evidence demonstrated that m^6A modification is involved in tumorigenesis, tumor proliferation, and migration of various types of cancers such as acute myeloid leukemia [11–14], glioblastoma [15, 16], lung cancer [17, 18], hepatocellular carcinoma [19–21], breast cancer [22], and colorectal cancer [23].

Previous studies also discovered a correlation between m^6A and ESCA. Nagaki et al. proved that knockdown of ALKBH5 can increase m^6A modification and delay cell cycle progression of esophageal squamous cell carcinoma (ESCC) cells [24]. ALKBH5 has been identified as m^6A demethylase that facilitates tumor cell proliferation, and a correlation between ALKBH5 and poor prognosis of ESCC patients has been illustrated [24]. Guo et al. observed that high expression of m^6A reader HNRNPA2B1 was positively associated with ESCA tumor size and lymphatic metastasis [25]. Knockdown of HNRNPA2B1 inhibits tumor cell progression of ESCA cells, indicating HNRNPA2B1 as an oncogenic protein in ESCA development [25]. In addition, HNRNPC and ALKBH5 have been screened and combined as a prognostic signature for predicting ESCA outcomes [26]. These findings provide potential application of m^6A regulators in clinical treatment.

As m^6A modification is strongly correlated with tumor proliferation, invasion, and migration, the present study aimed to exploit novel molecular subtypes of ESCA based on m^6A regulators (writers, readers, and erasers). Furthermore, hub genes associated with ESCA prognosis and potential small-molecule drugs were screened according to molecular subtypes. This study introduced a new strategy of bioinformatics analysis to explore potential drugs for ESCA treatment.

2. Materials and Methods

2.1. Data Information. TCGA-ESCA dataset with the data of gene expression, copy number variation (CNV), single nucleotide variant, methylation, and clinical information was downloaded from The Cancer Genome Atlas (TCGA, https://portal.gdc.cancer.gov/) database. The workflow of defining molecular subtypes of ESCA was shown in Figure 1.

2.2. Genes of m^6A Writers, Erasers, and Readers. Three types of enzymes (writers, erasers, and readers) related to m^6A were included. Specifically, m^6A writers were METTL3, METTL14, WTAP, and KIAA1429. m^6A erasers were FTO and ALKBH5. m^6A readers were YTHDC1, YTHDC2, YTHDF1, YTHDF2, YTHDF3, HNRNPA2B1, IGF2BP1, IGF2BP2, and IGF2BP3.

2.3. Data Preprocessing. RNA-seq and methylation data were further processed. For RNA-seq data, samples without clinical follow-up information, overall survival (OS), and survival status were excluded. Genes with transcripts per million (TPM) < 1 in over half of the samples were excluded. Primary solid tumor samples were included. For methylation data, NA value was completed by the KNN function in impute *R* package, and beta value was converted to *M* value. According to cross-reactive probes and polymorphic CpGs in the Illumina Infinium HumanMethylation450 microarray, CpGs present in the normal samples were excluded. Unstable methylation sites including CpGs in *X* and *Y* chromosomes as well as CpGs in single nucleotide were excluded. Finally, 161 ESCA samples were included (Supplementary Table S1).

2.4. Consensus Clustering. R package of ConsensusClusterPlus (v1.48.0) was used to cluster methylation sites related to ESCA prognosis [27] under the parameters of reps = 100, pItem = 0.8, pFeature = 1, distance = "spearman". D2 algorithm and Euclidean distance were employed for consensus clustering. Cluster numbers *k* from 2 to 10 were chosen, and the optimal clusters were screened by cumulative distribution function (CDF) curve and consensus CDF.

2.5. Gene Enrichment Analysis and Function Analysis. Single sample gene set enrichment analysis (ssGSEA) in GSVA *R* package was conducted to calculate the enrichment score of each sample to different functional pathways [28]. WebGestalt (v0.4.3) *R* package was performed to analyze Kyoto Encyclopedia of Genes and Genomes (KEGG) pathways and gene ontology (GO) enrichment for differentially expressed genes (DEGs).

2.6. Immune Correlation Analysis. We obtained immune checkpoint genes (BTLA, CD200, CD244, LAG3, IDO1, IDO2, PDCD1, CTLA4, PDCD1LG2, TNFRSF8, CD40, TNFSF18, CD86, and CD44) from previous studies to analyze the expression differences of these genes in various molecular subtypes. In addition, we evaluated 28 immune infiltrating cell components by ssGSEA method [29]. To analyze the differences of immune infiltrating cell components in different subtypes, we further evaluated the immune infiltrating score in the sample by using *R* software package estimate [30], analyzed the differences of immune infiltrating in different subtypes, and evaluated the potential benefits of immunotherapy of different subtypes in imvigor210 [31] by using *R* software package submap [32].

2.7. Protein-Protein Interaction (PPI) Analysis. STRING (https://string-db.org/) is a database to explore the interaction among known and unknown proteins, including

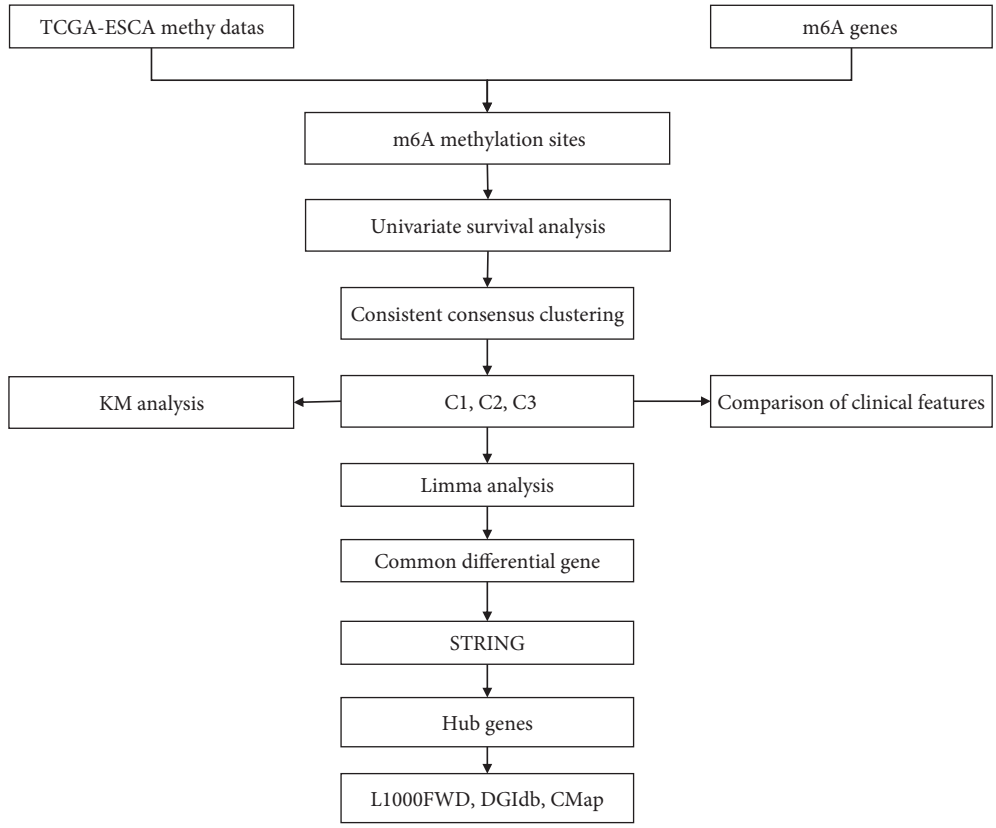

Figure 1: The workflow of developing m^{6}A-related molecular subtypes and screening potential small-molecular drugs for treating ESCA.

abundant data from current researches, other databases, and data by predicted bioinformatics [33, 34]. The protein interactions of DEGs were analyzed by STRING. PPI result was visualized by Cytoscape (v3.7.2) and further analyzed by cytoHubba to screen hub genes [35–37].

2.8. Databases of Small-Molecule Drugs. Databases of L1000 fireworks display (L1000FWD, https://maayanlab.cloud/L1000FWD/) [38], Drug-Gene Interaction database (DGIdb, https://dgidb.org/) [39, 40], and The Connectivity Map (CMap, https://clue.io/) [41, 42] were included for screening small molecules interacting with hub genes. L1000FWD includes over 16000 small molecules and gene expression data from tumor cell lines of 1000 drugs. DGIdb stores over 10000 drugs and 15000 interactions between drugs and genes. CMap contains over 19000 small molecules corresponding to 25200 biological entities. The function of small molecules associated with hub genes came from the National Library of Medicine (PubChem, https://pubchem.ncbi.nlm.nih.gov/#query=).

3. Results

3.1. Consensus Clustering of Methylation Sites on 15 m^{6}A-Related Genes. To develop a molecular subtyping system based on m^{6}A methylation sites, association between m^{6}A methylation sites and ESCA prognosis was analyzed. Coxph function in *R* package survival was used to perform univariate Cox regression analysis between 221 methylation sites and OS, survival status. 9 methylation sites associated with prognosis were screened ($p < 0.05$, Supplementary Table S2). Then 161 ESCA samples were clustered based on the 9 methylation sites with consensus clustering in ConsensusClusterPlus *R* package. As shown in Figure 2, when cluster number $k = 3$, CDF did not show great change; meanwhile, the relative change in area under CDF curve was the maximum, suggesting that $k = 3$ was the optimal. Therefore, under $k = 3$, 161 ESCA samples were clustered into three subtypes of C1, C2, and C3.

Survival analysis manifested significant OS difference in the three subtypes, with the most favorable prognosis detected in C3 subtype ($p = 0.018$, Figure 3). However, no difference of OS was observed between C1 and C2 subtypes. Gene mutation analysis showed that the top mutated gene was TP53 and that C3 subtype had the least mutations of the top 20 mutated genes among three subtypes (Supplementary Figure S1). Such results suggested a relation between gene mutations and prognosis.

3.2. The Relation between the Three Subtypes and Clinical Features. We next assessed the relation between subtypes and clinical features, including *T* stage, *N* stage, *M* stage, stages I to IV, grade, and risk factors of gender and smoking history. Although only the distribution of *G* stage (*G*1, *G*2, and *G*3) showed a close relation with the three subtypes ($p < 0.05$), there was a modest tendency indicating that C3

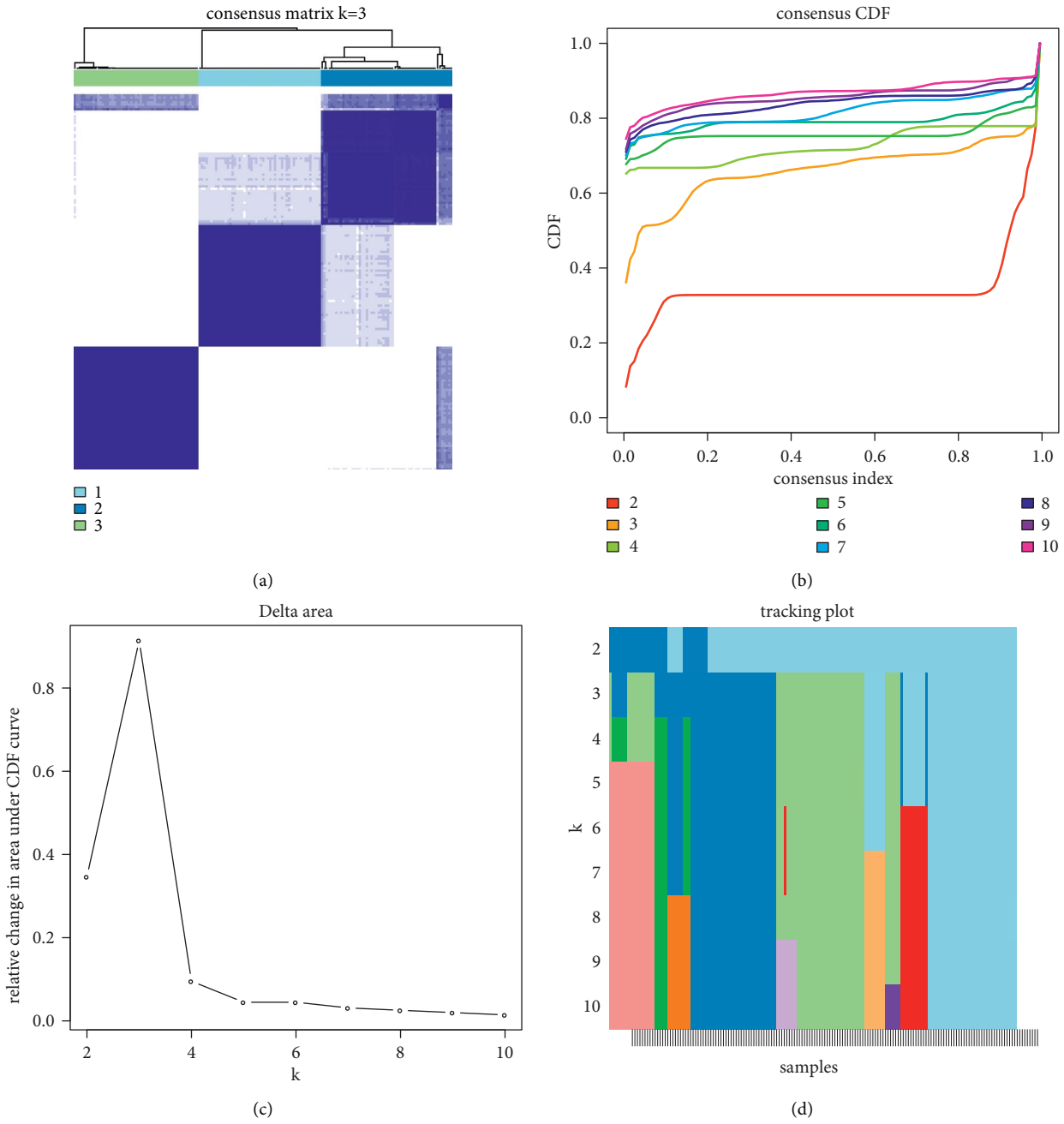

Figure 2: Consensus clustering of 161 ESCA samples based on m^{6}A methylation sites. (a) A consensus matrix when $k = 3$ where k represents cluster number. (b) Consensus CDF when $k = 2$ to 10. (c) The relative change in area under CDF curve when $k = 2$ to 10. (d) Tracking plot of samples when $k = 2$ to 10.

subtype had the lower proportion of stages with more invasive features than C1 and C2 subtypes (Figures 4(a)–4(e)). For risk factors, males accounted for a significantly higher proportion than female due to a higher smoking in males, and the female proportion was the highest in C3 subtype (Figure 4(f)). In addition, the number of nonsmokers was more in C3 subtype (tobacco = 1) than C1 and C2 subtypes; however, no significant difference was detected among tobacco groups (Figure 4(g)). We compared the three molecular subtypes with the previously reported three molecular subtypes (CIN, GS, and MSI) [43]. We observed that MSI subtypes are mainly related to C2 (Figure 4(h)). For example, the distribution of C1, C2, and C3 in CIN and GS subtypes is similar, suggesting that the new three molecular subtypes can be used as a supplement to the previously reported molecular subtypes.

3.3. The Enrichment of Metabolism Pathways in the Three Subtypes. Compared with normal cells, tumor cells are more active in acquiring energy through metabolism pathways to promote cell proliferation and migration.

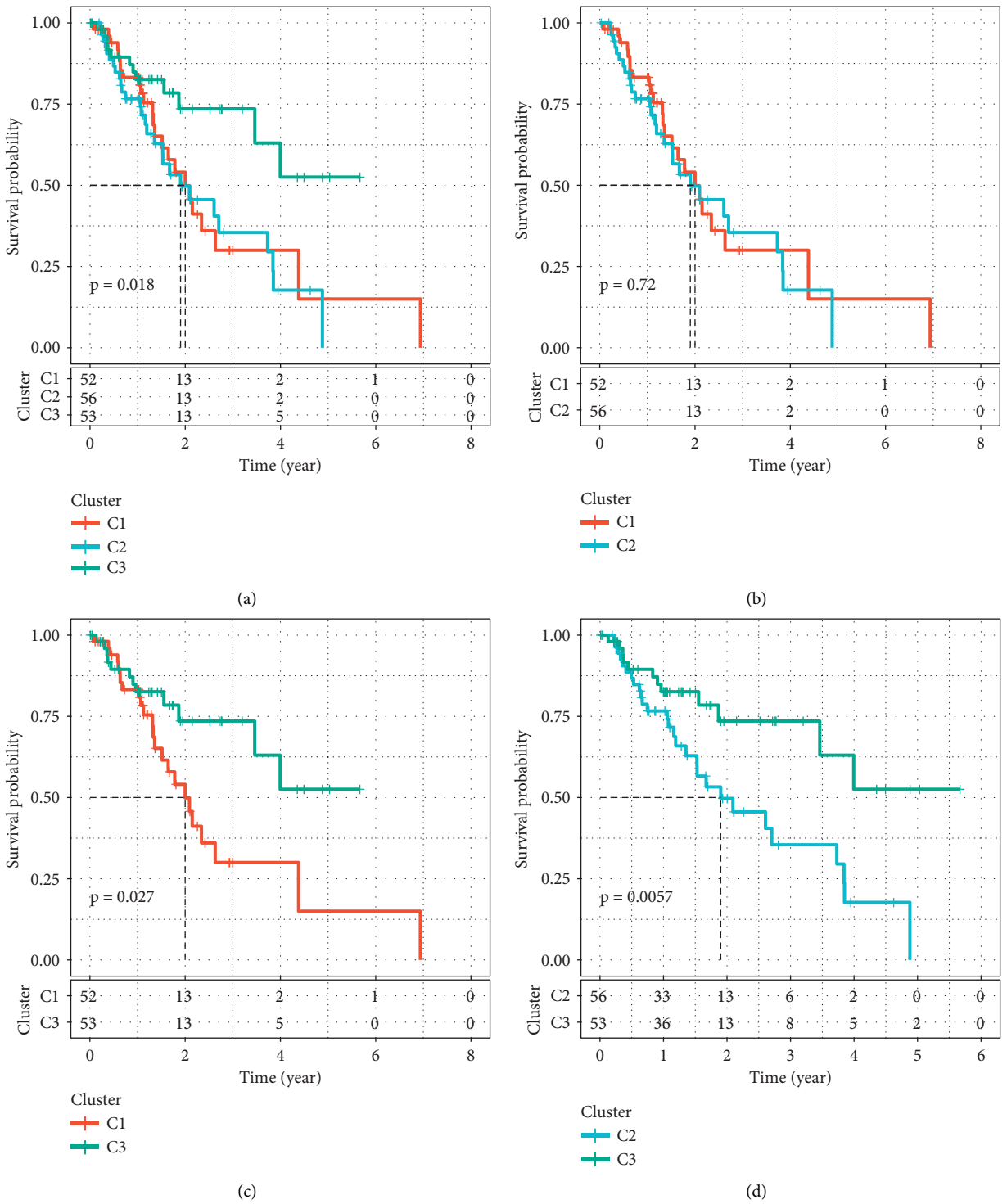

Figure 3: Kaplan-Meier survival curve of C1, C2, and C3 subtypes. (a) Survival analysis among three subtypes ($p = 0.018$). (b) Survival analysis between C1 and C2 subtypes ($p = 0.72$). (c) Survival analysis between C1 and C3 subtypes ($p = 0.027$). (d) Survival analysis between C1 and C3 subtypes ($p = 0.0057$). Log-rank test was performed.

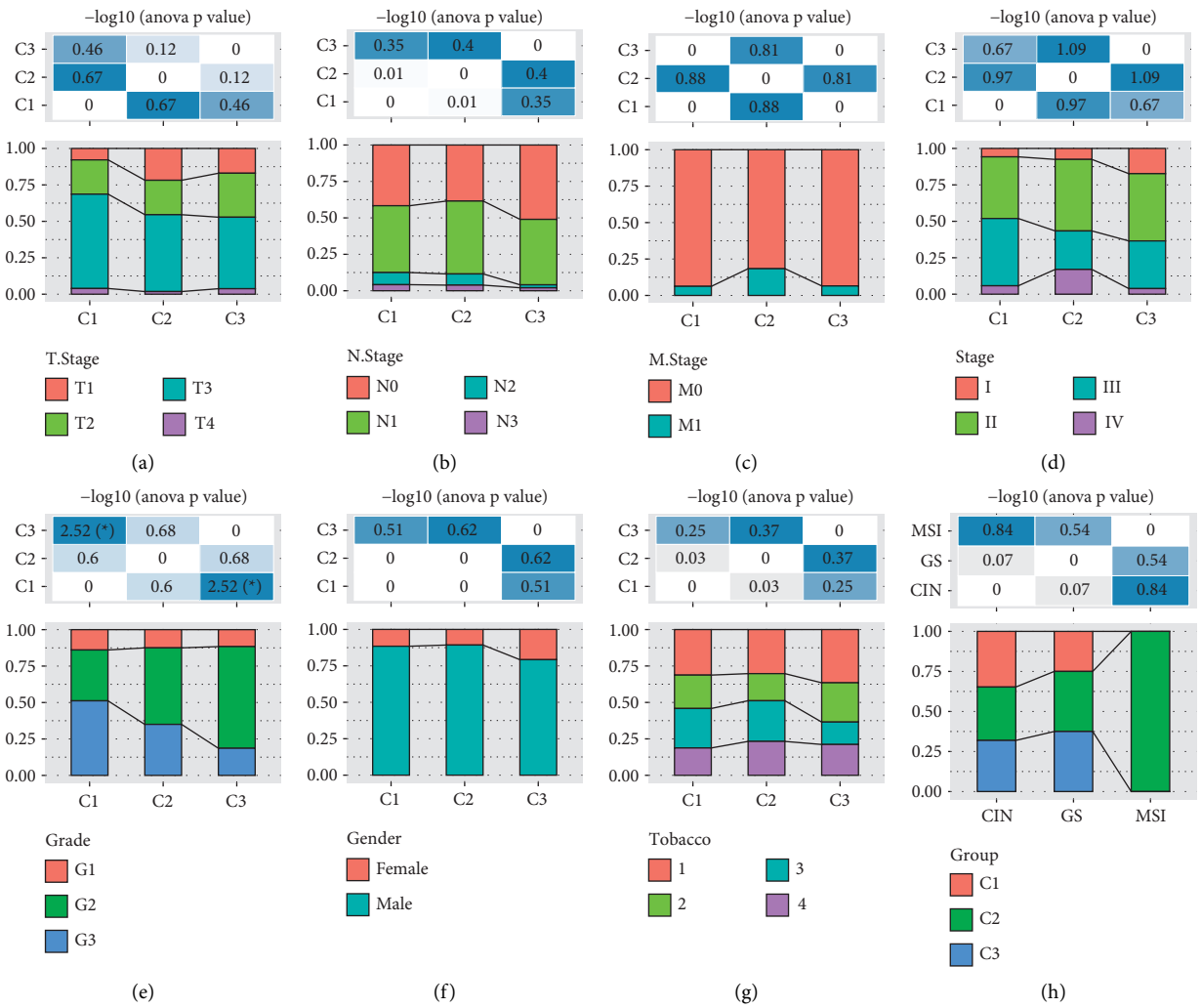

FIGURE 4: The relation between three subtypes and clinical features, including T stage (a), N stage (b), M stage (c), stages I to IV (d), grade (e), gender (f), tobacco (g), and TCGA molecular subtypes (h). ANOVA was performed. $^{*}p < 0.05$.

Therefore, we speculated that the activity of tumor cells in metabolism pathways could indicate the condition of cancer patients' prognosis. To examine whether there was an association between subtypes and metabolism pathways, ssGSEA was conducted to calculate the enrichment score of each sample. Eight major metabolism pathways, including nitrogen metabolism, nicotinate and nicotinamide metabolism, histidine metabolism, glyoxylate and dicarboxylate metabolism, glycerophospholipid metabolism, glycerolipid metabolism, drug metabolism cytochrome p450, and glutathione metabolism, were analyzed. The result exhibited that C3 subtype had the lowest enrichment score in these pathways, suggesting that C3 subtype with favorable prognosis was relatively inactive in metabolism pathways (Figure 5).

3.4. Immune Correlation of Different Molecular Subtypes. Immunotherapy is a promising clinical treatment method. In order to characterize the potential benefits of immunotherapy of different molecular subtypes, we first compared the differences of immune infiltration in the immune microenvironment of the three molecular subtypes. It can be observed that C1 subtype has higher matrix components and higher tumor purity (Figure 6(a)). We also observed the differences of multiple immune cell infiltration in patients with three molecular subtypes (Figure 6(b)). For example, C3 subtype has higher effector memory CD8 T cell and activated B cell, and C1 subtype has the highest regulatory T cell. These results show that the three molecular subtypes have different immune microenvironment characteristics. Further, we analyzed the expression differences of immune checkpoint genes in the three molecular subtypes and observed that 10 (71%) immune checkpoint genes had significant expression differences (Figure 6(c)), of which CD40 had the most significant expression difference. In addition, we also observed that C1 subtype was significantly correlated with CR/PR (Figure 6(d)). This suggests that C1 subtype may benefit from immunotherapy of PD-L1.

Identification of differentially expressed genes among the three subtypes and functional analysis were done.

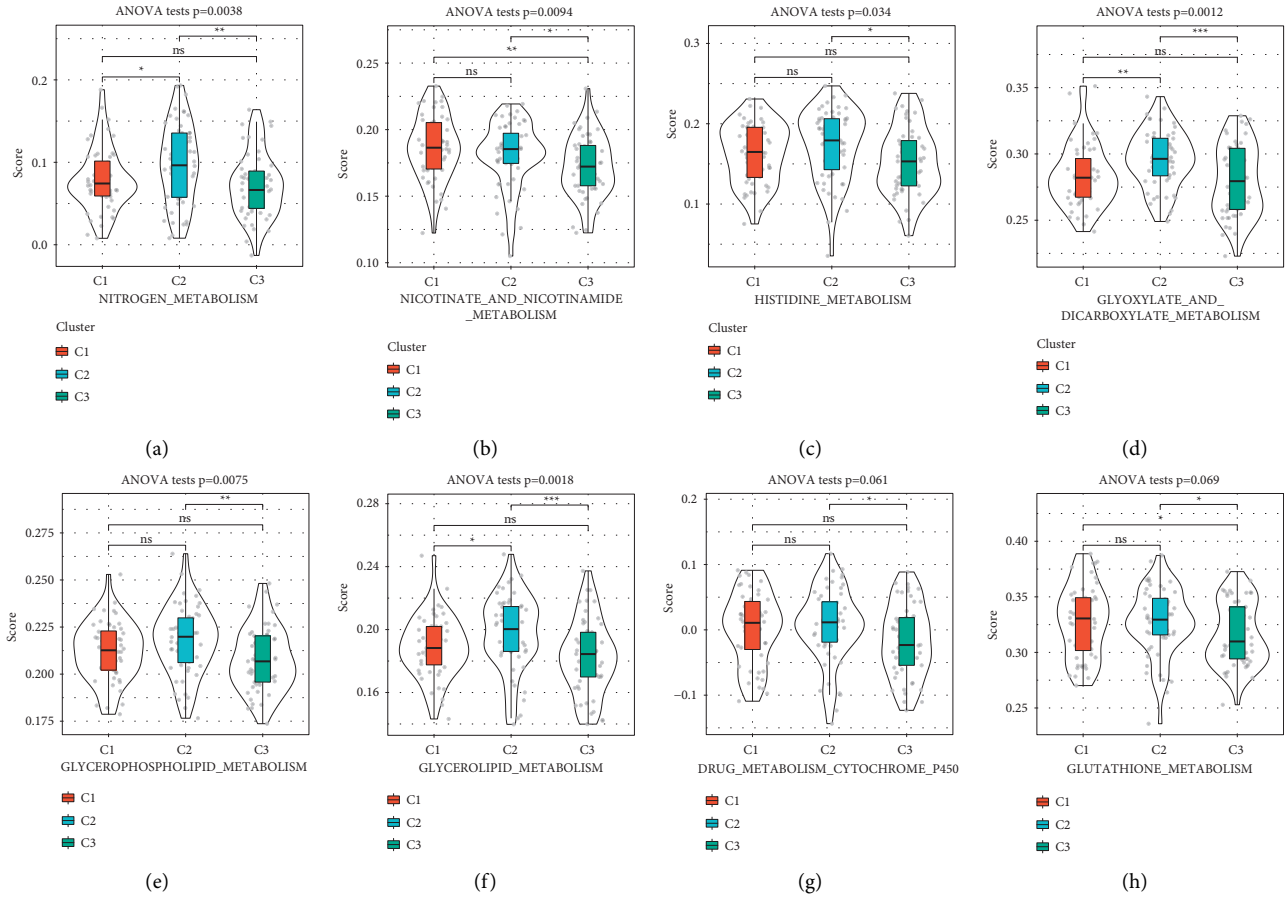

Figure 5: The relation between the three subtypes and metabolism pathways, including nitrogen metabolism (a), nicotinate and nicotinamide metabolism (b), histidine metabolism (c), glyoxylate and dicarboxylate metabolism (d), glycerophospholipid metabolism (e), glycerolipid metabolism (f), drug metabolism cytochrome p450 (g), and glutathione metabolism (h). ANOVA was performed. ns, no significance. $^{*}p < 0.05$, $^{**}p < 0.01$, $^{***}p < 0.001$.

As no difference of OS was found between C1 and C2 subtypes, and C3 subtype had the optimal prognosis, we also analyzed the DEGs between C1 and C3 and between C2 and C3 subtypes. Between C1 and C3 subtypes, 193 DEGs (132 upregulated genes and 61 downregulated genes) were identified under conditions of $p < 0.05$ and $|\text{fold change (FC)}| > 1.5$ using Limma *R* package (Figure 7(a)). Then 193 DEGs were further assessed with GO function analysis and KEGG pathways using WebGestalt *R* package. GO analysis showed that 432 terms of biological process, 27 terms of cellular component, and 41 terms of molecular function were annotated with significant differences between C1 and C3 subtypes ($p < 0.05$). The top 10 enriched terms of biological process, cellular component, and molecular function were displayed (Figures 7(b)–7(d)). However, no KEGG pathways with significant difference between C1 and C3 subtypes were found. Moreover, between C2 and C3 subtypes, we identified 1673 DEGs incorporating 685 upregulated and 988 downregulated genes (Supplementary Figure S2) and annotated 35 KEGG pathways, 1181 terms of biological process, 132 terms of cellular component, and 153 terms of molecular function. The top 10 enriched terms were shown in Supplementary Figure S3. Among these terms, epidermal cell differentiation, striated muscle cell differentiation, skin development, epidermis development, and epithelial cell differentiation were all annotated in the top 10 biological processes between C1 and C3 and between C2 and C3 (Figure 7 and Supplementary Figure S3).

3.5. Construction of PPI Networks and Hub Gene Identification. Next, mutually upregulated and downregulated DEGs between C1 and C3 and between C2 and C3 subtypes were examined. 146 mutual DEGs including 97 upregulated and 49 downregulated ones were identified for constructing PPI networks (Figure 8(a)). The bioinformatics tools in STRING database were applied to assess the interactions among 146 proteins of DEGs. Subsequently, Cytoscape was applied to visualize the PPI network and cytoHubba was performed to screen hub genes from the network (Figure 8(b)). Finally, the following top 15 hub genes were identified: OCLN, TFF1, BMP4, KRT18, CLDN3, CLDN4, KRT8, TFAP2A, PPARG, AGR2, GATA4, EPCAM, SNAI2, EGFR, and TMPRSS2. We further evaluated the expression differences of these 15 genes in cancer and adjacent tumors. We observed that GATA4, AGR2, and PPARG were significantly underexpressed in tumor samples (Supplementary Figure S4A). We further evaluated the

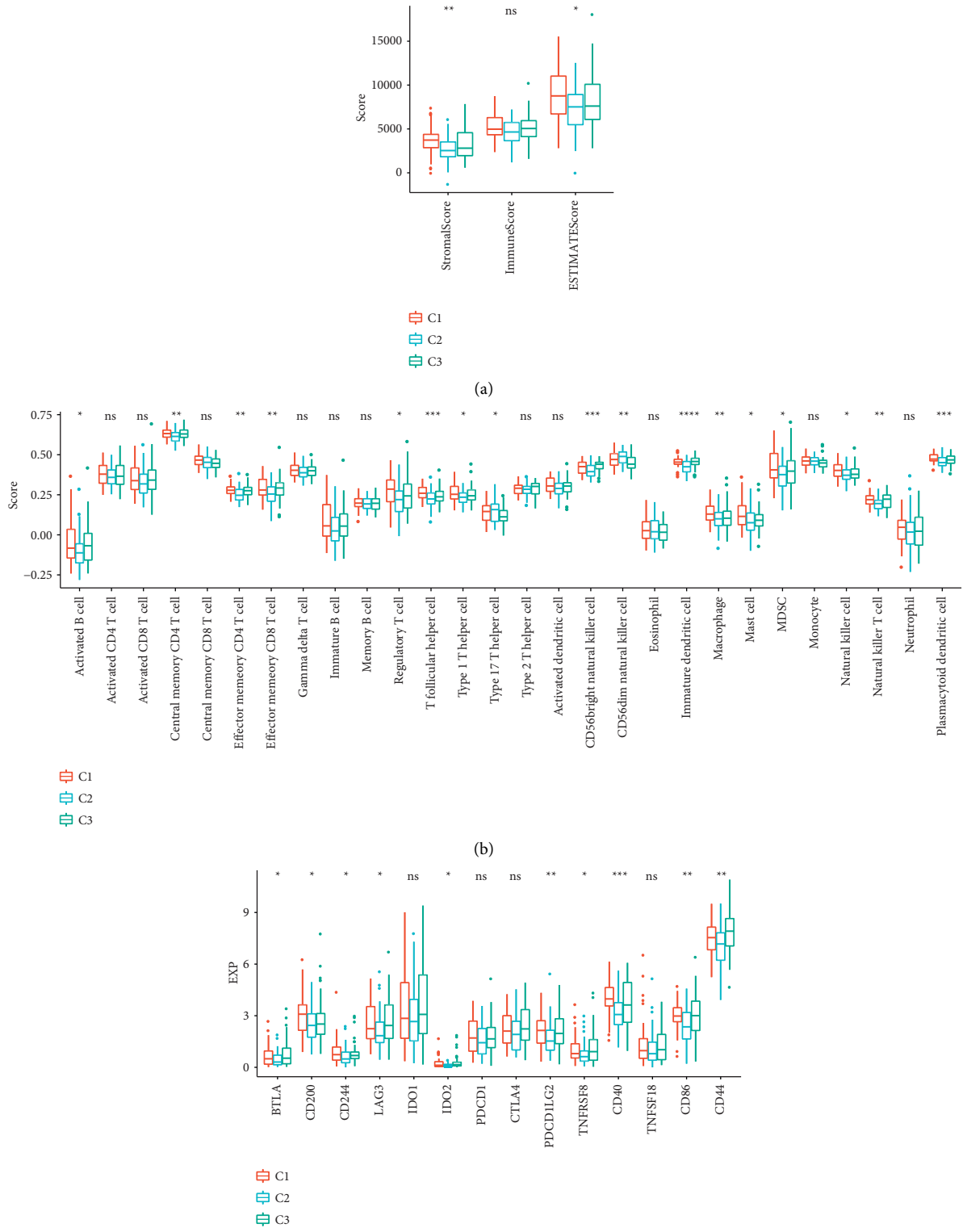

Figure 6: Continued.

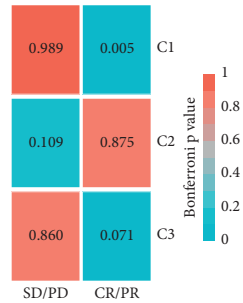

(d)

Figure 6: Immune correlation of three molecular subtypes. (a) Different distribution of immune infiltration of different molecular subtypes. (b) The distribution of immune cell infiltration in different molecular subtypes was different. (c) The expression and distribution of immune checkpoint genes of different molecular subtypes were different. (d) Correlation of immunotherapeutic response of PD-L1 with different molecular subtypes. Analysis of variance was used to test the difference between multiple groups of samples.

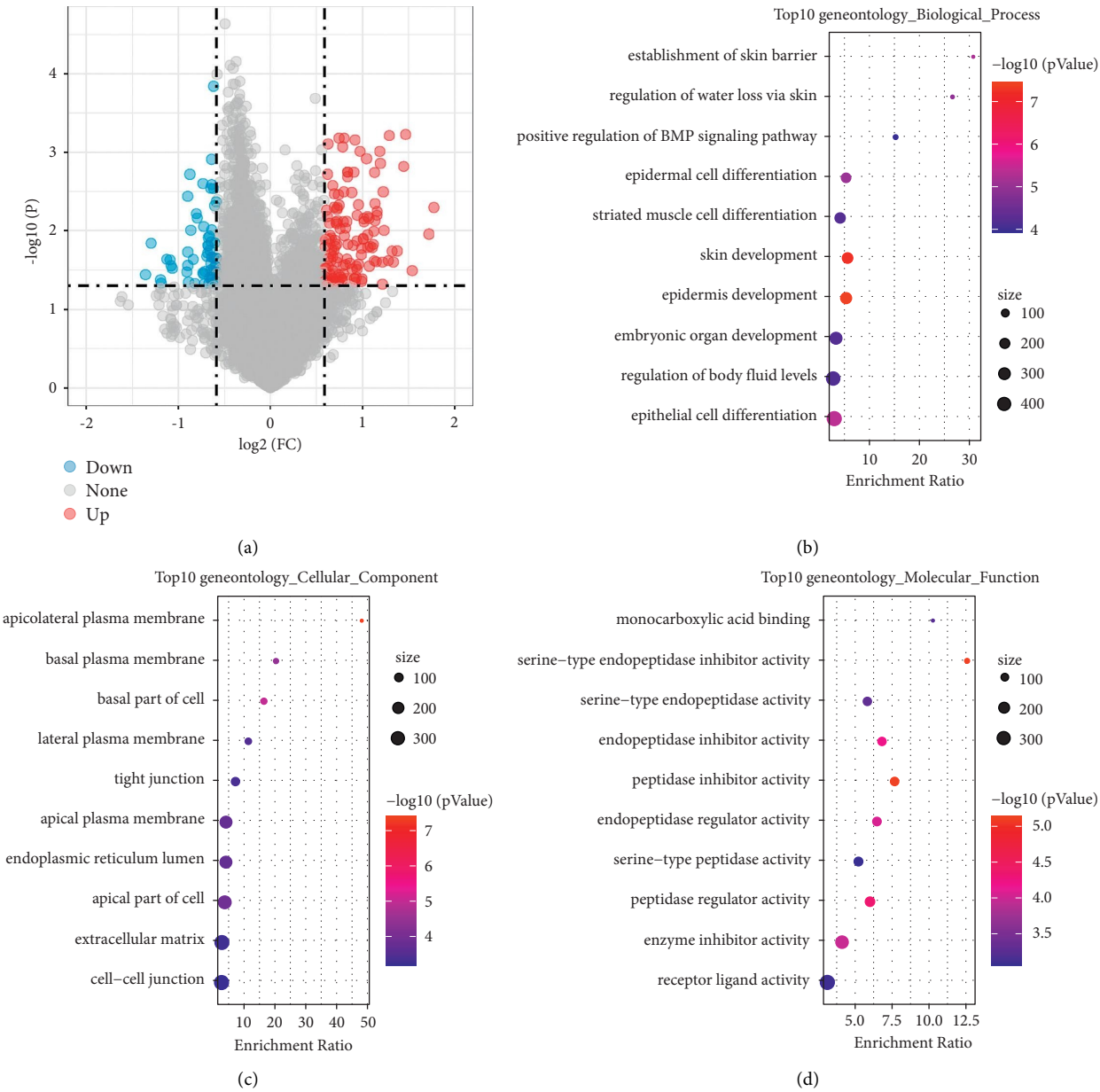

Figure 7: The volcano plot of DEGs between C1 and C3 subtypes. Blue represents downregulated genes and red represents upregulated genes. FC, fold change (a). The top 10 annotated terms of biological process (b), cellular component (c), and molecular function (d) between C1 and C3 subtypes. Dot size represents the gene numbers. The annotated terms were displayed in vertical axis and the enrichment ratio of each term was displayed in horizontal axis.

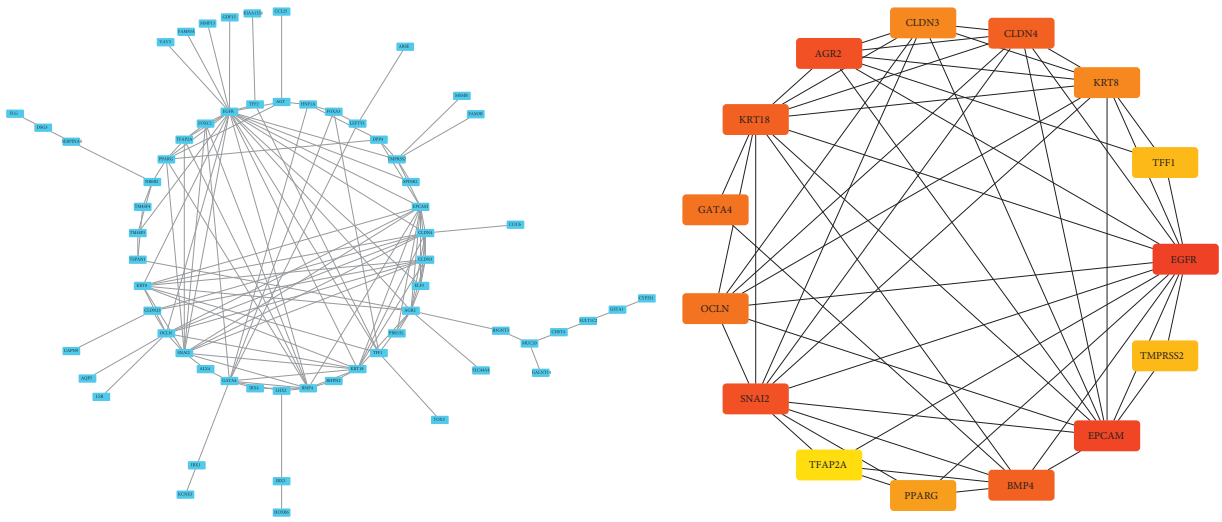

Figure 8: PPI analysis of 146 upregulated and downregulated genes. (a) A PPI network of 146 DEGs constructed by STRING. (b) A PPI network of 15 hub genes screened by Cytoscape and cytoHubba. Black line represents the interactions between proteins.

methylation level of CpG sites in the promoter region of these 15 genes in each sample. It can be observed that there is a higher methylation level in cancer samples as a whole, in particular, GATA4 and TFAP2A (Supplementary Figure S4B). We used ssGSEA to evaluate the enrichment scores of six important immune pathways and further analyzed the correlation between these 15 genes and these immune pathways. It was observed that there was a higher correlation between these genes and weak correlation with immune pathways, among which EPCAM was the most correlated with immune pathways (Supplementary Figure S4(c)).

3.6. Screening of Small Molecules Related to Hub Genes. The 15 hub genes were screened from DEGs between C1 and C3, C2 and C3 were considered to be closely related to ESCA prognosis, and this also suggested that these genes could be the targets for ESCA treatment. Therefore, we introduced three databases of L1000FWD, DGIdb, and CMap with abundant data of the interactions between small-molecule drugs and genes. If one drug is negatively associated with expression of one gene related to ESCA, the drug could be considered as a potential drug for ESCA treatment. Within three databases, we screened a total of 598 small molecules having interactions with hub genes, including 96 from L1000FWD, 439 from DGIdb, and 63 from CMap. By overlapping these small molecules in three databases, we observed 3 small molecules (BMS-754807, gefitinib, and neratinib) were overlapped between L1000FWD and DGIdb, 3 small molecules (zuclopenthixol, puromycin, and naringenin) were overlapped between L1000FWD and CMap, 2 small molecules (sulfasalazine and imatinib) were overlapped between DGIdb and CMap (Figure 9). Among these 8 small molecules, BMS-754807, gefitinib, neratinib, and imatinib have antitumor activity. Zuclopenthixol, as a Dopamine receptor antagonist, is a drug for treating

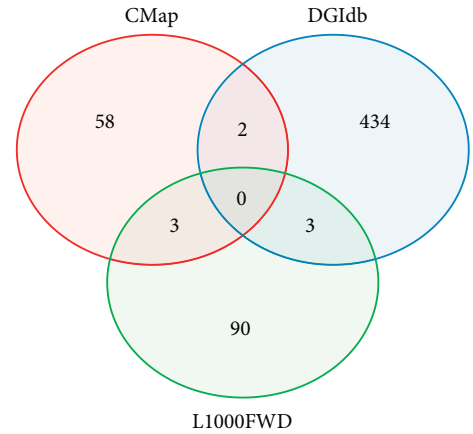

Figure 9: Screening of small molecules related to hub genes from L1000FWD, DGIdb, and CMap databases.

schizophrenia. Puromycin is an aminoglycoside antibiotic, and sulfasalazine is a nonsteroid anti-inflammatory drug. These drugs may specifically target hub genes and take function in suppressing tumor cell proliferation and invasion, although further experiment and analysis are needed for illustrating their function and mechanism in antitumor activity.

4. Discussion

A number of epigenetic studies on ESCA have revealed the significance of epigenetic regulation on ESCA development; however, the role of m^6A modification on ESCA has not been systematically studied. Only several studies have found that some m^6A regulators, such as ALKBH5, HNRNPA2B1, and HNRNPC, have strong relation with ESCA prognosis [24–26]. Inspired from the previous researches, we focused on analyzing a total of 15 m^6A regulators and identified three

new molecular subtypes associated with clinical features and ESCA prognosis. Furthermore, we constructed a PPI network based on DEGs screened from the three subtypes and determined 15 prognosis-related hub genes from the PPI network.

Some of the 15 hub genes have been reported to be associated with tumor progression of ESCA. For example, TFF1 encodes a mucosa protector factor, and it is silenced in the early stage of ESCA development resulting from high methylation of TFF1 promoter [44]. BMP4 and EPCAM are involved in inducing epithelial-mesenchymal transition (EMT) and promoting tumor cell migration of ESCA [45–47]. Low expression of CLDN4 is indicative of a poor prognosis of ESCC [48]. High expression of TFAP2A is correlated with favorable OS of ESCC patients [49]. EGFR is highly expressed in ESCA and some other cancer types; moreover, it is seen as a promising target for inhibiting tumor aggression [50]. Although some hub genes have not been found to be correlated with ESCA development, their relations with other cancer types have been previously demonstrated.

Using small-molecule databases, 8 potential drugs closely interacting with the 15 hub genes were identified. These drugs negatively associated with expression of the hub genes can be considered as potential drugs for treating ESCA. Among the 8 drugs, gefitinib, neratinib, and imatinib have been commercialized for clinical treatment of specific cancers. Gefitinib is an EGFR tyrosine kinase inhibitor that can hinder tumor cell proliferation and angiogenesis and has been commercially applied in treating non-small-cell lung cancer [51]. Clinical trials of gefitinib in advanced ESCA patients demonstrated a partial response and stable disease rate of between 24% and 39%, showing a relatively positive effect [52–54]. Neratinib is a tyrosine kinase inhibitor targeting HER1, HER2, and HER4 and can effectively improve disease-free survival of HER2-positive breast cancer patients given with chemotherapy and trastuzumab [55, 56]. Imatinib, a tyrosine kinase inhibitor targeting Bcr-Abl tyrosine kinase, could suppress disease progression and extend overall survival of chronic myeloid leukemia and gastrointestinal stromal tumors [57, 58].

BMS-754807 has not been used to treat cancers; however, evidence suggested a promising application of it in clinical practice. BMS-754807 is an inhibitor of targeting insulin-like growth factor-1 receptor/insulin receptor (IGF-1R/IR) signaling pathway, which has been proven to be effective in suppressing tumor cell proliferation of xenograft tumor models of several cancer types [59–61]. Study found that sulfasalazine could enhance cisplatin-induced cytotoxic effects on advanced gastric cancer and bladder cancer [62, 63]. The remaining two drugs zuclopenthixol and puromycin have not been reported to be related to cancer therapy, but they still may have the potential to target hub genes related to ESCA prognosis, according to our analysis.

This study did not differentiate two molecular types of esophagus cancer (squamous cell carcinoma and adenocarcinoma), which may affect the results of molecular subtypes to some extent. In addition, further study on these hub genes and small molecules are needed to demonstrate their functions in clinical practice. Importantly, this study applied a new approach to analyzing the relation between m^6A and ESCA prognosis and provided a valuable reference to explore potential targets and drugs for ESCA treatment.

5. Conclusions

In conclusion, this study determined three molecular subtypes of ESCA based on m^6A regulators and identified 8 potential small-molecule drugs closely interacting with hub genes through integrative analysis. The new molecular subtypes were effective in classifying ESCA patients into low-risk and high-risk groups. The 15 hub genes screened from DEGs among three subtypes can be potential targets for treating ESCA. The 8 small-molecule drugs closely interacting with the hub genes may be promising drugs for ESCA patients.

Abbreviations

CDF: Cumulative distribution function
CMap: The connectivity map
CNV: Copy number variation
DEGs: Differentially expressed genes
DGIdb: Drug-gene interaction database
EGFR: Epidermal growth factor receptor
ESCA: Esophagus cancer
ESCC: Esophageal squamous cell carcinoma
FC: Fold change
GO: Gene ontology
GRED: Gastroesophageal reflux disease
IGF-1R/IR: Insulin-like growth factor-1 receptor/insulin receptor
KEGG: Kyoto encyclopedia of genes and genomes
L1000FWD: L1000 fireworks display
m^6A: N^6-methyladenosine
OS: Overall survival
PPI: Protein-protein interaction
ssGSEA: Single sample gene set enrichment analysis
TCGA: The cancer genome atlas
TPM: Transcripts per million.

Data Availability

The data used to support the findings of this study are included within the article.

Conflicts of Interest

The authors declare that they have no conflicts of interest.

Acknowledgments

This work was supported by the Teaching Reform Research Project of University of South China (2020YB-XJG127), the Hunan Provincial Natural Science Foundation of Youth (2016JJ3108), and the Hunan Provincial Natural Science Foundation (2021JJ30610).

Supplementary Materials

Supplementary Figure S1. The mutation patterns of top 20 mutated genes in C1 (a), C2 (b), and C3 (c) subtypes. *Supplementary Figure S2.* The volcano plot of DEGs between C2 and C3 subtypes. Blue represents down-regulated genes and red represents upregulated genes. FC, fold change. *Supplementary Figure S3.* The top 10 annotated terms of biological processes (a), cellular component (b), molecular function (c), and KEGG pathways (D) between C2 and C3 subtypes. Dot size represents the gene numbers. The annotated terms were displayed in vertical axis and the enrichment ratio of each term was displayed in horizontal axis. *Supplementary Figure S4.* a: Differential expression of 15 genes in cancer and adjacent tissues; b: Heatmap of methylation distribution of promoter region methylation sites of 15 genes in various types of samples; c: Correlation heatmap of 15 genes and 6 immune related pathways. *Supplementary Table S1.* The clinical information of 161 ESCA samples. *Supplementary Table S2.* 9 m^6A methylation sites screened by univariate Cox regression analysis. (*Supplementary Materials*)

References

[1] H. Sung, J. Feerlay, R. L. Siegel et al., "Global cancer statistics 2020: GLOBOCAN estimates of incidence and mortality worldwide for 36 cancers in 185 countries," *CA: a Cancer Journal for Clinicians*, vol. 71, no. 3, pp. 209–241, 2021.

[2] M. J. D. Arnal, Á. Ferrández Arenas, and Á. L. Arbeloa, "Esophageal cancer: risk factors, screening and endoscopic treatment in Western and Eastern countries," *World Journal of Gastroenterology*, vol. 21, no. 26, pp. 7933–7943, 2015.

[3] A. Pennathur, M. K. Gibson, B. A. Jobe, and J. D. Luketich, "Oesophageal carcinoma," *The Lancet*, vol. 381, no. 9864, pp. 400–412, 2013.

[4] Y. Song, L. Li, Y. Ou et al., "Identification of genomic alterations in oesophageal squamous cell cancer," *Nature*, vol. 509, no. 7498, pp. 91–95, 2014.

[5] W. Zhang, H. Zhu, X. Liu et al., "Epidermal growth factor receptor is a prognosis predictor in patients with esophageal squamous cell carcinoma," *The Annals of Thoracic Surgery*, vol. 98, no. 2, pp. 513–519, 2014.

[6] Z. Gao, X. Meng, D. Mu, X. Sun, and J. Yu, "Prognostic significance of epidermal growth factor receptor in locally advanced esophageal squamous cell carcinoma for patients receiving chemoradiotherapy," *Oncology Letters*, vol. 7, no. 4, pp. 1118–1122, 2014.

[7] T. D. Ahrens, M. Werner, and S. Lassmann, "Epigenetics in esophageal cancers," *Cell and Tissue Research*, vol. 356, no. 3, pp. 643–655, 2014.

[8] A. Nebbioso, F. P. Tambaro, C. Dell'Aversana, and L. Altucci, "Cancer epigenetics: moving forward," *PLoS Genetics*, vol. 14, no. 6, Article ID e1007362, 2018.

[9] Q. Lan, P. Y. Liu, J. Haase, J. L. Bell, S. Hüttelmaier, and T. Liu, "The critical role of RNA m6A methylation in cancer," *Cancer Research*, vol. 79, no. 7, pp. 1285–1292, 2019.

[10] X.-Y. Chen, J. Zhang, and J.-S. Zhu, "The role of m6A RNA methylation in human cancer," *Molecular Cancer*, vol. 18, no. 1, p. 103, 2019.

[11] Z. Li, H. Weng, R. Su et al., "FTO plays an oncogenic role in acute myeloid leukemia as a N 6 -methyladenosine RNA demethylase," *Cancer Cell*, vol. 31, no. 1, pp. 127–141, 2017.

[12] L. P. Vu, B. F. Pickering, Y. Cheng et al., "The N6-methyladenosine (m6A)-forming enzyme METTL3 controls myeloid differentiation of normal hematopoietic and leukemia cells," *Nature Medicine*, vol. 23, no. 11, pp. 1369–1376, 2017.

[13] I. Barbieri, K. Tzelepis, L. Pandolfini et al., "Promoter-bound METTL3 maintains myeloid leukaemia by m6A-dependent translation control," *Nature*, vol. 552, no. 7683, pp. 126–131, 2017.

[14] H. Weng, H. Huang, H. Wu et al., "METTL14 inhibits hematopoietic stem/progenitor differentiation and promotes leukemogenesis via mRNA m6A modification," *Cell Stem Cell*, vol. 22, no. 2, pp. 191–205, 2018.

[15] S. Zhang, B. S. Zhao, A. Zhou et al., "m6A demethylase ALKBH5 maintains tumorigenicity of glioblastoma stem-like cells by sustaining FOXM1 expression and cell proliferation program," *Cancer Cell*, vol. 31, no. 4, pp. 591–606, 2017.

[16] Q. Cui, H. Shi, P. Ye et al., "m6A RNA methylation regulates the self-renewal and tumorigenesis of glioblastoma stem cells," *Cell Reports*, vol. 18, no. 11, pp. 2622–2634, 2017.

[17] S. Lin, J. Choe, P. Du, R. Triboulet, and R. I. Gregory, "The m 6 A methyltransferase METTL3 promotes translation in human cancer cells," *Molecular Cell*, vol. 62, no. 3, pp. 335–345, 2016.

[18] Y. Du, G. Hou, H. Zhang et al., "Sumoylation of the m6A-RNA methyltransferase METTL3 modulates its function," *Nucleic Acids Research*, vol. 46, no. 10, pp. 5195–5208, 2018.

[19] M. Chen, L. Wei, C.-T. Law et al., "RNA N6-methyladenosine methyltransferase-like 3 promotes liver cancer progression through YTHDF2-dependent posttranscriptional silencing of SOCS2," *Hepatology*, vol. 67, no. 6, pp. 2254–2270, 2018.

[20] J. Z. Ma, F. Yang, C. C. Zhou et al., "METTL14 suppresses the metastatic potential of hepatocellular carcinoma by modulating N 6 -methyladenosine-dependent primary MicroRNA processing," *Hepatology*, vol. 65, no. 2, pp. 529–543, 2017.

[21] S. Müller, M. Glaß, A. K. Singh et al., "IGF2BP1 promotes SRF-dependent transcription in cancer in a m6A- and miRNA-dependent manner," *Nucleic Acids Research*, vol. 47, no. 1, pp. 375–390, 2019.

[22] C. Zhang, D. Samanta, H. Lu et al., "Hypoxia induces the breast cancer stem cell phenotype by HIF-dependent and ALKBH5-mediated m6A-demethylation of NANOG mRNA," *Proceedings of the National Academy of Sciences*, vol. 113, no. 14, pp. E2047–E2056, 2016.

[23] A. Tanabe, K. Tanikawa, M. Tsunetomi et al., "RNA helicase YTHDC2 promotes cancer metastasis via the enhancement of the efficiency by which HIF-1α mRNA is translated," *Cancer Letters*, vol. 376, no. 1, pp. 34–42, 2016.

[24] Y. Nagaki, S. Motoyama, T. Yamaguchi et al., "m6A demethylase ALKBH5 promotes proliferation of esophageal squamous cell carcinoma associated with poor prognosis," *Genes to Cells*, vol. 25, no. 8, pp. 547–561, 2020.

[25] H. Guo, B. Wang, K. Xu et al., "m6A reader HNRNPA2B1 promotes esophageal cancer progression via up-regulation of ACLY and ACC1," *Frontiers in Oncology*, vol. 10, Article ID 553045, 2020.

[26] L.-C. Xu, J.-X. Pan, and H.-D. Pan, "Construction and validation of an m6A RNA methylation regulators-based prognostic signature for esophageal cancer," *Cancer Management and Research*, vol. 12, pp. 5385–5394, 2020.

[27] M. D. Wilkerson and D. N. Hayes, "Consensus cluster plus: a class discovery tool with confidence assessments and item tracking," *Bioinformatics*, vol. 26, no. 12, pp. 1572-1573, 2010.

[28] S. Hänzelmann, R. Castelo, and J. Guinney, "GSVA: gene set variation analysis for microarray and RNA-seq data," *BMC Bioinformatics*, vol. 14, no. 1, p. 7, 2013.

[29] P. Charoentong, F. Finotello, M. Angelova et al., "Pan-cancer immunogenomic analyses reveal genotype-immunophenotype relationships and predictors of response to checkpoint blockade," *Cell Reports*, vol. 18, no. 1, pp. 248–262, 2017.

[30] K. Yoshihara, M. Shahmoradgoli, E. Martínez et al., "Inferring tumour purity and stromal and immune cell admixture from expression data," *Nature Communications*, vol. 4, no. 1, p. 2612, 2013.

[31] A. V. Balar, M. D. Galsky, J. E. Rosenberg et al., "Atezolizumab as first-line treatment in cisplatin-ineligible patients with locally advanced and metastatic urothelial carcinoma: a single-arm, multicentre, phase 2 trial," *Lancet (London, England)*, vol. 389, no. 10064, pp. 67–76, 2017.

[32] Y. Hoshida, J.-P. Brunet, P. Tamayo, T. R. Golub, and J. P. Mesirov, "Subclass mapping: identifying common subtypes in independent disease data sets," *PLoS One*, vol. 2, no. 11, Article ID e1195, 2007.

[33] B. Snel, G. Lehmann, P. Bork, and M. A. Huynen, "STRING: a web-server to retrieve and display the repeatedly occurring neighbourhood of a gene," *Nucleic Acids Research*, vol. 28, no. 18, pp. 3442–3444, 2000.

[34] D. Szklarczyk, A. L. Gable, D. Lyon et al., "STRING v11: protein-protein association networks with increased coverage, supporting functional discovery in genome-wide experimental datasets," *Nucleic Acids Research*, vol. 47, no. D1, pp. D607–D613, 2019.

[35] P. Shannon, A. Markiel, O. Ozier et al., "Cytoscape: a software environment for integrated models of biomolecular interaction networks," *Genome Research*, vol. 13, no. 11, pp. 2498–2504, 2003.

[36] D. Otasek, J. H. Morris, J. Bouças, A. R. Pico, and B. Demchak, "Cytoscape Automation: empowering workflow-based network analysis," *Genome Biology*, vol. 20, no. 1, p. 185, 2019.

[37] C. H. Chin, S.-H. Chen, H.-H. Wu, C.-W. Ho, M.-T. Ko, and C.-Y. Lin, "cytoHubba: identifying hub objects and sub-networks from complex interactome," *BMC Systems Biology*, vol. 8, no. Suppl 4, p. S11, 2014.

[38] Z. Wang, A. Lachmann, A. B. Keenan, and A. Ma'ayan, "L1000FWD: fireworks visualization of drug-induced transcriptomic signatures," *Bioinformatics*, vol. 34, no. 12, pp. 2150–2152, 2018.

[39] M. Griffith, O. L. Griffith, A. C. Coffman et al., "DGIdb: mining the druggable genome," *Nature Methods*, vol. 10, no. 12, pp. 1209-1210, 2013.

[40] S. L. Freshour, S. Kiwala, K. C. Cotto et al., "Integration of the drug-gene interaction database (DGIdb 4.0) with open crowdsource efforts," *Nucleic Acids Research*, vol. 49, no. D1, pp. D1144–d1151, 2021.

[41] J. Lamb, E. D. Crawford, D. Peck et al., "The Connectivity Map: using gene-expression signatures to connect small molecules, genes, and disease," *Science*, vol. 313, no. 5795, pp. 1929–1935, 2006.

[42] A. Subramanian, R. Narayan, S. M. Corsello et al., "A next generation connectivity Map: L1000 platform and the first 1,000,000 profiles," *Cell*, vol. 171, no. 6, p. 1437, 2017.

[43] Cancer Genome Atlas Research Network, "Integrated genomic characterization of oesophageal carcinoma," *Nature*, vol. 541, no. 7636, pp. 169–175, 2017.

[44] I. M. Gonzaga, S. C. Soares Lima, M. C. Nicolau et al., "TFF1 hypermethylation and decreased expression in esophageal squamous cell carcinoma and histologically normal tumor surrounding esophageal cells," *Clinical Epigenetics*, vol. 9, no. 1, p. 130, 2017.

[45] C. Kestens, P. D. Siersema, G. J. A. Offerhaus, and J. W. P. M. van Baal, "BMP4 signaling is able to induce an epithelial-mesenchymal transition-like phenotype in barrett's esophagus and esophageal adenocarcinoma through induction of SNAIL2," *PLoS One*, vol. 11, no. 5, Article ID e0155754, 2016.

[46] J. Zhang, A. Luo, F. Huang, T. Gong, and Z. Liu, "SERPINE2 promotes esophageal squamous cell carcinoma metastasis by activating BMP4," *Cancer Letters*, vol. 469, pp. 390–398, 2020.

[47] C. Driemel, H. Kremling, S. Schumacher et al., "Context-dependent adaption of EpCAM expression in early systemic esophageal cancer," *Oncogene*, vol. 33, no. 41, pp. 4904–4915, 2014.

[48] C. O. Sung, S. Y. Han, and S.-H. Kim, "Low expression of claudin-4 is associated with poor prognosis in esophageal squamous cell carcinoma," *Annals of Surgical Oncology*, vol. 18, no. 1, pp. 273–281, 2011.

[49] Y. Zhang, Y. Xu, Z. Li et al., "Identification of the key transcription factors in esophageal squamous cell carcinoma," *Journal of Thoracic Disease*, vol. 10, no. 1, pp. 148–161, 2018.

[50] S. Sigismund, D. Avanzato, and L. Lanzetti, "Emerging functions of the EGFR in cancer," *Molecular oncology*, vol. 12, no. 1, pp. 3–20, 2018.

[51] R. S. Herbst, M. Fukuoka, and J. Baselga, "Gefitinib - a novel targeted approach to treating cancer," *Nature Reviews Cancer*, vol. 4, no. 12, pp. 956–965, 2004.

[52] D. J. Adelstein, C. P. Rodriguez, L. A. Rybicki, D. I. Ives, and T. W. Rice, "A phase II trial of gefitinib for recurrent or metastatic cancer of the esophagus or gastroesophageal junction," *Investigational New Drugs*, vol. 30, no. 4, pp. 1684–1689, 2012.

[53] D. R. Ferry, M. Anderson, K. Beddard et al., "A phase II study of gefitinib monotherapy in advanced esophageal adenocarcinoma: evidence of gene expression, cellular, and clinical response," *Clinical Cancer Research*, vol. 13, no. 19, pp. 5869–5875, 2007.

[54] Y. Xu, Z. Xie, Y. Shi et al., "Gefitinib single drug in treatment of advanced esophageal cancer," *Journal of Cancer Research and Therapeutics*, vol. 12, no. Supplement, pp. C295–c297, 2016.

[55] A. Chan, S. Delaloge, F. A. Holmes et al., "Neratinib after trastuzumab-based adjuvant therapy in patients with HER2-positive breast cancer (ExteNET): a multicentre, randomised, double-blind, placebo-controlled, phase 3 trial," *The Lancet Oncology*, vol. 17, no. 3, pp. 367–377, 2016.

[56] M. Martin, F. A. Holmes, B. Ejlertsen et al., "Neratinib after trastuzumab-based adjuvant therapy in HER2-positive breast cancer (ExteNET): 5-year analysis of a randomised, double-blind, placebo-controlled, phase 3 trial," *The Lancet Oncology*, vol. 18, no. 12, pp. 1688–1700, 2017.

[57] A. Hochhaus, R. A. Larson, F. Guilhot et al., "Long-term outcomes of imatinib treatment for chronic myeloid leukemia," *New England Journal of Medicine*, vol. 376, no. 10, pp. 917–927, 2017.

[58] J. A. Fernández, D. Ferreras, J. J. Ruiz-Manzanera et al., "Characteristics and prognosis of jejunoileal gastrointestinal

stromal tumours (GISTs) in the era of imatinib: a comparative study with gastric GISTs," *Clinical and Translational Oncology: Official Publication of the Federation of Spanish Oncology Societies and of the National Cancer Institute of Mexico*, vol. 23, no. 7, pp. 1368–1376, 2021.

[59] X. Hou, F. Huang, L. F. Macedo et al., "Dual IGF-1R/InsR inhibitor BMS-754807 synergizes with hormonal agents in treatment of estrogen-dependent breast cancer," *Cancer Research*, vol. 71, no. 24, pp. 7597–7607, 2011.

[60] N. Awasthi, C. Zhang, W. Ruan, M. A. Schwarz, and R. E. Schwarz, "BMS-754807, a small-molecule inhibitor of insulin-like growth factor-1 receptor/insulin receptor, enhances gemcitabine response in pancreatic cancer," *Molecular Cancer Therapeutics*, vol. 11, no. 12, pp. 2644–2653, 2012.

[61] S. E. Franks, R. A. Jones, R. Briah, P. Murray, and R. A. Moorehead, "BMS-754807 is cytotoxic to non-small cell lung cancer cells and enhances the effects of platinum chemotherapeutics in the human lung cancer cell line A549," *BMC Research Notes*, vol. 9, no. 1, p. 134, 2016.

[62] K. Shitara, T. Doi, O. Nagano et al., "Phase 1 study of sulfasalazine and cisplatin for patients with CD44v-positive gastric cancer refractory to cisplatin (EPOC1407)," *Gastric Cancer*, vol. 20, no. 6, pp. 1004–1009, 2017.

[63] K. Ogihara, E. Kikuchi, S. Okazaki et al., "Sulfasalazine could modulate the CD 44v9- xCT system and enhance cisplatin-induced cytotoxic effects in metastatic bladder cancer," *Cancer Science*, vol. 110, no. 4, pp. 1431–1441, 2019.

Hindawi
Journal of Oncology
Volume 2022, Article ID 9635218, 9 pages
https://doi.org/10.1155/2022/9635218

Research Article

Application of Circulating Tumor Cells and Circulating Free DNA from Peripheral Blood in the Prognosis of Advanced Gastric Cancer

Pengjie Yu,[1] Shengmao Zhu,[1] Yushuang Luo,[2] Ganggang Li,[3] Yongqiang Pu,[1] Baojia Cai,[1] and Chengwu Zhang[1]

[1]*Department of Gastrointestinal Oncology, Affiliated Cancer Hospital of Qinghai University, Affiliated Hospital of Qinghai University, Xining, China*
[2]*Internal Medicine-Oncology, Affiliated Cancer Hospital of Qinghai University, Affiliated Hospital of Qinghai University, Xining, China*
[3]*The Fifth People's Hospital of Qinghai Province, Xining, China*

Correspondence should be addressed to Chengwu Zhang; dtzhangcw@163.com

Received 15 November 2021; Accepted 21 December 2021; Published 11 January 2022

Academic Editor: Fu Wang

Objective. To explore the application value of circulating tumor cells (CTCs) and circulating free DNA (cfDNA) from peripheral blood in the prognosis of advanced gastric cancer (AGC). Here, we measured CTCs and cfDNA quantity for predicting the outcome of patients. *Patients and Methods*. Forty-five patients with advanced gastric cancer who underwent neoadjuvant chemotherapy and surgical treatment were enrolled in this study. All patients received neoadjuvant chemotherapy with paclitaxel + S-1 + oxaliplatin (PSOX) regimen, and CTCs and cfDNA of the peripheral blood were detected before and after neoadjuvant therapy. Relationships between the number/type of CTC or cfDNA and the efficacy of neoadjuvant chemotherapy were analyzed. *Results*. Among 45 patients, 43 (95.6%) were positive, and the positive rate of mesenchymal CTC was increased with the increase in the T stage. The proportion of mesenchymal CTC was positively correlated with the N stage ($P < 0.05$), and the larger N stage will have the higher proportion of mesenchymal CTC. Patients with a small number of mesenchymal CTC before neoadjuvant chemotherapy were more likely to achieve partial response (PR) with neoadjuvant therapy. Patients with positive CA-199 were more likely to achieve PR with neoadjuvant therapy ($P < 0.05$). Patients in the PR group were more likely to have decreased/unchanged cfDNA concentration after neoadjuvant therapy ($P = 0.119$). After neoadjuvant therapy (before surgery), the cfDNA concentration was higher and the efficacy of neoadjuvant therapy (SD or PD) was lower ($P = 0.045$). *Conclusions*. Peripheral blood CTC, especially interstitial CTC and cfDNA, has a certain value in predicting the efficacy and prognosis of neoadjuvant chemotherapy in advanced gastric cancer.

1. Introduction

Gastric cancer (GC) is one of the most common malignant tumors of the digestive tract according to World Health Organization (WHO) data [1]. Worldwide, the incidence of gastric cancer is 13.86 per 100,000 people [2]. Gastric cancer in China has a high mortality rate and is up to 20/100,000 [3]. Most case belong to advanced gastric cancer (AGC) based on standard tumor-node-metastasis (TNM) staging [4] when they were diagnosed in China. Surgery of no doubt is the best treatment tool for those who were classified as highly differentiated GC. However, the number of AGC patients for surgery was limited because of their staging. Recently, many studies suggested that patients with cancer can perform preoperative or perioperative neoadjuvant chemotherapy for shrinking tumor size or killing micrometastases [5–7]. This definitely increased successful chances for surgery. Therefore, the key for the treatment of the patients with GC is to identify sensitivity and specificity markers at their early stage. With the application of liquid

biopsy technology, circulating tumor cell (CTC) and circulating free DNA (cfDNA) have been used in effect evaluation of clinical tumor treatment and recurrence risk detection [8–10]. CTCs are cells that release into the blood stream from the primary tumor site. CTCs can become seeds of metastasis in distant organs and drive cancer to relapse [7]. CTCs are divided into epithelial, mesenchymal, and mixed CTCs based on their cell surface markers, in which epithelial CTCs are characterized with EpCAMplus CK8/18/19 and mesenchymal CTCs mark vimentin and twist, respectively [11, 12]. The measurement of CTCs from peripheral blood in cancer patients is used in the detection of breast cancer, bladder cancer, nonsmall cell lung cancer, and other solid tumors [13–16]. Circulating free DNA (cfDNA) is about 50–200 base pair (bp) length DNA fragment and can freely circulate in the bloodstream [17]. CfDNA may be from the cellular nucleus or mitochondria and has a specific genetic mutation or epigenetic abnormal information. These aberrant genetic materials can be used for diagnosis and predicting the prognosis of the disease [18]. Many studies revealed that cfDNA levels of patients with advanced-stage cancer were elevated [19–21]. However, CTCs and cfDNA levels of patients with advanced gastric cancer are limited. This study aimed to analyze the levels and types of peripheral blood CTC and cfDNA in patients with advanced gastric cancer during perioperative treatment. We also evaluated the application value of peripheral blood CTC and cfDNA in the outcomes of advanced gastric cancer.

2. Materials and Methods

2.1. Subjects. The patients with advanced gastric cancer (AGC) who had undergone neoadjuvant chemotherapy and surgery in the Department of Gastrointestinal Surgery of the Affiliated Hospital of Qinghai University between September 2019 and October 2020 were enrolled in this study. Enrollment criteria were as follows: (1) a total of 45 cases were diagnosed with gastric cancer by endoscopy and tumor tissues by biopsy; (2) TNM staging of all patients was T3-4N × M0 (according to the TNM staging standard of gastric cancer AJCC/UICC 8th edition, staging is mainly based on abdominal CT, combined with gastroscopy, B ultrasound, etc., if necessary, ultrasound endoscopy, MRI, etc.); (3) physical status score of eastern cooperative oncology group (ECOG) ≤2 points and could tolerate chemotherapy; (4) newly diagnosed patients with no previous radical or palliative surgery, radiotherapy, and chemotherapy history; (5) the functions of liver and kidney were in the normal range; and (6) age was between 18 and 80 years old. Exclusion criteria were as follows: (1) patients with pyloric obstruction, upper gastrointestinal hemorrhage, gastrointestinal perforation, severe infection, and other complications; (2) existed history of radical or palliative surgery, radiotherapy, and chemotherapy or biological therapy; (3) history of allergy to chemotherapy drugs; (4) pregnant or breastfeeding; (5) patients with distant metastases; and (6) other malignant tumors. In this study, 45 patients with advanced gastric cancer were enrolled, including 40 men, 5 women, and age of 29–69 years old with an average of 54.90 (±10.89) years old.

2.2. Study Method. All enrolled patients received 3 cycles of PSOX neoadjuvant chemotherapy. The peripheral blood for number and subtypes of CTC and cfDNA measurement were collected before (baseline) and after neoadjuvant therapy (postoperative) on the 10th day after surgery.

2.3. Chemotherapy Regimen. PSOX regimen was as follows: paclitaxel of 135 mg/m^2 and oxaliplatin of 85 mg/m^2 were injected in the vein on day 1. Tiggio was orally taken based on the patient's body surface area (BSA) from day 1 to day 14, twice a day (2 tablets in the morning and 3 tablets in the evening). 21 days was defined as a chemotherapy cycle. The clinical efficacy and toxicity of neoadjuvant chemotherapy were judged after at least 2 cycles. If the disease progresses during chemotherapy, it will be evaluated after 1 cycle. All cases were confirmed efficacy after 4 weeks.

2.4. Circulating Tumor Cell CTC Detection Method (Nanomembrane Filtration and RNA In Situ Hybridization Method). A total of 10 milliliters (mL) of venous blood from patients before and after chemotherapy and surgery was collected and placed in an ethylenediaminetetraacetic acid (EDTA) anticoagulant tube as a test sample. The samples were centrifugated at 1,500 r/m for 5 minutes within 4 hours, and the plasma phase was removed. CanPatrol® CTC enrichment counting was used to further separate CTC. Furthermore, multiple RNA in situ hybridization technology was used to perform CTC typing detection, and the epithelial type-specific genes (EpCAM, CK8, CK18, and CK19) and the mesenchymal-specific genes (vimentin and twist) were detected, respectively. The amplification probe was hybridized with the above-mentioned type-labeled probe labeled with a fluorescent group to generate a fluorescent signal, the fluorescent signal was read by an automatic identification system, and the CTC typing detection result was automatically judged through the fluorescent signal of different colors.

The CTC results were analyzed. The epithelial CTC was displayed as red fluorescent signal points, and the mesenchymal type was displayed as green fluorescent signal points. The red and green signal points in one cell were displayed as a mixed type.

2.5. CfDNA Isolation and Characterization. A total of 10 mL of peripheral venous blood was collected with an EDTA anticoagulation tube. KminTrak plasma extractor was used to extract plasma DNA. Qbit was used to determine the calculated concentration of cfDNA samples. Briefly, the Qbit quantifier reagent and the corresponding amount of DNA quantitative working solution were prepared according to the manufacturer's introduction. Qbit quantitative working solution was divided into QB tubes, and each tube contained 198 microliters (μL). About 2 μL of the extracted nucleic acid was taken and added into the aliquoted working solution, shaken, and mixed well. The standard nucleic acid working solution was used to formulate the standard curve of the Qbit quantifier, and the fluorescence value of the standard

Table 1: Basic information of enrolled patients.

	Items	Number (n)	Percentage (%)
Gender	M	40	88.89
	F	5	11.11
Age	>55	17	37.78
	≤55	28	62.22
Pathological typing	Adenocarcinoma	45	100
Degree of differentiattion	Low	16	35.55
	Moderate	16	35.55
	High	13	28.89
T staging	1–2	2	4.44
	3	26	57.78
	4	17	37.78
N staging	N0	0	0
	N+	45	100

M, male; F, female; T, tumor; and N, node.

curve was about 15,000, and then, the concentration of each nucleic acid was detected. The concentration of each sample was recorded.

2.6. Observation Indicators. Chemotherapy efficacy was identified according to the response evaluation criteria in solid tumor 1.1 (RECIST 1.1): (1) complete response (CR): all lesions disappeared and were maintained for 4 weeks; (2) partial response: reduced by 30% in tumor size and were maintained for 4 weeks; (3) progressive disease (PD): 20% increase in tumor size; (4) non-CR/PR/stable disease (SD) before lesions increase; new lesions appear; and (5) SD: based on the minimum sum of the longest diameters after the start of treatment, the reduction was less than the standard for PR, and the increase was not to the standard of PD.

2.7. Statistical Analysis. All data were input into spss 20.0 software for statistical analysis. Continuous data were expressed as mean ± standard deviation (Mean ± SD), and an independent sample t-test was used for comparison. Categorical data were expressed as examples (%), and the chi-square test was used for comparison. Spearman's correlation coefficient was used to analyze the correlation between CTC number change, cfDNA number change, and chemotherapy effect, and the Kaplan–Meier method was used for survival analysis. $P < 0.05$ indicated that the difference was statistically significant.

3. Results

3.1. Basic Information of Enrolled Patients. Basic information of 45 patients with AGC is shown in Table 1. Among 45 cases, there were 40 men (88.99%) and 5 women (11.11%). The patients aged more than 55 years old were 17 cases (37.78%), and the patients aged less than 55 years old were 28 cases (62.22%). The pathological typing of all patients was adenocarcinoma. Low, moderate, and high differentiation degrees accounted for 35.55% (16/45), 35.55(16/45), and 28.99 (13/45), respectively. The patients with T I-IV staging were 2 cases (4.44%, stage I-II), 26 cases (57.78%), and 17 cases (37.78%), respectively. All patients with TNM are N + M0.

3.2. Baseline Test Results of CTC. To investigate the CTC number and subtypes of 45 patients, we identified different CTC characteristics. The result is shown in Figure 1. A total of 87 tests were performed for 45 patients with gastric cancer, and all patients were in the advanced stage. Among them, 14, 14, and 17 patients were tested 3 times, 2 times, and only once, respectively. Neoadjuvant therapy efficacy was as follows: there were 27 patients with neoadjuvant efficacy evaluation results, with 10 PR, 16 stable diseases (SDs), and 1 progressive disease (PD); CTC statistical definition was as follows: when counting the positive rate of mesenchymal CTCs, if we set up mesenchymal CTC = 0, then it was negative and if the mesenchymal CTC ≥ 1, it was positive. Among the 45 patients, 39 were in cTNM stage III and 2 were in cTNM stage IIA. The T staging was used to show the baseline CTC. It can be seen from the above table that according to the tumor T stage stratification, comparing the number of CTC and the positive rate of mesenchymal CTC, it could be seen that the positive rate of mesenchymal CTC in stage 4 patients was higher than that in stage 2-3 patients. The results are shown in Table 2. The above table showed the relationship between the number of peripheral blood CTC and each type and the efficacy of chemotherapy. It could be seen that patients with a small number of mesenchymal CTC were more likely to achieve PR with neoadjuvant treatment.

3.3. Correlation between Baseline CTC and Relevant Clinical Indicators of Patients. The clinical information of the enrolled patients with gastric cancer mainly included the following parameters: age, gender, pathological type, tumor location, tumor diameter, degree of differentiation, cTNM staging, T staging, N staging, Lauren type, Borrmann type, whether CA19-9 was normal or not, and so on. The CTC value before neoadjuvant chemotherapy was the baseline CTC. The relationship between CTC and various clinical indicators of gastric cancer was mainly to analyze the total

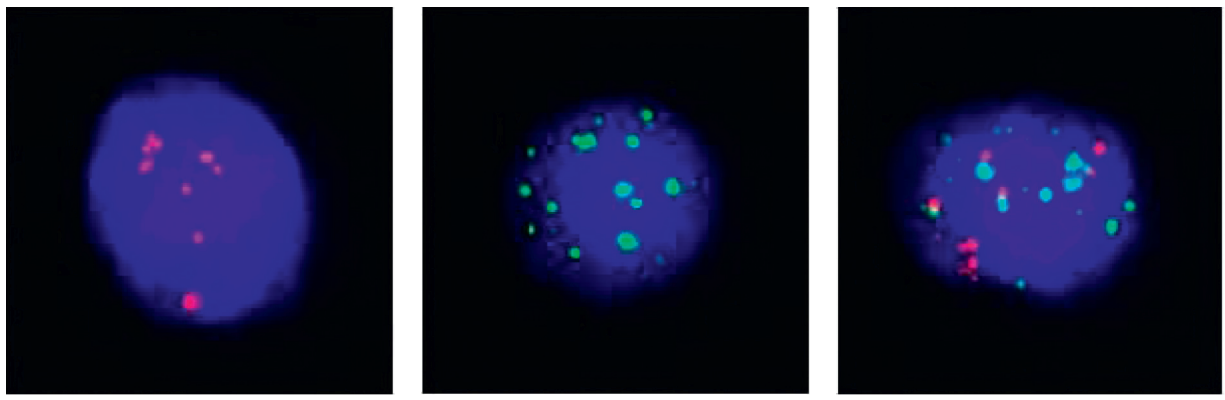

(a) (b) (c)

Figure 1: Images of CTCs. (a) Epithelial CTCs; (b) mesenchymal CTCs; and (c) mixed CTCs; CTC, circulating tumor cell.

Table 2: CTC test data before neoadjuvant therapy (baseline).

T Stage	CTC > 0	Median of CTC	Mean of CTC	Positive rate of mesenchymal CTC
2–3(30)	96.7%(29/30)	111	13.2	46.7%(14/30)
4(15)	93.3%(14/15)	88	10.9	60.0%(9/15)
Total ($n = 45$)	95.6%	110	12.4	51.5%

Table 3: Correlation between CTC and patients' clinical indicators before neoadjuvant therapy (baseline).

Spearman's rho			Total CTC	Total CTC(≤7/>7)	Epithelial CTC	Mixed CTC	Mesenchymal CTC	Mesenchymal CTC (≤0/>0)	Mesenchymal CTC proportion
Age (≤60/>60)	$N = 41$	0.2; 31	0.1; 81	0.1; 83	−0.214	0.23; 7	0.171	0.159	−0.231
		0.1; 27	0.2; 34	0.2; 30	0.158	0.11; 8	0.26	0.297	0.127
T stage (≤3/>3)	$N = 45$	r	0.0; 82	0.0; 12	0	0.22; 9	−0.138	0.155	0.126
		P	0.5; 93	0.9; 36	1	0.13; 0	0.365	0.308	0.41
N stage	$N = 40$	r	0.2; 32	0.4; 17	0.279	0.02; 5	0.244	0.092	0.134
		P	0.2; 17	0.0; 22	0.136	0.89; 7	0.193	0.63	0.481
CA-199 (normal/abnormal)	$N = 39$	r	0.1; 41	0.0; 36	−0.159	0.08; 4	−0.15	0.133	0.156
		P	0.3; 54	0.8; 13	0.298	0.58; 3	0.325	0.385	0.307

*When $P < 0.05$ (two-tailed) or $P < 0.01$ (two-tailed), it indicated a significant correlation; CTC, circulating tumor cells.

number of CTCs, whether the total number of CTCs >7, the number of each type, and the relationship between the positive/proportion of mesenchymal CTCs and the above parameters. The results of baseline CTC testing are summarized in Table 3 and Figure 2. The results showed that the ratio of mesenchymal CTCs was positively correlated with the N stage, indicating that the N stage was larger; the ratio of mesenchymal CTCs was higher. It was consistent with the positive correlation between mesenchymal CTCs and disease stage and prognosis proposed in the current related literature. However, there was no significant correlation between other clinicopathological indicators and the number/type of CTCs.

3.4. Correlation between CTCs before Neoadjuvant Treatment (Baseline) and Neoadjuvant Efficacy. CTCs before neoadjuvant chemotherapy were used as the baseline. We compared CTC number and subtype changes after three cycles of neoadjuvant chemotherapy. The efficacy of neoadjuvant treatment was performed according to the RECIST1.1 evaluation standard. There were 27 patients (27/45, 60%) with neoadjuvant efficacy evaluation results, including 10 cases of PR, 16 cases of SD, and 1 case of PD. The results are indicated in Table 4. The above table showed the relationship between the number of peripheral blood CTCs and each type and the efficacy of chemotherapy. It could be seen that patients with a small number of mesenchymal CTC were more likely to achieve PR with neoadjuvant treatment.

3.5. Correlation between Clinical Pathology and Neoadjuvant Efficacy. As shown in Table 5, the age, maximum tumor diameter, pathological stage, and carcinoembryonic antigen

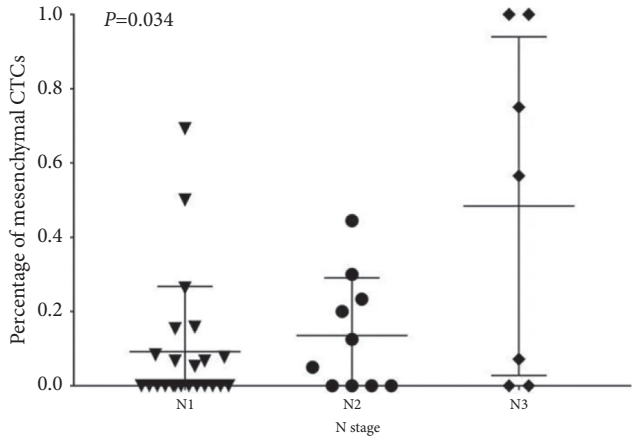

Figure 2: Relationship between mesenchymal CTC percentage and *N* stage. *Y*-axis, mesenchymal CTC percentage; *X*-axis, *N* stage. N1, tumor cells penetrated the second or the third layers of stomach. N2, tumor cells penetrated the second layer of stomach and more distant lymph nodes. N3, tumor cells penetrated the third layer of stomach and more distant lymph nodes.

Table 4: Correlation between CTC before neoadjuvant therapy (baseline) and neoadjuvant efficacy.

Spearman's rho			PR/SD	PR/SD + PD
Total of CTC	$N = 27$	r	0.127	0.069
		p	0.537	0.732
Total of CTC (≤0/>0)	$N = 27$	r	−0.158	−0.217
		p	0.44	0.277
Total of CTC (≤7/>7)	$N = 27$	r	0.22	0.182
		p	0.281	0.364
Epithelial CTC	$N = 27$	r	0.122	0.089
		p	0.553	0.661
Mixed CTC	$N = 27$	r	−0.09	−0.129
		p	0.662	0.522
Interstitial CTC	$N = 27$	r	0.435	0.394
		p	0.026	0.042
Interstitial CTC (≤0/>0)	$N = 27$	r	0.378	0.335
		p	0.057	0.087
Interstitial CTC proportion	$N = 27$	r	0.327	0.292
		p	0.103	0.139

*When $P < 0.05$ (two-tailed) or $P < 0.01$ (two-tailed), it indicated a significant correlation. CTC, circulating tumor cell; PR, partial response; SD, stable disease; PD, progressive disease; and *N*, case number.

(CEA) of the enrolled patients have no correlation with chemotherapy efficacy, but patients with abnormal CA19-9 achieved PR/SD = 0.015 after chemotherapy and PR/SD/PD = 0.018 after chemotherapy ($P < 0.05$). The level of CA19-9 was related to the efficacy of chemotherapy, and patients with positive CA19-9 were more likely to achieve PR with neoadjuvant therapy. Correlation between the end of neoadjuvant therapy (preoperative) CTC and neoadjuvant efficacy was seen that the number/type of mesenchymal CTC after neoadjuvant treatment was significantly related to the efficacy (Figure 3).

Table 5: Correlation between clinical pathology and neoadjuvant efficacy before neoadjuvant therapy (baseline).

Spearman's rho			PR/SD	PR/SD + PD
Age (≤60/>60)	$N = 27$	r	0.069	0.098
		p	0.734	0.635
T Stage (≤3/>3)	$N = 27$	r	0.217	0.184
		p	0.277	0.367
N stage	$N = 23$	r	0.174	0.157
		p	0.428	0.486
CA19-9 (normal/abnormal)	$N = 27$	r	0.174	0.157
		p	0.428	0.486

*When $P < 0.05$ (two-tailed) or $P < 0.01$ (two-tailed), it indicated a significant correlation. CTC, circulating tumor cell; PR, partial response; SD, stable disease; PD, progressive disease; and *N*, case number.

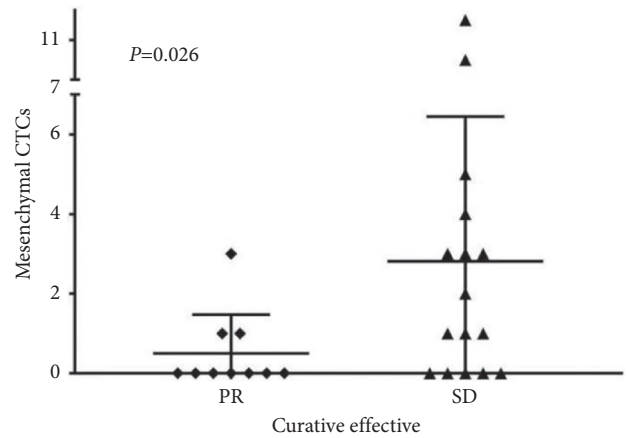

Figure 3: Relationship between mesenchymal CTC number and clinical pathology. *Y*-axis, mesenchymal CTC number; *X*-axis, clinical status. CTCs, circulating tumor cells; PR, partial response; and SD, stable disease.

Table 6: Correlation between the cfDNA concentration and the efficacy of neoadjuvant at the end of the neoadjuvant therapy (before surgery).

Spearman's rho			PR/SD	PR/SD + PD
cfDNA concentration	$N = 22$	r	0.432	0.405
		p	0.045	0.068

*When $P < 0.05$ (two-tailed) or $P < 0.01$ (two-tailed), it indicated a significant correlation. cfDNA, cell-free DNA; CTC, circulating tumor cell; PR, partial response; SD, stable disease; PD, progressive disease; and *N*, case number.

3.6. Correlation between cfDNA and Clinicopathological Indicators of Gastric Cancer and Neoadjuvant Efficacy. A total of 25 patients in this study were tested for CTCs before neoadjuvant and preoperative chemotherapy, and some patients were tested for cfDNA. Correlation between changes in the number/type of CTCs and changes in cfDNA concentration and neoadjuvant efficacy were analyzed, indicating that the changes in the total number of total CTCs and mesenchymal CTCs were similar in the PR and SD/PD groups, and there was no significant difference (Table 6). As

for cfDNA indicators (15 patients had matching cfDNA results before and after neoadjuvant therapy), the trend was that patients in the PR group were more likely to have a decrease/unchanged cfDNA concentration after neoadjuvant therapy ($P = 0.119$). The cfDNA concentration at baseline (before neoadjuvant therapy) was not significantly correlated with CTCs and neoadjuvant efficacy; however, the relationship could be seen that the number/type of CTCs after neoadjuvant treatment was not significantly related to the efficacy.

4. Discussion

Worldwide, cancer is the second cause of death affecting global residents after cardiovascular disease [22]. Of no doubt, early diagnosis and treatments of cancer are major methods for reducing the death rate in the future. Patients with advanced gastric cancer are still the main group of patients with gastric cancer in China [23] and are the focus of our work. Perioperative chemotherapy is an effective treatment for advanced gastric cancer [24, 25]. However, there is no uniform standard for the evaluation of the efficacy of preoperative chemotherapy [26, 27]. Traditional methods for evaluating the efficacy of gastric cancer treatment or chemotherapy include the following: tumor marker levels, imaging examinations, endoscopic ultrasound before and after treatment, or pathological regression after surgery. Spiral CT is a common method to evaluate the efficacy of chemotherapy for gastric cancer [28], and some studies suggested endoscopy, especially endoscopic ultrasound. A study by Wang et al. [29] pointed out that there was no significant difference in the accuracy of abdominal CT-enhanced scanning and ultrasound gastroscopy in the staging of gastric cancer after neoadjuvant chemotherapy. Considering the intolerance of ultrasound gastroscopy, routine ultrasound gastroscopy is not recommended. Currently, the main biomarkers for gastric cancer diagnosis include CA19-9, CA72-4, and CEA. However, these biomarkers are low specificity. Therefore, many studies explored more reliable and sensitive biomarkers for the early diagnosis of gastric cancer [30, 31].

With the continuous development of molecular technology, liquid biopsy is widely used in the field of tumors. In 2013, it was used as an early cancer detection method [32], which has the advantage of detecting cancer before symptoms appear. The commonly used biomarkers for liquid biopsy include circulating tumor DNA (ctDNA), CTCs, exosomes, and circulating tumor RNA (ctRNA). Currently, only ctDNA and CTC have been approved for clinical use by the FDA [33, 34]. Zhang et al. tested CTC in patients with bladder cancer planned for surgery and found that 44 cases (86.3%) were positive [35]. Many studies revealed that the detection of CTC in patients with colorectal cancer (CRC) [36], nonsmall cell lung cancer (NSCLC) [37], prostate cancer [38], and so on could predict the outcomes of the patients. The clinical findings of the perioperative CTC count and epithelial-mesenchymal transition classification of rectal cancer patients showed that the number of CTC in the peripheral circulation of colorectal cancer patients was reduced, especially for rectal cancer patients who underwent laparoscopic surgery [39]. However, the application of liquid biopsy technology in advanced gastric cancer is limited.

In this study, the total positive rate of CTCs (43/45) in this study was 95.6%, of which the positive rate of mesenchymal type (23/45) was 51.1%. In the study of patients with advanced gastric cancer, the CanPatrol® system monitored the detection rate of CTC capture in the peripheral blood of advanced gastric cancer >80%. The N staging in TNM staging indicates regional lymph node metastasis, but it is difficult to accurately evaluate the N stage before surgery. Generally, high-quality enhanced CT combined with invasive ultrasound gastroscopy is required for assessment, which increases the patient's radiation risk, economic burden, and physical pain. It has been reported that the number of mesenchymal CTC is closely related to the TNM staging and *N* staging of gastric cancer [40]. This study used CTC before neoadjuvant as the baseline, showing that baseline interstitial CTC and *N* staging were significantly correlated ($P = 0.034$) and positively correlated. The larger the *N* staging, the proportion of interstitial CTC was the higher. The higher *N* stage indicates that there is cancer cell infiltration in the lymph nodes or lymph vessels around the tumor, and these cancer cells are more likely to enter the peripheral blood system through the lymphatic circulation, which may be the reason why the higher the *N* stage, the easier it is to detect interstitial CTC in the peripheral blood. Therefore, the detection of interstitial CTC at the first diagnosis (before neoadjuvant therapy) may be another indicator for predicting N staging. In TNM staging, the T stage indicates the depth of primary tumor invasion. In the traditional TNM staging method, T staging is of great significance, but T staging reflects the local condition of the tumor, and CTC reflects the peripheral circulation. This may be the reason why T staging is not related to the number of CTCs, and it may also be related to the proportion of T stage in the enrolled patients.

This study found that patients with a small number of intermediate CTC types before neoadjuvant therapy were more likely to achieve PR with neoadjuvant therapy. After analyzing the relationship between the number and classification of CTC before and after neoadjuvant chemotherapy and the efficacy of chemotherapy, the total number of CTCs before and after neoadjuvant therapy was changed, and there was no significant difference in CTC before and after neoadjuvant therapy in patients in the PR, SD/PD, PR, or SD/PD groups. Comparison of changes in the total number of interstitial CTC before and after neoadjuvant therapy is as follows: patients with high interstitial CTC were more likely to have SD/PD ($P = 0.086$), but after grouping according to PR and SD/PD, the total number of interstitial CTC before and after neoadjuvant therapy in each group showed no significant difference. It can be seen that the total number of interstitial CTCs was related to the efficacy of neoadjuvant therapy, which was consistent with the conclusions of related studies. The less CTC before neoadjuvant therapy indicated the better effect of neoadjuvant chemotherapy. Therefore, interstitial CTC can be used as an index to predict the efficacy of chemotherapy. This result is consistent with

the other reports [41–43] and confirmed that CTC detection is a sensitive and reliable method for the prognosis of patients with AGC.

Normal cell apoptosis will produce cfDNA [44]. The acceleration of cell apoptosis in tumor patients leads to an increase in the number of cfDNA in the peripheral circulation. The tumor burden was greater, and the corresponding cfDNA level was higher. The cfDNA concentration before and after neoadjuvant treatment and the efficacy of chemotherapy were analyzed, and patients with higher cfDNA concentration after neoadjuvant treatment (before surgery) had the lower efficacy of neoadjuvant therapy (SD or PD) ($P = 0.045$). Patients in the PR group were more likely to have a decreased/unchanged cfDNA concentration after neoadjuvant therapy ($P = 0.119$). Chemotherapy acts on tumors with different cell cycles to prevent tumor cell replication and reduce tumor burden. PR after chemotherapy suggests a reduction in tumor burden in this group of patients through chemotherapy. So the cfDNA concentration of patients was decreased, cfDNA reflected the condition of circulating free DNA, and the concentration did not change, indicating that chemotherapy was effective. On the other hand, the cfDNA before neoadjuvant in the PR group was higher ($P = 0.073$), and the cfDNA after neoadjuvant in the SD/PD group was higher. This conclusion was similar to CA-199 and interstitial CTC, and it also reflected from the side that cfDNA concentration before neoadjuvant therapy can predict sensitivity and efficacy of chemotherapy. Comparing the cfDNA concentration before and after neoadjuvant, cfDNA before and after neoadjuvant treatment in the PR group showed a downward trend, but there was no significant difference. The concentration of cfDNA after neoadjuvant in the SD/PD group was significantly increased ($P = 0.008$), suggesting that the increase in cfDNA after chemotherapy reflected the poor efficacy of chemotherapy. In summary, the cfDNA concentration before neoadjuvant therapy can predict the efficacy of chemotherapy, and the higher cfDNA concentration before neoadjuvant therapy was relatively sensitive to chemotherapy and easy to achieve PR. If the cfDNA concentration remained elevated after neoadjuvant therapy, it indicated poor chemotherapy efficacy. It was worth noting that the total number of CTC in most patients showed a downward trend 10 days after surgery, but there were also some patients with PR who had an increase in the number of cfDNA after surgery. Follow-up of these patients should be strengthened because their risk of metastasis and recurrence may be higher.

5. Conclusions

CTC and cfDNA are safe and minimally invasive detection techniques compared to surgery and endoscopic biopsy. This study suggested that the level of mesenchymal CTC was positively correlated with tumor T staging and N staging, and patients with higher cfDNA concentration before neoadjuvant chemotherapy were easier to achieve PR, indicating that CTC and cfDNA had a certain value in evaluating the efficacy of neoadjuvant therapy for advanced gastric cancer. However, due to the small number of cases currently enrolled in this study, the follow-up has not yet been completed. After a large sample and follow-up study, it may better reflect the role of CTC and cfDNA in the perioperative treatment, recurrence risk assessment, and prediction of the recovery of advanced gastric cancer.

Data Availability

All data relevant to this study are included within the article and available from the corresponding author upon reasonable request.

Ethical Approval

This study was reviewed and approved by the Ethics Committee of Affiliated Cancer Hospital of Qinghai University (approval #: P-SL-2018008).

Consent

Written informed consent was obtained before the study.

Conflicts of Interest

The authors declare no conflicts of interest.

Authors' Contributions

The authors Pengjie Yu and Shengmao Zhu equally contributed to the study.

Acknowledgments

This study was supported by the Special Project for Transformation of Scientific and Technological Achievements in Qinghai Province (no. 2018-SF-113).

References

[1] D. M. Parkin, F. Bray, J. Ferlay, and P. Pisani, "Global cancer statistics," *CA: A Cancer Journal for Clinicians*, vol. 55, no. 2, pp. 74–108, 2002.

[2] C. A. González, N. Sala, and T. Rokkas, "Gastric cancer: epidemiologic aspects," *Helicobacter*, vol. 18, no. Suppl 1, pp. 34–38, 2013.

[3] W. Chen, R. Zheng, T. Zuo, H. Zeng, S. Zhang, and J. He, "National cancer incidence and mortality in China, 2012," *Chinese Journal of Cancer Research*, vol. 28, no. 1, pp. 1–11, 2016.

[4] J. S. Lim, M. J. Yun, M.-J. Kim et al., "CT and PET in stomach cancer: preoperative staging and monitoring of response to therapy," *Radio Graphics*, vol. 26, no. 1, pp. 143–156, 2006.

[5] R. Reddavid, S. Sofia, P. Chiaro et al., "Neoadjuvant chemotherapy for gastric cancer. Is it a must or a fake?" *World Journal of Gastroenterology*, vol. 24, no. 2, pp. 274–289, 2018.

[6] C. Schuhmacher, S. Gretschel, F. Lordick et al., "Neoadjuvant chemotherapy compared with surgery alone for locally advanced cancer of the stomach and cardia: European Organization for Research and Treatment of Cancer randomized trial 40954," *Journal of Clinical Oncology*, vol. 28, no. 35, pp. 5210–5218, 2010.

[7] D. Cunningham, W. H. Allum, S. P. Stenning et al., "Perioperative chemotherapy versus surgery alone for resectable gastroesophageal cancer," *New England Journal of Medicine*, vol. 355, no. 1, pp. 11–20, 2006.

[8] J. Müller Bark, A. Kulasinghe, G. Hartel et al., "Isolation of circulating tumour cells in patients with glioblastoma using spiral microfluidic technology-a pilot study," *Frontiers in Oncology*, vol. 11, Article ID 681130, 2021.

[9] K. Kolostova, E. Pospisilova, V. Pavlickova et al., "Next generation sequencing of glioblastoma circulating tumor cells: non-invasive solution for disease monitoring," *American Journal of Tourism Research*, vol. 13, no. 5, pp. 4489–4499, 2021.

[10] C.-K. Park, H.-J. Oh, M.-S. Kim et al., "Comprehensive analysis of blood-based biomarkers for predicting immunotherapy benefits in patients with advanced non-small cell lung cancer," *Translational Lung Cancer Research*, vol. 10, no. 5, pp. 2103–2117, 2021.

[11] S.-S. Jiang, C.-G. Mao, Y.-G. Feng et al., "Circulating tumor cells with epithelial-mesenchymal transition markers as potential biomarkers for the diagnosis of lung cancer," *World Journal of Clinical Cases*, vol. 9, no. 12, pp. 2721–2730, 2021.

[12] R. M. Bade, J. L. Schehr, H. Emamekhoo et al., "Development and initial clinical testing of a multiplexed circulating tumor cell assay in patients with clear cell renal cell carcinoma," *Molecular Oncology*, vol. 15, no. 9, pp. 2330–2344, 2021.

[13] X. Guan, C. Li, Y. Li et al., "Epithelial-mesenchymal-transition-like circulating tumor cell-associated white blood cell clusters as a prognostic biomarker in HR-positive/HER2-negative metastatic breast cancer," *Frontiers in Oncology*, vol. 11, Article ID 602222, 2021.

[14] M. Rink, S. Riethdorf, H. Yu et al., "The impact of circulating tumor cells on venous thromboembolism and cardiovascular events in bladder cancer patients treated with radical cystectomy," *Journal of Clinical Medicine*, vol. 9, no. 11, 2020.

[15] M. A. Papadaki, I. Messaritakis, O. Fiste et al., "Assessment of the efficacy and clinical utility of different circulating tumor cell (CTC) detection assays in patients with chemotherapy-naïve advanced or metastatic non-small cell lung cancer (NSCLC)," *International Journal of Molecular Sciences*, vol. 22, no. 2, 2021.

[16] E. Lin, A. W. Hahn, R. H. Nussenzveig et al., "Identification of somatic gene signatures in circulating cfDNA associated with disease progression in metastatic prostate cancer by a novel machine learning platform," *The Oncologist*, vol. 26, no. 9, pp. 751–760, 2021.

[17] S. Gravina, J. M. Sedivy, and J. Vijg, "The dark side of circulating nucleic acids," *Aging Cell*, vol. 15, no. 3, pp. 398-399, 2016.

[18] Y. Peng, W. Mei, K. Ma, and C. Zeng, "Circulating tumor DNA and minimal residual disease (MRD) in solid tumors: current horizons and future perspectives," *Frontiers in Oncology*, vol. 11, Article ID 763790, 2021.

[19] V. Casadio, D. Calistri, S. Salvi et al., "Urine cell-free DNA integrity as a marker for early prostate cancer diagnosis: a pilot study," *BioMed Research International*, vol. 2013, Article ID 270457, 5 pages, 2013.

[20] Y. V. Teo, M. Capri, C. Morsiani et al., "Cell-free DNA as a biomarker of aging," *Aging Cell*, vol. 18, no. 1, Article ID e12890, 2019.

[21] K. J. Lafata, M. N. Corradetti, J. Gao et al., "Radiogenomic analysis of locally advanced lung cancer based on CT imaging and intratreatment changes in cell-free DNA," *Radiology: Imaging Cancer*, vol. 3, no. 4, Article ID e200157, 2021.

[22] S. Sabiu and K. Idowu, "An insight on the nature of biochemical interactions between glycyrrhizin, myricetin and CYP3A4 isoform," *Journal of Food Biochemistry*, Article ID e13831, 2021.

[23] L. Yang, "Incidence and mortality of gastric cancer in China," *World Journal of Gastroenterology*, vol. 12, no. 1, pp. 17–20, 2006.

[24] T. Sano, T. Ichikawa, A. Iai et al., "[A case of advanced gastric cancer with para-aortic lymph node metastasis with long-term survival by chemotherapy and surgery]," *Gan To Kagaku Ryoho*, vol. 48, no. 6, pp. 825–827, 2021.

[25] Z. Pelc, M. Skórzewska, K. Rawicz-Pruszyński, and W. P. Polkowski, "Lymph node involvement in advanced gastric cancer in the era of multimodal treatment-oncological and surgical perspective," *Cancers*, vol. 13, no. 10, 2021.

[26] Y. Tian, Q. Wang, J. Wang et al., "[Neoadjuvant chemoradiotherapy combined with surgery versus direct surgery in the treatment of Siewert type II and III adenocarcinomas of the esophagogastric junction: long-term prognostic analysis of a prospective randomized controlled trial]," *Zhonghua Wei Chang Wai Ke Za Zhi*, vol. 24, no. 2, pp. 128–137, 2021.

[27] K. Miwa, E. Oki, M. Enomoto et al., "Randomized phase II study comparing the efficacy and safety of SOX versus mFOLFOX6 as neoadjuvant chemotherapy without radiotherapy for locally advanced rectal cancer (KSCC1301)," *BMC Cancer*, vol. 21, no. 1, p. 23, 2021.

[28] J.-X. Liang, X.-J. Bi, X.-M. Li et al., "Evaluation of multislice spiral computed tomography perfusion imaging for the efficacy of preoperative concurrent chemoradiotherapy in middle-aged and elderly patients with locally advanced gastric cancer," *Medical Science Monitor*, vol. 24, pp. 235–245, 2018.

[29] Y. Wang, Z. Liu, F. Shan et al., "Optimal timing to surgery after neoadjuvant chemotherapy for locally advanced gastric cancer," *Frontiers in Oncology*, vol. 10, Article ID 613988, 2020.

[30] L. Yao and Y. Xie, "Down-regulation of hsa_circ_0006470 predicts tumor invasion: a new biomarker of gastric cancer," *Journal of Clinical Laboratory Analysis*, vol. 35, no. 8, Article ID e23879, 2021.

[31] I. S. Lee, J. Ahn, K. Kim et al., "A blood-based transcriptomic signature for noninvasive diagnosis of gastric cancer," *British Journal of Cancer*, vol. 125, no. 6, pp. 846–853, 2021.

[32] J. C. Fischer, D. Niederacher, S. A. Topp et al., "Diagnostic leukapheresis enables reliable detection of circulating tumor cells of nonmetastatic cancer patients," *Proceedings of the National Academy of Sciences*, vol. 110, no. 41, pp. 16580–16585, 2013.

[33] E. Augustus, K. Zwaenepoel, V. Siozopoulou et al., "Prognostic and predictive biomarkers in non-small cell lung cancer patients on immunotherapy-the role of liquid biopsy in unraveling the puzzle," *Cancers*, vol. 13, no. 7, 2021.

[34] E. Rossi, M. Aieta, A. Tartarone et al., "A fully automated assay to detect the expression of pan-cytokeratins and of EML4-ALK fusion protein in circulating tumour cells (CTCs) predicts outcome of non-small cell lung cancer (NSCLC) patients," *Translational Lung Cancer Research*, vol. 10, no. 1, pp. 80–92, 2021.

[35] R. Zhang, J. Xia, Y. Wang et al., "Co-expression of stem cell and epithelial mesenchymal transition markers in circulating tumor cells of bladder cancer patients," *Onco Targets and Therapy*, vol. 13, pp. 10739–10748, 2020.

[36] I. Messaritakis, M. Sfakianaki, K. Vogiatzoglou et al., "Evaluation of the role of circulating tumor cells and microsatellite instability status in predicting outcome of advanced CRC

patients," *Journal of Personalized Medicine*, vol. 10, no. 4, 2020.

[37] A. Ntzifa, A. Kotsakis, V. Georgoulias, and E. Lianidou, "Detection of EGFR mutations in plasma cfDNA and paired CTCs of NSCLC patients before and after osimertinib therapy using crystal digital PCR," *Cancers (Basel)*.vol. 13, no. 11, 2021.

[38] H. I. Scher, A. J. Armstrong, J. D. Schonhoft et al., "Development and validation of circulating tumour cell enumeration (Epic Sciences) as a prognostic biomarker in men with metastatic castration-resistant prostate cancer," *European Journal of Cancer*, vol. 150, pp. 83–94, 2021.

[39] W. Yin, Y. M. Han, Z. L. Li, Z. X. Huang, L. Huang, and X. G. Zhong, "Clinical significance of perioperative EMT-CTC in rectal cancer patients receiving open/laparoscopic surgery," *Neoplasma*, vol. 67, no. 5, pp. 1131–1138, 2020.

[40] D. Ning, K. Cui, M. Liu et al., "Comparison of cell search and circulating tumor cells (CTC)-Biopsy systems in detecting peripheral blood circulating tumor cells in patients with gastric cancer," *Medical Science Monitor*, vol. 27, Article ID e926565, 2021.

[41] E. J. Moding, B. Y. Nabet, A. A. Alizadeh, and M. Diehn, "Detecting liquid remnants of solid tumors: circulating tumor DNA minimal residual disease," *Cancer Discovery*, 2021.

[42] Y. Shi, X. Ge, M. Ju, Y. Zhang, X. Di, and L. Liang, "Circulating tumor cells in esophageal squamous cell carcinoma - mini review," *Cancer Management and Research*, vol. 13, pp. 8355–8365, 2021.

[43] C. A. Dreyer, K. VanderVorst, S. Free, A. Rowson-Hodel, and K. L. Carraway, "The role of membrane mucin MUC4 in breast cancer metastasis," *Endocrine-Related Cancer*, vol. 29, no. 1, pp. R17–R32, 2021.

[44] Y. Guan, W. Zhang, X. Wang, P. Cai, Q. Jia, and W. Zhao, "Cell-free DNA induced apoptosis of granulosa cells by oxidative stress," *Clinica Chimica Acta*, vol. 473, pp. 213–217, 2017.

Hindawi
Journal of Oncology
Volume 2022, Article ID 6469523, 17 pages
https://doi.org/10.1155/2022/6469523

Research Article

DNA Repair and Replication-Related Gene Signature Based on Tumor Mutation Burden Reveals Prognostic and Immunotherapy Response in Gastric Cancer

Lei Zhang,[1,2] **Dahai Hu**,[1,3,4] **Shuchen Huangfu**,[1] **Jiaxin Zhou**,[4] **Wei Wang**,[2] **Shijin Liu**,[1] **Hui Tang**,[3,5] **Jinghua Pan**,[1] **and Yunlong Pan**[1]

[1]*Department of Gastrointestinal Surgery, The First Affiliated Hospital of Jinan University, Guangzhou 510632, China*
[2]*Department of Oncology Surgery, The Second Affiliated Hospital of Bengbu Medical College, Bengbu, Anhui Province 233080, China*
[3]*Clinical Medicine Research Institute, The First Affiliated Hospital of Jinan University, Guangzhou 510632, China*
[4]*International School, Jinan University, Guangzhou, Guangdong 510632, China*
[5]*Jiangmen Maternity and Child Health Care Hospital, Huizhou 52900, China*

Correspondence should be addressed to Hui Tang; feifei_085@126.com, Jinghua Pan; huajanve@foxmail.com, and Yunlong Pan; tpanyl@jnu.edu.cn

Received 4 November 2021; Accepted 1 December 2021; Published 11 January 2022

Academic Editor: Fu Wang

The genomic variant features (mutations, deletions, structural variants, etc.) within gastric cancer impact its evolution and immunogenicity. The tumor has developed several coping strategies to respond to these changes by DNA repair and replication (DRR). However, the intrinsic relationship between the associated DRR-related genes and gastric cancer progression remained unknown. This study selected DRR-related genes with tumor mutation burden based on the TCGA (The Cancer Genome Atlas) database of gastric cancer transcriptome and mutation data. The prognosis model of seven genes (*LAMA2*, *CREB3L3*, *SELP*, *ABCC9*, *CYP1B1*, *CDH2*, and *GAMT*) was constructed by a univariate and LASSO regression analysis and divided into high-risk and low-risk groups with the median risk score. Survival analysis showed that overall survival (OS) was lower in the high-risk group than that in the low-risk group. Moreover, patients with gastric cancer in the high-risk group have worse survival in different subgroups, including age, gender, histological grade, and TNM stage. The nomogram that included risk scores for DRR-related genes could accurately foresee OS of patients with gastric cancer. Interestingly, the tumor mutation burden score was higher in the low-risk group than that in the high-risk group, and the risk score for DRR-related genes was negatively correlated with tumor mutation burden in gastric cancer. Next, we further combined the risk score and tumor mutation burden to evaluate the prognosis of gastric cancer patients. The low-risk cohort had a better prognosis than the high-risk cohort in the high tumor mutation burden subgroup. The number of mutation types in the high-risk group was lower than that in the low-risk group. In the immune microenvironment of gastric cancer, more naïve B cells, memory resting CD4+ T cells, Treg cells, monocytes cells, and resting mast cells were infiltrated in the high-risk group. At last, PD-L1 and IAP expressions were negatively correlated with the risk scores; patients with gastric cancer in the low-risk group showed better immunotherapy outcomes than those in the high-risk group. Overall, the DRR-related gene signature based on tumor mutation burden is a novel biomarker for prognostic and immunotherapy response in patients with gastric cancer.

1. Introduction

Gastric cancer (GC) is one of the most common malignant tumors worldwide and the second leading cause of cancer-related death [1, 2]. Its high incidence, high mortality, and poor prognosis pose a severe threat to human health and life. At present, surgical resection is the leading choice for the treatment of patients with early GC, and chemotherapy is the essential treatment for patients who cannot be resected or have advanced metastasis [3, 4]. However, GC is highly

heterogeneous in biology and genes, resulting in less optimal surgical resection and chemotherapy results [5]. Therefore, there is an urgent need to explore more effective treatment strategies.

Tumor mutational burden (TMB) is defined as the total number of somatic gene coding errors, base substitutions, insertions, or deletions detected per million bases [6, 7]. TMB is a quantitative biomarker that reflects the total number of mutations carried by tumor cells, and tumor cells with high TMB will have higher levels of neoantigens [8]. It is thought to assist the immune system in recognizing tumors and stimulating the proliferation of antitumor T cells [9]. Both studies reported that TMB in GC was associated with OS and clinical benefit rate, and high TMB can be used as a biomarker for the clinical efficacy of immune checkpoint blocker (ICB) in GC patients [6, 10].

Defects in replication repair-associated DNA polymerases often manifest an ultrahigh TMB. DNA repair and replication (DRR) is an essential pathway for cells to cope with DNA damage [11, 12]. Recent studies have shown that increasing DNA damage and decreasing the DNA repair capacity of cancer cells lead to genomic distortion [13, 14]. Ying J et al. found that BRCA2, ATM, MSH6, and ATR exhibited high-frequency mutations in the DRR pathway, and TMB-high polymerase unknown significance variants were closely associated with DRR pathway genes and polymerase mutation features and prolonged OS, suggesting an essential role of DRR-related gene detection in cancer prognosis [15]. In addition, DRR-related genes are highly correlated with tumor chemotherapy resistance [16]. A recent clinical trial showed that cancer patients with BRCA1/2 mutations had higher response rates when treated with poly-ADP-ribose polymerase (PARP) inhibitors [17]. Moreover, numerous studies have shown that tumors with DRR mutations are more sensitive to platinum-based therapies. DRR-related genes may provide potential biomarkers for clinical prognosis and immunotherapy in GC. Combining the PARP inhibitor olaparib with the dual WEE1/PLK1 inhibitor AZD1775 to increases the effects of olaparib on GC cell growth inhibition and induction of apoptosis by blocking the DNA damage repair pathway [18]. Taken together, DRR-related genes may provide potential biomarkers for clinical prognosis and immunotherapy in GC.

To identify a novel biomarker for prognosis and therapeutic response in GC based on DRR-related genes, we first screened DRR-related genes in GC based on tumor mutation burden and constructed prognostic models. Then, we comprehensively evaluated the DRR-related gene signature that could predict the prognosis of GC patients and analyzed in detail the relationship between the DRR-related gene signature and the immune microenvironment in GC. Our study identified seven DRR-related genes as tumor signatures, with high sensitivity for GC's prognostic and immunotherapeutic response.

2. Materials and Methods

2.1. Patients and Clinical Specimens. RNA sequencing (RNA-seq) and matching complete clinical information (age, gender, histological grade, survival status, and stage) of GC ($n = 407$) were retrieved from the Cancer Genome Atlas (TCGA, https://portal.gdc.cancer.gov) on July 5, 2021. Fragments with a million per thousand base (FPKM) value are normalized to transcripts per thousand base million (TPM).

2.2. Identification of DRR-Related DEGs and Venn Graph. The limma package in R V4.0.5 (https://www.r-project.org; | log2 fold change |>1, FDR <0.05) analyzes DEGs, the volcano maps for differential genes are utilized the ggpolt2 package in R software. The Venn diagram of the intersecting genes of DEGs and TMBs uses the Venn package.

2.3. Univariate Cox Analysis and Construction of the Prognostic Model. Using DRR differential genes data, the survival package is used for univariate Cox regression analysis. The least absolute shrinkage and selection operator (LASSO) regression algorithm for feature selection, using 10-fold cross-validation, the above analysis uses the R software package glmnet. For Kaplan–Meier curves, p-value and hazard ratio (HR) with 95% confidence interval (CI) were generated by log-rank tests and univariate Cox proportional-hazards regression. All analytical methods above and R packages were performed using R software version 4.0.5 (The R Foundation for Statistical Computing, 2021). $p < 0.05$ was considered statistically significant.

2.4. Construction of the Nomogram Graph Based on the Prognostic Model. The "rms" package in R builds a nomogram based on OS with independent prognostic factors. Use the AUC value to test the ability of the nomogram to distinguish survival. Construct a calibration curve of the nomogram to test the 1-, 3-, and 5-year survival probabilities based on the nomogram and actual observations.

2.5. Estimation of Stromal and Immune Cells in Malignant Tumor Tissues Using Expression Data. The ESTIMATE algorithm-generated matrix and immune scores are used to estimate the level of infiltrating matrix and immune cells in GC tissue and tumor purity through expression profiles. Then, we used the Wilcoxon rank-sum test to compare the differences in tumor purity, stroma, and immune scores between the high- and low-risk groups. Deconvolution results for the tumor-infiltrating immune component were yielded with data gleaned from the TCGA database, which is analyzed by the CIBERSORT algorithm.

2.6. Calculation of TMB Scores and Somatic Mutation Analysis. TMB is defined as the total number of somatic gene coding errors, base substitution, insertion, or deletion detected per million bases. Perl script was used to calculate the mutation frequency of the number of variations/exon length of each sample. The "Maftools" package calculated the somatic mutations in different GCs and the mutation distribution was mapped using the ggplot2 package.

2.7. Statistical Analysis. Statistical analysis is performed by R (version 4.0.5). The Wilcoxon rank-sum test presents comparisons between the two groups, while the Kruskal–Wallis test assesses multiple comparisons. The survminer package determines the demarcation point of each subgroup in R. The Kaplan–Meier curve of OS analysis was presented between different subgroups, and then the log-rank test was performed. Multivariate Cox regression analysis is used to evaluate the association between OS and clinicopathological characteristics and risk scores. The forestplot package visualizes these in R. AUC depicts the 1-, 3-, and 5-year survival rates and is used to assess the predictive power of risk score. Bonferroni's test corrects the p-value. $p < 0.05$ on both sides was considered statistically significant.

3. Results

3.1. Identification of DNA Repair and Replication-Related Prognostic Genes in High and Low TMB GC Groups. Firstly, GC mutation data were downloaded from TCGA, and 816 differential genes were identified according to the high and low TMB GC groups (Figure 1(a), $|\log2FC| > 1$, $p < 0.05$)). Moreover, the high TMB group in GC has better survival (Figure 1(b), $p < 0.05$). A total of 10,315 genes were identified by entering the search term "DNA repair and replication" from GeneCards (https://www.genecards.org), and the top 5000 genes were selected. The two groups of genes were intersected, and 148 genes were overlapped (Figure 1(c)). Univariate Cox regression analysis screened 14 genes (*MAPK10*, *MEOX2*, *LAMA2*, *CREB3L3*, *RBMS3*, *GHR*, *SELP*, *EFEMP1*, *ABCC9*, *APOH*, *INHA*, *CYP1B1*, *CDH2*, and *GAMT*) that were associated with GC prognosis (Figure 1(d), $p < 0.05$).

3.2. Risk Score for DRR-Related Gene Correlated with Prognosis of GC Patients. Next, we constructed a risk score of DRR-related genes in GC. LASSO regression prognostic model was constructed from 14 genes screened by univariate Cox regression, and finally, a total of seven genes (*LAMA2*, *CREB3L3*, *SELP*, *ABCC9*, *CYP1B1*, *CDH2*, and *GAMT*) were constructed in this risk score (Figure 2(a)). The best performance of the risk score was achieved using these seven genes. The model function was as follows: risk score = (0.013918321 × *LAMA2* expression level) + (0.008279412 × *CREB3L3* expression level) + (0.71002582 × *RMI2* expression level) + (0.00495859 × *SELP* expression level) + (0.022154282 × *ABCC9* expression level) + (0.010346169 × *CYP1B1* expression level) + (0.01145852 × *GAMT* expression level). In total, 186 of the 371 GC samples were classified as a high-risk group, and the remaining 185 were classified as a low-risk group according to the median risk score. Survival analysis showed that overall survival (OS) was lower in the high-risk group than that in the low-risk group (Figure 2(b), $p < 0.05$). Receiver operating characteristic (ROC) curves verified AUC of 0.626, 0.638, and 0.623 at 1, 3, and 5 years, respectively (Figure 2(c)). The risk curves showed a positive correlation between prognostic model scores and patient risk values, and those low-risk patients had a higher survival rate than high-risk patients (Figure 2(d)). Heatmap visualizing the gene expression patterns used in the risk model showed that all seven genes in the prognostic model were highly expressed in the high-risk group (Figure 2(e)).

3.3. Construction and Verification of a DRR-Related Prognostic Model in GC. Moreover, we evaluated the prognostic value of risk score for DRR-related genes in different subgroups of GC patients. The risk score was higher in patients older than or equal to 65 years than those under 65 in GC patients (Figure 3(a)). There was no difference between GC gender subgroups (Figure 3(b)). The risk score was higher in the G3 group than that in the G1-2 group for the histological grade (Figure 3(c)). Regarding clinical TNM staging, there was no statistical difference between the risk score of patients with stages I-II and those with stages III-IV (Figure 3(d)). Next, we further analyzed the predictive value of the risk score in different clinical characteristics. In the age group less than or equal to 65 years, the prognosis was worse in the high-risk group, whereas in patients older than 65 years, there was no statistical difference in survival between the high- and low-risk groups (Figure 3(e)). The prognosis was worse in both male and female groups in the high-risk group (Figure 3(f)). There were differences in the prognosis of the high-risk and low-risk groups in the G1-2 group, whereas there was no difference in the prognosis of the G3 group (Figure 3(g)). In terms of clinical staging, survival was worse in the stage I-II and stage III-IV groups in the high-risk group (Figure 3(h)). Furthermore, multivariate analysis showed that the risk score was an independent prognostic factor for GC in the TCGA cohort (Figures 4(a) and 4(b)). To further apply the risk score in clinical prognosis prediction, we constructed the nomogram of GC that included risk score for DRR-related gene, TNM stage, gender, grade, and age. Attractively, the nomogram has accurate predictability in GC patients' 1-, 3-, and 5-year overall survival (Figure 4(c)). At the same time, the calibration diagram is listed in the following: decision curve analysis (DCA) demonstrated that the prognostic nomogram was clinically valuable (Figures 4(d) and 4(e)). In summary, the risk score for DRR-related genes can be used as an effective model for predicting survival outcomes of GC patients.

3.4. Relationship between Risk Score for DRR-Related Genes and TMB. To further elucidate the relationship between TMB and risk score and the effect of both on the prognosis of GC, we first observed that the TMB score was higher in the low-risk group than that in the high-risk group (Figure 5(a), $p < 0.01$) and that the risk score for DRR-related gene was negatively correlated with TMB in GC (Figure 5(b) $R = -0.5$, $p < 0.01$). Next, we further combined the risk score for DRR-related genes and TMB for evaluating the prognosis of GC patients. Interestingly, GC patients with low or high TMB can be further divided into two subgroups based on the risk score for DRR-related genes. Moreover, GC patients with the low-risk score have a superior prognosis than the high-risk score in both low and high TMB subgroups (Figure 5(c),

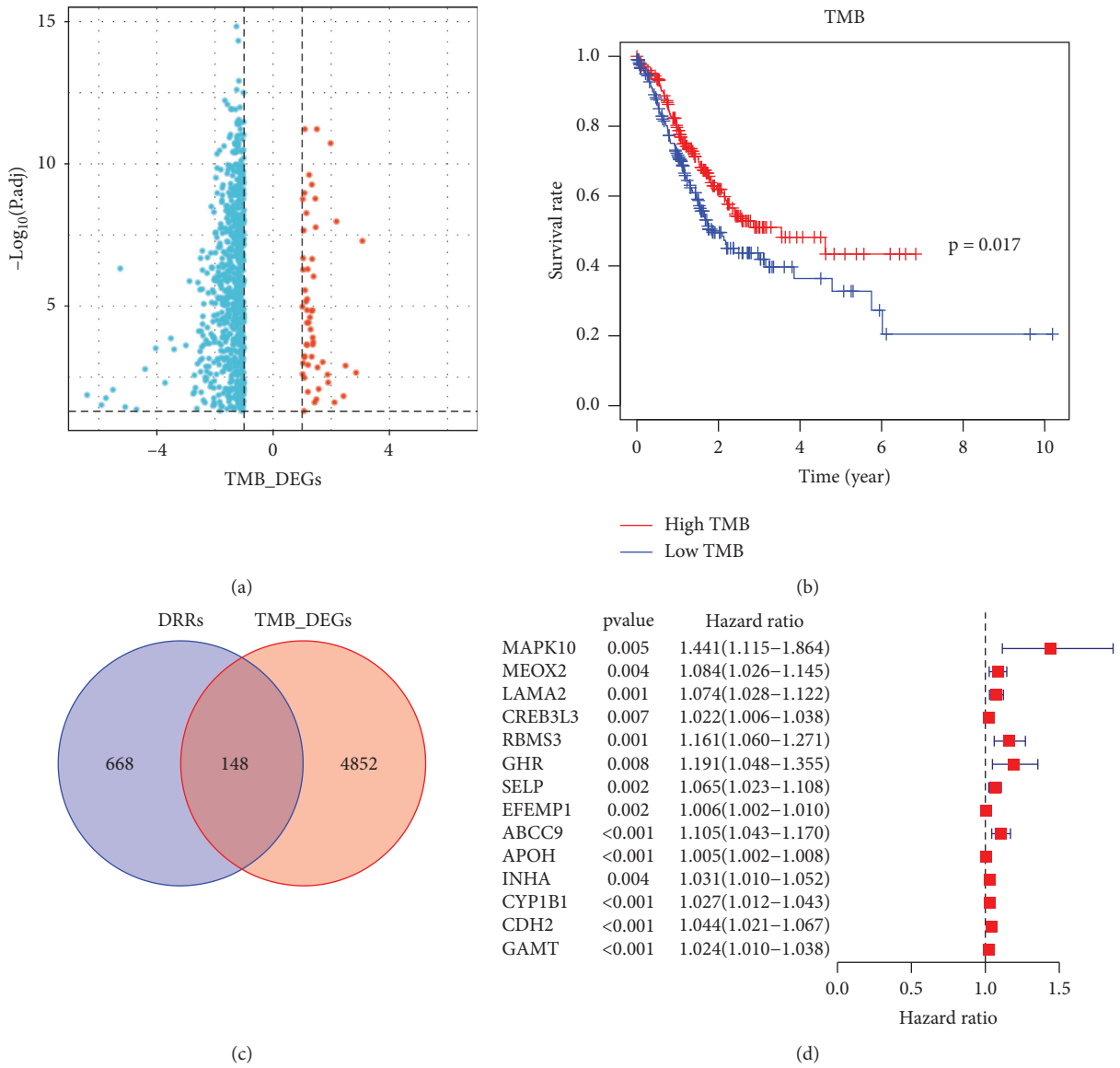

Figure 1: Identification of DRR-related prognostic genes in gastric cancer. (a) Volcano map of TMB differential genes. (b) Survival analysis of high and low TMB. (c) Venn diagram of DRR-related genes and TMB differential genes. (d) Univariate Cox regression analysis of intersecting genes.

$p < 0.001$). Subsequently, we compared the variation context of the high-risk group and low-risk group, which came from the combination of six variation types (T > G, T > A, T > C, C > T, C > G, and C > A) (Figure 5(d)). The number of each mutation type in the high-risk group was smaller than that in the low-risk group. There was a significant difference in somatic mutation rate among samples. The sweeping landscape of somatic variation shows the various patterns of the top 20 driving genes with the most frequent variation. The significant mutation gene (SMG) landscape showed that the mutation rate of the low-risk group was higher than that of the high-risk group among the top 20 mutation genes (Figures 5(e) and 5(f)). These findings may contribute to a new insight into the relationship between risk scores for DRR-related genes and somatic mutation in GC patients.

3.5. Relationship between Risk Score for DRR-Related Gene and TIME in GC. The ESTIMATE algorithm was used to score the immune microenvironment of the GC using an "estimation" package to calculate the ImmuneScore, StromalScore, and ESTIMATEScore for each GC patient resulting in four scores: Immunoscore, StromalScore, ESTIMATEScore, and TumorPurity. These four scores were correlated with the risk score for DRR-related genes. The results showed that ImmuneScore, StromalScore, and ESTIMATEScores were higher in high-risk patients and TumorPurity was higher in low-risk patients (Figures 6(a)–6(d), $p < 0.05$). In addition, to determine the relative abundance of tumor-infiltrating immune cells (TIICs) in GC samples, the degree of infiltration of TIICs was estimated using the CIBERSORT algorithm. The immune cell infiltration in the statistically different samples was significantly different in

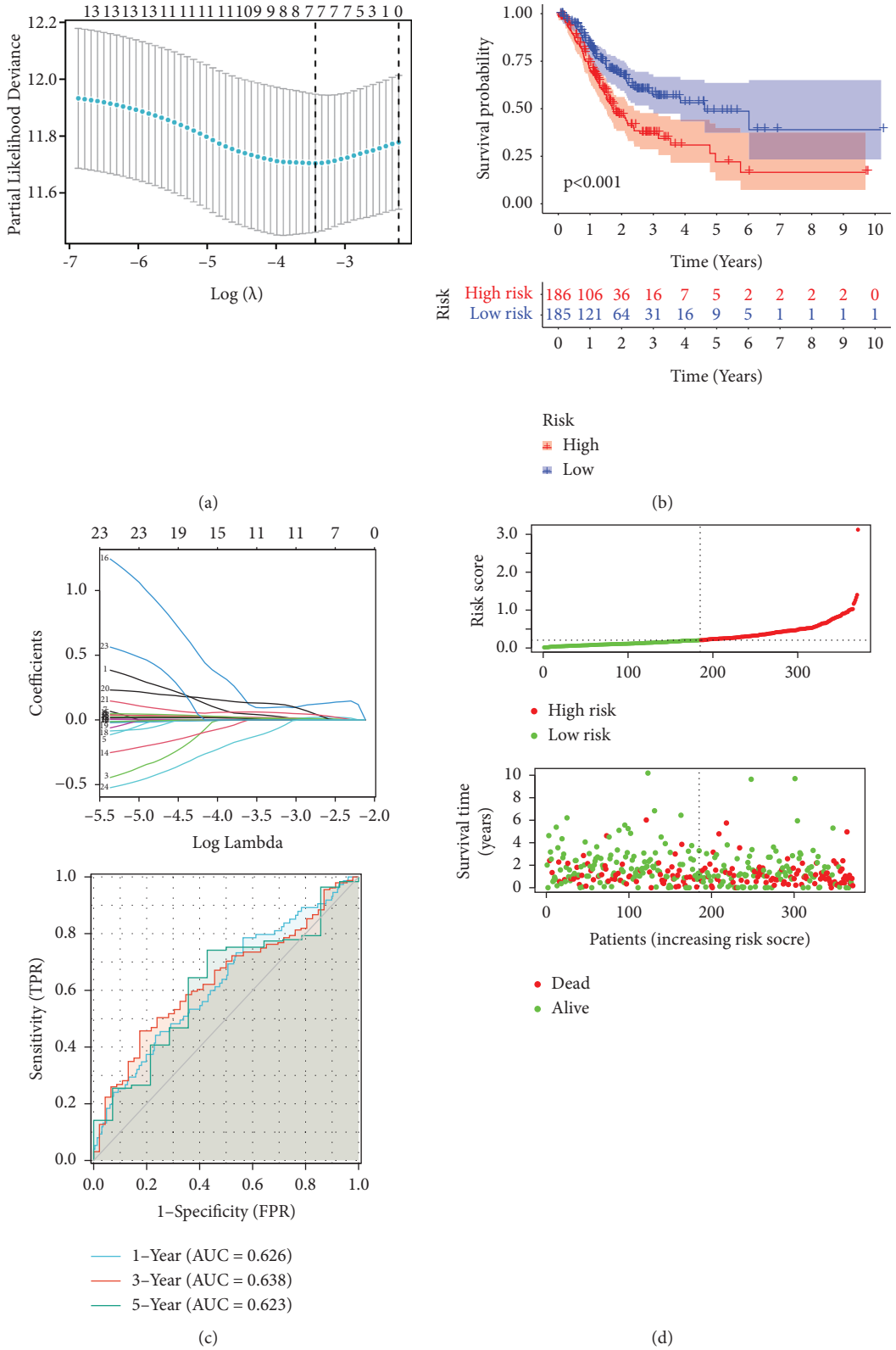

Figure 2: Continued.

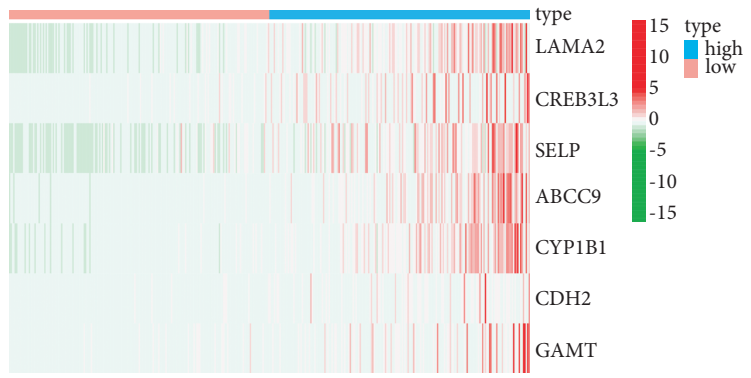

(e)

Figure 2: Risk score for DRR-related gene correlated with prognosis of GC patients. (a) LASSO analysis revealing the minimal lambda. (b) Survival status and risk score. (c) Time-dependent ROC curve. (d) Survival curve illustrating the overall survival of the GC patients. (e) Heatmap visualizing the expression pattern of the seven-candidate DRR-related genes.

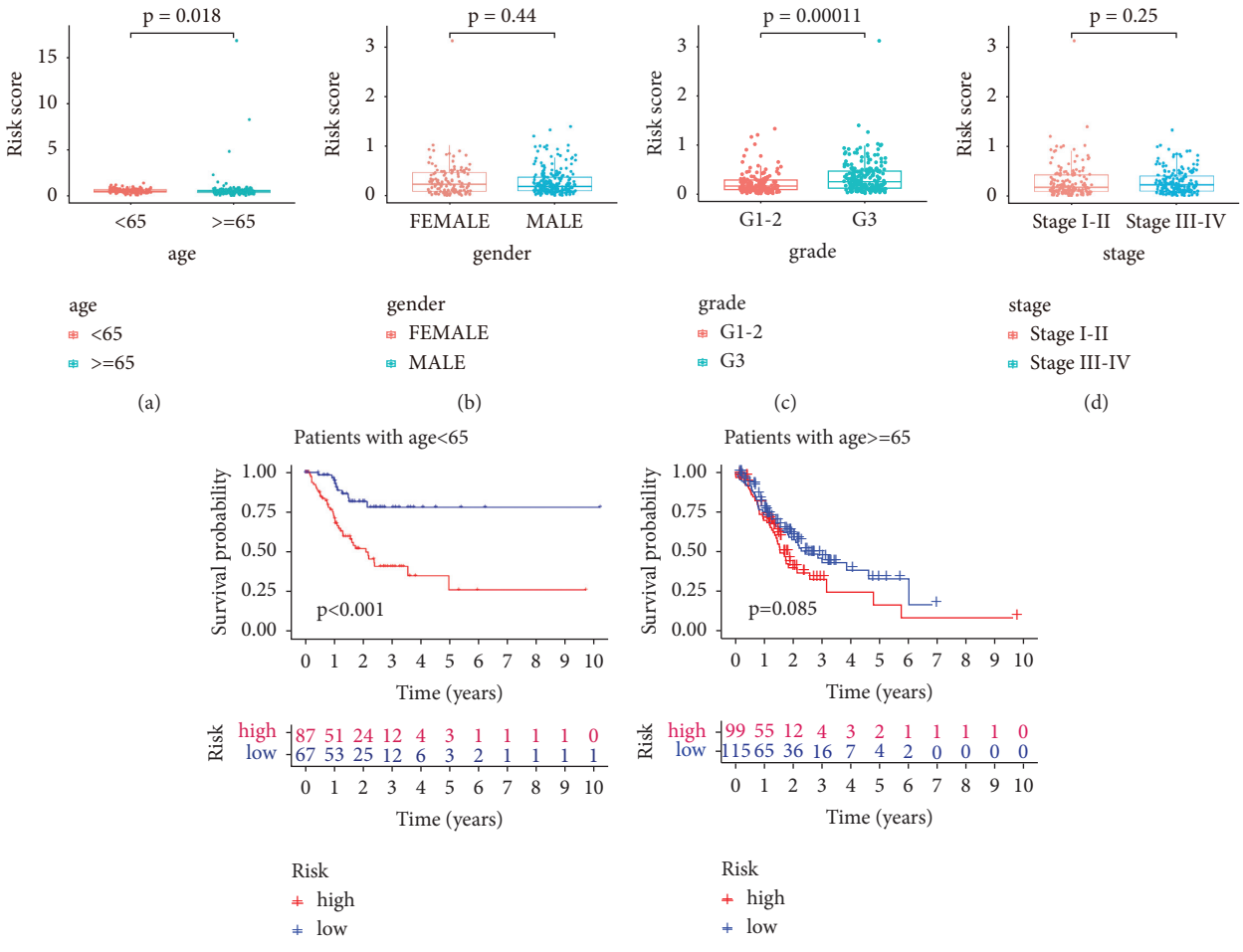

Figure 3: Continued.

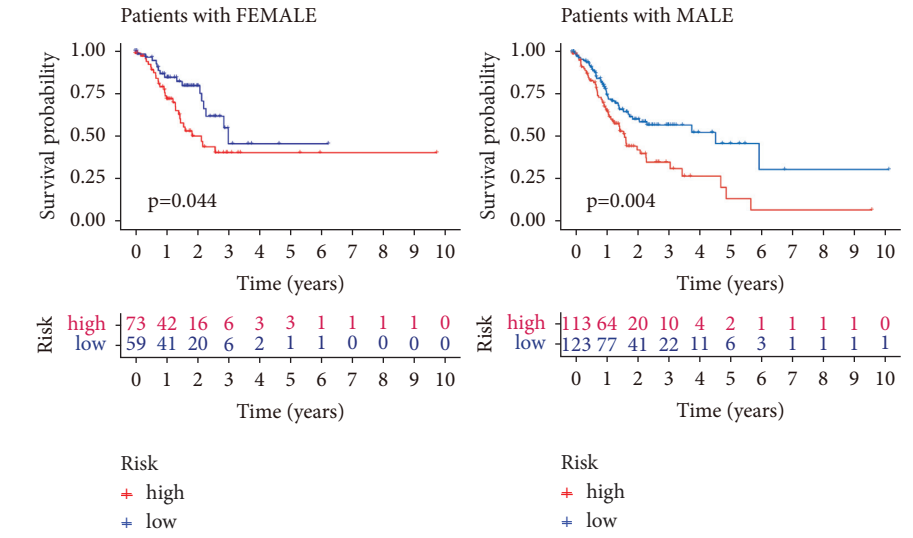

(f)

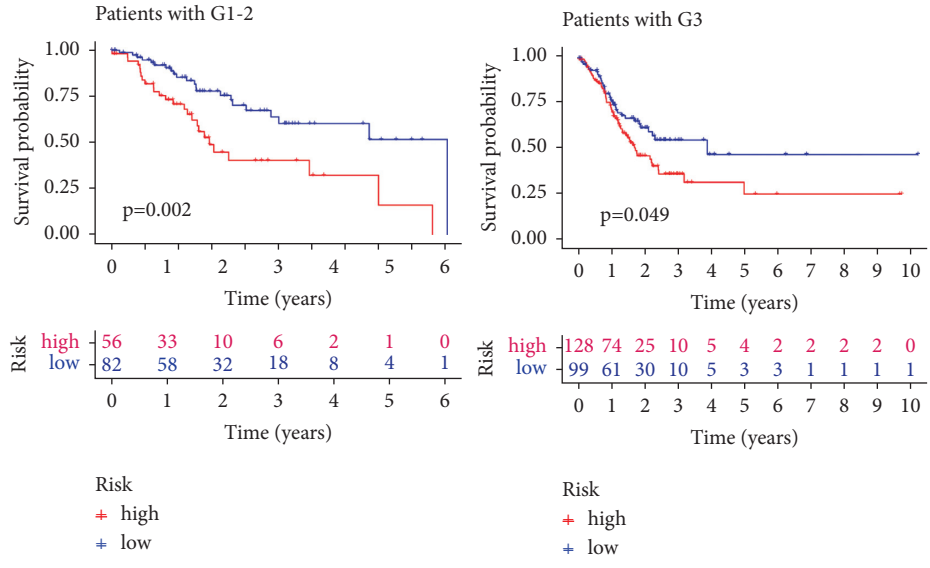

(g)

Figure 3: Continued.

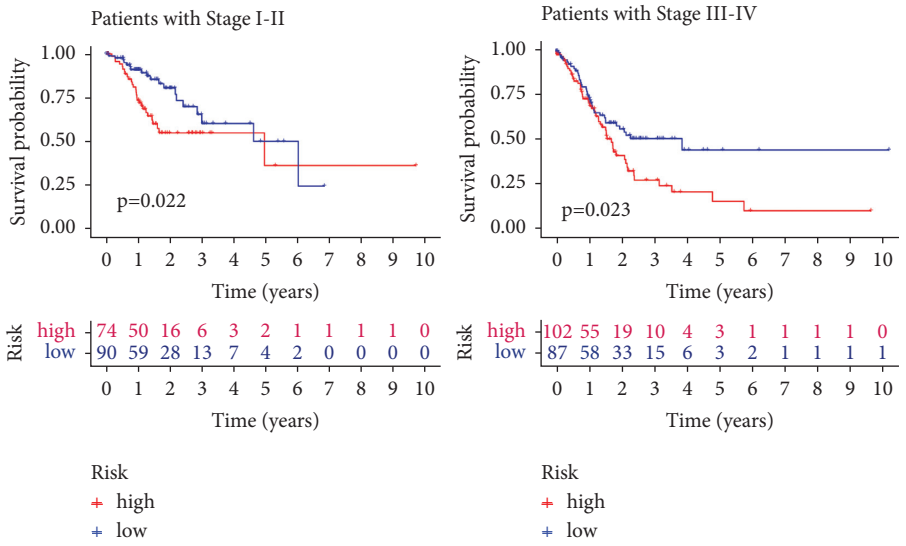

(h)

Figure 3: The correlation of risk score with gastric patients' clinicopathological characteristics. (a–d) The distribution of risk scores in the different ages, genders, histologic grades, and TNM stages. (e–h) The risk score could predict the survival of patients with different ages, genders, histologic grades, and TNM stages.

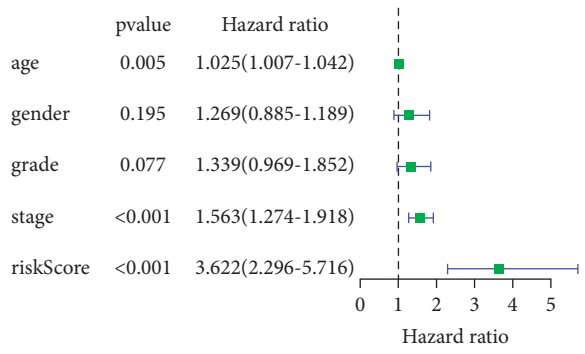

(a)

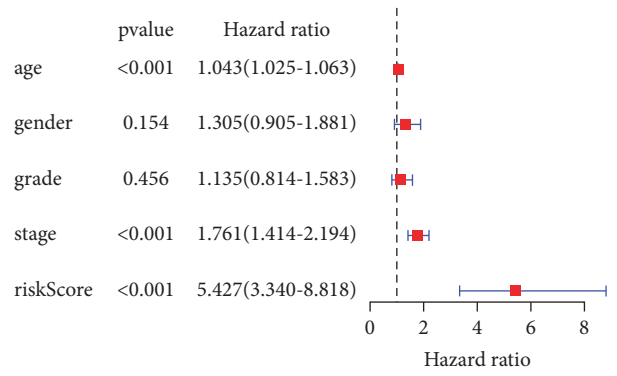

(b)

Figure 4: Continued.

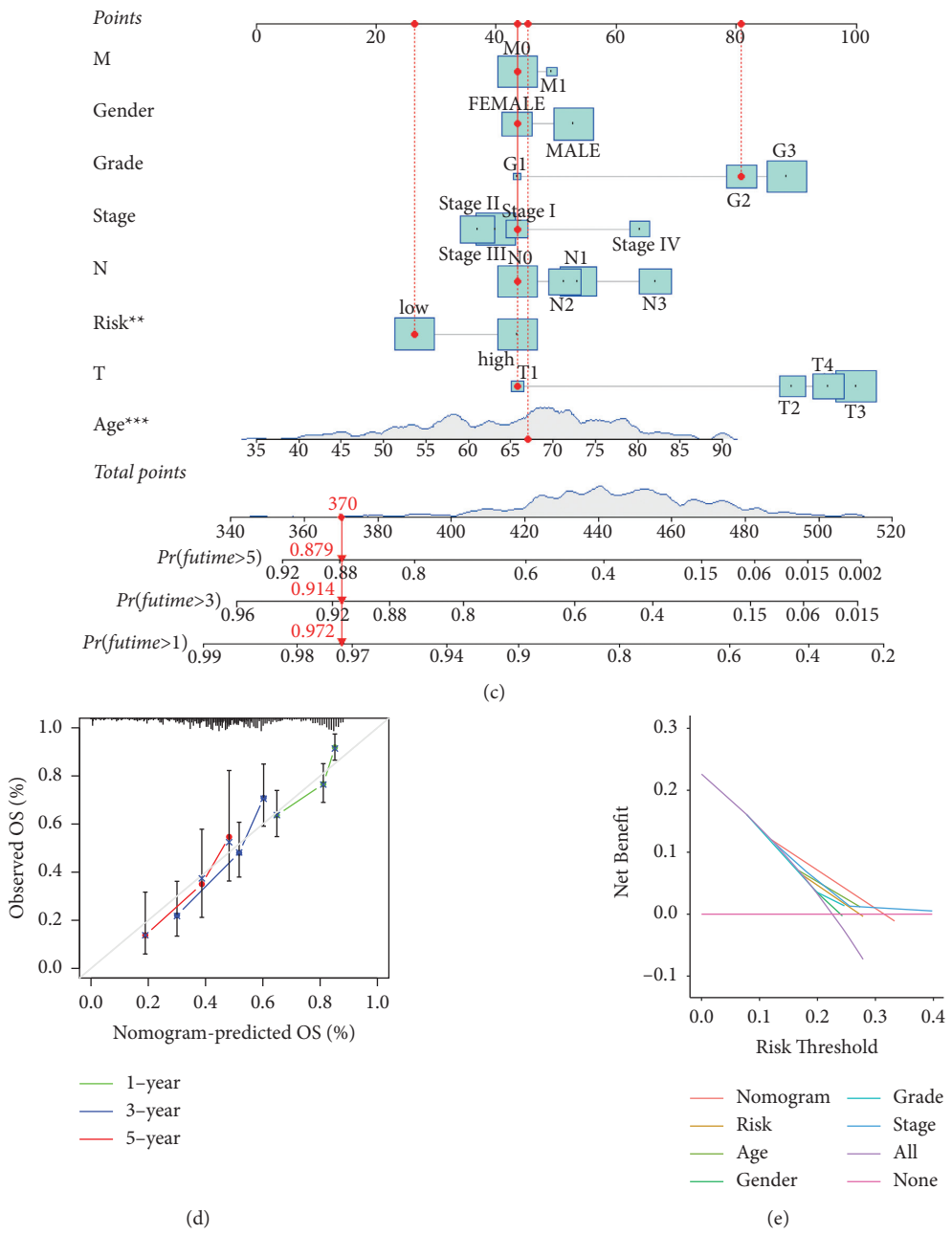

Figure 4: Construction and verification of a DRR-related prognostic model in gastric cancer. (a) Univariate analysis on the risk score. (b) Multivariate Cox analysis on the risk score. (c) Nomogram based on the prognosis associated DRR-related genes. (d) The calibration curves comparing the estimated 1-, 3-, and 5-year survival probability with the actual survival probability of GC patients. (e) DCA of clinical features and risk model.

the two groups with higher initial B naïve cells, CD4+ memory resting T cells, Treg cells, monocytes, and mast resting cells in the high-risk patients and more elevated CD4+ memory activated T cells in the low-risk patients (Figure 6(e), $p < 0.01$). The distribution of immune cells in the high- and low-risk groups was also visualized and analyzed (Figures 6(f) and 6(g)).

3.6. Prognostic Models with the Correlation between Immune Checkpoints and Immunotherapy of GC. Intending to ascertain the efficacy of the risk group for immunotherapy, we initially correlated six common immune checkpoints with the risk score. The results showed that PD-L1 and IAP expressions were negatively correlated with the risk score (Figures 7(a) and 7(b)), R <0, $p < 0.01$); however, PD1, CTLA4, TIGIT, and TIM-3 were positively correlated with the risk score (Figures 7(c)–7(f)), R >0, $p < 0.01$). Subsequently, the chi-square plot showed that 42% of the responders in the low-risk group were effective, and 58% were ineffective in the TIDE (Tumor Immune Dysfunction and Exclusion); 70% of the responders in the high-risk group were effective, and 30% were ineffective (Figure 7(g), $\chi^2 = 5.24$, $p = 0.022$). Ultimately, we

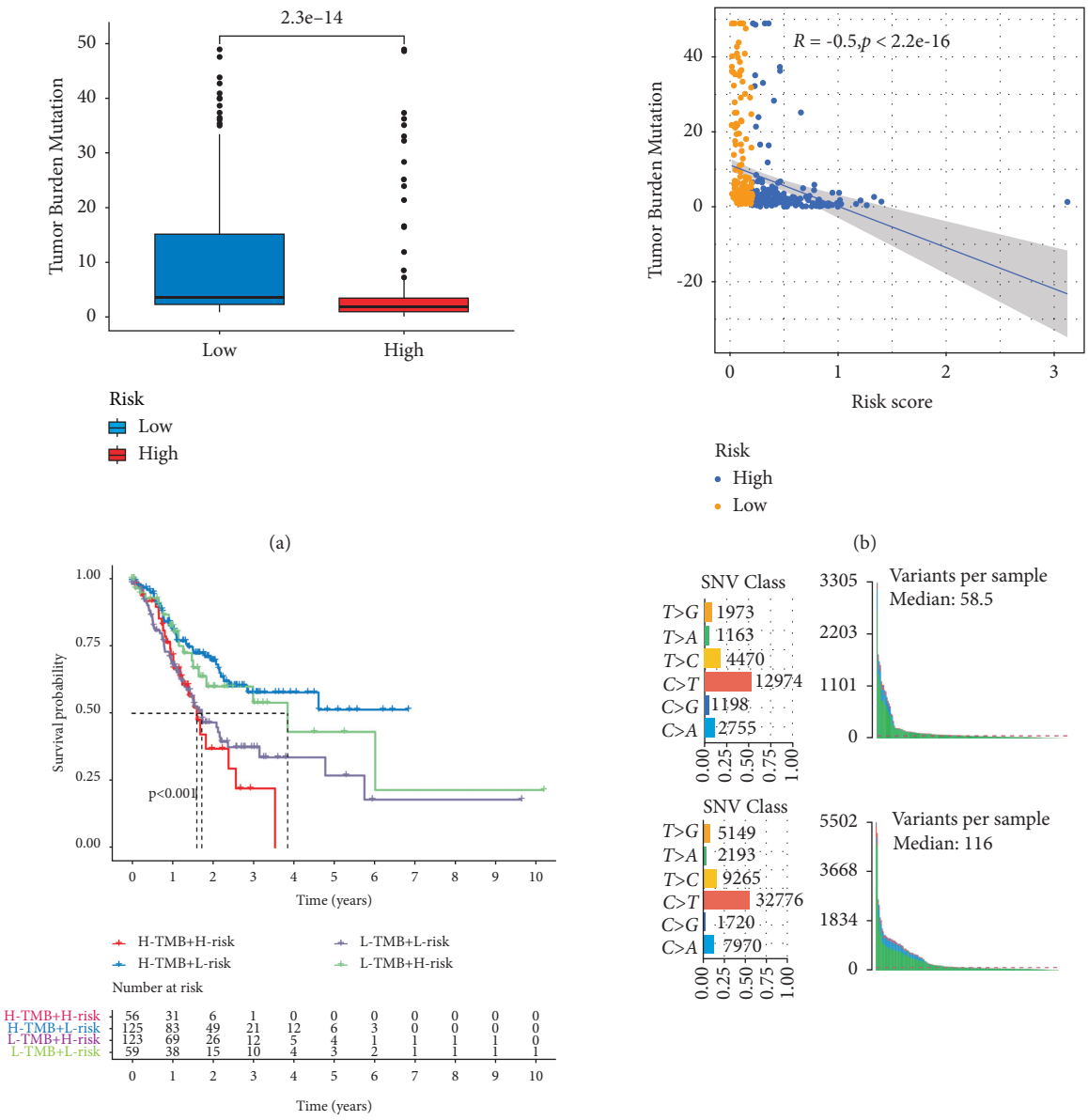

Figure 5: Continued.

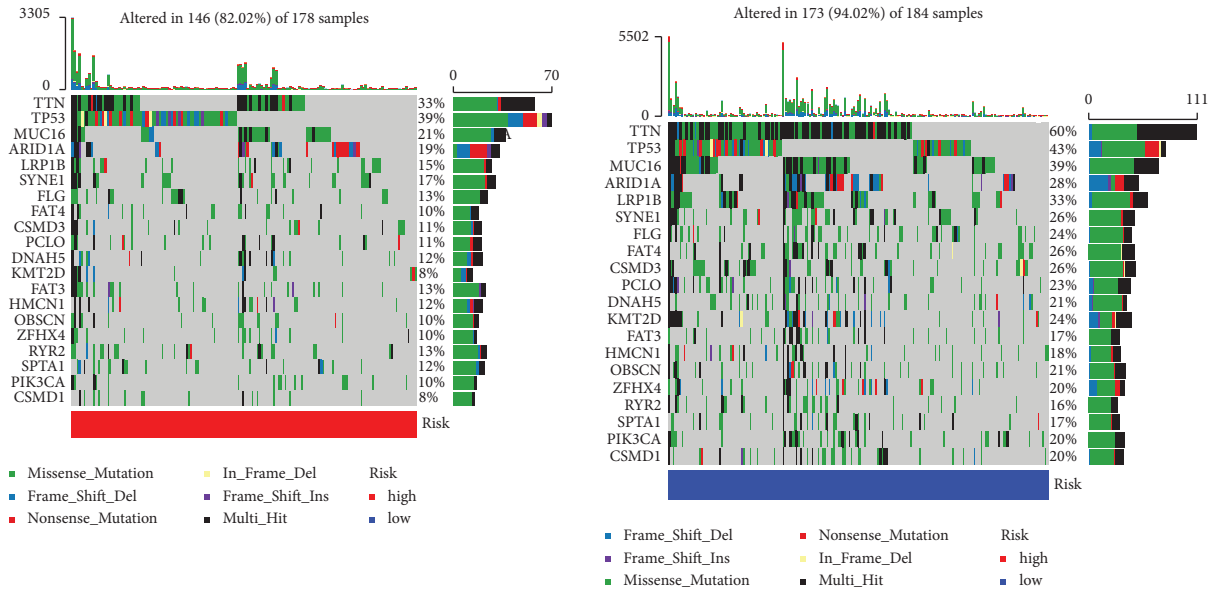

Figure 5: Characteristics of DRR-based risk score in tumor somatic mutation. (a) Difference of TMB between patients from the low-/high-risk subgroups. (b) Correlation between risk score and TMB. (c) Kaplan–Meier curves for patients stratified by both TMB and risk groups. (d) Mutation count per sample in nonsynonymous mutations. (e-f) The waterfall chart was constructed using the low-risk score and high-risk score.

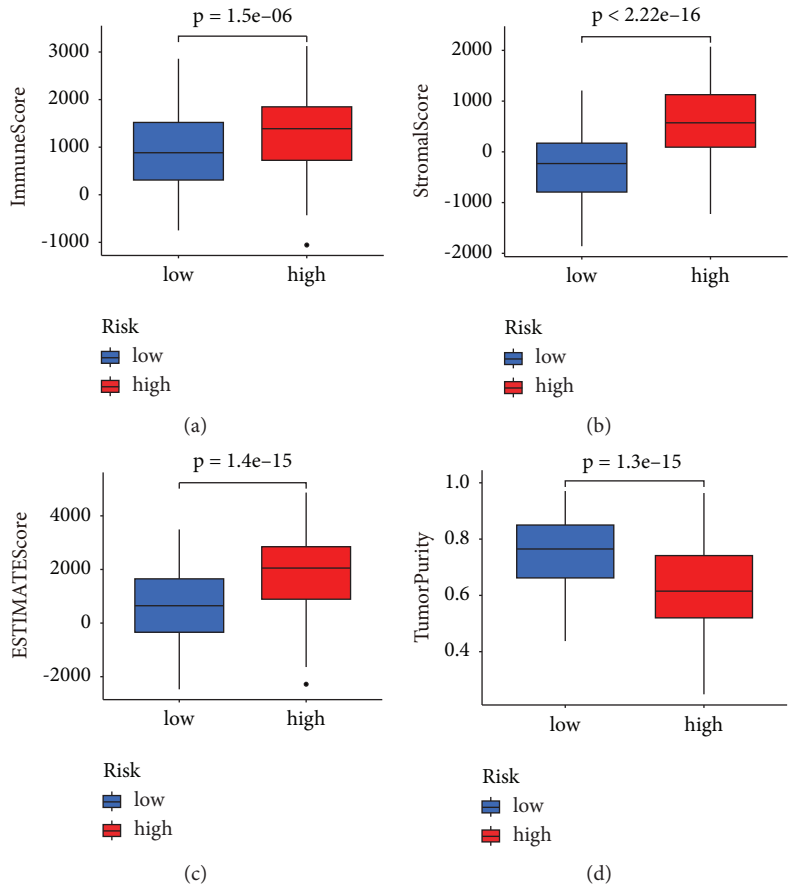

Figure 6: Continued.

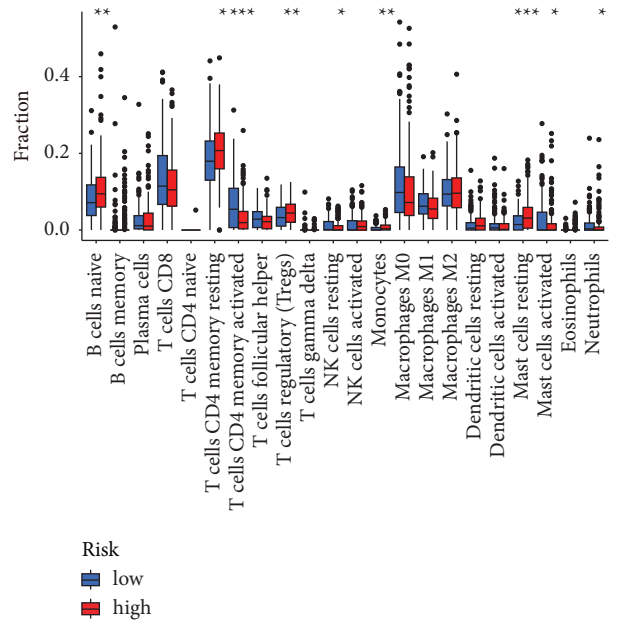

(e)

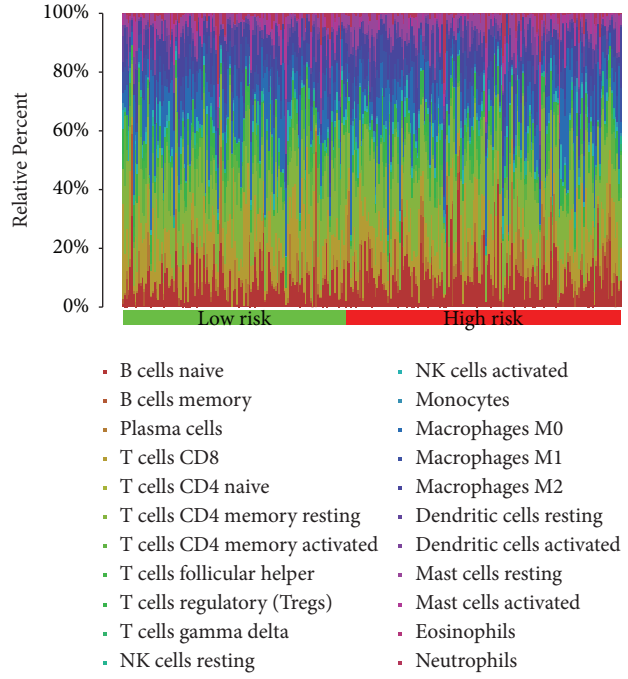

(f)

Figure 6: Continued.

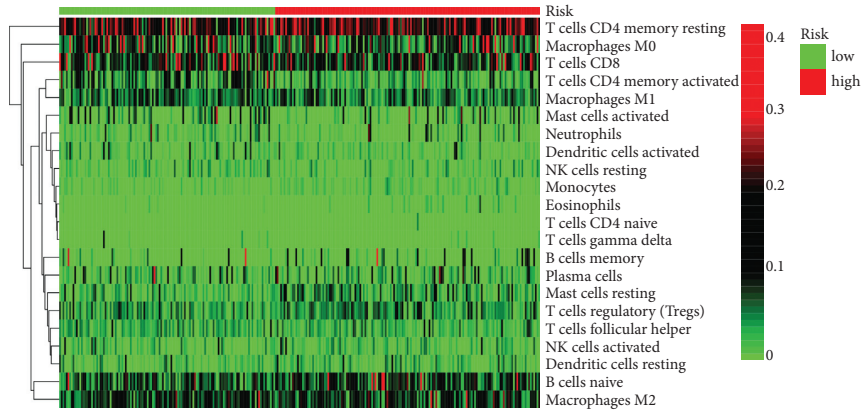

(g)

Figure 6: Correlation between prognostic model and immune microenvironment. (a–d) GC patients with high-risk scores have higher ImmuneScore, StromalScore, and ESTIMATEScore than those with low-risk scores. (e) The infiltrating levels of 22 immune cell types in high/low subtypes in the GC. (f) The relative proportion of immune infiltration in high/low-risk groups. (g) The landscape of immune cell infiltration between high/low-risk subtypes. $^{*}p < 0.05$, $^{**}p < 0.01$, and $^{***}p < 0.001$.

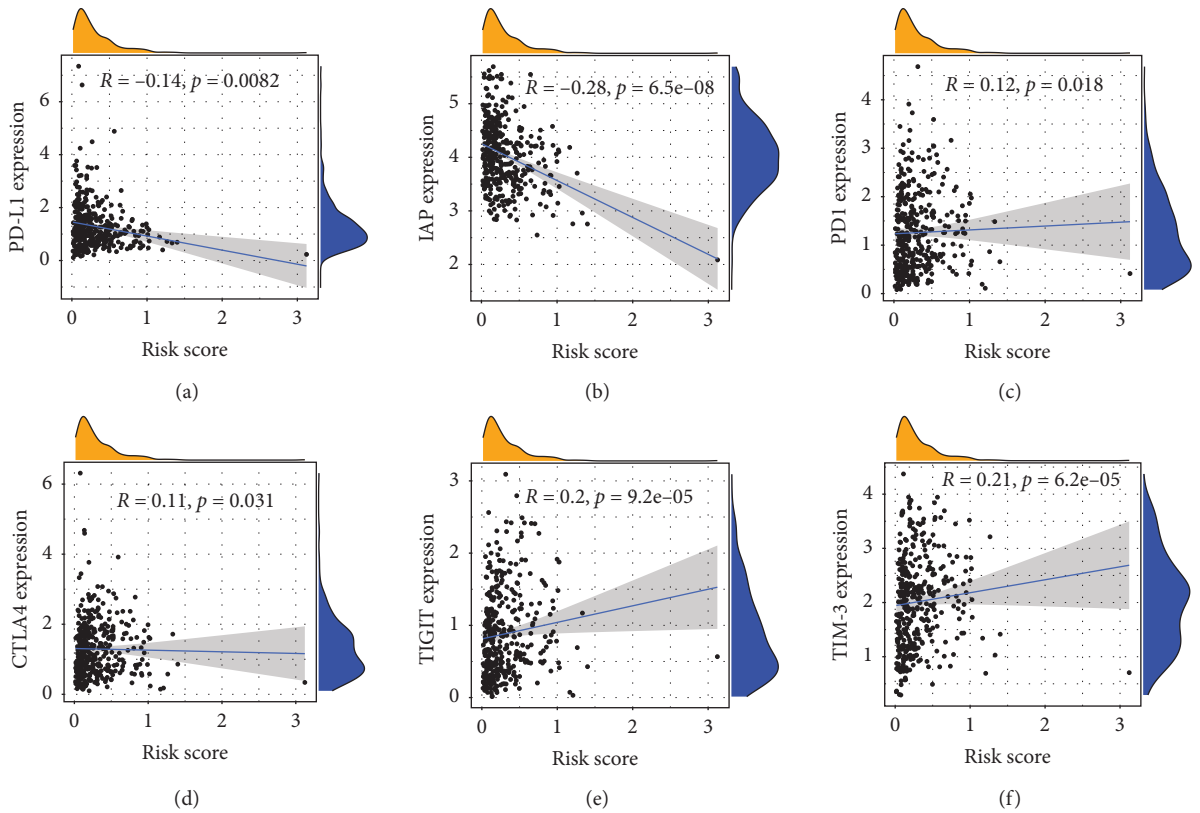

Figure 7: Continued.

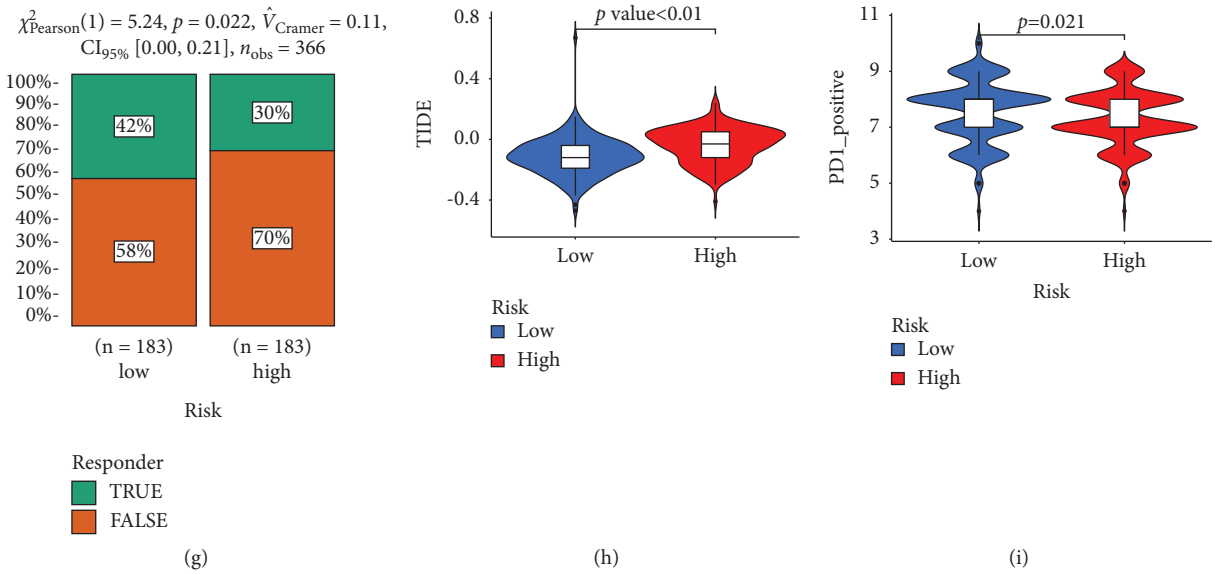

Figure 7: The estimation of two prognostic subtypes in immunotherapy response. (a–f) The expression of six immune checkpoint molecules (PD-L1, IAP, PD1, CTLA4, TIGIT, and TIM-3) in two prognostic subtypes. (g) Chi-squared test plot for immunotherapy in the responder. (h-i) Violin diagram showing the differential TIDE and TCIA between the high/low-risk groups.

evaluated the relationship between risk score and immunotherapy in GC at the TIDE and TCIA (The Cancer Immunome Atlas) (Figures 7(h) and 7(i), $p < 0.05$). Therefore, GC patients with the low-risk score for DRR-related genes showed better immunotherapy outcomes thanin the high-risk group.

4. Discussion

DNA is the place where cells store genetic information. The integrity of its structure and function is essential to maintaining life. Therefore, cells evolved specialized DNA repair mechanisms to maintain genome integrity [19, 20]. The significant feature of cancer cells is genomic instability, conducive to the accumulation of mutations and the expansion of tumor heterogeneity [21–23]. DRR mechanism can repair mutant genes in the early stage of the tumor and hinder cancer development. However, DRR-related genes may cause drug resistance of tumor cells to cytotoxic drugs with cancer progression [24]. The occurrence and development of cancer are often accompanied by the inactivation of one or more DRR pathways [25, 26]. Current studies of DNA repair gene prognostic models focused on immediate attachment to DNA repair genes, ignoring the impingement from the TMB [27–29]. Therefore, our research constructed a prognostic model based on a TMB filter of seven DRR-related genes that could better predict the clinicopathological characteristics, survival prognosis, role in the immune microenvironment, and efficacy of immunotherapy in GC patients.

In this study, we have developed a comprehensive description of DRR-related genes based on TMB. This prognostic model may better predict the prognosis and immune microenvironment of individuals with GC, providing a tangible contribution to immunotherapy. In this seven-gene prognostic model, GC patients are divided into a high-risk group and a low-risk group. The prognosis of the high-risk group was worse than that of the low-risk group. The ROC showed that survival at 1, 3, and 5 years had a high prognostic value. Risk curves were assessed and patients' risk increased with increasing scores in the model. Multivariate analysis showed that the prognostic score was an independent prognostic factor. Nomogram showed good prognostic value at 1, 3, and 5 years; calibration chart analysis showed accuracy. There were statistically significant differences between the high-risk and low-risk groups in terms of age and histological grading. At the same time, there were no significant differences in terms of gender and TNM staging. We observed no differences in survival curves in the subgroup survival analysis only for patients with G3 grading. In contrast, the high-risk group had worse prognostic survival than all other subgroups. We further observed habitual differences between prognostic models and tumor mutation profiles. Interestingly, the distribution of TMB was higher in the low-risk group, and the number and frequency of mutations were higher in the low-risk group than those in the high-risk group. The above results suggest that specific mutations in GC may be beneficial for tissue progression. DRR-related genes promote GC progression due to the repair of these mutations.

The high-risk group will have more Treg cell infiltration. It has been reported in the literature that Treg cells allow tumors to produce immune escape by suppressing CD8+ T cells and promoting tumors to express more immunosuppressive molecules [30]. This is consistent with our analysis of immunotherapy. The low-risk group had a lower TIDE and higher TCIA score due to a greater tendency to express PD-L1 and IAP immunosuppressive molecules, suggesting greater effectiveness of immunotherapy in the low-risk group. The findings further elucidate the function of these seven DRR-related genes in GC and may contribute to our understanding

of the biology of GC and provide new therapeutic targets. The poor prognosis of GC appears to depend on the multilayered relationship between DNA repair gene mutations, cell proliferation, and immune responses interactions.

LAMA2 is an extracellular protein and is the main component of the basement membrane [31]. It is believed to mediate cell attachment, migration, and tissue during embryonic development through interaction with other extracellular matrix components [32]. Li et al. identified LAMA2 as mediating the activation of the Src family of tyrosine kinase LCK-nondependent T cells by staphylococcal enterotoxin E [33]. Zhang et al. firmly established *LAMA2* as an immune-related gene associated with poor prognosis in pancreatic adenocarcinoma [34].

CREB3L3 encodes members of the alkaline leucine zipper family and the AMP-dependent transcription factor family. The encoded protein is located in the endoplasmic reticulum and acts as a transcription factor activated by cyclic AMP stimulation [35]. Resende et al. found that IL1β promoted the transition from chronic gastritis to GC through a CREB-C/EBPβ-related mechanism [36]. In the meantime, Luan B et al. reported that targeted disruption of CREB or cAMP-regulated transcriptional coactivators 2 and 3 (CRTC2/3) in macrophages downregulated M2 marker gene expression and promoted insulin resistance and facilitated insulin resistance, demonstrating that CREB-related molecules could initiate the human innate immune system [37].

SELP is stored in the alpha granules of platelets and Weibel–Palade vesicles of endothelial cells [38]. This protein redistributes to the plasma membrane during platelet activation and degranulation and mediates the interaction of activated endothelial cells or platelets with leukocytes [39]. Dai et al. screened the TCGA database and found that SELP was highly expressed in GC and significantly correlated with prognosis [40]. Singel et al. analyzed ascites from patients with advanced epithelial ovarian cancer (EOC) and identified that SELP activated neutrophil and platelet responses, promoted metastasis, and hindered antitumor immunity [41].

ABCC9 is a member of the ATP-binding cassette (ABC) transport protein superfamily, transporting various molecules through the outer and inner cell membranes. This protein is thought to form ATP-sensitive potassium channels in cardiac, skeletal, vascular, and nonvascular smooth muscle [42]. Mao et al. reported that ABCC9 was highly expressed in GC and negatively correlated with prognosis, which could be a potential biomarker for GC [43].

CYP1B1 encodes a member of the cytochrome P450 enzyme superfamily. Cytochrome P450 proteins are monooxygenases that catalyze many reactions involving drug metabolism and the synthesis of cholesterol, steroids, and other lipids [44]. Kwon et al. demonstrated that the oncogenic molecular mechanism of CYP1B1 action is associated with specificity protein one-mediated gene regulation, which induces cancer cell proliferation and migration [45]. D'Uva et al. concluded that CYP1B1 is considered a promising target for tumor chemoprevention in the tumor microenvironment due to the involvement of this oncogene in a positive loop with inflammatory cytokines [46]. Thus, evidence suggests that CYP1B1 may be involved in oncogenic events associated with the immune system.

CDH2 belongs to the calmodulin family and is involved in CNS cell adhesion, asymmetric cell division, and presynaptic/postsynaptic processes. For several cancer cells, including lung cancer, the role of CDH2 in cell migration and invasion has been reported. During epithelial-mesenchymal transition (EMT), tumor cells can transform to a CSC-like phenotype with an increase in CDH2 [47]. Hu et al. found that CDH2 promotes EMT in GC cells through LOXL1 overexpression, leading to peritoneal metastasis [48].

The protein encoded by GAMT is a methyltransferase that uses S-adenosylmethionine as a methyl donor to convert guanidinoacetate to creatine. Defects in this gene have been associated with neurological syndromes and hypotonia, possibly due to creatine deficiency and guanidinoacetate accumulation in affected individuals' brains [49]. Liu et al. have identified GAMT as a biomarker of prognosis in patients with advanced GC treated with docetaxel, cisplatin, and S-1 (DCS) [50]. Chen et al. also have demonstrated that high expression of GAMT, a gene driven by DNA methylation, was remarkably associated with poor prognosis [51].

The criteria explored in this study were based on objective indicators that may be more advantageous for detecting immune checkpoint inhibitors that were commonly used in clinical practice. Therefore, the prognostic model we developed was worthy of further study for its predictive efficacy. However, there were inevitable limitations in this study. Although high immune predictive efficacy was observed in the TCGA's STAD datasets, we could not obtain a GC cohort associated with immunotherapy to validate the utility of this study. Furthermore, the translation of these targets into clinical decision-making remains challenging. The mechanisms involved still need further validation in in vivo and in vitro experiments.

5. Conclusions

In conclusion, the signature of DRR-related genes are closely interrelated with the prognosis of GC patients. The model based on these seven genes can predict GC patients' response to immunotherapy in GC. Therefore, DRR-related gene signature based on tumor mutation burden is a novel biomarker for prognostic and immunotherapy response in GC patients.

Data Availability

Publicly available datasets were used in this study. These data can be found in the Cancer Genome Atlas (TCGA) database.

Conflicts of Interest

The authors declare that they have no conflicts of interest.

Authors' Contributions

Lei Zhang, Dahai Hu, and Shuchen Huangfu contributed equally to this work.

Acknowledgments

The authors acknowledge the TCGA database for providing the platform for uploading meaningful datasets. This research was supported by the First Affiliated Hospital of Jinan University Flagship Specialty Construction Project-General Surgery (711003), the Guangdong Basic and Applied Basic Research Fund Project (2018A030313145; 2019A1515011763; 2019A1515110543; 2021A1515010994), the Fundamental Research Business Expenses of Central Universities (21620306), Bengbu Medical College Translational Medicine Emphasis Project (BYTM2019050), and the Guangzhou Key Laboratory of Molecular and Functional Imaging for Clinical Translation (201905010003).

References

[1] R. L. Siegel, K. D. Miller, and A. Jemal, "Cancer statistics, 2020," *CA: A Cancer Journal for Clinicians*, vol. 70, no. 1, pp. 7–30, 2020.

[2] H. Sung, J. Ferlay, R. L. Siegel et al., "Global cancer statistics 2020: GLOBOCAN estimates of incidence and mortality worldwide for 36 cancers in 185 countries," *CA: A Cancer Journal for Clinicians*, vol. 71, no. 3, pp. 209–249, 2021.

[3] M. Das, "Neoadjuvant chemotherapy: survival benefit in gastric cancer," *The Lancet Oncology*, vol. 18, no. 6, p. e307, 2017.

[4] S.-E. Al-Batran, N. Homann, C. Pauligk et al., "Effect of neoadjuvant chemotherapy followed by surgical resection on survival in patients with limited metastatic gastric or gastroesophageal junction cancer," *JAMA Oncology*, vol. 3, no. 9, pp. 1237–1244, 2017.

[5] I. Gullo, F. Carneiro, C. Oliveira, and G. M. Almeida, "Heterogeneity in gastric cancer: from pure morphology to molecular classifications," *Pathobiology: Journal of Immunopathology, Molecular and Cellular Biology*, vol. 85, no. 1-2, pp. 50–63, 2018.

[6] R. M. Samstein, C.-H. Lee, A. N. Shoushtari et al., "Tumor mutational load predicts survival after immunotherapy across multiple cancer types," *Nature Genetics*, vol. 51, no. 2, pp. 202–206, 2019.

[7] G. De Velasco, D. Miao, M. H. Voss et al., "Tumor mutational load and immune parameters across metastatic renal cell carcinoma risk groups," *Cancer Immunology Research*, vol. 4, no. 10, pp. 820–822, 2016.

[8] A. M. Goodman, S. Kato, L. Bazhenova et al., "Tumor mutational burden as an independent predictor of response to immunotherapy in diverse cancers," *Molecular Cancer Therapeutics*, vol. 16, no. 11, pp. 2598–2608, 2017.

[9] D. P. Hurkmans, M. E. Kuipers, J. Smit et al., "Tumor mutational load, CD8+ T cells, expression of PD-L1 and HLA class I to guide immunotherapy decisions in NSCLC patients," *Cancer Immunology, Immunotherapy*, vol. 69, no. 5, pp. 771–777, 2020.

[10] F. Wang, X. L. Wei, F. H. Wang et al., "Safety, efficacy and tumor mutational burden as a biomarker of overall survival benefit in chemo-refractory gastric cancer treated with toripalimab, a PD-1 antibody in phase Ib/II clinical trial NCT02915432," *Annals of Oncology*, vol. 30, no. 9, pp. 1479–1486, 2019.

[11] X. Li and W.-D. Heyer, "Homologous recombination in DNA repair and DNA damage tolerance," *Cell Research*, vol. 18, no. 1, pp. 99–113, 2008.

[12] S. Bhattacharya, K. Srinivasan, S. Abdisalaam et al., "RAD51 interconnects between DNA replication, DNA repair and immunity," *Nucleic Acids Research*, vol. 45, no. 8, pp. 4590–4605, 2017.

[13] N. S. Gavande, P. S. VanderVere-Carozza, H. D. Hinshaw et al., "DNA repair targeted therapy: the past or future of cancer treatment?" *Pharmacology & Therapeutics*, vol. 160, pp. 65–83, Article ID 26896565, 2016.

[14] C. Ribeiro-Silva, W. Vermeulen, and H. Lans, "SWI/SNF: complex complexes in genome stability and cancer," *DNA Repair*, vol. 77, pp. 87–95, Article ID 30897376, 2019.

[15] J. Ying, L. Yang, J. C. Yin et al., "Additive effects of variants of unknown significance in replication repair-associated DNA polymerase genes on mutational burden and prognosis across diverse cancers," *Journal for ImmunoTherapy of Cancer*, vol. 9, no. 9, Article ID e002336, 2021.

[16] A. Yimit, O. Adebali, A. Sancar, and Y. Jiang, "Differential damage and repair of DNA-adducts induced by anti-cancer drug cisplatin across mouse organs," *Nature Communications*, vol. 10, no. 1, pp. 309–311, 2019.

[17] T. A. Yap, R. Kristeleit, V. Michalarea et al., "Phase I trial of the PARP inhibitor olaparib and AKT inhibitor capivasertib in patients with BRCA1/2- and non-BRCA1/2-mutant cancers," *Cancer Discovery*, vol. 10, no. 10, pp. 1528–1543, 2020.

[18] X. Lin, D. Chen, C. Zhang et al., "Augmented antitumor activity by olaparib plus AZD1775 in gastric cancer through disrupting DNA damage repair pathways and DNA damage checkpoint," *Journal of Experimental & Clinical Cancer Research*, vol. 37, no. 1, p. 129, 2018.

[19] D. Q. Tan, Y. Li, C. Yang et al., "PRMT5 modulates splicing for genome integrity and preserves proteostasis of hematopoietic stem cells," *Cell Reports*, vol. 26, no. 9, pp. 2316–2328, 2019.

[20] A. Travers and G. Muskhelishvili, "DNA structure and function," *FEBS Journal*, vol. 282, no. 12, pp. 2279–2295, 2015.

[21] L. Perkhofer, A. Schmitt, M. C. Romero Carrasco et al., "ATM deficiency generating genomic instability sensitizes pancreatic ductal adenocarcinoma cells to therapy-induced DNA damage," *Cancer Research*, vol. 77, no. 20, pp. 5576–5590, 2017.

[22] A. Tubbs and A. Nussenzweig, "Endogenous DNA damage as a source of genomic instability in cancer," *Cell*, vol. 168, no. 4, pp. 644–656, 2017.

[23] R. Böttcher, C. F. Kweldam, J. Livingstone et al., "Cribriform and intraductal prostate cancer are associated with increased genomic instability and distinct genomic alterations," *BMC Cancer*, vol. 18, no. 1, pp. 8–11, 2018.

[24] C. R. R. Rocha, M. M. Silva, A. Quinet, J. B. Cabral-Neto, and C. F. M. Menck, "DNA repair pathways and cisplatin resistance: an intimate relationship," *Clinics*, vol. 73, no. suppl 1, p. e478s, 2018.

[25] G. Damia and M. Broggini, "Platinum resistance in ovarian cancer: role of DNA repair," *Cancers*, vol. 11, no. 1, p. 119, 2019.

[26] D. L. Wilson, A. A. Beharry, A. Srivastava, T. R. O'Connor, and E. T. Kool, "Fluorescence probes for ALKBH2 allow the measurement of DNA alkylation repair and drug resistance responses," *Angewandte Chemie*, vol. 130, no. 39, pp. 13078–13082, 2018.

[27] D. Zhang, S. Yang, Y. Li et al., "Prediction of overall survival among female patients with breast cancer using a prognostic signature based on 8 DNA repair-related genes," *JAMA Network Open*, vol. 3, no. 10, Article ID e2014622, 2020.

[28] X.-q. Wang, S.-w. Xu, W. Wang et al., "Identification and validation of a novel DNA damage and DNA repair related genes based signature for colon cancer prognosis," *Frontiers in Genetics*, vol. 12, p. 635863, Article ID 33719345, 2021.

[29] W. Zhu, Q. Zhang, M. Liu, M. Yan, X. Chu, and Y. Li, "Identification of DNA repair-related genes predicting pathogenesis and prognosis for liver cancer," *Cancer Cell International*, vol. 21, no. 1, p. 81, 2021.

[30] X. Pei, X. Wang, and H. Li, "LncRNA SNHG1 regulates the differentiation of Treg cells and affects the immune escape of breast cancer via regulating miR-448/Ido," *International Journal of Biological Macromolecules*, vol. 118, no. Pt A, pp. 24–30, 2018.

[31] P. Barraza-Flores, C. R. Bates, A. Oliveira-Santos, and D. J. Burkin, "Laminin and integrin in LAMA2-Related congenital muscular dystrophy: from disease to therapeutics," *Frontiers in Molecular Neuroscience*, vol. 13, no. 1, p. 9, 2020.

[32] K. Ahmad, S. Shaikh, S. S. Ahmad, E. J. Lee, and I. Choi, "Cross-talk between extracellular matrix and skeletal muscle: implications for myopathies," *Frontiers in Pharmacology*, vol. 11, p. 142, Article ID 32184725, 2020.

[33] Z. Li, "Staphylococcal superantigens use LAMA2 as a coreceptor to activate T cells," *The Journal of Immunology (Baltimore, Md.: 1950)*, vol. 200, no. 4, pp. 1471–1479, 2018.

[34] M. Zhang, L. Zeng, Y. Peng, B. Fan, P. Chen, and J. Liu, "Immune-related genes LAMA2 and IL1R1 correlate with tumor sites and predict poor survival in pancreatic adenocarcinoma," *Future Oncology*, vol. 17, no. 23, pp. 3061–3076, 2021.

[35] Y. Nakagawa, Y. Wang, S.-i. Han et al., "Enterohepatic transcription factor CREB3L3 protects atherosclerosis via SREBP competitive inhibition," *Cellular and Molecular Gastroenterology and Hepatology*, vol. 11, no. 4, pp. 949–971, 2021.

[36] C. Resende, G. Regalo, C. Durães et al., "Interleukin-1B signalling leads to increased survival of gastric carcinoma cells through a CREB-C/EBPβ-associated mechanism," *Gastric Cancer*, vol. 19, no. 1, pp. 74–84, 2016.

[37] B. Luan, Y.-S. Yoon, J. Le Lay, K. H. Kaestner, S. Hedrick, and M. Montminy, "CREB pathway links PGE2 signaling with macrophage polarization," *Proceedings of the National Academy of Sciences*, vol. 112, no. 51, pp. 15642–15647, 2015.

[38] M. T. Rondina, D. Voora, L. M. Simon et al., "Longitudinal RNA-seq analysis of the repeatability of gene expression and splicing in human platelets identifies a platelet SELP splice QTL," *Circulation Research*, vol. 126, no. 4, pp. 501–516, 2020.

[39] Z. Zhang, Y. Guo, C. Qiu, G. Deng, and M. Guo, "Protective action of Se-supplement against acute alcoholism is regulated by selenoprotein P (SelP) in the liver," *Biological Trace Element Research*, vol. 175, no. 2, pp. 375–387, 2017.

[40] J. Dai, Z.-X. Li, Y. Zhang et al., "Whole genome messenger RNA profiling identifies a novel signature to predict gastric cancer survival," *Clinical and Translational Gastroenterology*, vol. 10, no. 1, Article ID e00004, 2019.

[41] K. L. Singel, K. S. Grzankowski, A. N. M. N. H. Khan et al., "Mitochondrial DNA in the tumour microenvironment activates neutrophils and is associated with worse outcomes in patients with advanced epithelial ovarian cancer," *British Journal of Cancer*, vol. 120, no. 2, pp. 207–217, 2019.

[42] P. T. Nelson, G. A. Jicha, W.-X. Wang et al., "ABCC9/SUR2 in the brain: implications for hippocampal sclerosis of aging and a potential therapeutic target," *Ageing Research Reviews*, vol. 24, no. Pt B, pp. 111–125, 2015.

[43] X. Mao, Z. He, F. Zhou, Y. Huang, and G. Zhu, "Prognostic significance and molecular mechanisms of adenosine triphosphate-binding cassette subfamily C members in gastric cancer," *Medicine*, vol. 98, no. 50, Article ID e18347, 2019.

[44] M. Maguire, M. C. Larsen, C. M. Vezina et al., "Cyp1b1 directs Srebp-mediated cholesterol and retinoid synthesis in perinatal liver; Association with retinoic acid activity during fetal development," *PLoS One*, vol. 15, no. 2, Article ID e0228436, 2020.

[45] Y.-J. Kwon, H.-S. Baek, D.-J. Ye, S. Shin, D. Kim, and Y.-J. Chun, "CYP1B1 enhances cell proliferation and metastasis through induction of EMT and activation of wnt/β-catenin signaling via Sp1 upregulation," *PLoS One*, vol. 11, no. 3, Article ID e0151598, 2016.

[46] G. D'Uva, D. Baci, A. Albini, and D. M. Noonan, "Cancer chemoprevention revisited: cytochrome P450 family 1B1 as a target in the tumor and the microenvironment," *Cancer Treatment Reviews*, vol. 63, pp. 1–18, Article ID 29197745, 2018.

[47] Q.-S. Zhuang, X.-B. Sun, Q.-Y. Chong et al., "ARTEMIN promotes oncogenicity and resistance to 5-fluorouracil in colorectal carcinoma by p44/42 MAPK dependent expression of CDH2," *Frontiers in Oncology*, vol. 11, p. 712348, Article ID 34422665, 2021.

[48] Q. Hu, T. Masuda, S. Kuramitsu et al., "Potential association of LOXL1 with peritoneal dissemination in gastric cancer possibly via promotion of EMT," *PLoS One*, vol. 15, no. 10, Article ID e0241140, 2020.

[49] S. A. Baker, C. R. Gajera, A. M. Wawro, M. R. Corces, and T. J. Montine, "GATM and GAMT synthesize creatine locally throughout the mammalian body and within oligodendrocytes of the brain," *Brain Research*, vol. 1770, p. 147627, Article ID 34418357, 2021.

[50] J.-B. Liu, T. Jian, C. Yue et al., "Chemo-resistant gastric cancer associated gene expression signature: bioinformatics analysis based on gene expression omnibus," *Anticancer Research*, vol. 39, no. 4, pp. 1689–1698, 2019.

[51] Z. Chen, B. Liu, M. Yi, H. Qiu, and X. Yuan, "A prognostic nomogram model based on mRNA expression of DNA methylation-driven genes for gastric cancer," *Frontiers in Oncology*, vol. 10, p. 584733, Article ID 33330065, 2020.

Hindawi
Journal of Oncology
Volume 2022, Article ID 8809469, 9 pages
https://doi.org/10.1155/2022/8809469

Research Article

Identification of DNA Repair-Related Genes Predicting Clinical Outcome for Thyroid Cancer

Ai-ying Zhang,[1] Wei Li,[2] Hai-yan Zhou,[3] Jing Chen,[4] and Li-bin Zhang[5]

[1]*Department of Clinical Laboratory, Affiliated Eye Hospital of Shandong University of Traditional Chinese Medicine, Eye Institute of Shandong University of Traditional Chinese Medicine, Jinan, Shandong, China*
[2]*Department of General Surgery, Qingdao Eighth People's Hospital, Qingdao, Shandong, China*
[3]*Department of Gynecology, Gaomi City Baicheng Center Hospital, Weifang, Shandong, China*
[4]*Department of Endocrinology, Weifang Hanting District People's Hospital, Weifang, Shandong, China*
[5]*Department of Endocrinology, The Second People's Hospital of Weifang, Weifang, Shandong, China*

Correspondence should be addressed to Li-bin Zhang; 73200048@sdutcm.edu.cn

Received 6 December 2021; Revised 27 December 2021; Accepted 28 December 2021; Published 6 January 2022

Academic Editor: Fu Wang

Recent studies have demonstrated the utility and superiority of DNA repair-related genes as novel biomarkers for cancer diagnosis, prognosis, and therapy. Here, we aimed to screen the potential survival-related DNA repair-related genes in thyroid cancer (TC). TCGA datasets were utilized to analyze the differentially expressed DNA repair-related genes between TC and nontumor tissues. The K–M approach and univariate analysis were employed to screen survival-related genes. RT-PCR was employed to examine the expression of DNA repair-related genes in TC samples and matched noncancer samples. CCK-8 analyses were used to determine cellular proliferation. Herein, our team discovered that the expression of four DNA repair-related genes was remarkably upregulated in TC samples in contrast to noncancer samples. Survival assays identified 14 DNA repair-related genes. In our cohort, we observed that the expression of TAF13 and DCTN4 was distinctly elevated in TC specimens in contrast to nontumor specimens. Moreover, knockdown of TAF13 and DCTN4 was observed to inhibit the TC cellular proliferation. Overall, the upregulation of TAF13 and DCTN4 is related to decreased overall survival in TC patients. Therefore, the assessment of TAF13 and DCTN4 expression may be useful for predicting prognosis in these patients.

1. Introduction

Thyroid cancer (TC) represents the most common endocrine malignancy, taking up 3.4% of the entire tumor diagnosis every year [1]. The transformation of thyroid follicle cells might cause the differentiation or undifferentiation of TC, via multiple steps which are the most adopted theories of follicle cell tumorigenesis [2]. Although some proofs have revealed that corpulency, smoking, hormone exposure, and some environmental pollution might be associated with TC, the only risk factor verified in TC is ionization radiation [3, 4]. The majority of TC sufferers at the early stage display beneficial prognoses posterior to thyroid resection and radioiodine. Nevertheless, the relapse is remarkably elevated when there is metastasis [5]. Therefore, finding new prognostic markers is critical for further treatment for TC.

Genome unsteadiness and the cumulation of variants are signatures of tumor development [6]. The anticipated cell reaction to DNA damages which cannot be restored is cellular death through aging or programmed cell death [7]. Various proteins at present are known to exert a pivotal impact on sustaining DNA integrity, especially with the identification and repairment of DNA damages via several signal paths which appear greatly conserved in terms of biology [8, 9]. In recent years, more and more DNA repair gene alterations have exhibited a vital modulatory function in the developmental process of various tumors [10, 11]. In recent years, researchers have determined genome flaws in

DNA repairment in the late period and primary TC, which has given rise to researchers clinically providing a potent reason to develop PARP suppressors and DNA-damage agents within such molecule-level TC subtype [12–14]. In addition, several DNA repair and replication-related gene signatures that could predict the prognosis and progression of tumors have been developed [15, 16]. However, the expression and function of DNA repair-related genes in TC were rarely reported.

In this study, we analyzed TCGA datasets and identified four dysregulated DNA repair-related genes in TC. In addition, we also identified 14 survival-related DNA repair-related genes in TC. Then, we chose six genes for further confirmation using 10 pairs of TC specimens and nontumor specimens from our cohort. Our findings focused on the possibility of DCTN4 and TAF13 utilized as new markers for TC.

2. Materials and Methods

2.1. Patients and Clinical Samples. TC samples and neighboring noncancer samples from sufferers who had undergone curative resection were collected between July 2020 and June 2021 from The Second People's Hospital of Weifang. All tissues were histopathologically confirmed by two experienced pathologists. No sufferers underwent chemotherapy, radiotherapy, or immunotherapy prior to surgeries. Cancer samples and neighboring healthy samples were harvested and reserved under −80°C for later assays. Written informed consent for the analysis of tissue specimens was obtained from all patients.

2.2. Data Collection. Genetic expression quantitation data and relevant clinic features of TC sufferers were acquired from the TCGA datasets (http://portal.gdc.cancer.gov/). The DNA damages and DNA repairment-associated genetic lists were acquired from GSEA genetic sets via the key word "DNA AND damage" or "DNA AND repair." Eventually, 150 genes associated with DNA damages and repairment were involved in the analyses. By comparing thyroid carcinoma tissues to normal tissues and using R package edgeR in R software (version 3.4.1), differentially expressed genes were identified with thresholds $|\log2\text{FoldChange}| > 2$ as well as adjusted $P < 0.05$.

2.3. Cox Regression and Survival Analyses. The TCGA specimens ($n = 510$) were separated into a high-expression group and low-expression group via the medium expressing level of every single candidate dysregulated DNA repair-related genes as the threshold. Univariate prognostic analyses and K–M analyses were afterwards finished for these two groups via the "survival" package of R program. To illustrate the intersection between dysregulated DNA repair-related genes and prognostic DNA repair-related genes, a Venn diagram program was employed.

2.4. Cell Lines and Transfection. Four mankind TC lineage cells (TPC, BHP5-16, K1, and BHP2-7) and mankind thyroid follicle epithelia (Nthy-ori 3-1) were acquired from the Type Culture Collection of the Chinese Academy of Sciences. The entire cells were maintained in DMEM (Gibco, America) in moist atmosphere with 5% carbon dioxide under 37°C. Such intermediary involved 10% FBS (Hyclone, America) and 1% penicillin/streptomycin.

DCTN4 and TAF13 expressions were knocked down by transiently transfecting TC cells with DCTN4-specific siRNA (si-DCTN4) or TAF13-specific siRNA (si-TAF13). In short, siRNAs were introduced into the cells via transfection by virtue of liposome transfection 2000 for 48 h; they were afterwards cultivated for later assays.

2.5. Quantitative Reverse-Transcription PCR (qRT-PCR). The overall RNA from TC samples and cells was abstracted via TRIzol® reagent (Invitrogen, America), and 200 ng abstracted RNA was converted to cDNA via reverse transcription through the ReverTra Ace qPCR RT Kit (Toyobo, Japan) prior to qRT-PCR. The qRT-PCR was employed to identify comparative RNA level, which was determined via a 7900 RealTime PCR System through the SDS 2.3 program sequence identification system (Applied Biosystem, America) by virtue of the SYBR Green (Takara) approach. The comparative expressing levels of mRNAs were evaluated via the $2^{-\Delta\Delta Cq}$ approach, with GAPDH as the internal reference. The primers are presented in Table 1.

2.6. Cell Proliferation Assay. TPC and BHP2-7 cells were inoculated into 96-well dishes (1×10^3 cells/well) and cultivated with 100 μl intermediary involving 10% FBS. Posterior to cellular transfection, they were cultivated for 0, 24, 48, and 72 h, before cultivation in 10 μl CCK-8 liquor (CK04, Dojindo, Yanhui Technology, Jiading, Shanghai, China) under 37°C or 60 min. The optical density was identified at 450 nm via a microplate reading device.

2.7. Statistical Analysis. The entire calculation was finished via the SPSS 17.0 (IBM, America) or R software, version 3.6.3. The diversity between these groups was studied via Student's *t*-test. The K–M approach was employed to draw the survival curves for prognosis analysis, and the log-rank test was leveraged to speculate the significance on statistics. The Cox proportion risk model was employed to identify the prognostic value of genes in TC. A $P < 0.05$ was deemed to be statistically significant.

3. Results

3.1. Determination of the Dysregulated DNA Repair-Associated Genes in TC. To identify the dysregulated DNA repair-associated genes in TC, we downloaded the list of DNA repair-associated genes from GSEA, and 135 genes were screened. Then, we analyzed TCGA datasets and identified 4 dysregulated DNA repair-related genes in TC including AK1, PNP, DDB2, and CD1 (Figure 1(a)). The expressing pattern of the abovementioned four genes was shown in heatmap (Figure 1(b)). In addition, we found the expression of AK1 (Figure 1(c)), PNP (Figure 1(d)), DDB2

Table 1: The primers used in this study for RT-PCR.

Names	Sequences (5′–3′)
AK1: F	GAAGAGTTTGAGCGACGGATT
AK1: R	CAGCCGCTTTTTGATGGTCTC
GTF2H5: F	AAGACATTGATGACACTCACGTC
GTF2H5: R	GGGAAAAAGCATTTTGGTCCATT
POM121: F	GCCTTTGTCCAGTCGGTTTG
POM121: R	TTGATGAGCGGAATAGCTTGC
TAF13: F	AGAAGACCCCACGTTTGAGGA
TAF13: R	TTGCCTTGTGAGTCATTTCAGT
DCTN4: F	CACACCCTCTCTACTCGGG
DCTN4: R	ACATGCCAGGTAATAGGCTTTC
DDB2: F	ACCTCCGAGATTGTATTACGCC
DDB2: R	TCACATCTTCTGCTAGGACCG
GAPDH: F	GGAGCGAGATCCCTCCAAAAT
GAPDH: R	GGCTGTTGTCATACTTCTCATGG

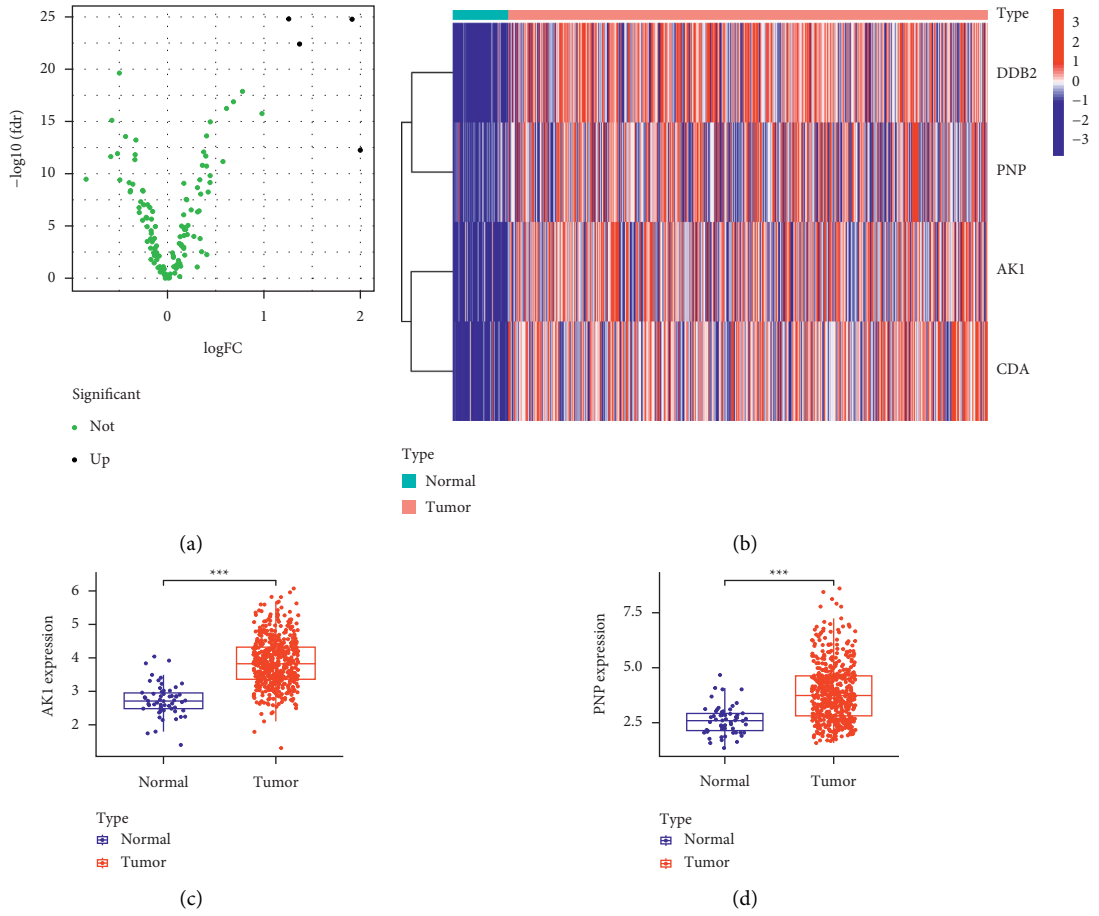

Figure 1: Continued.

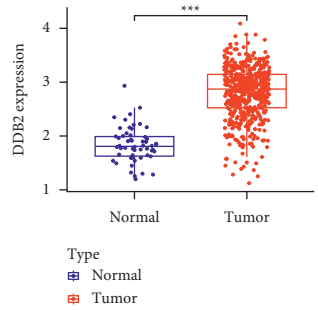

(e)

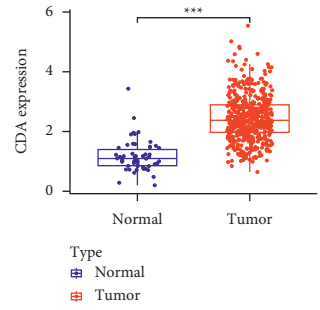

(f)

Figure 1: The dysregulated DNA repair-related genes in TC. (a) Aberrant expression DNA repair-related genes in TC tissues were reflected by the volcano plot. (b) Layer clustering analyses of differential expression DNA repair-related genes (fold change > 2; $P < 0.05$) in TC and healthy samples. (c–f) The expression of AK1, PNP, DDB2, and CDA was remarkably elevated in TC samples in contrast to healthy specimens. $^{***}P < 0.001$.

(Figure 1(e)), and CDA (Figure 1(f)) was remarkably elevated in TC samples in contrast to healthy specimens. Our findings suggested them as functional regulators in TC progression.

3.2. Determination of the DNA Repair-Associated Genes with Potential Prognostic Value in TC. To screen prognostic DNA repair-related genes, we performed the Kaplan–Meier method based on TCGA datasets and identified 13 genes, including ARL6IP1, DCTN4, GPX4, GTF2H5, LIG1, MPG, NT5C3A, POLR2E, POLR3C, RPA2, STX3, TYMS, and VPS37D (Figure 2). In addition, we also performed univariate analysis which revealed that high expression of DCTN4, PDE4B, PDE6G, POM121, TAF13, and VPS37D and low expression of DDB2, GPX4, GTF2H5, NT5C3A, PCNA, RPA2, STX3, and TSG101 were associated with survivals of TC patients (Figure 3). These findings provided a new clue for the identification of novel prognostic biomarkers in the section of DNA repair-associated genes.

3.3. The Distinct Upregulation of TAF13 and NCTN4 in TC and Their Oncogenic Roles. Then, we used Venn Diagram which confirmed DDB2 as a dysregulated DNA repair-related gene which had potentially prognostic value in TC (Figure 4(a)). Then, we performed RT-PCR to explore its expression, finding that DDB2 was not differentially expressed between TC specimens and nontumor specimens (Figure 4(b)). In addition, we chose AK1, GTF2H5, POM121, TAF13, and DCTN4 for further study. As shown in Figures 4(c)–4(e), the expression of AK1, GTF2H5, and POM121 between TC specimens and nontumor specimens remained unchanged. However, we discovered that the expressions of TAF13 and DCTN4 were distinctly elevated in TC specimens in contrast to matched nontumor specimens (Figures 4(f) and 4(g)). Moreover, high expression of TAF13 and DCTN4 was also observed in BHP5-16, TPC, K1, and BHP2-7 in contrast to nthy-ori 3-1 (Figure 5(a)). To investigate the potential role of TAF13 and DCTN4 in TC cells, our team used siRNA to decrease their levels in TPC and BHP2-7, which was confirmed by RT-PCR (Figures 5(b) and 5(c)). Finally, CCK-8 assays revealed that knockdown of TAF13 and DCTN4 distinctly suppressed the proliferation of TC cells (Figures 5(d) and 5(e)).

4. Discussion

There have been some developments in the therapies of TC over the past few decades [17]. Such development is facilitated by the progression in diagnosis and treatment modalities and new molecule-level target treatment [18]. Further endeavors are required to realize satisfactory prognostic results in this regard, which remains daunting. Clinical management highlights the significance of timely and valid identification and forecast of prognostic results, so as to achieve personalized therapies [19, 20]. The usage of prognosis models is helpful to guide decision making clinically and is pivotal for precise medical treatment [21, 22]. Given the important roles of DNA repair-related genes in tumor development, it is necessary to screen survival-related DNA repair-related genes.

Recently, epidemiology researchers have revealed that 2/3 tumors are induced by DNA replicational errors [23]. Particularly, errors in mRNA replications, such as the variant in the inhibitor gene P53, are especially vital for the tumor progression [24, 25]. In this study, we identified four dysregulated DNA repair-related genes, including AK1, PNP, DDB2, and CDA. Previously, several studies have reported the tumor-related function of the abovementioned four genes in different cancer types; e.g., DDB2 was reported to be greatly expressed in ovarian cancer and suppressed ovarian tumor cell dedifferentiation by suppressing ALDH1A1 [26]. CDA polymorphisms are found to be associated with clinical outcomes in gastroenteric cancer patients treated with capecitabine-based chemotherapy [27]. Then, we identified 14 prognostic DNA repair-related genes. However, we just found one gene DDB2 which exhibited a high level in TC and predicted a poor prognosis. DDB2 may be a novel biomarker for TC.

Then, we chose six genes for further confirmation, including DDB2, AK1, GTF2H5, POM121, TAF13, and DCTN4. RT-PCR assay revealed that DDB2 expression

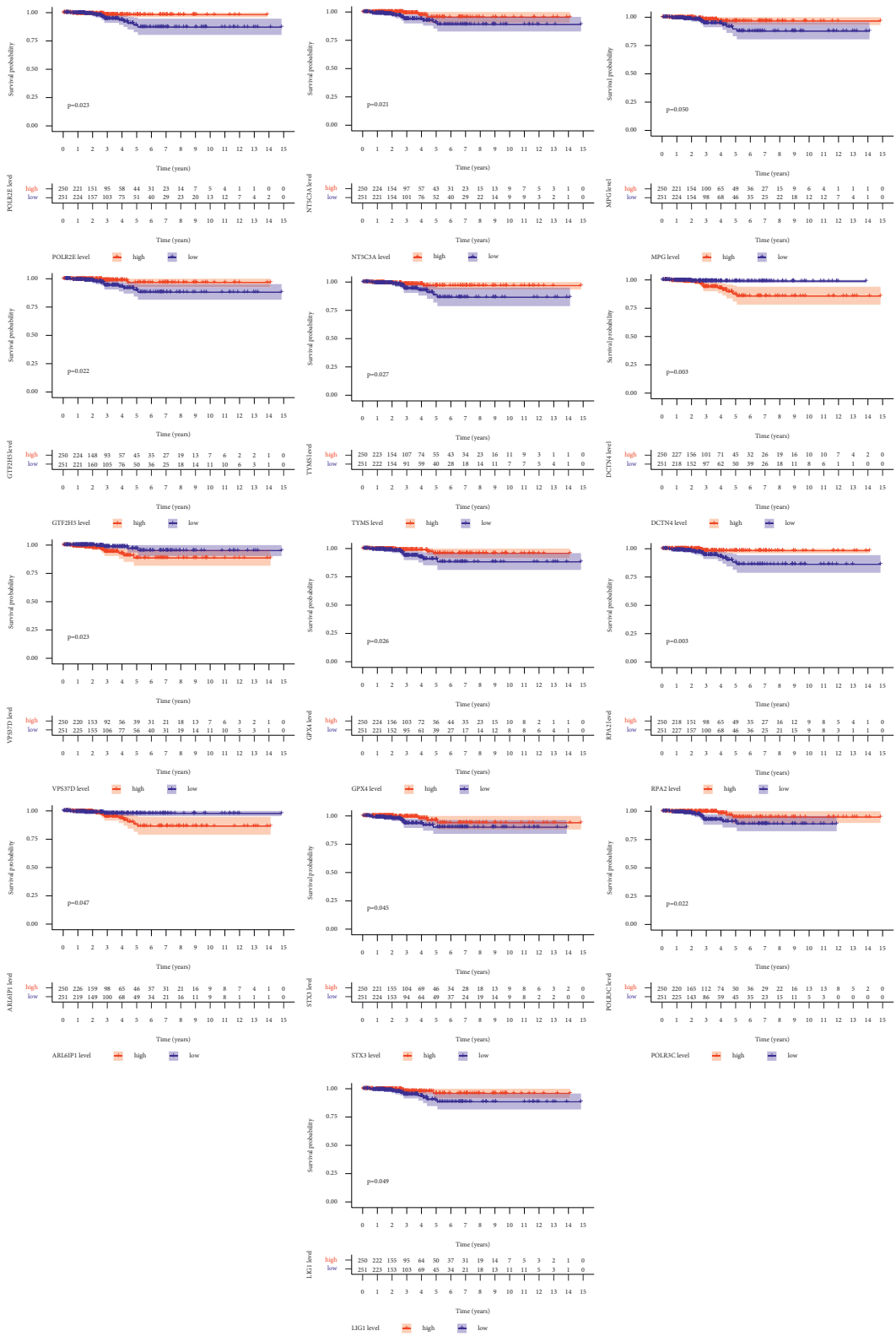

Figure 2: The K–M approach was employed to screen the survival-related DNA repair-related genes in TC.

remained unchanged between TC specimens and nontumor specimens, which was not consistent with the above-mentioned results. Importantly, we observed that TAF13 and DCTN4 expression was distinctly elevated in TC samples in contrast to paired noncancer samples. TAF13 produces a histone-fold-like heterodimer with TAF11, and such heterodimer is pivotal for the recruiting into the RNA polymerase II general TFIID protein complex [28]. To date,

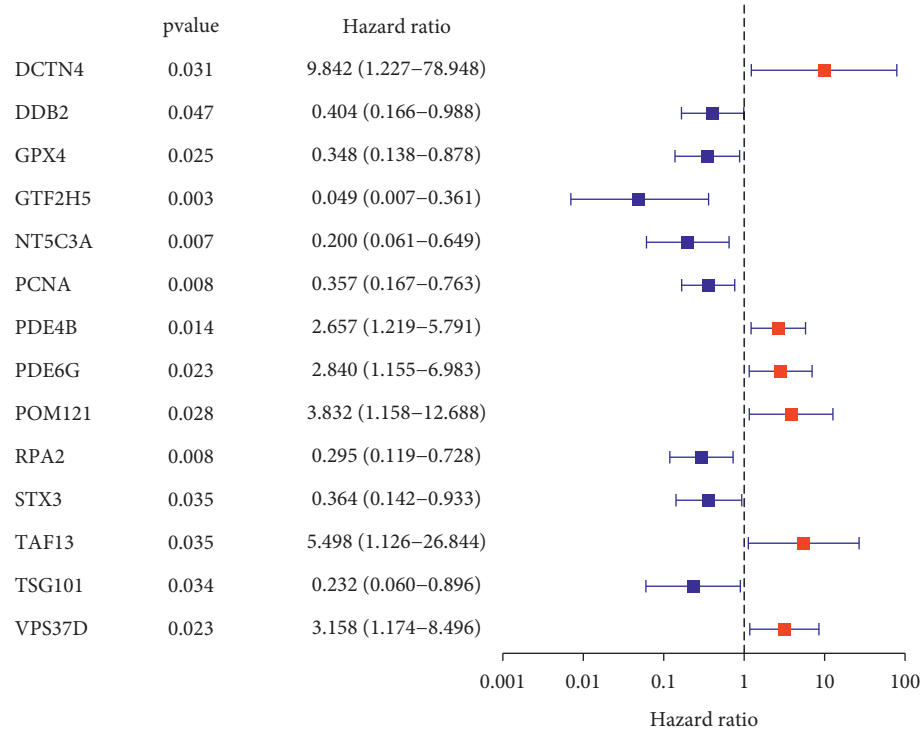

Figure 3: Univariate analysis of the 135 repair-related genes in TC.

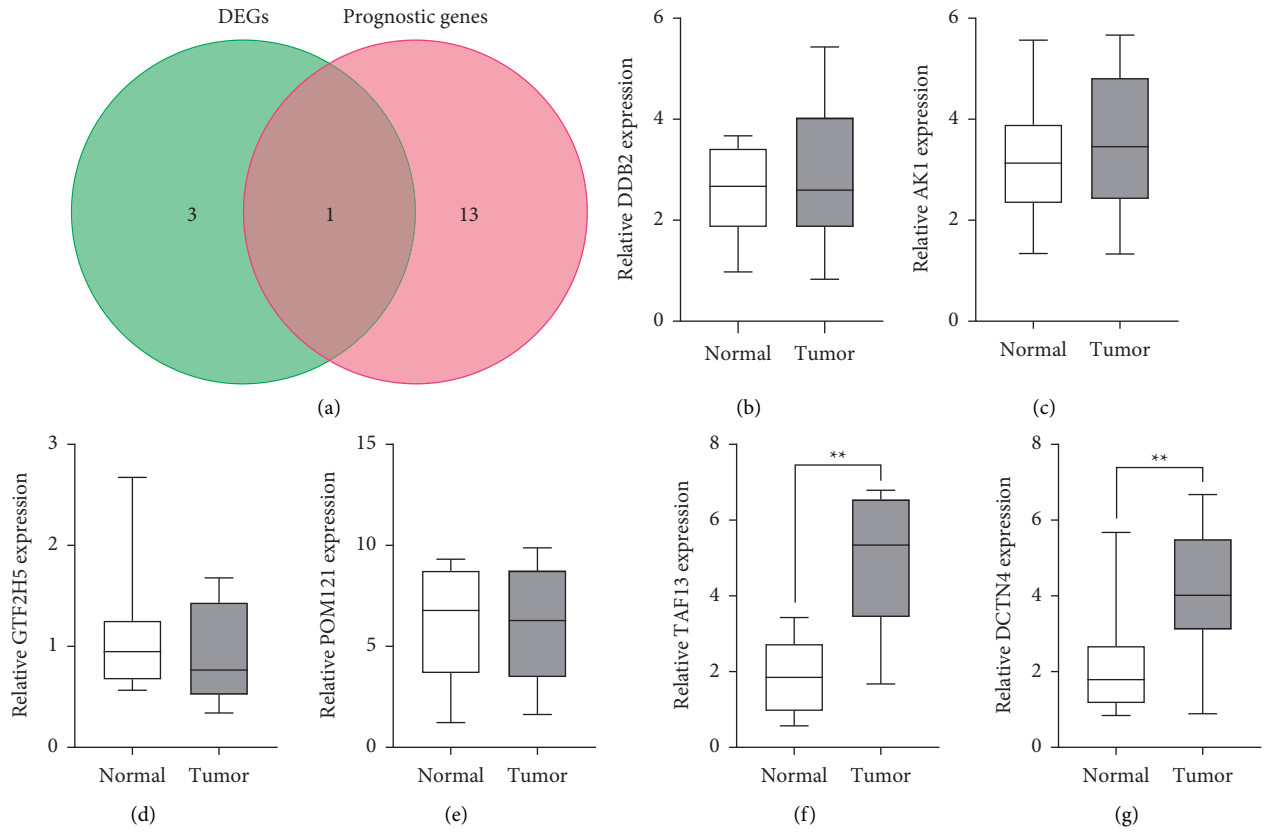

Figure 4: The distinct upregulation of TAF13 and DCTN4 in TC. (a) Venn diagram software of the common genes with dysregulated expression and potentially prognostic value in TC. (b–g) RT-PCR for the expressions of (b) DDB2, (c) AK1, (d) GTF2H5, (e) POM121, (f) TAF13, and (g) DCTN4. $^{**}P < 0.01$.

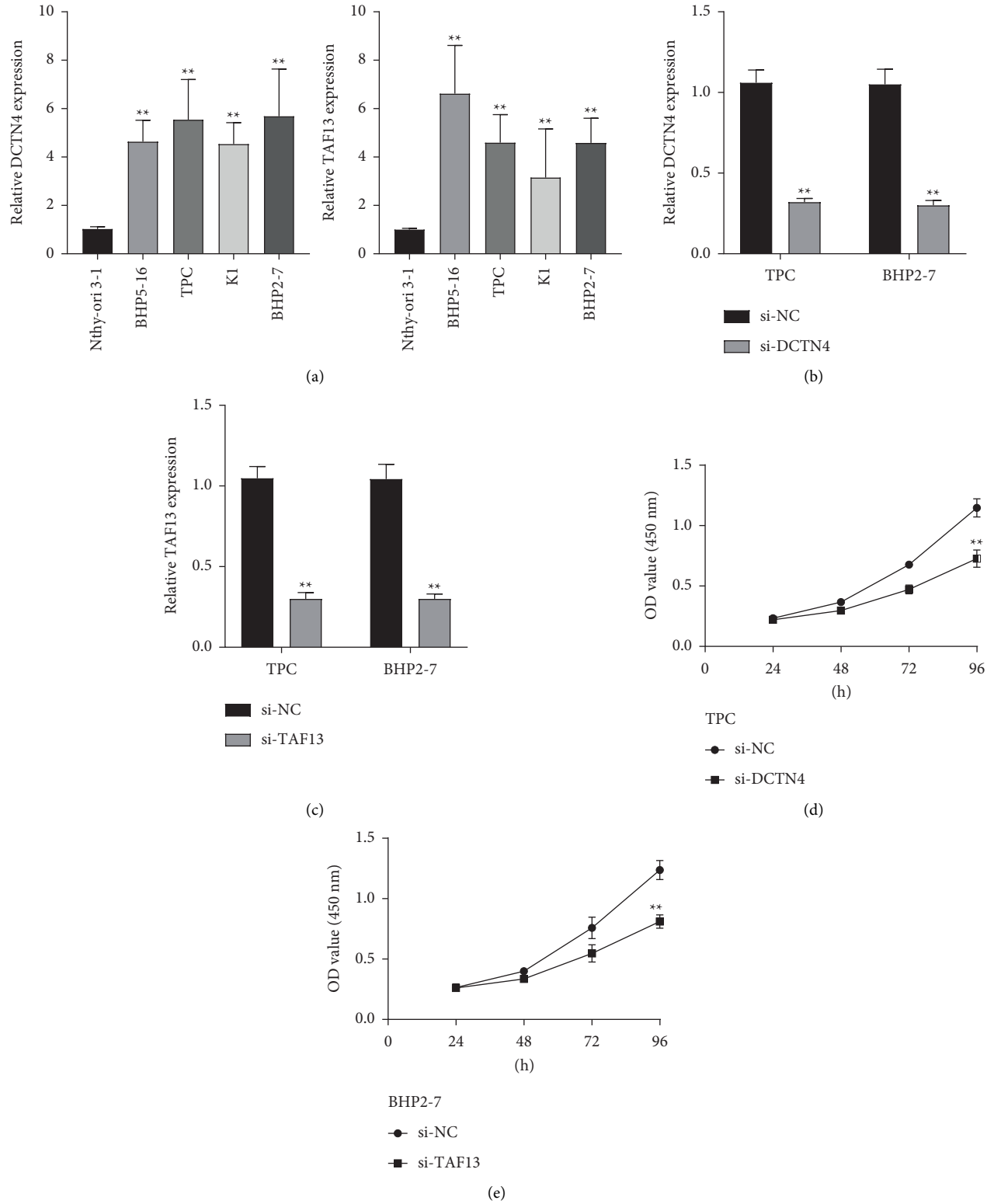

Figure 5: The oncogenic roles of DCTN4 and TAF13 in TC. (a) qRT-PCR analyses of DCTN4 and TAF13 expressing levels in four TC lineage cells (TPC, BHP5-16, K1, and BHP2-7) compared with the mankind thyroid follicular epithelial cells (Nthy-ori 3-1). (b, c) qRT-PCR analyses of DCTN4 and TAF13 expressions following treatment of TPC and BHP2-7 cells with siRNA targeting DCTN4 or TAF13. (d) CCK-8 analysis was performed to identify cellular proliferation. $^{**}P < 0.01$.

the expression and function of TAF13 were rarely reported. We observed that knockdown of TAF13 remarkably inhibited the TC cellular proliferation. Previous studies discovered that the DCTN family was related to several neurodegeneration illnesses [29]. DCTN4 belonged to the DCTN family. Previously, DCTN4 was reported to be associated with poor prognosis of colon adenocarcinoma and low-grade glioma [30, 31]. In addition, our team discovered the knockdown of DCTN4 in the TC cellular proliferation. Our findings provided a new clue for the determination of prognostic biomarkers for TC.

5. Conclusions

We identified 14 prognostic DNA repair-related genes and provided evidence that DCTN4 and TAF13 may serve as a tumor promotor in TC. The results herein elucidated an underlying causal link beneath the oncogenesis effect of DCTN4 and TAF13 in TC and revealed that DCTN4 and TAF13 could be a prospective biomarker and underlying treatment target for TC.

Data Availability

The analyzed datasets generated during the study are available from the corresponding authors on reasonable request.

Conflicts of Interest

The authors declare no conflicts of interest.

Authors' Contributions

Ai-ying Zhang and Li-bin Zhang contributed to the study's conception. Ai-ying Zhang and Wei Li contributed significantly to analysis. Hai-yan Zhou and Jing Chen performed the data analyses. Ai-ying Zhang and Li-bin Zhang wrote the manuscript. Jing Chen helped perform the analysis with constructive discussions. All authors read and approved the final manuscript.

References

[1] M. E. Cabanillas, D. G. McFadden, and C. Durante, "Thyroid cancer," *The Lancet*, vol. 388, no. 10061, pp. 2783–2795, 2016.

[2] T. Carling and R. Udelsman, "Thyroid cancer," *Annual Review of Medicine*, vol. 65, no. 1, pp. 125–137, 2014.

[3] A. Prete, P. Borges de Souza, S. Censi, M. Muzza, N. Nucci, and M. Sponziello, "Update on fundamental mechanisms of thyroid cancer," *Frontiers in Endocrinology*, vol. 11, p. 102, 2020.

[4] K. A. Araque, S. Gubbi, and J. Klubo-Gwiezdzinska, "Updates on the management of thyroid cancer," *Hormone and Metabolic Research*, vol. 52, no. 8, pp. 562–577, 2020.

[5] S. L. Asa, "The current histologic classification of thyroid cancer," *Endocrinology and Metabolism Clinics of North America*, vol. 48, no. 1, pp. 1–22, 2019.

[6] M. Li, R. Zheng, L. Dal Maso, S. Zhang, W. Wei, and S. Vaccarella, "Mapping overdiagnosis of thyroid cancer in China," *Lancet Diabetes & Endocrinology*, vol. 9, pp. 330–332, 2021.

[7] N. Chatterjee and G. C. Walker, "Mechanisms of DNA damage, repair, and mutagenesis," *Environmental and Molecular Mutagenesis*, vol. 58, no. 5, pp. 235–263, 2017.

[8] A. K. Basu, "DNA damage, mutagenesis and cancer," *International Journal of Molecular Sciences*, vol. 19, 2018.

[9] Z. Li, A. H. Pearlman, and P. Hsieh, "DNA mismatch repair and the DNA damage response," *DNA Repair*, vol. 38, pp. 94–101, 2016.

[10] M. J. O'Connor, "Targeting the DNA damage response in cancer," *Molecular cell*, vol. 60, no. 4, pp. 547–560, 2015.

[11] C. J. Lord and A. Ashworth, "The DNA damage response and cancer therapy," *Nature*, vol. 481, no. 7381, pp. 287–294, 2012.

[12] L. Stolarova, P. Kleiblova, M. Janatova et al., "CHEK2 germline variants in cancer predisposition: stalemate rather than checkmate," *Cells*, vol. 9, 2020.

[13] A. J. Sigurdson, M. Hauptmann, B. H. Alexander et al., "DNA damage among thyroid cancer and multiple cancer cases, controls, and long-lived individuals," *Mutation Research/Genetic Toxicology and Environmental Mutagenesis*, vol. 586, no. 2, pp. 173–188, 2005.

[14] A. A. Arbini, F. Guerra, M. Greco et al., "Mitochondrial DNA depletion sensitizes cancer cells to PARP inhibitors by translational and post-translational repression of BRCA2," *Oncogenesis*, vol. 2, no. 12, p. e82, 2013.

[15] W. Zhu, Q. Zhang, M. Liu, M. Yan, X. Chu, and Y. Li, "Identification of DNA repair-related genes predicting pathogenesis and prognosis for liver cancer," *Cancer Cell International*, vol. 21, p. 81, 2021.

[16] X. Q. Wang, S. W. Xu, W. Wang et al., "Identification and validation of a novel DNA damage and DNA repair related genes based signature for colon cancer prognosis," *Frontiers in Genetics*, vol. 12, Article ID 635863, 2021.

[17] O. V. Ancker, M. Krüger, M. Wehland, M. Infanger, and D. Grimm, "Multikinase inhibitor treatment in thyroid cancer," *International Journal of Molecular Sciences*, vol. 21, 2019.

[18] M. C. Kreissl, M. J. R. Janssen, and J. Nagarajah, "Current treatment strategies in metastasized differentiated thyroid cancer," *Journal of Nuclear Medicine*, vol. 60, no. 1, pp. 9–15, 2019.

[19] Y. Lu, N. Lan, Y. Zhang, X. Nie, S. Pu, and W. Yuan, "Role of extracellular vesicles in the progression, diagnosis and treatment of thyroid cancer (review)," *International Journal of Oncology*, vol. 57, pp. 881–889, 2020.

[20] J. P. Brito and I. D. Hay, "Management of papillary thyroid microcarcinoma," *Endocrinology and Metabolism Clinics of North America*, vol. 48, no. 1, pp. 199–213, 2019.

[21] C. Pierrakos and J.-L. Vincent, "Sepsis biomarkers: a review," *Critical Care*, vol. 14, no. 1, p. R15, 2010.

[22] V. A. Hristova and D. W. Chan, "Cancer biomarker discovery and translation: proteomics and beyond," *Expert Review of Proteomics*, vol. 16, no. 2, pp. 93–103, 2019.

[23] T. Wilhelm, M. Said, and V. Naim, "DNA replication stress and chromosomal instability: dangerous liaisons," *Genes*, vol. 11, 2020.

[24] D. Kolakofsky, L. Roux, D. Garcin, and R. W. H. Ruigrok, "Paramyxovirus mRNA editing, the "rule of six" and error catastrophe: a hypothesis," *Journal of General Virology*, vol. 86, no. 7, pp. 1869–1877, 2005.

[25] T. M. Mertz, V. Harcy, and S. A. Roberts, "Risks at the DNA replication fork: effects upon carcinogenesis and tumor heterogeneity," *Genes*, vol. 8, 2017.

[26] T. Cui, A. K. Srivastava, C. Han et al., "DDB2 represses ovarian cancer cell dedifferentiation by suppressing ALDH1A1," *Cell Death & Disease*, vol. 9, no. 5, p. 561, 2018.

[27] D. Liu, X. Li, X. Li et al., "CDA and MTHFR polymorphisms are associated with clinical outcomes in gastroenteric cancer patients treated with capecitabine-based chemotherapy," *Cancer Chemotherapy and Pharmacology*, vol. 83, no. 5, pp. 939–949, 2019.

[28] K. Gupta, A. A. Watson, T. Baptista et al., "Architecture of TAF11/TAF13/TBP complex suggests novel regulation properties of general transcription factor TFIID," *Elife*, vol. 6, 2017.

[29] A. Poersch, F. V. d. Santos, M. A. M. Maciel, J. K. P. d. Câmara, T. N. d. C. Dantas, and I. M. d. S. Cólus, "Protective effect of DCTN (trans-dehydrocrotonin) against induction of micronuclei and apoptosis by different mutagenic agents in vitro," *Mutation Research/Genetic Toxicology and Environmental Mutagenesis*, vol. 629, no. 1, pp. 14–23, 2007.

[30] S. Wang, Q. Wang, X. Zhang et al., "Distinct prognostic value of dynactin subunit 4 (DCTN4) and diagnostic value of DCTN1, DCTN2, and DCTN4 in colon adenocarcinoma," *Cancer Management and Research*, vol. 10, pp. 5807–5824, 2018.

[31] X. Su, H. Li, S. Chen, and C. Qin, "Study on the prognostic values of dynactin genes in low-grade glioma," *Technology in Cancer Research and Treatment*, vol. 20, Article ID 15330338211010143, 2021.

Hindawi
Journal of Oncology
Volume 2021, Article ID 1328444, 15 pages
https://doi.org/10.1155/2021/1328444

Research Article

ZC3H13 Inhibits the Progression of Hepatocellular Carcinoma through m^{6}A-PKM2-Mediated Glycolysis and Enhances Chemosensitivity

Qibo Wang,[1] Haichuan Xie,[2] Hao Peng,[1] Jianjian Yan,[1] Limin Han,[3] and Gang Ye[2]

[1]*Department of Hepatobiliary Surgery, Pingxiang People's Hospital of Southern Medical University, Pingxiang, Jiangxi 337055, China*
[2]*Department of Hepatobiliary Surgery, People's Hospital of Changshou Chongqing, Chongqing 401220, China*
[3]*Department of Endocrinology, People's Hospital of Changshou Chongqing, Chongqing 401220, China*

Correspondence should be addressed to Limin Han; hanlimin2018@sina.com and Gang Ye; yegang2021@163.com

Received 24 November 2021; Revised 14 December 2021; Accepted 16 December 2021; Published 30 December 2021

Academic Editor: Fu Wang

Objective. N^6-Methyladenosine (m^{6}A) is the most prevalent RNA epigenetic modulation in eukaryotic cells, which serves a critical role in diverse physiological processes. Emerging evidences indicate the prognostic significance of m^{6}A regulator ZC3H13 in hepatocellular carcinoma (HCC). Herein, this study was conducted for revealing biological functions and mechanisms of ZC3H13 in HCC. *Methods*. Expression of ZC3H13 was examined in collected HCC and normal tissues, and its prognostic significance was investigated in a public database. Gain/loss of functional assays were presented for defining the roles of ZC3H13 in HCC progression. The specific interactions of ZC3H13 with PKM2 were validated in HCC cells via mRNA stability, RNA immunoprecipitation, and luciferase reporter and MeRIP-qPCR assays. Moreover, rescue experiments were carried out for uncovering the mechanisms. *Results*. ZC3H13 expression was downregulated in HCC, and its loss was in relation to dismal survival outcomes. Functionally, overexpressed ZC3H13 suppressed proliferation, migration, and invasion and elevated apoptotic levels of HCC cells. Moreover, ZC3H13 overexpression sensitized to cisplatin and weakened metabolism reprogramming of HCC cells. Mechanically, ZC3H13-induced m^{6}A modified patterns substantially abolished PKM2 mRNA stability. ZC3H13 facilitated malignant behaviors of HCC cells through PKM2-dependent glycolytic signaling. *Conclusion*. Collectively, ZC3H13 suppressed the progression of HCC through m^{6}A-PKM2-mediated glycolysis and sensitized HCC cells to cisplatin, which offered a fresh insight into HCC therapy.

1. Introduction

Liver carcinoma represents the most frequent fatal malignant disease across the globe [1]. Among all liver carcinoma patients, hepatocellular carcinoma (HCC) occupies over 90% [2]. Patients' survival outcomes are dismal. Merely 5%–15% of patients benefit from radical resection, only for those in the earlier stages [3]. Therapeutic strategies for advanced-stage patients contain transarterial chemoembolization (TACE) as well as oral sorafenib [4]. Nevertheless, <33% of patients do not respond to this therapy as well as develop marked chemotherapy resistance within 6 months from starting therapeutic intervention [5]. Moreover, long-term usage of chemotherapeutic agents causes toxic response as well as chemotherapeutic inefficiency [6]. Therefore, neither TACE nor chemotherapeutic agents can remarkedly improve the outcome of liver cancer. In-depth exploration is required for finding a better way to treat liver cancer.

N^6-methyladenosine (m^{6}A) is the most prevalent form of internal mRNA modification [7]. m^{6}A modification has been proposed as the most frequent chemical modified form in eukaryotic mRNAs [8], which is of importance for controlling diverse cellular and biological events like RNA stability, translation, and splicing [6]. As estimated, about 0.1%–0.4% of adenosine in mRNAs may be modified via m^{6}A, with a mean of 2-3 m^{6}A modified sites per transcript

[9]. m^6A modification patterns are dominated through methyltransferase complex ("writer"), demethylase ("eraser"), and RNA-binding protein ("reader") [10]. Emerging evidences highlight the significance of deregulation of m^6A modification in liver carcinogenesis [9]. Through comprehensive analyses of m^6A regulators in TCGA-HCC project, Liu et al. proposed that METTL3, YTHDF2, and ZC3H13 acted as independent prognostic indicators of HCC outcomes [11]. METTL3 expression exhibited a frequent upregulation in HCC and promoted HCC development via YTHDF2-dependent posttranscriptional silence of SOCS2 [12]. Another study proposed the mechanisms of SUMOylated METTL3-mediated Snail mRNA homeostasis during HCC progression [13]. HBXIP triggered metabolism reprogramming of HCC cells through METTL3-dependent m^6A modified HIF-1α [14]. The hepatic microenvironment facilitated HCC proliferation and metastases through METTL3-mediated m^6A modification of YAP1 [15]. YTHDF2 triggered HCC stem cell phenotype as well as metastases through modulating OCT4 expression via an m^6A modification manner [16]. YTHDF2 deletion fueled inflammation as well as vascular abnormalization in HCC [17]. YTHDF2 weakened cellular proliferation and growth through destabilization of EGFR mRNA in HCC [18]. Nevertheless, to date, no experimental evidences have confirmed the biological significance of ZC3H13 in HCC pathogenesis.

Herein, we observed the biological roles of m^6A regulator ZC3H13 in HCC as well as addressed the underlying mechanisms. Our data suggested that ZC3H13 suppressed the progression of HCC with m^6A-PKM2-mediated glycolysis and sensitized HCC cells to cisplatin. Thus, our findings highlighted the critical functions of ZC3H13-mediated m^6A modification in HCC and provided a promising therapeutic regimen against HCC.

2. Materials and Methods

2.1. Patients and Specimens. Primary HCC as well as adjacent control tissue specimens from 30 patients in the People's Hospital of Changshou Chongqing were harvested for this study. The inclusion criteria were as follows: (i) patients with pathologic diagnosis of HCC and (ii) patients who received curative removal. Meanwhile, patients with distant metastases at diagnosis were excluded. Informed consent was acquired from each patient. This research was carried out in line with the guidelines of the Ethics Committee of the People's Hospital of Changshou Chongqing and approved following the ethical standards of World Medical Association Declaration of Helsinki.

2.2. Bioinformatics Analysis. The Gene Expression Profiling Interactive Analysis (GEPIA) web server [19] was adopted for determining the mRNA expression of ZC3H13 in HCC and normal tissues retrieved from The Cancer Genome Atlas (TCGA) and the Genotype-Tissue Expression (GTEx) projects. Survival analysis of HCC patients with high and low expression of ZC3H13 was presented via the Kaplan–Meier plotter (https://kmplot.com/analysis/). Difference of overall survival between groups was estimated with log-rank test.

2.3. Real-Time Quantitative Polymerase-Chain Reaction (RT-qPCR). Total RNA was extracted utilizing TRIzol reagent (Beyotime, China). In total, 500 ng RNA was reversed transcribed through HiScript II 1st-Strand cDNA Synthesis kits (Takara, Beijing, China). RT-qPCR was carried out via ChamQ Universal SYBR qPCR Master Mix (Takara, Beijing, China) as well as LightCycler 480 instrument. The sequences of primers included the following: ZC3H13: 5′-TCTGATAGCACATCCCGAAGA-3′ (forward) and 5′-CAGCCAGTTACGGCACTGT-3′ (reverse); PKM2: 5′-ATGTCGAAGCCCCATAGTGAA-3′ (forward) and 5′-TGGGTGGTGAATCAATGTCCA-3′ (reverse); and GAPDH: 5′- CTGGGCTACACTGAGCACC-3′ (forward) and 5′-AAGTGGTCGTTGAGGGCAATG-3′ (reverse). Data were quantified with a comparative Ct method ($2^{-\Delta\Delta Ct}$).

2.4. Western Blotting. Tissue and cell specimens were lysed with RIPA buffer (Beyotime, China) plus protease inhibitor cocktail. Lysed protein was extracted, and protein concentrations were evaluated with BCA kits (Sigma, USA). Afterwards, the equal amount of protein was separated with 12% SDS-PAGE as well as transferred to polyvinylidene difluoride membrane (Millipore, USA). After being blocked, the membrane was incubated by primary antibodies targeting ZC3H13 (1/2000; ab70802; Abcam, USA), GLUT (1/1000; ab156876; Abcam, USA), LDHA (1/5000; ab52488; Abcam, USA), LDHB (1/2000; ab264358; Abcam, USA), PKM2 (1/1000; ab85555; Abcam, USA), and β-actin (1/5000; ab179467; Abcam, USA). Then, protein bands were incubated by secondary anti-mouse or anti-rabbit secondary antibody (1/5000; ab7063/ab7090; Abcam, USA). Protein band was visualized with ECL assay kits.

2.5. Cell Culture. Human normal liver cells L-O2 as well as human liver cancer cell lines HUH-7, Hep3B, HepG2, and SMMC-7721 were retrieved from ATCC (USA). All cells were grown in Dulbecco's Modified Eagle's Medium (DMEM) supplemented with 10% fetal bovine serum (FBS) as well as 1% streptomycin/penicillin. Cells were grown in a humidified environment of 5% CO_2 at 37°C.

2.6. Transfection. Short interfering RNA (siRNA) against ZC3H13 as well as PKM2 was synthesized for specifically silencing ZC3H13 as well as PKM2 expressions in Hep3B and HUH-7 cells. HCC cells transfected with scrambled siRNAs acted as si-NC. The full-length ZC3H13 cDNA was synthesized and then subcloned into the pcDNA3.1 vector to establish pcDNA-ZC3H13 overexpression (OE-ZC3H13) plasmid. All plasmids were retrieved from GenePharma (Shanghai, China). Transient transfection was carried out lasting two days via Lipofectamine 3000.

2.7. Cell Counting Kit-8 (CCK-8) Assay. Hep3B as well as HUH-7 cells were planted onto 96-well plates (3,000 cells/well). In line with the protocols of CCK-8 kits (Dojindo, Japan), 10 μL CCK-8 solution that was diluted by 100 μL DMEM replaced the previous DMEM at diverse hours (24, 48, 72, and 96 h). After being cultured protecting from light at 37°C lasting an extra two hours, viable cells were determined through absorbance at 490 nm wavelength.

2.8. Clone Formation Assays. Hep3B as well as HUH-7 cells were seeded onto 6-well plates (1×10^3 cells/well). Following incubation in a 5% humidified CO_2 environment at 37°C lasting 2 weeks, HCC cells were gently washed by PBS twice as well as fixed by 4% paraformaldehyde lasting half an hour. Afterwards, the cells were stained by crystal violet lasting 30 min. The colonies formed (>50 cells/colony) were treated by crystal violet.

2.9. TdT-Mediated dUTP Nick-End Labeling (TUNEL) Staining. Hep3B and HUH-7 cells were planted onto 12-well plates. HCC cells were fixed with 4% paraformaldehyde lasting 15 min at room temperature, rinsed by PBS, and incubated by 3% H_2O_2 in methanol lasting 10 min. Afterwards, HCC cells were treated by 0.1% Triton X-100 lasting 2 min on ice as well as incubated by 50 μL TUNEL reaction mixture lasting 60 min at 37°C in the dark. Following being rinsed by PBS, nuclei were labeled with DAPI. Finally, images were captured with a fluorescence microscope (Olympus, Japan).

2.10. Transwell Assays. For migration assays, Hep3B and HUH-7 cells were seeded onto the upper chamber as well as DMEM plus 20% FBS was added to the lower chamber. For invasion assays, Hep3B and HUH-7 cells were planted onto the upper chamber containing a Matrigel-coated membrane (BD, USA). Following 48 h incubation, nonmigrative or noninvasive cells were moved away through wiping the upper side of the membrane utilizing sterile cotton bud; meanwhile, the migrative or invasive cells on the lower level of the membrane were stained by 0.5% crystal violet. Finally, HCC cells were counted for 6 randomly selected fields of view utilizing an IX71 inverted microscope (×200).

2.11. Cell Viability Assay. Hep3B as well as HUH-7 cells were planted onto 96-well plates (3,000 cells/well). Following being incubated overnight, DMEM plus distinct doses of cisplatin (0, 1, 2, 4, 8, 16, 60, and 32 μM) replaced the original medium lasting three days. Afterwards, viable cells were investigated through CCK-8 assays. The drug half-maximum inhibitory concentration (IC50) values were finally determined.

2.12. Measurement of Glucose Uptake and Lactate Production. Glucose uptake as well as lactate production was separately tested through Glucose Uptake Colorimetric Assay Kits (BioVision, USA) and Lactate Colorimetric Assay Kits (BioVision, USA) in Hep3B as well as HUH-7 cells following the manufacturer's protocols.

2.13. mRNA Stability Assay. Stability of mRNA assays in Hep3B as well as HUH-7 cells was evaluated through incubating cells with 5 μg/mL actinomycin D (Act-D, Sigma, USA). Afterwards, cells were harvested at the indicated time points, and mRNAs were drawn for RT-qPCR with GAPDH as the reference control.

2.14. RNA Immunoprecipitation (RIP) Assay. RIPA assay was conducted with Magna RIP RNA-Binding Protein Immunoprecipitation kits (Millipore, USA) in line with the manufacturer's instructions. Hep3B as well as HUH-7 cells were lysed utilizing RIPA lysis buffer. Cell lysate was immunoprecipitated through anti-ZC3H13 antibodies or nonimmunized IgG at 4°C overnight. Afterwards, RNA was purified and RT-qPCR was utilized for measuring the level of PKM2 transcript in ZC3H13 or IgG immunocomplex.

2.15. Luciferase Reporter Assay. Promoter sequence of PKM2 was cloned into pEZX-PL01 control vector containing firefly luciferase as well as Renilla luciferase. Luciferase assay was carried out utilizing Luc-Pair™ Duo-Luciferase HS Assay kits. In brief, pretreated Hep3B as well as HUH-7 cells were cotransfected by ZC3H13-wild-type (ZC3H13-WT) or ZC3H13-mutation-type (ZC3H13-MUT) as well as 250 ng pEZX-PL01 reporter plasmid (Promega, Shanghai, China) in 12-well plates. Following transfection lasting 6 h, HCC cells were seeded into 96-well plates. Following 36 h, cells were collected and analyzed utilizing Dual-Glo Luciferase Assay system. Activity of firefly luciferase was normalized to that of Renilla luciferase for evaluating the luciferase and transcriptional activity.

2.16. Methylated RNA Immunoprecipitation qPCR (MeRIP-qPCR). 1 μg·m^{6}A and IgG antibodies were treated by Protein G Magnetic Beads in 1x reaction buffer at 4°C lasting 3 h as well as treated by 200 μg isolated RNA at 4°C lasting 3 h. Bound RNAs were eluted via incubating by RNA-antibodies-conjugated bead plus 100 μL Elution Buffer lasting 30 min at room temperature. Eluted RNAs were extracted through phenol: chloroform method in line with ethanol precipitation. Extracted m^{6}A-RIP RNAs were reverse-transcribed as well as quantified via RT-qPCR. IPs enriched rates of transcripts were determined as the ratios of their amounts in IPs to those in the input generated from the same number of cells.

2.17. Statistical Analyses. Statistical analyses were conducted with GraphPad Prism 8 software (GraphPad Software, Inc., San Diego, CA, USA). Student's *t*-test and one- or two-way analysis of variance were utilized for comparisons between groups as appropriate. Kaplan–Meier method was

conducted for measuring the survival curves, and differences were assessed with log-rank test. P values less than 0.05 were indicative of statistical significance.

3. Results

3.1. ZC3H13 Displays Low Expression in HCC and Correlates with Survival Outcomes. For investigating the underlying function of ZC3H13 in liver carcinogenesis, this study firstly tested the mRNA expressions of m^6A methyltransferase ZC3H13 in 369 HCC tissues and 160 normal tissues from TCGA and GTEx projects. In Figure 1(a), ZC3H13 expressions were markedly downregulated in HCC relative to control tissues. Furthermore, similar mRNA expression patterns of ZC3H13 were verified in our cohort comprising of 30 paired cancerous and normal specimens (Figure 1(b)). Analysis of western blotting showed the decreased expression of ZC3H13 protein in HCC relative to normal tissues (Figures 1(c) and 1(d)). Moreover, our in vitro experiments confirmed the decreased mRNA expression of ZC3H13 in human liver cancer cell lines HUH-7, Hep3B, HepG2, and SMMC-7721 relative to human normal liver cells L-O2 (Figure 1(e)). Kaplan–Meier analysis uncovered that HCC patients with high ZC3H13 expression displayed a remarked survival advantage utilizing the online bioinformatics tool Kaplan–Meier plotter (Figure 1(f)). With the above evidences, ZC3H13 expression was remarkedly downregulated in HCC, which could be implicated in the pathogenesis and progression of HCC.

3.2. ZC3H13 Inhibits Cell Proliferation of HCC Cells. For addressing the effects of ZC3H13 on HCC progression, this study silenced ZC3H13 expression in Hep3B and HUH-7 cells (Figures 2(a)–2(c)), and its expression was upregulated in the two HCC cells (Figures 2(d)–2(f)) due to their relatively lower expression among all HCC cells, as determined with RT-qPCR and western blotting. CCK-8 results demonstrated that ZC3H13 deficiency enhanced cell growth in Hep3B as well as HUH-7 cells (Figures 2(g) and 2(h)). In contrast, cell growth of HCC cells was alleviated through overexpressed ZC3H13 (Figures 2(i) and 2(j)). As depicted in clonogenicity assay, clone formation of Hep3B and HUH-7 cells was remarkedly enhanced through ZC3H13 deficiency (Figures 2(k) and 2(l)). The opposite results were investigated when ZC3H13 was overexpressed (Figures 2(k) and 2(m)). Collectively, ZC3H13 might inhibit cell proliferation of HCC cells.

3.3. ZC3H13 Promotes Apoptosis and Suppresses Migration and Invasion in HCC Cells. TUNEL assays were utilized for evaluating the effects of ZC3H13 on apoptosis of HCC cells. Our data showed that ZC3H13 deficiency reduced cell apoptosis, whereas ZC3H13 overexpression enhanced cellular apoptotic levels of Hep3B as well as HUH-7 cells (Figures 3(a)–3(c)). Transwell assays revealed that migrative capacities of Hep3B as well as HUH-7 cells were enhanced through ZC3H13 deficiency; meanwhile, overexpressed ZC3H13 alleviated the migrative capacities of HCC cells (Figures 3(d)–3(f)). We also noticed the increase in the invasive abilities of Hep3B and HUH-7 cells induced by ZC3H13 knockdown (Figures 3(g) and 3(h)). However, invasive abilities were reduced by ZC3H13 overexpression (Figures 3(g) and 3(i)). Taken together, ZC3H13 promoted apoptosis as well as suppressed migrative and invasive capacities of HCC cells.

3.4. ZC3H13 Increases Sensitivity to Cisplatin in HCC Cells. We assessed the effects of ZC3H13 on sensitivity to cisplatin in HCC cells. Our CCK-8 data suggested that viable Hep3B as well as HUH-7 cells were suppressed as cisplatin was gradually increased (Figures 4(a) and 4(b)). ZC3H13 knockdown prominently reduced the inhibition rates of cisplatin in HCC cells relative to controls. Quantification analysis of IC50 values of cisplatin showed that ZC3H13 knockdown contributed to increased IC50 of cisplatin in Hep3B and HUH-7 cells, indicative of the reduced sensitivity to cisplatin (Figure 4(c)). Meanwhile, overexpressed ZC3H13 elicited the opposite effects (Figures 4(d)–4(f)). Moreover, our results uncovered that apoptotic levels of Hep3B as well as HUH-7 cells were markedly enhanced following treatment with cisplatin lasting 48 h (Figures 4(g)–4(j)). However, ZC3H13 knockdown weakened the inhibitory effects of cisplatin on apoptosis of HCC cells; meanwhile, overexpressed ZC3H13 enhanced the cisplatin-induced apoptotic levels. Above data demonstrated that ZC3H13 was capable of enhancing the cisplatin chemosensitivity of HCC cells.

3.5. ZC3H13 Reduces Metabolism Reprogramming of HCC Cells. The Warburg effect represents a sign of metabolism reprogramming of cancer, in which most cancer cells exhibit enhanced glucose uptake as well as lactic acid production when there is sufficient oxygen supply [20]. Herein, we measured the effects of ZC3H13 on bioenergy metabolism levels of HCC cells. Our data demonstrated that ZC3H13 deficiency increased glucose uptake of Hep3B and HUH-7 cells, whereas ZC3H13 overexpression reduced glucose uptake (Figures 5(a) and 5(b)). Moreover, we noticed that lactate production was enhanced by ZC3H13 knockdown, and the opposite results were investigated when ZC3H13 was overexpressed (Figures 5(c) and 5(d)). Through western blotting, the expressions of glycolysis-related proteins GLUT, LDHA, LDHB, and PKM2 were measured in Hep3B and HUH-7 cells (Figure 5(e)). As a result, ZC3H13 overexpression remarkedly decreased the expressions of GLUT, LDHA, LDHB, and PKM2 proteins in HCC cells (Figures 5(f)–5(i)). In conclusion, ZC3H13 modulated metabolism reprogramming of HCC cells.

3.6. ZC3H13-Mediated m^6A Modification Reduces PKM2 mRNA Stability. ZC3H13-silencing and overexpressing HCC cells were treated by Act D. Our results showed that ZC3H13 knockdown remarkedly increased the remaining PKM2 transcripts for Hep3B as well as HUH-7 cells (Figures 6(a) and 6(b)). Rather, ZC3H13 overexpression reduced the remaining

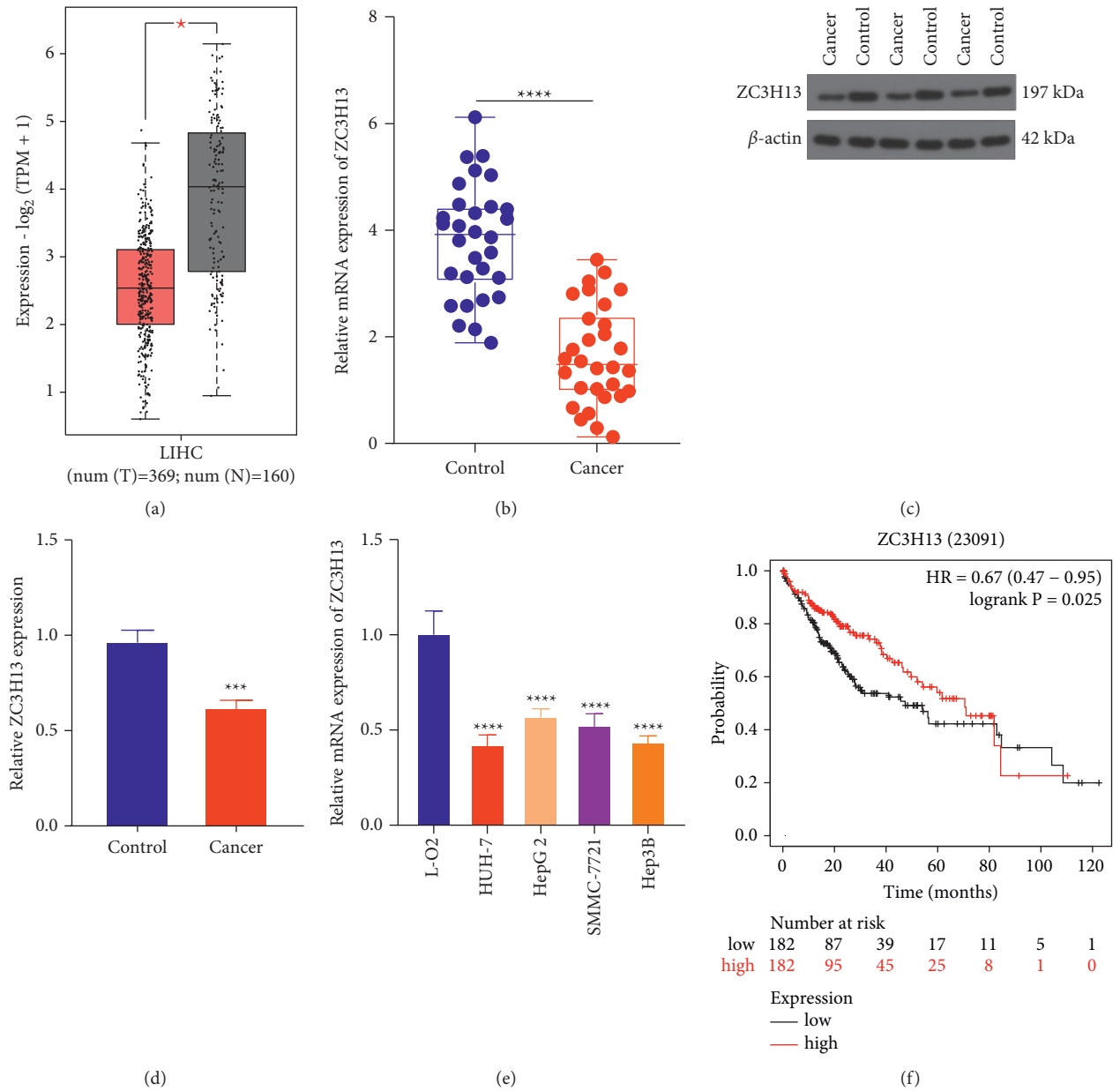

Figure 1: ZC3H13 displays low expression in HCC and correlates with survival outcomes. (a) Expression of ZC3H13 in 369 HCC and 160 control tissue specimens from TCGA and GTEx projects. (b) RT-qPCR examining the mRNA expression of ZC3H13 in 30 paired HCC as well as adjacent control tissue specimens in our cohort. (c, d) Western blotting detecting the protein expression of ZC3H13 in three HCC as well as adjacent control tissue specimens. (e) RT-qPCR testing the mRNA expressions of ZC3H13 in human normal liver cells L-O2 as well as human liver cancer cell lines HUH-7, Hep3B, HepG2, and SMMC-7721. (f) Kaplan–Meier survival analyses of HCC patients who possessed high and low expressions of ZC3H13 via the Kaplan–Meier plotter. $^{*}P < 0.05$; $^{***}P < 0.001$; and $^{****}P < 0.0001$.

PKM2 transcripts in two HCC cells (Figures 6(c) and 6(d)). The data indicated that ZC3H13 could decrease the stability of PKM2 mRNA. Moreover, RIP results showed that anti-ZC3H13 antibody prominently enriched the levels of PKM2 mRNA relative to anti-IgG antibody in Hep3B and HUH-7 cells (Figure 6(e)). However, GAPDH transcript was not detected in ZC3H13 or IgG immunocomplex. Thus, ZC3H13 possessed the capacity of binding to PKM2 transcript physically. Moreover, we further investigated whether PKM2 3′-untranslated region (3′-UTR) was required for ZC3H13 for reducing PKM2 expression. Therefore, dual-luciferase assay was carried out. Our data demonstrated that ZC3H13 overexpression remarkedly lowered the luciferase activities of PKM2 3′-UTR reporter vector for Hep3B as well as HUH-7 cells (Figures 6(f) and 6(g)). However, no effect was investigated for the empty vector. Thus, above data were indicated that ZC3H13 bound to PKM2 3′-UTR. In line with MeRIP-qPCR results, ZC3H13 overexpression reduced the m^6A levels of PKM2 mRNA for Hep3B as well as HUH-7 cells (Figure 6(h)). Thus, the findings indicated that ZC3H13

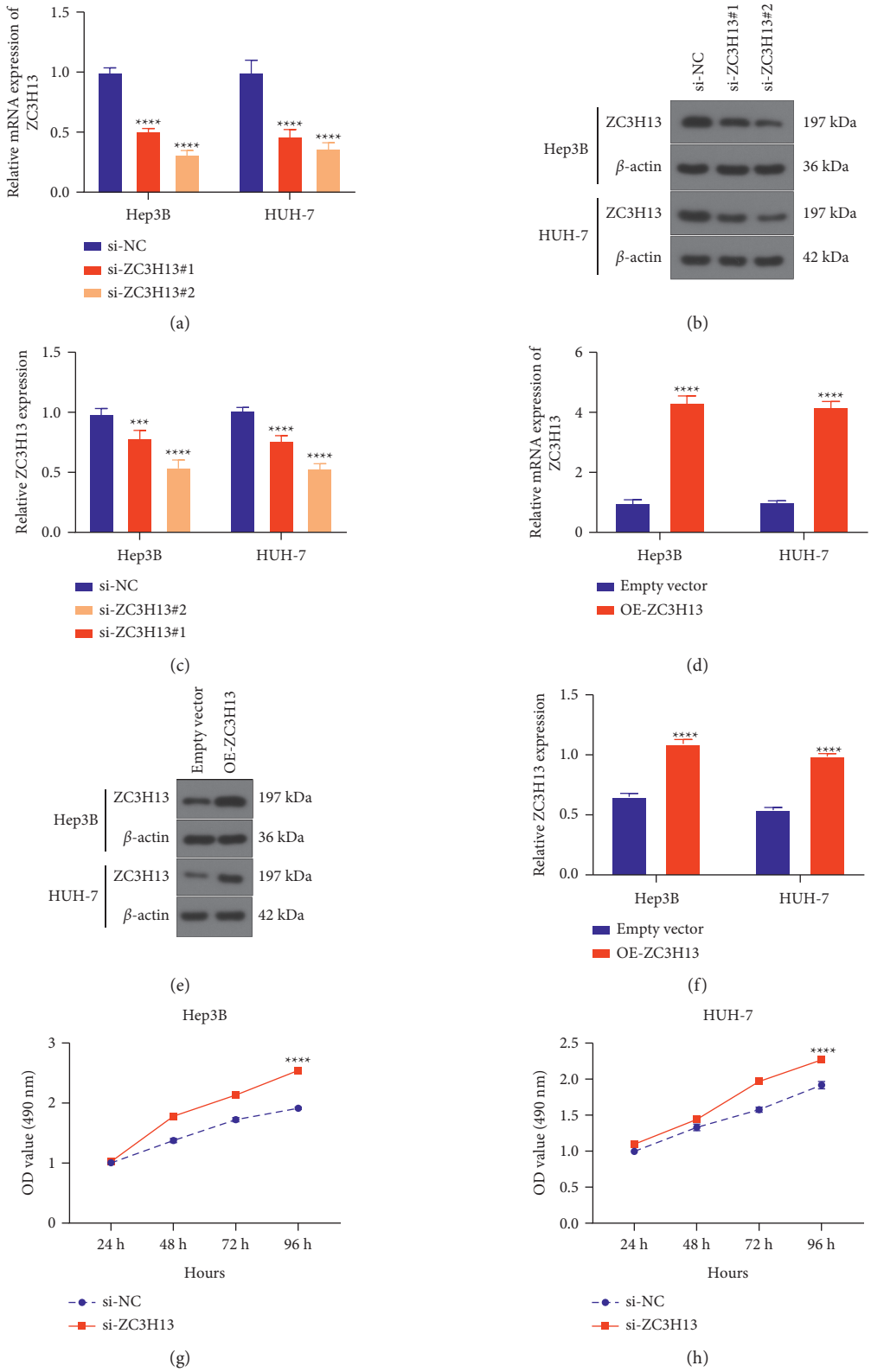

Figure 2: Continued.

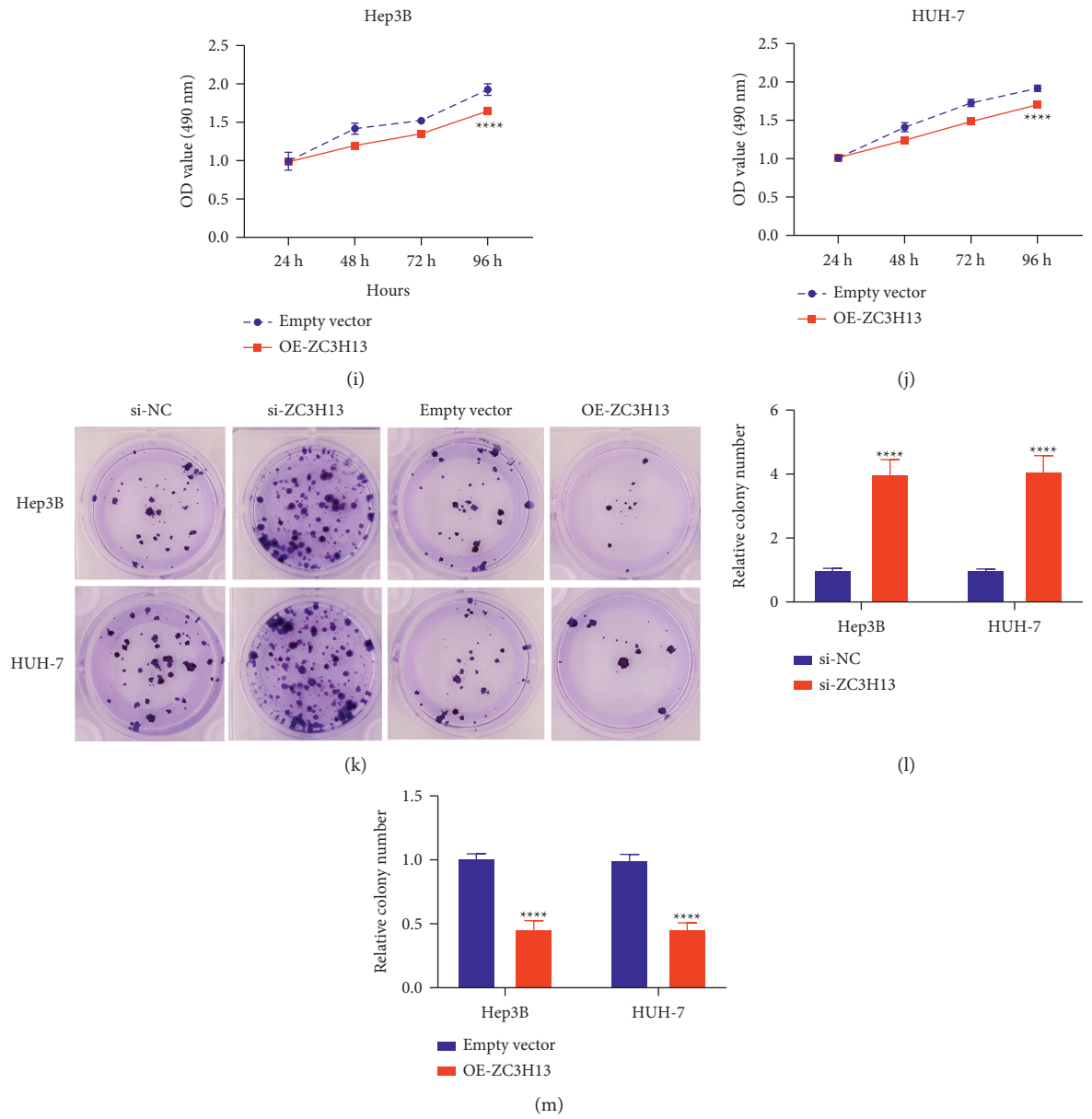

Figure 2: ZC3H13 alleviates cellular proliferative abilities of HCC cells. (a) RT-qPCR as well as (b, c) western blotting for detection of ZC3H13 expression in Hep3B and HUH-7 cells with siRNAs targeting ZC3H13. (d) RT-qPCR as well as (e, f) western blotting examining ZC3H13 expression for Hep3B as well as HUH-7 cells with ZC3H13 overexpression vectors. (g, h) CCK-8 examining the cellular growth for Hep3B as well as HUH-7 cells with ZC3H13 deficiency. (i, j) CCK-8 for evaluation for Hep3B as well as HUH-7 cells with ZC3H13 overexpression. (k–m) Clonogenicity assay for investigation of the colony formation for Hep3B as well as HUH-7 cells with ZC3H13 deficiency or overexpression. $^{***}P < 0.001$; $^{****}P < 0.0001$.

decreased the stability of PKM2 mRNA with an m^6A-dependent manner.

3.7. PKM2 Knockdown Weakens Cell Proliferation and Metabolic Reprogramming Mediated by ZC3H13 in HCC Cells. We further investigated the effects of interactions of ZC3H13 with PKM2 on HCC progression. We firstly confirmed the successful knockdown of PKM2 for Hep3B as well as HUH-7 cells with si-PKM2 transfections (Figure 7(a)). Afterwards, we assessed the cellular proliferation of PKM2 interacted with ZC3H13 in HCC through CCK-8. Our data demonstrated that PKM2 knockdown induced a prominent reduction in cell viability. Nevertheless, PKM2 knockdown reversed the cell growth mediated by ZC3H13 deficiency in Hep3B and HUH-7 cells (Figures 7(b) and 7(c)). Clone formation of HCC cells was weakened by PKM2 knockdown (Figures 7(d) and 7(e)). However,

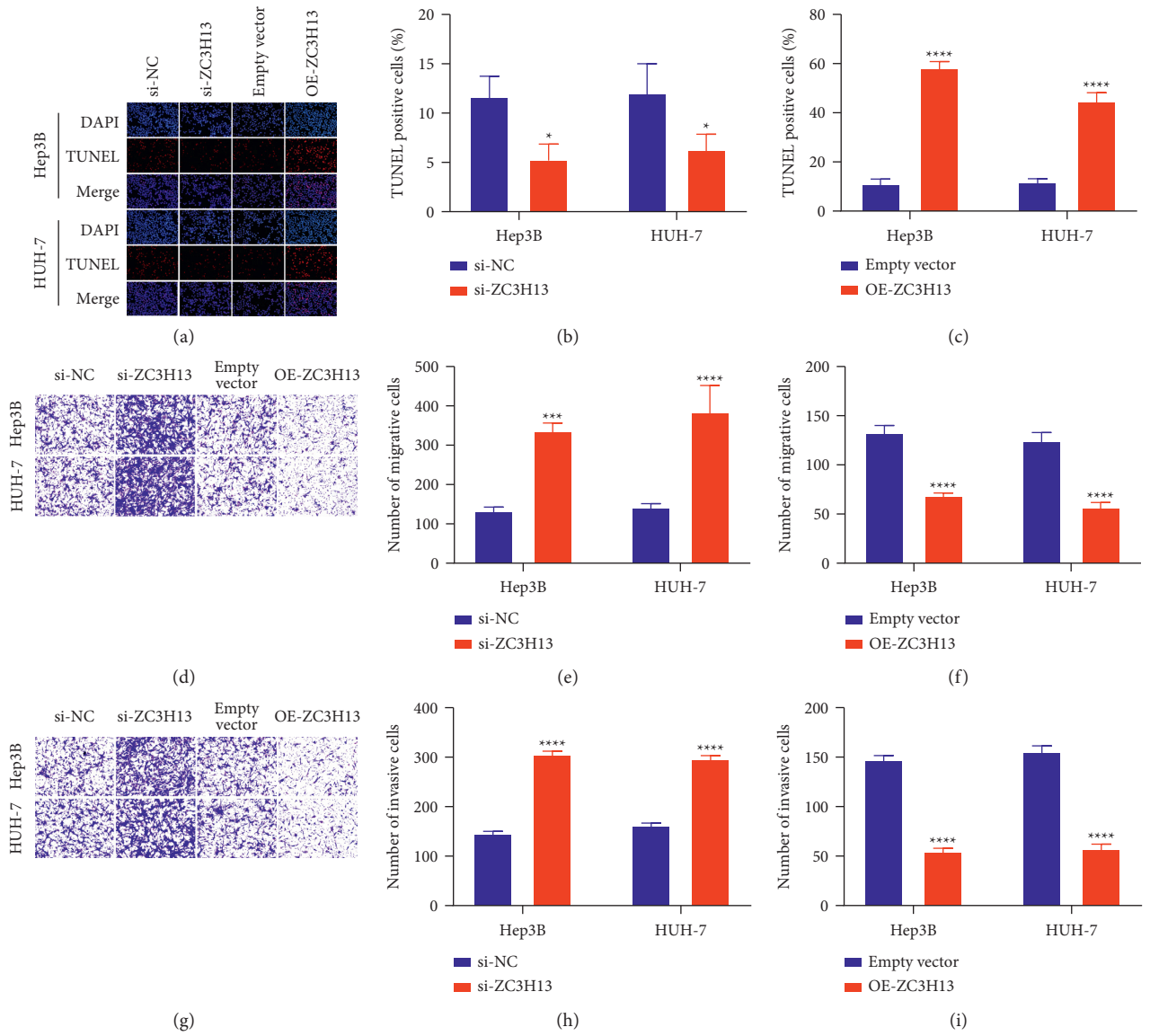

Figure 3: ZC3H13 promotes apoptosis and suppresses migration and invasion in HCC cells. (a–c) TUNEL for detecting the apoptotic levels for Hep3B as well as HUH-7 cells with ZC3H13 deficiency or overexpression. Magnification, 200×. (d–f) Evaluation of migration levels for Hep3B as well as HUH-7 cells with ZC3H13 deficiency or overexpression utilizing Transwell assays. Magnification, 200×. (g–i) Quantification of invasion levels for Hep3B as well as HUH-7 cells with ZC3H13 deficiency or overexpression utilizing Transwell assays. Magnification, 200×. $^{*}P < 0.05$; $^{***}P < 0.001$; and $^{****}P < 0.0001$.

silencing ZC3H13 remarkedly ameliorated the clone formation induced by ZC3H13 knockdown in HCC cells. By quantitative analyses of glycolysis, we noticed that PKM2 deficiency prominently reduced glucose uptake and lactic acid production for Hep3B as well as HUH-7 cells (Figures 7(f) and 7(g)). But silencing PKM2 alleviated glucose uptake and lactic acid production induced by ZC3H13 deficiency. Taken together, ZC3H13 alleviated HCC cell proliferation by PKM2-dependent glycolytic signaling.

3.8. PKM2 Deficiency Alleviates Migration and Invasion Induced by ZC3H13 in HCC Cells. The effects of interactions of ZC3H13 with PKM2 on HCC metastasis were investigated through quantification of migration and invasion via transwell assays. Our results demonstrated that PKM2 deficiency remarkedly alleviated the migrative capacities of Hep3B and HUH-7 cells (Figures 8(a) and 8(b)). Additionally, its deficiency reversed the migrative abilities induced by ZC3H13 knockdown in HCC cells. As depicted in Figures 8(c) and 8(d), silencing PKM2 led to a remarked

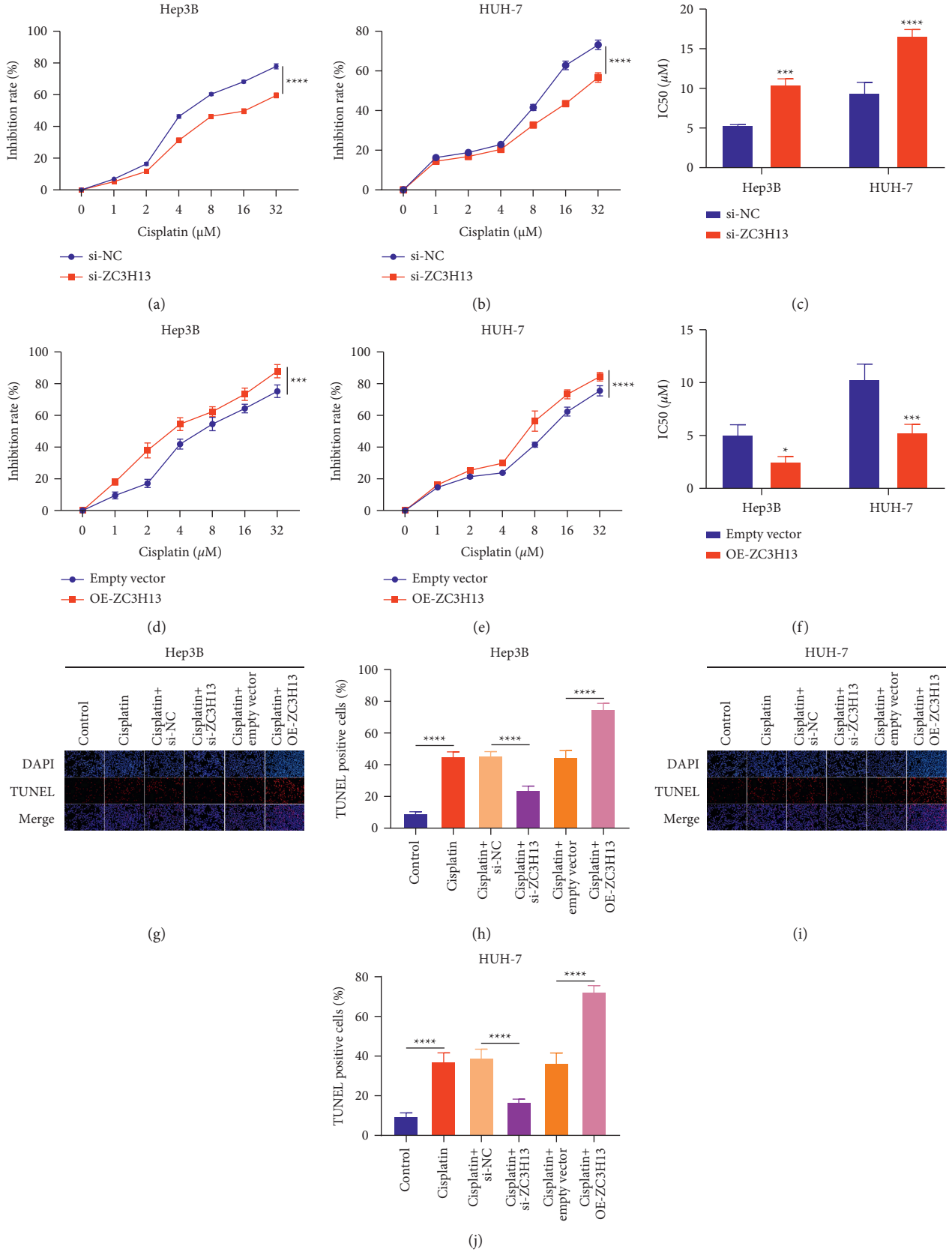

Figure 4: ZC3H13 increases sensitivity to cisplatin in HCC cells. (a, b) Inhibition rates of cisplatin for Hep3B as well as HUH-7 cells with ZC3H13 deficiency through CCK-8 assays. (c) Evaluation of IC50 values of cisplatin for Hep3B as well as HUH-7 cells with ZC3H13 deficiency. (d, e) Inhibition rates of cisplatin in Hep3B as well as HUH-7 cells with ZC3H13 overexpression by CCK-8 assays. (f) Assessment of IC50 values of cisplatin in Hep3B as well as HUH-7 cells with overexpressed ZC3H13. (g–j) TUNEL assays examining the apoptotic levels of Hep3B as well as HUH-7 cells with ZC3H13 deficiency or overexpression following exposure to cisplatin. Magnification, 200×. $^{*}P < 0.05$; $^{***}P < 0.001$; and $^{****}P < 0.0001$.

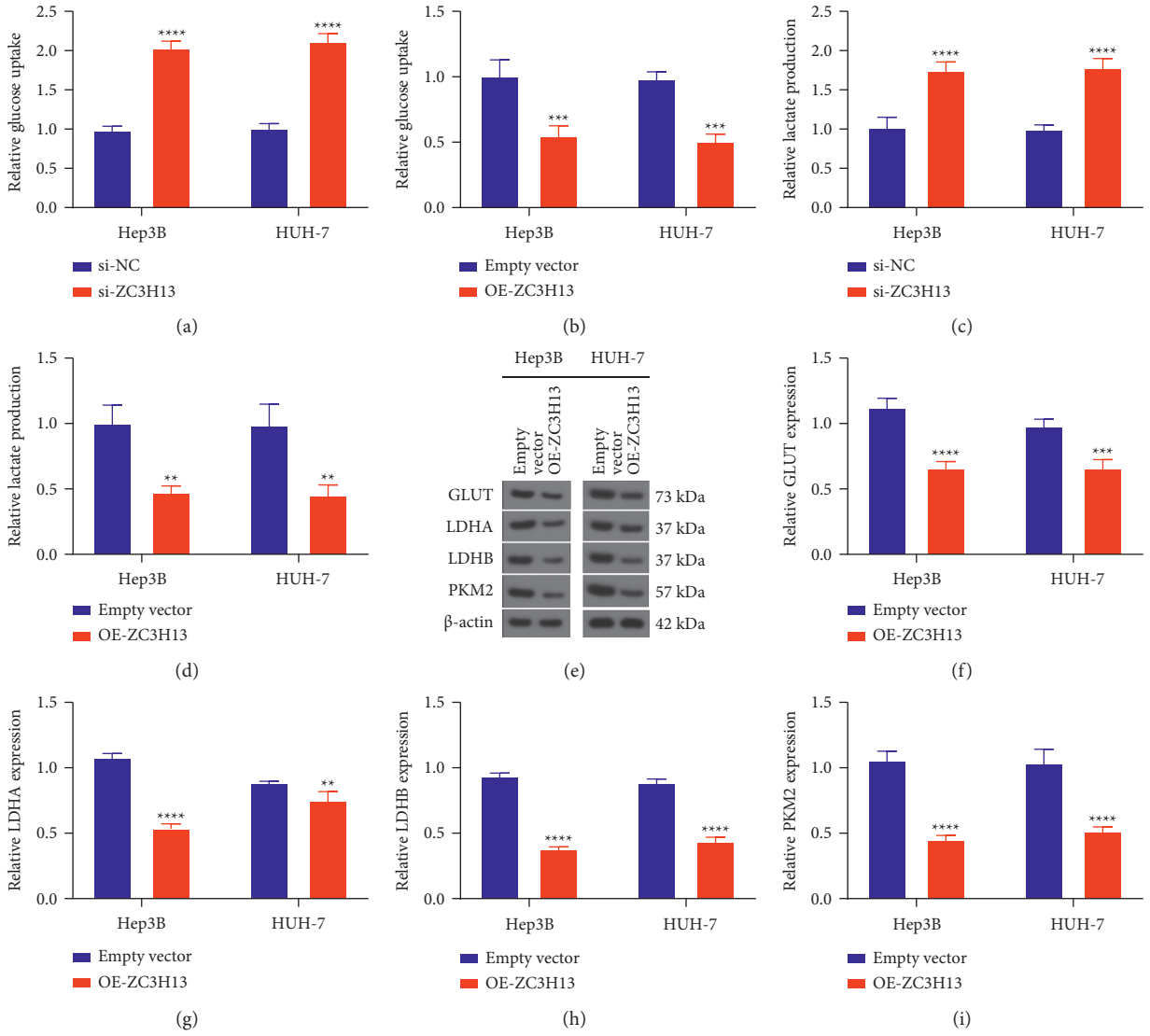

Figure 5: ZC3H13 weakens metabolism reprogramming of HCC cells. (a, b) Quantification of glucose uptake of Hep3B as well as HUH-7 cells with ZC3H13 deficiency and overexpression. (c, d) Quantification of lactate production of Hep3B as well as HUH-7 cells with ZC3H13 deficiency and overexpression. (e–i) Western blotting detecting the expression of metabolism reprogramming-related proteins including GLUT, LDHA, LDHB, and PKM2 in Hep3B as well as HUH-7 cells with overexpressed ZC3H13. $^{**}P < 0.01$; $^{***}P < 0.001$; and $^{****}P < 0.0001$.

decrease in the invasive abilities of Hep3B and HUH-7 cells. Also, PKM2 deficiency reversed the invasion of HCC cells mediated by ZC3H13 knockdown. Collectively, PKM2 deficiency alleviated migration and invasion induced by ZC3H13 in HCC cells.

4. Discussion

m^{6}A modification of RNAs acts as a novel layer of epigenetic modulation [8]. The biochemical event exerts critical roles in modulating growth, differentiation, resistance, and metabolic reprogramming of cancer cells via modulation of RNA splicing, translation, and stability [14, 21, 22]. Several evidences have proposed m^{6}A as a major modified type of mRNAs [23–25]. In our study, our evidences confirmed the important roles of m^{6}A regulator ZC3H13 in HCC progression and uncovered the underlying mechanisms. Our results demonstrated that overexpressed ZC3H13 weakened malignant behaviors of HCC cells through m^{6}A-PKM2-mediated glycolysis and enhanced chemosensitivity.

Consistent with bioinformatics analysis, ZC3H13 expression was downregulated in HCC as well as its loss correlated to dismal survival outcomes [26–28]. ZC3H13 weakens proliferative and invasive capacities of colorectal carcinoma cells through inactivating Ras-ERK pathway [29]. ZC3H13 is predictive of immune phenotype and therapeutic

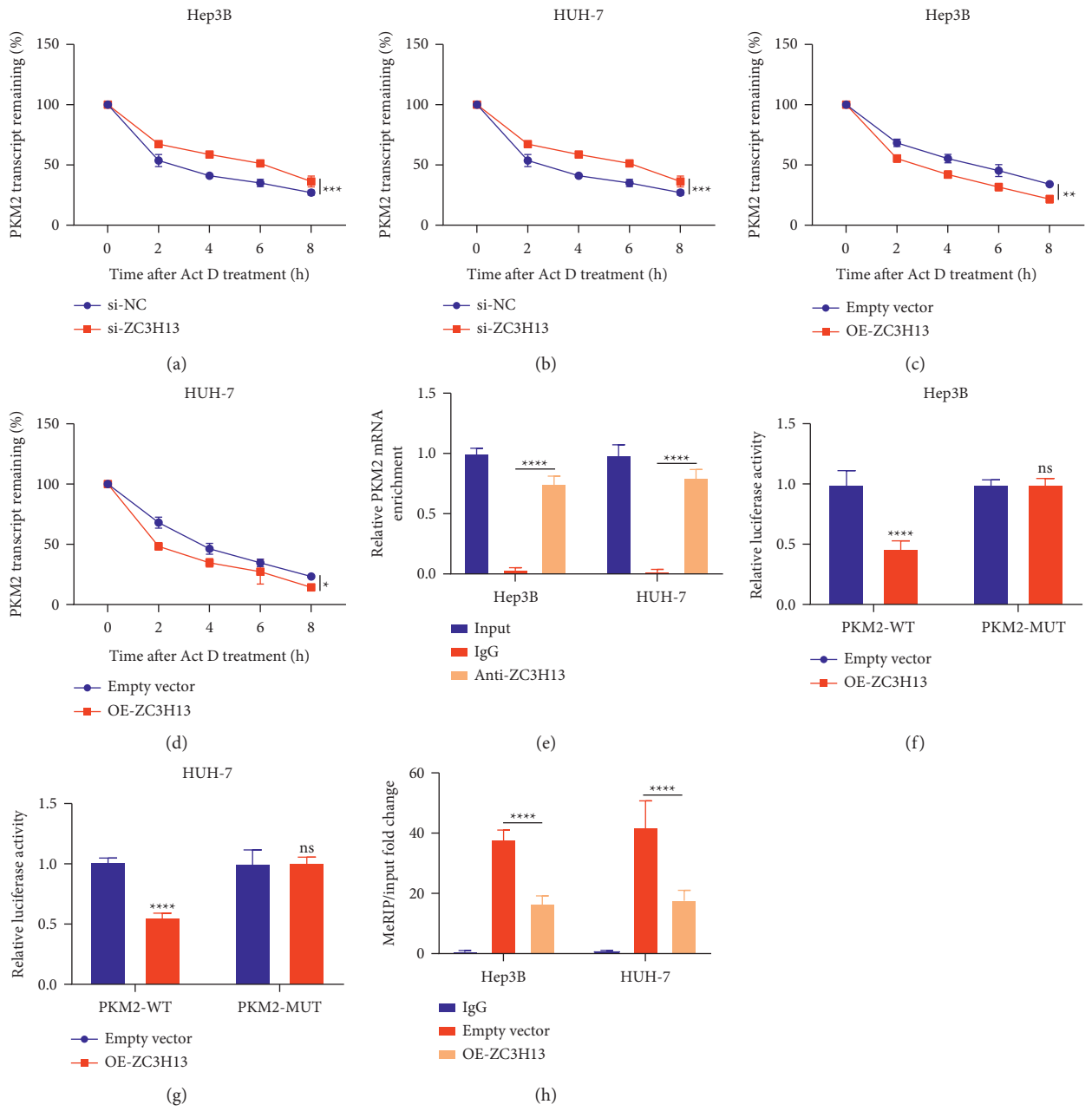

Figure 6: ZC3H13-mediated m^{6}A modification reduces PKM2 mRNA stability in HCC cells. (a, b) Detection of the remaining PKM2 transcript in Hep3B as well as HUH-7 cells with ZC3H13 knockdown following exposure to Act D for the indicated time points. (c, d) Detection of the remaining PKM2 transcript for Hep3B as well as HUH-7 cells with ZC3H13 overexpression under exposure to Act D for the indicated time points. (e) RIP assay examining the enrichment levels of PKM2 mRNA in Hep3B as well as HUH-7 cells under incubation by anti-ZC3H13 or anti-IgG antibody. GAPDH transcript was utilized as a control. (f, g) Luciferase reporter assay examining the effects of ZC3H13 on wild-type PKM2 (PKM2-WT) or mutant PKM2 (PKM2-MUT) vector for Hep3B as well as HUH-7 cells. (h) MeRIP-qPCR detecting m^{6}A modification levels of PKM2 through immunoprecipitation of m^{6}A-modified mRNA for Hep3B as well as HUH-7 cells with empty vector or ZC3H13 overexpression. Ns: not significant; $^*P < 0.05$; $^{**}P < 0.01$; $^{***}P < 0.001$; and $^{****}P < 0.0001$.

responses in renal carcinoma [30]. Our data demonstrated that overexpressed ZC3H13 alleviated proliferation, migration, and invasion as well as aggravated apoptosis in HCC cells, confirming that ZC3H13 exacerbated malignant behaviors of HCC cells. Tumor metastases and chemoresistance act as the major causes of therapeutic failure and increased mortality for HCC [31]. In line with the perspective of precision medicine, it is an urgency for finding novel molecular targets upon developing more effective therapeutic regimen. Herein, ZC3H13 overexpression could sensitize HCC cells to cisplatin, providing novel evidences for HCC chemotherapy.

HCC represents a heterogeneous malignancy, characterized by diverse etiological factors, that is implicated in

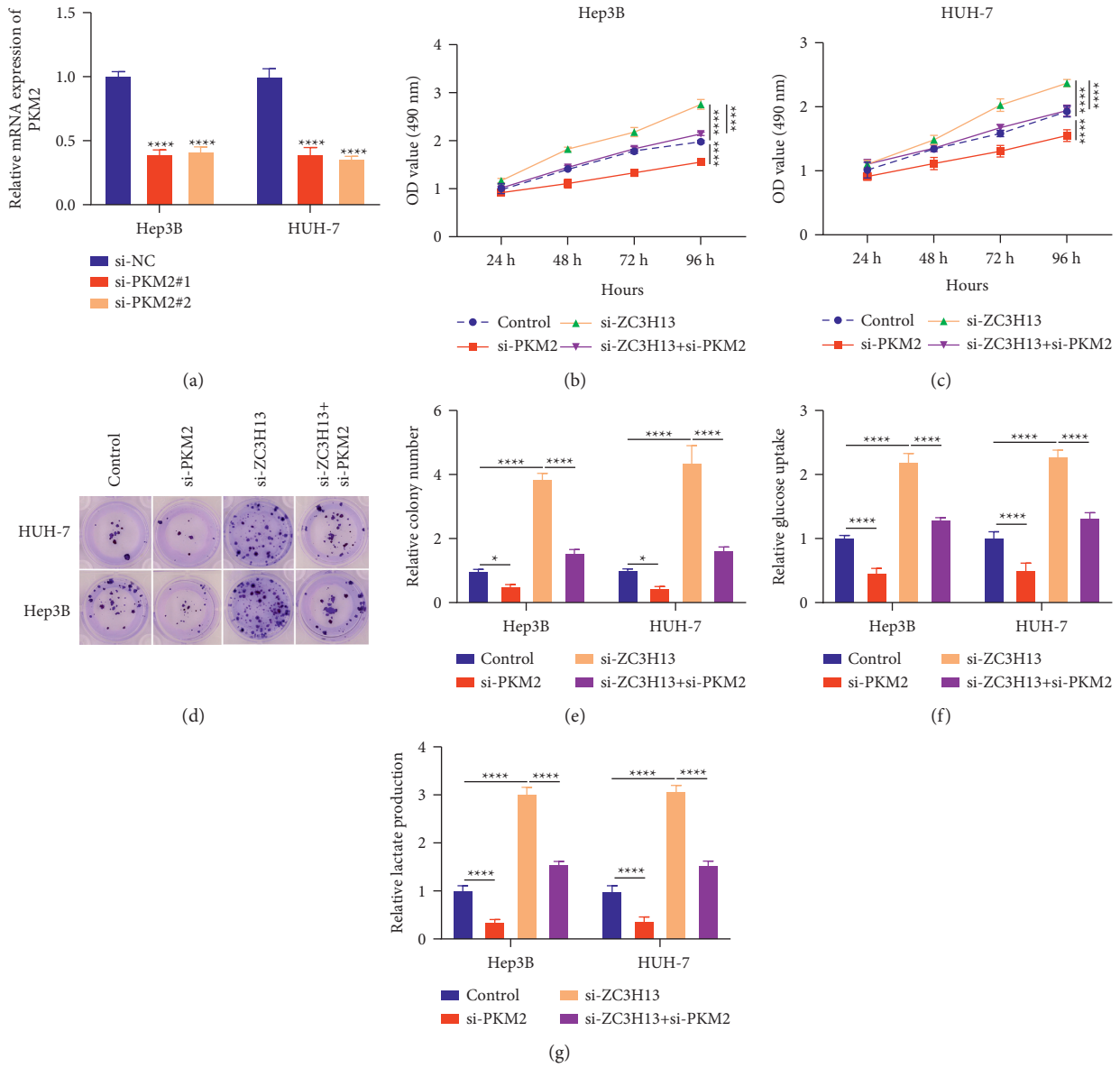

Figure 7: PKM2 knockdown weakens cell proliferation and metabolic reprogramming mediated by ZC3H13 in HCC cells. (a) RT-qPCR detecting the mRNA expression of PKM2 for Hep3B as well as HUH-7 cells transfected by siRNAs against PKM2. (b, c) CCK-8 examining the effects of PKM2 knockdown on cell growth for Hep3B as well as HUH-7 cells with ZC3H13 loss. (d, e) The effects of silencing or overexpressing PKM2 on clone formation of Hep3B as well as HUH-7 cells with ZC3H13 knockdown. (f, g) The effects of PKM2 knockdown on glucose uptake and lactate production in Hep3B and HUH-7 cells with ZC3H13 deficiency. $^{*}P < 0.05$; $^{****}p < 0.0001$.

metabolic alterations [32]. Previous evidences have demonstrated the significance of metabolic normalization to HCC inhibition [33–35]. The Warburg effect is fundamental to metabolic reprogramming in HCC progression [36]. Enhanced glucose uptake and lactate production maintain long-term growth of cancer cells. Hopefully, reprogramming of HCC cells may manifest itself as a new insight into developing therapeutic regimen against HCC. Our data demonstrated that ZC3H13 had much potential of inhibiting glycolysis in HCC through modulating metabolism reprogramming. Our further analyses uncovered that ZC3H13-mediated m^6A modification substantially alleviated PKM2 mRNA stability as well as overexpressed ZC3H13 facilitated malignant behaviors of HCC cells through PKM2-dependent glycolytic signaling. Even so, more selective and efficacious agents activating ZC3H13 will be developed upon HCC therapy in our future studies. There are several limitations in our study. Firstly, we collected 30 pairs of HCC specimens and matched nontumor specimens, and our results revealed that ZC3H13 expression was downregulated in HCC specimens. However, the sample size is small. The expression of ZC3H13 will be verified in larger HCC cohorts. Secondly, the biological function of ZC3H13 in HCC progression will be investigated through in vivo experiments.

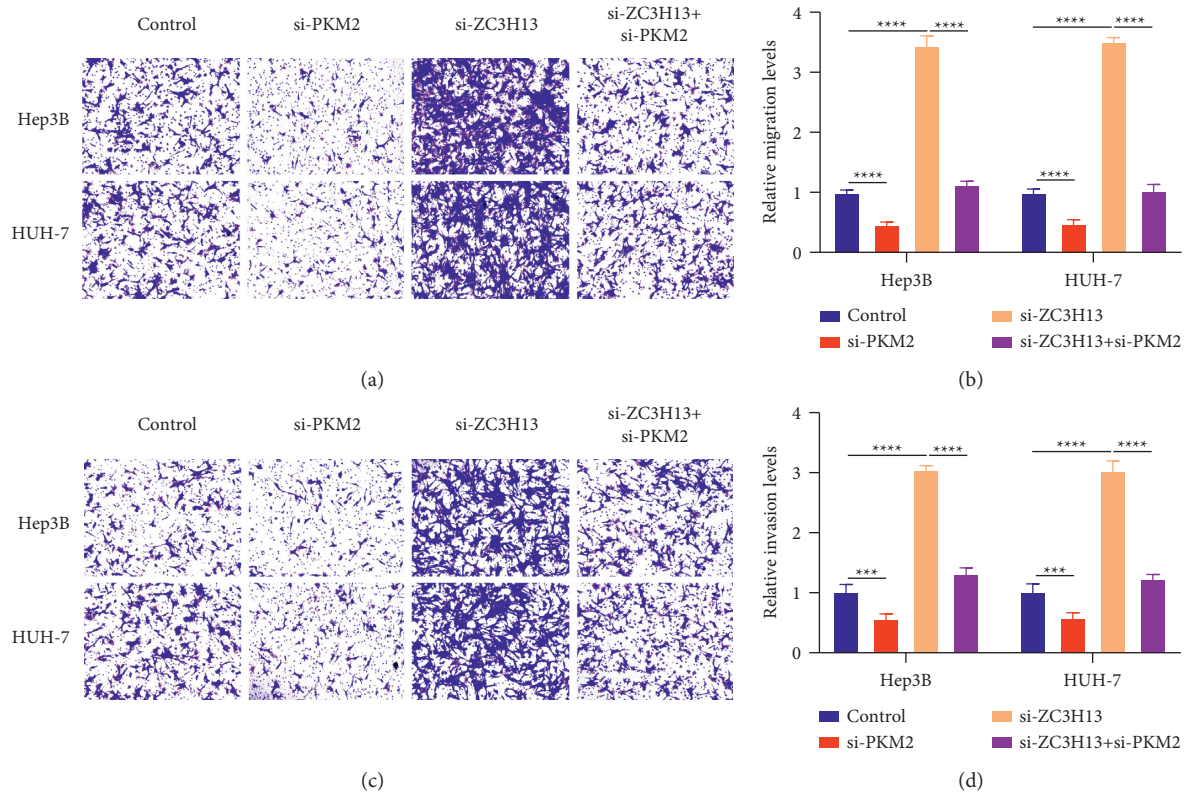

Figure 8: PKM2 deficiency alleviates migration and invasion induced by ZC3H13 in HCC cells. (a, b) Transwell assays detecting the effects of PKM2 knockdown on migrative capacities of Hep3B as well as HUH-7 cells with ZC3H13 deficiency. (c, d) Transwell assays detecting the effects of PKM2 knockdown on invasive capacities of Hep3B as well as HUH-7 cells with ZC3H13 deficiency. Magnification, 200×. $^{***}p < 0.001$; $^{****}p < 0.0001$.

5. Conclusion

In all, our evidences demonstrated that overexpressed ZC3H13 alleviated malignant behaviors and metabolism reprogramming of HCC cells through mediating the m^{6}A-modified PKM2 mRNA. Therefore, ZC3H13 possessed the potential as a therapeutic target against HCC. Effective treatments for HCC might be conducted on the basis of the new molecular mechanisms proposed in these observations.

Abbreviations

HCC: Hepatocellular carcinoma
TACE: Transarterial chemoembolization
m^{6}A: N^6-Methyladenosine
GEPIA: Gene Expression Profiling Interactive Analysis
TCGA: The Cancer Genome Atlas
GTEx: Genotype-tissue expression
RT-qPCR: Real-time quantitative polymerase-chain reaction
DMEM: Dulbecco's Modified Eagle's Medium
siRNAs: Short interfering RNAs
CCK-8: Cell counting kit-8
TUNEL: TdT-mediated dUTP nick-end labeling
IC50: Half-maximum inhibitory concentration
Act-D: Actinomycin D
RIP: RNA immunoprecipitation
MeRIP-qPCR: Methylated RNA immunoprecipitation qPCR.

Data Availability

The datasets analyzed during the current study are available from the corresponding author upon reasonable request.

Conflicts of Interest

The authors declare that they have no conflicts of interest regarding the publication of this paper.

Authors' Contributions

Qibo Wang and Gang Ye contributed equally to this paper.

References

[1] M. Arnold, C. C. Abnet, R. E. Neale et al., "Global burden of 5 major types of gastrointestinal cancer," *Gastroenterology*, vol. 159, no. 1, pp. 335–349, Article ID e315, 2020.

[2] Q. Zuo, J. He, S. Zhang et al., "PPARγ coactivator-1α suppresses metastasis of hepatocellular carcinoma by inhibiting warburg effect by PPARγ-dependent WNT/β-catenin/pyruvate dehydrogenase kinase isozyme 1 axis," *Hepatology*, vol. 73, no. 2, pp. 644–660, 2021.

[3] K. A. McGlynn, J. L. Petrick, and H. B. El-Serag, "Epidemiology of hepatocellular carcinoma," *Hepatology*, vol. 73, no. 1, pp. 4–13, 2021.

[4] M. Kudo, K. Ueshima, M. Ikeda et al., "Randomised, multicentre prospective trial of transarterial chemoembolisation (TACE) plus sorafenib as compared with TACE alone in patients with hepatocellular carcinoma: TACTICS trial," *Gut*, vol. 69, no. 8, pp. 1492–1501, 2020.

[5] D. Anwanwan, S. K. Singh, S. Singh, V. Saikam, and R. Singh, "Challenges in liver cancer and possible treatment approaches," *Biochimica et Biophysica Acta (BBA)-Reviews on Cancer*, vol. 1873, Article ID 188314, 2020.

[6] Z. Lin, Y. Niu, A. Wan et al., "RNA m^6 A methylation regulates sorafenib resistance in liver cancer through $FOXO_3$-mediated autophagy," *The EMBO Journal*, vol. 39, Article ID e103181, 2020.

[7] T. Wang, S. Kong, M. Tao, and S. Ju, "The potential role of RNA N^6-methyladenosine in Cancer progression," *Molecular Cancer*, vol. 19, Article ID 88, 2020.

[8] X. Niu, J. Xu, J. Liu, L. Chen, X. Qiao, and M. Zhong, "Landscape of N^6-methyladenosine modification patterns in human ameloblastoma," *Frontiers in Oncology*, vol. 10, Article ID 556497, 2020.

[9] M. Chen and C. M. Wong, "The emerging roles of N^6-methyladenosine (m^6A) deregulation in liver carcinogenesis," *Molecular Cancer*, vol. 19, Article ID 44, 2020.

[10] Z. Li, Y. Peng, J. Li et al., "N^6-methyladenosine regulates glycolysis of cancer cells through PDK4," *Nature Communications*, vol. 11, Article ID 2578, 2020.

[11] G.-M. Liu, H.-D. Zeng, C.-Y. Zhang, and J.-W. Xu, "Identification of $METTL_3$ as an adverse prognostic biomarker in hepatocellular carcinoma," *Digestive Diseases and Sciences*, vol. 66, no. 4, pp. 1110–1126, 2021.

[12] M. Chen, L. Wei, C.-T. Law et al., "RNA N^6-methyladenosine methyltransferase-like 3 promotes liver cancer progression through $YTHDF_2$-dependent posttranscriptional silencing of $SOCS_2$," *Hepatology*, vol. 67, no. 6, pp. 2254–2270, 2018.

[13] H. Xu, H. Wang, W. Zhao et al., "SUMO1 modification of methyltransferase-like 3 promotes tumor progression via regulating Snail mRNA homeostasis in hepatocellular carcinoma," *Theranostics*, vol. 10, no. 13, pp. 5671–5686, 2020.

[14] N. Yang, T. Wang, Q. Li et al., "HBXIP drives metabolic reprogramming in hepatocellular carcinoma cells via $METTL_3$-mediated m^6A modification of HIF-1α," *Journal of Cellular Physiology*, vol. 236, no. 5, pp. 3863–3880, 2021.

[15] X.-F. Ni, Q.-Q. Xie, J.-M. Zhao et al., "The hepatic microenvironment promotes lung adenocarcinoma cell proliferation, metastasis, and epithelial-mesenchymal transition via $METTL_3$-mediated N^6-methyladenosine modification of YAP_1," *Aging*, vol. 13, no. 3, pp. 4357–4369, 2021.

[16] C. Zhang, S. Huang, H. Zhuang et al., "YTHDF2 promotes the liver cancer stem cell phenotype and cancer metastasis by regulating OCT4 expression via m^6A RNA methylation," *Oncogene*, vol. 39, no. 23, pp. 4507–4518, 2020.

[17] J. Hou, H. Zhang, J. Liu et al., "YTHDF2 reduction fuels inflammation and vascular abnormalization in hepatocellular carcinoma," *Molecular Cancer*, vol. 18, Article ID 163, 2019.

[18] L. Zhong, D. Liao, M. Zhang et al., "YTHDF2 suppresses cell proliferation and growth via destabilizing the EGFR mRNA in hepatocellular carcinoma," *Cancer Letters*, vol. 442, pp. 252–261, 2019.

[19] Z. Tang, C. Li, B. Kang, G. Gao, C. Li, and Z. Zhang, "GEPIA: a web server for cancer and normal gene expression profiling and interactive analyses," *Nucleic Acids Research*, vol. 45, no. 1, pp. W98–w102, 2017.

[20] X. Huang, G. Gan, X. Wang, T. Xu, and W. Xie, "The HGF-MET axis coordinates liver cancer metabolism and autophagy for chemotherapeutic resistance," *Autophagy*, vol. 15, no. 7, pp. 1258–1279, 2019.

[21] Y. Chen, Y. Zhao, J. Chen et al., "ALKBH5 suppresses malignancy of hepatocellular carcinoma via m^6A-guided epigenetic inhibition of LYPD1," *Molecular Cancer*, vol. 19, Article ID 123, 2020.

[22] T. Zhou, S. Li, D. Xiang et al., "m^6A RNA methylation-mediated HNF3γ reduction renders hepatocellular carcinoma dedifferentiation and sorafenib resistance," *Signal transduction and targeted therapy*, vol. 5, no. 1, Article ID 296, 2020.

[23] T. Lan, H. Li, D. Zhang et al., "KIAA1429 contributes to liver cancer progression through N^6-methyladenosine-dependent post-transcriptional modification of GATA3," *Molecular Cancer*, vol. 18, Article ID 186, 2019.

[24] H. Ding, X. Zhang, Y. Su, C. Jia, and C. Dai, "GNAS promotes inflammation-related hepatocellular carcinoma progression by promoting STAT3 activation," *Cellular and Molecular Biology Letters*, vol. 25, p. 8, 2020.

[25] X. Cheng, M. Li, X. Rao et al., "KIAA1429 regulates the migration and invasion of hepatocellular carcinoma by altering m^6A modification of ID2 mRNA," *OncoTargets and Therapy*, vol. 12, pp. 3421–3428, 2019.

[26] Y. Huang, S. Chen, W. Qin et al., "A novel RNA binding protein-related prognostic signature for hepatocellular carcinoma," *Frontiers in Oncology*, vol. 10, Article ID 580513, 2020.

[27] J. Liu, G. Sun, S. Pan et al., "The Cancer genome atlas (TCGA) based m^6A methylation-related genes predict prognosis in hepatocellular carcinoma," *Bioengineered*, vol. 11, no. 1, pp. 759–768, 2020.

[28] J. Wei, D. L. Fang, W. Zhou, and Y. F. He, "N^6-methyladenosine (m^6A) regulatory gene divides hepatocellular carcinoma into three subtypes," *Journal of Gastrointestinal Oncology*, vol. 12, no. 4, pp. 1860–1872, 2021.

[29] D. Zhu, J. Zhou, J. Zhao et al., "ZC3H13 suppresses colorectal cancer proliferation and invasion via inactivating Ras-ERK signaling," *Journal of Cellular Physiology*, vol. 234, no. 6, pp. 8899–8907, 2019.

[30] T. Guo, H. Duan, J. Chen et al., "N^6-Methyladenosine writer gene ZC3H13 predicts immune phenotype and therapeutic opportunities in kidney renal clear cell carcinoma," *Frontiers in Oncology*, vol. 11, Article ID 718644, 2021.

[31] Q. Chen, P. Jiang, B. Jia, Y. Liu, and Z. Zhang, "RCC2 contributes to tumor invasion and chemoresistance to cisplatin in hepatocellular carcinoma," *Human Cell*, vol. 33, no. 3, pp. 709–720, 2020.

[32] Q. Li, X. Pan, D. Zhu, Z. Deng, R. Jiang, and X. Wang, "Circular RNA MAT2B promotes glycolysis and malignancy of hepatocellular carcinoma through the miR-338-3p/PKM2 Axis under hypoxic stress," *Hepatology*, vol. 70, no. 4, pp. 1298–1316, 2019.

[33] S. Ling, Q. Shan, Q. Zhan et al., "USP22 promotes hypoxia-induced hepatocellular carcinoma stemness by a HIF1α/USP22 positive feedback loop upon TP53 inactivation," *Gut*, vol. 69, no. 7, pp. 1322–1334, 2020.

[34] X. Zhang, Y. Li, Y. Ma et al., "Yes-associated protein (YAP) binds to HIF-1α and sustains HIF-1α protein stability to promote hepatocellular carcinoma cell glycolysis under hypoxic stress," *Journal of Experimental & Clinical Cancer Research: Climate Research*, vol. 37, Article ID 216, 2018.

[35] Q. Fan, L. Yang, X. Zhang et al., "Autophagy promotes metastasis and glycolysis by upregulating MCT1 expression and Wnt/β-catenin signaling pathway activation in hepatocellular carcinoma cells," *Journal of Experimental & Clinical Cancer Research: Climate Research*, vol. 37, p. 9, 2018.

[36] R. Shang, M. Wang, B. Dai et al., "Long noncoding RNA SLC2A1-AS1 regulates aerobic glycolysis and progression in hepatocellular carcinoma via inhibiting the STAT3/FOXM1/GLUT1 pathway," *Molecular Oncology*, vol. 14, no. 6, pp. 1381–1396, 2020.

Hindawi
Journal of Oncology
Volume 2021, Article ID 1920111, 12 pages
https://doi.org/10.1155/2021/1920111

Research Article

Identification of Latent Diagnostic Biomarkers and Biological Pathways in Dermatomyositis Based on WGCNA

Shaxi Ouyang,[1,2,3] Yifang Liu,[1,2,3] Changjuan Xiao,[1,2,3] Qinghua Zeng,[1,2,3] Xun Luo,[1,2,3] Xiaofang Hu,[4] and Shuoshan Xie [1,2,3]

[1]*Nephrology Department and Laboratory of Kidney Disease, Hunan Provincial People's Hospital, The First Affiliated Hospital of Hunan Normal University, Changsha, China*
[2]*Changsha Clinical Research Center for Kidney Disease, Changsha, China*
[3]*Hunan Clinical Research Center for Chronic Kidney Disease, Changsha, China*
[4]*Department of Clinical Medicine, School of Medicine, Hunan Normal University, Changsha, Hunan 410013, China*

Correspondence should be addressed to Shuoshan Xie; xie_shuoshan@hunnu.edu.cn

Received 10 November 2021; Revised 9 December 2021; Accepted 11 December 2021; Published 30 December 2021

Academic Editor: Fu Wang

Introduction. Dermatomyositis (DM) is a chronic autoimmune disease of predominantly lymphocytic infiltration mainly involving the transverse muscle. Its pathogenesis is remaining unknown. This research is designed to probe the latent pathogenesis of dermatomyositis, identify potential biomarkers, and reveal the pathogenesis of dermatomyositis through information biology analysis of gene chips. *Methods*. In this study, we utilised the GSE14287 and GSE11971 datasets rooted in the Gene Expression Omnibus (GEO) databank, which included a total of 62 DM samples and 9 normal samples. The datasets were combined, and the differentially expressed gene sets were subjected to weighted gene coexpression network analysis, and the hub gene was screened using a protein interaction network from genes in modules highly correlated with dermatomyositis progression. *Results*. A total of 3 key genes—myxovirus resistance-2 (MX2), oligoadenylate synthetase 1 (OAS1), and oligoadenylate synthetase 2 (OAS2)—were identified in combination with cell line samples, and the expressions of the 3 genes were verified separately. The results showed that MX2, OAS1, and OAS2 were highly expressed in LPS-treated cell lines compared to normal cell lines. The results of pathway enrichment analysis of the genes indicated that all 3 genes were enriched in the cytosolic DNA signalling and cytokine and cytokine receptor interaction signalling pathways; the results of functional enrichment analysis showed that all 3 were enriched in interferon-α response and interferon-γ response functions. *Conclusions*. This is important for the study of the pathogenesis and objective treatment of dermatomyositis and provides important reference information for the targeted therapy of dermatomyositis.

1. Introduction

Dermatomyositis (DM) is a relatively rare idiopathic multisystem inflammatory disease with a small incidence of just 1 in 100,000 and a significantly higher incidence in women than in men among adult patients [1–3]. Dermatomyositis is difficult to diagnose accurately without the presence of a characteristic dermatologic or myopathic condition [4]. Patients with typical dermatomyositis usually have a very abnormal skin surface, accompanied by progressive, symmetrical proximal muscle weakness. 30–50% of patients develop cutaneous disease 3–6 months before the appearance of myositis, while approximately 10% develop muscle symptoms before the appearance of cutaneous disease [5, 6]. About 20% of DM cases are classified as clinically amyopathic dermatomyositis (CADM), which is strongly associated with acute interstitial lung lesions, interstitial fibrosis, and has a very high mortality rate. In a study of 291 patients with CADM [7], 70% were diagnosed with non-amyopathic dermatomyositis and 13% with amyopathic dermatomyositis. Clinically, complete remission of cutaneous lesions is very difficult to achieve, which reflects the lack of understanding of the pathogenesis of dermatomyositis cutaneous lesions [8]. As the traditional view is that

the pathogenesis of autoimmune diseases is mainly due to excessive activation of effector T cells, glucocorticoids and immunosuppressive drugs are currently the main treatments for dermatomyositis [9]. The use of these drugs weakens the immunity of humoral and cellular immunity and also decreases the immune function of intrinsic immunity such as macrophages and NK cells, decreasing the body's resistance to pathogens and increasing the incidence of opportunistic infections, such as the Epstein-Barr Virus (EBV) and cytomegalovirus (CMV) blood disorders [10].

In addition, common histopathologic factors of DM skin lesions, often including vacuolar perivascular inflammation, interface dermatitis, increased skin mucin, and keratinised abnormal keratin-forming cells [11, 12], are also seen in cutaneous lupus erythematosus (CLE) lesions. This can make it more difficult to differentiate a rash associated with DM from one involving CLE, which makes the diagnosis of DM more difficult. In addition, dermatomyositis is closely associated with several types of cancer. Most patients have cancer within 1 year after the diagnosis of dermatomyositis, and thus, dermatomyositis is considered to be a paraneoplastic condition [13]. Therefore, it is urgent to find new diagnostic concepts and therapeutic approaches for dermatomyositis, and studies related to the identification of mRNA biomarkers for dermatomyositis are needed.

This manuscript is designed to probe the possible molecular mechanisms of DM. By identifying effective biomarkers through microarray analysis and then validating them through in vitro experiments, the pathogenesis of DM can be elucidated as well as the search for targeted therapies for DM.

2. Methods

2.1. Data Sources. The dermatomyositis gene datasets GSE142807 [8] (43 DM samples and 5 normal samples) and GSE11971 [14] (19 DM samples and 4 normal samples) were rooted in the Gene Expression Omnibus (GEO) databank, and the original document were processed and explained with the R package "affy" in a bioconductor for processing and annotation (http://www.bioconductor.org).

2.2. Cell Nurturing and Stimulation of Cells. Human skeletal muscle myoblasts (HSkM) were purchased from ScienCell Research Laboratories, located in USA. The myoblasts were cultured in Dulbecco's modified Eagle medium containing 4.5 mg/mL glucose + MEM 199 (ratio 4 : 1) with 20% fetal bovine serum, 100 IU penicillin, and 100 μg streptomycin. Myogenic cells were cultured in 6-well plates at a concentration of 5×104/mL at 37°C in a 5% CO_2 incubator, and the medium was renewed when the cells were fused to 60%. Lipopolysaccharides (LPS) [15] were used to stimulate myogenic cells to prepare a dermatomyositis cell model, after which the cells were collected for RNA-seq.

2.3. Methods for RNA Extraction and Transcript Library Formation. We first extracted total RNA from the cells using TRIzol reagent and then constructed RNA samples by RNA mass spectrometry using a Nanodrop microspectrophotometer. After enrichment of eukaryotic mRNA with polyA tails by magnetic beads with oligo (dT), mRNA was interrupted with buffer. We first synthesized cDNA first strand in the M-MuLV reverse transcriptase system using fragmented mRNA as template and random oligonucleotides as primers and then degraded RNA strand with RNaseH and synthesized cDNA second strand with dNTPs in the DNA polymerase I system. The purified double-stranded cDNA was end-repaired, A-tailed, and sequenced, and the cDNA of about 200 bp was screened with AMPure XP beads, then PCR amplified, and the PCR product was purified again with AMPure XP beads, and finally, the final result was achieved.

2.4. Differentially Expressed Gene Screening. Differential analysis of normal and dermatomyositis samples in the GEO dataset was performed using the "limma" package in R v4.0.4; differential analysis of normal and dermatomyositis model cell samples was performed using the DEseq2 package in R v4.0.4. The screening criteria were FDR < 0.05 and $\log2|FC| \geq 1$.

2.5. Weighted Gene Coexpression Network Analysis (WGCNA). WGCNA was executed using the WGCNA database in R v4.0.4 as follows. The correlation coefficients between pairs of all genes were calculated to construct the gene expression correlation matrix. After this, the correlation coefficients are weighted with power exponents, so that the correlation matrix of the expression is transformed into an adjacency matrix. The topological matrix (TOM) is used to calculate the association between genes, and the adjacency matrix is converted into a topological matrix based on the TOM values. The topological matrix has a prescribed algorithm for node dissimilarity, and the different gene modules are clustered using node dissimilarity. The expression of module eigengene (ME) and gene significance (GS) were calculated to associate different modules with phenotypes.

2.6. Protein-Protein Interaction Network (PPI). The mechanism of protein-protein interactions was established at the online analysis website, Metascape (https://metascape.org/gp/index.html#/main/step1). The MCODE algorithm in Cytoscape was used to extract hub genes and visualise the protein-protein interaction network.

2.7. KEGG and GO Enrichment Analyses. We established gene ontology (GO) and Kyoto Encyclopedia of Genes and Genomes (KEGG) pathway analysis of genes in the DAVID 6.8 database (https://david.ncifcrf.gov/). Enrichment results with $p < 0.05$ or FDR < 0.05 would indicate that it is statistically significant.

2.8. Gene Set Enrichment Analysis (GSEA). We wanted to know how gene expression affects the disease and divided the samples into high and low expression series on the

basis of the median expression values of the genes. The GSEA tool rooted in the Broad Institute (http://software.broadinstitute.org/gsea/downloads.jsp) was used to analyse the enrichment of KEGG and Hallmark pathways in the high and low expression series. Molecular characterisation was done making the use of the Hallmark gene set database (MsigDB, http://software.broadinstitute.org/gsea/msigdb). These pathways were considered meaningful gene sets when they satisfied $|NES| \geq 1$, FDR < 0.25, p value < 0.05.

2.9. Statistical Analysis. Statistical analyses were performed using R software v4.0.3 (R Foundation for Statistical Computing, Vienna, Austria). One-way ANOVA is taken for the samples with uniform variance, and the nonparametric test is taken for the samples with uneven variance. P value of <0.05 was considered statistically significant.

3. Results

3.1. Differentially Expressed Genes in Dermatomyositis. The GEO database was used to obtain the DM-related expression datasets GSE142807 (43 DM samples and 5 normal samples) and GSE11971 (19 DM samples and 4 normal samples). After differentially expressed gene screening, all 2746 upregulated genes and 382 downregulated genes were obtained from GSE142807 (Figure 1(a)); all 236 upregulated genes and 663 downregulated genes were obtained in GSE11971. Subsequently, the two differential gene datasets were combined using the ComBat function of the R package "sva" to remove the batch effect, and a total of 925 gene expression matrices were obtained. Functional and pathway enrichment analysis was established, and the results showed that the gene sets were significantly enriched in KEGG pathways, including shigellosis, endocytosis, and Alzheimer's disease (Figure 1(c)). GO functional enrichment analysis significantly enriched the gene set, mainly in protein binding, metabolic processes of organic nitrogen compounds, and intracellular fractions (Figures 1(d)–1(f)).

3.2. Analysis of the Weighted Gene Coexpression Network. The expression information of the combined GSE142807 and GSE11971 differential gene sets were used as input files, and the samples were first hierarchically clustered to eliminate outlier samples. To determine the scale-free network, we set power = 14 as a soft threshold parameter and then constructed a coexpression matrix (Figure 2(a)). The network graph was constructed using dynamic tree cuts and merging similarity modules, so we could obtain 3 groups of 925 genes, and these different sections have been marked with different color notations (Figure 2(b)). Next, the Pearson correlation between different modules and different clinical characteristics was calculated.

The Pearson correlation coefficients of different modules with different clinical features were calculated, and the most relevant module for dermatomyositis was obtained: the turquoise module (Figure 2(c)). The association between the genes in the turquoise module and the clinical phenotypes of dermatomyositis was analysed separately, and the correlation was good, with a significant linear correlation (Figure 2(d)).

3.3. Protein-Protein Interaction Network Analysis (PPI). Through the online analysis website Metascape, the genes in the turquoise module were analysed to obtain PPI protein network interactions, and the gene information was further visualized and the network was constructed (Figure 3). We use the MCODE plugin in Cytoscape to count the features of each node in the network graph, and the MCODE with the largest score value 4 was selected; genes in MCODE 4 were MX2, GBP2, OAS2, IFI6, IFIT2, BST2, OAS3, OAS1, IRF1, SAMHD1, RSAD2, EGR1, XAF1, and IRF2, which were mainly enriched in the interferon signalling pathway and immune system in the cytokine signalling pathway, as given in Table 1.

3.4. Cell Line RNA-Seq Analysis. Based on the FPKM values of each gene in the cell lines, we show the expression distribution of different sample genes or transcripts by an expression distribution map (Figure 4(a)). In general, the gene expression distribution map can be used to assess the differences between samples in the library in terms of building, sequencing, comparison, or quantification. In addition, based on the expression results of each sample, we used PCA analysis and calculated Pearson correlation coefficients between samples to determine the reproducibility between samples and to assist in excluding outliers (Figure 4(b)). The differentially expressed genes in the cell line samples are shown in a volcano plot (Figure 4(c)), and all 29 differentially expressed genes were obtained, including 27 differentially upregulated genes and 2 differentially downregulated genes. By overlaying the differentially expressed genes in the cell line samples with the previous genes in MCODE4, 3 key genes are obtained with the names MX2, OAS1, and OAS2.

3.5. Expression Validation of MX2, OAS1, and OAS2. The expressions of MX2, OAS1, and OAS2 in the 3 different datasets were compared. The results showed that MX2, OAS1, and OAS2 were significantly upregulated in the GSE11971 and GSE142807 datasets compared to normal samples in dermatomyositis samples (Figures 5(a) and 5(b)). In cell line samples, MX2, OAS1, and OAS2 were highly expressed in LPS-treated cell lines compared to normal cell lines (Figure 5(c)).

3.6. Genomic Enrichment Analysis. KEGG signalling pathway and Hallmark functional enrichment analyses were performed for each of MX2, OAS1, and OAS2. KEGG signalling pathway analysis showed that all 3 were enriched in the cytosolic DNA signalling and cytokine and cytokine receptor interaction signalling pathways; the results of Hallmark functional enrichment analysis showed that all 3 were enriched in interferon-α response and interferon-γ response functions (Figure 6).

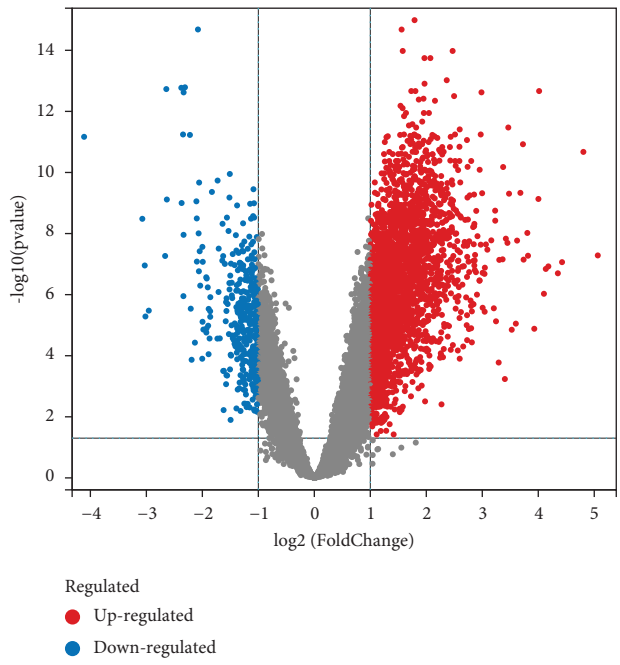

(a)

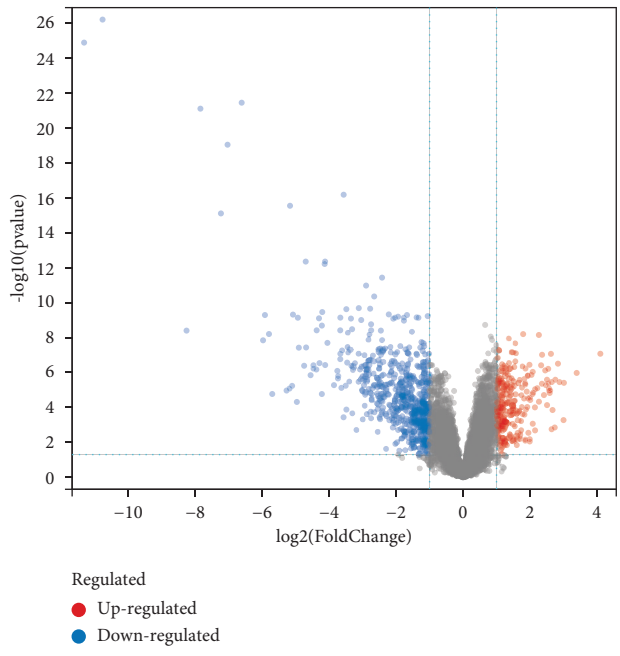

(b)

Figure 1: Continued.

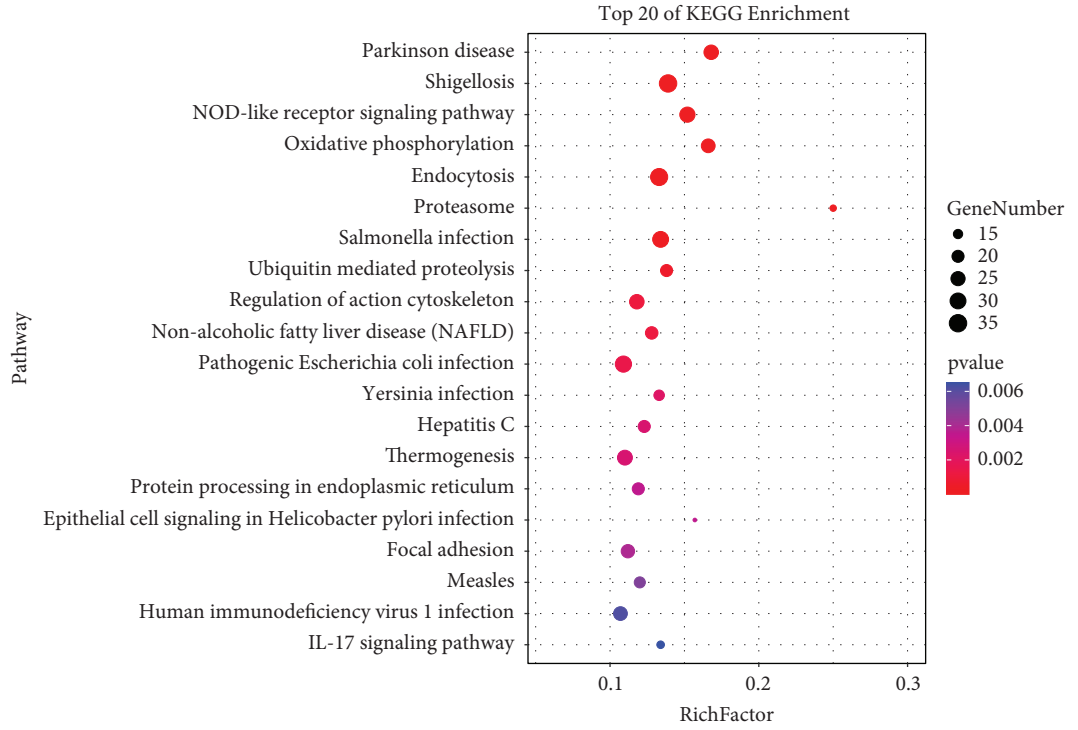

(c)

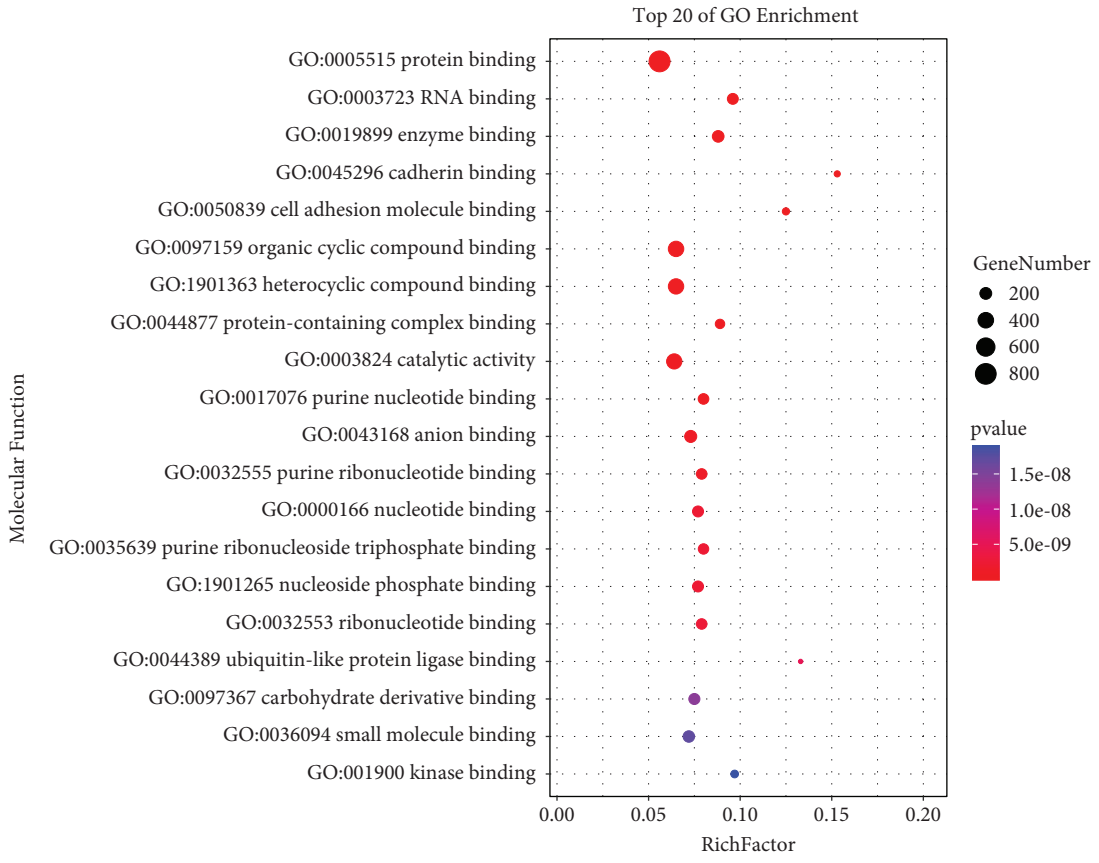

(d)

Figure 1: Continued.

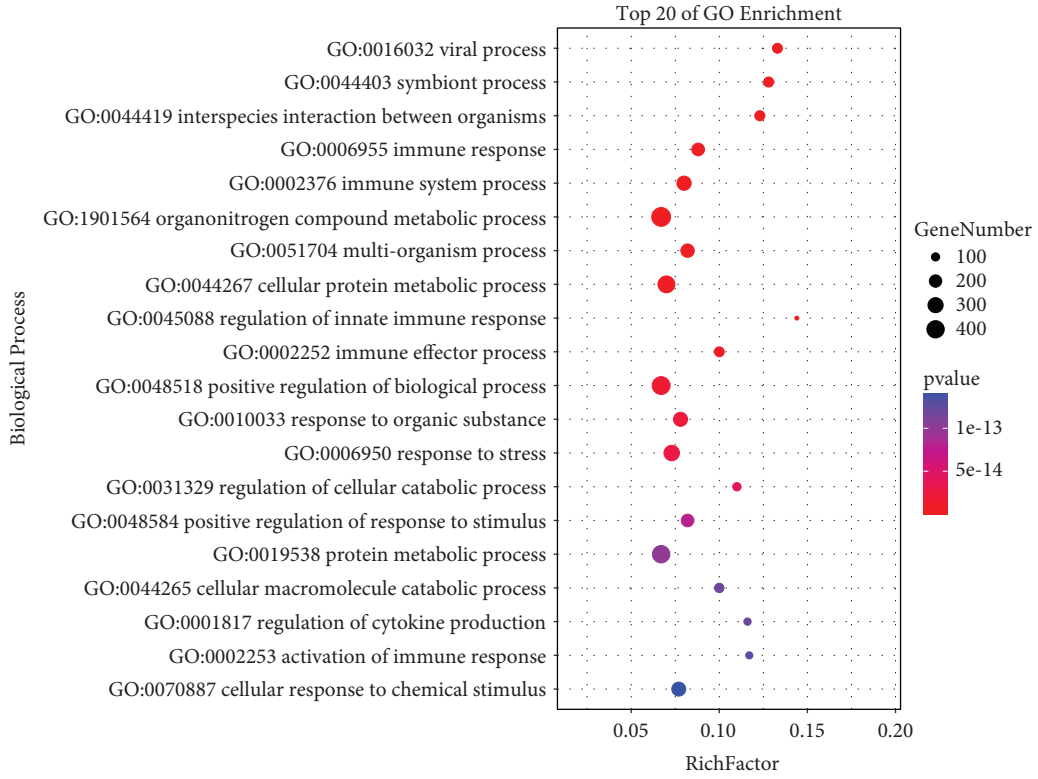

(e)

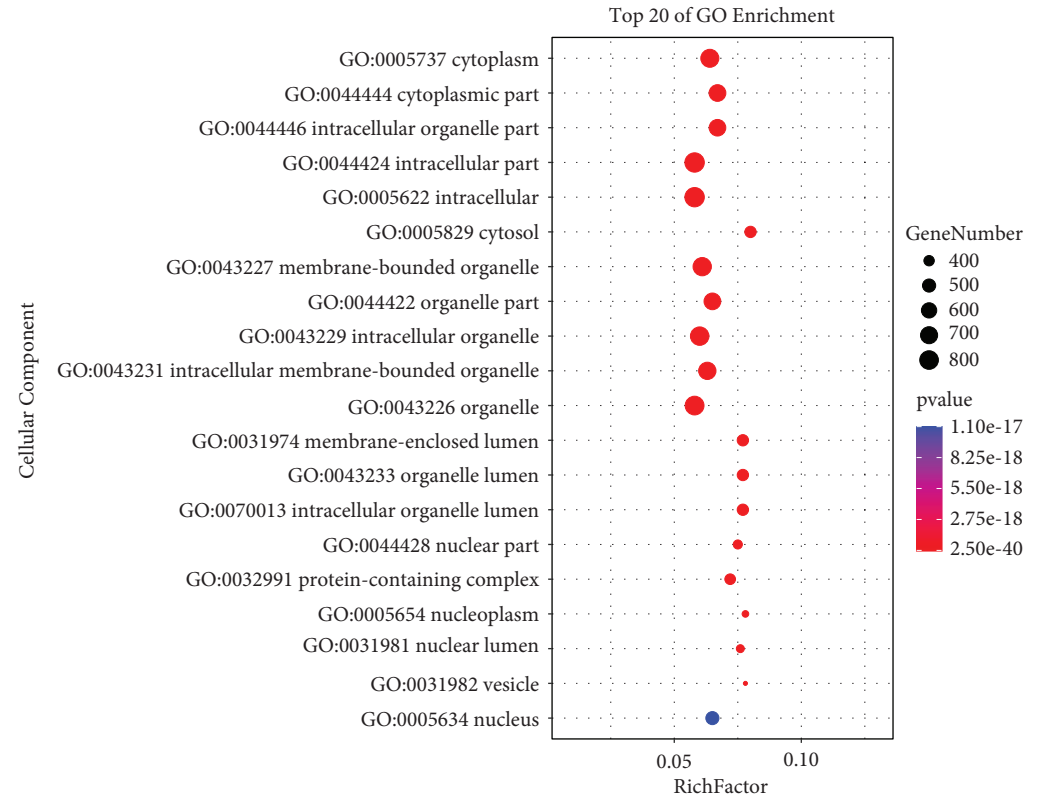

(f)

Figure 1: Analysis of differentially expressed genes in GSE14807 and GSE11971 datasets. (a) Volcano plot showing differentially expressed genes in GSE14807. (b) Volcano plot showing differentially expressed genes in GSE11971. (c) Enrichment analysis of KEGG pathway for differential gene ensemble. (d) Enrichment analysis of molecular function for differential gene ensemble. (e) Enrichment analysis of biological processes for differential gene ensemble. (f) Enrichment analysis of cellular components for differential gene ensemble.

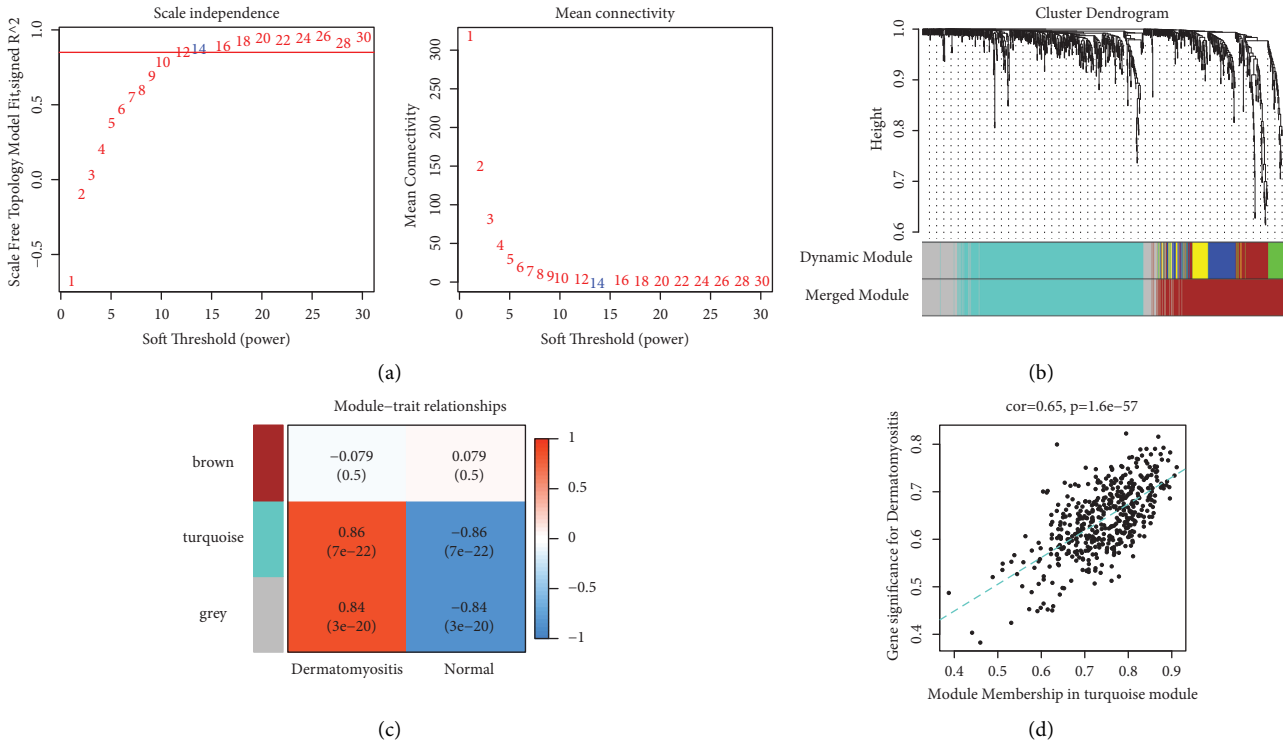

FIGURE 2: Construction of the weighted coexpression network and identification of key modules. (a) Network topology analysis of soft thresholds. (b) Identification of coexpression modules and cluster dendrogram. (c) Heat map analysis of module gene and clinical phenotype correlations. (d) Turquoise correlation of genes within modules with clinical phenotype data.

4. Discussion

Dermatomyositis is due to autoimmune connective tissue lesions, which usually include diseases such as autoantibody positivity and immune abnormalities. It has a complex clinical presentation, so there is little hope of a cure [16, 17]. Skin invasion is usually visible in all dermatomyositis subtypes, and skin problems often persist after successful treatment of muscle disease, greatly affecting patients' quality of life [18]. In a prospective cohort study of 74 patients with DM who received systemic therapy, only 38% of patients had remission of skin disease during the 3-year follow-up period [19]. Because many physicians have difficulty recognising dermatomyositis in the absence of muscle invasion, this often leads to misdiagnosis, as well as delays in treatment and initial investigations, and delays or misdiagnosis can increase the risk of cancer in patients [20, 21]. There is therefore a pressing need for appropriate biomarkers to identify dermatomyositis in clinical practice.

In this study, we used a multistep approach to identify differentially expressed genes in DM from microarray data and performed weighted gene coexpression network and protein interaction network analyses. Combined with in vitro experiments, we finally identified three key genes: MX2, OAS1, and OAS2. The results demonstrated that these 3 genes are highly expressed in dermatomyositis and are enriched in KEGG pathways, including the cytosolic DNA signalling pathway and cytokine-cytokine receptor interaction signalling pathway. Hallmark function was enriched in interferon-α response and interferon-γ response function.

Although the exact pathogenesis of dermatomyositis has not been fully elucidated, studies have suggested that the mechanism may cause upregulation or abnormalities in transduction signalling through the interferon pathway [22, 23]. There is substantial evidence that interferons (IFNs) are considered critical in skin disease and muscle disease in patients with dermatomyositis. Increased type I IFN signalling found in skin biopsies of lesions from 16 patients with dermatomyositis [24] and skin activity in adult dermatomyositis has been shown to correlate with type I IFN gene signatures [25, 26]. IFN signalling can be used to measure disease activity in adult and adolescent subjects with dermatomyositis markers, and identification of the signal in peripheral blood samples could be an alternative to the more invasive muscle biopsy technique [27]. Epstein-Barr virus (EBV) and cytomegalovirus (CMV) belong to the human herpes virus (HHV) family, and most adults worldwide are susceptible to these viruses [28, 29]. EBV infection leads to excessive production of interferons (IFNs) by T cells, which are proinflammatory cytokines essential for systemic autoimmunity. CMV can infect several cell types,

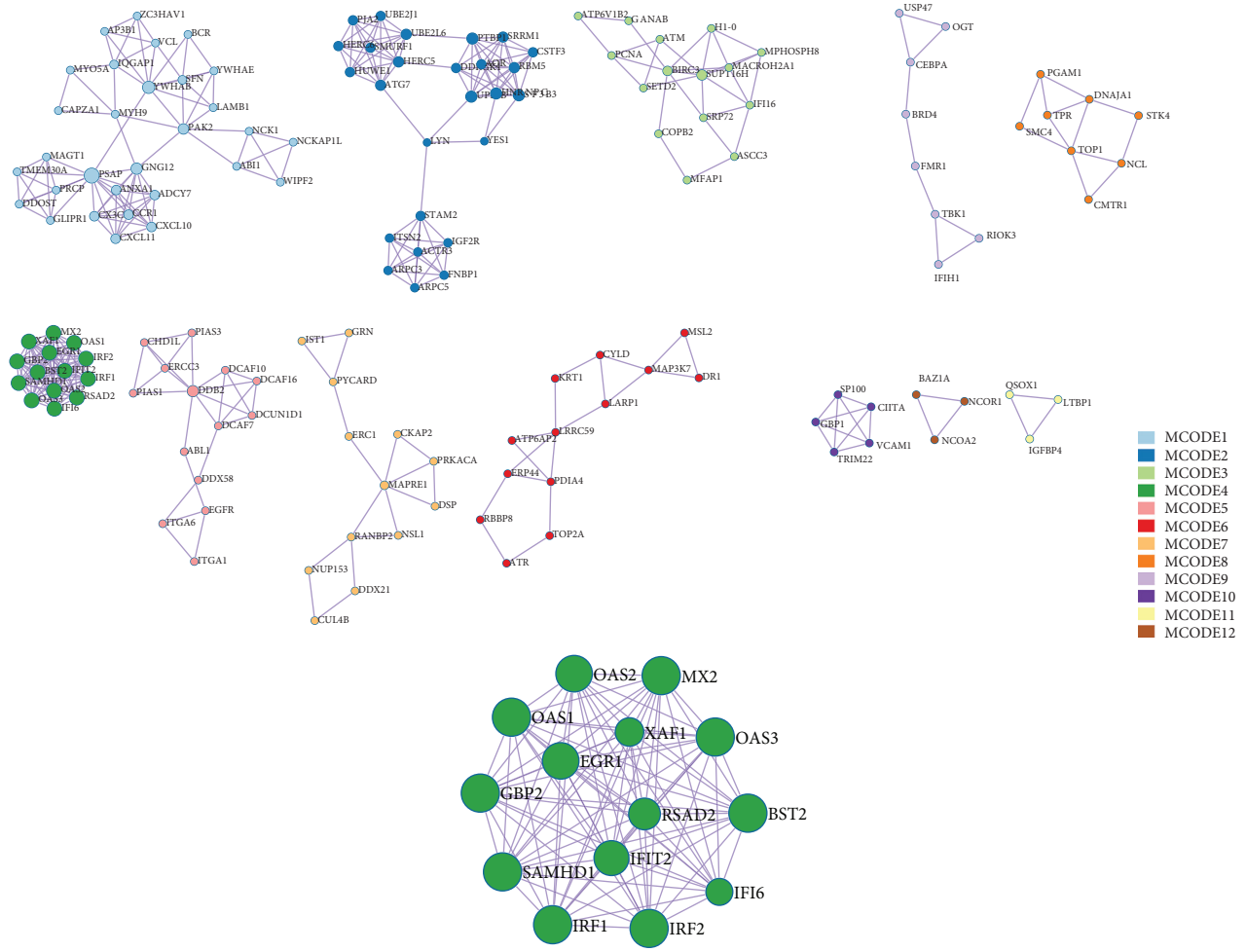

Figure 3: Map of gene interaction network in turquoise module.

Table 1: Top 5 MCODE pathway and process enrichment analysis for each group.

MCODE	GO	Description	Log_{10} (p)
MCODE 1	R-HSA-195258	RHO GTPase effectors	−12.0
MCODE 1	R-HSA-9664422	FCGR3A-mediated phagocytosis	−10.4
MCODE 1	R-HSA-9664417	Leishmania phagocytosis	−10.4
MCODE 2	R-HSA-72163	mRNA splicing—major pathway	−11.4
MCODE 2	R-HSA-72172	mRNA splicing	−11.3
MCODE 2	R-HSA-72203	Processing of capped intron-containing pre-mRNA	−10.4
MCODE 3	GO:0040029	Regulation of gene expression, epigenetic	−6.1
MCODE 3	GO:0051052	Regulation of the DNA metabolic process	−6.0
MCODE 3	GO:0034728	Nucleosome organization	−5.8
MCODE 4	R-HSA-909733	Interferon alpha/beta-signalling	−37.1
MCODE 4	R-HSA-913531	Interferon signalling	−30.3
MCODE 4	R-HSA-1280215	Cytokine signalling in the immune system	−22.4
MCODE 5	R-HSA-5696395	Formation of incision complex in GG-NER	−10.9
MCODE 5	R-HSA-5696399	Global genome nucleotide excision repair (GG-NER)	−9.4
MCODE 5	R-HSA-5696398	Nucleotide excision repair	−8.8

including epithelial cells, hematopoietic cells, and connective tissue [30]. EBV and CMV have been found to play a role in autoimmunity and may trigger a range of inflammatory factors that can exacerbate immune system disorders [31]. Although the pathogenesis of dermatomyositis is currently unclear, an immune imbalance is thought to be central to disease progression.

As an inhibitor of interferon (IFN) induction, myxovirus resistance-2 (MX2) has potent inhibitory activity against HIV-1 as well as herpes and hepatitis B viruses [32, 33].

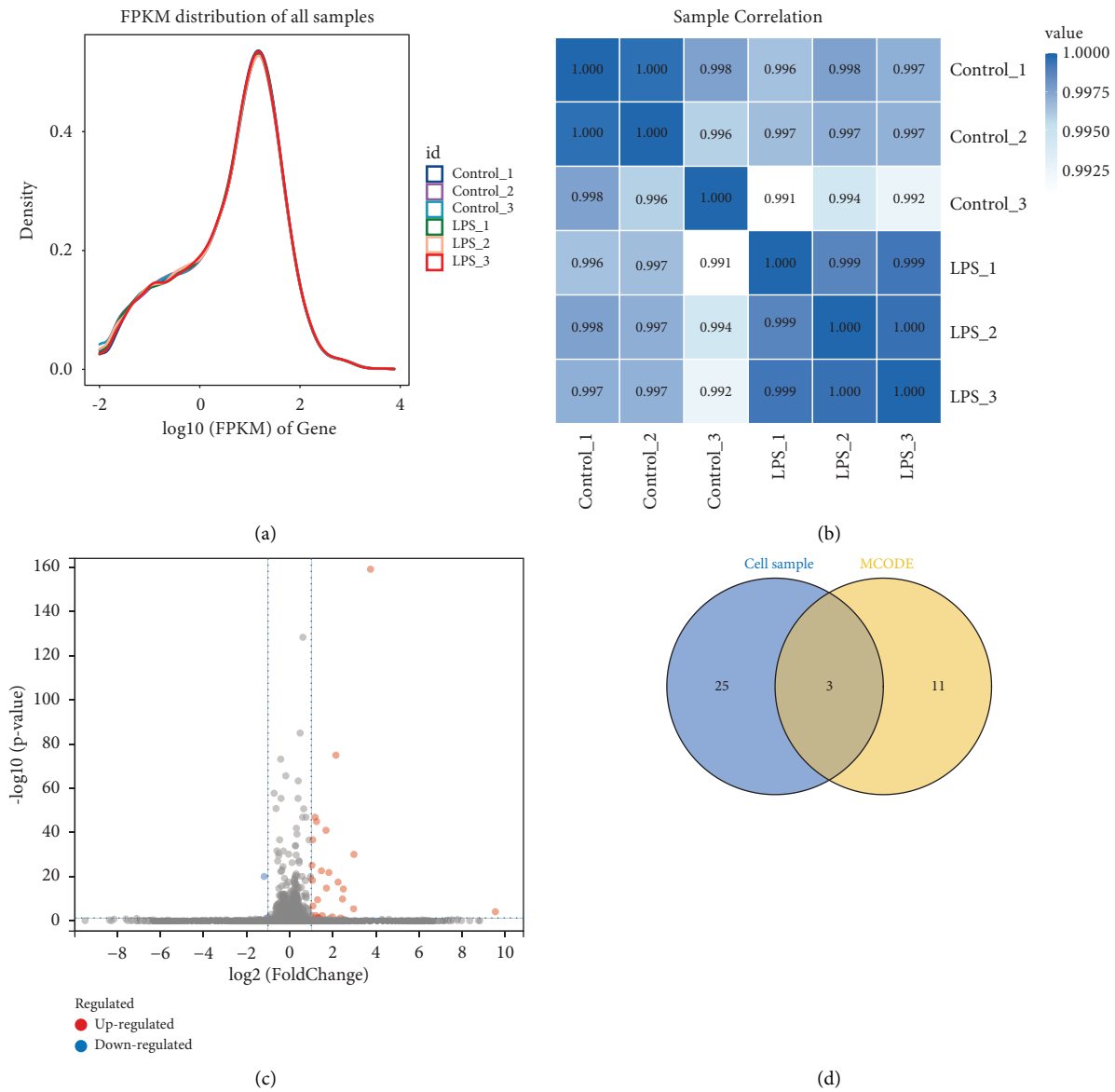

Figure 4: Cell line RNA-seq analysis. (a) Gene expression abundance map. (b) Sample correlation heat map. (c) Volcano map showing differentially expressed genes. (d) Overlap of differentially expressed genes in cell lines with genes in MCODE4.

Expression of MX2 reduces permissibility to various lentiviruses, and knockdown of MX2 expression using RNA interference has been shown to reduce IFN-α anti-HIV-1 potency [34]. It has been shown that MX2 is a cell autonomous anti-HIV-1 resistance factor whose purposeful mobilization may serve as a novel approach for the treatment of HIV/AIDS [35]. In the present study, MX2 is also expected to be a potential target for dermatomyositis treatment.

Interferon- (IFN-) induced double-stranded RNA activating enzymes are the so-called OAS proteins. The OAS patients includes 4 members: OAS1, OAS2, OAS3, and OASL [36]. Expression of the OAS gene family is highly regulated in patients with juvenile dermatomyositis, similar to the immune response to dsRNA virus infection [37]. Several studies have suggested that excessively keratinised cells may be responsible for the development of skin lesions in patients with dermatomyositis, in which OAS genes may activate one of the apoptotic cell death mechanisms [38] and resulted that the OAS/RNaseL pathway is a new effector of BRCA1 and IFN-γ-mediated apoptosis [39].

The present study has some drawbacks, as there is a lack of follow-up wet experiments to verify the mechanisms of the 3 genes identified to strengthen the results, in addition to the fact that the impact of the 3 genes on clinical prognosis has not yet been studied. This should be analysed in future studies in the context of clinical samples and survival.

In conclusion, a total of 3 genes associated with the development of dermatomyositis—MX2, OAS1, and OAS2—were identified in this study through a series of

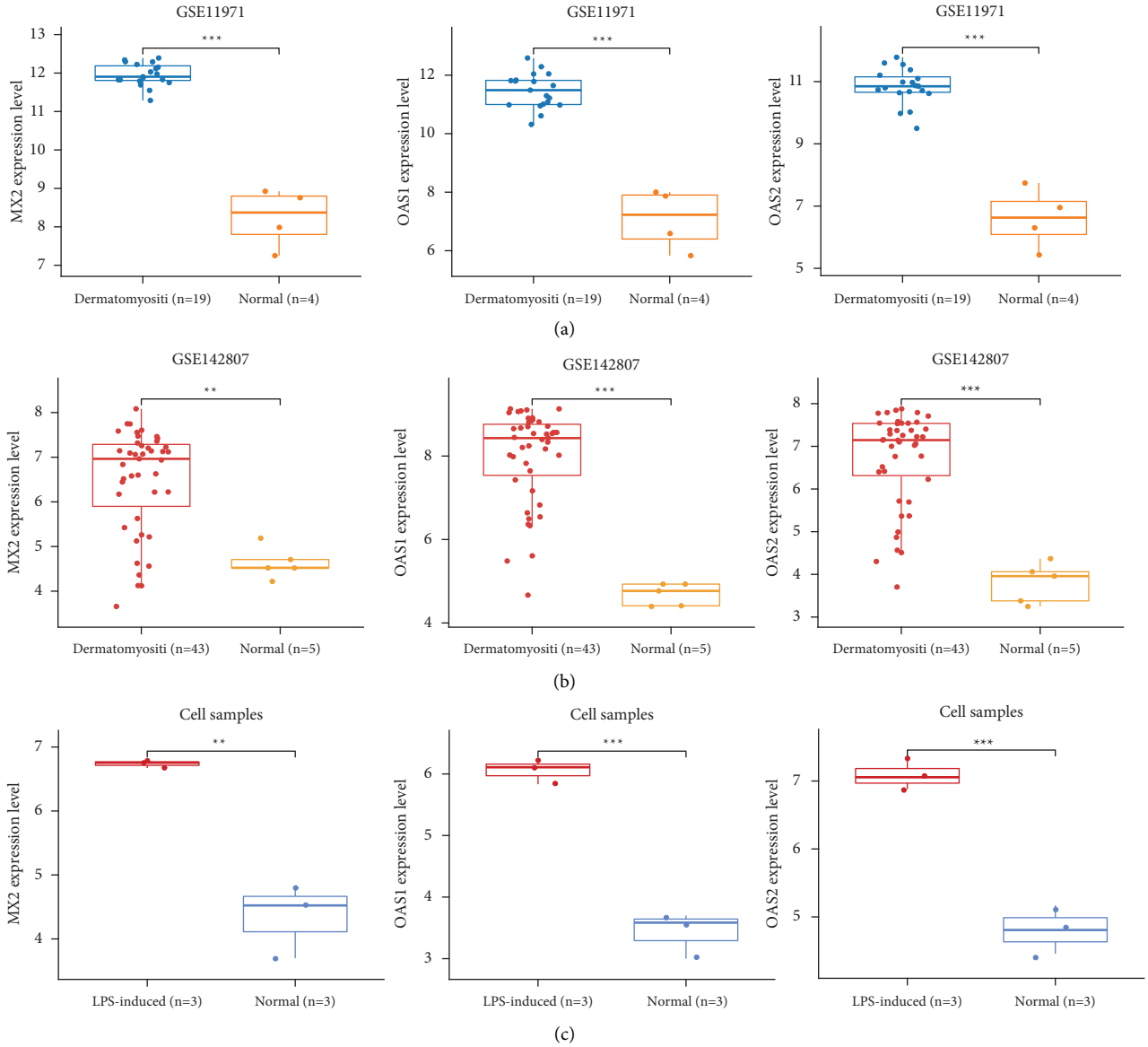

Figure 5: Expression validation of MX2, OAS1, and OAS2. (a) Expression of MX2, OAS1, and OAS2 in the GSE11971 dataset. (b) Expression of MX2, OAS1, and OAS2 in the GSE142807 dataset. (c) Expression of MX2, OAS1, and OAS2 in cell line samples.

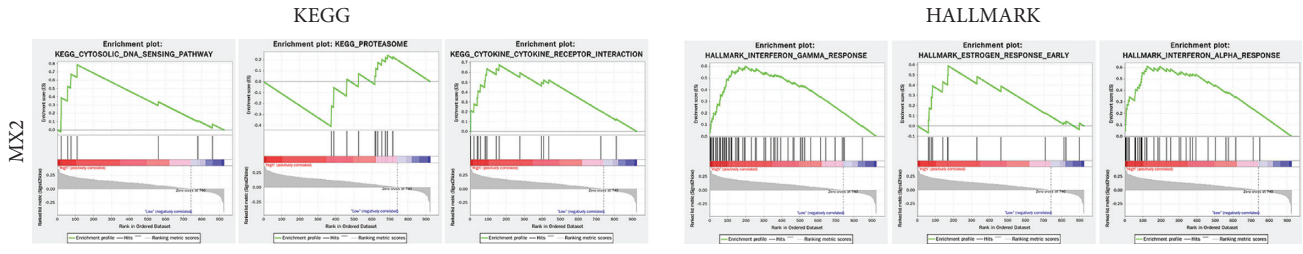

Figure 6: Continued.

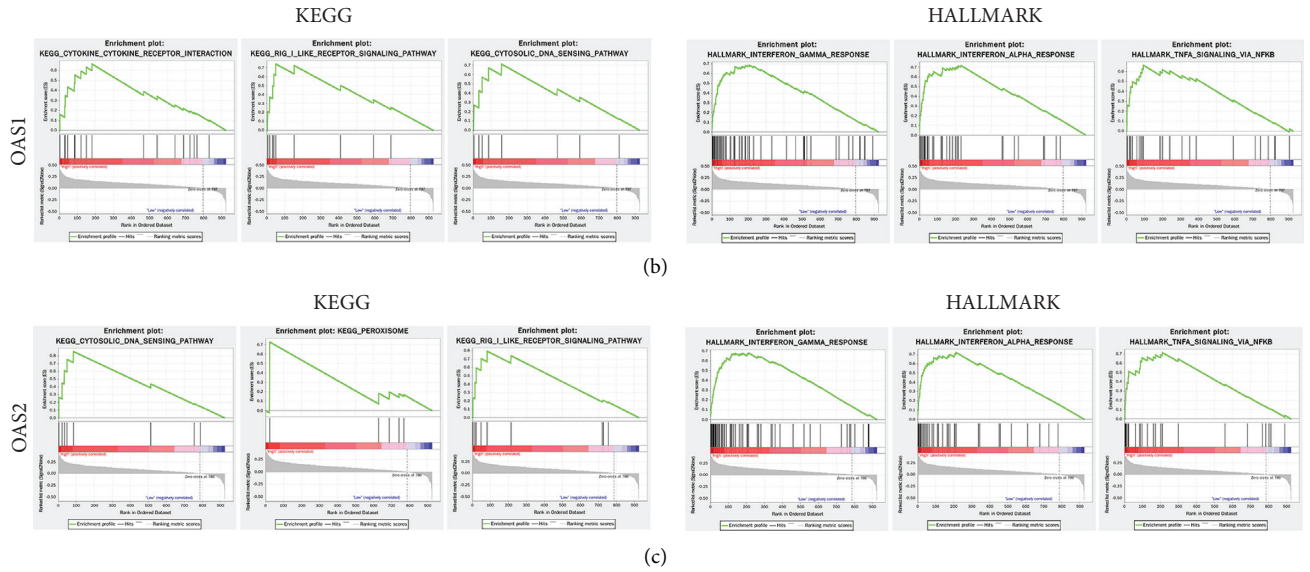

Figure 6: Gene set enrichment analysis. (a) MX2 in KEGG and Hallmark signalling pathway enrichment analyses results. (b) OAS1 in KEGG and Hallmark signalling pathway enrichment analyses results. (c) OSA2 in KEGG and Hallmark signalling pathway enrichment analyses results.

information biology analyses, which are expected to be biomarkers or drug targets to some extent for the diagnosis of dermatomyositis. Further studies are needed to elucidate the related mechanisms.

Data Availability

The data used to support the findings of this study are included within the article.

Additional Points

First time to explore the potential pathogenesis of dermatomyositis through the information biology analysis of gene chip. First time to identify diagnostic biomarkers and biological pathways in dermatomyositis based on WGCNA.

Conflicts of Interest

The authors declare that they have no conflicts of interest.

Acknowledgments

This work was supported by Application of Bioinformatics to Screen for Differentially Expressed Genes in Dermatomyositis and Related Experimental Studies (S2019JJKWLH0028).

References

[1] M. J. Bendewald, D. A. Wetter, X. Li, and M. D. Davis, "Incidence of dermatomyositis and clinically amyopathic dermatomyositis: a population-based study in olmsted county, Minnesota," *Archives of Dermatology*, vol. 146, pp. 26–30, 2010.

[2] L. C. Strowd and J. L. Jorizzo, "Review of dermatomyositis: establishing the diagnosis and treatment algorithm," *Journal of Dermatological Treatment*, vol. 24, no. 6, pp. 418–421, 2013.

[3] F. Galimberti, Y. Li, and A. P. Fernandez, "Clinically amyopathic dermatomyositis: clinical features, response to medications and malignancy-associated risk factors in a specific tertiary-care-centre cohort," *British Journal of Dermatology*, vol. 174, no. 1, pp. 158–164, 2016.

[4] M. E. DeWane, R. Waldman, and J. Lu, "Dermatomyositis: clinical features and pathogenesis," *Journal of the American Academy of Dermatology*, vol. 82, no. 2, pp. 267–281, 2020.

[5] J. P. Callen, "Cutaneous manifestations of dermatomyositis and their management," *Current Rheumatology Reports*, vol. 12, no. 3, pp. 192–197, 2010.

[6] R. D. Sontheimer, "The management of dermatomyositis: current treatment options," *Expert Opinion on Pharmacotherapy*, vol. 5, no. 5, pp. 1083–1099, 2004.

[7] P. Gerami, J. M. Schope, L. McDonald, H. W. Walling, and R. D. Sontheimer, "A systematic review of adult-onset clinically amyopathic dermatomyositis (dermatomyositis siné myositis): a missing link within the spectrum of the idiopathic inflammatory myopathies," *Journal of the American Academy of Dermatology*, vol. 54, no. 4, pp. 597–613, 2006.

[8] L. C. Tsoi, M. Gharaee-Kermani, C. C. Berthier et al., "Il18-containing 5-gene signature distinguishes histologically identical dermatomyositis and lupus erythematosus skin lesions," *JCI Insight*, vol. 5, 2020.

[9] M. Feng, H. Guo, C. Zhang et al., "Absolute reduction of regulatory t cells and regulatory effect of short-term and low-dose il-2 in polymyositis or dermatomyositis," *International Immunopharmacology*, vol. 77, p. 105912, 2019.

[10] Y. Shimojima, W. Ishii, M. Matsuda, and S. Ikeda, "Phenotypes of peripheral blood lymphocytes and cytokine expression in polymyositis and dermatomyositis before treatment and after clinical remission," *Clinical Medicine Insights: Arthritis and Musculoskeletal Disorders*, vol. 5, pp. 77–87, 2012.

[11] R. Su, Z. Li, Y. Wang et al., "Imbalance between th17 and regulatory t cells in patients with systemic lupus erythematosus

combined ebv/cmv viraemia," *Clinical & Experimental Rheumatology*, 2019.

[12] P. W. Wolstencroft, K. E. Rieger, H. W. Leatham, and D. F. Fiorentino, "Clinical factors associated with cutaneous histopathologic findings in dermatomyositis," *Journal of Cutaneous Pathology*, vol. 46, no. 6, pp. 401–410, 2019.

[13] C. Cassius, H. Le Buanec, J.-D. Bouaziz, and R. Amode, "Biomarkers in adult dermatomyositis: tools to help the diagnosis and predict the clinical outcome," *Journal of Immunology Research*, p. 2019, 2019.

[14] Y. W. Chen, R. Shi, N. Geraci, S. Shrestha, H. Gordish-Dressman, and L. M. Pachman, "Duration of chronic inflammation alters gene expression in muscle from untreated girls with juvenile dermatomyositis," *BMC Immunology*, vol. 9, pp. 43–13, 2008.

[15] T. Sugiura, M. Harigai, Y. Kawaguchi et al., "Increased IL-15 production of muscle cells in polymyositis and dermatomyositis," *International Immunology*, vol. 14, no. 8, pp. 917–924, 2002.

[16] J. Wienke, C. T. Deakin, L. R. Wedderburn, F. Van Wijk, and A. van Royen-Kerkhof, "Systemic and tissue inflammation in juvenile dermatomyositis: from pathogenesis to the quest for monitoring tools," *Frontiers in Immunology*, vol. 9, p. 2951, 2018.

[17] K. S. Berntsen, E. Edvardsen, B. H. Hansen, B. Flatø, I. Sjaastad, and H. Sanner, "Cardiorespiratory fitness in long-term juvenile dermatomyositis: a controlled, cross-sectional study of active/inactive disease," *Rheumatology*, vol. 58, no. 3, pp. 492–501, 2019.

[18] R. Goreshi, M. Chock, K. Foering et al., "Quality of life in dermatomyositis," *Journal of the American Academy of Dermatology*, vol. 65, no. 6, pp. 1107–1116, 2011.

[19] P. W. Wolstencroft, L. Chung, S. Li, L. Casciola-Rosen, and D. F. Fiorentino, "Factors associated with clinical remission of skin disease in dermatomyositis," *JAMA Dermatology*, vol. 154, no. 1, pp. 44–51, 2018.

[20] D. M. Da Silva, B. Patel, and V. P. Werth, "Dermatomyositis: a diagnostic dilemma," *Journal of the American Academy of Dermatology*, vol. 79, no. 2, pp. 371–373, 2018.

[21] Z. Yang, F. Lin, B. Qin, Y. Liang, and R. Zhong, "Polymyositis/dermatomyositis and malignancy risk: a metaanalysis study," *Journal of Rheumatology*, vol. 42, no. 2, pp. 282–291, 2015.

[22] L. Kao, L. Chung, and D. F. Fiorentino, "Pathogenesis of dermatomyositis: role of cytokines and interferon," *Current Rheumatology Reports*, vol. 13, no. 3, pp. 225–232, 2011.

[23] C. Huard, S. V. Gullà, D. V. Bennett, A. J. Coyle, R. A. Vleugels, and S. A. Greenberg, "Correlation of cutaneous disease activity with type 1 interferon gene signature and interferon β in dermatomyositis," *British Journal of Dermatology*, vol. 176, no. 5, pp. 1224–1230, 2017.

[24] D. Wong, B. Kea, R. Pesich et al., "Interferon and biologic signatures in dermatomyositis skin: specificity and heterogeneity across diseases," *PLoS One*, vol. 7, no. 1, Article ID e29161, 2012.

[25] S. Gao, H. Luo, H. Zhang, X. Zuo, L. Wang, and H. Zhu, "Using multi-omics methods to understand dermatomyositis/polymyositis," *Autoimmunity Reviews*, vol. 16, no. 10, pp. 1044–1048, 2017.

[26] B. Han and Q. Guo, "Clinically amyopathic dermatomyositis caused by a tattoo," *Case Reports in Rheumatology*, vol. 2018, Article ID 7384681, 4 pages, 2018.

[27] E. C. Baechler, J. W. Bauer, C. A. Slattery et al., "An interferon signature in the peripheral blood of dermatomyositis patients is associated with disease activity," *Molecular Medicine*, vol. 13, no. 1-2, pp. 59–68, 2007.

[28] L. Sternbæk, A. H. Draborg, M. T. Østerlund et al., "Increased antibody levels to stage-specific epstein–barr virus antigens in systemic autoimmune diseases reveal a common pathology," *Scandinavian Journal of Clinical and Laboratory Investigation*, vol. 79, pp. 7–16, 2019.

[29] H. T. Maecker, "Opening the door on the cmv immune response in aging," *The Journal of Infectious Diseases*, vol. 215, no. 8, pp. 1179-1180, 2017.

[30] V. Bhat, A. Joshi, R. Sarode, and P. Chavan, "Cytomegalovirus infection in the bone marrow transplant patient," *World Journal of Transplantation*, vol. 5, no. 4, p. 287, 2015.

[31] N. Rasmussen, A. Draborg, C. Nielsen, S. Jacobsen, and G. Houen, "Antibodies to early ebv, cmv, and hhv6 antigens in systemic lupus erythematosus patients," *Scandinavian Journal of Rheumatology*, vol. 44, no. 2, pp. 143–149, 2015.

[32] M. Kane, S. S. Yadav, J. Bitzegeio et al., "Mx2 is an interferon-induced inhibitor of hiv-1 infection," *Nature*, vol. 502, no. 7472, pp. 563–566, 2013.

[33] M. Crameri, M. Bauer, N. Caduff et al., "Mxb is an interferon-induced restriction factor of human herpesviruses," *Nature Communications*, vol. 9, pp. 1980–2016, 2018.

[34] N. M. Bourke, S. Napoletano, C. Bannan et al., "Control of HIV infection by IFN-α: implications for latency and a cure," *Cellular and Molecular Life Sciences*, vol. 75, no. 5, pp. 775–783, 2018.

[35] C. Goujon, O. Moncorgé, H. Bauby et al., "Human mx2 is an interferon-induced post-entry inhibitor of hiv-1 infection," *Nature*, vol. 502, no. 7472, pp. 559–562, 2013.

[36] A. J. Sadler and B. R. G. Williams, "Interferon-inducible antiviral effectors," *Nature Reviews Immunology*, vol. 8, no. 7, pp. 559–568, 2008.

[37] G. Musumeci, P. Castrogiovanni, I. Barbagallo et al., "Expression of the oas gene family is highly modulated in subjects affected by juvenile dermatomyositis, resembling an immune response to a dsrna virus infection," *International Journal of Molecular Sciences*, vol. 19, no. 9, p. 2786, 2018.

[38] J. L. Pablos, B. A. Santiago, M. Galindo, P. E. Carreira, C. Ballestin, and J. J. Gomez-Reino, "Keratinocyte apoptosis and p53 expression in cutaneous lupus and dermatomyositis," *The Journal of Pathology*, vol. 188, no. 1, pp. 63–68, 1999.

[39] P. B. Mullan, A. M. Hosey, N. E. Buckley et al., "The 2,5 oligoadenylate synthetase/RNaseL pathway is a novel effector of BRCA1- and interferon-γ-mediated apoptosis," *Oncogene*, vol. 24, no. 35, pp. 5492–5501, 2005.

Hindawi
Journal of Oncology
Volume 2021, Article ID 8223263, 13 pages
https://doi.org/10.1155/2021/8223263

Research Article

Weighted Gene Correlation Network Analysis Identifies Specific Functional Modules and Genes in Esophageal Cancer

Wei Xu, Jian Xu, Zhiqiang Wang, and Yuequan Jiang

Chongqing Key Laboratory of Translational Research for Cancer Metastasis and Individualized Treatment, Chongqing University Cancer Hospital, Chongqing 400030, China

Correspondence should be addressed to Yuequan Jiang; jyq1964@yahoo.com

Received 25 November 2021; Revised 12 December 2021; Accepted 14 December 2021; Published 27 December 2021

Academic Editor: Fu Wang

Objective. Esophageal cancer (ESCA) is one of the most aggressive malignancies globally with an undesirable five-year survival rate. Here, this study was conducted for determining specific functional genes linked with ESCA initiation and progression. *Methods*. Gene expression profiling of ESCA was curated from TCGA (containing 160 ESCA and 11 nontumor specimens) and GSE38129 (30 paired ESCA and nontumor tissues) datasets. Differential expression analysis was conducted between ESCA and nontumor tissues with adjusted p value <0.05 and |log2fold-change|>1. Weighted gene coexpression network analysis (WGCNA) was conducted for determining the ESCA-specific coexpression modules and genes. Thereafter, ESCA-specific differentially expressed genes (DEGs) were intersected. Functional enrichment analysis was then presented with clusterProfiler package. Protein-protein interaction was conducted, and hub genes were determined. Association of hub genes with pathological staging was evaluated, and survival analysis was presented among ESCA patients. *Results*. This study determined 91 ESCA-specific DEGs following intersection of DEGs and ESCA-specific genes in TCGA and GSE38129 datasets. They were remarkably linked to cell cycle progression and carcinogenic pathways like the p53 signaling pathway, cellular senescence, and apoptosis. Ten ESCA-specific hub genes were determined, containing *ASPM*, *BUB1B*, *CCNA2*, *CDC20*, *CDK1*, *DLGAP5*, *KIF11*, *KIF20A*, *TOP2A*, and *TPX2*. They were prominently associated with pathological staging. Among them, KIF11 upregulation was in relation to undesirable prognosis of ESCA patients. *Conclusion*. Collectively, we determined ESCA-specific coexpression modules and hub genes, which offered the foundation for future research concerning the mechanistic basis of ESCA.

1. Introduction

Esophageal cancer (ESCA) ranks the eighth major cancer type as well as the sixth major cause of cancer-relevant deaths across the globe [1]. Tobacco and alcohol consumption are the main environmental risk factors of ESCA. The five-year survival rate is nearly 15% [2]. It mainly contains two histological subtypes: esophageal squamous cell carcinoma (approximately 90%) and esophageal adenocarcinoma (around 10%) [3]. Patients' advanced clinical presentation is linked to locally late and distant metastasis, which contributes to undesirable survival outcome. Additionally, because of tumor heterogeneity and acquired drug resistance, inherent resistance to radiotherapy and chemotherapy triggers therapeutic failure and unfavorable survival rate [2]. ESCA therapy depends upon patients' and tumors' features, especially the tumor, node, metastasis (TNM) staging system [4]. In the early stage, patients are suitable for endoscopic resection, while those in the advanced stage receive surgical resection, chemotherapy, chemoradiotherapy, or their combination [4]. For patients with unresectable ESCA, systemic chemotherapy is applied. Additionally, immunotherapy has emerged as a therapeutic option for advanced or metastatic patients [5]. Although the therapeutic options have been steadily increasing, the molecular mechanisms underlying ESCA remain indistinct.

The pathogenesis of ESCA is a multistep process, involving distinct stages until eventually cancers [6]. Hence, to focus on the molecular mechanisms underlying the initiation and progression of ESCA may assist uncover underlying diagnostic markers or treatment targets. Weighted gene coexpression network analysis (WGCNA) is a reliable

systematic biological algorithm, which may emphasize coexpression genomic modules and effectively evaluate the interactions between coexpression modules and clinical phenotypes [7]. This algorithm has been widely utilized for discovering cancer-specific modules and hub genes like bladder cancer [7], hepatocellular carcinoma [8], and lung cancer [9]. Limited studies have applied the WGCNA method to uncover the pathogenesis of ESCA. For instance, Nangraj et al. identified hub genes shared between Barrett's esophagus and esophageal adenocarcinoma through integrated analysis of protein-protein interaction (PPI) and WGCNA [10]. Through WGCNA, *miR-92b-3p* was determined as a pathogenic gene in ESCA [11]. Integrated analysis of WGCNA and network pharmacology deciphered the molecular mechanisms of compound Kushen injection in ESCA treatment [12]. Here, this study adopted the WGCNA algorithm for determining specific functional modules and genes in ESCA, offering the foundation for future research concerning the mechanistic basis of ESCA.

2. Materials and Methods

2.1. Data Collection and Preprocessing. The RNA-seq data of ESCA were retrieved from the Cancer Genome Atlas (TCGA) GDC Application Programming Interface. Gene expression profiling data (read counts) were processed and transformed into gene ID Ensembl (version 90). In total, 160 ESCA and 11 normal tissues were included. Microarray expression profiling of 30 ESCC tumors and adjacent normal tissues was curated from the GSE38129 dataset [13] in the Gene Expression Omnibus (GEO; https://www.ncbi.nlm.nih.gov/gds/) repository. This dataset was in accordance with the GPL571 platform ((HG-U133 A_2) Affymetrix Human Genome U133A 2.0 Array). The raw expression profiling was background-corrected and normalized by quantile utilizing the robust multiarray average (RMA) method.

2.2. Differential Expression Analysis. Differentially expressed genes (DEGs) were selected utilizing the linear models for microarray data (limma; version 3.50.0) package through comparison of the expression profiling between ESCA and normal tissues [14]. The matched p values of gene symbols following the t-test were calculated, and adjusted p value <0.05 and $|\log2\text{fold-change}|>1$ were set as the selection criteria. The volcano and heatmap of the DEGs were drawn.

2.3. WGCNA. Coexpression networks were separately established in TCGA and GSE38129 datasets utilizing WGCNA package (version 1.69) [15]. The genes with the first 25% standard deviation were chosen as the input genes. For constructing a scale-free network, the optimal soft threshold power value (β; ranging from 1 to 20) was determined with the "pickSoftThreshold" function through calculation of the scale-free fit index. Pearson's correlation matrix was conducted for evaluating the similarity among the pairwise genes utilizing the "cor" function. Thereafter, the adjacency was determined in accordance with β and Pearson's correlation matrix utilizing the "TOMsimilarity" function. Meanwhile, the corresponding dissimilarity (dissTOM) was determined. The modules were segmented with a dynamic cut tree algorithm, and similar modules were merged into one. Module eigengenes (MEs) that were the first principal component of gene expression patterns within a specific module were identified for each module.

2.4. Identification of ESCA-Relevant Coexpression Models. In this study, the most crucial critical feature was tissue type that was designated as ESCA tumor and normal specimens. Pearson correlation between MEs and clinical feature was analyzed. Modules that possessed the strongest correlation coefficient were determined as the ESCA-relevant coexpression models. Module membership indicates the intramodule connectivity of any gene within a given module. The higher the absolute value of module membership, the higher the negative or positive correlation between the gene with the module eigengenes. Gene significance was utilized for incorporating external information to the coexpression network. The higher the absolute value of gene significance, the higher the biological significance of a gene for tissue type. ESCA-relevant genes within the ESCA-relevant coexpression models were determined in accordance with module membership >0.8 and gene significance >0.5.

2.5. Identification of ESCA-Specific DEGs. For achieving the intersection of DEGs and coexpressed genes, an online web tool (http://bioinfogp.cnb.csic.es/tools/venny/index.html) was adopted for plotting Venn diagram.

2.6. Function Enrichment Analysis. Functional annotation of ESCA-specific DEGs was presented with the clusterProfiler package (version 4.2.0), containing Gene Ontology (GO) and Kyoto Encyclopedia of Genes and Genomes (KEGG) pathway analysis [16]. GO terms comprised of the biological process (BP), cellular component (CC), and molecular function (MF).

2.7. Protein-Protein Interaction (PPI) Analysis. The PPI network of ESCA-specific DEGs was conducted on the basis of the Search Tool for the Retrieval of Interacting Genes/Proteins (STRING; version 11.0; https://string-db.org) online tool [17]. The CytoHubba plugin [18] of Cytoscape software (version 3.7.2) [19] was adopted for selecting the hub genes within the PPI network [18]. Herein, the first 10 genes were determined as hub genes.

2.8. Survival Analysis. In accordance with the optimal cutoff value determined by survival package, ESCA patients were stratified into high and low expression groups of the 10 ESCA-specific hub genes. Kaplan–Meier curves of overall survival were conducted between groups, and log-rank tests were utilized for comparing the survival differences.

2.9. Statistical Analysis. All the analyses in this study were implemented utilizing *R* software (version 3.5.1). Student's *t* test or Wilcoxon test was adopted for comparisons between groups. Spearman correlation analysis was carried out to evaluate the interactions of the 10 ESCA-specific hub genes with pathological staging of ESCA patients. P value<0.05 indicated the statistical significance.

3. Results

3.1. Exploration of DEGs in ESCA. For investigating the genetic alterations during the progression from normal to ESCA, we conducted differential expression analysis between ESCA tumors and normal tissues both in TCGA and GSE38129 datasets. In TCGA cohort, compared with 11 normal tissues, 1221 genes presented remarkable downregulation while 1169 genes displayed prominent upregulation in 160 ESCA tumors in accordance with adjusted p value <0.05 and |log2fold-change|>1 (Figures 1(a) and 1(b); Supplementary Table 1). With the same selection criteria, in the GSE38129 dataset, we determined 360 upregulated and 376 downregulated genes in 30 ESCA tumors in comparison to 30 nontumor tissues (Figures 1(c) and 1(d); Supplementary Table 2).

3.2. Establishment of a Coexpression Network and Discovery of ESCA-Specific Coexpression Module in the TCGA Dataset. We first curated gene expression matrix of ESCA patients from TCGA cohort and chose the genes with the top 25% variances for subsequent analysis. No outlier sample was found, and we conducted a sample clustering tree, as shown in Figure 2(a). Thereafter, the soft threshold power value was set as 10 (scale-free topology $R^2 = 0.90$) for constructing a scale-free network (Figure 2(b)). The adjacency matrix and the topological overlap matrix were separately developed. In total, 9 coexpression modules were clustered in accordance with the average hierarchical clustering and dynamic cutting tree (Figure 2(c)). The association of coexpression modules with clinical trait was analyzed. In Figure 2(d), the yellow module displayed the strongest correlation to tissue type, indicating that this module was strongly linked to ESCA progression. In line with module membership >0.8 and gene significance >0.5, we determined ESCA-specific genes (Figures 2(e) and 2(f)).

3.3. Development of a Coexpression Network and Discovery of ESCA-Specific Coexpression Module in the GSE38129 Cohort. The coexpression network was also developed in the GSE38129 dataset. In accordance with the mRNA expression matrix, we selected the genes with the top 25% variances. As shown in Figure 3(a), there was no outlier sample among 30 paired ESCA tumors and nontumors. Afterwards, we established a scale-free network in line with the soft threshold power value = 20 (scale-free topology $R^2 = 0.90$; Figure 3(b)). Following construction of the adjacency matrix and the topological overlap matrix, we determined 7 coexpression modules on the basis of the average hierarchical clustering and dynamic cutting tree (Figure 3(c)). In Figure 3(d), the turquoise module presented the strongest association with tissue type, demonstrating that this module was strongly linked to ESCA progression. Following module membership >0.8 and gene significance >0.5, ESCA-specific genes were determined (Figures 3(e) and 3(f)).

3.4. Identification of ESCA-Specific DEGs and Their Biological Significance. For determining ESCA-specific DEGs, we intersected the DEGs and the ESCA-specific genes in TCGA and GSE38129 cohorts. As a result, 91 ESCA-specific DEGs were finally identified (Figure 4(a) and Table 1). Their biological significance was further evaluated through GO and KEGG enrichment analysis. In Figure 4(b) and Table 2, we noted that the ESCA-specific DEGs were remarkably linked to cell cycle progression like chromosome segregation, nuclear division, mitotic nuclear division, and sister chromatid segregation. Additionally, the ESCA-specific DEGs were in relation to ESCA progression-relevant KEGG pathways like cell cycle, DNA replication, cellular senescence, base excision repair, mismatch repair, p53 signaling pathway, homologous recombination, nucleotide excision repair, and apoptosis (Figure 4(c) and Table 3).

3.5. Establishment of a PPI Network and Discovery of ESCA-Specific Hub Genes. For uncovering the interactions of the ESCA-specific DEGs, we conducted a PPI network in accordance with the STRING online tool. As shown in Figure 5(a), there were close interactions of proteins derived from the ESCA-specific DEGs. Utilizing CytoHubba plugin, we further determined the 10 ESCA-specific hub genes among them, containing *TOP2A* (score = 4.45 E + 23), *ASPM* (score = 4.45 E + 23), *CDK1* (score = 4.45 E + 23), *CDC20* (score = 4.45 E + 23), *CCNA2* (score = 4.45 E + 23), *KIF20 A* (score = 4.45 E + 23), *KIF11* (score = 4.45 E + 23), *DLGAP5* (score = 4.45 E + 23), *TPX2* (score = 4.45 E + 23), and *BUB1B* (score = 4.45 E + 23; Figure 5(b)). These ESCA-specific hub genes might exert crucial roles in ESCA progression.

3.6. Association of the ESCA-Specific Hub Genes with Pathological Staging of ESCA. Further analysis was carried out for evaluating the associations of the ten ESCA-specific hub genes with diverse pathological staging of ESCA patients in TCGA cohort. Our results demonstrated that *ASPM*, *BUB1B*, *CCNA2*, *CDC20*, *CDK1*, *DLGAP5*, *KIF11*, *KIF20 A*, *TOP2A*, and *TPX2* presented the different expression in diverse pathological stages across ESCA patients (Figures 6(a)–6(j)). This indicated that the 10 ESCA-specific hub genes were remarkably linked to pathological staging of ESCA.

3.7. Association of the ESCA-Specific Hub Genes with ESCA Patients' Prognosis. In accordance with the optimal cutoff value of the expression of the ESCA-specific hub genes, we stratified ESCA patients in TCGA cohort into high and expression groups of *ASPM*, *BUB1B*, *CCNA2*, *CDC20*,

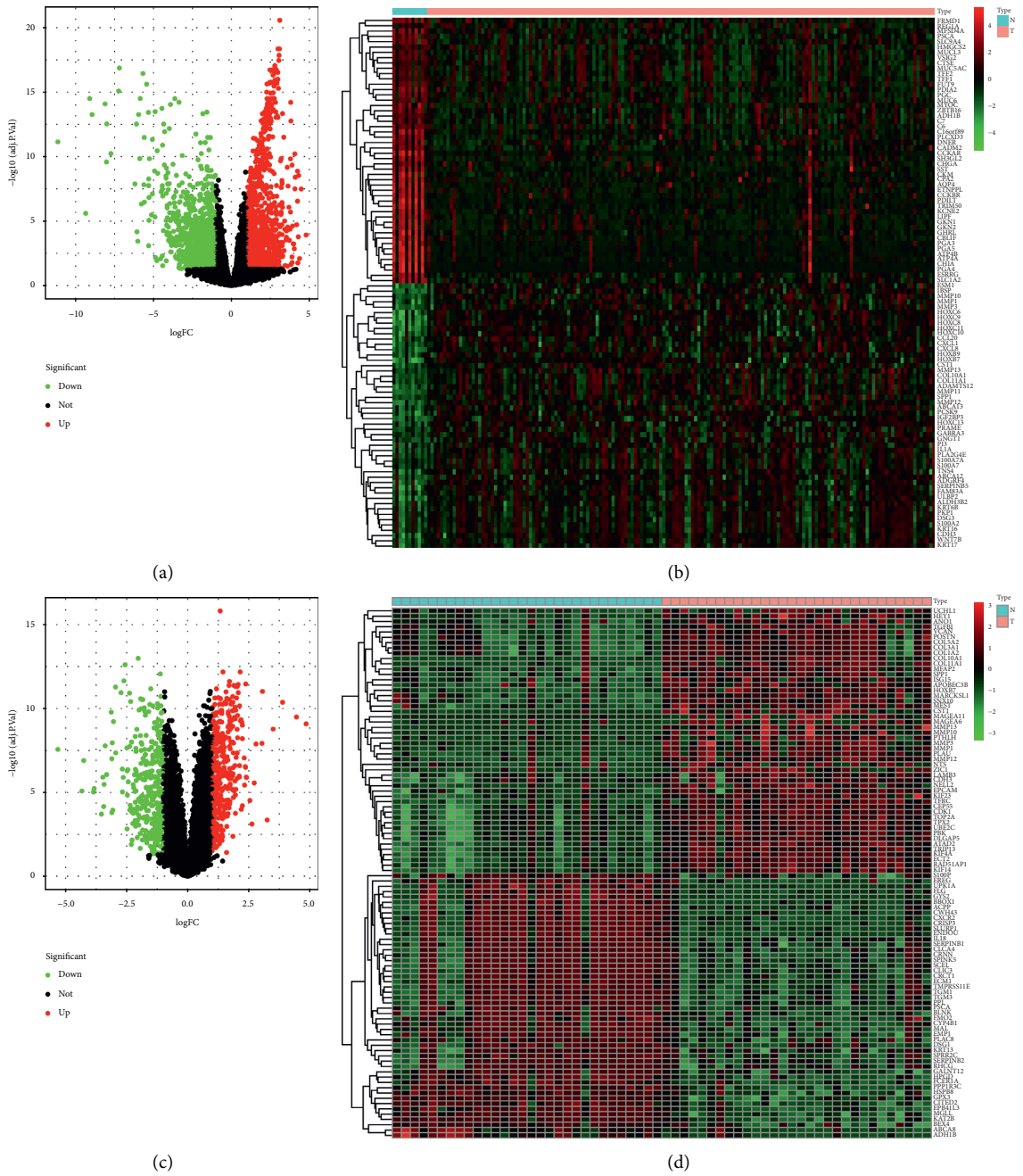

Figure 1: Analysis of DEGs of ESCA both in TCGA and GSE38129 datasets. (a) Volcano plots depict the results of differential expression analysis between 160 ESCA tumors and 11 normal tissues in TCGA cohort. Red bubble indicates upregulated gene in ESCA; green bubble represents downregulated gene in ESCA; black bubble is indicative of nonsignificant gene. (b) Heatmap visualizes the expression patterns of DEGs with adjusted p value <0.05 and |log2fold-change|>1 in 160 ESCA tumors (T) and 11 normal tissues (N) in TCGA cohort. Red represents upregulation, while green indicates downregulation. (c) Volcano plots present the results of differential expression analysis between 30 paired ESCA tumors and nontumor tissues in the GSE38129 dataset. Red bubble expresses upregulated gene in ESCA; green bubble is indicative of downregulated gene in ESCA; black bubble represents nonsignificant gene. (d) Heatmap displays the expression patterns of DEGs with adjusted p value <0.05 and |log2fold-change|>1 in 30 paired ESCA tumors (T) and nontumor tissues (N) in the GSE38129 dataset. Red is indicative of upregulation while green is indicative of downregulation.

*CDK*1, *DLGAP*5, *KIF*11, *KIF*20*A*, *TOP*2*A*, and *TPX*2 (Figures 7(a)–7(j)). Among them, we noted that ESCA patients in the high expression of the *KIF*11 group presented more undesirable overall survival outcome in comparison to those in the low expression of the *KIF*11 group.

4. Discussion

High-throughput sequencing technologies have improved our understanding about the heterogeneity and molecular basis underlying ESCA. At present, available biomarkers for

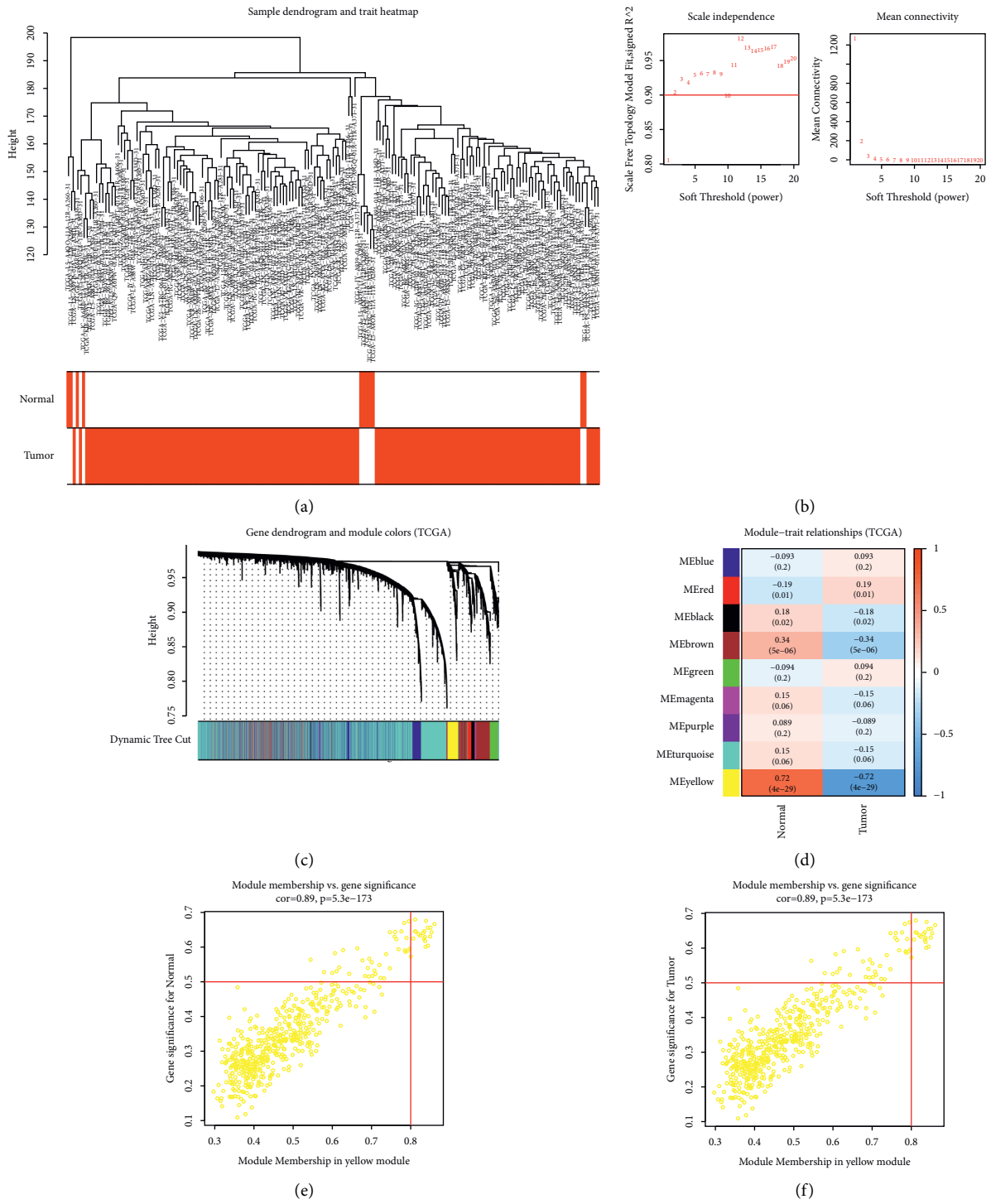

Figure 2: Establishment of a coexpression network and discovery of ESCA-specific coexpression module in the TCGA dataset. (a) Sample cluster analysis. (b) The scale-free network topology (left) as well as mean connectivity (right) under distinct soft threshold power values. (c) Gene dendrogram clustered in accordance with a dissimilarity measure. The upper panel indicates gene tree, and the bottom panel represents gene modules identified by diverse colors. (d) Heatmap visualizes the interaction between coexpression modules and clinical trait-tissue type. The upper number in each cell presents Pearson correlation coefficient between each module and tissue type. Meanwhile, the lower number indicates the p value. (e) Scatter plots depict the interaction between module membership and gene significance for normal tissue type for the yellow module. (f) Scatter plots present the interaction between module membership and gene significance for ESCA tumor tissue type for the yellow module.

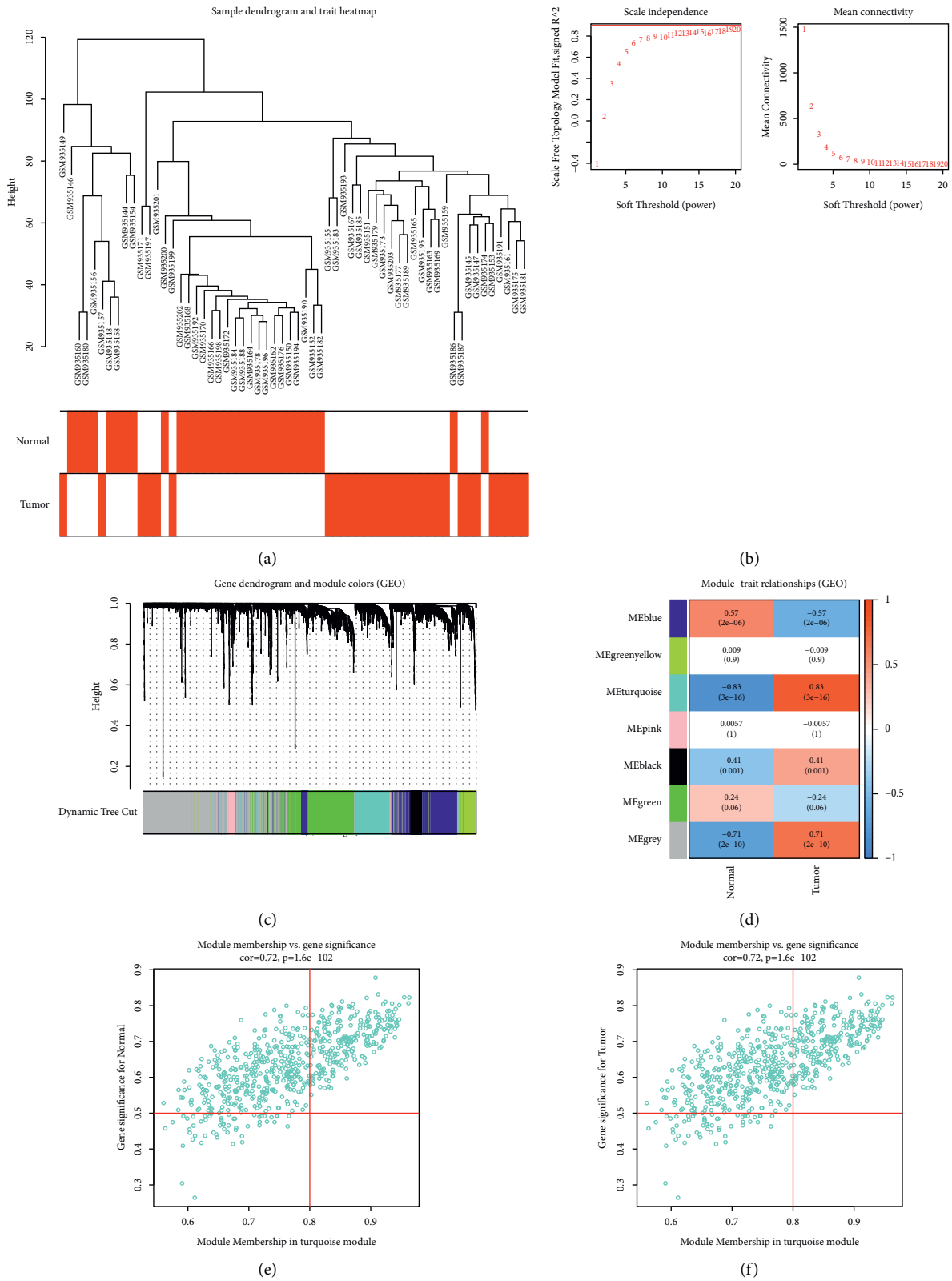

Figure 3: Development of a coexpression network and discovery of ESCA-specific coexpression module in the GSE38129 cohort. (a) Sample cluster analysis of 30 paired ESCA tumors and nontumors. (b) The scale-free network topology (left) and mean connectivity (right) following diverse soft threshold power values. (c) Gene dendrogram clustered in line with a dissimilarity measure. The upper panel presents gene tree and the bottom panel is indicative of gene modules signed by diverse colors. (d) Heatmap displays the relationship between coexpression modules and clinical trait-tissue type. The upper number in each cell presents Pearson correlation coefficient between each module and tissue type. Additionally, the lower number represents the p value. (e) Scatter plots showing the association between module membership and gene significance for normal tissue type for the turquoise module. (f) Scatter plots present the correlation between module membership and gene significance for ESCA tumor tissue type for the turquoise module.

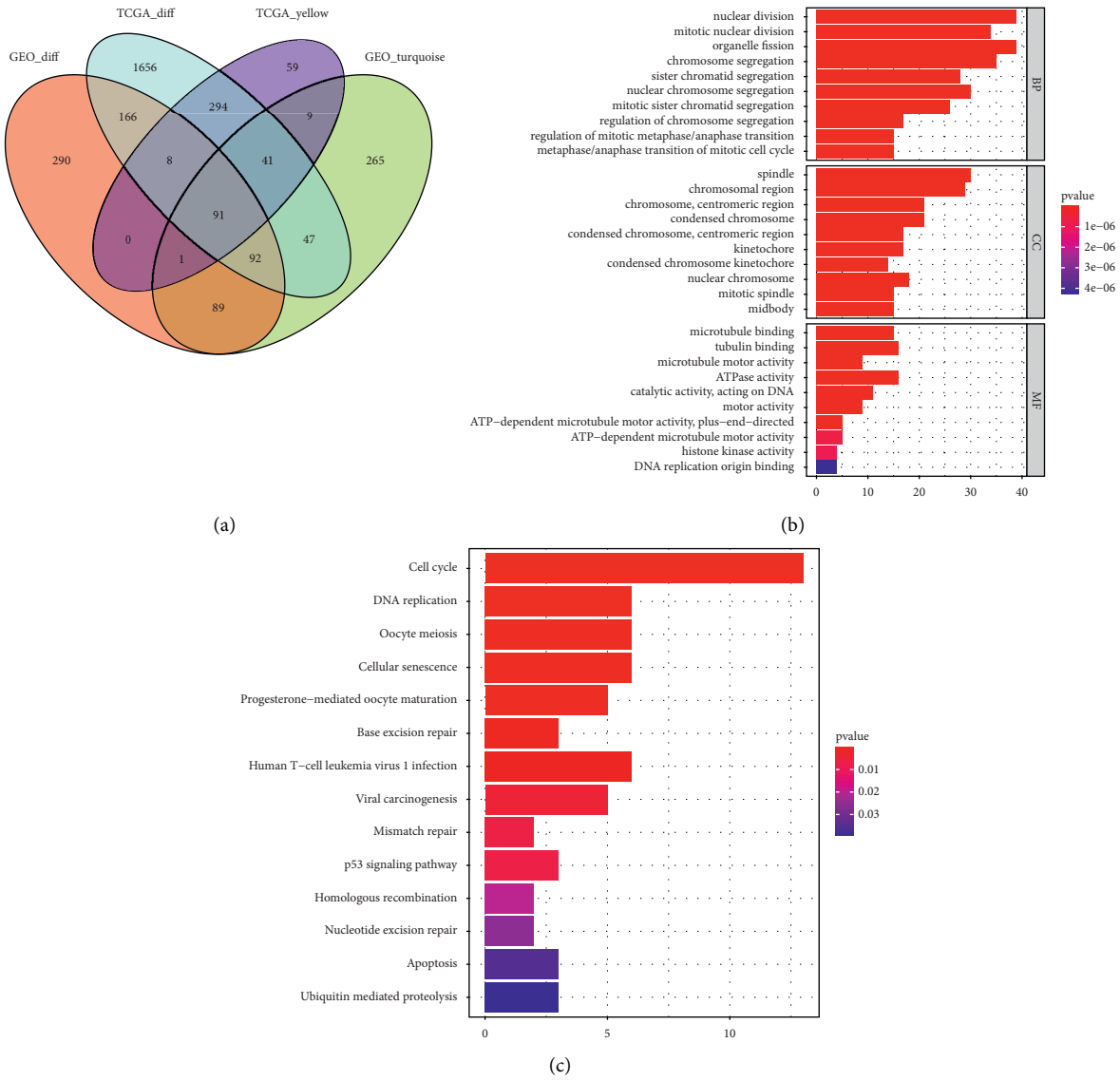

Figure 4: Identification of ESCA-specific DEGs and their biological significance. (a) Venn diagram depicts the intersection of the DEGs and the ESCA-specific genes in TCGA and GSE38129 cohorts. (b) GO enrichment results of the ESCA-specific DEGs. The first 10 enrichment results of BP, CC, and MF categories are separately displayed. (c) KEGG pathway enrichment results of the ESCA-specific DEGs.

prediction of ESCA patients' survival outcome remain nonsufficiently sensitive and specific. Hence, this study was conducted for discovering novel biomarkers for efficiently predicting ESCA patients' prognosis through the WGCNA algorithm, eventually lowering patients' morbidity and mortality.

Combining the DEGs and ESCA-specific genes in TCGA and GSE38129 cohorts, we determined 91 ESCA-specific DEGs. Our functional enrichment analyses uncovered that the ESCA-specific DEGs were remarkably linked to cell cycle progression and carcinogenic pathways like the p53 signaling pathway, cellular senescence, and apoptosis. This indicated that the ESCA-specific DEGs exerted crucial roles in ESCA progression. Additionally, there were prominent interactions between proteins derived from the ESCA-specific DEGs in accordance with the PPI network. Among them, the 10 ESCA-specific hub genes were finally determined, containing *ASPM*, *BUB1B*, *CCNA2*, *CDC20*, *CDK1*, *DLGAP5*, *KIF11*, *KIF20A*, *TOP2A*, and *TPX2*.

The tumorigenic roles of *ASPM* have been proposed in diverse cancer types. For instance, *ASPM* triggers prostate carcinoma stemness and progression through enhancing the Wnt-Dvl-3-beta-catenin pathway [20]. It is predictive of undesirable prognosis and modulates cellular proliferation in bladder carcinoma [21]. Its upregulation accelerates glioblastoma growth through modulating G1 restriction point progression as well as the Wnt-beta-catenin pathway [22]. Aberrantly expressed *ASPM* regulated by transcriptional factor *FoxM1* triggers the malignant progression of gliomas [23]. Additionally, it is linked to poor survival outcome as well as induces carcinogenesis in diffuse large B cell lymphoma [24]. Abnormally expressed *ASPM* induces the progression of lung squamous cell carcinoma through modulating *CDK4* [25]. Increasing evidences demonstrate

Table 1: The list of ESCA-specific DEGs.

ESCA-specific DEGs				
CBX3	FOXM1	DBF4	LMNB2	BLM
KAT2B	DLGAP5	MCM10	ASPM	C1orf112
KIF4A	PCNA	NUSAP1	UBE2S	AURKB
AURKA	KIF18B	CDT1	POLE2	FBXO5
CKS1B	CENPE	BUB1B	OIP5	MYBL2
ECT2	CDC6	BIRC5	CCNA2	CHEK1
HOXB7	CEP55	NCAPH	CCNB1	TFRC
KIF14	MCM6	DTL	MKI67	UBE2C
TRIP13	PRC1	NCAPG	DEPDC1	CDKN3
CITED2	CDCA3	FAM189A2	LMNB1	KIF20 A
MCM2	FEN1	HJURP	NDC1	GINS2
WDHD1	NUDT1	ORC6	KIF11	CENPF
RAD51AP1	RNASEH2A	HMMR	GINS1	STMN1
MAD2L1	PBK	ECHDC2	RUVBL1	EXO1
NDC80	CKS2	FYCO1	CENPM	DNMT1
NEK2	KIF18A	DDX39A	KNTC1	CDK1
KIF2C	SECISBP2L	MELK	CDC20	TPX2
KIF23	RAD54L	SHCBP1	TK1	TOP2A
SPC25				

Table 2: The detailed information of GO enrichment results of ESCA-specific genes.

ID	Description	Gene ratio	BgRatio	P value	Adjusted p	Q value	Count
GO: 0000280	Nuclear division	39/90	436/ 18862	$4.56E-40$	$6.17E-37$	$4.56E-37$	39
GO: 0140014	Mitotic nuclear division	34/90	296/ 18862	$2.13E-38$	$1.44E-35$	$1.07E-35$	34
GO: 0048285	Organelle fission	39/90	486/ 18862	$3.31E-38$	$1.49E-35$	$1.10E-35$	39
GO: 0007059	Chromosome segregation	35/90	337/ 18862	$5.24E-38$	$1.77E-35$	$1.31E-35$	35
GO: 0000819	Sister chromatid segregation	28/90	199/ 18862	$5.58E-34$	$1.51E-31$	$1.12E-31$	28
GO: 0098813	Nuclear chromosome segregation	30/90	273/ 18862	$4.07E-33$	$9.16E-31$	$6.77E-31$	30
GO: 0000070	Mitotic sister chromatid segregation	26/90	164/ 18862	$6.09E-33$	$1.18E-30$	$8.70E-31$	26
GO: 0051983	Regulation of chromosome segregation	17/90	89/18862	$4.02E-23$	$6.80E-21$	$5.02E-21$	17
GO: 0030071	Regulation of mitotic metaphase/anaphase transition	15/90	59/18862	$1.50E-22$	$2.25E-20$	$1.66E-20$	15
GO: 0007091	Metaphase/anaphase transition of mitotic cell cycle	15/90	61/18862	$2.63E-22$	$3.55E-20$	$2.63E-20$	15
GO: 0005819	Spindle	30/90	381/ 19520	$3.83E-29$	$4.34E-27$	$2.77E-27$	30
GO: 0098687	Chromosomal region	29/90	345/ 19520	$5.72E-29$	$4.34E-27$	$2.77E-27$	29
GO: 0000775	Chromosome, centromeric region	21/90	196/ 19520	$3.40E-23$	$1.72E-21$	$1.10E-21$	21
GO: 0000793	Condensed chromosome	21/90	217/ 19520	$3.00E-22$	$1.14E-20$	$7.26E-21$	21
GO: 0000779	Condensed chromosome, centromeric region	17/90	117/ 19520	$3.24E-21$	$9.84E-20$	$6.27E-20$	17
GO: 0000776	Kinetochore	17/90	137/ 19520	$5.31E-20$	$1.35E-18$	$8.57E-19$	17
GO: 0000777	Condensed chromosome kinetochore	14/90	106/ 19520	$5.13E-17$	$1.11E-15$	$7.10E-16$	14
GO: 0000228	Nuclear chromosome	18/90	250/ 19520	$7.75E-17$	$1.47E-15$	$9.38E-16$	18

Table 2: Continued.

ID	Description	Gene ratio	BgRatio	P value	Adjusted p	Q value	Count
GO: 0072686	Mitotic spindle	15/90	157/ 19520	$5.26E-16$	$8.89E-15$	$5.67E-15$	15
GO: 0030496	Midbody	15/90	193/ 19520	$1.17E-14$	$1.77E-13$	$1.13E-13$	15
GO: 0008017	Microtubule binding	15/89	269/ 18337	$3.07E-12$	$5.56E-10$	$3.91E-10$	15
GO: 0015631	Tubulin binding	16/89	368/ 18337	$2.33E-11$	$2.11E-09$	$1.49E-09$	16
GO: 0003777	Microtubule motor activity	9/89	69/18337	$4.41E-11$	$2.66E-09$	$1.87E-09$	9
GO: 0016887	ATPase activity	16/89	478/ 18337	$1.09E-09$	$4.92E-08$	$3.46E-08$	16
GO: 0140097	Catalytic activity, acting on DNA	11/89	204/ 18337	$4.22E-09$	$1.53E-07$	$1.08E-07$	11
GO: 0003774	Motor activity	9/89	129/ 18337	$1.26E-08$	$3.67E-07$	$2.59E-07$	9
GO: 0008574	ATP-dependent microtubule motor activity, plus-end-directed	5/89	17/18337	$1.42E-08$	$3.67E-07$	$2.59E-07$	5
GO: 1990939	ATP-dependent microtubule motor activity	5/89	35/18337	$6.96E-07$	$1.57E-05$	$1.11E-05$	5
GO: 0035173	Histone kinase activity	4/89	16/18337	$9.02E-07$	$1.81E-05$	$1.28E-05$	4
GO: 0003688	DNA replication origin binding	4/89	23/18337	$4.28E-06$	$7.06E-05$	$4.97E-05$	4

Table 3: The detailed information of KEGG pathways enriched by ESCA-specific genes.

ID	Description	Gene ratio	BgRatio	P value	Adjusted p	Q value	Count
hsa04110	Cell cycle	13/43	126/8104	$4.08E-14$	$2.08E-12$	$1.59E-12$	13
hsa03030	DNA replication	6/43	36/8104	$2.69E-08$	$6.85E-07$	$5.23E-07$	6
hsa04114	Oocyte meiosis	6/43	131/8104	$5.94E-05$	0.001009	0.000771	6
hsa04218	Cellular senescence	6/43	156/8104	0.000156	0.001923	0.001468	6
hsa04914	Progesterone-mediated oocyte maturation	5/43	102/8104	0.000189	0.001923	0.001468	5
hsa03410	Base excision repair	3/43	33/8104	0.00068	0.005776	0.004411	3
hsa05166	Human T cell leukemia virus 1 infection	6/43	222/8104	0.001031	0.007513	0.005737	6
hsa05203	Viral carcinogenesis	5/43	204/8104	0.004257	0.02714	0.020726	5
hsa03430	Mismatch repair	2/43	23/8104	0.006483	0.034097	0.026039	2
hsa04115	p53 signaling pathway	3/43	73/8104	0.006686	0.034097	0.026039	3
hsa03440	Homologous recombination	2/43	41/8104	0.019784	0.091726	0.070049	2
hsa03420	Nucleotide excision repair	2/43	47/8104	0.025565	0.108651	0.082974	2
hsa04210	Apoptosis	3/43	136/8104	0.035027	0.137412	0.104938	3
hsa04120	Ubiquitin mediated proteolysis	3/43	142/8104	0.039049	0.14225	0.108633	3

the crucial role of *ASPM* in cancer progression. For example, *BUB1B* accelerates prostate carcinoma proliferation through transcriptionally modulating *MELK* [26]. It triggers hepatocellular carcinoma development through activating *mTORC1* signaling [27]. It can facilitate extrahepatic cholangiocarcinoma development through *JNK/c-Jun* signaling [28]. Moreover, it participates in the tumorigenicity and radioresistance of glioblastoma [29]. For *CCNA2*, it can be suppressed by *miR*-219-5p, thereby affecting cellular proliferation and cell cycle progression in ESCA [30]. A previous study has proposed that *CDC20* modulates *E2F1* degradation and thymidylate synthase expression, thereby triggering ESCA chemoresistance [31]. Furthermore, *CDK1* has been considered as an underlying diagnostic and cancer progression biomarker as well as a drug target for ESCA [32]. Previous bioinformatics and experimental evidences have demonstrated the tumorigenic role of *DLGAP5* in ESCA [33]. *KIF11* is essential for spheroid formation of ESCA cells [34]. ScRNA-seq and qPCR analysis uncovered that *KIF20A* possesses the potential to diagnose and predict ESCA patients' prognosis [35]. For *TOP2A*, experimental data demonstrate that it can affect the resistance of ESCA cells to paclitaxel [36]. Targeting *TPX2* relieves ESCA progression through weakening tumor growth and invasion [37, 38]. Additionally, its upregulation is mediated by *LINC00337* and triggers autophagy and resistance to cisplatin in ESCA cells [39]. On the basis of previously published literature and our findings, *ASPM*, *BUB1B*, *CCNA2*, *CDC20*, *CDK1*,

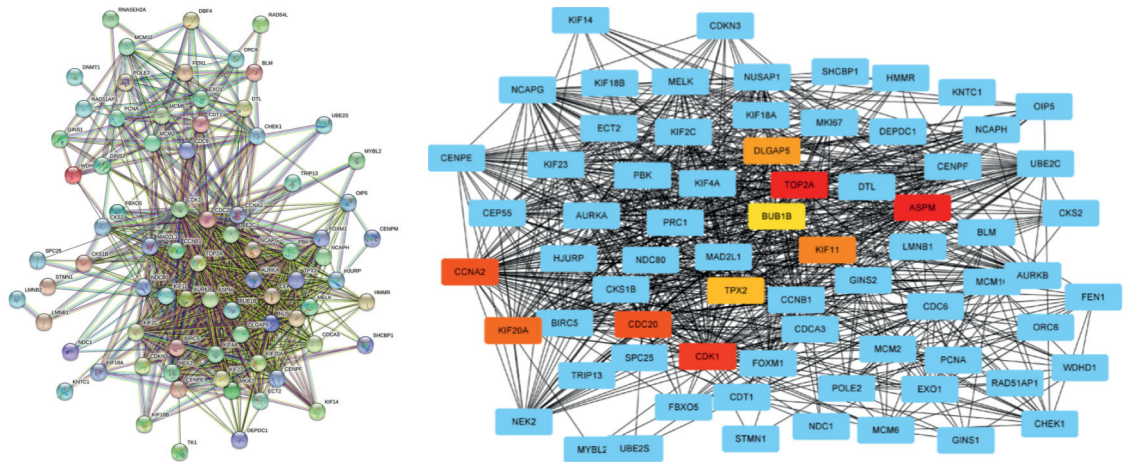

FIGURE 5: Establishment of a PPI network and discovery of ESCA-specific hub genes. (a) The PPI network of ESCA-specific DEGs through the STRING online tool. (b) Discovery of the ESCA-specific hub genes utilizing CytoHubba plugin. The ten hub genes are marked in orange.

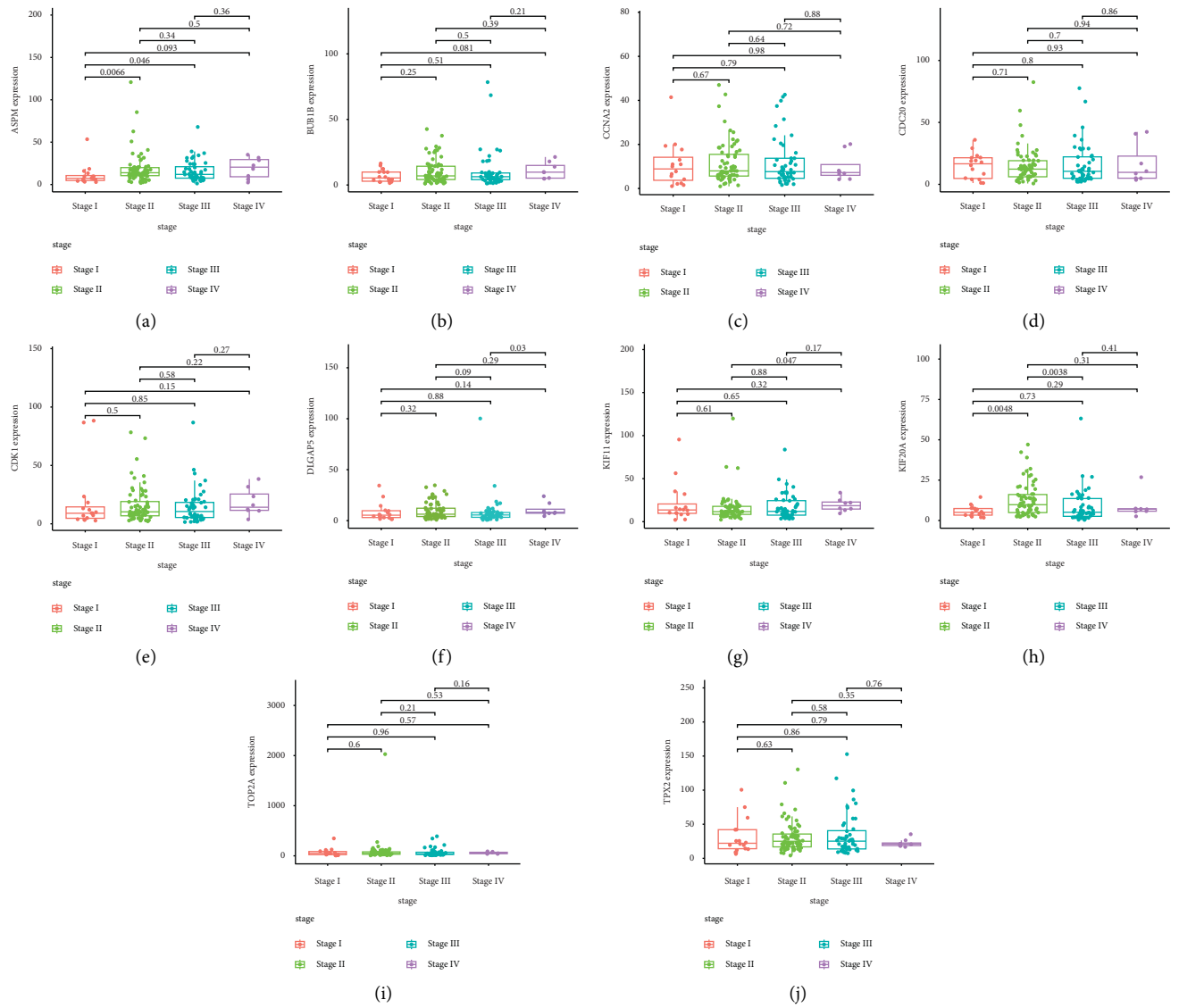

FIGURE 6: Association of the ESCA-specific hub genes with pathological staging of ESCA patients. (a–j) Box plots depict the difference in (a) *ASPM*, (b) *BUB1B*, (c) *CCNA2*, (d) *CDC20*, (e) *CDK1*, (f) *DLGAP5*, (g) *KIF11*, (h) *KIF20A*, (i) *TOP2A*, and (j) *TPX2* among diverse pathological staging of ESCA patients in TCGA cohort.

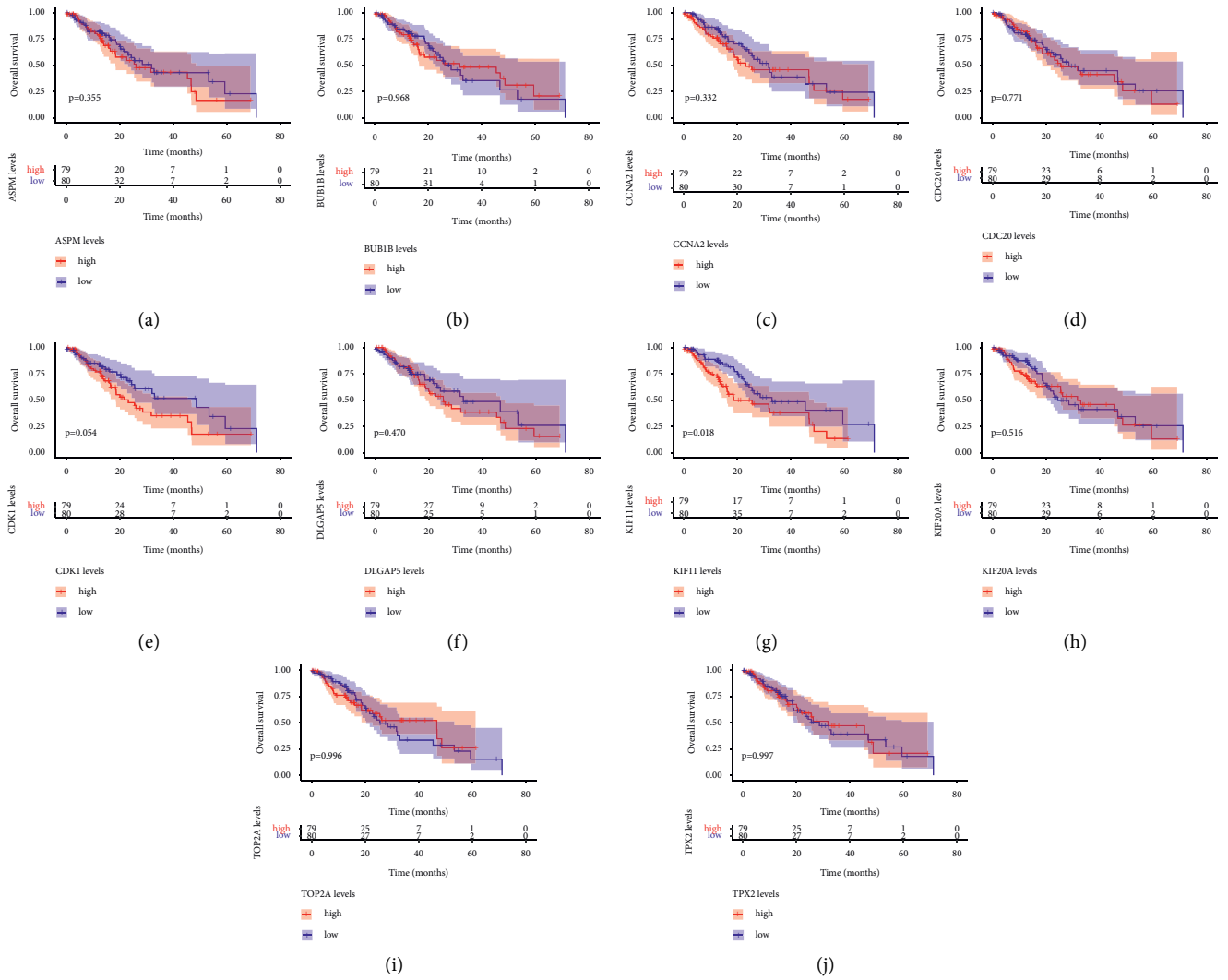

Figure 7: Association of the ESCA-specific hub genes with ESCA patients' prognosis in TCGA cohort. (a–j) Kaplan–Meier curves display the difference in overall survival between high and low expression of (a) *ASPM*, (b) *BUB*1*B*, (c) *CCNA*2, (d) *CDC*20, (e) *CDK*1, (f) *DLGAP*5, (g) *KIF*11, (h) *KIF*20*A*, (i) *TOP*2*A*, and (j) *TPX*2 groups. Survival difference between groups is determined with the log-rank test.

*DLGAP*5, *KIF*11, *KIF*20*A*, *TOP*2*A*, and *TPX*2 play crucial roles in ESCA progression.

Currently, approach of predicting ESCA patients' prognosis primarily depends on the conventional TNM staging system. Although conventional TNM staging is crucial for diagnosis and treatment interventions, it cannot roundly uncover the intrinsic biological processes and pathological development due to the high heterogeneity in tumor microenvironment and individual discrepancy. Our results demonstrated that the 10 ESCA-specific hub genes (*ASPM*, *BUB*1*B*, *CCNA*2, *CDC*20, *CDK*1, *DLGAP*5, *KIF*11, *KIF*20*A*, *TOP*2*A*, and *TPX*2) presented the remarkable associations with pathological staging, indicating that their roles in ESCA progression. Among them, KIF11 upregulation was indicative of an unfavorable survival outcome of ESCA patients, indicative of the potential of KIF11 as a prognostic indicator of ESCA.

However, there are certain drawbacks in our study. First, the influence of expression alteration of the ESCA-specific hub genes upon patients' prognosis remains to be explored. Hence, in our future, the interactions of the ESCA-specific hub genes with patients' prognosis will be monitored and verified in the large-scale clinical data. Additionally, it is of importance to consider statistical bias because the sample size is relatively small. Moreover, in-depth investigation will be presented for validating the biological significance of the ESCA-specific hub genes through in vitro and in vivo experiments.

5. Conclusion

Overall, this study determined the 10 ESCA-specific hub genes as novel markers for ESCA with the WGCNA algorithm based on distinct datasets, which offered promising targets for ESCA precision medicine. Nevertheless, in-depth exploration is required for validating the biological function of the specific hub genes in large-scale clinical cohorts.

Abbreviations

ESCA: Esophageal cancer
TNM: Tumor, node, metastasis
WGCNA: Weighted gene coexpression network analysis
TCGA: The Cancer Genome Atlas
GEO: Gene Expression Omnibus
DEGs: Differentially expressed genes
GO: Gene Ontology
KEGG: Kyoto Encyclopedia of Genes and Genomes
BP: Biological process
CC: Cellular component
MF: Molecular function
PPI: Protein-protein interaction
STRING: Search Tool for the Retrieval of Interacting Genes/Proteins.

Data Availability

The data used to support the findings of this study are included within the supplementary information files.

Conflicts of Interest

The authors declare that they have no conflicts of interest.

Authors' Contributions

Wei Xu and Jian Xu contributed equally to this work.

Acknowledgments

This work was funded by Chongqing Medical Scientific Research Project (Joint Project of Chongqing Health Commission and Science and Technology Bureau) (2021MSXM287) and The Planning Decision Consultation Project of Shapingba Science and Technology Bureau (Jcd202018).

Supplementary Materials

Supplementary Table 1. The detailed information of DEGs between ESCA tumors and normal tissues in TCGA cohort. Supplementary Table 2. The detailed information of DEGs between ESCA tumors and normal tissues in the GSE38129 dataset. . (*Supplementary Materials*)

References

[1] F. Bray, J. Ferlay, I. Soerjomataram, R. L. Siegel, L. A. Torre, and A. Jemal, "Global cancer statistics 2018: GLOBOCAN estimates of incidence and mortality worldwide for 36 cancers in 185 countries," *CA: A Cancer Journal for Clinicians*, vol. 68, no. 6, pp. 394–424, 2018.

[2] Z. Yuan, X. Wang, X. Geng et al., "Liquid biopsy for esophageal cancer: is detection of circulating cell-free DNA as a biomarker feasible?" *Cancer Communications*, vol. 41, no. 1, pp. 3–15, 2021.

[3] A. A. Bhat, S. Nisar, S. Maacha et al., "Cytokine-chemokine network driven metastasis in esophageal cancer; promising avenue for targeted therapy," *Molecular Cancer*, vol. 20, no. 1, p. 2, 2021.

[4] W. M. Grady, M. Yu, and S. D. Markowitz, "Epigenetic alterations in the gastrointestinal tract: current and emerging use for biomarkers of cancer," *Gastroenterology*, vol. 160, no. 3, pp. 690–709, 2021.

[5] Y. Kakeji, T. Oshikiri, G. Takiguchi et al., "Multimodality approaches to control esophageal cancer: development of chemoradiotherapy, chemotherapy, and immunotherapy," *Esophagus*, vol. 18, no. 1, pp. 25–32, 2021.

[6] W. Li, J. Liu, and H. Zhao, "Identification of a nomogram based on long non-coding RNA to improve prognosis prediction of esophageal squamous cell carcinoma," *Aging*, vol. 12, no. 2, pp. 1512–1526, 2020.

[7] Z. Tian, W. He, J. Tang et al., "Identification of important modules and biomarkers in breast cancer based on WGCNA," *OncoTargets and Therapy*, vol. 13, pp. 6805–6817, 2020.

[8] K. H. Bai, S. Y. He, L. L. Shu et al., "Identification of cancer stem cell characteristics in liver hepatocellular carcinoma by WGCNA analysis of transcriptome stemness index," *Cancer Medicine*, vol. 9, no. 12, pp. 4290–4298, 2020.

[9] M. Ding, F. Li, B. Wang, G. Chi, and H. Liu, "A comprehensive analysis of WGCNA and serum metabolomics manifests the lung cancer-associated disordered glucose metabolism," *Journal of Cellular Biochemistry*, vol. 120, no. 6, pp. 10855–10863, 2019.

[10] A. S. Nangraj, G. Selvaraj, S. Kaliamurthi, A. C. Kaushik, W. C. Cho, and D. Q. Wei, "Integrated PPI- and WGCNA-retrieval of hub gene signatures shared between Barrett's esophagus and esophageal adenocarcinoma," *Frontiers in Pharmacology*, vol. 11, p. 881, 2020.

[11] W. Wang, S. Fu, X. Lin et al., "miR-92b-3p functions as A key gene in esophageal squamous cell cancer as determined by Co-expression analysis," *OncoTargets and Therapy*, vol. 12, pp. 8339–8353, 2019.

[12] W. Zhou, J. Wu, J. Zhang et al., "Integrated bioinformatics analysis to decipher molecular mechanism of compound Kushen injection for esophageal cancer by combining WGCNA with network pharmacology," *Scientific Reports*, vol. 10, no. 1, Article ID 12745, 2020.

[13] N. Hu, C. Wang, R. J. Clifford et al., "Integrative genomics analysis of genes with biallelic loss and its relation to the expression of mRNA and micro-RNA in esophageal squamous cell carcinoma," *BMC Genomics*, vol. 16, no. 1, p. 732, 2015.

[14] M. E. Ritchie, B. Phipson, D. Wu et al., "Limma powers differential expression analyses for RNA-sequencing and microarray studies," *Nucleic Acids Research*, vol. 43, no. 7, p. e47, 2015.

[15] B. Zhang and S. Horvath, "A general framework for weighted gene co-expression network analysis," *Statistical Applications in Genetics and Molecular Biology*, vol. 4, Article ID 17, 2005.

[16] G. Yu, L.-G. Wang, Y. Han, and Q.-Y. He, "clusterProfiler: an R package for comparing biological themes among gene clusters," *OMICS: A Journal of Integrative Biology*, vol. 16, no. 5, pp. 284–287, 2012.

[17] D. Szklarczyk, J. H. Morris, H. Cook et al., "The STRING database in 2017: quality-controlled protein-protein association networks, made broadly accessible," *Nucleic Acids Research*, vol. 45, no. D1, pp. D362–d368, 2017.

[18] C. H. Chin, S. H. Chen, and H. H. Wu, "CytoHubba: identifying hub objects and sub-networks from complex interactome," *BMC Systems Biology*, vol. 8, no. Suppl 4, p. S11, 2014.

[19] P. Shannon, A. Markiel, O. Ozier et al., "Cytoscape: a software environment for integrated models of biomolecular interaction networks," *Genome Research*, vol. 13, no. 11, pp. 2498–2504, 2003.

[20] V. C. Pai, C.-C. Hsu, T.-S. Chan et al., "ASPM promotes prostate cancer stemness and progression by augmenting Wnt–Dvl-3–β-catenin signaling," *Oncogene*, vol. 38, no. 8, pp. 1340–1353, 2019.

[21] Z. Y. Gao, F. Yu, H. X. Jia, Z. Ye, and S. J. Yao, "ASPM predicts poor prognosis and regulates cell proliferation in bladder cancer," *The Kaohsiung Journal of Medical Sciences*, vol. 36, no. 12, pp. 1021–1029, 2020.

[22] X. Chen, L. Huang, Y. Yang et al., "ASPM promotes glioblastoma growth by regulating G1 restriction point progression and Wnt-β-catenin signaling," *Aging*, vol. 12, no. 1, pp. 224–241, 2020.

[23] W. J. Zeng, Q. Cheng, Z. P. Wen et al., "Aberrant ASPM expression mediated by transcriptional regulation of FoxM1 promotes the progression of gliomas," *Journal of Cellular and Molecular Medicine*, vol. 24, no. 17, pp. 9613–9626, 2020.

[24] J. Wu, Z. He, Y. Zhu, C. Jiang, Y. Deng, and B. Wei, "ASPM predicts poor clinical outcome and promotes tumorigenesis for diffuse large B-cell lymphoma," *Current Cancer Drug Targets*, vol. 21, no. 1, pp. 80–89, 2021.

[25] Y.-J. Yuan, Y. Sun, R. Gao, Z.-z. Yin, Z.-y. Yuan, and L.-M. Xu, "Abnormal spindle-like microcephaly-associated protein (ASPM) contributes to the progression of Lung Squamous Cell Carcinoma (LSCC) by regulating CDK4," *Journal of Cancer*, vol. 11, no. 18, pp. 5413–5423, 2020.

[26] J.-H. Tian, L.-J. Mu, M.-Y. Wang et al., "BUB1B promotes proliferation of prostate cancer via transcriptional regulation of MELK," *Anti-Cancer Agents in Medicinal Chemistry*, vol. 20, no. 9, pp. 1140–1146, 2020.

[27] J. Qiu, S. Zhang, P. Wang et al., "BUB1B promotes hepatocellular carcinoma progression via activation of the mTORC1 signaling pathway," *Cancer Medicine*, vol. 9, no. 21, pp. 8159–8172, 2020.

[28] C. Y. Jiao, Q. C. Feng, C. X. Li et al., "BUB1B promotes extrahepatic cholangiocarcinoma progression via JNK/c-Jun pathways," *Cell Death & Disease*, vol. 12, no. 1, p. 63, 2021.

[29] Q. Ma, Y. Liu, L. Shang, J. Yu, and Q Qu, "The FOXM1/BUB1B signaling pathway is essential for the tumorigenicity and radioresistance of glioblastoma," *Oncology Reports*, vol. 38, pp. 3367–3375, 2017.

[30] Q. Ma, "MiR-219-5p suppresses cell proliferation and cell cycle progression in esophageal squamous cell carcinoma by targeting CCNA2," *Cellular and Molecular Biology Letters*, vol. 24, no. 1, p. 4, 2019.

[31] B. Li, W. W. Xu, X. Y. Guan et al., "Competitive binding between Id1 and E2F1 to Cdc20 regulates E2F1 degradation and thymidylate synthase expression to promote esophageal cancer chemoresistance," *Clinical Cancer Research*, vol. 22, no. 5, pp. 1243–1255, 2016.

[32] D. E. Hansel, S. Dhara, R. C. Huang et al., "CDC2/CDK1 expression in esophageal adenocarcinoma and precursor lesions serves as a diagnostic and cancer progression marker and potential novel drug target," *The American Journal of Surgical Pathology*, vol. 29, no. 3, pp. 390–399, 2005.

[33] J. Hu, R. Li, H. Miao, and Z. Wen, "Identification of key genes for esophageal squamous cell carcinoma via integrated bioinformatics analysis and experimental confirmation," *Journal of Thoracic Disease*, vol. 12, no. 6, pp. 3188–3199, 2020.

[34] T. Imai, N. Oue, K. Sentani et al., "KIF11 is required for spheroid formation by oesophageal and colorectal cancer cells," *Anticancer Research*, vol. 37, no. 1, pp. 47–56, 2017.

[35] L. Zheng, L. Li, J. Xie, H. Jin, and N. Zhu, "Six novel biomarkers for diagnosis and prognosis of esophageal squamous cell carcinoma: validated by scRNA-seq and qPCR," *Journal of Cancer*, vol. 12, no. 3, pp. 899–911, 2021.

[36] S. Zhang, H. Jiang, Z. Xu et al., "The resistance of esophageal cancer cells to paclitaxel can be reduced by the knockdown of long noncoding RNA DDX11-AS1 through TAF1/TOP2A inhibition," *American journal of cancer research*, vol. 9, pp. 2233–2248, 2019.

[37] Y. Hou, H. Liu, and W. Pan, "Knockdown of circ_0003340 induces cell apoptosis, inhibits invasion and proliferation through miR-564/TPX2 in esophageal cancer cells," *Experimental Cell Research*, vol. 394, no. 2, Article ID 112142, 2020.

[38] H.-C. Liu, G.-H. Zhang, Y.-H. Liu et al., "TPX2 siRNA regulates growth and invasion of esophageal cancer cells," *Biomedicine & Pharmacotherapy*, vol. 68, no. 7, pp. 833–839, 2014.

[39] C. Yang, S. Shen, X. Zheng et al., "Long non-coding RNA LINC00337 induces autophagy and chemoresistance to cisplatin in esophageal squamous cell carcinoma cells via upregulation of TPX2 by recruiting E2F4," *The FASEB Journal*, vol. 34, no. 5, pp. 6055–6069, 2020.

Hindawi
Journal of Oncology
Volume 2021, Article ID 1827992, 8 pages
https://doi.org/10.1155/2021/1827992

Research Article

Clinicopathological and Prognostic Significance of ABCC3 in Human Glioma

Dan-Dong Fang,[1] Wei Huang,[2] Gang Cheng,[3] Xiao-Nan Liu,[1] Shi-Min Liu,[1] Bao-Sen Hou,[1] Jian Mao,[1] and Hu Zhou[2]

[1]*Department of Neurosurgery, The Sanmenxia Central Hospital, Sanmenxia, Henan, China*
[2]*Department of Neurosurgery, The First People's Hospital of Yunnan Province, Kunming, Yunnan, China*
[3]*Department of Neurosurgery, The First Medical Center, PLA General Hospital, Beijing, China*

Correspondence should be addressed to Hu Zhou; linze57@xjtu.edu.cn

Received 20 November 2021; Revised 11 December 2021; Accepted 13 December 2021; Published 23 December 2021

Academic Editor: Fu Wang

Glioma is the most common malignant primary brain tumor with an inferior survival period and unsatisfactory prognoses. Identification of novel biomarkers is important for the improvements of clinical outcomes of glioma patients. In recent years, more and more biomarkers were identified in many types of tumors. However, the sensitive markers for diagnoses and prognoses of patients with glioma remained unknown. In the present research, our team intended to explore the expression and clinical significance of ABCC3 in glioma patients. Sequential data filtration (survival analyses, independent prognosis analyses, ROC curve analyses, and clinical association analyses) was completed, which gave rise to the determination of the relationship between glioma and the ABCC3 gene. Clinical assays on the foundation of CGGA and TCGA datasets unveiled that ABCC3 expression was distinctly upregulated in glioma and predicted a shorter overall survival. In the multivariable Cox analysis, our team discovered that the expression of ABCC3 was an independent prognosis marker for both 5-year OS (HR = 1.118, 95% CI: 1.052–1.188; $P < 0.001$). Moreover, our team also studied the association between ABCC3 expression and clinical features of glioma patients, finding that differential expression of ABCC3 was remarkably related to age, 1p19q codeletion, PRS type, chemo status, grade, IDH mutation state, and histology. Overall, our findings suggested ABCC3 might be a novel prognosis marker in glioma.

1. Introduction

Glioma is the most commonly seen malignancy primary cerebroma and the most fatal type of cerebroma in adults [1]. Of the 4 categories of glioma categorized by the WHO, the most severe gradation (gradation IV) is GBM [2]. The morbidity and mortality of GBM cases have also increased year by year. GBM displays elevated aggressive proliferation and a tendency to invade and metastasize [3, 4]. Despite the fact that remarkable progresses have been made in the diagnoses and target treatment of this disease, the prognostic results of sufferers remain unsatisfactory [5, 6]. For that reason, more and more studies are conducted to find promising markers for tumor identification or forecast results, particularly in the early phases.

The progress in biological information and high-flux sequencing has realized the determination of various cancer markers which might assist the prognostic accurateness of GBM, which might give rise to more valid interventions in this regard [7, 8]. Tan et al. reported that serum long noncoding RNA HOTAIR was highly expressed in glioblastoma, and its positive association with long-term survival in tumors patients was also confirmed, indicating sera HOTAIR could be utilized as a novel prognosis and diagnostic marker for GBM [9]. Stanniocalcin 1 was reported to be overexpressed in glioma, and its upregulation in glioma patients predicted a poor prognosis [10]. Moreover, LAMC1 was also reported to be vital for the development of this disease and might be utilized in the diagnoses, prognoses, and target treatment of sufferers [11]. On the other hand,

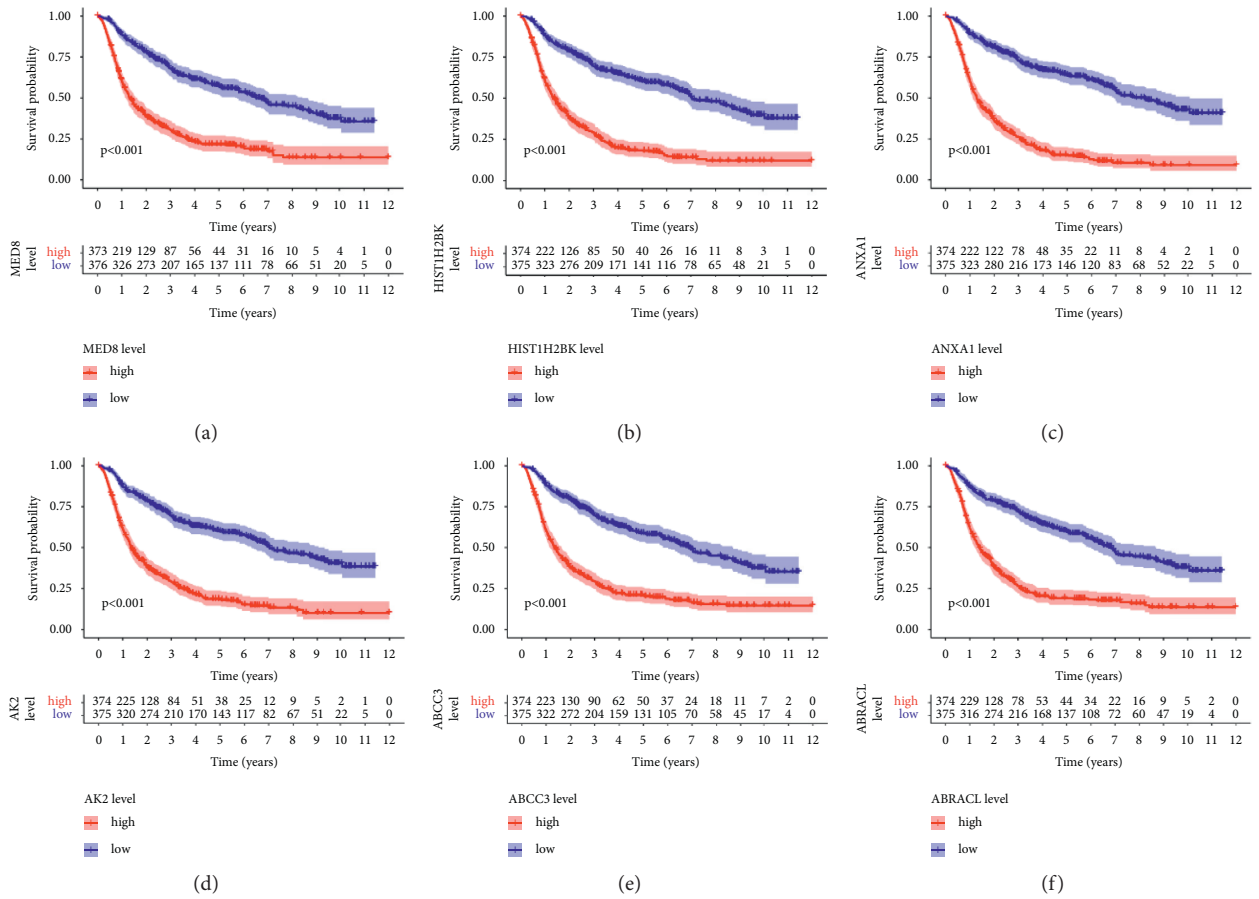

Figure 1: Kaplan–Meier curve of correlation between the top 6 genes including (a) MED8, (b) HIST1H2BK8, (c) ANXA1, (d) AK2, (e) ABCC3, and (f) ABRACL of glioma samples and overall survival of patients based on CGGA datasets.

more and more prognostic models based on multiple genes were also developed [12, 13]. Those biomarkers might be utilized for future sophisticated diagnosis and decision-making processes [14]. Despite these advances, more reliable prognostic indicators are needed for glioma.

Herein, we searched CGGA datasets and identified many survival-related genes based on several conditions. Finally, we identified 132 genes which may be the most important survival-related genes in glioma. Among those genes, our attention focused on ABCC3. Recently, some studies have discovered the dysregulation of ABCC3 in many cancers, including glioma [15–18]. However, its clinical significance in glioma patients was rarely reported.

2. Materials and Methods

2.1. Data Collection. We collected 1018 glioma sufferers for the following investigation. Clinic feature data and transcriptomic sequencing results of CGGA microarray and RNA-sequencing cohorts were acquired from the CGGA dataset [19]. Our team utilized FPKM to speculate the expression of RNA. Each sufferer without prognosis data was excluded at first. As the data were acquired from TCGA and the CGGA, the acceptance from the ethical board was not needed.

2.2. Survival Analysis Filtration. Survival and survminer packages were used in R program [20], and K–M and univariable Cox analysis were utilized for filtering genetic expression and survival data, with $P < 0.001$ being significant on statistics.

2.3. Analyses of the Expression of the Survival-Associated Genes in GBM. The information of differentially expressed survival-associated genes between tumor and matched normal tissues was from TCGA and GTEx databases. GEPIA was applied to analyze the expressions of the survival-associated genes in GBM [21].

2.4. Independent Prognosis Role of ABCC3 in Glioma Sufferers. To determine the impact of ABCC3 expression on prognoses, our team has to evaluate if the ABCC3 expression was related to the rest of the factors clinically, such as sex, age, IDH1 variant phase, and cancer WHO gradation. For that reason, univariable and multivariable Cox proportion assays were finished to identify the independent prognosis effects of ABCC3 with the forward stepwise procedure. The ABCC3 expression and clinical factors were considered to be independence factors when the modified P result was <0.05.

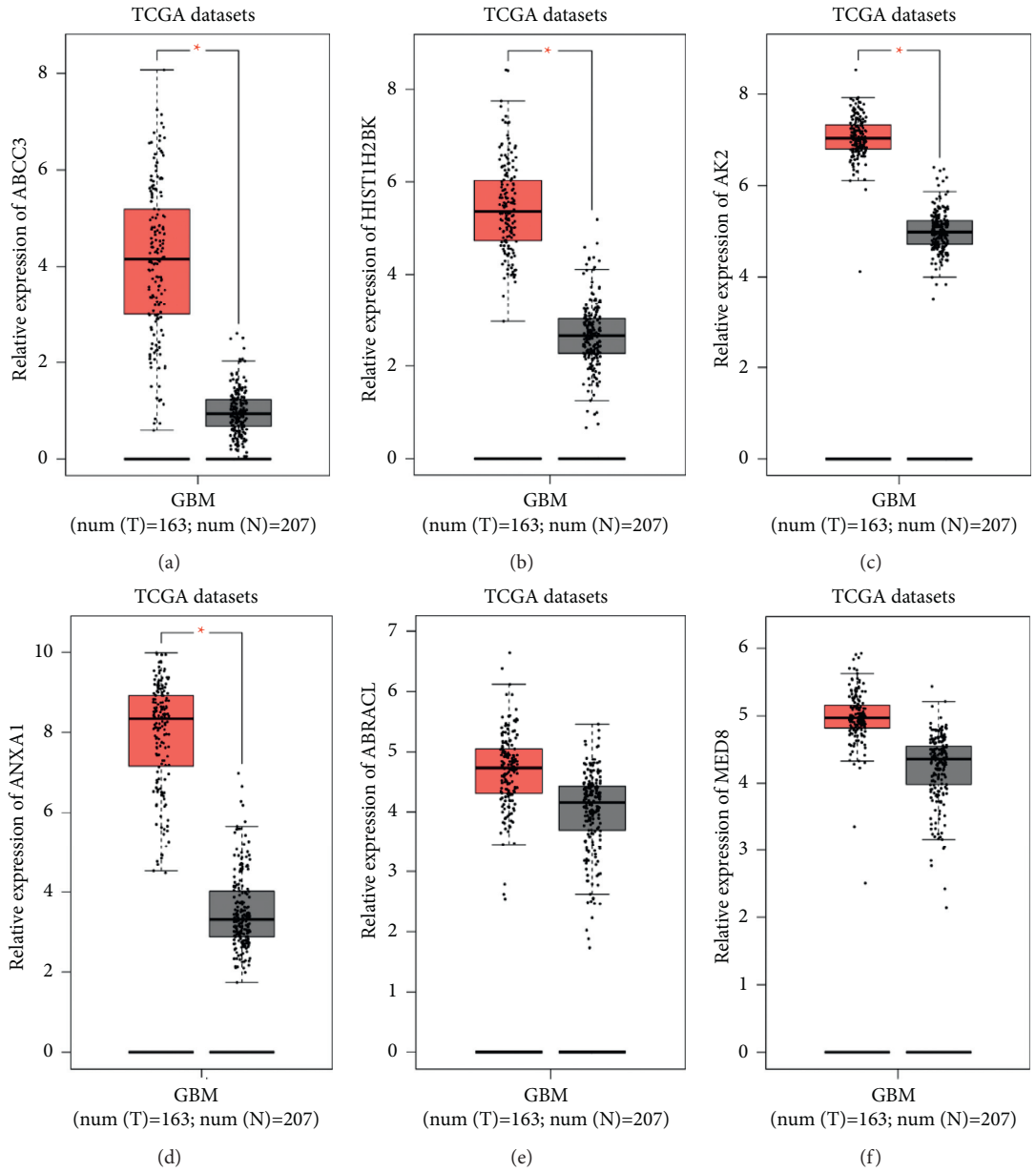

Figure 2: The expressing pattern of the top 6 genes in GBM based on TCGA datasets. The expression of (a) ABCC3, (b) HIST1H2BK8, (c) AK2, and (d) ANXA1 was distinctly increased in GBM samples. (e, f) The expression of ABRACL and MED8 remained unchanged between GBM samples and nontumor samples.

2.5. Clinic Relevance Filtration. The data of gene expressions acquired from ROC curve filtration and the relevant clinic data were studied via R program and subjected to filtration via $P < 0.05$.

2.6. Analyses of the Association between the Expression of ABCC3 and Clinical Features. Genetic expression and relevant clinic data acquired from ROC curve filtration were studied in R to abstract the clinic data related to the ABCC3 gene. The association between the expression of ABCC3 and a variety of clinic features was identified via beeswarm.

2.7. Statistical Analysis. All the statistical analyses were performed using R version 3.4.2 software. A two-tailed $P < 0.05$ was considered statistically significant.

3. Results

3.1. Identification of Survival-Related Genes in Glioma. We performed the K–M, univariable Cox method, and multivariable Cox analyses to screen the survival-related genes. Then, AUC >0.7 was taken as the liminal value for ROC curve analyses (Supplementary Table S1). Eventually, the association between genes and clinic features was studied, with $P < 0.05$ being the threshold. As shown in

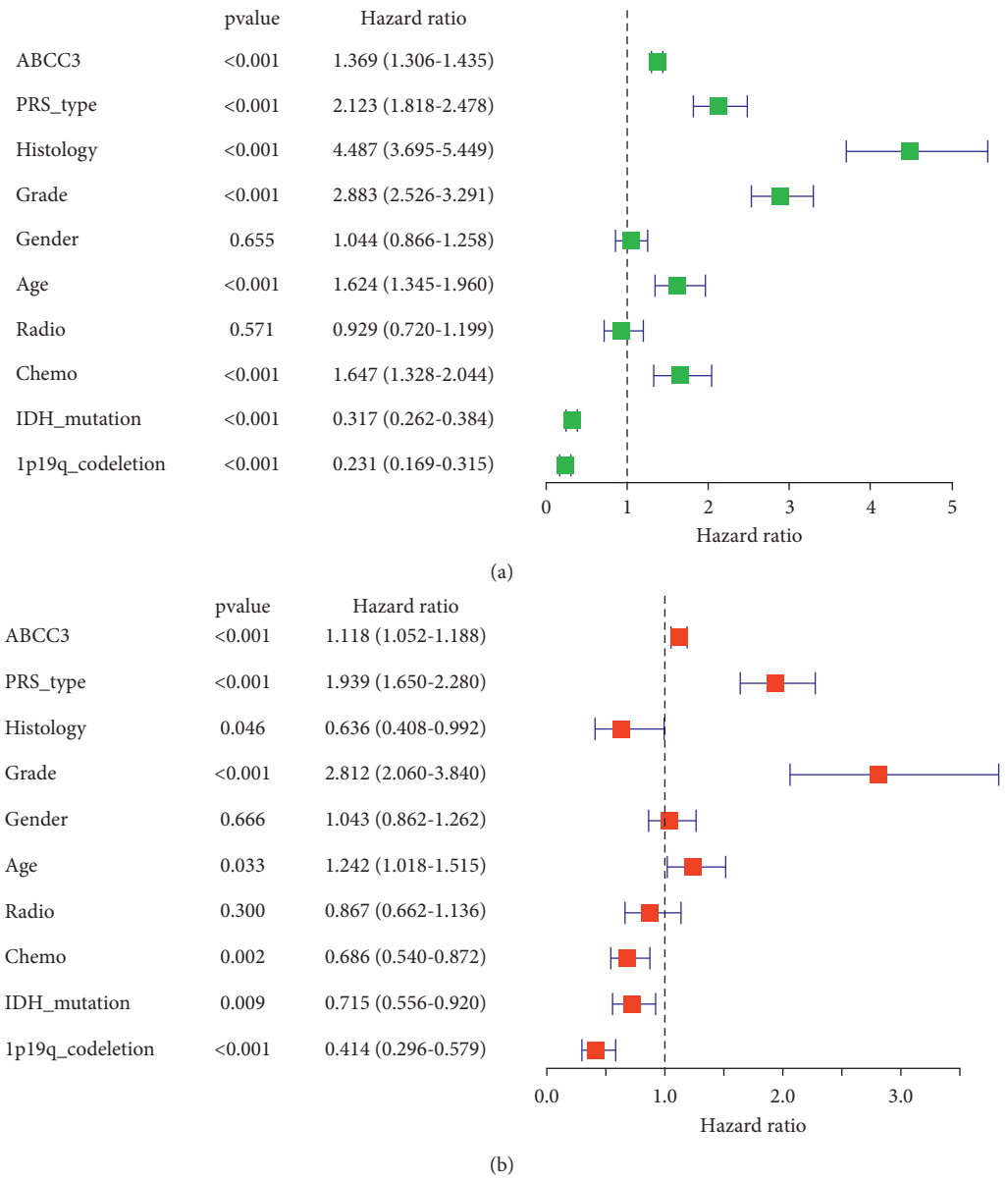

Figure 3: (a) Univariate and (b) multivariate analysis of ABCC3 expression and its correlation in patients with glioma based on CGGA data.

Figures 1(a)–1(f), we showed the top 6 survival-related genes including MED8 (Figure 1(a), $P < 0.001$), HIST1H2BK8 (Figure 1(b), $P < 0.001$), ANXA1 (Figure 1(c), $P < 0.001$), AK2 (Figure 1(d), $P < 0.001$), ABCC3 (Figure 1(e), $P < 0.001$), and ABRACL (Figure 1(f), $P < 0.001$).

3.2. The Distinct Upregulation of ABCC3 in GBM Specimens. Then, we used GEPIA to study the expressions of the abovementioned 6 genes and found that ABCC3 (Figure 2(a)), HIST1H2BK83 (Figure 2(b)), AK2 (Figure 2(c)), and ANXA1 (Figure 2(d)) exhibited an increased level in GBM specimens in contrast to healthy cerebrum specimens. However, the expressions of ABRACL and MED8 remained unchanged between GBM specimens and nontumor specimens (Figures 2(e) and 2(f)). Our attention focused on ABCC3.

3.3. The Prognostic Significance of ABCC3 in Glioma Patients from the CGGA Database. To investigate the prognostic value of the expression of ABCC3 in glioma patients, our team performed univariable Cox analyses and observed that ABCC3 (HR = 1.369; 95% CI = 1.306–1.435; $P < 0.001$), PRS types, histological status, gradation, ages, and chemotherapy were factors related to higher risks and IDH variant and 1p19q codeletion were related to lower risks (Figure 3(a)). Multivariable Cox analyses revealed that ABCC3 (HR = 1.118; 95% CI = 1.052–1.188; $P < 0.001$) was related to OS in an independent way, which unveiled that ABCC3 could serve as

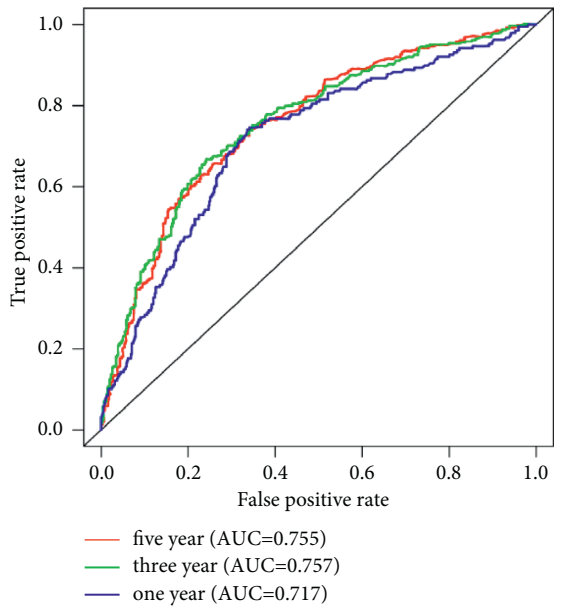

Figure 4: Time-dependent ROC curve for the patients in the CGGA dataset.

an independence marker for the clinical outcome of this disease. Moreover, PRS types, gradation, ages, chemotherapy, IDH variant, and 1p19q codeletion might be independent prognosis factors as well (Figure 3(b)). ROC curve analyses revealed that ABCC3 was a predicting factor of 1-year (AUC = 0.717), 3-year (AUC = 0.757), and 5-year survival (AUC = 0.755) (Figure 4). Finally, we analyzed the relationship between ABCC3 expressions and clinic characteristics of glioma patients, finding that differentially expressing ABCC3 was remarkably related to age (Figure 5(a)), 1p19q codeletion (Figure 5(b)), PRS type (Figure 5(c)), chemo status (Figure 5(d)), grade (Figure 5(e)), IDH mutation status (Figure 5(f)), and histology (Figure 5(g)). Our findings suggested ABCC3 might participate in the clinical development of glioma and may be a novel biomarker.

4. Discussion

Amongst inhomogeneous primary cancers of the CNS, gliomas are the most common type, with GBM featured by the most unsatisfactory prognoses [22, 23]. In the past 10 years, the variant in epigenesis modulator genes has been discovered to be crucial driving factor of the glioma subgroups with different clinic characteristics [24, 25]. More and more potential regulators display the potential to be used as novel diagnostic and prognostic biomarkers for glioma [26–28]. Among them, the dysregulated genes with positive regulatory functions in the tumor growth and metastasis were the most hopeful biomarkers [29, 30]. However, the expression and function of most genes remained largely unclear.

In this study, we analyzed CGGA datasets and identified 132 possible survival-related genes with a high score of ROC. Among the 132 genes, we showed the top 6 genes, including MED8, ABCC3, ABRACL, AK2, ANXA1, and HIST1H2BK. However, only ABCC3, HIST1H2BK, AK2, and ANXA1 exhibited a high level in GBM. Previously, several studies have reported the expressing pattern and function of HIST1H2BK and ANXA1 in glioma [31, 32]. For instance, knockdown of ANXA1 was reported to suppress the proliferation and metastasis of glioma cells via regulating the PI3K/Akt signaling pathway [33]. High HIST1H2BK expression predicted a shorter OS of glioma sufferers [34]. Nevertheless, the clinical significance of ABCC3 in glioma has not been investigated. Herein, our team offered proofs that the expression of ABCC3 was an independent prognostic marker for overall survival of glioma sufferers.

Previously, some studies have reported the effects of ABCC3 in many types of tumors. For instance, ABCC3 was found to be involved in the regulation of the sensitivity of doxorubicin in triple-negative breast cancer [17]. ABCC3 was highly expressed in urinary bladder cancer, and its knockdown inhibited cell growth, drug-resistant ability, and aerobic glycolysis of bladder oncocytes [35]. In glioma, ABCC3 was shown to predict reactions in GBM sufferers receiving combined chemo and DC immune therapy [36]. Those discoveries revealed the vital role of ABCC3 in cancer development. Herein, our team analyzed the clinical feature of glioma patients with ABCC3 expression, finding that differentially expressed ABCC3 was remarkably related to PRS types, histological status, gradations, ages, chemotherapy states, IDH variant, and 1p19q codeletion. Our findings suggested ABCC3 exhibited a prognostic value in glioma and may be involved in clinical progression of glioma via complex mechanisms.

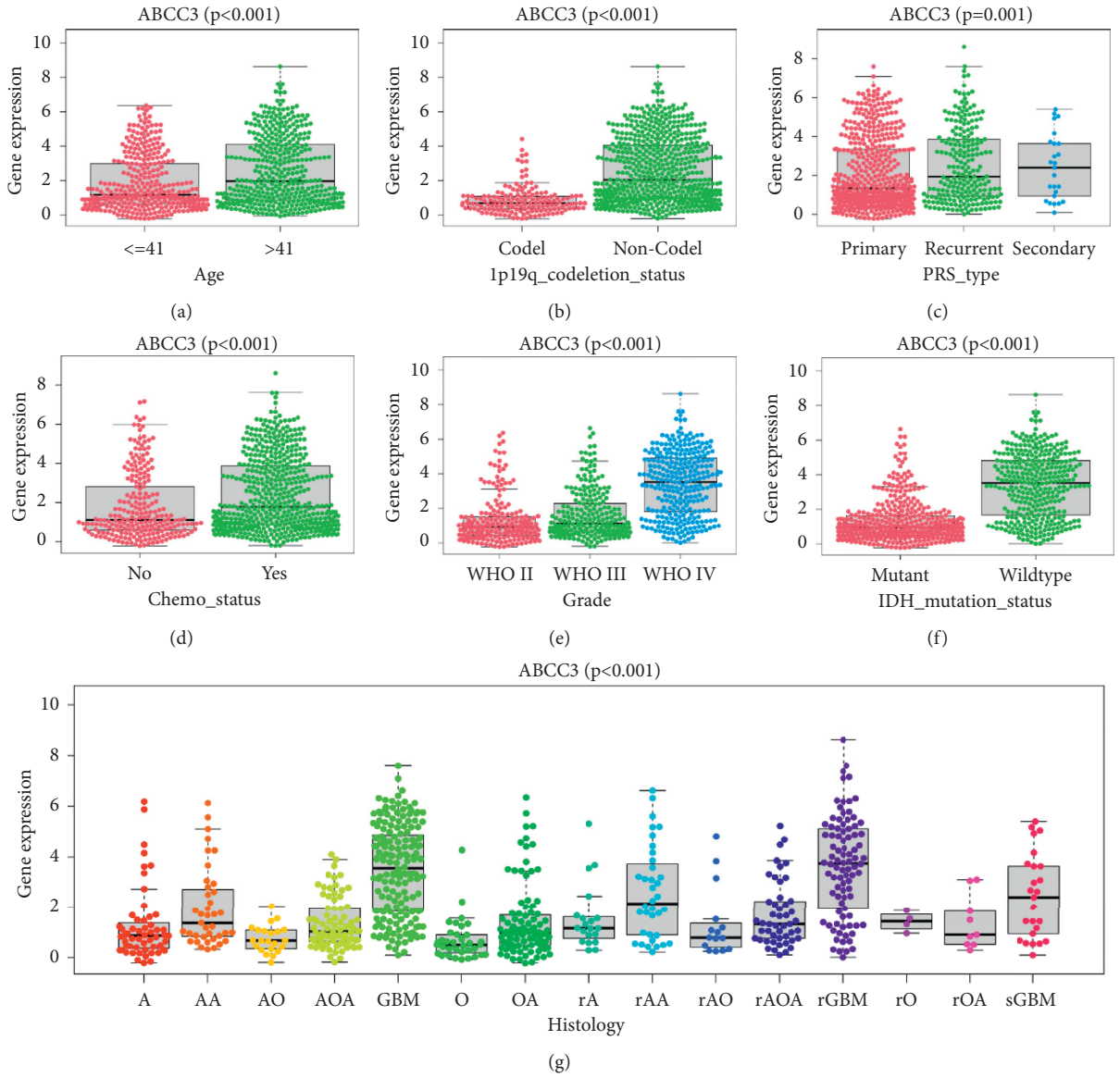

Figure 5: Association analyses between the expression of ABCC3 and clinical characteristics by virtue of the CGGA database. The upregulation of ABCC3 was remarkably associated with (a) ages, (b) 1p19q codeletion, (c) PRS types, (d) chemotherapy, (e) grade, (f) IDH variant, and (g) histology.

5. Conclusions

ABCC3 is upregulated in patients with glioma. Its abnormal expression can be utilized as an independent diagnostic and prognostic biomarker for this tumor. Nevertheless, its mechanisms and other effects remain unknown. Moreover, this study is limited by its small sample. Hence, further studies are needed.

Abbreviations

WHO: World Health Organization
GBM: Glioblastoma multiforme
CCGA: Chinese Glioma Genome Atlas
FPKM: Fragments per kilobases per million reads
K-M: Kaplan–Meier
GTEx: Genotype tissue expression
GEPIA: Gene expression profiling interactive analysis
CNS: Central nervous system
OS: Overall survival
ROC: Receiver operating characteristic
DCs: Dendritic cells.

Data Availability

The datasets used and/or analyzed during the present study are available from the corresponding author upon reasonable request.

Conflicts of Interest

The authors declare no conflicts of interest.

Authors' Contributions

Dan-dong Fang and Wei Huang contributed equally to this work.

Acknowledgments

This work was supported by grants from the Basic Research Program of Yunnan Province of China (No. 219FE001-209).

Supplementary Materials

Supplementary Table S1: ROC-related gene filtration in glioma patients. (*Supplementary Materials*)

References

[1] A. G. Rooney, P. D. Brown, J. C. Reijneveld, and R. Grant, "Depression in glioma: a primer for clinicians and researchers," *Journal of Neurology, Neurosurgery & Psychiatry*, vol. 85, no. 2, pp. 230–235, 2014.

[2] E. Le Rhun, S. Taillibert, and M. C. Chamberlain, "Anaplastic glioma: current treatment and management," *Expert Review of Neurotherapeutics*, vol. 15, no. 6, pp. 601–620, 2015.

[3] D. Bradley and J. Rees, "Updates in the management of high-grade glioma," *Journal of Neurology*, vol. 261, no. 4, pp. 651–654, 2014.

[4] P. Y. Wen and D. A. Reardon, "Progress in glioma diagnosis, classification and treatment," *Nature Reviews Neurology*, vol. 12, no. 2, pp. 69-70, 2016.

[5] N. A. O. Bush, S. M. Chang, and M. S. Berger, "Current and future strategies for treatment of glioma," *Neurosurgical Review*, vol. 40, no. 1, pp. 1–14, 2017.

[6] P. D. Delgado-López, E. M. Corrales-García, J. Martino, E. Lastra-Aras, and M. T. Dueñas-Polo, "Diffuse low-grade glioma: a review on the new molecular classification, natural history and current management strategies," *Clinical and Translational Oncology*, vol. 19, pp. 931–944, 2017.

[7] J. Jones, H. Nguyen, K. Drummond, and A. Morokoff, "Circulating biomarkers for glioma: a review," *Neurosurgery*, vol. 88, no. 3, pp. E221–e230, 2021.

[8] Y. Qi, B. Liu, Q. Sun, X. Xiong, and Q. Chen, "Immune checkpoint targeted therapy in glioma: status and hopes," *Frontiers in Immunology*, vol. 11, Article ID 578877, 2020.

[9] S. K. Tan, C. Pastori, C. Penas et al., "Serum long noncoding RNA HOTAIR as a novel diagnostic and prognostic biomarker in glioblastoma multiforme," *Molecular Cancer*, vol. 17, Article ID 74, 2018.

[10] W. Luo, D. Chen, H. Wang, and J. Hu, "Stanniocalcin 1 is a prognostic biomarker in glioma," *Oncology Letters*, vol. 20, no. 3, pp. 2248–2256, 2020.

[11] J. Liu, D. Liu, Z. Yang, and Z. Yang, "High LAMC1 expression in glioma is associated with poor prognosis," *OncoTargets and Therapy*, vol. 12, pp. 4253–4260, 2019.

[12] M. Zhang, X. Wang, X. Chen, Q. Zhang, and J. Hong, "Novel immune-related gene signature for risk stratification and prognosis of survival in lower-grade glioma," *Frontiers in Genetics*, vol. 11, Article ID 363, 2020.

[13] S. Zhuo, Z. Chen, Y. Yang, J. Zhang, J. Tang, and K. Yang, "Clinical and biological significances of a ferroptosis-related gene signature in glioma," *Frontiers in Oncology*, vol. 10, Article ID 590861, 2020.

[14] G. Reifenberger, H.-G. Wirsching, C. B. Knobbe-Thomsen, and M. Weller, "Advances in the molecular genetics of gliomas-implications for classification and therapy," *Nature Reviews Clinical Oncology*, vol. 14, no. 7, pp. 434–452, 2017.

[15] A. Adamska, R. Ferro, R. Lattanzio et al., "ABCC3 is a novel target for the treatment of pancreatic cancer," *Advances in Biological Regulation*, vol. 73, Article ID 100634, 2019.

[16] A. Adamska, A. Domenichini, E. Capone et al., "Pharmacological inhibition of ABCC3 slows tumour progression in animal models of pancreatic cancer," *Journal of Experimental & Clinical Cancer Research: CR*, vol. 38, Article ID 312, 2019.

[17] C. Zeng, D. Fan, Y. Xu et al., "Curcumol enhances the sensitivity of doxorubicin in triple-negative breast cancer via regulating the miR-181b-2-3p-ABCC3 axis," *Biochemical Pharmacology*, vol. 174, Article ID 113795, 2020.

[18] Z. Sun, X. Qi, and Y. Zhang, "Bioinformatics analysis of the expression of ATP binding cassette subfamily C member 3 (ABCC3) in human glioma," *Open Medicine*, vol. 15, no. 1, pp. 107–113, 2020.

[19] Z. Zhao, K.-N. Zhang, Q. Wang et al., "Chinese glioma genome atlas (CGGA): a comprehensive resource with functional genomic data from Chinese glioma patients," *Genomics, Proteomics & Bioinformatics*, vol. 19, no. 1, pp. 1–12, 2021.

[20] K. Ito and D. Murphy, "Application of ggplot2 to pharmacometric graphics," *CPT: Pharmacometrics & Systems Pharmacology*, vol. 2, Article ID e79, 2013.

[21] Z. Tang, C. Li, B. Kang, G. Gao, C. Li, and Z. Zhang, "GEPIA: a web server for cancer and normal gene expression profiling and interactive analyses," *Nucleic Acids Research*, vol. 45, no. 1, pp. W98–w102, 2017.

[22] N. H. Boyd, A. N. Tran, J. D. Bernstock et al., "Glioma stem cells and their roles within the hypoxic tumor microenvironment," *Theranostics*, vol. 11, no. 2, pp. 665–683, 2021.

[23] L. S. Hu, A. Hawkins-Daarud, L. Wang, J. Li, and K. R. Swanson, "Imaging of intratumoral heterogeneity in high-grade glioma," *Cancer Letters*, vol. 477, pp. 97–106, 2020.

[24] H. Wang, T. Xu, Q. Huang, W. Jin, and J. Chen, "Immunotherapy for malignant glioma: current status and future directions," *Trends in Pharmacological Sciences*, vol. 41, no. 2, pp. 123–138, 2020.

[25] M. Cheng, Z. W. Zhang, X. H. Ji, Y. Xu, E. Bian, and B. Zhao, "Super-enhancers: a new Frontier for glioma treatment," *Biochimica et Biophysica Acta: Reviews on cancer*, vol. 1873, Article ID 188353, 2020.

[26] W. Sun, H. Zhou, X. Han, L. Hou, and X. Xue, "Circular RNA: a novel type of biomarker for glioma (review)," *Molecular Medicine Reports*, vol. 24, 2021.

[27] A. Picca, G. Berzero, A. L. Di Stefano, and M. Sanson, "The clinical use of IDH1 and IDH2 mutations in gliomas," *Expert Review of Molecular Diagnostics*, vol. 18, no. 12, pp. 1041–1051, 2018.

[28] C. Yan, J. Wang, Y. Yang, W. Ma, and X. Chen, "Molecular biomarker-guided anti-angiogenic targeted therapy for malignant glioma," *Journal of Cellular and Molecular Medicine*, vol. 23, no. 8, pp. 4876–4882, 2019.

[29] C. Li, Z. Zhang, P. Lv, Y. Zhan, and Q. Zhong, "SCAMP3 promotes glioma proliferation and indicates unfavorable prognosis via multiple pathways," *OncoTargets and Therapy*, vol. 13, pp. 3677–3687, 2020.

[30] K. Zhou, Y. Liu, Z. Zhao et al., "ABCC8 mRNA expression is an independent prognostic factor for glioma and can predict chemosensitivity," *Scientific Reports*, vol. 10, Article ID 12682, 2020.

[31] S. X. Cheng, Y. Tu, and S. Zhang, "FoxM1 promotes glioma cells progression by up-regulating anxa1 expression," *PLoS One*, vol. 8, Article ID e72376, 2013.

[32] C. Berenguer-Daizé, L. Astorgues-Xerri, E. Odore et al., "OTX015 (MK-8628), a novel BET inhibitor, displays in vitro and in vivo antitumor effects alone and in combination with conventional therapies in glioblastoma models," *International Journal of Cancer*, vol. 139, pp. 2047–2055, 2016.

[33] J. F. Zhu, W. Huang, H. M. Yi et al., "Annexin A1-suppressed autophagy promotes nasopharyngeal carcinoma cell invasion and metastasis by PI3K/AKT signaling activation," *Cell Death & Disease*, vol. 9, Article ID 1154, 2018.

[34] W. Liu, Z. Xu, J. Zhou et al., "High levels of HIST1H2BK in low-grade glioma predicts poor prognosis: a study using CGGA and TCGA data," *Frontiers in Oncology*, vol. 10, Article ID 627, 2020.

[35] X. Liu, D. Yao, C. Liu et al., "Overexpression of ABCC3 promotes cell proliferation, drug resistance, and aerobic glycolysis and is associated with poor prognosis in urinary bladder cancer patients," *Tumor Biology*, vol. 37, no. 6, pp. 8367–8374, 2016.

[36] S. Pellegatta, N. Di Ianni, S. Pessina et al., "ABCC3 expressed by CD56(dim) CD16(+) NK cells predicts response in glioblastoma patients treated with combined chemotherapy and dendritic cell immunotherapy," *International Journal of Molecular Sciences*, vol. 20, 2019.